Proceedings

2000 IEEE International Conference on Phased Array Systems and Technology

May 21-25, 2000
Dana Point, California

Sponsored by

IEEE Antennas and Propagation Society

Technical Co-sponsorship by

IEEE Microwave Theory and Techniques Society
IEEE Aerospace and Electronic Systems Society
IEEE Communications Society

IEEE

20000627 032

2000 IEEE International Conference on Phased Array Systems and Technology
Proceedings

Additional copies of this publication may be ordered from

REPORT DOCUMENTATION PAGE	Form Approved OMB NO. 0704-0188

Public reporting burden for this collection of information is estimated to average 1 hour per response, including the time for reviewing instructions, searching existing data sources, gathering and maintaining the data needed, and completing and reviewing the collection of information. Send comment regarding this burden estimates or any other aspect of this collection of information, including suggestions for reducing this burden, to Washington Headquarters Services, Directorate for information Operations and Reports, 1215 Jefferson Davis Highway, Suite 1204, Arlington, VA 22202-4302, and to the Office of Management and Budget, Paperwork Reduction Project (0704-0188), Washington, DC 20503.

1. AGENCY USE ONLY (Leave blank)	2. REPORT DATE June 2000	3. REPORT TYPE AND DATES COVERED Final Report

4. TITLE AND SUBTITLE

2000 IEEE International Conference on Phased Array Systems & Technology

5. FUNDING NUMBERS

DAAD19-99-1-0377

6. AUTHOR(S)

Michael Thorburn, principal investigator

7. PERFORMING ORGANIZATION NAMES(S) AND ADDRESS(ES)

IEEE Lasers and Electro-Optics Society
455 Hoes Lane
Piscataway, NJ 08855-1331

8. PERFORMING ORGANIZATION REPORT NUMBER

9. SPONSORING / MONITORING AGENCY NAME(S) AND ADDRESS(ES)

U.S. Army Research Office
P.O. Box 12211
Research Triangle Park, NC 27709-2211

10. SPONSORING / MONITORING AGENCY REPORT NUMBER

ARO 40279.1-EL-CF

11. SUPPLEMENTARY NOTES

The views, opinions and/or findings contained in this report are those of the author(s) and should not be construed as an official Department of the Army position, policy or decision, unless so designated by other documentation.

12a. DISTRIBUTION / AVAILABILITY STATEMENT

Approved for public release; distribution unlimited.

12 b. DISTRIBUTION CODE

13. ABSTRACT (Maximum 200 words)

The technical program committee has developed an interesting and information packed five-day program with several special sessions. The conference is being held in Dana Point, Califorrnia on May 21-25, 2000 and promises to give academic, government, and industry professionals the latest in technical data in the increasingly important field of phased arrays. The excellent quality of papers received from about 20 countries demonstrate the vitality of this technology. The phased Array Conference has a long history since it was first organized in 1964.

14. SUBJECT TERMS

15. NUMBER IF PAGES

16. PRICE CODE

17. SECURITY CLASSIFICATION OR REPORT UNCLASSIFIED	18. SECURITY CLASSIFICATION OF THIS PAGE UNCLASSIFIED	19. SECURITY CLASSIFICATION OF ABSTRACT UNCLASSIFIED	20. LIMITATION OF ABSTRACT UL

NSN 7540-01-280-5500

Standard Form 298 (Rev. 2-89)
Prescribed by ANSI Std. 239-18
298-102

WELCOME FROM THE CHAIRMAN

Dr. Michael Thorburn
Chairman

On behalf of the Steering Committee, it is my pleasure to welcome you to the IEEE International Conference on Phased Array Systems and Technology at the Laguna Cliffs Marriott Resort in Dana Point, California, on May 21-25, 2000. The Antennas and Propagation Society of the Institute of Electrical and Electronic Engineers is proud to sponsor this event, and the IEEE Aerospace Electronics Systems Society, the IEEE Microwave Theory and Techniques Society and the IEEE Communications Society are equally proud to be technical co-sponsors.

The technical program committee has developed an interesting and information packed five-day program with several special sessions. Two concurrent technical sessions will run from Monday through Wednesday and a broad selection of short courses will be offered on Sunday and Thursday. Additionally, several meals have been arranged to provide an opportunity for conference attendees to assemble informally to discuss their interests and enjoy the warmth and beauty of Southern California. The conference promises to give academic, government, and industry professionals the latest in technical data in the increasingly important field of phased arrays.

I am confident that you will be stimulated by and enjoy our program. In this short week you will have ample opportunity to learn a great deal about the work of so many of the leaders in the phased array industry.

Welcome to Dana Point California and to the IEEE International Conference on Phased Array Systems and Technology.

Sincerely,

Michael Thorburn

MESSAGE FROM THE TECHNICAL PROGRAM CHAIRMAN
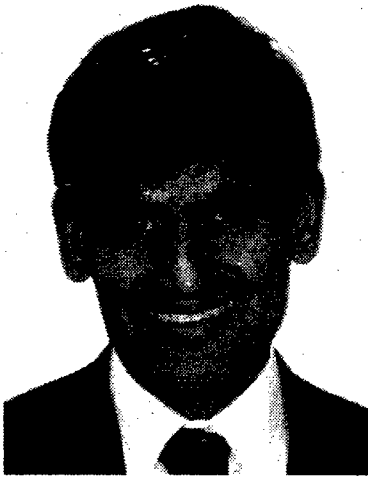
Dr. Sembiam R. Rengarajan
Technical Program Chairman

Welcome to the 2000 International Conference on Phased Array Systems and Technology at Dana Point, California. The Phased Array Conference has a long history since it was first organized in 1964 under the sponsorship of Rome Air Development Center. The second meeting was held in 1970, jointly sponsored by the US Army Advanced Ballistic Missile Defense Agency, MIT Lincoln Laboratory, and the Polytechnic Institute of Brooklyn. Rome Laboratory and MITRE jointly sponsored the 1985 symposium. Thanks to the sponsorship of IEEE, the 1996 symposium (held in Boston) and the present conference have attracted papers from all over the world.

The Technical program committee has worked hard to assemble outstanding papers on all aspects of Phased Array Systems and Technology. The excellent quality of papers received from about 20 countries demonstrate the vitality of this technology. We hope that you will find the technical program stimulating and very beneficial.

I look forward to seeing you at Dana Point.

Sincerely,

Sembiam R. Rengarajan

CONFERENCE COMMITTEE

Executive

Michael Thorburn,   Chairman
Aluizio Prata Jr.,   Vice Chairman
Sembiam Rengarajan, Technical Program Chairman
Mark Primich,   Treasurer

Technical Program

John Huang,   Co-Chairman
David Ksienski,   Co-Chairman
David Jenn,   Workshops and Short Courses

Publications

Ken Brown,   Advance Program
William Imbriale,   Compact Disc Proceedings
Michael Thompson,   World Wide Web Page
Allen Wang,   Printed Proceedings

Local Arrangements
Allan Love
John Wokurka

IEEE Liaison
W. Ross Stone

Conference Meeting Planners
Three Dimensions

TECHNICAL PROGRAM REVIEWERS

Ashok Agrawal
Makoto Ando
Ken Brown
John Huang
William Imbriale
Lars Josefsson
David Ksienski
J. J. Lee
Erik Lier
Allan Love
Robert Mailloux
Don Parker
Aluizio Prata, Jr.
Mark Primich
Daniel Purdy
Yahya Rahmat-Samii
Sembiam Rengarajan
Paul Rousseau
Shashi Sanzgiri
Tapan Sarkar
Daniel Schaubert
Hans Steyskal
W. Ross Stone
Michael Thompson
Michael Thorburn
Allen Wang
John Wokurka
Robert Yaccarino
Amir Zaghloul

SESSION INDEX

TABLE OF CONTENTS

ˊMONDAY AFTERNOON SESSION MP1
Phased Array Advances in Japan

MONDAY AFTERNOON SESSION MP2
Digital Beamforming

TUESDAY MORNING SESSION TA3
Active Arrays

TUESDAY AFTERNOON SESSION TP1
Analysis

TUESDAY AFTERNOON SESSION TP2
Array Applications of Photonics

WEDNESDAY MORNING SESSION WA1
European Session

WEDNESDAY AFTERNOON SESSION WP2
Phased Array Measurement and Calibration

Wednesday Afternoon Session WP3
Adaptive Array Antennas

MA1

Phased Array Overview, Current Trends, History

Phased Array Overview, Current Trends, History

PHASED ARRAYS FOR THE NEW MILLENNIUM

DR. ELI BROOKNER

Raytheon Systems Company
M/S 3-1-162
528 Boston Post Road
Sudbury, MA 01776
Telephone: 978-440-4007
Fax: 978-440-4040
E-Mail: Eli_Brookner@notes.res.ray.com

Abstract: This is a survey paper summarizing the recent developments and future trends in passive, active bipolar and Monolithic Microwave Integrated Circuitry (MMIC) phased arrays for ground, ship, air and space applications. Covered would be the THAAD (formerly GBR), European COBRA and Israel BMD radar antennas; Dutch shipboard APAR; airborne US F-22, European AMSAR, Swedish AESA, Japan FSX and Israel Phalcon; Iridium (66 satellites in orbit for total of 198 antennas) and Globalstar MMIC spaceborne antenna systems; Thomson-CSF wafer integration 94 GHz seeker antenna; digital beamforming; ferroelectric row-column scanning; optical electronic scanning for communications and radar; the MMIC C-band to Ku-band Advanced Shared Aperture Program (ASAP) antenna system for communications, radar, electronics countermeasures (ECM) and ESM; and continuous transverse stub (CTS) voltage-variable dielectric (VVD) antenna.

1.0 INTRODUCTION

Phased arrays have come a long way in the last three decades. This paper will cover phased array development over the last two and a half decades followed by future trends. Covered will be the dramatic entrance into the new era of active MMIC phase-phase steered arrays for ground, air and space; digital beamforming and its advantages; potential use of arrays for radar, communications, ESM, ECM and ECCM; how arrays can cope with jammers and ARM missiles through the use of ultra-low sidelobes and adaptive nulling; and the potential simultaneous use of an array for radar, communications, ESM and jamming. Presented will be example fielded phased arrays (COBRA DANE, PAVE PAWS, THAAD, IRIDIUM®) and arrays about to be fielded (F-22, APARS, AMSAR, SAMPSON). Covered will be the research work geared to reducing the cost and complexity of steered arrays. For example, by the use of row-column steering instead of element phase steering and through the novel electronically steerable plasma mirror antenna. Finally, covered will be the work toward the development of a 95 GHz reflectarray using 4 inch MMIC wafers!

2.0 PASSIVE PHASE-PHASE STEERED ARRAYS

The basics of phased arrays are described in References 1 and 2. Figures 1 through 3 show example passive phase-phase scanned arrays for ground and ship applications. There is the Patriot System [3, 4] -- the world's best known phase array, the USSR Flap Lid and finally the AEGIS SPY-1. These three arrays have seen very large production runs: respectively 173, > 100 (?) and 234 antennas. The total number of phase shifters produced for each of these systems is about 1 million.

Recent years have seen the development and deployment of passive phased-phase arrays by several other countries around the world. One example is the Swedish ARTHUR C-band 30 km range, artillery-locating system, which uses a traveling-wave tube (TWT) transmitter [40]. Another is the shipbased European Multifunction Phase Array Radar (EMPAR) C-band passive array [44]. This TWT radar, being built by Alenia (Italy) with the participation of Marconi Co. (UK), has a search range of up to 180 km, scans ± 45° in azimuth, ± 60° in elevation and rotates at 60 rpm. Still another is the ground or shipbased

---

® IRIDIUM is a registered trademark and service mark of Iridium, Incorporated

Thomson-CSF ARABEL multifunction radar that uses a space-fed rotating (also 60 rpm) X-band array [38]. This medium range (70 km) radar can electronically scan to zenith and backscan 60°. Finally India is selling an X-band space-fed array for a SAM-D system.

3.0 WIDE BANDWIDTH ARRAYS AND TIME DELAY STEERING

Phased arrays can have wide bandwidth waveforms. Such wide bandwidth waveforms are used for measuring the length of a target and imaging a target for target identification. One example radar system is the 95 ft diameter COBRA DANE radar of Figure 4 [3, 4, 6, 7]. It uses a 200 MHz bandwidth waveform having 5 ns compressed pulse width. With this waveform, the radar has a 2.5 ft range resolution which permits it to measure the length of ICBM reentry vehicles (RVs). Measuring the difference in arrival times between the RV tip and base returns does this.

4.0 ACTIVE PHASED ARRAYS

4.1 Bipolar Transistor Systems

Examples of active phased arrays using bipolar transistors for the power amplification are the UHF PAVE PAWS (Figure 5), the first solid state phase-phase steered array ever put in operation [1, 3, 4] and the UHF BMEWS upgrade radars which use the same T/R modules and radiating elements as used on the PAVE PAWS radar [3] (Figure 6). Countries around the worlds have developed active phased arrays using bipolar transistors. There is the Swedish Erieye airborne early-warning radar system that uses an S-band solid-state phased array placed in a dorsal fin over the top of the aircraft. The system has approximately 200 modules, which are shared with the array faces on both sides of the dorsal fin. Another system is the Israeli Phalcon airborne early-warning system that used four solid-state L-band phased arrays with each antenna having approximately 700 T/R modules [40]. The antenna are placed on the left and right sides of the aircraft forward of the wing, and on the underside toward the nose and tail or the aircraft. The system has been sold to Chile. Israel has also developed a theater missile defense system that is capable of detection ranges of hundreds of kilometers. This radar also uses an L-band solid-state active phased array. Two such systems have been built [45].

4.2 MMIC Systems: Ground-Based, Ship-Based and Airborne

An exciting new age of active phased-array antennas has begun using MMIC T/R modules, a technology that enables the production of solid-state T/R modules at a lower cost. One such system is the theater high altitude area defense (THAAD; formerly called GBR) X-band ground-based radar, which has 25,344 MMIC T/R modules and radiating elements [8]; see Figure 7. This is the largest active phased array built in the world in terms of number of modules. Like the COBRA DANE, it uses subarray time delay steering in order to prevent pulse distortion for its wideband waveforms. Three of these systems have been built. The first array was 50 percent populated with radiating elements and modules while the second and third arrays were fully populated. Approximately 65,000 MMIC T/R modules have been built for these systems. This program demonstrated that MMIC T/R modules could be manufactured for less than $1000 each at the end of the production run [9]. Many more of the THAAD systems are schedule to be built.

A second MMIC active phased-array system is the counter battery radar (COBRA) artillery and mortar weapon-locating system. This system, being built jointly by Lockheed-Martin, Siemens, Thomson-CSF and Thorn-EMI, has 2700 MMIC T/R C-band modules and radiating elements in its antenna. Three of these systems have been built [40] and a production contract at $576 million for 29 has been awarded [61].

A number of countries are in the process of developing active phased arrays using MMIC T/R modules for fighter aircraft, including the US for the F-22 fighter; Japan for the FSX; the consortium of France, Germany and the UK developing the airborne multiroll solid-state active-array radar (AMSAR) [47, 53-55, 58]; and Sweden, which is developing the active electronically scanned antenna (AESA) [48]. All of these radar systems operate at X-band. Over 300 F-22 X-band phased arrays, shown in Figure 8, are scheduled to be built, each having approximately 2000 elements and MMIC T/R modules for a total production run of over 600,000 million MMIC T/R modules [5].

For shipboard application the UK Defense Evaluation and Research Agency (DERA) in cooperation with Siemens Plessey has been developing the S-band Multi-function, Electronically Scanned, Adaptive Radar (MESA) [34, 49]. This radar uses a thinned array of 918 elements and 156 2W peak power T/R modules. Initial production has started for a twin-faced version called the SAMPSON to be deployed on future Royal Navy frigates [49, 60]. To support air defense and ballistic missile defense a second-generation ground based MESAR2 is under construction with completion expected in 1999.

Hollandse Signaalapparaten (Signaal) of the Netherlands is developing the four-faced X-band Active Phased Array Radar (APAR) shipboard radar [50, 59]. Each face as 4096 elements fed by 4096 MMIC T/R modules. Its bandwidth is to be 30% and its scan $\pm$ 60°.

5.0 MULTIBEAM ROTMAN LENS

It is possible to build a multibeam array antenna by the use of a Rotman lens feed [10]; see Figure 9. An advantage of the Rotman lens feed is its wide bandwidth like a 2.5 to 1 instantaneous bandwidth. By placing the elements on a semicircular surface a 180° coverage is achieved. When used for transmit, power amplifiers can be placed between the antenna elements and the Rotman lens. Using TWTs a peak ERP (effective radiated power) of over 1MW is achievable. The applications for such Rotman lens arrays are ECM, ESM, DF, communications and radar.

Figure 10 shows the block diagram of a Rotman lens system used for ECM, ESM and DF. It consists of separate multibeam receive and transmit Rotman lens arrays. The multibeam receive array determines the direction of arrival of various signals impinging on the antenna and then processes these signals to determine their parameters--carrier frequency, PRF, pulse width and amplitude. The transmit Rotman lens array is used to transmit jammer signals in the direction of some of these signals. A jammer signal could be either a repeater jammer type signal using range-gate pull-off, velocity gate pull-off or inverse gain, or it could be a CW or barrage noise jammer generated by the transponder circuit of Figure 10 [11]. Such a system is the shipboard SLQ-32.

By using a 2-dimensional array and the 2-dimensional Rotman lens feed, it is possible to form a 2-dimensional array of pencil beams as done for the MUSTRAC (Multiple-Simultaneous-Target Steerable Telemetry Tracking System). For the MUSTRAC system, only 4 independent beams are processed simultaneously with these being switched to any position in the coverage. Each of these 4 independent beams is formed as a weighted sum of a contiguous cluster of 4 of the 2-dimensional Rotman lens beam former outputs. This allows each of the 4 independent beams to be steered so as to have the beam peak pointed at the signal source, avoiding the scalloping loss. The MUSTRAC was used for receiving telemetry data from ballistic missiles fired over the Atlantic Eastern Test Range.

Raytheon has found the Rotman lens feed to be attractive for use in a novel, low cost 76-77 GHz millimeter automotive Intelligent Cruise Control (ICC) radar because of its low weight, small size and low cost [42]. The Rotman lens is formed as a printed circuit on a 5 mil thick soft flexible substrate. The antenna elements are columns of series-fed patch elements etched onto the same substrate. Switching to different beam ports of the Rotman lens scans the beam. GaAs MMIC circuitry is being developed for small size, low weight and low cost.

6.0 NEW AGE REVOLUTIONARY SPACEBORNE-ACTIVE-MMIC-COMMERCIAL-PATCH-PHASED-ARRAY

Above a 2-dimensional array of beams was formed for the MUSTRAC using a 2-dimensional Rotman lens beamformer. Alternately such a 2-dimensional array of beams could be formed using a Butler matrix [2, 12] or Blass [12] feed. One antenna that does just this is the IRIDIUM® antenna (see Figure 11) which uses a 2-dimensional Butler matrix feed to generate 80 simultaneous beams [13]. Weighted combinations of these beams are then used to form 16 simultaneous shaped beams for coverage of a sector the earth. Figure 12 shows the 16 ground footprints realized by one such antenna. In Figure 11 three of the active IRIDIUM arrays are shown mounted on the satellite bus for testing in an anechoic chamber. These arrays have everything. They use MMIC T/R modules, microstrip patch radiating elements, 16 simultaneous beams, are space qualified, have had a large production run of over 200 arrays, and are commercial. The MMIC T/R modules use linear PAs. The IRIDIUM is the revolutionary new commercial global satellite personal communication system, which uses low orbiting satellite

5

constellation. The IRIDIUM constellation consists of 66 satellites in six circular 765-km altitude near polar orbits (eleven satellites per orbit). The constellation provides coverage for global communications. Each satellite has three antennas pointed toward the earth for horizon-to-horizon coverage [13]. The antennas are active L-band (1.6 GHz) phased arrays using about 100 MMIC T/R modules and patch radiating elements. As a result, there are about 20,000 MMIC T/R modules and radiating elements per constellation. A subscriber holds a hand-held phone (similar to those used for the conventional cellular phone systems) which communicates directly with one of the satellites. In turn, the signal is cross linked to other satellites for final passage down to the earth to another subscriber with a hand-held IRIDIUM phone or to a gateway which directs the call to a conventional telephone user via land lines. Alternately, the signal could be transmitted directly down from the satellite to a user in view of the same satellite as the first user. The satellites were launched by USA Delta II rockets, Russian Proton rockets and Chinese Long March rockets. The system went into operation November 1, 1998. The IRIDIUM system has been a technical success - - all specs were met and the antenna built to cost.

IRIDIUM is not the only low-altitude satellite voice communications system using active arrays employing MMIC modules. Another is the GlobalStar system consisting of 48 satellites providing near global coverage up to 65-north latitude and down to 65 south latitude. Each satellite uses a 2.5 GHz 91 element transmit array of 91 transmit MMIC modules and a 1.6 GHz 61 element receive array of 61 receive MMIC modules for a total of 7300 modules for the constellation.

Following on the heels of the IRIDUM and GlobalStar voice communication systems are high data rate digital communications systems (1 Mbps) for computer-to-computer and video conferencing communications. One such system is the Bill Gates Teledesic satellite system using 20 GHz for transmit onboard the satellites and 30 GHz for receive.

There has been much talk about the transfer of military technology to the commercial world, especially with the end of the cold war. The IRIDIUM Program is an excellent example of this. The technology for the IRIDIUM Space Based L-band antenna is derived from the Air Force's and Navy's Space Based Radar Program. The Space Based Radar was originally being developed for surveillance of CONUS and US Fleets to warn of possible attack by enemy bombers [14]. The lightweight (one ounce) L-band module developed by the Air Force for the SBR Program forms the basis for the IRIDIUM L-band module. The SBR was never deployed by the Air Force and Navy because of the end of the cold war and also because of the expense of building the system. It is nice to see the IRIDIUM system taking its place for a total cost of $3.5 billion dollars, including the cost of satellite launch services, ground stations and software. And now, in a fair turn around, with the deployment of the IRIDIUM and GlobalStar systems the US government is looking to take advantage of the experience gained with these commercial systems to deploy a military tactical Surveillance Targeting and Reconnaissance Satellite (STARLITE) system consisting of 24 low-orbiting, low-cost 24 satellites capable of seeing moving ground targets [51]. Consideration is being given to the use of 1-dimensional electronically scanned arrays.

7.0   THE JAMMER AND ARM THREAT AND THE RESPONSE TO THEM

Table 1 gives various ECM threats and the electronic counter-counter measures (ECCM) to them. The countermeasure to the sidelobe barrage jammer is a sidelobe canceller (SLC) [15-18, 56]. MIT Lincoln Laboratory demonstrated a jammer cancellation of 50 dB for an L-band linear array of 32 elements [19, 20]. The measurements were made in a near field range. The null was obtained for a 1 MHz wide noise jammer.

The response to a sidelobe repeater jammer is to use a sidelobe blanker [15, 16]; see Table 1. Another response to the sidelobe barrage and/or repeater jammers, as well as the ARM (Anti-Radiation Missile) threat, is to use an ultra-low sidelobe antenna; see Table 1 and Chapters 2 and 6 of [3] and Ref. [21]. The T/R modules of an active array could be calibrated over temperature and frequency to reduce their rms phase and amplitude errors from unit-to-unit to respectively 3° and 0.4 dB to support an rms SLL of -17 dBi [22].

For a nonscanning rectangular dipole array antenna a SLL below -28 dBi was achieved along the principal plane beyond ± 60° from the beam peak [3]. Here the rms element-to-element errors were 0.8° and 0.07

dB. Using calibration and digital beam forming, such sidelobe levels may be achievable in the future for an electronically scanned array; see Sects. 8.1 and 8.3 and Refs. [23] and [29].

To cope with the mainlobe (ML) jammer threat and jammers in close-in high sidelobes, a multiple beamformer would be used to generate a number of independent high gain beams overlapping with and/or close to the main beam. These high gain beams would be pointed toward the jammers and act as auxiliary antennas. Their outputs would be connected to a sidelobe canceller. This approach can also be used for far out sidelobes with it being possible to use lower gain auxiliaries. Its performance is as good as or almost as good as obtained with a fully adaptive array without the complexity and long transient response of a fully adaptive array, the computations required and the transient response being reduced by orders of magnitude [3, 24]. This technique has been referred to in the literature as adaptive-adaptive array processing [3, 24, 56], beam space processing and eigenbeam processing.

8.0 RESEARCH AND DEVELOPMENT WORK FOR FUTURE PHASED ARRAYS SYSTEMS

8.1 Clutter Rejection for an Airborne System (STAP and DPCA)

To cope with ground clutter and sidelobe jamming for an airborne radar, extensive work is on-going toward the development of an airborne phased array using Space-Time Adaptive Processing (STAP) [25, 26]. STAP is a general form of Displaced Phase Center Antenna (DPCA) processing. STAP had been demonstrated several years ago on a modified E2-C system by NRL [27, 28]. More recently a flight demonstration STAP provided 52 to 69 dB of sidelobe clutter cancellation relative to the mainbeam clutter [29]; see Figure 13. This system used an array mounted on the side of an aircraft. The antenna had 11 degrees of freedom in azimuth and 2 in elevation for a total of 22. Before STAP, the antenna rms sidelobe level was -30 dBi, with STAP it was -45 dBi.

8.2 C- to Ku-band Multi-User Advanced Shared Aperture Program (ASAP) MMIC Array and Dual Band Array

Earlier we presented the COBRA DANE radar system that had a 16% bandwidth and the Rotman lens multibeam array systems that had a 2.5 to 1 frequency bandwidth. Work is under way to develop an active MMIC phase-phase steered array that has over a 2 to 1 frequency bandwidth and at the same time is shared by multiple users. Specifically the Naval Air Weapons Center (NAWC) and Texas Instruments (TI, now part of Raytheon) were developing a broadband array having continuous coverage from C-band through Ku-band that would share the functions of radar, passive ESM (Electronic Support Measures), active ECM (Electronic Counter Measures) and communications [30]; see Figures 14 and 15. To achieve this wide bandwidth, a flared notch-radiating element is used. Cross notches are used so that horizontal, vertical or circular polarization can be obtained. They have built a solid state T/R module that provides coverage over this wide band from C-band to Ku-band continuously. The module has a power output of 2 to 4 W per element over the band, a noise figure between 6.5 and 9 dB over the band and power efficiency between 5.5 and 10% over the band. A 10 x 10-element array having eight active T/R modules was built for test purposes. A typical full up array would be approximately 29" wide by 13" high. With this type of array it would ultimately be possible to use simultaneous part of the array as radar, part of the array for ESM, part of the array for ECM and part of the array for communications. The parts used for each function would change dynamically depending on the need. Also, these parts could be nonoverlapping or overlapping, depending on the needs.

DERA of the UK is developing a dual frequency array which would enable a single radar to use L-band for search at and X-band for track so as to avoid the use of a single compromise frequency for search and track [52]. Consideration is being given to the use of waveguide L-band radiating elements and dipole X-band elements.

8.3 Digital Beamforming and Its Potential

Table 2 list where digital beamforming (DBF) has been operationally used, some developmental systems that have been built, and its significant advantages. The first operational radars to use digital beamforming are the over-the-horizon (OTH) radars. Specifically the GE OTH-B and the Raytheon ROTHR (Relocatable OTH Radar). The ROTHR receive antenna is about 8,500 feet long. More recently Signaal used digital beamforming for their deployed 3-D stacked beam SMART-L and SMART-S

shipboard radars. The digital beamforming is done only on receive. For the SMART-L system the antenna consists of 24 rows. The signal from each row is down converted and pulse compressed with SAW lines and then A/D'd with 12-bit 20 MHz Analog Devices A/D. The signal is then modulated onto an optical signal and passed down through a fiber optic rotary joint to a digital beamformer where 14 beams are formed [31].

A number of experimental DBF systems have been developed; see Table 2. One is the Rome Laboratory (Hanscom AFB, MA) 32 column linear array at C-band that can form 32 independent beams and which uses a novel self-calibration system [32]. Rome Lab. also has developed a fast digital beamformer that utilizes a systolic processor architecture [3] based on the Quadratic Residue Number System (QRNS) [32]. MICOM (U. S. Army) built a 64 element feed that used DBF for a space fed lens [33].

The experimental British MESAR S-band system does digital beamforming at the subarray level [34]. This experimental system has 16 subarrays and a total of 918 waveguide-radiating elements and 156 T/R solid state modules. Roke Manor Research Ltd. of Britain has built an experimental 13 element array using digital beamforming on transmit as well as on receive [35]. This experimental system uses the Plessey SP2002 chip running at a 400 MHz rate as a digital waveform generator at every element. Doing digital beamforming on transmit allows one to put nulls in the direction of an ARM threat or where there is high clutter.

Finally the National Defense Research Establishment of Sweden has built an experimental S-band antenna operating between 2.8 and 3.3 GHz which does digital beamforming using a sampling rate of 25.8 MHz on a 19.35 MHz IF signal [23]. The advantage of using IF frequency sampling rather than baseband sampling is that one doesn't have to worry about the imbalance between the two channels, that is, the I and Q channels, or the DC offset. They demonstrated that, by using digital beamforming, they could compensate for amplitude and phase variations that occur from element-to-element across angle and across the frequency band. Via a calibration, they were able to reduce an element-to-element gain variation over angle due to mutual coupling from ±1 dB to about ±0.1 dB. Using equalization, they were also able to reduce a ±0.5 dB variation in the gain over the 5 MHz bandwidth to a less than ±0.05 dB variation; see Figure 16. With this calibration and equalization, they were able to demonstrate peak sidelobes 47 dB down over a 5 MHz bandwidth; see Figure 17. A 50 dB Chebyshev weighting was used. They demonstrated that the calibration was maintained fairly well over a period of two weeks. This work demonstrates the potential advantage offered by digital beamforming with respect to obtaining ultra-low antenna sidelobes.

MIT Lincoln Laboratory is developing an all-digital radar receiver for an airborne surveillance array radar like that of the UHF E-2C [43]. They are A/D sampling directly at UHF (~430 MHz) using a Rockwell 8 bit 3 Gigabit per sec A/D running at room temperature. Three stages of down conversion are done digitally and because the A/D quantization noise is filtered the effective number of bits of the A/D is increased. For example if the signal bandwidth was only 5 MHz the increase in signal-to-noise ratio is 3 GHz/2 (5 MHz) = 25 dB so the increase in the number of effective bits is 25 dB divided by 6 dB/bit or 4.2 bits to yield 12 bits total. The whole digital receiver is on an 8 inch x 8 inch card that uses three 0.6 μm chips. In the future these three chips are expected to be replaced by a single 0.35 μm CMOS chip.

With the digital processing field being moved forward rapidly by the commercial world, by the year 2016 it is expected that one 9U 16 inch x 14.5 inch board would provide a throughput of 600 GFLOPS. It would consist of 64 chips each providing 10 GFLOPS, use 0.07 μm and have a 1.25 GHz clock. Such processing capability should help make the above experimental Swedish ultra-low sidelobe antenna and above airborne STAP array feasible.

8.4   Row-Column Steered Arrays

The Naval Research Laboratory (NRL) is developing two row-column array steering techniques which have the potential for low cost 2-dimensionally steered arrays [36, 37]. The first technique, the one closest to possible deployment, involves using two arrays back-to-back; see Figure 18. The first array steers the beam in azimuth, the second in elevation. The first array consists of columns of slotted waveguides with each column having at its input one ferrite phase shifter to provide azimuth scanning. The second array is a RADANT lens array consisting of parallel horizontal conducting plates between

8

which are connected many diodes. The velocity of propagation of the electromagnetic signal passing through a pair of parallel plates of the array depends on the number of diodes that are on or off in the direction of propagation. By appropriately varying this number as one goes from one pair of plates to the next in the vertical direction one creates a gradient on the signal leaving the lens in the vertical direction so as to steer the beam in elevation. The estimated production cost of the hybrid row-column steered array of Figure 18 is $3 million. It is possible to use two RADANT lenses to provide 2-dimensional electronic scanning, one RADANT lens providing elevation scan while the second provides azimuth scan [38]. Thomson-CSF has developed such a RADANT antenna for the DASSAULT Aviation RAFALE Multi-Roll Combat Aircraft [38].

The second NRL row-column steered array involved using two ferroelectric lenses; see Figure 19 [37]. The first lens consists of columns of ferroelectric placed between conducting plates. A DC voltage is applied across each pair of plates. The dielectric constant of the ferroelectric material between a pair of plates depends on the DC voltage applied across that pair of plates. As a result the phase of the electromagnetic signal passing through a ferroelectric column will depend on this DC voltage. Consequently by applying appropriate DC voltages across the ferroelectric columns one can create a phase gradient in the horizontal direction for the signal leaving the first lens and thus scan the beam in azimuth. A second such lens rotated 90° would steer the beam in elevation; see Figure 19.

For a ferroelectric lens, it is necessary that the electric field be linearly polarized and perpendicular to the conducting plates as shown in Figure 19. Hence the first ferroelectric lens of Figure 19 requires a horizontally polarized signal while the second lens requires a vertically polarized signal. A 90° polarization rotator is used between the lens in order to have the horizontally polarized signal out of the first lens become vertically polarized at the input to the second lens; see Figure 19. Considerable work is necessary before a practical ferroelectric phased array is produced. This work is going on at present.

Raytheon Company is developing a row-column steered array that employs phase shifters for steering in the H plane (see Figure 20) and a Voltage Variable Dielectric (VVD) ceramic material used for a Continuous Transverse Stub (CTS) antenna architecture for steering in the E plane (see Figure 20) [41]. Changing the voltage across the VVD changes its dielectric constant and in turn the velocity of propagation along the VVD. It provides for a lightweight, low cost, small thickness antenna. They are looking to apply this technology to aircraft radar antennas and commercial antennas.

Engineers and scientists have been talking about achieving electronic scanning of lasers since the 1960s. Some thought this was a pipe dream, but these doubters have since been proven wrong. Raytheon [40, 57] has demonstrated an electronically steered phased array for laser and optical beams. This array, which is carried around in a briefcase, represents a major breakthrough in the scanning of laser and optical beams. The scanning is achieved using a row-column scanning architecture similar to that of the ferroelectric scanner described above with liquid crystal used instead of the ferroelectric material. In production, the cost per phase shifter for an optical phased array will be pennies [40, 57].

8.5   Novel Electronically Steerable Plasma Mirror

NRL is also pursuing the development of a novel electronically steerable plasma mirror in order to provide electronic beam steering; see Figure 21 [39]. Here a plasma sheet is rotated to steer the beam in azimuth and is electronically tilted to steer the beam in elevation. Switching to different initiation points in the cathode rotates the plasma mirror. Tilting the magnetic field around the plasma tilts the plasma mirror. This is done using coils placed around the plasma. These coils are placed so as not to block the microwave signal. A 50 cm x 60 cm plasma mirror has been generated whose measured antenna patterns had sidelobes of about 20 dB down [39].

8.6   95 GHz Reflect-Array Using 4 Inch MMIC Wafers!!

Colin [38] described a very aggressive effort wherein MMIC was taken to the point of wafer integration - - 4" wafers. Specifically, Thomson-CSF is developing a missile seeker antenna which uses two 4" wafers [38]. One wafer has printed on it the dipole elements and one bit PIN diode phase shifters. The second 4-inch wafer contains the driving circuits that are linked to the first through bumps. The antenna has 3,000 elements. The beam width is 2° and can be steered ±45°. They have reported having obtained low sidelobes [38]. Figure 22 shows this experimental antenna.

9.0 CONCLUSIONS

Based on the above accomplishments, ongoing developments, research and large numbers of programs that are looking to effectively use phased arrays, it is apparent that the future for phase arrays is very promising and should lead to exciting developments. Phased arrays have come a long way and can be expected to make major strides in the future. For further reading on recent developments in phased arrays around the world the reader is referred to the proceedings of the excellent 1996 IEEE International Symposium on Phased Array Systems held October 15-18, 1996 in Boston, Massachusetts area. Over 500 attended and 92 papers were presented by authors from 16 countries. The reader is also referred to References 1 - 4, 6, 7, 40, 46 and 62.

REFERENCES:

1. Brookner, E., "Phased-Array Radars," Scientific American, February 1985, pp. 94-102.

2. Brookner, E., (Editor), Practical Phased Array Antenna Systems, LexBook 282 Marrett Rd., Lexington, MA 02173 (formerly published by Artech House), 1991.

3. Brookner, E., Aspects of Modern Radar, Chapter 2, LexBook, 282 Marrett Rd., Lexington, MA 02173 (formerly published by Artech House), 1988.

4. Brookner, E., Radar Technology, LexBook, 282 Marrett Rd., Lexington, MA, 02173 (formerly published by Artech House), 1977.

5. Rhea, J., "Active Array Antennas Head for the Sky's" Military and Aerospace Electronics, August 1996.

6. Brookner, E., "Radar Imaging for Arms Control," Chapter 11 in Arms Control Verifications, The Technologies That Make It Possible, edited by K. Tsipis, D. W. Hafemeister, and P. Janeway, Pergamon-Brassey's, London, 1986.

7. Brookner, E., "Large Phased-Array Radars", Chapter 7 in Nuclear Arms Technologies in the 1990s, Editors: Dietrich Schroeer and David Hafemeister, American Institute of Physics, New York, 1988.

8. Sarcione, M., J. Mulcahey, D. Schmidt, K. Chang, M. Russell, R. Enzmann, P. Rawlinson, W. Gluzak, and R. Howard and M. Mitchell, "The Design, Development and Testing of the THAAD (Theater High Altitude Area Defense) Solid State Phased Array (formerly Ground Based Radar)," 1996 IEEE International Symposium on Phased Array Systems and Technology, October 15-18, 1996, pp. 260-265, Boston, MA.

9. Cohen, E. D., "Trends in the Development of MMICs and Packages for Active Electronically Scanned Arrays (AESAs)," 1996 IEEE International Symposium on Phased Arrays Systems and Technology, October 15-18, 1996, pp. 1-4, Boston, MA.

10. Archer, D., "Lens-fed Multiple Beam Arrays," Electronic Progress, Vol. 16, No. 4, Winter 1974, pp. 24-32; or, D. Archer, "Lens- Fed Multiple-Beam Arrays," Microwave Journal, Oct, 1975, pp. 37-42.

11. Black, A., "Multibeam Systems," Electronic Progress, Vol. 17, No. 3, Fall 1975, pp. 32-42.

12. Skolnik, M. I., Introduction to Radar Systems, McGraw Hill, 2nd edition, 1980.

13. Schuss, J. J., J. Upton, B. Myers, T. Sekina, A. Rohwer, P. Makridakas, R. Francois, L. Wardle, W. Kreutel, and R. Smith, "The IRIDIUM Main Mission Antenna Concept," 1996 IEEE International Symposium on Phased Array Systems and Technology, October 15-18, 1996, pp. 411-415, Boston, MA.

14. Brookner, E. and T. S. Mahoney, "Derivation of a Satellite Radar Architecture for Air Surveillance," Microwave Journal, Vol. 29, No. 2, February 1986, pp. 173-191; see also M.I. Skolnik (ed.), Radar Applications, IEEE Press, New York, 1988.

15. Farina, A., Antenna-Based Signal Processing Techniques for Radar Systems, Artech House, 1992.

16. Nitzberg, R. Adaptive Signal Processing for Radar, Artech House, 1992.

17. Brookner, E., "Sidelobe Cancellation," and "Adaptive Arrays," The Institution of Electrical Engineers (IEE) Tutorial Seminar on "Adaptive Radar Processing," Oct 22-23, 1987, pp. 1-74, London, England.

18. Brookner, E., "Ubiquitous Orthonormal Transformation--in Sidelobe Canceling, Adaptive Arrays, and Tracking," Proceedings of the IEEE Long Island Section, Adaptive Antenna Systems Symposium, Nov, 1992, pp. 23-30.

19. Johnson, J. R., F. G. Willworth, H. M. Aumann and A. J. Fenn, "Receiver Channel Equalization for Adaptive Antennas: Experimental Results," 1990 International Symposium Digest, Antennas and Propagation, IEEE Catalog No. 90CH2776-3, Library of Congress No. 89-80729, pp. 194-197.

20. Fenn, A. J., H. M. Aumann, F. G. Willwerth and J. R. Johnson, "Focused Near-Field Adaptive Nulling: Experimental Investigation, 1990 International Symposium Digest, Antennas and Propagation, IEEE Catalog No. 90CH2776-3, Library of Congress No. 89-80729, pp. 186-189.

21. Carlson, B. D., L. M. Goodman, J. Austin, M. W. Gantz and Lee O. Upton, "An Ultralow-Sidelobe Adaptive Array Antenna," The Lincoln Laboratory Jour, Summer 1990, pp. 291-310.

22. Private Communication from D. Laighton, Raytheon Company.

23. Pettersson, L., M. Danestig, and U. Sjostrom, "An Experimental S-Band Digital Beamforming Antenna," 1996 IEEE International Symposium on Phased Array Systems and Technology, October 15-18, 1996, pp. 93-98, Boston, MA.

24. Brookner, E., and J. M. Howell, "Adaptive-Array Processing," Phased Arrays Symp. Proc., The Mitre Corp., Bedford, MA, October 15-18, 1985, pp. 133-146. See also: RADC Rep. No. RADC-TR-85-171, Electromagnetics Science Div., RADC, Hanscom AFB, Bedford, MA, Air Force Systems Command, August 1985; IEE Int. Conf. Radar-87, London, October 19-21, 1987; Proc. IEEE, Vol. 74, No. 4, April 1986, pp. 602-604.

25. Brennan, L. E., J. D. Mallett, and I. S. Reed, "Adaptive Arrays in Airborne MTI Radar," IEEE Trans. on Antennas and Propagation, Vol. AP-24, No. 5, September 1976, pp. 607-615.

26. Ward, J., "Space-time Adaptive Processing for Airborne Radar," MIT Lincoln Laboratory, Technical Report 1015, Dec. 13, 1994.

27. Lee, F. W. and F. Staudaher, "The NRL Adaptive Array Flight Test Database," Proceedings of the IEEE Long Island Section Adaptive Antenna Systems Symposium, Nov 1992, pp. 101-104.

28. Brennan, L. E., D.J. Piwinski and F. M.Staudaher, "Comparison of Space-Time Adaptive Processing Approaches Using Experimental Airborne Radar Data," The Record of the 1993 IEEE National Radar Conference, Lynnfield, MA, April 20-22, 1993, pp. 176-181.

29. Fenner, D. K., and W. F. Hoover, Jr., "Test Results of a Space-Time Adaptive Processing System for Airborne Early Warning Radar," IEEE 1996 National Radar Conference, May 13-16, 1996, Ann Arbor, Michigan.

30. Hemmi, C., R. T. Dover, A. Vespa, and M. Fenton, "Advanced Shared Aperture Program (ASAP) Array Design," 1996 IEEE International Symposium on Phased Array Systems and Technology, October 15-18, 1996, pp. 278-282, Boston, MA.

31. de Heig, I. W. T. A. and I. H. T. Muskens, "Multi-Channel Receiver and Optical Data Link for Radar Systems with Digital Beamforming," The Record of the IEEE 1995 International Radar Conference, May 8-11, 1995, pp. 201-206, Alexandria, VA.

32. Steyskal, H., "Digital Beamforming at Rome Laboratory," The Rome Laboratory Technical Journal, Vol. 1, No. 1, June, 1995, pp. 7-22.

33. Rose J. F., B. A. Worley, and M. M. Lee, "Antenna Patterns for Prototype Two-Dimensional Digital Beamforming Array," 1993 IEEE Antennas and Propagation International Symposium, June 28-July 2, 1993, pp. 1544-1547, University of Michigan, Ann Arbor, Michigan.

34. Billam, E. R. and D. H. Harvey, "MESAR--An Advanced Experimental Phased Array Radar," IEEE International Conference on Radar," October 19-21, 1987, pp. 37-40.

35. Garrod, A., "Digital Modules for Phased Array Radar," 1996 IEEE International Symposium on Phased Array Systems and Technology, October 15-18, 1996, pp. 81-86, Boston, MA.

36. Rao, J. B.L., P. K. Hughes, III, G. V. Trunk and J. C. Sureau, "Affordable Phased-Array for Ship Self-Defense Engagement Radar" Proceedings of the 1996 IEEE National Radar Conference, May 13-16, 1996, Ann Arbor, Michigan, pp. 32-37.

37. Rao, J. B. L., G. V. Trunk and D. P. Patel, "Two Low-Cost Phased Arrays," 1996 IEEE International Symposium on Phased Array Systems and Technology, October 15-18, 1996, pp. 119-124, Boston, MA.

38. Colin, Jean-Marie, "Phased Array Radars in France: Present and Future," 1996 IEEE International Symposium on Phased Array Systems and Technology, October 15-18, 1996, pp. 458-462, Boston, MA.

39. Mathew, J., R. A. Meger, J. A. Gregor, D.P. Murphy, R. E. Pechacek, R. F. Fernsler, and W. M. Manheimer, "Electronically Steerable Plasma Mirror," 1996 IEEE International Symposium on Phased Array Systems and Technology, October 15-18, 1996, pp. 58-62, Boston, MA.

40. Brookner, E., "Major Advances in Phased Arrays: Part I," Microwave Journal, May 1997, pp. 288-294, "Major Advances in Phased Arrays: Part II," Microwave Journal, June 1997, pp. 84-92.

41. T. W. Bradley et al., "Development of a Voltage-Variable Dielectric (VVD), Electronic Scan Antenna," IEE 1997 International Radar Conference, Edinburgh, Scotland, October 14-16, 1997, pp. 383-385.

42. Russell, M. E., A. Crain, A. Curran, R. A. Campbell, C. A. Drubin, and W. F. Miccioli, "Millimeter-Wave Radar Sensor for Automotive Intelligent Cruise Control (ICC)," IEEE Trans. on Microwave Theory and Techniques, Vol. 45, No. 12, Dec. 1997, pp. 2444-2453.

43. Song, W. S., "A New 3-GSPS 65-GOPS UHF Digital Radar Receiver and Its Performance Characteristics," 1997 ALISOMAR Conf.

44. Palumbo, B., "Some Examples of System Developments in Italy Based on Phased Array Technology," 1996 IEEE International Symposium on Phased Array Systems and Technology, Boston, MA, October 15-18, 1996, pp. 444-449.

45. Dryer, S., E. Levine, M. Peleg and A. Schrift, "EL/M 2080 ATBM Early-warning and Fire-control Radar System," 1996 IEEE International Symposium on Phased Array Systems and Technology, Boston, MA, October 15-18, 1996, pp. 11-16.

46. Brookner, E., "Report on 1996 Phased Array Symposium," IEEE Antennas of Propagation Magazine, Vol. 39, No. 1, February 1997, pp. 114-118.

47. Albarel, G. J., J. S. Tanner and M. Uhlmann, "AMSAR Antenna Architecture and Predicted Performance," 1996 IEEE International Symposium on Phased Array Systems and Technology, Boston, MA, October 15-18, 1996, 450-453.

48. Josephson, L., L. Erhage, and T. Emanuelsson, "An AESA Development Model for Next-generation Fighter Aircraft," 1996 IEEE International Symposium on Phased Array Systems and Technology, Boston, MA, October 15-18, 1996, pp. 454-457.

49. Moore, A. R., D. M. Salter and W. K. Stafford, "MESAR Multi-Function, Electronically Scanned, Adaptive Radar," IEE 1997 International Radar Conference, Edinburgh, Scotland, October 14-16, 1997, pp. 55-59.

50. Smolders, A. B., "Design and Construction of a Broadband Wide-Scan Angle Phased-Array Antenna with 4096 Radiating Elements," 1996 IEEE International Symposium on Phased Array Systems and Technology, Boston, MA, October 15-18, 1996, pp. 87-92.

51. Fulghum, D. A. and J. C. Anselmo, "DARPA Pitches Small Sats for Tactical Reconnaissance," Aviation Week and Space Technology, June 9, 1997, pp. 29, 30.

52. Moore, S. A. W and G. A. Hockham, "Dual Frequency Multi-Function Radar Antenna Research," IEE 1997 International Radar Conference, Edinburgh, Scotland, October 14-16, 1997, pp. 50-54.

53. Gruener, W., J. P. Toernig, and P. J. Fielding, "Active-Electronically-Scanned-Array Based Radar System Features," IEE 1997 International Radar Conference, Edinburgh, Scotland, October 14-16, 1997, pp. 339-343.

54. Albarel, G., J. S. Tanner, and M. Uhlmann, "The Trinational AMSAR Programmer: CAR Active Antenna Architecture," IEE 1997 International Radar Conference, Edinburgh, Scotland, October 14-16, 1997, pp. 344-347.

55. Feldle, H. P. A. D. McLachlan and Y. Mancuso, "Transmit/Receive Modules for X-band Airborne Radar," IEE 1997 International Radar Conference, Edinburgh, Scotland, October 14-16, 1997, pp. 391-395.

56. Brookner, Eli, "Filtering and Kalman Filtering Made Easy," Section 4.4: "Adaptive Nulling, the Orthonormal Transformation, and the LSE," pp. 188-200, John Wiley and Sons, Inc., New York, NY, 1998.

57. T. A. Dorschner, L. Friedman, M. Holz,, D. P. Resler, R. C. Sharp and I. W. Smith, "An Optical Phased Array for Lasers," Proceedings of the 1996 IEEE International Symposium of Phased Array Systems and Technology. October 15-18, 1996, Boston, MA, pp. 5-10.

58. Albarel, G. J., J. S. Tanner, and M. Uhlmann, "AMSAR Active Antenna Technology and First Measured Performance", 5th International Conference and Exhibition on Radar Systems, Brest, France, May 17-21, 1999, Session 2.2.

59. Golshayan, A. K., S.v.d. Schoot and P. vanGenderen, "Active Phased Array Radar (APAR)," 5th International Conference and Exhibition on Radar Systems, Brest, France, May 17-21, 1999, Session 1.5.

60. Scott, R., "PAAMS Deal Switches SAMPSON to Active Mode", Janes Defense Weekly, December 15, 1999.

61. Foss, C. F., "Long-Awaited Deal for COBRA Radar is Awarded", Janes Defense Weekly, March 18, 1998.

62. Special Issue on Phased Arrays of IEEE Trans. on Antenna and Propagation, March 1999.

TABLE 1. JAMMING AND ITS RESPONSE

THREAT	COUNTERMEASURE
SIDELOBE NOISE OR CW JAMMING	SIDELOBE CANCELLING OR ADAPTIVE ARRAY NULLING ● 50 DB SIDELOBE CANCELLING ACHIEVED IN NEAR FIELD TEST RANGE BY LINCOLN LABORATORY
SIDELOBE REPEATER JAMMER	SIDELOBE BLANKER
MAINLOBE JAMMER	MULTIPLE INDEPENDENT BEAMS
SIDELOBE JAMMER, ARM MISSILE	ULTRA-LOW SIDELOBE LEVEL (SLL) ANTENNA ● SLL <-40DB OR -20 DBI ● T/R MODULE CAN BE CALIBRATED TO GIVE -17 DBI (3°, 0.4DB RMS) OPEN-LOOP NULLS WHERE JAMMERS ARE EXPECTED

TABLE 2. DIGITAL BEAMFORMING (DBF)

WHERE USED:
- OTH-B (GE); 1-D
- ROTHR (RAYTHEON); 1-D
- SMART-L AND SMART-S (SIGNAAL); 1-D STACKED BEAM SYSTEMS

DEVELOPMENTAL SYSTEMS
- ROME LAB: 32 COLUMNS, 32 INDEPENDENT BEAMS
- MICOM: ARRAY FEED OF 64 ELEMENTS
- BRITISH MESAR: SUBARRAY DBF
- BRITISH: DBF ON TRANS. AND REC., 13 EL
- LINCOLN LAB. ALL-DIGITAL UHF RECEIVER: 8 BIT 3 GSPS A/D

ADVANTAGES:
- FLEXIBILITY:
  - ANTENNA WEIGHTING
  - GROWTH WITH TECHNOLOGY
- ADAPTIVE PROCESSING
- IMPROVED PERFORMANCE
  - SLL
  - DYNAMIC RANGE
  - JAMMER AND CLUTTER SUPPRESSION
  - EMI

- C-BAND
- 5000 EL/PER
- NO. MAN.:173
- 865,000 PHASE SHIFTERS TOTAL
- RAYTHEON

FIGURE 1 — PATRIOT - THE WORLDS BEST KNOWN PHASED ARRAY SYSTEM

- X-BAND
- 10,000 EL/PER
- NO. MAN.:>100(?)
- >1,000,000 PHASE SHIFTERS TOTAL

FIGURE 2 — USSR FLAP LID FOR SA-10 (S300 PMU)

14
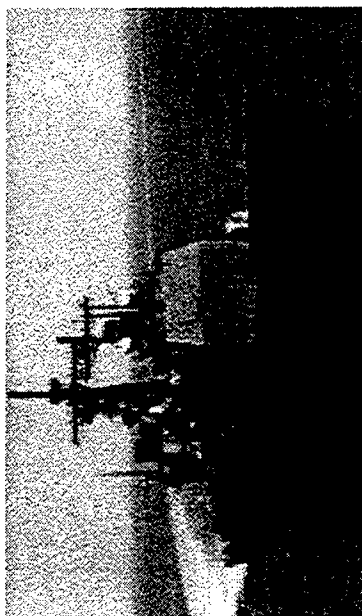
- S-BAND
- 4000 EL/PER ANTENNA
- NO. MAN.: 234 ANTENNAS
- 936,000 EL. TOTAL
- LOCKHEED MARTIN

FIGURE 3 – AEGIS SPY-1

- L-BAND (1175-1375 MHZ)
- BANDWIDTH: 200 MHZ (16% BW)
- POWER:
  PEAK: 15.4 MW
  AV. 0.92 MW
- DIAMETER: 95 FT
- NO. EL.: 15,360 ACTIVE
  34,746 TOTAL
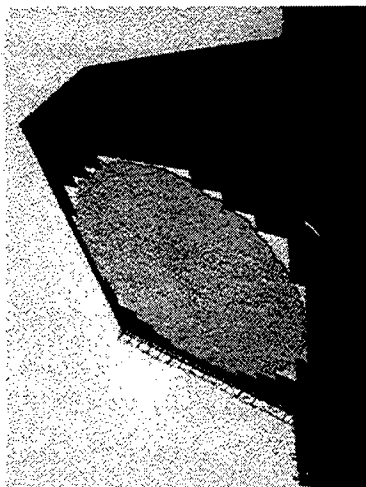
(BROOKNER, '88)

FIGURE 4 – COBRA DANE (AN/FPS-108)
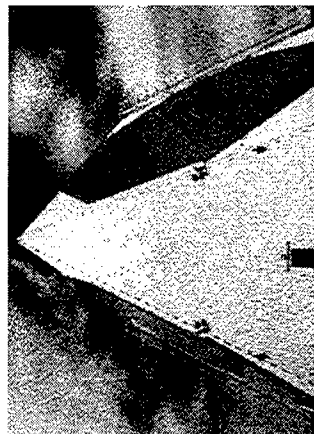
- UHF (420-450 MHZ)
- NO. T/Rs/FACE: 1,792
  EL./FACE: 2,677
- NO. MAN.: 4
- TOTAL NO. T/R MODULES
  MANUFACTURED >14,336
- DIAMETER: (72 FT/102 FT)
- RAYTHEON

(BROOKNER, SCI. AM, 2/85)

FIGURE 5 – PAVE PAWS (AN/FPS-115)
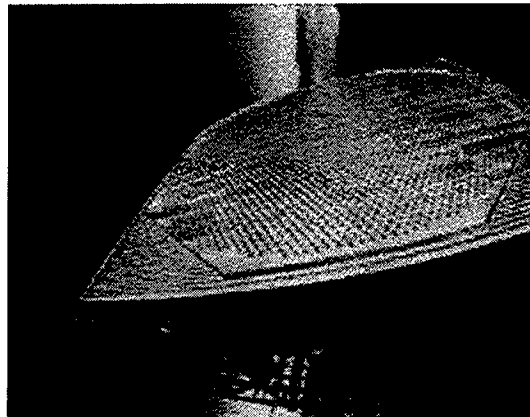
- UHF
- NO. T/Rs/FACE: 2,560
  ELEMENTS/FACE: 3,584
- NO. MANUFACTURED: 2
- TOTAL NO. T/Rs
  MANUFACTURED 12,800;
  ELEMENTS: 17,920
- DIAMETER: 84 FT
- RAYTHEON

FIGURE 6 – BMEWS UPGRADE (AN/FPS-123(V)5)

- X-BAND
- NO. T/Rs/FACE: 25,344
- NO. MANUFACTURED: 2.5
- TOTAL NO. T/Rs MANUFACTURED: 63,360 (MMIC)
- RAYTHEON

(SCARCIONE, ET AL., ARRAY-96)

FIGURE 7 – THEATER HIGH ALTITUDE AREA DEFENSE (THAAD; FORMERLY GBR)

- X-BAND
- ~2000 ELEMENTS/PER ANTENNA
- NO. MANUFACTURED: OVER 300 TO BUILD
- TOTAL ELEMENTS AND T/Rs: ABOUT 600,000
- NORTHRUP GRUMMAN (WESTINGHOUSE)/TI (NOW RAYTHEON)

(RHEA, MIL. & AEROSPACE ELECT., 8/96)

FIGURE 8 – F-22 ACTIVE MMIC ARRAY

- FREQUENCY: 0.5-70 GHZ
- INST. BW: MULTI OCTAVE
- ANGLE COV.: TO 180°
- PEAK EFFECTIVE RADIATED POWER: TO 1 MWs
- NO. BEAM: 1 TO MANY SIMUL.
- APPLICATIONS:
  - ECM
  - ESM
  - DF
  - COMMUNICATIONS
  - RADAR

FIGURE 9 – ROTMAN LENS ARRAY

DF, FREQ. MEAS., WAVEFORM PAR. (PRF, PW, AMP.)

RCV SW

REPEATER

MODE SW

TRANS-PONDER

RECEIVE ARRAY

LENS

RANGE-GATE PULL-OFF, INVERSE GAIN, VEL. GATE PULL-OFF

XMT SW

ECM WAVEFORM GENERATOR

TRANSMIT ARRAY

LENS

PA

(BLACK, ELECT. PROGRESS, FALL '75)

FIGURE 10 – ECM/ESM/DF MULTIBEAM ROTMAN LENS ARRAY SYSTEM

IRIDIUM®: THREE L-BAND MMIC ARRAY PANELS DEPLOYED ON BUS

- REVOLUTIONARY COMMERCIAL GLOBAL SATELLITE PERSONAL COMMUNICATION SYSTEM
- NO. T/Rs: >100/ANT.
- NO. ANT./SAT.: 3
- NO. SATS.: 66
- TOTAL NO. T/Rs/CONST.: >19,800
- NO. BEAMS/PANEL: 16

(BLACK, ELECT. PROGRESS, FALL '75)

FIGURE 11 – AN ARRAY ANTENNA THAT HAS IT ALL – ACTIVE, MMIC, MULTIBEAMS, MICROSTRIP-PATCH ELEMENTS, SPACEBORNE, COMMERCIAL, LARGE PROD.

(SCHUSS, ET AL., ARRAY-96)

FIGURE 12 – GROUND FOOTPRINTS OF 16 BEAMS

MOCK UP OF ASAP

- NAVAL AIR WEAPONS CENTER (NAWC)/TI (NOW RAYTHEON)
- SHARED APPLICATIONS: RADAR, ESM, ECM, COMMUNICATIONS
- WIDEBAND (C-TO KU-BAND)
- STRIKE/FIGHTER A/C
- MMIC ACTIVE ARRAY
- MULTIPLE POLARIZATIONS (H,V,C)
- FLARED NOTCH RADIATING ELEMENT
- NF: 6.5DB - 9DB OVER BAND
- POWER: 2-4 W/EL. OVER BAND
- EFF: 5.5 - 10% OVER BAND
- STATUS: UNDER DEVELOPMENT

(HEMMI, ET AL., ARRAY-96)

FIGURE 14 – ADVANCED SHARED APERTURE PROGRAM (ASAP)

- L-BAND
- DEGREES OF FREEDOM:
  2 IN EL
  11 IN AZ
- SLL BEFORE STAP: -30DBI
  AFTER STAP: -45DBI
- STAP CLUTTER CANCELLATION: 52-69DB

CANCELLATION RATIO

BEFORE STAP

AFTER STAP

RANGE CELL

CLUTTER LEVEL (dB)

(FENNER AND HOVER, RADAR-96)

FIGURE 13 – STAP FLIGHT DATA

ELEMENTS EQUALIZED

EQUALIZED
TO <±0.05 dB

Frequency (MHz)

(PETTERSSON, ET AL., ARRAY-96)

FIGURE 16 – EQUALIZED ELEMENT PATTERNS
FOR SWEDISH EXPERIMENTAL S-BAND
ANTENNA USING DBF

RADANT LENS
(COST $ 1.0M)
ELEVATION SCAN

FERRITE PHASE
SHIFTERS
(COST $250K)
MONOPULSE
BEAMFORMING
NETWORK
(COST $125K)

TPQ-36
SLOTTED
WAVEGUIDE
ANTENNA
4 FT. X 8 FT.
(COST $150K)
AZIMUTH SCAN
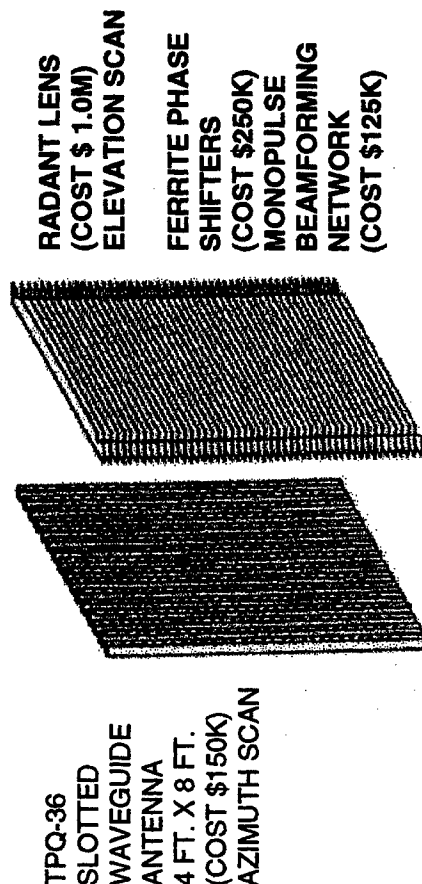
(RAO, ET AL., ARRAY-96)

FIGURE 18 – NRL HYBRID PHASED ARRAY

Ku-BAND
CO-POL
CROSS-POL

ANGLE (DEGREES)

AMPLITUDE

(HEMMI, ET AL., ARRAY-96)

FIGURE 15 – ASAP ANTENNA PATTERNS

C-BAND
CO-POL
CROSS-POL

ANGLE (DEGREES)

AMPLITUDE

ANTENNA PATTERNS

● BW = 5 MHz
● 50 dB CHEB
   WTG

Angle

dB

(PETTERSSON, ET AL., ARRAY-96)

FIGURE 17 – ANTENNA PATTERNS
FOR SWEDISH EXPERIMENTAL S-BAND
ANTENNA USING DBF

18
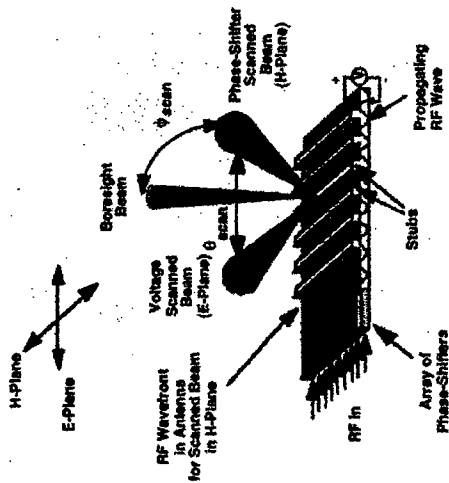
FIGURE 20 – LOW-COST 2D ELECTRONICALLY SCANNED ANTENNA APPROACH BASED ON TWO TECHNOLOGIES: CTS ANTENNA ARCHITECTURE AND VVD MATERIALS

(RAU, ET AL., ARRAY-96)

- 2 4" WAFERS
- 3000 ELEMENTS
- ±45°, 2° BEAMWIDTH
- DIPOLES PRINTED ON SI PASSIVATED WAFER (4") USING PIN DIODES
- 2ND WAFER FOR CONTROLLING CKTS CONNECTED VIA BUMPS
- MONOPULSE FEED
- LOW SLL WITH 1 BIT
- THOMSON - CSF

(COLIN., ARRAY-96)

FIGURE 22 – 94 GHZ WAFER SEEKER REFLECT ARRAY

(RAU, ET AL., ARRAY-96)

FIGURE 19 – NRL FERROELECTRIC LENS ANTENNA

(MATHEW, ET AL., ARRAY-96)

FIGURE 21 – NRL ELECTRONICALLY STEERABLE PLASMA MIRROR

19

Overview of Advanced Multifunction RF System (AMRFS)

Paul K. Hughes, Joon Y. Choe

Radar Division, Naval Research Laboratory, Washington, DC 20375

Introduction

The Office of Naval Research in 1996, initiated an Advanced Multifunction RF System (AMRFS) Program to address and resolve the serious technological challenges posed by the US Navy for supporting an increase in the number of shipboard topside RF functions, while significantly increasing requirements for ship signature control/reduction. The AMRFS Program is focused on a proof-of-principle demonstration of the concept of broadband RF apertures that are capable of simultaneous performance of a large number of radar, electronic warfare and communications functions from common, low signature apertures. The goals then of the program are to reduce the number of topside RF system apertures dramatically while increasing effective functionality and bandwidth. This will reduce the aggregate radar cross section (RCS) contribution of the topside RF system apertures. This multifunction RF system concept puts the functionality into the software. In addition to the proof-of-principle demonstration, the AMRFS Program is developing new component technologies that allow more efficient cost-effective design architectures.

The underlying concept of AMRFS is to divide the frequency band into an optimal number of segments based on cost and functionality and then utilize separate, electronically scanned, solid state transmit and receive apertures. For the initial AMRFS test-bed the goal is to obtain as large of a bandwidth as technically possible to permit cost-function trade-offs to be made for a tactical system evaluation. The use of very large percentage bandwidths minimizes the number of apertures required for a given frequency coverage, while, on the other hand, optimal choice of spectral band partitioning could reduce the size of specific arrays. The choice of 4 to 1 or 5 to 1 operation bandwidth has been selected as being marginally within the available or near-term state-of-the-art in components. Using separate transmit and receive apertures, similarly, but less obviously, minimizes the number of required apertures. In a single transmit/receive (T/R) aperture for radar applications, a small fraction of the timeline is utilized for transmitting whereas a much larger fraction of the timeline is used for receiving. Further, transmit and receive times cannot overlap because of the requirement for very high isolation between transmit and receive signal paths within the system. For multifunction radar, the need for significantly longer receive times, leads to relatively underutilized transmitter capability. In a truly multifunction aperture, electronic attack (EA) and communications functions may require high duty or even continuous operation from the transmitter (or receiver), allowing insufficient time for receive (or transmit) functions. Separate transmit and receive apertures allow full utilization of the entire timeline for the transmitter as well as for the receiver and thereby support a greater compression of the numbers of required apertures.

TRANSMIT ARRAY   **RECEIVE ARRAY**
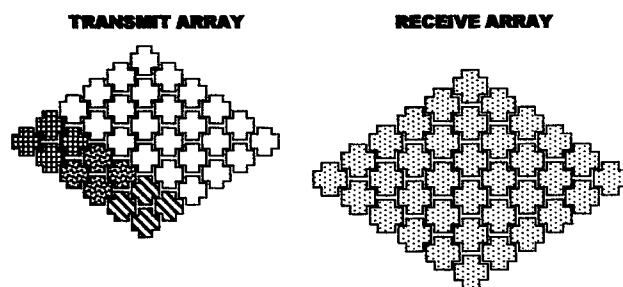
Figure 1 – AMRFS Top-Level System Conceptual Architecture

Figure 1 shows a high level conceptualization of an AMRFS concept. It consists of a transmit array composed of dynamically allocable subarrays that are sectioned to form multiple simultaneous transmit beams. In the figure, four sections of the transmit array are shown. Having more than one signal present in a power amplifier at the same time is not currently feasible. So each transmit subarray is used by one function at a time. However, for the receive array, more than one signal can be present simultaneously in a subarray. All or portions of the receive array can be used by multiple functions simultaneously with section sizes depending on the gain

and beamwidth requirements of the function. In the test-bed, each receive subarray can support up to three independent beams.

The AMRFS development is being conducted by a Government and Industry team comprised of the Naval Research Laboratory, the Naval Surface Warfare Center, the Naval Air Warfare Center and the SPAWAR Systems Center, Lockheed Martin, Northrop-Grumman, Boeing, and Raytheon. Other industry partners and other Government facilities are being included when and as appropriate to the development effort. The initial test-bed is being designed and built with advanced development funds from the Office of Naval Research (ONR).

RF Functions and Functional Requirements

For the AMRFS Test-Bed System and concept demonstration, a representative set of RF functions has been identified from the communications, electronic warfare and radar types of functions. The functional requirements selected are typical for the types of functions supported by today's surface Navy. In several cases (radar and electronic warfare), the functional requirements have been selected from a class of federated systems, which will be logically combined in AMRFS. In other cases (communications), where an existing infrastructure dictates the function being supported, the functional requirements are pulled directly from the legacy systems.

During the AMRFS study these top-level functional requirements have provided a basis for initial strawman implementations and a means to calibrate each implementation in terms of functional performance versus asset requirements (i.e., size of arrays, receive channels, bandwidths, and etc.). Initial focus was on functional implementation concepts and not on design details. Additional refinement of both the concepts and designs has been part of the latest AMRFS Test-Bed activities.

The present AMRFS functions for the initial demonstration were identified as:

	Radar	Communications	Electronic Warfare
Low Band (1 – 5 GHz)	VSR CV Marshalling TBMD IFF	JTIDS IMMARSAT-B Challenge Athena	Electronic Attack High Gain High Sensitivity High Probability Of Intercept
High Band (4.5 – 18 GHz)	LPI Navigation Radar	Ku Band SATCOM	Electronic Attack High Gain High Sensitivity High Probability Of Intercept

These functions are typical of what might be use on a future ship. They are not all the functions that could be included, but the low band functions provide all the stressing requirements that the integrated sets of equipment would need. To manage the cost of the proof-of-principle demonstration, the emphasis has been placed on the low band. There are additional high band functions (mostly radar) that would bring even more stressing requirements to the high band arrays if they were included.

AMRFS System Concepts and Trades

This section presents the top-level system block diagram for the AMRFS test-bed and some of the trade study analysis results leading up to the Test-Bed architecture.

The object of the AMRFS program, "…to develop and demonstrate an integrated RF shipboard system, which can support the simultaneous requirements of radar, communications and electronic warfare." requires that significant system trades be made. Traditionally, radar systems have enjoyed the luxury of dedicated hardware tuned to provide low sidelobes, high spectral purity, and low noise figures. Similarly, communications systems have been able to optimize data link communications with link margins supportive of acceptable bit error rates. Electronic warfare systems have always been able to selectively trade some of these key radar and communications performance parameters for bandwidth in order to achieve the probability of intercept required against a wide range of signal conditions and types. Additionally, spectral and spatial isolation has been used extensively by co-located systems to minimize interference and aid time-line asset allocation.
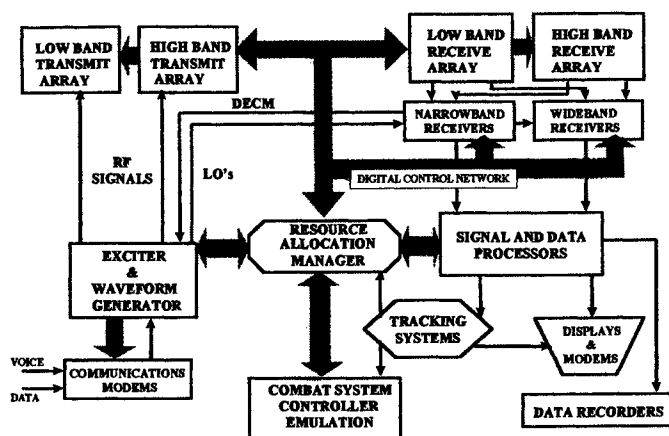
Figure 2 – AMRFS Test-bed Block Diagram

Figure 2 shows the test-bed system design for implementing the proof-of-principle demonstration. The design is comprised of a low band transmit and a low band receiver array (1-5GHz), and a high band transmit and a high band receive array (4.5-18GHz). Also included is a resource allocation manager (RAM) to schedule receive and transmit functions, a digital receiver/signal processor, a display console, and an interface to the rest of the platform combat systems. There must be a source for signals to be transmitted, so a waveform generation capability is included. The commands generated by the RAM control the entire integrated RF sensor suite. These commands are distributed to all subsystems via a digital control network.

The basic concept of a single shared phased array aperture to support radar, communication, and electronic warfare functions over a 5:1 RF band introduces numerous architectural concerns. In addition to the fundamental problems associated with asset sharing, aperture front-end elements must be able to support the extremes of the combined system functions simultaneously (i.e., polarization diversity, low noise figure, high dynamic range, bandwidth, power-aperture product, etc.). Unlike conventional dish apertures, the phased array does not benefit from spatial isolation. All front-end elements within the phase array are exposed to the RF environment incident on the surface of the planar array resulting in significant introduction of sources for inter-modulation products, which in turn result in potential system performance degradation.

Figure 3 is a more detailed diagram for the proposed AMRFS test-bed that has been developed as a result of the system design. At the core of the test-bed concept are the four ONR funded low band and high band transmit and receive array apertures. Fundamental to the selected AMRFS architecture is the physical separation of receive and transmit and the partitioning of the 1 - 20 GHz frequency coverage into two bands, low band (1-5 GHz) and high band (4-18 GHz). Both receive arrays include the receive array subsystem, RF down-conversion and digital receivers and local processing and control necessary to support simultaneous and time-interleaved multi-function receive functions from RF through to digitized I&Q samples of the received environment. Similarly, both transmit subsystems include the array transmit system, RF up-conversion and digital waveform generation synthesis and local processing and control necessary to support simultaneous and time-interleaved multi-function transmit functions.

Peripheral to the basic receive/transmit building blocks is the High Probability of Intercept (HPOI) receiver subsystem, wideband Electronic Attack (EA) processing and communication legacy modems required to support multi-function demonstrations. Because of the unique requirement of the HPOI function to support omni azimuth and elevation interferometry, only the basic antenna receive elements of the interferometer are integrated into the receive array subsystem. In a similar fashion, legacy communications modems are proposed for test-bed use to minimize the cost of demonstrating shared array functionality with legacy communications functions and infrastructure.

Test-bed elements will be integrated together under the control of centralized Signal and Control Processing. Key to signal and control processing will be the test-bed's Resource Allocation Management (RAM) function. RAM will have cognizance over the test-bed's receive/transmit subsystems and peripheral hardware and software elements through digital control network interfaces for the setup of receive/transmit configurations supporting simultaneous radar, communications, and electronic warfare functionality. Data received as a result of RAM is routed to Receive Signal/Data Processing software functions within the Signal and Control Processing subsystem. Similarly, generation of digital
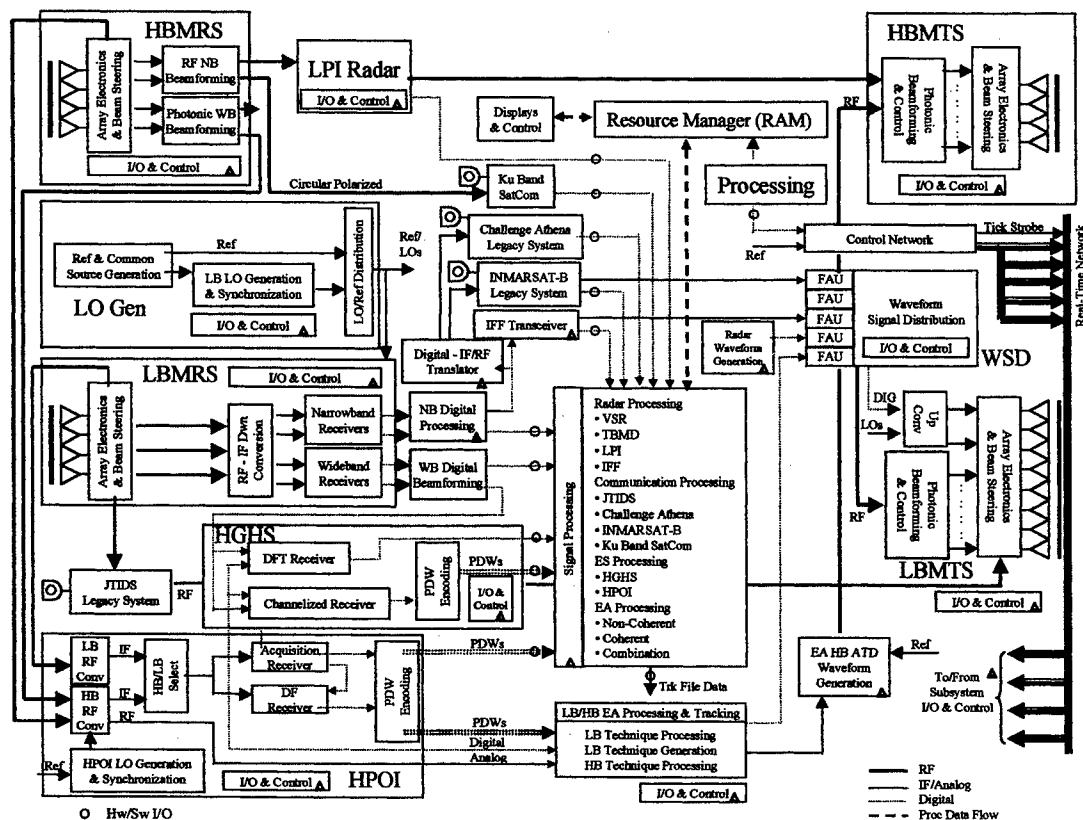
Figure 3 – AMRFS Test-Bed System Architecture

technique/waveform data to support transmit functions is provided through software functions within Signal and Control Processing.

In support of the AMRFS test-bed system, special provisions will be provided through instrumentation and control for operator tasking and data collection for performance analysis. At various levels of testing and evaluation, both cooperative and non-cooperative emitters will be introduced into the test environment. System performance evaluation is planned for laboratory controlled environments as well as land-based open environment testing.

Summary

The AMRFS Program consists of two equal but distinct parts. This program description has provided details of design for equipment that would provide a "proof-of-concept" demonstration to be carried out by building an experimental test-bed and showing in real-time that the integration of RF functions, such as radar, electronic warfare, and communications, into a single system is technically feasible. This part of the Program deals with all the issues of establishing requirements, designing, building, testing, and demonstrating an integrated RF system. One purpose of this part of the Program is to provide risk reduction within a science and technology program. This is deemed important because of the large risk involved in building a first-of-a-kind multifunctional integrated RF system. The other part of the Program is concerned with advanced new components and subsystems technologies that would enable a more practical, cost effective, tactical system to be developed and deployed by the Navy. The ultimate objective of both parts of the Program is the transition of the integrated RF system technology to operational platforms within the Navy. An attempt was and is being made to provide acquisition Program Managers with risk reduced new technology and combat capabilities, in a timely manner, to allow insertion decisions at the earliest possible date.

24

Time-Domain Properties of Phased Array Antennas

Daniel A. Leatherwood, Larry E. Corey, Rickey B. Cotton, and Barry S. Mitchell
Georgia Tech Research Institute, Atlanta, GA 30332-0852

I. Introduction

This paper describes initial findings from a research program to investigate the main beam and sidelobe impulse responses of large phased array antennas and reflector antennas typically used for radar applications. Particular emphasis is given to the way that the impulse response changes from the main beam to the sidelobe region of the antenna. Antennas are designed to radiate a plane wave with a given polarization and frequency in a specified main beam direction. However, the time-domain impulse response will vary according to the actual implementation of the antenna design. Reflectors are designed to collimate a radiated beam by creating equal path delays and tend to have few parts. This produces a relatively simple and short time-domain impulse response. A phased array, on the other hand, generally collimates the beam by adjusting phases instead of path delays. In addition, there are more parts, which introduce multiple reflections. This gives the phased array a more complicated and longer impulse response than a reflector. These time-domain effects affect transmit and received waveforms and therefore advanced signal processing algorithms such as adaptive digital beamforming (ADBF) and space-time adaptive processing (STAP). GTRI has instituted an internal research program to investigate the time-domain phenomenology of phased array antennas and develop computer simulation tools and measurement capability for characterizing these phenomena. Section II provides a brief discussion of the time-domain phenomena and the effects that antenna architecture produce. An overview of the method GTRI is using to investigate these phenomena is given in Section III. Finally, initial results of these efforts are presented in Section IV.

II. Architecture Effects on Time-Domain Phenomena

A variety of architectures exists for directing radiated RF energy in a specified direction. Two broad classes of architectures are reflector and phased array antennas. A simple parabolic reflector antenna collimates energy from a feed located at the focal point of the parabola by providing equidistant path delays from the feed to a plane perpendicular to boresight of the antenna. In the direction of the main beam, this produces a very narrow impulse response, which implies that the transmitted waveform in the main beam direction will be very similar to the waveform input to the antenna terminals. Deviations from a true impulse result from multiple reflections and dispersion within the feed, multiple reflections between the feed and reflector, diffraction off the reflector edge, and scattering off the feed and feed struts. In addition, the gain increases with frequency. In the sidelobe regions, the impulse is broadened by dispersion that results from differences in path lengths from the feed to the reflector to a plane perpendicular to the sidelobe direction. Some sidelobes may also be affected by spillover from the feed.

Most phased array antennas collimate a beam by using phase shifters to adjust the phase of the waveform radiated from each element in the array. In general, this implies that the path delay from the antenna terminals to the plane perpendicular to the main beam direction is different for every element. Some radars use time-delay units (TDUs) at the subarray level to decrease the dispersion in the main beam. However, phase shifters are still used at the subarray level, so some dispersion still exists. In addition, when the beam is scanned away from broadside, the TDUs actually increase the dispersion in the far-off sidelobes. Other sources of time-domain effects in phased arrays are multiple reflections between the different components in the phased array and dispersion within the feed waveguides and phase shifters. Some architectures such as a space-fed array will have direct radiation from spillover that will affect sidelobes. If polarized screens and polarizing grids are used, polarization misalignments will produce

polarization transients at the beginning of the pulse. A time-varying effect will result if the pulse is transmitted before the phase shifters have settled into a steady state.

Several phased array architectures are used for radar applications. They are space-fed lens arrays, corporate-fed arrays, reflect arrays, and subarrayed arrays. Each of these architectures has a distinct time signature. A series-fed corporate feed phased array, such as shown in figure 1 will have large differences in the delay time to each of element radiators. On the other hand, a parallel-fed corporate feed phased array, as shown in figure 2 will have the same delay time to each element. Figure 2 shows the phased array with TDUs controlling each subarray, which produces a different time-domain signature when the beam is scanned than a phased array without TDUs.

III. Approach

The first step in studying the time-domain phenomena is to catalog all of the sources of time-domain effects and then determine which of these effects are significant. Using this analysis, computer simulation models are being developed to investigate these effects. For the initial modeling effort, it is assumed that the antennas are linear and time-invariant, which allows the use of the Fourier transform convolution theorem so that calculations can be performed in both the frequency and time domains. The transmitted waveform is the convolution of the input waveform with the antenna impulse response.

Measurements are performed to validate the modeling. GTRI has upgraded its near-field measurement range so that measurements can be multiplexed at a number of frequencies. The near-field measurement at each frequency is transformed to the far-field domain, which gives a wide-band frequency response over a large range of observation angles. Transformation of these frequency responses to the time-domain produces measured impulse responses for the antenna as a function of observation angle. In addition, the far-field range has been upgraded to perform swept-frequency measurements. This allows time-domain impulse measurements of backlobes and measurements of antennas mounted on vehicles. These measurements are not suitable for the near-field range.

IV. Results

Time-domain measurements have been made of both a simple four-foot parabolic reflector antenna and a large limited field-of-view (LFOV) target engagement radar (TER) antenna. The TER is a series-fed corporate feed phased array with ferrite phase shifters. The antenna comprises 24 rows and 24 columns of element radiators with a 3 wavelengths by 3 wavelength element lattice. The elements are divided into 4 quadrants that are parallel-fed, where each quadrant has a horizontal corporate waveguide that series-feeds 12 vertical corporate waveguides that each series-feeds the 12 elements on that column. Figure 3 shows the frequency domain response in the main beam of both the four-foot reflector and the TER with the beam steered to broadside over the frequency range of 12.4 to 18 GHz. The phase shifters of the TER are set to collimate the beam at 14.523 GHz. It is seen that the reflector is a wide-band antenna with the gain increasing with frequency. The ripples in the response are likely due to diffraction and scattering off the feed and feed struts. The TER has a much narrower instantaneous bandwidth. This is a result of the different path delays, which cause the main beam to quickly decollimate away from the collimation frequency. Actually, as we move away from the collimation frequency, the main beam splits into four beams that scan diagonally away from boresight as the frequency increases. As the frequency increases further, these four beams move towards the center again and the beam recollimates, which accounts for the peak seen in the graph at 18 GHz.

Fourier transforming the frequency response produces the impulse response of the antenna. Figure 4 shows the magnitude of the complex envelope at 14.523 GHz for the main beam of the two antennas. It is seen that the reflector has a very narrow impulse response. This results from the identical delay times for

all the radiation paths. The different path delay times for the TER produces a broadened impulse response lasting about 6 or 7 ns, which corresponds to the difference in delay times from the center elements to the outer elements of the array.

The impulse function of an antenna changes with observation angle. Figure 5 shows the measured impulse response of the TER in the sidelobe region for two different observation angles. The main beam is steered to broadside, and the impulse responses at 10 degrees and 20 degrees in azimuth off broadside are plotted. The shapes of the two impulse responses are significantly different. The impulse response can produce interesting transmitted waveforms in the sidelobe regions. Even in a null of the antenna pattern, a CW pulse will have a transient spike at the beginning and end of the pulse. A linear FM pulse is even more interesting because the angular location of the null will scan with frequency.

Figure 4 shows differences in the simulated impulse response for two different phased array architectures. In this simulation, two arrays with 30 horizontal elements are constructed. The first array is a series-fed corporate feed phased array, which is fed from the center of the array. In the second array, the elements are divided into three subarrays with the subarrays series-fed from the center of the array and controlled by TDUs. Each subarray is series-fed from the center of the subarray and phase shifters are used to control each element of the subarray. The main beam is steered to an azimuth angle of 45 degrees. The plot shows the impulse response for the two arrays at an azimuth of –60 degrees. The TDUs reduce the dispersion in the main beam of the antenna. However, the differences in the time delays in the far-off sidelobe directions are increased. Thus, the first array has an impulse response that is only about 3 ns wide, whereas the second array has an impulse response that is about 8 ns wide.

V. Conclusions

All antenna architectures are designed to produce a radiated wave in a given direction, but the differences in the implementation can produce significant differences in the time-domain response of the antenna. These responses will vary with the beam-scanning angle of the antenna and with observation angle. Reflector antennas have very simple impulse responses that will not induce noticeable changes to transmitted or received waveforms. However, as indicated above, phased array antennas can have complex and extended impulse responses that have the potential to modify the transmitted or received waveforms in significant ways. The ways in which this time-domain phenomenon can affect the radar's performance will be the subject of a future paper.
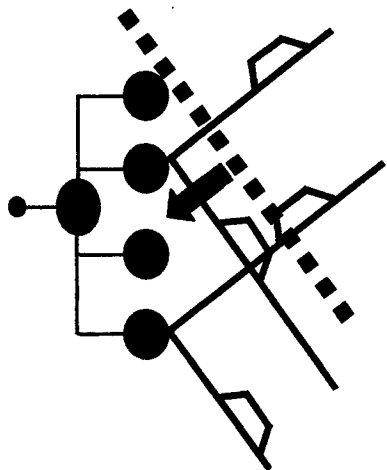
Figure 1. Series-fed phased array
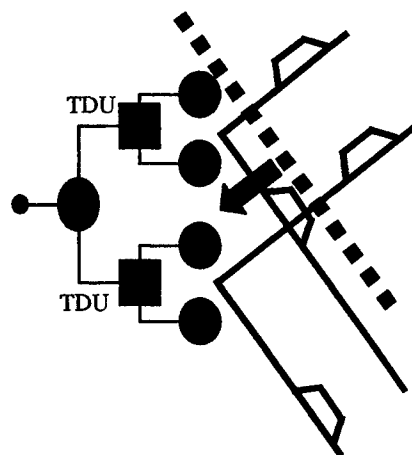
Figure 2. Parallel-fed phased array with TDUs
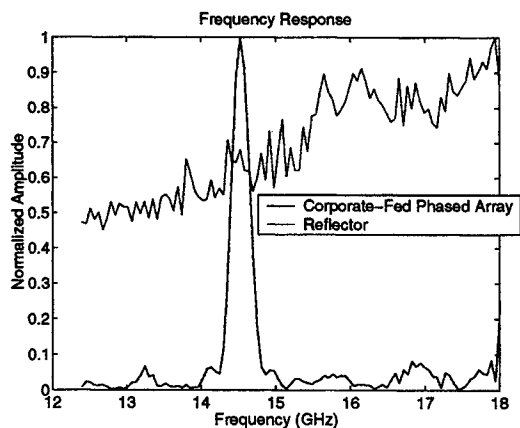
Figure 3. Frequency response of four-foot reflector and TER
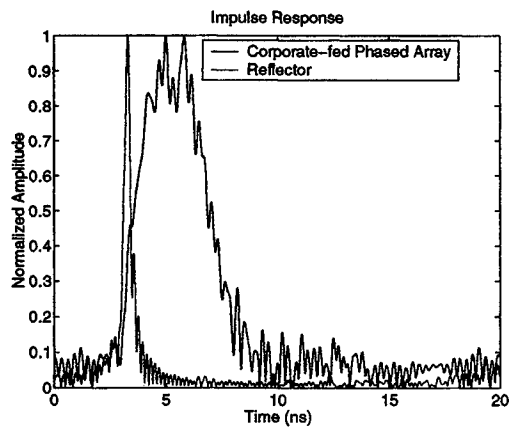
Figure 4. Impulse response of four-fout reflector and TER
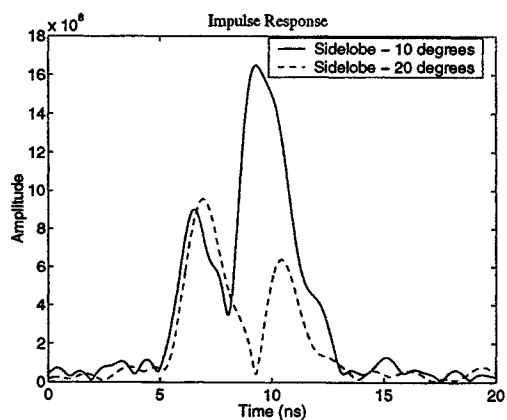
Figure 5. Impulse response of TER in sidelobe regions
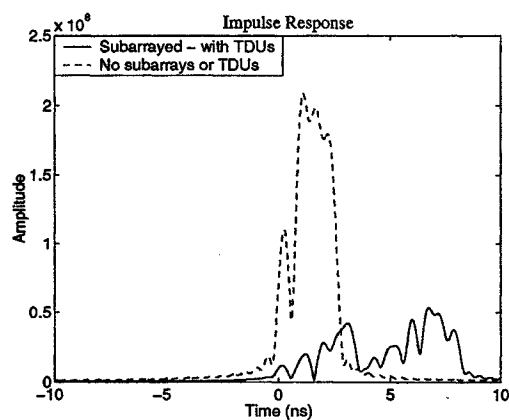
Figure 6. Impulse response of two phased array architectures

THE FIRST APPLICATION OF ARRAY ANTENNA

Dr. Probir K. Bondyopadhyay
GSA SYSTEMS INC.
14418 Oak Chase Drive
Houston, Texas 77062
[E.Mail : p.bondy@worldnet.att.net]

ABSTRACT

The world's first application of array antenna is described in this historical paper. Wireless wizard Guglielmo Marconi was the first in the use of arrays as the transmitting antenna for the epoch making transatlantic wireless communication experiment of December 1901. This successful use is outlined in this paper. A video clip describing this event will also be presented in this Symposium.

1. INTRODUCTION

In the introduction to his recent book on Phased Array Antennas[1] Robert C. Hansen wrote, *"Discovery of the first works on array antennas is a task best left to historians, but the two decades before 1940 contained much activity on array theory and experimentation."*

The first work on array antennas is not at all an obscure event. Guglielmo Marconi in his epoch making transatlantic wireless communication experiment employed an array antenna to transmit the grounded Hertzian waves. The actual antenna used is shown in Figure 1.
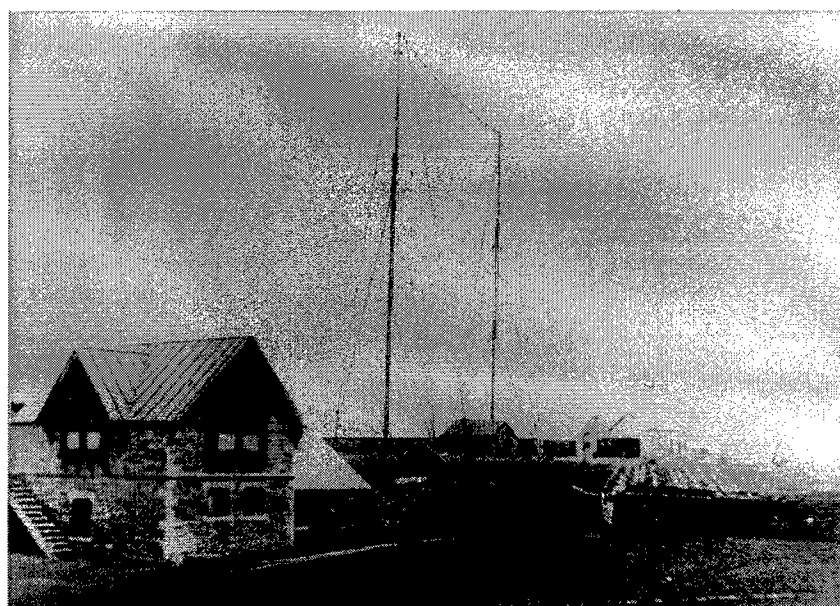
Figure 1. The world's first array antenna actually used by Guglielmo Marconi to transmit the first transatlantic wireless signal from Poldhu, Cornwall, U.K. on 12 th December 1901.

2. THE FIRST ARRAY ANTENNA

The first array antenna (Figure 2) was designed by Guglielmo Marconi (Figure 3) himself in 1901. Sir John Ambrose Fleming(Figure 4) as technical advisor to the Marconi's Wireless Telegraph Co., Ltd., was in charge of the design of the high power wireless transmitting system capable of sending Morse codes. The original
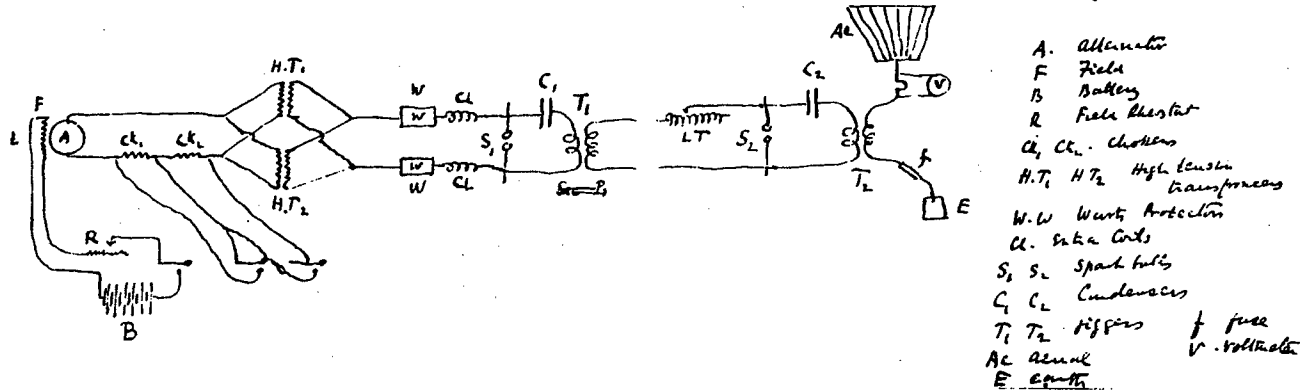
Figure 2. Sketch of the Poldhu Wireless Transmitting System as recorded by Sir Fleming in his Notebook[2].

Figure 3. Guglielmo Marconi

Figure 4. J. Ambrose Fleming

array antenna designed by Marconi for this purpose is shown in Figure 5. According to the original plan two identical such antennas were designed, one for Poldhu, Cornwall and the other for Cape Cod, Massachusetts for two way communications. Both of these array antennas were destroyed by devastating storms, the one at Poldhu, on September 17th, 1901 as shown in Figure 6.
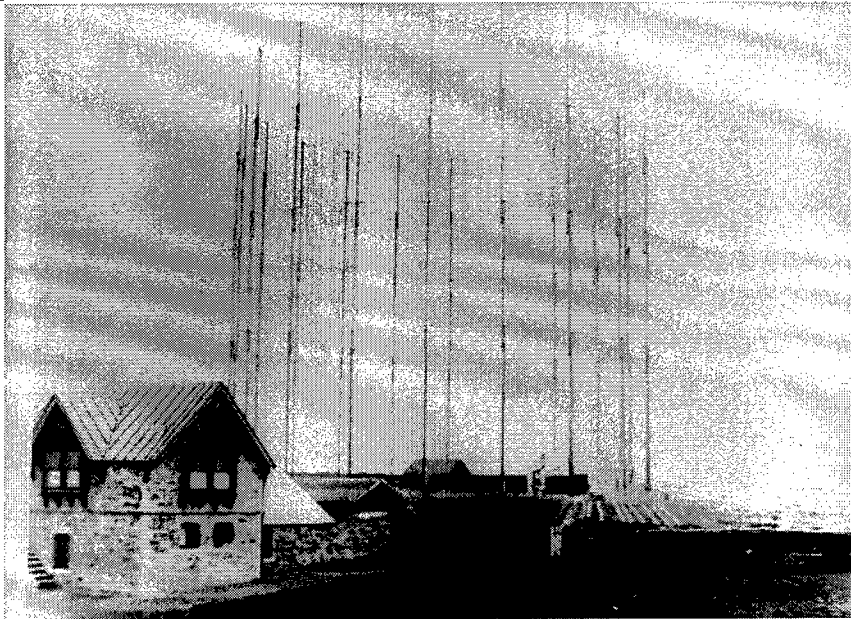
Figure 5. The original design of the array antenna by Guglielmo Marconi to transmit the first transatlantic wireless signal from Poldhu, Cornwall, U.K. This antenna was destroyed by very strong winds on 17th September 1901.

Figure 6. The array antenna first designed by Guglielmo Marconi for two way transatlantic wireless communication was destroyed at both ends by very strong winds. This picture was taken at Poldhu, Cornwall, U.K.

3. SPECIFICATIONS OF THE FIRST ARRAY ANTENNA

The array antenna that was actually used in the first transatlantic wireless communication was a simpler aerial. Two poles, instead of twenty in the original configuration, were erected. A triatic stay was stretched between the masts and from it were suspended fifty four copper wires(or was it fifty five ?). They were about a yard apart at the top and converged at the bottom, forming a planar fan shaped aerial.

Figure 7. Description of the first array antenna designed and used by Marconi as described in Sir Fleming's Notebook in his own handwriting[2].

The first transatlantic wireless signal in the form of a repeated Morse Code Signal representing the letter 'S' was received by Marconi at St. Johns, Newfoundland, using a single wire receiving antenna floated high with a Kite and a solid state diode detector- the iron-mercury-iron contact detector, known at that time as a self restoring coherer, invented by Sir J. C. Bose[5].

4. REFERENCES

[1] Robert C. Hansen, "Phased Array Antennas", John Wiley & Sons, New York, 1998, Chapter 1, page 5.

[2] Sir John Ambrose Fleming, Personal Notebook, 1901, MS. Add 122/20, Fleming Collections, Rare Manuscripts Division, University College London, Library, Gower Street, London, U.K.

[3] Orrin E. Dunlap Jr., **Marconi - The Man and His Wireless**, The MacMillan Co, 1937, New York, (Reprint Ed. 1971, Arno Press), Chapter VIII, pp. 87-102.

[4] Vivian J. Phillips, "The 'Italian Navy Coherer' Affair - A Turn-of-the-Century Scandal", Reprint Paper, Proceedings of the IEEE, Vol. 86, No. 1, January 1998, pp. 248-258.

[5] Sir J. C. Bose, "On a Self-Recovering Coherer and the Study of the Cohering Action of Different Metals", Proc. Royal Society, London, Vol. LXV, No. 416, pp. 166-172.

MA2

Modules/Components

Modules/Components

KU-BAND PLANAR TRANSMIT-ARRAY MODULE WITH TRANSISTOR AMPLIFIERS

Marek E. Bialkowski and Hyok J. Song
Department of Computer Science and Electrical Engineering
The University of Queensland, Brisbane, QLD 4072, Australia

ABSTRACT
This paper presents the design, development and testing of a Ku-band planar transmit-array module of transistor amplifiers excited by either a pyramidal horn or a patch array. Investigations are performed into the power combining efficiency of these structures. After establishing optimal distances between the active transmit-array and the illuminating antenna, either the patch array or horn, the entire structure is tested in terms of gain, operational bandwidth and radiation pattern. The experimental results show that the use of a corporate-fed array as an illuminating device leads to a slightly higher gain and a significantly larger operational bandwidth.

1. INTRODUCTION
Significant research into spatial power combining techniques of solid-state devices has been observed during the past decade. The motivation is the inherent low power handling capability of individual solid-state devices at upper microwave and millimeter-wave frequencies and a strong demand for high-power solid-state sources in applications such as satellite communications and airborne radar. Spatial power combining has the advantage over classical waveguide or cavity-type power combining in that conductive losses are minimised. A variety of spatial power combiners have been proposed and significant advancements have been achieved in terms of power combining efficiency [1], [2]. Although oscillators and amplifiers can be spatially combined to produce solid-state sources, most of the recent activities have been devoted to amplifiers combined using *tile* or *tray* array configurations.

In this paper, only the tile configuration of amplifiers is considered. This is a planar active transmit-array of transistor amplifiers illuminated by a pyramidal horn or a corporate-fed array of microstrip patches. An optimal distance between the active stage and the illuminating device for maximum gain at the design frequency is ascertained and then the behavior of the entire module is assessed in terms of gain and radiation pattern over a given frequency band in an anechoic chamber.

2. EXPERIMENTAL INVESTIGATIONS
Fig. 1 shows the detailed configuration of an active transmit-array and a corporate-fed illuminating array. In an alternative arrangement, a pyramidal horn replaces the corporate-fed array as an illuminating device. Note that the arrays employ two varieties of antenna elements: an aperture-coupled microstrip patch antenna and an edge-fed microstrip patch antenna.

As seen in Fig. 1, the active transmit-array receives a vertically polarized signal on one side, amplifies it and radiates it in free space using horizontal polarization on the other side. Note that the active stage can involve a couple of transmit-arrays in cascade. In addition, if necessary a single amplifier can be incorporated at a feed point of each 4-element sub-array of the illuminated array, to overcome conductive losses and simultaneously satisfy circuit space constraints. This option has not been considered here. For the purpose of investigations, 4×2-element passive corporate-fed patch arrays and 4×2-element active transmit-arrays for operation at 12.5 GHz were designed. The designs followed guidelines presented for passive arrays in [3].
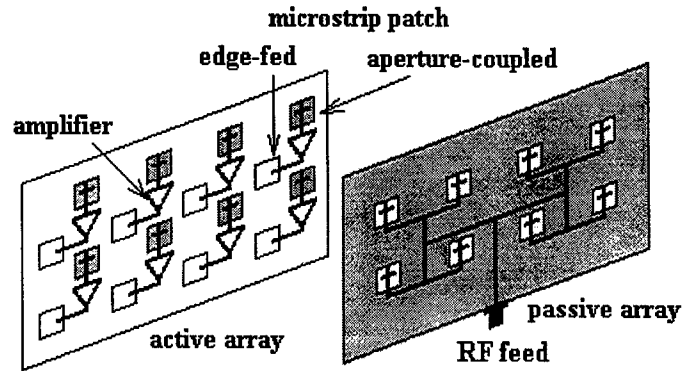
Fig. 1 Perspective view of an active transmit-array excited in reactive near-field region by a corporate-fed aperture coupled patch array.

Both the passive and active arrays use a 0.483mm-thick low loss Ultralam substrate ($\varepsilon_r = 2.45$) from Rogers. In order to increase the operational bandwidth, a 0.8mm thick layer of air is applied between the patch and aperture layers. Both aperture-coupled patch elements and edge-fed patch elements are designed for 50-ohm operation. For the edge-fed patch antenna, an inset in the patch is used to obtain the 50-ohm impedance match. The fabricated aperture-coupled patch has the dimensions of 7.2mm in width and 7.6mm in length, with a rectangular slot 0.3mm × 6.9mm. Similarly, the dimensions of the edge-fed patch are 7.4mm in width and 7.63mm in length with a 2.5mm inset. These antenna elements feature respectively 0.6GHz and 0.2GHz 10-dB return loss bandwidth when tested in isolation. The resulting 4×2-element transmit-array dimensions are 70mm × 35mm using inter-element spacing of 0.8 free-space wavelength (λ_0). The array uses a finite size ground plane of 120mm × 80mm to match the dimensions of two horns' apertures of 124mm and 92mm in H- and E-plane, which feature an axial length of about 30cm from apex to aperture. During measurements, transmit-arrays are centered with respect to the apertures of the transmitting horn.

For the active array, NE32484A FET transistors from NEC are selected. The input and output matching circuits of the amplifiers are initially designed for the 50-ohm characteristic impedance using HP-EEsof Series IV. In the active array these loads are realised by aperture-coupled and edge – feed microstrip patch antennas. The design employs the S-parameter data provided by the manufacturer for the bias condition of $V_{DS} = 2V$, $I_D = 10mA$. The resulting amplifiers with coaxial input/output are unconditionally stable and exhibit a broad flat 3-dB gain from 11.5 to 13GHz. The measured gain at 12.5GHz is 11.5dB. These amplifiers are included in the array using 0.8 λ_0 spacing.

3.   RESULTS

The 4×2-element active transmit-array including two alternative signal launching devices were initially tested using the HP8510C VNA and a specially designed test jig with rails providing precisely controlled spacing between signal launching device and transmit-array. For these structures spacing d_1 between the receiving device and the active array, and d_2 between the launching device and the active array were varied until the maximum measured gain at the design frequency of 12.5 GHz was obtained. For the module involving the corporate-fed patch array as the launching/receiving device, the optimal spacing was $d_1 = 9mm$ and $d_2 = 10mm$ and the measured gain was 7.21dB. When sweeping the frequency from 12 to 13 GHz, it was found that the maximum gain was 7.21dB at the design frequency and the 3dB-gain bandwidth was approximately 0.7GHz. For the module with horns as signal launching/receiving devices, the optimal distances were $d_1 = 6.5mm$ and $d_2 = 6mm$ and the respective gain was 6.36dB at the design frequency. By sweeping the frequency from 12 to 13 GHz the maximum gain was found at the design frequency with the 3dB-gain bandwidth of 0.1GHz.

38

Having obtained the optimal spacing between the signal launching device and the active transmit-array, the receiving antennas used in the near-field test setups were removed and the active transmit array excited by either a passive array or a horn, was tested in a far-field range. The studied parameters included gain and radiation patterns.

Fig. 2 compares the measured gain of the active 4×2-element module when illuminated either by a corporate-fed patch array or a horn. The gain was measured with reference to the known gain of an X-band horn antenna.
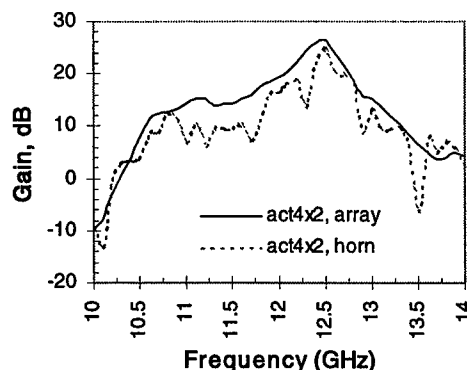
Fig. 2   Comparison between gain of the active 4×2-element module when excited in the reactive near-field region by a corporate-fed patch array or a standard pyramidal horn.

As seen in Fig. 2, the maximum gain in the two cases occurs at the design frequency of 12.5GHz. For the patch array excited module, the peak gain is 26.54dB. The horn-excited active transmit-array exhibits the maximum gain of 24.71dB, which is about 1.8dB lower than for the patch array acting as an illuminating device. A 3-dB gain bandwidth of the patch array excited module is about 0.5GHz and ranges from 12.2 to 12.7GHz whereas the horn excited module features a 3-dB gain bandwidth of only 0.2GHz.

Fig. 3 shows E-plane and H-plane far-field radiation patterns at 12.5GHz as obtained for the active transmit-array excited by the corporate-fed patch array.
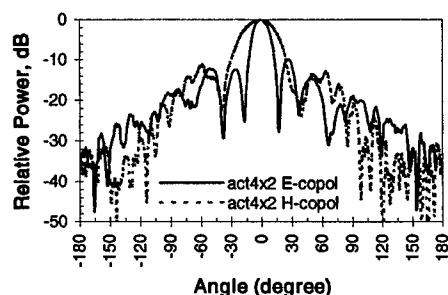
Fig. 3   E- and H-plane far-field radiation patterns of the 4×2-element active array excited by a corporate-fed patch array.
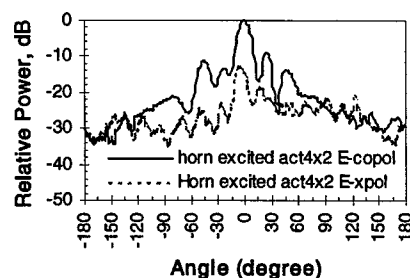
Fig. 4.   E-plane co-polar and cross-polar far-field radiation patterns of active 4×2-element transmit-array excited by a pyramidal horn.

The corresponding E-plane co-polar and cross-polar far-field radiation patterns of the transmit-array excited by the horn at the same frequency of 12.5 GHz is shown in Fig. 4. The comparison between

the results in Fig. 3 and 4 reveals that the sidelobes of the patch array excited module are smoother than the ones obtained for the horn-excited counter-part. Also for the E-plane pattern the level of first side lobes is closer to the theoretical value of –12.2dB for the uniform excitation.

In order to further investigate the uniformity of excitation of the 4×2-element active array, the measured E-plane patterns were compared with the E-plane pattern, predicted by PCAAD software [4] for the uniform excitation.
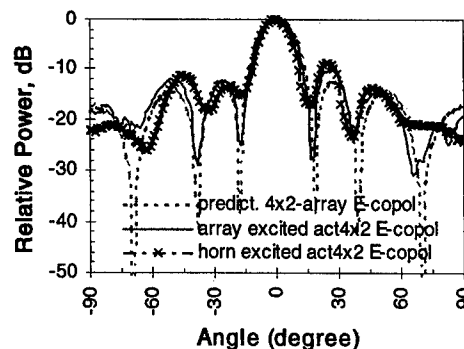
Fig. 5 Comparison of measured E-plane patterns of the active 4×2-element transmit-array with the predicted E-plane pattern of a uniformly excited 4×2-element array at 12.5GHz.

This comparison, shown in Fig. 5, reveals that the measured E-plane pattern of the patch array excited module is almost identical to the PCAAD predicted pattern for uniform excitation, indicating the required excitation of the active stage. In the case of the horn excited module there are some discrepancies in sidelobe levels and null positions.

4. CONCLUSION

In this paper we have presented experimental results for a Ku-band active 4×2-element microstrip patch transmit-array excited by either a passive corporate-fed array or a pyramidal horn, both operating in the near-field zone of the active stage. The results concern gain, operational bandwidth and radiation pattern. They reveal that the illumination by the corporate-fed patch array offers a slightly higher active directive gain and more importantly a larger operational bandwidth than the horn. This is due to a more uniform excitation of the active stage by this device. The distinct advantage of the active array being illuminated by a patch array is the significantly smaller size of the entire system.

REFERENCES

[1] J. A. Navarro and K. Chang, *Integrated active antennas and spatial power combining*. New York: Wiley-Interscience, 1996.

[2] R. A. York and Z. B. Popovic, *Active and Quasi-Optical Arrays for Solid-state Power Combining*, Wiley Inter-Science, 1997.

[3] M. E. Bialkowski and H. J. Song, "Investigations into power combining efficiency of microstrip patch transmit-arrays," *Microwave Opt. Technol. Lett.*, vol.22, no.4, pp.284-287, Aug. 1999.

[4] D. M. Pozar, PCAAD (Personal Computer Aided Antenna Design), Version 2.1, Dec. 1991.

AIRBORNE RADAR ANTENNA MODULES USING LIGHTWEIGHT TEMPERATURE-RESISTANT MATERIALS

Pawel Kabacik[†], Krzysztof Sachse[†], Andrzej Sawicki[†], Grzegorz Jaworski[†]
and Marek E. Bialkowski[‡]

[†] Inst. of Telecommunications & Acoustics,
Wroclaw University of Technology,
50-370 Wroclaw, Poland,
E-mail: pawel@zr.ita.pwr.wroc.pl

[‡] Computer Science & Electrical Eng. Dept.,
University of Queensland, St Lucia,
Qld 4072, Brisbane, Australia
E-mail: meb@csee.uq.edu.au

ABSTRACT

In contemporary radar technology, increasingly complex antennas must maintain a low weight requirement and provide sufficient robustness to a harsh environment. Among many desired features, a high degree of antenna integration and the ability to incorporate the design into a plane's fuselage or wings are of the highest priority. In order to meet such demands, advanced power dividing and phasing networks together with digital signal processors should be located close to the transmitting and receiving antennas preferably in multi-layer architectures. Such architectures put stringent requirements on electrical and mechanical properties of dielectric substrates. This paper presents some results concerning the design and development of multi-layer antenna elements and the associated signal dividing and phasing networks using honeycomb and quartz-fibre composite materials, which are widely used in the aerospace industry.

I. INTRODUCTION

In contemporary radar antenna technology, *smart antennas* have gained a great deal of attention due to their capability of supporting complex functions of radar. Their role is to produce directional beams towards moving or stationary targets using specially developed scanning algorithms. In order to perform the role of "smart beam forming" these antennas require a large number of elements – usually densely packed. For easy deployment, the radiating and processing modules should preferably be accomplished in lightweight highly reliable integrated technology and should be easy to maintain. Thus if any of the sub-modules fail, this technology should allow easy repair, replacement or an adaptive failure correction. These requirements motivate investigations of planar or conformal array technologies to build such antenna systems. Of the many possible planar technologies, the microstrip patch technology seems to be most suitable for the manufacture of radiating layers [1]. For reasons of technological compatibility, the use of multi-layer microstrip technology for the construction of other high frequency components, such as power dividing and phasing networks, is a logical choice.

Although easy to propose, microstrip technology faces challenges in the present application. One problem is that for many of the available substrates electrical properties change excessively when subjected to temperature variations which are unavoidable in airborne radar. One cause is a fast varying environment and the other is the heat from the beamforming modules. In our recent paper [2], classes of available microwave materials have been proposed for a limited set of dielectrics whose electrical parameters are resistant to temperature changes. The purpose of the present paper is to demonstrate the practical use of these materials to develop antenna elements integrated with power dividing/phasing networks for possible use in airborne radar.

II. ANTENNA ELEMENTS

Elements for use in radar antennas should have a number of desirable features: a suitable operational bandwidth, high radiation efficiency and low mutual coupling with other elements in the array. In addition they should feature low-level passive intermodulations, repeatability of transmission characteristics and hence low sensitivity to manufacturing tolerances. Also they should offer suitable means for integration with the associated dividing/phasing networks and polarization switches, which preferably should be conformal to the carrier-platform.

The present study assesses a rectangular antenna element fed by microstrip lines via two orthogonal rectangular apertures as a basic candidate for the airborne array antenna design. The main goal is to establish the feasibility of manufacturing this element using microwave materials with parameters resistant to temperature changes. The two types of materials selected here are the Nomex honeycomb composites and quartz-fiber composites. The former is predominantly air-filled and has electrical properties close to that of air [2]. The quartz-fiber composite material also exhibits ultra stable electrical properties with temperature variations. It has a relative dielectric constant close to 1.7 and a *tanδ* value approaching 0.00045 at room temperature [2]. In our study we decided to use these two selected composite materials in two different combinations to manufacture dual-feed aperture coupled antennas, which can also incorporate a polarization switch.

Fig. 1 depicts the cross-sectional view of the antenna aperture entirely formed by a honeycomb composite material, which is interleaved with conducting patches and the feed network. The individual layers are joined together using a bonding film (*prepreg*). Fig. 2 shows the modification of the patch antenna configuration manufactured with both the quartz-fiber composite and honeycomb composites. In terms of the electrical properties, the two designs differ in dimensions, radiation properties and mutual coupling characteristics.
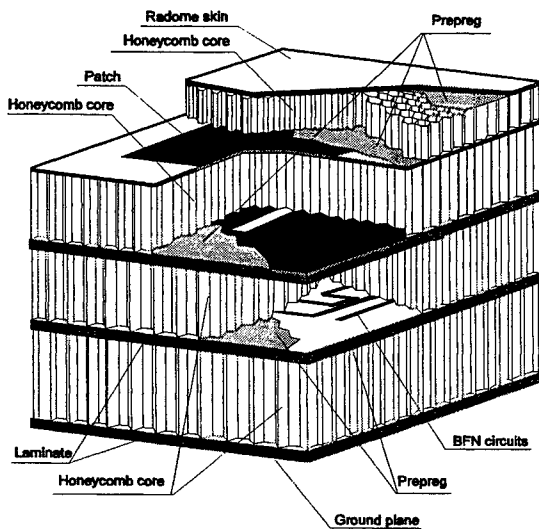
Fig. 1. Generic configuration of a patch antenna integrated with the feeding network in honeycomb composite technology.
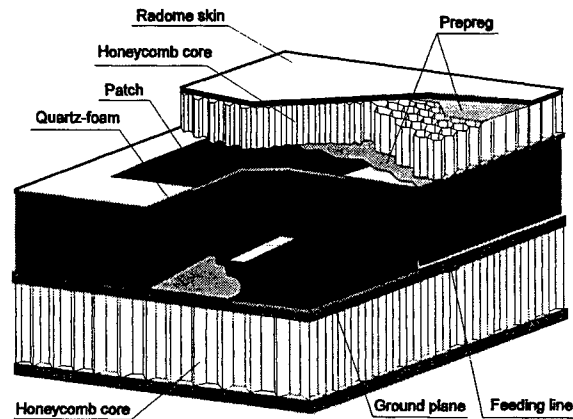
Fig. 2. Generic configuration of a patch antenna using a quartz-fibre composite as the antenna's substrate.

Using the two generic configurations of Fig. 1 and 2, we designed numerous antenna elements in frequency bands from about 1GHz to 2.5GHz. The designs of these antenna elements have been accomplished using Ensemble of Ansoft. Fig. 3 presents the calculated and measured return loss characteristics for the antenna element developed entirely in the honeycomb technology (core

42

thickness 25 mm). The element is dual-polarized and is to operate in the 890 to 960 MHz frequency band. The element does not include radome.
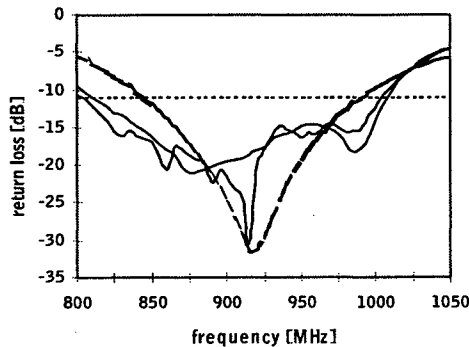
Fig. 3. Calculated (dashed line) and measured (continuous line) return loss characteristics of a dual-polarised antenna element made entirely of honeycomb composites.
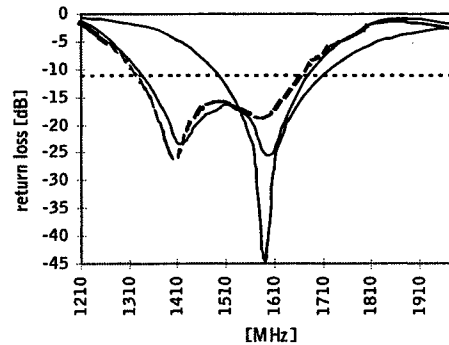
Fig. 4. Calculated and measured return loss characteristics of antenna element made entirely of honeycomb composites (measured data for antenna with radome shown by dashed line).

The comparison between the measured and calculated results shows good agreement. Discrepancies can be due to the short feeding lines used to preserve the compact size of the module. The overall agreement indicates that the performance of the manufactured antenna element with a honeycomb composite is predictable. Calculated and measured characteristics of another element (for operation) in the frequency band from 1530 to 1660 GHz are shown in Figure 4. Also included is the measured return loss of the element with radome made of a 12.7 mm honeycomb core and a polystyrene laminate skin. Again, quite satisfactory agreement between the measured and calculated results is observed confirming the predictability of the design of antenna elements using the mixture of honecomb and quartz-fibre composites. It is worthwhile mentioning that the two elements can be made conformal to curved surfaces.

III. RF SIGNAL DISTRIBUTION NETWORKS

In order to support antenna beamforming, both analogue and digital beamforming networks can be used. In our research we have concentrated on the development of multi-layer directional couplers, power dividers and fixed phase shifters that accomplish these tasks. Cross-sectional views of four configurations (a, b, c, d) of the investigated coupler structures are shown in Fig. 5. Such passive devices are accurately analysed using numerical quasi-static and full-wave analysis methods [3]. A major advantage of the chosen configurations is that the printed circuits can be located on a small-sized rectangular piece of a dielectric material for example a thin polyimide film. This superstrate plate can be firmly fixed onto the main substrate using a suitable bonding film. Thus, the coupler can be manufactured separately, tested and approved independently before mounting onto the antenna, irrespective of how large the antenna beamforming network is.

Fig.5 (e) and (f) present the amplitude and phase characteristics of a 3dB coupler developed using the three-strip configuration (d). The results show that the developed device exhibits almost equal power division over one octave band and that the signal phase difference between the output ports is very close to 90° over a multi-octave band.

In addition to equal power dividers, we also developed non-equal power dividers having considerable asymmetry, as well as couplers featuring high isolation (in the range of 40dB). However, due to space limitation we do not present these results here.
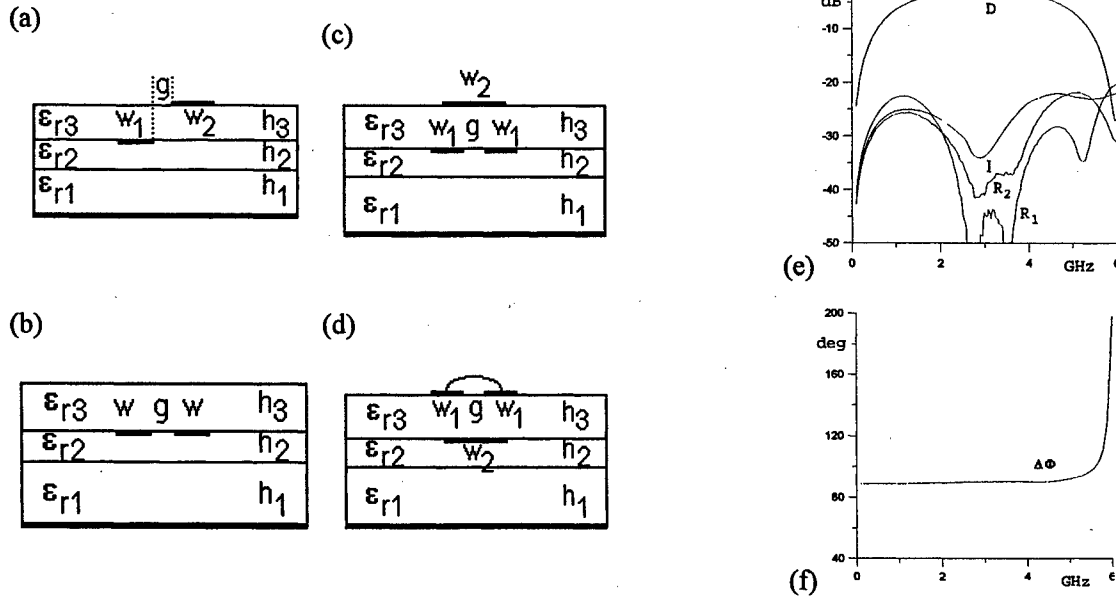
Fig. 5. (a)-(d) Cross-sectional views of the investigated two-, three- and four-strip directional couplers involving stratified dielectrics. (e), (f) - Measured characteristics of a *three-strip* 3 dB directional coupler developed using structure d (C - coupling; D – directivity; I-isolation; R1 and R2 - return loss).

IV. CONCLUSIONS

The design and development of highly integrated antenna modules for airborne radar using multi-layer honeycomb and quartz-fiber composite technologies, which are commonly employed in aerospace industry, has been described. These antenna elements offer easy integration with directional couplers, power dividers and phase shifters. Their robustness to environmental stresses is adequate. The designed associated directional couplers and dividers involving a bi-level structure, exhibit not only a wide operational bandwidth, but also exceptionally good isolation and transmission characteristics. The manufacturing cost of these components is moderate and their integration into large antenna arrays is not labor-intensive. The presented structures should well withstand large temperature drifts due to a varying environment or when down-conversion modules, power supply and control wires are incorporated in close proximity.

REFERENCES

[1] P. Kabacik, A. Sawicki, K. Sachse and G. Jaworski, "An advanced technology of integrating lightweight microstrip arrays", 10th International Symposium on Antennas JINA'98 Symposium, Nice, France, November 17 - 19, 1998.

[2] P. Kabacik and M. Bialkowski, " The temperature dependence of substrate parameters and their effect on microstrip antenna performance", IEEE Trans. on Antennas and Propagation, vol. 47, No. 6, pp. 1042-1049, June 1999.

[3] K. Sachse and A. Sawicki, "Quasi-ideal multilayer 2- and 3-strip directional couplers for monolithic and hybrid MIC", Special Issue on Multilayer Circuits, IEEE Trans. on Microwave Theory and Techniques, vol. 47, No. 9, pp. 1873-1882, Sept. 1999.

The Effects of Nonlinear High Power Amplifiers on Space Based Phased Array Antenna Patterns

Monica Obermier, ARFL, Edward J. Powers
Department of Electrical and Computer Engineering
The University of Texas at Austin, Austin, Texas 78712

Abstract: This paper investigates the effects of intermodulation (IM) distortion produced by the nonlinear high power amplifiers (HPAs) of the space based phased array antenna. Several HPA models are investigated, which include the TWTA, SSPA, an "ideal" HPA which is perfectly linear up to saturation, and a "perfect" HPA which is perfectly linear and experiences no saturation. This paper demonstrates that to achieve the optimal EIRP for a given system, there is a tradeoff between the main beam power loss at a low input backoff (IBO) due to IM distortion and the power loss at a high IBO due to decreased input power.

I. Introduction. As the need for satellite communication systems increases, so does the need for space based active phased array antennas. Each radiating element of an active phased array antenna is preceded by a HPA which produces IM distortion. This IM distortion adds vectorially in the far field to generate IM beams. The location of these IM beams was studied by Sandrin in 1973 [1], and several other studies have recently been done to measure the IM beams produced by personal communication system antennas, such as Globalstar [2]. However, not much work has been done to characterize the degradation in performance of the phased array antenna due to power loss in the main beam directions. As the IBO is decreased, the power is spread from the main beam directions to the IM beams. This power loss changes the directivity, antenna gain, and EIRP of the antenna. The objectives of this paper are to:

- Study the effects of IM distortion on the array factor of a phased array antenna using several different HPA models, including traveling wave tube amplifiers (TWTAs), solid state power amplifiers (SSPAs), an "ideally" linearized HPA, and a "perfect" linear HPA which experiences no saturation.
- Investigate the changes in EIRP for each HPA model.
- Introduce a method to calculate the optimal operating point for the HPAs which will yield the greatest EIRP for a given antenna.
- Introduce the IMAF, which is a way of indicating the severity of the array factor distortion due to HPA nonlinearity.

Section II of this paper will describe the phased array antenna simulation, which will include the HPA and antenna models used for the calculations. The distortion of the array factor will be presented in this section. Section III will discuss the degradation in performance of a phased array antenna due to IM distortion, and EIRP calculations will be presented. The optimal HPA operating point, or IBO, which gives the greatest EIRP will be introduced and the tradeoffs which influence this IBO will be discussed. The focus of this paper is on EIRP, since energy per bit (E_b) is proportional to EIRP, and the probability of error is related to the energy per bit (actually E_b/N_o). The IMAF, which indicates the change of the locations and magnitudes of the beams in the array factor, will be introduced in Section IV. Finally, conclusions will be presented in Section V.

II. Simulation. Active phased array antennas consist of several components. Multiple input beams are fed into a Beam Forming Matrix (BFM), in which the appropriate phases and/or amplitudes are applied to each signal. The BFM has N outputs, each of which leads to a HPA and a radiating element. Because of this architecture, the active phased array antenna has N HPAs, with each HPA contributing to the IM distortion of the array factor of the antenna. Four separate types of HPA models are used for this simulation. The AM/AM and AM/PM functions are shown in Table 1. The AM/AM characteristics are also graphed in Figure 1. Their input and output voltages have been normalized to their corresponding values at saturation. The four models are as follows: the TWTA model proposed by Saleh [3], the SSPA

model used by Bogenfeld [3],the *ideal* amplifier model, and the *perfect* amplifier model. The *ideal* model has a constant gain and is perfectly linear up to saturation. This model was chosen because this is the most linear amplifier that can be achieved in practice. The *perfect* HPA model is perfectly linear until infinity and does not saturate. While this model is only achievable in theory, it presents a good reference for comparison with the other models as it produces no IM distortion.

	TWTA	SSPA	Ideal	Perfect
G(A)	$G(A) = \dfrac{\alpha_1 A}{(1 + \alpha_2 A^2)}$	$G(A) = \dfrac{v_k A}{\left[1 + \left(\dfrac{v_k A}{A_0}\right)^{2pk}\right]^{1/2pk}}$	$G(A) = \begin{cases} vA : A \le A_0 \\ A_0 : A > A_0 \end{cases}$	$G(A) = vA$
Φ(A)	$\Phi(A) = \dfrac{2\Theta_1 A^2}{(1 + \Theta_2 A^2)}$	Φ(A)=0	Φ(A)=0	Φ(A)=0
Variables	$\alpha_1 = 2; \alpha_2 = 1; \Theta_1 = \pi/6; \Theta_2 = 1$	$v_k = 1; A_o = 1; p_k = 2$	N/A	N/A

Table 1: HPA Model Functions and Parameters

For simplicity, a 40 element linear array with λ/3 spacing was used for these simulations. The two inputs are sinusoidal signals at 2 GHz and 2.05 GHz, and the main beam directions are 30° and 60° for these signals respectively, with a third order IM beam of the form 2f2-f1 at 82°. The magnitude of the normalized array factor for this antenna is shown in Figure 2 at 10 dB IBO, where IBO is defined as:

$$IBO = 10\log 10(P_{yi}^{max} / P_y) \quad [dB]$$

The maximum input power of the HPA is denoted as P_{yi}^{max} and P_y is the mean power of the signal at the HPA input. The four traces in Figure 2 represent the same antenna with each separate HPA model discussed above. Each array factor has been normalized to the case of the perfect HPA antenna which experiences no IM distortion. The main beams at 30° and 60° of the perfect HPA antenna have been normalized to unity. It can be seen from Figure 2 that the perfect HPA antenna, the ideal HPA antenna, and the SSPA HPA antenna have array factors which are very similar. By looking at Figure 1 it can be seen that far from saturation these models are very similar, and they therefore should exhibit a similar array factor. The TWTA HPA antenna has main beams with magnitudes that are much larger than the other models. This is due to the higher gain of the TWTA. Also, it can be seen that the IM beam of the TWTA has a larger magnitude. This is due to the increased nonlinearity of the TWTA over the other models. Figure 3 shows the array factor of the same four HPA models at 0 dB IBO. The first thing to notice is the decreased magnitude in the main beam directions for the TWTA, SSPA, and ideal HPA antenna cases. This magnitude is proportional to electric field strength, and the radiated power is proportional to the field strength squared. This decrease in main beam power is due to the distribution of power from the main beams to the IM beams. Figure 3 also shows the growth of the IM beams as the HPAs approach saturation. The following section discusses the degradation in antenna performance due to power loss in the main beam.

III. Effects of IM Distortion on the Performance of a Phased Array Antenna

Several parameters such as antenna gain, directivity, and EIRP are used to measure antenna performance. The gain of an antenna can be calculated as [4]

$$G(\Theta) = eD(\Theta) = \frac{U(\Theta)}{U_o} = \frac{[(AF)]^2}{avg[(AF)]^2}$$

where G(Θ) is the antenna gain, e is the antenna efficiency, D(Θ) is the antenna directivity, U(Θ) is the radiation intensity, Uo is the average value of the radiation intensity, and [(AF)] is the normalized array factor. The EIRP for an antenna can then be written as

$$EIRP = P_T G = N(P_{inHPA})(G_{HPA})G$$

Where P_T is the transmitted power, N is the number of radiating elements, P_{inHPA} is the input power to each HPA, G_{HPA} is the gain of the HPA, and G is the antenna gain. Figure 4 shows the EIRP calculated in the 30° main beam direction for the antenna described in Section II. The EIRP is plotted versus IBO. It can be seen from Figure 4 that the EIRP curves for the antennas which experience IM distortion are convex and experience a maximum EIRP. This is due to the tradeoff between operating the HPAs near saturation which produces IM distortion and operating the HPAs at a high IBO. As seen in the figure, as the HPAs are operated at a high IBO, the EIRP decreases in value due to a decrease in input power to the HPA and consequently a decrease in transmit power. Conversely, near saturation at a low IBO, the EIRP decreases due to a decrease in main beam power as the power is spread to the spurious IM beams. This decrease was illustrated in Section II. There is an optimal operating point for each HPA which yields the maximum EIRP for the antenna. This optimal operating point is about 2.5 dB IBO for the ideal and SSPA models, and about 7 dB IBO for the TWTA model. Another interesting aspect of Figure 4 is the relatively high EIRP values for the TWTA HPA antenna. This again is due to the high gain of the TWTA. Yet while the TWTA has a much higher gain, it is more nonlinear than the other models and this is evident by the sharp decrease in EIRP as the TWTA approaches saturation. The last thing to notice from Figure 4 is that the behavior of the perfect HPA antenna experiences no IM distortion, and therefore the EIRP continues to increase as the IBO is decreased.

IV. IM Factor. The change in EIRP can be attributed to a change in the array factor of the antenna due to intermodulation distortion. A parameter called the IM Factor can be used to demonstrate the variation of the array factor. The array factor produced by an antenna with IM distortion can be thought of as the multiplication of the array factor of the perfect antenna with a IM factor which introduces the IM distortion. The IM factor is a function of both angle and IBO, and can be expressed as:

$$IM\ factor(\Theta, IBO) = (AF_{IM}) / (AF_{perfect})$$

To minimize the effect of IM distortion, both array factors should be equal for all angles, which will yield a IM factor of unity for all angles. Figure 5 shows the IM factor for the SSPA HPA antenna at 10 dB IBO. This IM factor is very close to unity in all directions, which indicates that there is little IM distortion at this IBO. Figure 6 illustrates the IM factor for a TWTA HPA antenna at 0 dB IBO, which is at saturation. This plot is very jagged and has peaks of large magnitudes, which indicates a large difference between the two array factors as a result of the IM distortion. Figures 5 and 6 demonstrate the ability of the IMAF to indicate the severity of the degradation of the array factor due to nonlinearity.

V. Conclusions. This paper presents a way to determine the optimal operating point for the HPAs in a phased array antenna which will provide the maximum EIRP. This paper also demonstrates that when considering several HPA models, the TWTA gives the largest EIRP value for a given system. This illustrates another tradeoff: the nonlinear TWTA model has higher IM beam strengths, yet it has a higher gain and thus has a higher EIRP value. The ideal model, which is linear up to saturation, has lower IM beams but also yields a lower EIRP value. This indicates that when designing the HPAs for the phased array antenna, the requirements of the system (i.e. link budget, IM beam levels) can dictate whether to strive for absolute linearity or high HPA gain.

References
[1] W. A. Sandrin, "Spatial Distribution of Intermodulation Products in Active Phased Array Antennas", *IEEE Transactions on Antennas and Propagation*, November 1973, pp. 864-868.
[2] Riccado De Guadenzi, Amnon Silberger, "Payload Nonlinearity Effects on the Globalstar Forward Link", Proceedings of ICUPC 1997, pp. 311 – 315.
[3] E. Bogenfeld, R. Valentin, K. Metzger, W. Sauer-Greff, "Influence of Nonlinear HPA on Trellis-Coded OFDM for Terrestrial Broadcasting of Digital HDTV", *Globecomm 1993*
[4] C. Balanis, "Antenna Theory", John Wiley and Sons, 1997
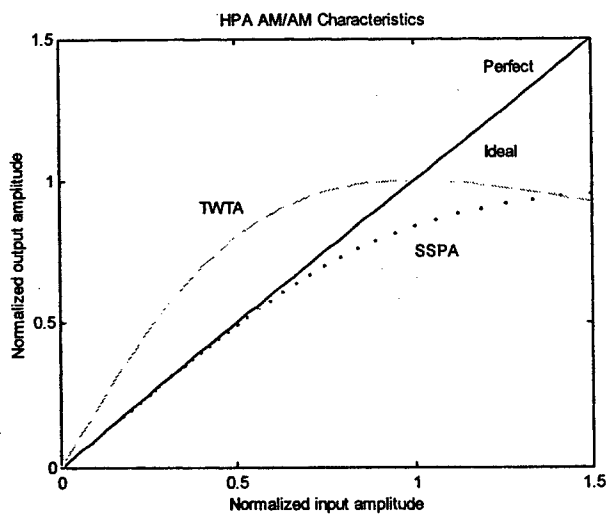
Figure 1: HPA AM/AM Characteristics
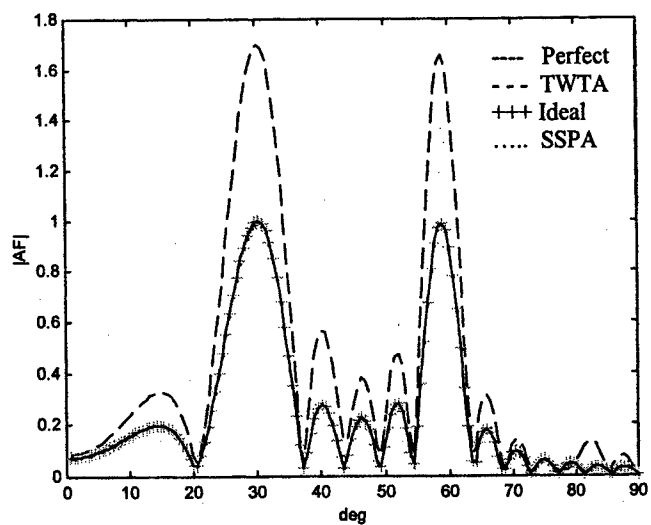
Figure 2: Normalized Array Factor at 10 dB IBO
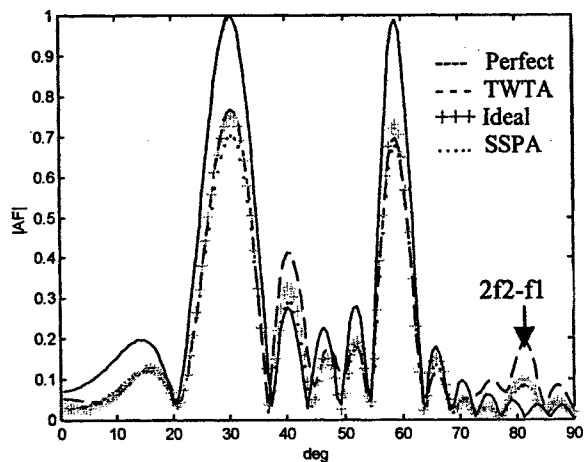
Figure 3: Normalized Array Factor at 0 dB IBO
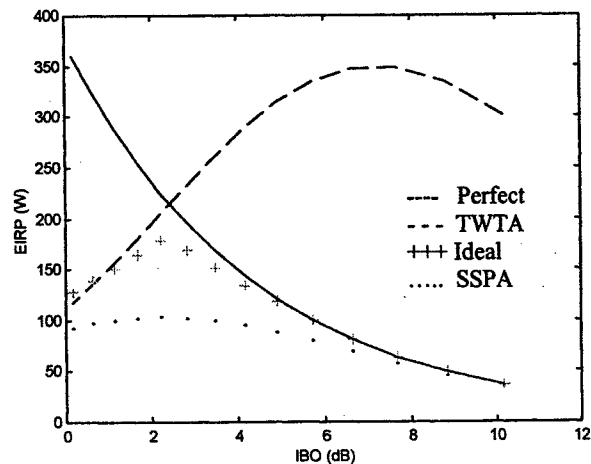
Figure 4: EIRP at 30° vs IBO
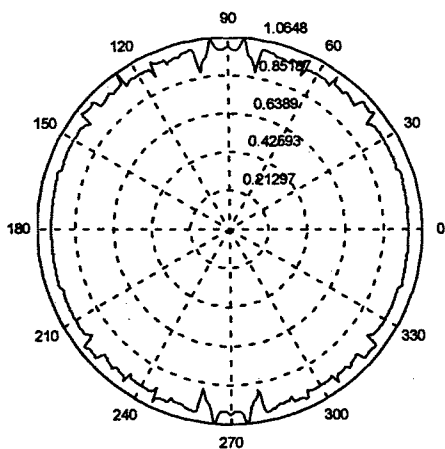
Figure 5: IMAF for the SSPA at 0 dB IBO
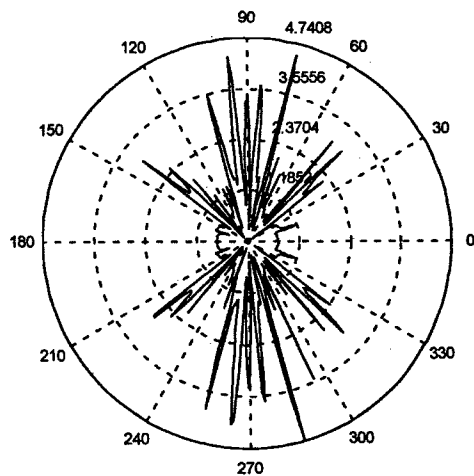
Figure 6: IMAF for the TWTA at 10 dB IBO

Vertically Interconnected 3D Module for Conformal Phased Array Antennas

Bosui Liu, Yu Albert Wang, George Kang, Altan M. Ferendeci, *Misoon Mah
Electrical and Computer Engineering and Computer Science Dept.
University of Cincinnati, Cincinnati, Ohio 45221-0030
Phone: (513) 556-4759, Fax: (513)556-7326
email: aferende@uceng.uc edu
*AFRL, Paterson AFB, OHIO

ABSTRACT

Development of a basic X-band 3DIC/MEMS microwave transmit module has been investigated for the possibility of a *conformal* phased array technology. An innovative approach using the microelectronics and MEMS processing technologies was implemented to develop 3D-IC processing technology. This allows us to investigate technology development needed for minimum module depth to enable distribution on any arbitrary surface. For the initial phase, as a demonstration vehicle, a basic passive transmit module was designed, fabricated and characterized at microwave frequencies.

INTRODUCTION:

Current T/R module technology has a distinct disadvantage because the depth of a typical module is too large compared to its lateral dimensions to be used in a conformal configuration as shown in Figure 1. In order for a module to be universally conformal to any arbitrarily curved surface, the depth of the module must be negligibly small compared to the maximum lateral dimension of the module.

Figure 2 shows various antenna topologies that can provide the technology advancements needed for implementing affordable conformal phased arrays for next generation aircraft and commercial applications. As aerodynamic requirements and lower radar cross section (RCS) requirements of the future aircraft become more demanding, it becomes more difficult to meet the requirements with conventional radome technology. Conformal phased array technology is one possible alternative to meet these requirements. However, the curvature of the particular conformal surfaces and the positional relationships of the radiating elements introduce many problems which are different from those associated with electronically controlled planar arrays. Linear or planar arrays do not have depth restrictions as long as the separation between the modules does not exceed more than $\lambda/2$. If the present day modules are stacked in circular or any arbitrary plane the separation between the antennas will exceed $\lambda/2$ and lead to unwanted lobes. On the other hand, thin modules can be stacked on any arbitrary surface.

Because of these complicated radiating elements and required control circuits, many of these arrays need to have active transmit/receive modules located behind the radiating elements. This demands more compact and efficient microwave and millimeter MCAs. The proposed approach will provide one step in the technical advancement to achieve affordable conformal phased array technology.

In this paper, an innovative vertically interconnected multilayer microwave monolithic (M^3) circuit approach is presented. Various developments of this new technology will allow us to implement vertically interconnected 3D M^3IC for an affordable

conformal phased array antenna development. The proposed development is based on deposition of multiple dielectric and conductor layers including an integral planar antenna. The extensions required for development of major components of the T/R module and the specific areas will be further discussed.

Issues on 3D MODULE

Figure 3 shows the schematic depicting diagram of the 3D module that is being developed for affordable conformal phased array antenna systems.

A substrate such as GaAs or Silicon wafer is used as a substrate. The active devices for a power amplifier are processed on the substrate. Some of the necessary passive circuit elements are also processed on the substrate layer. Then a dielectric layer is deposited followed by the ground metal deposition. A second dielectric layer is then deposited over the ground plane followed by another metal deposition. This metal becomes the circuit plane. The circuit includes passive elements such as the matching and bias networks. Then another dielectric layer is deposited prior to deposition of the upper ground plane. This plane also becomes the lower ground plane of the next circuit layer. A metal/dielectric/metal/dielectric/metal combination constitutes a circuit layer. Prior to processing the subsequent layer various via holes and trenches is then processed to interconnect the circuit elements with different levels.

One of the hurdles to overcome during development is the problem associated with the two ground planes between the previous and subsequent circuits. The two ground planes act as a parallel transmission lines and the signal from one circuit layer to the subsequent layer may not follow the circuit transmission line and tends to leak through the side openings. In order to prevent this, metal side walls are inserted to short all ground planes to the same potential.

Among possible distributed transmission line elements that can be used for 3D-IC circuitry are striplines and CPWs. Currently,

the only element library that can satisfy the 3D circuitry elements is the stripline library. On the other hand, other element libraries, such as CPW is limited with only the top surface open to air or with an air filled metal cover. Therefore, CPW transmission lines with more complicated structures should be reformulated from the conventional structures. Thus extensive development work is needed to build the necessary circuit element libraries for the 3D-IC modules.

This work also incorporates a planar antenna as a radiating element. Various patch and slot antennas are prime candidates for these types of applications.

EXPERIMENTAL WORK

Design, simulations and processing of various sub-circuits were undertaken to provide initial implementation of the various sub-circuits of the 3D-IC.

a) ANTENNA

Figure 4 shows the perspective and the top view of the cavity-backed slot antenna. A design frequency of 13 GHz was chosen.

ANTENNA CAVITY

As shown in Figure 4, a cavity was created between the top and bottom ground planes by building four vertical metal walls in the dielectric layers. The field distribution in the slot was dependent on the excitation of higher cavity modes. Since the whole cavity is very thin, the depth of the cavity (44 μm) was much less than one half of the guide wavelength (λ_g) at 13GHz. With the cavity's depth of 44 μm, the closest higher order mode was then TM_{120} that resonates at 13.27GHz.

ANTENNA STRIPLINE OFFSET-FED SLOT

The slot antenna was fed by a 50 Ohm stripline. The stripline was short-circuited at one of the metal side walls. In the initial design, no matching elements were used.

The input impedance of the cavity backed slot antenna was measured using HP 8510 network analyzer. The measured input impedance of the antenna is shown in Figure 5. The magnitude of S_{11} was -42.9dB at 13.35GHz. EM simulation of the cavity and slot using Ansoft HFSS predicted -8.7dB of S11 at 14.36GHz with no significant insertion loss.

b) INTERMEDIATE LAYER T/R SWITCH

Contrary to the conventional MEMS type microwave switches, spin-coated polyimide was used in place of silicon as a supporting dielectric substrate. Micromachined switch and the coplanar waveguide were sandwiched between two 30μm polyimide layers. A bottom and a top ground planes were used to shield the switch layer from interference with other layers.

The movable part of the switch consisted of a 2μm thick rectangular Au plate with four serpentine beams attached at each corner. Four electroplated Au posts were used to raise it 5 μm above the CPW. Beam width was chosen to be 4μm so that the top plate can be easily pulled down with relatively low voltage while providing the necessary mechanical strength. Other parameters such as the switch metal plate length, serpentine beam length, and coplanar waveguide center strip width were optimized. Figure 6 shows the top view of the processed switch with perforated top plate.

c) PROCESSING:

An innovative combination of the microelectronics and MEMS processing technologies was implemented for 3D-IC processing development.

- Dielectric deposition: Polyimide is used for the dielectric material. It was spin coated followed by soft and hard cures. With multiple depositions, up to 70 μm thick layers were obtained.

- Metal deposition: Cr/Au/Cr was used for the metal layers deposition. Initially Cr/Au was sputtered. Using electrodeposition, the thickness was increased to 2μm. Then it was followed by Au/Cr sputtering.

- Vertical posts and trenches: RIE was performed using an $O_2/CF_4/Ar$ gas mixture. The flow rates were varied to determine the etch rate of polyimide. Au was used as a mask for RIE.

CONCLUSIONS:

A new technology is being developed to implement a vertically interconnected 3D module for affordable conformal phased array antenna technology development. Initial design, simulation and processing steps were taken to realize some of the essential sub-circuits of the module.

REFERENCES:

[1] Altan M. Ferendeci, Bosui Liu, Ho Huang, Misoon Mah, and Lee Liou, "3D Multilayer Monolithic Microwave (M^3) Passive Transmitter Module," IEEE MTT-S Digest, 445-48(1999).

[2] Warren L. Stutzman, Gary A. Thiele, *Antenna Theory and Design*. 2nd Edition, New York John Wiley & Sons, Inc. c1998.

[3] C. Goldsmith, T-H. Lin, B. Powers, W-R. Wu, and B., Norvell, "Micromechanical Membrane Switches for Microwave application", IEEE MTT-S Digest 1995, pp91~94
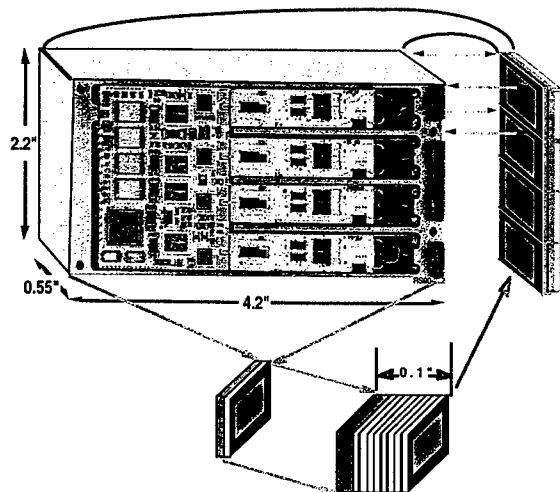
Figure 1. Present day quad phased array module and the future 3D-IC module.
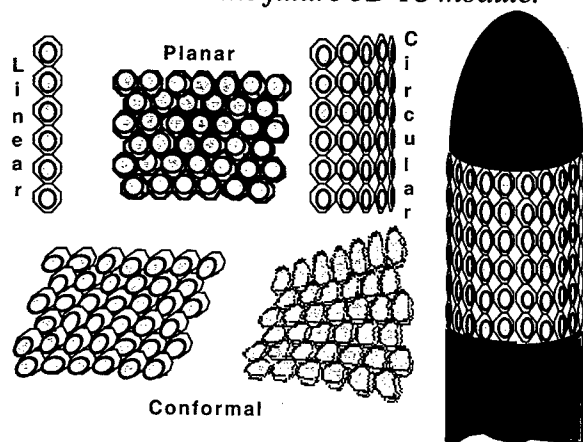
Figure 2. Various topologies for phased array antenna systems.
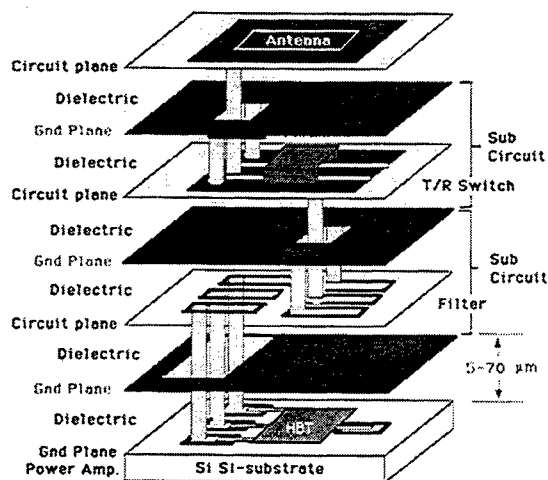
Figure 3. Vertically interconnected 3D passive transmitter module.
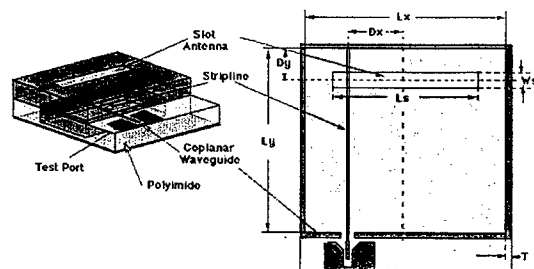
Figure 4. Cavity backed slot antenna.
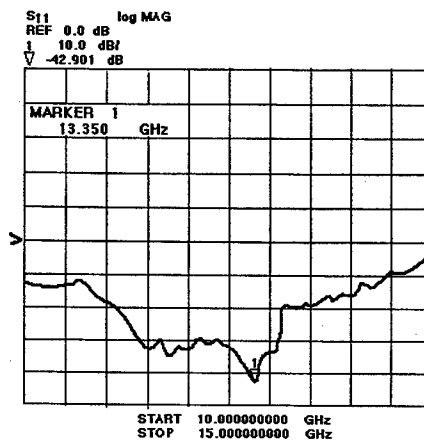
Figure 5. Measured S_{11} of the cavity backed slot antenna.
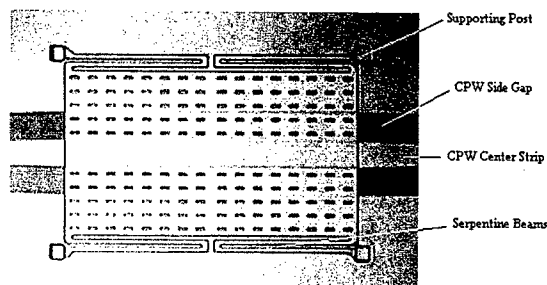
Figure 6. Processed MEMS RF switch with a CPW line and perforated upper plate.

Low-Loss Phase Shifters for Ka Band Phased Array

Alexander E. Martynyuk, Yuri K. Sidoruk*

Division de Ingenieria Electrica, Facultad de Ingenieria, Universidad Nacional Autonoma de Mexico, Cd.
Universitaria, Coyoacan, C.P. 04510, Mexico, D.F.,Mexico
*Kiev Polytechnic Institute, Radioengineering Faculty, Department of Theoretical Grounds of Radioengineering,
Kiev-252137, Kiev, Ukraine

Abstract – Results of the investigation of polarization reflective phase shifters are presented. It is proved that application of the polarization principle of phase changing results in effective fast low loss phase shifters. It is shown that insertion loss level less than 1dB can be achieved in Ka band. Peak phase errors were reduced to 5 degrees, and observed switching time was in the nanosecond range.

Introduction

Rapid development of Ka-band satellite communication systems causes a growing interest to the research works in the area of Ka-band phased arrays. However, one of the main obstacles that delays the design of the millimeter-wave phased arrays is the absence of the fast low-loss phase shifters.

We have investigated the possibility of the design of reflective phase shifter based on the polarization principle of phase changing. Firstly this principle was applied by Fox [1], when the mechanical phase changer was developed. According to the mentioned principle, the mechanical rotation of the differential 180-degree phase section results in the additional phase shift in the circularly polarized wave traveling through mentioned section. Polarization principle of phase changing has such advantages as small phase errors and low level of accompyining amplitude modulation. Application of the electronic simulation of mechanical rotation resulted also in the successful design of the spyraphase reflective phased array [2].

We propose a new design of reflective polarization phase shifter. Special design of the phase shifter permits to achieve the optimal transformation of the p-i-n diode impedance. Therefore, the insertion loss level can be reduced significantly. Earlier, the proposed approach resulted in the successful design of the amplitude phase modulator [3].

Phase shifter design

Polarization phase shifter is realized as a special control diaphragm, installed in the cross-section of the circular waveguide terminated in a short circuit (Fig. 1). The presence of the control diaphragm causes the difference in the reflection conditions for two orthogonal components of the incident circularly polarized wave. Therefore, the orthogonal components of the incident wave are reflected from the control diaphragm with the different reflection coefficients Γ_{II} and $\Gamma_{\perp}$. For this case, the electric field of the incident wave ($\vec{E}_i$) and the electric field of the reflected wave ($\vec{E}_r$) can be expressed as follows:

$$\vec{E}_i = E_0 \left(\vec{e}_x + j\vec{e}_y\right)e^{-j\beta z}$$
$$\vec{E}_r = 0.5 E_0 e^{2j\gamma} \left(\Gamma_{II} - \Gamma_{\perp}\right)\left(\vec{e}_x - j\vec{e}_y\right)e^{j\beta z} + 0.5 E_0 \left(\Gamma_{II} + \Gamma_{\perp}\right)\left(\vec{e}_x + j\vec{e}_y\right)e^{j\beta z} \tag{1}$$

where E_0 is the magnitude of the incident wave, $\vec{e}_x$ and $\vec{e}_y$ are the unit vectors in the directions $\vec{x}$ and $\vec{y}$ respectively, β is the propagation constant, $j = \sqrt{(-1)}$, γ is the angle that determines the angular position of the control diaphragm (Fig. 1).

According to (1), the reflected wave is divided in two components. The first component is a circularly polarized wave with the same direction of rotation of electric field vector as compared to $\vec{E}_i$. The phase of

this component is determined by the angle γ. The second component is the circularly polarized wave with the opposite direction of rotation as compared to $\vec{E}_i$. It is impossible to control the phase of this wave. When

$$\Gamma_\perp = -\Gamma_{II}, \tag{2}$$

the magnitude of the second component of the reflected wave is zero. One can control the phase of reflected wave by changing angle γ. Hence, the mechanical rotation of the control diaphragm leads to the appearance of additional phase shift in the reflected wave. This phase shift is equal to 2γ.

The velocity of mechanical rotation is not sufficient for the phased array applications. Therefore, the electronic simulation of mechanical rotation should be used [2]. We need to situate switching elements (p-i-n diodes) on the surface of control diaphragm. Switching of these diodes should be equivalent to the mechanical rotation of the control diaphragm.

Design of the Control Diaphragm

Two designs of the control diaphragm were proposed and investigated. According to the first design, the control diaphragm of one-bit phase shifter consists of a ring slot resonator 1, two radial inductive stubs 2 and 3 and two p-i-n diodes 4 and 5 connected in parallel to the radial stubs (Fig. 2). At any time, one p-i-n diode is switched on and one is switched off.

The control diaphragm operates in the following way. Assume that diode 4 situated at stub 2 is switched-off. Hence, stub 3 is shorted by the switched-on diode and can not be excited. In this case, the control diaphragm is equivalent to the ring slot resonator for the vertical component of the incident wave because stub 2 can not be excited by mentioned component. The parallel resonance of the control diaphragm occurs when the average diameter of the ring slot resonator is approximately equal to λ/π, where λ is the wavelength. At the resonant frequency, the control diaphragm is transparent with respect to the vertical component of the incident wave. Therefore, no-load condition is assured in the plane of the control diaphragm for the vertical component when the metal wall is placed at the distance of $\lambda/4$ from the control diaphragm.

The control diaphragm reflects a horizontal component of the incident wave in the different manner. This horizontal component excites stub 2, where switched-off diode 4 is situated. In this case, the series resonance occurs because of the series connection of the capacitance of switched-off diode 4 and the inductance of the outer metal ring 7 (Fig.2). At the resonant frequency, the control diaphragm reflects the horizontal component of the incident wave with the reflection coefficient that is approximately equal to -1. It is possible to change the frequency of the series resonance by changing the length of radial stub 2. When the frequency of series resonance becomes equal to the frequency of the parallel resonance; additional differential phase shift of 180 degrees appears between the orthogonal components of the reflected wave. This is equal to the fulfillment of condition (2), when the insertion loss in the p-i-n diodes is neglected. Furthermore, switching of the p-i-n diodes is equivalent to the rotation of control diaphragm on the angle of 90 degrees. Hence, one-digit phase shifter has been realized.

The control diaphragm of M-bit phase shifter should contain 2^M radial inductive stubs with the diodes installed in each stub. At any time, one diode is switched off and $2^M - 1$ diodes are switched on. The principle of operation is the same, but now it is possible to simulate the mechanical rotation on the angles $n\pi/2^M$, where $n = 0,1,2...2^M - 1$. As a result, corresponding phase shifts appear in the reflected circularly polarized wave.

The fulfillment of the condition (2) is more difficult when the insertion loss in the p-i-n diodes are taken into account. For this case, only the optimal transformation of the diode impedance leads to the fulfillment of (2). It was proved [3] that the proper choice of the width w of ring slot resonator 1 (Fig. 2) assures mentioned optimal transformation.

The second design of the control diaphragm is shown in fig. 3. The absence of the central metal circle 6 is the unique difference from the design described above. The frequency of the series resonance does not change when the central metal circle is removed. However, the distance between the control diaphragm and the metal wall should be more than $\lambda/4$ in order to compensate the inductive reactance of the metal ring 7. In this case, the optimal transformation can be achieved by the correct choice of the diameter of the metal ring. In both cases all switching diodes and bias circuits are arranged in a unique plane. Therefore, planar technologies can be applied during the fabrication process.

Fabrication and performance
The two bit phase shifter had been fabricated using the first design of the control diaphragm. The control diaphragm was printed on the microfiber reinforced PTFE substrate. In the 29.3-31.9 GHz frequency range, experimentally observed insertion loss were less than 1dB. The minimum insertion loss was 0.75dB. The peak phase error was less than 15 degrees in the mentioned frequency band. This phase error appeared because of the 10% spread in the values of capacitance of the switched-off p-i-n diodes. Accompanying amplitude modulation was less than 0.2dB. Measured switching time was less than 50 ns.

Then the two-bit phase shifter that used the second design of the control diaphragm was built. Special technology, proposed by Dr. Skachko [4] was used to fabricate bias circuits. In the 36-38 GHz frequency band, measured insertion loss was less than 1dB. The minimal insertion loss was less then 0.6 dB. Peak phase errors of 15 degrees were observed. These phase errors can be attributed to the 15% spread in the capacitance of the switched-off diodes. Theoretical predictions [3] indicate that this phase shifter can handle up to 2.5 W of continuos microwave power.

Finally, it is useful to mention the results of experimental investigation of the amplitude-phase modulator [3]. The main element of the modulator was the three-bit phase shifter that used the first design of control diaphragm. The separation of the diodes according to it capacitance and the stub tuning were used to reduce phase errors. As a result, measured maximum phase errors were reduced to 5 degrees in the 36-37.5 GHz frequency range. Insertion loss of the phase shifter was less than 1dB in the mentioned frequency range, while amplitude imbalance between two different phase conditions was less than 0.3dB. Switching time less than 35ns was achieved. This phase shifter was able to operate under the 400mW of continuous microwave power without any significant change of performance.

Conclusions
The new design of the Ka band phase shifters is presented. Fabricated phase shifters demonstrated insertion loss level less than 1dB. With the special measures applied, the peak phase errors were reduced to 5 degrees while accompanying amplitude modulation was less than 0.3 dB. These phase shifters are suitable for the usage in the passive reflective phased arrays due to the fast and accurate performance.

References
[1] Fox, "An Adjustable Waveguide Phase Changer," *PIRE*, vol. 35, no. 12, pp. 1489-1498, Dec. 1947.
[2] H. Phelan, "Spyraphase-a New, Low-Cost, Lightweight Phase Array. Part 1. Theory and Concept," *Microwave Journal*, vol. 19, no. 12, pp. 41-44, Dec. 1976
[3] Martynyuk, N.Martynyuk, S. Khotiaintsev, V. Vountesmeri, "Millimeter-Wave Amplitude-Phase Modulator," *IEEE Transactions on Microwave Theory and Techniques*, vol. MTT-45, no. 6, pp. 911-917, June 1997.
[4] Chenakin, V. Skachko, A. Martynyuk, "A New Hybrid Technology for Millimeter-Wave Integrated Circuits," *1997 IEEE-MTT-S International Microwave Symposium Digest*, pp. 921-924.
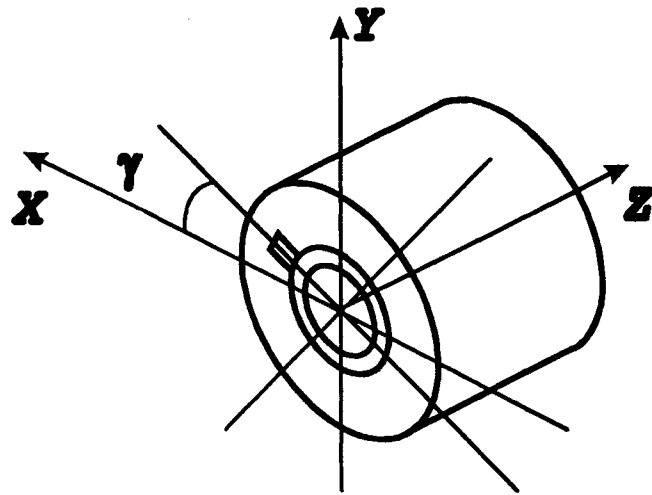
Fig.1. Design of the polarization reflective phase shifter
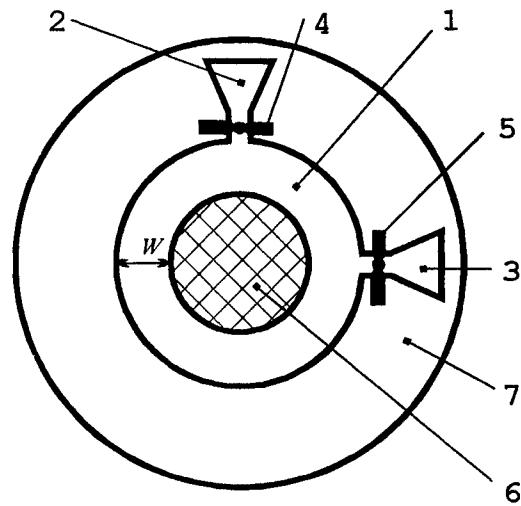
Fig.2. The first design of the control diaphragm (one-bit phase shifter is assumed)
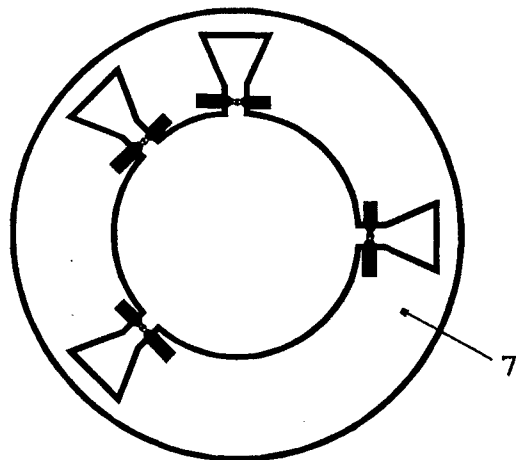
Fig.3. The second design of the control diaphragm (two-bit phase shifter is assumed)

MA3

Phased Arrays for Mobile Communications

Phased Arrays for Mobile Communications

Antenna Design Considerations for High-Speed Millimeter-Wave Wireless/Mobile Access Systems

Hiroyo Ogawa[1], Hiroyuki Tsuji[1], Mitsuru Hirakawa[2], and Yoji Okada[2]

[1]Communications Research Laboratory, M.P.T. Japan
[2]Sumitomo Electric Industries, Ltd., Japan
3-4, Hikarino-oka, Yokosuka, 239-0847 Japan

ABSTRACT

In this paper, we mention the array antennas and the directional antennas, which are designed for millimeter wave band, to realize high-speed wireless access systems between base stations and mobiles. We also describe a view of the proposed system and design the channel models between the base station and the mobile. Finally, we show the characteristics of the antennas.

INTRODUCTION

A great interest of high-speed wireless access communication systems has been growing because of a need of large-capacity wireless access systems [1][2]. We have been investigating the technical feasibility of the system which realizes high-speed wireless access systems between the base station (BS) and the high-speed mobile terminals. The millimeter-wave (MMW) band spectrum should be employed in the system because of the congestion at lower frequencies, the available wide bandwidth, and the compactness of antenna and radio components [3]. However, the MMW is characterized by obstruction by buildings and other structures and by transmission loss in air [4]. To overcome these problems and extract the advantages of the MMW band, we have proposed a concept of a new MMW system, as shown in Fig.1, in which the distance between the base station and the mobile terminal is shorter than that of the other microwave mobile systems [5]. In this system, each base station has array antennas to track mobile terminals and provide the maximum gain to the desired signal direction and suppress the interference from the other terminal. Moreover, the radio-on-fiber technique is introduced to simplify and miniaturize the equipment of the base station. In this technique, the base stations are connected to the control station via optical fiber. Furthermore, by using the optical wavelength division multiplexing subcarrier (WDMSC) transmission, the control station can directly manage the array antenna of the base stations.

In this paper, we propose new cell configurations for MMW access systems which can transmit high-speed data signals to the mobile terminals. Then the most suitable antenna configurations for these cell configurations will be proposed. We also clarify the specifications of the antennas to establish communications between the BS and mobile terminals. Finally, the experimental results of each antenn developed by our study will be discussed.
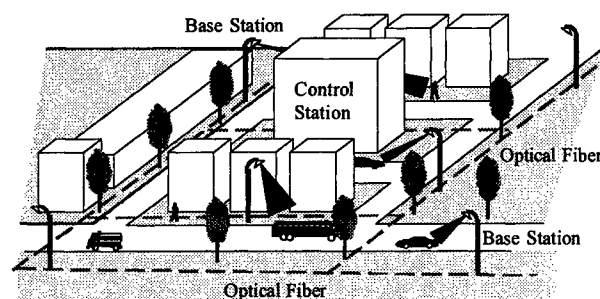
Figure 1. System Overview

ANTENNA CONFIGURATIONS FOR MMW ACCESS SYSTEMS

A. Antenna Design Considerations

First let us consider the specifications of the antenna design. In the system we proposed here, the transmission between the base station and mobile terminal will be characterized by a line-of-sight propagation path and multipath propagation. However, for simplicity, we consider a single line-of-sight propagation path to design the antennas. We assume the following conditions to design the antennas for the base station.

● The free space propagation model is used.
● The center frequency of signal is 59.5 GHz.
● The transmitted power is 10 dBm.
● The maximal separation distance between BS and mobile is 50 m
● Carrier-to-noise ratio (CNR) is required to be at least 15 dB.
● The bandwidth of the channel is 50 MHz.
● Noise figure (NF) is 10 dB.

The CNR is defined as

$$\mathrm{CNR} = P_T + G_T + L_{free} + G_R - N_P$$

where P_T is the transmitted power, G_T is the transmitter antenna gain, G_R is the receiver antenna gain, N_P is the noise power which is calculated at -87 dBm when $NF = 10$ dB. Using these parameters, the cell configurations of the MMW access systems have to be considered.

Two cell configurations, as shown in Fig.2, are proposed here. One is a single-side-radiation system, which covers the area of the left (or right) side of the BS. The other is a both-side-radiation system, which covers the both sides of the BS. These two systems have the following characteristics:

The single-side-radiation system:
● The propagation distance is longer.
● The efficient utilization of the signal power
● The influence of multipath signals may increase.

The both-sides-radiation system:
● The propagation distance is shorter.
● The probability of intercept is lower.
● The electric field strength at both sides is low.
● The antenna beam at the mobile should be changed when the mobile passes under the BS.

(a) Single-Side-Radiation System

(b) Both-Side-Radiation System
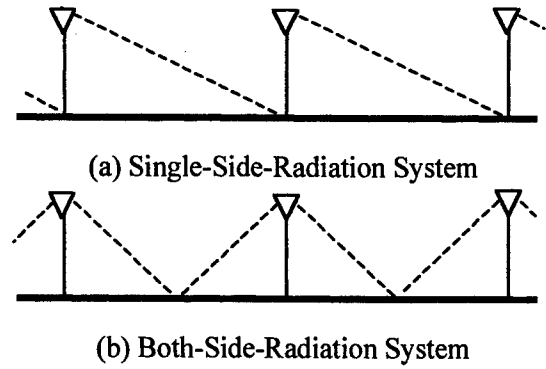
Figure 2. Cell Configuration of Each System

Let us consider the requirements of the BS antenna. We assume the patch antenna with a gain 5.74 dBi is used at the mobile terminal. First we consider the case of the single-side-radiation system. Fig. 3 shows the calculation results of the CNR of the single-side-radiation system using a cosecant-beam antenna whose direction of boresight is $80°$ and beam width is $20°$, and a patch antenna whose direction of boresight is $50°$. and beam width is $80°$. These results reveal that at least two antenna beams are required at the BS to obtain the CNR at 15 dB. Moreover, the antenna gain is required about 18 dBi when the mobile is at the end of the cell. The usage of array antennas seems to be ideal for tracking the mobile terminals and beamforming the BS antenna in our system. However, the array antenna with several elements cannot obtain enough gain when

(b) Boresight=80°, Beam width=20°

Boresight=70°, Beam width=80°

(a) Boresight =50°, Beam width=80°

(a) Boresight=50°, Beam width=80°

(b) Boresight=80°, Beam width=20°
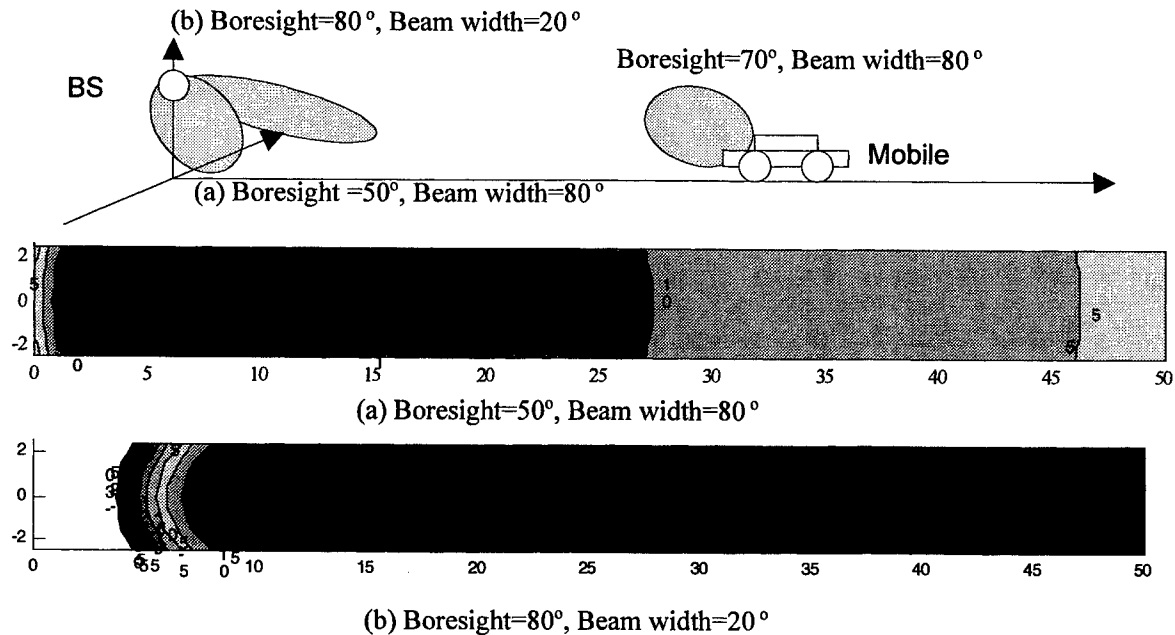
Figure 3 Calculated CNR by two beam patterns at the BS

the mobile terminal is at the far distance from the BS. As shown in Fig.3, the multibeam antenna which consists of the patch and cosecant antennas can realize the single-side-radiation system. In general, the cosecant antenna is suitable for making a narrow beam, while a patch antenna is good for making a wide beam.

Next, consider the case of both-side-radiation system, the angle of the antenna beam should be smaller than that in the previous case because the propagation distance is shorter. For example, the antenna beam with the boresight of 70° and beamwidth of 60° can obtain the CNR=15 dB at the both sides of the cell. Therefore, an array antenna seems to be suitable for both-side-radiation system.

Table 1 summarizes the relation ship between the systems and the antenna configurations. As for the antenna for mobile terminals, it should be compact and simple. The patch antenna ca be considered as one of candidates.

	Single-Side Radiation System	Both-Side Radiation System
Base Station	Cosecant & Patch Antenna	Array Antenna
Mobile Terminal	Patch Antenna	

Table 1 Antenna Structures for Base Station and Mobile Terminal

B. Millimeter-Wave Cosecant-Beam Antenna for Single-Side-Radiation System

The cosecant-beam antenna is made of aluminum which is polished mechnically. The external view of the antenna is shown in Fig.4. Fig.5 showns the experimetal results as well as the theory. The high gain characteristics have been
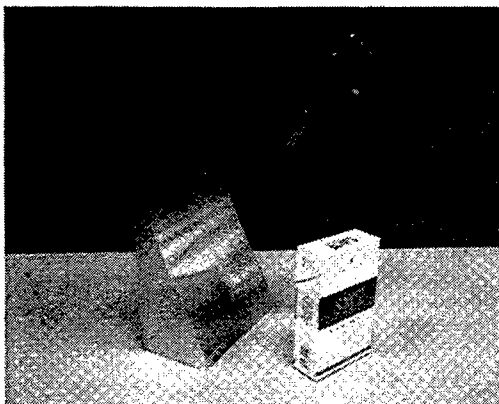
Figure 4. Cosecant-Beam Antenna Structure

achieved at the direction of boresight of 80°. Therefore, the combination of the cosecant-beam antenna and the patch antenna can make the single-side-radiation antenna pattern.
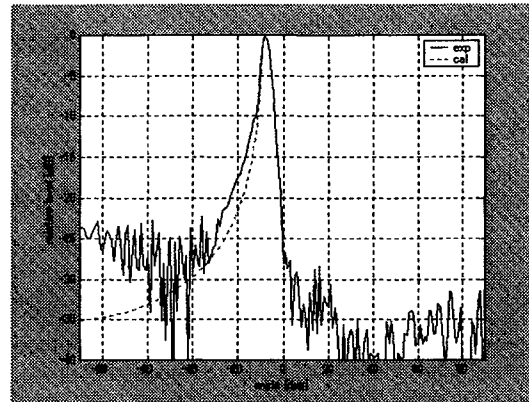
Figure 5. Radiation Patern of Cosecant-Beam Antenna

C. Millimeter-Wave Array Antenna for Both-Side-Radiation System

In the introduction, we mentioned that the BS can estimate the location of the mobile to make a antenna beam toward the mobile. We have already proposed a tracking method and developed a real-time processing unit [6]. According to our study, we realize that the direction of arrival of the signal from the mobile can be estimated precisely using 4-element array antenna and the tracking algorithm [7].

The making of an array antenna at MMW requires great skill because the frequency of MMW is extremely high. We developed an array antenna that applied a microstrip antenna (MSA) as the antenna element. Since a directivity of a MSA is generally wide, it has no trouble to steer the main beam when used as an array antenna. In addition, an MSA is manufactured by using the photolithographic etching technology, and so it can easily build an array antenna with interelement spacing of a half-wavelength.

The array antenna we developed has a multi layer structure, shown in Fig. 6. This type of MSA is called an "electromagnetically-coupled microstrip antenna" or a "proximity-coupled microstrip antenna." The center frequency of this antenna is 59.5 GHz. This antenna has a 4-element linear array of rectangular patch antennas with uniform interelement spacing of a half-wavelength. To make the mutual coupling between the elements equal, parasitic elements are placed at both ends of the array. The radiating patch is fed by a feed

line in the middle layer and excited by the interaction between the radiation patch and the feed line. Although different substrates can be used on the radiating patch side and the ground plane side of this type of antenna, the same substrate is used on both sides.

The actual beam patterns of the array antenna are shown in Fig. 7 when the phase difference between element is set at 0 and 120 degrees. A good agreement between the experimetal results and the calculations has been obtained.
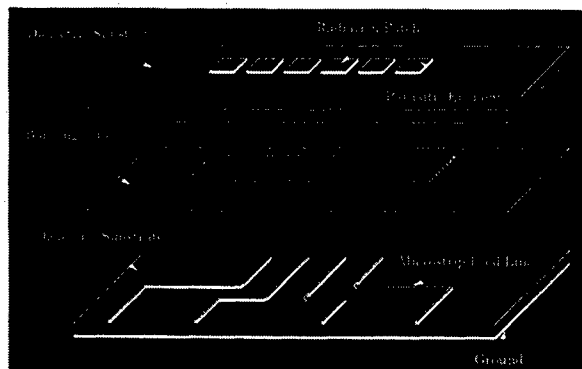
Figure 6. Structure of Proximity-Coupled Microstrip Array Antenna.

CONCLUSION

The antennas of the base station for millimeter-wave wireless/mobile access systems have been discussed. Two cell configurations, the single-side-radiation and the both-side-radiation systems are proposed for the MMW access systems. The requirement of the cosecant-beam antenna the array antenna has been discussed. The results described in this paper will be used for designing the base station for the MMW access systems.

Figure 7. Beam Pattern of Proximity-Coupled Microstrip Array Antenna.

REFERENCES

[1] "Introduction To Mobile and Wireless ATM," *IEEE Communications Magazine*, vol. 35, no.11, Nov. 1997.

[2] "Wireless ATM," *IEEE Personal Communications*, vol. 3, no. 4, Aug. 1996.

[3] M. Umehira, M. Nakura, H. Sato and A. Hashimoto, "ATM Wireless Access for Mobile Multimedia: Concept and Architecture," *IEEE Personal Communications*, vol. 3, no. 5, Oct. 1996.

[4] A. Plattner, "Technology and Demonstrator of the RACE Project 'Mobile Broadband System'," *1994 IEEE MTT-S Digest*, paper WEID-4, pp. 639-642.

[5] Y. Okada, H. Tsuji, H. Kagiwada, and A. Sano, "Millimeter-wave broadband wireless access system with tracking technology of moving targets," in Proc. 1998 IEEE VTC Conf.,Ottawa, 1998, pp. 2057-2061.

[6] Y. Okada, H. Tsuji, S. Yoshimoto, H. Kagiwada, and A. Sano, "Tracking Method of Moving Targets for Millimeter-Wave Multimedia Mobile Access Communications System," *Technical Report of IEICE*, vol. RCS97, no. 194, pp. 83-88, 1997.

[7] H. Kagiwada, H. Ohmori, and A. Sano, "A recursive algorithm for tracking DOA's of moving targets by using linear approximations," IEICE Trans. Fundamentals, vol. E-81A, 1998.

[8] S. Komaki and E. Ogawa, "Trends of Fiber-Optic Microcellular Radio Communication Networks," *IEICE Trans. Electron.*, vol. E-79C, no. 1, pp. 98-104, Jan. 1996.

[9] N. Ohmi, M, Hirakawa, Y. Okada, H. Tsuji, and S. Yoshimoto, "Measurement of the Array Antenna for Millimeter-Wave Multimedia Mobile Access Communication System," *IEICE Soc. Conf.*, B-5-131, Japan, 1997.

ANTENNA DIVERSITY ARRAY DESIGN FOR MOBILE COMMUNICATION SYSTEMS

Juha Juntunen, Keijo Nikoskinen, Kari Heiska*
Helsinki University of Technology
Electromagnetics laboratory
P.O. Box 3000, FIN-02015 HUT, Finland
email: Juha.Juntunen@hut.fi, Keijo.Nikoskinen@hut.fi
tel: +358-9-451-2260, fax: +358-9-451-2267

* Nokia Networks, P.O. Box 300, FIN-00045 NOKIA GROUP, Finland
email: Kari.Heiska@nokia.com

Diversity reception is a technique in radio communications to provide better spectrum efficiency with a cost of an extra set of antennas. The basic requirement of antenna diversity is to have more than one way to receive incoming electromagnetic waves provided usually by a multi-element antenna configuration. The reception modes should be as uncorrelated as possible since the received signal to interference ratio can be optimized in basis of the correlation properties of the signals. A well known example of the antenna diversity usage is the reduction of signal fading in multi-path environments such as downtown areas in large cities or indoor environments. Antenna diversity in its various forms and implementation techniques is found to be a very useful and cost-effective addition to many narrow bandwidth TDMA/FDMA-systems, as well as low-chiprate CDMA-systems. Applications of diversity reception include for instance cellular phone networks and wireless local area networks (WLAN).
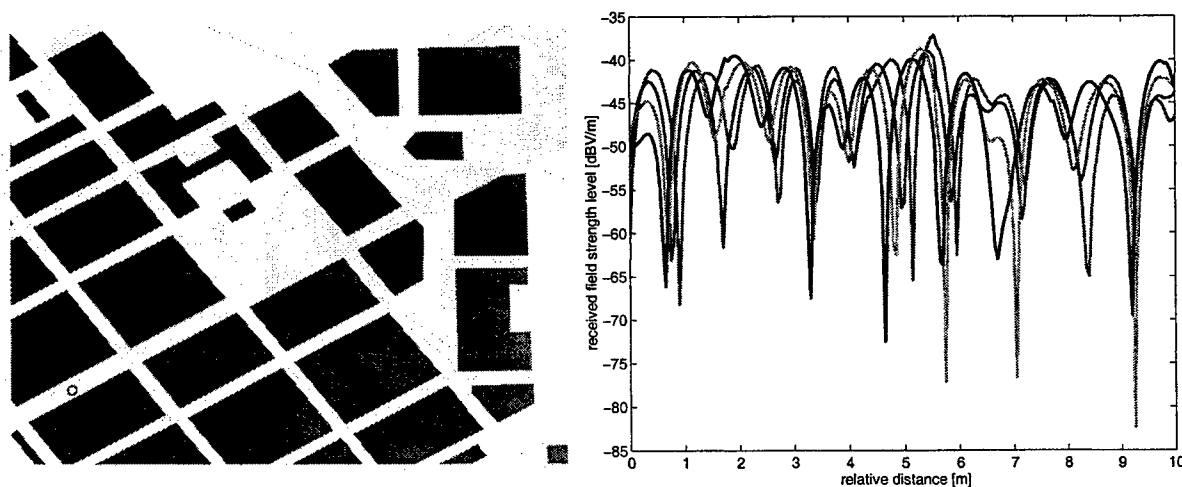
Figure 1: The simulated microcellular environment and an example of the received signals as a function of distance.

The operation of antenna arrays and its radiation properties are generally understood in the form of power patterns. Likewise, one approach to produce uncorrelated reception modes with

antenna arrays is to create uncorrelated power patterns. However, array antennas inherently also have the possibility to vary their phase characteristics ie. the phase pattern [1]-[3]. This is another and quite opposite approach in utilizing array antennas and the antenna diversity concept.
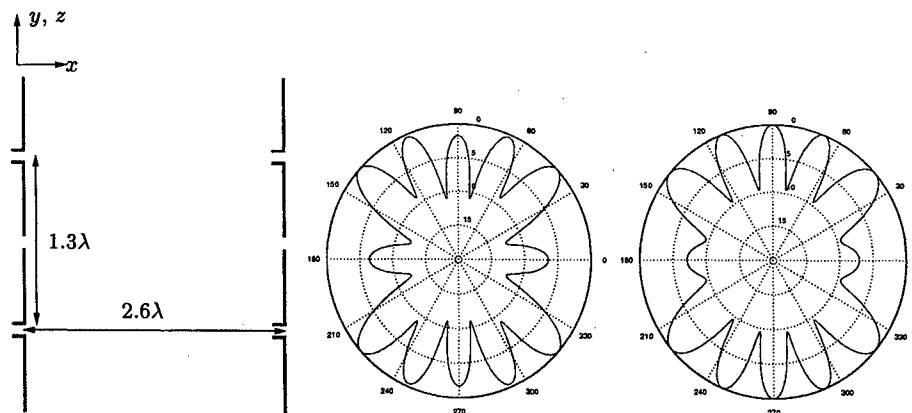
Figure 2: 2-dimensional diversity array and horizontal plane antenna patterns for both horizontal and vertical alignments of the array.

An antenna pattern synthesis method is introduced, which results in exactly the same power pattern but disssimilar phase patterns for the array. The theory of the pattern synthesis is rather general and can be applied for linear, planar or 3-dimensional array pattern design. The antenna patterns provided by the synthesis method can be applied in diversity reception while the dissimilar phase patterns offer uncorrelated signals to be utilized in reducing destructive interference. The antenna diversity would therefore be implemented in selection combining between the different antenna pattern excitation and thus fulfilling the desired coverage planning requirements.

This theoretical study of antenna array diversity is followed by assessments of the technique in various simulated surroundings. In a microcellular urban environment, where antenna heights are clearly below rooftops, a 2-dimensional radio channel simulation model is used. Wall reflections, corner diffractions and the ground reflection are taken into account in a city perspective as linear polarization is being used.

In an indoor radio propagation channel, reflections from the floor and the ceiling are important sources of signal interference, thus making the propagation environment more complex and prone to severe signal fading. A small 2-dimensional array (Figure 2) in a base station could be a simple but effective method to neutralize the effects of fading. The fading reduction performance is assessed from a signal response of a 3-dimensional ray-tracing radio channel program. The simulator program takes into account the polarization effects of the propagating signal, which leads to a good estimate of the signal correlation between different array responses and antenna diversity methods. The use of an antenna array in a base station provides means to design the radiation pattern according to coverage needs and, on the other hand, to utilize the signals in all array elements in diversity reception.
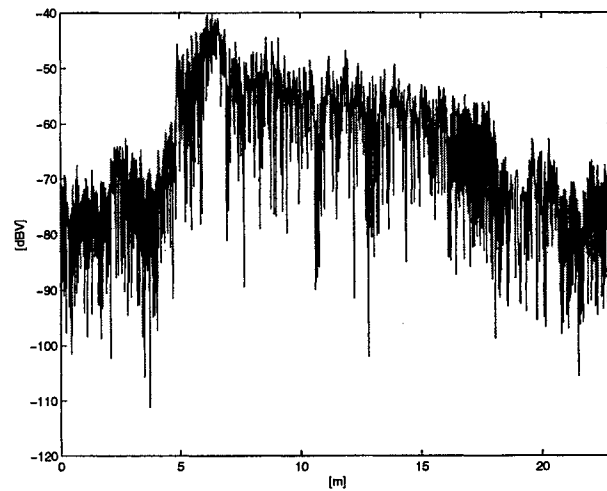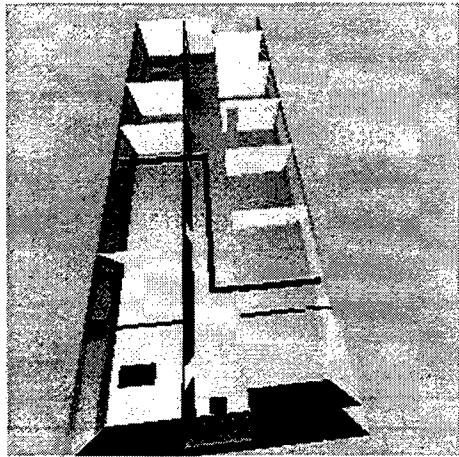
Figure 3: The simulated office environment and the corresponding receiver signal response

References

[1] J. Lempiäinen, K. Nikoskinen, J. Juntunen, *"Multistate phase diversity microcell antenna."* Electronic letters, Vol. 33, No. 6, pp. 438-440, March 1997.

[2] J. Juntunen, K. Nikoskinen, K. Heiska, *"Binomial array as a multistate phase diversity antenna."* to appear in IEEE Transactions in Vehicular Technology.

[3] J. Juntunen, K. Nikoskinen, K. Heiska, *"Phase diversity arrays for mobile communication networks."* 10e Journèes Internationales de Nice Sur les Antennes (JINA'98), Nice, France, pp. 734-737, 17-19 November 1998.

Smart Antennas for 3G and Future-Generation Code Division Multiple Access Wireless Communications

[1]Yoo S. Song, [2]Hyuck M. Kwon, and [3]Byung J. Min

[1,2]Dept. of Electrical and Computer Engineering, Wichita State University, Wichita, KS 67260-0044
[3]SK Telecom, 9-1 Sunae-dong, Pundang-gu, Sungnam City, Kyunggi-do 463-020, Korea
Correspondent: Hyuck M. Kwon, Tel: (316) 978-6308, Fax: (316) 978-3853 Email: hmkwon@ece.twsu.edu

Abstract – This paper presents three simple smart antenna algorithms without eigenvector findings and compares them with a conventional smart antenna with eigenvector finding. Either the maximum output power or the maximum signal-to-interference-plus-noise-output power ratio ($SINR_0$) criteria are used to develop the simple smart antennas. The proposed smart antennas require computational loads of the order $4M$ or $4M+2M^2$ per snapshot where M is the number of antennas while the conventional smart antenna requires order larger than M^2 due to the generalized eigenvector finding. Furthermore, the proposed simple antennas can show lower bit error rate (BER) results than the conventional one when multipath channels have unequal strength and interference comes from a cluster of many other users, e.g., users in a building.

1. Introduction

Recently a technique for estimating the vector channel and the corresponding adaptive beamformer has been developed for CDMA wireless systems [1]. The adaptive algorithms in [1] are based on generalized eigenvector and eigenvalue finding and are designed to maximize $SINR_0$. They require enormous amounts of computation and not simple to apply in practical fields. These heavy computations are due to the calculations of eigenvalues and eigenvectors of $M \times M$ auto-covariance matrices for the antenna array outputs.

Simple smart antennas based on maximum output power instead of maximum $SINR_0$ were introduced in [2-4] to significantly reduce the number of computations. The research in [2] shows performance similar to results in [4]. However, the maximum output power criteria in [2] employs a Lagrange multiplier method and introduces slightly higher computational loads ($5.5M$ compared to $4M$ in [4]). A weak point of the maximum output power based algorithms is that the optimum weight vector for a weak path signal can track an undesired user or strong path signal direction, if the power of the undesired signal is strong or signal-to-interference input power ratio (SIR_i) is low.

It is desirable to develop a smart antenna algorithm, which maximizes not only the SINR but also has smaller computation loads. In this paper two such smart antenna algorithms are proposed and compared with the existing smart antenna with eignevector finding in [1] and one is based on the maximum output power criteria in [4]. Two of four algorithms only require computational loads of the order $4M$ per snapshot where M is the number of antennas in a sector at a base station. The other proposed algorithm that is based on the maximum $SINR_0$ criteria requires computational loads of order $4M+2M^2$. All three algorithms do not require any computation of eigenvalue and eigenvectors.

2. System Models

In a transmitter, the input data stream $d_n^I(k)$ in the pilot channel is I and the input data stream $d_n^Q(k)$ in a traffic channel is a random sequence of $\pm I$ where k denotes code symbol (or snapshot) index. The pilot amplitude A_0 is chosen to $\sqrt{8}$ times that of a reverse traffic channel according to the specification in [5]. The pilot and traffic channels are multiplied with the orthogonal Walsh codes $b_n^I(i)=I$ and $b_n^Q(i)=\pm I$ alternating sequence, and the in-phase and quadrature-phase data are pseudonoise (PN) spread with $a_n(i)=a_n^I(i)+ja_n^Q(i)$ where i denotes the chip index. PN spreading gain is assumed to be 64 chips per code symbol. The PN spread signal can be written as $\{A_0 d_n^I(k)b_n^I(i)+jd_n^Q(k)b_n^Q(i)\}$ $(a_n^I(i)+ja_n^Q(i)) = \{A_0+jd_n^Q(k)b_n^Q(i)\} (a_n^I(i)+ja_n^Q(i))$.

Figure 1 shows a receiver with a smart antenna processor for the cdma2000 reverse link [5]. It is assumed that the directions of arrival angle (DOA) from N users are independent random variables and

also the DOAs of L multipath signals from the same mobile user are independent. The antenna spacing d in a linear array of M antennas is chosen to be $\lambda/2$ where λ is the wavelength. The identical signals are received by all antennas and the M antenna output signals are equal except the spatial phase difference. The antenna array response vector $\underline{a}(\theta)$ is written as

$$\underline{a}(\theta) = [1 \quad e^{-j\pi\sin\theta} \quad \cdots \quad e^{-j(M-1)\pi\sin\theta}]^T \quad (1)$$

where T is the transpose and θ the incident angle. The received signal at the m-th antenna can be written as

$$r_m(t) = \sum_{n=1}^{N}\sum_{l=1}^{L}\left\{\begin{array}{l} s_n(t-\tau_{l,n})\alpha_{l,n}(t) \\ e^{j\phi_{l,n}(t)}e^{-j(m-1)\pi\sin\theta_{l,n}(t)} \end{array}\right\} + n_m(t) \quad (2)$$

where $\tau_{l,n}$, $\alpha_{l,n}(t)$, $\phi_{l,n}(t)$, and $\theta_{l,n}(t)$ are respectively the multipath dealy, amplitude, phase and incident angle of the l-th path from user n, and $n_m(t)$ is the thermal noise with two-sided power spectral density $N_0/2$.

3. Smart Antenna Algorithms

3.1 Smart Antenna Based on Maximum Output Power without Lagrange Multiplier:

Figure 2 shows the flow chart of the proposed smart antenna in [4], which minimizes the mean square error (MMSE) by using projection approximation subspace tracking with deflation (PASTd) instead of maximizing the SINR. It takes only $4M$ computation cycles per snapshot, which is significantly smaller than the existing algorithms. The power of the array output $z(k)$ is maximized when the weight vector $\underline{w}(k)$ minimizes the cost function. A weak point of this algorithm is that the optimum weight vector can track an undesired user signal direction if the power of the undesired user signal after PN despreading is strong.

3.3. Smart Antenna Based on Maximum SINR Output without Eigenvector Finding:

Figure 3 shows a simplified smart algorithm based on the maximum SINR criteria in [1]. Smart antenna weight vector is applied after post-PN processing as in [1]. This smart antenna requires neither any computations of eigenvalues or eigenvectors nor the inverse of any matrices, but only requires multiplication between scalars and vectors and products between a matrix and vectors. Thus, the overall computational load to get the array output $z(k)$ in the proposed algorithm is $2M^2+4M$ per snapshot, which is significantly smaller than those of the existing algorithms in [1].

3.4. More Simplified Smart Antenna Based on Maximum SINR Output w/o Eigenvector Finding:

Figure 4 shows further simplified smart antenna algorithm based on maximum SINR output. This algorithm only requires multiplication between scalars and vectors. Thus, the overall computation load to get the array output $z(k)$ with the simplified algorithm is only $4M$ per snapshot, which is much smaller than those of the existing algorithms.

4. Analysis

The universal BER formula under L independent Rayleigh fading paths in [6, pp. 959] can be employed for the CDMA with smart antenna processor and can be written as

$$P_b(E) = p^L \sum_{l=0}^{L-1}\binom{L+l-1}{l}(1-p)^l \quad (3)$$

where p is the symbol error probability under the l-th multipath fading, and can be written as

$$p = \frac{1}{2}\left(1 - \sqrt{\frac{\rho_c}{1+\rho_c}}\right) \quad (4)$$

and ρ_c denotes the average output SINR of the l-th multipath. The ρ_c can be written as

$$\rho_c = \overline{\alpha_l^2}\frac{E_b}{L\left(\dfrac{N_0}{M} + G_{avg}(\theta_1)I_0\right)} \quad (5)$$

where $G_{avg}(\theta_l)$ denotes the suppression gain against interference obtained by a smart antenna when the incident angle from the desired signal is θ_l [3] and $\overline{\alpha_l^2}$ is the average power of the l-th multipath fading.

5. Simulation and Analysis Results

The incident angle of the desired user changes linearly with $0.01°$ per snapshot. Convergence parameter $\mu=0.0001$ and the pilot channel estimation window $N_p=128$ was used throughout the simulation.

Figure 5 shows the corresponding simulation BER results for four smart antenna algorithms under *unequal* strength multipath with $\overline{\alpha_{l=1}^2} = 0.9$ and $\overline{\alpha_{l=2}^2} = 0.1$, and scattered users. Equal strength is assumed for theoretical BER results. It is observed that all four smart antenna simulation BER results under *unequal* strength fading are placed between theoretical smart antenna BER results with $L=1$ and $L=2$ path. As the number of users increases, all four smart antenna simulation BER results under *unequal* strength fading approach to theoretical smart antenna BER results with $L=1$ path fading because the finger output from the strong path with strength 0.9 is dominant under severe interference environment, compared to the weak path. It is also observed that

the smart antenna based on the maximum SINR criteria without eigenvector finding is slightly better than other smart algorithms. As the number of users decreases, the smart antenna based on the maximum SINR criteria with eigenvector finding is slightly worse than other smart algorithms.

Figure 6 shows the corresponding simulation BER results by assuming all other users are located in a cluster region and their incident angles are within $\pm 5°$. The four smart antenna algorithms are also considered under *unequal* strength multipath with $\overline{\alpha_{l=1}^2} = 0.9$ and $\overline{\alpha_{l=2}^2} = 0.1$. It is observed that three smart antenna simulation BER results under *unequal* strength fading are placed between theoretical smart antenna BER results with $L=1$ and $L=2$ path *equal* strength fading. However, it is observed that the smart antenna based on the maximum SINR criteria with eigenvector finding can be worse than the theoretical smart antenna BER results with $L=1$ as the number of users increases. Again the smart antenna based on the maximum SINR criteria without eigenvector finding may yield better BER results than the other algorithms. This is due to that the proposed algorithms employ a small convergence parameter $\mu=0.0001$ and the update increment for the weight vector is small, while the algorithm with eigenvector finding in [1] does not employ any convergence parameter.

6. Conclusion

Four smart antenna algorithms were employed for the pilot-aided CDMA system with cross PN spreading and de-spreading. For practical channel models, *unequal* strength multipath fading was considered with Jake model. Also, a cluster of interfering users and scattered interference users were considered. It was observed that both a smart antenna based on the maximum output power criteria with no Lagrange multiplier and a smart antenna based on the maximum output SINR criteria without eigenvector finding perform slightly better than others. Furthermore, computation loads of both algorithms per snapshot are significantly smaller than the existing ones. Therefore, the proposed smart antenna algorithms may be recommended for 3G and future CDMA systems to increase capacity with reasonable and practical computational loads.

References

[1] Ayman F. Naguib and Arogyaswami Paulraj, "Performance of Wireless CDMA with M-ary Orthogonal Modulation and Cell Site Antenna Arrays," IEEE Journal on Selected Areas in Communications, Vol. 14, No. 9, pp. 1770-1783, December 1996.

[2] D. Shim and S. Choi, "A New Blind Adaptive Algorithm Based on Lagrange's Formula for a Smart Antenna System in CDMA Mobile Communications," IEEE Vehicular Technology Conference, pp. 1160-1664, Ottawa, May 1998.

[3] Yoo S. Song and Hyuck M. Kwon, "Simple Analysis of a Simple Smart Antenna for CDMA Wireless Communications," IEEE Vehicular Technology Conference, Houston, TX, pp. 254-258, May 16-20, 1999.

[4] Yoo S. Song and Hyuck M. Kwon, "Analysis of a Simple Smart Antenna for Code Division Multiple Access Wireless Communications," the 4th CDMA International Conference and Exhibition, vol. II, pp. 253-257, Seoul, Korea, September 8-11, 1999.

[5] TIA, Interim V&V Text for cdma2000 Physical Layer (Revision 8.3), March 16, 1999.

[6] J. S. Lee and L. E. Miller, CDMA Systems Engineering Handbook, Artech House Publishers, 1998.
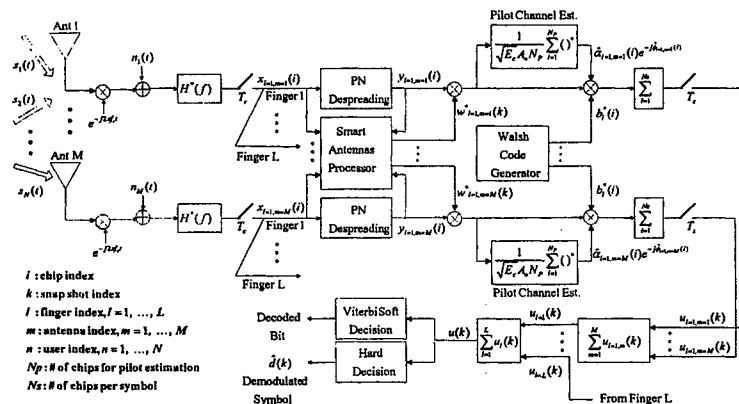
Figure 1. Overall block diagram of a receiver with a smart antenna processor for the cdma2000 reverse link.

Figure 2

Initial Guess
$\underline{w}(0),\lambda(0)$

New Signal
$\underline{y}(k)$

Array Output
$z(k)=\underline{w}^H(k-1)\underline{y}(k)$
$\lambda(k)=f\cdot\lambda(k-1)+|z(k)|^2$

$\underline{w}(k)=\underline{w}(k-1)+[\underline{y}(k)-\underline{w}(k-1)z(k)]\dfrac{z^*(k)}{\lambda(k)}$

$\underline{w}(k)=\dfrac{\underline{w}(k)}{w_1(k)}$
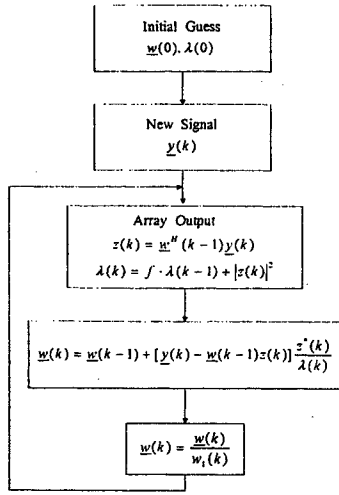
Figure 2. Maximum output power based algorithm.

Figure 3

Initial Guess
$\underline{w}(0),\mu$

New Signal
$\underline{x}(i),\underline{y}(i)$

$R_{xx}(k),\underline{y}(k)$
$z(k)=\underline{w}^H(k-1)\underline{y}(k)$
$D(k)=G\cdot\underline{w}^H(k-1)R_{xx}(k)\underline{w}(k-1)-|z(k)|^2$

$\underline{w}(k)=\underline{w}(k-1)+\dfrac{2(G-1)}{D^2(k)}\cdot$
$\left((D(k)+|z(k)|^2)z^*(k)\underline{y}(k)-G\cdot|z(k)|^2 R_{xx}(k)\underline{w}(k-1)\right)$

$\underline{w}(k)=\dfrac{\underline{w}(k)}{w_1(k)}$
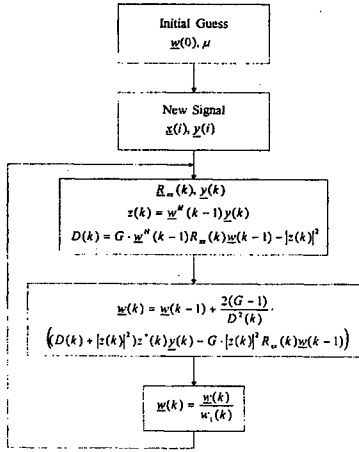
Figure 3. Maximum SINR criteria based algorithm.

Figure 4

Initial Guess
$\underline{w}(0),\mu$

New Signal
$\underline{x}(i),\underline{y}(i)$

$g(k)=\underline{w}^H(k-1)\underline{x}(k)$
$z(k)=\underline{w}^H(k-1)\underline{y}(k)$
$C(k)=f\cdot C(k-1)+G\cdot|g(k)|^2-|z(k)|^2$

$\underline{w}(k)=\underline{w}(k-1)+\dfrac{2(G-1)}{C^2(k)}\cdot$
$\left((C(k)+|z(k)|^2)z^*(k)\underline{y}(k)-G\cdot|z(k)|^2 g(k)\underline{x}(k)\right)$

$\underline{w}(k)=\dfrac{\underline{w}(k)}{w_1(k)}$
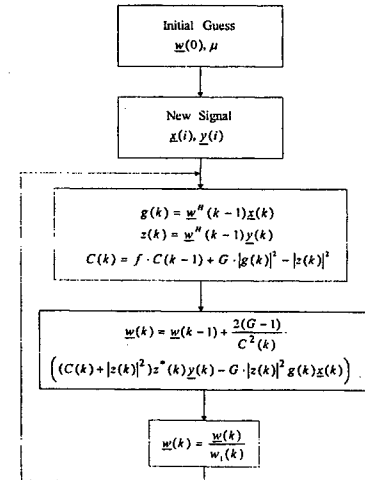
Figure 4. Simplified maximum SINR criteria based algorithm.

Figure 5

Unequal Strength Channel(0.9,0.1). M=3 L=2, SNR=20dB

___ : Conv. w/o Smart Ant. (M=3,L=2)
..... : Theory (M=3,L=1)
---- : Theory (M=3,L=2)
-+- : Max SINR w/ Eigen.
-o- : Max SINR w/o Eigen.
-*- : Simplified Max SINR w/o Eigen.
-x- : Max Output Power

Bit Error Rate
Number of Users, N
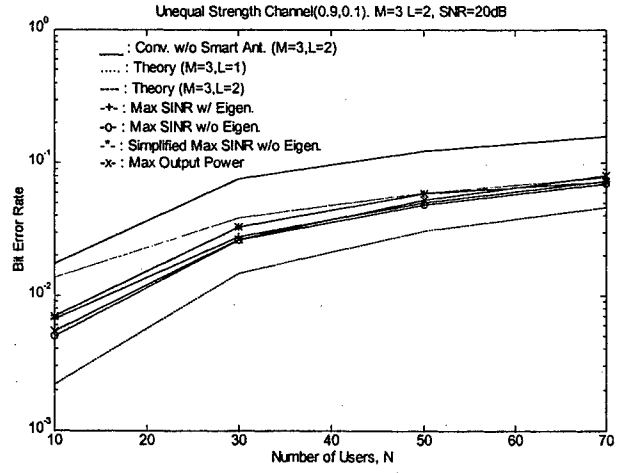
Figure 5. BER results for the smart antennas under unequal strength multipath fading.

Figure 6

Cluster of Interference & Unequal Strength Channel(0.9,0.1). M=3 L=2, SNR=20dB

___ : Conv. w/o Smart Ant. (M=3,L=2)
..... : Theory (M=3,L=1)
---- : Theory (M=3,L=2)
-+- : Max SINR w/ Eigen.
-o- : Max SINR w/o Eigen.
-*- : Simplified Max SINR w/o Eigen.
-x- : Max Output Power

Bit Error Rate
Number of Users, N
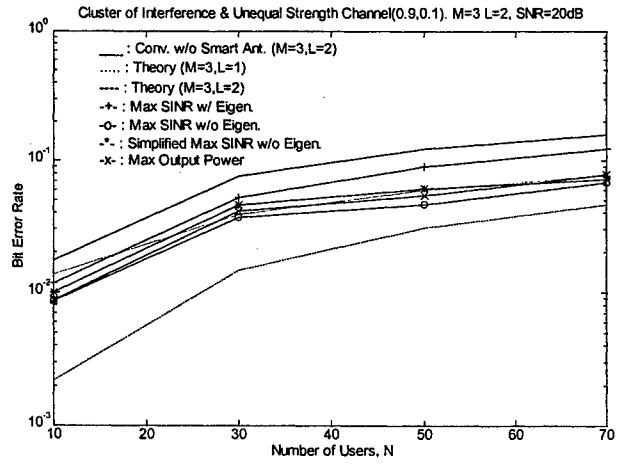
Figure 6. BER results for the smart antennas under a cluster of interference and unequal strength multipath fading.

Blind Adaptive H^∞ Multiuser Detection for CDMA Systems

Ann-Chen Chang[1], Ching-Tai Chiang[2] and Yuan-Hwang Chen[1]

[1]Dept. of Electrical Engineering, National Sun Yat-Sen University, Kaohsiung, Taiwan 804, ROC

[2]Dept. of Electronic Engineering, South Taiwan University of Technology, Tainan, Taiwan, ROC

Abstract — This paper addresses the issue of employing a generalized sidelobe canceler (GSC) without and with subweight partition scheme to describe blind H^∞ multiuser detection. Although the recursive least-squares (RLS) algorithm with subweight partition can improve the performance of multiuser detector, it only suits for uncorrelated signal. It has shown that the adaptive H^∞ algorithm with subweight approach demonstrates the advantages of faster convergence speed, insensitivity of dynamic estimate error, and suitable arbitrary noise signals than the H^∞ and RLS-based adaptive algorithms.

I.   INTRODUCTION

Code-division multiple access (CDMA) is a multiplexing method that effectively allows many users to commonly use a communication channel. Often, the near-far problem presents a major limitation to CDMA system performance. The conventional approach to multiuser detection is to employ a match filter [1] for each user, which is optimal in the absence of multiple access interference. A constrained technique for adaptive interference suppression based on minimizing the receiver output variance has shown great promise [2]. Recently, H^∞ minimum estimation spectrum error criterion [3] is designed to guarantee that the operator relating the noise signals to the resulting estimation error should possess an H^∞ norm less than a prescribed positive value. The adaptive H^∞ algorithm has been previously proposed in the context of channel equalization [3] under decision feedback structure, but its adaptive implementation requires the transmission of training sequences. The main drawback of the H^∞ filtering is computational complexity. An adaptive RLS algorithm based on the GSC-based subweight partition [4] is derived to update the weight subvectors. Faster convergence speed and less computational complexity can be achieved by using the technique of [4]. Although the RLS algorithm with subweight partition can improve the performance of multiuser detector, it cannot deal with nonorthogonal spreading codes.

In this paper, we combine the GSC-based subweight approach [4] and adaptive H^∞ algorithm [3], termed the H^∞-based, which can reduce the computation burden, overcome the model error due to reducing the degree of freedom and against the uncertainty of correlated codes in the sub-correlation matrix.

II.   GSC-BASED SUBWEIGHT PARTITION

Let the multiuser CDMA system with K users and a set of normalized signature waveforms $s_i(t)$, $i = 1, 2, \cdots, M$, where $K < M$. Assuming that the desired user is user 1 and the timing of the desired

user can be accurately estimated. After chip sampling the received signal can expressed as an $M \times 1$ column vectors $\mathbf{x}[k]$ for the k-th bit duration. The correlation matrix of received data vectors is $\mathbf{R}_{xx} = E[\mathbf{x}\mathbf{x}^T]$, where the superscript T denotes the transpose. The solution weight vector $\mathbf{W}$ decomposition motivates the GSC structure and expresses as $\mathbf{W} = \mathbf{w}_q - \mathbf{B}\mathbf{w}_a$. The nonadaptive weight vector, $\mathbf{w}_q = \mathbf{s}_1(\mathbf{s}_1^T\mathbf{s}_1)^{-1}$ where $\mathbf{s}_1$ denotes the desired user code, is not data dependent in the upper branch. The blocking matrix $\mathbf{B}$ with rank $M-1$ is chosen to satisfy $\mathbf{B}^T\mathbf{s}_1 = \mathbf{0}$ and the optimal adaptive weight vector $\mathbf{w}_a$ is given by

$$\mathbf{w}_{ao} = (\mathbf{B}^T\mathbf{R}_{xx}\mathbf{B})^{-1}\mathbf{B}\mathbf{R}_{xx}\mathbf{w}_q = \mathbf{R}_{uu}^{-1}\mathbf{P} \tag{1}$$

The solution in (1) is developed by [4] to implement the efficient GSC-based adaptive multiuser detection technique with subweight vectors. Let the lower branch data vector which passed the blocking matrix $\mathbf{B}$ be denoted as an $(M-1) \times 1$ vector $\mathbf{u} = \mathbf{B}^T\mathbf{x}$ and be partitioned into $\mathbf{u} = [u_1^T, u_2^T, \cdots, u_L^T]^T$, where u_i is an $N_i \times 1$ data vector and $\sum_{i=1}^{L} N_i = (M-1)$. The autocorrelation matrix $\mathbf{R}_{uu} = E\{\mathbf{u}\mathbf{u}^T\}$ can be constructed by submatrices $\mathbf{R}_{ij} = E[u_i u_j^T]$ for $i, j = 1, 2, \cdots, L$. And, the vector $\mathbf{P}$ partition as

$$\mathbf{P} = \mathbf{B}^T\mathbf{R}_{xx}\mathbf{w}_q = [\mathbf{P}_1^T \quad \mathbf{P}_2^T \quad \cdots \quad \mathbf{P}_L^T]^T \tag{2}$$

where each subvector $\mathbf{P}_i = E\{u_i d^*\}$ with $d = \mathbf{w}_q^T\mathbf{x}$ and the superscript $*$ denoting the complex conjugate, for $i = 1, 2, \cdots, L$ has size of $N_i \times 1$. Finally, the adaptive weight vector $\mathbf{w}_a$ can be reconstructed by

$$\mathbf{w}_{ao} = [\mathbf{w}_1^T \quad \mathbf{w}_2^T \quad \cdots \quad \mathbf{w}_L^T]^T \tag{3}$$

with $\mathbf{w}_i = \mathbf{R}_{ii}^{-1}(\mathbf{P}_i - \sum_{j=1, j \neq i}^{L} \mathbf{R}_{ij}\mathbf{w}_j)$,

for $i = 1, 2, \cdots, L$. $\tag{4}$

The solution in (4) is developed by [4] to implement the RLS-based technique with subweights, but it has dynamic estimate modeling error that occurs by recursive algorithm. Owing to the resulting spreading codes are the cyclically shifted versions of $\mathbf{s}_k$, the partition subvector may be confused for different user in the $\mathbf{R}_{ii}$, especially when the large cross-correlations exists.

III. BLIND ADAPTIVE H^∞ ALGORITHMS

This section describes new implementation of blind H^∞ algorithm multiuser detection and evaluates the required computational complexity.

A. The conventional H^∞ algorithm

Based on the adaptive H^∞ algorithm [3], then the adaptive algorithm for computing the adaptive weight vector $\mathbf{w}_a$ of (1) is given by

$$\mathbf{w}_{k+1} = \mathbf{w}_k + \mathbf{F}_{k+1}[\sigma^{-1/2}d_{k+1} - \mathbf{w}_k^T\mathbf{u}_{k+1}]^* \tag{5}$$

where σ denotes the forgetting factor, $0 < \sigma \leq 1$, and the required reference signal is $d_{k+1} = \mathbf{w}_q^T\mathbf{x}_{k+1}$,

$$\mathbf{F}_{k+1} = \frac{\Phi_k\mathbf{u}_{k+1}}{\sigma + \mathbf{u}_{k+1}^T\Phi_k\mathbf{u}_{k+1}} \tag{6}$$

and $\Phi_{k+1}^{-1} = \sigma\Phi_k^{-1} + \mathbf{u}_k\mathbf{u}_k^T - \gamma_{k+1}^{-2}\mathbf{u}_{k+1}\mathbf{u}_{k+1}^T \tag{7}$

$\gamma_{k+1} = \varsigma\max\{eig[\sigma^{-1}\mathbf{u}_{k+1}\mathbf{u}_{k+1}^T(\mathbf{I}_{L-1} - \mathbf{F}_k\mathbf{u}_k^T)\Phi_k]\}^{0.5} \tag{8}$

where $\max\{eig(\Sigma)\}$ and $\mathbf{I}_{L-1}$ denote the maximum eigenvalue of the matrix Σ and the identity matrix, respectively. ς is a constant close to one, but larger than one to ensure that γ is always greater than the maximum square root value of Σ. For this adaptive H^∞ algorithm, the initial condition are $\mathbf{w}_0 = \mathbf{0}$ and $\Phi_0^{-1} = (\sigma\delta)^{-1}\mathbf{I}_{L-1}$.

B. The H^∞-based adaptive algorithm

According to the technique of [4] which shows that uniformly partitioning the weight vector can

offer the advantages of faster convergence rate over nonuniformly partitioning the weight vector, it is easy to derive an unconstrained H^∞-based adaptive algorithm for computing the subweights. Therefore, the adaptive algorithm for computing the subweights $\mathbf{w}_i$ of (5) are given by

$$\mathbf{w}_{i(k+1)} = \mathbf{w}_{i(k)} + \mathbf{F}_{i(k+1)}[f_{(k+1)} - \sum_{j=1, j\neq i}^{L} \Delta h_{j(k+1)}]^* \quad (9)$$

where $\quad \mathbf{F}_{i(k+1)} = \dfrac{\Phi_{i(k)}\mathbf{u}_{i(k+1)}}{\sigma + \mathbf{u}_{i(k+1)}^T \Phi_{i(k)}\mathbf{u}_{i(k+1)}} \quad (10)$

$$\Phi_{i(k+1)}^{-1} = \sigma\Phi_{i(k)}^{-1} + \mathbf{u}_{i(k)}\mathbf{u}_{i(k)}^T - \gamma_{i(k+1)}^{-2}\mathbf{u}_{i(k+1)}\mathbf{u}_{i(k+1)}^T \quad (11)$$

$$\gamma_{i(k+1)} = \varsigma \max\{eig[\sigma^{-1}\mathbf{u}_{i(k+1)}\mathbf{u}_{i(k+1)}^T$$
$$(\mathbf{I}_{N_i} - \mathbf{F}_{i(k)}\mathbf{u}_{i(k)}^T)\Phi_{i(k)}]\}^{0.5} \quad (12)$$

$$f_{k+1} = \sigma^{-1/2} d_{k+1} - \sum_{j=1}^{L} \mathbf{w}_{j(k)}^T \mathbf{u}_{j(k+1)} \quad (13)$$

and $\quad \Delta h_{i(k+1)} = (\mathbf{w}_{i(k+1)}^T - \mathbf{w}_{i(k)}^T)\mathbf{u}_{i(k+1)} = \Delta \mathbf{w}_{i(k+1)}^T \mathbf{u}_{i(k+1)}$ for $i = 1, 2, \cdots, L$, which may be occur dynamic estimate model error, are given by solving the following matrix equation

$$\begin{bmatrix} 1/g_{1(k+1)} & 1 & \cdots & 1 \\ 1 & 1/g_{2(k+1)} & \cdots & 1 \\ 1 & 1 & \vdots & \vdots \\ 1 & 1 & \cdots & 1/g_{L(k+1)} \end{bmatrix} \begin{bmatrix} \Delta h_{1(k+1)} \\ \Delta h_{2(k+1)} \\ \vdots \\ \Delta h_{L(k+1)} \end{bmatrix} = \begin{bmatrix} f_{k+1} \\ f_{k+1} \\ \vdots \\ f_{k+1} \end{bmatrix} \quad (14)$$

with $\quad g_{i(k+1)} = \mathbf{F}_{i(k+1)}^T \mathbf{u}_{i(k+1)}$.

C. Computational Complexity Analysis

In this subsection, the computational complexity requires by the adaptive H^∞ algorithm [3] and the H^∞-based algorithm are evaluated. Since the blocking matrix is fix and the blocked signal can be computed with special purpose high-speed hardware, we ignore the computational complexity of the blocked signal $\mathbf{u}$. Additionally, utilizing the eigenvalue decomposition method of [5] on (8) requires $12(M-N)^3$ complex multiplications (CM)

where N denotes the number of constraints. The H^∞ algorithm requires about $12(M-N)^3 + 3(M-N)^2 + 8(M-N)$ CM when using adaptive H^∞ algorithm. The RLS algorithm requires about $2(M-N)^2 + 6(M-N)$ CM [4]. Let the number of subweights be L and the size of the i-th subweight $\mathbf{w}_i$ be N_i. Based on the weight partition technique [4], the number of CM is about $\sum_{i=1}^{L}(12N_i^3 + 3N_i^2 + 8N_i) + (L^3/2) + L^2 + M - N$ CM. To compare the required CMs between the H^∞ and H^∞-based algorithms, we plot the number of required complex multiplications in logarithmic scale versus the number of subweights $\mathbf{w}_i$ in Fig. 1 with $M - N = 126$ for each subweight $\mathbf{w}_i$ has the same number of elements. It is seen that the H^∞-based algorithm can reduce the computational complexity of the conventional adaptive H^∞ algorithm.

IV. SIMULATION RESULTS

The system parameters are $K = 6$ users and Gold sequence of processing gain 31 with BPSK modulation. The length of subweight is $N_i = 10$ for $i = 1, 2, 3$. The value of δ for the presetting the initial value of Φ_o is set to 100, while the forgetting factor is set to 1. To ensure that steady-state performance is being assessed, simulations are allowed to run long enough for the weights to converge. Fig. 2 and Fig. 3 show the effect of convergence rate and bit error rate with additive white Gaussian noise channel for the synchronous CDMA system. The users except user 1 have equal power, which are 6dB more than that of user 1. It is seen that the RLS-based detector exhibits worst performance due to that it cannot mitigate the

uncertainty of the correlation of codes under subautocorrelation matrix. Again, these figures show that the proposed technique possesses much robust capabilities than the RLS-based and the H^∞ algorithms.

V.　CONCLUSION

Blind adaptive H^∞ multiuser detectors in CDMA systems have been presented. Since the design criterion is based on the worst case disturbance, the H^∞ filtering is less sensitive to uncertainty in the exogenous signals statistics and dynamical model. It can combat the model error resulting by subweight partition and unknown noise, also has fast convergence rate.

REFERENCES

[1] J. PROAKIS, Digital Communications. New York: McGraw Hill, 1989.

[2] J.B. Schodrof and D.B. Williams, "A constrained optimization approach to multiuser detection," IEEE Trans., vol. SP-45, pp. 258-262, Jan. 1997.

[3] W. Zhuang, "Adaptive H^∞ channel equalization for wireless personal communications," IEEE Trans., vol. VT-48, pp. 126-136, Jan. 1999.

[4] S.J. Yu and J.H. Lee, "Adaptive array beamforming based on an efficient technique," IEEE Trans., vol. AP-40, pp. 1094-1101, Aug. 1996.

[5] G.H. Golub and C.F. Van Loan, Matrix Computations, Baltimore, MD: Johns Hopkins Univ. Press, 1983.
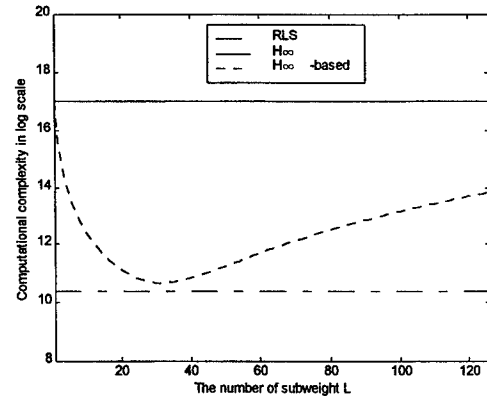
Fig. 1 The computational complexities analysis.
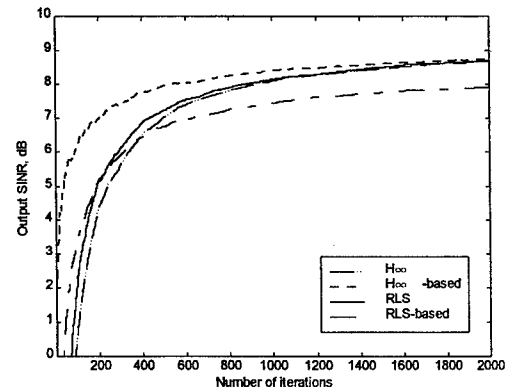
Fig. 2 The output SINR versus the number of iterations with synchronous AWGN channel. The desired user power is 10 dB.
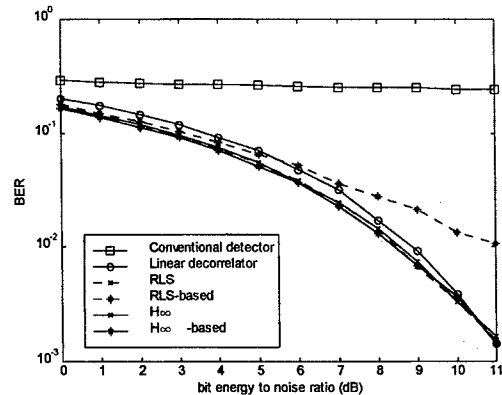
Fig. 3 Average bit error rate of desired user 1 with synchronous AWGN channel.

An Electronically-Stabilized 915 MHz Phased Array Antenna for Ship-Borne Atmospheric Wind Profiling

D. C. Law[1], S. A. McLaughlin[2], D. A. Merritt[1], and S. A. Pezoa[2]

1. National Oceanic and Atmospheric Administration
Environmental Technology Laboratory
325 Broadway
Boulder, CO 80303 USA
www.etl.noaa.gov

2. Science and Technology Corp.
10 Basil Sawyer Drive
Hampton, VA 23666 USA

1. INTRODUCTION

Wind profilers are vertically-directed, sensitive pulsed Doppler radars that measure horizontal and vertical wind velocities from about 100 meters to over 20 km above ground, depending on the operating frequency (typically VHF or UHF), antenna aperture, and transmit power [1,2]. In clear air (devoid of rain, snow and ice targets), profilers measure the Doppler shift of extremely weak radar returns from gradients of the radio refractive index due to atmospheric turbulence. The sensitivity required to detect these weak signals is obtained primarily through long dwell times, on the order of tens of seconds. Radial velocities from two to five beam directions are combined to form the horizontal and vertical wind vectors. The addition of vertically-directed acoustic sources allows the radar to also retrieve profiles of virtual temperature by the radio-acoustic sounding system (RASS) [1].

The meteorologic research community has identified the need for wind and temperature data over the oceans for such applications as improved severe weather forecast of coastal areas [3], and studies of the El Niño-Southern Oscillation [4]. The adaptation of ground-based wind profilers for ship-borne applications has proven to be a formidable engineering challenge. Limited deck space, the harsh marine environment, high levels of radar sea clutter, and the need for antenna stabilization to achieve the beam pointing accuracy over long dwell times all indicate the need for a system specifically designed for ship-borne wind profiling.

2. THE ELECTRONICALLY-STABILIZED PHASED ARRAY SYSTEM

Figure 1 is an artist concept showing one beam from the profiler antenna mounted on a National Oceanic and Atmospheric Administration (NOAA) research vessel. Enclosed in a fiberglass radome, the 2.75 m (9 ft) diameter, 1 m (3 ft) tall antenna is mounted rigidly to the deck of the ship. The radome encloses the phased-array antenna, final RF power amplifier and preamplifier, power supplies, and heating/cooling units. The 10° profiler radar beam is sequentially switched among 5 beam directions; typically a vertical beam and about 15° from zenith in the north, east, south, and west directions. The computers and other radar electronics are located below deck.
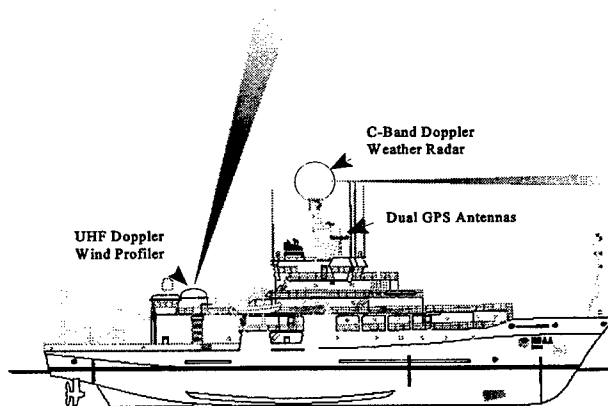
Figure 1. Mounting location of 915 MHz profiler on a NOAA research vessel. Beam directions are typically 0° to 20° off-zenith in four azimuthal directions in contrast to a conventional horizontally-scanning Doppler weather radar. Differential phase GPS is used for accurate heading measurement.

Figure 2 is a diagram of the phased-array profiler system developed by the NOAA Environmental Technology Laboratory. In operation, the radar computer determines the geocentric beam direction and communicates its choice to the motion control and monitor computer (MCM) which steers the phased-array antenna beam to the desired direction while compensating in real time for the ship orientation as measured by a commercial GPS-based inertial attitude, position, and velocity measuring system. The antenna beam position is updated at a 10 Hz rate to accommodate maximum ship roll rates (Table 1). The MCM software is written in a commercial graphical programming environment for data acquisition and control. The user computer combines radial wind velocities from the radar computer with ship velocities from the MCM to generate meteorologic products and archives all radar and ship motion data.
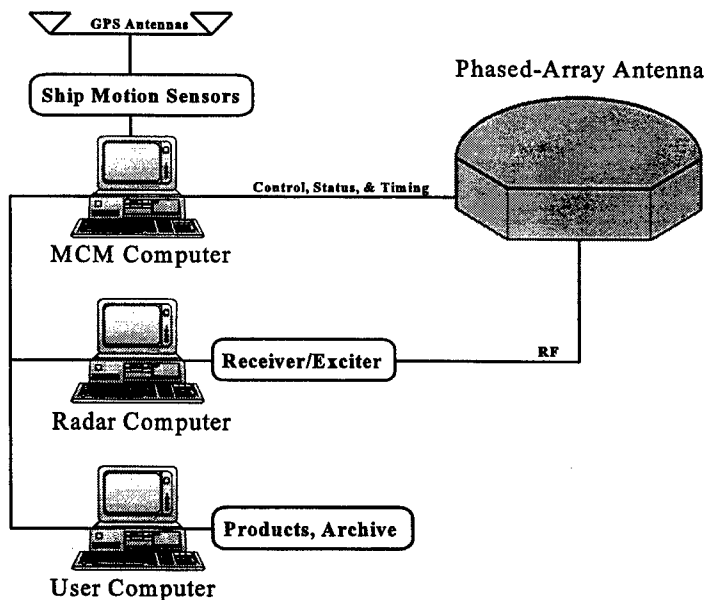
Figure 2. Electronically-stabilized profiler system consists of the phased-array antenna and three computers. The MCM computer steers the antenna beam to compensate for ship motion indicated by GPS-based inertial attitude, position, and velocity measurements.

3. THE PHASED-ARRAY ANTENNA

Figure 3 shows the positions of the 90 identical elements that comprise the phased-array antenna. The elements are arranged on an equilateral triangle with 0.66-wavelength (21.6 cm at 915 MHz) spacing. The absence of the element in the center of the array improves the low-elevation side lobe performance of the antenna and simplifies the RF feed network. To electronically steer the radar beam, the RF transmit signal is split and distributed to each antenna element which shifts the phase of the signal based on its position in the array and the desired beam pointing direction as communicated simultaneously to all modules by the MCM. Received RF signals are likewise phase shifted and combined. Timing signals ensure that phase switching is synchronized to the radar pulse period.
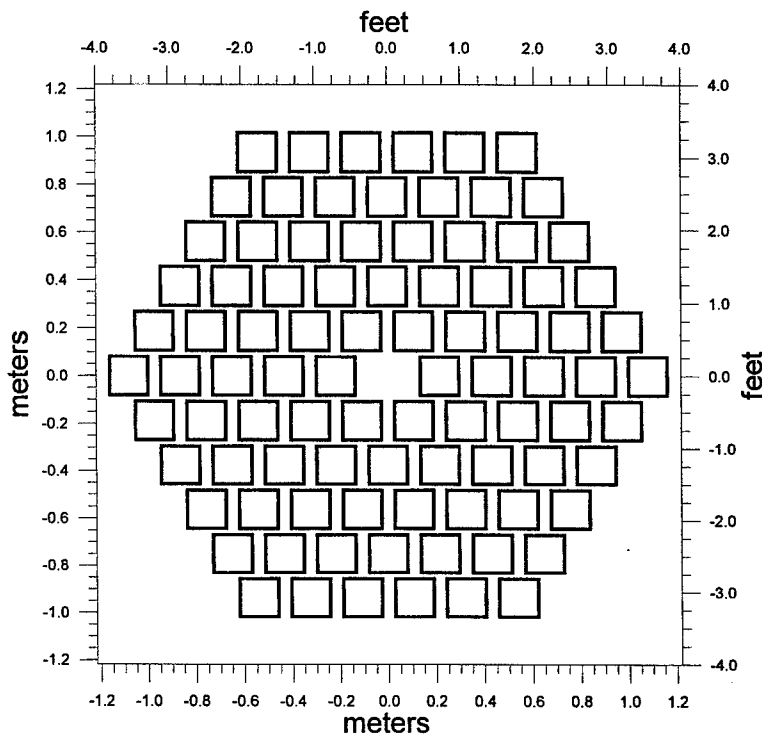
Figure 3. Ninety identical elements with equilateral triangular spacing of 0.66-wavelengths comprise the phased-array.

Figure 4 shows an assembly diagram of the antenna element module, a 215 x 185 x 75 mm (8.5" x 7.3" x 3.0") unit weighing 2.5 kg (5.5 lbs). Each module comprises a microstrip patch antenna, a 4-bit diode phase shifter, and an 8-bit microcontroller arranged in a "tile" architecture [5] and costs about $1000 to manufacture. Although the elements are all physically identical, each is programmed with a unique identification address and a phase control look up table appropriate for its location in the array.

Microstrip Patch Radiator

4-Bit Diode Phase Shifter

8-Bit Microcontroller
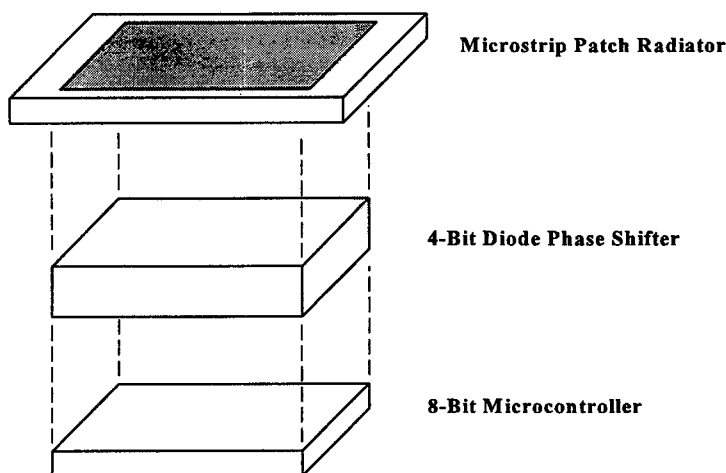
Figure 4. Antenna element components in a "tile" architecture.

To increase the bandwidth and to minimize the low-elevation radiation, the rectangular microstrip patch antenna is printed on the underside of a .79 mm (.031") thick fiberglass board and positioned 6.35 mm (.25") in air above the aluminum ground plane. The effective dielectric constant is close to 1. The ground plane spacing results in a bandwidth of 20 MHz (about 2%) for VSWR < 2:1 (RL > 10 dB). The feed point impedance is adjusted to 55-j25 Ω to compensate for mutual coupling among elements.

In order to meet the mechanical and electrical requirements, the 4-bit diode phase shifter was custom designed using an RF computer-aided design (CAD) system which proved to be very accurate in simulating the operation of the PIN diodes and resulting impedance match, transmission loss, and insertion phase of the shifter. The shifter has an insertion loss of 1.0 dB and an RMS phase and amplitude error over all phase angles of less than 1° and 0.1 dB, respectively. The circuit also includes a dual directional coupler which allows the measurement of forward and reflected RF power. This is used to monitor the antenna and phase shifter circuitry since a failure in these components results in high reflected power.

A single-chip, 8-bit microcontroller in each antenna element communicates with the MCM computer over a four-wire multidrop EIA RS-485 network using a commercial serial communication protocol. Additional radar timing signals are distributed to all modules using RS-422/485 balanced differential drivers and receivers. The microcontroller board also includes a 128 Kbyte nonvolatile memory which is loaded by the MCM with the phase table unique to the module position in the array. The microcontroller also has an 8 channel 8-bit A/D converter which is used to measure module temperatures, voltage, and RF power levels. The MCM polls all of the modules sequentially and maintains a status map of the array hat is updated about every 60 seconds.

4. SUMMARY

Table 1 lists the performance requirements of the NOAA ETL phased-array antenna. Phased-arrays are often complicated, expensive devices which can be justified only for demanding applications such as military radars. However, the falling prices of CAD tools, digital and RF electronic components, and software development products makes the development of phased-arrays for a wide range of application economically feasible. The new ship-borne profiler is scheduled for field trials in 2000.

Table 1. Performance Requirements

Range of Ship Motion

Speed:	0 to 8 m s^{-1} (15 knots)
Roll:	± 8°
Roll Rate:	~ 5 deg s^{-1} max.
Pitch:	± 3°
Pitch Rate:	~ 1.7 deg s^{-1} max.
Heave:	± 3 m (20 ft. waves)
Heave Rate:	1.75 m s^{-1}

Antenna Beam Steering

Zenith Angle:	0° to 31.5° in 0.5° steps
Azimuth:	0° to 359.5° in 0.5° steps
Pointing Error:	± 1° RMS
Rate:	10 Hz
Switching Time:	1 μs (cold-switched)

Antenna Size: 2.75 m dia. x 1 m high

Antenna Beam Characteristics:

Gain:	≥ 23 dBi over all scan angles
-3 dB Beamwidth	≤ 10°
Antenna Loss:	≤ 2.5 dB includes RF distribution network

0° to 10° elevation one-way side lobes, relative to main beam

0° ≤ θ_0 ≤ 15° steering	≤ -40 dB
15° ≤ θ_0 ≤ 30° steering	≤ -30 dB

Amplitude/Phase Errors: 0.5 dB, 3° RMS radiated at each element

REFERENCES

[1] Röttger, J., and M. F. Larsen, "UHF/VHF Radar Techniques for Atmospheric Research and Wind Profiler Applications", Chapter 21a, *Radar in Meteorology*, Atlas, D. (ed.), American Meteorological Society, Boston, 1990.

[2] Balsley, B. B., "Clear-Air Radar Technology: Panel Report", Chapter 21b, *Radar in Meteorology*, Atlas, D. (ed.), American Meteorological Society, Boston, 1990.

[3] The California Land-Falling Jets Experiment (CALJET)
NOAA Environmental Technology Laboratory. http://www7.etl.noaa.gov/programs/CALJET/

[4] El Niño-Southern Oscillations (ENSO)-related web sites.
NOAA Pacific Marine Environment Laboratory. http://www.pmel.noaa.gov/toga-tao/el-nino/
National Center for Atmospheric Research. http://www.ucar.edu/publications/lasers/elnino/

[5] Fourikis, N., *Phased Array-Based Systems and Applications*, John Wiley & Sons, New York, 1997.

ELECTRONICALLY STEERABLE ARRAY ANTENNAS FOR MOBILE SATELLITE COMMUNICATIONS – A REVIEW

Nemai C. Karmakar

School of Electrical and Electronic Eng.
Nanyang Technological University,
Singapore 639798
Email: enckarma@ntu.edu.sg

Marek E. Bialkowski

Department of Computer Science and Electrical
Engineering, University of Queensland, St. Lucia,
Australia 4072
Email: meb@csee.uq.edu.au

ABSTRACT

Mobile satellite communications has flourished since the last decade. Different research groups have conducted research on electronically steerable array antennas for mobile ground stations and commercial vendors now reap the benefits marketing this technology. This paper reviews the technical details of these antenna arrays.

INTRODUCTION

Mobile satellite communications (MSAT) is an emerging technology and a major factor in shaping the global village. Satellite mobile communications can be defined as the link established between an earth base station and a mobile unit via a satellite. The mobile unit can be a satellite phone carried by a person or fitted to a land vehicle, aircraft or ship. In contrast to cellular based mobile communications, land mobile satellite communications (LMSS) now represent an ideal way of putting people in remote areas in touch with the rest of the world. Over the years, a number of global MSAT services have been in operation around the world [1]. Individual satellite communication systems may cover the entire surface of the earth with a large number of satellites as does Inmarsat, an international satellite consortium covering the globe with headquarters in London, whereas other systems may cover only certain populated areas with a lesser number of satellites, as for example, American Mobile Satellite Corporation (AMSC) in America, Optus Mobilesat™ an Australian domestic mobile satellite communications and TMI Communication's MSAT™ service in Canada.

Antennas play a significant role in establishing satellite communications [1]. The signal is beamed into space with a *ground* antenna, received by the satellite antenna, electronically processed, sent back to earth using a *downlink* antenna, received by the *ground* antenna and processed by the electronic receiver. A mobile user further complicates the scenario since the *ground* mobile antenna needs to track the satellite. At present, two types of antenna systems can be used to access these MSAT services. These are: (i) fixed position portable systems of a briefcase type, and (ii) fully mobile systems such as those installed on a land vehicle. The fixed position antenna system is relatively easy to accomplish by the antenna designer. The design involves standard procedures that concern the operational bandwidth, polarization and moderate gain. One inconvenience of the portable briefcase type systems is that they require the user to be stationary with respect to the ground. This inconvenience can be overcome with the *mobile* antenna system. The design of such a system is more challenging as new features associated with the system's mobility have to be incorporated. For the current GEO systems, this task is non-trivial as the antenna has to feature gain in the range of 10dBi. This requirement leads to a narrow antenna beamwidth, for which satellite tracking is required as the vehicle moves around. This paper reviews recent developments of *mobile* antennas by different research groups. The technical details of the antenna are also highlighted.

ANTENNA SYSTEMS FOR MSAT

Antennas for mobile satellite communications can be classified into two main types according to their modes of operation. They are *fixed beam portable* antennas, usually of briefcase type, and *fully mobile* systems such as those installed on a land vehicle. The fixed position antennas can be further divided into two types according to their gain: *briefcase type* and *suitcase type*. The *briefcase type* is a low gain option and uses microstrip patch antennas. The *suitcase type* is a high gain option and uses parabolic reflectors made of a foldable parabolic mesh like an umbrella [2]. This is to facilitate transportation. Different

varieties of *briefcase type* and *suitcase type* MSAT terminals are commercially available in the MSAT market [2].

The *fully mobile* antennas can be further classified into fixed beam low gain *omni-directional* antennas and medium to high gain *steerable beam* antennas. *Omni-directional* antennas include rod antennas of bifilar or quadrifilar helical antennas, cross-drooping dipoles and higher-order-mode microstrip patch antennas [3]. These antennas are used for data communications where gain values in the range of 2-4 dBi are sufficient. Medium to high gain *steerable* antennas can be further divided into three different types according to their scanning techniques. They are *electronically steerable* antennas, *mechanically steerable* antennas or they can be a combination of the two. In this case, they are called *electro-mechanically steerable* antennas. *Electronically steerable* antennas can be further divided into four groups. They are *phased array* antennas, *switched beam array* antennas, *adaptive array* antennas and *self-scanned array* antennas. The following is a detailed discussion of different medium gain electronically steerable antennas that have been introduced.

HIGH GAIN STEERABLE ANTENNAS

Directional steerable antennas are medium to high gain antennas that tend to have a gain value in the range of 8 to 20 dB. These antennas are made up of an array of small antenna elements. The advantage of most directional antennas as opposed to *omni-directional* antennas is that the former tends to have better performance and suffer less from signal fading. The disadvantage of most directional antennas is that they require a satellite tracking system to point the focused beam of the antenna in the direction of the satellite. Such antennas are therefore more costly to produce than omni-directional antennas. In addition, the higher gain directional antennas are usually much larger in size. Nevertheless, while size and cost are disadvantages, the extra performance of directional antennas is desirable in LMSS applications. A block diagram of the high gain electronically steerable antennas is presented in Fig.1.
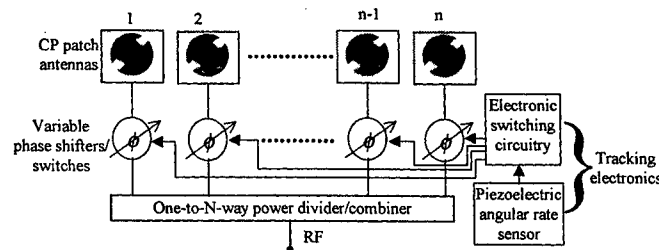
Fig.1. Block diagram of an electronically steerable antenna.

The satellite tracking can be established using the combination of *closed-loop* and *open-loop* control systems. In the initial state of the antenna operation, the transceiver unit (TU) activates antenna beams and locks the antenna to the satellite with the strongest beam. This is called the *initial acquisition*. As the antenna is locked to the satellite, the CPU of the TU records the received signal strength during an interval of milliseconds. If the vehicle is in smooth transition, the received signal drop can be adjusted internally by activating the nearby beams of the original beam configuration. This mode of tracking operation is called *closed loop* tracking. If the received signal drops by a significant amount due to a sharp turn of the vehicle, a steep terrain or obstacles, the TU's CPU receives information from the angular rate sensor. The CPU then calculates the amount of angular rotation and the direction of rotation. Based on this calculation, the CPU decides which beam should be activated. The CPU then sends appropriate information to the switching circuitry of the tracking electronics. The digitised information from the switching electronics actuates phase shifters or switches so that the antenna can regenerate directional beams. The beam is redirected to the satellite and the system regains communications immediately after the obstacle is removed. This mode of operation is called *open loop* tracking. The *open loop* tracking system is particularly useful when the vehicle takes a sharp turn or passes through an obstacle such as tunnels, bridges and buildings.

- **Phased Array Antennas**

Researchers around the world have proposed a number of phased array antennas for use in MSAT. Ball Aerospace Corporation [4] in USA, Teledyne Ryan Electronics [5] in USA, CRL [6] in Japan, The Toyota Central R & D Laboratories [7] in Japan and CSELT in Italy [8] have developed low profile phased array antennas consisting of 19 elements, a 19-way power divider/combiner and 18 digital phase shifter arrays. These antennas are capable of capturing signals in 0° to 90° elevation and 360° azimuth coverage. The basic differences in these designs are the antenna radiating elements. Most of the radiating elements are in microstrip format. As antennas are very similar in dimensions and construction, they have very similar performance. With careful designs, they have low loss and high gain at the higher elevation angles. The only disadvantage is their low gain at low elevation angles and relatively high cost as expensive PIN diodes are used in the phase shifters that form a beamforming network. Recently the smaller version of the phased array antenna with only 12 antenna elements and very low cost phase shifters has been developed by the authors [9].

- **Switched Beam Array Antennas**

The alternative to the *phased array antenna* is the *switched beam array antenna*. In [10], Bialkowski *et al* proposed a configuration/system of 14 elements around a truncated cone structure with 3 elements active at a time. For such an antenna, a 14-way-3-element-on radial switch is used to energise the radiating elements. The advantage of switched beam arrays is that they do not required phase shifters and therefore have simpler and cheaper feed network development. The disadvantages are a higher profile than that of a phased array antenna and a considerable null between adjacent beams. The many connectors and coaxial cable assemblies between different modules make the manufacture of this antenna a difficult task.

An improvement in the null region between adjacent switched beams can be obtained by using a combination of switching and phase shifting actions simultaneously [11]. While switching a few elements ON and the rest OFF, gain drop is minimized with the beam steering in limited azimuth angles. In a *switched beam phased array*, the total number of beams can be increased significantly in comparison with the standard *switched beam array*. Due to a larger number of beams, the gain drop at the null can be improved by 1 dB. The advantages of the *switched beam phased array* over the phased arrays are: (i) fewer phase shifters are required, therefore the production cost is less; and (ii) less complex control algorithm and control electronics are needed as the action requires less involvement of active antenna elements. The disadvantages are: (i) the antenna is not a planar design, therefore it requires many coaxial connections; (ii) modules are arranged in tiered layers, therefore they are labor intensive to manufacture; and (iii) antenna elements need to be mounted on an inclined surface to eliminate the requirement of elevation steering. Hence the design results in a high profile antenna.

- **Adaptive Array Antennas**

In *adaptive antenna arrays*, beamforming is carried out by a digital signal processor (DSP), so that both excitations and phases can be controlled more precisely in *adaptive arrays* than in conventional phased arrays. The rapid development of VLSI techniques has made it feasible to take advantage of digital hardware. J. I. Alonso *et al* [12] has reported a 6-element *adaptive array* for integrated GPS and MSAT applications. The array consists of six broadband rectangular patches that are arranged in a hexagonal fashion. They are connected to six hybrid couplers followed by six monolithic low noise amplifiers (LNAs). Outputs from six elements pass through six quadrature phase shift keyed (QPSK) modulator HPMX2001 integrated circuits (ICs). The ICs are controlled by two DC control signals I' and Q' that are obtained through two 8-bit digital-to-analogue (D/A) converters associated with two 8-bit latch registers. The QPSK modulators produce the desired attenuation and phase shifts to the RF signal. A six-way combiner adds the six output signals of each RF channel. The user's transceiving terminal processes the output of the combiner.

R. Miura *et al* [13] and I. Chiba [14] have reported a 4×4-element DBF square array. This antenna has the capability of allowing the nulls to be steered in the directions of interference signals. The elements are connected to LNAs followed by down converters (D/Cs). D/Cs directly convert the RF signals (at 1.54 GHz) to the intermediate frequency (IF) signals at 32 kHz. The IF signals are then passed through

the band pass filter (BPF) and digitised by A/D converters. The digitised signals are then fed into DSPs. The DSP precisely controls the antenna beam according to the algorithm that is loaded in it. The disadvantage of the adaptive array is that it is very hardware and software intensive and, therefore, very costly.

- **Self Scanned Array Antennas**

L. Shafai [15] has proposed a new approach of beam steering called a *self-scanning* array. Two microstrip patch antennas that operate at two adjacent modes are stacked one above/over the other. The beam steering is achieved by introducing a phase shift between the stacked elements resulting in the development of a low cost *self-scanning* array element. Two different types of antennas are designed. One is a single element unit (with stacked patches operating at TM_{11} and TM_{21} modes respectively) providing a moderate gain of about 7 dBi at 32° elevation angle, and the other is a 7-element array with a peak gain of about 14 dBi. Two different sets of phase shifters (seven 2-bit or 3-bit phase shifters and three 4-bit phase shifters) are necessary to scan beams of the 7-element array.

CONCLUSIONS

In this paper different ground station antennas for mobile satellite communications have been discussed. Two different types, fixed beam portable antennas and electronically steerable antennas are used for MSAT. The operation of electronically steerable antennas requires switching electronics and gyro sensors for open look satellite tracking. Finally different electronically steerable antenna systems developed by different researchers have been presented with their technical details.

REFERENCES

1. B.R. Elbert, *The Satellite Communication Applications Handbook*, Artech House Inc., Boston, USA, 1997
2. *TRANSAT*, "Inmarsat-M and B Buyer's Guide", Inmarsat, London, UK, No. 27, July 1994, pp. i-viii.
3. A.W. Jongejans, P.J. Rinous and A. G. Roederer, "Review of ESA Mobile Antenna Developments for Satellite Communications", *IEEE AP-S Int. Symp. Digest*, 1995, pp. 1838-1341.
4. F. Schmidt and B. Cox, "Electronic Steered Phased Array Antenna For MSAT", *MSN*, Vol. 18, No. 11, 1988, pp. 41-43.
5. G. Schaffner, "Low Cost Cartop Phased Array Steering", *1987 IEEE MTT-S Digest*, pp. 949-952.
6. S. Ohmori, S. Yamamoto and K. Tanaka, "Phased Array Tracking Antenna System for Vehicles", *Proc. of IREECON 1992*, pp.17-20.
7. K. Nishikawa, K. Sato, T. Hirako, T. Yamanaka and N. Takahashi, "Phased Array Antenna for Land Vehicle Satellite Communications", *Denshi Tokyo*, No. 29 (1990), pp. 87-90.
8. P. Ansbro, D. Finotto and P. Gianola, "A Phased Array Antenna System for Mobile Communications in L-band", *Proc. of 1995 Asia-Pacific Microwave Conference*, Korea, pp. 944-947.
9. M.E. Bialkowski and N.C. Karmakar, "A Two-Ring Circular Phased Array for Mobile Satellite Communications", *IEEE AP-S Magazine*, Vol. 41, No. 3, June 1999, pp. 14-23.
10. M.E. Bialkowski, S.T. Jellett and R.S. Varnes, "Electronically Steered Antenna System for the Australian Mobilesat", *IEE Proc. Microw. Antennas Propag.* Vol. 143, No. 4, August 1996, pp. 347-352.
11. N.C. Karmakar and M.E. Bialkowski, "A Compact Switched-Beam Array Antenna for Mobile Satellite Communications", *Microwave and Optical Technology Letters*, John Wiley & Sons, USA, vol. 21, No. 3, May 1999, pp. 186-191.
12. J.I. Alonso, J.M. Blas, L.E. Garcia, J. Ramos, J. Pablos, J. Grajal, G.G. Gentili, J. Gismero and F. Perez, "Low Cost Electronically Steered Antenna and Receiver System for Mobile Satellite Communications", *Trans. IEEE MTT*, Vol. 44, No. 12, Dec., 1996, pp. 2438-2449.
13. R. Miura, T. Tanaka, A. Horie, T. Sekiguchi, T. Inoue and Y. Karasawa, "A Land Mobile Satellite Experiment on a DBF Self-beam Steering Array Antenna", *Proc. of Int. Symp. Ant. Prop.*, ISAP '96, Chiba, Japan, pp. 1189-1193.
14. I. Chiba, "Adaptive and Digital Beam Forming Antennas for Mobile Communications", Proc. Of Asia-Pacific Microw. Conf., 1994, Korea, pp. 831-834.
15. L. Shafai, "MSAT Vehicular Antennas with Self Scanning Array Elements", *Proc. of 2nd Int. Mobile Satellite Conf.*, Ottawa, 1990, pp. 523-527.

3-bit Digital Phase Shifter for Mobile DBS Active Phased Array Antenna System Application

S.Y. Eom, S.I. Jeon, D.G. Oh, H.K. Park[*]

Electronics and Telecommunications Research Institute
161 Kajong-Dong, Yusong-Gu, Taejeon, 305-350, R.O.Korea
Tel.: +82-42-860-4853, FAX.: +82-42-860-5740, eMail: syeom@etri.re.kr
* Dept. of Electrical & Computer Engineering, Yonsei Univ.

Abstract — In this paper, the 3-bit digital pin diode phase shifter of the hybrid-coupled reflection type is designed and fabricated for the mobile DBS application of an active phased array antenna system. Its fractional bandwidth is about 17%(VSWR=2:1). The theoretical considerations for the phase shifter design are briefly described. The experimental results for the fabricated 3-bit phase shifter such as the insertion loss and phase response, and its variations according to each phase state are presented, and also the overall insertion loss variations due to the forward current variations of each pin diode used in the phase shifter are given and the discussion about those results will be made in the system application aspect.

I. INTRODUCTION

As direct broadcasting satellite(DBS) services in the Ku-band become more widespread, the need for TV programs reception by vehicles, such as small cars, buses, trains, ships and so on, is more growing[1]. Since DBS system covers a wide region, it is inherently suitable for mobile reception. DBS reception services by vehicles have advantages in propagation conditions compared to its terrestrial TV broadcasting services due to suffering less interference by receiving directly TV signal from DBS, not multi-path environment.

The Ku-band mobile active phased array antenna system(APAA) which could receive DBS signal from Koreasat, as engineering and also practical model, had been already developed[2,3] by ETRI in Korea.

As the two-port key element of a phased array antenna system, the phase shifter gives the role to change the phase of the input signal ideally without the insertion loss, but practically it has the insertion loss variation according to each phase state. The electronic phase shifter can be broadly classified into two groups, that is, the reflection type and the transmission type. A variety of electronic digital phase shifters can be configured by mounting on the one or more diodes in different types of transmission line circuit elements, but in general, two or more diodes in arbitrary 1-bit phase shifter design are required for the simultaneous perfect matching at two control states. But, the phase shifter with less than 11.25° phase quantity using one diode can give good simultaneous matching performances.

The 3-bit digital phase shifter using the branch-line hybrid-coupled reflection type uses beam lead pin diodes as a microwave semiconductor control device, which can approximately give the desired short-circuit(practically,

low forward series resistance) and open-circuit(practically, very low capacitance) conditions at microwave frequencies under forward and reverse bias states, respectively. The 3-bit digital phase shifter requires the electrical specification summarized in Table I.

Table I. Electrical specification of the phase shifter

Item description	Specification
Operating band	10.5~12.5 GHz
Phase range	360°
Insertion loss	5 dB Typ.
Insertion loss variation	± 1 dB Max.
Digital control bit	3-bit
Min. phase increment	45°
Phase error	±22.5° Max.
I/O return loss	9.5 dB Min.
I/O impedance	50 Ω
Operating temperature	-30 ~ 55° C

II. PHASE SHIFTER DESIGN

The hybrid coupled phase shifter makes use of a 3-dB, 90° hybrid coupler with two of its ports terminated in symmetric phase-controllable reflective networks. Fig. 1 shows the general schematic of the phase shifter, which uses reflection type circuit of the open-circuited transmission line with a series switch(pin diode), and its configuration is available in this paper.
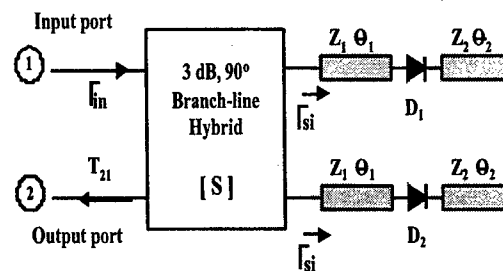
Fig. 1. Schematic of the used hybrid coupled phase shifter

The hybrid coupled phase shifters are slightly superior to others due to a lower number of switching pin diodes per bit, and higher power-handling capacity and the ability to obtain any desired phase shift[4]. Expressions for the phase shift and insertion loss, taking a complete equivalent circuit of a pin diode, have been derived[5]. Optimization

of matching networks has been made[6]. But, the hybrid coupler and reflection networks including pin diodes should be considered simultaneously in the phase shifter design to obtain the constant phase shift versus frequency in the operating band. For this, the scattering parameters of the overall network are needed. The transmission and reflection parameters of the overall network are given in the following equation (1) and (2) [4].

$$T_{21} = S_{12} + \Gamma_{si} \begin{bmatrix} S_{41} & S_{31} \end{bmatrix} \begin{bmatrix} 1-\Gamma_{si}S_{11} & -\Gamma_{si}S_{21} \\ -\Gamma_{si}S_{21} & 1-\Gamma_{si}S_{11} \end{bmatrix}^{-1} \begin{bmatrix} S_{31} \\ S_{41} \end{bmatrix} \quad (1)$$

$$\Gamma_{in} = S_{11} + \Gamma_{si} \begin{bmatrix} S_{31} & S_{41} \end{bmatrix} \begin{bmatrix} 1-\Gamma_{si}S_{11} & -\Gamma_{si}S_{21} \\ -\Gamma_{si}S_{21} & 1-\Gamma_{si}S_{11} \end{bmatrix}^{-1} \begin{bmatrix} S_{31} \\ S_{41} \end{bmatrix} \quad (2)$$

where, Γ_{in}, i=0,1, is reflection coefficient under forward or reverse bias states, respectively. In this paper, first of all, the base element of branch-line hybrid was optimized in the operating band using HP Eesof simulator. The each reflection network for three phase bit(45°, 90°, 180°) was designed and optimized with the fixed parameters of the base element, and real electrical parameters of a pin diode was considered in this simulation. The Alpha beam lead pin diode, DSG6405 was used in this design, and its forward resistance is typically 4.5Ω(@100MHz, 20mA) and total capacitance is typically 0.017pF(@1MHz, 50V).

The forward resistance R_s versus forward current I_d curve of the above pin diode is shown in Fig. 2 and its curve response was obtained by the direct measurement.

Rs vs. Id Curve
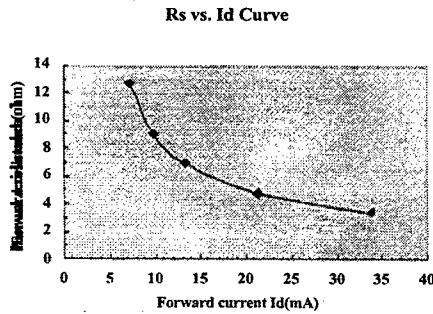
Fig. 2. Measured forward resistance vs. forward current

The base element of branch-line hybrid was designed as 100 Ω system to design the phase shifter with small size. Because the input and output of the phase shifter requires 50 Ω characteristic impedance, the coupled line impedance transformer, which blocks the reference DC voltage of the circuit and converts from 50 Ω to 100 Ω, was used between the input or output port and the base element. Its structure is shown in Fig. 3. When the electrical length of the coupled line is 90°, the even and odd mode impedance is given in equation (3) and (4)[7].

$$Z_{Oe} = Z_L \left[1 + \sqrt{\frac{Z_S}{Z_L}} \right] \quad (3)$$

$$Z_{Oo} = Z_L \left[1 - \sqrt{\frac{Z_S}{Z_L}} \right] \quad (4)$$
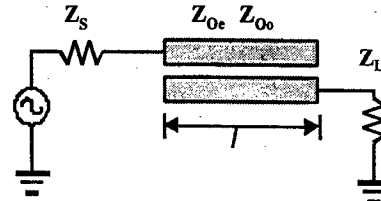
Fig. 3. The structure of the coupled line impedance transformer

From (3) and (4), the values of Z_{Oe} and Z_{Oo} are 170.71 Ω and 29.29 Ω, respectively.

The reflection circuit of the phase shifter uses the open-circuited transmission line with a series pin diode as shown in Fig. 1. If the used pin diode is ideal, the required phase shift form the circuit can be easily obtained from the electrical length $2\theta_2$. But, a real microwave semiconductor pin diode has low capacitance under reverse bias condition. And, this value brings the effect to extend the electrical length θ_1 to the following equation (5).

$$\theta' = \beta l' = \cot^{-1} \left[\frac{1}{\omega C_j Z_o} \right] \quad (5)$$

where, Z_o is 100 Ω, and from (5), additional phase shift is about 7° at center frequency.

In the phase shifter structure which is composed of the branch-line 90° hybrid and the open-circuited transmission line with a series pin diode, its bandwidth has an influence on the electrical length variation θ_1.

III. EXPERIMENTAL RESULTS AND DISCUSSION

Taconic TLY-5A soft substrate with ε_r=2.17, H=20mils, T=0.5oz., and tanδ=0.0009@10GHz as the PCB of the phase shifter was used. Each phase bit was tested independently, and the overall 3-bit phase shifter was cascaded in series as shown in Fig. 4.

Fig. 4 Fabricated 3-bit digital phase shifter

The electrical performances of the 3-bit phase shifter were measured using the HP 8510C vector network analyzer and the phase shifter driver circuit, and a notebook PC with the phase control program.

The input and output return loss performances by each phase state are shown in Fig. 5 and Fig. 6, respectively. They are more than 10 dB within the operating band. The phase responses by each phase state are shown in Fig. 7. They show 45° increment within the phase error boundary of the operating band. From Fig. 8 to Fig. 13, the insertion

various forward current(or forward resistance) conditions. From the figures, the average insertion loss is about 4 dB including I/O SMA connectors which have about 0.5~0.6 dB loss in operating band, and its variation is less than ±1.5 dB within the operating band. It is due to the upper band characteristic. One reason is that impedance matching characteristic of the coupled line impedance transformer circuit in upper band are not so good due to the etching tolerance. Second one is that the base element for 180° bit was a little modified compared with them for 45° and 90° bit to decrease the phase error within 17% bandwidth, and its reflection networks have two microstrip benders which degrade the impedance matching. These will be considered in the next version.

Also, from Fig. 8 to Fig. 13 , it can be known that the forward resistance of a pin diode increases, the insertion loss and its variation increase. Because the mobile DBS APAA system uses many phase shifters including active modules, it requires the limited DC power budget. Therefore, these results show that it should be proper trade-off considering the performances, system bandwidth and the overall DC power consumption of the pin-diode phase shifter. For example, in the system application, if it is assumed that the number of the phase shifter is twelve, and each 3-bit phase shifter is composed of six pin-diodes, then total DC current consumption only by the phase shifter in the system is 2.33A, 1.47A, 0.99A, 0.75A, 0.50A and 0.30A, respectively. If the upper band problem is overcome, 0.5 A current consumption is enough.

The active module including the 3-bit phase shifter designed in this paper is shown in Fig. 14. It is low-cost and is available in the Ku-band mobile APAA system which could receive DBS signal from Koreasat(DBS band : 11.7~12GHz).

Fig. 7. Phase responses vs. frequency
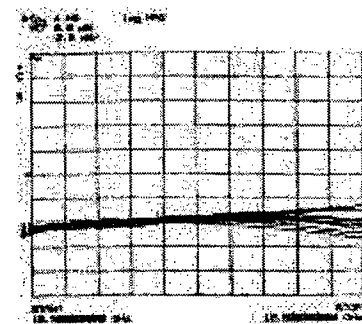
Fig. 8. Insertion loss responses vs. frequency

$(I_d$=32.3 mA, R_s=3.4Ω)
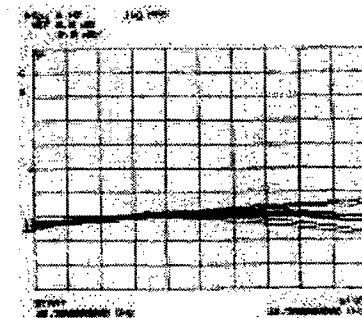
Fig. 9. Insertion loss responses vs. frequency

$(I_d$=20.4 mA, R_s=4.7Ω)

Fig. 5. Input return loss responses vs. frequency

Fig. 6. Output return loss responses vs. frequency
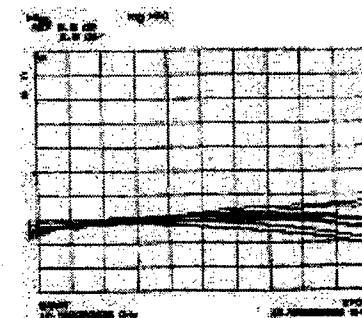
Fig. 10. Insertion loss responses vs. frequency

$(I_d$=13.8 mA, R_s=6.9Ω)
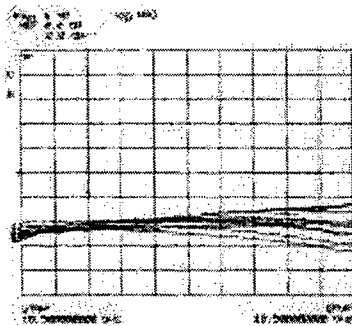
Fig. 11. Insertion loss responses vs. frequency

(I_d=10.4 mA, R_S=9.0Ω)
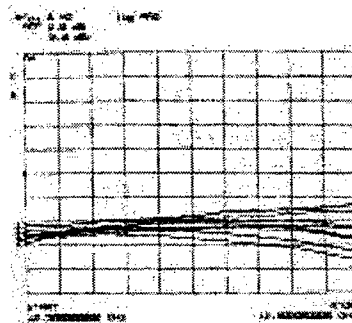
Fig. 12. Insertion loss responses vs. frequency

(I_d=6.9 mA, R_S=12.7Ω)
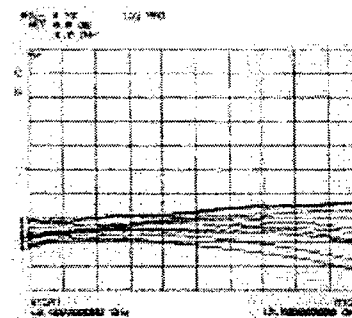
Fig. 13. Insertion loss responses vs. frequency

(I_d=4.1 mA, R_S=18Ω)
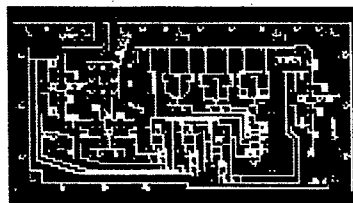
Fig. 14. Active module including 3-bit phase shifter

IV. CONCLUSION

The 3-bit digital pin diode phase shifter of the hybrid-coupled reflection type was designed and fabricated for the mobile DBS APAA system application. The theoretical described. The phase shifter showed the 45° phase increment within 17% fractional bandwidth, and the insertion loss variation was less than ±1.5 dB within the operating band. The insertion loss variations according to forward current conditions of each pin diode were given and the discussion about them was made in the system application aspect. In the future, it will be extended to higher bits and its size will be reduced with various coupled line structures.

REFERENCES

[1] K. Fujimoto, J.R. James, "*Mobile Antenna Systems Handbook*," Artech House, Inc., 1994.

[2] S.I.Jeon, et al., "Active Phased Array Antenna for the Vehicular DBS System of Ku-band", *XXVII Moscow ICATT IEEE AP-S*, pp. 253-256, Sept. 1998.

[3] S.Y.Eom, et al., "Design and Test of RACM in Ku-band Vehicular APAA System for DBS Reception," Proc. of ICEAA '99, pp. 215-218, Sept. 1999.

[4] M. H. Kori and S. Mahapatra, "Integral Analysis of Hybrid-Coupled Semiconductor Phase Shifters," *IEE Proc.*, Vol. 134, Pt. H, No. 2, pp. 156-162, April 1987.

[5] Shiban K. Koul, Bharathi Bhat.,"Microwave nad Millimeter Wave Phase Shifters," Artech House, Inc., 1991.

[6] P.J. Starski, "Optimization of Matching Network for a Hybrid Coupled Phase Shifter," *IEEE Trans. Microwave Theory Tech.*, Vol. MTT-25, pp. 662-666, Aug. 1977.

[7] Kajfez, D.,and B. S. Vidula, "Design Equations for Symmetric Microstrip DC Blocks," *IEEE Trans. Microwave TheoryTech.*, Vol. MTT-28, pp. 974-981, Sept. 1980.

A LOW SIDELOBE, DIRECTIVE ANTENNA AT 2200 MHz

C.SABATIER, P.COUSIN

FRANCE TELECOM
CNET/DMR/ANT
1581 Fort de la Tête de Chien
06320 LA TURBIE
FRANCE

Introduction

Mobile communications have grown rapidly these last years. UMTS will be soon available. This novel activity has generated new research in the antenna domain. Compact antennas or multiband antennas are two examples of these new developments. To improve mathematical models for propagation in various

Figure 1: Schematic view of the elementary antenna.
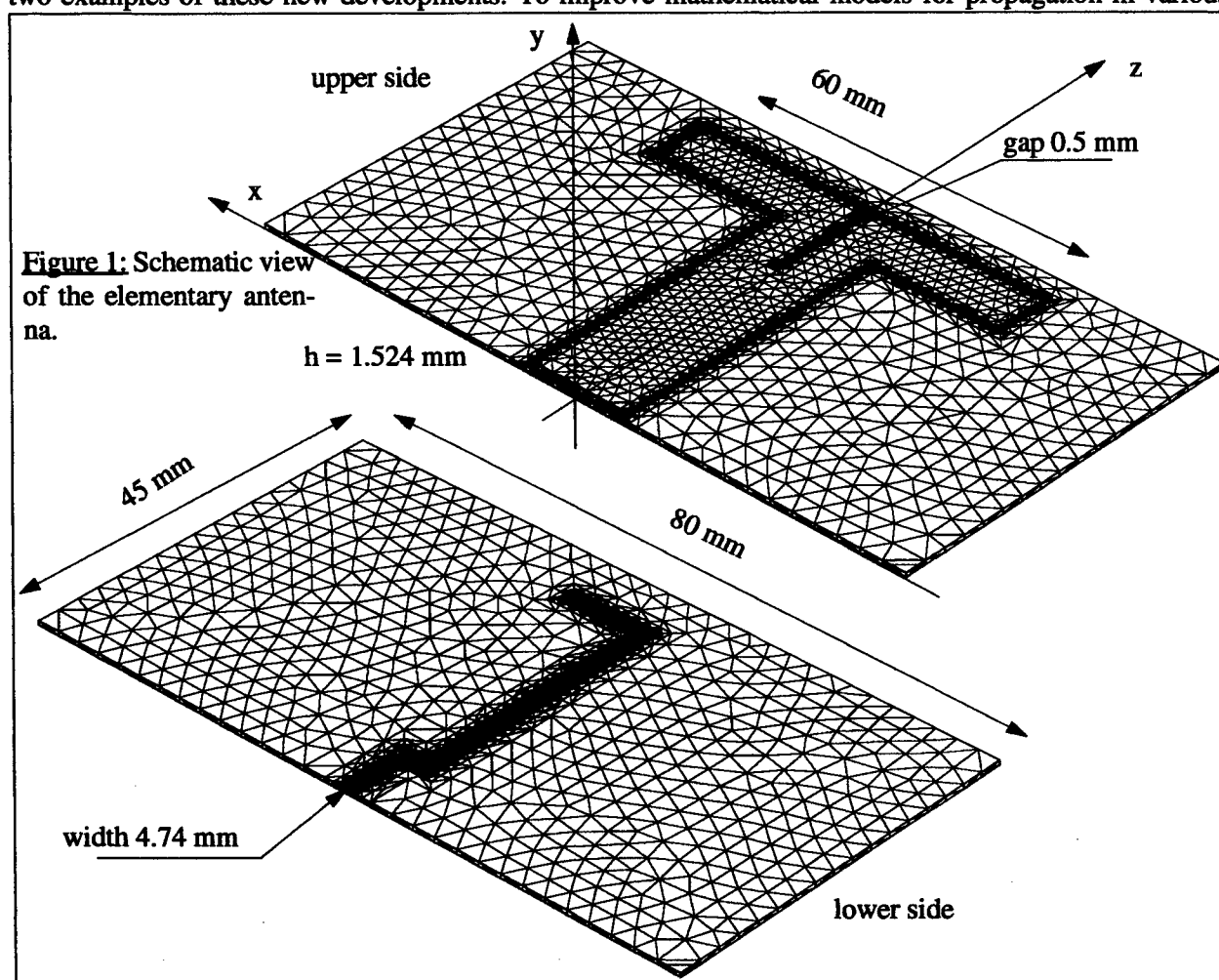
environments, our laboratory was involved in the design of an antenna exhibiting the following performances:

- beam width at 3 dB under the maximum: around 15 degrees
- side lobe level: less than -25 dB under the maximum
- frequency band: 100 MHz around 2200 MHz

- polarization: vertical
- rear gain: around -30 dB under the maximum gain

As the antenna is to mounted on a rotating arm for the characterization of the direction of arrival of the microwave signal, the mass of this antenna must be light.

Isolated dipole

The elementary antenna that we chose, was a dipole etched on a duroid substrate (thickness=1.524 mm, permittivity=2.2), as shown figure 1. This planar antenna, called a T-dipole was designed with our internal software SR3D [1]. Matching is achieved with the help of two stubs: a parallel stub located between the two horizontal arms of the T-dipole and a serial stub at the end of the microstrip. Although the bandwidth of such an element is large (more than 40% for a VSWR <2) because it is a non-resonant antenna, we chose this kind of element due to its mass (15g per antenna). In our frequency band, the maximum VSWR is less than 1.10. The far field of such an element is presented figure 2 at the mid frequency of the bandwidth. Di-

Figure 2: Far field pattern of the isolated dipole.
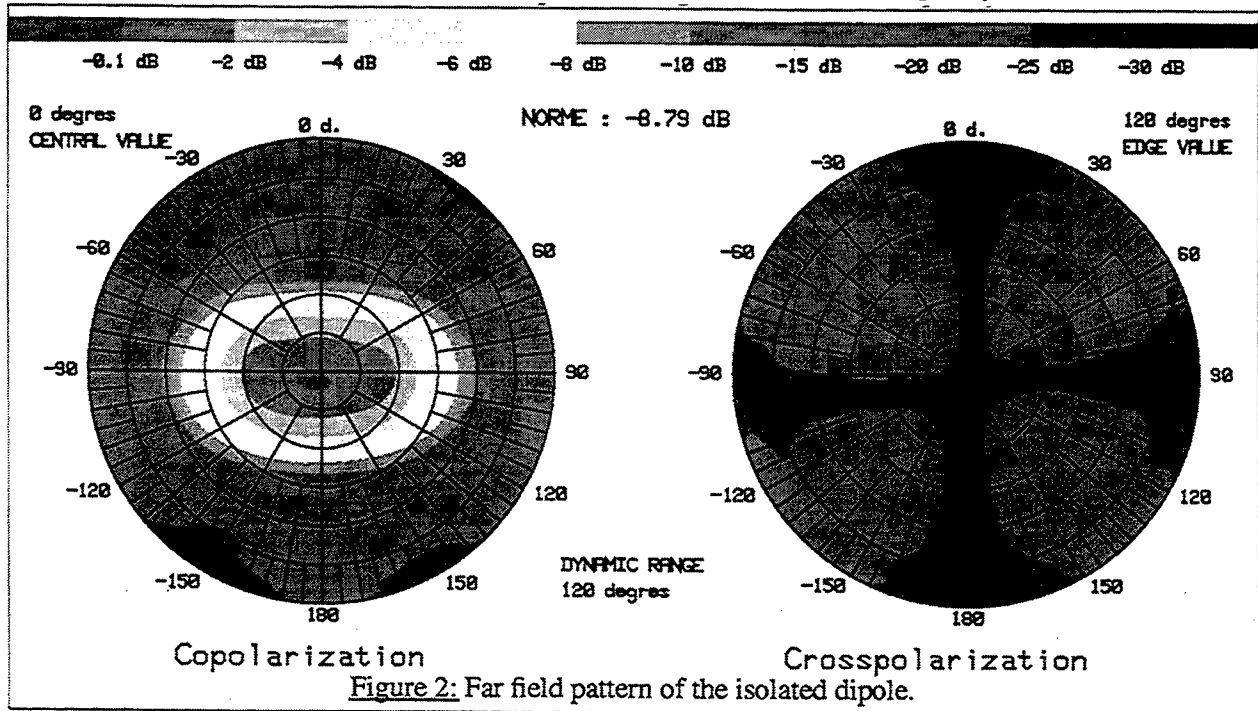
rectivity, obtained by integration of the diagrams up to $\theta = 120$ degrees is 8.79 dB. Losses (ohmic and matching) aren't taken into account. On this map, θ moves along the radius from 0 degrees at the center to 120 degrees at the edge. This limitation of 120 degrees is due to our far field measurement range. The angle φ moves from 0 degrees to 360 degrees.

Simulation of the complete antenna

The far field pattern of the elementary antenna is then expanded in spherical modes [2] for designing the bi-directional array which is made up of 36 identical elements (6 in each direction), spaced at 0.75λ. A specific law is needed to obtain low side lobes (under -25 dB). The amplitude weighting is presented in table 1 (a quarter of the complete structure due to the symmetry along the x and y axes) and the phase is similar for all the antennas. The computed far field pattern of the complete antenna can be obtained without taking into account the coupling between the elements. Figure 3 presents the co and the cross-polarization at 2200 MHz of the simulated complete antenna which agreed with the performances presented in the introduction.

Figure 3: Theoretical far field pattern of the antenna.
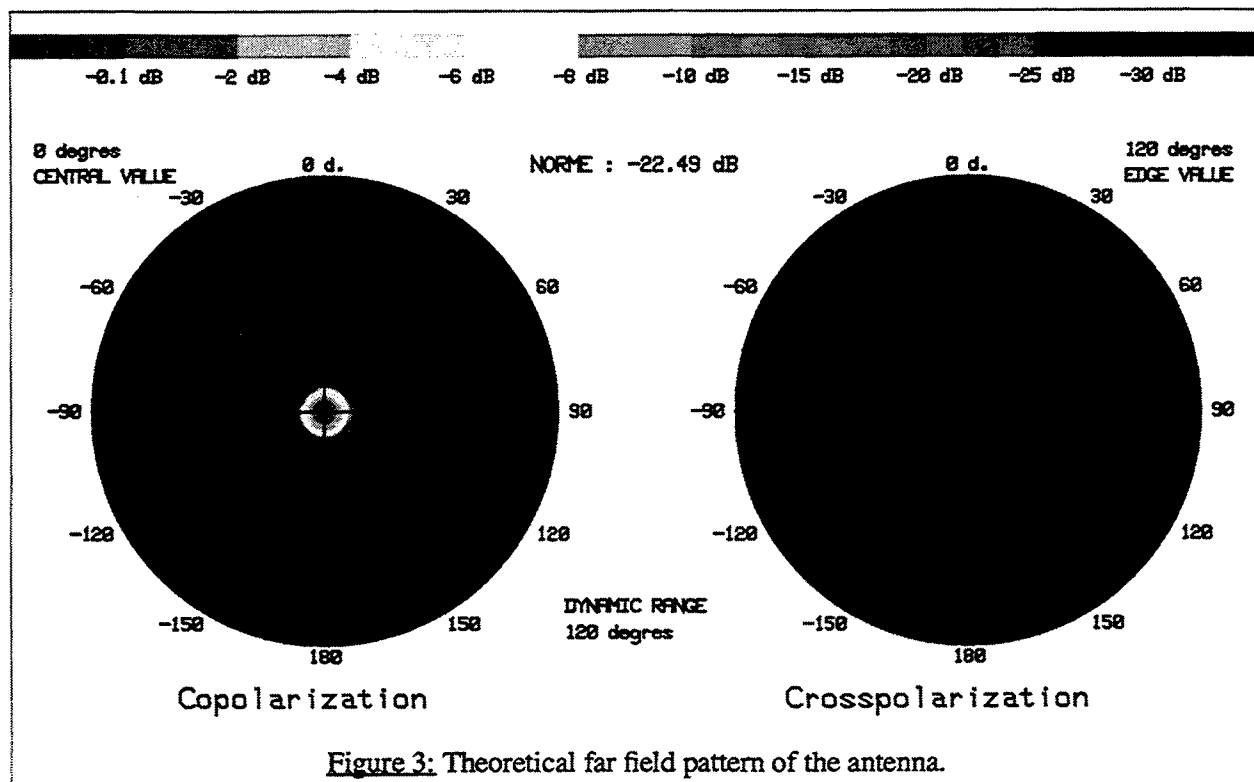
.13 (outer element)	.2	.3
.2	.45	.67
.3	.67	1. (inner element)

Table 1:amplitude excitation of a quarter of the structure

Experimental results

The feeding circuit (1 entry, 36 exits) was designed with MDS and etched on the same substrate as the antennas. The link between the circuit and the antennas is assumed to be via cables having the same length. The antennas and the circuit are set inside a metallic box (600x600x160 mm) to obtain a low level back lobe. The experimental far field pattern is shown figure 4 at 2200 MHz. We note a good correlation between experimental and theoretical results. The level for all the side lobes is under -25 dB and the rear gain is also under -30 dB. The width of the main lobe at 3 dB under the maximum is around 15 degrees and is independent of the elevation angle. The other characteristics of the antenna are 1.35 for the VSWR and 20.5 dB for the gain at the mid frequency of the frequency bandwidth. The losses due to the cables, the connections, the substrate,etc,... are around 1.8 dB. The mass of the antenna is 8.5 kg. Pictures of the antenna are shown in figure 5. The left-hand photo is the radiating T-dipole array and the right-hand photo represents the feeding circuit without the inter-connecting cables.

Conclusion

The antenna developed is compliant in regard to the specifications. The impact of coupling between the elements or with the edge of the metallic structure wasn't taken into account for the design of the antenna. The good agreement between the simulated and measured results shows that this impact is low for the radiated fields.

Figure 4: Experimental far field pattern of the antenna.

Figure 5: Views of the radiating array and of the feeding circuit during the assembling of the antenna.
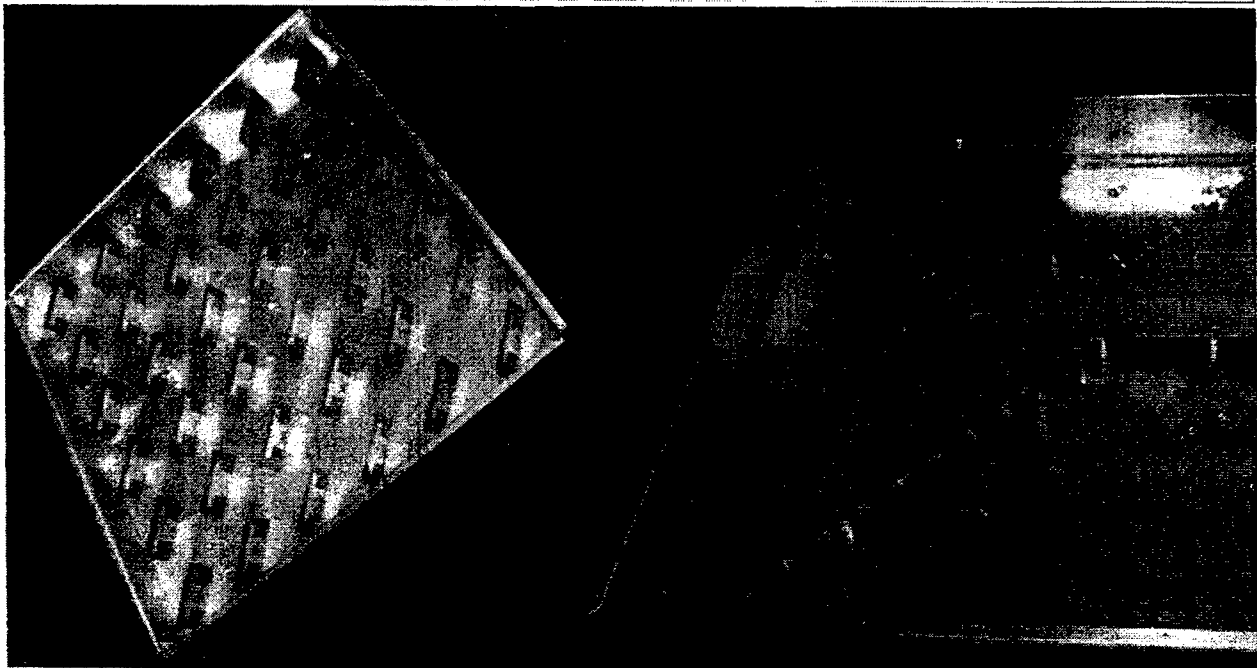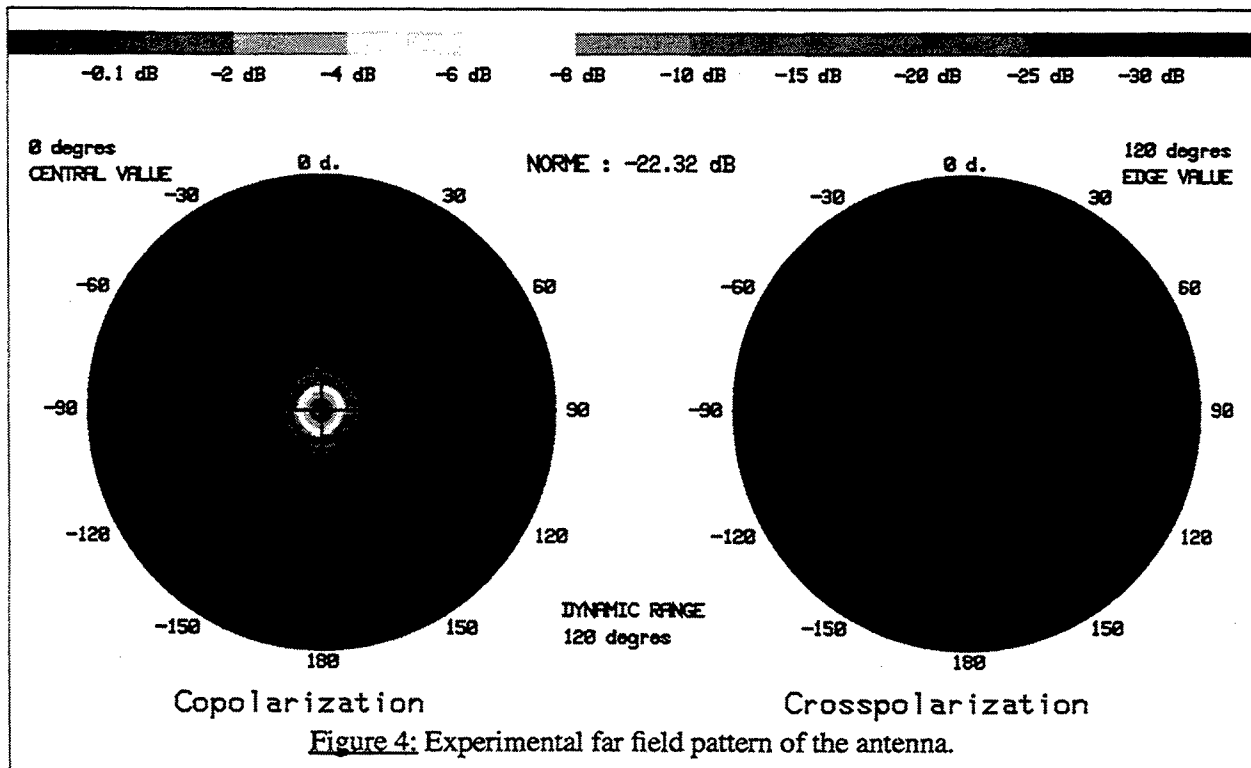
References

[1] P.RATAJCZAK, P.BRACHAT and C.DEDEBAN, "Modeling of arbitrarily radiating elements using the CAD tool SR3D",IEEE /AP-S International Symposium and USNC/URSI Radio Science Meeting, Montréal, 1997.

[2] J.E.HANSEN, "Spherical Near-Field Antenna Measurements", Peter Peregrinus Ltd., Londres, 1988.

MP1

Phased Array Advances in Japan

Phased Array Advances in Japan

Analysis of Phased Arrays of Printed Microstrip Patches with Parasitic Elements

Tsunehisa Marumoto and Ryuichi Iwata

Microwave and Satellite Communications Division, NEC Corporation
4035, Ikebe-Cho, Tsuzuki-ku, Yokohama 224-8555, Japan

Abstract: The mutual coupling effect in phased arrays of patch elements on relatively high permitivity substrates is discussed. Mutual coupling properties of a single layer (un-stacked) patch and stacked patches with/without an air layer are compared as for both port coupling and re-radiation level. To estimate the mutual coupling effects in 2-dimensioanl array environments, 4x4 element arrays are simulated.

1. INTRODUCTION

Phased arrays employing printed microstrip patch antennas as radiation elements have many features such as compact, lightweight, easy-to-manufacture, etc. Especially, in high frequency bands above sub-millimeter wave, patch antenna elements can be integrated with phase shifting devices on the same substrate. Thus, properties of phased arrays using patch antennas have been investigated by many authors [1]-[4].

However, bandwidth of patch antennas is comparably narrow especially when substrates with high permitivity are employed. To solve this problem, practically, patch antennas with parasitic elements (stacked patch antennas) are widely used. As for this type also, mutual coupling effects have already been investigated in [5] and [6], which analyzed mutual coupling effects in substrates with relatively low dielectric constant, implicitly on the condition that the devices are mounted on a different layer from the radiation elements.

This paper discusses the mutual coupling effect in stacked patch antenna phased arrays on relatively high permitivity substrates, which enables integration or mounting of phase shifting devices on the same layer as radiation elements. Firstly, this paper compares mutual coupling between two elements for (A) single layer (un-stacked) patch, (B) stacked patch without an air layer, and (C) stacked patch with an air layer, introducing a method to calculate re-radiation level due to mutual coupling. Secondly, this paper discusses mutual coupling effects in 4x4 element arrays, showing surface wave directional patterns, and reflection / surface wave losses for the above elements. According to the analysis, the mutual coupling decreases by inserting an air layer between the lower substrate (for radiation elements) and the upper substrate (for parasitic element).

2. ELEMENT CONFIGURATION

Configurations of analyzed microstrip patches are shown in Fig.1 and Table 1. In all cases, the thickness and ε_r of the radiation element layer are set at $0.02\lambda_0$ and 6.0, respectively. In these configurations, rectangular patch antennas can be integrated easily with 4-5 bit phase shifters on the same plane.

Both element (C_1) and (C_2) include an air layer between the upper and the lower substrate (the thickness of the air layer is different). This air layer enables integration of devices without physical interference.

Table 1   Microstrip patch antenna configuration

Element Type		Un-stacked	Stacked without Air Layer	Stacked with Air Layer	
		(A)	(B)	(C_1)	(C_2)
Parasitic Element Layer	t	——	$0.05\lambda_0$	$0.05\lambda_0$	$0.05\lambda_0$
	ε_r	——	4.1	4.1	4.1
Air Layer	t	——	——	$0.02\lambda_0$	$0.05\lambda_0$
Radiation Element Layer	t	$0.02\lambda_0$	$0.02\lambda_0$	$0.02\lambda_0$	$0.02\lambda_0$
	ε_r	6.0	6.0	6.0	6.0

t : Thickness of Layer
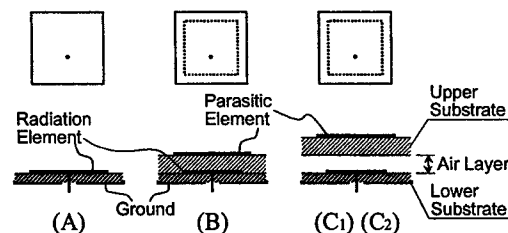
Fig. 1   Microstrip patch antenna configuration

3. MUTUAL COUPLING BETWEEN TWO ELEMENTS

The mutual coupling between two elements were calculated by the method of moment for the elements listed in Table.1.

Fig. 3 shows the mutual coupling between two elements; the output level from the other port (○ : port coupling), and the re-radiated level form the other element (● : re-radiation) that was obtained by the procedure described below.

Fig.4 shows the schematic diagram that explains the calculation method of the re-radiated level. By combining two isolated element patterns multiplied by each appropriate excitation coefficient, 2-element pattern can be reproduced. The excitation coefficients were numerically calculated so as to minimize the error δ expressed by the following equation.

$$\delta = \int \; | \; (\; a_1 e^{j\varphi_1} p_{i1}(\theta,\phi_0) + a_2 e^{j\varphi_2} p_{i2}(\theta,\phi_0) \;)$$
$$- p_{a1}(\theta,\phi_0) \; |^2 \cdot \sin\theta d\theta$$

where,

a_1 : radiation amplitude of #1 element
φ_1 : radiation phase of #1 element
a_2 : re-radiation amplitude of #2 element
φ_2 : re-radiation phase of #2 element
$p_{i1}(\theta,\phi)$: isolated element pattern at #1 location
$p_{i2}(\theta,\phi)$: isolated element pattern at #2 location
$p_{a1}(\theta,\phi)$: element pattern, #1 element is fed,
#2 element is terminated by matched load.
ϕ_0 : angle between x-axis and the line connecting #1–#2 element (see Fig. 4)

The above expression is not accurate in the case of stacked patch antennas, since the excitation mode for "re-radiation" is not the same as that for "radiation" of the isolated element. However, it gives useful information for prediction of the effective re-radiation level.

As shown in Fig. 3, in the case of single layer patch (A) or stacked patch without an air layer (B), the port re-radiation level agrees with the port output level, and the both level decrease gradually as the element distance increases. However, in the case of stacked patches with an air layer ((C₁) and (C₂)), the re-radiation level does not coincide with the port output level especially in the E-plane, and dips can be observed at around 0.5 λ₀ to 0.9 λ₀.

As for the coupling level, that of (B) is higher than that of (A). However, by inserting an air layer ((C₁) or (C₂)), the coupling level decreases obviously in E-plane compared with element (B).

4. BEAM SCANNING CHARACTERISTICS

To estimate mutual coupling effects in 2-dimensional phased arrays, 4x4 element arrays shown in Fig.2 with the elements in Table 1 were investigated.

Fig. 5 shows surface wave pattern from the arrays when the elements are fed with uniform amplitude and scanned to θ=50° in φ=0°, 45° and 90° plane (φ=0° : H-plane, φ=90° : E-plane). The amplitude is normalized by surface wave level from an imaginary source that excites only surface wave isotropically (omni-directionally) with neither radiation nor reflection.

When the array is scanned in φ=0° plane (H-plane), many lobes can be observed but the peak level of each lobe is small. When it is scanned in φ=45° plane, the largest lobe is observed at φ=45°, and the second lobe at around φ=45±90°. And when it is scanned in φ=90° plane (E-plane), where the surface wave loss is maximized as shown later, the largest lobe is observed at φ=–90° (backward), and the second lobe at φ=90°. In practical arrays, these lobes are diffracted from the substrate edges, and affect radiation characteristics (sidelobes, antenna gain, XPD, etc.).

In most cases, the surface wave level of the stacked patch antennas ((B), (C₁) or (C₂)) is higher than that of the un-stacked patch antenna (A). Comparing (C₁) or (C₂) with (B), the surface wave level in most of direction is decreased by 2–5 dB.

Fig. 6 shows the loss due to reflection and surface wave when the elements are fed with uniform amplitude and scanned in φ=0°, 45° and 90° plane. The surface wave loss was calculated by integrating the surface wave pattern obtained in Fig.5. For comparison, the surface wave loss of single element is also shown in the same graph.

Comparing (B) with (A), the excitation of surface wave increases obviously in each plane. However, by inserting an air layer (C₁), both surface wave loss and reflection loss decrease. When the thickness of the air layer is increased from 0.02 λ₀ (C₁) to 0.05λ₀ (C₂), the improvement is comparably small.
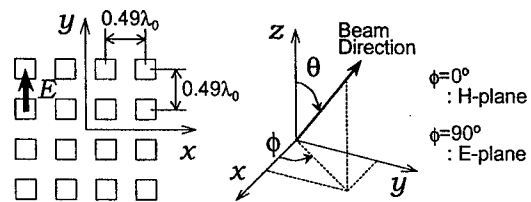
Fig. 2   4x4 array configuration

5. CONCLUSION

Mutual coupling effects on single layer (un-stacked) patches and stacked patches with/ without an air layer were simulated, on the condition that the substrate ε_r for radiation elements is relatively high (ε_r=6.0). According to the analysis, the mutual coupling effects in stacked patches are more than that in single layer patches. However, by inserting an air layer between the upper and the lower substrates, the characteristics can be improved.

REFERENCES

[1] D. M. Pozar, "Finite phased arrays of rectangular microstrip patches," *IEEE trans. Antennas Propagat.*, vol. AP-34, pp. 658-665, May 1986.

[2] ——, "Considerations for millimeter wave printed antennas," *IEEE trans. Antennas Propagat.*, vol. AP-31, pp. 740-747, Sep. 1983.

[3] A. K. Skrivervik and J. R. Mosig, "Analysis of finite phase arrays of microstrip patches," *IEEE trans. Antennas Propagat.*, vol. 41, pp. 1105-1114, Aug. 1993.

[4] S. G. Pan and I. Wolff, "Computation of mutual coupling between slot-coupled microstrip patches in a finite array," *IEEE trans. Antennas Propagat.*, vol. 40, pp. 1047-1053, Sep. 1992.

[5] B. J. Jang, Y. K. Lee, H. W. Moon, Y. J. Yoon and H. K. Park, "Analysis of finite-phased arrays of aperture-coupled stacked microstrip antennas," *IEEE trans. Antennas Propagat.*, vol. 45, pp. 1201-1204, Aug. 1997.

[6] A. K. Skrivervik and J. R. Mosig, "Analysis of printed array antennas," *IEEE trans. Antennas Propagat.*, vol. 45, pp. 1411-1418, Sep. 1997.
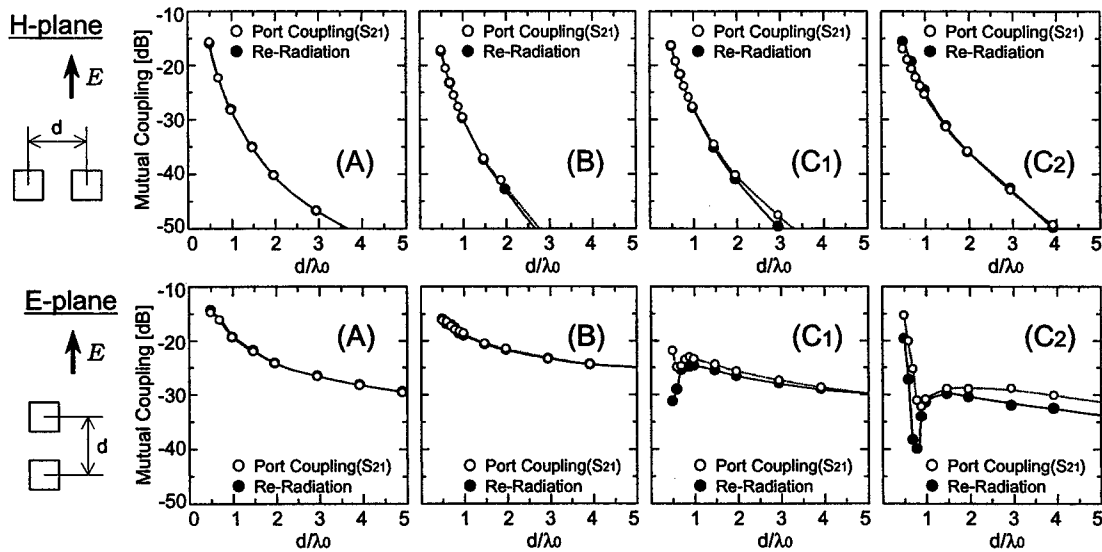
Fig. 3 Mutual coupling between two elements
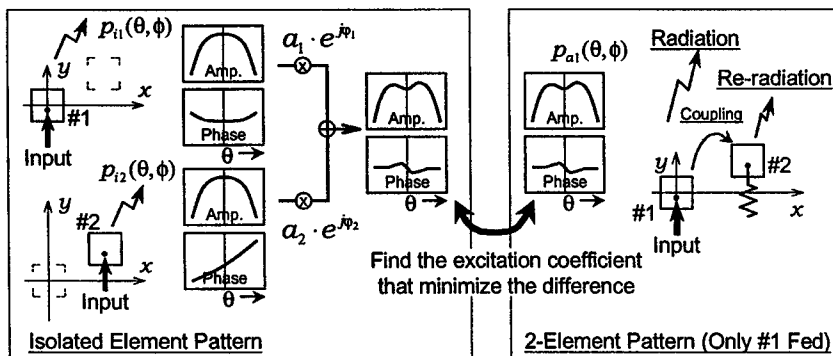
Fig. 4 Calculation of re-radiation coefficients
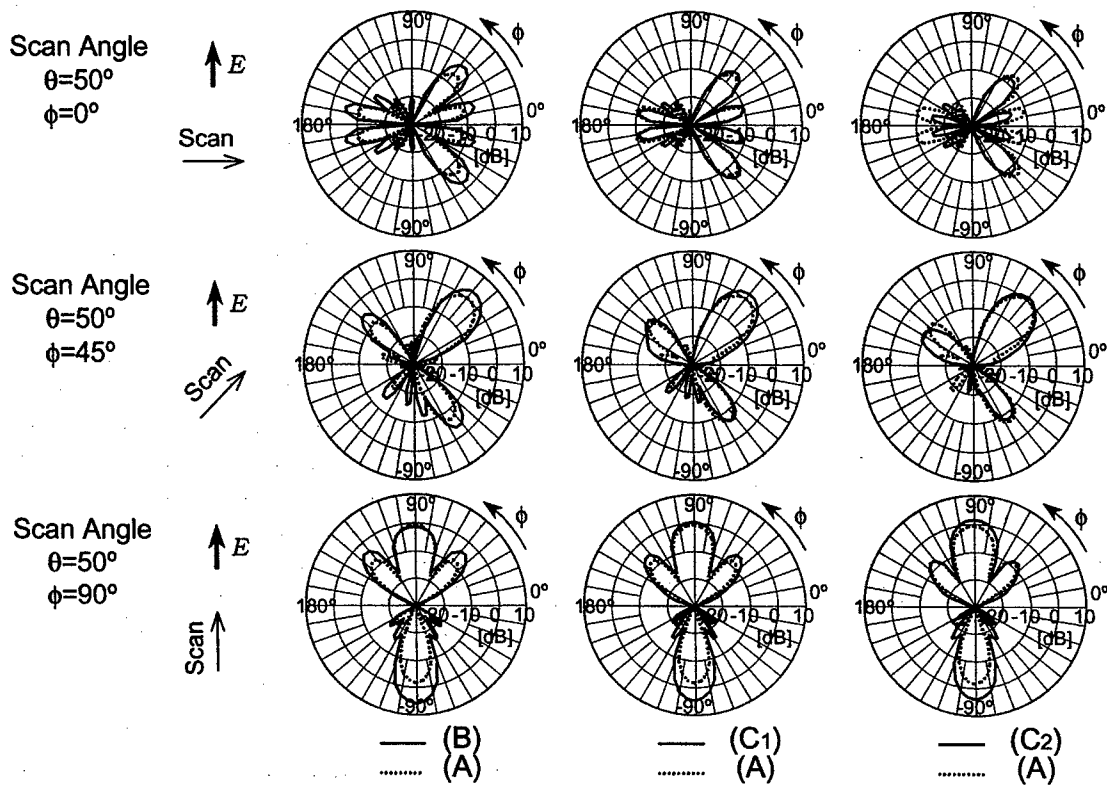
Fig. 5 Surface wave pattern
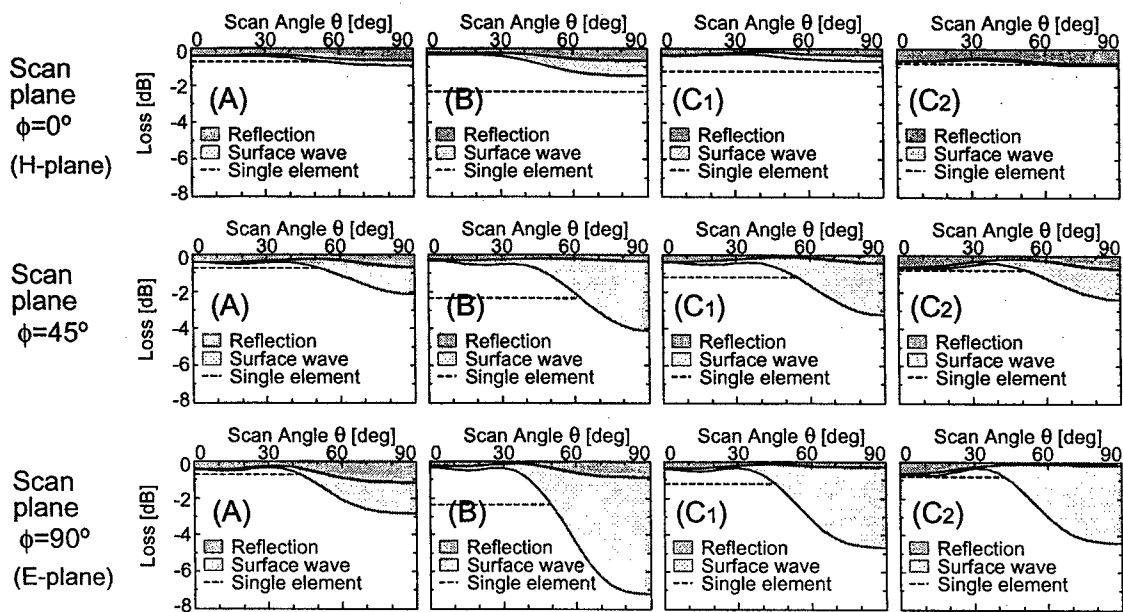
Fig. 6 Loss of 4x4 element array

Electronically Steerable Passive Array Radiator Antennas
for Low-Cost Analog Adaptive Beamforming

Takashi Ohira *and* Koichi Gyoda
ATR Adaptive Communications Research Laboratories
2-2 Hikaridai, Seikacho, Sorakugun, Kyoto 619-0288 Japan
phone:+81-774-95-2710   e-mail:ohira@ieee.org

Abstract   Electronically steerable passive array radiator antennas are proposed for low-cost analog adaptive beamforming. Unlike conventional digital beamforming, they require only one transmitter or receiver. For 2-, 3-, 4- and 5-element antennas, beam and null steering characteristics are estimated by the method of moments. It is numerically shown that full 360-degree continuous azimuthal beam/null steering is possible by at least 4 elements. Also shown is that a directive gain of 9 dBi +/-1 dB and null depth of -50 dBi +/-10 dB are obtained by 5 elements, along with an associated return loss of better than 20 dB at the feeding port. Their drastically low cost and low power consumption could help to achieve adaptive antennas for portable wireless user terminals.

I. INTRODUCTION

EVEN THOUGH adaptive array antennas offer the powerful functionality of variable beamforming and null steering, their use has been almost restricted to military applications due to their complex configuration and high fabrication cost. In recent years, they have been used in some commercial cellular base stations in mobile communication systems. However, the high cost still prevents their use from spreading to the general population in uses such as wireless user terminals. The cost generally increases with the number of radiator elements, since the array needs the same number of RF high-power or low-noise amplifiers as the elements in conventional array antennas. Especially for digital beamforming (DBF) antennas, the same number of frequency converters and D/A or A/D converters is needed in addition to the RF amplifiers. This leads to high weight, high power consumption, and high fabrication costs, which becomes more serious as the number of elements increases.

To reduce the required circuit scale, beamforming in the RF stage is an attractive alternative instead of DBF. Some key technologies toward this alternative are emerging, such as a GaAs single-chip microwave signal processor for variable beamforming [1] and a constant modulus algorithm (CMA) modified specially for microwave analog beamforming adaptive arrays [2].

For further cost reduction, a variable antenna with only one RF port could be a potential candidate. The history of single-port-fed variable antennas dates back to Harrington's dipole array [3]. As an example of the numerical analysis, he showed that the beam direction can be controlled by varying the loaded reactances for a 7-element circular array. However, the theory did not consider the minimum number of elements required to offer 360-degree continuous beam steering. The return loss (VSWR) deviation due to beam steering was not considered either.

Another single-port-fed approach was proposed by Preston et al [4]. Their antenna has 13 elements with switched parasitic or active elements to achieve 360-degree azimuthal coverage with a 30-degree minimum step. However, continuous azimuthal angle adjusting would be desired for adaptive applications because, unfortunately, a deep null is likely to appear only in a very narrow angle.

As an attempt to achieve high-resolution null steering, Dinger [5] demonstrated a planar array antenna that consists of closely coupled microstrip elements with adjustable reactive terminations. It has 9 elements to steer its null continuously in both the elevation and azimuth directions. However, it is difficult to cover full azimuthal angles due to its planar structure.

This paper pursues an ultimate low-cost solution that meets the requirement of full azimuthal continuous beam/null steering. Circularly arrayed monopole passive radiators are analyzed by the method of moments. The radiation patterns and steering characteristics are estimated for 2-, 3-, 4-, and 5-element arrays. Although the steering causes unwanted i/o port impedance deviation in general, a steering scheme with constrained return loss degradation is also proposed.

II. CONFIGURATIONS

A single quarter-wavelength vertical monopole radiator on a ground plane is excited from the bottom in a coaxial fashion. This radiator itself exhibits an omni-directional radiation pattern. To establish directivity in it, the passive radiators are placed in equal intervals around the active radiator and loaded with variable reactors in the bottom. To control the directivity by electronic means, each reactor is implemented with a varactor diode and two fixed inductors in series and parallel, which can carry out any positive and negative value of variable reactance. Figure 1 shows 2-, 3-, 4-, and 5-element versions. These are called electronically steerable passive array radiator antennas or ESPAR antennas in this paper.

III. STEERING CHARACTERISTICS

The radiation pattern was calculated for 2- to 5-element ESPAR antennas by the method of moments.

The ground plane was assumed to have an infinite diameter for simplicity. The space between the center and the passive radiators is a quarter wavelength. According to the Monte Carlo technique, the loaded reactances were randomly varied with a minimum step of 1 ohm and within the range of +/- 250 ohms. The maximum directive gain and the deepest null during 50,000-cycle variations were plotted for each direction on the radar charts shown in Figs. 2 and 3.

It is found that the 2-element ESPAR antenna cannot exhibit high maximum gain, i.e., only 2 dBi in the worst direction (almost broadside). It also cannot exhibit a deep null, i.e., only -8 dBi even in the best direction. This performance is far from sufficient for adaptive applications. A deep null is formed by the 3-element version, only in the broadside directions though. This version has higher gain than the 2-element one, and is symmetrical, but it is still unsatisfactory due to the direction-limited steering ability. Null steering in an arbitrary direction becomes successful with the 4-element version. It can offer gain higher than 7 dBi and null deeper than -40 dBi in an arbitrary direction. Even better performance is obtained by the 5-element version. It can offer gain of 9 dBi +/- 1 dB and null deeper than -50 dBi in an arbitrary direction.

IV. PORT IMPEDANCE DEVIATION

The steering of the ESPAR antennas is based on the strong coupling among the radiator elements. The impedance of the feeding port is also deviated with the steering. The port impedance was calculated by the method of moments for the 5-element ESPAR antenna and plotted on the Smith chart shown in Fig. 4(a). It has a fairly large deviation of $3\sigma = 40$ ohms. This leads the return loss (VSWR) to a level of degradation that will not be acceptable for various practical applications. Therefore, we placed a constraint on the value of the variable reactors. In other words, we employed only the reactances that exhibit the port impedance that satisfies the tolerance of return loss degradation. To determine the boundary of this constraint, the mean value of port impedance plotted in Fig. 4(a) is estimated as $34.4 + j34.4$ ohms. The boundary is determined to be the circle centered at this impedance with a radius of 9.7 ohms. The resulting impedance is plotted in Fig. 4(b). Since it is constrained within the circle, the return loss is much improved, yielding better than -20 dB (VSWR < 1.22).

The constraint of the reactances adversely affects the radiation patterns. The gain and null were calculated again for the 5-element ESPAR antenna but this time with the above mentioned constraint. Figure 5 shows the results. The gain is quite similar to that of the constraint-free steering shown in Fig. 2(d). The null is a little less deep but still maintains almost -40 dBi.

Under this constraint, the radiation patterns in 24 different reactance states were estimated and shown in Fig. 6. The main beam is fixed in the direction of 0 degree keeping the gain at 9 dBi +/- 1 dB throughout these states. The null is successfully steered in various directions as designated by the arrow state by state. For receiver applications, the null should be steered in the direction from which an interference or jamming wave is assumed to arrive. For applications where the receiver is unable to presume the incident direction of the jammer, a blind steering algorithm such as perturbation-based CMA [2] will be effectively used for nulling.

V. CONCLUSIONS

It has been shown for the first time that 360-degree continuous beam/null steering is possible with at least 3 passive radiators around the active one. Four passive elements offer a higher performance in directive gain, null depth, and associated return loss deviation, making it acceptable for practical antenna applications.

Since the ESPAR antenna has much higher gain than omni-directional antennas, the RF power necessary to transmit in wireless systems can be effectively reduced. The co-channel interference in wireless links is associatedly decreased. Even compared with conventional DBF adaptive arrays, the ESPAR antenna consumes much lower dc power as well as, and can be fabricated much more cheaply. This advantage is of great importance especially for implementation in battery-operated wireless devices. Such a simple and low-cost analog beamforming scheme could make it possible for every user's terminal to have an adaptive antenna and bring the idea of smart mobile communication networks closer to reality.

Acknowledgment

References

[1] T. Ohira, Y. Suzuki, H. Ogawa, and H. Kamitsuna, "Megalithic microwave signal processing for phased-array beamforming and steering", IEEE Trans. Microwave Theory Tech., MTT-45, 12, pp.2324-2332, Dec. 1997.
[2] S. Denno and T. Ohira, "Modified constant modulus algorithm for digital signal processing adaptive antennas with microwave analog beamforming", to be published in Proc. IEEE Aerospace Conference, Big Sky, Mar. 2000.
[3] R. F. Harrington, "Reactively controlled directive arrays", IEEE Trans. Antennas and Propagation, AP-26, 3, pp.390-395, May 1978.
[4] S. Preston, D. Thiel, and J. Lu, "A multibeam antenna using switched parasitic and switched active elements for space-division multiple access applications", IEICE Trans. Electron., E82-C, 7, pp.1202-1210, July. 1999.
[5] R. J. Dinger, "A planar version of a 4.0 GHz reactively steered adaptive array", IEEE Trans. Antennas and Propagation, AP-34, 3, pp.427-431, Mar. 1986.

2-element espar antenna

3-element espar antenna

4-element espar antenna

5-element espar antenna

#0 : active radiator   #1-4 : passive radiators
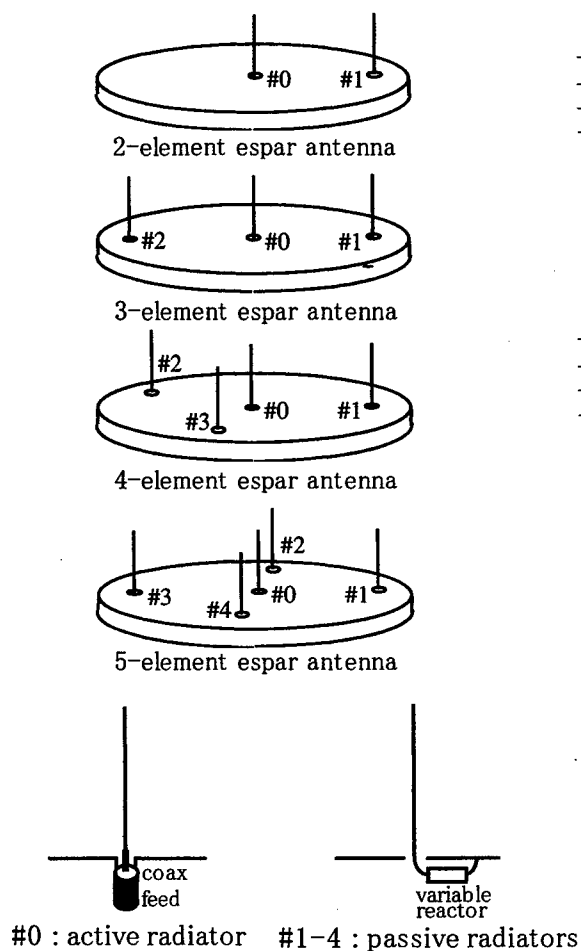
Fig. 1 Espar antenna configuration

(a) 2 elements

(b) 3 elements

(c) 4 elements

(d) 5 elements

Fig. 3 Deepest null in each direction

(a) 2 elements

(b) 3 elements

(c) 4 elements

(d) 5 elements

Fig. 2 Maximum gain in each direction

(a) Random steering

(b) Steering with return loss constraint better than 20dB (VSWR<1.22)
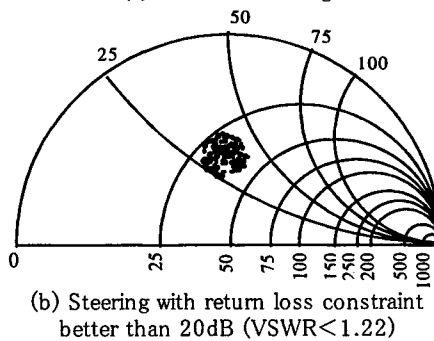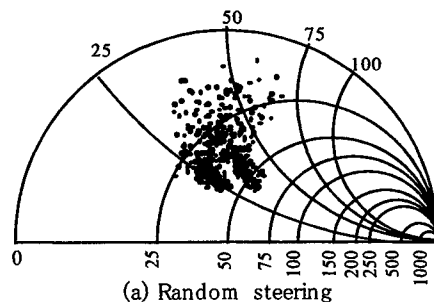
Fig. 4 Port impedance of the 5-element espar antenna

(270)
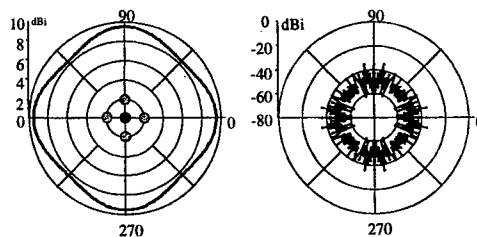
Fig. 5 Maximum gain and deepest null with the return loss constraint

(a) nulled at 62°

(b) nulled at 70°

(c) nulled at 80°

(d) nulled at 90°

(e) nulled at 100°

(f) nulled at 112°

(g) nulled at 120°

(h) nulled at 125°

(i) nulled at 130°

(j) nulled at 135°

(k) nulled at 139°

(l) nulled at 153°
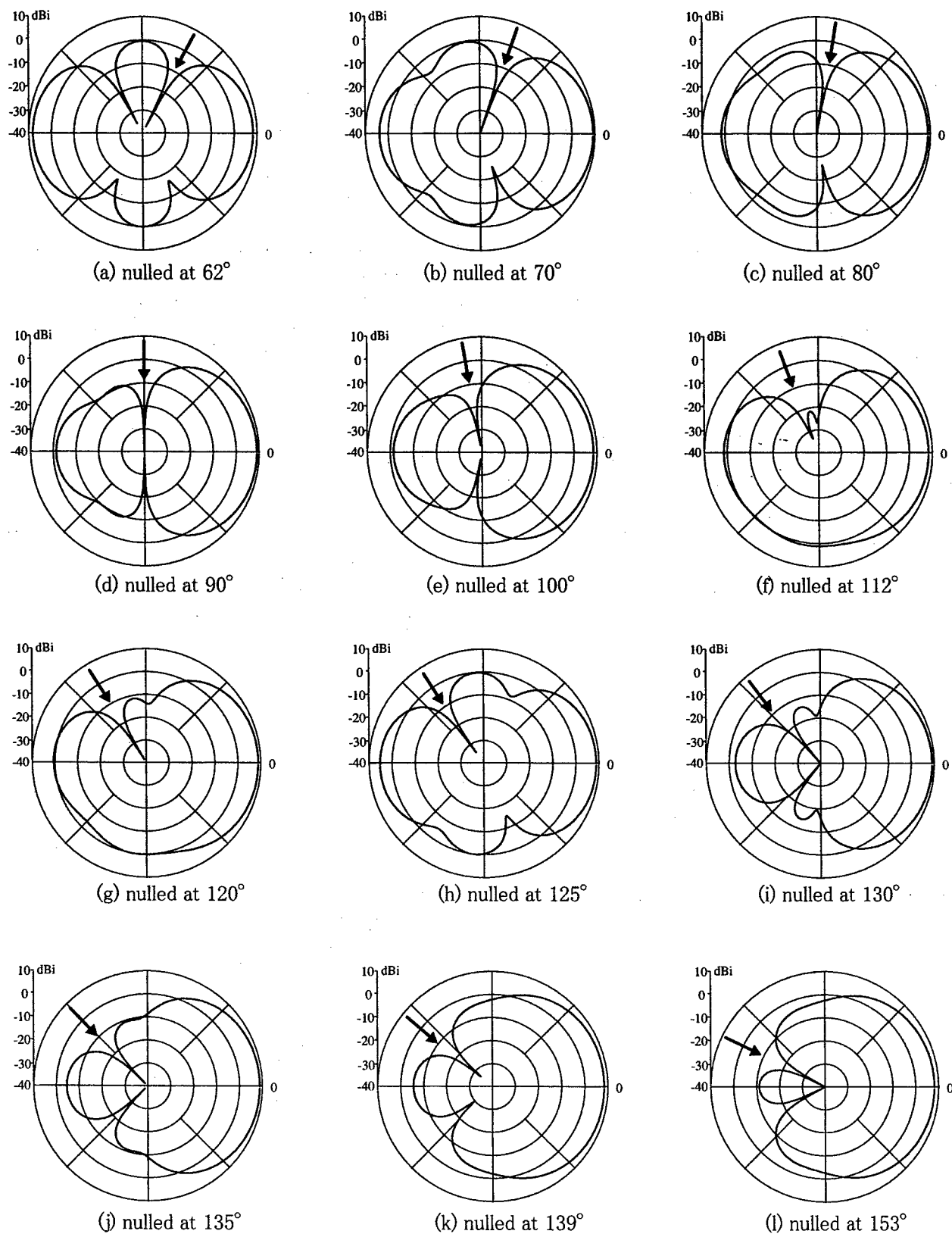
Fig. 6   Null steering of the 5-element espar antenna with the main beam fixed in the direction of 0°

Closed-loop beam forming experiment for an onboard Phased array fed reflector antenna

Yutaka IMAIZUMI, Satoshi HARADA,
Masashi SHIMIZU, Kazuichi YAMAMOTO§ and Katsuhiko ARAKI

NTT Network Innovation Laboratories
1-1 Hikarinooka, Yokosuka-shi, Kanagawa, 239-0847 Japan
TEL: +81-468-59-2463, FAX: +81-468-59-3351, e-mail: yutaka@wslab.ntt.co.jp
§NTT Docomo

Abstract

This paper describes the beam forming procedure for phased array fed reflector antennas and gives the results of a beam forming experiment for a receiving phased array fed reflector antenna. In the experiment, the main beams were aimed at two target directions. The results indicated that the procedure adequately compensates for the mechanical errors of the reflector, alignment errors of the antenna system, and phase and amplitude errors of BFN. The experimental results confirm the effectiveness of the proposed beam forming procedure and algorithm.

Introduction

Recently, phased array fed reflector antennas has been developed for onboard antennas. This antenna can get high gain by a large deployable reflector, and a large number of beams can be achieved by a phased array feed which promise low sidelobe, beam steering and shaping flexibility. But for practical purposes, it is very difficult to steer and shape the beam because this antenna system has various beam pointing error factors, such as excitation coefficient errors, a misalignment between the feed and the reflector, alignment errors between each module of the reflector, mesh surface errors, and so on. The performance index for the beam forming control thus becomes too complex for analytical approach because the performance index involves a non-linear equation. We have developed a pattern tuning method for these cases [1]. This method uses the gradient of the performance index in the genetic algorithm (GA) optimization [2].

This paper describes the beam forming procedure for phased array fed reflector antennas and gives the results of a beam steering experiment for a receiving phased array fed reflector antenna that consisted of 31-element phased array feed and two hexagonal mesh reflector modules.

Beam forming procedure

Phased array feed should be able to compensate for beam pointing errors caused by small mechanical alignment errors. However, if these mechanical errors become too large, antenna performance, particularly antenna gain is significantly reduced. Therefore, one has to ensure that these mechanical errors can be minimized. Figure 1 shows our beam forming procedure. First, the position and the shapes of the reflector and the feed are measured, for example, by using the 3D digital photogrammetry system called V-STARS, and the mechanical alignments of the antenna system are adjusted. V-STARS can measure only the positions that the optical targets are put in advance. In this case 100 optical target put on the reflector. This measurement and adjustment procedure is repeated until antenna's actual geometry nearly fits the designed parameters. This step removes mechanical alignment errors between reflector and feeds from the antenna system. Next, the RF signal is radiated

from the transmission antenna as a reference signal for determining the boresight direction, and the antenna pointing error for this direction is detected by the RF sensor, which is in the array feed section. After that, the adjustment mechanisms attached the feed and the reflector are adjusted until the measured pointing error becomes zero. This step removes the effect of the reflector's surface distortion that is too detailed and cannot measure by V-STARS. This procedure can determine the boresight direction of phased array fed reflector antennas that have complex error factors. The excitation coefficient of the phased array is controlled as follows.

Beam forming algorithm

Figure 2 illustrates the elements involved in the control procedure in the case of the receiving antenna. The beam direction is intended to aim at the direction of a transmission antenna. The RF signal radiated from the transmission antenna is received at each phased array element, and the signals from the elements are synthesized into one signal in the BFN. This synthesized signal is measured and is used as the performance index. Our beam forming algorithm is used to vary the excitation coefficient for the beam steering control until this performance index reaches a maximum value. This algorithm is based on the gradient of the performance index and a special excitation coefficient matrix generated by GA operations [1]. This special matrix is generated by cross over from the elite condition of the preceding generation. This algorithm, as verified by simulation, is faster and stronger versus local minimums than is the normal GA.

Experimental Setup

Figure 3 shows the setup of the main beam direction control experiment for a receiving phased array fed reflector antenna. This phased array fed reflector antenna was composed of a 31-element phased array feed and two hexagonal deployable mesh reflector modules [3] that had an aperture diameter of 4.8 m. The reflector could be steered by the antenna positioner in 2 dof, and by the deployable adaptive supporting structure attached the module reflectors [4] in 2 dof. The feed array's orientations was controlled by the feed positioner in 4 dof. The RF sensor was composed of a monopulse antenna using 4 horns. Two transmission antennas were located on the roof of NTT Yokosuka R&D center; a semi-open-type anechoic chamber holding the receiving antenna system was located about 1.6 km away. One transmission antenna was used to determine the boresight direction, and the other was positioned at an angle of −3.4 degrees in azimuth with respect to the boresight. The beam direction was controlled by using a BFN to change the excitation coefficient of the phased array feed. This BFN is composed of voltage-controlled attenuators and phase shifters [5]. The excitation coefficient can be varied by the added voltage for these circuits, and these voltages are controlled by 8 bit D/A converters.

Experimental Results

The beam steering control was started from the 6 bit's initial excitation coefficient. This initial excitation coefficient was determined as follows. At first, all attenuators were set at maximum attenuation. Next, one attenuator was set at minimum attenuation, and the phase of the signal was changed by the phase shifter on that attenuator's path. The phase shifter was adjusted using the loop shown in the figure until the received power of that signal become the maximum amount of power. This procedure was repeated until all 31 paths were included in the loop. This initial excitation coefficient was determined for both beam directions. The 8 bit's optimal excitation coefficient was found by the beam forming algorithm. Figures 4 (a) and (b) plot the received power when only the reflector was turned in the azimuth direction. In these figures, the horizontal axis shows the angle of

the reflector with respect to the boresight. To convert to the angles observed at the primary feed, the horizontal axis values have to be multiplied by two. The dashed line shows the target beam steering direction, i.e., the direction of the transmission antenna. The beam controlled directions were in good agreement with the desired directions.

Conclusion

This paper described a beam forming procedure for phased array fed reflector antennas and reported on the results of a beam steering experiment on such an receiving antenna. The results indicated that the procedure adequately compensates for the mechanical errors of the reflector, alignment errors of the antenna system, and phase and amplitude errors of BFN. The experimental results confirm the effectiveness of the proposed beam forming procedure and algorithm.

References

[1] M. Shimizu, "Pattern Tuning of Defocus Array-Fed Reflector Antennas," IEEE AP-S Symp., vol. 4, pp. 2070-2073, Jun. 1998.

[2] M. Shimizu, "Determining the Excitation Coefficients of an Array using Genetic Algorithms," Proc. IEEE Conf. Antennas and Propagation, vol. 1, pp. 530-533, June 1994.

[3] M. Watanabe, J. Mitsugi, A. Miyasaka and M. Shimizu, "Large Space Antenna Structure Design Technology Status," 49th International Astronautical Congress, IAF-98-I.1.01, 1998.

[4] S. Harada and M. Shimizu, "Using Variable Length Members on an Attachment Support Structure for Initial Pointing Control of a Large Deployable Antenna Reflector," Ninth International Conference on Adaptive Structures and Technologies, pp. 418-426, Oct. 1998, Boston, U.S.A.

[5] T. Ohira, Y. Suzuki, H. Ogawa and H. Kamitsuna, "Megalithic Microwave Signal Processing for Phased-Array Beamforming and Steering," IEEE Trans. Microwave Theory Tech., MTT-45, pp. 2324-2332, Dec. 1997.
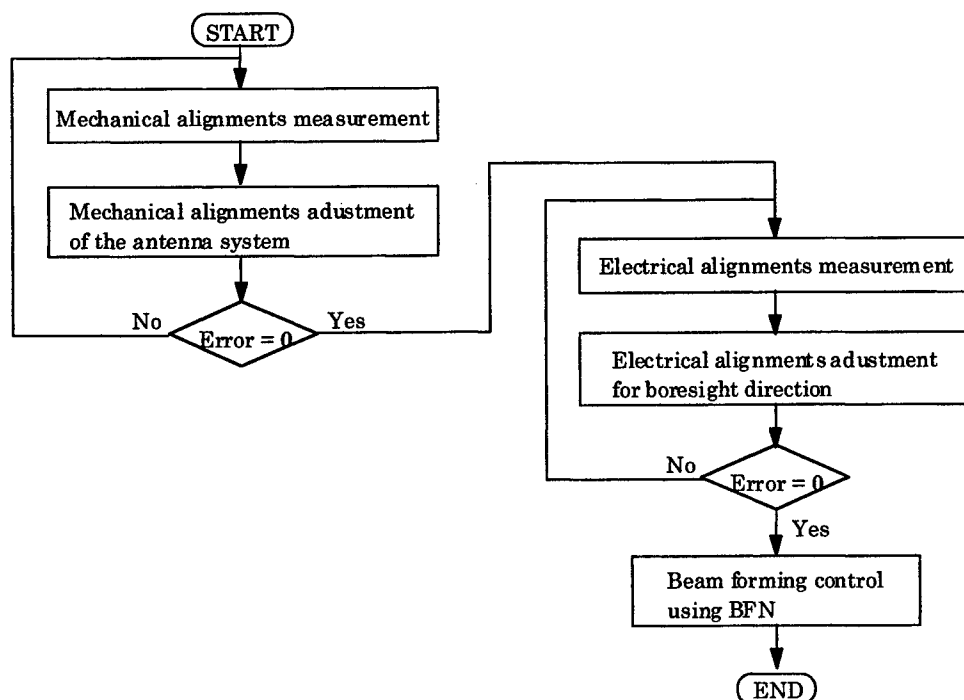
Fig 1. Beam forming procedure.
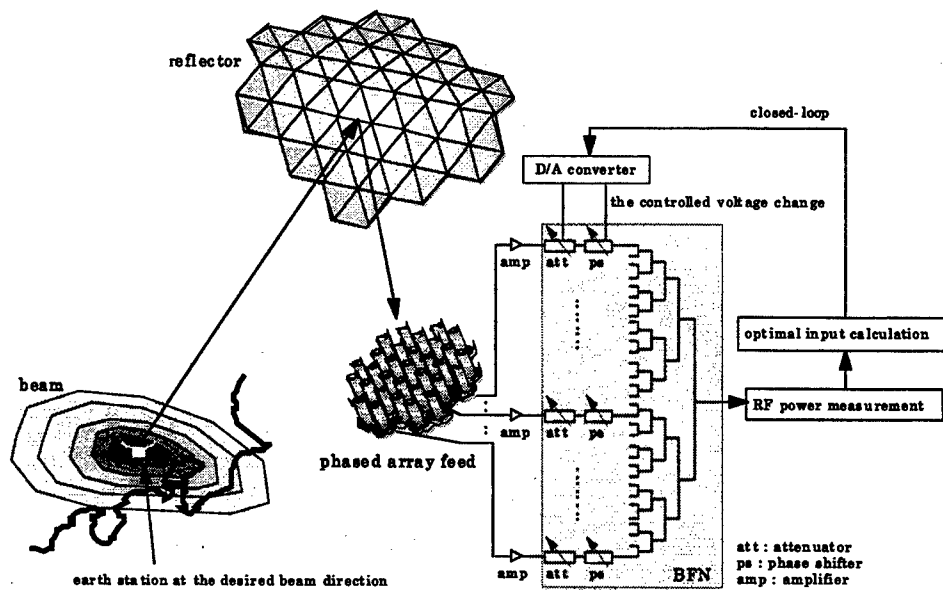
Fig 2. Beam forming method for phased array fed reflector antennas.
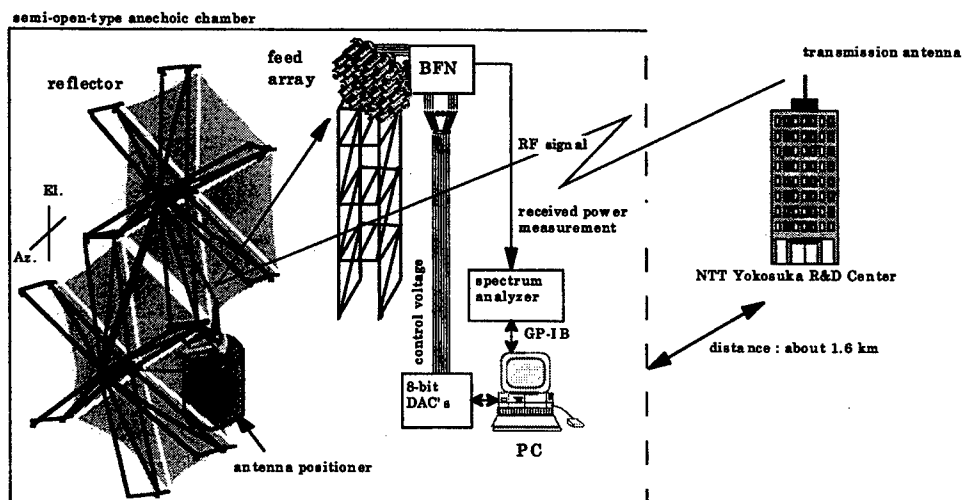
Fig 3. The experimental setup for controlling the beam direction for a phased array fed reflector antenna.

(a) The boresight direction

(b) Az.=-3.4 degree direction
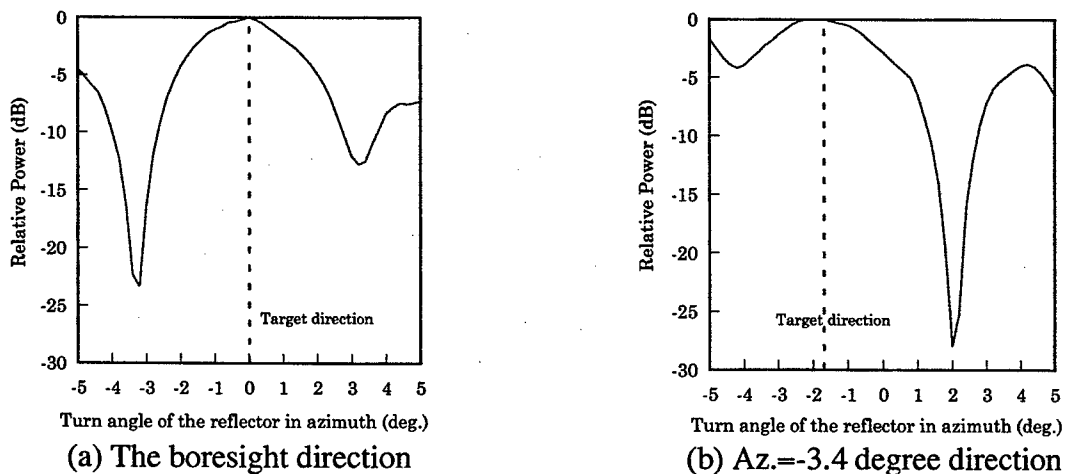
Fig 4. Beam steering results.

Adaptive Array Antenna for Mobile Communication

Isamu Chiba, Rumiko Yonezawa and Kazunari Kihira

chiba@ isl.melco.co.jp   rumiko@isl.melco.co.jp kihira@isl.melco.co.jp

MITSUBISHI ELECTRIC CORPORATION

5-1-1 Ofuna, Kamakura, Kanagawa 247-8501 Japan

ABSTRACT

Digital beam forming (DBF) antennas are developing as advanced phased array antennas. The microwave signal received at each element antenna of the DBF array antenna is converted to a digital signal after down-converting. Beam-forming is carried out in a digital processor, so both excitation amplitudes and phases can be controlled more precisely in the DBF than in the conventional phased array antenna(Fig.1). The DBF also has the advantage of adaptive array antenna signal processing. This allows the nulls of an antenna radiation pattern to be steered in the directions of interference signals. Adaptive array antennas are applied to the base station antennas of mobile communications. In this presentation, in TDMA and CDMA communication systems, the adaptive array antenna fit to each system is shown.
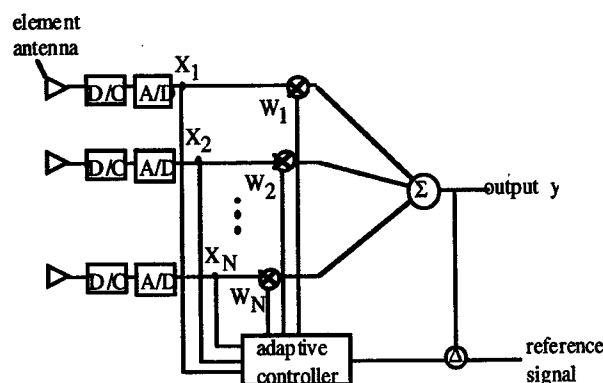
Fig.1 Adaptive array configuration.

1. ADPTIVE ARRY FOR TDMA SYSTEM

In TDMA system, communication signal is divided in time region. The main beam can be directed to one specific user. The ordinary adaptive antenna algorithm, SMI[1](Sample Matrix Inversion) or CMA[2](Constant Modulus Algorithm), is useful in this system. We developed CMA combined with SMI algorithm for reducing the error occurred when the signal level is lower than that of interference.

CMA (Constant Modulus Algorithm) method has been known as blind adaptive beamforming because it requires no knowledge about the signal except that the transmitted signal waveform has a constant envelope. Although the CMA has the merit of blind operation, it possesses problems in its convergence property. First, the ill convergence of giving false solution when the interfering signal is stronger than the desired signal, and second, its slow convergence time limiting its application in dynamic environments.

On the other hand, SMI has been known as an approach with high convergence rate. Using the information of the output signal and the reference signal, the optimum weights could be computed by directly calculating the inversion of the covariance matrix. Although it has a rapid convergence property, there are systems which the reference signal cannot be known at all times while the signal environment frequently changes. Also, inversion of a large matrix requires heavy computational capacity.

This paper presents a method which takes advantage of the merits of both the SMI algorithm and CMA. This is useful in systems when the information of the reference signal can only be used at a certain fracture of time. In the first stage of the operation, the initial weights are determined by using SMI algorithm and in the next stage while the environment changes, CMA method is introduced to update the weights until the next opportunity arrives to capture the reference signal. By using this approach, the convergence time in CMA operation could be decreased and the problem of ill convergence capturing the interference

signal could be solved.

1.1 Adaptive Algorithm

The combined method for adaptive beamforming proposed in this paper is very simple. We assume a system in which the reference signal cannot be used continuously. First, at the early stage of the operation when the reference signal can be used, the SMI algorithm is introduced to determine the optimum weights assigned to each element antennas of the array. These weights and the output of the array are stored. Next, the CMA method is introduced in the operation. Here, the weights derived from the SMI algorithm W_{opt}, are chosen as the initial weights in the CMA.

$$W(1) = W_{opt} - \mu \nabla_W J_1 \qquad (1)$$

This operation implies that the antenna beam is already scanned to the incident direction of the desired signal when the CMA starts its operation, except in cases which the change of the signal environment is extremely rapid. Here, we consider systems which the environmental change is slow compared to the digital signal calculation. Under this condition, with the signal environment change, CMA system can track the desired signal with more rapid convergence time than the conventional CMA method.

1.2 Algorithm Simulation

[1]Simulation Conditions

The performance evaluation of the proposed algorithm has been accomplished in a typical application using a computer simulation. A QPSK signal was generated and transmitted. For convenience in evaluation, one direct path (desired) signal and one multipath (or interference) signal model is used. Fig.2 shows a configuration of 4-element array antenna used in this simulation.
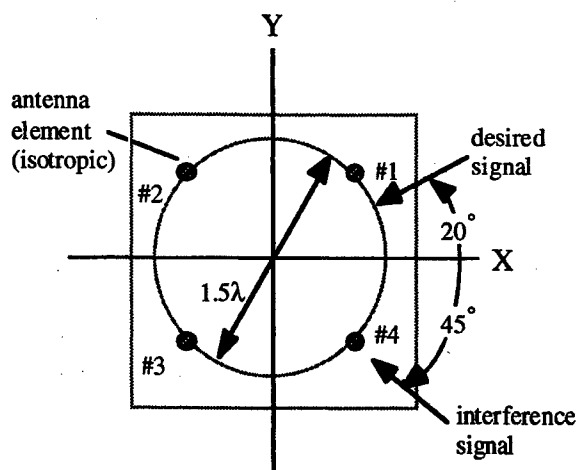
Fig.2 4-element array antenna configuration.

The direction of the paths is 20 degrees and -45 degrees, respectively. An isotropic antenna was assumed as an element antenna and the incident desired signal level is set to be 3dB greater or less than the interference signal level. The evaluation was carried out only in azimuth plane (i.e. the X-Y plane in Fig.2). To evaluate the time of convergence and the captured signal, both the antenna pattern and the time variation of the SINR (Signal to Noise Ratio) was simulated.

[2]Simulation and Discussion

Next, the case when the interference signal level is greater than the desired signal level is evaluated. When the initial antenna pattern is an isotropic one, the antenna beam directs to the interference signal resulting in an inferior SINR. This is shown in Fig.3. Here, the adaptive antenna assumes the higher level signal as the desired one and the lower level signal as the interference. On the other hand, when the results of the SMI method is used in the initial weight vector in CMA, the antenna pattern after 500 iteration time is calculated as shown in Fig.4. As can be seen from the figure, the antenna beam stays with the desired signal, confirming the effectiveness of the proposed method.
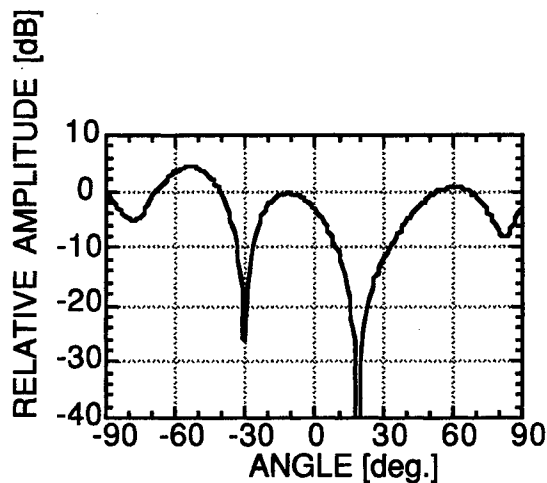
Fig.3 Adaptive pattern when interference level
is higher than the desired one (CMA only).
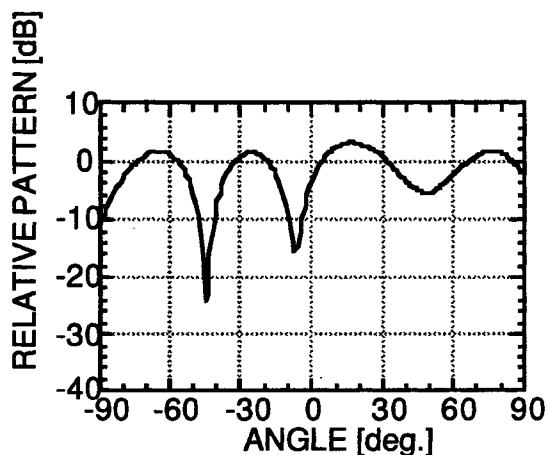
Fig.4 Adaptive pattern when interference
level is higher than the desired one
(SMI+CMA).

2. ADPTIVE ARRAY FOR DS-CDMA SYSTEM

We propose two adaptive array
configurations fit to DS-CDMA system. One
is for increasing communication capacity on
condition that all signal power is almost the
same. In the future, high bit rate signal will
be used mixed with low bit ones. Adaptive
arrays that have the function for cancellation
of interference have to be used in such case. We
also propose the adaptive array antenna
suitable for such demand.

2.1 Smart Antenna for increasing communication capacity

In the DS-CDMA system, all the signal
power being almost the same, the beam
combining algorithm according to

maximization of signal to interference and
noise ratio is sufficient for increasing
communication capacity. This antenna
should be called as smart antenna rather than
adaptive array antenna.
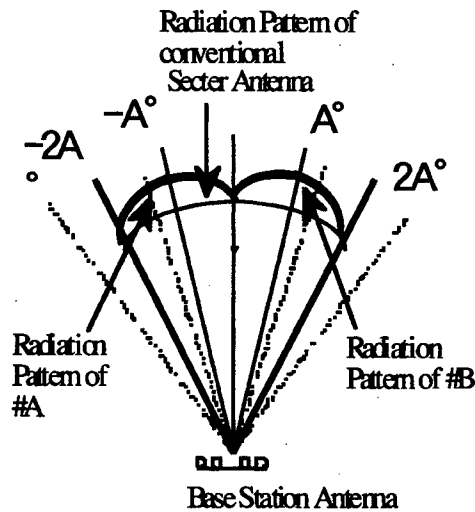
Fig. 5 Beam configuration.

In this smart antenna, as shown in Fig.5,
there are two beams(Beam#A and Beam#B)
in one sector. These two beams are combined
by the weight with the phase being the same
and the amplitude being proportional to the
SINR.
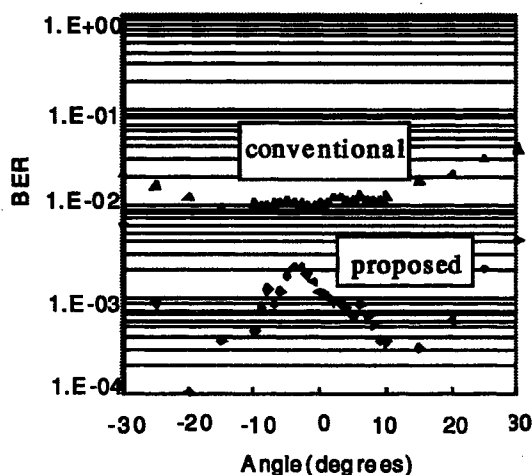
Fig.6 Results of BER measurement.

We carried out experiments of BER
measurements. Results are shown in Fig.6.
From this figure, the BER is improved in the
proposed antenna system.

111

2.2 Adaptive Array Antenna for High Bit Rate Communication

When the high bit rate signal are used mixed with low bit ones, there would be a high power level interference even in DS-SDMA system. Adaptive arrays that have the function for cancellation of interference have to be used in such case. But in almost all the communication system, the conventional antenna is used for base station antenna at first. To introduce the adaptive array antenna, simple calculation procedure is necessary and the impact to the hardware, for example digital signal processor and antenna setting, has to be reduced.

We propose an adaptive array antenna suitable for this system. Configuration of this is shown in Fig.7. PIAA(Power inversion Adaptive Algorithm[3]) is adopted as the signal-processing algorithm. By using this algorithm, the interference with the power larger than the noise power is cancelled. PIAA procedure should be carried out before matched filtering, so that the amount of calculation is reduced compared to that of conventional adaptive array antenna. Also small size antenna can be used as the auxiliary antenna. The high bit rate signal could be received by the flow without power inversion procedure, as shown in Fig.7. The simulation result is shown in Fig.8. From this figure, the SINR is improved to sufficient level for the desired signal to be demodulated.

array antenna.

Fig.8 Relation of input and output SIR

REFERENCES

[1] R.T.Comptom,Jr., *Adaptive Antennas: Concepts and Performance*, Prentice Hall, Englewood Cliffs, NJ, 1988.

[2] J.R.Treichler and B.G.Agee, "A new approach to multipath correction of constant mudulus signals," *IEEE Trans. on Acoustics, speech and signal processing*, Vol.ASSP-31, No.2, pp.459-472, April 1983.

[3] R.T.Comptom,Jr., " The Power-Inversion Adaptive Array,"*IEEE Trans. On Aero Space and Electronic Systems*, Vol.AES-15, No.6, , Nov. 1979.

Fig.7 Configuration of proposed adaptive

A Smart Antenna Receiver Testbed with Directional Antenna Elements

Hidehiro Matsuoka, Yasushi Murakami, Hiroki Shoki, and Yasuo Suzuki

Corporate Research & Development Center, Toshiba Corporation

1, Komukai Toshiba-cho, Saiwai-ku, Kawasaki 210-8582, Japan

Abstract

This paper reports the configuration of a smart antenna receiver testbed for land mobile communication base stations and the experimental results obtained for it. The antenna pattern and bit error rate (BER) is measured in a radio anechoic chamber. These results show the interference can be suppressed effectively by beamforming using adaptive algorithm, e.g. LMS or CMA.

1 Introduction

A smart antenna, which performs adaptive beamforming and interference suppression, is expected to significantly increase the system capacity and extend the coverage for wireless communication systems[1]. Particularly, a digital beamforming (DBF) smart antenna offers advantages in that its calibration is relatively easy and various algorithms can be flexibly implemented by software without changing hardware components because most of the signal processing is handled by a digital signal processor (DSP)[2]. In recent years, increasing efforts have been devoted to development of the smart antenna for land mobile communications and results of the experiments have been reported[3, 4, 5].

On the other hand, progress has been made in research on adaptive arrays with temporal equalization (space-time processing) to handle both co-channel and inter-symbol interference optimally[6, 7, 8]. The authors have also proposed the space-time processing smart antenna. This proposed antenna can reduce interference by adaptive arrays (spatial processing) and combine each of delayed components of a desired wave by path diversity (temporal processing) as shown in the block diagram of Fig.1. It selects some appropriate elements from plural directional antenna elements based on the results of all delay profile estimation, and combines some outputs of the adaptive array for each delayed wave. The selecting of antenna elements can reduce the computing time for signal processing. The performance improvement by interference suppression and multipath diversity combining has already been evaluated by computer simulation, and significant improvement was confirmed even in the case that delayed waves are incident from the same directions as a desired wave[9].

To verify its performance from the practical point of view, the authors developed a smart antenna receiver testbed and conducted experiments in a radio anechoic chamber. In this paper, the first step of the experiment is reported, namely the use of this testbed to examine only space domain processing.

2 Testbed overview

The structure of the developed smart antenna testbed is shown in Fig.2. The developed smart antenna receiver testbed is implemented for Time Division Multiple Access (TDMA) systems and only the receiver mode is carried out by non-real-time processing. The modulation scheme is $\pi/4$-DQPSK with differential detection, and an adaptive signal processing runs using Least Mean

Squares (LMS) algorithm or Constant Modulus Algorithm (CMA). A step size parameter on which the convergence of weight update depends is 0.05 in both algorithms. The converged weights during this reception time slot are held and used as the initial weights for the next slot. The radio frequency is 2GHz-band and the data rate is 384kbps. A TDMA burst format consists of 112-symbol information data and 8-symbol guard time.

The antenna array consists of eight rectangular microstrip antennas which are circularly arranged spaced at equal distances of a half wavelength. And, each of the directional antenna elements used is directed in a different direction from the others. The 3dB beamwidth is about 90 degrees for each.

After a certain time slot of the TDMA frame is stored to peripheral buffer memory, the data burst is processed in a DSP. But any other received data bursts are not inputted to the memory until the DSP finishes the adaptive processing of the data burst. In this testbed, the complex baseband signals are obtained at quadrature demodulator after down-converting, and are calculated in a DSP to form interference suppression patterns. In the DSP, at first, data extraction of each branch, roll-off filtering, sampling from 5-fold oversampling timing are performed, and then adaptive signal processing is implemented. Data synchronization and clock recovery are handled in a control unit. This system can sequentially capture data out of the DSP by interrupt request from a PC, and monitor the received signal sequences and the state of updating of the complex spatial weights and the errors in an adaptive array. This configuration makes it easy to change the adaptive algorithms by rewriting the program installed on the DSP.

3 Experimental results

The external overview of the experimental setup using the testbed is shown in Fig.3. A receiver antenna array is set up on a turntable as shown in Fig.4. A desired wave and an interference wave are generated from a different modulated signal generator (SG). An entire 112-symbol data sequence is employed as the reference sequence for weight update in LMS because it is assumed that the bit sequence of desired signal is already known at receiver side. Frame timing synchronization is adjusted by burst trigger from testbed to the desired SG. Four antenna elements are selected from all elements for adaptive array processing since the element which does not receive a desired signal exists due to the directivity of each element under this condition. At the beginning of experiments, the deviation of the signal strength and phase shift for each branch is measured and compensated in the digital signal processing.

A typical antenna pattern measured in a radio anechoic chamber is shown in Fig.5. This figure indicates the pattern by LMS under the condition that a desired wave is incident from $\theta_D=20°$ and an interference wave is incident from $\theta_U=-7°$, and average desired-to-undesired ratio (D/U) is 3dB. It is confirmed that beam and null are formed toward the direction of arrival (DOA) of a desired wave and an interference wave respectively, and the output signal-to-interference ratio (SIR) is 20dB.

The BER performance of adaptive array using LMS and CMA, respectively, is shown in Fig.6. Those of only omnidirectional and directional antenna elements are also shown in this figure. Here, the antenna plane is pointed toward transmitter antenna of desired signal in the case of only one directional element.

From this figure, it is confirmed that the BER in the case of using a smart antenna is improved by about two figures compared to that in the case of one antenna reception at $D/U = 3$dB. Compared with the performance of smart antennas using LMS and CMA, when D/U is low, BER of CMA greatly degrades. This is because the miscapture of interference wave occurs. On the contrary,

when D/U is high, LMS degrades. In this experiment, the obtained adaptive weights in the last slot are employed as initial weights in weight update calculation. But, in LMS, the converged weights are not always optimum for the next reception time slot. Thus, bad initial weights may be given depending on the carrier phase condition. In LMS smart antenna, increased interference tolerance of 11dB at BER $= 10^{-2}$ is demonstrated for this system using four directional antenna elements.

4 Conclusion

The authors developed a smart antenna receiver testbed with directional antenna elements and conducted experiments in a radio anechoic chamber. From the experiment result, it is confirmed that this smart antenna can form the beam pattern to obtain high output SIR and improve the interference tolerance. In the near future, the experiments for space-time processing will be conducted.

References

[1] J. H. Winters, "Smart Antennas for Wireless Systems," *IEEE Personal Communications*, vol.4, no.11, pp.23-27, Feb. 1998.

[2] J. Razavilar, F. Rashid-Farrokhi and K. J. R. Liu, "Software Radio Architecture with Smart Antennas: A Tutorial on Algorithms and Complexity," *IEEE J. on Selected Areas in Commun.*, vol.17, no.4, pp.662-676, April 1999.

[3] F. P. S. Chin and M. Y. W. Chia, "Smart Antenna Array for High Data Rate Mobile Communications," *Proc. of AP-S'97*, pp.350-353, July 1997.

[4] G. Tsoulos, M. Beach and J. McGeehan, "Wireless Personal Communications for the 21st Century: European Technological Advances in Adaptive Antennas," *IEEE Commun. Mag.*, vol.35, no.9, pp.102-109, Sep. 1997.

[5] S. Anderson, B. Hagerman, H. Dam, U. Forssen, J. Karlsson, F. Kronestedt, and S. Mazur, "Adaptive Antennas for GSM and TDMA Systems," *IEEE Personal Communications*, vol.6, no.3, pp.74-86, June 1999.

[6] A. J. Paulraj, E. Lindskog, "Taxonomy of Space-time Processing for Wireless Networks," *IEE Proc. -Radar, Sonar Navig.*, vol.145, no.1, pp.25-31, Feb. 1998.

[7] G. E. Bottomley and K. Jamal, "Adaptive Arrays and MLSE Equalization," *Proc. of IEEE VTC'95*, pp.50-54, June 1995.

[8] Y. Ogawa, R. Sasaki, T. Ohgane, K. Itoh, "An Adaptive Antenna for a Multipath Propagation Environment," *Proc. of IEEE VTC'98*, pp.1345-1349, June 1998.

[9] H. Matsuoka, H. Shoki, Y. Suzuki, "Path Diversity Using an Adaptive Array with Directional Antennas for High Bit Rate Mobile Communication Systems," *Proc. of IEEE GLOBECOM'98*, pp.171-176, Nov. 1998.
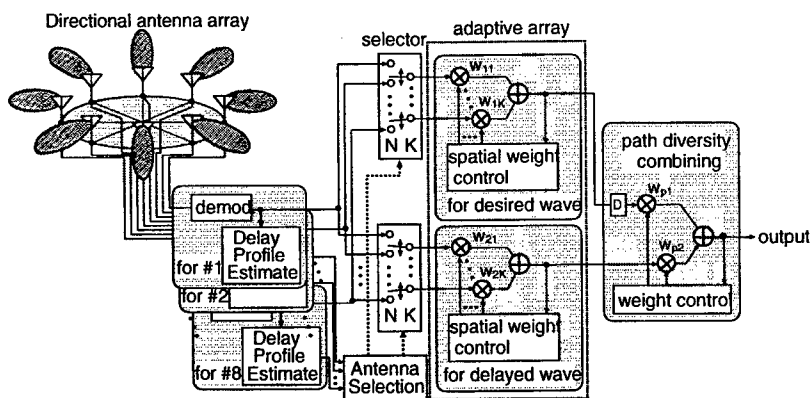
Figure 1: Block diagram of smart antenna using space-time processing
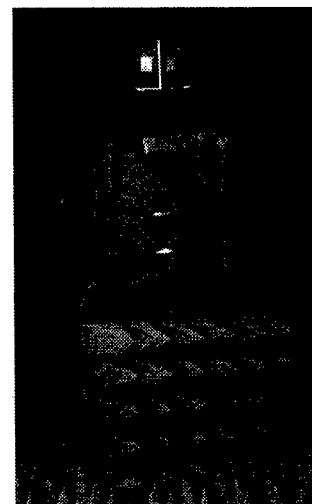
Figure 4: Receiver antenna array
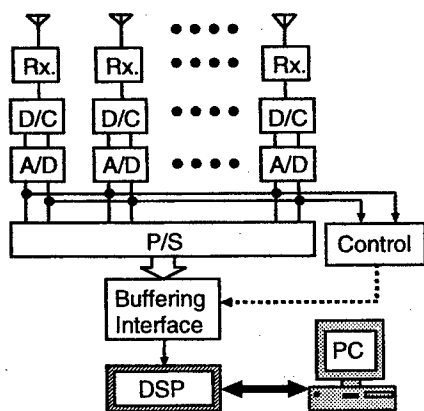
Figure 2: Structure of smart antenna testbed
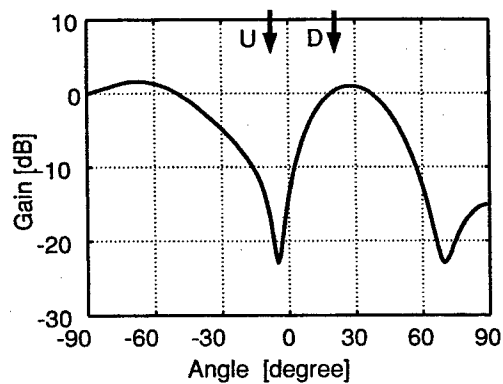
Figure 5: Antenna pattern ($\theta_D=20°$, $\theta_U=-7°$)
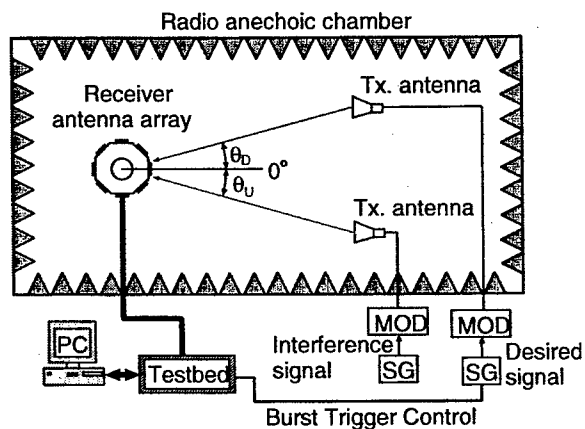
Figure 3: Experimental setup
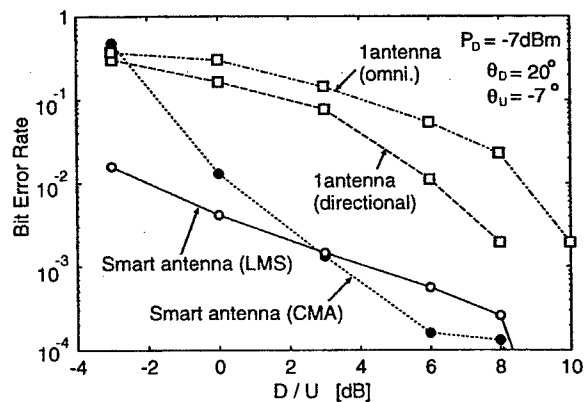
Figure 6: BER performance

Experimental Results on Multi-beam Receiving Antenna
for Satellite Broadcasting

Masaru FUJITA[†], Kouichi TAKANO[††], Shoji TANAKA[†], Yozo UTSUMI[†] and Takao MURATA[†]

[†]NHK Science and Technical Research Laboratories

1-10-11 Kinuta, Setagaya-ku, Tokyo 157-8510, Japan

([††]Advanced Space Communications Research Laboratories)

1. Introduction

Satellite broadcasting services are currently provided in Japan using four orbital positions, one operates in the BSS band (11.7 - 12.2 GHz) and the other operate in the FSS band (12.2 -12.75 GHz). A number of satellites located in different orbital positions will provide in the future. A commonly used dish antenna can receive signals from only one satellite at a time. A multihorn-feed reflector antenna can receive signals simultaneously from several satellites in different orbital positions, but the number of satellites may be limited by the arrangement of the feed horns. A multi-beam phased-array antenna can receive signals simultaneously from a great number of satellites in different orbital positions.

This paper describes the fundamental design of a multi-beam receiving antenna[1] and measured results of an experimental model.

2. Antenna design

The multi-beam receiving antenna receive signals simultaneously from many satellites in different orbital positions (Fig.1). Figure 2 shows a block diagram of the antenna. Multiple beams are formed using multiple beam forming circuits, one for each satellite direction. To receive both linearly polarized waves with an arbitrary angle and circularly polarized waves, the waves are received as two orthogonal components.

We designed this antenna to meet the following requirements.

• Receive signals from satellites in range of ±20 degrees (corresponding 110°E - 150°E)
• Suppress interference from adjacent satellites
• Provide a gain of 32 dBi, which corresponds to the gain of a ϕ45 cm dish antenna[2]
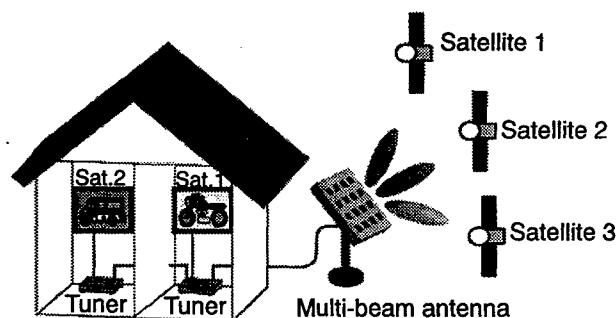
Figure 1 Multi-beam receiving antenna

Antenna elements receive two orthogonal components
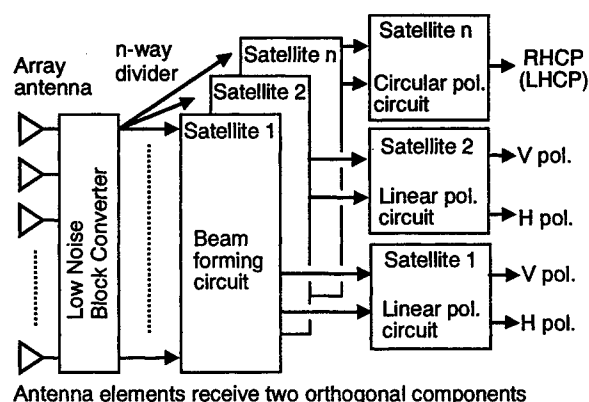
**Figure 2 Brock diagram of multi-beam
receiving antenna**

117

2-1. Range of beam position

Figure 3 shows the orbital positions of the four satellites providing satellite broadcasting in Japan. These four satellites are positioned within 40 degrees in azimuth and 0.4 degrees in elevation. We set the range of the beam position to ±20 degrees only in the direction of the azimuth axis, because the difference in elevation angles is negligible compared with the beam-width of the antenna. To form a beam along the azimuth axis, we used the antenna configuration shown in Fig. 4.

2-2. Antenna size

The radiation pattern along the azimuth axis, which coincides with the orbital arc, depends on the width of the antenna. To suppress interference from adjacent satellites, the antenna width should be designed taking into consideration the side-lobe level in their directions. To make nulls in the azimuth pattern that coincide with the directions of the adjacent satellites (±4.4 and ±6.6 degrees), the antenna width needs to be 65 cm (Fig. 5). However, to reduce the number of subarrays, we set the width to 37 cm. In this case, the first side-lobes occur in the directions between ±4.4 and ±6.6 degrees; they have the same levels in the directions of the adjacent satellites. To achieve a gain of 32 dBi with a width of 37 cm, the antenna needs to be 70 cm long (assuming 50% aperture efficiency).
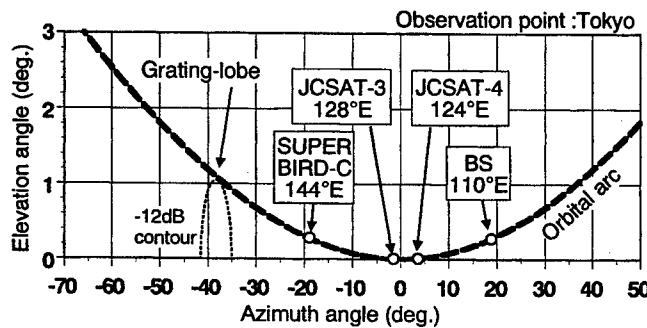
Figure 3 Orbital positions of satellites providing satellite broadcasting
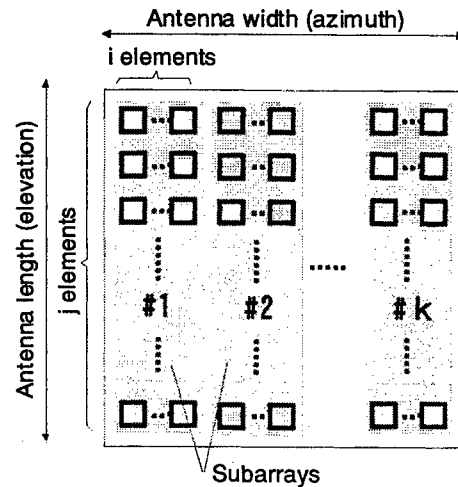
Figure 4 Subarray configuration
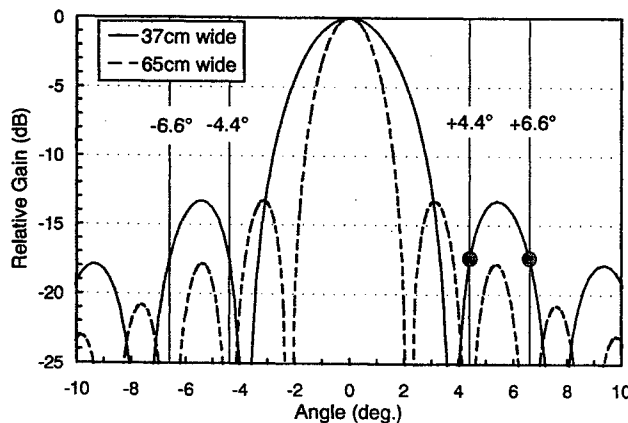
Figure 5 Calculated azimuth pattern
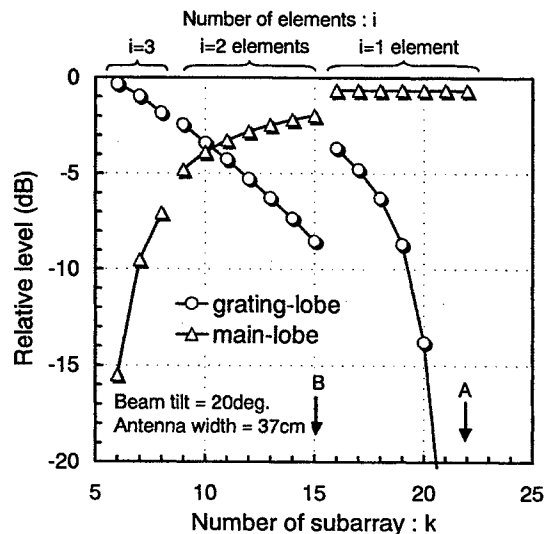
Figure 6 Main-lobe level and grating-lobe level

118

2-3. Number of subarrays

Figure 6 shows the calculated results for both the main-lobe level and the grating-lobe level when the beam is tilted to 20 degrees. To avoid the occurrence of a grating-lobe, the number of subarrays must be at least 22 (Fig. 6, A). If we allow the occurrence of the grating-lobe in order to reduce the number of subarrays, the subarrays can be reduced to 15 while still keeping the condition that the difference between the main-lobe and grating-lobe level is large (Fig. 6, B).

2-4. Grating-lobe

When the beam is tilted to 20 degrees, the grating-lobe occurs in the direction of −39 degrees, and its relative level is −7 dB. The distance between the azimuth axis and the orbital arc is 1.2 degrees in the direction of the grating-lobe (Fig. 3). Therefore, the relative level of the grating-lobe at the orbital arc is reduced to −12 dB.

3. Measured results on experimental model

3-1. Experimental model

Figure 7 shows the configuration of a two-beam experimental model. Delay lines are used as phase shifters to simplify the beam forming circuits. Figure 8 shows an external view of the experimental model. The antenna consists of 960 microstrip patch elements (0.76 mm thick PTFE substrate, $\varepsilon_r = 2.17$). The size of the antenna aperture is 372×672 mm.

3-2 Radiation pattern

Figure 9 shows the measured radiation pattern for a beam formed at 0 degrees in the azimuth axis. The maximum side-lobe level is −17.5 dB in the direction of adjacent satellites (−4.4 degrees). Figure 10 shows the measured radiation pattern when the beam is tilted to 20 degrees. The grating-lobe occurs in the direction of −39 degrees, and its relative level is −7.3 dB.

3-3. Reception experiments

We performed a reception experiments in an anechoic chamber. The two beams were tilted to ±20 degrees. Figure 11 shows their measured radiation patterns. In the direction of each main-lobe, isolation levels of over 20 dB were obtained. We transmitted two different TV programs on the same frequency from two points 40 degrees apart. The experimental model was able to receive both programs simultaneously.
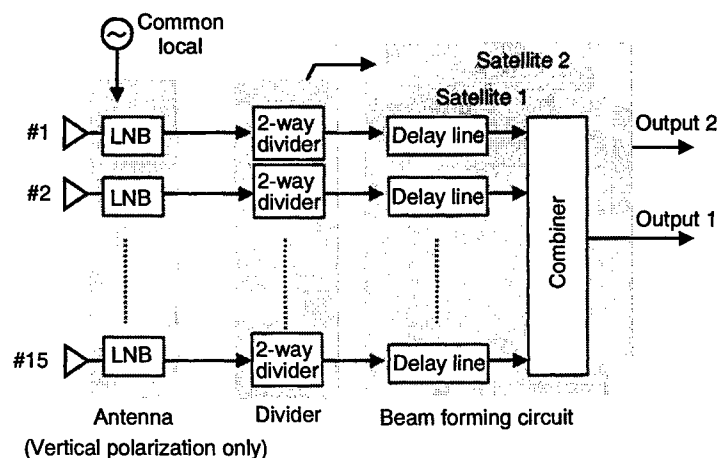
**Figure 7 Configuration
of experimental model**
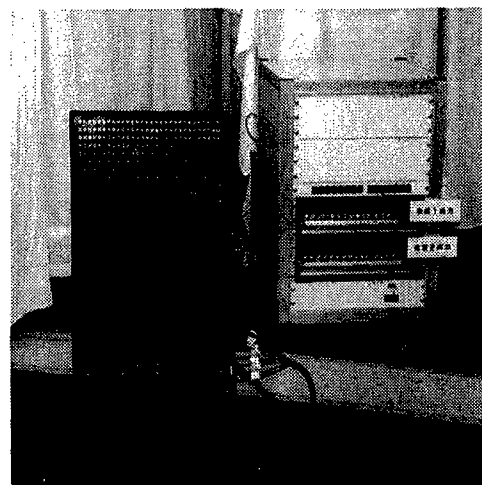
**Figure 8 External view
of experimental model**

4. Conclusion

We performed a fundamental study on a multi-beam receiving antenna for a satellite broadcasting. We presented that 15 subarrays are suitable for the antenna considering interference from adjacent satellites while trying to minimize the number of subarrays. The experimental model was able to form two beams separated by 40 degrees.

Even though multi-beam receiving antennas have superior performance capabilities, the large number of discrete components, such as phase shifters and down-converters, is a major obstacle to their realization. To reduce the component count and cost, we have been studying an active integrated subarray antenna and a simplified feed system. In the future, we expect that beam forming circuits will be integrated into satellite TV tuners to handle both satellite and frequency selection.
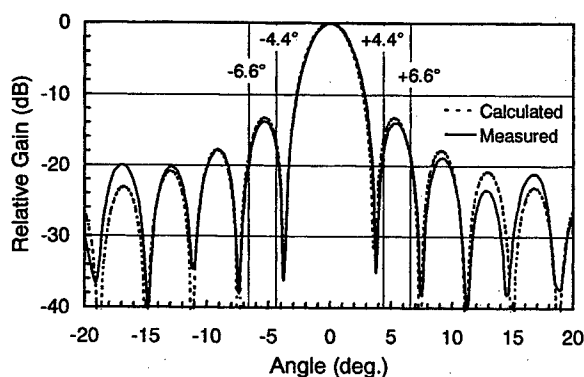
Figure 9   Azimuth pattern

(Beam position : 0 deg.)
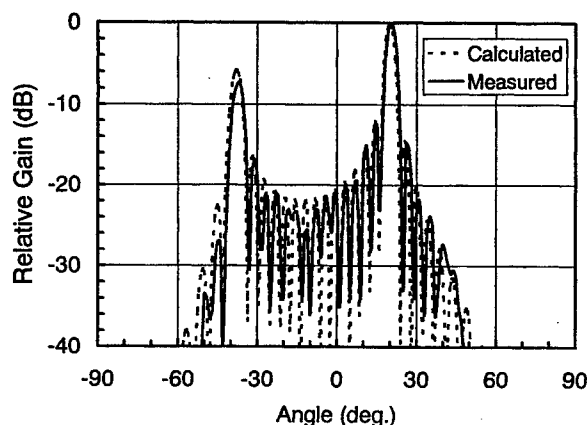
Figure 10 Azimuth pattern

(Beam position : 20 deg.)
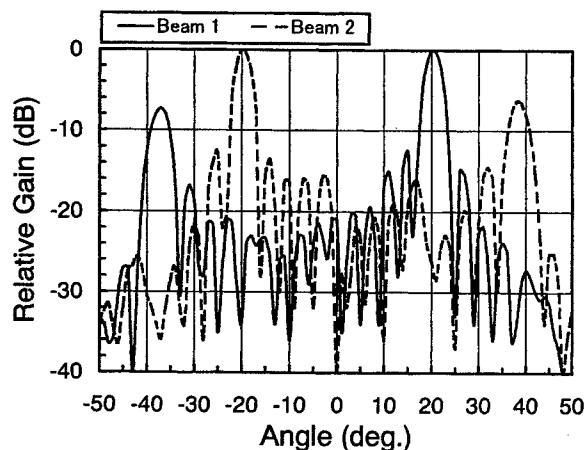
Figure 11 Two-beam pattern

(Beam position : +20 deg., -20 deg.)

References

[1] K. Takano et al., "Fundamental Study of Multi-beam Receiving Antenna for Satellite Broadcasting", 1999 Spring Natl. Conv. Rec., IEICE, B-1-166

[2] Technical Report of Electronic Industries Association of Japan, "Electrical, Mechanical & Environmental Characteristics on Receiving Antenna for SHF Satellite Broadcast Transmission", EIAJ CPR-510A

Alternating-Phase Fed Single-Layer Slotted Waveguide Arrays
with Chokes Dispensing with Narrow Wall Contacts

Yuichi Kimura*, Takashi Hirano, Jiro Hirokawa and Makoto Ando

Department of Electrical & Electronic Engineering, Tokyo Institute of Technology

2-12-1 Ohokayama, Meguro-ku, Tokyo 152-8552, JAPAN

1. Introduction

Demands for high-gain and mass-producible planar antennas are rapidly increasing because various millimeter-wave applications are focused on and is being developed actively. In Japan, 25/26 GHz bands are released for LMDS (Local Multi-point Distribution System), for example. Single-layer slotted waveguide arrays [1] is a leading candidate for these applications because the transmission loss of hollow waveguides is very small even in millimeter-wave frequency in comparison with microstrip or triplate lines.

Figure 1 presents single-layer slotted waveguide arrays fed in co-phase and alternating-phase, respectively. They are simple structures consisting of a slotted plate and a grooved feed structure. The co-phase fed array has a series of π-junctions which excite the radiating waveguides in equal amplitude and phase. It is inevitable to have electrically tight contacts on all the narrow walls between the slotted plate and the feed structure. The co-phase fed array has been developed at 22GHz band [2]. The brazing contact provides 35.8dBi gain with 76% efficiency. but it is not good for mass-production in terms of its fabrication cost. The co-phase fed array has also been applied to 60GHz band. The highest gain is 35.2dBi and the efficiency is 64%, which means that the co-phase fed array keeps the high efficiency in millimeter wave band [3].

In the alternating-phase fed array, the radiating waveguides are excited in the same amplitude but with 180-degree out-of-phase between adjacent waveguides by a series of T-junctions. Currents on the narrow walls do not flow across the contact points with the slotted plate and the tight contacts can be neglected without gain reduction in the radiating waveguide array except the periphery of the antenna. The authors have already confirmed this feature experimentally [4]. High-gain and high-efficiency slot design has succeeded in obtaining 35.5dBi gain with 67% efficiency in the 25GHz antenna [5][6].

This paper proposes the alternating-phase fed array with a choke surrounding the periphery as shown in figure 2. The choke can prevent from the leakage between the slot plate and the feed structure. It dispenses with any tight contacts between them. This structure is very suitable for the mass-production. The choke in straight waveguides is discussed and the transmission loss is measured. Then, the application to the alternating-phase array of the choke is demonstrated [7].

2. Choke in a straight grooved waveguide

In order to check how the choke prevents from the leakage between the slotted plate and the groove feed structure, straight waveguides are fabricated by adding chokes beside the narrow walls as

shown in figure 3. The top plate and the bottom groove are just fixed   by screws. The dimension of the choke is designed to minimize the leakage by using a mode matching analysis. The measurement is done at 40GHz.

Figure 4 presents the transmission loss of the waveguide as a function of the length, in which "gap" means that a thin paper with negligible loss is put between the top plate and the bottom groove to keep the height of a small gap constant. The intercept of the graph corresponds the loss at the input apertures on the both terminals. The gradient of the lines gives the loss of the waveguide in dB/cm. The loss of the choke waveguide is 0.01dB/cm, which is much less than 0.29dB/cm in a waveguide without the choke. Furthermore, in case of the gap, the increase of the loss of the choke waveguide is quite smaller than that of the waveguide without the choke. It is confirmed the choke works well to prevent the leakage in the straight grooved waveguide and reduces the transmission loss.

3. Experimental results of the alternating-phase array with choke

The choke structure is applied to the alternating-phase fed array to keep the good performance without any tight contacts. Two types of the slot arrays are designed. Type (A) has 26 radiating waveguides with 16 slots. Type (B) has 12 radiating waveguides with 33 slots. The aspect ratio of the two-dimensional slot array is different between them..The design frequency is at 25GHz band for (A) and 26 GHz band for (B). The design of the slot arrays are based on the moment method using an anaysis model withthe periodic boundaries to simulate the mutual coupling in the external region. The backward beam tilting is adopted to increase the aperture efficiency and to suppress the reflection from the slots. Three types of placement of the slotted plate on the feed structure are done: (i) bonding, (ii) screwed on the antenna periphery with no choke and (iii)   screwed on the antenna periphery with a choke.

Figure 5 presents the amplitude distribution on the aperture at the design frequency. Uniform illumination is created by the bonding antenna (i) while the power in the feed waveguide cannot reach enough till the ends by the screwed antenna (ii). The choke antenna (iii) obtains almost the same results as the bonding antenna (i) in spite of neglecting tight contact. Figure 6 presents the measured gain. The highest gain is obtained in the bonding antenna (i) to be about 32.8dBi with 65% efficiency. The choke antenna (iii) goes up to 32.4dBi, 60%. This is comparable to the bonding antennas (i). The screwed antenna (ii) suffers from serious gain reduction. This points out that leakage in the feed waveguide takes place without tight contact and it results in the gain reduction. The choke structure is valid for keeping both the aperture illumination and the gain without the tight contact.

4. Conclusion

The choke structure in the alternating-phase array is discussed. It is demonstrated the choke works very effectively to prevent from the leakage in the feed waveguide and to keep the antenna efficiency.

the test antennas.

References

[1] N.Goto, IEICE Technical Report, AP88-39, Jul. 1988 [2] K.Sakakibara *et al.*, IEICE Trans. Commun., vol. E79-B, No.8, pp.1156-1164, Aug. 1996 [3] M.Matsuura *et al.*, IEICE Comm. Societ. Conf., B-1-81, Oct. 1998 [4] K.Sakakibara *et al.*, IEE Proc., Antennas and Propagation, Vol.144, No.6, Dec. 1997 [5] Y.Kimura *et al.*, IEEE AP-S Digest, pp.142-145, Jul. 1999 [6] Y.Kimura *et al.*, JINA98 digest, pp.702-705, Nov. 1998 [7] T.Hirano *et al.*, IEICE Comm. Societ. Conf., B-1-102, Sep. 1999

(a) Co-phase fed array   (b) Alternating-phase fed array
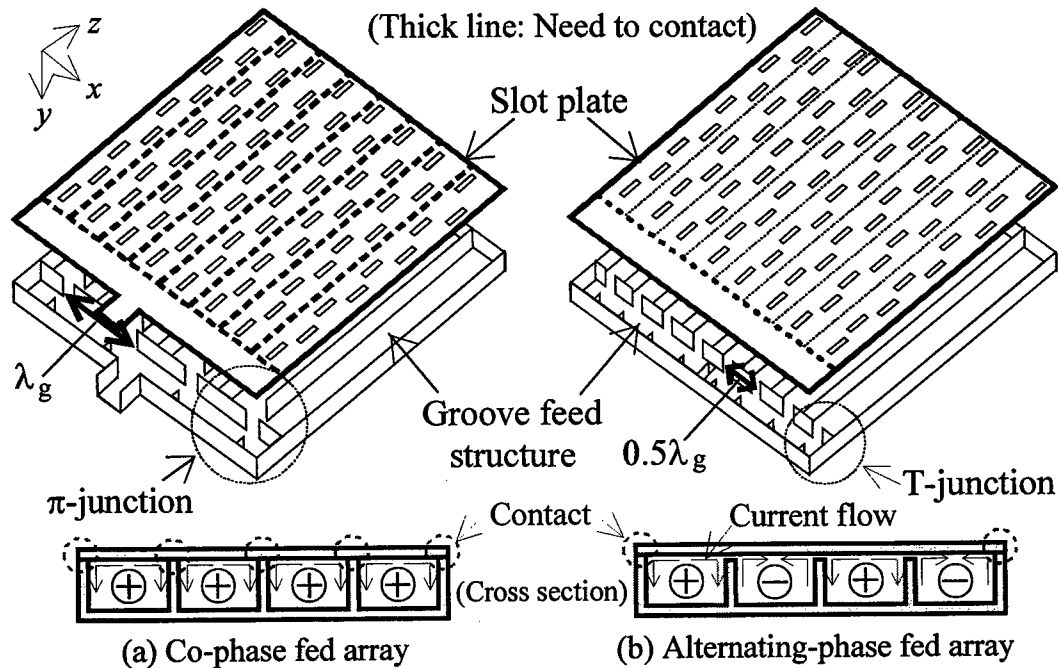
Figure 1   Single-layer slotted waveguide arrays
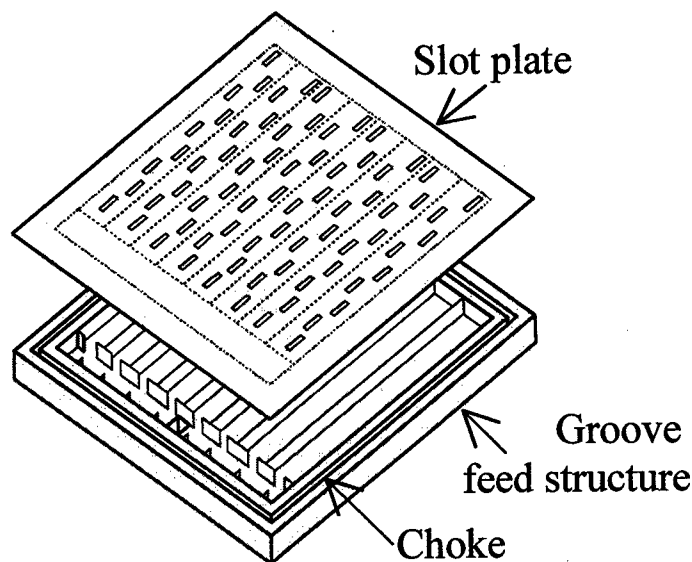
Figure 2   Alternating-phase fed array with a choke

123
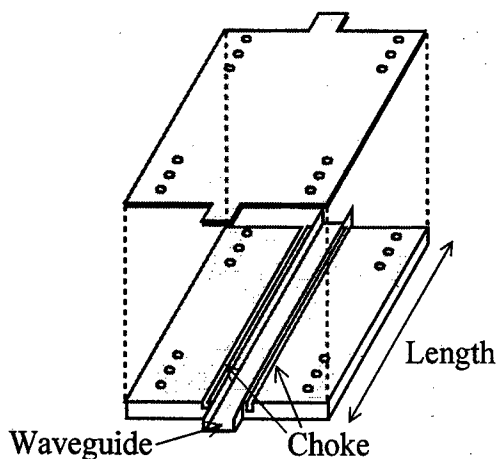
Figure 3 A straight waveguide with chokes
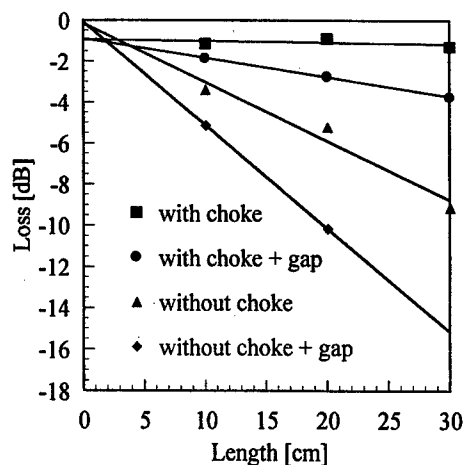
Figure 4 Loss of the straight waveguide

Type(A) : (i) Bonding   (ii) Screw   (iii) Screw+Choke

Type(B) : (i) Bonding   (ii) Screw   (iii) Screw+Choke
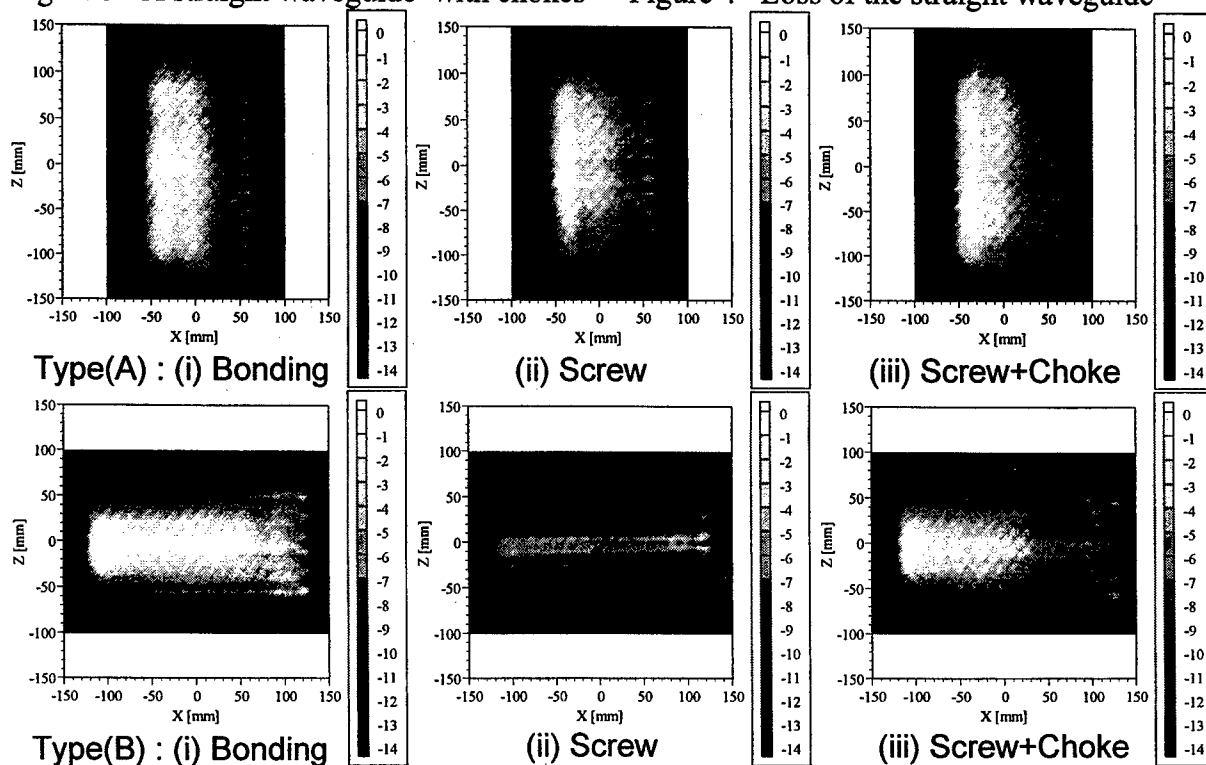
Figure 5 Aperture illumination (Amplitude in dB)
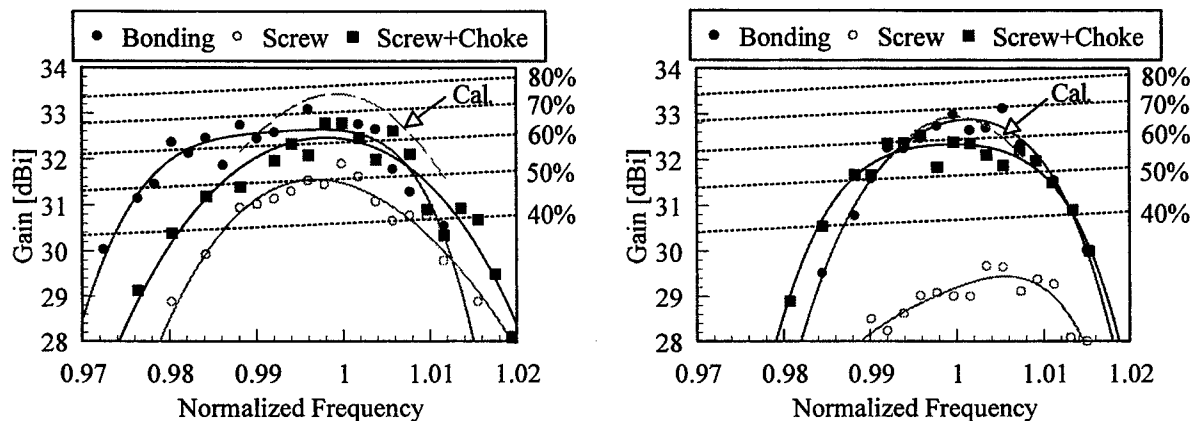
Figure 6 Measured gain (Left: Type(A)   Right: Type(B))

Onboard DBF Antenna for Stratospheric Platform

Masayuki Oodo, Ryu Miura and Yoshihiro Hase

Communications Research Laboratory, Ministry of Posts and Telecommunications
3-4 Hikarino-oka, Yokosuka-shi, Kanagawa 239-0847, Japan

1. Introduction

The wireless network by using stratospheric platforms (SPF) [1-5] is attracting interest as a new network infrastructure that is different from terrestrial networks and also satellite networks. A national project to develop a large airship system and onboard missions to be operated in the stratosphere at an altitude of about 20km has been progressing since 1998 in Japan [1,2]. Communications, broadcasting and earth observations will be its main applications. Wide area can be covered for service by multiple platforms deployed with certain separations and connected to each other by wireless inter-platform links as shown in Fig.1. Each platform provides a service coverage for access link to user terminals on the ground with the minimum elevation angle of 20-45degrees. The maximum bit rate will be more than 20Mbps per carrier to support high-speed internet or high-quality digital broadcasting services in commercial stage. By using inter-platform links, the users separated with a long distance can be connected in an all-wireless link including access links and trunk links. The optical link may be appropriate for inter-platform connection to support large capacity more than 10Gbps.
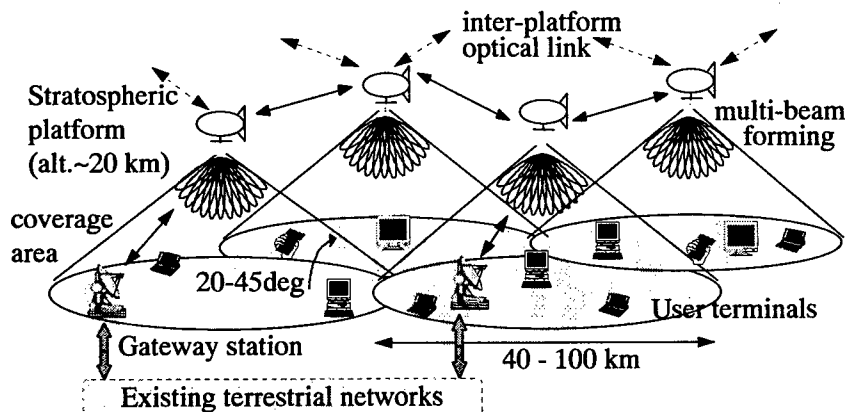
Fig. 1.   SPF network for high-speed wireless access

Now we are developing two types of multibeam antennas for access link for the test flight model that will be launched in 2003-2004. One is a multi-horn antenna in 47/48GHz bands that are officially allocated for the fixed service (FS) using High Altitude Platform Stations (HAPS) [6]. The other is a digital beamforming (DBF) antenna in 20/30GHz bands that have not been officially allocated yet and are selected as one example. Japan is now proposing the allocation of additional frequency bands in the range of 18-32GHz for FS using HAPS to ITU-R [7] because 47/48GHz bands are too high for the access link of stratospheric platform network to provide a high-speed and high-reliability service due to much rain attenuation in rainy country such as Japan.

This paper focuses upon the 20/30GHz bands DBF antenna under development. Requirements for the onboard antenna for SPF and basic characteristics of the DBF antenna are presented.

2. Onboard DBF Antennas

2.1 Requirements for onboard antenna

The access link of SPF network using the band above 20GHz is regarded as a power-limited channel with small power margin. Service coverage for one platform is about 40-100km in diameter on the ground. Considering these conditions, requirements for onboard antennas can be summarized as follows:

(a) Directional antennas will be needed to get high e.i.r.p. and G/T.

(b) Multibeam antennas will be needed to get a large traffic capacity with efficient use of frequency. Minimum service elevation angle will be 20-45degrees and the number of multiple beams will be about 60-400 for one platform.

(c) Since the platform will fluctuate or drift within about one kilometer due to the variation of wind and pressure, antenna beams should be controlled to compensate them and to fix the footprint on the ground as far as possible.

(d) Broad bandwidth to transmit more than 20Mbps will be needed.

(e) Reliability against the stratospheric environment will be needed.

2.2 Basic characteristics of onboard DBF antenna

Due to the limitation of time and budget, the specifications of an onboard DBF antenna on the test flight model will be limited with minimum performance for technological proof. The DBF antenna under development uses Ka band (20.2-21.2 GHz/30.0-31.0 GHz) for experiment. Development cost of devices may not be very expensive because this band has already been used widely in satellite systems. On the other hand, although the performance of digital devices is being rapidly improved, it may not be sufficient for real-time processing of multiple signals coming from many antenna elements in the array antenna. Consequently, the target for transmission data rate with the DBF antenna on the test flight model will be about 2-4 Mbps at most. In spite of such an aspect, achievement of several 10Mbps can be expected in near future. Therefore, the development target of the DBF antenna is placed on the establishment of a high-performance beamforming rather than a high-speed transmission in the meantime. The development and evaluation of the DBF antenna in Ka band is also important for seeking feasibility of frequency allocation in ITU-R. The DBF antenna has the following features:

(a) Flexible beam steering for each of the user terminals will become possible by adaptive multiple beams. Fixed cells are no longer needed. This feature should lead increased traffic capacity.

(b) Consequently, the hand-over in the coverage of one platform will not be basically needed except for the case that the locations of some user terminals get close to each other. High link quality is expected with the maximum antenna gain provided to each of the user terminals on their request.

(c) Spatial signal processing can reduce interference reception of undesired signals and interference emission to other systems such as satellite systems. Direction of arrival (DOA) of communication signal or illegal radio can be estimated.

(d) Partial defection of antenna elements will not affect seriously the total performance of the array antenna.

(e) High-speed array calibration will be possible by signal processing in transmitting and receiving array.

The DBF antenna for test flight model will have as much as 16 antenna elements (4x4 square array) and will be used to obtain technical data for future large-scale DBF antenna. The antenna will be designed to allow transmission of 5-10 carriers with 2-4Mbps in one beam and 4 beams simultaneously available in transmission or reception. The simultaneous number of signals also depends on the number of onboard modems. Two types of digital signal processing devices will be jointly used: FPGA/CPLD (Field Programmable Gate Array/Complex Programmable Logic Device) and high-speed MPU (Micro Processing Unit). The FPGA/CPLD is suitable for high-speed parallel processing and the MPU allows easy programming capability. Table 1 shows the specifications of the DBF antennas.

Table 1. Specifications of the onboard DBF antenna for test flight model: 150-200m-class

	DBF antenna
Frequency band	TX: 30.0-31.0 GHz (LHCP)
	RX: 20.2-21.2 GHz (RHCP)
Number of antenna elements	16
Type of antenna element	Microstrip antenna
Number of multiple beams	Fixed beams: 9 Adaptive beams: 3
Antenna gain	15 dBi
Saturated output power (TX)	>16 dBm
Noise figure (RX)	<5.4 dB
Bandwidth	>3 MHz
Sampling rate	32 Msps
A/D quantization	12 bits

Figure 2 shows the schematic configuration of transponder on the test flight model fully-equipped with DBF antenna and multi-horn antenna. It is pending whether the inter-platform optical communication equipment can be equipped or not on board the test flight model. Table 2 shows the link budget examples for an experimental system using the test flight model. The minimum elevation angle 45degrees is assumed in this link budget, which will be achieved in the experiment with the test flight model by an appropriate phase shift for DBF antenna.   The aperture diameter will be reduced to about 13 cm for 30 GHz and 20 cm for 20GHz even with the link availability as much as 99.7 %. Then the beam width will be about 5 degrees, which does not require antenna tracking even when the platform drifts within the above range.

3. Conclusion

This paper presented the outline of the onboard DBF antenna for the test flight model that will be launched in 2003-2004. Details of the other basic technologies such as SDMA using DBF on SPF [8] and calibration for DBF antenna in reception [9] and transmission[10] are now being studied and will be experienced by the test flight model.

127
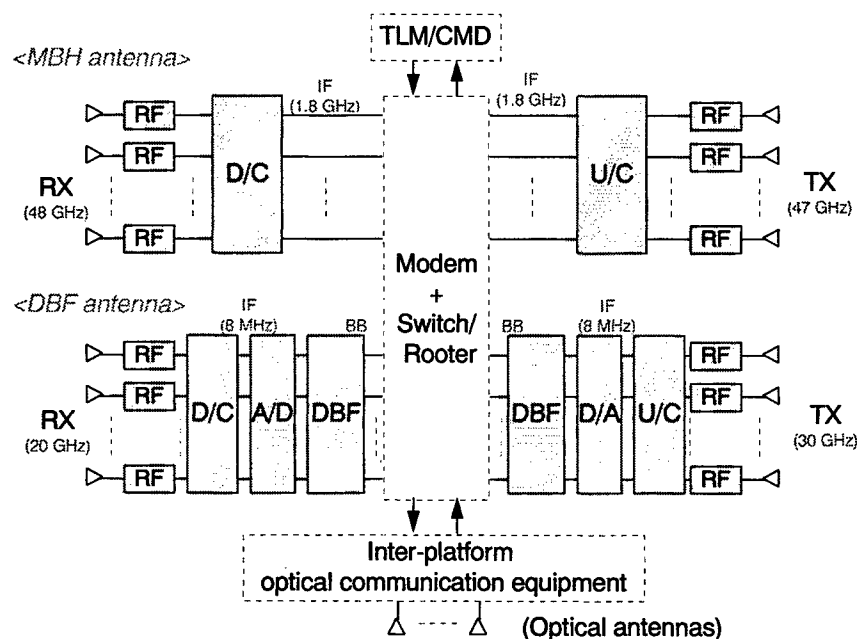
Fig. 2. Fully-equipped transponder on board test flight model
DBF antenna (30/20 GHz)

	unit	elev. angle=45 deg		elev. angle=90 deg	
		up-link	down-link	up-link	down-link
Frequency	GHz	20.0	30.0	20.0	30.0
Bandwidth	MHz	2.0	2.0	2.0	2.0
TX antenna					
output powe	dBW	-20.0	-17.0	-20.0	-17.0
gain [*1]	dBi	30.0	19.0	30.0	15.0
aperture [*2]	cm	19.5	5.2	19.5	3.3
beam width	deg	5.2	13.1	5.2	20.7
eirp	dBW	9.5	1.3	9.3	-2.7
Path loss	dB	147.5	151.0	144.5	148.0
Rain atten. [*3]	dB	4.0	8.0	3 0	6.0
RX antenna					
gain [*1]	dBi	19.0	30.0	19.0	30.0
aperture [*2]	cm	7.8	13.0	7.8	13.0
noise temp.	K	700.0	500.0	700.0	500.0
Req'd Eb/No	dB	5.5	5.5	5.5	5.5
Req'd C/N0	dBHz	71.5	71.5	71.5	71.5
Link margin	dB	5.1	1.8	8.8	2.7

[*1] On-board antenna gain: Peak gain - 3 dB

[*2] Aperture efficiendy: 60 %

[*3] Link availability: 99.7 %

Table 3 Example of Link Budget

Acknowledgment

References

[1] Proceedings of "The First Stratospheric Platform Workshop (SPSW'99)", Yokosuka, May 1999

[2] Y.Hase, R.Miura, and S.Ohmori, "A novel broadband all-wireless access network using stratospheric platforms," Proc. VTC'98, pp. 1191-1194, Ottawa, 1998

[3] http://www.broadband.com/

[4] http://www.skystation.com/

[5] Y.Lee and H.Ye, "Sky station stratospheric telecommunications system, a high speed low latency switched wireless network," Proc. 17th AIAA ICSSC, pp. 25-32, Yokohama, Feb. 1998

[6] ITU-R Final Acts, WRC-97, pp. 60 and 398, Geneva, Nov. 1997

[7] ITU-R Doc. 9B/126 (4-9S/115), Geneva, Apr. 1999

[8] R.Miura, A.Kanazawa, M.Oodo, and Y.Koyama, "Non-blind maximal-ratio-combining array beamforming for SDMA in power-limited channels, " Proc. WPMC'98, pp. 121-125, Yokosuka, Nov. 1998

[9] R.Miura et al. AP97-96(in Japanese) , Sep. 1997

[10] M.Oodo and R.Miura, "A Remote Calibration for DBF Transmitting Array Antennas by Using Synchronous Orthogonal Codes", Digest of IEEE AP-S. July 1999

A novel technique based on power combining mechanism
that yields HPA arrays with high power efficiency

Yoshinori NAKASUGA, Takana KAHO and Kohji HORIKAWA*

Wireless Systems Innovation Laboratory / NTT Network Innovation Laboratories
1-1 Hikarinooka Yokosuka-Shi Kanagawa 239-0847 Japan
TEL:+81-468-59-2084, FAX:+81-468-59-3351, e-mail:nakasuga@wslab.ntt.co.jp
*Radio Network Development Department / NTT Mobile Communication Network Inc.

Abstract

This paper proposes a new concept: utilizing a novel technique to reduce the intermodulation distortion products (IM) allows the efficiency of a high-power amplifier (HPA) array to increased by operating the array in the saturation region. Since we use even-order distortion implemented intermodulation distortion controllers (EODIC), IM is controlled independently of the carriers and thus IM power is reduced while maintaining carrier power. This improves the carrier power to intermodulation power ratio (C/IM) of the HPA array in the saturation region. The improvement in C/IM is 10logN [dB] where N is the number of HPA. The effect is demonstrated experimentally by using a 4-parallel HPA array. The measured C/IM improvement, 6 (10log4) dB, confirms the feasibility of the proposed technique and the feasibility of highly efficient active phased array operation in the saturation region with large N.

1. Introduction

In mobile satellite communication systems, demands for high-speed access and large capacity are increasing due to the advent of the multimedia era. To satisfy these requests, it is necessary to generate RF powers in the kW class. However, the thermal loading becomes extremely large with current RF components. This is a serious problem for satellite systems which are poor at shedding heat. Figure 1 shows the relationship between power efficiency and thermal load for the three RF powers of 1, 2, and 3 kW. Mobile satellite communication systems generally use multi-carrier transmission so a high carrier power to intermodulation power ratio (C/IM) is required. Since the power efficiency of current onboard HPAs is about 25 %[1,2], the thermal load is about 6 kW, for the RF power of 2 kW. To overcome this problem, HPA efficiency must be greatly increasd. In general, HPA output power and power efficiency increase as the operating point approaches the saturation point. Unfortunately, undesirable intermodulation distortion products (IM) also increase due to the non-linear characteristics of HPAs. In operation, the output back-off (OBO) level is typically a few dB lower than the output

saturation point. In the saturation region, the power efficiency decreases by 5% for every 1 dB increase in the OBO level [2]. Any reduction in OBO is valuable in increasing HPA efficiency and thus reducing the thermal load. Many approaches based on linearizers have been advanced to compensate the non-linear distortion but they are not strong enough in the saturation region. This paper utilizes a novel technique to reduce IM and create a high efficiency HPA array. The technique distributes IM power while maintaining carrier power. The effect is demonstrated experimentally by using 4-element HPA array.

2. Distortion distribution method

An HPA array with power combining is necessary to generate kW class RF power. In this case, IM output power is lower than the sum of the individual IM powers of the HPAs because the IMs are slightly imbalanced. Accordingly, HPA arrays offer slightly better C/IM an equivalent single HPA. The proposed concept reinforces this IM reduction effect; IM power is distributed while carrier power is maintained. The image of the concept as applied to a phased array antenna (PAA) is shown in Fig. 2.

In this case, carrier power is increased by voltage summation while IM power is increased by power summation. The combined carrier and IM powers can be expressed by the next equations,

$$P_C = p_C + 20 \log N \quad [dB] \cdots\cdots\cdots\cdots\cdots\cdots\cdots\cdots\cdots\cdots\cdots (1)$$

$$P_{IM} = p_{IM} + 10 \log N \quad [dB] \cdots\cdots\cdots\cdots\cdots\cdots\cdots\cdots\cdots (2)$$

Where,

P_C : output power of the carriers of HPA array P_{IM} : output power of the IM of HPA array

p_C : output power of the carriers of one HPA p_{IM} : output power of the IM of one HPA

N : the number of HPA

Therefore, C/I was expressed next equation.

$$(C / IM)_{array} = P_C - P_{IM}$$
$$= (p_C + 20 \log N) - (p_{IM} + 10 \log N)$$
$$= (p_C - p_{IM}) + 10 \log N$$
$$= (C / IM)_{HPA} + 10 \log N \quad [dB] \cdots\cdots\cdots\cdots\cdots\cdots (3)$$

Where,

(C/I)$_{array}$: C/I of HPA array   *(C/I)$_{HPA}$* : C/I of single HPA

Consequently, the improvement of C/IM becomes 10logN [dB].

3. Experimental results

The effectiveness of the proposal was demonstrated experimentally using a 4-element HPA array. The HPA was a 20 W class SSPA for the S-band. In the proposed technique, the key technology is that IM is controlled independently of the carriers. The even-order distortion implemented intermodulation distortion controller (EODIC)[3] is useful here because pre-distortion signals are controlled in a frequency band different from the transmission band. Moreover, the EODIC has high control

performance against higher-order distortion, which is important in the saturation region because the higher-order distortion can reach the same level as the 3rd-order distortion. A block diagram of the experiment is shown in Fig. 3. An EODIC was set in front of each HPA. In these experiments, multi-tone (27-tone) signals were used to evaluate the effect of the higher-order distortion products. The number of higher-order distortion products increases with the number of carriers because the products are produced from the combination of carriers. The 27-tone signals were located as shown in Fig. 4. All signals were equal spaced except for the center signal. The center frequency (C) was shifted to a slightly lower frequency. When those 27-tone signals are distorted, the primary intermodulation products (IM1) not caused by the shifted center frequency and the secondary intermodulation products (IM2) caused by the shifted center frequency appear at a higher frequency. The C/IM of the 27-tone signals, (C/IM)multi, is given by:

$$(C/IM)_{multi} = C - 10\log(10^{\frac{IM1}{10}} + 10^{\frac{IM2}{10}}) \quad [dB] \cdots\cdots\cdots(4)$$

Output spectra of the combining matrix are shown in Fig. 5. Those with (without) EODIC are shown on the right (left) side. The vertical axes plot output power [dB] relative to the maximum power of IM1. Without EODIC, IM power was concentrated at Port#4. With EODIC, IM power was evenly distributed to all ports. At Port#4, IM power with EODIC was lower 6 [dB] than without EODIC. Therefore, C/IM was improved by 6 [dB] This result agrees with the expected value of 10log4 [dB].

4. Conclusion

A new concept of increasing the efficiency of an HPA array by IM distribution was proposed. The effect of IM distribution was demonstrated by experiments using a 4-element HPA array. The experiments show that C/IM was improved by 6 (10log4) [dB]. This result agrees with the expected value. When this method is applied to an PAA, the carrier power is combined according to the feeding coefficients of PAA to form the appropriate beam while the IM power is spread over as well as noise. Accordingly, C/IM is improved within the service area.

Reference

[1] T. ONO, et al,: "Linearized C-Band SSPA Incorporating Dynamic Bias Operation for GLOBALSTAR," Proc. of AIAA 16th ICSSC, pp. 123-130,1996.
[2] M. Sigaki, et al,: "S-Band High-Power and High-Efficincy SSPA for On Boarding Satellite," Proc. of AIAA 16th ICSSC, pp. 108-112,1996.
[3] K. Horikawa and H. Ogawa: "Even-order distortion enveloping method to linearizer saturated high power amplifiers," MTT-S Symp. Tech. Wireless Appli. Digest, pp. 79-82 1997
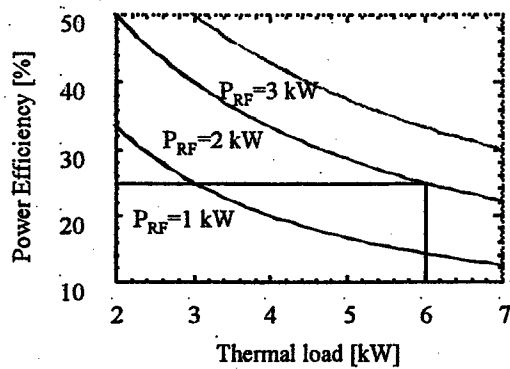
Fig. 1   Efficiency VS Thermal Load
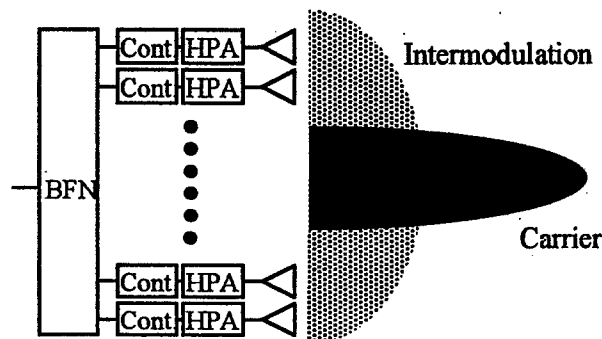
Fig. 2   Image of distribution of intermodulation
         in PAA
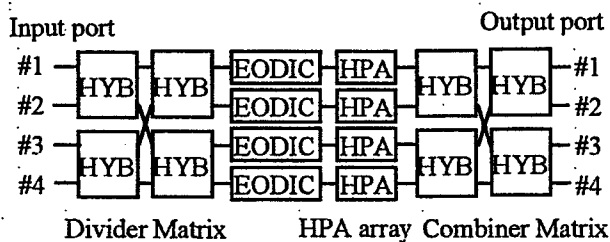
HYB : 3dB Hybrid
HPA : High Power Amplifier
EODIC : Even-Order Distortion
         implemented Intermodulation distortion Controllers

Fig. 3   Block diagram of experiments
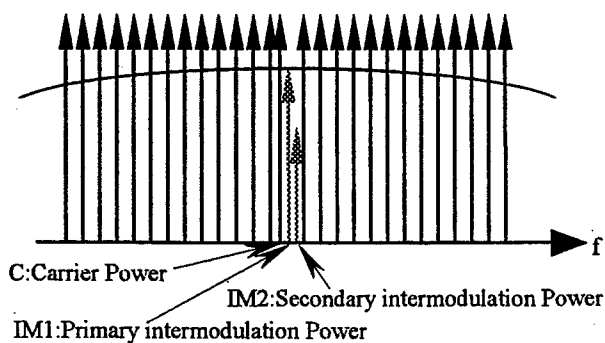
Fig. 4   Output spectrum in 27-tone evaluation
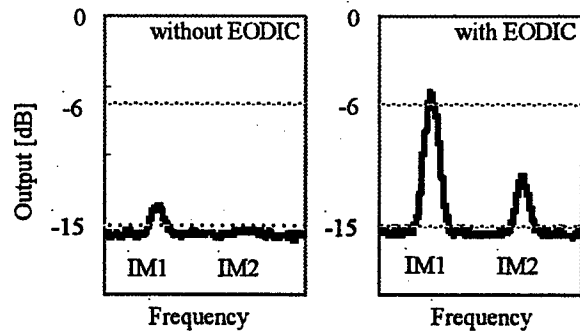
(1) Output Port #1
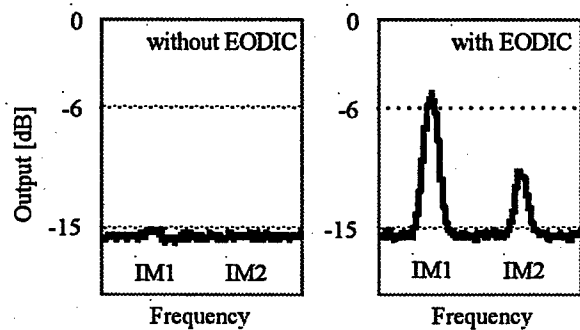
(2) Output Port #2
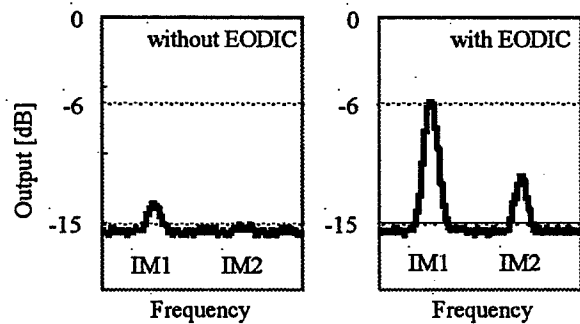
(3) Output Port #3
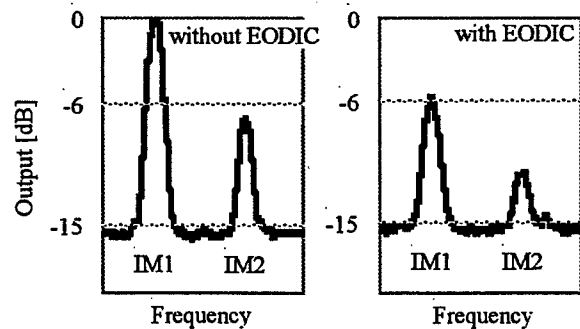
(4) Output Port #4

Fig. 5   Output spectra of combining matrix

Beam Forming Network Design for Cluster Feeding of Scanning Antenna

Fumio KIRA and Toshikazu HORI

NTT Network Innovation Laboratories

Nippon Telegraph and Telephone Corporation

1-1 Hikari-no-oka, Yokosuka-shi, Kanagawa 239-0847 Japan

TEL:+81-468-59-5108, FAX:+81-468-59-3351

E-mail:kira@wslab.ntt.co.jp

Abstract

This paper proposes a new beam-forming network (BFN) for a scanning antenna system that generates a steerable beam using a reflector illuminated by an array of feeding elements. This BFN comprises several variable phase shifters, a power divider, and a Butler matrix (FFT circuit) [1], which is a multi-beam matrix network, and forms a primary beam pattern by using the Fourier transform. This BFN can obtain a primary radiation pattern that is very similar to the input signal distribution of the beam port, and does not require deep consideration of the excitation distribution of the antenna elements to obtain the desired pattern. Moreover, the beam pattern generated by this BFN effectively illuminates only the reflector. We confirm that this BFN was able to improve the antenna efficiency by 11%.

1. Introduction

There are roughly two kinds of the feeding method for electric beam scanning reflector antennas. One type is an array feeding that feed power from the off-focal position, and the other is a cluster feeding that feed power from the focal plane. The former suitable for making a shaped-beam, but in general, the antenna efficiency is not high [2]. A variation of the phasing between the reflector and the feed array is obtained when a large number of element antennas are used. The number of antenna elements can be decreased in the latter. However, a BFN usually involves many switches because different antenna elements must be excited depending on the beam orientation, and phase/amplitude correction is achieved in the considerable configuration complex. When a reflector must be uniformly illuminated to increase aperture efficiency, spillover increases and the antenna efficiency deteriorates.

This paper propose a new BFN configuration for cluster feeding, which removes switches in the BFN and can easily form a flat beam that uniformly radiates the reflector only. This paper first describes the configuration and operation principle. After that, two examples adopting the proposed BFN using Gaussian beam and flat beam are presented and the effectiveness of the proposed BFN are evluated by numerical analysis.

2. Configuration and Principle of BFN

Figure 1 shows the basic configuration of the proposed BFN. Signals are divided by the power divider and are input to the beam port of the Butler matrix through variable phase shifters. Each signal to the beam

port is distributed and output to all element ports with phase differences depending on the position of the input beam port. The number of the exciting beam ports is less than the total number of the beam ports. The rest of the ports is terminated. The input signal distribution, $f(x)$, and the output signal distribution, $F(\omega)$, of the Butler matrix are related through the Fourier transform [3]. Here x and ω represent the position of the beam ports and the position of the element ports, respectively.

From the time-shifting property of the Fourier transform, the changes in the position, $\Delta \omega$, of the output signal distribution, $F(\omega)$, can be given as the relation between $f(x) \, e^{-j\omega\Delta x}$ and $F(\omega + \Delta \omega)$ [4]. Therefore, by feeding signals with phase differences to multiple beam ports of the Butler matrix, it is possible to change antenna elements to an excited state without using switches to change the beams. It is a well-known fact that output signal distribution $F(\omega)$ and the primary radiation pattern are related through the Fourier transform. Thus, it is expected that input signal distribution $f(x)$ and the primary radiation pattern will have a very similar form.

In practical use, it is important to determine how many beam ports must be used to feed signals. If the element antennas connected to the Butler matrix have an equal spacing of d, the beam direction of the i-th beam, θ_i, is given by $kd\sin\theta_i = (2i-N-1)\,\pi/N$, where k is the wave number and N is the number of beam ports (or element ports). That is to say, when all beam ports are used, the primary beam can be roughly radiated within the range of $\pm\pi$ in u dimensions ($u = kd\sin\theta$). Moreover, if half the beam ports are used, the range of $\pm\pi/2$ can be covered, and should be sufficient for an average antenna configuration.

3. Numeric Analysis Applied to Offset Parabolic Antenna

3.1. Side-lobe suppression by Gaussian beam

The results of applying the proposed BFN to the feeder of a circular aperture parabolic antenna with the aperture radius of 20λ and $f/D = 1$ shown in Fig. 2 are described below as an example. The number of Butler matrix ports is $N = 16$, the beam scanning direction is horizontal, element antennas are circularly polarized microstrip antennas and element spacing d is 0.5λ. To narrow the primary radiation pattern to vertical, four antenna elements are vertically arranged with the power distribution ratio of 1:2:2:1. When the primary radiation pattern is a Gaussian distribution with a -20 dB edge, $F(\omega)$ is a Gaussian distribution with the half-amplitude of 3.8. This means that 99.3% of the signal power is concentrated on the central six beam ports. Figure 3 shows the signal distribution $F(\omega)$ of the element ports when signals are fed using the six ports (#6–#11). The phase differences between adjacent beam ports, $\Delta\phi$, are 15, 45, 75 and 105 degrees and the power distribution ratio is 1:5.1:11:11:5.1:1 in this figure. Figures 4 and 5 show the primary radiation pattern and antenna radiation pattern in this case, respectively. The above results show that an adequate low side-lobe pattern was obtained. In this case, antenna efficiency is about 69%, the half-power beamwidth (HPBW) is about 4.0 degrees, the maximum value of the spillover is 8%, and that the sidelobe levels are below -32dB. The efficiency deterioration due to the loss of variable phase shifters becomes a problem in the BFN usually, but if the phase of beam ports are adjusted based on the beam port #8 (or #9), one number of variable phase shifters can decreases and the loss is reduced by 33%.

3.2. Efficiency improvement by implementing flat beam

Figure 6 shows $F(\omega)$ when the same input signals are fed to all six ports to obtain a flat beam that uniformly illuminates the reflector. The aperture angle of the reflector is ±24.9 degrees and the range of the flat beam is calculated as $sin^{-1}\pm3/16 = \pm22.0$ degrees. Figures 7 and 8 show the primary radiation patterns and antenna radiation patterns, respectively. These figures show that the primary beam patterns are a flat beam, and a narrow beam is obtained as the antenna radiation pattern. In this case, antenna efficiency is about 85%, the HPBW is about 3.1 degrees, and the maximum value of the spillover is 14%. When $F(\omega)$ is excited by Gaussian distribution without using the proposed BFN and the HPBW is 3.2 degrees, the spillover is 20%. When the HPBW is 3.1 degrees, the spillover is 27% and the antenna efficiency is 64%.

4. Conclusion

We proposed a BFN configuration that is suited to cluster feeding by using the Butler matrix, and demonstrated its ability to offer good pattern characteristics. Moreover, the BFN provides a beam steering function by using fewer variable phase shifters. A low side-lobe pattern and flat beam are easily achieved by changing the power ratio of the fed power to the beam ports. Furthermore, the BFN improved antenna efficiency by reducing spillover.

References

[1] J. Butler and R. Lowe, "Beamforming matrix simplifies design of erectronically scanned Antennas," Electron. Design, Vol. 9, No. 7, pp. 170-173, April 1961.

[2] K.ueno, "Multibeam Antenna Using a Phased Array Fed Reflector," IEEE AP-S Int. Sym. Dig, pp. 840-843, JOINT-42.2, July 13-18, 1997.

[3] J.P. Shelton, "Fast Fourier transforms and Butler matrices," Proc. IEEE, Vol. 56, No. 3, p. 350, March 1968.

[4] R.N. Bracewell, "The Fourier transforms and Its Applications," chapter 6, McGraw-Hill, Inc., 1978.
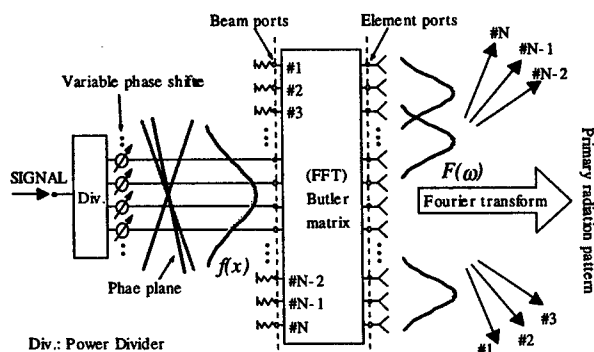
Fig. 1 Proposed BFN configuration
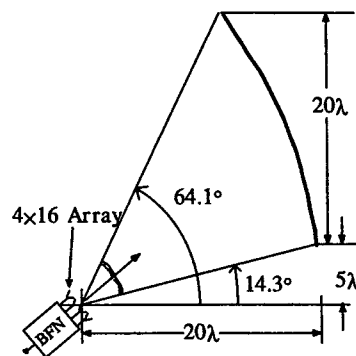
Fig. 2 Example of antenna configuration

135

beam port	Amplitude
6	-15.45 dB
7	-8.39 dB
8	-4.86 dB
9	-4.86 dB
10	-8.39 dB
11	-15.45 dB

$\Delta\phi = 15°, \ 45°, \ 75°, \ 105°$
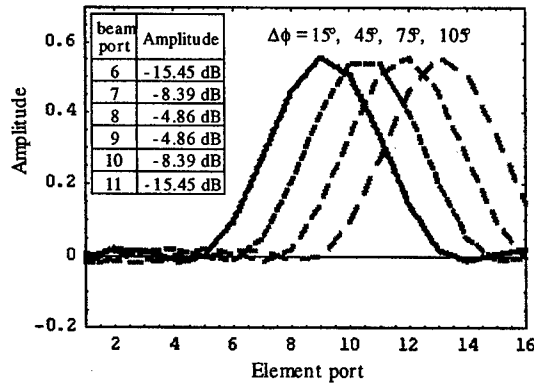
Fig. 3 Amplitude distribution of $F(\omega)$
(for Gaussian beam)

beam port	Amplitude
6	-7.78 dB
7	-7.78 dB
8	-7.78 dB
9	-7.78 dB
10	-7.78 dB
11	-7.78 dB

$\Delta\phi = 15°, \ 45°, \ 75°, \ 105°$
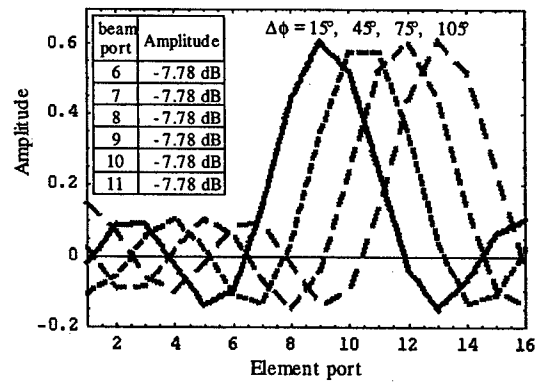
Fig. 6 Amplitude distribution of $F(\omega)$
(for Flat beam)
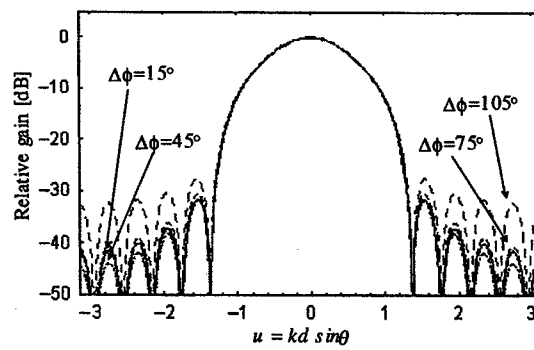
Fig. 4 Primary radiation pattern
[Array pattern]
(Gaussian beam)
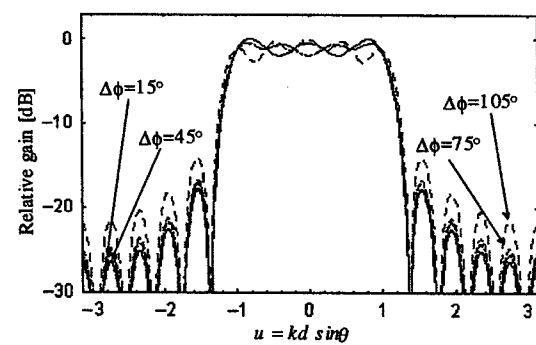
Fig. 7 Primary radiation pattern
[Array pattern]
(Flat beam)
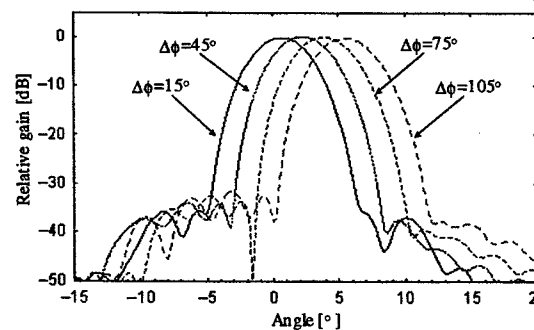
Fig. 5 Antenna radiation pattern
(Gaussian beam)
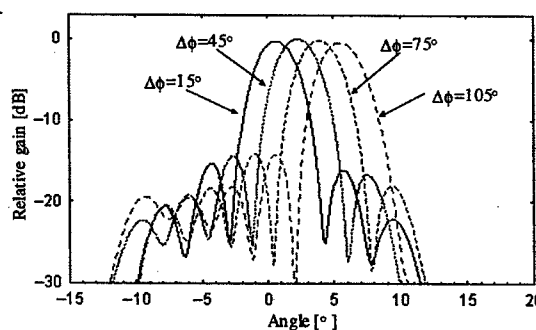
Fig. 8 Antenna radiation pattern
(Flat beam)

MP2

Digital Beamforming

Digital Beamforming

Spectral Analysis of Nonuniformly Sampled data
Using a Least Square Method
For Application in Multiple PRI System

Jinhwan Koh and Tapan K. Sarkar
Department of Electrical Engineering & Computer Science
121 Link Hall
Syracuse University
Syracuse, New York 13244-1240
Phone : 315-443-3775
Fax : 315-443-4441
Email : jikoh@mailbox.syr.edu, tksarkar@mailbox.syr.edu

Michael C. Wicks
Rome Laboratory
Sensors Directorate
Email : wicksm@rl.af.mil

Abstract

This paper addresses the problem of spectrum analysis from nonuniformly sampled data using the least square method for applications in multiple PRF radar system. The benefits of using a direct spectrum analysis using nonuniformly spaced data instead of using a FFT based CR(Chinese Remainder) theorem has been presented. Using a spectrum analysis based on nonuniformly spaced data, the blind bursts that the target frequency is folded into the clutter band could be overcome easily. Additional benefits of using an unevenly spaced data spectrum is its robustness to noise. It is shown that the least square method outperforms conventional Chinese remainder theorem based on FFT method by 2.5[dB] of SNR. This can also be an efficient method when there exist multiple interferences with same magnitude as the target. To obtain a spectrum from nonuniformly sampled data, the well known Lomb periodogram has been modified to fit a complex sequence. Phase component has also been recovered from the power representation to determine whether the target is opening or closing. The result of a modified scheme is compared to the result of the Lomb periodogram.

1. Introduction

There are several methods to enhance doppler ambiguities. The best method depends on the application and of the choice of the constraints. Generally speaking, the multiple pulse repetition frequency (PRF) or staggered PRF system performs better than other systems [1]. By using several fixed PRFs enables one to discriminate the aliased response of a single PRF system by comparing it with the responses of other PRFs. In this way one can eliminate Doppler ambiguity or range ambiguity.

Previous researches have been done in developing methods for resolving doppler and range in multiple PRFs systems. Ludloff and Minker [3] presented a curve of reliability of velocity measurement from simulations. Vrana [4] dealt with the problem in a statistical manner. The two steps used to get the optimum estimation in Vrana's research lies in making a decision resolving the ambiguity of the estimate and smoothing of the data. In many papers, the Chinese remainder (CR) theorem is a commonly used algorithm to resolve doppler frequencies or a range and it is a method to solve a set of residue problems [1,2]. The CR theorem has a couple of defects when applied to the multiple PRF systems. First, it can

only operate with a single target. If there are several targets which have the same scattered power at one look angle, the results of the CR theorem would be ambiguous since there are too many folded doppler frequencies to discern for an actual doppler frequency and therefore there should be another algorithm to cope with this situation. If the measured frequency folded into the clutter spectral band, which may be due to the movement of the radar with respect to the ground, the contact to the target is not clear. Other problem with this approach is that a small range error on a single PRF system can cause a large error in the resolved range and there is no indication that this has happened. To overcome this problem of CR theorem, a clustering algorithm has been proposed by Trunk and Brockett [5]. They used a variance to each PRF data to test if it is real doppler or range. Even with the clustering algorithm, the fundamental drawback of the CR theorem approach cannot be resolved in the previous researches since they dealt with the problem of solving the congruences problem by some numerical techniques. However, none of them addressed the problem about the unevenly spaced data itself.

Instead of dealing with each PRF one at a time, one can use all the PRFs simultaneously in the time domain. The problem then reduces to finding a spectrum for an unevenly sampled signal. If we can find the spectrum of the unevenly sampled signal, we would not have the problem of solving for congruences and other disadvantages associated with CR theorem. Moreover the present method deals with multiple targets and it can also resolve blind speed and the blind range problems.

In this paper, the frequency domain response is generated from an unevenly sampled sequence by using a least square method. Additional benefit of using an unevenly spaced analysis is that it can reduce the distortion in the spectrum of a signal affected by noise due to the correlation of each frequency component as indicated by Lomb [6]. It is generally known that if the sampling is completely random, and is a Poisson process, then the spectrum of that sequence is alias free [8, 9].

2. Least Squares Method

The periodogram approach [6-10] to solve a problems of nonuniformly sampled spectrum provides a scan of a given frequency range obtained by fitting sine and cosines in a least squares fashion to the data and plotting the correlation of data at each frequency. The least square spectrum provides the best measure of the power contributed by the different frequencies to the overall variance of the data. Therefore this can be regarded as the natural extension of the Fourier methods to nonuniformly spaced data. The frequency increment can be determined with any precision and that is a benefit of using this method.

Let a continuous complex signal $x(t)$ be sampled at time instants, $t = t_k$, for k=0,1,2,...,N-1.
A complex version of the Lomb periodogram can be derived in a similar fashion as a Lomb periodogram of a real sequence [6, 7] using the least square method. The resulting power in the harmonic component for a complex sequence at frequency ω is given by

$$P(\omega) = \frac{\left\{\sum_{k=0}^{N-1} x(t_k)\cos[\omega(t_k - \tau)]\right\}^2}{\sum_{k=0}^{N-1}\cos^2[\omega(t_k - \tau)]} + \frac{\left\{\sum_{k=0}^{N-1} x(t_k)\sin[\omega(t_k - \tau)]\right\}^2}{\sum_{k=0}^{N-1}\sin^2[\omega(t_k - \tau)]}, \tag{1}$$

$$\text{where } \tan(2\omega\tau) = \frac{\sum_{k=0}^{N-1}\sin(2\omega\, t_k)}{\sum_{k=0}^{N-1}\cos(2\omega\, t_k)}. \tag{2}$$

142

Observe that (1) yields the same value for ω and $-\omega$ since it is squared. Obviously this expression is not suitable for negative frequencies (opening target). To obtain the phase component of the spectrum from the power representation (1), a frequency response $E(\omega)$ of the form is assumed:

$$E(\omega) = \sum_{k=0}^{N-1} \alpha \cos[\omega \ (t_k - \tau)] + i\sum_{k=0}^{N-1} \beta \sin[\omega \ (t_k - \tau)],$$ (3)

where τ is a free parameter same as defined in (2).

The corresponding power spectrum can be written as

$$P(\omega) = \mid E(\omega) \mid^2 = \left| \sum_{k=0}^{N-1} \alpha \cos[\omega \ (t_k - \tau)] \right|^2 + \left| \sum_{k=0}^{N-1} \beta \sin[\omega \ (t_k - \tau)] \right|^2.$$ (4)

Matching (1) and (4) for all $x(t_k)$ will give the unknown coefficients α and β. The resulting expression turned out to be:

$$E(\omega) = \frac{\sum_{k=0}^{N-1} x(t_k)\cos[\omega \ (t_k - \tau)]}{\sqrt{\sum_{k=0}^{N-1} \cos^2[\omega \ (t_k - \tau)]}} + i\frac{\sum_{k=0}^{N-1} x(t_k)\sin[\omega \ (t_k - \tau)]}{\sqrt{\sum_{k=0}^{N-1} \sin^2[\omega \ (t_k - \tau)]}}.$$ (5)

The phase information is obtained through this expression.

To illustrate the significance of (1) and (5), consider a signal of the form

$$f(x_k) = 1.2\exp(10\cdot10^3 \cdot 2\pi i x_k) + 2\exp(-20\cdot10^3 \cdot 2\pi i x_k) - 2.5\exp(25\cdot10^3 \cdot 2\pi i x_k),$$

where x_k are the sampling points from a 4 PRF systems of 1kHz, 1.35kHz, 1.6kHz and 1.7kHz, sequentially for $k = 1, 2, \ldots, 128$. Now (1) and (5) are used to estimate the spectrum of the nonuniformly sampled data and the result is shown in figure 1. Average sampling frequency is 5.5kHz which is much lower than the Nyquist sampling rate (25kHz since this is a complex signal). As seen in figure 1-(b) the negative frequency component located at -20kHz is now distinguishable through the use of equation (5). This is not possible in figure 1-(a) which is the original formulation for the Lomb periodogram. Note that the absolute value has been taken and squared values in figure 1-(b) are suitable for comparison with figure 1-(a).

The performance to noise depends on situations and we considered a single test signal which is located at 10kHz with unit magnitude sampled by 4 PRFs, 1kHz, 1.35kHz, 1.6kHz and 1.7kHz. Gaussian white noise of real and imaginary components having equal power density has been added to the signal. The signal has been sequentially sampled at 32 sampling points by PRF1, 32 points using PRF2, 32 points from PRF3 and other 32 points due to PRF4. We assumed that an error occurred if the magnitude of the sidelobe is larger than the magnitude of the signal frequency. The result shows that the least square approach outperformed the CR theorem based on the FFT method. Figure 2 is a plot of the increase in the noise power versus the probability of false alarm for both the methods and an error occur when the maximum does not occurs at the real signal frequency. 1000 simulations have been tried to get the estimation of probability. Around -2.5 dB of SNR, the CR theorem starts to fail and around -5 dB of SNR, the least square method starts to fail. Note that only one false alarm for any of the 4 PRF may lead to a failure of the CR theorem (clustering algorithm) method. Therefore the least square method outperformed CR theorem method by 2.5dB of SNR. If we consider 5 or 6 PRFs system, the least square method will provide better result than the CR theorem.

3. Conclusion

This paper addresses the problem of a spectrum analysis from nonuniformly sampled data using the least square method for applications in multiple PRF radar system. The benefits of using a direct spectrum analysis from nonuniformly spaced data instead of using a FFT based CR theorem has been presented. The direct spectrum analysis can detect a target easily in the presence of ground clutter. This can also be an efficient method when there exist multiple interferences with same magnitude as the target.

4. References

[1] M. I. Skolink, Radar Handbook, McGrawHill, 1970.

[2] H. R. Raemer, Radar System Principles, CRC press, 1996.

[3] A. Ludloff and M Minker, "Reliability of Velocity Measurement by MTD Radar," IEEE Transactions on Aerospace and Electronic Systems, AES-23, 4, July 1985, pp.522-528.

[4] I. Vrana, "Optimum Statistical Estimates in Conditions of Ambiguity," IEEE Transactions on Information Theory, 39, 3, May 1993, pp.1023-1030.

[5] G. Trunk and S Brockett, "Range and Velocity Ambiguity Resolution," IEEE National Radar Conference, 1993, pp.146-149.

[6] N. R. Lomb, "Least squares frequency analysis unequally spaced data", Airophysics and space science, vol. 39, pp. 447-462. May. 1975.

[7] J. D. Scargle, "Studies in astronomical time series analysis. II. Statistical Aspects of spectral analysis of unevenly spaced data", The Airophysical Journal, vol. 263, pp835-853, Dec. 1982.

[8] I. Bilinskis and A. Mikelsons, Randomized Signal Processing, Prentice Hall, New York, 1992.

[9] F. J. Beutler, Error-Free Recovery of Signals from Irregularly Spaced Samples, SIAM Review, vol 8, No. 3, pp328-335, July 1966.

Figure 1. Comparison between the Lomb periodogram and the new modified scheme
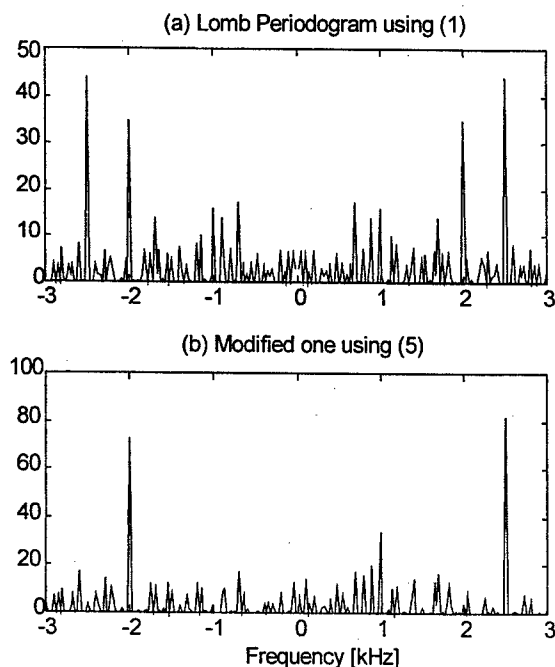
Figure 2. Comparison of least square method and CR theorem based on the FFT method. A false alarm occurred when the sidelobe is greater than the mainlobe. As SNR decreases least square method outperforms the FFT method about 2.5 dB
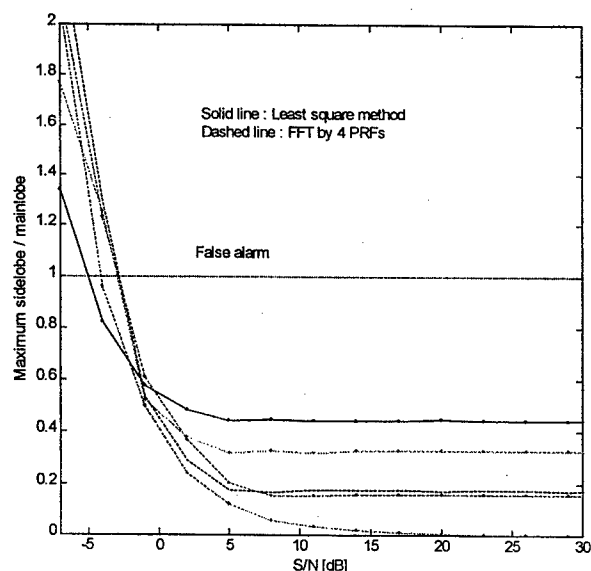
Digital Active-Aperture Phased-Array Radar

Dr. B.H. Cantrell, Mr. J.W. de Graaf, and Dr. L.M. Leibowitz
Naval Research Laboratory
Washington, DC 20375

Background: Twenty-first century U.S. Navy radar requirements call for reduced production costs with improved reliability and maintainability. The Naval Research Laboratory (NRL) has addressed this problem with consideration of various radar architectures.[1] NRL recently performed analysis and initial testing leading to a digital phased-array radar approach providing the performance required by the Fleet. Digital radar has the potential for unprecedented performance in the presence of jamming and clutter such as in the littoral environments in which the Fleet often operates. NRL has a hardware design being developed to demonstrate digital radar technology for future Navy radars. The approach uses commercial-off-the-shelf (COTS) cell-phone and other commercial technologies.

Technical Approach: The NRL approach utilizes a new digital radar architecture as shown in Fig. 1. A below-decks COTS processor generates digital waveform codes and control messages and provides a 60 MHz basic clock. The codes and messages are generated offline and stored in memory. During radar operation these data and the 60 MHz clock are each transferred on a single fiber-optic line and directed up the mast to an optical distribution network at the array aperture. Each fiber-optic line in this network is fanned out to a group of m 8-element digital T/R modules. Each digital T/R module element consists of digital-to-analog converter (DAC) and analog-to-digital converter (ADC), field programmable gate array (FPGA) modules, up/down frequency converters, filters, and a power amplifier and receiver with a duplexer and receiver protector behind a simple antenna element. Echo data from the m T/R modules is routed to the processor via fiber-optic lines.

Digital T/R Module: A more detailed block diagram of a T/R module element is shown in Fig. 2 with performance specifications indicated in Table 1. The module element consists of fiber-optic distribution with electrical-to-optical (E/O) and optical-to-electrical (O/E) conversion, a digital section, a clock and LO distribution section, a microwave section consisting of up/down converter, multi-stage amplifier chain, and module calibration. The below-decks fiber-optic transmitter sends optical pulses, containing serial digital controls/waveform data and 60 MHz clock, to fiber-optic distribution at the antenna aperture. The fiber-optic distribution presents the optical 60 MHz clock and waveform data to a photo detector in each T/R module. After photo detection and buffering, the noise performance of the 60 MHz clock is improved by a phase-locked loop and passed to a microwave circuit that generates the 2nd LO frequency. The 1st LO frequency is generated by an FPGA-based module and a multiplier in a microwave circuit. The digital controls/waveform data are decoded and conditioned at baseband by several operations in an FPGA-programmed module. The baseband waveform is then digitally frequency translated and converted to the last IF via a DAC. The IF waveform is upconverted to the transmitted frequency band, power amplified, and coupled to an antenna element via a duplexer/circulator. Echo signals are received and passed through a duplexer with receiver protector to a downconverter. In the digital section, the baseband echo signal is converted to digital and passed by the fiber-optic distribution system to the below-decks processor. T/R module calibration presents a major challenge to equalize and maintain hardware errors throughout the active aperture over a reasonable period of operation.

Up/Down Frequency Converter: The up/down converter primarily consists of COTS components. A simple block diagram of the exciter and receiver is shown in Fig. 3. In the exciter chain, the bandpass filters are designed with lump elements inside a surface-mount package and the amplifiers are broadband monolithic in design. The mixers are double balanced with a high third-order intercept point (IP3). Also, the low-noise amplifier (LNA) has a high IP3 with moderate gain. The noise figure of this LNA is less than 3 dB.

Fiber-Optic Up/Down Link and Distribution: The creation and encoding of the transmitted radar waveform are performed in the VME processor as shown in Fig. 4. To set dwell times and waveform parameters, the FPGA-based module takes timing information from the VME processor and appends a short word to the radar waveform data. The entire word is then converted to serial data for the fiber-optic transmitter. The optical data stream from this transmitter is then up-linked to the aperture antenna and distributed to all the digital T/R modules. To clock the ADC and DAC in the digital T/R module and to generate the LO frequencies, the 60 MHz clock is converted to optical and distributed similarly at the aperture. On the receive side, the FPGA module at each digital T/R module conditions the baseband signal by several operations, converts it to optical, and sends the data stream below decks for additional processing.

Digital Section: Prior to the up/down converter, the digital section performs transmit and receive of digital data as shown in Fig. 5. The transmit side of the digital section converts the optical serial data streams from below decks into electrical serial data. This serial data stream, containing the waveform and control words, is then converted into a parallel word at the 60 MHz base clock rate. The parallel digital words are then conditioned by an FPGA-based module, which performs phase/amplitude control, amplitude and phase equalization, injection of a lowpass dither signal, and frequency translation from baseband to the last IF. The last IF is demultiplexed into 8 separate channels for an 8-element sub-array. Each channel is piped into a 14-bit DAC for the upconverter. The addition of the dither signal aids in lowering the spurious content generated in the DAC. The receive side of the digital section essentially performs the reverse of the transmit function. As shown in Fig. 5, the input waveform at the last IF is sampled by an ADC (14 bits at 60 MHz). The digitized data in the FPGA module conditions the received data by first converting from real data to I/Q samples. Applying a finite impulse response (FIR) filter to the data performs the conversion to I and Q by a method derived by J.P. Hansen of NRL.

Summary and Conclusions: Digital active-aperture architecture for phased-array radars has been proposed by NRL to improve performance and reduce the life-cycle cost of future U.S. Navy radars. Considering various approaches, NRL has been procuring and testing various component alternatives and is implementing the design described above in order to demonstrate this technology. The simulations, analysis, and laboratory measurements that have been performed support this development. Although much progress has already been made, several important issues must still be resolved. These include the amount of processing required in the digital section for high precision, the size and performance of the up/down converters, and the size and cost of on-module generation of the LO and the digital clock. Under a new FY00 ONR program, MIT Lincoln Laboratories, Naval Surface Warfare Center Dahlgren Division, and NRL will draw on their individual developments to collectively construct a 100-T/R module phased-array radar. To be considered viable, digital active aperture array radar must demonstrate high performance with relatively low life-cycle cost and complexity. NRL results to date hold the promise of unprecedented performance in jamming and EMI with low life-cycle cost and high availability for U.S. Navy applications.
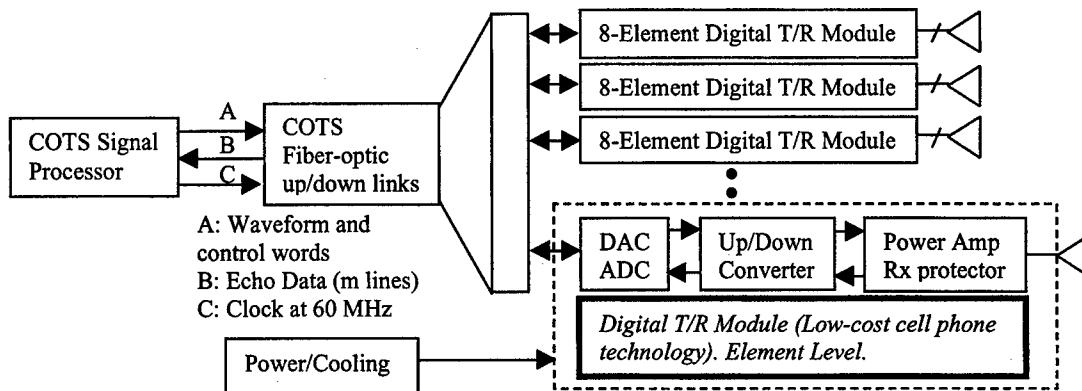
Fig. 1 – Digital radar architecture
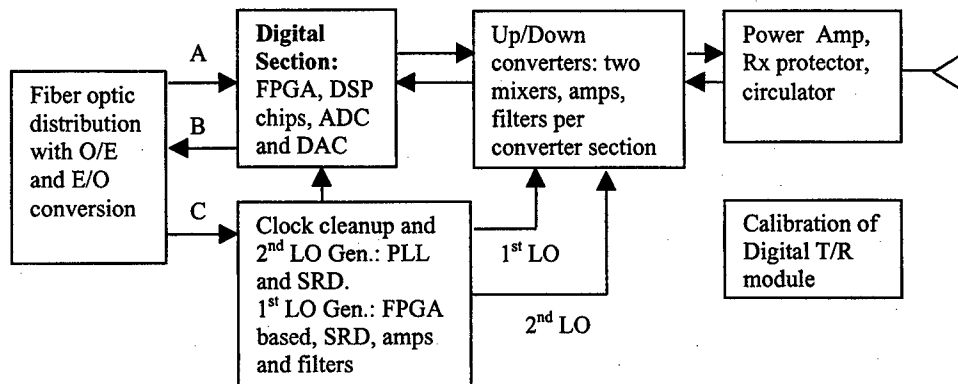
Fig. 2 – Digital T/R module concept

Table 1 _ Digital T/R Module Performance Specifications

Parameter	Value	
Frequency	1215 to 1400 MHz	
Peak/Average Power	50/5 W - Couple of stages. Class C final	
Module Efficiency	>25%	
Bandwidth	<10 MHz	
Noise Figure	4 dB	
Front-End Dynamic Range	Single-Tone (I MHz)	85 dB
	Two-Tone	70 dB
Phase Noise (CW)	Floor	-160 dBc/Hz
	100 Hz	-110 dBc/Hz
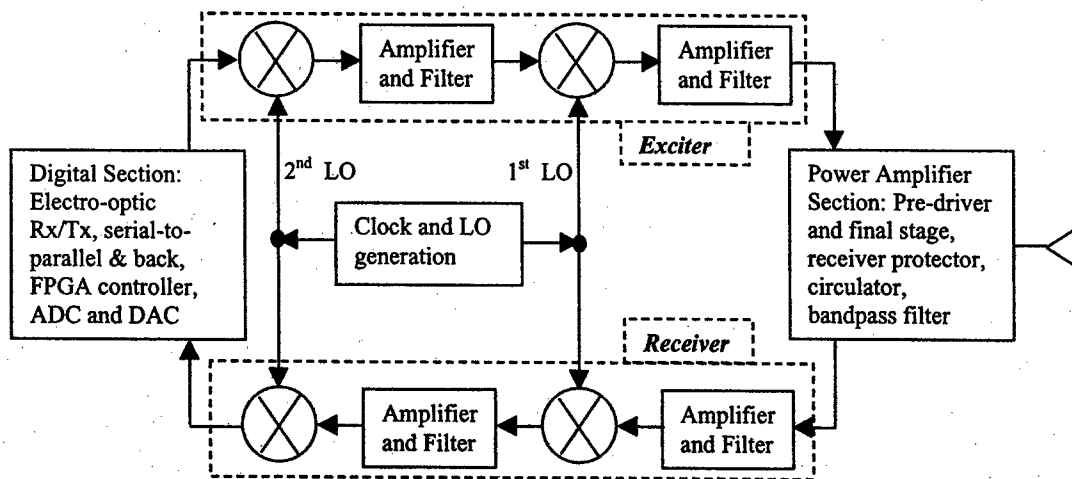
Fig. 3 – Up/Down frequency converter
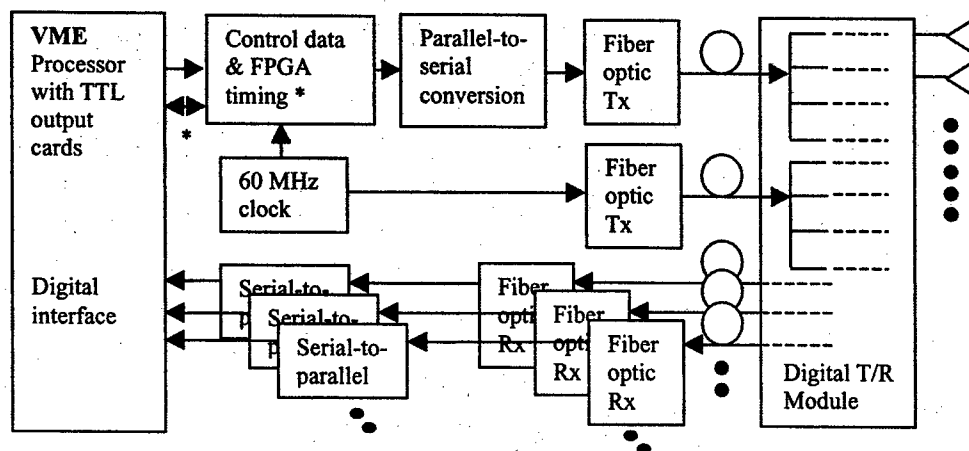
Fig. 4 – COTS processor, fiber-optic up/down link and distribution
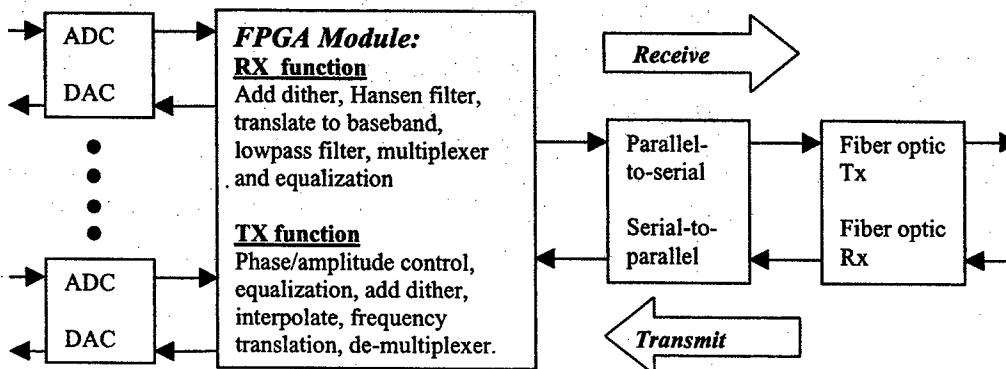
Fig. 5 – T/R module digital-section transmit/receive signal-flow diagram

148

Digital Beamforming in a Compact 20 – 32 MHz Radar

Robert J. Dinger
Erik L. Nelson
Code D73J, SPAWAR Systems Center
San Diego, CA 92152

Richard L. Powers
Sanders, A Lockheed Martin Company
Nashua, NH 03061

1. Introduction

Most current research and development programs in the field of digital beamforming are concerned with systems that operate in the traditional microwave frequency bands or higher. This paper discusses digital beamforming in a novel high frequency (HF) radar that operates from 20 to 32 MHz. Under the STEEL TRAP sensor program of the Department of Defense, we developed a semi-portable HF radar to measure the scattering properties of air targets. Earlier semi-portable HF radars, as well as most skywave HF radars, have used analog beamforming and frequency-modulated continuous wave (FMCW) waveforms. The STEEL TRAP HF radar (STHFR) radiates a pulsed waveform and has an eight-element receiving array that forms beams digitally. This paper describes the beamforming approach and the technique used for determining target angular position, and presents examples taken from a series of scattering measurements of a sounding rocket.

2. HF Radar Description

Figure 1 is a block diagram of the STHFR, and Figure 2 is a photograph of the receiving array. The V-shaped configuration, shown in Figure 3, was chosen as a compromise between the highest possible gain of a linear array and the elevation discrimination offered by an array with a projected aperture in the elevation plane. A separate transmitting antenna, located about 100 m from the receiving array, radiates about 150 W (average). The STHFR uses a pulsed waveform, typically with a pulse width of about 200 µs and a pulse repetition interval of 800 µs. The linear FM waveform has a swept bandwidth of 75 kHz.

The antennas are log-periodic dipole arrays (LPDA) with vertically and horizontally polarized elements. A wire ground screen, combined with the downward pointing angle of the LPDA feedline evident in Figure 2, improves the antenna pattern at high elevation angles. The antennas provide coverage over an azimuth sector of 90 deg and elevation angles from 10 to 60 deg above the horizon.

Each receiving antenna is connected by a phase-matched coaxial cable to a receiver and A-to-D converter in a portable shelter. The digital outputs are generated with a 16-bit resolution at a rate of 160 kHz and are recorded on a RAID disk array for post processing.

3. Post Processing

The beamforming and target range, velocity, and azimuth/elevation angle processing are carried out after the mission by the following steps. (1) Closed-loop calibration data, injected into the receiver inputs, are used to generate matched filters for each channel to compensate for phase and amplitude differences in the receivers. In-phase and quadrature (I and Q) components of the signal return are recorded for every channel. (2) Pulse compression is accomplished by performing an FFT on the return signal and applying the matched filter response. An inverse FFT returns the data to its original domain. (3) Doppler filtering is achieved by applying a Hamming window and performing an FFT across a coherent integration time for each range cell. The resulting 2-D image is comprised of signal returns arrayed in range and Doppler.

(4) The azimuth and elevation of targets of interest are determined using the method described in Section 5. (5) Each of the eight range-Doppler arrays (RDA) is multiplied by a complex weight and summed to yield a beamformed RDA. Determination of the beamforming weights is discussed in the next section. (6) The amplitude, range, and velocity of the target are determined from the beamformed RDA.

4. Beamforming

The challenge in beamforming is to derive the correct values of the complex weights $W_i = A_i exp(j\varphi_i)$, where i is the index of the antenna element, given a desired azimuth and elevation angle (and in general other beam parameters, such as sidelobe level). Because of the physically large near-field scattering region at HF (10's of meters), which can produce distortions in the incident signal, we would prefer to determine the beamforming weights based on the element responses to calibrated targets positioned in the array far field. However, for the measurements described below, this was not possible. Hence, we used uniform weighting ($A_i = 1$ for all i) and calculated the phase weights from the standard free-space phase relationship $\varphi_i = (2\pi/\lambda) e_r(\alpha,\varepsilon) \bullet r_i$, where $e_r(\alpha,\varepsilon) = e_x cos\alpha cos\varepsilon + e_y sin\alpha cos\varepsilon + e_z sin\varepsilon$ is a unit vector in the desired mainbeam direction, and r_i is the position vector of the ith element in the array. We made no attempt to include the dielectric effects of the earth or otherwise account for near-field scattering effects.

5. Target Azimuth and Elevation Angle Determination

The target azimuth and elevation angles were determined by a correlation technique borrowed from HF direction finding. First, a set of reference vectors is computed that encompasses the range of possible azimuth and elevation angles to be searched. In the sample results shown below, these reference vectors assume a uniform amplitude and linear progressive phase (i.e., the same assumptions as were used for the beamforming). Then, the correlation is computed between the similarly constructed vector produced by apparent targets on the RDAs and each reference phase vector. The reference vector yielding the highest correlation identifies the azimuth and elevation angle of the target. Mathematically: The elements of the reference vector are given by $V_r(i,m,n) = exp[j\varphi_i(m,n)]$, where m and n index a grid defined by α_m and ε_n over which the target angle is searched. The measurement vector for a target of interest is given as $V_t(i) = exp(j\varphi_{ti})$, where φ_{ti} is the measured target phase extracted from the RDA. The target azimuth and elevation angles are then determined as the $(\alpha_m, \varepsilon_n)$ grid point that maximizes the correlation given by

$$\rho_{m,n} = \frac{1}{8}\left[\sum_i V_r^*(i,m,n)V_t(i)\right]$$

Note that this approach does not require beamforming in the usual sense, since no use is made of weighted sums of the receiver outputs.

6. Examples

In September 1997 the STHFR measured the radar signatures of modified 10-m-long two-stage sounding rockets launched from the northwest coast of Australia. The radar was installed at a point 47 km from the launch point; the site was very flat and free of any nearby man-made structures. The sounding rockets attained an apogee of 180 km and impacted 120 km downrange. The sounding rockets used a Terrier booster and an Orion second stage. Four such rockets were launched.

We observed the target over a time span from 6 s after liftoff to 60 s after liftoff. Figure 4 is an example of a RDA formed at a point when the target was at an elevation angle of 12 deg, an azimuth of 62 deg, a range of 48 km, and line-of-sight velocity of 119 m/s. To assess digital beamforming ability,

150

beamformed RDAs (Step 5 of Section 3) were computed as described in Section 4 as the commanded mainbeam direction was "scanned" in azimuth past the Orion target, with the beam elevation angle fixed at 12 deg. The value of the Orion target peak occurring at a (range,Doppler) of (48 km,119 m/s) was then plotted as a function of the azimuth angle, resulting in Figure 5. The procedure is similar to plotting the response as the antenna of a microwave radar is physically scanned in angle past a fixed point target. Figure 5 shows a well formed beam with a beam-forming gain of 10.5 dB, which is in good agreement with a calculated value of 11 dB. A theoretical curve calculated from the array geometry shows good agreement with the experimental results.

In Figure 6 we show an example of the target azimuth and elevation angle determination using the correlation technique of Section 5. The large excursions near the end of the measurement interval are the result of a low SNR. The high correlation values observed (Fig 6c) are indicative of a nearly distortion-free wavefront. The raw azimuth rms error is 4.7 deg and the smoothed error is 0.9 deg. The errors in target elevation are larger than in azimuth because the aperture is much smaller in the elevation plane.

7. Conclusions

We have described digital beamforming in a compact HF radar. The beamforming coefficients were generated solely from the geometry of the array without any explicit far-field calibration sources. We achieved very good beamforming because of the flat, clean, and uncluttered site available in these measurements. We have also presented a correlation technique for determining the target azimuth and elevation angles, and demonstrated very good accuracy. This technique also relied on phase values derived only from the array geometry. We do not expect radar sites with nearby scattering structures such as buildings and towers to yield as high a level of performance.
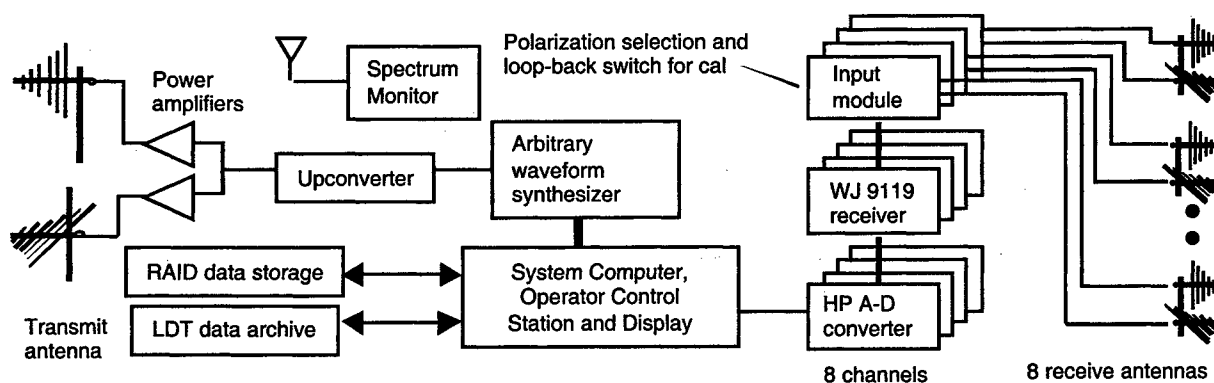
Figure 1. Block Diagram of STHFR
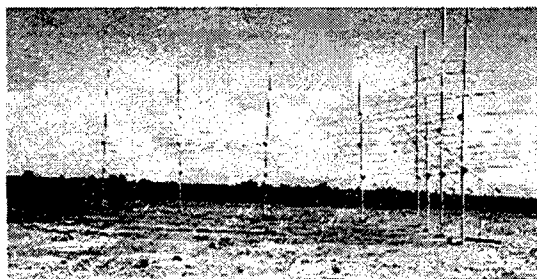
Figure 2. STHFR Receiving Array
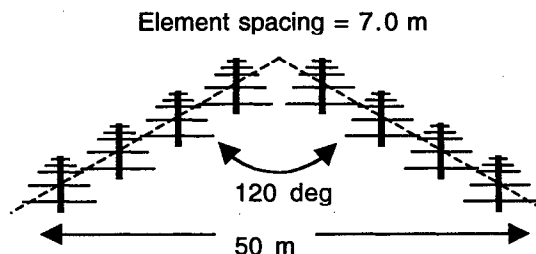
Figure 3. Receiving Array Layout

151
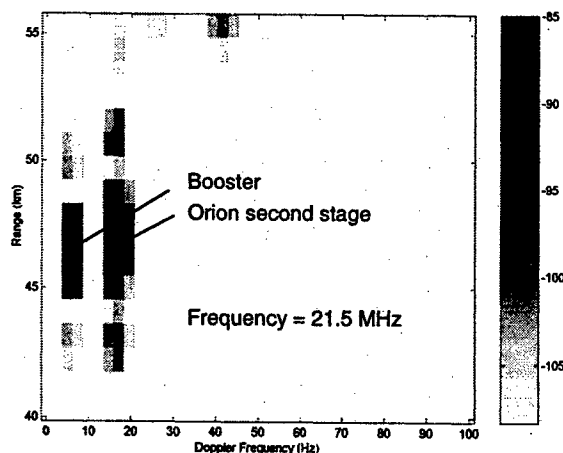
Figure 4. Range-Doppler array 17.5 sec after launch. The booster and Orion second stage have separated. Both targets show sidelobes in the range dimension. Intensity scale in dBm.
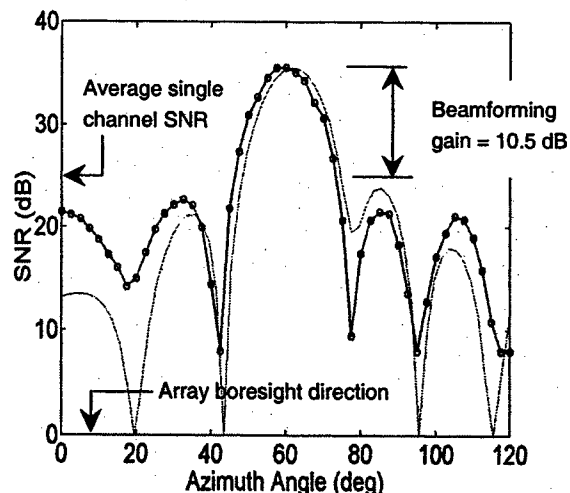
Figure 5. Beam formed in the azimuth plane by digitally "scanning" the beam pointing angle past the Orion rocket at TALO = 17.5 s (curve with points). Theoretical curve (curve without points). Experimental curve is displayed in dB above noise threshold of -114 dBm.
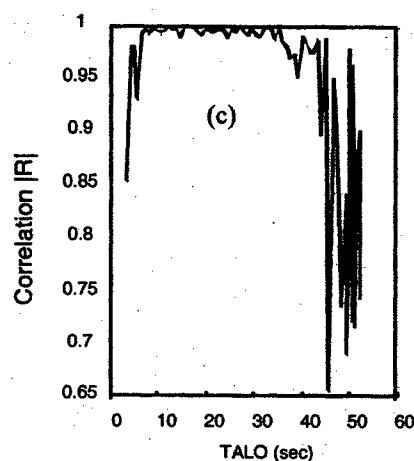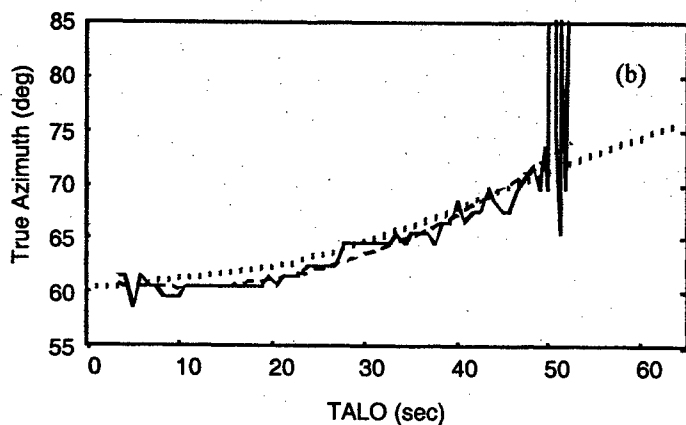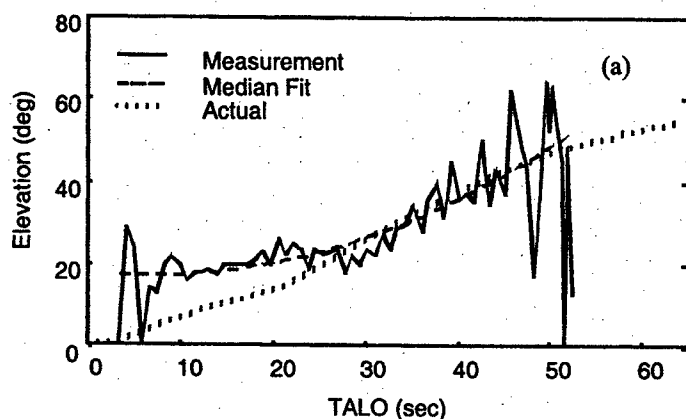
Figure 6. Azimuth and elevation angles as determined by STHFR for Mission Three. (a) Elevation angle; (b) Azimuth angle; (c) Maximum correlation between Orion measurement phase vector and reference phase vector.

A GPS Digital Phased Array Antenna and Receiver

Dr. Alison Brown, Randy Silva; *NAVSYS Corporation*

ABSTRACT

NAVSYS High Gain Advanced GPS Receiver (HAGR) uses a digital beam-steering antenna array to enable up to eight GPS satellites to be tracked, each with up to 10 dBi of additional antenna gain over a conventional receiver solution. This digital, PC-based architecture provides a cost-effective solution for commercial applications where more precise GPS measurements are needed.

The additional gain provided on the satellite signals by the HAGR enables sub-meter pseudo-ranges to be observed directly on the C/A code and also improves the accuracy of the GPS carrier phase observations. The directivity of the digital beams created from the antenna array also reduces multipath errors, further improving the accuracy of DGPS corrections generated by the HAGR and the navigation and timing solution computed. This paper describes the beam steering array and digital receiver architecture and includes test data showing the HAGR performance.

HIGH GAIN ADVANCED GPS RECEIVER DESIGN

The HAGR design is based on NAVSYS' Advanced GPS Receiver (AGR) PC-based digital receiver architecture[1] integrated with a digital beam steering array. Using a proprietary digital beam steering (DBS) board NAVSYS is able to combine data from as many as 16 antennas and create a multi-beam antenna pattern to apply gain to up to eight GPS satellites simultaneously.[2]

The HAGR phased array antenna is shown in Figure 1 and the HAGR electronics includes the components shown in Figure 2. The multi-element antenna array is assembled using commercial antenna elements. The antenna outputs are fed to a Digital Front End (DFE) assembly that includes a custom RF-board that digitizes each of the received L1 signals. The digital output from the DFE assembly is then passed to a custom Digital Beam Steering (DBS) board installed in the AGR Personal Computer that performs the digital signal processing required to implement the digital beam steering operations. The AGR PC also includes a custom Correlator Accelerator card (CAC) that performs the C/A code correlation and carrier mixing on each satellite channel.

Depending on the level of performance desired, the antenna array and DFE assembly can be populated with two, four, nine or sixteen antenna elements. The antenna elements are spaced ½ wavelength apart. The Digital Beam Steering board is operated through software control from the AGR PC. This applies the array spatial signal processing algorithms to form the digital antenna array pattern from the multiple antenna inputs, adjusts the antenna array pattern to track the satellites as they move across the sky, and applies calibration corrections to adjust for offsets between the individual antenna and DFE channels and alignment errors in the positioning of the antenna elements and array assembly.

The GPS signal processing is performed by the HAGR Correlator Accelerator Card (CAC) also operated under software control from the PC. This performs the code and carrier tracking on each satellite signal. The HAGR PC-based software computes the navigation solution using the satellite data and can also be configured to record raw measurement data or generate differential GPS (DGPS) or kinematic GPS (KGPS) corrections.

ANTENNA ARRAY BEAM PATTERNS

The beam pattern created by the digital antenna array is a function of the number of elements used in the array and the elevation angle of each satellite being tracked. In Figure 3, simulated beam patterns are shown for the different HAGR antenna configurations.

HAGR SIGNAL-TO-NOISE RATIO COMPARISON TESTING

The HAGR digital beam forming has the effect of increasing the signal-to-noise ratio from the GPS satellites. In Figure 4 to Figure 6, performance data is shown from a HAGR unit compared against two conventional GPS reference receivers[3]. From these plots, it can be seen that the HAGR C/N_0 is significantly higher than the reference receiver, demonstrating the effect of the gain from the digital beam forming.

HAGR PSEUDO-RANGE NOISE

The HAGR pseudo-range measurement accuracy was demonstrated by plotting the difference between the pseudo-range and the contiguous carrier phase observations. This difference is a function of the pseudo-range measurement noise, the carrier-phase noise (a minimal effect) and the code/carrier divergence caused by the ionosphere (which is constant over short time intervals). This data is plotted in Figure 7 through Figure 9 and shows that the pseudo-range variance is between 0.6 to 1 meter for the underlined <u>unfiltered</u> HAGR data. It should be noted that with carrier smoothing, this variance is reduced even further. The observed pseudo-range noise compares closely with that predicted by the improved C/No. For example, at a C/No of 54 dB-Hz, theory predicts a pseudo-range variance of 0.4 meters. Our data shows an observed variance of 0.5 meters for the same C/No.

KINEMATIC GPS TEST RESULTS

The kinematic performance of the HAGR antennas was tested by setting each of the antennas on two survey marks separated about 1.5 meter apart. The NAVSYS's kinematic GPS software was used to process the data. A 10 degree elevation mask angle was selected. Figure 10 shows the processing results. During the test, 6 valid satellites were available. These test results show that the kinematic GPS positioning error achieved a standard deviation of 3 mm (1-sigma) in the north and east directions and 7 mm (1-sigma) vertically. This is consistent with a carrier phase measurement accuracy of 3 mm (1-sigma). This shows that the multipath errors on the carrier phase are maintained on the order of a few millimeters by the HAGR beam forming.

CONCLUSION

In this paper, the design, performance and test results of the NAVSYS High Gain Advanced GPS Receiver (HAGR) have been presented. The benefits of the HAGR for the following applications are summarized below.

<u>Differential Reference Station</u>
The gain applied to the GPS signals by the antenna array improves the signal strength observed in the tracking loops by up to 10 dBi (for the 16-element array option). This will improve the pseudo-range residual noise from the HAGR's delay lock loops by a factor of 3. The improved pseudo-range accuracy results in higher precision in differential corrections generated by this reference receiver. The variance on unfiltered 1-Hz pseudo ranges collected into the HAGR was shown to be between 0.5 and 1 meters.

<u>Multipath Rejection</u>
The antenna array digital signal processing algorithms applied by the programmable Digital Beam Steering (DBS) PC-board. This attenuates any multipath signals received while applying gain to the direct path GPS satellite signals. The combination of these effects is to significantly reduce the residual multipath error in the AGR's delay lock loops and pseudo-range and comer phase observations.

154

Interference Rejection

The antenna array digital signal processing algorithms applied by the programmable DBS-board can be programmed to apply nulls as well as generate gain through forming beams. By placing nulls on interfering signals, the DBS-board can also be used to reject interference sources or signals from GPS jammers.

Kinematic GPS

The high-accuracy pseudo-range and carrier phase observations provided by the HAGR allow it to provide kinematic positioning accuracies of better than 1 cm.

ACKNOWLEDGEMENT

[1] E. Holm, A. Brown, R. Slosky "A Modular Reprogrammable Digital Receiver Architecture," ION 54th Annual Meeting, Denver, CO, June 1998

[2] A. Brown, R. Silva, G. Zhang, "Test Results of a High Gain Advance GPS Receiver," ION 55th Annual Meeting, Cambridge, MA, June 1999.

[3] A. Brown, J. Wang, "High Accuracy kinematic GPS Performance Using a Digital Beam-Steering Array," ION GPS '99, Nashville, TN, Sept. 1999.
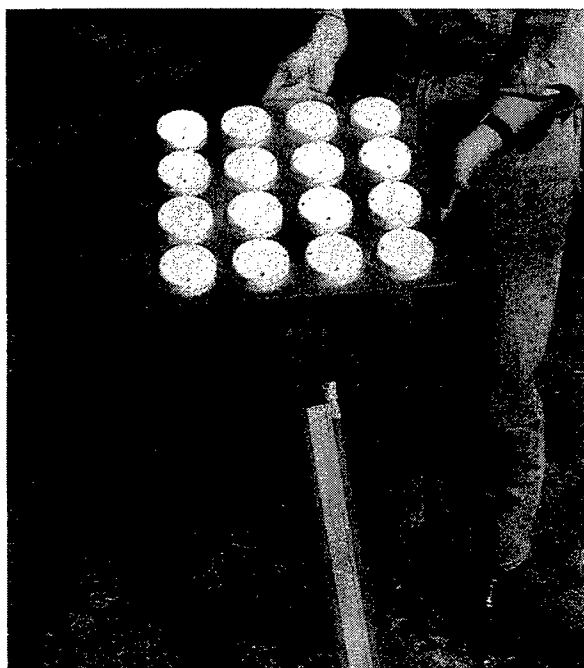
Figure 1 HAGR 16 element antenna array
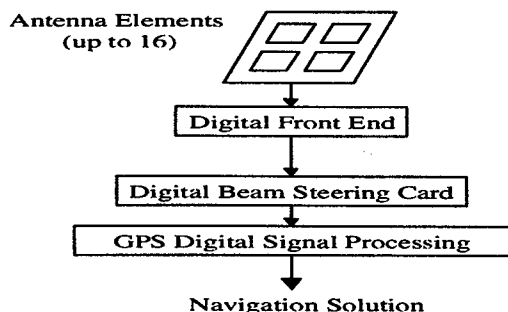
Figure 2 High Gain Advanced GPS Receiver Design
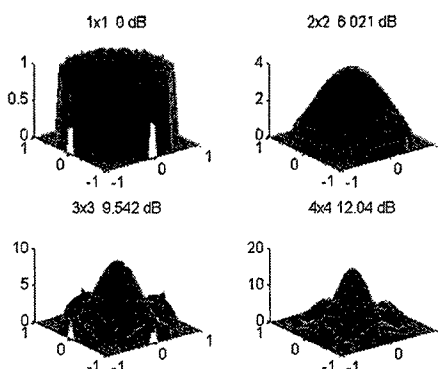
Figure 3 Typical antenna beam patterns
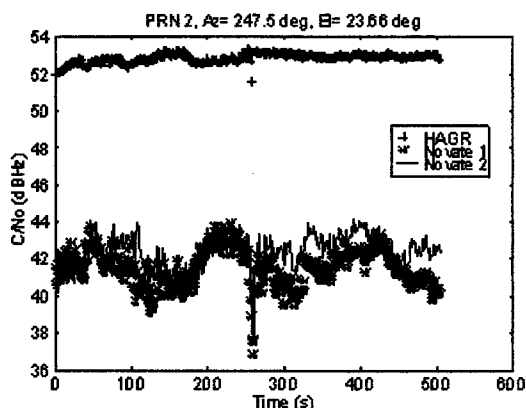
Figure 4 SNR Comparison Between 16-Antenna HAGR and Reference Receiver for PRN 2
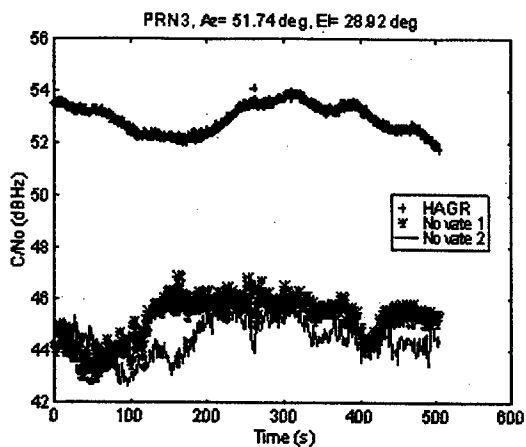
Figure 5 SNR Comparison Between 16-Antenna HAGR and Reference Receiver for PRN 3
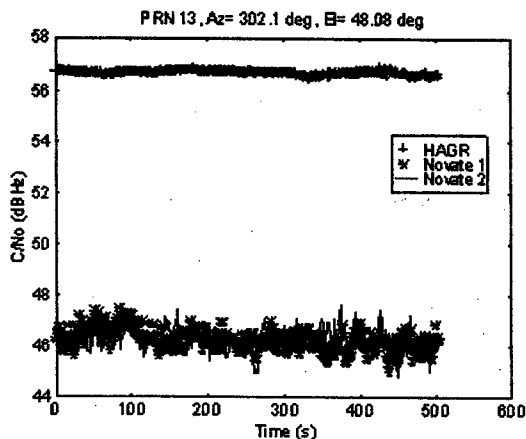
Figure 6 SNR Comparison Between 16-Antenna HAGR and Reference Receiver for PRN 13
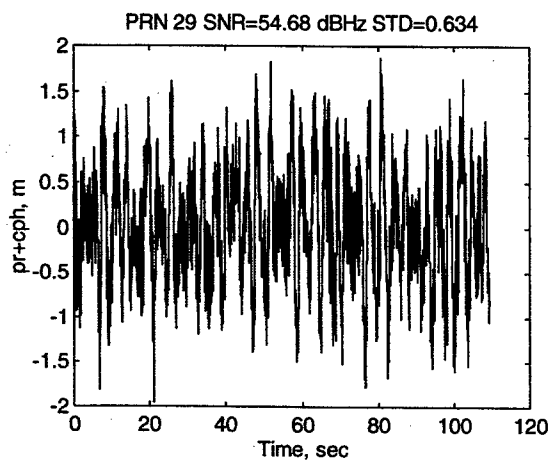
Figure 7 HAGR Difference between Pseudo-Range and Carrier Phase for PRN 29
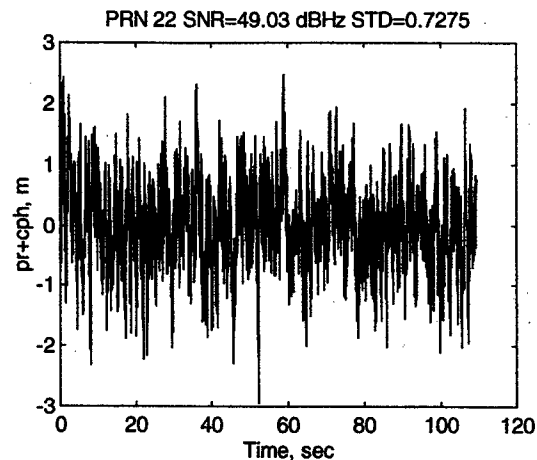
Figure 8 HAGR Difference between Pseudo-Range and Carrier Phase for PRN 22
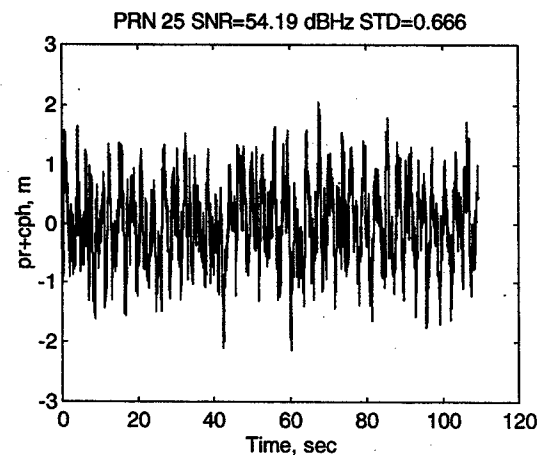
Figure 9 HAGR Difference between Pseudo-Range and Carrier Phase for PRN 25
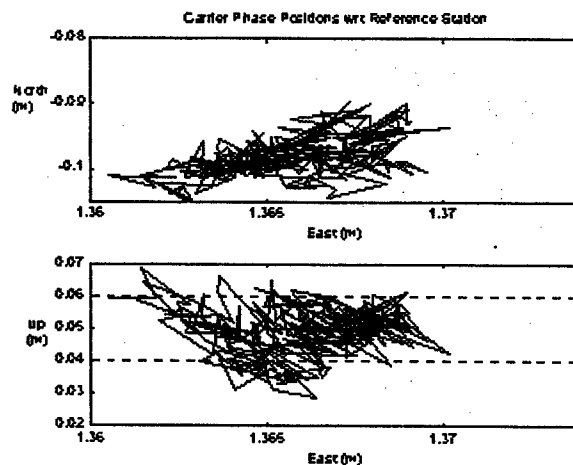
Figure 10 KGPS positioning error

A novel approach for the mitigation of the effects of the RFI on radiotelescopes

N. Fourikis
Phased Array Systems
3 / 48 Adelaide Tce
ASCOT PARK   SA 5043
AUSTRALIA
fourikis@camtech.net.au

Abstract: For single dish radiotelescopes the proposed approach for the mitigation of the radio frequency interference, RFI problem calls for the illumination of the reflector antenna by a monopulse feed and the Dicke-switching of the input of its radiometer between the sum and difference ports. The same approach can be used for array-based radiotelescopes.

1   INTRODUCTION

The outputs of single dish radiotelescopes are affected by tropospheric noise when operation above 3 GHz is required and some approaches that mitigate the effects of tropospheric noise on radiometers are outlined in reference [1]. The approaches call for the Dicke-switching of the input of the telescope's radiometer between the main and a reference beam. The celestial source under observation is placed in the main beam of the telescope while the reference beam is slightly offset from it. With these approaches the effects of tropospheric noise on the radiometer's output are minimized to a degree that depends on the proximity of the two beams in the spatial domain.

Existing phased array-based radiotelescopes have excellent spatial resolutions but their sensitivity is only adequate because the arrays are highly thinned. Their other defining characteristics are:
- One narrow field of view, FOV is observed at a time.
- Minimum redundancy arrays are used
- Dual-polarization capability; and
- One narrow frequency band is observed at a time.

The essential requirements for future array radiotelescopes under consideration are [2-4]:
- High sensitivity and moderate spatial resolution. More explicitly, the required sensitivity is equal to that attained by a radiotelescope fully populating an area of one hectare or one square kilometer.
- The availability of one or more wide fields of view simultaneously.
- Inexpensive realizations are preferred; and
- Operation at many frequency bands simultaneously.

The last requirement not only minimizes the observation time required to attain maps of celestial sources at many frequency bands but also meets the requirement for observations of variable sources at many frequency bands simultaneously. Lastly, the same radiotelescopes are also suitable for searches of extra terrestrial intelligence, SETI.

All types of radiotelescopes receiving weak signals emanated by distant celestial radio sources are affected by unwanted transmissions that are either Earth-bound or satellite borne.

The strong Earth-bound transmissions originate from broadcast stations, communication and radar systems while the latter transmissions originate from medium / low Earth orbiting constellations of satellites designated to perform the navigation / communication functions. As the approaches to mitigate the effects of RFI caused by Earth-bound transmitters are considered in many references, we shall focus attention on the mitigation of the RFI caused by constellations of Earth-orbiting constellations of satellites.

2   THE RFI PROBLEM

The current constellations of Earth-orbiting satellites cover the Earth's surface comprehensively. In Table 1 we listed some of the essential characteristics of existing / future navigation and communications constellations of satellites drawn from references [5, 6]. As can be seen there are several systems in the planning stage and their frequency of operation can be as high as 40 GHz. As several satellites are 'visible' from any location on Earth we require the excision of the interfering signals when the positions and number of satellites in view from a particular location vary with time.

Table 1 – Essential characteristics of existing / future navigation and communication constellations of satellites.

System	Up Link Frequency [GHz]	Down Link Frequency [GHz]	Cross link Frequency [GHz]	Capacity
GPS		1.237, 1.575 ±0.020		Navigation system
Odyssey	1.6, 29	2.5, 19		3,000-9,500 voice channels
ICO	2.2, 5	2.0, 7		4,500 voice channels
Globalstar	1.6, 5	2.5, 7		2,000-3,000 voice channels
Iridium	1.6, 28	1.6, 19	23	1,100 voice channels
Teledesic	Ka[1]	Ka[1]	60	100,000 voice channels

[1] 27-40 GHz

In an experimental 8-element array the rejection of interfering signals in the spatial domain with the aid of nulls generated in the direction of interfering signals can yield up to 37 dB rejection [7]. Furthermore, no a priori knowledge of the number of interferers or their position is required by the adaptive minimum variance beamformer used. For the same array, a non-adaptive Fourier beamformer rejects interference only in the sidelobes by between 13 and 30 dB depending on the location of the interference within the array's sidelobes.

A real-time adaptive interference cancellation technique has also been used to mitigate the effects of RFI on a prototype receiver [8]. In the presence one interferer, a main channel containing the required signal and that of the interferer is used in conjunction with a reference channel that contains the interfering signal only. The reference channel input is processed using a digital adaptive filter and then subtracted from the primary channel input producing the system output. An attenuation of strong frequency modulated interference to 72 dB has been measured by the experimental setup. In an

environment where M interferers exist, the approach calls for M reference channels that are used in conjunction with the main channel to cancel the interfering signals.

3 A NOVEL APPROACH

For single dish radiotelescopes we propose the illumination of the antenna reflector by a monopulse feed that yields the sum and difference beams. Ideally the sum / difference beams are defined by Gaussian / Rayleigh functions respectively and working monopulse feeds yield beams that have shapes approximating these functions. Monopulse feeds are commonly used for satellite communications / radar applications and descriptions of these feeds are found in reference [9]. Monopulse feeds are used in satellite communications applications to ensure the alignment between the satellite and ground station antennas; the same types of feeds are used in radar applications to measure the angle of arrival of signals transmitted by targets on a monopulse basis.

The celestial source is placed at the maximum of the sum beam, which coincides with the minimum of the difference beam, and the input of the radiometer is Dicke-switched between the sum and difference beams. With this arrangement, the output of the radiometer is the difference between the two beams and the radiotelescope gains immunity from tropospheric noise and unintentional jammers, the transmitters of the Earth-orbiting constellations of satellites. Furthermore, knowledge of the number of transmitters in view from the radiotelescope site or their position is not required.
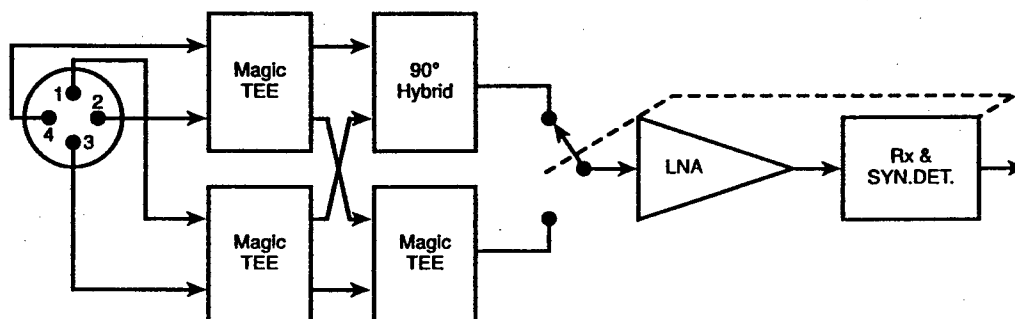
Figure 1   A block diagram illustrating the generation of sum and difference beams from a frequency independent four-arm spiral antenna. The input of the radiometer of the telescope is Dicke-switched between the sum and difference beams.

While the above proposal is suitable for narrow band applications, the arrangement shown in figure 1 is suitable for wideband applications. The antenna element used to illuminate the reflector is a four-arm frequency independent spiral antenna and the sum and difference patterns are derived with the aid of the signal processing shown in the same figure. Lastly, the input of the radiometer is again Dicke-switched between the sum and difference beams.

Phased array-based radiotelescopes consist of several antennas followed by sensitive receivers operating either in the aperture or image synthesis mode. Radiometric arrays on the other hand operate in the image synthesis mode. If all antennas are illuminated by monopulse beams and the inputs of the receivers are again Dicke-switched between the sum and difference beams, immunity from the RFI is gained. With this approach, knowledge of the number of intrerferers and their positions is not required.

4   DISCUSSION

The proposed approach does not call for one or more separate reference channels but the radiometer's rms minimum detectable signal when compared to that of a total power radiometer is doubled; this is not a high penalty to pay for the mitigation of the RFI. High efficiency monopulse feeds and low-loss Dicke-switching systems have evolved by the satellite / radar and radioastronomy communities respectively over a long period. Developmental risks are therefore minimal for the realization of systems using the proposed approach.

The effectiveness of the cancellation of the RFI depends on how low the antenna sidelobes are and experimental work is required to quantitatively assess its effectiveness.

5   REFERENCES

1   Fourikis N. and Thomas McA. Beam-separation constraints in a beam-switched radio-telescope. Proc IREE (Aust), Vol 35, No 7, 1974, p 199-201.
2   The one hectare telescope (1HT) Project. http://www.usska.org/papers.html
3   The Square Kilometer Array: Astronomy for the Next Millennium. http://www.usska.org/project.html
4   Fourikis N. Novel radiometric phased array systems. Microwave & Optical Tech Letters. June 5, 1998, p 100-108.
5   Greiling P and Ho N. Commercial satellite applications for heterojunction microelectronics technology. IEEE Trans Microw Theory Techn. Vol 46, No 6, June 1998, p 734-7.
6   Pozar D M and Duffy S M. A dual-band circularly polarized aperture-coupled stacked microstrip antenna for global positioning satellite. IEEE Trans Antennas Prop., Vol 45, No 11 Nov 1997, p1618-1625.
7   Goris M., Joseph A., Hampson G. and Smits F. Adaptive beamforming system for radio-frequency interference rejection. IEE Proc.-Radar, Sonar Navig., Vol 146, No 2, April 1999, p 73-77.
8   Barnbaum C. and Bradley R F. A new approach to interference excision in radio astronomy: Real-time adaptive cancellation. The Astronom. J. Vol 115, Nov 1998, p 2598-2614.
9   Love A W Edit. *Electromagnetic horn antennas.* IEEE Press, 1976.

MP3

Direction Finding

Direction Finding

RF Direction Finding with a Reduced Number of Receivers by Sequential Sampling

Josef G. Worms
FGAN-FHR
Neuenahrerstrasse 20
D-53343 Wachtberg-Werthhoven, West Germany
Tel.: +49 228 9435 216   Fax: +49 228 9435 627   Email: worms@fgan.de

INTRODUCTION:

In this paper we consider the RF direction finding of arriving narrowband sources by a passive sensor array. Modern superresolution methods e.g. projection based methods, like the MUSIC method, the Capon method or Maximum Likelihood based methods require the same number of receiver channels as antenna elements. In contrast to the Maximum Likelihood methods the MUSIC and Capon method have less numerical load at the cost of a reduction in resolution. Expensive receivers and the need of their calibration make superresolution methods unattractive for RF direction finding with array antennas.

A solution with less receivers is the introduction of subarrays (comp. Nickel [1]). Considering the subarrays as so called 'superelements', all known superresolution methods can be applied to the subarray output signals. Another proposal, very attractive with respect to receiver cost, is a preprocessing beamforming network. The network can be realized by a Butler- or Blas-matrix. Considering the received signals of the different output channels of the network as element signals, the superresolution methods can be applied to a restricted number of output channels corresponding to the directions of the received signals (comp. Buckley [2]). A reduction of the receiver channels by building subarrays or using a restricted number of output channels of a beamformer network implies a "sequential scanning" of the angular space.

This paper aims at the use of superresolution methods with a reduced number of receivers by sequential sampling of the antenna elements, the subarray channels or the output signals of a preprocessing beamforming network in time.

Sequential sampling of subarrays or preprocessing networks were discussed by Sheinvald and Wax in [3] and [4]. Sheinvald and Wax derived an estimator based on the corresponding 'Maximum Likelihood' problem (ML). Based on their work in this paper the Capon and MUSIC method are modified for sequential sampling. The resulting new 'Sequential-MUSIC' (S-MUSIC) respectively 'Sequential-Capon' method (S-Capon) build approximations of the conventional MUSIC and Capon methods, where all element channels are processed. The resolution properties of the proposed methods are superior to the conventional MUSIC or Capon method with a number of element antennas restricted to the number of receivers.

ASSUMPTIONS

In our investigations we assume that the number of received signals n_s is smaller than the number of receivers n_{sub}. The received signals are normal distributed. We assume that during the whole sampling period the emitter directions and their signal power do not change. The antenna array consists of n_a antenna elements, where $n_a = n_1 \cdot (n_{sub}-1)+1$, $n_1 \in \mathbb{N}$. Building n_1 subarrays of $(n_{sub}-1)$ antenna elements and taking the remaining element as part of all subarrays, at a given time t only the signals of one subarray can be received (comp. figure 1). The received signals of subarray k are given by

$$\underline{X}_k(t) = \sum_{l=1}^{n_s} \underline{S}_k(\theta_l) \cdot c_{kl}(t) + \underline{n}_k(t)$$

$$:= \underline{\underline{S}}_k(\underline{\theta}) \cdot \underline{c}_k(t) + \underline{n}_k(t)$$

(1)

where $\underline{S}_k(\theta_l)$; $1 \le l \le n_s$; is the DOA vector and $c_l(t)$ of the l'th received signal arriving from direction θ_l. The thermal noise of the element channels of the k'th subarray is given by $\underline{n}_k(t)$. Taking sequential sampling into account and starting the measurement at t_0, we obtain the sampling points of the k'th subarray

$$ t_o + m \cdot \Delta_t \cdot n_1 + (k-1) \cdot \Delta_t \qquad (2) $$

with $m \in \mathbb{N}$ and $1 \le k \le n_1$.
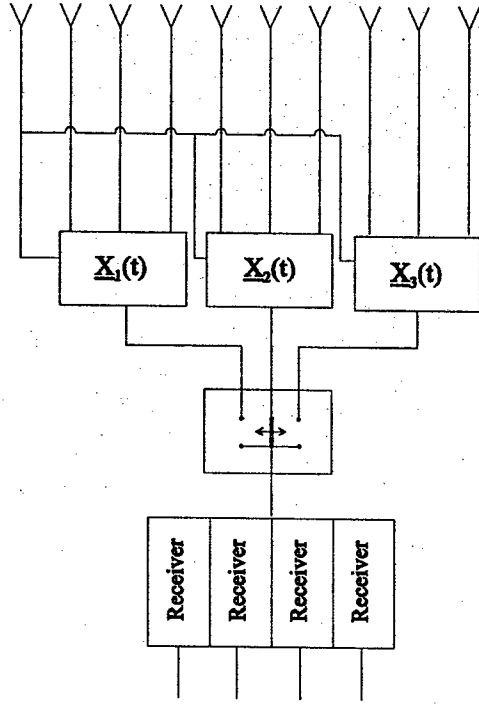
Figure 1: Sketch of Sequential Sampling of an Array Antenna

MAXIMUM LIKELIHOOD ESTIMATOR (MLE) AND THE MUSIC ALGORITHM

Similar to [5] in the sequential sampling case 'deterministic' and 'stochastic' 'Maximum Likelihood Estimators' (MLE) can be derived. While the 'stochastic' MLE was discussed in [4], in this paper we restrict us to the 'deterministic' MLE. Maximizing the probability density function of the received signals, given by

$$ P(\underline{X}_1,....,\underline{X}_{n_1} / \underline{\theta}, \underline{c}_1,....,\underline{c}_{n_1}) = $$

$$ \prod_{k=1}^{n_1} N(k,n,n_{sub},\sigma) \cdot $$

$$ \exp\left\{ \frac{-1}{\sigma^2} \sum_{m=1}^{n} \left| \underline{X}_k(t_0 + m \cdot \Delta_t \cdot n_1 + (k-1) \cdot \Delta_t) - \underline{\underline{S}}(\theta) \cdot \underline{c}_k \right|^2 \right\} $$

$$ (3) $$

with respect to the parameter vectors θ, $\underline{c}_1$, ..., $\underline{c}_{n1}$, we obtain after a maximization of the amplitude vectors $\underline{c}_i$ the optimization task

$$ \min_{\underline{\theta}} \left\{ trace\left(\sum_{k=1}^{n_1} \left[\underline{\underline{I}} - \underline{\underline{S}}_k(\theta) \left(\underline{\underline{S}}_k(\theta)^* \underline{\underline{S}}_k(\theta) \right)^{-1} \underline{\underline{S}}_k(\theta)^* \right] \underline{\underline{Q}}_{k,n} \right) \right\} $$

$$ (4) $$

where $N(k,n,n_{sub},\sigma)$ is a normalization factor and the covariance matrix $\underline{\underline{Q}}_{k,n}$ is given by

$$ \underline{\underline{Q}}_{k,n} = \frac{1}{n} \sum_{m=1}^{n} \underline{X}_k(t_0 + m \cdot \Delta_t \cdot n_1 + (k-1) \cdot \Delta_t) \cdot \underline{X}_k(t_0 + m \cdot \Delta_t \cdot n_1 + (k-1) \cdot \Delta_t)^* \qquad (5) $$

Equation (4) and (5) yield the 'deterministic' MLE of the angles of arrival of the received signals. In contrast to the multidimensional search methods (e.g. (4)), the MUSIC and Capon method as well as 'conventional' beamforming methods belong to the class of onedimensional search methods (comp. Viberg [5]), which can be derived as follows. Assuming that only one signal is received equation (4) can be written as

$$ \max_{\theta} \left\{ \sum_{k=1}^{n_1} \frac{\underline{S}_k(\theta)^* \cdot \underline{\underline{Q}}_{k,n} \cdot \underline{S}_k(\theta)}{\underline{S}_k(\theta)^* \cdot \underline{S}_k(\theta)} \right\} \qquad (6) $$

If we assume now that all antenna elements (resp. subarray outputs) receive the arriving signal in the mean with the same power, the optimization task (6) can be approximated by

$$\max_{\theta}\left\{\sum_{k=1}^{n_1}\frac{\underline{S}_k(\theta)^*\,\underline{p}_{k,1}\cdot\underline{p}_{k,1}^*\cdot\underline{S}_k(\theta)}{\underline{S}_k(\theta)^*\cdot\underline{S}_k(\theta)}\right\}=\min_{\theta}\left\{\sum_{k=1}^{n_1}\frac{\underline{S}_k(\theta)^*\cdot(\underline{\underline{I}}-\underline{p}_{k,1}\cdot\underline{p}_{k,1}^*)\cdot\underline{S}_k(\theta)}{\underline{S}_k(\theta)^*\cdot\underline{S}_k(\theta)}\right\}$$

$$=\max_{\theta}\frac{1}{\left\{\sum_{k=1}^{n_1}\dfrac{\underline{S}_k(\theta)^*\cdot(\underline{\underline{I}}-\underline{p}_{k,1}\cdot\underline{p}_{k,1}^*)\cdot\underline{S}_k(\theta)}{\underline{S}_k(\theta)^*\cdot\underline{S}_k(\theta)}\right\}} \tag{7}$$

where $\underline{p}_{k,1}$ is the eigenvector of the covariance matrix $\underline{Q}_{k,n}$ belonging to the maximal eigenvalue. We define a spatial spectrum via

$$fs(\theta)=\frac{1}{\displaystyle\sum_{k=1}^{n_1}\frac{\underline{S}_k(\theta)^*\cdot(\underline{\underline{I}}-\underline{p}_{k,1}\underline{p}_{k,1}^*)\cdot\underline{S}_k(\theta)}{\underline{S}_k(\theta)^*\cdot\underline{S}_k(\theta)}} \tag{8}$$

If more than one signal is received by the array antenna, we obtain the wanted S-MUSIC spectrum with equation (8) by

$$S-MUSIC(\theta)=\frac{1}{\displaystyle\sum_{k=1}^{n_1}\frac{\underline{S}_k(\theta)^*\cdot(\underline{\underline{I}}-\underline{\underline{P}}_k)\cdot\underline{S}_k(\theta)}{\underline{S}_k(\theta)^*\cdot\underline{S}_k(\theta)}} \tag{9}$$

where the matrix $\underline{\underline{P}}_k$ is a projection on the so called signal space. The projection matrix $\underline{\underline{P}}_k$ can be built by the eigenvectors belonging to the n_s most significant eigenvalues of the matrix $\underline{Q}_{k,n}$. Since

$$\underline{\underline{I}}-\underline{\underline{P}}_k\approx\underline{\underline{Q}}_{k,n}^{-1} \tag{10}$$

we obtain the S-Capon-spectrum by (9) and (10)

$$S-Capon(\theta)=\frac{1}{\displaystyle\sum_{k=1}^{n_1}\frac{\underline{S}_k(\theta)^*\cdot\underline{\underline{Q}}_{k,n}^{-1}\cdot\underline{S}_k(\theta)}{\underline{S}_k(\theta)^*\cdot\underline{S}_k(\theta)}} \tag{11}$$

SIMULATION RESULTS

In order to check the resolution properties of the S-MUSIC and S-Capon method, computer simulations were conducted. In our simulations we consider a uniform linear array antenna (ULA) consisting of 10 antenna elements. The distance between neighboring antenna elements was 0.8λ. The number of receivers was restricted to 4, i.e. the signals of 3 subarrays had to be sampled sequentially. In the experiments, proposed here, two signals arriving from 10° and 15° with a signal-to-noise ratio (SNR) of 30 dB, related to a single antenna element, were investigated. First 256 time sample vectors were used to estimate the covariance matrices of each of the subarrays. In figure 2a the MUSIC spectra of a 4 element ULA, i.e. the MUSIC spectrum of the first subarray, the conventional MUSIC spectrum of the considered 10 element ULA, i.e. 10 receivers, 256 time sample vectors to estimate the covariance matrix, and the S-MUSIC spectrum are compared. The MUSIC spectrum of the 4 element ULA has less resolution and higher spectral values compared to the other spectra. The resolution properties of the S-MUSIC method are nearly the same as those of the MUSIC spectrum obtained with the 10 element array antenna. Similar results are obtained with respect to the Capon and S-Capon method. In figure 2b the number of time sample vectors was reduced from 256 to 10 time sample vectors.

The maxima of the MUSIC spectra are less than with 256 time sample vectors and the resolution of the MUSIC spectrum of the ULA, consisting of the 4 neighboring antenna elements, is reduced. If the
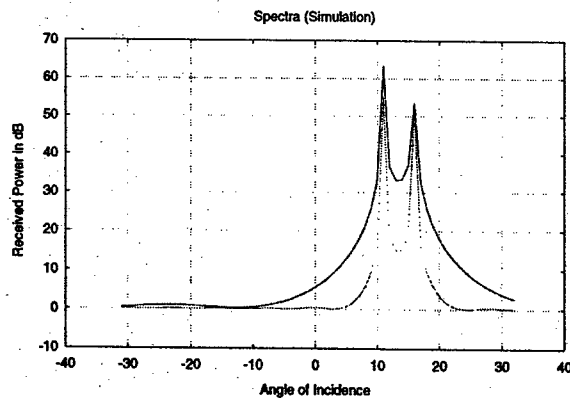
Figure 2a: A comparison of the MUSIC spectra of a 4 element ULA (blue), a 10 element ULA (red) and the S-MUSIC spectrum (green) (256 time samples)
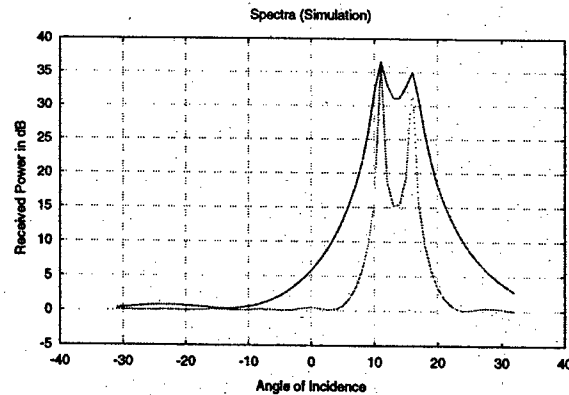
Figure 2b: A comparison of the MUSIC spectra of a 4 element ULA (blue), a 10 element ULA (red) and the S-MUSIC spectrum (green) (10 time samples)

covariance matrices are estimated by only 10 time sample vectors, the Capon spectrum of the 10 element ULA is strongly fluctuating in contrast to the MUSIC spectrum of the 10 element ULA. The S-Capon spectrum obtained with 10 time sample vectors has no fluctuation and is comparable to the spectrum obtained with 256 time sample vectors.

CONCLUSIONS

Because of the high receiver costs superresolution methods applied to array antennas with a smaller number of receivers than antenna elements are very attractive. Thus, in this paper the Capon and MUSIC method are modified to apply them to array antennas with a restricted number of receiver channels. In comparison to the MUSIC or Capon method of an array antenna with the same number of antenna elements as receivers, the proposed configuration conserves the resolution given by the aperture without yielding grating lobes. With a restricted number of receivers the necessary number of time samples to estimate the covariance matrix respectively the S-MUSIC or S-Capon spectra does not correspond to the number of antenna elements but to the number of receivers. A limitation of the proposed methods is given by the stationarity constraint of the received signals during the total sampling period.

REFERENCES

[1] U. Nickel: Aspects of Implementing Superresolution Methods into Phased Array Radar. To appear in AEÜ Int. Journ. of Electronics and Comm., Vol. 53, No. 6, 1999.

[2] K.M. Buckley, X.L. Xu: Recent Advances in High Resolution Spatial-Spectrum Estimation. Proc. of EUSIPCO-90, Barcelona, Spain, Sep. 1990, pp. 17-25.

[3] J. Sheinvald, M. Wax: Detection and Localization of Multiple Signals Using Subarrays Data. in *Advances in Spectrum Analysis and Array Processing* S. Haykin Ed., Englewood Cliffs, NJ: Prentice Hall, 1995. Ch. 7, Vol. 3, pp. 324-351

[4] J. Sheinvald, M. Wax: Direction Finding with Fewer Receivers via Time-Varying Preprocessing. IEEE Trans. on Sig. Proc. Vol. 47, No. 1, Jan. 1999, pp. 2-9

[5] M. Viberg: Subspace Fitting Concepts in Sensor Array Processing. Dissertation No. 217, Linköping, Sweden, 1989

High Resolution DF Architectures Using a
Robust Symmetric Number System Encoding

D.J. Wickersham, P.E. Pace, D. Styer, D.C. Jenn, R. Vitale and N.S. York

Center for Joint Services Electronic Warfare
Department of Electrical and Computer Engineering
Naval Postgraduate School
Monterey, CA 93943, USA
pepace@nps.navy.mil

Abstract: A direction finding architecture that implements an innovative number system encoding of phase samples, the robust symmetric number system (RSNS), is described. The RSNS possesses Gray Code properties and provides significant advantages over conventional phase scanning methods and other symmetric number system encoding techniques. The design equations for a RSNS array are presented. Simulation results for a prototype RSNS array are shown, and its performance compared to previously published results for other number system encoded direction finding architectures.

I. Introduction

Direction finding systems provide an emitter's bearing that can be used as a sorting parameter in the identification of radar and communication systems. The phase sampled linear interferometer is a common DF approach that uses the known spacing between two or more array elements to obtain time-of-arrival measurements [1]. The time-of-arrival measurements can be converted into phase differences that are then used to determine the angle of arrival (AOA).

This paper describes the development of a new type of phase-sampled DF array based on the robust symmetrical number system (RSNS) [2]. The RSNS DF antenna architecture uses the RSNS to decompose the analog spatial filtering operation into a number of parallel sub-operations or moduli that are of smaller complexity. One two-element interferometer is used for each sub-operation and only requires a precision in accordance with its modulus. A much higher spatial resolution is achieved after the spatial filtering results from the individual low-resolution arrays are recombined.

II. RSNS Antenna Architecture

The RSNS DF array is a modular scheme in that the integer values within each modulus (phase sampling comparator states), when considered together, change one at a time between adjacent positions (a Gray code property). Although the dynamic range of the RSNS is somewhat less than that of the optimum SNS (OSNS) [3], the RSNS Gray code properties make it particularly attractive for error control. With RSNS encoding, the errors due to comparator thresholds not being crossed simultaneously are eliminated. As a result, the interpolation circuits can be removed, and only a small number of comparators are required.

Table 1 illustrates a RSNS and compares it to an OSNS for the two moduli case. The shaded cells (bins) are unique combinations of integers, that are mapped into spatial angles over the antenna's field of view (FOV). The entries also correspond to the number of comparators ON in each channel. The DF resolution is the FOV divided by the number of unique combinations (shaded cells). The number of unique combinations is also referred to as the dynamic range. From computer results the dynamic range, $\hat{M}$, for a two-channel system is conjectured to be [2]:

$$\hat{M} = 4m_1 + 2m_2 - 5, \text{ for moduli spaced 1 or 2 apart, and} \qquad (1)$$

$$\hat{M} = 4m_1 + 2m_2 - 2, \text{ for moduli spaced 3 or more apart.} \qquad (2)$$

The dynamic range of the OSNS is the product of the moduli. The dynamic range of the OSNS grows faster than the RSNS dynamic range, so for practical systems (which require dynamic ranges greater than 50), the OSNS can achieve larger values with smaller moduli.

The dynamic range determines the angular resolution of the system and the antenna element spacing. A RSNS array based on N moduli $(m_1, m_2, ..., m_N)$ has $N+1$ array elements. For an array using mixers for phase detection, the spacing between the reference element and element i is

$$d_i = \frac{\hat{M}\lambda}{4Nm_i}. \qquad (3)$$

Table 1: Comparison of Dynamic Range of RSNS and OSNS.

System	Modulus	0	1	2	3	4	5	6	7	8	9	10	11	12	13	14	15	16	17	18	19	20	21
RSNS	m_1=3	0	0	1	1	2	2	3	3	2	2	1	1	0	0	1	1	2	2	3	3	2	2
	m_2=4	0	1	1	2	2	3	3	4	4	3	3	2	2	1	1	0	0	1	1	2	2	3
OSNS	m_1=3	0	1	2	2	1	0	0	1	2	2	1	0	0	1	2	2	1	0	0	1	2	2
	m_2=4	0	1	2	3	3	2	1	0	0	1	2	3	3	2	1	0	0	1	2	3	3	2

Figure 1: RSNS Direction Finding Antenna Architecture.
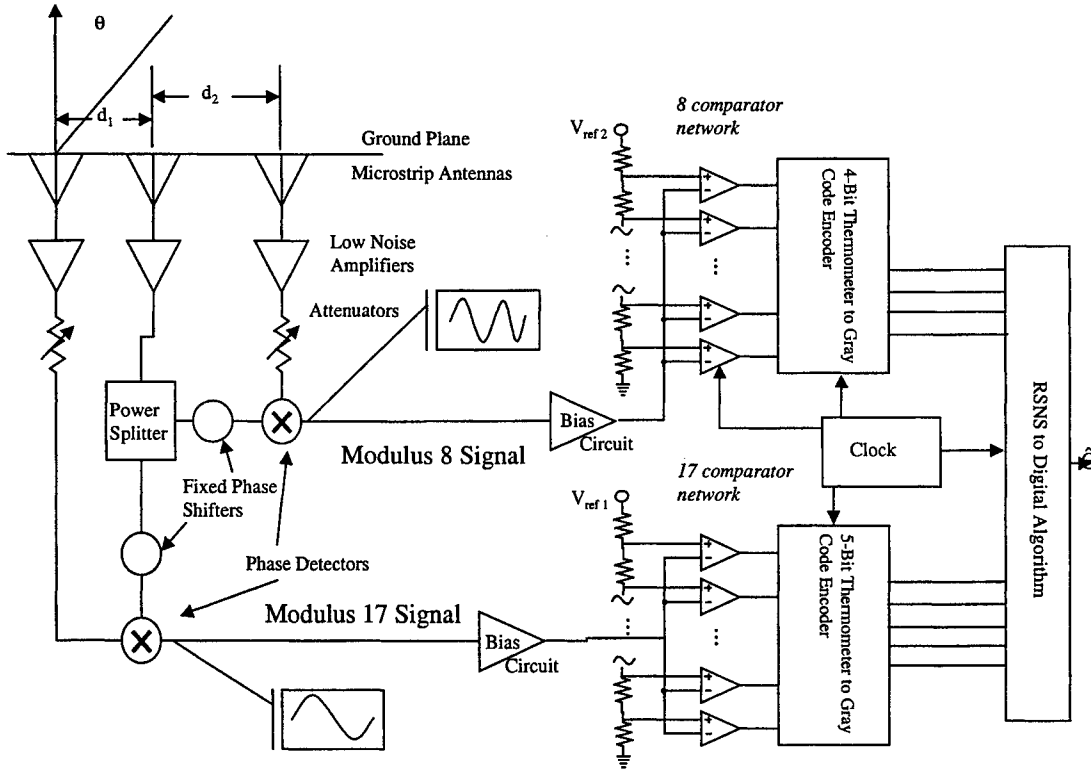
To demonstrate the RSNS antenna, a two channel system was selected with modulus of m_1= 8 and m_2=17. The prototype architecture is shown in Fig. 1. Three receiving elements are used to measure an 8 GHz incident signal. The receiving elements are microstrip dipoles designed for 8 GHz. The spacing between elements is defined by (3). A summary of the system parameters is shown in Table 2 along with

170

those of the OSNS design for comparison. Each channel contains a low noise amplifier and the center element serves as a common element for both interferometers. The phase detector output (PDO) for channel i is a symmetrical folding waveform

$$PDO_i(\theta) = \cos(kd_i \sin\theta + \phi_i) \qquad (4)$$

where ϕ_i is a known phase shift, $k = 2\pi / \lambda$ and θ is the angle of arrival. The separation between interferometer elements, d_1 and d_2, defines the number of folding waveforms within the FOV

$$n_i = \frac{\hat{M}}{2m_i N} = \frac{2d_i}{\lambda}. \qquad (5)$$

System	OSNS	RSNS
Method	Experimental	Simulated
Moduli	6, 11	8, 17
Spacings (inches)	3.82, 2.08	1.18, 0.56
Resolution (ave)	2.02	2.08
RMS error (degrees, 120 degree FOV)	> 25	0.66
Dynamic range (bins)	66	64
Number of comparators	17	25
Frequency band (GHz)	8.2-10	7-8
Number of channels	2	2

Table 2: Prototype Antenna Comparison.
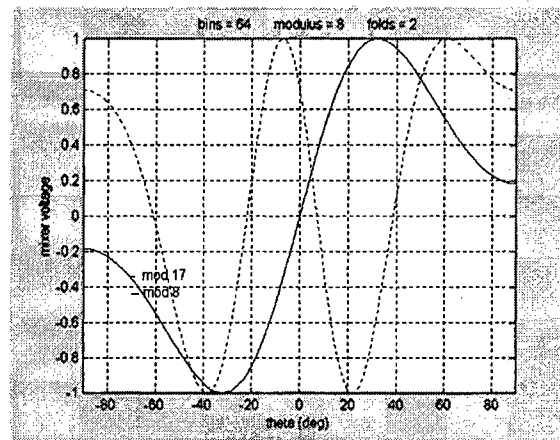
Figure 2: RSNS Folding Waveforms

A simulation of the detected phase (symmetrical folding waveform) is shown in Fig. 2. The $m_1 = 8$ channel has two folds and the $m_2 = 17$ channel has 0.941 folds as shown in the figure. The detected voltage is processed by a dc restoration amplifier to bring the folding waveform above dc so that the comparator threshold levels lie between ground and the bias voltage. The amplifier output is sampled in both channels by a small network of comparators. The normalized value for the 17 threshold levels is $T = \cos(2n - 1/2m_i)$ for $n=1$ to 17. A similar process can determine the threshold levels for the modulus 8 comparators. A channel with modulus m_i has m_i comparators (see Table 1). The number of comparators that are ON in each channel is mapped onto an EEPROM chip that converts the RSNS vector into a bin number that corresponds to a known AOA.

Using the phase waveforms shown in Fig. 2, the transfer function of the RSNS antenna is shown in Fig. 3. As is typical with phase scanned arrays, the $\sin(\theta)$ dependence in (4) causes the folding waveforms to expand as the AOA diverges from broadside. Since the outputs from both channels expand at the same rate, the unique relative relationship between channels is maintained. However, it does increase the bin size resulting in reduced DF resolution for angles near endfire relative to those near broadside, as shown in Fig. 3.

The dynamic range for the prototype system is 64. This dynamic range was chosen to provide a 5-bit output for the angle of arrival. At broadside the bin width is 1.6° and at 60° off broadside, the bin width is 3.4°. More importantly, the RMS reporting error is 0.66° for the FOV of ±60° off broadside and 2.20° over a 180° FOV.

The most significant impact of the Gray Code characteristic of the RSNS is the absence of encoding errors. Fig. 4 shows the experimental results from the OSNS DF antenna [3]. The OSNS does not possess Gray Code properties since multiple comparators are required to change state simultaneously at each code transition, resulting in large errors. The RSNS has the Gray Code property, so only one comparator must change state to transition between bins. If a comparator fails to change state at the correct AOA, the system will report that the signal is in the adjacent bin resulting in a small error.

III. Conclusion

The robust symmetric number system provides a unique and innovative means of mapping directions of arrival in the spatial domain to a digital representation with no encoding errors. There are no theoretical limits on the array baseline or unambiguous AOA resolution. In the absence of noise and system errors, the minimum element spacing and AOA resolution are limited only by the physical size of the array elements and the complexity of the decoding electronics (i.e., number of comparators required).

The RSNS antennas have the potential to perform high resolution DF with very small baselines. The simplicity of the microwave components allows operation over wide bandwidths. The prototype antenna will be capable of a RMS DF error of less than one degree. The system's small weight and size make it an ideal candidate for small unmanned air vehicles.
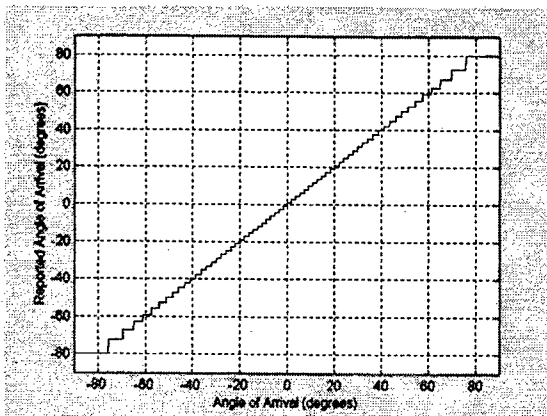
Figure 3: RSNS Transfer Function.
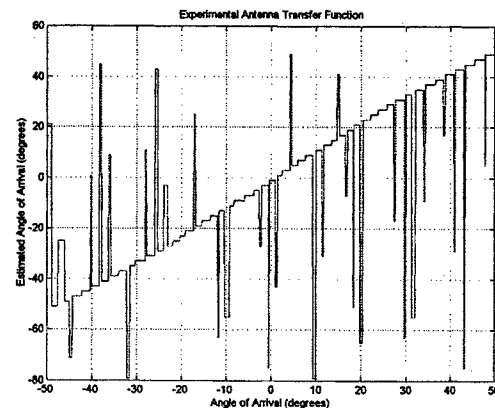
Figure 4: OSNS Transfer Function [3].

IV. References

1. S. Lipsky, *Microwave Passive Direction Finding*, Wiley, 1987.
2. P. Pace, D. Styer, and I. Akin, "A Folding ADC Employing a Robust Symmetrical Number System with Gray Code Properties," ISCAS'98.
3. D. Jenn, P. Pace, T. Hatziathanasiou, "High resolution wideband direction finding arrays based on optimum symmetrical number system encoding," *Electronics Letters*, Vol 34, No. 11, May 28, 1998, pp. 1062-1063.

EFFECTS OF AMPLIFIER NONLINEARITIES ON DOA ESTIMATION

J. Yin, Y. Lu, and B. P. Ng

School of Electrical and Electronic Engineering,
Nanyang Technological University
Singapore 639798
eylu@ntu.edu.sg

Abstract -- This article presents the study of the nonlinear effects of amplifier gain compression and intermodulation on the accuracy of direction of arrival (DOA) in a digital array receiving system. Based on analysis and realistic computer simulation, it is shown that the gain compression has little effect on DOA estimation but the third-order intermodulation may significantly degrade DOA estimation.

INTRODUCTION

DOA estimation is very important in many wireless communication and radar systems [1]-[3]. In an adaptive antenna array system, the system always estimates DOA first and then uses DOA information for beamforming and related critical applications. The accuracy of DOA estimation is very important and critical in applications.

In a practical antenna array receiving system, no real antenna and receiver are free from physical or electrical aberrations. Any distortion in the RF/IF chain will alter the accuracy of the look direction. Some of the fixed mismatches among channels can be corrected using calibration/compensation techniques, but nonlinearity effects in this chain can not be effectively compensated in any practical way [4],[5]. It is necessary to analyze and understand the effect of nonlinearity on DOA estimation.

NONLINEAR DESCRIPTION

Consider a RF digital receiving array system, as shown in Fig. 1, and DOA estimation is carried out after IF stage and analog to digital converters (ADCs) [6]. The phase behavior of a small-signal amplifier can be considered linear enough, since the maximum value of small-signal amplifiers normally never exceeds a few degrees per dB near amplifier saturation, and it is generally ignored. And since the higher order intermodulation (IMD) products are at much lower levels than third-order

products, the nonlinear characteristic of an amplifier can be modeled in an analytical way in terms of the small signal gain, the 1 dB compression point, second order and the third order interception points of the amplifier. Thus, the output characteristic of the small signal nonlinear amplifier can be modeled by:

$$y = a + bx + cx^2 + dx^3 \qquad (1)$$

The coefficients a, b, c and d can be determined by the above amplified parameters. In our simulation, the amplitude-to-amplitude transfer curve of the nonlinear amplifier is shown in Fig. 2.

SYSTEM DESCRIPTION

As shown in Fig. 1, a typical two stage downconversion RF digital receiving system with uniform linear antenna array is considered. After frequency downconversion, filtering, and amplification, signals are sampled at second IF with ADCs. All elements in RF/IF chain are considered as linear except for the last IF stage amplifiers. The overall system is built and modeled on Signal Processing Workstation (SPW) [7]. Signals arrive at the N antenna elements can be represented by a vector $\mathbf{X}$ as:

$$\mathbf{X} = \{x(t - \tau_i)\} \qquad (2)$$

where τ_i is the relative signal time delay at the i-th element/channel. The digital output of the array system after ADCs can be expressed in complex form as:

$$\mathbf{Y} = \{f(x(t - \tau_i))\} \qquad (3)$$

Next a covariance matrix $\mathbf{R}$ of the array needs to formed via:

$$\mathbf{R} = E\{\mathbf{Y}\mathbf{Y}^H\} \qquad (4)$$

where $E\{\bullet\}$ denotes the expectation operator, H denotes complex conjugate transpose. DOA estimation can then be done by one of various DOA estimation algorithms. In this study, we use the Capon algorithm [8], and the DOA estimation can be obtained by:

$$DF(\theta) = \mathbf{s}^{-1}\mathbf{R}(\mathbf{s}^{-1})^H \qquad (5)$$

where $\mathbf{s}$ denotes the array steering vector. We will use a 4-element system and the Capon algorithm to obtain the DOA estimation.

NONLINEAR EFFECT ON DOA

A. Gain Compression Effect With Single Tone

Consider a single desired signal $x(t)$:

$$x(t) = A(t)\cos[\omega_d t + \varphi(t)] \qquad (6)$$

From equation (1), (2), (3) and (6), the output complex vector $\mathbf{Y}$ can be expressed as

$$\mathbf{Y} = \mathbf{F}_0 + \mathbf{F}_1 + \mathbf{F}_2 + \mathbf{F}_3 + \mathbf{F}_4 \qquad (7)$$

$$\mathbf{F}_0 = \left\{a' + \tfrac{1}{2}c'A^2(t-\tau_i)\right\}$$

$$\mathbf{F}_1 = \left\{b'A(t-\tau_i)e^{j[\omega_d(t-\tau_i)+\varphi(t-\tau_i)]}\right\}$$

$$\mathbf{F}_2 = \left\{\tfrac{1}{2}c'A^2(t-\tau_i)e^{j[2\omega_d(t-\tau_i)+2\varphi(t-\tau_i)]}\right\}$$

$$\mathbf{F}_3 = \left\{\tfrac{1}{4}d'A^3(t-\tau_i)e^{j[3\omega_d(t-\tau_i)+3\varphi(t-\tau_i)]}\right\}$$

$$\mathbf{F}_4 = \left\{\tfrac{3}{4}d'A^3(t-\tau_i)e^{j[\omega_d(t-\tau_i)+\varphi(t-\tau_i)]}\right\}$$

where $\mathbf{F}_1$ corresponds to the signal vector, $\mathbf{F}_2$ the second harmonic, $\mathbf{F}_3$ the third harmonic, and $\mathbf{F}_0$ and $\mathbf{F}_4$ the temporal variations. The coefficients $a' = ak_2$, $b' = bk_1k_2$, $c' = ck_1^2k_2$, $d' = dk_1^3k_2$, k_1 is the linear system gain before the nonlinear amplifier and k_2 the linear system gain after the nonlinear amplifier.

From (4) and (7), the covariance matrix can be obtained by

$$\mathbf{R} = E\{\mathbf{Y}\mathbf{Y}^H\} = \sum_{0 \le i,j \le 4} E\{\mathbf{F}_i\mathbf{F}_j^H\} \qquad (8)$$

Thus the DOA spectrum can be obtained by using (5). It can be seen that when the signal is single tone, the DOA spectrum will include the harmonic powers and temporal variations caused by the compression of the nonlinear amplifier. These distortion terms will degrade the DOA estimations.

The above DOA performance is simulated for a 4-element array system, illustrated by Fig.2. The model is constructed on SPW using 50 Monte-Carlo trials, the nonlinear amplifier parameters are shown in Fig.1, and the results are shown in Fig.3(a) and (b). In the example, the signal arrives at in the direction of 48.59 degrees. To better illustrate the results, we introduce a variable

$OBO = 10\log(P_{-1}/P_{out})$, where P_{-1} is the power of 1dB compression point of the nonlinear amplifier, $P_{out} = P_{in} + G$, P_{in} is the input power of the amplifier, and G is its gain. When the OBO is equal to 0 dB, it indicates that the output power of the amplifier is just at compression point. The larger the OBO value the smaller the output powers of the amplifier. The negative OBO values mean that the amplifier works at compression and saturation status. It can been seen that when the input signal level approaches or exceeds the compression point, the deviations of the estimations are increased rapidly. Combined with the input/output characteristic of this amplifier in Fig.1, it can be observed that when the OBO is equal to 10dB, the output power has been compressed and entered the nonlinear section though the compression is less than 1dB. This is why the DOA estimation fluctuates largely before the output level reaches the 1dB compression point. This means the DOA estimation is very sensitive to the nonlinearity. As long as the nonlinearity occurs, the DOA estimation will degrade rapidly.

On the other hand, since the harmonic products are located outside of the channel passband, they can be significantly suppressed by the filter before they reach to ADCs. Thus, though the compression can affect the DOA significantly, the DOA estimated values have relatively small changes. For instance, the maximum mean difference is just 0.0308 degrees when OBO changes from -8 dB to 25 dB.

B. Intermodulation Effect With The Presence Of Interference

Consider the signal $x(t) = x_d(t) + x_i(t)$. $x_d(t)$ is the desired signal and $x_i(t)$ is the interference. Let

$$x_d(t) = A(t)\cos[\omega_d t + g_1(t)]$$
$$x_i(t) = B(t)\cos[\omega_i t + g_2(t)] \qquad (9)$$

where $\omega_d \ne \omega_i$, $(2\omega_d - \omega_i)$ and $(2\omega_i - \omega_d)$ fall in the channel passband. Because of the nonlinearity, the system outputs will have rich frequencies including the originals, the harmonics, the sum and difference of the frequencies, third-order intermodulation and some temporal variations. It is known in section A that the products outside the channel passband will be

largely suppressed and should have relatively small effects on DOA estimation. Since intermodulation product can not be filtered out and it will be kept in channels with signals, the IMD will be a dominant factor that affect DOA estimation. The output vector Y can be derived from equation (1), (2) and (9):

$$Y = \sum_{i=1}^{15} Y_i \qquad (10)$$

$$Y_1 = \{a' + \tfrac{1}{2}cA^2(t-\tau_i) + \tfrac{1}{2}c'B^2(t-\tau_i)\}$$

$$Y_2 = \{b'A(t-\tau_i)e^{j[\omega_d(t-\tau_i)+g_1(t-\tau_i)]}\}$$

$$Y_3 = \{b'B(t-\tau_i)e^{j[\omega_i(t-\tau_{ii})+g_2(t-\tau_{ii})]}\}$$

$$Y_4 = \{\tfrac{1}{2}c'A^2(t-\tau_i)e^{j[2\omega_d(t-\tau_i)+2g_1(t-\tau_i)]}\}$$

$$Y_5 = \{\tfrac{1}{2}c'B^2(t-\tau_i)e^{j[2\omega_i(t-\tau_i)+2g_2(t-\tau_i)]}\}$$

$$Y_6 = \{c'A(t-\tau_i)B(t-\tau_i)e^{j[(\omega_d+\omega_i)(t-\tau_i)+g_1(t-\tau_i)+g_2(t-\tau_i)]}\}$$

$$Y_7 = \{c'A(t-\tau_i)B(t-\tau_i)e^{j[(\omega_d-\omega_i)(t-\tau_i)+g_1(t-\tau_i)-g_2(t-\tau_i)]}\}$$

$$Y_8 = \{kA^2(t-\tau_i)B(t-\tau_i)e^{j[(2\omega_d-\omega_i)(t-\tau_i)+2g_1(t-\tau_i)-g_2(t-\tau_i)]}\}$$

$$Y_9 = \{kA(t-\tau_i)B^2(t-\tau_i)e^{j[(2\omega_i-\omega_d)(t-\tau_i)+2g_2(t-\tau_i)-g_1(t-\tau_i)]}\}$$

$$Y_{10} = \{kA^2(t-\tau_i)B(t-\tau_i)e^{j[(2\omega_d+\omega_i)(t-\tau_i)+2g_1(t-\tau_i)+g_2(t-\tau_i)]}\}$$

$$Y_{11} = \{kA(t-\tau_i)B^2(t-\tau_i)e^{j[(2\omega_i+\omega_d)(t-\tau_i)+2g_2(t-\tau_i)+g_1(t-\tau_i)]}\}$$

$$Y_{12} = \{\tfrac{1}{4}d'A^3(t-\tau_i)e^{j[3\omega_d(t-\tau_i)+3g_1(t-\tau_i)]}\}$$

$$Y_{13} = \{\tfrac{1}{4}d'B^3(t-\tau_i)e^{j[3\omega_i(t-\tau_i)+3g_2(t-\tau_i)]}\}$$

$$Y_{14} = \{[k_3A(t-\tau_i)B^2(t-\tau_i)+kA^3(t-\tau_i)]e^{j[\omega_d(t-\tau_i)+g_1(t-\tau_i)]}\}$$

$$Y_{15} = \{[k_3A^2(t-\tau_i)B(t-\tau_i)+kB^3(t-\tau_i)]e^{j[\omega_i(t-\tau_i)+g_2(t-\tau_i)]}\}$$

Y_2 and Y_3 are the original signals, Y_4, Y_5, Y_{12} and Y_{13} are harmonic products, Y_6 and Y_7 are the products of sum and difference of frequencies, Y_8, Y_9, Y_{10} and Y_{11} are intermodulation products and Y_8 and Y_9 fall in the channels, Y_1, Y_{14} and Y_{15} are temporal variations, $k = \tfrac{3}{4}d'$, $k_3 = \tfrac{3}{2}d'$.

Similarly, the covariance matrix R is:

$$R = E\{YY^H\} = \sum_{1 \le i,j \le 15} E\{Y_i Y_j^H\} \qquad (11)$$

$DF(\theta)$ can be obtained by using (5). Thus, the DOA spectrum includes original signal power, intermodulation products and some temporal variations in addition of the harmonics and the sum and difference components. Since the intermodulation products Y_8 and Y_9 cannot be filtered out, the distortion will affect DOA estimation.

The above DOA performance is simulated based on the same computation model and the Monte-Carlo results are shown in Fig.4(a) and (b). Combined with Fig.1, it can be seen that when the input power is larger than –6 dBm (OBO is 16 dB), the amplifier just enter the compression status (less than 1dB). And from this point on, the deviations of the means and variances are increased significantly, for example, the maximum mean difference is 12.0559 degrees when OBO changes from 10 dB to 25 dB. It indicates that as long as the intermodulation products exist and fall in the channel passband, they will degrade the DOA performance significantly and promptly even though the intermodulation level is small. Since the intermodulation product can not be eliminated, it always accompanies the signals and thus degrades the DOA performance. This is different from that of the single tone.

CONCLUSIONS

This study revealed that when signal is a single tone, the harmonic components caused by gain compression has little effect on DOA estimation. But if the interference is present and the intermodulation products fall in the channel passband, and it may severely degrade the accuracy of DOA estimation.

REFERENCES

[1] J. Litva and T. K.-Y. Lo, *Digital Beamforming in Wireless Communications*, Artech House, 1996.

[2] E. Nicolau and D. Zaharia, *Adaptive Arrays*, Elsevier, 1989

[3] N. Fourikis, *Phased Array-Based Systems and Applications*. John Wiley, 1997

[4] S. Merchan, "OFDM Performance in Amplifier Nonlinearity," *IEEE Trans. Broadcasting*, vol.44, No.1, Mar. 1998.

[5] A. Chini, Y. Wu and S. Mahmoud, "Hardware Nonlinearites in Digital TV Broadcasting Using OFDM Modulation," *IEEE Trans. Broadcasting*, vol.44, No.1, Mar.1998.

[6] C. Olmstead and M. Petrowski, "Digital IF Processing," *RF Design*, Sep.1994.

[7] *Signal Processing Workstation Users' Guide*, Cadence Design System, Inc, 1998.

[8] S. Haykin, et al. (ed), *Radar Signal Processing*, New York: Springer-Verlag, 1993.

175
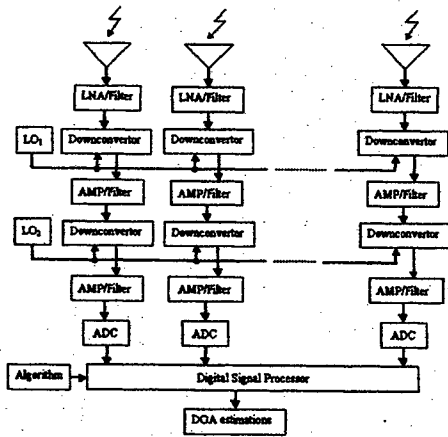
Fig. 1. System structure – antenna array with RF digital receivers and digital signal processor.

Fig. 3(b). Variances of DOA estimation for a signal arriving at angle 48.59° via OBO with single tone.
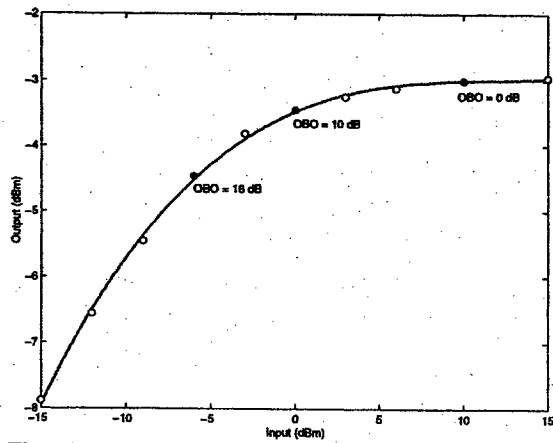
Fig. 2. Characteristic of the input/output of a nonlinear amplifier (IP$_2$= 39 dBm, IP$_3$= 35 dBm, Gain =10 dB, P$_{-1}$= 20 dBm).
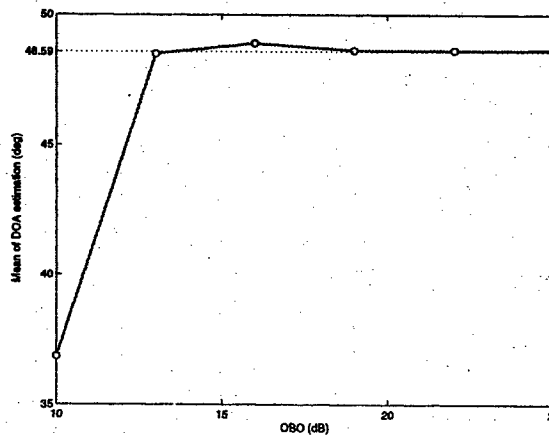
Fig. 4(a). Mean of DOA estimation for a signal arriving at angle 48.59° with two tones.

Fig. 3(a). Mean of DOA estimation for a signal arriving at angle 48.59° via OBO with single tone.
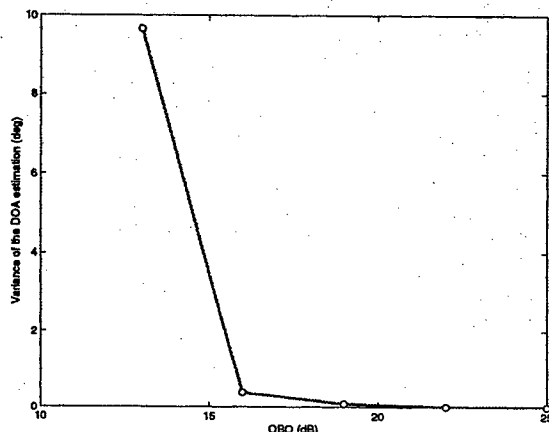
Fig. 4(b). Variance of DOA estimation for a signal arriving at angle 48.59° with two tones.

ARRAY ROBUSTNESS TO SENSOR FAILURE

A. Alexiou* and A. Manikas
Communications and Signal Processing Research Group
Department of Electrical and Electronic Engineering
Imperial College of Science, Technology and Medicine, London, SW7 2BT, UK

*currently with Global Wireless Systems Research, Bell Labs, Lucent Technologies, Swindon, SN5 7YT, UK

Abstract

The presence of uncertainties in the array response results in a performance degradation often greater than the application requirements can afford. Although various attempts have been made to measure the effect of uncertainties on Direction-Finding algorithms performance, the impact of sensor response uncertainties on the ultimate array DF capabilities has not been considered thoroughly. In this paper, the sensitivity of an array's DF capabilities to sensor response errors is formulated. Robustness and reliability measures are proposed, which can be used as tools for the evaluation of each sensor's importance within the array geometry and as criteria for the comparison of a number of array geometries.

1. Array signal model in the presence of failure

The response of a planar array of N sensors to a signal incident from azimuth $\theta \in [0, 360°]$ and elevation $\phi \in [0, 90°]$ is described by the *manifold vector*,

$$\underline{a}(\theta, \phi) = \underline{\gamma} \odot \exp\{-j\underline{\underline{r}}\,\underline{k}(\theta, \phi)\} \qquad (1)$$

where $\underline{\gamma} \in \mathcal{C}^N$ is the vector of sensor gain responses, $\underline{\underline{r}} \in \mathcal{R}^{N \times 3}$ is the sensors locations matrix (in meters) and $\underline{k}(\theta, \phi) = \frac{2\pi}{\lambda}[\cos\theta\cos\phi, \ \sin\theta\cos\phi, \ \sin\phi]^T \in \mathcal{R}^3$ denotes the wavenumber vector. For the fully operational array, the effect of the array structure on the system performance may be assessed quantitatively by determining the local properties (*shape* and *orientation*) of the array manifold, through the study of the manifold's differential geometry [1],[2]. However, in the presence of sensor response uncertainties, the actual array configuration and the resulting performance depend on the location of the sensors whose actual response differs from the nominal one, as well as on the operational state of each one of the malfunctioning sensors.

Let F_i be a complex number denoting the operational state of the i-th sensor, with $F_i = 1$, representing the fully operational state and $F_i = 0$ the complete failure. The **effective array manifold vector** in the presence of sensor response uncertainties can be written as

$$\underline{a}_F(\theta, \phi) = \underline{F} \odot \underline{a}(\theta, \phi) \qquad (2)$$

where $\underline{F} = [F_1, F_2, ..., F_N]^T$. It is interesting to observe that, when the sensors have identical operational states, i.e. $F_i = F$, $\forall i$, the effective array manifold is a scaled version of the nominal one and spans the same subspace.

2. Array robustness

In order to quantify the array robustness, the **array performance structure function** is defined as the ratio,

$$\Phi_{pc} = \frac{\text{performance criterion in the presence of array uncertainties}}{\text{performance criterion for the fully operational array}} \qquad (3)$$

and is equal to zero when all sensors fail, whereas it is equal to one when all sensors are fully operational.

Let now the deviation ΔF_i of F_i from its nominal value F_{oi} result in a change $\Delta\Phi_{pc,i}$ of the array state from its nominal value $\Phi_{pc}(\underline{F}_o)$. The **sensitivity function** of Φ_{pc} in terms of F_i is defined as the ratio $\frac{\Delta\Phi_{pc,i}}{\Delta F_i}$ and indicates the i-**th sensor's structural importance**. When ΔF_i is 'large' (compared to F_{oi}), $\Delta\Phi_{pc,i}$ is a measure of sensitivity for the array state and is called **sensitivity-in-large** $S_{pc,i}^L$ or **structural importance-in-large of the i-th sensor**. Thus,

$$S_{pc,i}^L(\underline{F}_o, \underline{\Delta F_i}) = \Phi_{pc}(\underline{F}_o) - \Phi_{pc}(\underline{F}_o + \underline{\Delta F_i}) \qquad (4)$$

where $\underline{\Delta F_i}$ is a vector with the i-th element equal to ΔF_i and all other elements equal to zero. In a sensor failure scenario $S_{pc,i}^L \in [0,1]$, with $S_{pc,i}^L = 1$ when the i-th sensor absolutely determines the array performance and $S_{pc,i}^L = 0$ when it has no effect on performance.

When ΔF_i is 'small', so that $\lim_{\Delta F_i \to 0} \frac{\Delta\Phi_{pc,i}}{\Delta F_i}$ exists, then the **small or absolute sensitivity** function of Φ_{pc} in terms of F_i evaluated at the nominal value $\underline{F}_o$ is a measure of the **(absolute) performance structural importance** of the i-th sensor. Thus,

$$S_{pc,i}(\underline{F}_o) = \left.\frac{\partial\Phi_{pc}}{\partial F_i}\right|_{\underline{F}_o} \qquad (5)$$

As $S_{pc,i}(\underline{F}_o) \to \infty$, the state of the i-th sensor determines the array performance, whereas $S_{pc,i}(\underline{F}_o) \to 0$, the state of the i-th sensor tends to be of no consequence. While

the absolute structural importance reflects the *local* robustness and is intended for perturbation analysis, the structural importance-in-large represents the *global* robustness and is more suitable for sensor failure analysis.

3. Array reliability

In the case of random sensors operational state, the effective array manifold vector $\underline{a}_F(\theta, \phi)$ becomes a random variable with stochastic characteristics depending on each sensor's location within the array geometry and its statistical properties. These properties determine the **sensor reliability**, which can be defined as the probability that the sensor's operational state is within the range required for the satisfactory operation of the array system with respect to a chosen performance criterion. In the special case, when the sensors operational states are assumed independent binary variables, the sensors reliability [3] is *independent of the chosen performance criterion* and is given by

$$R_i = \Pr\{F_i = 1\} = \mathcal{E}\{F_i\}, \ i = 1, 2, ..., N \quad (6)$$

Given the sensors reliability, the expectation of the structure function can provide a *stochastic measure of the array performance effectiveness*, the so-called **performance effectiveness index** (PEI), defined as:

$$\text{PEI}_{pc} = \mathcal{E}\{\Phi_{pc}(\underline{F})\} \quad (7)$$

and taking values in [0,1], with 1 corresponding to ideal operation and 0 to complete system failure.

In the presence of failure, the objective must be to ensure that the array provides a minimal performance level Φ_{thr} or in other words, it remains *operational* according to the particular application requirements. The **array reliability** R_{pc} with respect to a chosen performance criterion and given a prespecified required performance level is defined as the probability that this performance level will be reached or exceeded, i.e.

$$R_{pc} = \Pr\{\Phi_{pc} \geq \Phi_{thr}\} \quad (8)$$

The array reliability is a decreasing function of Φ_{thr} and equals 1 when $\Phi_{thr} = 0$, whereas it tends to 0 for $\Phi_{thr} = 1$.

In order to develop a measure which quantifies the combined effect of both array geometry and sensors reliability on the array reliability, the **reliability importance of sensor** i is introduced as

$$I_{R_{pc},i} = \frac{\partial R_{pc}(\underline{R})}{\partial R_i} \quad (9)$$

Under the assumption of independent random binary sensors operational states, the array reliability is an

increasing function of sensors reliability R_i [3] and it can be deduced that:

$$I_{R_{pc},i} = R_{pc}(\underline{R}|F_i = 1) - R_{pc}(\underline{R}|F_i = 0) \quad (10)$$

Thus, the reliability importance of the i-th sensor is independent of its reliability and depends on the array geometry and the reliability of the other sensors.

4. Comparison of robustness and reliability of a number of array geometries

In the previous sections, the framework of how to quantitatively assess the array robustness and reliability and to evaluate the impact of each sensor has been described. Consider, for instance, the scenario of two equi-powered uncorrelated signals impinging from azimuth directions $\theta \pm 2.5°$, on the array geometries depicted in Figure 1 and let the estimation accuracy, as determined by the inverse of the Cramer-Rao lower bound [2][4], be the performance criterion of interest.
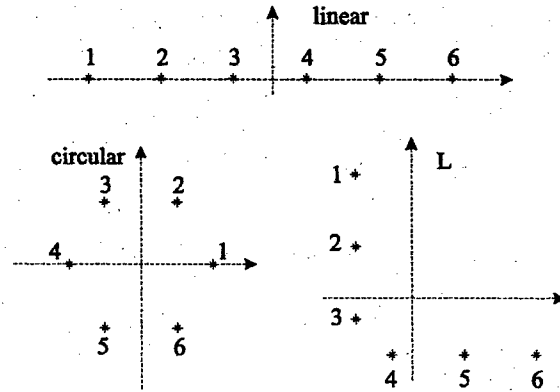
Figure 1: Array geometries

Four criteria are proposed aiming at exemplifying the utilisation of the measures presented as figures of merit for the comparison of array geometries in terms of robustness/reliability.
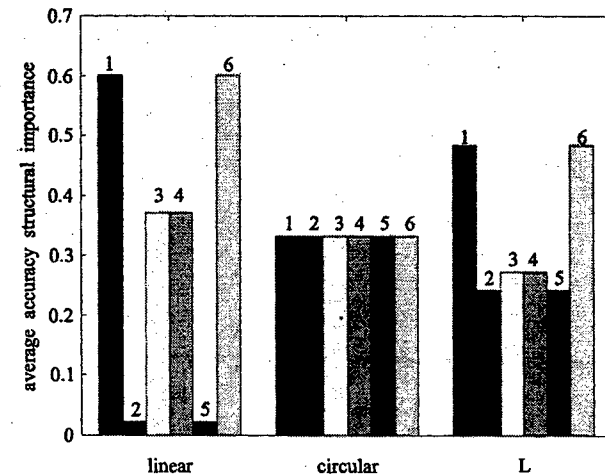
Figure 2: Sensors accuracy structural importance

CRITERION 1: **Sensors structural importance**

In Figure 2 the linear, circular and L-shaped arrays are compared in terms of accuracy structural importance averaged over azimuth. As it was expected, all the sensors of the circular array have the same average structural importance due to the circular symmetry (sensitivity is uniformly distributed along the array), whereas for the linear and L-shaped arrays, sensors 1 and 6 are the most important. It is interesting to observe that the linear array is almost perfectly robust to failure of sensors 2 and 5.

CRITERION 2: **Minimum robustness**

Although the performance structural importance averaged over all azimuths provides a measure of the way in which robustness is distributed along the array geometry, it eliminates the information concerning the cases of very low robustness along some particular DOAs. In order to depict this 'worst case scenario' and assuming one malfunctioning sensor only, the notion of *minimum robustness*, i.e. maximum sensitivity over all sensors can be expressed along the azimuth DOAs. When large sensor response deviations are assumed in the analysis, the sensitivity-in-large is employed. Thus,

$$S_{pc,max}^{L} = \max_{i}\{S_{pc,i}^{L}(\boldsymbol{F_o}, \boldsymbol{\Delta F_i})\} \qquad (11)$$

In a sensor failure analysis $\Delta F_i = -1$ and $1 - S_{pc,max}^{L}$ denotes the minimum array robustness in the presence of one failed sensor. In Figure 3 the minimum accuracy robustness of the arrays depicted in Figure 1 is illustrated along with the 'most important' sensors.
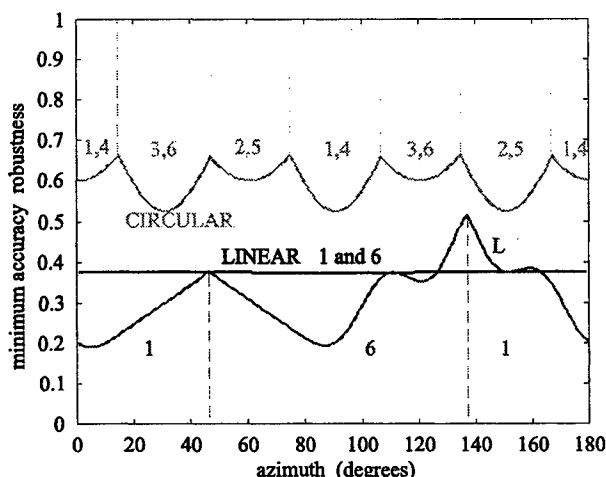
Figure 3: Minimum robustness-in-large

Observe that for the linear array the sensors at the ends are the most important along the whole azimuth range. For the circular array, the maximum sensitivity is periodical with period equal to 60° and the geometrical relation between the azimuth DOA and the

corresponding most important sensors is preserved within each period. For the L-shaped array, the minimum robustness in $[0°, 45°]$ and $[45°, 90°]$, $[90°, 135°]$ and $[135°, 180°]$, as well as the corresponding most important sensors are mirror images of each other with respect to 45° and 135° respectively. In absolute terms the L-shaped array is the less robust, with worst case robustness 20%. The circular array is the most robust to sensor failure, with minimum robustness 50%.

When 'small' perturbations of sensors response are assumed, the absolute sensitivity must be employed,

$$S_{pc,max} = \max_{i}\{S_{pc,i}(\boldsymbol{F_o})\} \qquad (12)$$

which is a measure of the induced performance degradation to a first order approximation. In Figure 4 the maximum absolute accuracy sensitivity is depicted for the linear, circular and L-shaped arrays. Similar conclusions to the ones made for Figure 3 can be drawn regarding the arrays relative robustness, taking into account the inverse relation between robustness and sensitivity. Nevertheless, the variation with azimuth and the corresponding 'most important' sensors may be different, e.g. for the L-shaped, reflecting the fact that absolute sensitivity is related to sensitivity-in-large through differentiation.
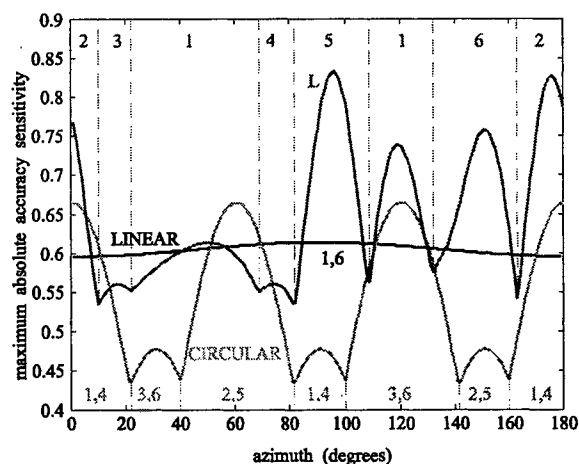
Figure 4: Maximum absolute sensitivity

CRITERION 3: **Performance Effectiveness**

Assume that the linear, circular and L-shaped arrays consist of equi-reliable sensors with reliability equal to 0.9. Their accuracy effectiveness indices are compared in Figure 5. The circular array is the most 'effective'. The effectiveness of all three arrays varies with azimuth according to the involved geometrical symmetry. In Figure 6 the accuracy effectiveness indices of the three arrays are compared for sensors reliabilities equal to $[0.95, 0.85, 0.9, 0.9, 0.85, 0.95]^T$. In this way, the

reliability is 'distributed' along the linear and L-shaped arrays according to the sensors structural importance relative order, as depicted in Figure 2. This combination of reliabilities results in change of order in terms of effectiveness (now the linear array is the most effective), increased effectiveness of all the arrays and different variation with azimuth. That is to say that the sensors reliability 'distribution' along the array geometries determines their relative merits in terms of effectiveness.
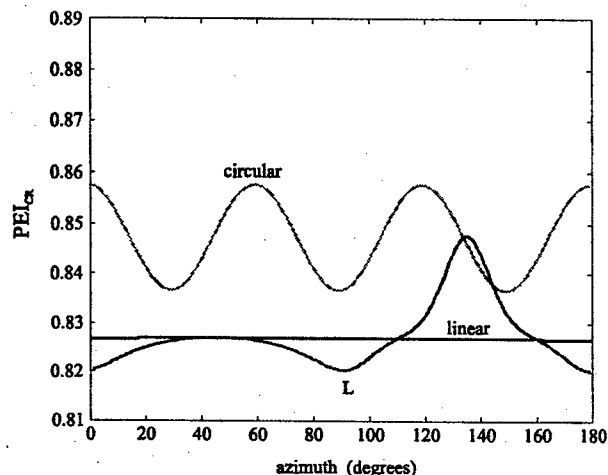
Figure 5: Accuracy effectiveness index (sensors reliabilities = 0.9)
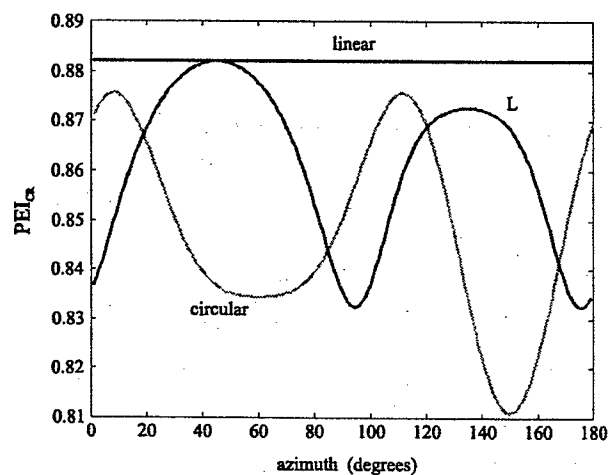
Figure 6: Accuracy effectiveness index (sensors reliabilities = $[0.95, 0.85, 0.9, 0.9, 0.85, 0.95]^T$)

CRITERION 4: **Sensors reliability importance**

The reliability importance of the sensors is a measure -to a first order approximation- of the impact of a change in the sensor reliability on the array system reliability. In Figure 7 the linear, circular and L-shaped arrays are compared in terms of accuracy reliability importance averaged over all azimuth directions. The arrays are assumed to be consisted of equi-reliable sensors with reliability equal to 0.9 and the required performance

level is 0.6. Notice for example that sensors 2 and 5 of the linear array do not at all affect the reliability sensitivity, which is determined almost exclusively by sensors 1 and 6. This is the case for sensors 1 and 6 of the L-shaped array, whereas the order of importance of sensors 2,5 and 3,4 is reversed compared to their structural importance depicted in Figure 2.
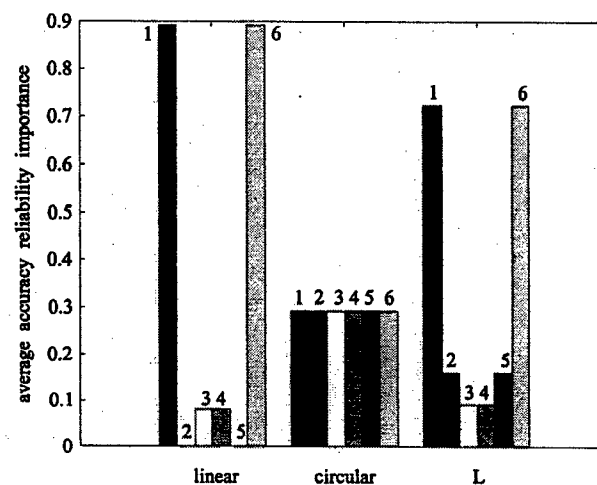
Figure 7: Accuracy reliability importance ($\Phi_{thr} = 0.6$)

5 Conclusions

In this paper, novel measures have been introduced for the array robustness and reliability assessment in the presence of sensor failure and the evaluation of each sensor's importance. Using these measures as criteria, a number of array geometries were compared. The knowledge of sensors' importance was shown to reveal the 'distribution' of robustness and reliability along the array geometry and therefore it is a useful tool for the design of arrays satisfying certain performance sensitivity and reliability constraints.

References

[1] A. Manikas, H. R. Karimi, I. Dacos, "Study of the detection and resolution capabilities if a one-dimensional array of sensors by using differential geometry", *IEE Proc. on Radar, Sonar & Navigation*, Vol.141, No. 2, pp.83-92, April 1994.

[2] A. Manikas, A. Alexiou, H. R. Karimi, "Comparison of the ultimate direction-finding capabilities of a number of planar array geometries", *IEE Proc. on Radar, Sonar & Navigation*, Vol.144, No. 6, December 1997.

[3] R. E. Barlow, F. Proschan, "Statistical Theory of Reliability and Life Testing: Probability Models", Silver Spring: To Begin With, MD, 1981.

[4] P. Stoica, A. Nehorai, "MUSIC, Maximum, Likelihood, and Cramer-Rao Bound", *IEEE Trans. on Acoustics, Speech, and Signal Processing*, Vol.37, No. 5, pp.720-741, May 1989.

LOCATOR WITH SUPER-SCANNING PHASED ARRAY AND ITS BASIC FEATURES

Dr.Sci.Vera Ginzburg
IEEE member No: 40360208, SPIE member No: 00373899
3085 Brighton 13th st., Apt. 2A
Brookllyn, NY 11235
Phone: 718-891-3753; E-mail: veraginz@worldnet.att.net

INTRODUCTION

Imaging of reflecting objects by locators with phase array, super-scanning during both the emission of probing pulses and reception of reflected signals, rejects the principal feature of traditional pulsed locating systems, which is the necessity to wait for the arrival of a reflected signal. Like a circus juggler, the antenna hurls a long pulse over the whole surveyed space and then rapidly comes back to the initial position to start the next scanning period according to the same or another scanning law. The reception of reflected signals is possible only from certain (known beforehand) visibility layers (VLs), similar to the tomograph's cuts, separated by "dead" zones. When proposed in the 50s[1, 2], this method was outright discarded on the assumption that energy and the information would be lost in these dead zones. In this connection, the author has carried out theoretical studies and established that, on the contrary, the new technique ensured a substantial gain in energy and information as compared to traditional radar systems[3, 4]. It was shown that the "super-scanning" (SS) locator could be adaptive and provide optimum distribution of energy in the surveyed space as well as super-resolution of observable objects (at distances smaller, than required by the Rayleigh criterion). An ultrasonic version of the SS locator was built, performing beam scanning in an-echoic chamber at a frequency of 115 KHz (i.e., in the range of dolphin and bat locators). The experiments totally confirmed the theoretical conclusions. A known hypothesis about super scanning mechanism in dolphin locators[5] is also mentioned. The obtained results are briefly presented in this report. They are described in detail in the first three chapters of the book[4] and partly in the SPIE's Conferenses[6-8].

SUPERSCANNING PHASE-ARRAY OPERATION

The equation of the dynamic beam pattern of an SS phase-array is described by the expression

$$g(\theta, t) = \int_{D/2}^{D/2} A(x) \exp\{i[kx\sin\theta - \psi(x, t)]\}\, dx \tag{1}$$

$\psi(x, t)$ is the phase distribution in the antenna aperture D, θ is the angle between the direction of signal reception (radiation) and the normal to the antenna aperture, $A(x)$ is the field amplitude distribution, $k = 2\pi/\lambda$, and λ is the wavelength. In the simplest case, when $A(x) = $ const and $\psi(x, t) = b(t)x$, where $b(t)$ is the tangent of the angle of phase distribution along the antenna aperture. In this case the dynamic beam pattern $g(\theta, t) = (\sin U)/U$, where $U = (kD/2)(\sin\theta - b/k)$. The directivity maximum is determined by the equation $\sin\theta_{max} = b/k$ and varies with b. **Fig 1** demonstrates the operation of the locator for the simplest saw-toothed scanning law over the sector Θ. The antenna emits pulses of the duration τ and repetition period T. During scanning the beam crosses direction R, θ during the time interval $t_0 \le t \le t_0 + \tau_0$, where t_0 is the initial moment of transmission and $\tau_0 = \tau\theta_0/\Theta$ is the time taken by the beam to turn through its width θ_0. In the course of scanning, the initial transmission's time t_0 vary with the angle according to the scanning law. The emitted energy occupies in space a moving section A of the Archimedes spiral having the thickness $c\tau_0$ and depth $c\tau$. The energy reflected from a point object comes back to antenna in the form of part of spherical layer B, at the time $t = t_0 + 2R/c$. Reflected signal may be received if the antenna beam is directed at the same angle as at the initial moment of signal transmission.

Therefore, the reflected signals are received from the discrete VLs separated by the dead zones. The depth of VLs - δR, the repetition period - ΔR, and the inclined VLs depth - δR_r (caused by the reverse beam motion) are equal to

$$\delta R = (c\tau/2)(\theta_0/\Theta); \quad \Delta R = c(\tau + \tau_r)/2; \quad \delta R_r = (c\tau_r/2)(\theta_0/\Theta), \qquad (2)$$
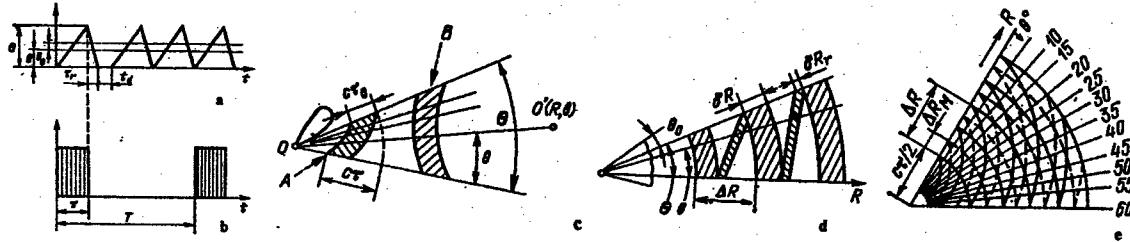
Fig.1. SS locator operation: (a) saw tooth scanning law; (b) emitted pulses; (c) spatial shape of emitted (A) and reflected (B) energy; (d) positions of VLs; (e) surveying net. T- recurrent period, τ -pulse duration, τ_d – delay time; R, θ - object coordinates, θ_0 – antenna's beam width, Θ - observation sector.

The emitted energy occupies in space a confined section in the form of Archimedes spiral (**Fig. 1c**) having the thickness $c\tau_0 = c\tau\ (\theta_0/\Theta)$. The energy reflected from an object comes back in the shape of spherical layer B. It can be totally received only when antenna beam is directed at the same angle as at the initial moment of signal transmission. The reflecting signals are received from certain visibility layers (VL) (Fig. 1d) with the depth $\delta R = c\tau_0/2$ and repetition period $\Delta R = c\ (\tau + \tau_r)/2$, where τ_r is the reverse travel time of the beam forming the inclined visibility layers. By using additional antenna beams with shifted delay times and different antenna scanning laws, a surveying net can be formed in space (see Fig. 1e).

The SS Phase-Array is a parametric converter changing the form and duration of emitted and receiving pulses. Their form acquires that of the beam pattern for $\theta/\Omega \ll 1$. The form and duration of receiving pulses depend on the object's velocity crossing a VL and on the relationship between the object dimension L, the VL width δR, and their repetition period ΔR. For a point object crossing VLs the receiver records pulse trains. The train duration t_+, the number of pulses in the train n, and interval between the trains t_- (crossing neighboring VLs) are accordingly equal to

$$t_+ = \delta R / V_r = c\tau_0/2 V_r; \qquad t_- = (\Delta R - \delta R)/V_r; \qquad n = t_+/2 V_r T \qquad (3)$$

The repetition period (survey period) T_0 and the average number of pulses, $<n>$ are

$$T_0 = t_+ + t_- = (C\tau_0/2 V_r)(\theta/\Theta); \qquad <n> = n/T_0) = \text{const} \qquad (4)$$

The Eqs (3) and (4) show: the pulse's numbers in the train and survey period depend on the velocity of the object. Hence, the increase in the object velocity results in higher data acquisition rates with the average number of received pulses being const.

When extended objects having dimension L_r are observed, the duration of pulse train increases by L_r / V_r for the same survey time T_0. When the object's dimension exceeds that of dead zones, the object have to be seen continuously as a moving "striped" image (tomogram)

To verify the theoretical conclusions, a working ultrasound prototype version of the locator with phased super-scanning array, has been constructed. Figure 2 a, b shows two positions of an aircraft model crossing the visibility layers of the locator. Figure 2 c, d illustrates how the part of an object's image can be separated.

a   b   c   d
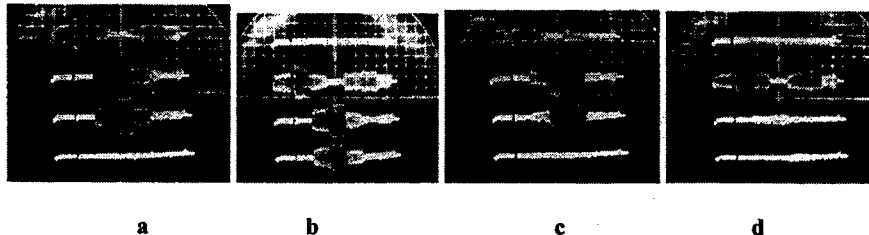
Fig 2. Two positions of a moving object crossing several VLs: for the same scanning direction (a,b); for the opposite scanning directions at radiation and receiving (c,d).

Such images are the same in the near and the far zones. Only the width of VLs can decrease with distance dependent of the admissible SNR

EFFECT OF SUPER_RESOLUTION

If objects dimensions are smaller than VL's depth, the objects still can be resolved even when distance between them is less then required by the Rayleigh criterion. **Fig 3 a, b, c** demonstrate such possibilities received by changing VL's direction during observation.
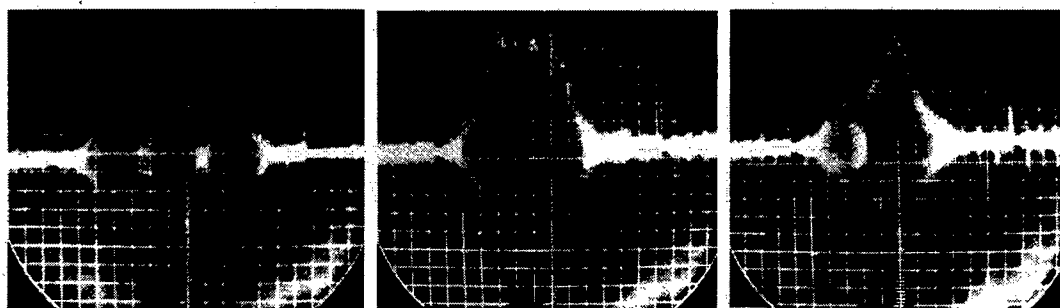
Fig.3. Signals from three objects (with sizes smaller than the width of VLs) at the equal distances from the locator disposed: a) The distance between the objects correspond to Rayleigh criterion; b) 3 time lesser then the Rayleigh criterion; (c) the same distance but opposite directions of beam scanning: effect of "super-resolution" - excretion of the middle object

OPTIMAL ENERGY DISTRIBUTION

Since the position of the surveying net is known beforehand, the coordinates of objects crossing the net are also known. This circumstance opens many new opportunities in location. Specifically, the emitted energy can be optimally distributed within the surveyed space. **Fig. 4** illustrates the example of calculation the locator with constant-altitude space surveying mode for the distance R_{max} = 300 km, the angular observation sector Θ = 60°, the limiting inclination angle θ_s = 8°, the angular beam width 1°, and the wavelength 10 cm.
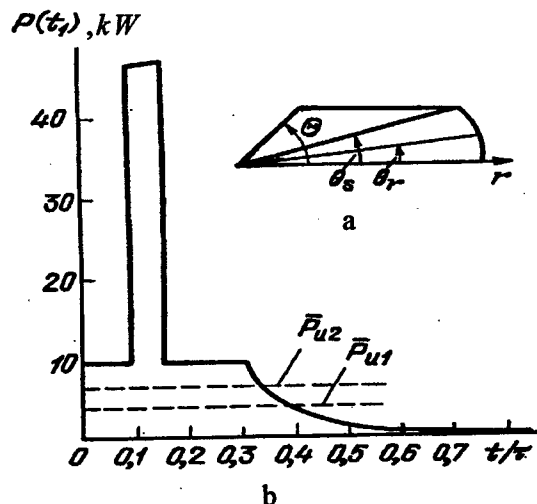
Fig.4 The example of the energetically optimal SS locator: (a) area of observation; (b) a synthesized pulse of the transmitter

It follows from this figure that only the fraction of the pulse, corresponding to the surveying region, with maximum range, should provide the maximum energy. The whole constant altitude's

surveying region is ensured by the dragging rear front of the emitted pulse. When intensive interference is on at maximum range, it is sufficient to send a powerful short pulse in the interference direction (the calculation has been made for the interference energy with equivalent temperature 100 KT). The total emission power P_u will change insignificantly in this case.

AN EXAMPLE OF REAL SUPER SCANNING PHASE ARRAY ANTENNA
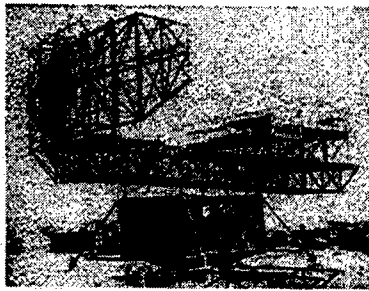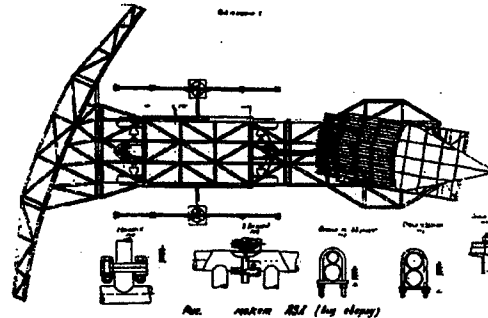
a   b

Fig 5 a, b show the photo and the design of the SS phased-array antenna for λ = 10 cm with the scanning sector ± 7° at period 8 μs. It consisted the parabolic reflector and scanner - the flat horn with the set of gas-discharge phase-rotators. The ground locator with frequency scanning SS antenna for λ = 10 cm with the scanning sector ± 5°, with period 10μs, also was created

CONCLUTIONS

The locator (tomograph) with Super-Scanning Phase-Array Antenna has the following basic unique possibilities:

Optimal energy distribution and resolving power in the surveyed space redistribution;

Reception of contour object's images in the far (Fraunhofer) zone with the linear resolution independent of distance;

Super-resolution the objects in a group within VLs due to intentional increase of interval between reflected signals;

Increase the potential of the locator due to redistribution of the energy in survey zone;

It is shown that the Locator with SS Phase array antenna can be adaptive i.e. the maximum ratio of information to spending energy from survey area, can provide.

This possibility can decreases vastly the total energy radiated in the Atmosphere, in comparison with existing Radars and Lidars, i.e. decreases the warming of the Atmosphere.

REFERENCES

1. V.M.Ginzburg and K.A.Petrov, «A technique to survey space by a radar», Certificate of Authorship No.596061, USSR, (September 15, 1950), declassifyed at *Bull*. No.32,1982.
2. V.M. Ginzburg, «Radars antenna arrangement», Certificate of Authorship No.596062 (April 23, 1958), declassifyed at *Bull*. No.32, 1982.
3. V.M.Ginzburg, «3D image formation by transformation time signals into spatial structures», *Opt. Communicattions*, 42 (5) pp. 298-300, 1982.
4. V.M.Ginzburg, *Real time image formation and processing. Fast scanning methods*, Radio I Sviaz, Moscow, 1986 (in Russian)
5. V.M.Belkovich and A.E.Reznicov, Nature, No.11, 1971 (in Russian)
6. Vera M. Ginzburg, "Real-time imaging and recognition of moving objects by pulsed "super-scanning" locator (tomograph)" *Proc. SPIE*: 3068 38, 1997;
7. ,Imaging of the static and dynamic objects by pulsed super-scanning locator (tomograph) with resolution higher than by the Rayleigh criterion" *Proc. SPIE*: 3370-01, 1998;
8. Vera Ginzburg "Superscaning locator and its possibilities, *SPIE Proc*.3749-181, 1999.

Phase Optimized Beam Design for Direction Sensing Aboard Communication Satellites[†]

Gregory M. Kautz

General Electric – Corporate Research & Development

kautz@crd.ge.com

Abstract

Accurate estimation of directions to terrestrial reference sites is a key component for stabilized pointing of customer beams aboard communication satellites. Direction estimation is enabled through the formation of beams on the payload phased arrays. To minimize downtime of channels otherwise used to provide service, phase-optimized beamforming strategies are considered for both coherent and non-coherent methods of signal reception. Direction estimation accuracy is derived from Monte-Carlo simulation and used to assess the quality of the optimized beams relative to those commonly employed in conventional monopulse and sequential lobing.

1. Introduction

The application of phased array technology to communication satellites provides extensive flexibility over conventional reflector antenna designs. A phased array is easily programmed to efficiently tailor the beam pattern to the arbitrary distribution of customer sites. New or changing customer profiles over the mission lifetime or during the course of a day are accommodated. Also, the benefit of frequency re-use is enabled for customers with displaced service zones. Phased array technology also poses unique challenges. First, there is a need for a high-performance calibration scheme to properly characterize the array elements. Second, the solid state power amplifiers existing at each active element typically operate inefficiently relative to a conventional system. Recently, a calibration method capable of *accurately* measuring the RF characteristics of the array was proposed[1]. To compensate for the reduced component conversion efficiencies, large arrays with high gain are implemented. For systems offering point-to-point service, the high-gain beams have smaller footprints, requiring a higher degree of pointing accuracy.

More accurate pointing is achieved by augmenting the sensor suite with Star Trackers. The error signal of finer granularity drives onboard momentum wheels to physically stabilize the craft. The additional sensors add both weight and cost to the system, especially if there are multiple, gimbaled array structures. In an alternative approach[2], electrical compensation provides fine-pointing stability while the conventional physical attitude control operates in a comparitively coarse manner. Here, multiple terrestrial reference points are located relative to the array via conventional Radar Monopulse [3]. Measuring the apparent directions to two or more sites, the full 3D array attitude may be determined. While continually sensing the drift, customer beams are re-pointed to compensate for the orientation error.

To determine the attitude, the satellite must sequentially generate a set of transmit or receive beams. This paper considers the generation of beam shapes that are "optimal" in the sense that the accuracy of the direction finding approach is maximized. Both coherent and non-coherent signal reception methods are considered with a goal minimizing the onboard hardware complexity and the down-time of channels otherwise used to handle customer traffic. As similar for the design of transmit beams for communication, a constant amplitude beamforming strategy over the aperture is adopted. This is desired to (1) maximize radiated power and (2) provide a common operating point for all amplifiers within the transmit array, as important when the amplifiers are operated in the non-linear regime to realize increased RF conversion efficiencies.

[†] This work supported under contract through Lockheed Martin, Missiles & Space

2. Direction estimation – general form for coherent and non-coherent systems

The key component process to electronic beam stabilization is the estimation of directions to two or more terrestrial references. Considered herein are coherent and non-coherent signal reception methods where the direction estimator formulations are based on minimizing the least-squared error. Let the applied $N \times N_b$ constant-amplitude beamforming matrix be denoted as $\mathbf{W}_{BF}$ so that the response of a unit-amplitude signal arriving direction (T_x, T_y) be written in vector form as $\mathbf{g}(T_x, T_y) = \mathbf{W}_{BF}^H \exp\left(j\frac{2\pi}{\lambda}[\mathbf{x}T_x + \mathbf{y}T_y]\right)$. Here the T-space coordinates of the terrestrial reference location are $T_x = \cos\theta_{AZ}\sin\theta_{EL}$, $T_y = \sin\theta_{AZ}\sin\theta_{EL}$; $\mathbf{x}$ and $\mathbf{y}$ are the N_e-element coordinates and λ is the wavelength. Note that bold lowercase/uppercase variables represent vectors/matrices. The shorthand notation $\exp(j\psi)$ is intended to represent a vector of unit-amplitude elements where the k'th element is $\exp(j\psi_k)$.

The assumed form of the baseband measurements for both coherent and non-coherent reception methods are included in Table I below. The form of the least-squares estimators is also given. J represents the number of beams in use, a, α and σ are unknown amplitudes which are parasitic parameters in the estimation. The noise for the coherent system is modeled as Gaussian. For the non-coherent system, the noise is not Gaussian but may be reasonably modeled as such under sufficiently high SNR conditions.

	Signal measurement model	Estimator
Coherent Reception	$\mathbf{z} = a\begin{bmatrix} g_1(T_x,T_y) \\ \vdots \\ g_J(T_x,T_y) \end{bmatrix} + \begin{bmatrix} n_1 \\ \vdots \\ n_J \end{bmatrix}$,	$(\hat{T}_x,\hat{T}_y,\hat{a}_R,\hat{a}_I) = \min_{a,Tx,Ty} \boldsymbol{\varepsilon}^H \boldsymbol{\varepsilon}$ $\boldsymbol{\varepsilon} = \begin{bmatrix} z_1 \\ \vdots \\ z_J \end{bmatrix} - (a_R + ja_I)\begin{bmatrix} g_1(T_x,T_y) \\ \vdots \\ g_J(T_x,T_y) \end{bmatrix}$
Non-coherent Reception	$\mathbf{z} = \alpha\begin{bmatrix} |g_1(T_x,T_y)|^2 \\ \vdots \\ |g_J(T_x,T_y)|^2 \\ \cdots \\ 0 \end{bmatrix} + \begin{bmatrix} E_n \\ \vdots \\ E \\ \cdots \\ E_n \end{bmatrix} + \begin{bmatrix} n_1 \\ \vdots \\ n_J \\ \cdots \\ n_J+1 \end{bmatrix}$,	$(\hat{T}_x,\hat{T}_y,\hat{a},\hat{\sigma}) = \min_{a,\sigma,Tx,Ty} \boldsymbol{\varepsilon}^H \boldsymbol{\varepsilon}$ $\boldsymbol{\varepsilon} = \begin{bmatrix} z_1 \\ \vdots \\ z_J \\ \cdots \\ z_{J+1} \end{bmatrix} - \alpha\begin{bmatrix} |g_1(T_x,T_y)|^2 \\ \vdots \\ |g_J(T_x,T_y)|^2 \\ \cdots \\ 0 \end{bmatrix} - \begin{bmatrix} \sigma \\ \\ \\ \\ \end{bmatrix}$

Table I: Model of measurements and coherent/non-coherent direction estimators

3. Phase-Only Beam Design for Direction Estimation

In the conventional (coherent) monopulse method, three beams are employed: the sum, azimuthal difference, & elevation difference[3]. This set provides a high degree of accuracy at boresight and results in a simple implementation. However, such simplicity is not important in this application. As the difference beams possess a symmetric *power* pattern in one dimension, the set cannot be used in combination with a non-coherent reception method. Historically, reflector antennas which radiate a (spot) beam are adapted to direction estimation using the technique of sequential lobing[3]. Here, the antenna is gimbaled about a point in space in a tight oval pattern to provide samplings of the power pattern of effectively multiple spot beams. One could produce the equivalent effect here by phasing the beamformer to produce spot beams directed to a small set of points about the direction of the ground station. As the full flexibility of the phased array is available to us, one could ask what set of beams provides the best localization performance. Appropriate with the normal operational mode where constant-amplitude weighting across the transmit aperture is employed, only optimization of the phase profile is allowed. Preliminary results on this topic are provided in this section.

The beam design criteria is that of providing a set with a high composite sensitivity to signal position in the two T-space dimensions. This implies that the beam set should have a large gradient with respect to the T_x and T_y directions over the Region Of Interest (ROI). The physical stabilization system of a conventional geo-stationary system *guarantees*, to ~3σ confidence, that the pointing direction is within 0.1 degrees of nominal. With assumed pointing uniformly distributed over this $0.1°$ disk, the optimization approach is to maximize the minimal derivative as described in Table II.

Optimization strategy	Coherent system	Non-coherent system
$\varphi = \max\limits_{\phi} \min\limits_{ROI} \left\{ \dot{G}_x^H(T_x,T_y)\dot{G}_x(T_x,T_y), \right.$ $\left. \dot{G}_y^H(T_x,T_y)\dot{G}_y(T_x,T_y) \right\}$	$\dot{G}_x = \dfrac{d}{d\tilde{T}_x}\left[\begin{array}{c} g_1(\tilde{T}_x,\tilde{T}_y) \\ \vdots \\ g_J(\tilde{T}_x,\tilde{T}_y) \end{array}\right]_{\substack{\tilde{T}_x=T_x \\ \tilde{T}_y=T_y}}$ $\dot{G}_y = \dfrac{d}{d\tilde{T}_y}\left[\begin{array}{c} g_1(\tilde{T}_x,\tilde{T}_y) \\ \vdots \\ g_J(\tilde{T}_x,\tilde{T}_y) \end{array}\right]_{\substack{\tilde{T}_x=T_x \\ \tilde{T}_y=T_y}}$	$\dot{G}_x = \dfrac{d}{d\tilde{T}_x}\left[\begin{array}{c} \left|g_1(\tilde{T}_x,\tilde{T}_y)\right|^2 \\ \vdots \\ \left|g_J(\tilde{T}_x,\tilde{T}_y)\right|^2 \end{array}\right]_{\substack{\tilde{T}_x=T_x \\ \tilde{T}_y=T_y}}$ $\dot{G}_y = \dfrac{d}{d\tilde{T}_y}\left[\begin{array}{c} \left|g_1(\tilde{T}_x,\tilde{T}_y)\right|^2 \\ \vdots \\ \left|g_J(\tilde{T}_x,\tilde{T}_y)\right|^2 \end{array}\right]_{\substack{\tilde{T}_x=T_x \\ \tilde{T}_y=T_y}}$

Table II: Beam optimization strategy

Practical broadband, point-to-point communication using a geostationary satellite may require phased arrays of at least dimension 40x40 elements (2.5 λ spacing). In order to gain general insight into optimal beam design, a small array of size 4x4 was considered. The region of interest was appropriately scaled by a factor of ten (disk of ~1° radius). Using the optimization procedure outlined in Table II, the optimal beam shapes were derived. Figure 1a)-c) show the shapes of the optimal three beams for the non-coherent reception method. Figure 2 shows the "best" beam shape for the three-beam, coherent method. The magnitude pattern applies to all three beams.

A simulation was conducted to assess the performance using the optimal beams relative to conventional shapes. For all cases, the total process time was constant, divided evenly amongst the J beam dwells. A signaling scheme representative of wideband digital communication was employed, with components representative of the RF/IF path modeled. A detailed discussion of the system and signal model are beyond the scope of this paper. The results of a Monte-Carlo simulation are shown in Figure 3, with salient observations included in Section 4 below.

4. Conclusions

The optimal beamforming strategy for non-coherent methods of reception consist of beam shapes very nearly that of spot beams. This is not surprising as the spot beam provides the highest localization of power. The beams are situated nearly at a constant radius from the nominal boresight. For the coherent reception case, conventional monopulse is approximately 20% from optimal in terms of the standard deviation in the location error. The optimal beam set features a common amplitude response with a null situated at the nominal boresight. Although the design provides maximal sensitivity, the estimation process is not robust. A robustness constraint is easily incorporated, taking the form of a minimal imposed gain of the composite beam set across the ROI.

References
[1]   S. Silverstein, "Application of Orthogonal Codes to the Calibration of Active Phased Array Antennas for Communication Satellites," *IEEE Trans. Sig. Proc.*, Vol. 45, No. 1, Jan. 1997.

[2]   S.D. Silverstein, J.M. Ashe, G.M. Kautz, F.W. Wheeler, "Tripulse: An Accurate Orientation/Attitude Estimation System for Satellite Borne Phased Arrays," ICASSP 98, Seattle, WA.

[3]   M. Skolnik, "Radar Handbook," 2nd edition, McGraw-Hill Book Company, NY, 1990
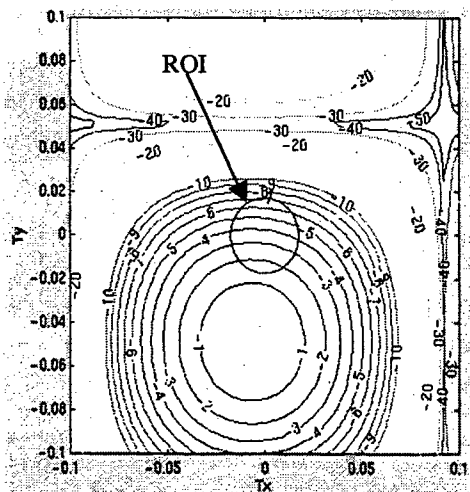
Figure 1a) Best non-coherent, beam 1 of 3
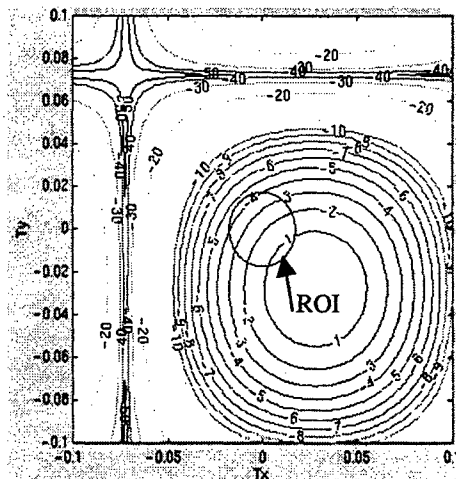
Figure 1b) Best non-coherent, beam 2 of 3
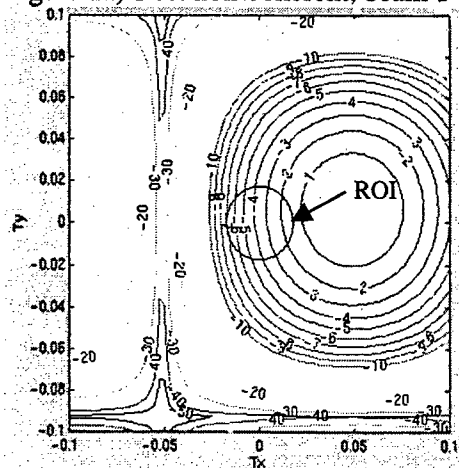
Figure 1c) Best non-coherent, beam 3
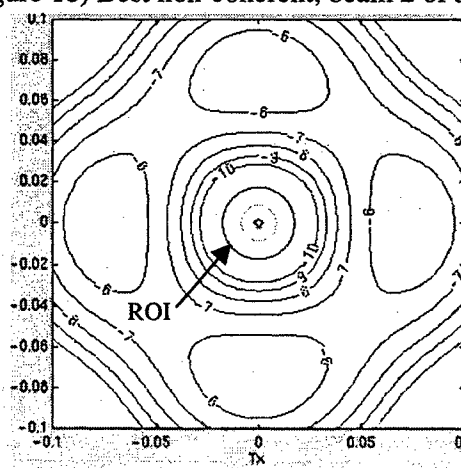
Figure 2) Best coherent, beams 1-3
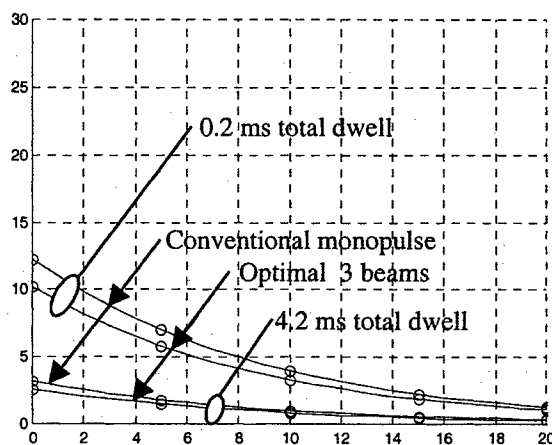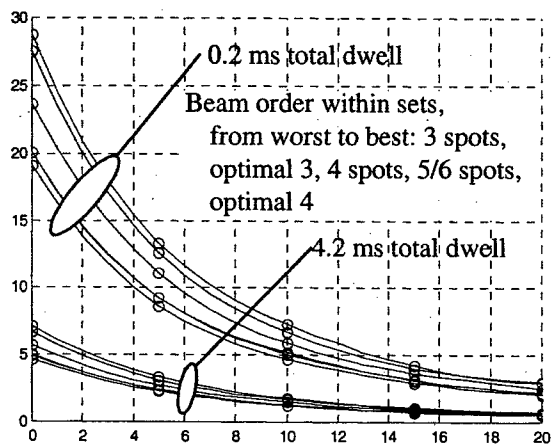
Figure 3: Performance assessment: Left panel: non-coherent, right panel: coherent reception methods.

TA1

Phased Arrays for Satellite Communications

Phased Arrays for Satellite Communications

PHASED ARRAYS FOR SATELLITE COMMUNICATIONS:
A SYSTEM ENGINEERING APPROACH

Dr. Ing. Marco LISI [*]
Alenia Aerospazio – Space Division
Via Saccomuro, 24 – 00131 Roma (Italy)
Phone: +390641512586 – Fax: +390641514336
E-mail: m.lisi@roma.alespazio.it

1. Introduction

Today's space industry is living a very exciting and promising phase of its history, due, to a large extent, to the enormous success of wireless cellular telephony and to the worldwide diffusion of Internet.

The increasing complexity of satellite communication payloads, mainly characterized by the widespread adoption of phased array antennas, and the parallel growth of a strongly competitive, commercially oriented satellite market, caused a marked shift towards new technological and organizational paradigms, such as:

- Concurrent Engineering;
- Design for cost, producibility and testability;
- Modular approach to design;
- Large scale production techniques;
- Short time-to-market.

Phased array antennas require a wide range of state-of-the-art technologies and a large number of electronic equipment, such as printed-circuit radiators, solid-state amplifiers, beam-forming networks (sometimes implemented with Digital Signal Processing techniques), power supply units and power distribution networks.

A system engineering approach to the design and development of phased arrays is hence mandatory in order to achieve a synergic integration of all functions and to implement large-scale production and testing techniques.

In the field of Satellite Personal Communication Networks (S-PCN's), the three main non-geostationary systems (Iridium, Globalstar, ICO), together with some regional GEO systems (e.g. AceS, Thuraya, EAST), triggered a substantial break-through in satellite active phased array techniques [1].

Major advancements were achieved in printed array technologies; receive and transmit RF modules miniaturization and performances; passive Butler matrices and beam-forming networks in multi-layer, printed-circuit technology; digital beam-forming and signal processing techniques; thermo-mechanical design and integration techniques. Moreover, the above mentioned regional GEO satellites will qualify in orbit unfurlable reflectors of up to 15 meter diameter.

Further developments are likely to be required for the future provision of Third Generation (3G) mobile communications via satellite (S-UMTS), as a result of more stringent requirements in terms of link performances (G/T, EIRP) and frequency reuse.

Multimedia LEO constellations, working at Ka-band (Teledesic) and Ku-band (Skybridge), will also rely on the development of active multiple beam antennas in a direct-radiating array configuration.

2. The Phased-Array Antenna as a System

In satellite communications missions where a limited number of medium-gain shaped or spot beams have to be generated on earth, the antenna configuration is usually based on a parabolic reflector illuminated by an array of feeds; the feed array is located in the focal plane of the parabolic reflector geometry.

Whenever multiple high-gain beams are required, such as in case of mobile communications satellites in MEO or LEO orbits, active phased array configurations have to be considered. In an active phased array the reflector and its feed array are most often replaced by a direct radiating array (DRA) of size comparable to that of the original parabolic aperture. The direct radiating array is usually composed of a number of individually-fed array radiators, or subarrays. A phased array is named "active" when each subarray is individually connected to the receive (Low–Noise Amplifiers, LNA's) or transmit (Power Amplifiers, PA's) modules [2].

It is also possible to envision an antenna configuration where a small active array is magnified by a double or single reflector optical system (Imaging Antennas). This second configuration allows, through the magnification effect provided by the reflector optics, a feed array smaller in size and lighter than that required for a DRA; it has to be

---

[*] Senior Member IEEE

noted, however, that the number of controlled feeds (or subarrays)is substantially the same in the two configurations.

It is worth mentioning, because of its widespread use in recent satellite missions (e.g. Inmarsat 3), a third class of active antennas, known as Semi-active Multi-matrix Reflector Antennas [3] [4]. The name "Semi-active" derives from their performance somehow "in between" DRA's and conventional Multi-beam Reflector Antennas. In a DRA all PA's (or LNA's) contribute to the formation of any single beam (unless heavy amplitude weighting is applied to form shaped beams); this implies that the overall RF power can be dynamically shared among the beams (Traffic Reconfigurability). On the opposite end, in conventional focussed reflector antennas each feed (and its corresponding power amplifier) is virtually associated to only one beam, hence traffic reconfigurability is impossible. In Semi-active Multi-matrix Reflector Antennas the number of PA's contributing to any beam is increased by slightly de-focussing the feed array and by using hybrid matrixes in a multi-port amplifier configuration.

With the coming of age of active antennas, the traditional separation in a satellite communications payload between antennas and repeater is disappearing. Moreover, the performance of an active antenna system can not be separated into the contributions of its constituent components, as in conventional designs. A system engineering approach is hence deemed essential for the successful design and development of this type of antennas.

It has to taken in due account that the antenna's architecture, implementation and performance ultimately determine the communications capacity and the spacecraft's physical characteristics, i.e. configuration, weight and size. Therefore, the active antenna configuration best suited to a specific satellite communications mission is to selected on the basis of trade-off analyses on many factors, such as EIRP, G/T, mass, power consumption, overall efficiency and, last but not least, production cost.

3. Satellite Antenna Requirements

Future satellite communications missions will realize the convergence of broadband (multimedia) applications with mobility (e.g. S-UMTS).

Multiple Beam Antennas (MBA's) are required to cope with the gain, beam shaping and frequency reuse requirements of such missions.

Multiple spot beam antennas can provide higher EIRP and G/T than those achievable by regional coverage shaped beam antennas because of their higher gain beams.

Multiple spot beam antennas implement frequency re-use techniques in order to increase the over-all system throughput. These frequency re-use schemes typically utilize a portion of the available bandwidth per beam: one quarter or sometimes as much as one third (4:1 and 3:1 frequency re-use schemes). The same spectrum can be re-used multiple times over the multiple beam coverage area. In practice, frequency re-use is limited by the achievable beam to beam isolation and interference rejection.

As far as mobile satellite communications are concerned, The EIRP from handsets is limited because of radio frequency power density limitations by International Telecommunications Union (ITU) Radio Regulations. Health and safety standards also constraint power.

The return link margin (from the handset to the satellite) is the most critical for reliable communications. As the receiver noise figure is limited by device technology, satellite antenna receive gain is one of the most important parameters in system design.

The forward link is less critical since satellite EIRP is usually only restricted by power flux density (pfd) limitations in the ITU radio Regulations. These limits depend on the elevation angle. Since acceptable pfd levels are reduced at low elevation angles, the peripheral beams in a satellite antenna multiple-beam coverage are then more likely to exceed the specified pfd values and should hence roll off rapidly.

Antenna systems for MEO and LEO satellite constellations require quite demanding scanning capabilities, being the Field of View (F.O.V.) up to +/- 60 degrees. In these applications Direct Radiating Arrays (DRA's) are preferred to reflector MBA configurations, as they provide better off-boresight performance (lower scan loss) and consequently lower mass (smaller apertures and fewer controlled elements are required).

4. Phased Array Antenna Components

A phased array antenna is a complex assembly constituted of many active and passive components [5].

The widespread development of active phased arrays in the recent years largely depends upon the use of highly efficient and uniform monolithic microwave integrated circuit (MMIC) amplifiers. Novel packaging and interconnection techniques allow MMIC amplifiers to be directly coupled to the radiating elements, thus substantially reducing signal losses and resulting in very high G/T's or EIRP's.

The dominant component, the true "hearth" of all phased array antennas is the Beam Forming Network (BFN) [6].
A "passive" BFN generates a time invariant set of spot beams of different shapes; in one such network amplitude and phase coefficients are fixed at time of design. An "active BFN allows on-orbit control of amplitude and/or phase excitation coefficients; this type of network, generating M beams and interfacing N radiating feeds, will need M x N control elements (variable phase shifters and variable attenuators, most often in MMIC technology).

As far as passive BFN's are concerned, the state-of-the-art technology is that of multi-layer caseless microwave circuit design with inter-layer connections. The three dimensional nature of the multi-layer approach allows flexibility in packaging topography as well as input/output port location. Utilizing a lamination process in autoclaves under high pressure and high temperature conditions, the multi-layer stack of "soft" material substrates is fused into a solid, high integrity assembly.

Some Beam Forming Networks (BFN's) for DRA's are based on a two-tier configuration: an upper tier Beam Forming Matrix (BFM), based on a two-dimensional Butler matrix, and a lower tier Beam Combining Network (BCN), as a multiple layer stripline circuit, combining a number (typically seven) of orthogonal beams (beamlets) to form a shaped "composite" beam ("beam synthesis" technique).

5. Mechanical and Thermal Design Aspects

The thermal design of active phased array antennas to be flown on LEO or MEO satellites has to cope with the fact that for three quarter of the time DC power consumption and associated thermal dissipation are usually small over the oceans, to rapidly rise to very high levels over land areas, especially if densely populated. In order to avoid the sizing of the thermal radiating panels for the periods of peak traffic, the adoption of heat sinks with high thermal capacity and of integral heat pipes to drain the generated heat towards the radiating panels is advisable.

As far as mechanical design is concerned, ease of assembly is achieved through the adoption of self-indexing and self-aligning techniques at modules level and the use of commercially available precision blind-mate connectors and adapters (e.g. the GPO ^{TM} type).

6. Digital Beam-Forming Techniques

The adoption of digital signal processing architectures strongly suggests multiple beam antennas based on Digital Beam Forming (DBF) techniques. Such techniques allow the implementation of phased-array antennas (both in a Direct Radiating Array or in an Array-Fed Reflector configuration) with full control of their potential capabilities, i.e. beam steering and shaping, interference rejection, nulling, etc..

Given the requirement for increased beam gain, deriving from the higher data rates being handled, the combination of digital beam-forming and digital signal processing, already adopted in the ICO MEO satellites and in regional GEO satellites of Second Generation (such as Garuda, Thuraya and EAST), might result as on optimal choice for S-UMTS satellites in similar orbits, although at the expense of additional on-board mass, power consumption and complexity.

7. Assembly, Integration and Test of Phased Array Antennas

The testing of active antennas and of communication payloads integrating active antennas involve a series of technical problems, both for the wide variety of technologies adopted at component level and for the large number of parts being integrated.

Passive antennas are usually verified in terms of their radiated characteristics, such as radiation patterns and directive gain, and do not require the test of such parameters as EIRP, G/T, Gain and Group Delay variations vs. frequency, since these parameters are more meaningfully assessed at overall payload level.

On the contrary, active antennas integrate active components (SSPA's, LNA's) and narrow band components (filters), which heavily affect the end-to-end performance of the payload.

A typical Assembly, Integration and Test (AIT) flow applicable to flight model active antennas is that adopted at Alenia Aerospazio for the production of the Globalstar L and S-band active phased array antennas [7]. After integration of all components except for the radiating array, the partially integrated active antenna is hard-line tested (S-parameters) to check the correct integration of the Beam-Forming Network (BFN) and the active modules.

In the Hard-Line test stations, robotic arms are used in conjunction with radiofrequency test systems, with high performance in terms of test velocity and repeatability.

The active antenna is then completed with the installation of the radiating array and environmentally tested (thermal cycling and vibrations).

The final steps are the pattern verification in the Near-Field range and the telecommunication performance verification in the Far-Field range.

At integrated spacecraft level, the end-to-end performance testing of communication payloads integrating active antennas requires the realization of a radiated interface.

One possible implementation of such interface, particularly suitable to the high-rate check-out of communication payloads, is that constituted of a small anechoic chamber and of a number of probes sampling the near-field of the active antennas.

8. Large Scale Production of Phased Array Antennas

In a competitive global environment the space industry is currently transitioning from a not yet forgotten past when it was funded mostly by public institutions (national space agencies, international organizations, departments of defense, etc.) to a very near future when funds will have to be raised entirely from private shareholders.

Commercial investors participating in satellite ventures will require high internal rates of return (IRR's) to compensate for the high risks and long development times often associated with many space projects.

Competitive products need to be on the market at the right time and with the right price. To this objective, reductions in development and deployment times are a must.

The realization of satellite constellations for mobile or multimedia communications asks for large number of spacecraft's to be produced in a very short time. The traditional concepts for space production are no longer adequate to meet the requirements of these innovative projects, hence new approaches to design and to production are needed.

In Europe a good example of this evolving mentality is the Small Satellites Center, the production plant developed by Alenia Aerospazio in the frame of the Globalstar project.

Located in Rome near other Alenia Aerospazio production sites for easy access to consolidated expertise in specific related disciplines, this plant of new conception, expressly conceived for the large scale production of spacecraft's and payload subsystems, covers an area of 6,000 square meter and includes a 4,000 square meter clean room (class 100,000), maintained at controlled environmental conditions.

The approach selected for the assembly, integration and testing (AIT) of small spacecraft's and of active phased array antennas is based on the concept of «islands», i.e. working areas where a series of homogeneous activities is performed.

The Small Satellites Center is equipped with a complete set of electrical and environmental test equipment able to check spacecraft and payload behavior in their real operative conditions. More specifically, for the radiated testing of the active phased array antennas, completely automated Near-field and Far-field test ranges were realized.

Most of the test equipment is in fact automated and connected to a Data Management System (DMS) to collect and analyze test results.

Some of the most innovative management and quality control methodologies, such as Concurrent Engineering, Total Quality Management (TQM) and Statistical Process Control (SPC), were successfully applied, building into the organization a culture of quality awareness, continuous improvement and constant learning.

9. Conclusions

A synthetic overview of the most fascinating topic of phased array antennas for satellite communications was presented.

A system engineering approach to the design and development of phased array was shown essential in order to achieve an effective and synergic design and to implement large-scale production techniques.

It is an author's firm opinion that a broadband technical background and an open, "laterally thinking" mentality are key factors for the successful design, development and production of active phased arrays.

References

[1] M. Lisi, "Satellite Communications Systems in the 90's and for the Next Millenium, MEE, May 1999

[2] A. I. Zaghloul et alii, "An L-band Active Array System for Global Coverage", Comsat Review, Spring 1985

[3] M. Lisi, "An Introduction to Multiport Power Amplifiers", MEE, February 1992

[4] A. G. Roederer et alii, "Some European Satellite-Antenna Developments etc.", IEEE APS Mag., April 1996

[5] P. L. Metzen, "Satellite Communication Antennas for Globalstar", JINA 1996

[6] M. Lisi, "Beam Forming Network Technologies for Satellite Multibeam Antennas", 17th EuMC , 1987

[7] M. Lisi et alii, "Large Scale RF Testing of Active Antennas and Payloads", AIAA ICSSC 1997

Design and Performance Assessment of Active Phased Arrays for Communications Satellites

A.I. Zaghloul, R.K. Gupta, E.C. Kohls, and O. Kilic
COMSAT Laboratories
Clarksburg, MD, 20871 USA

Abstract:

This paper discusses the use of active phased arrays for communications satellite systems that require simultaneous multiple beams. The design of the complete phased array aims at satisfying the system requirements. The emphasis in the paper is on the evolution of the MMIC-driven highly modular technologies at Ku-, C- and X-bands. The paper reviews the designs of the different arrays in the development programs.

Introduction:

The design of the satellite antennas depends on the beam definition, which in turn is a function of the system capacity and projected traffic patterns. Several systems require a large number of fixed narrow spot beams to cover the service area. A single reflector with a large number of feeds may provide such coverage. However, if the scanning loss is excessive due to the large number of beams scanned in one direction, multiple reflectors may be required. Alternatively, single or multiple phased arrays may be used. The phased array may have lower scan loss and a single phased array can handle a large number of beams. The phased array solution also offers higher reliability due to the use of the beam former versus the switching arrangement in a focal-region-fed reflector antenna. For a small number of beams at a time, a microwave beam former represents a simple and attractive solution, while if the number of beams is large a digital beam former is a more viable alternative. In many applications the choice between the microwave and the digital beam formers becomes a payload system issue.

Active phased arrays can also meet high flexibility requirements which are becoming the feature of future communications satellites. Among the flexibility requirements are the ability to form multiple beams, provide power-sharing among beams through distributed amplification, and rapidly reconfigure and/or repoint the beams. The requirements also include high reliability and the ability to readjust the feed or array coefficients to compensate for component failures. The conventional drawbacks of active antennas pertaining to mass, nonuniformity of performance of a large number of elements, and reliability have been largely overcome by the advances in monolithic microwave integrated circuits (MMICs), printed-circuit antennas and digital beam forming networks. The MMICs allow the beam-forming network, which may include signal conditioning circuitry such as MMIC phase shifters and attenuators, to be incorporated in a lightweight transmission medium. The resulting antenna configurations have the potential for dramatic reductions in mass while providing increased efficiency, flexibility, and capacity. Similar features apply also to digital beam formers.

COMSAT Laboratories initiated an evolutionary research and development program to assess the feasibility of implementing MMIC-driven active phased-array antennas on future high-capacity communications satellites. A number of advanced concepts employing active phased arrays have been investigated. Among the first arrays developed during this effort is a Ku-band array using 64 elements to produce a single reconfigurable shaped beam. A second array, also at Ku-band, uses higher power SSPAs feeding 24 elements to produce four simultaneous and independently steerable spot beams [1]. A third array in this effort is a 69-element high-power C-band array, designed to produce eight simultaneous and independently shaped and steerable beams [1]. A fourth 8-element array was designed at X-band and built as a proof of concept for a four-beam array providing spot coverages over the earth disc [2]. The Ku-band arrays use dual-linearly polarized square horns as the radiating elements, while the C- and X-band arrays use circular polarizations produced by printed circuit radiators and scalar ring horns, respectively. Three of the four arrays are described in the following sections.

Ku-Band Multiple-Beam Active Phased Array:

A Ku-band array consists of 24 active radiating elements, each equipped with orthomode transducers OMTs for dual-linear polarization [1]. This array represents only a portion of the actual array that would be required to achieve typical INTELSAT zone coverages. Figure 1 shows the complete array assembly. In some implementations, the array will be

required to form a number of simultaneous and independent beams. Thus, a beam-forming matrix (BFM) is used to satisfy this requirement. Directly behind each element is a 2-W SSPA. The SSPAs are located in separate housings which are mechanically cooled by a liquid cooling loop that simulates the use of heat pipes for space application. The output of the amplifiers are probe coupled to the input of the OMTs. The inputs to the amplifiers are connected to the respective outputs of the BFM, which is capable of forming four simultaneous beams. Each beam is independently steerable through the use of digital phase shifters located in the BFM. The logic circuitry necessary to drive and store the respective states of the phase shifters is also located within the BFM. The
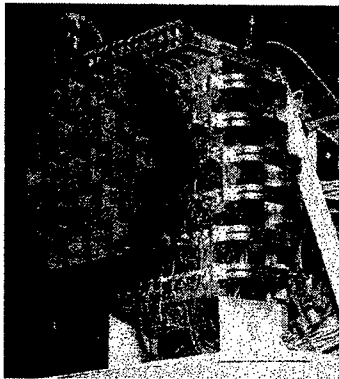
SSPA and BFM designs both make extensive use of MMICs. The signal path from the output of the BFM to the input of the amplifiers is provided by phase-matched RF cables.

Figure 1. Ku-Band Active Phased Array

The BFM consists of four 1-to-24 way power dividers and 24 four-way power combiners. Each transmission path in the BFM consists of an MMIC 5-bit phase-shifter module, input and output distribution networks. A total of 96 MMIC phase-shifter modules are located in the BFM housing.

A modular architecture was selected for implementation of the MMIC-populated BFM in the form of 4-input, 8-output shelves, corresponding to the four beams and eight elements, respectively. The three shelves are identical in assembly and performance. Each shelf shown in Figure 2 contains four 1-to-8 way dividers, eight 4-to-1 way combiners, thirty-two MMIC phase-shifter modules and associated control electronics. Four 1-to-3 way dividers distribute the signals for each beam to the three shelves. The input plane of the BFM shelf contains four eight-way Wilkinson dividers and MMIC phase shifter modules. The MMIC phase-shifters are assembled on separate carriers for individual testing. The output plane of the BFM shelf

also contains the phase-shifter driver and level-shifter electronics which is mounted on multilayer alumina boards. The ground plane in the middle serves as an RF and DC ground and also provides isolation between input and output planes.
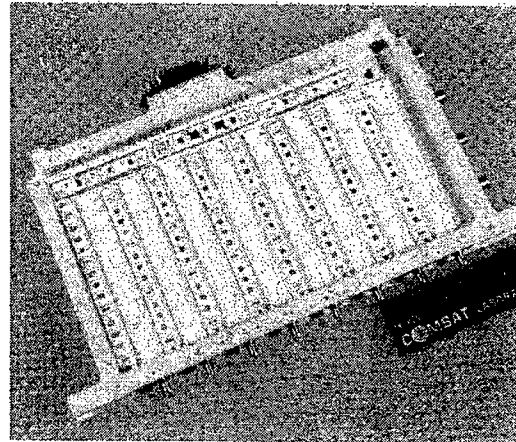
Figure 2. 4 X 8 Shelf in Ku-Band BFM

This design approach for the BFM provides several advantages including modularity, reproducible assembly and performance. Broadband Wilkinson dividers and combiners provide inherently good amplitude and phase balance between the paths. Furthermore, path-to-path insertion loss variations can be minimized by the appropriate selection of MMIC phase shifter modules so that low loss phase shifters are matched with high loss paths, and vice versa.

The power amplifier design combines MMIC and quasi-monolithic technology to achieve optimum DC-to-RF conversion and linearity, while simultaneously meeting output power and size requirements. The amplifiers are designed to be integrated directly in back of the array to minimize total output losses.

C-Band Multiple-Beam Active Phased Array:

The linearly polarized Ku-band array described above demonstrated the concept of active phased arrays for communications satellites. It used large pyramidal horns as the radiating elements. One of the most desirable features which has to be achieved is light weight. Because the size of the array can be large, especially at lower frequencies, the need for compact, lightweight radiating elements became paramount. The next array in this development series used printed-circuit patch radiators in order to achieve this goal. The array, shown in Figure 3, was designed at C-band (3.6-4.2 GHz) and featured printed-circuit radiators, a highly modular approach for the beam forming matrix as well as for the active aperture, and

an integrated thermal control system [1]. The array consists of 69 electromagnetically coupled patch (EMCP) elements, each producing two orthogonal circular polarizations. The elements are fed with 2-Watt SSPAs which are integrated in the array structure. The BFM provides independent control of eight simultaneous beams.
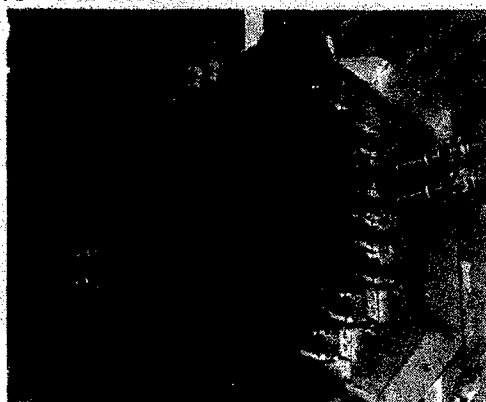
Figure 3. C-Band Active Phased Array

The array active elements demonstrates a high level of integration. The integrated element includes the EMCP radiating element, redundant SSPAs, MMIC gain blocks, redundancy switches, and monitoring circuit at the SSPA output. The SSPA consists of a high-efficiency power amplifier preceded by multistage MMIC preamplifiers and an MMIC linearizer to predistort the signal such that high linearity is achieved simultaneously with the required efficiency.

The active array is controlled by a 8X69 BFM which consists of nine 8x8 shelves and accommodates up to eight beams connected to a maximum of 72 elements. For the 69-element array, three outputs are match terminated. The modular architecture of the Ku-band BFM described above has been further enhanced by implementing the C-band BFM shelf with eight 1x8 BFM modules. Each of these modules is realized by modular MMIC packages, each containing phase and amplitude control elements and associated digital control for each BFM crosspoint. This additional modularity further offers improved design flexibility for larger size BFMs, ease of repairability and reduced manufacturing costs. The 8 x 8 shelf, shown in Figure 4, is composed of eight 1x8 BFM modules on the top side and eight 8-way power combiners on the bottom surface. Each 1x8 BFM module is an independently testable unit and includes the control circuits for eight MMIC packages and also provides the RF signal paths from the top to the bottom of the BFM shelf. Each 1x8 module consists of an eight-way power divider, eight MMIC packages and the digital control circuits. The most basic building block

of the BFM is the MMIC package, shown in Figure 5, which contains an MMIC 5-bit phase-shifter, a 5-bit MMIC attenuator and three digital control ICs. This MMIC package can be individually tested and hermetically sealed to provide a ruggedized design.
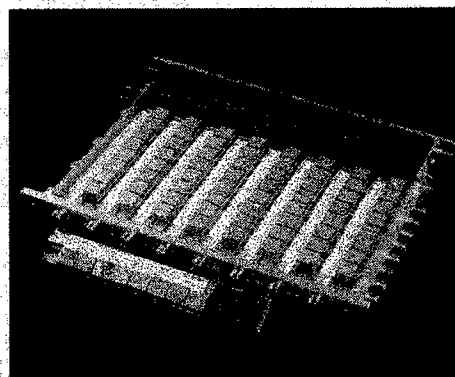
Figure 4. 8 X 8 Shelf in C-Band BFM
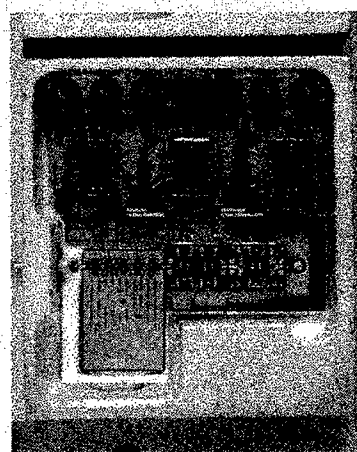
Figure 5. Basic C-Band MMIC Module

X-Band Multiple-Beam Active Phased Array:

A proof-of-concept subarray was developed to demonstrate active phased arrays at X-band, where the transmit and receive frequencies of operation are closer than the corresponding ones at C- and Ku-bands. The subarray consists of eight elements in two rows composed of four scalar ring horns each [2]. The elements are arranged in a triangular lattice with the horns tangent to each other. The array element is sized in accordance with scanning over the angle subtended by the face of the earth as viewed from the geostationary orbit ($\pm 9°$) without forming interfering grating lobes. Since the beams utilize the same set of power amplifiers, they share the same available power pool, with each beam capable of flexibly drawing upon the pool for the amount of power required to support its traffic.

The antenna, shown in Figure 6 is composed of three parts: the modular active radiating element which also incorporates the 2-Watt SSPA, the BFM which is positioned in the middle of the array, and the chassis which also provides thermal control for the array. The BFM and the elements are interconnected by means of a set of phase matched cables. The array chassis serves a dual purpose: to support the elements, and serve as a heat sink for the power amplifiers. The reverse side of the chassis includes a set of fins which are located directly beneath each SSPA. A pair of blowers positioned at the end of the chassis cool the array by forcing air over the heat fins. The heat fins are designed to provide sufficient cooling to maintain the temperature of the amplifiers FETs at the temperature of 110°C.
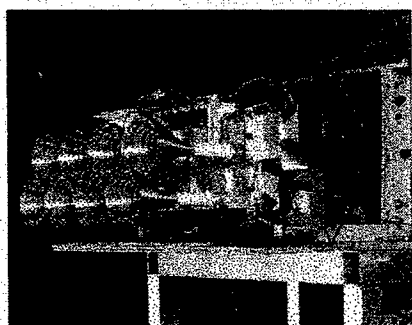
Figure 6. X-Band Active Phased Array

The active radiating element consists of a scalar ring horn radiator, its polarizer, a feed section, and an amplifier housing that serves as the input to the element and contains the SSPA along with the microstrip-to-waveguide transition. Together the feed section and the amplifier housing constitute the OMT of the radiating element. This structure provides input to two polarizations while maintaining a high degree of port-to-port isolation and a good input match. The element is fabricated in these four separate parts which are assembled after being tested separately.

The BFM design is similar to the one used for the C-band array described above. The BFM architecture is easily expandable to a larger size, as would be required for the complete array. The modularity of the BFM also enhances its manufacturability. The RF circuits, power distribution, and controller architecture all provide a substantial level of fault tolerance, to minimize the propagation of failures from one cross-point to others. The BFM consists of two 1 x 8 modules on the front side and eight 2-way power combiners on the back. Each 1 x 8 module is independently testable, including the associated

control circuits. The housing for the 2 x 8 unit represents a shelf. Larger BFMs use a number of shelves which are connected through power dividers.

The SSPA assembly, shown in Figure 7, consists of a two-stage MMIC driver and power chips in cascade to achieve an overall gain greater than 40 dB. The individual stages of the overall SSPA were designed for a compromise between linearity and efficiency performance. The MMIC design approaches and circuit layouts are chosen to minimize the impact of process variations on the circuit performance. This approach is necessary for maintaining performance uniformity over all the modules required for the antenna array.
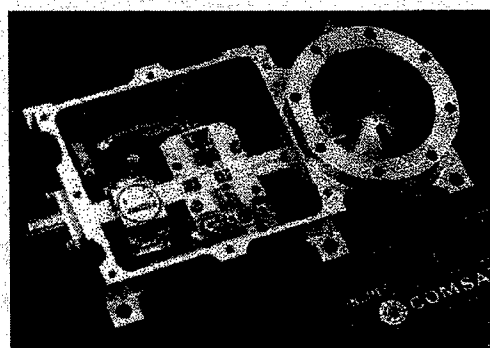
Figure 7. X-Band SSPA

Conclusion:

This paper presented an overview of a progressive development of active phased arrays for satellite applications. Ku-, C- and X-band arrays represent an evolutionary process for the highly modular, highly integrated active array design. The arrays demonstrated the use of MMICs in the active circuit modules to control the amplitude and phase distribution across the array aperture and in the SSPA modules to achieve the required EIRP. These arrays represent a significant departure in antenna architecture from existing multibeam reflector antenna designs. The hardware demonstration validates the advanced antenna concepts which can be considered for flexible communications satellite systems. Some of these concepts have found their way to implementations in recent multiple-beam satellite systems such as Iridium and Globalstar. These concepts will find more applications in high-capacity multiple-beam systems for both commercial and military applications.

References:

[1] A.I. Zaghloul, R.K. Gupta, F.T. Assal, J.E. Martin, and S.B. Wernek, "Active Phased-Array

Development at C- and Ku-Band," AIAA 15th Internatl. Comm. Sat. Sys. Conf., San Diego, CA, February/March 1994.

[2] A.I. Zaghloul, L. Sichan, J.I. Upshur, G.C. Estep, and R.K. Gupta, "X-Band Active Transmit Phased Array for Satellite Applications," 1996 IEEE Internatl. Sym. on Phased Array Sys. and Tech., Boston, MA, October 1996.

EIRP and C/I Analysis of Multibeam Active Phased Array Transmit Antennas for Communication Satellites

Daniel S. Purdy* and Erik Lier
Communications and Power Center
Lockheed Martin
100 Campus Drive
Newtown, PA 18940

Abstract -- A comprehensive model was developed to analyze performance of a multibeam active phased array antenna used in a high traffic capacity, TDMA satellite communications system. The model includes the effects of intermodulation distortion, sidelobe level interference, partial array failure, pointing errors, and amplitude and phase errors. The performance of a Ka-Band 64 beam satellite antenna system based on a modular tile approach was assessed in terms of C/I and EIRP performance. The results presented show the graceful degradation characteristics in high communication traffic applications in terms of partial array failures and array errors.

Introduction

Effective Isotropic Radiated Power (EIRP) and Carrier to Interference (C/I) are two important performance parameters that must be considering when designing a satellite antenna. This paper investigates the performance issues regarding active array performance in the presence of high communications traffic capacity requirements as would be expected in a multibeam system with hopping beams. For active arrays it is especially important to consider the array performance over the life of the satellite, including performance degradation due to thermal effects and aging. In this paper the overall performance of the array is summarized as failures and errors occur thus impacting the system performance. The satellite transmitter antenna system was assumed to consist of four active phased arrays that utilize frequency reuse, polarization reuse, and beam hopping in the multibeam application.

Analysis

The active phased array considered in this analysis is comprised of 'tile' architecture, where a tile is defined as a 20x20 wavelength section of the phased array that is feed by a single RF cable for each beam. Each antenna is assembled from a 5x5 tile array with the corner tiles removed forming the 21 tile array shown in Figure 1. The results presented in this analysis include a 1.0 dB RMS amplitude error, and 12 degrees RMS uncorrelated phase error among array elements. A beam forming network (BFN) is utilized to provide multibeam performance, with 4 beams per frequency channel at a given polarization sense. This results in an active array antenna providing 16 independently steered beams. Each satellite has 4 active phased arrays with 2 operating at each of the orthogonal polarization

senses, forming 64 total beams. The satellite antenna system therefore is assumed to provide a total of 8 beams occupying a given frequency channel and polarization. The antenna is assumed to have a 0.05° RMS pointing error over the beam service cell on the ground.

Each of the 64 beams are steered to earth cell locations, designated by a specified template. In order to maximize traffic capacity in densely populated regions it is desirable to place cells as close together as possible. The template under study consists of 2 clusters of 4 cells shown in Figure 2. The cells shown represent 8 co-frequency and co-polarized beams which provide desired power density at receiving terminals within the cell. In order to maximize efficiency it is further desirable to maintain a uniform level of saturation across all small signal power amplifiers (SSPAs) within the transmit array. Since the aperture is assumed to have uniform amplitude weighting and inherently high sidelobes, the technique of phase synthesis (optimization) must be employed to reduce sidelobe levels within co-frequency and co-polarized beams.

A Monte Carlo computer model was developed to simulate the transmitter antenna system performance in terms of EIRP and C/I. Since the interfering signals can be treated as uncorrelated total interference is obtained by summing the interference powers. The power contained in the interference signal for the C/I analysis is calculated by

$$I = I_{IMD} + I_{SL} + I_{XPOL} \tag{1}$$

where I_{IMD} is the intermodulation distortion due to amplifier nonlinearity described by [1,2], I_{SL} is the sidelobe energy interference due to co-frequency co-polarized cells, and I_{XPOL} is the cross-polar and co-frequency interference due to the radiating element. The small signal amplifiers were experimentally measured in the 1dB back-off nonlinear region and the data were incorporated into the envelope model. All 3rd order intermodulation products were retained in the analysis for signals passing through the same small signal power amplifier. Other interference factors such as spectral re-growth and inter-satellite interference are not presented in this analysis.

Results

Given the above antenna system and cell template, two parameters were investigated including tile correlated phase errors and tile failures. Thermal gradients may effect the phase of the signal due to changes in path lengths of the RF cable and BFN. Tile correlated phase errors were used to simulate the performance of the array due to thermal, aging, manufacture and mechanical tolerance effects. Figure 3.a shows EIRP degradation as the tile correlated errors vary from 0 to 25 degrees. Shown are both the 50-percentile degradation and the 95-percentile (2 standard deviations) for all 8 beams in the template. A similar plot shown in Figure 3.b is the C/I degradation as a function of correlated phase

errors over the tile. A 10 degree correlated phase error will result in EIRP and C/I degradation of about .3 dB and 1.2 dB respectively.

For satellite communications system it is especially important to assess system performance in the presence of partial array failures, as summarized in Figures 4 and 5. When a tile failure occurs and one has knowledge of which tile failed, the phase can be re-optimized and performance of C/I and EIRP recovered to achieved the best performance possible. As shown the failure of one tile can result in an EIRP degradation of 0.4 to 0.8 dB EIRP, depending on the location of the failed tile. In failure mode the degradation of C/I is dependent on the location of the failed tile. Failure of the inner tile (#13) can result in a 0.5 dB C/I degradation while failure of an outer tile (#15) has no adverse effect on C/I.

Acknowledgments

References
[1] W. Sandrin, "Spatial Distribution of Intermodulation Products in Active Phased Array Antennas," IEEE Transactions on Antennas and Propagation, November 1973.
[2] O. Shimbo, "Effects of intermodulation, AM-PM conversion, and additive noise in multicarrier TWT systems," Proc. IEEE, vol. 59, pp. 230-238. Feb. 1971.

	22	23	24	
16	17	18	19	20
11	12	13	14	15
6	7	8	9	10
	2	3	4	
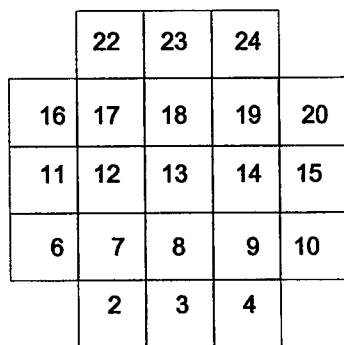
Figure 1.
Active array tile designations.
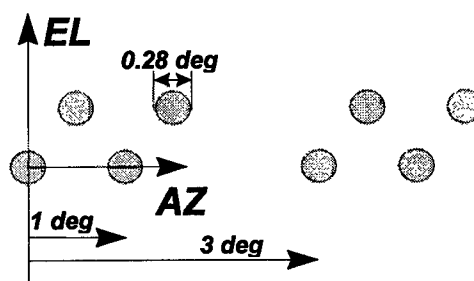
Figure 2. Frequency reuse cell
template used in the simulations.
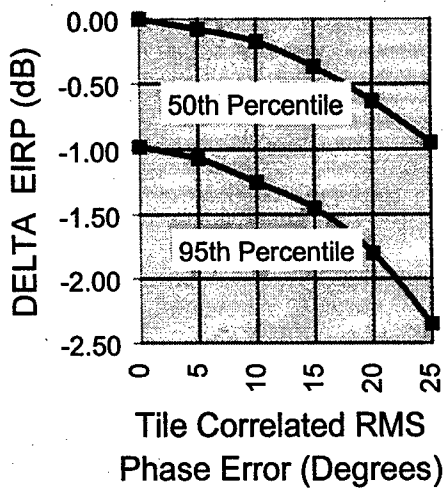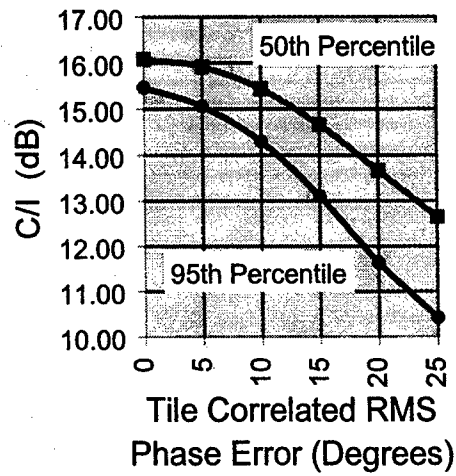
Figure 3.a.   Figure 3.b.

Figure 3. System performance degradation as a function of tile correlated phase errors.
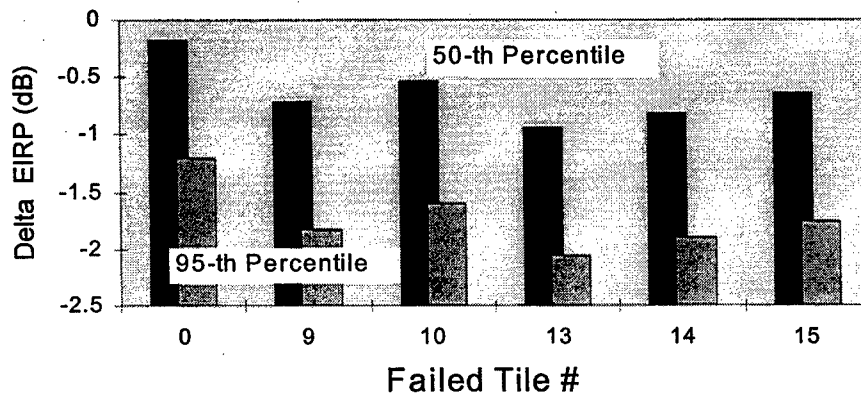
Figure 4. EIRP degradation during tile failure mode. A 10 degree tile correlated phase error was assumed (normalized to no phase errors).
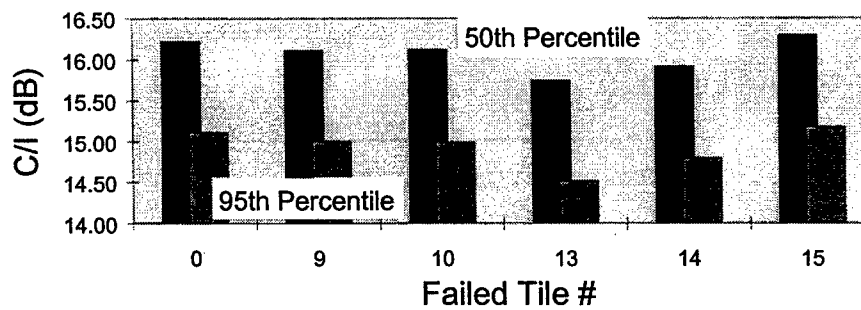
Figure 5. C/I degradation during tile failure mode. A 10 degree tile correlated phase error was assumed.

Globalstar Satellite Phased Array Antennas

P. L. Metzen, Space Systems/Loral

Introduction

The Globalstar worldwide satellite system will provide voice, facsimile, paging, and data transmission to subscribers with hand-held mobile and fixed services, covering locations in all areas of the world except the far reaches of the Arctic and Antarctic. The complete system is a constellation of 48 three-axis-stabilized satellites located in low Earth orbit at an altitude of 870 miles. The Earth subtends an angle of ±55° from nadir at this altitude. Each satellite weighs about 1012 pounds and orbits the Earth in 114 minutes. Mission life is 10 years, after which the satellite will be raised to a higher orbit. Globalstar is a trademark of Globalstar, L.P. All rights reserved.

Globalstar Communication Antennas

The communication antennas, located on the Earth-facing deck of the satellite, consist of multibeam active L-band receive and S-band transmit array antennas. Figure 1 presents a view of the Earth deck of the Globalstar satellite, including the transmit and receive array antennas. The receive and transmit array antennas communicate directly with the subscribers.

The active multibeam transmit array antenna forms 16 simultaneous circularly polarized beams, covering the visible Earth with isoflux radiation patterns, as shown in Figure 2. The hexagonal shape of the antenna results from the use of an equally spaced triangular lattice array of 91 radiation elements. Figure 3 presents an electrical block diagram and Figure 4 presents an exploded view drawing of the S-beam active transmit antenna. Each radiating element input is connected to the output of a small module containing a Solid State Power Amplifier (SSPA) and a bandpass filter. The 91 modules are mounted on a solid Beryllium heat sink. DC bias and control lines in the form of multilayer printed circuit boards are also mounted on the heat sink. Integral heat pipes in the heat sink and external radiation panels complete the thermal control system. Inputs to the 91 modules are connected through the heat sink to the 91 output ports of the Beamforming Network (BFN). Figure 5 presents the RF interfaces of the Globalstar S-band multibeam active transmit array. Phase-only equal-amplitude beamforming is used to avoid the phase errors associated with SSPAs driven at different input amplitudes. The BFN has 16 input ports with each input producing one of the 16 independent beams. Ease of assembly is achieved through the reduction in the number of piece parts, the use of captured quarter-turn fasteners, the self-indexing and self-aligning features on the modules, and the use of commercially available precision GPO™ blind-mate connectors and adapters. Figure 6 is a photograph of an S-band array antenna engineering development model with one of the radiating array sections (containing 15 of the 91 radiating elements) removed, exposing the internal components.
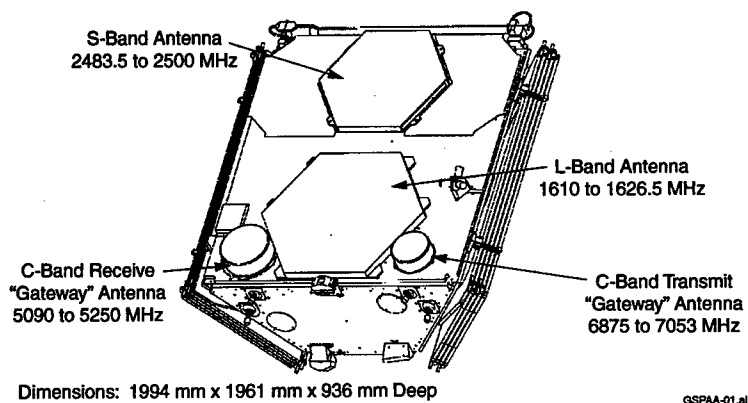
Figure 1. Globalstar Satellite with Solar Panels in Stowed Position
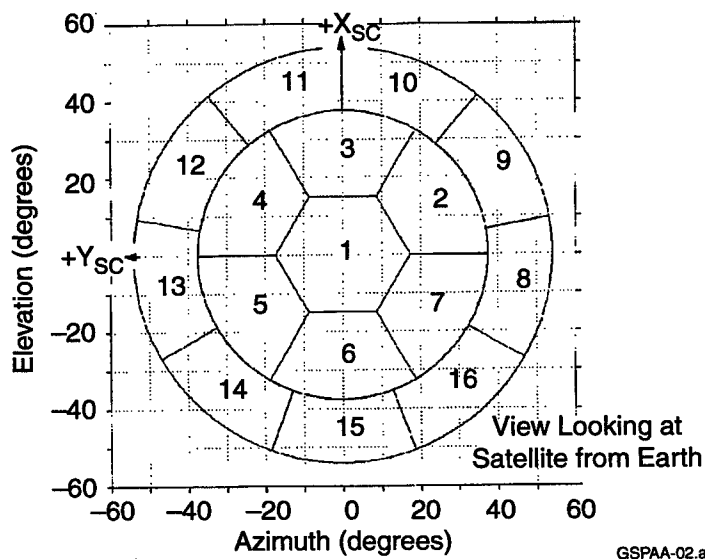
Figure 2. Globalstar S-Band Transmit Array Antenna Pattern Coverage Requirement

The transmit antenna's BFN is composed of 16 equal-amplitude 1-to-91 Strip Transmission Line (STL) power dividers and 91 interconnected equal-amplitude 16-to-1 STL power combiners, resulting in 16 input beam ports and 91 output array ports. Independent fixed-line-length "trombone" sections in the 1-to-91 power dividers are used to set the required phase values for the beam shapes. Figure 3 includes a block diagram of the BFN assembly. A one-piece 68-copper-layer composite BFN is formed by bonding the individual photo-etched Teflon Fiberglass (TFG) STL layers under pressure and at an elevated temperature. Figure 7 presents one photo-etched copper layer of the S-band BFN. The inner area of this 0.020 inches thick TFG board contains a 1-to-91 equal-amplitude power divider with a trombone phase-setting section located at each of the 91 outputs. The combination of the 1-to-91 power divider and the 91 trombone sections is used to establish the correct phase and amplitude necessary to produce one of the 16 required beams. The 16 photo-etched 1-to-91 power dividers required to form 16 beams are identical, while each trombone phase-setting section is unique. The outer area of the board contains one layer of the 91, 16-to-1 power combiners. The power combiners are formed vertically through the 32 board STL stack, as shown in Figure 8. An STL distribution circuit composed of two hexagonal-shaped 0.060 inch thick TFG boards is used to route the 91 signals from the periphery of the 22 inch-diameter BFN stack of 32, 0.020 inch boards to the correct SSPA input. Figure 9 is a photograph of the underside of an S-band antenna array engineering qualification model with the BFN visible. The measured BFN is 24.1 mm thick excluding the connector plate, the hexagonal section is 25 inches from flat to flat, and the mass is 40.5 pounds. There are no internal solder joints or vias passing through more than two boards. This approach results in a singular, compact, accurately reproducible, robust, high-reliability part with good, repeatable RF performance.

As shown in Figure 6, the transmit radiating array assembly is composed of 91 individual radiating elements. The radiating elements are photo-etched STL annular slot radiators operating in the dominant TE_{11} coaxial transmission line mode. Two orthogonal probes excite the slot radiator through the use of a STL branch-line coupler to produce circular polarization. For ease of assembly, the hexagonally shaped array assembly is constructed in six "pie-shaped" sections.
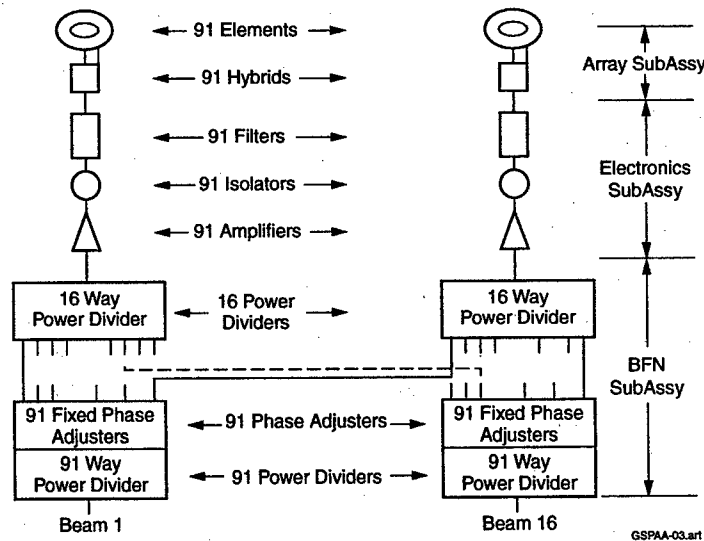
Figure 3. Electrical Block Diagram of S-Band Multibeam Active Transmit Array Antenna
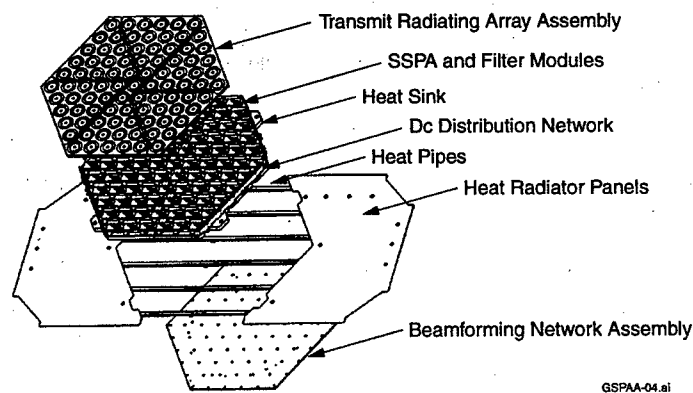
Figure 4. Exploded View of S-Band Multibeam Active Transmit Array Antenna
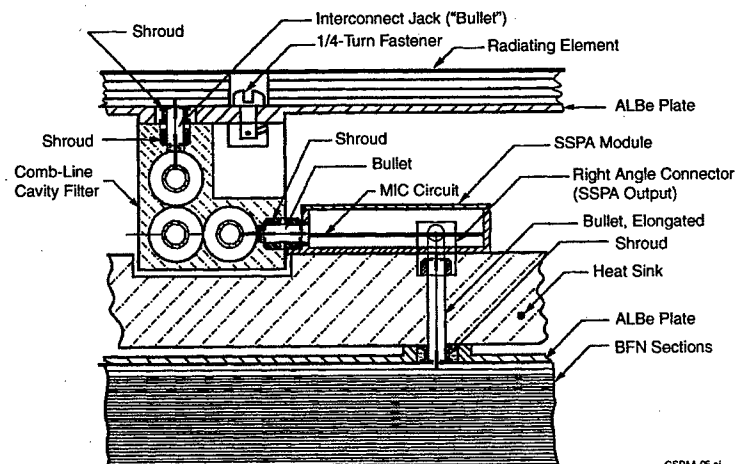
Figure 5. RF Interfaces of the Globalstar S-Band Multibeam Active Transmit Array Antenna

208
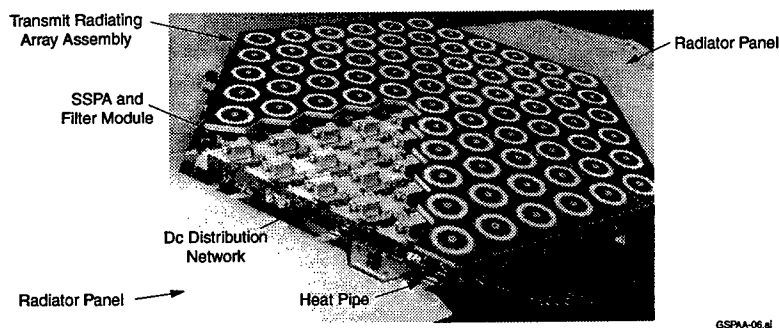
Figure 6. Photograph of an S-Band Multibeam Active Transmit Array Antenna Development Model

559 mm Diameter

1-to-91
Power Divider

"Trombone"
Phase Adjuster
(91 places)

One Layer of a
16-to-1 Power Combiner
(91 places)

GSPAA-07.ai
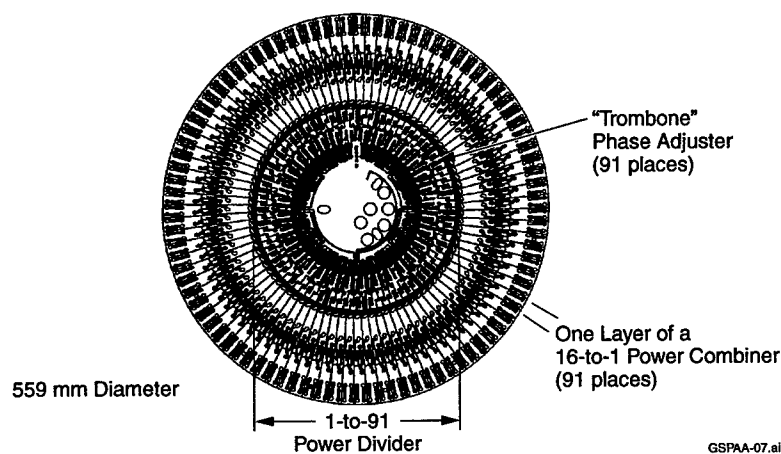
Figure 7. One Layer of the S-Band Transmit Antenna Beamforming Network

BFN Interface

Power
Division
Junction

32-Board "Stack"

Schematic Equivalent
(Four-Level Binary Split)

GSPAA-08.ai
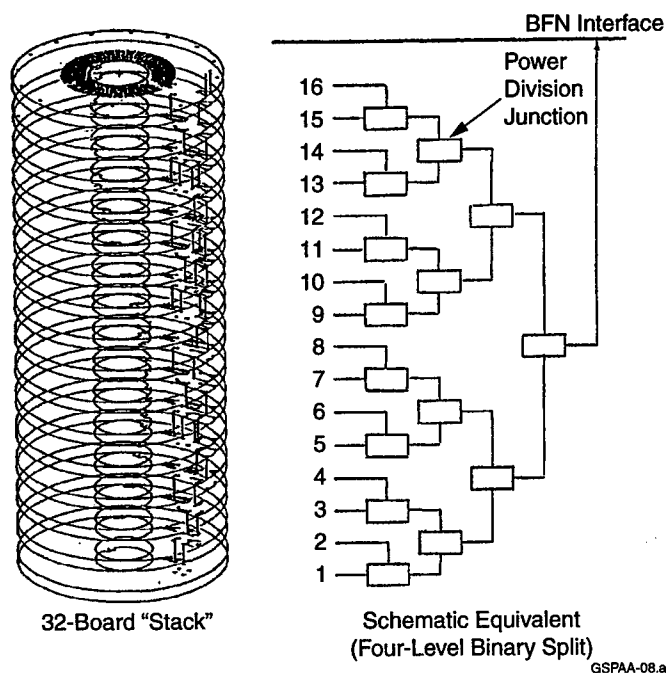
Figure 8. 16-to-1 Power Combiner Implementation

Each of the six sections is a one-piece, eight-layer bonded composite that is manufactured using the same procedures and techniques used to fabricate the BFN.

The SSPA module, presented in Figure 10, is composed of two parts, the SSPA package, which is made with a copper-moly base supported by a brazed nickel-alloy frame, and a three-pole comb-line filter, which is machined from aluminum alloy and silver plated. Formed into an "L," the filter housing provides a more compact package, while providing support for the antenna array. The hermetically sealed SSPA package contains a three-stage Monolithic Microwave Integrated Circuit (MMIC) driver, a Psuedomorphic High Electron Mobility Transistor (PHEMT) power Field Effect Transistor (FET), phase trim adjustment, output-power adjustment, bias-protection circuitry, temperature compensation, and an output isolator. The dc interface is made through a six-conductor ceramic feed-through brazed into the package. The S-band antenna has its own dc/dc converter to provide bias and control for the 91 SSPAs. This converter responds to user traffic (total drive power) by adjusting bias voltage to minimize SSPA power consumption. The SSPA modules have 49 dB of gain and an output power of 4.5 watts at an efficiency of 30%.

The active multibeam receive array antenna, like the transmit array antenna, forms 16 simultaneous circularly polarized beams covering the visible Earth with isoflux radiation patterns. It is fabricated and assembled using the same procedures and techniques, but differs from the transmit array antenna in the following ways: there are 61 radiating elements instead of 91, the heat sink, pipes, and radiators are replaced by a honeycomb support panel, Low Noise Amplifiers (LNAs) are used instead of SSPAs, and both amplitude and phase beamforming is used to produce the required beam shapes and beam-pointing angles. Amplitude taper values for the concentric rings of radiating elements are restrained to multiples of 3 dB to simplify the BFN. Figure 11 is a photograph of an L-band array antenna, with and without the radiating array assembly in place. The six segments of the radiating array, the LNA and filter module, the dc distribution network, and the upper facing panel on the honeycomb support panel are visible. Figure 12 presents the 16-beam antenna pattern coverage requirement of the L-band receive array antenna.
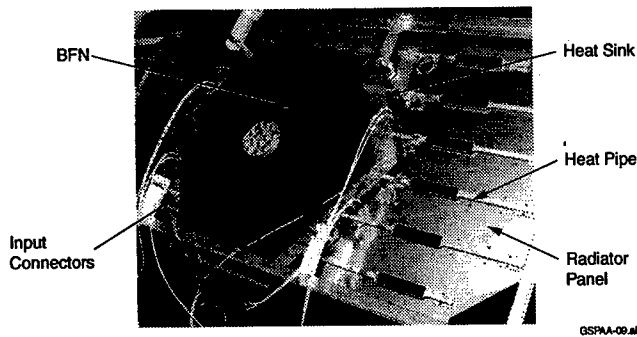
Figure 9. Photograph of the Underside of the S-Band Multibeam Active Transmit Array Antenna Engineering Qualification Model
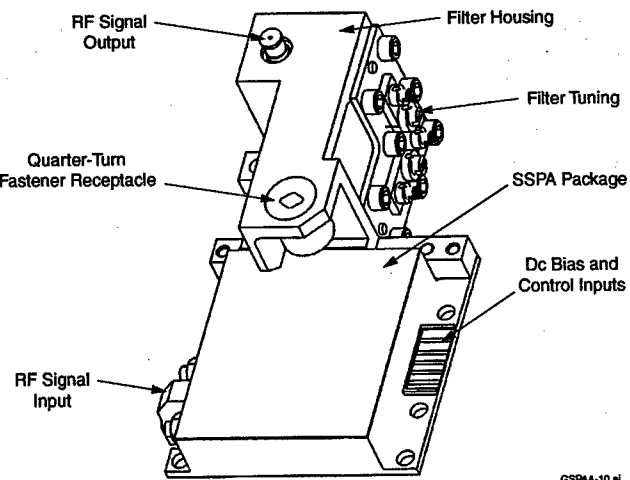
Figure 10. S-Band SSPA Module
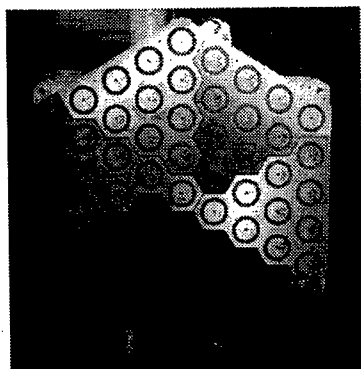
With Array Assembly in Place
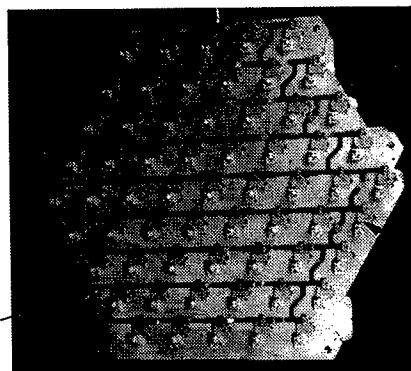
Without Array Assembly in Place

Figure 11. Photograph of an L-Band Multibeam Active Receive Array Antenna Engineering Model
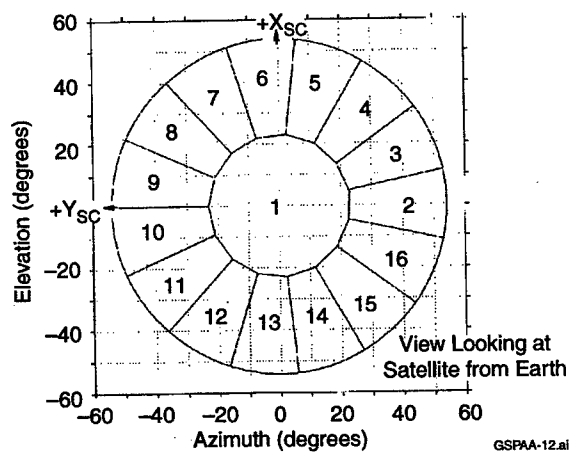
Figure 12. Globalstar L-Band Receive Array Antenna Pattern Coverage Requirement

DESIGN OF A K-BAND TRANSMIT PHASED ARRAY FOR LOW EARTH ORBIT SATELLITE COMMUNICATIONS

Thomas Watson*, Stephen Miller*, Dennis Kershner*, G. Art Anzic**

*Raytheon Systems Company
**NASA-Glenn Research Center

Abstract

The design of a light weight, low cost phased array antenna is presented. Multi-layer printed wiring board (PWB) technology is utilized for RF and DC/Logic manifold distribution. Transmit modules are soldered on one side and patch antenna elements are on the other, allowing the use of automated assembly processes. The 19 GHz antenna has two independently steerable beams, each capable of transferring data at 622 Mbps. A passive, self-contained phase change thermal management system is also presented.

Experiment Description & Objectives

Rapid deployment of low and medium Earth orbit (LEO/MEO) satellite constellations, which will offer various narrow to wide band wireless communications services, will require phased array antennas which feature wide-angle and super agile electronic steering of one or more antenna beams. Phased array antennas are perfectly suited for this application. A MMIC-based, K-band phased array antenna is in development, under a cooperative agreement between NASA Glenn Research Center and Raytheon Systems Company. The transmit array, operating at 19 GHz, is a state-of-the-art design that features dual, independent, electronically steerable beam operation ($\pm$ 42°), a stand-alone thermal management system and a high-density tile architecture. The tile integration technology ("flip chip MMIC tile") represents a major advancement in phased array engineering and holds much promise for reduced manufacturing costs.

The antenna system is scheduled to be completed in mid-2000. The array will be a critical component of the Direct Data Distribution (D^3) flight experiment on a future Space Shuttle mission, as early as 2001, with the objective of down linking wide band data rates to a small, tracking Earth terminal. Phased array antennas capable of providing a rapid direct downlink of large volumes of data from various space platforms are high on NASA's and the communications industry's priority lists.

Array Requirements

Requirements for the D^3 Array were determined

DC/LOGIC CABLE (4)
QUAD Tx MMIC SUBASSEMBLIES (64)
PATCH ANTENNA ELEMENTS (256)
RF CABLE (2)
MANIFOLD CLAMPING RING
BELLOWS ACCUMULATOR (3)
PHASE CHANGE HOUSING
POROUS ALUMINUM AND PHASE CHANGE MATERIAL
MANIFOLD MOUNTING RING
MANIFOLD ASSEMBLY
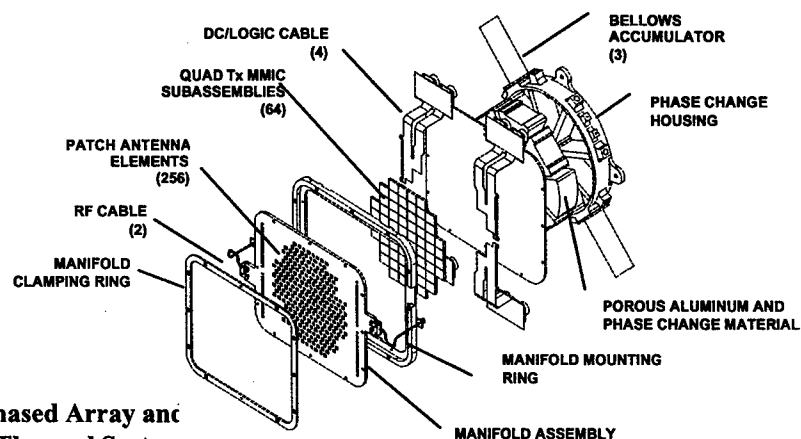
Figure 1. Phased Array and Thermal System

from a combination of functional needs of NASA's D^3 flight experiment and performance requirements taken from the experiment link budget analysis. Functional requirements of the experiment include: frequency/bandwidth, number of beams, scan limits, polarization, DC power and weight/volume. Performance requirements derived from the link budget include: EIRP, cross-polarization, and intermodulation. A summary of the phased array performance goals is listed in Table 1.

Table 1. Array Performance Goals

Parameter	Value
Frequency/Bandwidth	18.8 to 19.3 GHz
Transmit Power	20 Watts/beam
EIRP at max. scan	39.1 dBW
Number of Beams	2
Maximum Scan Angle	± 42° in Az and El
Polarization	RHCP & LHCP
Cross-polarization	-15 dB
Beamwidth	6.4° × 6.4°
Sidelobe level	-20 dB, peak
Intermodulation	-25 dBc
DC power	<390 Watts
Array Weight	< 3.8 kg
Array Volume	<5000 cm^3

Additional requirements due to the planned experiment on the Shuttle are environmental and safety related. The space environment requires special attention to thermal design of the active array. A separate thermal management system is required to handle the heat generated by the transmit modules. Special materials are used to accommodate the temperature and vacuum conditions. Space radiation is low at the Shuttle altitude, but radiation must be considered in selection of high speed digital circuits. Three levels of hardware and software interlocks are designed into the controller to eliminate the risk of RF radiation to the astronauts.

Array Description

The array aperture is circular with edges formed due to the use of quad modules as tiles for array construction. Microstrip stacked patch radiating elements are arranged in an equilateral triangular grid with a separation of 9.75 mm to allow the

antenna to scan to 42° from boresight without grating lobes. To achieve the required 39.1 dBW effective isotropic radiated power (EIRP) at full scan, the array consists of 256 radiating elements. A 6 dB step taper has been implemented to control sidelobe levels. The 96 central and 160 outer elements are fed by 0.25 μm pHEMPT 150 mW and 37.5 mW MMIC amplifiers, respectively.

Each quad module contains 8, 4-bit phase shifters and 4 dual channel power amplifiers, allowing the array to form two independent, simultaneous beams. The output power is 20 Watts per beam. Array power dissipation is estimated at 346 Watts during the ON state with both beams active. The total dc power required by the array is estimated at 386 Watts.

The two beams are generated with opposite sense polarization, one right-hand circularly polarized, one as left-hand circularly polarized. This approach minimizes interference between beams and allows both beams to be simultaneously received by a single ground terminal. The current estimate is that the worst case polarization coupling level will be –15 dB. Predicted pattern performance is shown at the end of this paper.

As shown in Figure 1, the antenna is fabricated using a tile method of construction producing a high-density, low-profile assembly. The main internal assembly, the RF/DC manifold, is a multi-layer printed wiring board consisting of 27 metal layers separated by dielectric material of various thicknesses. These layers include the etched circuits for the two corporate feed RF divider networks for the two beams, the dc power distribution circuits, the logic and control networks, and the microstrip patch elements with their associated 90° branch-line hybrids to form circularly polarized waves. The layer count also includes all of the ground and joining layers required between sub-panels of the multi-layer board assembly. The quad modules are attached directly to the RF/DC manifold with a solder ball reflow process.

A beam steering computer (BSC) has been developed by Raytheon to control all operations

of the antenna. The BSC consists of a commercially available VME processor card and a custom mezzanine card to control array functions in response to commands received from the payload control computer via the VME bus.

Tile Description

The D³ Array is populated with 64 tile modules mounted to the RF DC manifold in a rectangular grid. Tile size is 16.4 mm W x 19.0 mm L x 2.67 mm H weighing approximately 3.5 grams. Each tile consists of a quad module as shown in Figure 2. The tile modules each contain 8 independently controlled RF paths partitioned in quadrants since each tile must feed the two independent beams to four radiating elements. The array 6 dB step taper is implemented with 24 high power modules in the center of the array and 40 low power modules around the periphery.
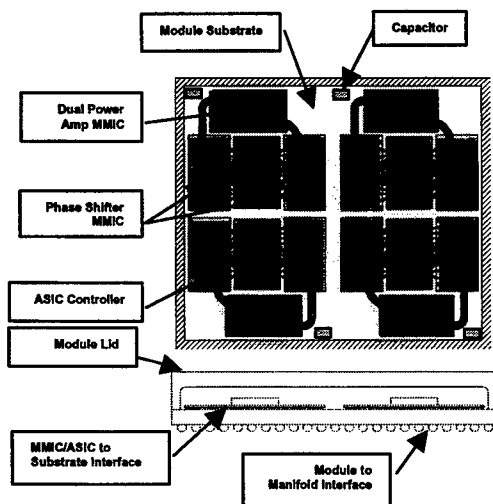
Figure 2. Module Layout

The D³ tile module design evolved from RF and thermal performance, available area, fabrication/production issues and cost goals. The major module components are shown in Figure 2. The module mounts to the RF/DC manifold using a Ball Grid Array (BGA) using 0.508 mm diameter 90Sn/10Pb alloy solder balls. The module substrate is 0.381 mm thick Alumina with appropriate metallization for signal routing,

thermal conduction and BGA attachment with 0.127 mm diameter filled through vias for RF/DC/logic I/O and thermal conduction. Each quadrant contains a silicon ASIC controller, a GaAs dual channel power amplifier MMIC, and two GaAs phase shifter/attenuator MMICs. The ICs are flip chip mounted to the substrate using 0.127 mm diameter 63SN/37Pb alloy solder balls. There are 4 surface mount chip capacitors for local energy storage and RF bypass. The MMICs and capacitors account for 60% of the substrate area demonstrating the increased packing density afforded by flip chip IC mounting. A copper alloy lid attached to the substrate completes the module package and serves as the main thermal interface.

Monolithic Microwave Integrated Circuit (MMIC)

The D³ Array modules contain Embedded Transmission Line (ETL) MMICs on a GaAs substrate as shown in Figure 3 [1]. ETL MMICs utilize matching circuits, transmission lines, and lumped, passive components in a low loss dielectric with a topside ground plane. The ground plane reduces unwanted interactions between the MMIC and its surrounding environment producing more consistent RF performance during production process development.
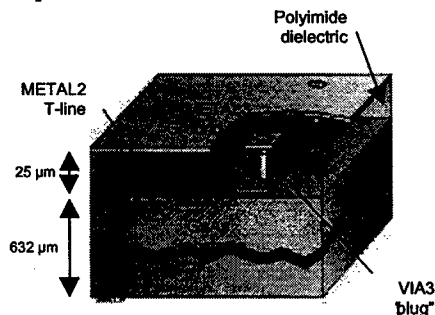
Figure 3. ETL MMIC

There are three MMIC designs: the phase shifter/attenuator, high power dual channel power amplifier and low power dual channel power amplifier. The phase shifter/attenuator MMIC size is 4.47x2.47 mm. The RF signal enters the MMIC and travels through an

213

amplifier followed by 4 attenuator bits, another amplifier stage, 4 phase shifter delay line and then exits the MMIC. The amplifier stages offset transmission line losses within the MMIC for a nominal net gain of 0 dB.

The dual channel high power amplifier MMIC size is 4.47x2.47 mm. Two RF signals enter the MMIC and each signal path travels through three amplifier stages before exiting the MMIC. Net gain is +21 dB with +22 dBm RF output power at 1 dB compression. The dual channel low power amplifier MMIC is similar to its high power counterpart except there are only two amplifier stages producing +15 dB gain with +16 dBm RF output power at 1 dB compression.

Thermal Management System

A phase change thermal management system has been developed to provide a platform independent heat management system. The system also provides the structural interface between the array and the Shuttle Hitchhiker canister. It is sized to maintain transistor junction temperatures below $100^{\circ}C$ and to maintain an array thermal gradient below $1^{\circ}C$. The phase change system is a 20 cm diameter brazed housing with porous aluminum "foam" inside, as shown in Figure 1. The "foam" is filled with paraffin wax phase change material. As the antenna modules heat up, the solid wax absorbs the heat energy and changes to the liquid phase. During the phase change period, the wax temperature is maintained at approximately the melt point. This provides a constant-temperature interface for the array electronic modules. During periods in which the antenna modules are off, the wax releases its stored heat and changes back to the solid phase, thereby tempering extreme temperature excursions. Heat pipes are arranged radially to maintain the array temperature gradients at an acceptable level. This is made necessary due to the higher power center modules described above.

Conclusions

High performance, lightweight, low cost antennas are needed for future satellite communication systems. A recent advance has been the development of a two beam, K-band, transmit array to demonstrate high data rate link from the Shuttle to a NASA ground station. Many advanced technologies have been designed into this antenna in order to meet the requirements of the experiment. A successful demonstration will validate these technologies for future satellite applications.

Acknowledgements

References

[1] H. Tserng, et. al., "Embedded Transmission-Line (ETL) MMIC for Low-Cost High-Density Wireless Communication Applications," IEEE Transactions on Microwave Theory and Techniques, vol. 45 No. 12, December, 1997.

Array Patterns on Boresight
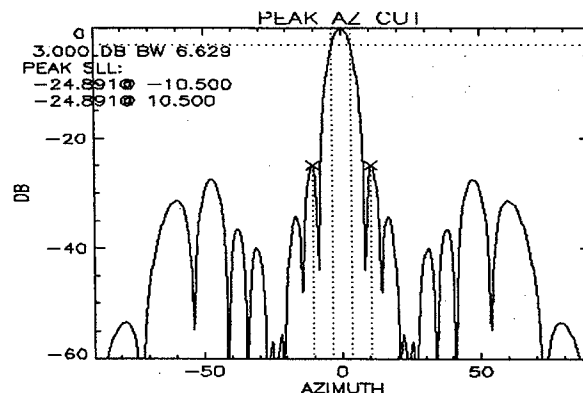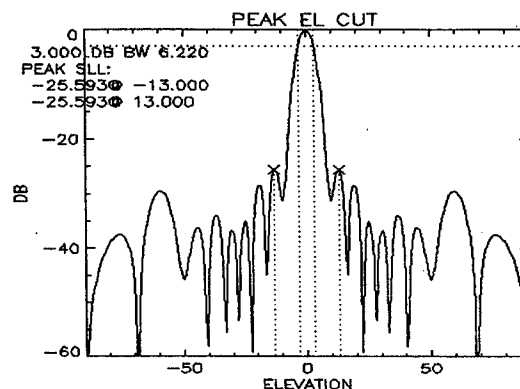
PATCH-EXCITED CUP ELEMENTS FOR SATELLITE-BASED MOBILE COMMUNICATION ANTENNAS

Per Ingvarson, Ulf Jostell, Patrik Svedjenäs

Saab Ericsson Space, SE-405 15 Göteborg, Sweden

Background

Antennas for mobile communication satellites have been studied for 25 years at Saab Ericsson Space. The first multibeam antenna array consisted of 18 circularly polarised Short Backfire radiators in a triangular lattice giving 19 beams covering the earth. A complete demonstration model including the IF beamforming network, amplifiers and filters was manufactured and tested.

The Short Backfire elements have a size of 2.2 wavelengths. Several smaller element types have also been developed, mainly in microstrip technology. They include self-diplexing elements and wide-band double-patch elements. The rf performance of the latter was improved by adding a cup to the microstrip radiator. This is what we call a patch-excited cup.

ARTEMIS

ARTEMIS is a geostationary technology demonstrator. It contains an L-band, 1.5/1.6 GHz, mobile communication payload with an arrayfed reflector antenna. The array is used both for receive and transmit, with very stringent requirements on PIM (passive intermodulation). PIM gives spurious frequency components that are generated when two or more signals mix in a non-linear passive device. Metal to metal junctions and non-linearities in dielectric material are typical PIM sources and must be avoided in the design.

The test power in ARTEMIS was 2x20 W and the PIM requirements −145 dBm over ±80 °C and −140 dBm over the extended range ±100 °C. A new PIM test chamber was developed, which allowed these low levels to be accurately measured. In the antenna development, the patch-excited cup radiator was developed.

The patch-excited cup of the ARTEMIS L-band feed array, figures 1 and 3, consists of 0.8 λ diameter and 0.37 λ deep cups excited by a pair of stacked circular discs with an integral central support attached to the cup bottom. In order to minimize the generation of PIM, all the cups in the array are made in one piece. The lower disc is excited by a pair of capacitively coupled probes. The first development model contained 12 cups, figure 3, and had dual circular polarisation generated by foam supported, unbalanced for cross-polarisation control, stripline quadrature hybrids in compartments below each cup. The system concept was changed to 5 cups and dual linear polarisation for the flight hardware. A patented device for compensation of the detrimental effects of interprobe coupling on the cross-polarisation performance, was implemented. A typical transmit frequency antenna pattern of a top edge element of the array in figure 1 is shown in figure 2. Measured aperture efficiency is ≥100 % and ohmic loss ≤ 0.1 dB.

EMS

Similar 4-element arrays, figure 4, were delivered for EMS (European Mobile Service) on board the ITALSAT F2 satellite. The use of separate reflector antennas for transmit and receive alleviated in this case the PIM requirement somewhat to −130 dBm at 2x30 W input power.

The patch-excited cup elements are here sequentially rotated to improve the cross-polarisation performance. Feed probes of neighbour elements are connected by tee stripline networks giving four input ports in total. The cups are slightly non-circular to give room for a centrally mounted Ka-band feed array.
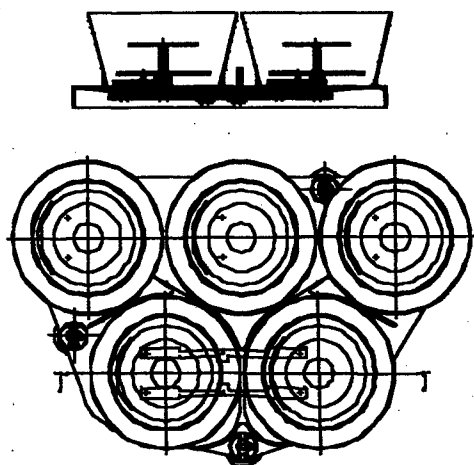
Figure 1. ARTEMIS L-band feed array.
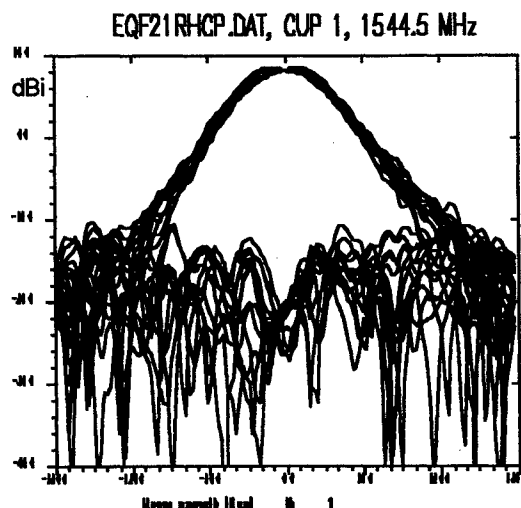
Figure 2. Polar pattern cuts each 15 degree of top edge element in ARTEMIS L-band feed array.
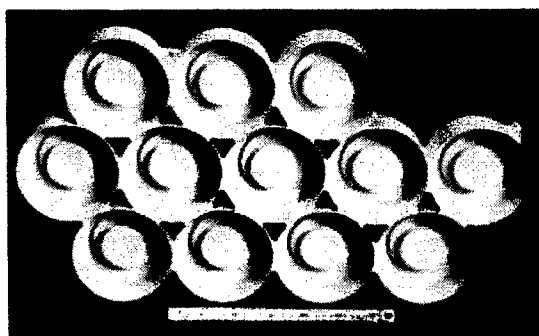
Figure 3. 12-element development model of the ARTEMIS L-band feed array
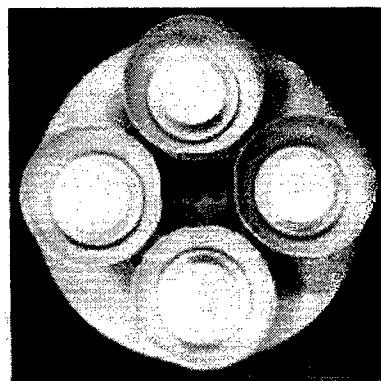
Figure 4. EMS receive feed array.

ICO

The ICO satellite system consists of 12 satellites in MEO orbit (10400 km). Each satellite has one transmit array at 2.185 GHz, and one receive array at 2.0 GHz, see figure 5. Both arrays consist of 127 radiating elements in a hexagonal lattice with 1.3 wavelength spacing. All feed chains are active, i e they contain radiating element, filter, amplifier, frequency conversion and D/A (A/D) conversion. All beamforming is digital.

The arrays cover the earth with 163 circularly polarised beams, with a four beam reuse pattern. Up to 4500 simultaneous users can be accommodated. Saab Ericsson Space has developed and delivered the array elements to Hughes Space and Communications Company, the prime contractor.

The radiating elements have very stringent requirements on aperture efficiency and cross-polarisation. The multicarrier transmit signal and the small separation to the receive band give strict limits on PIM. Also, requirements on ESD (electrostatic discharge) are stricter than for most other satellites due to the orbit. The large number of radiators leads to very low mass and cost targets.

The radiator has been redesigned compared to ARTEMIS. To keep high aperture efficiency with the larger radiator, a third patch has been added in the feed. The "patch tower" is mounted within a very thin aluminium cup with a rim height of about $\lambda_0/4$. The two lower patches form a resonant cavity, allowing broadband- or double tuning. The upper patch acts mainly as a reflector that affects the illumination of the aperture and is used to improve the aperture efficiency and thereby the gain.

The lower patch is fed in phase quadrature at four points by a stripline network to give circular polarisation. The symmetric feeding is used to obtain good cross-polar performance. It is important that the stripline network is a robust design from a production point of view and meets the tough PIM requirements. A metallic box together with the cup, forms a compartment for the feeding network.

Measured co- and cross-polar radiation patterns from a single element as well as in the array environment are shown in figure 6 for the transmit radiator.

Figure 6.   Measured co and cross polar radiation pattern of the S-band transmit element. (a) Isolated element. (b) In terminated 18-elements environment. Each plot shows 6 polar cuts with steps of 30°.

Figure 5. ICO satellite being tested in the Integrated Satellite Factory at Hughes Space and Communications Company. Saab Ericsson Space supplies antenna elements and microwave equipment to the ICO satellite program at Hughes.

The PIM requirements have forced the patch tower to be machined in one part as well as the stripline network. Metal to metal contact is avoided by using dielectrics. The rf connection between the feed network and the lower patch is done with non-contacting probes, i.e. through a capacitive coupling. All grounding resistances are kept as high as possible to keep rf current low which is a trade off against the ESD requirement.

Due to the large number of radiators (Saab Ericsson Space have delivered 3048 radiators for ICO), the design has to be lightweight and have a low unit cost. The radiators have to be exchangable, and therefore essentially identical. The selected design is to use separate elements mainly made of thin aluminium parts. The mass per element is less than 100 g.

Thuraya

For geostationary satellites, a direct-radiating array as in ICO would have to be very large in order to give a sufficiently dense cell-grid on ground. Therefore, array-fed reflectors are used. A common transmit-receive radiator allows the use of only one reflector. This gives even stricter requirements on PIM compared to ICO. Saab Ericsson Space has developed L-band radiators for geostationary applications in a technology similar to the one for ICO, and has delivered 256 radiators to Hughes Space and Communications Company for Thuraya. Measured patterns in an array environment are shown in figure 9.

Figure 8. Thuraya elements mounted on panel for rf testing.
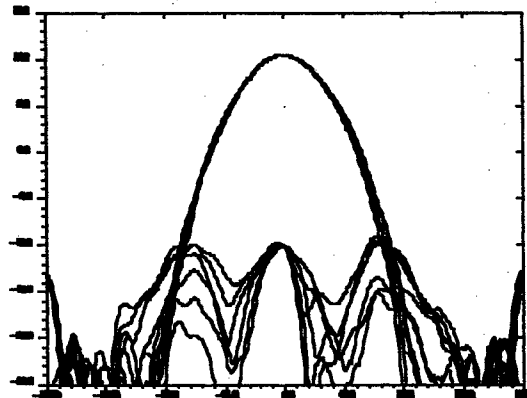
Figure 9. Measured co and cross polar radiation pattern of the L-band transmit/receive element in terminated 6-elements environment. Each plot shows 6 polar cuts in steps of 30°.

A Low-Cost, Injection-Molded Satellite Phased Array

P. L. Metzen
Space Systems/Loral

Introduction

The current trend in synchronous orbit satellites and satellite antennas is toward increased power, increased payload capability, and more independent antenna beams. Spacecraft antennas must also be low in cost, be quickly produced, and fit within the available spacecraft mounting locations. Furthermore, spacecraft with antennas and solar arrays must fit within the launch vehicle shroud. Spacecraft mounting space and shroud volume are limited, and larger launch vehicles with larger shrouds are costly.

The transmit and receive functions are often performed by separate antennas, each antenna covering a narrow bandwidth, to reduce the transmit feed system losses and improve the efficiency of the antenna beam shape optimization. Improved transmit antenna performance reduces the high costs of supplying more solar array Direct Current (dc) power, Traveling Wave Tube Amplifier (TWTA) Radio Frequency (RF) power, and thermal control. A deployed shaped-reflector antenna is frequently used to satisfy the transmit requirements, and an Earth-facing, deck-mounted reflector antenna is used to satisfy the receive functions. An Earth-deck structure is necessary to hold the receive antenna reflector, subreflector, and feed. At Ku-band, the projected aperture of the Earth-deck antenna diameter is typically 1.2 m. The reflector, subreflector, and structure are made of graphite composite materials.

An Earth-deck-mounted passive array antenna is being developed that has the same RF performance and the same mass as the 1.2-m reflector antenna, yet costs 75% less and occupies 80% less Earth-deck area and 95% less shroud volume. Furthermore, the array has a lower center of gravity that improves spacecraft inertial characteristics. (A U.S. patent is pending.)

RF Design

A 256-element, passive, direct-radiating receive array operating from 13.75 GHz to 14.5 GHz with a two wavelength element spacing was developed to have the equivalent RF performance of a 1.2-m Gregorian,

dual-polarized shaped-reflector antenna. Figure 1 presents a block diagram of the phased array. Each of the 256-horn radiating elements contains an Orthomode Junction (OMJ) to produce 256 vertically and 256 horizontally polarized outputs. Each element also contains a crossed septa in each aperture to increase the directivity and improve E-plane and H-plane equalization. Separate Beamforming Networks (BFNs) are used for each polarization to establish the unique phase and amplitudes necessary to produce two separate outputs associated with two independent beams of any desired shape.

Only the horizontally polarized BFN is described in this paper. The vertically polarized BFN is very similar. The horizontally polarized output from each horn/OMJ passes through a predetermined, fixed-phase phase shifter, and is then combined with the output of a neighboring horn/OMJ and phase shifter in one of 128 two-way power combiners. The 128 outputs of the two-way power combiners are then combined by 16 eight-way power combiners resulting in 16 outputs that are combined by 5 four-way power combiners to produce a single horizontally polarized output. Each eight-way power combiner consists of 7 two-way power combiners, and each four-way power combiner consists of 3 two-way power combiners, for a total of 255 two-way power combiners in each vertically and horizontally polarized BFN. Each power combiner will have a predetermined, fixed output power ratio that, together with the phase shifters, uniquely determines any desired output beam shape.

Table 1 presents the calculated loss budget and Edge-of-Coverage (EOC) gain for a typical Contiguous United States (CONUS) coverage. The BFN is constructed in WR62 and half-height WR62 waveguide operating in the TE_{11} mode, and uses U-shaped waveguide phase shifters and internally terminated four-port hybrid ring power combiners. The RF performance of each component was computer-optimized and then verified with aluminum models. The aperture cover can be replaced by a three-layer meanderline polarizer with an added 0.1 dB of loss if circular polarization is desired.
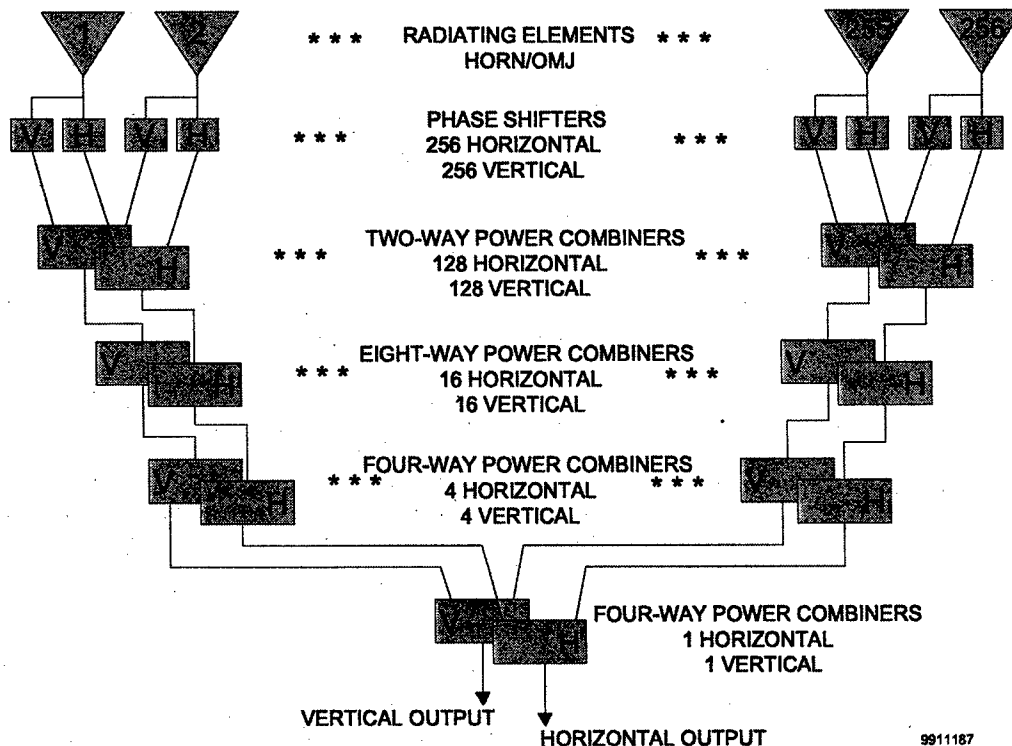
Figure 1. Phased Array Block Diagram

Table 1. Calculated Loss Budget and EOC Gain

CONUS Coverage	
EOC Directivity	
Rectangular Horn	31.0 dB
Crossed Septa	0.5 dB
Total Directivity	31.5 dB
Array Antenna Losses	
Mismatch Loss	0.2 dB
Insertion Loss	0.4 dB
Aperture Cover Loss	0.1 dB
Total Loss	0.7 dB
Antenna EOC Gain	30.8 dB

Mechanical and Manufacturing Design

To significantly lower the cost of the finished array, metallized, injection-molded, fiber-reinforced, thermoplastic waveguide array components are being developed. The material being used has excellent physical and thermal properties, produces highly repeatable parts, and is lightweight and easy to machine. Good metallization and easy injection molding is assured by splitting the power combiner assemblies along the waveguide broadwall axis to expose the inside surfaces. The power combiner components are designed and molded to near-net shape, and are then lightly machined in the "ring"

areas to predetermined, fixed power ratios using high-speed Computer Numerical Control (CNC) machining. Internal RF loads for the power combiners are molded to net shape, and self-capture features allow them to be captured when installed in the power combiners. Injection molding to net and near-net shape allows all components to be produced in quantity for lower cost and placed in inventory in advance of their need, reducing the delivery time for the finished array.

Ease of assembly, integration, and test is included in the design. Part counts are minimized where possible, flanges are eliminated, waveguide slip-joints are used, and threaded fasteners are replaced by clips and self-capture features. Where threaded fasteners are required, lightweight composite versions are used. Excess material is designed out of the injection-molded pieces and interlocking, self-jigging features are designed in. The injection-molding tools are constructed from three-dimensional Computer-Aided Design (CAD) file models of the injection-molded parts. The CAD files are verified using stereo-lithography models.

Figure 2 presents the antenna array assembly with the aperture cover and aperture cover support panels removed on two sides for clarity. The complete assembly is 0.84 m by 0.76 m in cross section and 0.37 m in height, and weighs 28.7 kg.

220

Figure 3 presents a pair of horn/OMJ assemblies, a pair of two-way power combiners, and four phase shifters, all securely interconnected with simple Beryllium copper spring clips to form an assembly. This assembly is a simple building block and, when repeated numerous times, forms a major portion of the antenna. The phase shifters are set to predetermined values between 0° and 360° by CNC machining material from the open ends to produce the proper length and are easily interchanged to produce the desired phase distribution. The horn/OMJ is injection-molded in two pieces, the 90° bend in two pieces, and the crossed septa in one piece. The five pieces are bonded together with structural adhesive and then plated with electroless copper to produce the finished component. The phase shifters and all versions of power combiners are molded in two pieces and, after machining, electroless plating, and inserting the RF loads in the combiners, the two pieces are joined together using molded-in self-aligning features, and mechanically fastened with rivets.

Figure 4 presents a 4 x 16 element subarray assembly formed by fastening the 32-horn/OMJ phase shifter assembly and the two-way power combiner assembly to an intermediate structural panel. The waveguide

outputs of the two-way power combiners pass through the intermediate structural panel and slip into the input ports of four horizontally polarized and four vertically polarized eight-way power combiners. The eight-way power combiners are fastened to the underside of the structural panel and are offset with respect to each other for proper waveguide alignment.

Figure 5 presents an exploded view of the antenna array assembly. Four 4 x 16 element subarray assemblies are fastened to the main structural panel. Two output combiner networks are fastened to the underside of the structural panel. For clarity, only one of the two output combiner networks—composed of five two-way power combiners—is shown. The other combiner network is offset and passes through the one shown. Sixteen interconnecting waveguide ports pass through the main structural panel and slip into eight horizontally polarized and eight vertically polarized output ports located on the eight-way power combiners. On the underside of the middle pair of the four-way power combiners are two output ports, one horizontally polarized and one vertically polarized. Fastening the aperture cover assembly to the main support panel completes the antenna assembly.
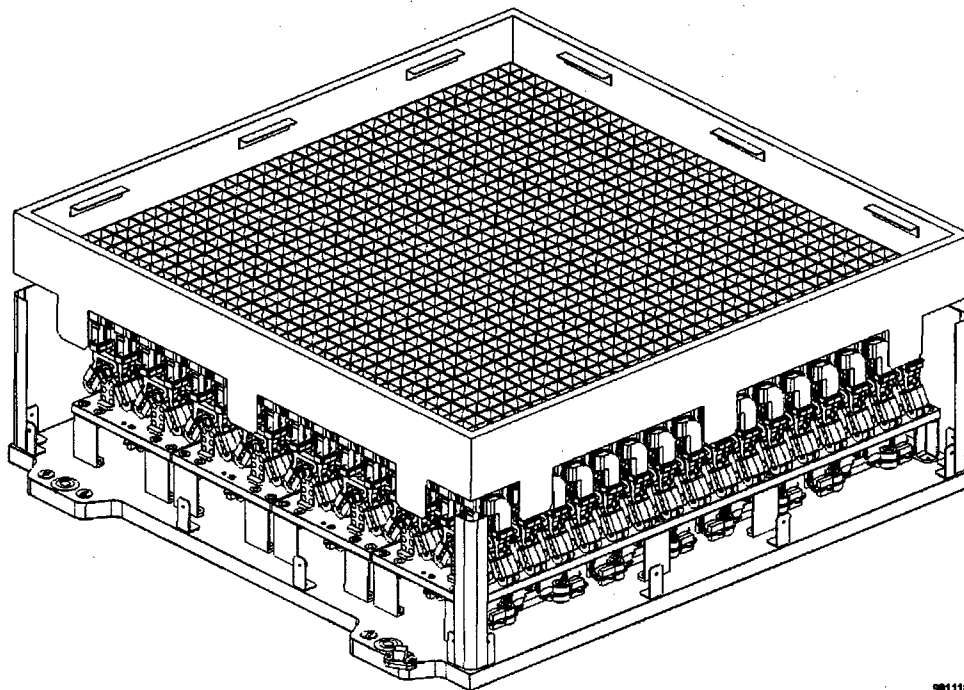
Figure 2. Antenna Array Assembly
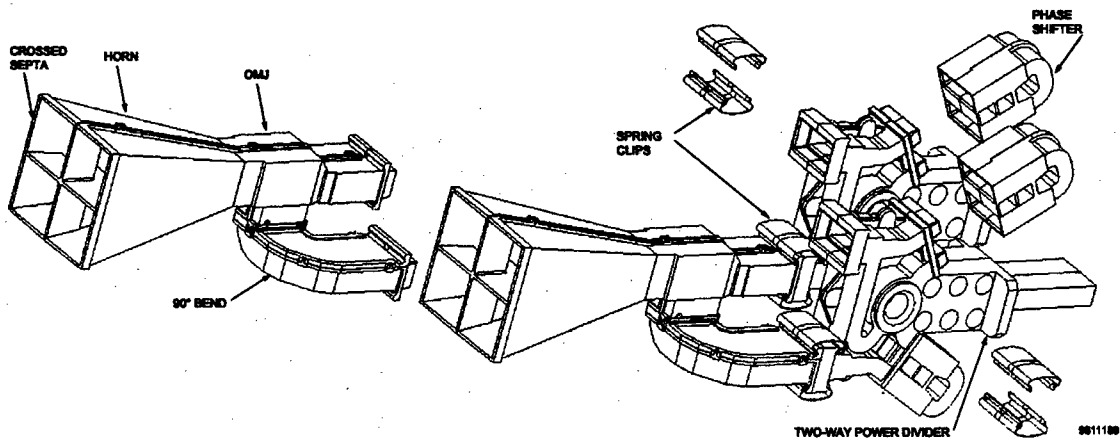
Figure 3. Horn/OMJ, Phase Shifters, and Two-Way Power Combiner Assembly
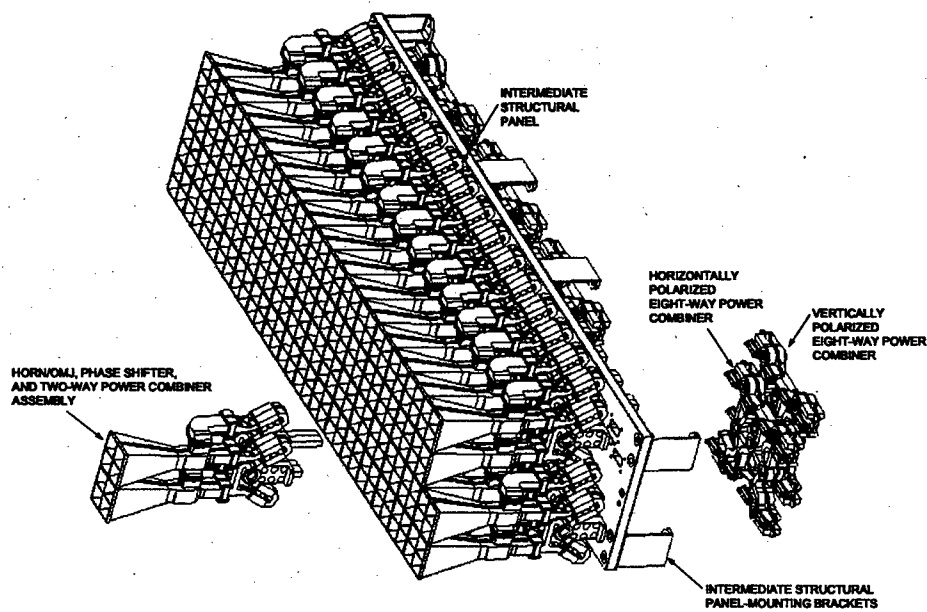
Figure 4. 4 x 16 Element Subarray Assembly
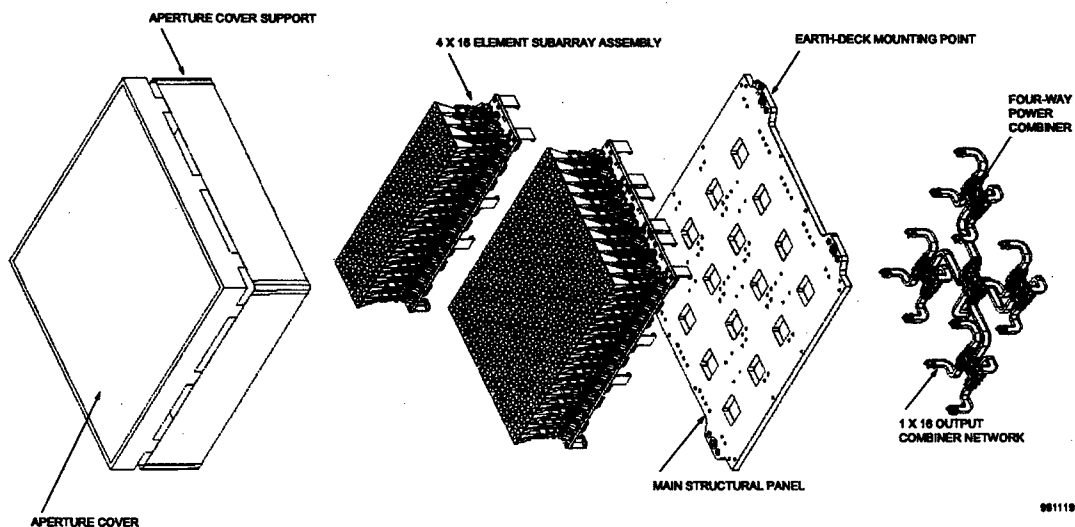
Figure 5. Exploded View of Antenna Array Assembly

222

AIRBORNE RECEPTION OF DATA AND DIRECT BROADCAST TV USING A PHASED ARRAY ANTENNA

Charles O. Adler, Derek J. Van Alen, Ronald S. Carson, Arthur F. Morrison,
Mathew E. Lavelle, Eric D. Anderson, Gordon R. Onorati, Jeffrey K. Cunningham

Boeing, Space & Communications
P.O. Box 3999 MC 8Y-98
Seattle, WA, USA, 98124-2499

ABSTRACT

The rapid growth of ground based broadband services and the advent of high power Ku band broadcast satellites compatible with relatively small aperture terminals have provided the incentives and the channels for providing broadband services to highly mobile users such as aircraft. There are a number of antenna system options that provide a capability for tracking a satellite broadcast from a moving platform. This paper describes one of these options - the Boeing commercial Ku band receive phased array antenna system.

This antenna system is a proven, production system. It is currently being used to provide worldwide broadband data and commercial satellite television services for a variety of business and military aircraft customers.

1.   INTRODUCTION

An earlier paper described the Boeing commercial Ku band phased array receive antenna with a focus on antenna details [1]. This paper focuses on a system level description, starting with a summary of the developmental and operational history of the system in section 2. Section 3 follows with an antenna system level description. Section 4 is a discussion of the system level performance with respect to the operational satellite environment. Section 5 provides a summary.

2.   A SHORT DEVELOPMENTAL AND OPERATIONAL HISTORY

Over the past 12 years, and with significant investments, Boeing has developed a phased array technology that is in production, space qualified, and has been applied successfully to receive and transmit applications from 7 to 44 GHz.

Work on applying this technology to a commercial Ku band antenna for satellite broadcast reception by airborne users began in 1993. By 1996, three prototype Single-Polarization Receive (SPR) antennas had been built. That same year, these antennas were installed and flown on aircraft including a Cessna 206 light aircraft, a military aircraft and a privately owned Boeing 757 business jet. The Boeing 757 installation was left in place through the end of 1999 and amassed over 3000 flight hours of fault free operation. The SPR antennas were successful antennas but they were not optimized for mass production and operationally they had a single (switchable) circular polarization output with an instantaneous bandwidth of 100 MHz.

To provide a more commercially viable antenna system, Boeing built a production dual polarization receive, circular/linear antenna system with a 500 MHz instantaneous bandwidth. The first production versions of the Dual-Polarization Receive (DPR) antenna system came off the production line in late 1997.

By the latter half of 1998 a capability to electronically switch between linear and circular polarization was added to allow operation with a worldwide range of services. This capability was demonstrated using European and Middle Eastern broadcast services and has been added to all production units.

At the end of 1999 an initial production run of over 25 antenna systems has been completed, and DPR systems are available as 'off the shelf' systems. Proven, highly automated production processes are in place for follow-on production runs.

Figure 1 summarizes the operational history for a subset of the Boeing SPR and DPR Ku band antennas through the end of November 1999. All of the Business Jet DPR system installations have been FAA Supplemental Type Certifications (STCs). Most of these installations have been Multiple STCs and all of these installations have been certified for multi-region (3&4) service. Flight operations with a variety of US, European and Middle Eastern

broadcast TV services are routinely taking place. A system with in-flight broadband internet/intranet access has been installed on several privately owned Boeing 757 and 737 business jets and broadband in-flight data downloads for customers have been accomplished using US (both Broadcast Satellite Service (BSS) and Fixed Satellite Service (FSS)) and European satellite services. This service history demonstrates the flexibility of the system.
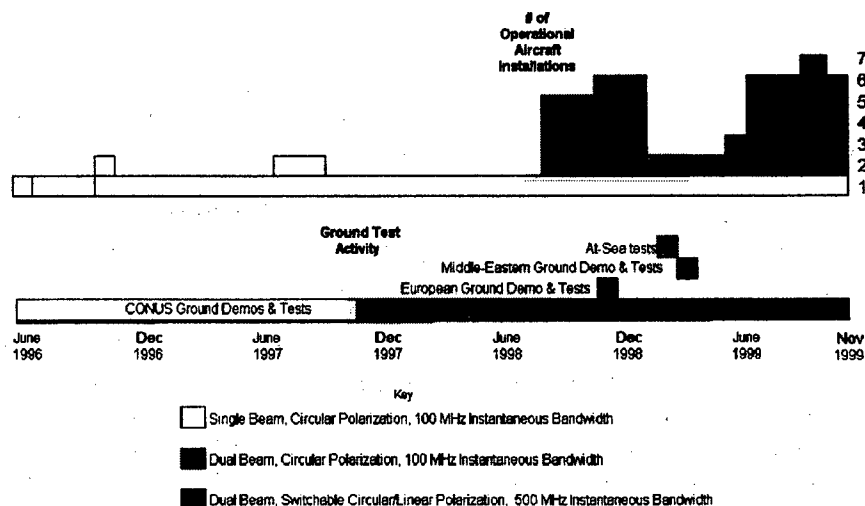
Figure 1. Boeing Ku Band Operational Summary

3. ANTENNA SYSTEM DESCRIPTION

The system is applicable to a wide range of air, land and sea mobile platforms. The target aircraft market for this antenna system includes commercial, military, and business-jet airliner class aircraft. Common system level attributes important to the customers operating these aircraft include ease of operation, ease of integration to aircraft (IFE) systems, high quality reception, high reliability, ease and low cost of installation and maintenance, low aerodynamic profile, and high operational flexibility. These are areas where this phased array technology can offer significant advantages. For example, the DPR antenna is designed for a minimum ten-year maintenance free installation. Table 1 summarizes a number of important system level parameters. Figure 2 shows a representative antenna installation.

Figure 3 is a block diagram of the antenna system. The DPR antenna is a dual beam, circular polarization antenna. It outputs simultaneous, independently steerable Left-Hand Circular Polarization (LHCP) and Right-Hand Circular Polarization (RHCP) Ku band signals. These signals are fed into a Linear-Polarization Converter (LPC) box that takes the dual circular inputs and converts them to dual linear outputs as required. Following the LPC is a Low-Noise amplifier, Block down-converter (LNB). This has dual band, dual channel functionality and outputs L-band IF (950-1450 MHz) signals. There is also a product improvement of a fully tunable LNB/LPC unit with a 950 to 2150 MHz IF range. The output of the LNB is fed through the system controller where RF detector functionality is tied in with digital beam control functionality to provide a variety of tracking options. In a typical installation the IF signal is fed from the System Phased Array Controller (SPAC) into an RF multiswitch for distribution to a variety of satellite television or data Integrated Receiver Decoders (IRDs).

Table 1. DPR System Level Parameters

• Polarization – Dual Circular or Dual Linear (Electronically Selected)
• # of independently steerable beams (circular polarization) = 2
• Overall Bandwidth – 11.45 GHz to 12.75 GHz
• Instantaneous Bandwidth – 500 MHz
• Satellite Tracking Rate - Up to 30° /s
• G/T at 0° Scan – 12.5 dB/K
• Active Aperture - 17" x 26"
• Antenna Thickness - 1.7"
• Antenna Beamwidths – 2° x 3°
• Aerodynamic Drag (typical at cruise) ~20 Lbs.
• Aircraft navigation data input - ARINC 429 IRU data
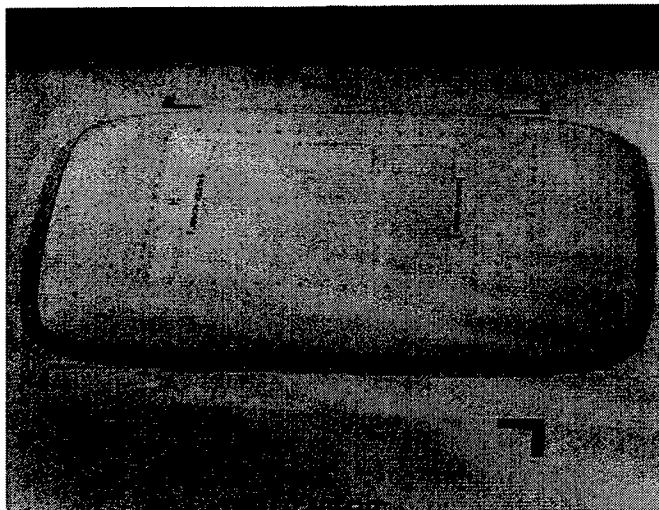
Figure 2. Representative DPR Antenna Installation
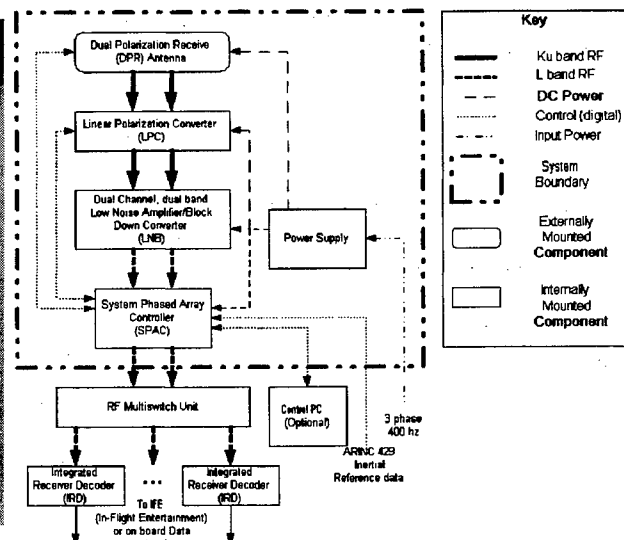
Figure 3. DPR Antenna System Block Diagram

4. SYSTEM PERFORMANCE

Two of the key performance specifications for this system are maximum scan angle, i.e. the antenna look angle measured from antenna broadside, and the capability to maintain track under dynamic conditions, i.e. the ability to handle angular rates. All phased array antennas exhibit scan loss: decreasing gain with increasing scan angle. Assuming the absence of grating lobes, the maximum antenna scan angle is that angle at which the link just closes. Therefore, the maximum scan angle is determined by antenna scan loss, satellite power, and the desired data rate. The Boeing phased array scan performance is very close to the theoretical maximum, falling off with scan angle (theta) very nearly as cos(theta). The design specifications for this system allow for scan angles of 63° with typical services and the ability to maintain track with angular rates of up to 6°/sec. The system has routinely exceeded both of these specifications with operations at 70° scan angle and rates of up to 30°/sec. This performance though, can be dependent on operational considerations, in particular, the satellite environment.

Satellite Environment: As touched on in the operational history, there are two primary commercial Ku band satellite service types: FSS and BSS. In the US, BSS satellites are used by the major direct satellite TV services while FSS satellites are much more plentiful and are used for a variety of commercial and direct-to-home data services as well as broadcast TV services. In the US, Ku band FSS satellites are linearly polarized with a frequency range of 11.7-12.2 GHz. US BSS satellites are circularly polarized with a frequency range of 12.2 - 12.7 GHz. The GE-2 satellite with twenty-four 36 MHz transponders and max EIRPs of better than 48 dBW is representative of FSS satellites in the US. The DBS-1 satellite with sixteen 24 MHz transponders giving max EIRPs of better than 54 dBW is typical of US BSS satellites. Co-frequency spacing on FSS satellites is typically 2°, while it is limited to 9° for BSS satellites [2]. The tighter orbital spacing and lower power levels of the FSS satellites can present challenges for a small-aperture mobile antenna system.

The antenna supports communications with both FSS and BSS satellites. It covers both frequency bands, and is capable of tracking either sense circular polarization, or linear polarization. Because of their (typically) higher power, and wider spacing, the antenna (typically) supports a higher data rate with BSS satellites.

Actual performance from flight tests in the US, Europe, Middle East and North Africa has been determined on aircraft with production DPR Antenna systems installed. BSS and FSS satellite reception has been verified for all of CONUS. Satellite coverage in Europe, including all of UK, has been verified for services on Astra 2A, Astra 1 and Hotbird 2/3. North African coverage has been verified for most of southern Mediterranean Sea and the North Africa land mass covered by services on NileSat 101. Finally, coverage for services on Arabsat 3A have been verified for all of Saudi Arabia and other areas of the Middle East.

Performance with BSS Satellites: The antenna is capable of receiving simultaneous, full rate (up to 30 Mbps per transponder) video from two direct broadcast satellites. Figure 4 shows the roll-off of *signal quality* with increasing

225

scan angle for a BSS based service (*signal quality* is a measure of Bit Error Rate). In this case, high quality video outputs were maintained to about 70° of scan angle.

Using an RF power-tracking mode, rates of 30°/sec with stable, high quality video output have been achieved repeatedly in test with actual BSS satellite services. These high track rates are a major strength of this technology and are being significantly increased with ongoing product improvements.

Performance with FSS Satellites: The antenna is capable of tracking linear polarization from an FSS satellite, and has been used successfully with a number of FSS satellites. Because of their lower power, and closer spacing, the signal to interference plus noise ratio (SINR) with these satellites tends to support a lower data rate than with a BSS satellite. The DPR antenna has a rectangular aperture, resulting in main beam dimensions and side lobes that vary with azimuth. At broadside the main beam width varies from about 3° to about 2° (depending on heading) - the same magnitude as US FSS satellite spacing. Link performance (E_b/N_o) can be maintained in the face of reduced power and increased interference by lowering the data rate. The lower bandwidth associated with lower data rate allows reductions in both noise and interference power, without affecting signal power. The antenna can be operated simultaneously with two FSS satellites, albeit at a lower data rate per satellite (half at best) than with single satellite. In this case, the cross-polarization must be clear - a condition satisfied in the guard band of most FSS satellites.

Over the past three years, the system has been used for numerous in-flight operations with broadband data services (with data rates up to 6 Mbps). In flight, broadband, FSS operations have been recorded at close to 70° scan angle.
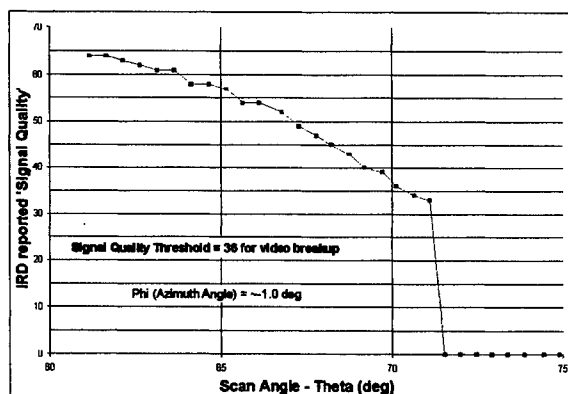
Figure 4. Measured Maximum IRD Reported Signal Quality vs. Scan Angle for a DPR Antenna Operating with a BSS Satellite

5.   SUMMARY

The Boeing DPR antenna provides a proven, in-production, technology and architecture. It has a record of high operational reliability, performance, and flexibility, including providing world-wide FSS or BSS operations from a single system. Ongoing product improvements are strengthening the already impressive performance of the system while decreasing costs.

This system has the architecture and performance to handle a wide variety of operational scenarios. With its dual, completely independently controlled beams, high track rates and near instantaneous re-pointing capability, the DPR system can even potentially handle non-geo satellites (in the appropriate frequency band) with no modification.

In the area of phased array technology, the combination of the wide variety of systems built and fielded and the production and operational experience gained by having a phased array antenna system in commercial production and deployed on a range of private and military platforms has given Boeing a proven product line with significant performance and operational advantages.

6.   REFERENCES

[1] C. Adler, D. Vacanti, D. Van Alen, G. Fitzsimmons, W. Walker, T. White, R. Ott, D. Pietila, J. Freeman, "A Phased Array Antenna For The Airborne Reception Of Data And Direct Broadcast TV", in press, to be published in AP2000 Millennium Conference on Antennas & Propagation Conference Proceedings (ESA SP-444).

[2] Dr. Frank Baylin, *1998/2000 World Satellite Year Book*, 6th ed., Baylin Publications, pp. T-157, S391-S426, T-210, 1998.

Ku-Band Transmit Phased Array Antenna for use in FSS Communication Systems

S. A. Raby, R. Y. Shimoda, P. T. Heisen, D. E. Riemer, B. L. Blaser, G. R. Onorati
Boeing Phantom Works
P.O. Box 3999, Seattle, WA 98124

Abstract. Boeing has developed an active transmit phased array for use in the 14–14.5 GHz Fixed Satellite Service (FSS) spectrum. The array consists of 254 actively controlled elements that radiate variable linear polarization. Measured boresight EIRP is 41 dBW with a beamwidth of 6°. Cross-polarization isolation is better than 25 dB at boresight. The antenna can track a satellite from a fixed or moving platform with angular tracking rates better than 30 degrees/sec and at grating lobe-free scan angles greater than 60° from zenith. The antenna, when used with Boeing's commercially available 1515 element ku-band receive array, provides mobile users a highly capable communications link utilizing geostationary FSS satellites.

Introduction. To meet the growing demands of mobile communications users, and to utilize the large number of resources available in the commercial satellite FSS band (11.7-12.2 GHz downlink, 14.0-14.5 GHz uplink), Boeing has introduced a commercially available receive phased array antenna and a prototype transmit phased array antenna. Two transmit antennas have been built; one of which was delivered to NASA John H. Glenn Research Center for use in their ongoing research exploring next-generation air traffic control systems. The other transmit antenna was built for internal Boeing use. These systems allow a high-data-rate satellite uplink (typically greater than 20 Mbps) to a mobile platform (e.g., aircraft) and a lower rate satellite backhaul (typically 0.4-0.6 Mbps) from the mobile platform to a fixed ground station.

Antenna Design. The transmit antenna architecture combines features of many of the communication phased arrays that Boeing has developed [1]-[4] and is shown in Figure 1. RF energy is distributed by a corporate feed network integrated into a multilayer wiring board (MLWB). The MLWB also distributes dc and logic signals to the 254 element locations. Vertical connectors (termed 'fuzzbuttons') electrically and thermally join the MLWB to each module. The modules are connected to circular waveguide radiators that are tightly spaced in a triangular lattice and form a 16x16 element rectangular array.

Each module contains a multilayer hermetic ceramic package which houses a silicon ASIC phase shifter buffer and two GaAs devices that provide gain and define appropriate phase to the RF signal. The phase shifter buffer interfaces the beam steering controller to the module phase shifters. The incoming RF signal is split in-phase into two channels. Each channel is assigned four-bit phase information, amplified through two stages, combined via a Lange-type coupler, and radiated by orthogonal waveguide probes that are embedded in a dielectrically loaded circular waveguide. Varying the phase offset between the two-phase shifters generates linear polarization of arbitrary orientation. A multilayer wide-angle impedance matching (WAIM) substrate is used to provide environmental protection and to optimize scan performance.

Array Performance. The transmit antenna is shown in Figure 2 alongside the receive antenna for purposes of size comparison. The transmit antenna is approximately 13"x9" with a thickness of 1.5". For testing and characterization, it was installed in a five foot near-field scanner facility and insertion phase compensation was developed at 14.25 GHz. Additionally, linear polarization scans were taken to obtain an optimized directivity of 29.0 dBi and an aperture efficiency of 95.6%. Measured directivity was within 0.1 dB of expected. The antenna was then installed in a 32 foot indoor antenna range, where antenna patterns were taken at 14, 14.25, 14.5, and 15 GHz for a variety of elevation/azimuth scan angles.

The measured co-polarization and cross-polarization EIRP at 14.25 GHz for various main beam elevation scan angles and $\phi = 0°$ are shown in Figure 3. EIRP was measured when the antenna was driven at the 1 dB compression point. This EIRP corresponds to an output power of approximately 75 mW per element and an input power to the array of approximately 27.5 dBm. Input power to achieve 1 dB compression varied by 3 dB from 14-15 GHz. Measured half power beamwidth at boresight was 6° and 12° at 60° scan. At 60°, measured scan loss was 3.3 dB which compares well with a $\cos(\theta)^{1.1}$ distribution. Cross-polarization isolation was better than 25 dB at boresight and 16 dB at 70° scan from 14-15 GHz.

Measured versus commanded polarization angle at 14.25 GHz and the 1-dB compression point are shown in Figure 4. Measured polarization angle was within 5° of the commanded angle for all angles considered, resulting in negligible EIRP loss. A summary of measured versus commanded pointing angles is shown in Table 1. Pointing error was less than 10% for all scan angles considered.

Table 1. Measured vs. commanded scan angle and associated % error.

Commanded Scan Angle – Degrees Theta,phi	Measured Scan Angle (Theta)- Degrees	% Error
0,0	0	0
20,0	19.6	2.0
40,0	39.4	1.5
60,0	58.4	2.7
70,0	66.4	5.1
0,90	0	0
20,90	20.2	1.0
40,90	39.6	1.0
60,90	60.0	0
70,90	66.2	5.4

System Operation. The beam steering controller functions are calculated by a separate controller and serially transmitted to the antenna. A programmable gate array located inside the array performs a serial-to-parallel conversion and distributes the logic signals to the appropriate module locations via the MLWB. For polarization and closed-loop tracking, the receive antenna system must be used in conjunction with the transmit antenna in order to track signal level and polarization orientation. Using a sequential lobing technique, the receive antenna autonomously tracks the intended satellite, and the resulting beam pointing information is communicated to the transmit antenna via the system phased array controller (SPAC). One SPAC can control both the receive and transmit antenna arrays. An ARINC 429 interface to a navigation system can be used to acquire/reacquire satellite location.

The antenna has been used with the Telstar VI satellite at data rates of 200 kbps at 60° scan. A data rate of 400 kbps was achieved at broadside. The architecture is eminently scalable; much higher data rates would be possible with larger arrays.

Conclusion. Boeing has successfully developed a prototype actively controlled transmit phased array antenna for use in the commercial FSS frequency band. The antenna offers an EIRP of 36-41 dBW over a conical scan volume of greater than 120°, variable linear polarization and angular tracking rates in excess of 30°/sec. The design is based on a successful, low cost commercial architecture making future development of the antenna very affordable. It can be easily scaled to accommodate larger apertures for users with higher throughput demands. When used with Boeing's complementary receive phased array antenna, this transmit/receive antenna system provides users with a highly capable mobile communications solution.

Acknowledgments. The authors would like to thank D. N. Rasmussen for his work characterizing the transmit antenna in the antenna range and near-field scanner facility.

References
[1] E.J. Vertatschitsch, G.W. Fitzsimmons, "Boeing Satellite Television Airplane Receiving System (STARS) Performance," International Mobile Satellite Conference, Ottawa, Canada, June 6-8, 1995.
[2] R.Y. Shimoda, E.A. Sorenson, G.R. Onorati, "SHF Transmit/Receive Communication Phased Array Antenna," MILCOM, Atlantic City, NJ, Nov 2-4, 1999.
[3] R.W. Huggins, P.T. Heisen, G.E. Miller, D.J. McMeen, "Phased Array Transmit Antenna for a Satellite," *IEEE AP-S Intl. Symposium Digest,* vol. 1, July 1999, pp. 150-153.
[4] M. Chen, D.E. Reimer, D.N. Rasmussen, J.E. Wallace, H.J. Redd, R.C. Ettore, D.B. Peterson, R.N. Bostwick, G.E. Miller, "A 20-GHz Active Receive Phased Array Antenna for Navy Surface Ship Satellite Communications Applications," *IEEE AP-S Intl. Symposium Digest,* vol. 4, July 1999, pp. 2310-2313.
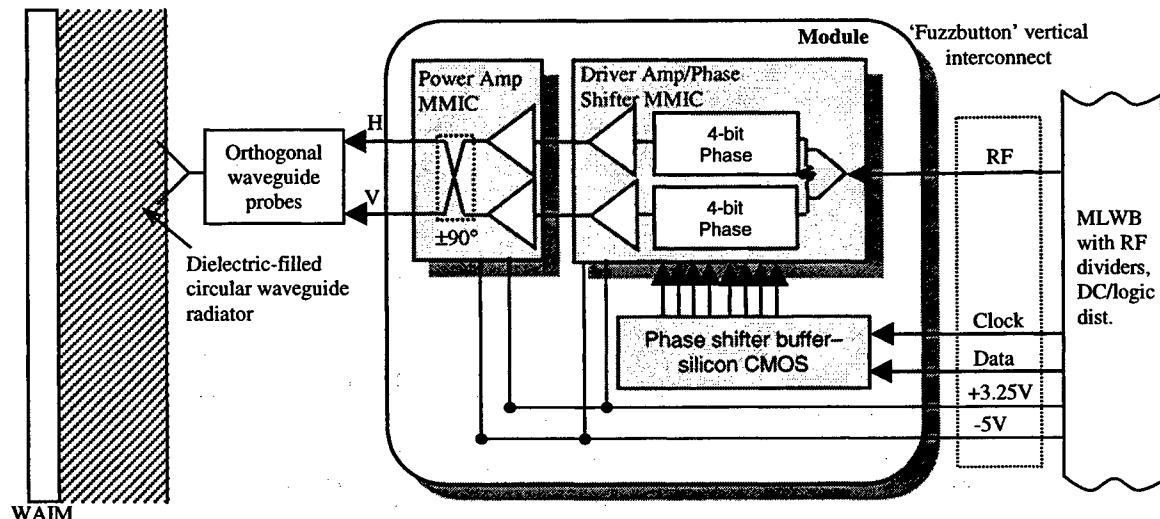
Figure 1. Antenna architecture.
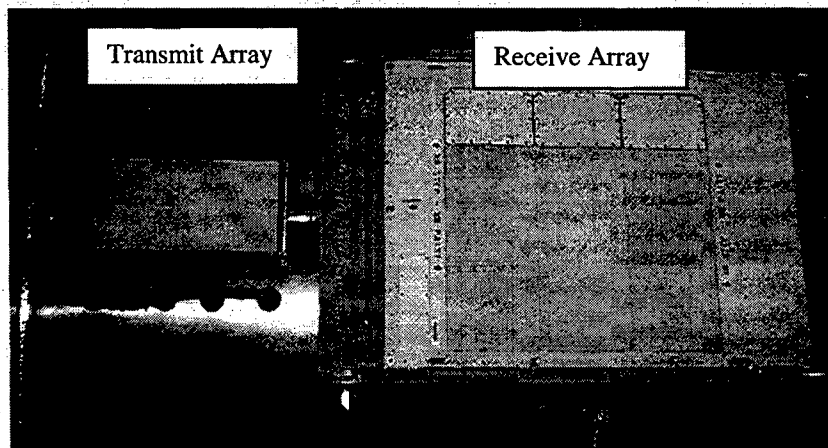
Figure 2. Transmit and receive phased array antennas.
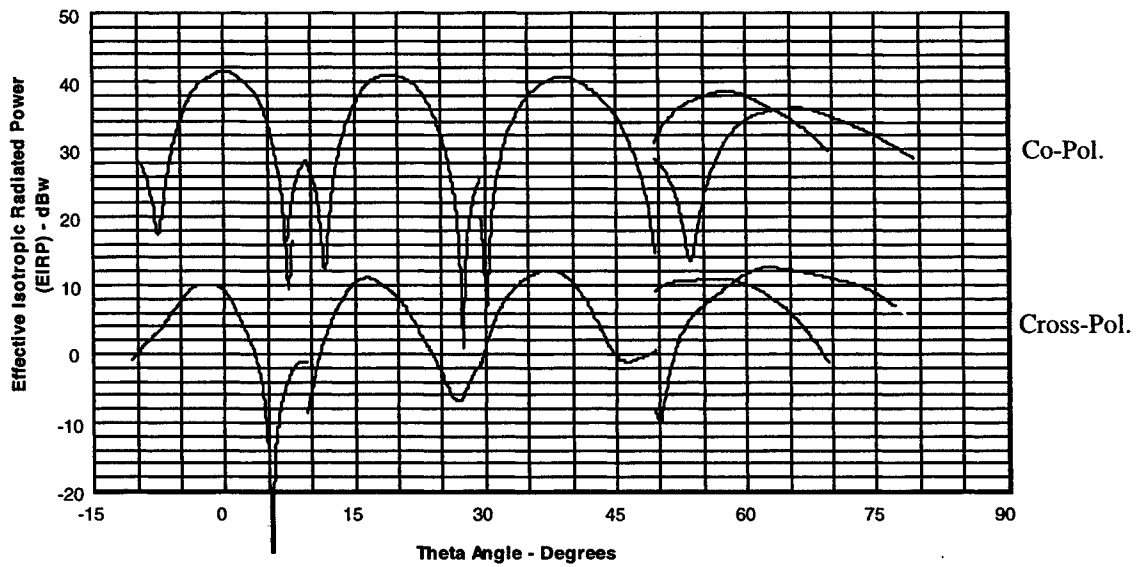
Figure 3. EIRP vs. main beam scan angle for $\phi=0$.
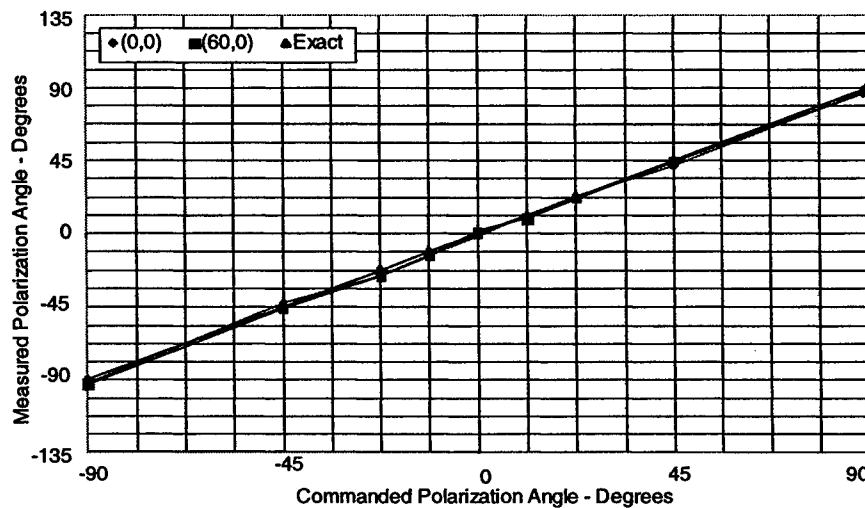
Figure 4. Measured vs. commanded polarization angle.

A Low Profile X-Band Active Phased Array
For Submarine Satellite Communications

Kuan M. Lee, Jay Edie, R. Krueger, J. Weber, and T. Brott
Raytheon Systems Company, El Segundo, CA
William Craig
Naval Undersea Warfare Center, Newport, Rhode Island

I. Introduction

There is currently a strong desire to achieve a level of connectivity for U.S. submarines that is comparable to other Naval platforms. To meet this goal, the submarine must support higher data rate communications via satellite. A candidate link is through the Defense Satellite Communications System (DSCS). The Submarine SHF Phased Array Antenna program, funded by the Office of Naval Research (ONR 313), has developed a phased array antenna that will support communications via DSCS while addressing the stringent volumetric and environmental constraints imposed by the submarine. An overview of this program is described in more detail in reference [1]. The DSCS operating band is in the low X-Band with right-hand circular polarized (RHCP) uplink and left-hand circular polarized (LHCP) downlink and therefore requires a dual-polarized antenna. The high static seawater pressures and other environmental conditions require a very high strength array structure. In order to fit within the existing submarine sail, the antenna must be very thin. In this paper, a low-profile X-Band phased array providing dual circular polarizations for submarine satellite communications is described. Representative test results will be shown. The calibration procedures used for the assembly of the array panel will be discussed. It is shown that good test results have been obtained from a near field probe test and various interesting array patterns can be obtained by adjusting the transmit/receive (T/R) modules.

II. Array Design

For the submarine application, the antenna will be subjected to the harsh sea water environment and be required to withstand an external hydrostatic pressures of over 1000 pounds per square inch (psi) and also dynamic wave slap conditions of over 9 psi. Figure 1 shows a cross-section of the thin (2.5") tile-based array design. To meet the design goals, wideband low-profile stacked disk radiators are chosen for the aperture with a conformal radome. A discussion of the design and analysis of these low profile stacked disk radiators is given in reference [2]. Incompressible material such as Duroid TMM3 and R4003 must be used to withstand the water pressure. Figure 2 shows an assembly view of the completed wideband, four-channel radiator tile. The feeding circuits for the stacked disks are printed on multiple layers in order to fit within the radiator spacing. Two wideband 180° hybrid circuits and one 90° hybrid are used with each radiator for dual polarization application. The array housing structure is made from titanium due to the environmental constraints of the submarine platform. This provides a lightweight and stiff structure. An assembly view of the T/R module is shown in Figure 3. Four T/R channels are packaged within each module. Each channel is made up of a transmit amplifier driving the RHCP radiator port and a receive low noise amplifier accepting signals from LHCP radiator port. Each channel provides 5 bits (31 dB) of gain control and 6 bits of phase control. The maximum power out used is 17 dBm, which is adequate for this application. The module noise figure is around 2.5 dB from 7-11 GHz. The module tiles are constructed from multi-layer low-temperature cofired ceramic (LTCC) material. The modules are held in place within an egg-crate titanium structure that will protect the modules from hydrostatic pressures. The RF feeds and the power/signal distribution boards are built in a layered configuration. Compressive interconnects are used for interconnects between the power distribution boards. The overall thickness of the array panel is 2.5 inches.

To verify the performance of the radiator and the T/R module prior to the installation of these components to the array, a test array with 2x6 active elements (Figure 4) has been successfully tested. Measured and predicted results are in good agreement as shown in Figure 5.

III. Assembly and Test

Figure 6 shows a front view of the assembled array panel. The array consists of 12 small signal/power distribution boards, 7 small azimuth feeds, one large elevation feed, one large signal/power distribution board and numerous vertical vias and coaxial connectors. The aperture consists of 196 four-channel T/R modules (784 T/R channels) and 784 low profile radiators. Liquid cooling is provided for the array through cooling channels and cold plates on the backside of the array. At the front of the array we have a thin radome and radome bezel (not shown in the figure). This forms the outer water barrier for the array.

In order to ensure the performance of the array, several functional tests were conducted at different levels of the assembly using appropriate special test equipment (STE). The STE hardware simulates full panel distribution functions for small sections of the array and checks the functions of control signal system, power system, RF system and cooling system. The lower level STEs are progressively replaced by actual components and interconnects for higher level test during the assembly of the array. Extensive test results have been obtained from these STE tests. The completed subarrays are then tested in a near field probe range to verify their performance. Typical results are shown in Figure 7 for a broadside beam for a 72-element (4x18) subarray. The measured results are close to the expected results. Many interesting patterns have been obtained from the subarray by varying T/R module amplitude and phase weighting as shown in Figure 8 for a 30 degree scan case and in Figure 9 for a Taylor distribution case. A phase-up procedure with the near field back transform calibration techniques has been demonstrated successfully in these results.

III. Conclusion

The assembly and test of a low profile X-Band active phased array for satellite communications is presented in this paper. An array panel consisting of 784 active elements has been assembled. The functions of the radiator and T/R modules and signal distribution boards in the array have been verified using special test equipment. Good array performance has been demonstrated in a near-field probe range.

IV. References

[1].   Edie, J. L., and W. P. Craig, "A Low Profile, Multifunction, Active ESA for High Data Rate Satellite Communications", MILCOM 97 Classified Proceedings, vol. 1, pp. 321-324, November 1997.

[2].   A. Wang, R. S. Chu, and K. M. Lee, "Planar, Low-Profile, Wideband, Wide-Scan Phased Array Antenna Using Stacked-Disc Radiator", IEEE AP-S International Symposium, Montreal, Canada, 1997, pp. 702-705.
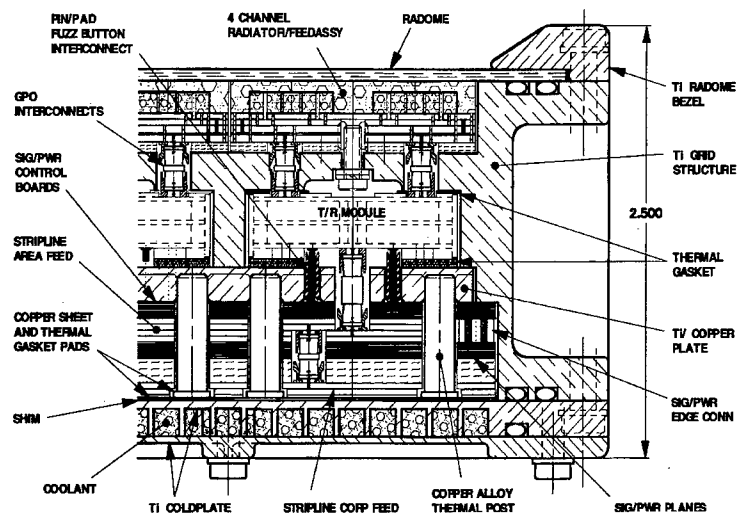
Figure 1. Cross-section of the thin tile-based phased array antenna.
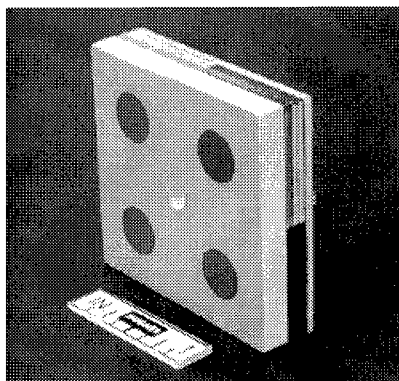
Figure 2. Wideband, four-channel radiator tile.
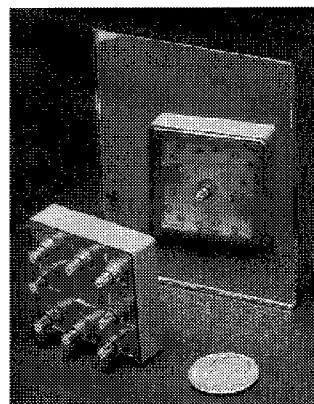
Figure 3. Four-channel Transmit/Receive (T/R) module.
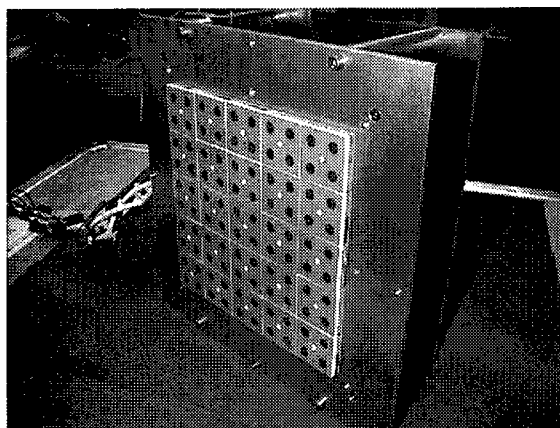
Figure 4. A 2x6-element test array for aperture test.
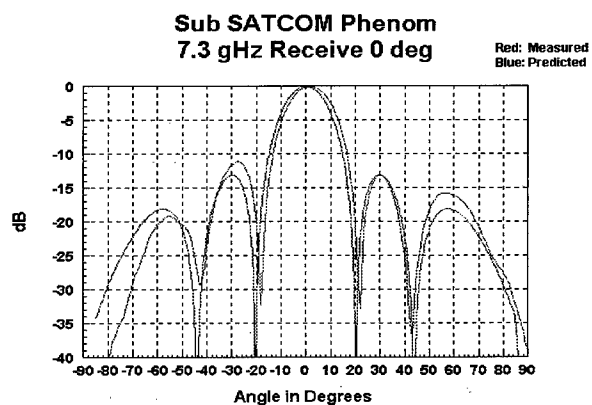
Figure 5. Test array measured results.

233
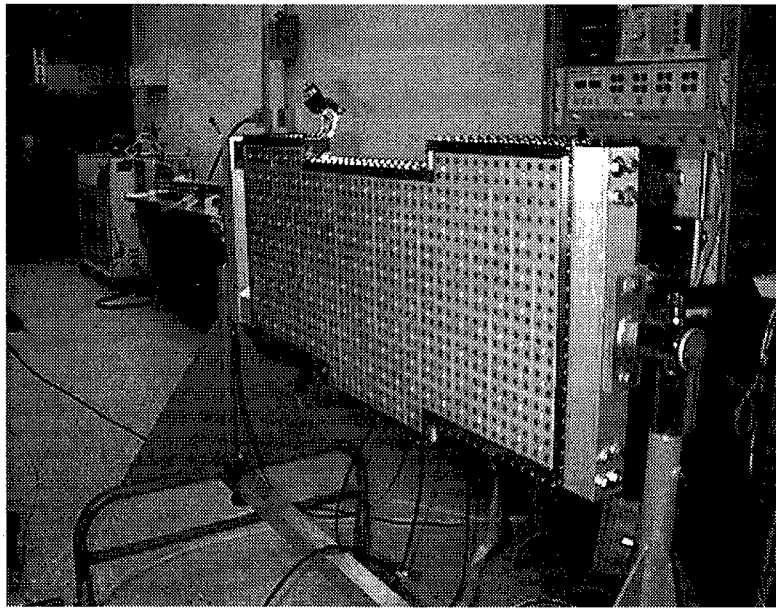
Figure 6. An overview of the 784 element array panel
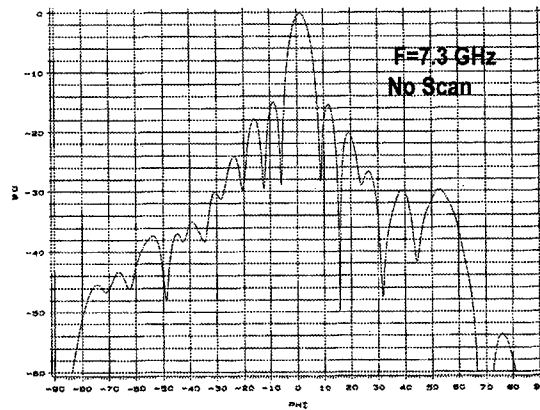
Figure 7. Measured pattern for a broadside case.
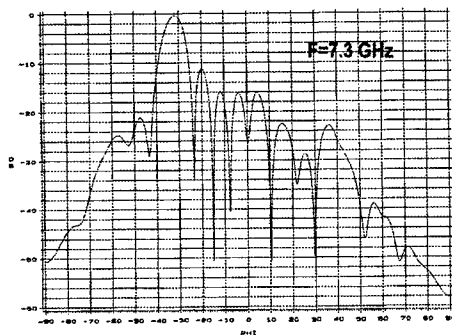
Figure 8. Measured pattern for a scan case.
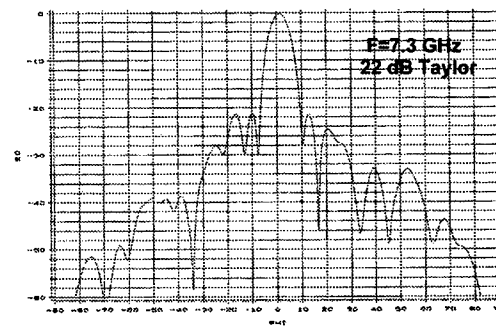
Figure 9. Measured pattern for a Taylor distribution.

234

TA2

Microstrip/Conformal Array Antennas

Chair: Johan Granholm

Microstrip/Conformal Array Antennas

Integrated RF Antenna and Solar Array
for Spacecraft Application

Mark Zawadzki
John Huang

Jet Propulsion Laboratory
California Institute of Technology
Pasadena, CA 91109

Introduction

There is a critical need for enabling technologies that will reduce the mass, physical size and cost of major spacecraft components. Virtually all spacecraft include at least one large-aperture telecommunications antenna and a large-aperture solar array. Combining these large apertures will achieve critical goal of reducing spacecraft mass, stowage volume, cost, and deployed surface area, without significantly affecting the performance of either the antenna or solar array [1]. This will also facilitate spacecraft maneuvers and attitude control, and increase the field of view of scientific instruments. The performance of the RF antenna and solar array both vary with the cosine of the angle from their broadside directions. This would allow significant mission flexibility and the potential to optimize the integrated array pointing-angle between the Sun and the Earth to obtain the proper combination of electrical power and RF gain. Most deep space missions have Sun/Earth subtended angles of less than 40°. If an integrated array were pointed half-way between the Sun and the Earth with a 40° subtended angle, then this would represent only a 0.5 dB loss for the antenna and only a 6% reduction in solar array output.

The objective of this research effort was to develop and demonstrate an integrated high-gain RF antenna and solar array technology for spacecraft application. The RF antenna technology selected was a printed microstrip reflectarray, which uses a large number of thin crossed-dipoles as the radiating elements. A microstrip reflectarray has the capability of integration with a solar array for the following reasons:

1) the reflectarray consists of many array elements printed on a flat panel, which is illuminated by a feed horn and does not require a power division network
2) the electrical characteristics of a reflectarray are similar to those of a conventional curved parabolic reflector, but since its aperture is physically flat and its elements function without power division network, it is amenable to integration with a flat solar panel; and,
3) the microstrip dipoles that are used as array elements are physically very thin, and will not significantly reduce blockage of sunlight to the solar cells situated below the RF elements.

Although both the microstrip reflectarray and the solar array are very thin in profile and low in mass, they separately require massive and large support panels to maintain their required aperture flatness. By combining the antenna and solar panels, thus eliminating one support structure, significant mass and launch vehicle stowage volume savings can be achieved. The goal of this research effort was to breadboard and test a half-meter-diameter aperture that was populated by both X-band reflectarray crossed-dipole elements and silicon solar cells.

Antenna Description

The reflectarray in this design consists of 408 X-band crossed-dipole elements that are etched onto a Kapton substrate, which is then laid on top of a standard solar array. The element spacing on the reflectarray was chosen to fit the solar cell size. The integrated solar/RF array consists of four basic components: 1) a mechanical support structure; 2) an X-band feed horn; 3) a solar array with 198 silicon solar cells; and, 4) a thin-film polyimide material (Kapton) with 408 printed reflectarray crossed dipoles. Fig. 1 shows a photograph of the final antenna, and Fig. 2 shows a sketch of the antenna cross-section with a top view of a single solar cell. Support for both the reflectarray and the solar cells is provided by a circular anodized aluminum plate, which is 0.5m in diameter and 6.4mm thick. A tripod strut assembly is used to hold a circularly-polarized, conical feed-horn with a 3dB-beamwidth of 39° and a -9dB edge taper to the aperture. The f/D ratio of the structure is 0.75. The solar cells are secured directly onto of the anodized aluminum plate with a silicon-based adhesive. A 1.52mm-thick (60mil) coverglass, which serves to protect the solar cell in space, is bonded to the top of each cell. This coverglass also provides the necessary vertical separation between the solar cells and the dipoles. The printed crossed-dipoles are etched onto a sheet of 0.051mm-thick (2mil) Kapton membrane, and secured to the top of the coverglasses with a silicon-based adhesive. Even though Kapton absorbs a significant amount of light energy in the same spectral region as the solar cells, which reduces the amount of light that reaches the solar cells, it was chosen because it is readily available in large pieces with a thin copper coating that is easily etched. This was a carefully considered trade. Polymers with higher optical transparency would be favored for future versions of the integrated array.

The reflectarray was designed using software developed by The University of Massachusetts [2], and used the Moment Method technique. Since the effect of the inhomogeneous nature of the cross-section, particularly the irregular ground plane (see Fig. 2), on the performance of the reflectarray was unclear, the strategy adopted was to etch three separate reflectarrays - one designed at the desired center frequency of 8.4GHz, and the other two ±3% away.

Results and Discussion

The solar array results were very good. While the Kapton membrane alone (no dipoles) reduced the power output of the cells by 40.5% (from the reference of using just coverglasses), the addition of the dipoles only reduced the output by about 10%, which would then be the expected overall loss if an optically clear membrane were used. This loss in power could be easily regained by increasing the area of the solar array by 10%, or by increasing the sides of a square array by only 5%. This is a very small amount considering the overall reductions of mass and volume realized by combining the RF and solar arrays.

The news for the RF portion, while encouraging, was not as good. As can be seen from the radiation patterns in Fig. 3, the reflectarray did form a coherent beam in the far field; however, the measured aperture efficiency was only about 10% - far from the expected value of 40%. This relatively low efficiency is likely the result of two main factors. First, the electrical characteristics of the overall reflectarray substrate, especially the inhomogeneous ground plane, were not well-understood or well-considered in the design, mainly because the fine, inhomogeneous silver grid on the top surface of the solar cells is difficult to characterize. The second factor has to do with the reflectarray element itself. It was felt that elements other than crossed-dipoles should be examined in an attempt to find an optimal element. Future work to improve the RF performance would focus on these two areas. Nevertheless, the result of this

240

development indicates that the integration of large antenna and solar array apertures is highly feasible.

Acknowledgements

References

1.   J. Huang, "Capabilities of Printed Reflectarray Antennas", IEEE Phased Array Systems and Technology Symposium, Boston, Massachusetts, October 1996, pp. 131-134.

2.   D. M. Pozar, "Reflectarray Antenna and Solar Array Integration for Spacecraft Applications", University of Massachusetts at Amherst, Final report prepared for JPL under Contract No. 960740, March 1997.
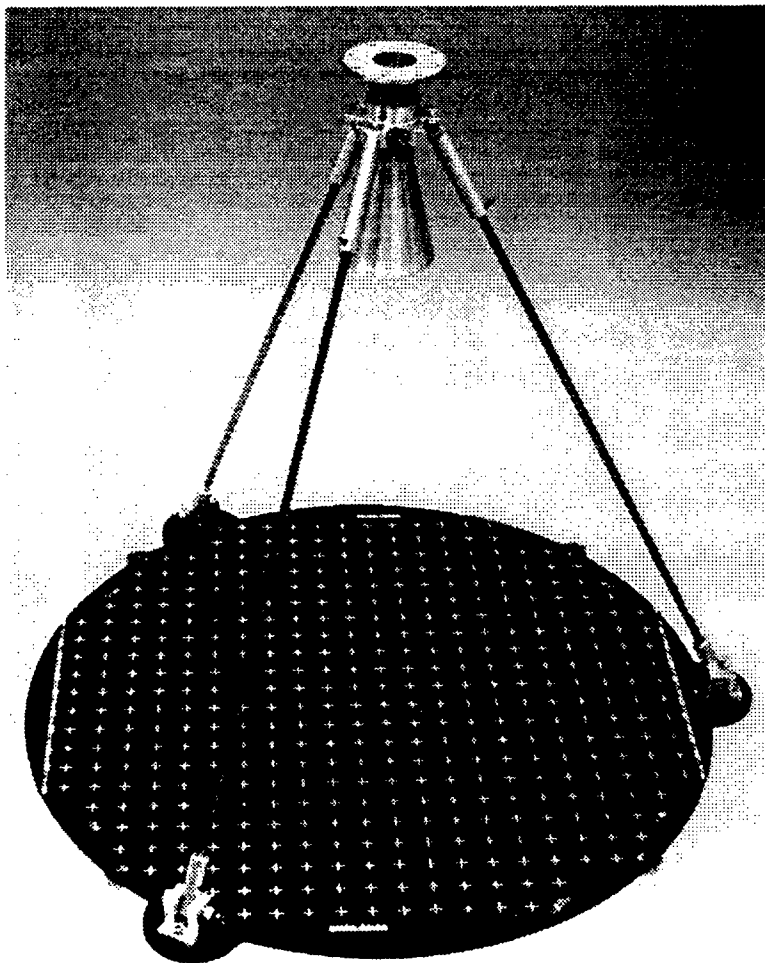
Figure 1. Photograph of integrated solar array with reflectarray crossed-dipole elements.

KAPTON SHEET WITH
COPPER DIPOLES

ADHESIVE

FUSED SILICA COVERGLASSES
(OVER SOLAR CELLS ONLY)

SILVER GRID (ANODE)

SILICON SOLAR CELL

SILVER PLATING (CATHODE)

ADHESIVE

ANODIZED ALUMINUM PLATE

CROSS-SECTION OF ANTENNA

SILVER GRIDDING
ON ANODE
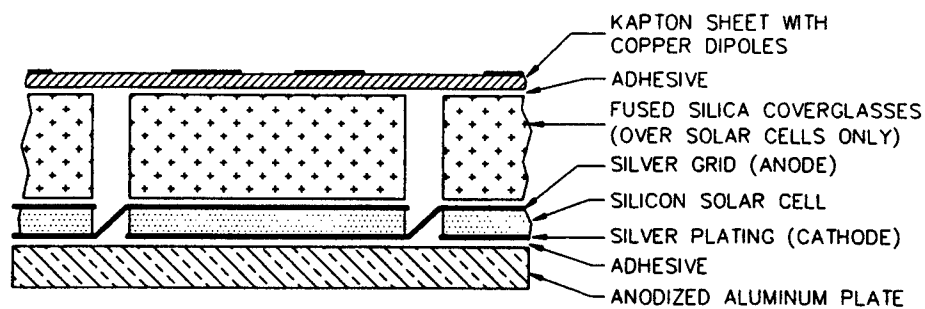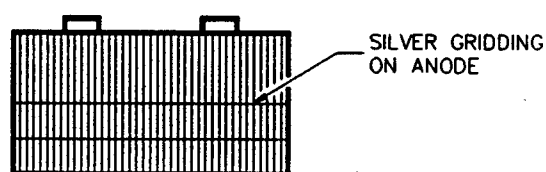
TOP VIEW OF SOLAR CELL

Figure 2. Cross-section of antenna and top view of solar cell.
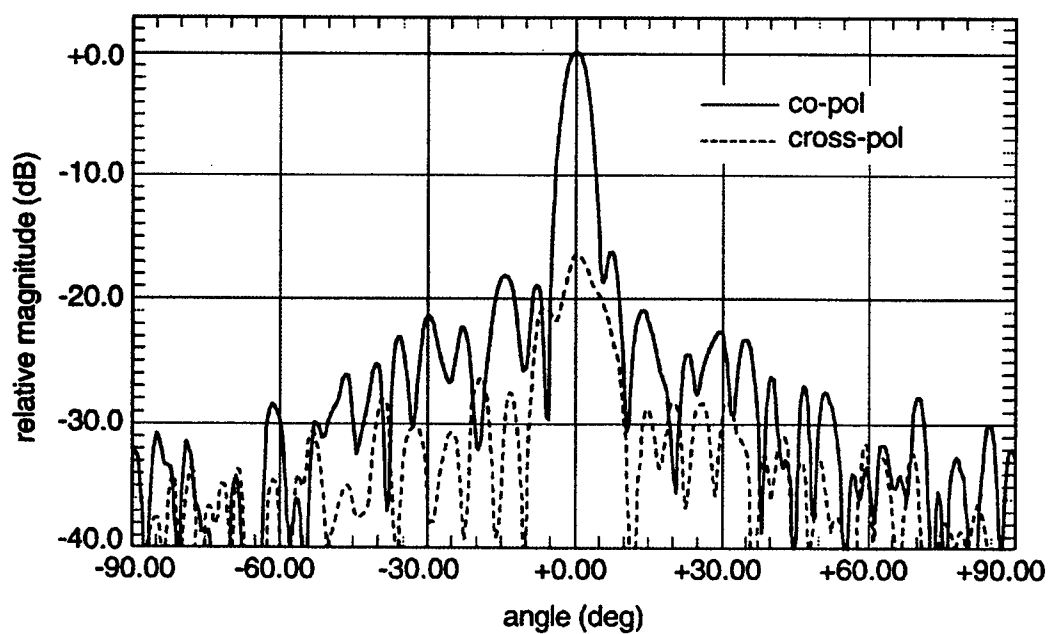
Figure 3. Measured radiation pattern of the integrated antenna at 8.5GHz

DUAL-POLARIZATION, WIDEBAND MICROSTRIP ANTENNA ARRAY FOR AIRBORNE C-BAND SAR

Johan Granholm & Niels Skou

Danish Center for Remote Sensing, Department of Electromagnetic Systems, Technical University of Denmark, Building 348, DK-2800 Lyngby, Denmark (jg@emi.dtu.dk, ns@emi.dtu.dk)

Abstract
The paper describes the development of a C-band, dual-linear polarization wideband antenna array, for use in the next-generation of the Danish airborne polarimetric synthetic aperture radar (SAR) system. The array is made of probe-fed, stacked microstrip patches. The design and performance of the basic stacked patch element, operating from 4.9 GHz to 5.7 GHz, and a 2x2 element test-array of these, are described.

Introduction
High-resolution airborne and spaceborne imaging of the Earth is often carried out using remote sensing techniques, such as SAR. Early SAR systems were single-polarization instruments, but time has seen a growing interest in dual-polarization (i.e. "polarimetric") SAR systems. The reason for this trend is the additional amount of geophysical information, which it is possible to extract from polarimetric SAR data, compared to single-polarization data. It is well known, that radar signatures of e.g. crops are polarization dependent. An intuitive physical explanation of this dependence is, that the vertical polarization primarily are reflected by the vertical structures (e.g. straws, trunks), whereas the horizontal polarization are in stead reflected by the predominantly horizontal structures (e.g. branches). Mapping an area with polarimetric SAR thus provides more information, hence allows more details to be distinguished and increases the ability to classify targets. Future SAR systems for e.g. crop study and monitoring are therefore required to be polarimetric instruments. Several space agencies and other institutions are currently developing such next-generation polarimetric SAR systems, [1] - [4].

Resolution requirements for future SAR systems
Several polarimetric SAR systems have already been built and flown, incl. the Danish L- and C-band system, EMISAR, developed at Department of Electromagnetic Systems, Technical University of Denmark (EMI), [5]. The EMISAR system has a resolution of approx. 2 m in both range and elevation. At the time of design (1993) this was state-of-the-art, but not least due to the rapidly advancing digital technology (especially high-speed data acquisition and storage systems), higher resolutions are possible today. At the same time user demands, e.g. for surveying applications, continue to call for increased resolution. Both for scientific and commercial mapping purposes, there are a desire to achieve resolution of 0.25 x 0.25 m.

The maximum SAR azimuth resolution is not dependent on the bandwidth of the transmitted radar chirp, but on the pulse-repetition frequency and to a first approximation to the physical antenna length, l_A. The SAR azimuth-resolution, δR_A is limited to:

$$\delta R_A = l_A/2$$

This (frequency independent) result shows, that to obtain an azimuth resolution of 0.25 m the antenna should be max. 0.5 m long. Lower frequency results in less gain with this limited antenna length. High-resolution SAR systems therefore are difficult at lower microwave frequencies.

The maximum range-resolution in SAR systems, δR_R, and the bandwidth requirement are inversely proportional:

$$\delta R_R = c/(2B_R)$$

where B_R is the bandwidth of the transmitted pulse and c is the speed of light. The present EMISAR system has 100 MHz bandwidth in both L-band and C-band, translating to approx. 2 m resolution in range, including proper weighting. To obtain 0.25 m resolution in range, the pulsed chirp must therefore have an eightfold increase in bandwidth. Although the range resolution of both the L-band SAR (with centre frequency 1.25 GHz) and the C-band SAR (centered at 5.3 GHz) is desired to be increased in the next-generation EMISAR system, technology will not allow for this in L-band. In C-band, however, it may be possible to achieve up to 800 MHz bandwidth. The goal therefore is to upgrade the, today medium resolution, C-band EMISAR to a high-resolution system, capable of 800 MHz operation. To be compatible with existing and planned civilian and scientific air- and spaceborne SAR's (to allow for data comparison), the centre frequency shall remain 5.3 GHz.

Requirements for polarimetric SAR antenna arrays
Future polarimetric SAR-systems require compact and lightweight dual-linear polarization antenna arrays, which should preferably be flat to facilitate easy installation; e.g. conformal on the fuselage of aircrafts. The arrays' elevation plane radiation patterns shall be shaped to resemble a modified cosecant-squared shape (to compensate for the range-dependence), while the azimuth plane radiation patterns shall be narrow, with a moderately low sidelobe level, and symmetrical w.r.t. boresight. In order to obtain a high degree of polarization discrimination of the overall SAR system, it is a further requirement to the array, that it should have a low cross-polarization level. An antenna element, which complies with these requirements, is the microstrip patch. Although it is very narrowbanded as a single-layer structure, a stacked patch can be added to significantly increase the bandwidth.

Aperture coupled microstrip patches, although capable of offering wide bandwidth, has the drawback that, in a practical antenna, a closed cavity is required to be placed behind the aperture. Such cavities may lead to a reduction of the bandwidth of the "naked" element but, worse, the cavity will take up valuable board space underneath the aperture. Due to this "real-estate" problem, this cavity may prevent, or at least severely complicate, the (already challenging) design and layout of the necessarily multilayer beamforming network (BFN), which must reside under the groundplane, below the aperture. Furthermore, apertures are known to excite surface waves far stronger, than probe-fed patches. For these reasons aperture-coupled patches is not the optimum choice in this application. Probe-fed patches are attractive from the a feeding network point of view, since the probes does not take up any board space, and easily connect the patch to its beamforming network, which is e.g. located several layers down from the patch groundplane. For this reasons probe-fed patches are chosen.

The existing C-band EMISAR system [6], operating over an approx. 2 % bandwidth, uses a single, probe-fed patch. The L-band EMISAR system [7], which is also operating over a 100 MHz bandwidth (translating to 8 %), uses a stacked probe-fed patch. The idea thus was to investigate, if the stacked patch concept could be adopted and optimized to operate over an 800 MHz bandwidth in C-band.

Selection of dielectric substrate
The bandwidth of microstrip patches depends strongly on the substrate thickness and -permittivity. For practical reasons, C-band patch probes shall be fabricated as "integrated via's". Although electrical attractive, this mechanical requirement preclude the use of low loss, low permittivity foam materials, since via's can neither be grown, nor supported, by such soft materials. Hence, for bandwidth reasons, it is desirably to use a thick, low

permittivity hard substrate. On the other hand, the maximum thickness is limited for several reasons: A thick substrate may support the (undesirable) propagation of excessive surface waves, and will also be heavy. Furthermore, it will necessarily imply a long feeding probe, which electrically act as a large series-inductance, thus reducing the element bandwidth.

Due to fabrication and reliability issues, the multi-layer stripline BFN and the radiating patch layer should preferably be fabricated using the same type of substrate. The wide bandwidth requirement will demand that the elements must be fed through a binary-type network in the azimuth direction. In the elevation direction, it is desired to shape the elevation pattern, so that it will resemble a modified cosecant-squared pattern. This elevation BFN will be implemented using couplers and lines. It is desirable to be able to vary the characteristic impedance of the striplines over a wide range (w.r.t. 50 Ω), within acceptable linewidths (e.g. 5 mm to 0.5 mm) to facilitate the design of these couplers, lines and necessary impedance matching networks. This requirement also calls for the use of a low permittivity substrate, although its thickness can be chosen independently of the patch substrate thickness. The design of the BFN, however, is a separate task, and will not be covered in this paper.

In this work, 32 mil (0.8128 mm) Rogers RO4003 substrate was initially chosen for the driven patch, having a dielectric constant ε=3.38 and loss tangent tanδ=0.0027 @ 10 GHz. The RO4003 material is constructed as woven glass cloth, impregnated with a ceramic loaded thermoset plastic resin to yield a thermally stable rigid laminate with electrical properties suitable for microwave frequencies Although the RO4003 permittivity and dielectric loss factor is somewhat higher than PTFE-based materials (e.g. Rogers RT/duroid 5870 having ε=2.22 and tanδ=0.0009 @ 10 GHz), RO4003 is attractive in an antenna feasibility study like the present, since RO4003 resembles FR4 in mechanical integrity and can be fabricated like basic FR4 material (and also because of its much lower price). Hence prototype development of stripline PCB's with integrated via's is much faster and cheaper if using RO4003 materials, than if using a PTFE-material.

Design of the C-band wideband element

The starting point in the design of a stacked patch, is the design of the driven (i.e. single-layer) patch, shown in Fig. 1. It is designed so that its resonance frequency is in the centre of the band, i.e. 5.3 GHz.

L = 14.5 mm
D = 0.3 mm

a)   b)
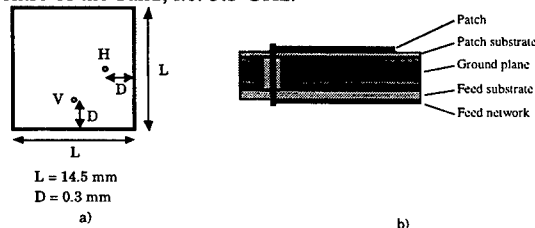
Fig.1. Dual polarization probe-fed microstrip single patch;
a) Top view of the patch, b) cross section.

The patch is fed close to its edges using 0.6 mm diameter probes (in the laboratory patch, the probe is directly made from the center conductor of a SMA-connector). Two probes (designated "H" and "V"), located on the patch' center lines, are used to excite the patch in orthogonal modes. This orthogonality will have the effect, that the coupling between the H and V-ports (i.e. the scattering parameter S_{21}) remains fairly low in the vicinity of the patch resonance frequencies ("resonance frequency" is defined as the frequency at which the real part of the patchs' input impedance achieves its maximum value, when the reference plane is at the upper side of the ground plane). The measured input impedance of the driven patch alone is shown in Fig. 2.
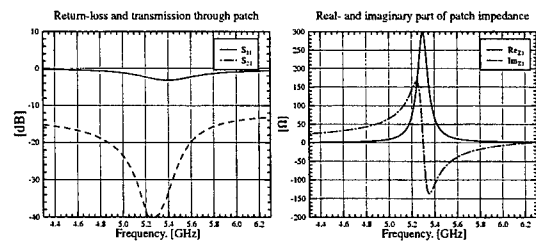
Fig. 2. Measured S-parameters and input impedance of single-layer C-band microstrip patch.

There is only one resonance in the band shown (approx. at 5.3 GHz). The impedance for the two ports is identical. An interesting experimental observation is, that the resonance frequency occurs at the same frequency where the two ports are best de-coupled (i.e. at the frequency where the scattering parameter S_{21} exhibits its minimum). At this frequency it can therefore be expected, that the cross-polarization level of the patch will be best, because S_{21} is minimum. When designing microstrip patches for dual-polarization purposes, it is important to obtain a low level of the element S_{21}, since the "cross-coupled" power will directly affect the cross-polarization level.

The impedance match of the single-layer patch to 50 Ω (i.e. the scattering parameter S_{11}) is quite poor, but this is a direct consequence of the patch being fed at the edge. Here the input impedance is on the order of 300 Ω. If a single-layer patch is desired to have a good intrinsic match to a lower impedance level (e.g. 50 Ω), this can easily be accomplished simply by moving the feed points towards the patch center.

The measured radiation pattern of the single-layer probe-fed microstrip patch is shown in Fig. 3. All pattern measurements presented in this paper have been performed in the spherical near-field test facility of EMI, [8].
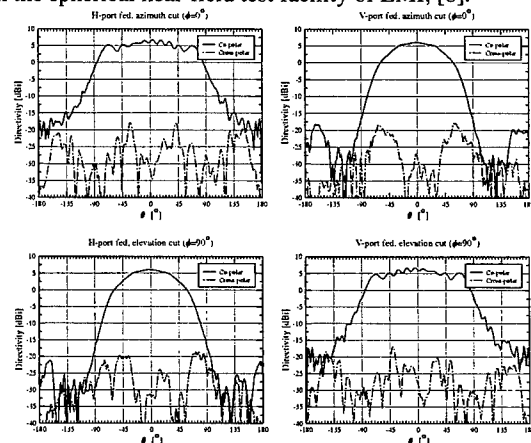
Fig. 3. Radiation pattern of single (unstacked) microstrip patch (f = 5.3 GHz).

The co-polarized fields in the E-planes (i.e. H-port fed, azimuth cut and V-port fed, elevation cut) show the typical rippled behaviour due to diffraction at the edges of the finite sized (0.5 m x 0.5 m) ground plane. The co-polarized fields in the patch's H-plane, on the other hand, have a much smoother appearance. The cross-polarization level in the main beam is seen to be approximately of the same magnitude as the level of the transmission through the patch (approx. -30dB at 5.3 GHz which is almost the same as the "intrinsic element-S_{21}", i.e. S_{21} measured, but corrected for mismatch loss). The peak directivity is approx. 6 dBi.

As shown in Fig. 2 a single-layer patch can far from achieve the 800 MHz bandwidth required, and a stacked patch is therefore added. This configuration is shown in Fig. 4.

L = 14.5 mm
D = 0.3 mm

a)   b)
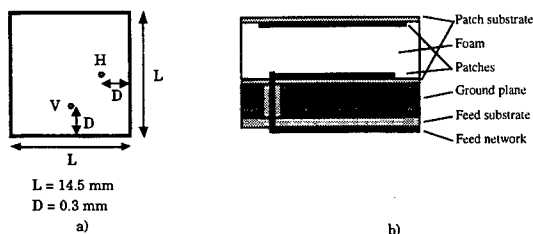
Fig. 4. Dual polarization probe-fed microstrip stacked patch; a) Top view of the lower patch, b) cross section.

The driven patch is identical to the one shown in Fig. 1. The upper patch acts as a passive parasitic element. Although the impedance of the single (i.e. unstacked) driven patch, when fed on its edge, is very high (see Fig. 2), it is significantly reduced when being loaded by the stacked patch. Hence, to obtain an approx. 50 Ohm input impedance of the stacked patch, the driven patch is fed on the edges. The dual linear polarization requirement implies, that the stacked microstrip patch must be constructed symmetrically. A pair of quadratic and co-axially aligned patches is therefore used.

Since no direct synthesis method for the design of wideband stacked microstrip patches is known, an iterative numerical design process, using an electromagnetic simulator, was adopted. The sizes of and the distance between the two patches were varied, until the desired wideband performance was obtained. During this process it was found, that a good starting point was to design the driven patch first, having its resonance frequency lying in the centre of the band of interest. The stacked patch adds a second resonance, and the task is now to find the parameters so that the two resonances balance in value (i.e. are excited equally strong), and are spaced in frequency so, that the impedance remains constant over the band.

Using this "numerical iterative design", combined with impedance measurements to validate the approach, a stacked C-band microstrip patch yielding an near-optimum result was found, when the size of the quadratic lower and upper patches were 14.5 mm and 19.5 mm, respectively. The upper patch is etched on a 0.1 mm FR4 substrate, and mounted inverted to let the FR4 material act as environmental protection. The spacing between the patches is 4.5 mm, using a Rohacell 31 HF foam material having ε_r of 1.05. All layers are glued together, using a 0.1 mm thick adhesive film (supplied by 3M; type 665). The measured scattering parameters for this element are shown in Fig. 5.
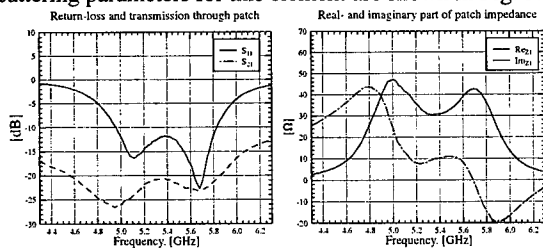
Fig. 5 Measured S-parameters and input impedance of wideband, stacked C-band microstrip patch.

A wideband behaviour for the stacked patch is indeed observed. Note, that the two "peaks" of the real-part input impedance balance quite well. Also, note how the parasitic loading of the lower patch leads to a significant decrease of the input impedance, compared to the single-layer patch. It is seen, that the intrinsic impedance of the stacked patch is not very different from 50 Ω (S_{11} of the unmatched patch remains below -10 dB in a 50 Ω system, over a 860 MHz bandwidth). This typical characteristic of the stacked patches eases the matching of the element to 50 Ω.

Rather than matching the element to 50 Ω, it should be considered to design the entire BFN using a slightly lower reference impedance (e.g. 40 Ω). This will only require one transformation from 40 Ω to 50 Ω (at the input of the array), thus saving board space and reducing the losses (since the

loss in a 40 Ω system will be lower than the loss in a 50 Ω system). If reducing the system impedance to 40 Ω and implementing a simple microstrip matching network at the patch feeding point, this has been found to bring S_{11} of the patch down below -20 dB, over the 800 MHz bandwidth.

Note that the transmission through the patch (i.e. the scattering parameter S_{21}) is seen to exhibit a similar "stagger-tuned" characteristic as seen in the real-part of the input impedance. The average level of S_{21} for the stacked patch is somewhat poorer than for the single-layer patch, but from a network point-of-view this stagger-tuned behaviour is not surprising. Due to this characteristic of S_{21} it must be expected, that the cross-polarization of the stacked patch is slightly worse, than for the single-layer patch. The "stagger-tuned" behaviour of S_{21} of a stacked patch may probably be the reason why stacked patches are sometimes claimed in the literature to have a poorer cross-polarization performance, than single-layer patches. The above level of S_{21} (between -20 dB and -25 dB) is typical for wideband, probe-fed stacked microstrip patches.

The measured radiation pattern of the stacked microstrip patch is shown in Fig. 6.
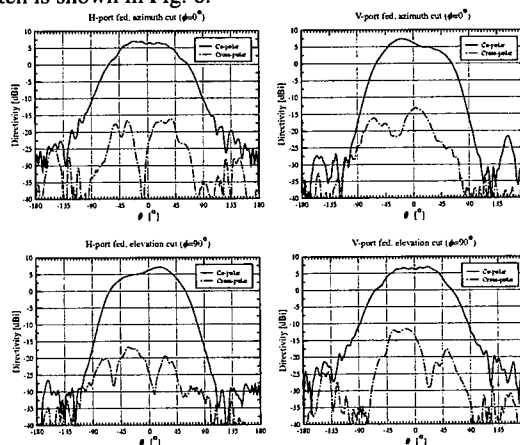
Fig. 6. Measured radiation pattern of stacked microstrip patch (f = 5.3 GHz).

The stacked patch radiation pattern has a slightly higher directivity, compared to the unstacked patch. The H-plane pattern of the stacked patch is somewhat asymmetrical (elevation-plane for the H-port fed; azimuth plane for the V-port fed). This behaviour is neither expected, nor understood, and is believed to have been caused by either improper alignment of the two patches or by passive loading of the driven patch by adjacent (non-driven, but still mutually coupled) patches. A new measurement is planned to investigate this further, and will be reported at the conference (previously stacked patches designed at EMI have all had well-behaved patterns). Despite this slight pattern anomaly, the co- and cross-polarization patterns are both quite usable for arrays. The influence of the ground plane is much less significant, than for the single-layer patch. The pattern remain stable over the full 800 MHz bandwidth, but the main beam narrows with increasing frequency, and the associated peak directivity increases from 6.5 dBi at 5.1 GHz to 10 dBi at 5.9 GHz.

The cross-polarization level for the stacked patch is worse than for the single-layer patch, but this was expected, due to its higher S_{21}-level. If this level of cross-polarization is not compliant with array requirements, simple, yet very efficient, techniques can be employed in the large array to substantially improve the overall array cross-polarization suppression over that of the basic stacked patch element. A cross-polarization improvement of typical 15 dB in microstrip patch arrays has been achieved using the method described in [9] and [10]. A practical example of the implementation of this cross-polarization improvement technique is found in [7].

245

To investigate wideband array-issues, four stacked patch elements were combined into a 2 x 2 element group, as shown in Fig. 7. The S-parameters of the array was measured in the case where the elements were connected to two four-way Wilkinson power splitters/combiners using coaxial cables (i.e. all elements were fed in equal amplitude and phase). The element spacing was approx. 0.7 λ_0.
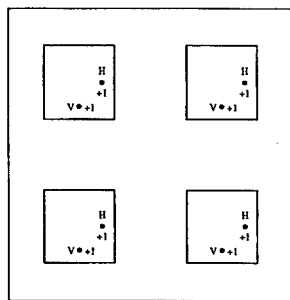
Fig. 7. Layout of 2 x 2 element stacked microstrip array.

The measured S-parameters are shown in Fig. 8, and are compared with the calculated S-parameters in the two cases: a) Mutual coupling between the elements is neglected in the calculation, b) All mutual couplings between the elements are taken into account. In the a) case only the four eigen-impedances of the patches were connected together (in the computer) with the measured S-parameters of the four-way Wilkinson power splitters and associated cables. In the b) case, all S-parameters of the 2 x 2 element dual-polarized array (i.e. the full eight-port), all cables, and the power dividers were measured and connected.
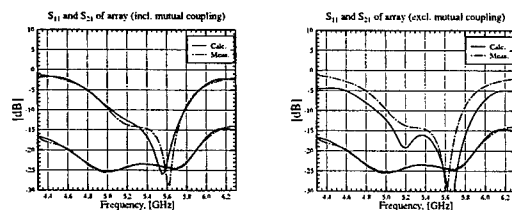
Fig. 8. Measured S-parameters of the 2 x 2 element stacked C-band microstrip array

From Fig. 8 it is observed, that the bandwidth of the 2 x 2 element group is slightly lower than for the individual stacked element. This is due to mutual coupling between the elements, and to a lesser extent due to the finite bandwidth of the Wilkinson divider. Note that S_{21} of the array is practically identical to S_{21} for the element. Also note, that the mutual coupling certainly must be taken properly into account, otherwise measured vs. calculated data does not agree very well. The measured radiation pattern of the 2 x 2 element array is shown in Fig. 9.
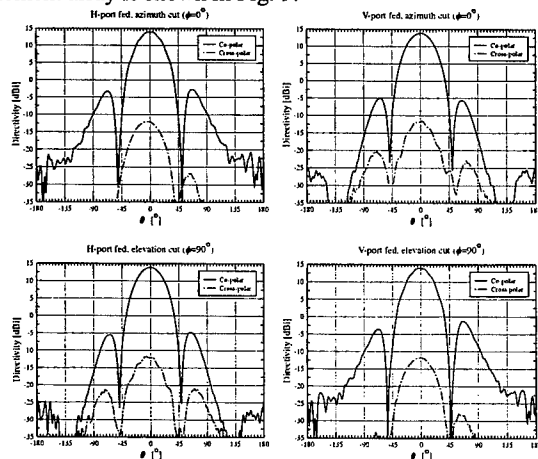
Fig. 9. Radiation pattern of 2 x 2 element array of stacked microstrip patches (f = 5.3 GHz, uniform excitation).

The radiation pattern is symmetrical, does not show any sign of anomaly, and has deep nulls. The peak directivity is 13.9 dBi at 5.3 GHz, increasing to 14.8 dBi at 5.9 GHz. The cross-polarization level is on the order of -25 dB, which is slightly better than for the individual element. Measurements confirm that the pattern is stable over a very wide frequency range (in excess of 1 GHz), and that the cross-polarization level remains low.

As demonstrated, low-cost stacked microstrip probe-fed patch arrays can be designed, capable of operating over a 15 % bandwidth in C-band. What still remains in order to arrive at a complete antenna, is the design of the azimuth and elevation beam forming networks.

Future work
The C-band element described here is presently being integrated into a full dual-frequency array (L- and C-band). This array will be based on the use of perforated, stacked L-band patches [11], inside the perforations of which the C-band elements are placed.

Conclusion
The design and performance of a wideband, dual-polarization probe-fed microstrip C-band antenna element, and a small test array, have been described. The element will be used in an 800 MHz dual-polarization array, being designed for use with the next-generation of the Danish airborne SAR system, EMISAR. The dual-polarization probe-fed microstrip array described here is believed to be the most widebanded antenna of its kind yet reported, for use in polarimetric SAR systems.

References

[1] JPL's "LightSAR", see e.g. http://lightsar.jpl.nasa.gov/

[2] European Space Agency's "Envisat", see e.g. http://envisat.estec.esa.nl/

[3] Canadian Space Agency's "RADARSAT II", see e.g. http://www.space.gc.ca/eng/about/radarsat/rad8.html

[4] Department of Electromagnetic System, Technical University of Denmark's next-generation SAR, "SAR++"; see http://sarppsrv.emi.dtu.dk/~sarpp/

[5] E.L. Christensen, N. Skou, J. Dall, K. Woelders, J.H. Jørgensen, J. Granholm, S.N. Madsen, "EMISAR: An absolutely calibrated polarimetric L- and C-band SAR", *IEEE Trans. on Geoscience and Remote Sensing Applications*, Vol. 36, no. 6, Nov. 1998, pp. 1852-1865.

[6] J. Granholm, K. Woelders, M. Dich, E. Lintz Christensen, "Microstrip antenna for polarimetric C-band SAR", *IEEE Int. Symp. on Antennas and Propagation*, Seattle, WA, June 1994, pp. 1844-1847.

[7] J. Granholm, K. Woelders, "Dual polarization microstrip antenna array with very low cross-polarization", submitted for publication in *IEEE Trans. on Antennas and Propagation*.

[8] J.E. Hansen, F. Jensen, "Spherical near-field scanning at the Technical University of Denmark", *IEEE Trans. on Antennas and Propagation.*, Vol. 36, June 1988, pp. 734-739.

[9] J. Granholm, K. Woelders, "Dual-polarization antenna array with very low cross-polarization and low side lobes", *International PCT Patent Application no. PCT/DK97/00141*, filed March 26, 1997.

[10] K. Woelders, J. Granholm, "Cross-polarization and sidelobe suppression in dual linear polarization antenna arrays", *IEEE Trans. on Antennas and Propagation*, Vol. 45, No. 12, Dec. 1997, pp. 1727-1740.

[11] J. Granholm, "Dual-frequency and polarization antenna arrays for future SAR systems", *21" ESTEC Antenna Workshop on Array Antenna Technology* (ESTEC publication WPP-142), Noordwijk, The Netherlands, 6-8 May 1998, pp. 29-35.

A Novel Design for the Microstrip Leaky-Mode
Antenna Array with High-Efficiency

Cheng-Nan Hu, Ching-Kuang C. Tzuang and Shyue-Dar Chen

Institute of Electrical Communication Engineering, National Chiao Tung University,
Hsinchu, TAIWAN; e-mial:cktzuang@cc.nctu.edu.tw

Abstract – A novel design of a closely coupled microstrip leaky-mode antenna array is proposed, built, and tested, showing the gain of 19.35 dB, directivity of 19.8 dB, and overall radiation efficiency of 83%. Detailed analyses and array design are presented for prototyping an eight-element antenna array. Excellent agreement between the theoretical and measured results is obtained.

I. Introduction

Recently we witnessed a rapid growth of wireless communication systems where antennas play a paramount role in establishing a communication link between different destination points. With diversified applications of wireless communications, there has been an increasing demand for high performance antennas for use in the commercial market that a low-cost, low profile, low weight, and more aesthetic antenna is often required. One popular design is the microstrip-array antenna, since it has the above-mentioned desired features. One problem with this type of antenna array, however, is the lack of efficiency when the desirable gain is high. Recently, Ando, et al. [1], proposed a variety of RLSAs (radial line slot antennas) to achieve antenna efficiency as high as 85%. Malherbe [2] reported a novel NRD (nonradiating dielectric) antenna array, showing almost 100% of aperture efficiency, when excluding the power loss in the load. All of these antennas have one common disadvantage in that they are not realized in the printed-circuit form, needing extra transition circuit to interface to a typical MIC (microwave integrated circuit) transceiver.

Hu and Tzuang [3] reported a novel microstrip leaky-mode antenna array, by which a pencil beam could be produced using a linear, one-dimensional array, thereby greatly reducing the complexity of feeding network. It, however, showed only 30% antenna efficiency. Careful antenna loss budget analyses indicated that two fundamental reasons caused such high losses, namely, large backlobe due to finite array length and high insertion loss from the corporate feeding network. One may enlarge the array length to reduce the backlobe radiation. This in turn will reduce the antenna efficiency because of large area is involved while gain improves fairly little. Regarding the improvement on the feeding network, one may design a better feed structure to reduce losses. This paper presents a novel design of microstrip leaky-mode array that simultaneously tackles the two fundamental problems, thus enhancing the antenna efficiency over 80%.

Figure 1 illustrates the proposed, eight-element, leaky-mode microstrip antenna array, showing one power divider, two series-fed networks, and eight matched balun feeding structures for exciting the EH_1 (the first higher-order) mode of the corresponding array with each microstrip of length L and width W, which is placed very close to the adjacent microstrip at gap distance S much smaller than W. To rigorously analyze the mode coupling of leaky modes inherent in the array, the coupled-mode approach is employed [4]. Consequently the 8-element array under uniform excitation can be designed by the modal analysis based on the eigenfunction approach, which explicitly reveals the guided waves aspect of the closely coupled leaky-mode array under development. Finally, the prototype of an 8-element microstrip leaky-mode array is designed and tested, showing overall efficiency of 83%, gain of

19.35 dBi, which is twice as large than that was90 in the past [3], i.e., the loosely coupled microstrip leaky-mode array.

II. Analysis and Design
A. Dispersion Characteristics of the Coupled EH_1 Leaky Modes

As shown in Fig 1, microstrips are placed tightly to form a compact, linear array. However, the modal characteristics of the higher EH_1 modes will be altered by the coupling between the adjacent microstrip lines. Incorporating the rigorous full-wave analysis and the coupled-mode approach [4], one can obtain both the undisturbed (before coupling) EH_1 mode and the coupled EH_1 modes of the 8-element array. Fig. 2 clearly shows the effect of the mutual coupling of the leaky lines on the dispersion characteristics. The coupled-mode approach states that all of the coupled EH_1 modes of an N-element array are governed by a system of the linear differential equations expressed as follows

$$dI(z)_i = -\gamma I_i(z) + \sum_{j=1}^{N} c_{ij} I_i(z) \qquad (1),$$

where $I_i(z)$ is the modal current vector on the microstrip i and c_{ij} is the mutual coupling coefficient between the *ith* and *jth* elements. Using matrix notation, (1) is abbreviated as

$$[A] \cdot \overline{X} = \overline{I}^{inc}(0) \qquad (2),$$

where $\overline{I}^{inc}(0)$ is the excitation vector at z = 0 plane, $\overline{X}$ is the eigenvector to be solved, and [A] is the square characteristic matrix with dimension of N by N (N is the number of microstrip lines). The contribution of each coupled EH_1 mode to the far-field radiation pattern is determined by the excitation ($\overline{I}^{inc}(0)$) vector. For the case of the uniform excitation, only four out of the eight coupled EH_1 modes, which happen to have their α/ko of the dispersion curves above that of a single, isolated microstrip in this particular case of study as shown in Fig. 2, have contribution. This implies that the back-lobe is significantly reduced while the main beam can almost be kept in the specified direction. From the

modal characteristics of the closely coupled microstrip array as shown in the Fig. 2, one can predict that more than 90% of the radiated power is attained by the array with length of 6.5 cm.

B. Antenna Design

The linear microstrip leaky-mode array is fabricated on a 20-mil (0.0508 cm) thick RO4003™ substrate with relative permittivity of 3.38. In the case of a single microstrip leaky-mode antenna with a balun matching circuit to excite the EH_1 leaky mode, the input signal is applied at the input end of the balun matching circuit where a T-junction splits the signal into two paths. One travels along a $1/4\lambda_g$ microstrip line while also acting as an impedance transformer. The other travels along a longer path of $3/4\lambda_g$, thus rendering 180° phase delay to the previous path. There two paths terminate at microstrip of low impedance, respectively, which are the shunt stubs to compensate the inductive part of the input impedance looking into the leaky line. Realization of the compact balun matching circuit needs the quantitative assessment of the characteristic impedance for the microstrip leaky mode to provide insightful circuit-domain view of the leaky line. The input impedance of an open-circuited microstrip leaky line of length of L can be expressed as:

$$Z_{in}(\omega) = -jZ_c(\omega)\cot(k_z L) \qquad (3),$$

where Z_c is the characteristic impedance of the leaky line as expressed below [5]-[6]:

$$Z_c = \frac{1}{2}\int_S \overline{E} \times \overline{H}^* \cdot \hat{z}\, da \Big/ |I_t|^2 \qquad (4),$$

where I_t is the total current on the metal strip. It is well known that the leaky line solution exhibits nonstandard exponential growth to infinity at the transverse plane, resulting in unbound Poynting power. N. K. Das [5] reported the method for obtaining the leaky-mode characteristic impedance by decomposing the transverse field into bound fields and leaky fields and considering bound fields only for the Poynting power. Applying this definition, the characteristics impedance

of microstrip leaky line can be computed by using 2-D space-domain integral equation method [6]. Figure 3 plots the theoretical results of the input impedance, where the solid-line (dash-line) plots the real part (imaginary part) of the input impedance for the leaky line of length equal to 65 mm. With Z_{in} at the desirable operating frequency, one can design the input feed network of the antenna. A combination of series and parallel power dividers is used to form a very compact feed network. Thus, we may maximize the aperture efficiency and minimize the dissipation at the feed network.

III. Measured Results

According to the antenna design discussed in section II, a proof-of-concept prototype is built and tested. Three performance indexes are measured, including 1) the return loss to understand the degradation of the input matching as the result of the strong mutual coupling, 2) the reduction in back-lobe and 3) the antenna gain.

Figure 4 plots the measured $|S_{11}|$ (input reflection coefficient) at the input port of the array, showing VSWRs of less than 2.0 ($|S_{11}|<-10$ dB) in the entire leakage regime (11 to 13 GHz). Unlike the serious bandwidth limitation for the patch array of resonant type [7], here 16% VSWR bandwidth can be achieved with ease. Observing the excellent input matching, we find the positive effect of strong coupling on the input impedance of the prototype. Fig. 5 plots the measured and theoretical far-field patterns corresponding to a single element and an eight-element microstrip leaky-mode antenna array, respectively. Excellent agreement between the theoretical and measured results is obtained near the mainlobe region. The patterns is measured along the H-plane along the y-z cut ($\phi = 90°$) and normalized by the peak value, showing that the back-lobe is greatly reduced from −12 dB (single element) to −25 dB (array). Finally, the antenna gain is measured by calibrated to the standard gain horn and compared to the area gain to obtain the overall radiation efficiency. Fig. 6 plots

the antenna gain and the overall radiation efficiency, showing that the maximum efficiency of 83%, gain of 19.35 dBi is achieved at the frequency of 11.8 GHz.

IV. Conclusion

A first-pass design of a proposed closely coupled microstrip leaky-mode antenna array is presented. Excellent measured results confirm that the new printed antenna array is feasible for high efficient antenna design.

V. Acknowledgment

References

[1] M. Ando, J. Hirokawa, "Design of planar slotted waveguide arrays and the application to millimeterwave," 1996 *Asia Pacific Microwave Conference*, pp. 91-94.

[2] J. A. G. Malherbe, "An array of coupled nonradiative dielectric waveguide radiators," *IEEE Trans. Antenna Propagat.*, vol. 46, no. 8, pp. 1211-1125, Aug. 1998.

[3] C. -N. Hu and C. -K. C. Tzuang, "Microstrip leaky-mode antenna array," *IEEE Trans. Antenna Propagat.*, vol. 45, no. 11, pp. 1698-1699, Nov. 1997.

[4] C. -K. C. Tzuang and C. -N. Hu, "The mutual coupling effects in large microstrip leaky-mode array," *1998 IEEE MTTS, THIF-51*, pp. 1791-1794.

[5] N. D. Das," Power leakage, characteristic impedance, and leakage-transition behavior of finite-length stub sections of leaky printed transition lines," IEEE Trans. MTT-.44, no.4., Apr. 1996, pp.526-536.

[6] C. -K. C. Tzuang," Leaky mode perspective of printed antenna," 1998 *APMC, TH4C-1*, pp. 1471-1478.

[7] D. M. Pozar, "Finite phased array of rectangular microstrip patches," *IEEE Tans. on Antennas and Propaga.*, vol.-34, no.5, pp. 658-665, May. 1986.
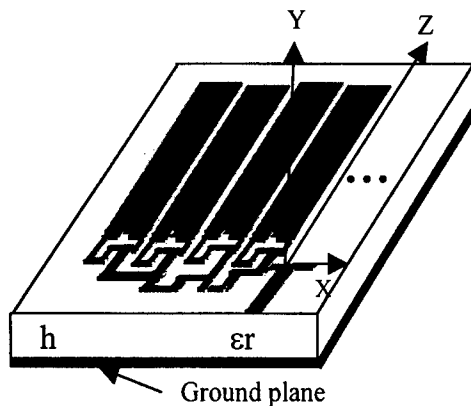
Fig.1 Proposed proof-of-concept design of an eight-element, closely coupled, microstrip leaky-mode antenna array.
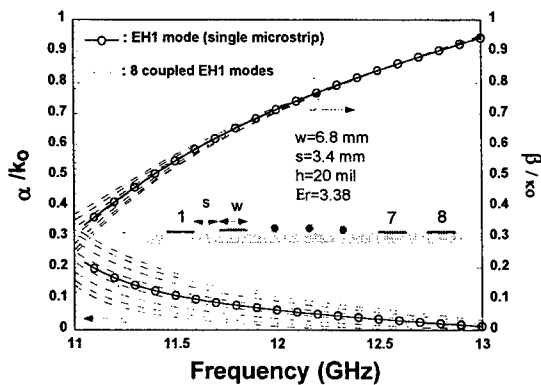
Fig.2. Comparison of the dispersion characteristics of a single microstrip line and those of an eight-element microstrip array, clearly indicating the effect of mutual coupling on the dispersion curves.
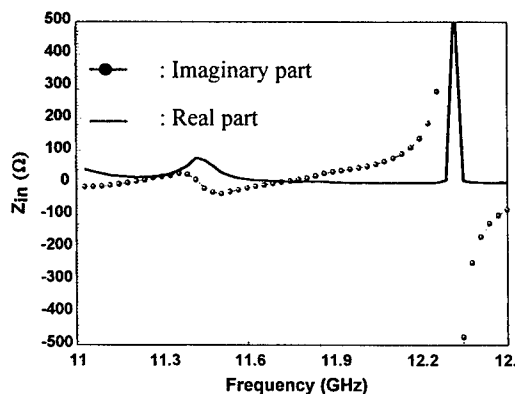
Fig. 3 The input impedance of a single microstrip leaky-mode antenna with length L=6.5 cm as computed by the 2-D spatial-domain integral equation method [6].
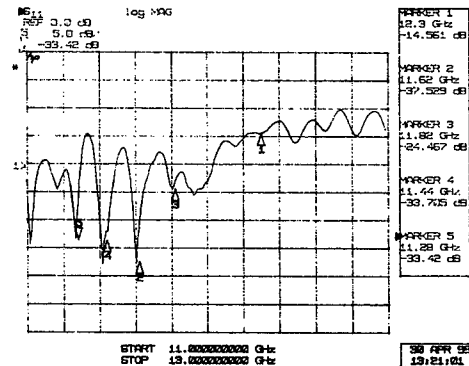
Fig.4 The measured input reflection coefficient $|S_{11}|$ against the frequency, showing good match at input.
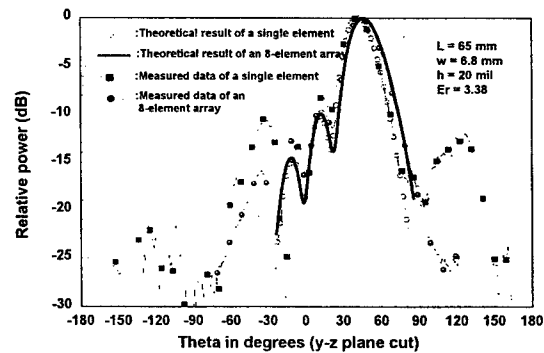
Fig. 5. Measured and theoretical patterns (y-z plane cut) of a single-element antenna and an eight-element array.
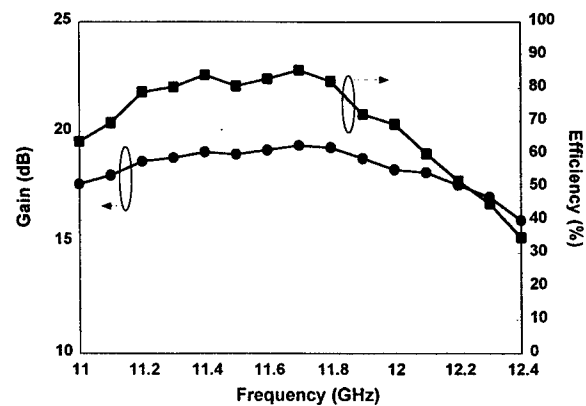
Fig. 6 Measured antenna gain and overall radiation efficiency of the prototype.

250

PERFORMANCE SIMULATION STUDIES FOR A CLASS OF "SMART", CONFORMAL ARRAY ANTENNA ARCHITECTURES

D. Chatterjee
ECE Department, 370-H Robert H. Flarsheim Hall
University of Missouri-Columbia/Kansas City (UMKC)
5100 Rockhill Road, KC, MO 64110-2499

and

S. Chakrabarti, K. Shanmugan and G. E. Prescott
EECS Dept., Information Telecomm. Tech. Center (ITTC)
University of Kansas, 2291 Irving Hill Road, Lawrence, KS 66044-7541

Abstract

Numerical comparisons between Radial Basis Function Neural Networks (RBFNN) and Linearly Constrained Least Square Method (LCLSM) are investigated for azimuth plane beamsteering for an array of axial sources about a PEC circular cylinder. The results show reasonably good agreement in pattern predictions for the two cases. The preliminary results suggest that the RBFNN can be a promising technique for practical realization of Digital BeamForming for adaptive, phased arrays on conformal surfaces.

I. Introduction

Adaptive (or "smart") antenna arrays require extensive modeling and simulations prior to their practical implementation [1]. In the recent past Digital BeamForming (DBF) techniques [2] have been hardware-implemented in wireless packet radio networks [3]. The subject of this paper is explore the feasibility of realizing beamsteering, adaptive antenna arrays on cylindrical structures [4]. Conventional techniques, such as the Linearly Constrained Least Square Method (LCLSM) [5], has been applied to realize arbitrary sidelobe topography in cylindrical geometries. Implicit in [4], is the fact that DBF techniques can be applied to realize adaptive beamforming and beamsteering for cylindrical arrays as demonstrated in [6]. This concept was further pursued in [7] where the application of Artificial Neural Networks (ANN) was found to be suitable for real-time applications. The purpose of this paper is to provide preliminary results for comparison between ANN and LCLSM as applied to a azimuth plane beamforming for a cylindrical array of axial electric dipoles. In section II the salient aspects of the formulation are outlined followed by some results in section III and a brief summary in section IV.

II. Formulation of the Problem

The radiation pattern for N excited elements in an array is:

$$\vec{\mathbf{E}}(R,\theta,\phi) = \frac{e^{-\jmath kR}}{R} \sum_{n=1}^{N} \mathtt{w}_n \vec{\mathbf{e}}_n(\theta,\phi) e^{+\jmath k\hat{\mathbf{u}}_R \cdot \vec{\mathbf{r}}_n}, \tag{1}$$

where:

(a) $\hat{\mathbf{u}}_R$ and $\vec{\mathbf{r}}_n$ are the appropriate unit and position vectors in the the far-field for the observation point and the nth array element, respectively.

(b) $\vec{\mathbf{e}}_n(\theta,\phi)$ is the element pattern of the nth element in the array and may/may not include mutual coupling

(c) $\mathtt{w}_n$ are the unknown excitation weights (coefficients) that are determined from the information about $\vec{\mathbf{E}}(R,\theta,\phi)$ and other quantities in Eq. (1)

The principal (or $\hat{\theta}-$) component of the $\vec{\mathbf{e}}_n(\theta,\phi)$ in Eq. (1), for the geometry in Fig. 1, are given in [4] that read:

$$E_\theta^e \simeq E_o \frac{e^{-\jmath kr}}{r} \mathcal{F}_d(\theta) \sum_{n=0}^{N-1} \sum_{m=-\infty}^{+\infty} e^{-\jmath p\phi} \mathcal{S}_p \mathcal{Z}_p(k,\theta,\rho_o,a) \tag{2}$$

where

$$\mathcal{Z}_p(k,\theta,\rho_o,a) = J_p(k\rho_o \sin\theta) - \frac{J_p(ka\sin\theta)}{H_p^{(2)}(ka\sin\theta)} H_p^{(2)}(k\rho_o \sin\theta), \tag{3}$$

and

$$\mathcal{F}_d(\theta) = \frac{\cos(\frac{kL}{2}\cos\theta)}{(\frac{\pi}{L})^2 - (k\sin\theta)^2} \tag{4}$$

are the "cylinder" and "dipole" factors, respectively. The quantity

$$\mathcal{S}_p = \frac{\sin(\frac{pw}{2\rho_o})}{\frac{pw}{2\rho_o}}. \tag{5}$$

In Eqs.(4),(5) L and w are the length and widths of the dipole elements, and $\rho_o = a + h$ where h is the distance of the dipole from the PEC cylinder curved surface. In Eqs. (3) $J_p(z)$ and $H_p^{(2)}(z)$ stand for the standard Bessel and Hankel functions of second kind, with the order $p = m + nN$ and the limits of indices m and n can be obtained from Eq. (2).

Subject to the beamsteering and sidelobe constraints in the (adaptive) excitation weights in Eq.(1), via LCLSM method, can be found from [4, Eq. (10)]

$$[\mathtt{W}] = [\mathtt{R}]^{-1}[\mathtt{C}]([\mathtt{C}]^{\mathtt{H}}[\mathtt{R}]^{-1}[\mathtt{C}])^{-1}[\mathtt{d}] \tag{6}$$

where [R] is the covariance matrix for the input data, [C] is the constraint matrix and [d] is a $N \times 1$ column matrix with all zero entries except the 1st element. In (6), H stands for hermitian form. Other details of these matrices are omitted here for brevity, and will be provided at the time of the presentation.

III. Preliminary Results and Discussion

The computation of Eq. (2) is quite intensive for $ka \geq 10$. For the purposes of this paper, in order to demonstrate the applicability of ANN, the following simplification [4, Eq. (12)]

$$e_n(\theta, \phi) = \frac{1}{3}\sin\theta[1 + 2\max(\cos\phi, -5.0 \times 10^{-1})] \tag{7}$$

to Eq. (2) for the preliminary results in this paper. Equation (2) predicts oscillations at and near the boresight [4, Figs. 7-9], while (7) does not predict this behavior. The effects of creeping and space wave interferences in (2) is absent in (7).

For comparisons between LCLSM and ANN, a single-ring array on a cylinder with: $a = 12.5\lambda, N = 18, \theta = 90°$ and $\Psi_s \simeq 39°$ was used. As in [7] a Radial Basis Function Neural Network(RBFNN) was used. The training angles for the RBFNN were at $\phi = -30°, -25°, -20°, \cdots, \cdots, +20°, +25°, +30°$. The RBFNN was used to compute weights for mainbeam steering angle at $\phi = +17.5°$ and a peak sidelobe constraint of -30 dB. The LCLSM, $i.e.$ Eq. (6), was used to predict the weights for the same geometry and pattern constraints. The resulting azimuth ($\theta = 90°$) plane pattern from, RBFNN and LCLSM are shown in Fig. 2. The agreement between the two is reasonably good, even though RBFNN predicts at an angle for which it is not trained.

An interesting issue is to examine the RBFNN and LCLSM predictions for the more complicated yet realistic case in Eq. (2). It would also be interesting to see how close can the RBFNN, *trained* by the simplified pattern in Eq. (7) at the various angles, can *predict* for actual situations defined by Eq. (2). These results will be discussed at the time of presentation.

IV. Summary

In this paper a comparison between neural network and conventional optimization techniques (LCLSM) have been studied for a circular array of axial dipoles about a cylinder with $ka \simeq 79$. The results show that neural networks can predict reasonably satisfactorily even at those angles for which it has not been originally trained. Additional investigations are underway for a more robust comparison of the two approaches.

References

[1] L. C. Godara, "Applications of Antenna Arrays to Mobile Communications, Part II: Beam-Forming and Direction of Arrival Considerations," *Proc. of IEEE*, vol. 85, no. 8, pp. 1195-1245, August 1997.

[2] H. Steyskal, "Digital Beamforming at Rome Laboratory", *Microwave Journal*, pp. 100-126, February 1996.

[3] J. B. Evans *et. al.*, "The Rapidly Deployable Radio Network", *IEEE Journal on Selected Areas in Comm.*, vol. 17, no. 4, pp. 689-703, April 1999.

[4] J. C. Herper, A. Hessel and B. Tomasic, "Element Pattern of an Axial Dipole in a Cylindrical Phased Array, Part I: Theory," *IEEE Trans. Antennas Propagat.*, vol. AP-33, no. 3, pp. 259-271, March 1985.

[5] S. R. Nagesh and T. S. Vedavathy, "A Procedure for Synthesizing a Specified Sidelobe Topography Using an Arbitrary Array," *IEEE Trans. Antennas Propagat.*, vol. AP-43, no. 7, pp. 742-745, July 1995.

[6] D. Chatterjee and R. G. Plumb, "Modeling Far Field Patterns of Cylindrical Arrays For Rapidly Deployable Radio Networks (RDRN) Using the NEC-Basic Scattering Code," *IEEE Antennas and Propagation* and *URSI/USNC Symp.*, vol. 1, pp. 714-717, Baltimore, MD, July 21-26, 1996.

[7] D. Chatterjee, S. Chakrabarti, K. Shanmugan and G. Prescott, "Application of Some Optimization Techniques to Adaptive, Conformal Array Antennas for Mobile Communications," *IEEE Antennas and Propagation and URSI/USNC Symp.*, (URSI Abstract Digest), p. 135, July 11-16, Orlando, FL, 1999.
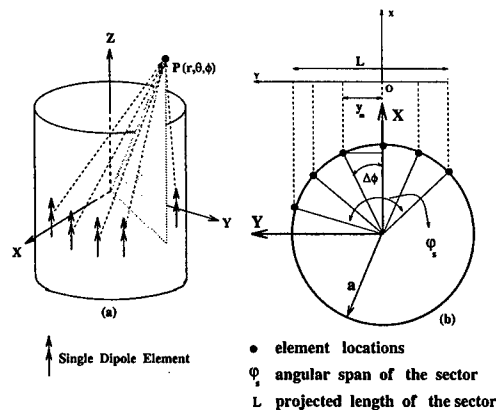
Figure 1: Geometry of the conformal cylindrical array problem
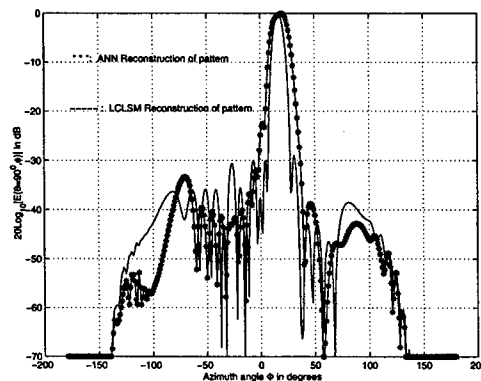
Figure 2:

BROADBAND CHARACTERIZATION OF THE ACTIVE REFLECTION COEFFICIENT OF FINITE-SIZED PHASED ARRAY MICROSTRIP ANTENNAS

Javier Gómez-Tagle* and Christos G. Christodoulou**

*Electrical Engineering Department, ITESM, Guadalajara, México

** EECE Department, The University of New Mexico, Albuquerque, New Mexico, USA

Introduction

This paper describes the application of the Finite-Difference Time-Domain Method (FDTD) for calculating broadband characteristics of finite-sized phased array antennas consisting of microstrip elements fed with coaxial probes. The motivation is to develop a computer-aided analysis technique that can be applied to the design and evaluation of an antenna array system. It is important to consider the effects of increased mutual coupling and the impedance of the radiating element, since they vary as the array is scanned. The most significant contribution is the calculation of broadband characteristics of phased array microstrip antennas using a full time-domain approach from the scan element patterns, and the use of a full time-domain approach to analyze finite-sized phased array microstrip antennas for different scan conditions.

Theory

From the definition of the S-parameters, it can be easily shown that the active reflection coefficient for element n of an N-element array, the scanning angle (θ_o, ϕ_o) can be represented by the following expressions

$$\Gamma_{in}^n(\theta_o, \phi_o) = \frac{b_n}{a_n}$$

$$\Gamma_{in}^n(\theta_o, \phi_o) = \sum_{m=1}^N S_{nm} \frac{a_m}{a_n}$$

(1)

The first expression for the active reflection coefficient can be easily implemented with the FDTD method, since we can feed the array element at port n with the incident wave a_n and measure the reflected wave b_n.

The second expression is very useful if the S-parameters of the array are known. The coupled energy from the other ports into port n can be calculated with FDTD, or it can be measured exciting the input element while all other elements are terminated with a matched load.

Figure 1 shows the setup between the source and the $n - th$ array element. Therefore, the scan element pattern $E_e^n(\theta, \phi)$ for the $n - th$ element of the array can be obtained from the knowledge of the far-field radiation pattern of an isolated element $E(\theta, \phi)$ and after making the substitution for b_s yields the final expression for the scan element pattern

$$E_e^n(\theta, \phi) = E(\theta, \phi)|a_n|e^{jk[x_n(\sin\theta\cos\phi - \sin\theta_o\cos\phi_o) + y_n(\sin\theta\sin\phi - \sin\theta_o\sin\phi_o)]}[1 - \Gamma_{in}^n(\theta, \phi)\Gamma_s^n(\theta, \phi)]$$

(2)

where $\Gamma_{in}^n(\theta, \phi)$ is the active reflection coefficient of the $n - th$ element, and $\Gamma_s^n(\theta, \phi)$ is the reflection coefficient as seen into the excitation source. The scan element pattern can be obtained experimentally or with the FDTD model, exciting one element and terminating the others to 50 ohms.

For an array with N elements, the array radiation pattern $E_a(\theta, \phi)$ can be obtained adding the contributions of all the scan element patterns in the far field

$$E_a(\theta,\phi) = \sum_{n=1}^{N} E_e^n(\theta,\phi)$$ (3)

In order to use the FDTD algorithm to analyze finite phased arrays antennas [1,2], a phase shift can be implemented in the time domain to model the effects of the scanning angle. The sources that excite each one of the array elements can be modeled using the shift property of the Fourier Transform, using $\Delta\phi_o$ as the excitation phase difference between the $n - th$ array element and a reference element and t_d is the time delay in the excitation of both elements.

A fixed delay in the time domain will yield a frequency-dependent phase shift. The introduction of a constant time delay is equivalent to the introduction of a line of length $L = ct_d$ at the excitation point. And that renders this approach viable for the modeling of the excitation and broadband analysis of phased array antennas.

The excitation phase-difference $\Delta\phi_o = \phi_n - \phi_{ref}$ between element n and the reference element in the array can be determined in terms of a constant $\Delta\phi_{min}$ [5,6]. For simplicity, the time delay is chosen to be proportional to the time step used in the FDTD calculations. Thus [3,4],

$$\Delta\phi_o = m\Delta\phi_{min} = \varpi \cdot t_d = 2\pi f \cdot m\Delta t$$

$$\Delta\phi_{min} = 2\pi f \Delta t$$ (4)

If β_x and β_y are the progressive phase shift, hence:

$$\beta_x = m\Delta\phi_{min}$$

$$\beta_y = n\Delta\phi_{min}$$ (5)

Thus, delaying the phase excitation by m time steps ($m \cdot \Delta t$) in the x-direction and n time steps ($n \cdot \Delta t$) in the y-direction renders a time domain approach for modeling a phased array antenna. In order to avoid modeling time advances, only time delays are represented with this approach. The excitation of every array element occurs at delayed times with respect to the reference element.

$$t = t_o + (i - 1)m\Delta t + (j - 1)n\Delta t$$ (6)

Figure 2 is a three-dimensional representation of the Active Reflection Coefficient where one axis represents the frequency and another represents the scanning angle. Figure 3 is a contour plot obtained from Figure 2. One can easily predict the scanning characteristics of the antenna versus frequency for a specified design value of the SWR. Figure 4 depicts the gain of the scan-element. Broadband results have been obtained for the scanning-array when all the elements are active. The radiation pattern for the array can be obtained based on the scan-element characteristics and the mutual coupling.

List of References

[1]   J. Gómez-Tagle, C. G. Christodoulou and P. F. Wahid, "Active Impedance Analysis of Finite Phased Array Microstrip Antennas", IEEE AP/S International Symposium, Atlanta, July 1998.

[2]   J. Gómez-Tagle, C. G. Christodoulou and P. F. Wahid, "Time Domain Simulation of Circularly Polarized Phased Array Microstrip Antennas", IEEE AP/S International Symposium, Orlando, Florida, July 1999.

[3]   R. P. Jedlicka et al, "Measured Mutual Coupling Between Microstrip Antennas", IEEE Trans. Antennas Prop., vol. 29, no. 1, pp. 147-149, Jan. 1981.

[4]   D. M. Pozar, "Input Impedance and Mutual Coupling of Rectangular Microstrip Antennas", IEEE Trans. Ant. Prop., vol. 30, no. 6, pp. 1191 – 1196, Nov. 1982.

[5]   K. Uehara and K. Kagoshima, "Rigorous Analysis of Microstrip Phased Array Antennas using a new FDTD Method", Electronics Letters, vol. 30, no. 2, pp. 100 – 101, Jan. 1994.

[6]   D. Crouch, "On the Use of Symmetry to Reduce the Computational Requirements for FDTD Analyses of Finite Phased Arrays", Microwave Opt. Tech. Letters, vol. 13, no. 3, pp. 123 – 128, Oct. 1996.
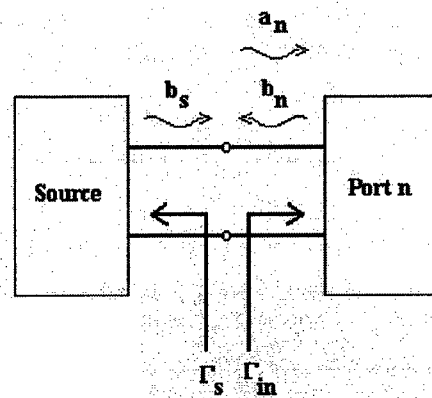
Figure 1. Two-port network setup for the excitation of the $n - th$ array element.
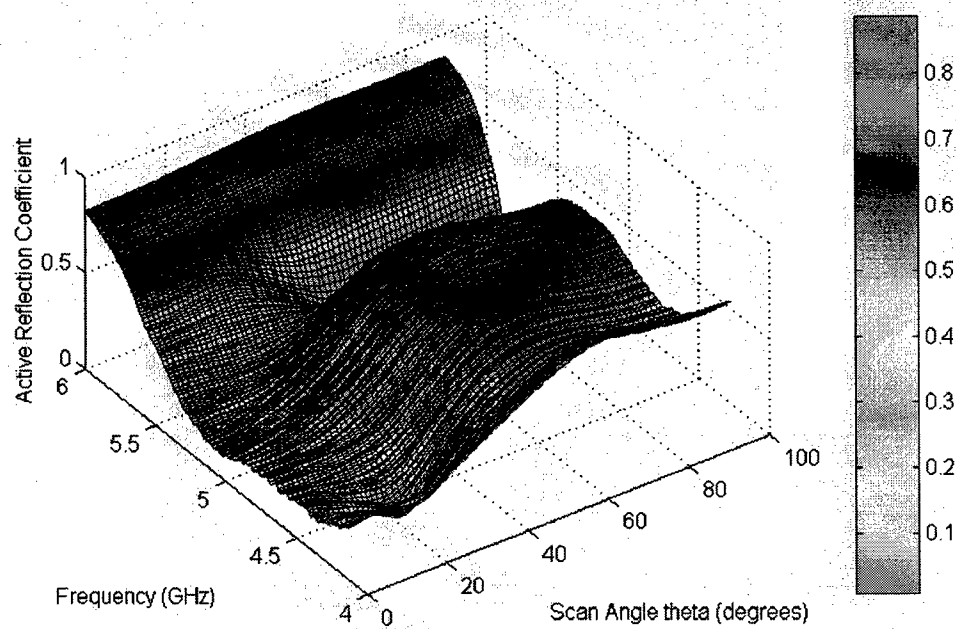
Figure 2. Active Reflection-Coefficient for the eight-element E-Plane Array.
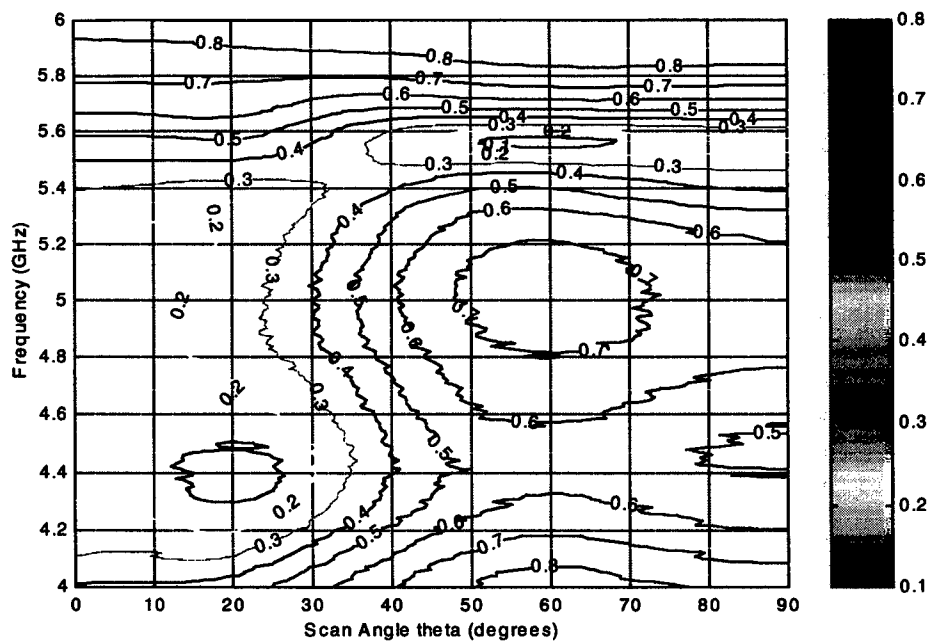
Figure 3. Contour Plot of the Active Reflection-Coefficient for the 8-element E-Plane Array.

Figure 4. Gain of the Scan Element for the E-Plane Array at 4.75 GHz.

TA3

Active Arrays

Active Arrays

Coupled-Oscillator Arrays: Beamsteering without Phase Shifters

L. W. Pearson and J. Shen
Department of Electrical and Computer Engineering
Clemson University
Clemson, SC 29634-0915
pearson@ces.clemson.edu

1. Abstract

Arrays of coupled oscillators have been proposed as signal sources for beam-steered array antennas by York, Pogorzelski, and their coworkers. The engineering considerations for designing an array based on coupled oscillators is discussed herein and performance features are compared with those of conventional phased arrays wherever possible. It is shown that there is a direct relationship between departure of the free-running frequencies of individual oscillators and phase errors in the signal produced by the oscillator. Considerations for minimizing the sensitivity to frequency errors and the achievability of reproducible free running frequencies are discussed. The correspondence between the phase of an individual oscillator in an array in phase-shifted state and the phase setting of a phase shifter is discussed.

2. Introduction

Coupled oscillator arrays were proposed as a means for electronic beam-scanning of array antennas by York and his protégés [1,2,3]. Liao and York [2] established proof of principle with a four-element linear array. Pogorzelski, et. al. [4,5] demonstrated that in the weak-coupling, small-phase-shift limit, the phase shift moves across an array through a mechanism of discrete diffusion. Pearson and Shen [7] showed through numerical demonstration, where an explicit diffusion equation is no longer valid, the transport of phase across the array continues to be diffusive in character. The critical time parameter is the reciprocal of the locking range of the individual oscillators. Numerical experiments in [7] suggest that low quality-factor (Q) oscillators are mutually compatible with minimizing the sensitivity to variations in free running frequency and to rapid stabilization of the array when its phase state is changed.

Results to date are encouraging, and it is desirable to seek a thorough understanding of parameter interactions in designing coupled oscillator systems with a focus on eventual practical deployment. Indeed, coupled oscillator arrays provide a technology that lends itself to full integration as millimeter wavelength arrays emerge. In that regard, coupled oscillator array technology is an alternative to microelectromechanical (MEMS) switches, which have yet to be evaluated for reliability.

3. A Generic Architecture Employing Coupled Oscillators

Fig. 1 shows a generic architecture employing coupled oscillators as the source of phase information for exictation of individual array elements. The principal of operation of the coupled oscillator array is that either phase shift or equivalently frequency detuning on the perimeter of the array introduces progressive phase shift across the entire array [1,2,3,4,5]. The first work in coupled oscillator arrays viewed the oscillator signals as the actual RF signals eventually to be radiated. With this point of view, the processing layer shown in Fig. 1 would have the role of modulating and amplifying the signals. This is a relatively limited perspective, however, and a broader view of the middle layer is useful in considering all possibilities. Specifically, it is useful to consider broader possibilities for mixing in the middle layer. This suggest the possibility of using the middle layer for detection in a receiving mode, as well as for modulation in a transmitting mode. The coupled oscillator array is then viewed as the generator of phase references, as opposed to the generator of primary RF signals.
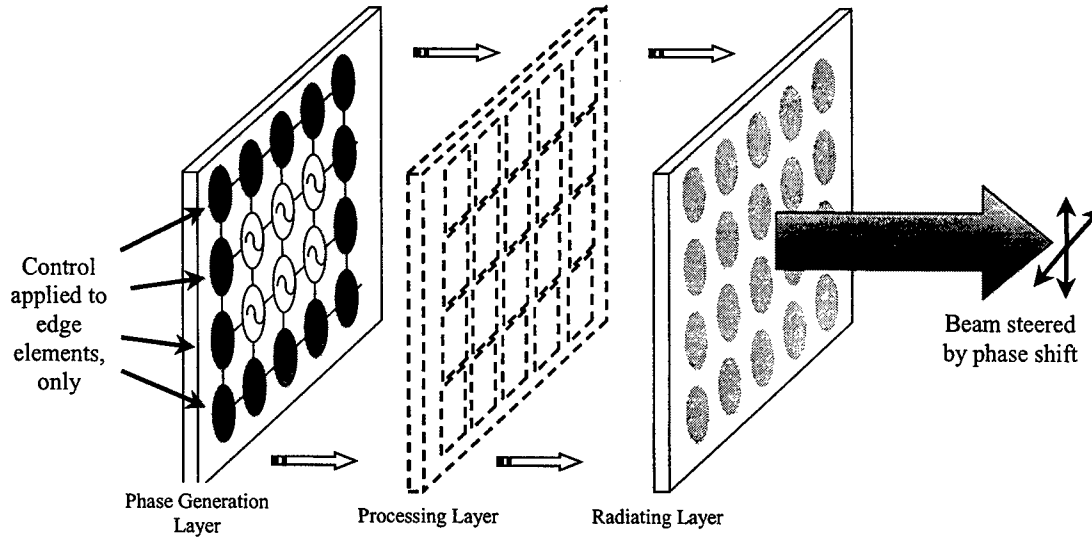
Fig. 1. Generic Representation of an Array whose Beam is Steered by Coupled Oscillators (from [7]). Details of the processing layer and of interconnections are omitted.

3. Steady-State Phase Distribution

The equations governing the dynamic behavior of the phase distribution of a coupled oscillator system is given by Liao and York [2]. The steady state (*i.e.*, late time) form of the steady state equations may be written

$$\omega_0 = \omega_i - \frac{\omega_i \kappa}{2Q} \cdot [\sin(\Phi + \theta_i - \theta_{i-1}) + \sin(\Phi + \theta_i - \theta_{i+1})], \quad i = 2,3,...,N-1. \tag{1}$$

where θ is the instantaneous phase of each oscillator, Φ is the phase of the coupling factor between two neighboring oscillators, ω_i is the free-running frequency of the ith oscillator, κ is the coupling strength between adjacent oscillators, and Q is the oscillator quality factor, and ω_0 is the locking frequency—the ensemble average of all of the free-running frequencies. The first and Nth oscillators are fixed with either frequency or phased controlled to introduce phase shift. We consider the one-dimensional case here for clarity. We consider only the case where a single coupling factor $\kappa e^{j\Phi}$ applies to the coupling of all oscillators in an array and where a single Q applies for all oscillators. The form in (2) includes nearest-neighbor coupling only, although, mutual coupling among all elements can be characterized by replacing the second term on the right hand side of each equation with a sum over all oscillators other than the ith oscillator.

The set (1) reveals both the phase shifting feature of a linear array of coupled oscillators and the source of phase error due to free-running frequency errors. To see the origin of the intended phase shift, let us assume that all of the free-running frequencies ω_i are precisely ω_0, the ensemble average frequency. Let us assume further that the phase of the coupling factors is zero. With these assumptions, the equations reduce to

$$\sin(\theta_i - \theta_{i-1}) + \sin(\theta_i - \theta_{i+1}) = 0, \quad i = 2,3,...,N-1 \tag{2}$$

If a phase difference is introduced between the first and N^{th} oscillators, the system of equations above is satisfied through the difference's being distributed equally among all oscillator pairs. The influence of frequency error is also discernable from (1). Let us define $\Delta\omega_i = \omega_0 - \omega_i$ as the error in the free-running frequency of the ith element. With this notation, we form from (1)

$$\frac{\Delta\omega_i}{\omega_i} = -\frac{\kappa}{2Q} \cdot [\sin(\theta_i - \theta_{i-1}) + \sin(\theta_i - \theta_{i+1})], \tag{4}$$

where we have retained the assumption of zero coupling factor phase. It is seen here that any frequency error, $\Delta\omega_i$, leads to an unwanted adjustment in the angles in the arguments of the sine functions to compensate for the non-zero left hand side.

4. Engineering of a Coupled Oscillator Array

From the point of view of array design, one wishes to achieve the following outcomes for the performance of a coupled oscillator system that is used to generate phases of radiating elements:

1. Minimum departure of element phases from the sought-after linear phase progression. (This can be thought of as corresponding to the bit-precision of phase shifters in a phased array.)

2. The ability of the array to change phase states rapidly for fast scanning.

3. The ability of the array to maintain lock as it is scanned

4. Precise spectral properties (low phase noise) for the array in locked state.

We can observe directly from (4) how to control the phases precisely. Namely, the free-running frequencies among oscillators need to be as close to the operating ensemble average as possible and the factor $\frac{\omega_i \kappa}{2Q}$, which functions as a sensitivity factor, must be as large as possible. The large $\frac{\omega_i \kappa}{2Q}$ condition ensures that a small adjustment in oscillator phase angles is translated into a significant $\Delta\omega_i$. This factor is made large by designing for large coupling factor and low Q. It is generally assumed that low Q oscillators have concomitantly imprecise frequency. There is no evident physical constraint that imposes this. It is a reality in the way that design is *practiced* for at least two reasons. First, it is difficult to *adjust* an oscillator to a precise frequency when its spectrum is broad. Second, applications of low-Q oscillators are typically frequency tolerant. We are currently pursuing oscillator design from the perspective of degrading the Q of an oscillator whose frequency is set by a precisely formed filter. We believe that this conceptual framework will lead to low-Q realizations with precise center frequencies.

The second feature in the list above is also satisfied by low-Q designs. A low Q means that the oscillator has a large locking range, which in turn dictates a fast slew rate when a phase change control is applied [4,5]. Wide locking range also leads to stable lock state during scanning. It is conceivable that the difference across the array may need to be several hundred degrees for wide-angle scanning. In this case, one would achieve the desired phase difference incrementally so that no 360 degree ambiguities are introduced in the change in phase state. Pogorzelski [8] has suggested that it may be desirable to introduce frequency multipliers at the input of the processing layer in Fig. 1. In this way, the phase of each element is multiplied by the multiplier factor. In this way, operating the coupled system at an overall phase difference $\theta_N - \theta_1$ produces an effective phase difference $M(\theta_N - \theta_1)$ across the array at the M-fold harmonic frequency, so that even while $\theta_N - \theta_1$ is held to less than 360 degrees.

The fourth point is, of course, the *sine qua non* in the implementation of this technology as an alternative means for beam steering. The employment of low-Q elements even suggests that the final goal is not achievable. The key to achieving the fourth goal is the precise spectral control of the *exterior elements*.

These elements do not need to adjust since they are the control elements of the array. All other elements lock to them and therefore the ensemble's spectrum matches the spectrum of the locking sources. These elements must be of synthesizer quality. Indeed, these exterior elements must be synchronized to a common clock. This may be accomplished either by phase locking of the perimeter oscillators to a reference clock or by dividing a single signal source and distributing it to the perimeter of the array.

5. Acknowledgment

References:

1. R.A. York, "Nonlinear analysis of phase relationships in quasi-optical oscillator arrays", *IEEE Trans. Microwave Theory and Tech.*, Vol. MTT-41, No.10, Oct.1993, pp. 1799-1809

2. P.Liao and R.A. York, "A new phase-shifterless beam-scanning technique using arrays of coupled oscillators," *IEEE Trans. Microwave Theory and Tech.*, Vol. MTT-41, No.10, Oct.1993, pp. 1810-1815

3. H.C. Chang, E.S. Shapiro and R.A. York, "Influence of the oscillator equivalent circuit on the stable modes of parallel-coupled oscillators," *IEEE Trans. Microwave Theory and Tech.*, Vol. MTT-45, No.8, Aug.1997, pp. 1232-1239

4. R. J. Pogorzelski, P. F. Maccarini, and R. A. York, "A Continuum Model of the Dynamics of Coupled Oscillator Arrays for Phase-Shifterless Beam Scanning," *IEEE Trans. Microwave Theory and Tech.*, Vol. 47, no. 4, April, 1999, pp. 463-470

5. R. J. Pogorzelski, P. F. Maccarini, and R. A. York, "Continuum Modeling of the Dynamics of Externally Injection-Locked Coupled Oscillator Arrays," *IEEE Trans. Microwave Theory and Tech.*, Vol. 47, no. 4, April, 1999, pp. 471-478

6. L. Wilson Pearson and Ronald J. Pogorzelski, "A Fresh Look at Spatial Power Combining Oscillators," National Radio Science Meeting, Boulder, CO, January, 1999.

7. L. W. Pearson and J. Shen, "Coupled-Oscillator Spatial Power Combining," XXVth General Assembly of the International Radio Science Union, Montreal, CA, August, 1999.

An Agile Beam Transmit Array Using Coupled Oscillator Phase Control

R. J. Pogorzelski, R. P. Scaramastra, J. Huang, R. J. Beckon, S. M. Petree, and C. Chavez
Jet Propulsion Laboratory
California Institute of Technology
Pasadena, CA 91109-8099

I. BACKGROUND

Some years ago it was suggested that an array of coupled oscillators could be used to control the phase distribution across the aperture of an array antenna in such a manner as to effect steering of the beam without the use of phase shifters.[1] The behavior of such arrays of oscillators has been described in detail using a coupled set of non-linear differential equations.[2][3] These equations are derived by first describing the behavior of an individual oscillator with injection locking in the manner of Adler [4] and then allowing the injection signals to be provided by the neighboring oscillators in the array. More recently, an alternative description was developed by Pogorzelski, Maccarini, and York [5] in which the phase distribution across the array is represented by a continuous function governed by a partial differential equation of diffusion type. This formalism provides considerable insight concerning the relationship between the phase distribution and the tuning of the oscillators.

One result of the above theoretical treatments is detailed understanding of the beam steering scheme proposed by York and demonstrated in four element X-band arrays by Liao and York [1][2]. Their approach made use of the mutual coupling between the radiating elements of the array to achieve mutual locking of the oscillators. Thus, the element spacing was constrained by the necessary coupling strength. In another experiment, the coupling was accomplished by connecting the radiating elements by microstrip lines.[6] In the approach described here, the coupling is achieved through microstrip transmission lines between the oscillator *resonators*. The oscillator outputs are isolated from the resonators by buffer amplifiers intrinsic to the MMICs which were used. Thus, the element spacing is independent of the coupling and can be chosen for optimum performance of the radiating aperture. The theory provides the relationship between coupling phase (the phase shift through the coupling lines) and the ensemble frequency and locking range, relationships which were observed experimentally during the development of the present seven element array. Moreover, the theoretical results were shown to accurately predict the beam steering behavior of this array.

In this paper, we describe the fabrication of the array of voltage controlled oscillators, the experimental determination of the behavior of this array, and comparison of the experimentally observed behavior with theoretical predictions. We further discuss the design of the microstrip patch radiating aperture and describe the experimental measurement of the antenna patterns under various scan conditions.

II. THE VOLTAGE CONTROLLED OSCILLATORS (VCOs)

A commercial MMIC VCO suitable for operation at a nominal 2.5 GHz was selected and a number of preliminary characterizations were performed to ascertain its suitability for the present application. [We gratefully acknowledge the assistance of Professor R. A. York and Mr. P. F. Maccarini of the University of California, Santa Barbara in selecting the Pacific Monolithics MMIC for the experiment and designing the initial board layout.]

Full wavelength lines were used for coupling the oscillators. This choice was made for compatibility with the parallel resonance determining the free running frequency of the oscillators.[3] However, the end oscillators were fitted with half wavelength lines to provide a one wavelength round trip path through which the end oscillators inject themselves resulting in the desired Neumann boundary condition.[5]

III. FABRICATION AND BENCH TESTING OF THE ARRAY

A seven oscillator linear array was fabricated. The theoretical treatment is based on the assumption that the Q of the coupling circuit is much lower than that of the oscillators. To assure that this is the case in our implementation, we terminated the 100 ohm coupling lines in their characteristic impedance using 100 ohm chip resistors. This reduced reflections from the ends of the line so that energy storage on the line in the form of standing wave was minimized. Minimum energy storage implies minimal Q.

The inter-connecting (coupling) lines were meandered in a U shape such that their length could easily be adjusted by moving a shorting bar along the U shaped portion. The actual electrical length of the inter-connecting coupling line is 360 degrees (one wavelength). The phase shift of the oscillator tuning circuit adds some 100 ohm additional electrical length to the coupling circuits. It was conjectured that the additional coupling circuit phase shift might be involved in the initially observed 180 degree output relationship. Shortening the line lengths by approximately ¼ wave allows the adjacent oscillators to lock in-phase. Two theoretically predicted behaviors were observed and thus confirmed during this investigation. First, when the coupling lines are an odd multiple of a quarter wavelength in effective length, the locking range of the array is reduced to zero and no locking is possible. Second, when the coupling lines are an even multiple of a quarter wavelength in effective length, the ensemble frequency is equal to the tuning frequency of the individual oscillators whereas it differs from this value for other line lengths. This difference is maximized at odd multiples of a quarter wavelength.

Linear aperture phase distribution was achieved by adjusting the tuning bias upward in voltage (and frequency) on one end oscillator and downward in voltage (and frequency) on the other end oscillator thus maintaining a constant average tuning frequency. The oscillators, being locked to their neighbors, do not actually change oscillation frequency. The result is that the array oscillator output signals remain at the same frequency but their differential phase is controlled by the tuning. It is believed that the inability to achieve the full 90 degree phase difference between adjacent oscillators was due to the limited tuning range available. That is, before 90 degrees was reached, one or more oscillator outputs decreased in amplitude to a level at which they no longer participate in the interaction.

IV. DESIGN AND FABRICATION OF THE RADIATING APERTURE

Each oscillator in the array provides an output RF signal properly phased with respect to the others. To radiate this signal, one must provide each oscillator with a properly designed radiating antenna element. Each element must be properly impedance-matched to the oscillator and must radiate the RF energy with a wide enough beamwidth to achieve wide-angle beam scanning capability. The overall array antenna beam will then be a result of the spatial power combining which takes place in the radiating aperture. A microstrip patch was selected as the radiator. This choice also provides negligible mutual coupling between the elements, a property which was confirmed by the agreement between the measured array pattern and that predicted theoretically neglecting mutual coupling. In addition, all array elements can be

fabricated on a single slab of substrate material with a single chemical etching process, which can significantly lower the production time and cost.

A seven element array achieves sufficiently narrow beamwidth to demonstrate the beam scanning with adequate beam resolution. A resonant frequency of 2.503 GHz and a bandwidth of 33 MHz were measured for the individual patches. The seven elements are spaced uniformly with half free-space wavelength spacing of 6.0 cm at 2.50 GHz. They are fabricated by etching on a rectangular substrate panel of 51 cm x 15 cm. The elements are arrayed in the H-plane. In other words, the array is vertically polarized.

V. RANGE TESTING OF THE ARRAY ANTENNA

Having established that the seven element oscillator array could be mutually injection locked and could provide linear phase distributions suitable for beam steering and controllable by detuning the end oscillators, a matched set of seven cables was fabricated with which to connect the outputs of each of the seven oscillators to a corresponding microstrip patch element in the radiating aperture. In preparation for the measurement, each of the oscillators was tuned to 2.522 GHz measured with a spectrum analyzer (HP-8562A) and the voltage necessary to do this was recorded. However, it was found that the amplitudes of the oscillator outputs were not equal. In fact they varied over a range of approximately plus or minus 3.5 dB. Therefore, attenuators (pads) were inserted in each of the lines to equalize the amplitudes while maintaining equal phase change in each line. Having done this, the end oscillators were detuned by an amount necessary to create phase progressions corresponding to steering angles of 6.38, 9.59, and 12.84 degrees (phase differences between the end oscillators of 120, 180, and 240 degrees) and the necessary tuning voltages recorded. In anticipation of the need for a reference signal to which to lock the range receiver, provision was made to injection lock the center oscillator of the array to a master oscillator (HP-8648C) which would provide the necessary locking signal to the receiver. A uniform set of 10 dB pads was installed, one at the back of each of the patch elements in the radiating aperture to eliminate the effects of the mismatch due to operation off resonance. Then, the array was placed on the measurement range and patterns were measured using each of the above four tuning voltage configurations.

The results for one of the measurements are shown in Figure 1 in which the ensemble frequency and injection frequencies were 2.522 GHz. The chart associated with the graph shows the free running frequency to which each oscillator was tuned and the voltage required to tune it. Also shown is the relative output power level and relative phase of each oscillator under locked conditions. These levels, read from the spectrum analyzer, and phases, measured with a network analyzer (HP-8410A), were used to computationally predict the pattern shown in long dashes for each scan angle. These results show very satisfactory agreement between the measured and predicted patterns and close alignment with the desired beam scanning. Based on these results, it is believed that the array is performing in a manner consistent with utility in a communications application.

VI. CONCLUDING REMARKS

A seven element S-band phased array based on the coupled oscillator beam steering concept has been fabricated. We have described an experimental investigation of the behavior of this array in which several theoretically predicted characteristics of such an array have been verified. The array provides an agile beam which can be steered from boresight to nearly 13 degrees by merely adjusting the voltages applied to the tuning ports of the end VCOs in the array. High efficiency, however, will require additional attention to the impedance match between the oscillator outputs and the radiating elements; a

match which was not optimal in the present experiment due to the difference between the design frequency of the patch elements and the ultimate ensemble frequency of the array.

ACKNOWLEDGMENTS

REFERENCES

1. P. Liao and R. A. York, "A New Phase Shifterless Beam-Scanning Technique Using Arrays of Coupled Oscillators," IEEE Trans. Microwave Theory and Tech., MTT-41, pp. 1810-1815, October 1993.
2. R. A. York, "Nonlinear Analysis of Phase Relationships in Quasi-Optical Oscillator Arrays," IEEE Trans. Microwave Theory and Tech., MTT-41, pp. 1799-1809, October 1993.
3. H.-C. Chang, E. S. Shapiro, and R. A. York, "Influence of the Oscillator Equivalent Circuit on the Stable Modes of Parallel-Coupled Oscillators," IEEE Trans. Microwave Theory and Tech., MTT-45, pp. 1232-1239, August 1997.
4. R. Adler, "A Study of Locking Phenomena in Oscillators," Proc. IEEE, 61, pp.1380-1385, October 1973.
5. R. J. Pogorzelski, P. F. Maccarini, and R. A. York, "A Continuum Model of the Dynamics of Coupled Oscillator Arrays for Phase Shifterless Beam-Scanning," IEEE Trans. Microwave Theory and Tech., MTT-47, April 1999.
6. R. A. York, P. Liao, and J. Lynch, "Oscillator Array Dynamics with Broadband N-Port Coupling Networks," IEEE Trans. Microwave Theory and Tech., MTT-42, pp. 2040-2045, November 1994.
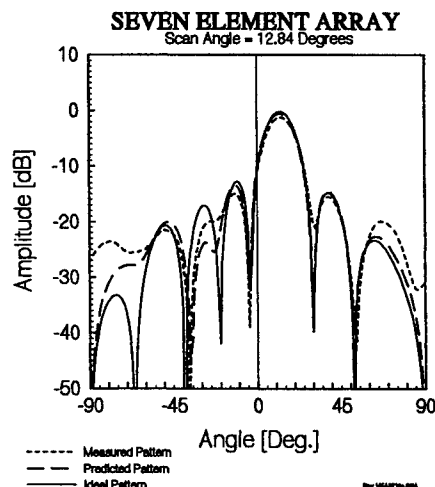
Osc.	Freq. (GHz)	Pwr (dBm)	Tuning Voltage	Phase (Deg.)
1	2.554	-8.83	8.07	0.0
2	2.530	-9.67	8.40	- 49.4
3	2.530	-9.50	9.65	- 71.6
4	2.546	-10.33	6.99	-128.0
5	2.530	-9.17	8.01	-156.0
6	2.530	-9.50	8.29	-192.0
7	2.496	-12.50	7.95	-242.0

Figure 1. Experimental array pattern for 12.84 degree scan.

DEVELOPMENT AND TESTING OF AN X-BAND ACTIVE REFLECT-ARRAY WITH 137 MESFET AMPLIFIERS

Ashley W. Robinson[†‡], Marek E. Bialkowski[‡], Hyok J. Song[‡]

[†]Filtronic Components Australia
43 Metroplex Avenue
Murarrie, Queensland 4170 Australia
Ashleyr@filtronic.com.au

[‡] Computer Science and Electrical
Engineering Dept.
University of Queensland
St Lucia Queensland 4072 Australia
E-mail: meb@csee.uq.edu.au

ABSTRACT

The development of a 137-element active reflect-array with MESFET amplifiers operating at X-band is presented. The array uses dual feed aperture coupled patch antennas to reduce the element size and allow for a tighter packing density. Test results for the array, including gain and radiation pattern at two frequencies, are presented to allow discussion of the array performance.

INTRODUCTION

Arrays of microstrip patches fed by a circuit network [1], and microstrip reflect-arrays [2], [3] fed by a horn antenna, have been proposed as a replacement for the frequently used parabolic reflector antenna. These structures each have their own advantages and disadvantages, such as the fully planar format of the microstrip patch array but with conduction losses in the feed network for large, highly directive, arrays. The reflect-array features a fully planar reflector, however, the entire structure including the feed is 3-dimensional. In comparison with the microstrip array with the circuit-type feed network, its advantage is that the feed losses are reduced. This is because the horn and the array act as a spatial power combiner, for which conductive losses are negligible.

In comparison with a conventional parabolic reflector, both planar microstrip arrays and reflect-arrays feature a reduced bandwidth. The reason is that in order to efficiently combine power in a given direction in space, as measured in terms of the directive gain, microstrip patch elements require a suitable phasing, which can only be achieved over a limited bandwidth before beam squint occurs.

In addition to exploring them as antennas, the most recent interest has been to use microstrip patch arrays as spatial power combiners of solid state sources, in which transistor oscillators or amplifiers [4] augment passive patches. Previous reflect-arrays presented in the literature have been passive reflectors only. In the present paper, an active reflect-array is considered as a candidate for a spatial power combiner of transistor amplifiers.

ARRAY DESIGN

The 137 elements of the active reflect-array use a combination of an aperture coupled patch antenna and a MESFET amplifier. To minimise spacing between elements in the array, the aperture coupled patch antenna has dual, orthogonal, feeds with 'dog-bone' slots. These dual feed antennas allow for much greater packing density in the array than would be possible if separate antennas were used for receive and transmit. A return loss of better than 10dB is achieved for this antenna element across a frequency range of 11GHz to 11.7GHz with a minimum isolation between the feeds of 13dB at 10.3GHz. This isolation sets the maximum gain possible for the active stage for stable, oscillation free, operation, however as the gain approaches the isolation the gain ripple with respect to frequency

will increase. The wide bandwidth of the antenna is achieved through the use of a 1.3mm thick foam layer in between the 0.635mm thick Rogers 6010 (dielectric constant 10.2) feed substrate and the 1.57mm thick Rogers 5880 (dielectric constant 2.2) patch antenna substrate.

The MESFET amplifier is based around a Mitsubishi MGF1302 with a microstrip matching network to produce approximately 10dB of gain across a bandwidth of 10GHz to 12GHz when operating with 50 ohm source and load impedances. Bias for each element is established via an active auto-bias network to set each FET for a drain to source voltage of 3V with 30mA of drain current.

To convert the spherical wavefront from the feed horn to a planar wavefront each element in the array requires suitable phasing. This is achieved by the addition of sections of microstrip transmission line between the transistor amplifier and the transmit portion of the aperture coupled patch antenna. Standard design equations are applied to obtain the required microstrip line section lengths at the design frequency of 11.4GHz. The layout for the central 25 elements of the array can be seen in Figure 1a.
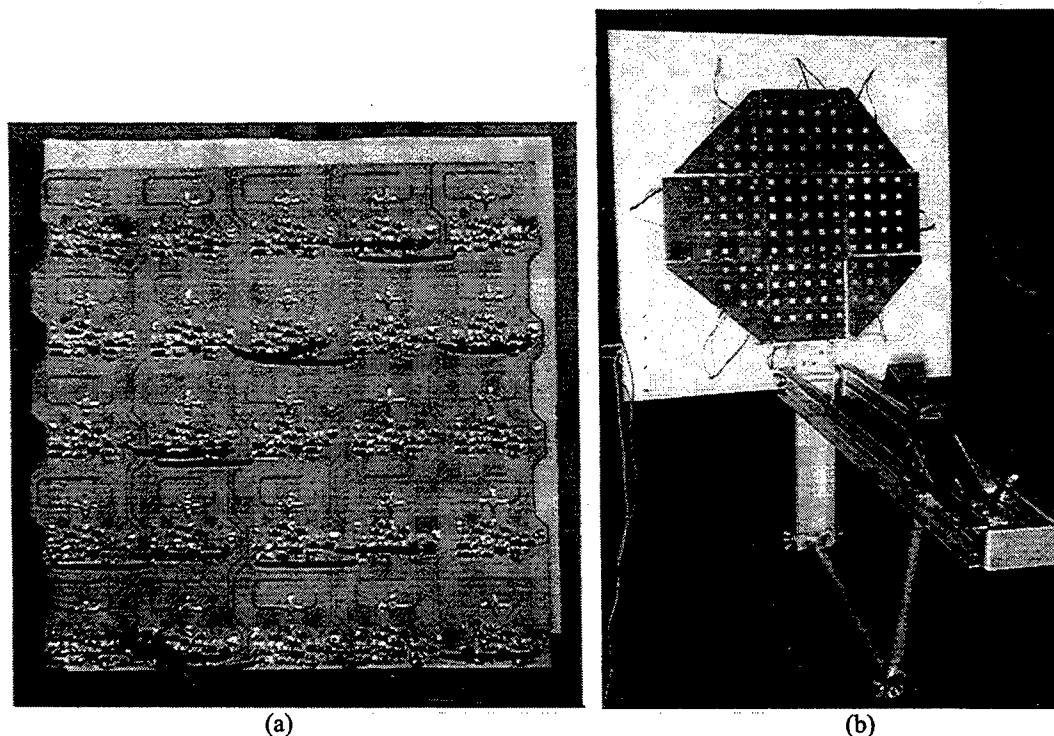
Figure 1: Photograph of (a) the amplifier side of the central tile, and (b) complete 137 element active reflect-array

The active reflect-array has 137 elements separated by 24mm, or 0.92 wavelengths at 11.5GHz, arranged on a rectangular lattice with a circular border. The element spacing is set by the size required for the active bias network for each amplifier. A spacing of 0.8 wavelengths is the preferred spacing to avoid grating lobes in the radiation pattern, however simulation of the performance of the antenna indicated that at the 0.92 wavelength spacing the grating lobes had not risen by an excessive amount. A small WR90 horn antenna with a 44mm (E-plane) by 38mm aperture, and an axial length of about 60mm, feeds the array. In order to avoid feed blockage an offset feed design is explored. The horn is positioned at 180mm down from the centre of the array and 360mm out from the array. It is mounted onto an adjustable aluminium arm that is screwed to the bottom of the array-backing sheet.

As seen in Figure 1b, the complete array is broken up into 9 separate tiles to suit the size of the available substrate in the etching process and to ease the assembly of the amplifier elements. Note that this approach may be required to create large size reflect-arrays. Each tile is assembled using M2 nylon screws and nuts with the foam layer sandwiched in between the thick patch antenna substrate and the circuit substrate. The array is mounted on a sheet of HMW plastic to obtain a rigid construction with a gap of approximately 10mm between the amplifier substrate and the mounting sheet.

To verify the performance of the array design tests were initially performed on a passive prototype. In this stage the dual-feeds in each element were connected using suitable lengths of the 50ohm characteristic impedance microstrip transmission line. Results and discussion on the performance of this array can be found in [5]. Having confirmed the array design as sound, the amplifier layer was fully populated with transistors and bias components to form the active array. The developed active array underwent similar tests as the passive prototype. In both cases, the measurements were performed in an anechoic chamber.

ACTIVE REFLECT-ARRAY RESULTS

The gain and radiation pattern for the active reflect-array was measured across a frequency range of 10GHz to 12GHz. The measured gain for the array is given in Figure 2 where the measurements were performed relative to a horn antenna of known gain. Also in Figure 2(a) is the measured gain for the array when the FET drain supply is removed. In this case the amplifier acts as an attenuator with a loss relatively constant with frequency. The gain response for no drain supply is the same shape as for the passive reflect-array explored in [5], but at a lower level due to the attenuation of the FET. In contrast the gain of the active array at full bias shows gain over that of the passive array across 10GHz to 11.3GHz.
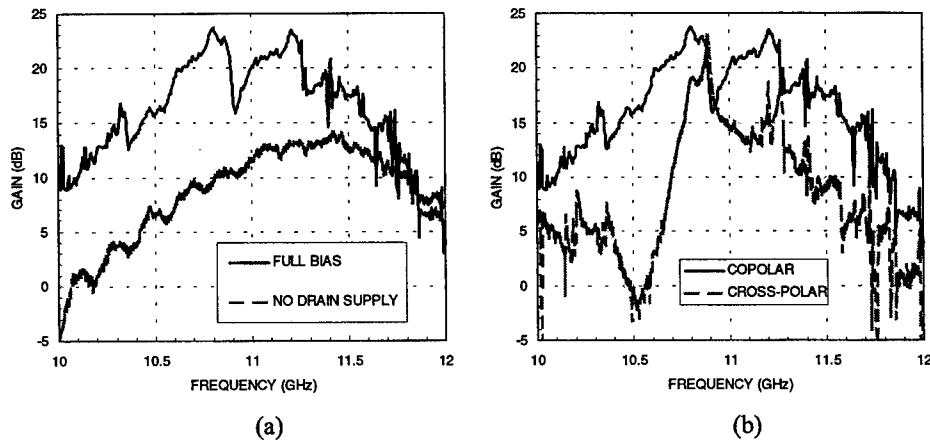
Figure 2: Measured gain for active reflect-array when co-polarised with receive antenna compared to (a) array with drain supply removed (b) cross-polar response

The cross-polar gain of the array is given in Figure 2(b). This plot shows that the active reflect-array has high cross polarisation for frequencies in the range of 10.8GHz to 11GHz. It is also useful to note that a peak in the cross-polarisation occurs at the same frequency as a trough in the co-polarised gain. The high levels of cross-polarisation are most likely due to the combination of the return loss of the active stage, both input and output, leading to low levels of isolation between the two feeds of the antenna, and therefore radiation of the cross-polarised signal from the input feed. The coupling between the feeds of the antenna could also be increased over that measured on the antenna alone by reflections from the array backing plate.
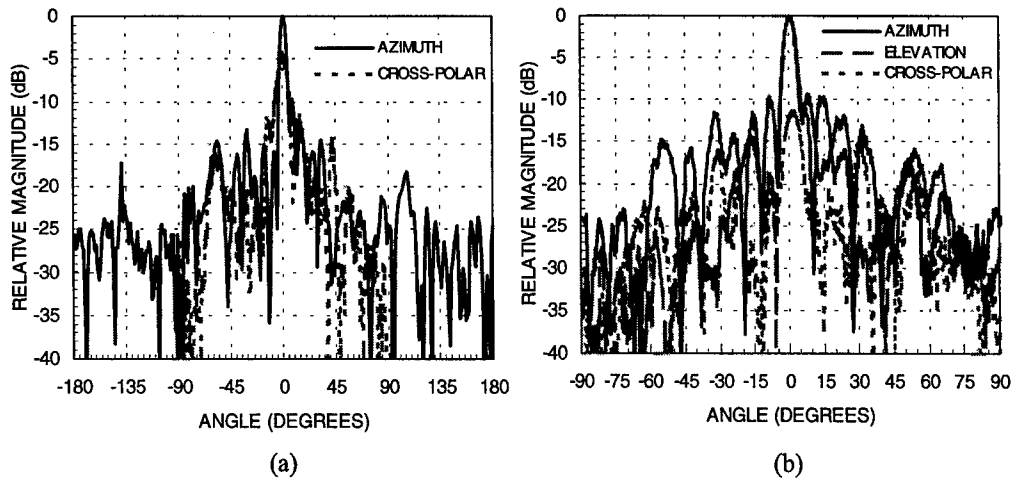
Figure 3: 137-element active reflect-array measured radiation pattern (a) at 11GHz in the azimuth principle planes across full 360 degrees, along with the cross-polarised azimuth radiation pattern, relative to the co-polarised peak gain; (b) at 11.15GHz for the azimuth and elevation principle planes and the cross-polarised azimuth radiation pattern.

Figure 3 shows the azimuth, elevation and cross-polar (azimuth) radiation patterns for the active array as measured at 11GHz and 11.15GHz. At 11GHz the gain of the array is in a dip with respect to the surrounding frequencies. This plot, Figure 3(a), shows that the at this gain dip the array is still radiating in a broadside direction, and in particular the array does not radiate in an end fire mode. At 11.15GHz the active antenna exhibits good gain over the passive array discussed in [5]. Similarly as its passive partner, this array features a significant side lobe level. The peak of cross-polarisation is about 12 dB from the peak of main lobe.

CONCLUSIONS

The design, development and testing of an X-band 137 element active reflect-array including transistor amplifiers has been presented. In this array dual-feed slot/aperture coupled patch antenna elements are used to minimise the inter-element spacing. The required phasing to obtain broadside radiation is achieved by using sections of transmission lines coupled between the input/output ports of the transistor amplifiers and the apertures. The array features broadside radiation although with increased side lobes and undesired cross-polarisation. The improved performance can be expected in the next design iterations.

REFERENCES

[1] Song, H.J. and Bialkowski, M.E., "Ku-band 16×16 Array of Aperture Coupled Microstrip Patches", IEEE Antennas and Propagation Magazine, vol. 40, No 5, pp. 25-29, Oct 1998.

[2] J. Huang, "Microstrip Reflectarray and its Applications", Proceedings of ISAP 96, Chiba, Japan, pp 1177-1180

[3] S. D. Targonski, D.M. Pozar, "Analysis and Design of a Microstrip Reflectarray Using Patches of Variable Size", IEEE Antennas and Propagation Conf. Proc. Vol 3, pp 1820 - 1823, June 1994.

[4] J. A. Navarro and K. Chang, Integrated Active Antennas and Spatial Power Combining, Wiley Inter-Science, 1996.

[5] A. W. Robinson, M. E. Bialkowski, H. J. Song, "A Passive Reflect-Array with Dual-Feed Microstrip Patch Elements", Microwave and Optical Technology Letters, Vol.23, No.5, Dec. 5, 1999, pp.295-299.

Phase-Only Pattern Synthesis for the Design of
an Active Linear Phased Array

Cheng-Nan Hu, Ching-Song Chuang, and Chia-I Hung

Antenna Section, Depatment of Electronics, Chung Shan Inst. of Sci. and Tech.
P.O. Box 90008-16-24, Lung-Tan, Taiwan, R. O. C. Fax. +886-3-4717897

Abstract

The paper presents a new technique for synthesizing the radiation pattern of an active linear phased array. The approach taken in the paper is to integrate the power response of the array over a spatial region of interest and force it to less than or equal to the desirable value. The closed form equation of the objective function is derived such that numerical technique based on the gradient search can be used to optimize the far-field patterns in a fast and efficient manner.

I.   Introduction

Recent advance in modern telecommunication systems (such as ground based high-performance radars, satellite antennas, etc.) has been an increasing demand for more sophisticated antenna systems. On one hand, such antennas must future improved performance. On the other hand, they must fulfill a number of additional requirements, including reconfigurable antennas, i.e. antenna systems able to radiate more than one pattern. This trend is particular true for the consideration of avoiding the use of radiating systems using many antennas, one for each task, and of employing antennas able to reconfigure the radiated pattern according to the task to be performed [1]. Thereby, a growing of synthesizing antenna patterns has emerged. One immediate application of this work is for the design of a 16-element, reconfigurable, active, linear phased array. Fig. 1 shows the functional block diagram of the array. As shown in Fig. 1, array antenna can be controlled by completely electronic techniques, operating separately on each element, so that the pattern synthesis can easily be achieved in array antenna by optimizing the weightings of radiation elements. There are number of existing optimization methods for far-field pattern synthesis which allow for the control of either the sidelobe structure (including multi-nulls or broad nulls [2] in the unwanted directions) or the main-lobe (including the shaped beam design [1],[3]). Among the various kinds of optimization methods, phase-only pattern control is becoming a significant relevance with the introduction of solid-state active integrated antenna systems. Because it allows one to fully exploit the limited available power of amplifiers driving each element of an active array thus maximizing the total radiated power. Also, the phase-only control is less complicated and far cheaper to dynamically modify the phase of a RF-signal, rather than its amplitude level.

The phase-only pattern synthesis problem is inherently nonlinear. In general it can only be solved numerically. The methods used can be classified into two main groups: (1) methods

based on the perturbation technique [4]; (2) methods based on general nonlinear optimization [1],[5]. As a rule the second type are more reliable, but have poor convergence rates and require considerable computer resources, especially for large arrays, so they cannot be used for pattern real-time control. To improve their performance, the aims of this paper is deriving the closed form equations for the objective function in pattern synthesis problems so that a simple and efficient numerical procedure based on gradient searching can be employed to optimize the antenna patterns in the sense of least mean-square-error. A number of significant examples for a 16-element linear array will assess the feasibility and effectiveness of the approach

II. Analysis

Consider a generic linear array located on the z-axis which should radiate different patterns, $g^{(k)}(\theta)$, with the control of different phase distribution, $\Phi^{(k)}(z_i)$. The array factor of far-field can be obtained from the excitation, $a_i e^{j\Phi i}$, of the individual elements as

$$f(\theta) = \sum_{i=1}^{N} a_i e^{j(kd(i-1)\cos\theta + \Phi_n)} \tag{1},$$

where d is the inter-element spacing, k is wavenumber $(2\pi/\lambda)$, θ is the angle from array axis (z-axis), and $a_i \angle \Phi_i$, is the amplitude and phase of $i'th$ element. If we let $\varphi = kd\cos\theta$, we can define the complex error function as

$$\varepsilon(\varphi) = f(\varphi) - g(\varphi) \tag{2},$$

where $g(\varphi)$ is the desired array pattern. Then the mean square error function, $\sigma(\varphi)$, can be obtained and given as

$$\sigma_{\Omega_i}(\varphi) = \int_{\Omega_i} \|\varepsilon(\varphi)\|^2 d\varphi / \Delta\varphi \tag{3},$$

where Ω_i is the specified integral region $(\varphi \in [\theta_1, \theta_2])$ and $\Delta\varphi = \varphi_1 - \varphi_2$. Introducing equation (2) into equation (3), we can express equation (3) as

$$\sigma_{\Omega_i}(\varphi) = \left\{ \int_{\Omega_i} |f(\varphi)|^2 d\varphi - \int_{\Omega_i} [g(\varphi)^* f(\varphi) + g(\varphi) f^*(\varphi)] d\varphi + \int_{\Omega_i} |g(\varphi)|^2 d\varphi \right\} / \Delta\varphi \tag{4},$$

where '*' means complex conjugate. In this particular case of study, $g(\theta) = C$ (C equal to zero for nulling in sidelobes and C equals to a constant value for the shaped beam design) is discussed. The closed form equations of the gradient of the error function, $\sigma(\varphi)$, is accomplished and expressed as following

$$\frac{\partial\sigma(\varphi)}{\partial\Phi_i} = \sum_{j=1}^{N} \frac{a_i a_j}{kd(i-j)} \sin[\frac{kd}{2}(j-i)(x_1 + x_2) + \Phi_i - \Phi_k] \sin[\frac{kd}{2}(j-i)(x_1 - x_2)]$$
$$+ \frac{ca_i}{2kd(i-1)} \{\cos[kd(i-1)x_1 + \Phi_i] - \cos[kd(i-1)x_2 + \Phi_i]\} \tag{5},$$

where i = 1,2 ,···, N. Using (5), the POGS (phase-only gradient search) algorithm [6] can be

276

employed to optimize the objective function (4) in the sense of least mean square error efficiently.

III. Numerical Results

Using this approach, three examples for the phase-only pattern synthesis problems of a 16-element active linear phased array are studied and presented. There are:1) flat-topped pattern for mainlobe, 2) multi-nulls, and 3) broad nulls for sidelobe of the far-field radiation patterns.

As an example of this capability, firstly, a flat-topped pattern for an array with 16 elements was designed and plotted in Fig. 2 to meet the specifications of the extent of flat-topped region form 75-105° with deviation of +/- 0.35dB in flat region and beamwidth of 57° between zero crossings. Fig. 2 also plots the directive pattern design of a 16-element array with uniform distribution to obtain the maximum gain.

Fig. 3 demonstrates the multi-nulling capability of this approach, clearly showing two nulls are placed to the desirable directions of 100° and 115° in respectively and, however, causing the degradation in directivity of –0.55 dB.

Fig. 4 illustrates the broad nulls capability of this approach, clearly showing a broad nulls in the specified spatial region from 100° to 155° with only – 0.85 dB dropping in directivity. Finally, table I lists the computed phase distribution of numerical examples in Fig. 2, 3, and 4.

IV. Conclusion

A new approach for the design of a linear, active, phased array by phase-only control has been proposed. The closed form solution of the objective function is derived so that a simple gradient search method can be used to synthesize the pattern in a fast and efficient manner. Excellent results shown in numerical examples validate the approach.

References

[1] O. M. Bucci and G. D. Eli, "Power synthesis of reconfigurable conformal arrays with phased-only control," *IEE Proc., Vol. 145, Pt. H, No. 1*, Feb. 1998, pp. 131-136.

[2] M. H. Er, "Thechnique for antenna array pattern synthesis with controlled broad nulls," *IEE Proc. Vol. 135, Pt. H, No. 6*, Dec. 1988, pp. 375-380.

[3] D. J. Shpak, "A method for the optimal pattern synthesis of linear arrays with prescribed nulls," IEEE Trans., AP-44, Vol. 44, No. 3, Mar. 1996, pp. 286-295.

[4] Steyskal H., Shore R. A., "Methods for null control and their effects on the radiation pattern," *IEEE Trans., AP-34, No. 3*, 1986, pp. 404-409.

[5] Shore R. A., "Nulling at symmetric pattern location with phase-only weight control," *IEEE Trans., AP-32, No. 5*, 1984, pp. 530-533.

[6] D.–C. Chang, C.–N. Hu, C.–I. Hung, and K.–T. Ho, "Pattern synthesis of the offset reflector antenna system with less complicated phased array feed," *IEEE Trans., AP-42, No. 2*, 1994, pp. 240-245.
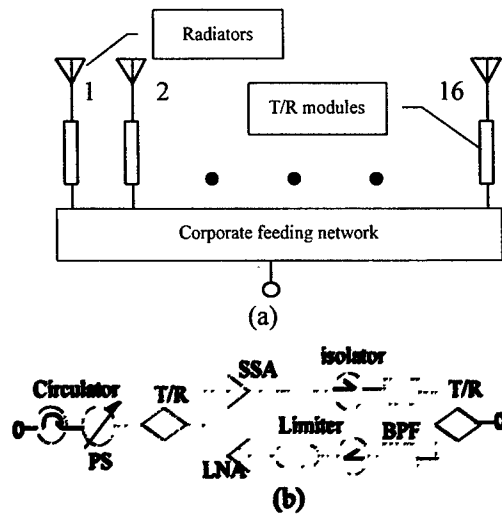
Fig.1 Functional diagram of (a) a generic, linear, active phased array and (b) a T/R module

Fig. 4. Array pattern with broad nulls from 100° to 155°.
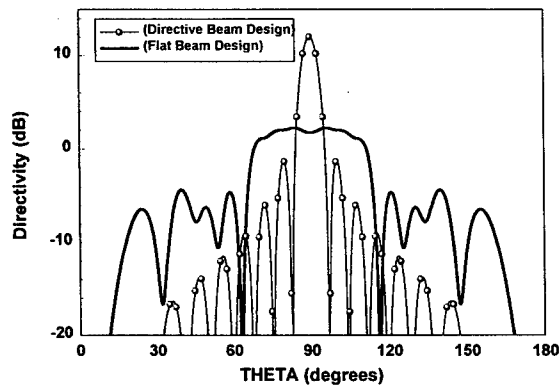
Fig. 2. Flat-topped array pattern, showing the extent of a topped region of 75-105° with the deviation in flat region of +/-0.35 dB.
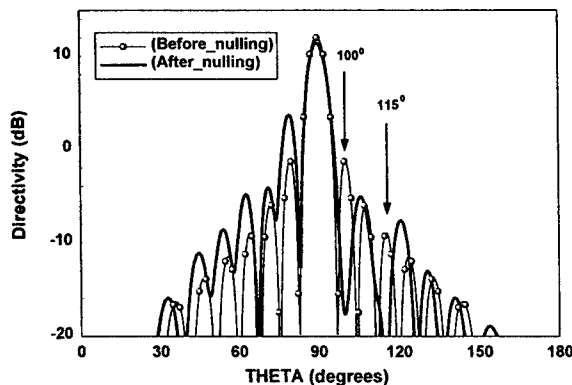
Fig. 3. Array pattern with nulls at 100° and 115°.

Table I. Computed phase distribution of patterns plotted in Fig. 2, 3, and 4.

NO.	Φ (FIG.2)	Φ (FIG.3)	Φ (FIG.4)
1	- 5.6°	-65.1°	-78.8°
2	157.5°	-69.0°	-25.3°
3	84.4°	-61.3°	-32.3°
4	-140.6°	-56.7°	-5.6°
5	-106.9°	-59.4°	-36.6°
6	-78.8°	-57.6°	-4.2°
7	-50.6°	-45.2°	-47.8°
8	-22.5°	-48.5°	-15.5°
9	-22.5°	-69.0°	-63.3°
10	-50.6°	-90.2°	-30.9°
11	-78.8°	-95.1°	-74.5°
12	-106.9°	-79.5°	-42.2°
13	-140.6°	-74.6°	-73.1°
14	84.4°	-76.0°	-46.4°
15	157.5°	-49.4°	-53.4°
16	- 5.6°	0°	0°

Focussed Reflections off Spherical Radomes for Active Phased Arrays

Dr. Kaichiang Chang and Leigh Martinson
Raytheon, Sudbury, MA

Dr. Larry Corey, William Guzak, Rob Hemphill, and Dr. Daniel Leatherwood
Georgia Tech Research Institute, Atlanta, GA

Danny Pollard
GBR-P Product Office, Huntsville, AL

I   Introduction

Spherical radomes have successfully been used as environmental protection for large reflector and passive array antennas for many years. However, with the advent of active solid-state phased arrays, an additional phenomenon must be considered that previously was not important. This new phenomenon is the focusing properties of spherical surfaces. When the antennas transmits, a portion of the energy is reflected off the surface of the radome and focused to a small spot about half way between the surface and the center of the radome. The power density in this focal region is not large enough to be of concern for passive arrays of reflectors. However, if it happens to be focused on a small group of solid-state modules, it can exceed the power handling capability of the solid-state receive module. This paper presents an analysis of this phenomenon and provides radome design criteria to avoid potential problems.

In Section II, the analogy is made between analysis of this problem and the design of spherical reflectors, plus two modeling methods are presented. A design criterion used to avoid the problem is presented in Section III. Two radome geometries are analyzed in Section IV. Finally, measured data used to validate the models is shown in Section V.

II   Analysis and Modeling

It is well known that a spherical reflector is desirable for beam scanning applications. All parallel rays incident on the sphere generate reflected rays which cross a line through the origin and parallel to the incident rays [1]. As shown in figure 1 a typical incident ray AB is reflected through points C1 and C2, where C1 and C2 are the caustics of the reflected ray. This caustic surface intersects any plane through the x-axis in the form of an epicycloid called the nephroid because of its resemblance to a kidney. A suitable primary feed can thus lie near the paraxial focus at $x=0.5 R_0$, $y=0$ where the caustics cusp and focal line and near which most of rays pass. The Arecibo 1000ft diameter spherical reflector is an example of this application. The same model can be used to analyze the radome problem if the reflection coefficient of the radome is considered.
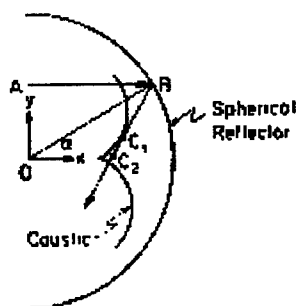
Ray Behaviour of Spherical Reflector

Figure 1 Parallel Rays off of a Spherical Reflector

When the array antenna radiates parallel rays through the spherical radome, the reflected rays from the radome produce caustics inside the radome. If the antenna is situated near the paraxial focus at $x=0.5\ R_0$, the power received by an antenna element can exceed 100% of the radiated power of a T/R module.

Since the radome is in the far field range of each array element, a far field model of the radome reflection on the array face is developed to determine the initial position and direction of each ray radiated from each array element to the radome. Next the position and direction of each ray reflected back onto the array face is calculated using the ray tracing method. Finally, at array element level, the reflected rays are summed, whose amplitudes and phases are determined by the element pattern as function of the ray's direction and ray path length, in order to calculate the total reflected power into each array element. Modeling results are shown in figure 2 for when the radome reflection is focused and defocused on the array.
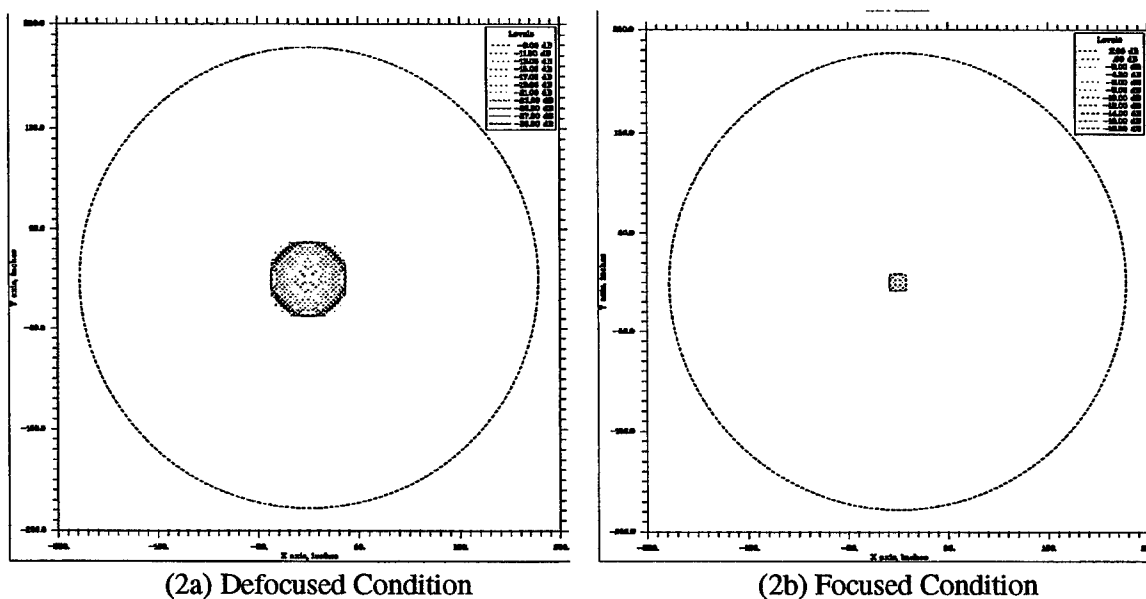
(2a) Defocused Condition   (2b) Focused Condition
Figure 2. Examples of Far-Field Modeling Results

Since ray tracing is a far-field technique and accounts for two points (mainbeam and grating lobe direction) on the element pattern, a second modeling approach was established in order to include the effect from the full element pattern. A phased array near field model was used to determine the field on a grid of points on the spherical radome. Each of these points was then considered to be point sources. A second model then added up the field from each of these point sources onto a second grid of points on the array face. There were some minor differences with the ray tracing results, but these differences were not significant. Modeling results are shown in figure 3 for when the radome reflection is focused and defocused on the array.

III   Design Criteria

Typically radomes are designed for low loss and small radome reflection coefficients, therefore the power reflected off radomes is around -10 to -15 dB. T/R modules are normally designed to handle no more than full-reflected power. In order to obtain less than 5 dB of focussing gain, the antenna position should be within $0.21\ R_0$ from the radome center as determined by ray tracing analysis. Given a typical radome reflection of -11 dB, only -6 dBr (relative to T/R module transmit power) of reflected power will be received by a T/R module, which is well below the safe level of full reflected power (0 dBr).
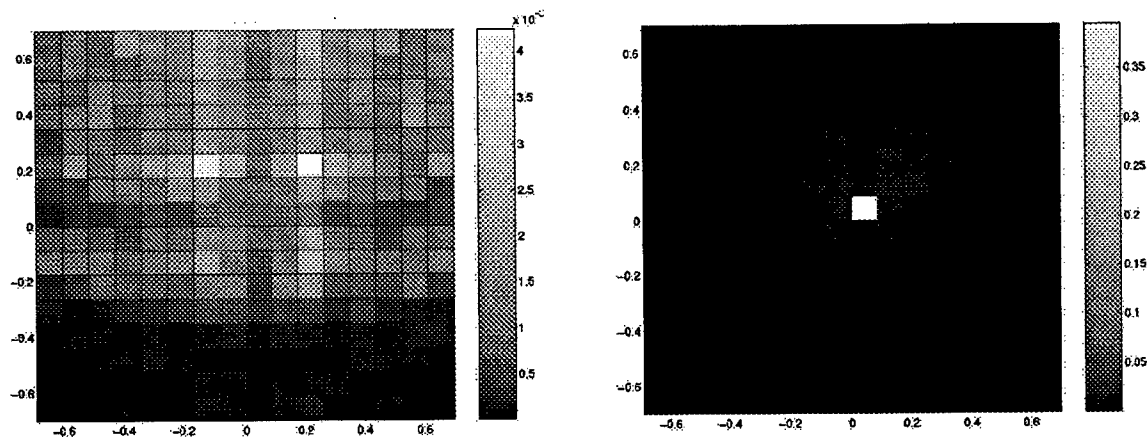
(3a) Defocused Condition   (3b) Focused Condition

Figure 3. Examples of Near-Field Modeling Results

IV   Two Radome Geometries

Two radome geometries are presented to illustrate having the caustic point near the array face and off the array face. The first geometry is a 38ft diameter phased array enclosed inside an 85ft spherical air-supported radome as shown in figure 4a. The elevation axis of the antenna is about 14ft above the radome center and the aperture of the antenna is about 9ft from the elevation axis. When the antenna is pointing at the horizon, the aperture of the antenna is $0.21 \, R_0$ (i.e. 9ft) away from the radome center, where R_0 is the radome radius of 42.5 ft. In this case, reflected rays are defocused so that no significant reflected power enters the T/R module. When the antenna is pointing at zenith, the aperture of the antenna is $0.54 \, R_0$ (i.e. 23ft) away from the radome center at which all rays pass through to produce more than a 22 dB focussing gain. Given a typical radome reflection of –11 dB, then 11 dBr (relative to T/R module transmit power) of reflected power will be received by a T/R module, which will damage the T/R module.

The second geometry is similar to the first but the radome is raised 12ft higher in respect to the antenna as shown in figure 4b. When the antenna is pointing at the horizon, the position of the antenna with respect to the radome is not different from the first geometry. When the antenna is pointing at zenith, the aperture of the antenna is $0.26 \, R_0$ (i.e. 11ft) away from the radome center and the reflected rays are still defocused.

V   Measured Results

Measured data was taken using the Ground Based Radar-Prototype (GBR-P), which has the first radome geometry. Two different element locations were used to measure the radome reflections versus elevation tilt. Both models predicted approximately the elevation tilt where the peak radome reflection would occur and the magnitude of the received power for that element position (see figure 5). The predictions were slightly off due to the fact the GBR-P radome may not be truly spherical as was modeled.

REFERENCES
[1] Kohei Hongo and Yu Ji, "Study of the Field Around the Focal Region of Spherical Reflector Antenna", IEEE Transactions on Antennas and Propagation, Vol. 36, No. 5, pp. 592-598.
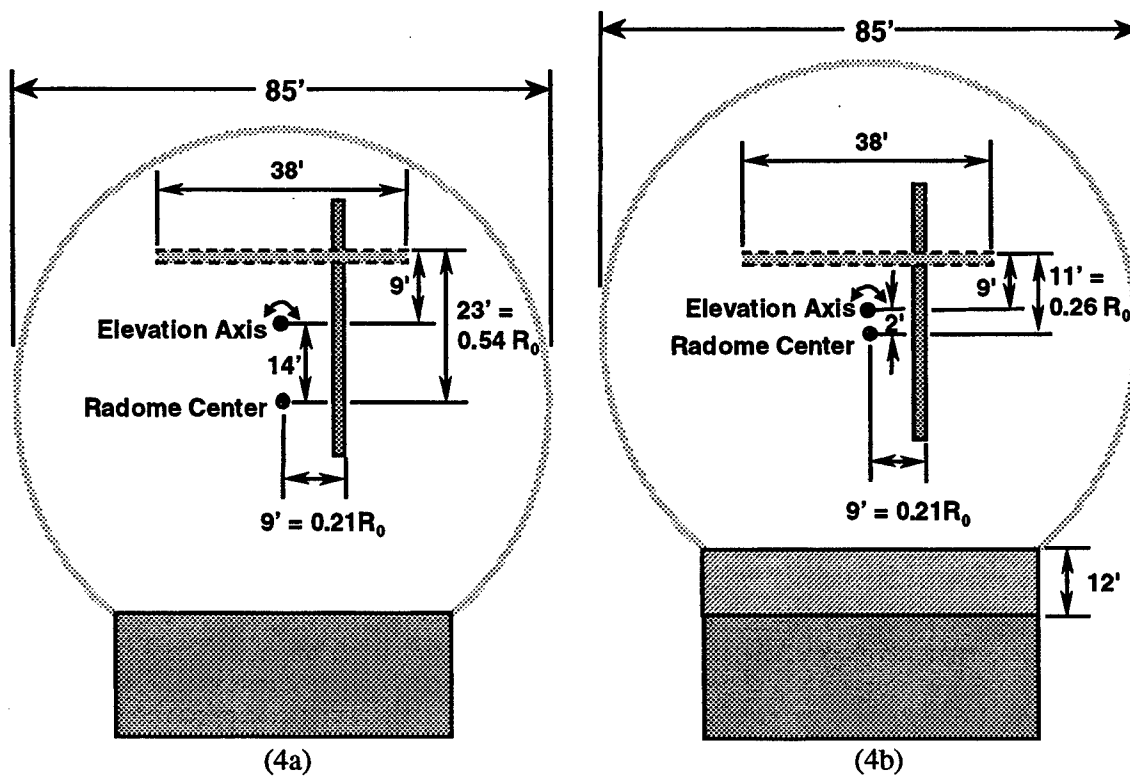
Figure 4. Two Radome Geometries

(5a) Position 1   (5b) Position 2
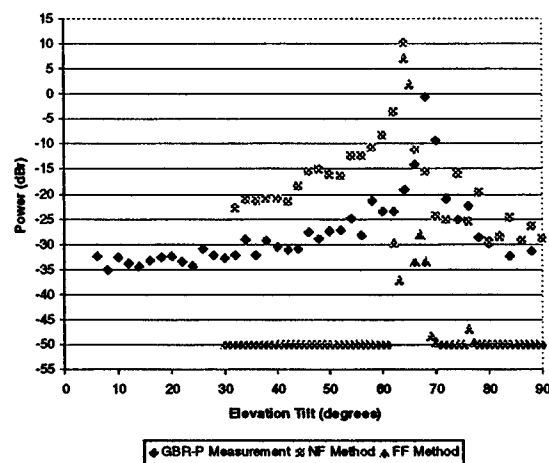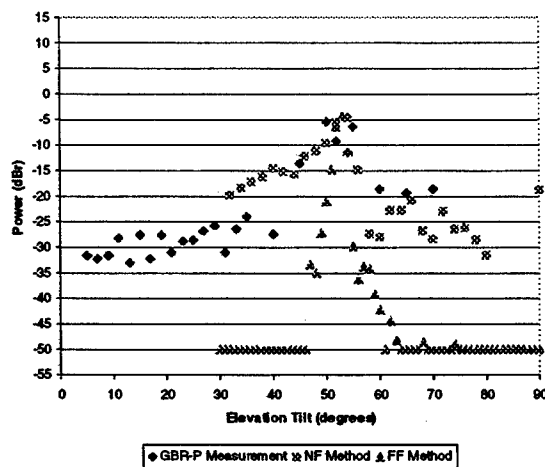
Figure 5. Comparision of Analyses and Measurements at Two Element Positions

TP1

Analysis

Analysis

Constant Elevation Pattern Notch Design in a Rectangular Phased Array Having a Triangular Lattice

Joseph K. Mulcahey and Kaichiang Chang
Raytheon Company
528 Boston Post Rd.
Sudbury, MA 01776-3375 USA
(978) 440-3291   Joseph_K_Mulcahey@res.raytheon.com

Abstract - When designing the aperture distribution for a constant elevation pattern notch in a rectangular, planar phased array with a triangular lattice, the designer may be tempted to set the excitation of each element individually, based on sampling a desired continuous distribution at each element's unique location. It can be shown that for some types of aperture distributions, such as a principal-plane notch on one side of the main beam, this can cause unacceptable lobes to appear away from the principal planes. The resolution to this problem is to first generate the distribution for the elements in one (odd) column, and then directly apply these excitations to the elements in the adjacent (even) column. This has the effect of increasing the periodicity of sidelobe features in k-space, which causes a notch to appear in the sidelobe structure of the grating lobes at the desired location.

Introduction

An active phased array antenna can be designed to permit the adjustment of the individual element amplitude and phase settings. In radar or communications applications this flexibility can be used to implement aperture distributions in order to generate the required antenna pattern. Frequently, a region of reduced sidelobe energy (or notch) is required for clutter or interference suppression in elevation. Lowering the sidelobes everywhere unnecessarily reduces aperture efficiency and broadens the beamwidth. A pattern synthesis technique such as that of Orchard [1] or Guella [2] can be used to generate an aperture distribution that will produce the desired antenna pattern with a low sidelobe region. Figure 1 illustrates the concepts of column-dependent and column-independent sampling.
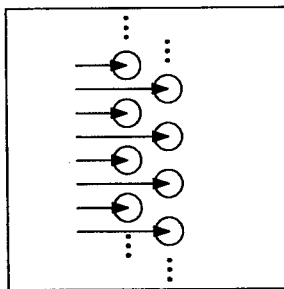
Fig. 1 (a). Column-Dependent Distribution Sampling
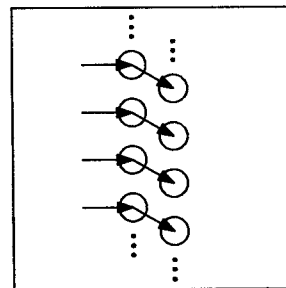
Fig. 1 (b). Column-Independent Distribution Sampling

Simulation

To demonstrate this effect, an array of 38 columns, 32 rows per column, and an unstable equilateral triangular lattice is simulated. If the lattice is set so that no grating lobe main beam peaks can enter real space for scan angles from boresite of up to 45°, then the column spacing is $d_x = \lambda/(1+\sin(45°)) \approx 0.586\lambda$, and the row spacing within one column is $d_y = 2*d_x/\sqrt{3} \approx 0.676\lambda$. Figure 2 illustrates the array geometry.
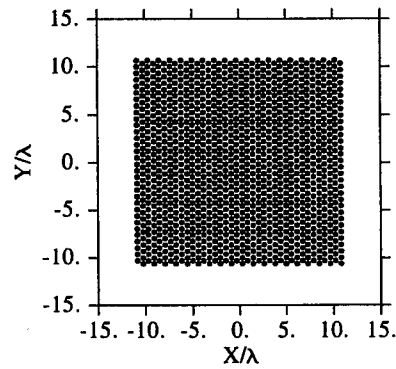
Fig. 2. Array Geometry

Two aperture distributions will be considered. In each case, the azimuth distribution is a 25 dB, $\bar{n} = 4$ linear Taylor [3]. The elevation distributions for the two cases are as follows:

1. 25 dB, $\bar{n} = 4$ linear Taylor, modified with a notch -60 dB below the unscanned main beam from v ≈ -0.2 to -0.4, using Orchard Synthesis. Synthesized at 64 row locations (column-dependent).
2. 25 dB, $\bar{n} = 4$ Linear Taylor, modified with a notch -60 dB below the unscanned main beam from v ≈ -0.2 to -0.4, using Orchard Synthesis. Synthesized at 32 row locations (column-independent).

In this array, with 32 rows per column and an unstable triangular lattice, there are 64 unique y-values for the element locations. In order to force the desired notch into the sidelobes of the grating lobes, however, the notch must be synthesized over the 32 elements in a single column, and the same complex element weights applied to the 32 elements in each column, regardless of whether the elements are in an odd or even column. The effects of errors, mutual coupling, edge effects and bandwidth are neglected here.

Column-Dependent Distribution

In the column-dependent case, the notch is synthesized for the 64 different y-values. Figure 3 shows the complex aperture distribution. Figure 4 shows the elevation and azimuth principal plane cuts. Figure 5(a) shows the sine space contour. The notch is present below the main beam, but the sidelobes of the grating lobe appear in the notch. Figure 5(b) shows an elevation cut through the grating lobe series at u = λ/(2d_x), which is approximately equal to u = 0.854 sines. The peak sidelobe level in the notch is –44.8 dBr, or more than 15 dB above the notch design level.
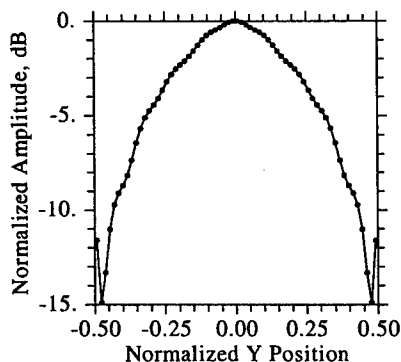
Fig. 3 (a). Column-Dependent Notch Amplitude Distribution
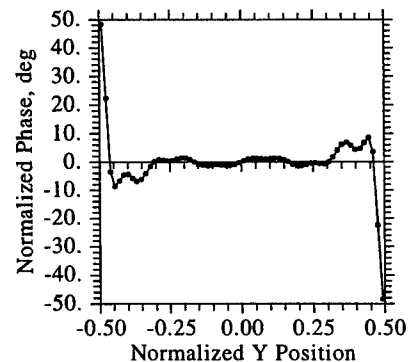
Fig. 3 (b). Column-Dependent Notch Phase Distribution
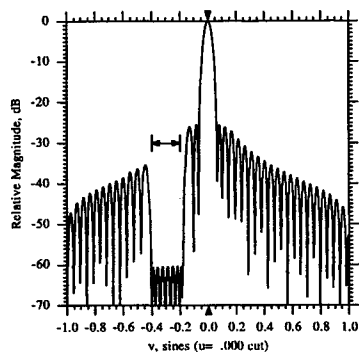
Fig. 4 (a). Column-Dependent Notch
Elevation Principal Plane Cut
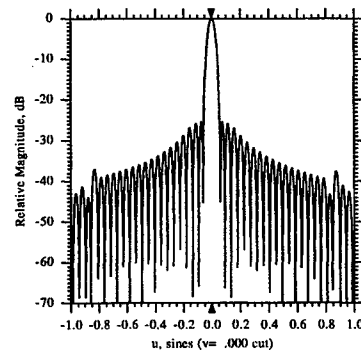
Fig. 4 (b). Column-Dependent Notch
Azimuth Principal Plane Cut
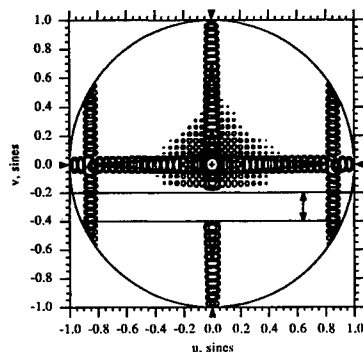
Fig. 5 (a). Column-Dependent Notch Sine Space Contour
(peak notch sidelobe level = -44.8 dBr)
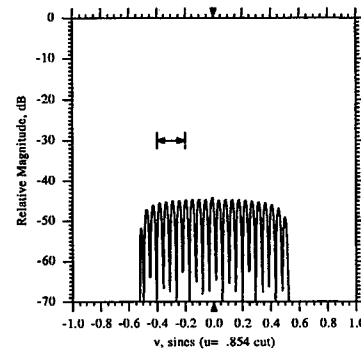
Fig. 5 (b). Column-Dependent Notch
Elevation Cut through u = +0.854

Column-Independent Distribution

In the column-independent case, the notch amplitude and phase distribution is synthesized over the 32 elements in the odd columns, and the complex voltages are used for the 32 elements in the even columns. Figure 6 shows the complex aperture distribution. Figure 7 shows the elevation and azimuth principal plane cuts. Figure 8(a) shows the sine space contour. The notch is still present below the main beam, but the sidelobes of the grating lobes are now also notched over the range $v \approx$ -0.2 to -0.4 sines. Figure 8(b) shows an elevation cut through the grating lobe series at u = 0.854 sines. The sidelobe level in the notch is now −60.5 dBr, which is approximately the notch design level.
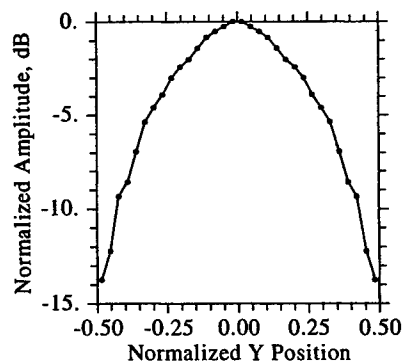
Fig. 6 (a). Column-Independent Notch Amplitude Distribution
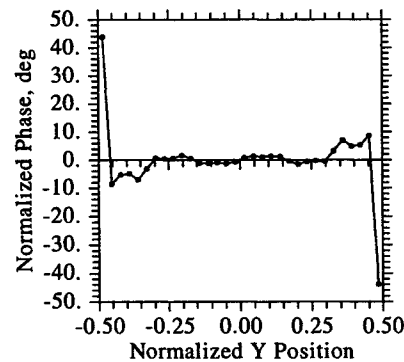
Fig. 6 (b). Column-Independent Notch Phase Distribution
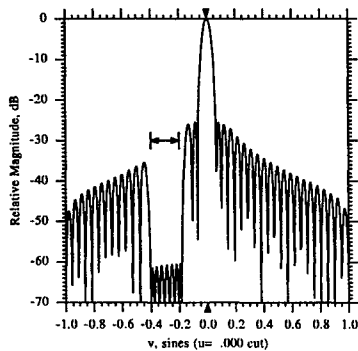
Fig. 7 (a). Column-Independent Notch
Elevation Principal Plane Cut
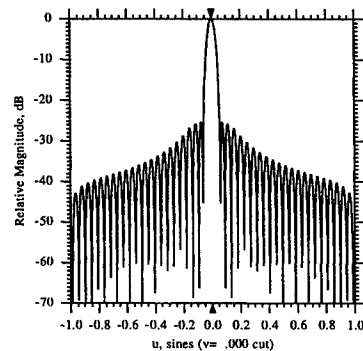
Fig. 7 (b). Column-Independent Notch
Azimuth Principal Plane Cut
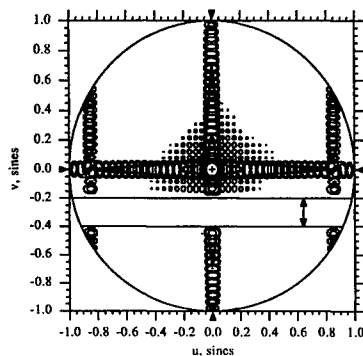
Fig. 8 (a). Column-Independent Notch Sine Space Contour
(peak notch sidelobe level = -60.5 dBr)
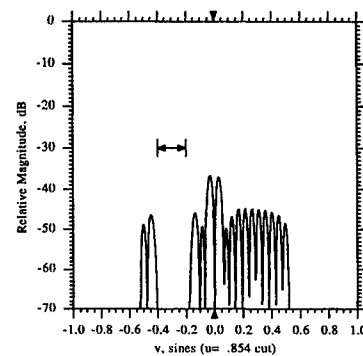
Fig. 8 (b). Column-Independent Notch
Elevation Cut through u = +0.854

Conclusion

It has been shown that in a planar phased array with a triangular lattice, an elevation pattern notch will not be present over all azimuth angles unless care is taken in synthesizing the aperture distribution. While intuition may indicate that synthesizing the distribution over each unique element position would be advantageous, it actually is not. Only if the distribution is synthesized over the element positions in one column and then applied to the corresponding elements in the next column will the notch also appear in the grating lobe sidelobes in the correct location. For the example shown here, the difference in peak notch sidelobe levels is greater than 15 dB.

References

1. H. J. Orchard, R. S. Elliot, and G. J. Stern, "Optimizing the synthesis of shaped beam antenna patterns," *IEE Proc.*, vol. 132, pt. H, no. 1, Feb. 1985.
2. T. P. Guella and R. M. Davis, "Synthesis of notched antenna patterns for wideband processing," *IEEE Trans. Antennas Propagat.*, vol. 43, pp. 1465-1471, Dec. 1995.
3. T. T. Taylor, "Design of line-source antennas for narrow beamwidth and low sidelobes," *IRE Trans. Antennas Propagat.*, vol. AP-7, pp. 16-28, 1955.

Limited Scan Antenna Systems Using Phased-Array Feeds (versus Direct Radiating Array Apertures) Require Fewer Array Elements; Or Do They?

Paul A. Chiavacci, Raytheon Company
528 Boston Post Road, Sudbury, MA 01776
phone 978-440-1061; fax 978-440-2414; email 'chiavacci@ieee.org'

Abstract: It is generally accepted that a limited-scan antenna system with a phased-array feed uses significantly fewer elements than a direct-radiating, phased-array aperture (planar array) for similar scan coverage. This paper presents an analysis showing this is not necessarily the case. The author derives the relative number of elements for both cases (phased-array fed lens and direct radiating aperture) using two grating lobe conditions: 1) elimination of grating lobes in "real space" and 2) elimination of grating lobes within the antenna coverage area. The former grating lobe condition does result in fewer array elements for the phased-array feed as expected. But imposing the latter grating lobe condition, often of interest in GEO satellite communication, yields no benefit in element count between a direct-radiating, phased-array aperture and the phased array fed, dual-lens antenna system used in the analysis.

Introduction: It is often assumed that in limited scan applications an antenna system utilizing a phased array feed will require fewer elements than a direct-radiating, phased-array antenna i.e. planar array. It is often stated that in a dual lens system (a dual reflector antenna system would be equivalent) with phased-array feed the element advantage of a phased-array feed versus a direct-radiating phased array is in the ratio $(f/F)^2$ [1]. Where f is the focal length of the Feed lens and F the focal length of the Aperture lens. Under the defined conditions for a modest ratio of focal lengths (e.g. $f/F = 1/2$) a significant reduction in the number of required elements (a cost driver in phased-array antennas) would be achievable. That's the perception. Reality, under reasonable operating conditions, is not necessarily the same.

The above element reduction is achievable if the element spacing for the planar array (direct radiating aperture) and the phased-array feed are the same. That is usually not the case, since the phased-array feed, to achieve the aperture magnification (F/f) which yields the element reduction, is required to scan over a larger angle than the direct-radiating phased array. The larger scan angle necessitates a reduction in the element spacing for a phased array feed resulting in additional elements.

Furthermore there are two conditions, defined by the imposed grating lobe requirement, which result in a change in the element spacing. Condition 1 requires that all grating lobes be eliminated from "real space". This provides for a planar array aperture with fewer required elements than the (F/f) ratio would imply since the element spacing on the planar array is greater than is required for the phased array feed. Condition 2 only requires that all grating lobes be eliminated from the primary coverage area of the antenna. This would be the case, for example, if one wanted to eliminate grating lobes from impinging on the disk of the Earth as viewed from geosynchronous orbit. Under this latter condition the ratio of the element spacing required for a direct-radiating planar array and the phased-array feed is such that the number of elements required for both the phased-array feed and the direct radiating aperture are the same.

The following section derives the size and structure of a limited-scan, dual-lens antenna system in the manner of Chen and DuFort [1], to determine the size of the required phased-array feed. Further sections define the grating lobe criteria and derive the number of array elements required for both antenna structures: direct radiating array aperture and the array-fed, dual-lens antenna system. Finally, the element ratio between antenna system types using both grating lobe conditions is determined.

Size and Structure of a Dual-Lens Antenna System with Phased Array Feed

Prior to beginning an analysis of element count it is necessary to determine the size (diameter) of the array feed that must be populated with elements. To do so requires an extension of the analysis employed by Chen and DuFort [1]. The analysis assumes that the Aperture lens is efficiently utilized consequently, the diameter **D** of the Aperture lens is equivalent to the diameter of the direct radiating array. Also, all angles are in radians and the small angle approximation is employed for the limited scan conditions. Refer to Figure 1 for an overview of the dual lens system.
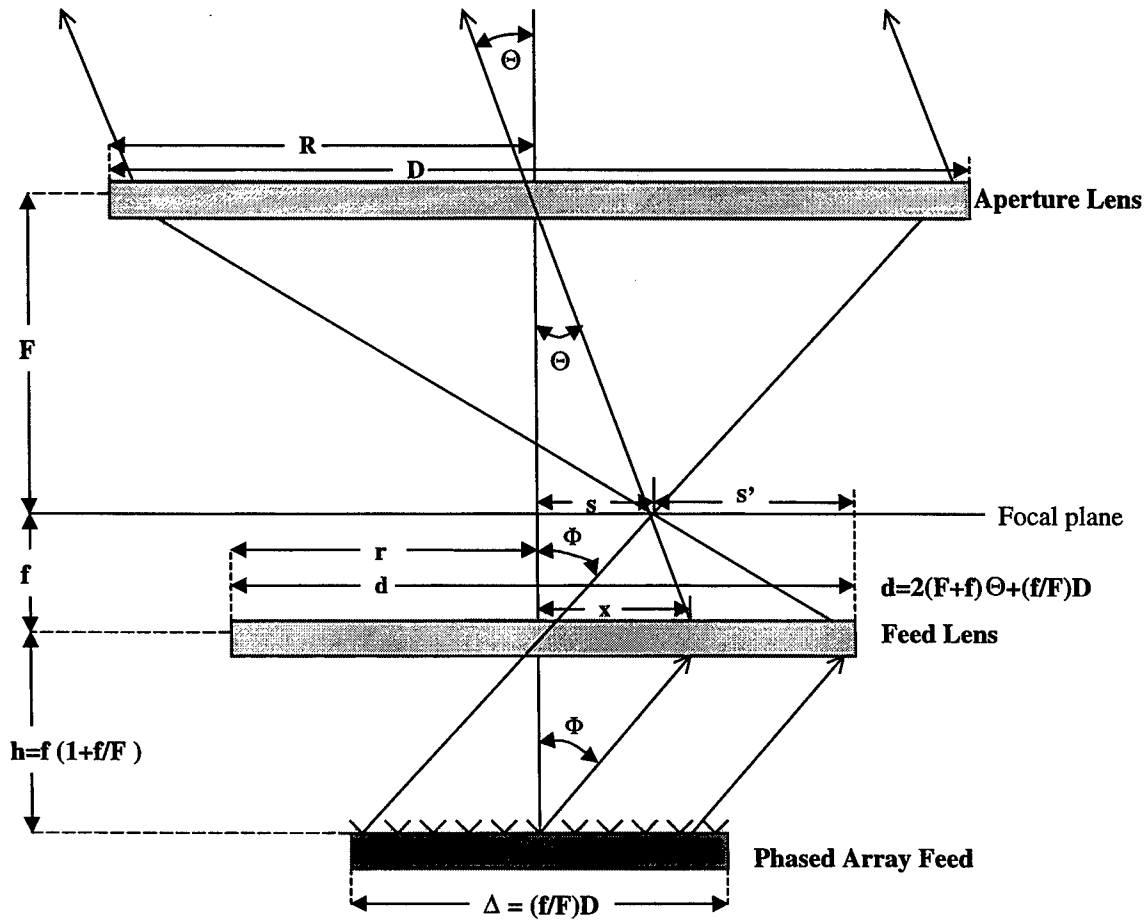
Figure 1. Dual Lens Antenna System with Phased Array Feed

The Aperture lens, Feed lens and Array feed are placed coaxially. The Aperture lens and Feed lens are also confocal. For angle of arrival Θ (i.e. lens system in a receive configuration) the ray intercepts the focal plane at a distance $s = F\Theta$ from the axis. Since parallel incident rays cross at the focal spot that is common to both the Aperture and Feed lenses, the rays will exit the feed lens at an angle Φ to the coaxial line. Therefore, $s = F\Theta$ and $s = f\Phi$ or

$$1)\ \Phi = (F/f)\Theta$$

From this relationship it can be seen that the scan angle Φ required of the array feed is equal to the magnification of the lens antenna system (F/f) multiplied by the far-field scan angle Θ. In other words to achieve lens system magnification the array scan angle must increase correspondingly.

The size of the Feed lens can be determined by reference to Figure 1, where r = s+s' and F/(R+s) = f/s'. Substituting from the previous equation for s', setting s = FΘ from Figure 1 and combining terms yields r = (F+f)Θ + (f/F)R. Therefore, the diameter (d= 2r) of the Feed lens

$$\text{2) } d = 2(F+f)\Theta + (f/F)D$$

To provide maximum utilization of the Aperture lens it is necessary to place the Array feed at the proper distance from the Feed lens. We want to ensure that energy leaving the Feed lens, at all scan angles and without spillover, will be intercepted by the Aperture lens. The location of the Feed lens can be determined by considering a central ray through the lens system. To implement the above condition it is necessary that a ray through the center of the Aperture lens also intercept the Array feed at the center of the array.

Given the above we can determine the proper distance (h) between the Feed lens and the Array feed. Notice that x = (F+f)Θ and x = hΦ. Equating the expressions and solving for h yields, h = (F+f)(Θ/Φ). Substituting equation 1 into the previous result yields

$$\text{3) } h = (F+f)(f/F) = f(1 + f/F)$$

We can now determine the diameter Δ of the phased array feed. From Figure 1 we set Δ/2 = r – hΦ. Substituting r (r=d/2) from equation 2) and h from equation 3) results in Δ/2 = (F+f)Θ + (f/F)R – f(1+f/F)Φ. Further substitution of equation 1) for Φ and combining terms results in Δ/2 = (f/F)R or,

$$\text{4) } \Delta = (f/F)D$$

The above analysis defines the gross dimensions of a dual-lens antenna system with phased-array feed and is useful as an initial approximation to begin a baseline design. A final design will require application of geometric optics and extensive ray tracing. Such a design is not the intent or purpose of this paper.

Given the diameter Δ of the phased-array feed we can now determine the number of elements required to populate a feed of this size. This is done in a later section. In the next section we define the grating lobe conditions of interest.

Grating Lobe Criteria

The textbook grating lobe criteria [2][3] that restricts the scan angle of a phased array to eliminate grating lobes from entering "real space" is defined as

$$\text{5) } \sin \Theta \le [\lambda / d] - 1$$

Where Θ is the scan angle of the radiating array, λ the operating wavelength and d the spacing between elements. Such a condition eliminates any beam, other than the mainbeam, from forming in visible space and the antenna designer need not be concerned about radiating energy or receiving energy (other than normal sidelobes) from unwanted directions. This is a desirable condition (no grating lobes in real space) but imposes a strict limit on element spacing. For a non-scanned antenna –main beam on boresight- the

theoretical element spacing can approach λ. For large scan –approaching 90 degrees- the element spacing approaches a $\lambda/2$ limit.

Although eliminating grating lobes from "real space" is a desirable condition, the antenna designer may choose other means to eliminate/reduce grating lobes such as providing an element pattern that minimizes the effect of grating lobes in real space. If grating lobes can be mitigated by other means, such as the above element pattern approach, then the antenna designer need not be as concerned about grating lobes entering "real space". The designer then only needs to be concerned about grating lobes that enter into the primary coverage area of the antenna.

The grating lobe condition that applies in such a case –no grating lobes in the primary coverage area of the antenna [4]- is

$$6) \sin\Theta \le \frac{1}{2}\left[\lambda/d\right]$$

Such a condition might apply to Earth coverage from geosynchronous orbit. In other words, allow grating lobes into real space, mitigate the effect of grating lobes using the element pattern or other techniques, but do not allow grating lobes to impinge on the Earth's disk as seen from geosynchronous orbit (+/-8.7 degrees). Under such conditions the less stringent grating lobe condition is a desirable design point.

The following sections of this paper discuss and compare the relative element count required for the direct-radiating, phased-array aperture as compared to the phased-array feed under both grating lobe conditions.

Number of Elements required; No Grating Lobes in "Real Space"

For the first grating lobe condition, no grating lobes in "real space" (equation 5), we will now determine the number of elements for a direct radiating phased array aperture. The number of radiating elements is proportional to $[D/d]^2$. Where **D** is the required radiating aperture and $d \le \dfrac{\lambda}{\sin\Theta+1}$. Now utilizing the limiting condition for **d** the number of required elements is proportional to $\left[\dfrac{[D(\sin\Theta+1)]}{\lambda}\right]^2$. For limited scan conditions ($\sin\Theta = \Theta$) then,

$$7) \text{ # of required elements} \propto \left[\frac{D(\Theta+1)}{\lambda}\right]^2 \text{ for the direct radiating aperture.}$$

For a phased array feed we can calculate the number of required elements in a similar manner by substituting the diameter Δ for the phased array feed in place of **D**. The number of required elements is proportional to $\left[\dfrac{\Delta}{d}\right]^2$, where $\Delta = \left[\dfrac{f}{F}\right]D$ (equation 4), and $d=\dfrac{\lambda}{(\sin\Phi+1)}$. Substituting for Φ from equation 1) and utilizing the small angle approximation yields,

$$8) \text{ # of required elements} \propto \left[\frac{\dfrac{f}{F}D\left[\dfrac{F}{f}\Theta+1\right]}{\lambda}\right]^2 \text{ for the phased array feed.}$$

Now we can determine the relative number of elements for a direct radiating aperture versus a phased array feed for a dual lens system. The ratio (number of elements required for the direct radiating aperture divided by the number of elements required for the phased array feed),

$$9) \quad ratio = \left[\frac{D(\Theta+1)}{\left(\frac{f}{F}\right)D\left[\left(\frac{F}{f}\right)\Theta+1\right]}\right]^2 = \left[\frac{\Theta+1}{\Theta+\left(\frac{f}{F}\right)}\right]^2$$

The following Table summarizes the element ratios for practical values of the scan angle Θ (radians) and the inverse of the lens magnification ratio, $\dfrac{f}{F}$:

Θ \ f/F	1	1/2	1/3
0	1	4	9
0.1	1	3.4	6.4
0.2	1	2.9	5.1

Table 1. Ratio of the Required Elements for a Direct Radiating Phased Array Aperture versus a Phased Array Fed, Dual-Lens Antenna System

As can be seen in Table 1 and equation 9, for zero scan ($\Theta = 0$) we achieve the familiar $(F/f)^2$ ratio of elements for the direct radiating phased array aperture versus the phased array fed dual lens. Consequently, for a f/F ratio of ½ the direct radiating aperture requires 4 times as many elements as the phased array feed.

As the scan angle increases the benefit of a phased array feed is reduced but the element savings is still significant: the direct radiating aperture requires 3.4 times as many elements for $\Theta = 0.1$ radians (5.7 degrees) and 2.9 times as many elements for $\Theta = 0.2$ radians. See results in Table 1 for a range of focal lengths (f/F) and scan angles (Θ).

The above results because the direct radiating aperture is restricted to a maximum element spacing of d = λ. Using the grating lobe criteria that eliminates grating lobes from the antenna coverage area (equation 6) imposes no such condition and consequently, the result is quite different, as we will see in the next section.

Number of Elements required; No Grating Lobes within the Antenna Coverage Area

For the second grating lobe condition, no grating lobes within the antenna coverage area (equation 6), we will again determine the ratio of the required number of elements: direct radiating aperture versus a phased array feed.

The number of radiating elements for the direct radiating aperture is again proportional to $\left[\dfrac{D}{d}\right]^2$ but

under the present grating lobe condition, $d \leq \dfrac{\lambda}{2\sin\theta}$. Now putting it into equation form, utilizing the limiting condition for **d**, and the small angle approximation for $\sin\theta$ yields,

$$\textbf{10)} \quad \textbf{\# of required elements} \propto \left[\frac{2D\theta}{\lambda}\right]^2 \text{ for the \textbf{direct radiating aperture.}}$$

Continuing the analysis for the phased array feed; the number of required elements is proportional to $\left[\dfrac{\Delta}{d}\right]^2$ where $\Delta = D\dfrac{f}{F}$ and $d = \dfrac{\lambda}{2\sin\Phi}$. Substituting for $\phi = \dfrac{F}{f}\theta$ from equation 10) and again using the small angle approximation, results in

$$\textbf{11)} \quad \textbf{\# of required elements} \propto \left[\frac{2D\theta}{\lambda}\right]^2 \text{ for the \textbf{phased array feed.}}$$

Now dividing equation 10) for the direct radiating aperture by equation 11) for the phased array feed yields,

$$\textbf{12) ratio} = \left[\frac{2D\theta\big/\lambda}{2D\theta\big/\lambda}\right]^2 = \textbf{1}$$

Therefore, from equation 12) we can see that if we are willing to allow grating lobes to enter "real space" but eliminate them from impinging on the defined coverage area of the antenna, there is no advantage in element count between a phased array feed and a direct-radiating aperture (planar array). This is due primarily to the fact that allowing grating lobes into "real space" allows the antenna designer to use element spacing (element size) of multiple wavelengths. For example, from equation 6) keeping the grating lobes out of a coverage area of 0.2 radians (11.4 degrees) half-cone angle, allows an element spacing of $\textbf{d} \cong \textbf{2.5}\lambda$. This super-element design (element diameter greater than λ) allows for an equivalent number of elements and supporting components (power amplifiers or LNA's and phase shifters) as one would achieve using a phased-array feed in a dual-lens antenna system.

Summary and Conclusions: In this paper we have derived the size of the phased-array feed necessary to support an array-fed, dual-lens antenna configuration (a dual reflector configuration should provide a similar result). We then determined the element ratio between a direct radiating, phased-array aperture (planar array) and the phased-array fed, dual-lens antenna configuration. It is shown that for the grating lobe condition which eliminates grating lobes from "real space" the element advantage of the phased array feed approaches the familiar ratio of f/F. Where F/f is the ratio of the focal lengths of the dual lenses and equals the aperture magnification of the dual-lens antenna system. This is as expected.

It is also shown that if the antenna designer allows grating lobes to enter "real space" but remain outside of the defined antenna coverage area (as might be the case for an antenna system illuminating the Earth's disk from geosynchronous orbit), then the phased-array fed, dual-lens system has no advantage (reduction) in element count over a direct-radiating aperture (planar array).

References:

[1] Chao C. Chen and Edward C. DuFort, "Optical Limited Scan Antenna System", United States Patent #3,835,469, September 10, 1974

[2] E. Brookner (ed), " Practical Phased Array Antenna Systems", Artech House, 1991

[3] Robert J. Mailloux, "Phased Array Antenna Handbook", Artech House, 1994

[4] Paul A. Chiavacci, "Planar Phased Array Relationships for FFT & Butler Matrix Generated Beamlets with Graphical Display of Results", IEEE International Symposium on Phased Array Systems and Technology, Boston, MA, 15-18 October, 1996

ON THE USE OF YAGI-UDA ELEMENTS IN ARRAY ANTENNAS FOR LIMITED SCAN APPLICATIONS

Sergei P. Skobelev and Alexander V. Shishlov

JSC "RADIOPHYZIKA", 10, Geroev Panfilovtsev str., Moscow 123363, RUSSIA
Ph.: +7 095 494 9565, Fx.: +7 095 496 8790, E-mail: apex@glas.apc.org

1. INTRODUCTION

Some applications require development of array antennas providing high-gain electronic beam scanning in a wide-angle sector in one plane and in a limited (small) sector in another plane. In principle, such arrays with the correspondingly minimized number of controlled elements in the limited-scan plane can be designed by using the constrained circuits of overlapped subarrays with flat-topped radiation patterns [1], [2]. Another approach, though less universal but resulting in simpler feed systems, is the use of longitudinally radiated antenna elements like dielectric rods, [3], allowing forming the required overlapped subarrays at the expense of natural interaction between the elements over free space. More convenient longitudinal elements for the indicated arrays designed for operation at linear polarization in the L-to-K_u frequency ranges could be director Yagi-Uda antenna elements. Performance of such elements in an infinite array for wide-angle scanning in both planes is studied in [4]. Some experimental data concerning a linear array are used in [5] as a material for comparison, but they are obviously insufficient for making reliable conclusions on capabilities of shaping the flat-topped patterns by the director array elements. Any other studies on the use of the director elements in the limited-scan arrays are unknown for the authors, and performing such studies is of interest.

The arrays of director elements can be realized in different modifications, and this gives a wide field for research. To begin with, we consider below a simplified model in the form of an infinite planar periodic array of thin-wire director elements arranged above an infinite perfectly conducting screen.

2. FORMULATION AND SOLUTION OF THE PROBLEM

Geometry of the array under consideration is shown in Fig. 1 together with a rectangular coordinate system $Oxyz$. The director elements are arranged in a rectangular lattice with spacing d_x and d_y along the x-axis and y-axis, respectively. The array element consists of M perfectly conducting wires arranged symmetrically in a plane parallel to the Oyz-plane. Each wire is parallel to the screen, and characterized by diameter $2a$, length $2d_m$, and height above the screen h_m, where $m = 1, 2, ..., M$. The first wire is treated as a driven dipole, and the rest ones are passive directors. The dipoles are assumed to be fed in the infinitely narrow gaps in their centers via transmitting lines with wave resistance W_f. The amplitude and phase distributions of the excitation over the array elements are assumed to be uniform and linearly progressing, respectively.

To calculate the array characteristics, we assume that the wire diameter $2a$ is much less than the operating wavelength λ, element spacing, and distance between any two wires. This allows us to replace the surface currents on the wires by y-directed currents $I_m(y)$, $m = 1, 2, ..., M$, on the wire axes. The boundary condition on the wire surfaces and subsequent standard procedure aimed at determining the indicated currents give the following system of integral equations

$$\sum_{\mu=1}^{M} \int_{-d_\mu}^{d_\mu} G_{m\mu}(y,y')I_\mu(y')dy' + C_m \cos ky + D_m \sin ky = -\frac{iV\delta_{1m}}{2W_0}\sin k|y|, \quad (1)$$

where $|y| \leq d_m$, $m = 1, 2, \ldots, M$, C_m and D_m are unknown constants, V is the voltage in the gap of the central dipole, δ_{1m} is the Kronecker symbol, $k = 2\pi/\lambda$, $W_0 = 120\pi\ \Omega$, and

$$G_{m\mu}(y,y') = \delta_{m\mu} \frac{1}{4\pi} \sum_{p=-\infty}^{\infty} \sum_{q=-\infty}^{\infty} \frac{e^{-k''R_{pq}}\cos k'R_{pq}}{R_{pq}} e^{-ipu-iqv} +$$

$$\frac{1}{2d_x d_y} \sum_{p=-\infty}^{\infty} \sum_{q=-\infty}^{\infty} \left[\frac{e^{-\Gamma_{pq}|h_m-h_\mu|} - e^{-\Gamma_{pq}(h_m+h_\mu)}}{\Gamma_{pq}} - \delta_{m\mu} \mathrm{Re}\left\{ \frac{e^{-\Gamma'_{pq}|h_m-h_\mu|}}{\Gamma'_{pq}} \right\} \right] e^{-i\beta_q(y-y')} \qquad (2)$$

with $R_{pq} = [(pd_x)^2 + (y - y' - qd_y)^2 + (h_m - h_\mu)^2 + a^2\delta_{0p}\delta_{m\mu}]^{1/2}$, $\Gamma_{pq} = [\alpha_p^2 + \beta_q^2 - k^2]^{1/2}$, $\alpha_p = (u + 2\pi p)/d_x$, $\beta_q = (v + 2\pi q)/d_y$, $\Gamma'_{pq} = [\alpha_p^2 + \beta_q^2 - k^2 + 2ik'k'']^{1/2}$, $u = kd_x \sin\theta\cos\varphi$, $v = kd_y \sin\theta\sin\varphi$. The angles θ and φ specify the main lobe direction.

The kernel (2) has been obtained from the free space periodic Green's function with accelerating the convergence of the latter when $m = \mu$ by generalizing the approach proposed in [6]. As a result for the indicated cases, the first series in (2) converges exponentially, and the second one converges as $1.5(k'k'')^2\Gamma_{pq}^{-5}$. An optimum proportion between k' and k'' satisfying the condition $k'^2 - k''^2 = k^2$ is determined by a concrete scheme of calculations. Note that the present approach is more efficient than that in [7] providing the convergence as Γ_{pq}^{-3}, and much simpler than the algorithms based on the Ewald transformation [8].

Determining the voltage V in the gap from formula $V = 2V^i - W_f I_1(0)$, [9], where V^i is the voltage of the incident wave in the transmitting line, breaking the wires into intervals by collocation points at $y_{mn} = (n - 1 - N_m)d_m / N_m$, $n = 1, 2, \ldots, 2N_m+1$, using the piece-wise linear approximation for the currents on the intervals, and satisfying (1) in the indicated points, we reduce (1) to the algebraic system

$$C_m \cos k y_{mn} + \sum_{\mu=1}^{M} \sum_{\nu=2}^{2N_\mu} G_{m\mu,n\nu} I_{\mu\nu} + D_m \sin k y_{mn} = -\frac{iV^i\delta_{1m}}{W_0} \sin k|y_{mn}|, \qquad (3)$$

where $m = 1, 2, \ldots, M$, $n = 1, 2, \ldots, 2N_m+1$, $I_{\mu\nu}$ are currents at the collocation points,

$$G_{m\mu,n\nu} = -\frac{iW_f\delta_{1m}\delta_{\nu,N_1+1}}{2W_0} \sin k|y_{mn}| + \int_{y_{\mu,\nu-1}}^{y_{\mu,\nu+1}} (1 - |y' - y_{\mu\nu}|/\Delta_\mu) G_{m\mu}(y_{mn}, y')dy',$$

$\Delta_\mu = d_\mu / N_\mu$, and it is taken into account that the currents at the wire ends are equal to zero, so that the number of unknowns is exactly equal to the number of equations.

After solving the system (3), the array reflection coefficient is determined as $R(u,v) = 1 - W_f I_{1,N_1+1}(u,v)/V^i$, and the components of the array element pattern corresponding to the unit incident power are calculated by formulas

$$F_\theta(\theta,\varphi) = F_y(\theta,\varphi)\cos\theta\sin\varphi, \quad F_\varphi(\theta,\varphi) = F_y(\theta,\varphi)\cos\varphi, \qquad (4)$$

where

$$F_y(\theta,\varphi) = \frac{1}{k}\sqrt{\frac{W_f W_0}{d_x d_y}} \sum_{m=1}^{M} \left[\frac{\sin(0.5\Delta_m v/d_y)}{0.5\Delta_m v/d_y}\right]^2 \sin(kh_m \cos\theta) \sum_{n=2}^{2N_m} I_{mn}(u,v)e^{iy_{mn}v/d_y}.$$

3. RESULTS OF CALCULATION

The algorithm described above has been realized in a *FORTRAN* code tested by comparing the results for the array parameters available in [4]. After testing there have been performed a number of calculations with optimization of the array element parameters for shaping the flat-topped patterns. The study has shown that the director elements are capable both to provide high wide-angle scanning performance in the E-plane and to shape the flat-topped pattern of high quality for spacing up to $d_y=\lambda$. The results to be discussed below have been obtained for the cases when the directors have identical lengths, and the wires in the element are arranged at an identical distance $\Delta h=h_{m+1}-h_m$ from each other. In these cases the parameters under optimization have been the number of directors $M-1$, the director length, and the distance between the wires. Some results of such optimization are presented in Figs. 2 through 5. The same for all these results are the following values $2d_1=0.48\lambda$, $h_1=0.25\lambda$, $2a=0.014\lambda$, $2d_m=0.35\lambda$ for $2 \le m \le M$, $d_x=0.6\lambda$, at a reference frequency f_0, and $W_f=75\ \Omega$.

Figs. 2 and 3 contain the element patterns in the E- and H-planes, respectively, of an array with $d_y=0.8\lambda$ and four directors arranged in the element with $\Delta h=0.12\lambda$. The similar E- and H-plane patterns for an array with $d_y=\lambda$ and six directors in the element where $\Delta h=0.14\lambda$ are shown in Figs. 4 and 5, respectively. The solid curves with crosses presented for comparison correspond to the elements having no directors. The comparison shows that the quality of the obtained flat-topped patterns is rather high, and the VSWR calculated from the reflection coefficient is less than 1.2 in the area corresponding to the flat tops of the patterns. However we have failed to obtain such quality for the spacing greater than wavelength. As for the H-plane (Figs. 3 and 5), we observe that, like in [4], the patterns have narrow notches at the angles slightly smaller than those corresponding to arising the grating lobes. We can also observe that the greater notches correspond to the longer (in the z-direction) director elements. As shown in [4], the indicated effects are not observed in the arrays with triangle lattices. However the study of such arrays for limited-scan application is beyond the present paper.

The results in Figs. 2 and 4 show that the flat-topped pattern shape is kept well within a 10% frequency band, and the changes of the pattern width correspond to the natural changes of the element spacing. The bandwidth can be even wider if the element spacing in the E-plane does not exceed the wavelength.

Thus, the obtained results have shown good capabilities of the director elements to use them in the array antennas for limited-scan application, and allow us to draw a conclusion on promises of the further studies in this area.
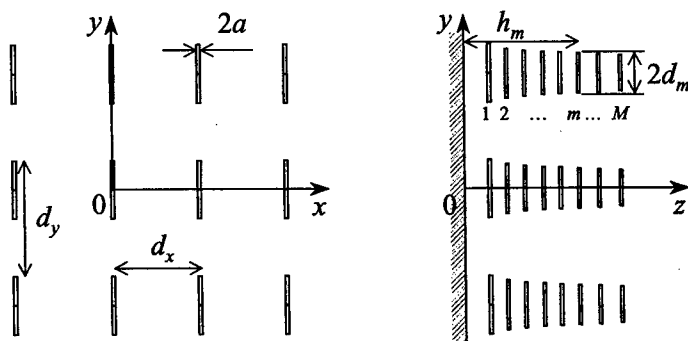
Fig. 1. Geometry of a planar array of Yagi-Uda elements.
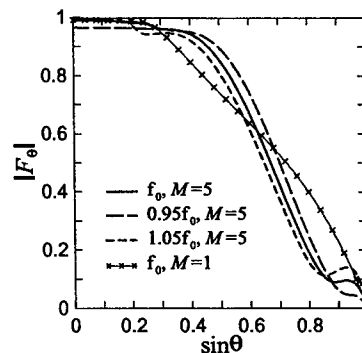
Fig. 2. E-plane patterns of array with $d_y=0.8\lambda$, $\Delta h=0.12\lambda$.
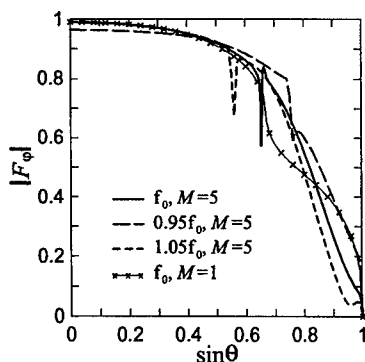
Fig. 3. H-plane patterns of array with d_y=0.8λ, Δh=0.12λ.
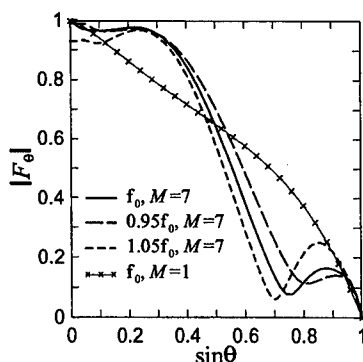
Fig. 4. E-plane patterns of array with d_y=λ, Δh=0.14λ.
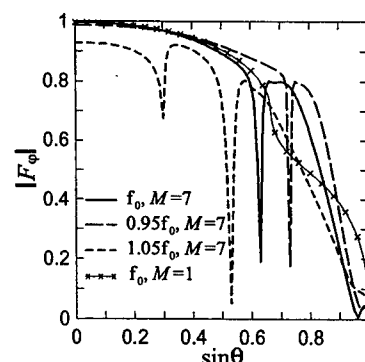
Fig. 5. H-plane patterns of array with d_y=λ, Δh=0.14λ.

REFERENCES

[1] R. J. Mailloux, *Phased Array Antenna Handbook*. Boston: Artech House, 1993.

[2] S. P. Skobelev, "Methods of constructing optimum phased-array antennas for limited field of view," *IEEE Antennas and Propagat. Magazine*, vol. 40, April 1998, pp. 39-50.

[3] A. A. Tolkachev, V. V. Denisenko, A. V. Shishlov, and A. G. Shubov, "High Gain Antenna Systems for Millimeter Wave Radars with Combined Electronical and Mechanical Beam Steering," *1996 IEEE Int. Symposium on Phased Array Systems and Technology*, Boston, MA, 15–18 Oct. 1996, pp. 266-271.

[4] M. V. Indenbom and V. S. Filippov, "Analysis and optimization of director radiators in plane array," *Izvestiya Vuzov – Radioelectronika*, vol. XXII, no. 2, pp. 34-41, 1979 (Rus.).

[5] E. V. Baklanov, V. A. Bokhan, Yu. A. Vainer, and L. M. Novikova, "Radiation pattern of a longitudinal element in an infinite periodic array," *Radiotekhnika & Electronika*, vol. 17, no. 1, pp. 30-36, 1972 (Rus.).

[6] M. M. Ivanishin, "Use of integral equations in the problem on a cylinder inside a rectangular waveguide," *Radio Engin. & Electr. Phys.*, vol. 29, no. 12, pp.1-8, 1984.

[7] S. Singh, W. F. Richards, J. R. Zinecker, and D. R. Wilton, "Accelerating the convergence of series representing the free space periodic Green's function," *IEEE Trans. Antennas Propagat.*, vol. 38, pp. 1958-1962, Dec. 1990.

[8] P. P. Ewald, "Die Berechnung optisher und electrostatischer Gitterpotentiale," *Annalen Der Physik*, vol. 64, pp. 253-287, 1921.

[9] V. V. Bodrov and G. T. Markov, "Excitation of periodic antenna arrays," In *Collected Volume of Papers on Applied Electrodynamics*, no. 1, pp. 129-162, 1977 (Rus.).

Design of the Cross-Dipole Antenna with Near-Hemispherical Coverage in Finite-Element Phased Array by Using Genetic Algorithms

Cheng-Nan Hu, Ching-Song Chuang, Der-Chorng Chou, Koong-Jeng Liu and Chia-I Hung

Antenna Section. Depatment of Electronics,Chung Shan Int. of Sci. and Tech.
P.O. Box 90008-16-24. Lung-Tan, Taiwan, R. O. C: Fax: +886-3-4717897

Abstract

A cross-dipole antenna surrounded by four pins is used as a radiating element for a finite-element phased array. To achieve near-hemispherical radiation coverage and high gain under the consideration of mutual coupling effects, a method of using genetic algorithms to optimize the design parameters of a cross-dipole antenna is presented. A method of moment's code, performs the task of evaluating each of antenna designs generated by the genetic algorithm (GA) during the optimization process. To illustrate capabilities of this approach, the numerical results are compare to the measured ones, showing excellent agreement in the comparison.

I. Introduction

Genetic algorithms (GA's) are a class of search techniques that use the mechanics of natural selection and genetics to conduct a global search of a solution space. The goal of the search is to find a good solution to the given problem. Other optimization techniques (such as gradient decent method) search a region of the solution space around an initial guess for the best local solution. However, a local search is limited to finding the best of these poor solutions provided that the initial guess falls in a region of the solution space. This is particular true as design parameters are large, resulting in difficulty for searching the entire solution space by using gradient decent methods.

In the designing and synthesis of the finite element phased array, one of the most important goals is to find the optimal radiating element that meets a set of performance criteria that usually include gain, beamwidth, input impedance, and physical size. Generally, there are a large number of design variables that affect the antenna performance because of the mutual coupling effects inhering in the phased array. Thereby, it is often difficult to provide good initial guesses for the design. For such a complex problem, the GA approach become attractive to conduct a global search for a solution that satisfies some specified performance criteria.

Adapting this point of view, there has been a recent interest in applying GA's to the problem in the field. Haupt [1] used GA's to thin dense arrays of active elements for minimizing sidelobe levels, and Marcano *et al.* [2] determining phase and amplitude setting for array beamforming with GA's. In wire antenna design, Boag *et al.* [3] designed electrically loaded wire antenna with GA's and Jones's *et al.* [4] have used GA's to design the optimal Yagi-

Uda antennas.

The aim of this paper focuses on using of genetic algorithms to optimize the design of a circular-polarized cross-dipole antenna with near-hemispherical coverage for the application of finite-element phased array. The dipole with arms sloped down at 45° and surrounded by four pins is proposed to enhance the radiation coverage and to maximize the gain as well. During the optimization process, a developed method of moment code [5] performs the task of evaluating each of designed parameters, including the length of dipole and pin's length and location, generated by the GA. The results are compare to the measured data, showing excellent agreement in the comparison.

II. Genetic Algorithms for Antenna Design

Figure 1 shows a cross-sectional and top view of the cross-dipole antenna with arms sloped down at 45° and two pins surrounded. The goal of this design in determining the design parameters (such as the length of dipole (l_d), and the length (l_p) and location (x_d) of pins) such that antenna gain can be maximized and near-hemispherical radiation coverage can be achieved. To consider the effect of mutual coupling on the antenna performance, we use five elements arranged in triangular lattice with central driven element, as shown in Fig. 2, in this case of study since the coupling fields among the radiating elements other that the adjacent ones is negligible.

The objective function rewards an antenna design x for having a high gain G of g_{max} and penalizes the design if the radiation far-field pattern F is not equal to a constant C over the hemispherical coverage. Thus, the object function can be expressed numerically as

$$O(x) = a|G(x) - g_{max}|^2 + b|F(x) - C|^2 \qquad (1),$$

such that the performance can be optimized in the sense of least square error. The constant a and b are weights that control the contribution from each term to the overall objective function.

Figure 3 shows a flow diagram of the GA used in this paper. Most of steps shown are common to any genetic algorithm regardless of the problem being solved. Before applying the GA's algorithms, one should represents the antenna as a chromosome, which are abstract representations of the solution to the problem. Then three basic genetic operators: reproduction, crossover, and mutation are processing. Reproduction, the simplest of the operators, directly copies an individual from the old generation into the new generation. In crossover, information between two chromosomes is exchanged by cutting the chromosomes at a random chosen location and swapping the ends of the chromosomes to create two new chromosomes. In order to maintain a more diverse population, the mutation operator is introduced. If a particular bit in a chromosome is chosen for mutation, the value of the bit is simply changed from zero to one or from one to zero.

III. Results

In this optimization, we set the constant a = 1, b = 10, g_{max} = 5dB, and C = 1.8 so that the near-hemispherical coverage receives more emphasis than gain of the antenna. There are four adjustable element length and two-location spacing resulting in total six adjustable parameters. Each parameter is discretized using eight bits to form a total chromosome length of 48 bits. To thoroughly cover the search space, the population size of 100 is chosen. It required about 10 min on Pentium II-233 personal computer. The simulated result is tabulated in Table I. According to the simulated results listed in table I, a five-element, proof-of-concept design is built for experimental validation. Fig.4 plots a comparison of the radiation coverage between the theoretical pattern with 4 pins and that without 4 pins, showing greatly enhancement in coverage by using 4 surrounded pins. Furthermore, the simulated patterns at two orthogonal plane cuts are plotted in Fig.5 to compare with measured ones, showing well agreement at the radiation coverage of interest.

IV. Conclusion

A circular polarized cross-dipole antenna with near-hemispherical coverage is presented for a finite-element phased array antenna. A method of GA is employing in the performance optimization, showing that the design performance not only satisfies the system requirement but also well agrees with the measured result.

Reference

[1] R. L. Haupt, "Comparison between genetic and gradient-based optimization algorithms for electromagnetics problem," *IEEE Trans. Mag.*, vol. 31, pp. 1932-1935, July 1994.

[2] D. Marcano, F. Duran, and D. Chang, "Synthesis of multiple beam linear antenna arrays using genetic algorithms, in *IEEE AP-S, Int. Symp. Proc.*, Newport Beach, CA, Hune 1995, vol. 2, pp. 938-941.

[3] A. Boag, E. Michielessen, and R. Mittra, "Design of electrically loaded wire antennas using genetic algorithms," *IEEE Trans*. AP-44, pp. 687-695, May 1996.

[4] E. A. Jones and W. T. Joines, "Design of Yagi-Uda antennas using genetic algorithms," *IEEE Trans*. AP-45, pp. 1386-1392, Sep. 1997.

[5] C. -N. Hu, *et. al.*, "Analysis and design of circular polarization antenna by using cross-dipole," *Proceeding of 1996 Asia-Pacific Electronic Defence Symposium & Exhibition, Taipei*, pp.4-22~4-26

Table I. Design Parameters and Performance Comparison

	$L_{P1}(\lambda_0)$	$L_{P2}(\lambda_0)$	$X_{P1}(\lambda_0)$	$X_{P2}(\lambda_0)$	$L_{D1}(\lambda_0)$	$L_{D2}(\lambda_0)$	GAIN(d B)
Simulation	0. 191	0. 193	0. 308	0.305	0. 386	0. 388	4.81
Experiment	0. 19	0. 19	0. 31	0. 31	0. 39	0. 39	4.65
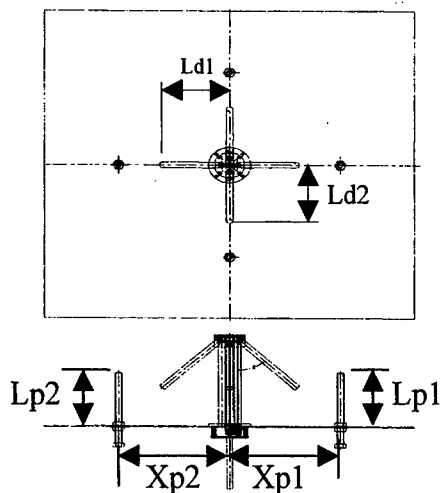
Fig. 1 The schematic layout of the antenna
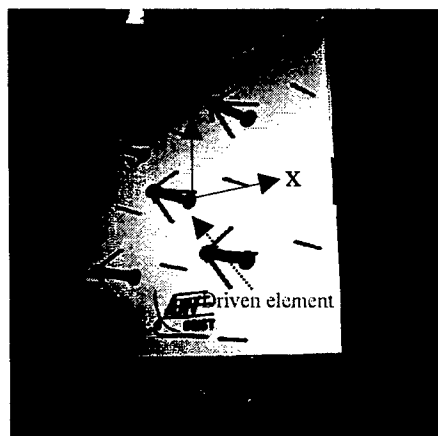
Fig. 2 The photo of measured 5-element array
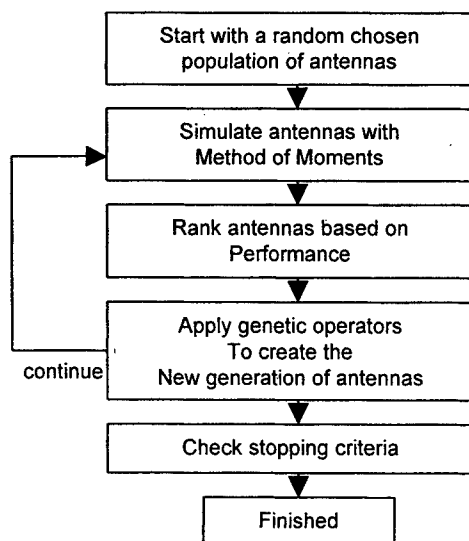
Fig. 3 Flow diagram for the genetic algorithm [4]
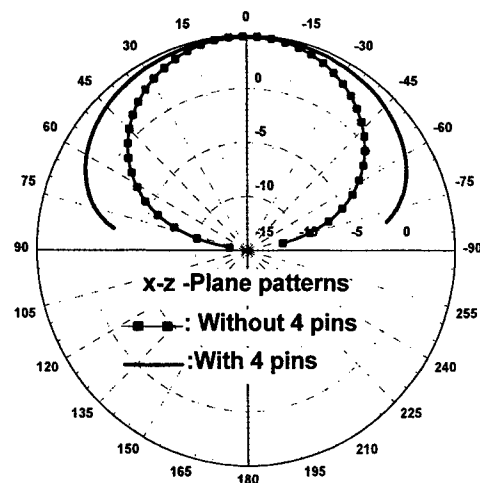
Fig.4 A comparison of radiation coverage between antenna with and without 4 pins
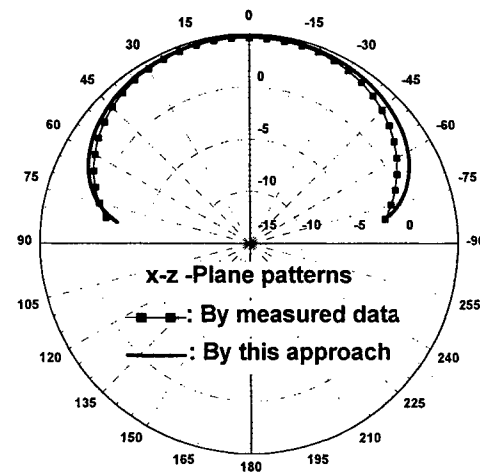
(a) x-z plane cut patterns
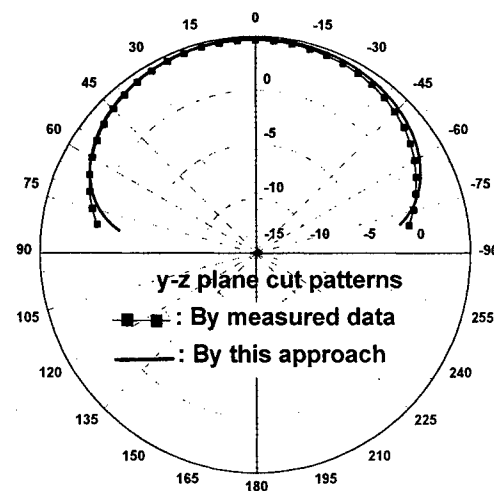
(b) y-z plane cut patterns

Fig.5. A comparison between measured and theoretical patterns at two orthogonal plane cuts.

Analysis of Multilayer Array Structures with Different Cell Size and Axes Orientations

Arun K Bhattacharyya
Hughes Space and Communications Company
S12/V348, Box 92919
Los Angeles, CA 90009.

INTRODUCTION:

Multilayer patch array structures are useful for bandwidth enhancement purposes or for dual band applications [1]. Floquet modal expansion followed by Generalized Scattering Matrix (GSM) formulation are commonly used to analyze such structures [2,3]. This analysis assumes equal cell size for all the layers. For many useful structures, however, the layers may not have identical cell sizes. A typical example of this kind is a patch array antenna loaded with a frequency selective surface (FSS). Generally, the cell size of the radiating patch layer is different from that of the FSS. A more complex multilayer array structure is a patch array loaded with a polarizing screen. The patch layer and the polarizer layer have different cell sizes and the cell orientations are non-parallel. To analyze such useful but complex structures, no systematic procedure is available in the open literature.

We present a general analysis of multilayer structures. The analysis accommodates different cell sizes of the layers, including angular rotations. We first find the global unit cell dimensions, which is equal to the lowest common multiple of the cell dimensions of the layers. We then find the GSMs of the individual layers with respect to the global unit cell. Construction of the global GSM for each layer is necessary in order to apply the GSM cascading rule [2] for analyzing a multilayer structure. It is found that a set of local GSMs (GSMs with local unit cell and local coordinate system of an individual layer) can be used to construct the global GSM for that layer. The mode numbers (Floquet mode indices), however, will be different for the two different cells. Therefore, if one could find a mapping relation between the mode number associated with a local cell and a global cell, then one can construct the global GSM for the layer using the local GSM elements. We have established such mapping relations for different cases. To find a local GSM of an individual layer, we use Floquet modal analysis and Galerkin's method of moment [3]. Once we find the global GSMs for all the individual layers, we can find the overall GSM of the structure. The following three examples illustrate the analysis method and verify the accuracy.

Example 1: Patch-fed patch subarray: Figure 1 shows the geometry of a unit cell of the structure. The array consists of two patch layers on a dielectric coated ground plane. Probes excite the lower layer patches. Each lower layer patch electromagnetically couples four upper layer patches. The driven patch in the lower layer and the four coupled patches in the upper layer make a subarray of an infinite array system. The lower layer patches have the periodicity [a,b], while the upper layer patches have the periodicity [a/2,b/2]. In a unit cell, the driven patch is symmetrically located below four upper layer patches. Analysis of an isolated subarray is reported in [4]. However, our analysis is applicable for infinite array of such subarrays.

In Fig. 1 we have plotted the input impedance of a unit cell. The geometry of a unit cell is shown within the figure. For comparison we have also plotted the impedance data of an isolated subarray [4]. High Q resonances are found to occur for the infinite array case. The high Q resonances near 4.4 GHz and 5 GHz are due to the parallel plate modes that couple with higher order Floquet modes. The uncharacteristic behavior of the array impedance near 4.16 GHz is due
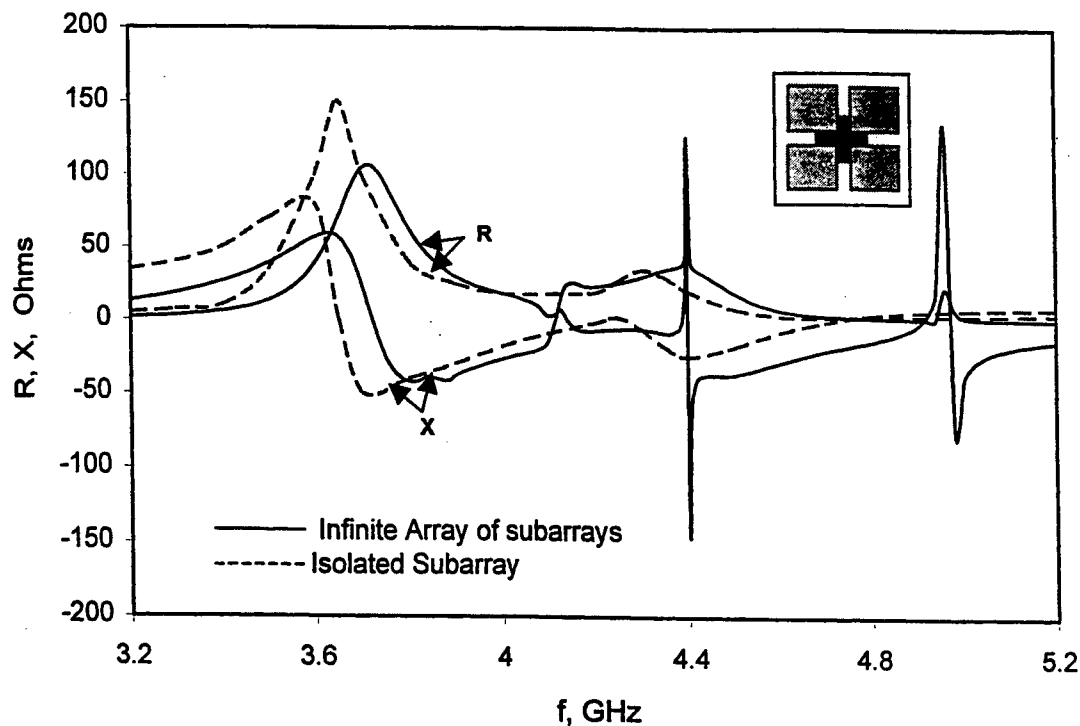
Fig. 1: *Input impedance versus frequency of a two-layered patch-fed-patch subarray. Subarray dim. = 7.2 x 6.4 sq-cm, lower layer patch dim.=2.13 x 2 sq-cm, upper layer patch dim. = 2 x 1.6 sq-cm. Fig.1:Subs. thk. =0.16cm, eps=2.55, probe at 0.8 cm from center.*

to the appearance of the first grating lobe. If the high Q resonance points are ignored (which are pertinent to an infinite array), the general shapes (including the number of peaks) of the impedance curves are very similar to each other.

Example 2: Array of Subarrays: For a limited scan requirement, the subarray concept is useful because it allows a lesser number of phase shifters than normal. The usual way of analysis is to consider the entire subarray as a unit cell of the array and then solve the patch currents using the method of moments [5]. This method requires excessive analytical and computational efforts because all patch currents in a subarray are solved simultaneously with a large number of unknowns. In the present approach, we use the general procedure outlined before with necessary modifications for [Z] matrix representation of a subarray. In order to validate the above subarray analysis, we compute the impedance matrix of three subarrays with elements 1 x 1, 2 x 1 and 3 x 1, respectively. From the impedance matrix, we derive the reflection coefficient seen by an equal split power divider. Figure 2 shows the reflection coefficient data. Also plotted are the results published in [5]. For our numerical results, we assume the probes to be located near a radiating edge of the patch elements. Excellent agreements between the two sets of results are found. For 3 x 1 element-subarray, discrepancies are found near θ = 20 degree and θ = 75 degree scan angles. These two angles correspond to the array blind spots. The magnitude of the reflection coefficient near the blind spot is very sensitive to the feed location. Since the feed location is not mentioned in [5], we assume the feed locations near the edge of the patch elements, which may be different from that in [5].
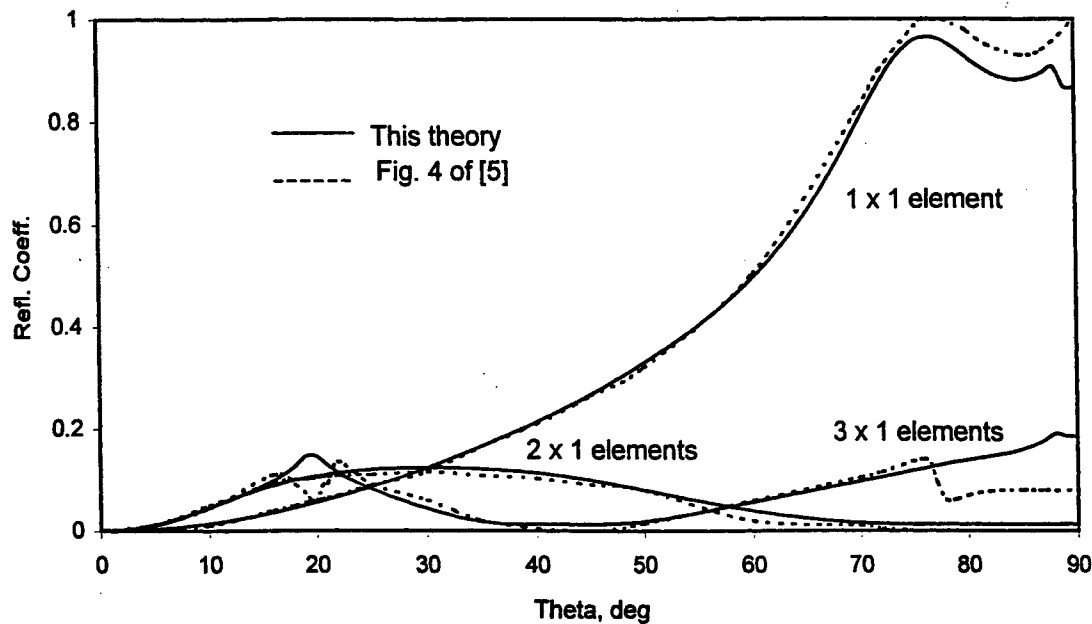
Fig.2: *Reflection coefficient versus E-plane scan angle of an infinite array of subarrays. Element spacing within a subarray = 0.5 x 0.5 sq-wl. Element size = 0.28 x 0.3 sq-wl, eps = 2.55.*

Example 3: Slot-fed Patch Array Loaded with Screen Polarizer: An exploded view of the structure is shown in Fig 3(a). The patch array is designed to radiate linearly polarized wave. The screen polarizer converts the fields from linear polarization to circular polarization. The analysis of such an integrated structure (patch & polarizer) has not been reported. It is found that the scan performance of an isolated screen polarizer differs considerably from that when coupled to a patch array. The periodicity of the patch elements is 0.99 cm in both directions. For the screen polarizer, the spacing between two grid-lines is 0.35 cm and the grids are oriented at an angle 135 degree with the E-plane of the patch array. Figure 3(b) shows the input impedance of an element with and without screen polarizers. Two different polarizers (meander line and strip line polarizers) are considered in this study. The impedances are computed for bore-sight beams. Expectedly, the polarizers reduce the impedance bandwidth of the array. The strip line polarizer introduces high Q resonances, which are due to coupling between strip line modes and higher order Floquet modes. For meander line polarizer no such resonance occurs for the bore-sight beam. Figure 3(c) shows the axial ratio versus frequency for three different screen locations. By adjusting the spacing between patch surface and the screen polarizer, the array structure can be tuned to some extent, to improve the axial ratio of the radiated fields. For the strip line polarizer, the axial ratio degrades significantly at the resonance locations. More results will be shown during the presentation, which are omitted here due to space limitations.

REFERENCES
[1] Y. Lubin and A. Hessel, "Wide-band, wide-angle microstrip stacked-patch-element phased arrays", IEEE Trans., Antennas Propagat., AP-39, pp. 1062-1070, Aug. 1991.

[2] R. Mitra, C.H. Chan and T. Cwik, "Techniques for analyzing frequency selective surfaces- a review", Proc. IEEE, Vol. 76, No. 12, pp. 1593-1615, Dec. 1988.

[3] A.K. Bhattacharyya, "A numerical model for multilayered microstrip phased array antennas" IEEE Trans., Antennas Propagat., Vol. AP-44, pp. 1386-1393, Oct. 1996.

[4] H. Legay and L. Shafai, "New stacked microstrip antenna with large bandwidth and high gain", Proc. IEE, MAP, Vol. 141, No. 3, pp. 199-204, June 1994.

[5] D.M. Pozar, "Scanning characteristics of infinite array of printed antenna subarrays", IEEE Trans., Antennas Propagat., Vol. AP-40, pp. 666-674, June 1992.
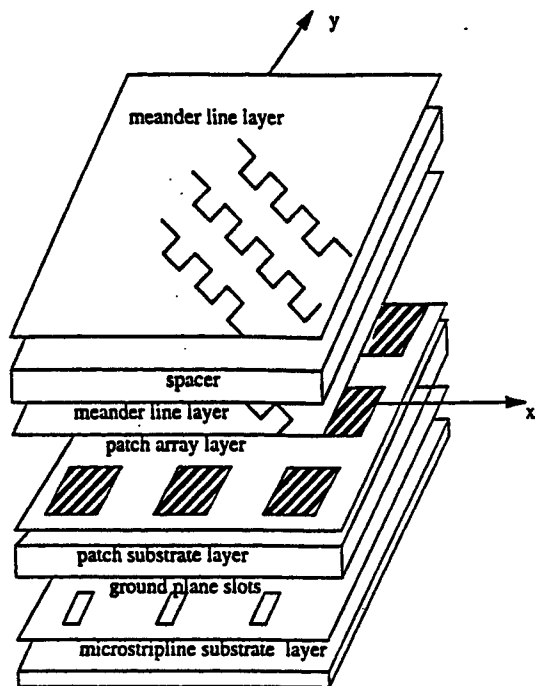
(a)
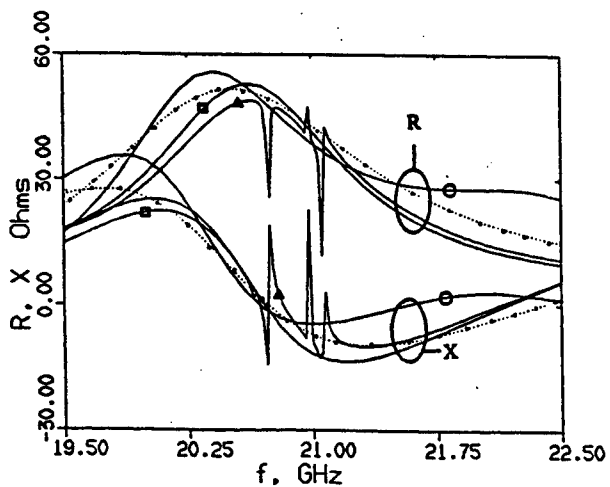
(b)
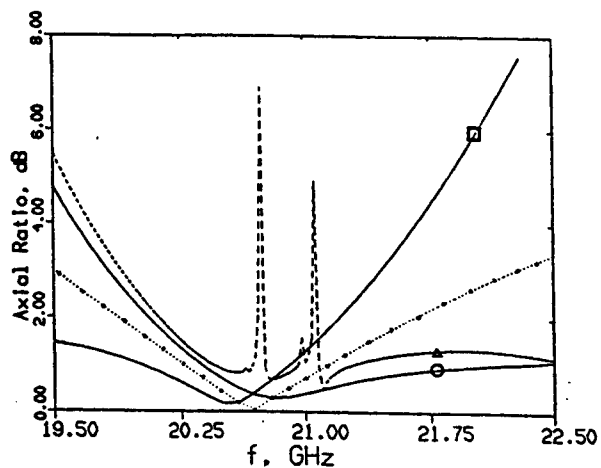
(c)

Fig. 3: *(a) Exploded view of a slot-fed patch array loaded with meander line screen polarizer. (b) Input impedance versus frequency,* •••• *patch array without polarizer, -△- with strip line pol.(d=0.5 cm), -□- with meander line pol. (d = 0.5 cm), -O- with meander line pol. (d=0.7 cm), d = distance between patch surface and polarizer bottom surface. (c) Axial ratio versus frequency.*

SUPPRESSION OF SUB-ARRAY QUANTIZATION LOBES

R. C. Hansen
Consulting Engineer
Tarzana, CA 91357
818-345-0770

A new method for decollimating the quantization lobes (QL) of a scanned array of sub-arrays applied pseudorandomization to the sub-array phases [1]. This breaks the QL up into several lobes, of roughly equal, and lower, amplitude, providing the number of elements is large and the random numbers are good. Most random number tables (and generators) of 100 numbers are only partially random; the random number table should spread out the QL energy, with no excessive peaks. New test cases utilize a linear array of 100 or 102 isotropic radiators, with sub-arrays of 2 or 3 elements, and half-wave element spacing. A random number table (from 0 to 1) is used to adjust the phase applied to each sub-array. Fig. 1 shows a conventional array of 2 element sub-arrays, with 5 bit phase excitations, for a 30 deg. scan. Note the low non-monotonic sidelobes caused by the 5 bit phase quantization. As expected the main beam (MB) and QL are equal, each about 3 dB down [2]. Instead of adding a pseudorandom phase to that of each sub-array, the 5 bit phase is calculated at a virtual phase center for each sub-array. In Fig. 2 each sub-array phase center is selected at the element whose position most closely matches the random number. While the amplitude and position of the main beam is unchanged, the QL is suppressed to -14 dB, or 11 dB below the MB. The random number table used was not optimum, but was the best of a dozen tries. For a scan of 45 deg., the MB is down 7 db and the QL is down only 1 dB, as seen in Fig. 3. This of course, is because the first QL moves closer to broadside as the MB scans away. Fig. 4 shows the decollimated pattern: the MB is unchanged, while the QL is down 12 dB, or 6 dB below the main beam. The same random number table is used.

For 3 element sub-arrays the results are less useful, primarily due to the narrower sub-array pattern. Fig. 5 is for a 102 element array at 30 deg. scan: the MB is down 9 dB, and there are two QL. The decollimated pattern of Fig. 6 shows the MB unchanged, but the first QL is down 12 dB, or roughly 4 dB below the main beam. In both patterns the sub-array pattern null at ±42 deg. can be observed. Thus for a 45 deg. scan the results are poor.

Four element sub-arrays, with a sub-array null at 30 deg. are severely scan limited, although the QL are nicely suppressed.

Pseudorandomization appears useful for two element sub-arrays, with modest scan ranges. These sub-arrays can provide a QL 12 dB below the main beam at 30 deg. scan, and 6 dB below the main beam at 45 deg. scan. This may allow some systems to utilize this new method. A planar array would require only 1/4 the number of TR modules compared to a conventional array with one module per element.

REFERENCES

[1]   R. C. Hansen and G. G. Charlton, "Subarray Quantization Lobe Decollimation," *Trans. IEEE*, Vol. AP-47, Aug. 1999, pp. 1237-1238

[2]   R. C. Hansen, *Phased Array Antennas*, Wiley, 1998
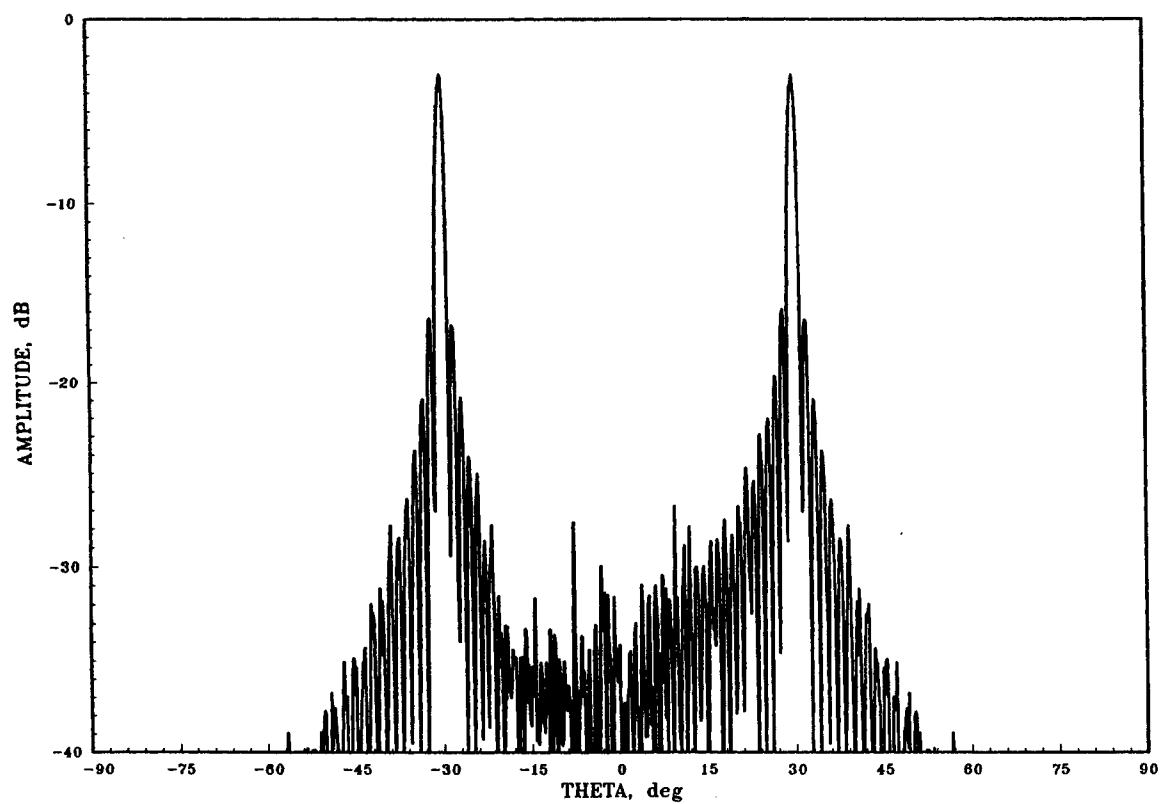
LINEAR ARRAY, 100 ELEMENTS, 50 SUBARRAYS, THETA=30 deg

Fig. 1
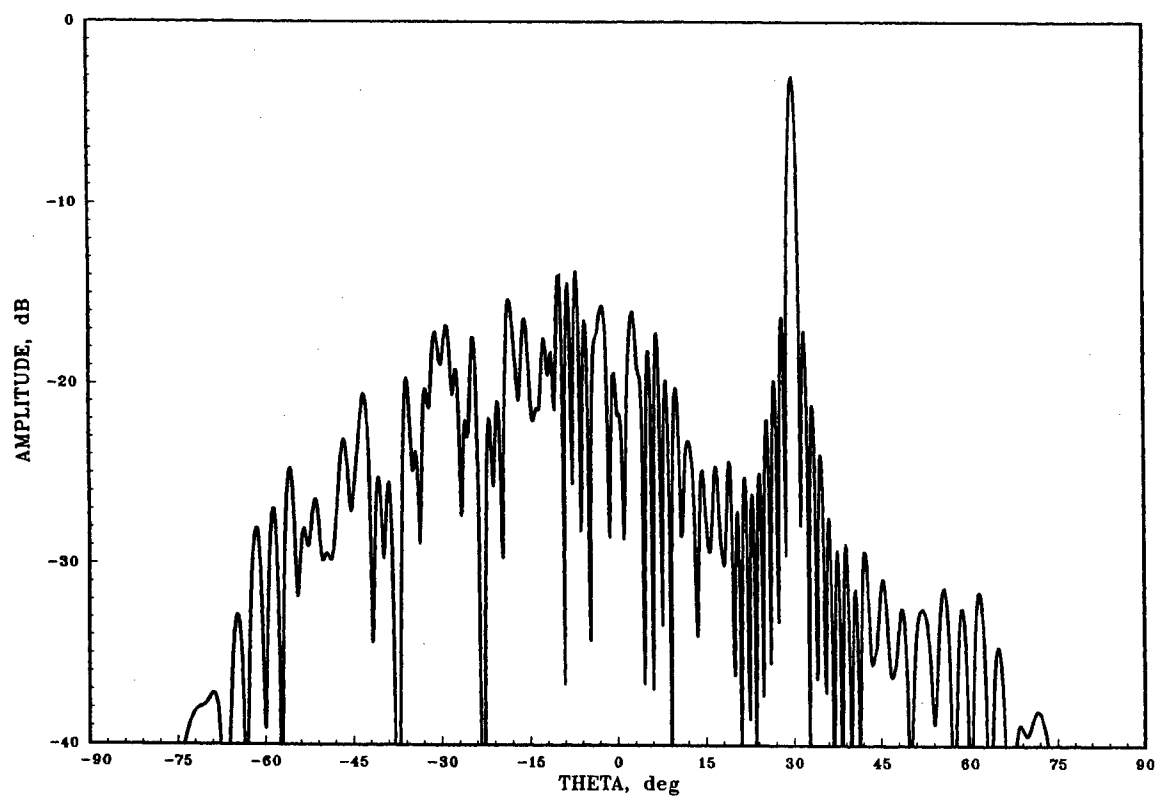
LINEAR ARRAY, 100 ELEMENTS, 50 SUBARRAYS, THETA=30 deg

Fig. 2
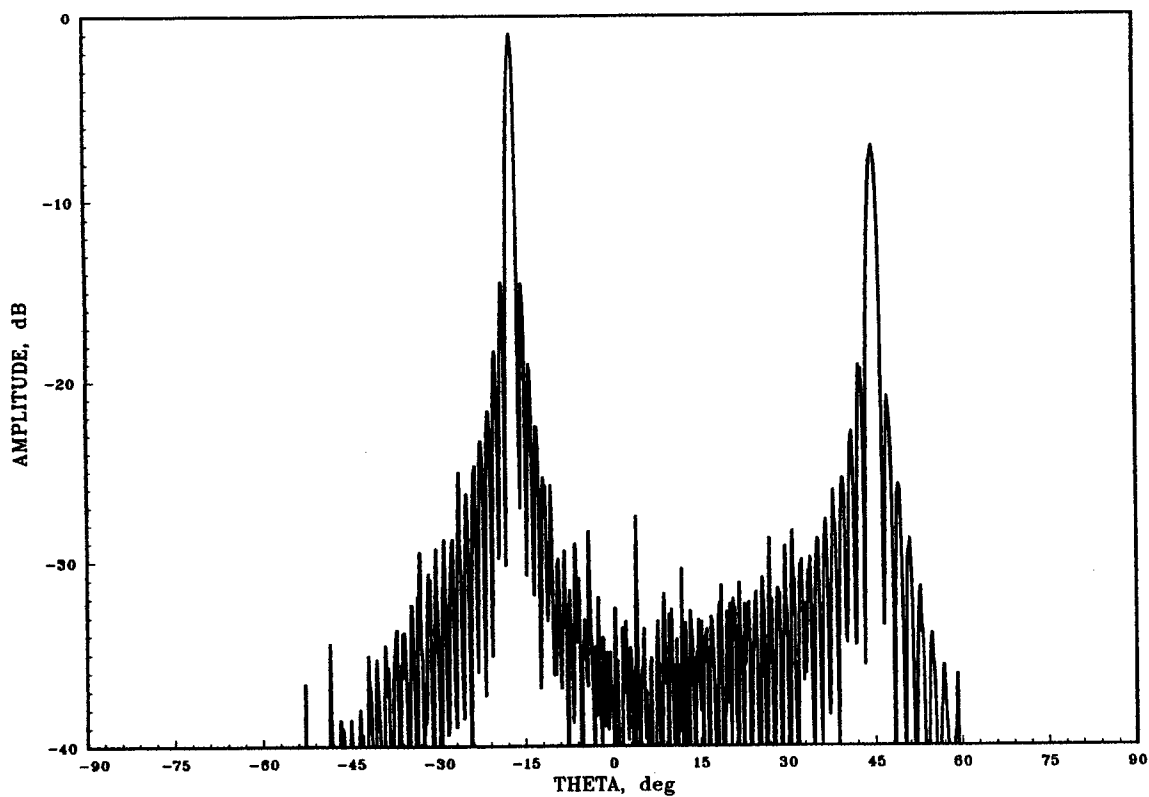
LINEAR ARRAY, 100 ELEMENTS, 50 SUBARRAYS, THETA=45 deg

Fig. 3
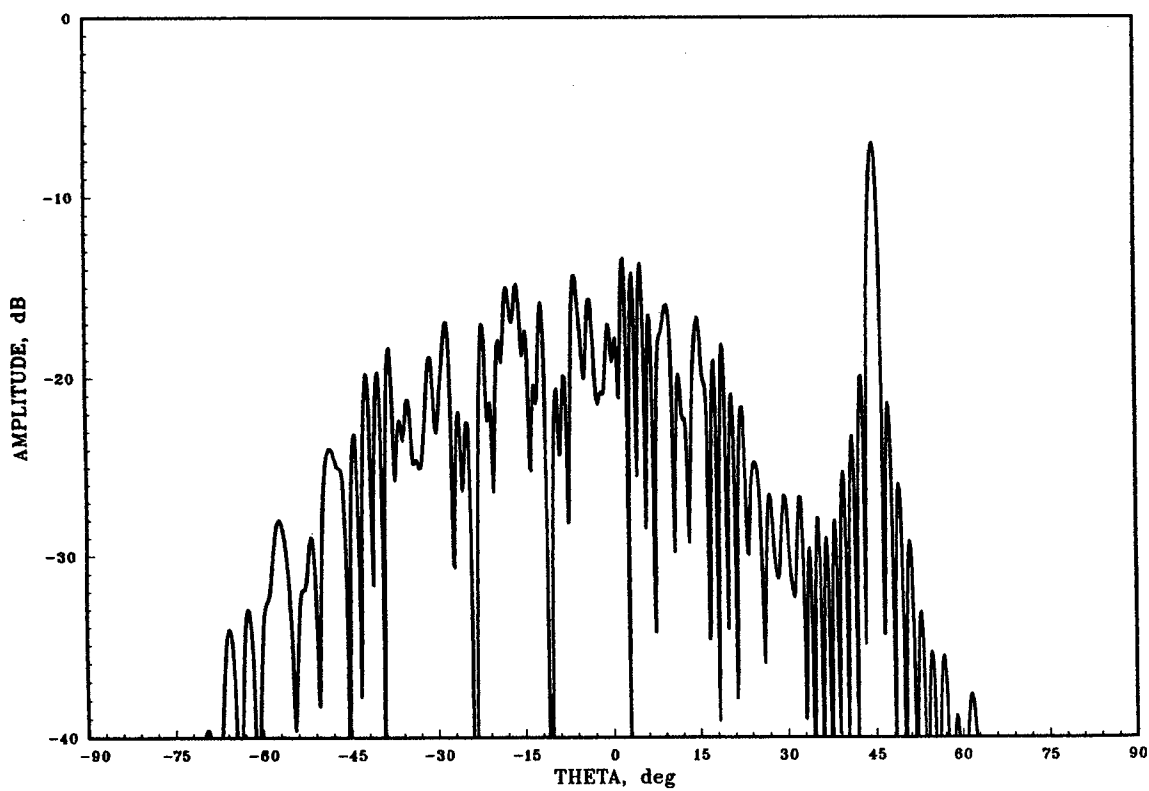
LINEAR ARRAY, 100 ELEMENTS, 50 SUBARRAYS, THETA=45 deg

Fig. 4
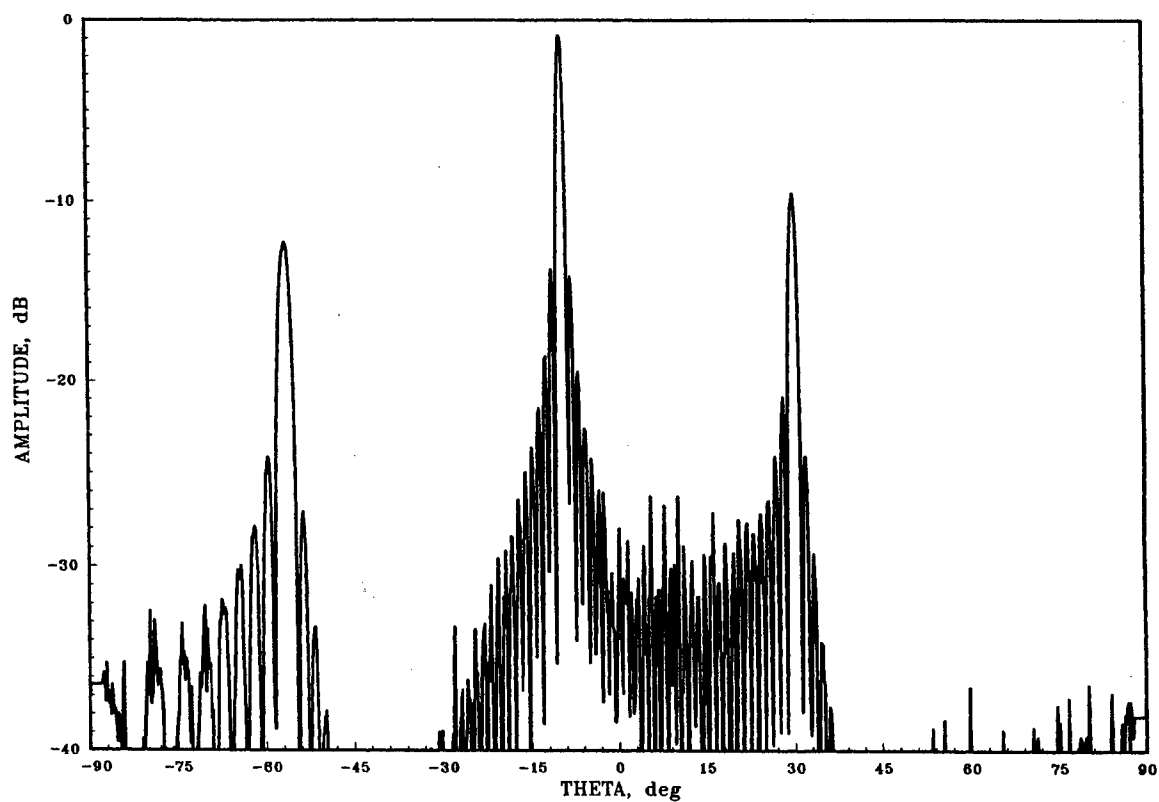
LINEAR ARRAY, 102 ELEMENTS, 34 SUBARRAYS, THETA=30 deg

Fig. 5
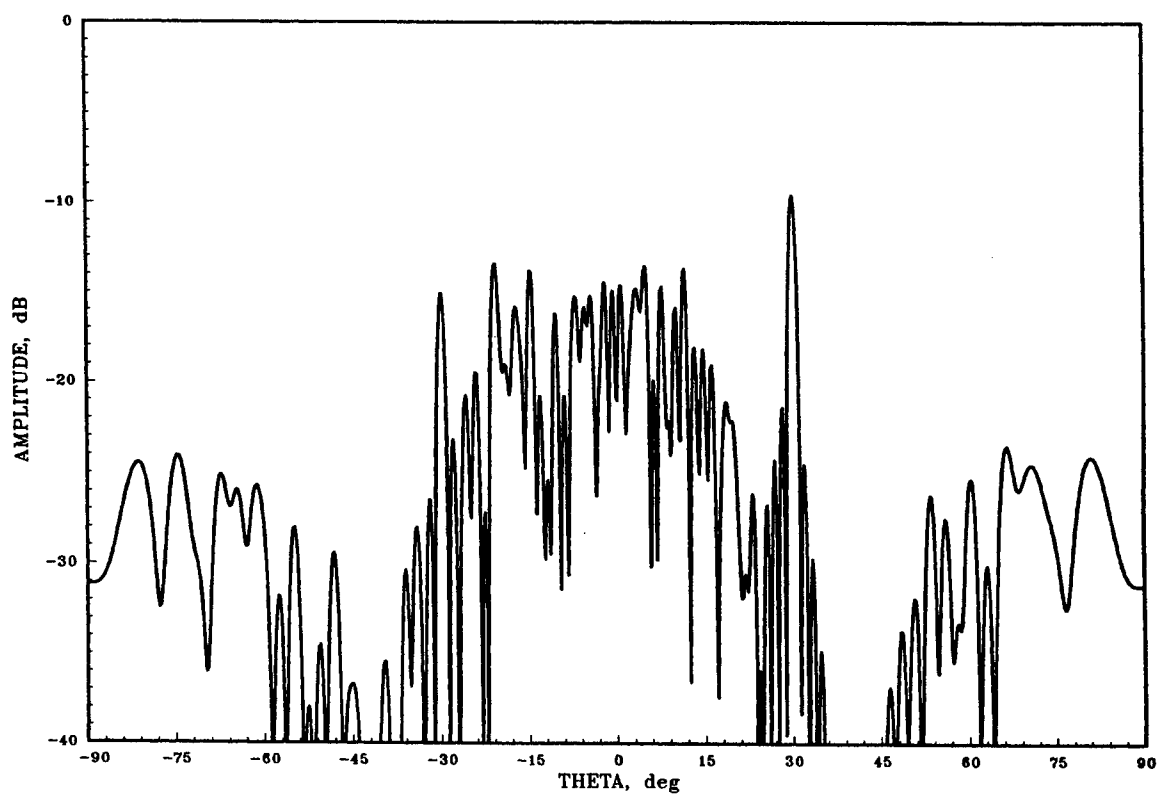
LINEAR ARRAY, 102 ELEMENTS, 34 SUBARRAYS, THETA=30 deg

Fig. 6

314

Fractal Loop Elements in Phased Array Antennas: Reduced Mutual Coupling and Tighter Packing

John P. Gianvittorio and Yahya Rahmat-Samii

Department of Electrical Engineering
University of California, Los Angeles
Los Angeles, CA 90095-1594

Introduction

A common goal for array antennas has been to pack the elements tighter for lower scan angles while fighting mutual coupling. The emergence of wireless networks as a rapidly expanding market has brought about a need for very small and efficient phased array antennas. An optimal design would incorporate tightly packed elements for efficient directed transmissions that radiate effectively without significant mutual coupling.

This paper presents arrays for a wireless LAN configuration, designed at 2 GHz for operation at the PCS band, that scan lower angles more efficiently than conventional designs. We show the benefits of using fractal elements in linear phased arrays to achieve denser packing while minimizing mutual coupling.

Previous work has shown that fractal geometries are an effective means of miniaturizing antennas [1]. The smaller elements can work in an array in two ways: the first is to increase the gap size between the elements, thus reducing the coupling between them; the second is to allow more elements into a fixed length array for broader scan angles.

Also, there are two methods for utilizing fractals in arrays. One method is fractal arrays, which arrange elements in fractal patterns [2] [3]. The other method, analyzed here, uses fractals as elements. Linear arrays of fractal square loop elements were analyzed using a Method of Moments computer code developed at UCLA [4].

Reduced Mutual Coupling with Fractal Elements

Mutual coupling adversely affects the feeding voltages of the array elements, typically raising the level of the back radiation and filling in the nulls of the antenna pattern [5].

This problem can be managed by using smaller array elements, which maintain interelement spacing while increasing the physical gap between elements. Fractal geometries exhibit similar radiation patterns and input impedances as standard geometries, while requiring less space.

The fractal geometry that is utilized is a second iteration of a square Koch loop [6] [7]. This geometry, fed as a loop antenna, as well as the square loop antenna, can easily be matched to 50Ω at the PCS band and shows significant reduction in width, $\frac{2}{3}$, compared to a square loop. The second iteration was chosen to keep the array easily printable on a PCB. The element patterns of the two geometries and the input match are shown in Figure 1.

A five element, Dolph-Chebyshev array, scanned to 150° off of the axis of the array, shown in Figure 2, was designed for -30 dB sidelobe levels for minimal back radiation. However, the volatile ratio of the excitation coefficients, 1 : 2.41 : 3.14 : 2.41 : 1, increase the level of mutual coupling between the elements [5]. Standard square elements yield unpredictable

results with this level of coupling, but the reduced coupling of the fractal elements permit this design.

The arrays, both having identical excitation and 0.3λ spacing, give the normalized far field patterns shown in Figure 3a. The patterns, when compared to the ideal pattern, a Dolph-Chebyshev array factor as described above with a $sin(\Theta)$ element pattern, show how mutual coupling foils the design of the square element array and increases the back radiation 25 dB above that of the fractal element array.

Figure 3b shows a physical implementation of a tightly packed two-element array, printed on Duroid, fed by a microstrip to co-planar strip transition.

Tighter Array Packing Using Fractal Elements

Modern wireless devices limit the physical size of arrays, making it desirable to pack as many elements as possible into a confined space for broad scan angles without grating lobes. In the space of a 0.5λ spaced array of five square elements, seven fractal elements spaced 0.35λ will fit, as seen in Figure 4, while maintaing the gap between the elements to control mutual coupling.

These uniformly excited arrays yield a grating lobe using square elements when scanned to 150°, but not for the fractal element case, as seen in Figure 5. The normalized patterns are compared with an ideal pattern comprised of an array factor of five uniformly excited 0.5λ spaced elements and seven 0.35λ spaced elements, scanned to 150°, with a $sin(\Theta)$ element pattern, showing how mutual coupling affects both arrays in a limited fashion. Nevertheless, the back radiation of the fractal element array is 15 dB below that of the square element array.

Conclusion

By tightly packing arrays and decreasing mutual coupling, phased arrays with enhanced performance may be designed for future wireless and radar devices.

Acknowledgement

References

[1] C. Puente, J. Romeu, R. Pous, J. Ramis, and A. Hijazo. Small but long koch fractal monopole. *Electronics Letters*, 34(1):9–10, January 1998.

[2] Douglas H. Werner, Randy L. Haupt, and Pingjuan L. Werner. Fractal antenna engineering: The theory and design of fractal antenna arrays. *IEEE Antennas and Propagation Magazine*, 41(5):37–59, October 1999.

[3] C. Puente-Baliarda and R. Pous. Fractal design of multiband and low side-lobe arrays. *IEEE Transactions on Antennas and Propagation*, 44(5):730–9, May 1996.

[4] R.E. Hodges and Y. Rahmat-Samii. An iterative current-based method for complex structures. *IEEE Transactions on Antennas and Propagation*, 45(2):265–276, February 1997.

[5] W. L. Stutzman and G. A. Thiele. *Antenna Theory and Design.* John Wiley and Sons, second edition, 1998.

[6] H.N. Kritikos and D.L. Jaggard, editors. *Recent Advances in Electromagnetic Theory*, chapter 6, pages 183–224. Springer-Verlag, 1990.

[7] N. Cohen. Fractal antenna applications in wireless telecommunications. In *Professional Program Proceedings*, pages 43–9. Electronic Industries Forum of New England, May 1997.
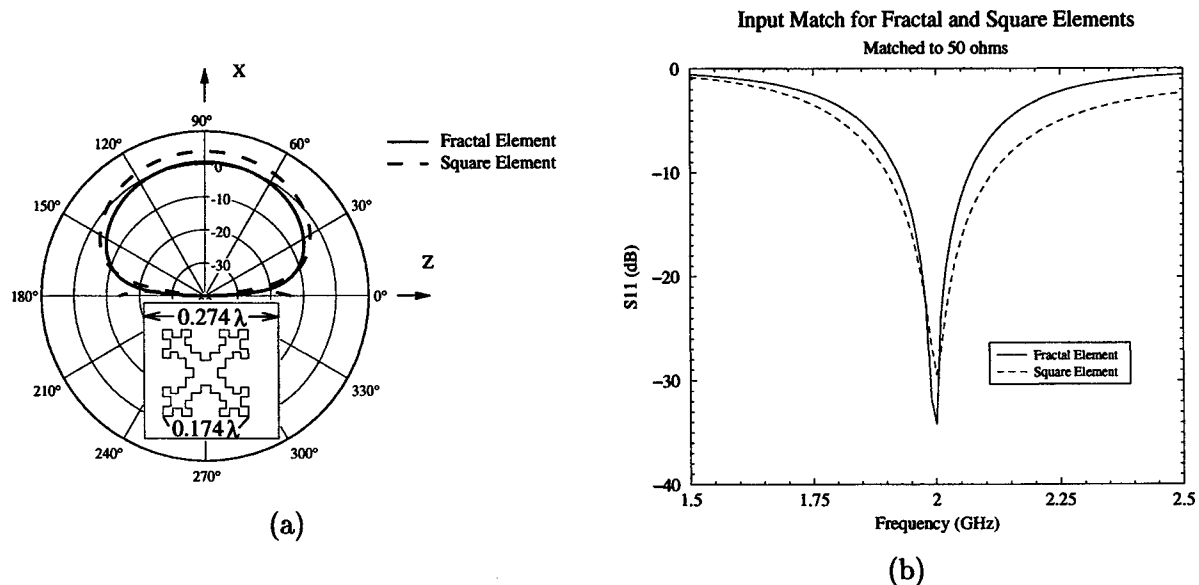
Figure 1: a) Element patterns for an isolated fractal loop and square loop. The inset figure shows the relative sizes for matched fractal and square loops. b) Simulated input match for the two elements matched to 50Ω.
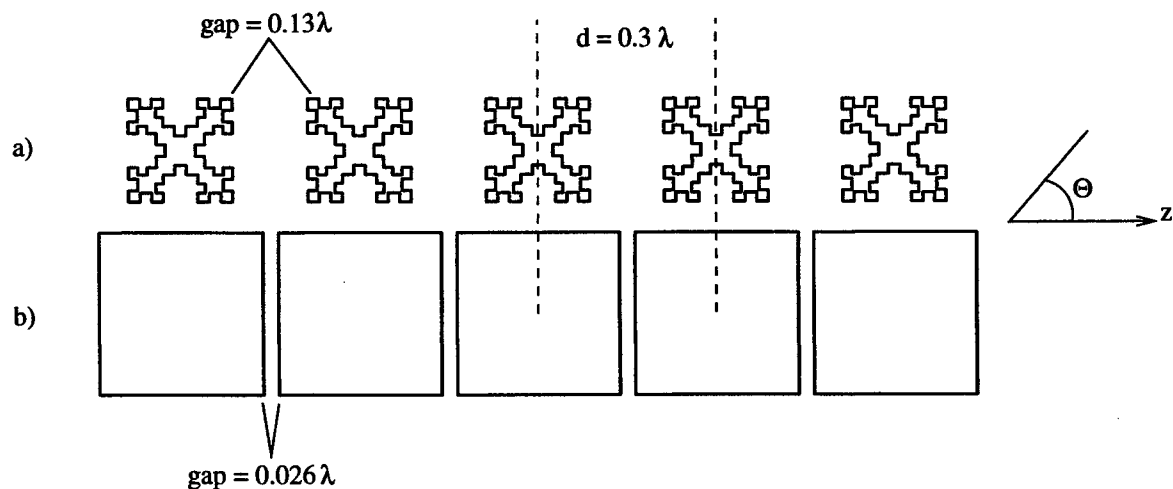
Figure 2: Relative sizes of the two arrays, a) using fractal loop elements, and b) using square loop elements. The fractal element is the second iteration of a square Koch loop.
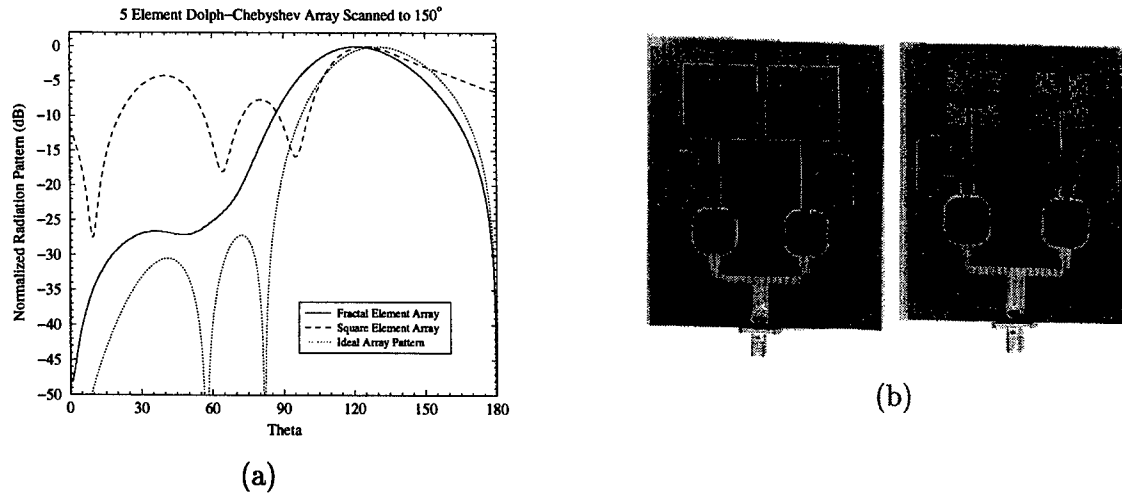
Figure 3: a) Simulated far field pattern for a 5 element, Dolph-Chebyshev, 0.3λ spaced linear array scanned to 150°. The three plots shown are with fractal elements, square elements, and the ideal pattern as expected without mutual coupling. b) Square loop and fractal square loop element arrays printed on Duroid and fed with a microstrip to co-planar strip transition.
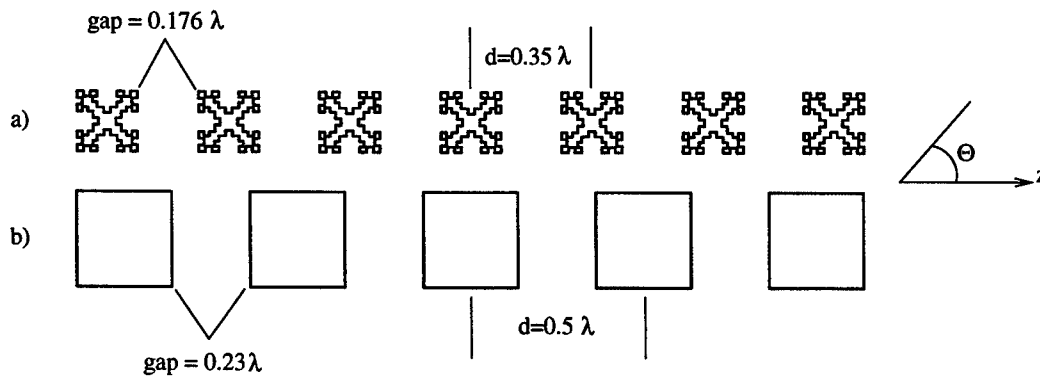
Figure 4: Relative sizes of the two arrays, a) using fractal loop elements, and b) using square loop elements. The overall length of the two arrays are the same.
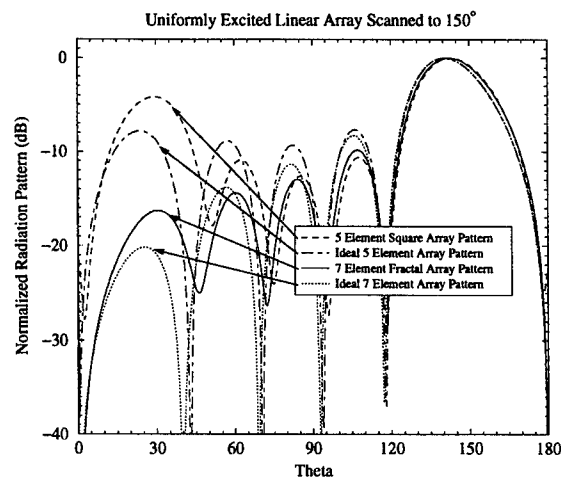
Figure 5: Simulated far field pattern for a 5 square element and a 7 fractal element uniform linear array scanned to 150°. Both arrays have identical overall lengths. Also shown are the ideal patterns of 5 and 7 element uniform arrays neglecting mutual coupling.

ACCELERATED PERIODIC HYBRID FINITE ELEMENT METHOD ANALYSIS FOR INTEGRATED ARRAY ELEMENT AND RADOME DESIGN

Daniel T. McGrath

Raytheon Electronic Systems, McKinney, TX*

I. INTRODUCTION

Earlier, a computational technique known as the periodic hybrid finite element method was developed for finding the active reflection coefficient and active element gain of general phased array radiators [1]. It uses periodic radiation conditions based on an integral equation, hence it is a hybrid of FEM and the periodic moment method (PMM). An extension of the method incorporates the effects of homogeneous dielectric cladding layers without including those layers in the FEM mesh. The result is an efficient means of modeling structures that include wide angle impedance matching sheets and planar radomes.

II. FORMULATION FOR ARRAY RADIATION

The generic structure to be modeled is depicted in Fig. 1. The FEM region, Ω, is one unit cell of a planar structure that is periodic and infinite in both x and y. The unit cell is truncated at two planes transverse to z, denoted Γ_A and Γ_B. Any material structure exterior to Ω above Γ_B must be a homogeneous, isotropic material with constant thickness. The surface Γ_A is a waveguide aperture in a ground plane.
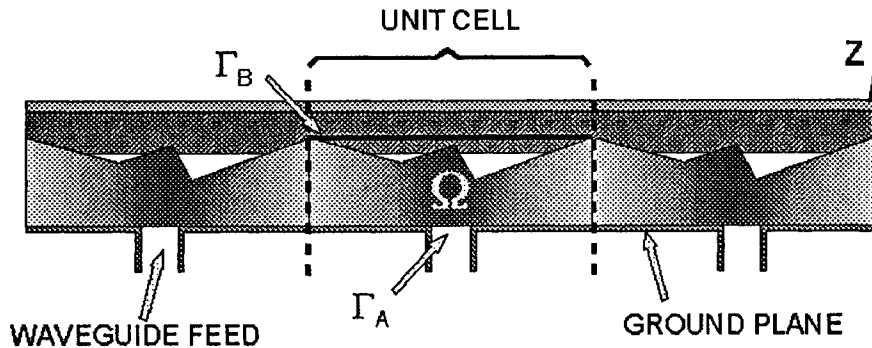
Figure 1. Generic Array Radiating Element with Waveguide Feed

Within the unit cell, the electric field is expanded in terms of finite elements. On the boundaries Γ_A and Γ_B, the radiation condition is enforced using a magnetic field integral equation (MFIE), recast as an infinite summation by representing the exterior fields in terms of Floquet modes. As detailed in [1], the resulting matrix terms for Γ_B are

$$S_{st}^B = jk_0\,\eta_0 \int\limits_{\Gamma_B} \bar{\psi}_t \cdot \sum_{p=1}^{2} \sum_{m=-\infty}^{\infty} \sum_{n=-\infty}^{\infty} Y_{pmn}\,\bar{g}_{pmn}\,dx\,dy \int\limits_{\Gamma_B} \bar{\psi}_s \cdot \bar{g}_{pmn}^{*}\,dx\,dy \tag{1}$$

---

where $\bar{\psi}_t$ is the "vector edge element," $\bar{g}_{pmn}$ is the m,n Floquet mode with $p=1$ or 2 for TE or TM, respectively, and Y_{pmn} is the corresponding modal admittance. Eq. (1) has nonzero terms for each pair of edges s,t on Γ_B. The summations over m and n need only be carried out over a relatively small number of modes, typically ± 5 (121 total). Solution of the system of equations gives the electric field along all mesh edges. The reflection and transmission coefficients are found from the field solution on Γ_A and Γ_B, respectively.

The effect of an arbitrary number of homogeneous exterior dielectric layers is accounted for by finding effective admittances to be substituted for Y_{pmn} in (1). Its derivation follows the approach used by Amitay et. al. [2:219-222] for multimode calculations with waveguide phased arrays. Only the end results are given here, since a complete derivation is already available [3].

For a single superstrate layer of thickness δ outside Γ_B, the following effective admittance is used in place of Y_{pmn} in (9) for calculating the terms of S^B:

$$Y_{pmn}^{<1>} = Y_{pmn}^{(1)} \frac{\left(Y_{pmn}/Y_{pmn}^{(1)}\right) + j\tan(\kappa_{mn}^{(1)}\delta)}{1 + j\left(Y_{pmn}/Y_{pmn}^{(1)}\right)\tan(\kappa_{mn}^{(1)}\delta)} \tag{2}$$

where $Y_{pmn}^{(1)}$ and $\kappa_{mn}^{(1)}$ are the modal admittances and transverse wavenumbers in the dielectric. Y_{pmn} is, as usual, the modal admittance in free space.

If there is a second layer of thickness δ_2 inside the first layer, then the effective admittance to be used in place of Y_{pmn} in (9) is

$$Y_{pmn}^{<2>} = Y_{pmn}^{(2)} \frac{\left(Y_{pmn}^{<1>}/Y_{pmn}^{(2)}\right) + j\tan(\kappa_{mn}^{(2)}\delta_2)}{1 + j\left(Y_{pmn}^{<1>}/Y_{pmn}^{(2)}\right)\tan(\kappa_{mn}^{(2)}\delta_2)} \tag{3}$$

where $Y_{pmn}^{(2)}$ and $\kappa_{mn}^{(2)}$ are the modal admittances and transverse wavenumbers in the inner layer. Eqs. (2) and (3) constitute a recursion procedure for multiple layers, by starting at the outermost layer and working inwards until reaching Γ_B.

The transmission coefficient for the p,m,n mode (which may include Bragg lobes for which $m \neq 0$ or $n \neq 0$) for M exterior layers is

$$\tau_{pmn} = \sqrt{\frac{Y_{pmn}}{Y_{inc}}} \left[\left(y_{pmn}^{(1)} y_{pmn}^{(2)} \cdots y_{pmn}^{(M)}\right) \int_{\Gamma_B} \bar{E}^t \cdot \bar{g}_{pmn}^* \, dx \, dy\right] \tag{4}$$

The integral is the excitation coefficient for the p,m,n mode, found from the field solution over Γ_B. Y_{pmn} is the free space admittance. Y_{inc} is the modal admittance for the incident mode in the feed waveguide. The admittance ratio $y_{pmn}^{(i)}$ for the i'th layer is

$$y_{pmn}^{(i)} = \left[\cos(\kappa_{mn}^{(i)}\delta_i) + j\frac{Y_{pmn}^{<i-1>}}{Y_{pmn}^{<i>}}\sin(\kappa_{mn}^{(i)}\delta_i)\right]^{-1} \tag{5}$$

The $(i-1)$'th layer is the next one on the side away from Γ_B. Note that this formula does not involve a recursion since $y_{pmn}^{(i)}$ does not depend on $y_{pmn}^{(i-1)}$. The terms $Y_{pmn}^{<i>}$ are the effective admittances computed from (3).

III. VALIDATION

Consider the circular waveguide phased array shown in Figure 2 [2:299]. The waveguides

open into free space through a ground plane, and there may also be a dielectric layer just outside the waveguide openings. Figure 2b is a view of the finite element model, which represents a short section of a single waveguide just below the ground plane. The boundary Γ_A, the hidden face, is inside the waveguide, where circular waveguide mode boundary conditions are imposed to represent an arbitrarily-long, match-terminated waveguide as discussed in [1]. The incident field carried by the waveguides is in the TE_{11} mode, polarized in the y direction. The boundary Γ_B is the near mesh face, which conforms to the waveguide-ground plane junction.

(a)   (b)
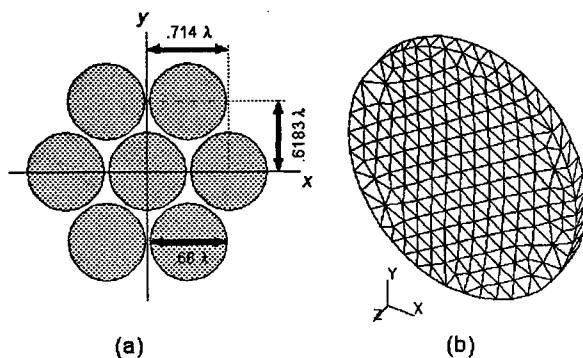
Figure 2. Circular Waveguide Array and FEM Representation
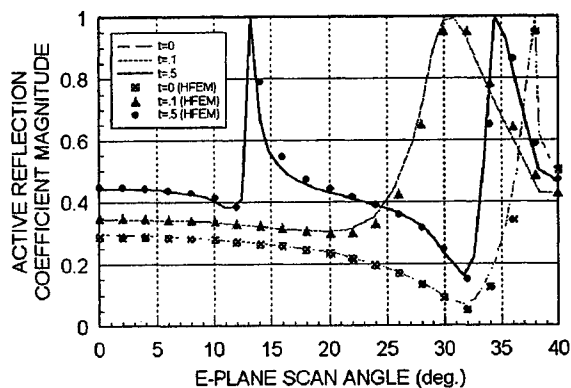
Figure 3. Active Reflection Coefficient Calculations by HFEM and Multimode Method [2] for Array of Figure 2

Figure 3 compares HFEM calculations with multimode results from Amitay et. al. [2:299] for the active reflection coefficient magnitude for scanning in the E plane ($\phi = 90°$). The three solid curves are the multimode results for slab thicknesses of 0, .1 λ, and .5 λ. The three sets of discrete points are the corresponding HFEM results. The close agreement confirms the validity of the effective admittance given by (2), as well as for the modal transmission coefficients from (4) and (5).

A second case, whose geometry is shown in Fig. 4, is a rectangular waveguide array whose waveguides are dielectrically-loaded, with the dielectric protruding a small distance above the ground plane [4],[5]. The finite element inhomogeneous dielectric region above the ground plane. Calculated results for active element gain are shown in Figure 5, both with and without a cover layer of thickness .1 λ and ϵ_r=2.56 attached to the ends of the protruding dielectric plugs. The results with no exterior layer agree with those from Herd and D'Angelo, also obtained with HFEM [4], and with those from Lewis et. al. for a parallel-plate waveguide array with the same E plane dimensions. Clearly, the addition of the matching layer improves the element gain at all angles and supresses the E-plane scan blindness. Both results are discontinuous at 60° scan due to the onset of a grating lobe.

IV. CONCLUSIONS

A method for incorporating the effects of exterior stratified dielectric layers in hybrid finite element calculations for phased array radiating elements has been developed and demonstrated. This extension to the method makes it more efficient for modeling antennas that have wide-angle matching layers and/or radomes. It was previously necessary to extend the finite element mesh through all such layers, adding to the problem size and execution time. Calculations demonstrated a factor of five savings in execution time for an array antenna with a radome.

321
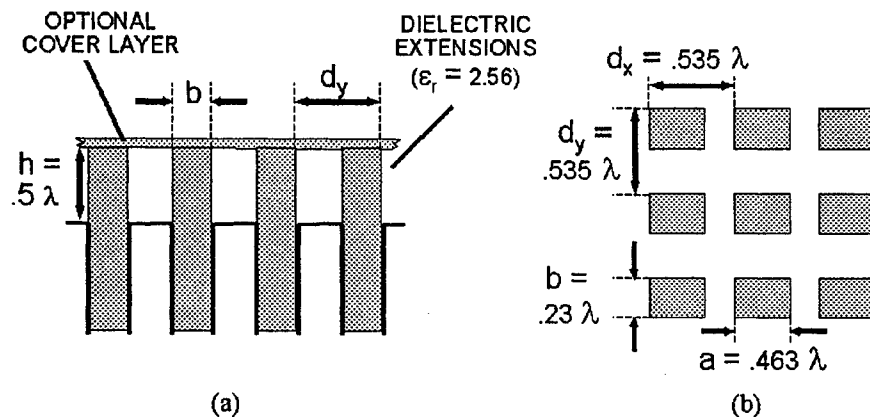
Figure 4. Rectangular Waveguide Array with Protruding Dielectric Plugs: (a) Side View; (b) Top View
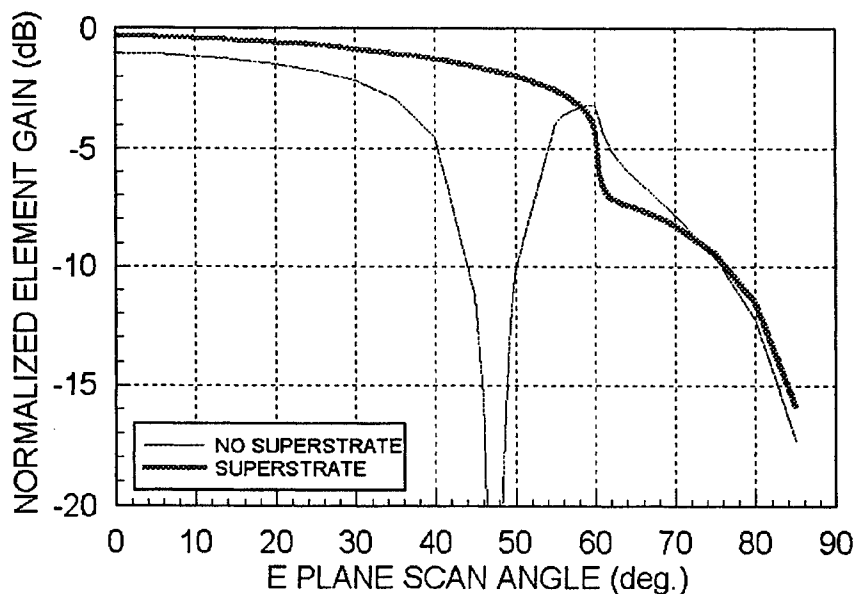
Figure 5. HFEM Calculations for Rectangular Waveguide Array Active Element Gain with & without Cover Layer

REFERENCES

1. McGrath, D.T. and V.P. Pyati, "Phased Array Antenna Analysis with the Hybrid Finite Element Method," *IEEE Transactions on Antennas and Propagation*, AP-42, pp. 1625-1630, Dec. 1994.

2. Amitay, Noach, Victor Galindo and Chen-Pang Wu, *Theory and Analysis of Phased Array Antennas*, Wiley Interscience, 1972.

3. McGrath, D.T., "Extension of the Periodic Hybrid Finite Element Method for External Stratified Dielectrics," USAF Research Laboratory, Kirtland AFB, NM, Mar 1988, AFRL-DE-PS-TR-1998-1017.

4. Herd, J. and J. D'Angelo, "Efficient Modeling of Complex Three Dimensional Antenna Elements in Finite Arrays," *Digest, 1998 IEEE AP International Symposium*, Altanta, GA, pp. 768-771.

5. Lewis, L.R., A. Hessel and G. Knittel, "Performance of a Protruding-Dielectric Waveguide Element in a Phased Array, *IEEE Transactions on Antennas and Propagation*, AP-20, pp. 712-721, Nov. 1972.

Modeling Phased Array Antennas in Ansoft HFSS

Naresh Appannagaari   Istvan Bardi   Roman Edlinger   John Manges   Martin Vogel   Zoltan Cendes
Ansoft Corporation
Pittsburgh, PA 15219

John Hadden
Raytheon Systems Company
El Segundo, CA 90245-0902

A number of algorithms and procedures have been developed for the commercial 3D finite element solver Ansoft HFSS, to model antennas. Primary among these is the application of periodic boundary conditions and array factors to speed the simulation of phased arrays. Another key component is a new procedure for mesh truncation called adaptive PML's that improve upon traditional PML's and eliminate the layers used in earlier publications. And still another is the parametrics and optimization module Optimetrics^{TM} by which design studies of antenna metrics such as directivity and gain can be efficiently automated.

Adaptive PML's

A key development is a new theory for the application of Perfectly Matched Layers (PML's) to absorb electromagnetic waves and thus provide an "open" boundary condition for antenna simulation. None of the published methods on PML's work well with general-purpose codes such as HFSS that employs an unstructured, adaptively-refined mesh. The problem is that the uniform layers in PML's generate a large number of elements and thus result in poor efficiency.

However, the layers are not an essential attribute of PML's; we may show that more efficient absorption is in fact obtained by eliminating the conventional layered structure of PML's. First, consider what happens when the PML is perfectly layered. In this case, an incoming wave sees a constant change in impedance (slight, but nonzero) along several planes at regularly-spaced intervals. As a consequence, reflections are reinforced in certain directions. With an irregular mesh, this change in impedance is broken into a random pattern unlikely to reinforce reflections. Second, by using Huygen's principle, the error caused by back reflections from the PML layer is seen to be proportional to the incident electric and magnetic field. Thus, it is important to refine the mesh in locations where the electromagnetic field is dominant, but it is unnecessary to refine it in locations of small field where the error caused by the local back reflections is negligible. Since a fine mesh is not required on the PML sections where the field is small, great savings in solution time are possible by using large elements in these locations.

Periodic Boundary Conditions and Infinite Arrays

HFSS employs periodic boundary conditions (PBC's) to simulate phased arrays. In describing array simulation using PBC's, it is important to distinguish between the physical array being modeled and the idealized structure analyzed by HFSS. It is assumed that the physical array consists of a large, but finite number of radiating structures arranged in a regular lattice. The "infinite" array analyzed by HFSS approximates this situation with an infinite number of radiators arranged periodically, with lattice geometry identical to the physical array case. Due to its strict periodicity, the infinite array analysis reduces to that of a finite volume called the unit cell. The unit cell then serves as the problem domain for the finite element solution.

The cross-sectional geometry of the unit cell is determined by the geometry of the infinite array lattice. In using HFSS, the opposite pairs of sidewalls of the unit cell are PBC pairs and have the fundamental requirement that they be separated by integer multiples of the array lattice unit vectors so that a PBC may be applied. For a given array lattice, there are an infinite number of possible unit cells, but generally the smallest one is selected, for purposes of solution efficiency. If the array elements are spaced widely apart relative to element dimensions, the unit cell cross section may take the form of a parallelogram, with two pairs of PBC's. In the special case of a rectangular array, the parallelogram is a rectangle. Large array

elements and/or more complicated array geometries may require more than two pairs of PBC's; this is handled automatically in HFSS.

Once the cross section of the unit cell has been defined, a "master-slave" (M/S) relationship is defined between each of the PBC boundary pairs. This entails enforcing a phase shift between the tangential electric fields appropriate to the desired array scan angle. In the discrete world of the HFSS finite element solution, the M/S relationship is enforced by constraining the mesh to be identical on opposite wall pairs and requiring each edge-based degree of freedom on the slave boundary to be tied to that on the master boundary, both in value and orientation. The slave degrees of freedom are then eliminated prior to matrix solution. Typically, the unit cell is excited via addition of a port boundary. Finally, the unit cell is truncated using the PML boundary to provide a high-accuracy open boundary condition, even for antennas scanned at large angles.

Once the finite element problem is formulated, within the unit cell, an arbitrarily accurate approximation to the infinite array fields may be obtained. Additionally, S-parameters are determined at the port boundary of the unit cell. These might more properly be called "active" S-parameters, since they represent the situation where all elements of the infinite array are simultaneously excited.

Of particular interest to array designers is "scan blindness". In this case, the fields above the array consist primarily of energy propagating along the array face, rather than in the desired direction. This condition occurs for certain scan directions and its principal manifestation is a near-unity reflection coefficient at the input ports of the elements. Scan blindness is nearly impossible to predict without detailed electromagnetic analysis, such as available in HFSS. Since multiple scan angle settings must be computed, Optimetrics, the parametrics and optimization module in Ansoft HFSS, is ideally suited for this task.

Concerning antenna patterns, the first thing to note is that an infinite array radiates one or more plane waves that are sometimes referred to as propagating Floquet modes. Using the HFSS postprocessor, the portion of the radiating plane waves within the unit cell may be observed by animating a field plot, but a traditional polar plot of such a pattern is not meaningful. However, having obtained the unit cell field solution, one can compute a radiation pattern for the *finite* array that neglects edge effects by arraying the unit cell pattern. For this purpose, HFSS offers an interactive routine for the definition of array lattice geometry. Here the user can define a wide variety of configurations, not just rectangular, and can even switch individual elements in the array off and on.
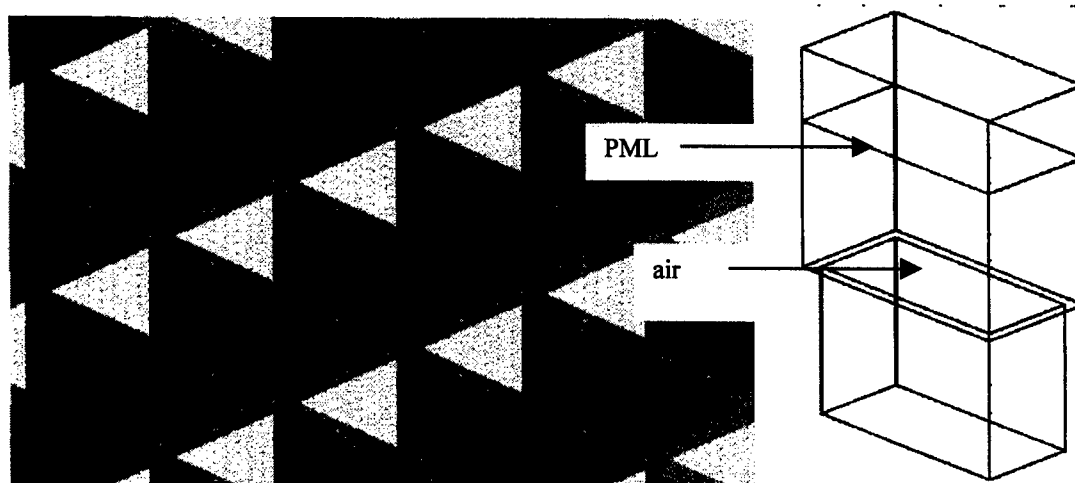
Figure 1: (a) The phased-array antenna. (b) The HFSS model of the antenna, consisting of one unit cell.

324

A Rectangular Array

Consider an array consisting of 0.9" × 0.4" rectangular waveguides in a 1.0" × 0.5" rectangular lattice, as shown in Figure 1. In the HFSS simulation, only a unit cell containing one radiating element is modeled, as shown on the right. The model consists of a section of 0.9" × 0.4" waveguide, one inch long, and an airbox of 1.0" × 0.5" × 1.0". The air is covered by a Perfectly Matched Layer (PML) to absorb radiated fields. The periodicity of the phased array is incorporated in the model by two pairs of periodic boundaries on the side faces of the air and PML objects.

Using Optimetrics with the antenna's scan angle as a parameter to be varied, the simulation was performed for scan angles in the E plane ranging from 0 degrees to 80 degrees. The electromagnetic field corresponding to each row in the table computed by Optimetrics can be displayed as shown in Figure 2, with each row containing the solution for one scan angle. Figure 3 compares Ansoft HFSS results and the results obtained by using a modal code developed by the Raytheon Systems Company. Note that this phased-array antenna is extremely well matched near 42 degrees: its return loss is well below –40 dB. Even at very low return loss values, Ansoft HFSS produces accurate results.
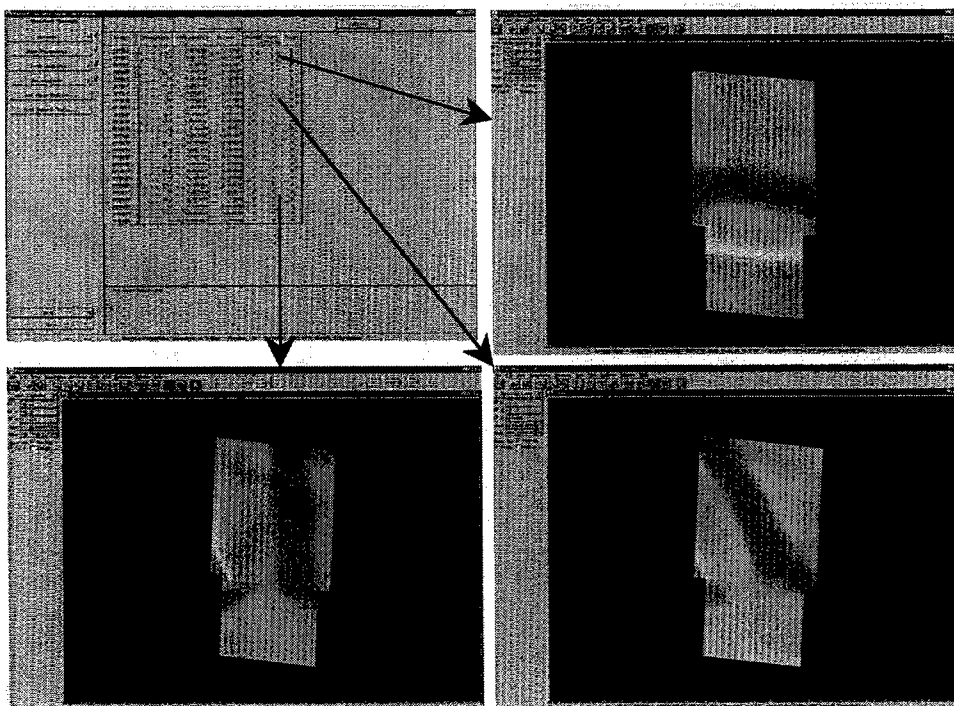
Figure 2: Unit cell electric field magnitude at three different scan angles.

Modeling complex materials

A final example illustrates the power of a versatile finite element solver such as HFSS to incorporate a variety of material properties and boundary conditions.   In array simulation, this allows beam-forming network components to be incorporated simultaneously into the field analysis of the radiating element. Figure 4 displays a snapshot of the electric field solution for a rectangular array unit cell coupled to its exciting port by a ferrite-filled circulator. The exciting and decoupled ports and non-reciprocal action of the three-port circulator are clearly evident in the field pattern.
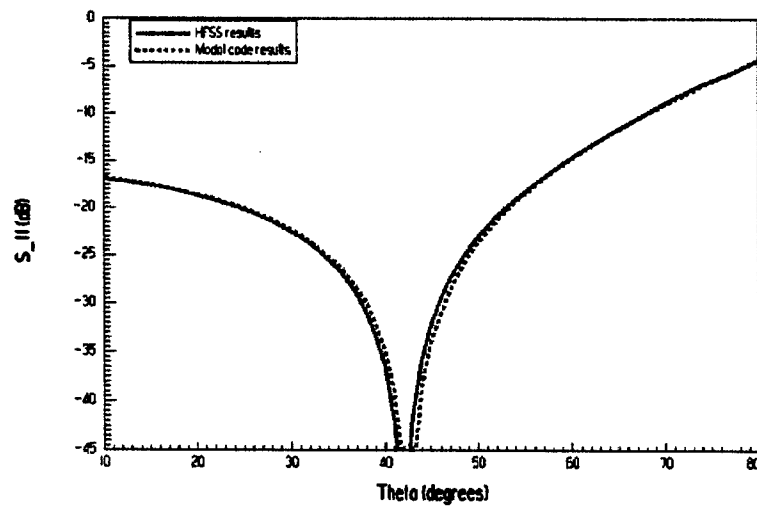
Figure 3: Agreement with modal code of reflection coefficent vs. E-plane scan angle.
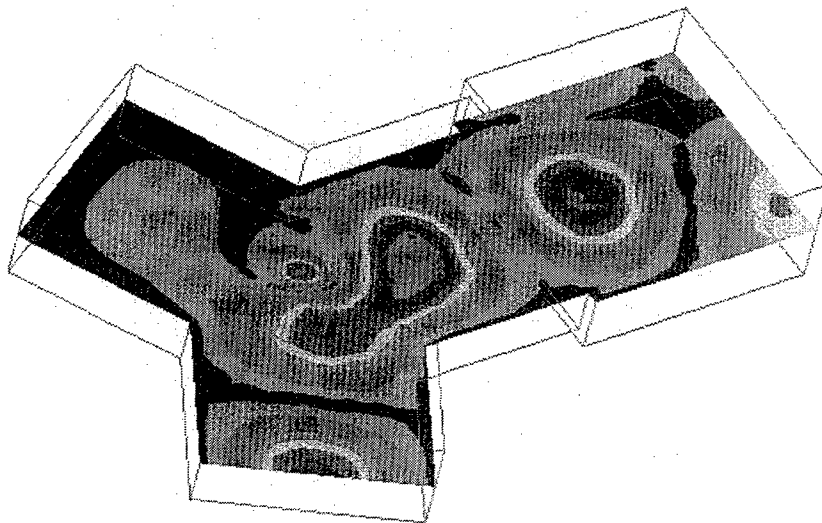
Figure 4:   Field solution for rectangular array unit cell with ferrite circulator

Conclusion

Advances in computational techniques such as adaptive PML modeling and new features such as optimization have been incorporated into Ansoft HFSS. More traditional capabilities such as radiated field computation have been enhanced with array factor and display options. For large, regular arrays, the infinite array approximation is fully exploited by the use of periodic boundary conditions. The resulting combination of features in HFSS offers designers unprecedented ability to simulate phased array antennas and their associated components.

Transmit Antenna pattern synthesis for secondary surveillance Radar.

Yin Liansheng (CIE senior member)

Nanjing Research Institute of Electronic Technology (210013 Nanjing China)

Abstract -A new method of transmit pattern synthesis for secondary surveillance radar (SSR) is presented. This method is concerned with an active phasedarray antenna .In order to eliminate the interference introduced by the interrogation side lobe signal which triggers the transponder mounted on the airplane. A cosine on pedestal excitation for aperture distribution which is used to synthesize the desired directional pattern, which is used to transmit the P_1 and P_3 pulse for interrogation. Using stationary phase method, the phase function over aperture on the specified aperture amplitude distribution is obtained and the desired pattern to transmit the P_2 pulse is synthesized for interrogation side lobe suppression (ISLS).The antenna and relevant equipment which transmits only the P_2 pulse is saved.

I. INTRODUCTION

When the airplane is nearby the SSR, due to SSR's antenna with the high side lobe, as a result, the transponder of airplane may be triggered by the transmitting signal from antenna's side lobe. So there are answer signals in all directions of the PPI display of the SSR,[1] it is called the "ring effect". Due to the "ring effect" it will cause:

(1) The azimuth accuracy and resolution of the SSR seriously deteriorate, sometime the azimuth recognition of the target could be impossible.

(2) The interference increases, i.e. when the target in the side lobe direction is near by the SSR it may be recognized as the target in the main lobe direction.

To eliminate this phenomenon, the international civil aviation organization (ICAO) recommends and stipulates a "three pulse method" as a measure of the interrogation side lobe suppression. The interrogation pulse P_1 and P_3 are transmitted via the directional antenna of the interrogator, and the reference pulse P_2 (sometimes it is called the control pulse) is transmitted via the omni-antenna, but their power level are equal. In the main lobe direction of the interrogation antenna the P_1 and P_3 is higher than P_2, but in the side lobe direction of the interrogation antenna the P_2 is higher than P_1 and P_3. Compare the amplitude of P_1 and P_3 with P_2 in the transponder, if P_1 and P_3 is 9dB large than the P_2, transponder transmits answer signal, if P_1 and P_3 is less than or equal to P_2, the transponder does not transmit any answer signal. Otherwise the transponder will be transmitting answer signal or not. So the P_2 pulse is called the control pulse.

In order to obtain the excellent ISLS result, the omni-antenna design must ensure:

(1) Its azimuth pattern covers the side lobe of the directional antenna.

(2) Its elevation pattern matches with the elevation pattern of the directional antenna to ensure the action of the ISLS system not to suffer from the elevation of the target.

Although the SSR with some features of the radar and communication can obtain more information, but it is only a desire to have a transponder mounted on the target, this limits its useful field. In order to reduce the effect from the disadvantage, in general the SSR cooperates with the radar in its operation. For the target mounted on the transponder, the SSR can provide more information. The normal target position is determined by the radar. Due to the difference of the system and the function for the SSR and radar, the transmission power and antenna gain of the radar is higher than SSR. So the antenna of the SSR is mounted on the top of the radar's antenna. It synchronously scans with radar's antenna. When the phasedarray antenna is used for the radar, the SSR adapts also the azimuth scanning phasedarray antenna.

Since the phasedarray antenna is used, the omni-antenna to transmit P_2 pulse and the directional interrogation antenna to transmit P_1 and P_3 may be integrated, i.e. the above two functions can be done by an antenna. Hence, not only an antenna, but also the relevant equipment of the antenna that transmits the P_2 pulse can be omitted, and the complication of the system and the production cost reduced. Furthermore, due to phasedarray antenna scans rapidly and quickly, the phasedarray antenna of the SSR not only can synchronize scan with the radar antenna in azimuth, but also can be controlled according to different requirements.

II. PATTERN SYNTHESIS OF INTERROGATION ANTENNA

Due to need of the interrogation antenna for SSR transmitting P_1 and P_3 pulses with low side lobe level, we use the cosine

on pedestal amplitude aperture distribution[2]. The formula (1) and Fig.1 shows the aperture amplitude distribution,

$$f(x)=b+(1-b)\cos(\pi x/2L)^2 \tag{1}$$

where: x—antenna element's position; 2L—dimension of the antenna aperture of the SSR; b—selected constant for the side lobe level.

Hence, the pattern $E(\theta-\theta_0)$ of the azimuth scan phasedarray antenna for interrogation antenna is expressed by

$$E(\theta-\theta_0)=\frac{\cos\left(\frac{\pi}{2}\sin\theta\right)}{F_1\cos\theta}\sum_{n=1}^{N}F_n\exp\left[j\left(\frac{2\pi}{\lambda}X_n(\sin\theta-\sin\theta_0)\right)\right] \tag{2}$$

where: $\cos\left(\frac{\pi}{2}\sin\theta\right)\bigg/\cos\theta$ —the pattern of element; F_n—the normalized current amplitude of the nth element;

λ—Wave length; N—the total number of elements; X_n—the position of the nth element; $F_1=\sum_{n=1}^{N}F_n$.

III. PATTERN SYNTHESIS OF ISLS ANTENNA

Since ISLS antenna and interrogation antenna is the same phasedarray antenna, hence the pattern synthesis of the ISLS antenna is based on the determined aperture amplitude distribution. In order to obtain the omni-pattern of the ISLS antenna in azimuth ±60° range, we use phase weighting method to synthesize its pattern[3]. The formula of the pattern is shown by

$$E_0(\theta)=\frac{\cos\left(\frac{\pi}{2}\sin\theta\right)}{F_1\cos\theta}\sum_{n=1}^{N}F_n\exp\left[j\left(\frac{2\pi}{\lambda}X_n\sin\theta+\psi_n\right)\right] \tag{3}$$

where: ψ_n—phase at the nth element.

When the mainbeam scans to θ_0, the pattern is shown by

$$E_0(\theta-\theta_0)=\frac{\cos\left(\frac{\pi}{2}\sin\theta\right)}{F_1\cos\theta}\sum_{n=1}^{N}F_n\exp\left[j\left(\frac{2\pi}{\lambda}X_n(\sin\theta-\sin\theta_0)+\psi_n\right)\right] \tag{4}$$

On the determined aperture amplitude distribution the stationary phase method[4] is used to find the aperture phase distribution function.

From the ISLS antenna pattern synthesis, one- dimensional angular spectrum of plane waves generated by the antenna aperture in the azimuth is given by

$$g(u)=\sqrt{\cos\left(\frac{\pi}{a}u\right)} \qquad (-u_0\le u\le u_0) \tag{5}$$

its distribution is shown in Fig.2

where: a—constant selected when the pattern of the ISLS antenna is synthesized.

According to Parseval's theorem, write down the relation (6),(7) for the energy.

$$\frac{L}{\lambda}\int_{-u_0}^{u_0}g^2(u)du=\int_{-L}^{L}f^2(x)dx \tag{6}$$

$$\frac{L}{\lambda}\int_{-u_0}^{u}g^2(u)du=\int_{-L}^{x}f^2(x)dx \tag{7}$$

where: f(x)—the antenna aperture amplitude distribution to synthesize the interrogation antenna's pattern(see formula(1)).

From the formula (6) we obtain

$$\frac{L}{\lambda}=\frac{\int_{-u_0}^{u_0}g^2(u)du}{\int_{-L}^{L}f^2(x)dx} \tag{8}$$

Formula (5) is substituted into the formula (7) and obtain the formula

$$u(x)=\frac{a}{\pi}\arcsin\left[\frac{\pi}{a}\cdot\frac{\lambda}{L}\int_{-L}^{x}f^2(x)dx-\sin\left(\frac{\pi}{a}u_0\right)\right] \tag{9}$$

Formula (8) is substituted into the formula (9) and obtain the formula

$$u(x) = \frac{a}{\pi} \arcsin \left[\frac{\pi}{a} \cdot \frac{\int_{-L}^{L} f^2(x)dx}{\int_{-u_0}^{u_0} g^2(u)du} \int_{-L}^{x} f^2(x)dx - \sin\left(\frac{\pi}{a}u_0\right) \right] \tag{10}$$

As a result we can obtain the aperture phase distribution function $\psi(x)$ with the determined aperture amplitude distribution function $f(x)$.

$$\psi(x) = \frac{2\pi L}{\lambda} \int_{-L}^{x} u(x)dx \tag{11}$$

Then the phase of the signal fed to each element ψ_n can be obtained.

$$\psi_n = \psi(x_n) \tag{12}$$

IV. EXAMPLE OF THE PATTERN SYNTHESIS

As an example, assume N=44; b=0.32; a=3, Compute the amplitude and phase of the current signal fed to every element (see table.1) and the antenna pattern in some condition(see Fig.3~Fig.5). The SSR's pattern used to transmit without the error is shown in Fig.3. The SSR's pattern used to transmit with error of the amplitude and phase $(\sigma_A = \sigma_\phi = 0.05)$ is shown Fig.4. The SSR's pattern used to transmit and scan to +60° in the azimuth is shown Fig.5 and the error of the amplitude and phase $(\sigma_A = \sigma_\phi = 0.05)$ is considered.

It is seen in Fig.5 that when the ISLS antenna pattern scans simultaneously with the interrogation antenna pattern to +60° in azimuth, in the −30°~0° range exist some pits.This is a disadvantage and useless for interrogation side lobe suppression. So that it is decided the ISLS antenna do not scan following after the interrogation antenna (Fig.6) and satisfactory result can be obtained.

V. CONCLUSION

From the synthesized result given above, we see that the phasedarray antenna is used to the SSR, via controlling the phase shifter, not only the function of the directional interrogation antenna and ISLS omni-antenna is realized but also two pattern full match in elevation is ensured. The antenna and relevant equipment which transmits specially the P_2 pulse is also saved. Due to phasedarray antenna scan rapidly and quickly and can be controled simply, especially in the active phasedarray the phase shifter is operating on lower power level and it is of great advantage to realize the program.

VI. ACKNOWLEDGEMENT

Author loyally thanks the companions for the help and support in forming this paper.

REFERENCES

(1) Paul R .Drouilhet. "The development of the ATC Radar Beacon System :past, present and future". JR.IEEE. Transaction on communications, Vol, Com-21 No.5 May 1973.

(2) T.T.Taylor. "Design of circular apertures for narrow beam width and low side lobes", IRE Trans Antennas propagat...pp17-22 Jan 1960.

(3) Y. C. Gip et al, "Principles of Pased Array and Frequancy-scanning Antennas", Defence Industry Press, 1978.

(4) H. E. Shanks. "A geometrical optics method of pattern synthesis for linear array". IRE Trans Antennas Propagat... pp485-490, Sept, 1960.

Table.1   Amplitude and phase of the current signal fed to every element

n	1	2	3	4	5	6	7	8	9	10	11
F_n	0.321	0.328	0.341	0.362	0.388	0.42	0.456	0.497	0.541	0.588	0.636
ψ_n (radian)	1.518	4.533	7.515	10.464	13.374	16.24	19.055	21.81	24.492	27.091	29.589
n	12	13	14	15	16	17	18	19	20	21	22
F_n	0.684	0.732	0.779	0.823	0.864	0.9	0.932	0.958	0.979	0.992	0.999
ψ_n (radian)	31.972	34.222	36.319	38.245	39.981	41.508	42.81	43.871	44.678	45.222	45.496
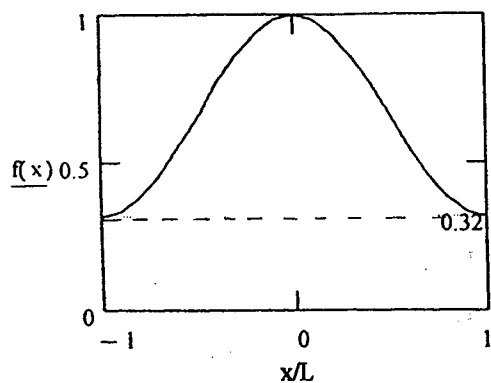
Fig.1   Cosine on pedestal aperture amplitude distribution
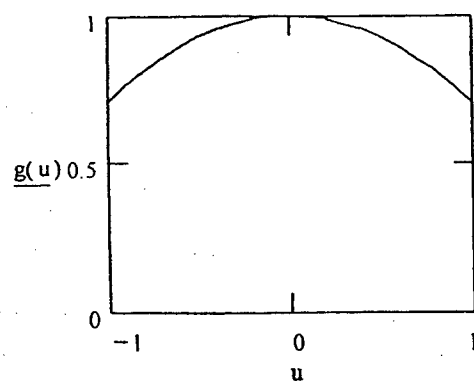
Fig.2   One-dimensional angular spectrum distribution of plane waves generated by the antenna aperture in the azimuth
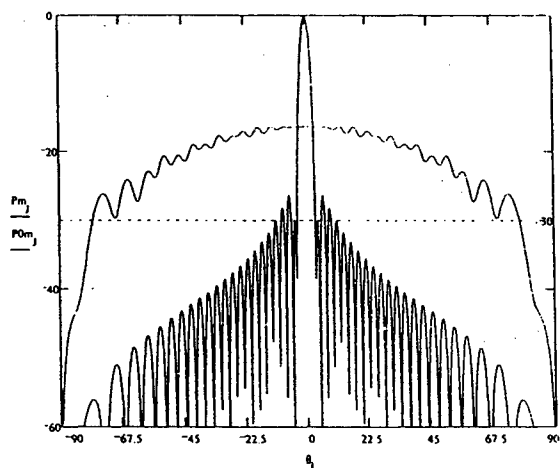
Fig.3   SSR's pattern used to transmit without the error
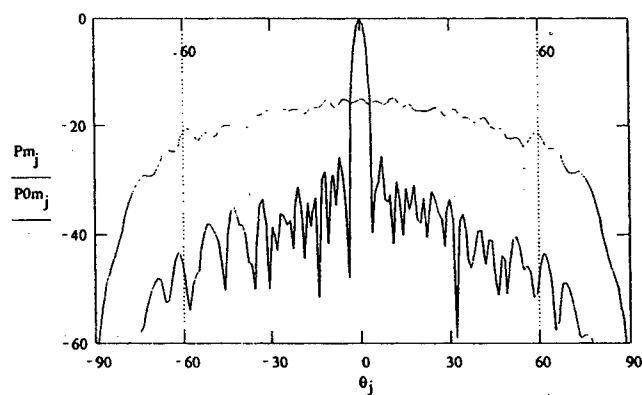
Fig.4   SSR's pattern used to transmit with error of the amplitude and phase ($\sigma_A = \sigma_\phi = 0.05$)
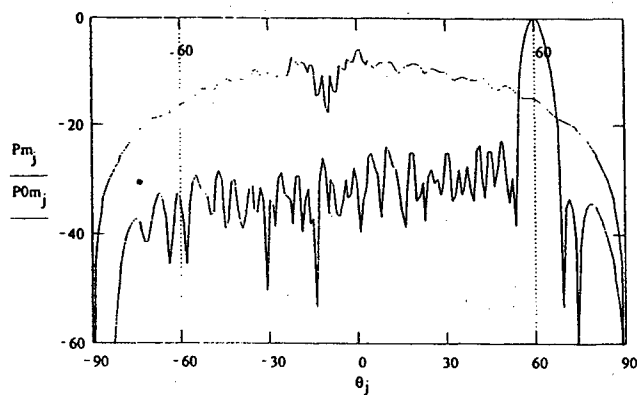
Fig.5   SSR's pattern used to transmit and scan to +60° in the azimuth and considered the error of the amplitude and phase ($\sigma_A = \sigma_\phi = 0.05$)
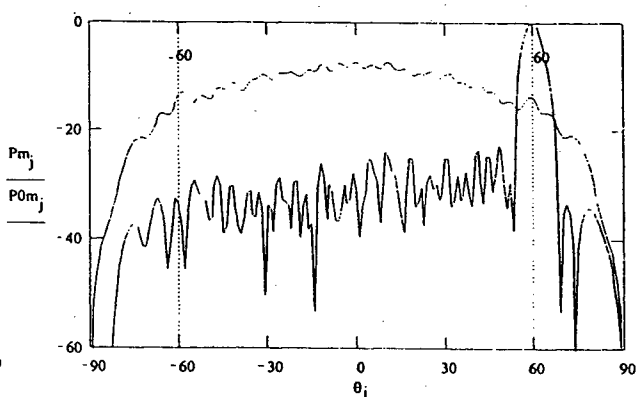
Fig.6   ISLS antenna do not scan following after the interrogation antenna ($\sigma_A = \sigma_\phi = 0.05$)

330

Phase-only Synthesis of the Shaped Beam Patterns
for the Satellite Planar Array Antenna

Shi-Ming LIN ,   Ye-Qing WANG   and   Pei-Li SHEN
P.O.Box 645, Northwestern Polytechnical University
Xian 710072, P.R.China

1. Introduction

In this paper, the phase-only synthesis method is proposed to produce the shaped beam patterns for the satellite planar array antenna. This method is based on the Fourier analysis and iterative method. The simulation results show that the shaped beam patterns can be obtained for the earth coverage case and the desired coverage area case,respectively.

2. Synthesis Method

The far-field pattern of a planar array can be written in the form

$$F(u,v) = \sum_{m=0}^{N-1}\sum_{n=0}^{N-1} a_{mn}^* \exp\{j(m\omega_0 u + n\omega_0 v)\} \tag{1}$$

where $N \times N$ is the total number of the elements, $\omega_0 = 2d/\lambda$, $d(= d_x = d_y)$ is the spacing between elements, $a_{mn} = I_{mn}\exp\{j\phi_{mn}\}$, * denotes the conjugation, I_{mn} and ϕ_{mn} are the magnitude and phase of the mnth current element, respectively, and

$$u = \pi\sin\theta\cos\phi, \qquad v = \pi\sin\theta\sin\phi \tag{2}$$

According to the Fourier analysis, we have

$$a_{mn}^* = \frac{1}{T_1 T_2}\int_{-T_1/2}^{T_1/2}\int_{-T_2/2}^{T_2/2} F(u,v)\exp\{-j(m\omega_0 u + n\omega_0 v)\}dudv \tag{3}$$

where T_1 and T_2 are the periods of function $F(u,v)$ along the u-and v-axes, respectively, Suppose that all I_{mn} are given, $I_{mn}=1$, and the magnitude function of the ideal pattern $|E(u,v)|$ is known. Then, we want to find the fitting values of ϕ_{mn} such that the desired pattern can be obtained. In fact, the phase ϕ_{mn} can be obtained from the following formulas:

$$a_{mn} = \left[\frac{1}{T_1 T_2}\int_{-T_1/2}^{T_1/2}\int_{-T_2/2}^{T_2/2}|E(u,v)|\exp\{-j\varphi(u,v)\}\cdot\exp\{-j(m\omega_0 u + n\omega_0 v)\}dudv\right] \tag{4}$$

$$\phi_{mn} = \frac{1}{j}\ln\frac{a_{mn}}{|a_{mn}|} \tag{5}$$

if the argument function of $E(u,v)$, $\varphi(u,v)$, is found. To solve the problem of $\varphi(u,v)$, an iterative method is proposed as follows:

Let $a_{mn}^{(l)}$ and $\phi_{mn}^{(l)}$ are the complex currents and phases, respectively, in the lth step. Then, we suppose that

$$a_{mn} = \begin{cases} I_{max}\exp\{j\phi_{mn}^{(l)}\} & I_{max} < \left|a_{mn}^{(l)}\right| \\ I_{mn}\exp\{j\phi_{mn}^{(l)}\} & I_{min} \leq \left|a_{mn}^{(l)}\right| \leq I_{max} \\ I_{min}\exp\{j\phi_{mn}^{(l)}\} & \left|a_{mn}^{(l)}\right| < I_{min} \end{cases} \tag{6}$$

where $I_{max} = \max\{I_{mn}\}$ and $I_{min} = \min\{I_{mn}\}$. So, from (1), we have

$$F^{(l)}(u,v) = \sum_{m=0}^{N-1}\sum_{n=0}^{N-1}(a_{mn})^* \exp\{j(m\omega_0 u + n\omega_0 v)\} \tag{7}$$

$$\varphi^{(l)}(u,v) = \frac{1}{j}\ln\frac{F^{(l)}(u,v)}{\left|F^{(l)}(u,v)\right|} \tag{8}$$

where a_{mn} are given by (6). Now, $\varphi^{(l)}(u,v)$ will be regarded as the argument function in (4). So, we have

$$a_{mn}^{(l+1)} = \left[\frac{1}{T_1 T_2}\int_{-T_1/2}^{T_1/2}\int_{-T_2/2}^{T_2/2}|E(u,v)|\exp\{-j\varphi^{(l)}(u,v)\}\cdot\exp\{-j(m\omega_0 u + n\omega_0 v\}dudv\right] \tag{9}$$

$$\phi_{mn}^{(l+1)} = \frac{1}{j}\cdot\ln\frac{a_{mn}^{(l+1)}}{\left|a_{mn}^{(l+1)}\right|} \tag{10}$$

It means that the $l+1$ step is finished. For the stationany of convergence, the function $|E(u,v)|$ in (4) is displaced by

$$|E(u,v)| \sim \alpha^{(l)}\left|F^{(l)}(u,v)\right| + \beta^{(l)}|E(u,v)| \tag{11}$$

where $\alpha^{(l)} + \beta^{(l)} = 1$ and $\alpha^{(l)} = 1$ if $l \to \infty$.

3. Simulation Results

Suppose that the total number of elements is 19×19, and the spacing between elements d is equal to 0.65λ.

3.1 The earth coverage case

It is known that the antenna is assumed to yield an $18°$ earth view. For the earth coverage case, an ideally shape beam pattern was introduced in [2]. Now, the mathematical model of such beam is proposed as

$$E(u,v) = \begin{cases} A/\cos wr & r \leq r_0 \\ 1 & r_0 < r \leq r_1 \\ A/r^s & r_1 < r \leq r_2 \\ 0.075 & r > r_2 \end{cases}$$

weher $r = \sqrt{u^2 + v^2}$, $A = 10\exp\{-B/20\}$, $B = 1.5$, $w = (\arccos A)/r_0$, $\omega_0 = 1.3$, $r_0 = 0.124\pi/\omega_0$, $r_1 = 0.156\pi/\omega_0$ and $r_2 = 0.3\pi/\omega_0$. Then, the above synthesis method can be used to find the phases of currents ϕ_{mn}. Note that the total number of the iterative loops is 2000. The simulation result is shown in Fig.1. The values of gain are calculated for moving the point along the circle $r = \sqrt{u^2 + v^2} = \pi\sin 9° = 0.156\pi$. The minimum of these values is larger than 18.44dB.

For designing the antenna, the effect of phase error is considered. Let the phase errors e_{mn} be independent random variables, they possess the same normal distribution. Assume that $E\{e_{mn}\} = 0$ and $\sigma^2 = 5° (= 0.0873)$. According to the case of $\phi_{mn} + e_{mn}$, some resuts are shown in Fig.2. It can be seen that the above synthesis method will be effectual for the earth coverage case.

3.2 The desired coverage area case

The above synthesis method will be effectual for the desired coverage area case. The simulation results of two examples are shown in Fig.3 and Fig.4. The levels of sidelobes are smaller than -16dB. It can be shown that the effect of phase eror is small for the examples.

References

[1] Y.T.Lo and S.W.Lee, Antenna Handbook, VAH Nostrand Reinhold, N.Y., U.S.A., 1993
[2] J.S.Ajioka and H.E.Harry, Jr., Shaped beam antenna for earth coverage from a stabilized satellite, IEEE Trans. on AP, Vol. AP-18, No.3, 1970, pp.323~327
[3] A.R.Dion and L.J.Rieardi, A variable-coverage satellite antenna system, Proc. of IEEE, Vol.59, No.2, 1971, pp.252~262
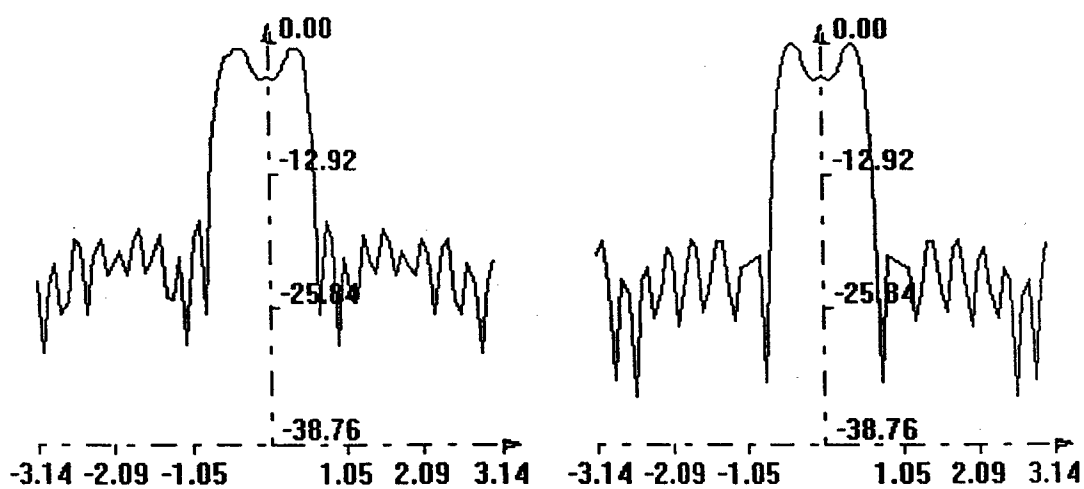
Fig.1   Earth coverage pattern: left:u =0; right: v = 0
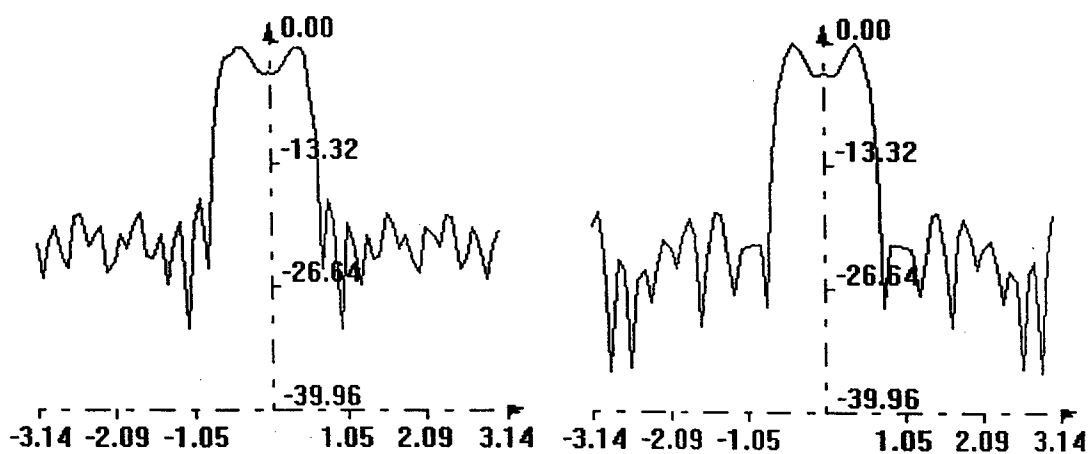
Fig.2   Earth coverage pattern with phase error: left: u = 0; right, v = 0
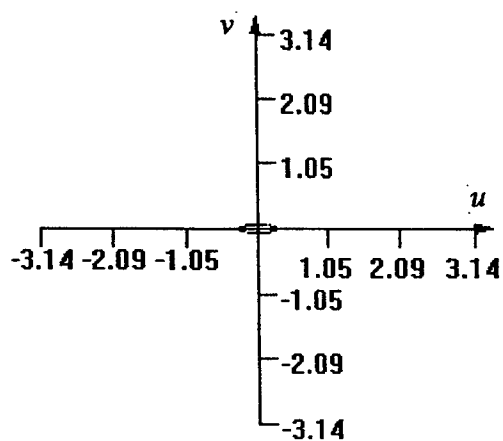
Fig.3   Beam contour in the -3dB plane
rectangular
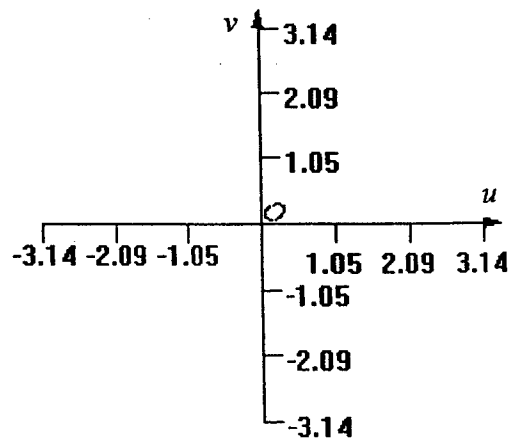
Fig.4   Beam contour in the -3dB plane
ellipse

TP2

Array Applications of Photonics

Array Applications of Photonics

Steps Towards Photonic Antennas

Charles H. Cox, III
MIT

Abstract

One of the present application areas for RF fiber optic links (as opposed to digital links) is the remoting of antennas from the electronics, i.e. the receiver, transmitter, controls, user interface, etc. Examples of antenna remoting can currently be found in both the commercial and defense markets. RF photonic links are being used to convey signals between base stations and cellular antennas as well as between the receiver and antennas of advanced radars.

Important as these initial applications are in establishing the credibility of this new technology, they are really just the first step along a path that eventually could lead to the evolutionary merging of two fields: photonics and antennas. However in these present applications, the photonics are basically *replacing* conventional components, such as the coax that would have interconnected the antenna and electronics.

In the replacement stage, the design of the electronics is largely, if not completely, unaffected by the photonics. Although the RF photonic link provided advantages, such as increased immunity to EMI and the ability to increase the distance between the antenna and the electronics, the RF photonics did not change the system in the sense that no new capabilities were introduced.

A second step in the evolution, which we are beginning to see signs of already, is the *integration* of photonics with antennas. In this stage the system design treats the photonics and electronics as two complementary technologies that can be blended together to obtain performance that was not previously possible from either technology alone.

It is important to note that the term "integration" is being used here to refer to both physical as well as functional integration of the two technologies. An example of physical integration would be designing the filter, LNA and diode laser as one sub-assembly and locating them on the same substrate. An example of functional integration would be a frequency conversion photonic link that can replace the first stage of down conversion in an RF heterodyne receiver. By conveying a lower frequency IF over the photonic link, it is possible to remote 60 GHz antennas over 10's of kilometers of distance. A defining feature of this stage is that it introduces new capabilities that were not possible in stage one.

The third step in the evolution is a *photonic antenna*. In this stage the photonics performs the *sensing* of the electro-magnetic field, thereby replacing conventional antennas. One or two examples of antenna designs along this direction have been reported at the Photonic Systems for Antenna Applications (PSAA) conference. At this stage, entirely new types of antennas would be possible, since photonics would permit sensing as well as remoting the RF field without any electrically conductive elements to interfere with the antenna pattern.

This talk will present examples and status of work in each of the three areas discussed above.

Some Aspects of the Use of Photonics in Large Sensor Manifolds

R.H. Buckley

Surveillance and Reconnaissance Systems, Raytheon Electronic Systems

2000 E. El Segundo Blvd., M/S J132, El Segundo, CA 90245

The advantages of fiber optic transmission are often stated as cable size and weight, freedom from RFI and large instantaneous bandwidth. Although these benefits are intuitively applicable to large sensor manifolds they are insufficient by themselves to be conclusive. Further technology developments will be required by the evolution of modern manifold design. It is likely that future sensor platform incorporating photonics will be large airframe or satellite systems where the above advantages will preclude any other medium for transmission of signals between highly distributed sensor arrays. The insertion points for photonics will then be identified in that context. These insertion points will be determined by two important considerations:

a) The future sensor suite, will to the greatest extent possible, use broadband or reconfigurable antenna arrays; it will utilize a common or shared aperture for transmit and receive; it will allow the formation of multiple beams in a wide range of frequency bands for different applications, and it will require that these signals be routed and controlled via switches to banks of digital receivers controlled by a common processor and resource manager.

b) The architecture of the future sensor manifold will depend strongly on functionality of the sensor suite at the system level and the rate of migration of the ADC towards the antenna element at the component level. Conventional wisdom is that an ideal architecture would digitize directly received signals at the antenna element and route them using optical fiber to the digital signal processor. This view is in line with the rapid growth in the speed and availability of DSP. However ADCs are not yet available with sufficient resolution and bandwidth at microwave frequencies to permit direct digitization. Constraints of size and power consumption as well as the ongoing need for down-conversion continue to dictate that the analog receiver front end is the architecture of choice.

One area of great importance is the persistently high insertion loss of analog fiber optic links due largely to the efficiency penalty of dual electo-optical conversions in the simple link. This ultimately leads to degradation of noise figure and dynamic range. One of the primary goals is the development of more efficient optical modulation devices. There is also a parallel line of attack which is more focussed on the subsystems of the manifold itself. That is to devise methods by which the photonic elements assume a greater share of the functionality of the system by performing more sophisticated tasks than that of "a copper replacement." The more processes that can be done in the optical domain prior to the initial conversion to RF, the less is conversion efficiency an issue.

The author believes in exploiting both approaches to the problem with the ultimate goal of developing the "photonic manifold", a sensor system incorporating radar and other sensor suites in a manner which will reduce cost and weight and add the unique bandwidth and agility properties that photonics has to offer.

Figure 1 shows a schematic of a generalized manifold for a large distributed phased array radar. The building blocks highlighted in blue show the areas of the system for which photonic technology is sufficiently developed to allow component and sub-system solutions to be proposed or developed (both at

Raytheon and within the photonics community at large.) The other shaded areas represent functions which are expected to be addressable by components developed under RFLICS and other photonic technology programs. The upper half of the figure is the transmit side and the lower half the receive side. Most of the functions of the manifold have optical insertion potential. increase Without describing these in detail, three particular points can be made.

a) Optical beamforming using true time delay (particularly suited too widely spread frequency bands and large arrays) or other means has been included.

b) There is extensive use of photonics to generate and distribute waveforms and reference/calibration signals. These signal elements are of various kinds, e.g. transmit waveform generators, mixers, local oscillators, reference tones, clocks etc.

c) Various alternative forms of optical preprocessing have been suggested. For example, one can imagine a receiver in which signals at the antenna are split into parallel paths. One path would consist of a photonic correlation receiver from which a computer would develop cues fed to the second path. This path might comprise a wideband delay, optical channelizer and optical block down-converter to a common IF and filter prior to A/D conversion. The down-converter is cued from the correlation receiver.

It is important, if not essential, that contemplated innovations in photonic devices and their implementation in analog links be designed from the outset with a focus that concentrates on the nature and demands of real military systems applications. Particular requirements, such as those of cost, availability of prime power and physical footprint must be taken into account along with performance. It is particularly helpful when the system integrator has extensive experience in the development and deployment of photonic solutions.

Figure 1 Conceptual Areas for Photonic Insertion within a Radar Manifold

The second part of this paper deals in a non tutorial manner with the interpretation of common subsystem "black box" parameters as they apply in the presence of photonic elements, and the most important of these are noise figure and dynamic range. Analog designers are familiar with the use of these parameters to characterize active and passive elements of a RF circuit, and with well known cascade formulas, such as that of Friis, to calculate the overall parameters of their subsystem. These kinds of calculations lead to the common "power diagram" of Figure 2 which is often used to summarize the result in a convenient graphical form. This displays concepts such as intercept point, orders of distortion, and noise floor in a way that makes the concept of say, spurious free dynamic range, very clear. Further based on extensive experience of different materials used in active devices designers have little difficulty in estimating a compression dynamic range from a SFDR.

The question arises whether the user of photonics can characterize the elements of his optical system in a similar fashion, and then similarly cascade them together. The answer is in general yes, but the behavior of photonic devices such as lasers and photodetectors is quite unique, requiring an understanding of their

Figure 2 RF power out versus power in showing distortions and noise floor

A- 1st order.slope=1

B- 3rd order.slope=3

C- 5th order.slope=5

D- Third order intercept

E- Third order spurious free

F- Fifth order spurious free

G- Output noise
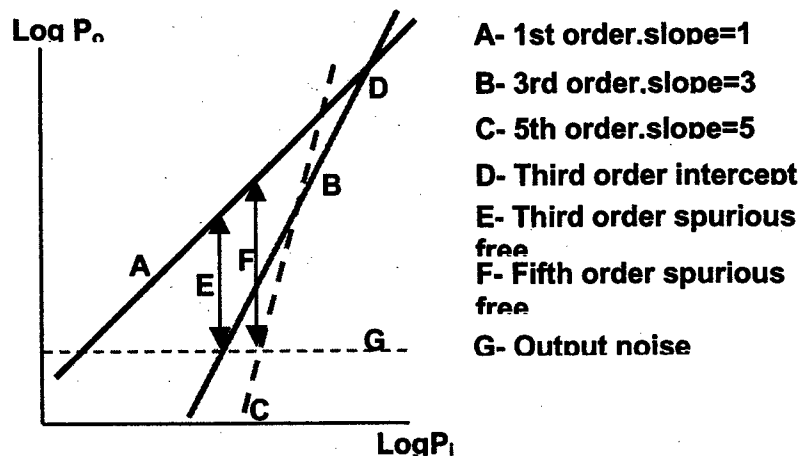
operation in detail, and the expressions for cascading them to the subsystem level much more arcane than those of the electrical designer. In particular the properties of the photonic devices are much more dependent on operating point than are electrical devices, due in part to the unipolar nature of light but also to the basic

physics of the interactions between light and matter on which they depend. With such caveats it is possible to hand to the user an optical system with RF inputs and outputs and an eqvualent set of useful electrical parameters.

To illustrate the point, we describe in general terms the noise and linearity properties of three typical devices found in extrenally and directly modulated point to point analog photonic links, which are the basic building block of the photonic manifold. Figure 3 shows a cartoon of a link of each basic kind. The external link contains an electro-optic modulator (Mach-Zehnder interferometer shown) which intensity modulates an externally supplied CW laser beam in response to a received signal. The modulator is a voltage to optical power converter. The directly modulated link contains a laser diode which acts as a current to optical power converter. In both cases modulated light is returned to a photodiode detector at the receiver location. The photodiode converts the optical power modulation to an electrical current. (Additional signals, including power may also be supplied optically to a distributed sensor array.)
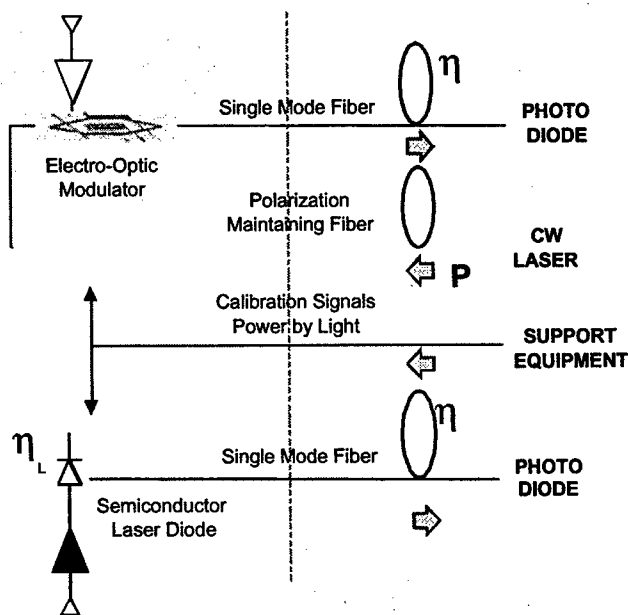
Figure 3 An externally modulated (top) and directly modulated (bottom) antenna remoting link

The properties of the modulator are easiest to discuss. Because it is a passive device it adds no noise to the link. Because an analog photonic link normally operates at high optical power the received noise level is dominated by

that contained in the CW source laser. The harmonic generation of the modulator is determined by its transfer function which is sinusoidal in shape (see Figure 4). Ordinarily the modulator is biased at its half

343

power point where it is most linear. The voltage Vpi required to extinguish transmission is called the switching voltage. The static distortions are readily calculated from the transfer curve and depend on the modulating voltage and Vpi. A typical modulator with a 4 volt switching voltage from a 50 ohm source will have an input IP3 of 21 dBm. The diode laser is a very different matter. It is inherently noisy as a result of randomly generated stimulated emission events inside the cavity and dominates the link noise. Its noise spectrum is strongly frequency dependent as are its distortions; causes for distortion include mode switching, spatial hole burning, threshold clipping and resonance distortion. In addition such a device often displays interferometric distortion due to its inherent AM-FM conversion. Because distortion and noise are both generated by the laser it may be said to possess a dynamic range of its own. Considering only resonance distortion, we have calculated C/IM3 and C/IM5 of a typical laser diode as shown in Figure 5. Note the strong frequency dependence and multiple resonances. In either case the receiver photodiode contributes distortion to the link. It does so in response to space charge saturation caused by the very high average received optical power. The onset of saturation is very sudden and depends on the design and operating point of the device. Because the minimum received noise is the quantum limited value of the average power the detector too can be said to possess an intrinsic dynamic range. A typical example is plotted in Figure 6. Note the rapid degradation with increasing photocurrent density.
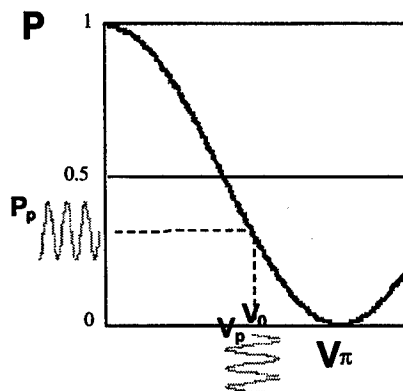
Figure 4 Transfer function of the electro-optic modulator

Figure 6 : The narrow band dynamic range of the Si PiN photodiode with frequency. ∞>>1

Frequency (MHz)

Figure 5 IM free dynamic range of the laser diode

In summary we see photonics as a cornerstone of the architecture of future large distributed sensor manifolds. The technology continues to improve in key requirements of reliability, cost and performance. The examples we have shown , without detailed explanation, of the unique behavior of some of the basic components are intended to convey the sense that as sensor systems come to require increased dynamic range above 125 dB-Hz $^{2/3}$, the successful design and implementation of the photonic elements demands a profound knowledge of the details of their operation.

344

Microwave fiber optic links for shipboard antenna applications

S. A. Pappert, C. K. Sun, R. J. Orazi and T. E. Weiner
U.S. Navy SPAWAR Systems Center, San Diego
SSCSD D895, 53560 Hull Street, San Diego, CA 92152-5001
Tel: (619) 553-5704; Fax: (619) 553-1060; E-mail: spappert@spawar.navy.mil

ABSTRACT

Microwave photonic link technology suitable for shipboard RF antenna applications is presented. High performance narrowband (sub-octave) direct modulation links designed for shipboard GPS and UHF communications antenna remoting are described along with a novel broadband (multi-octave) photonic link linearization approach.

SUMMARY

The U.S. Navy has recently begun deployment of analog fiber optic links for remoting shipboard antenna information. Microwave photonic links offer advantages in size, weight, bandwidth, EMI immunity, minimum bend radius, and RF loss flatness across frequency and fiber length (<1 km), all of which are important issues for Navy surface ships. In spite of these attractive features and rapid advance of fiber optic link technology over the past twenty years, the widespread deployment into analog-based military communication, radar, and surveillance systems has been slow. Reasons for this include the continued high electrical-to-optical (E/O) and optical-to-electrical (O/E) conversion losses incurred as well as the environmental stability, ruggedness, and cost of the photonic links. In terms of link RF insertion loss, the optical fiber provides an extremely low loss transmission media, however there is typically significant loss associated with the E/O and O/E conversions. Most limiting is the optical modulation efficiency or E/O conversion loss. Consequently, the transmission loss advantage of fiber over copper diminishes for most shipboard antenna remoting links (<100 m). Copper transmission loss can be made quite low (e.g. 6.5 dB/100 m @ 2 GHz with 7/8 inch diameter heliax) if rigid, larger diameter cable can be tolerated resulting in stiff competition for fiber in microwave antenna systems aboard Navy surface ships. Topside antenna systems that have recently selected single-mode optical fiber as their preferred microwave transmission medium include GPS (Global Positioning System) and MERS (Multifunction Electromagnetic Radiating System). As microwave photonic links continue to improve and become more affordable, more topside antenna systems will opt for optical remoting/distribution/processing of RF signals [1,2]. This paper focuses on the high performance fiber optic links developed for the shipboard GPS and MERS antennas that require operation up to 2 GHz.

For microwave systems operating below 3 GHz, direct current modulation of a laser diode offers a good solution for remoting shipboard antenna information. A broadband microwave photonic link consisting of a high-performance commercially available 1.3 μm DFB strained QW laser diode, SMF-28 single-mode fiber (2 km), and a high efficiency (>0.85 A/W) InGaAs p-i-n photodiode has been assembled for test and measurement purposes. The frequency response and two-tone spurious free dynamic range (SFDR) measurement results for the unmatched (25 Ω laser diode input impedance and high impedance detector output) laser diode link are shown in Fig. 1 and Fig. 2, respectively. The link exhibits an RF loss of <10 dB out to 3 GHz with a value of 8.4 dB at 1.5 GHz, close to the 6.5 dB heliax value at 2 GHz cited above. The fiber-coupled modulation slope efficiency of the temperature controlled DFB laser is estimated to be near 0.35 W/A, which explains the very

low link RF insertion loss. The high-performance link has a noise figure of <30 dB, a >125 dB-Hz$^{2/3}$ narrowband (sub-octave) SFDR, and a >100 dB-Hz$^{1/2}$ broadband (multi-octave) SFDR out to 1 GHz. The 1 dB compression point for the link optimized for transmit mode operation is >15 dBm. The photonic link exhibits a residual phase noise of <-110 dBc/Hz at 1 Hz from a 780 MHz carrier and an amplitude stability of better than 1 dB. Using these optoelectronic link modules as building blocks, microwave fiber optic links have been constructed specifically to meet shipboard GPS and MERS requirements. One fiber optic link has been designed to function in a narrowband receive system, another in a broadband receive system, and still another has been designed for a narrowband transmit system. For improved VSWR performance (better than 2:1 input and output VSWR), the links are broadband matched to 50 Ω at the detector output which sacrifices about 6 dB of link gain over the unmatched case.
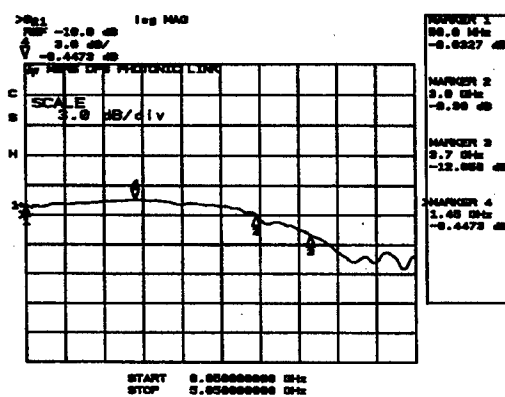
Fig. 1. Frequency response of the 1.3 μm laser diode link.
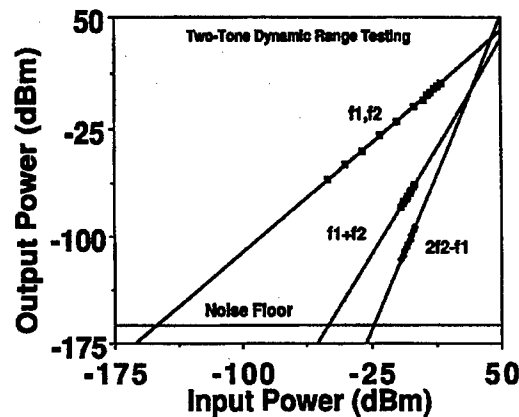
Fig. 2. SFDR measurement of the laser diode link.

The GPS fiber optic antenna links (FOALs) operate near 1.5 GHz and take received satellite navigation and timing information at two topside antenna sites and remote this information to below deck processing receivers. Employing an LNA in front of the laser diode as well as a post-amplifier behind the optical detector, a fully connectorized link noise figure of <3 dB and a 35 dB gain for single-mode fiber runs up to 100 m are achieved. The GPS FOAL has a nominal SFDR of 100 dB-Hz$^{2/3}$. The FOAL system has been tested from –55°C to +85°C degrees, exceeding the shipboard requirement, and over full shipboard shock and vibration levels, over which ranges excellent RF performance has been achieved. The links use MIL/AERO qualified single-pin and multi-pin single-mode fiber optic connectors. The FOAL system meets all shipboard environmental and GPS receiver system requirements and is currently being deployed on Navy surface ships throughout the fleet. As receive-mode antenna remoting using photonic links matures and is reduced to practice, microwave photonic link antenna remoting of topside radiating systems requiring transmit-mode operation in addition to receive-mode operation becomes more the R&D focus.

Microwave fiber optic links are ideally suited for feeding and distributing RF and LO signals to and from broadband multifunction antennas. As a first step in integrating multifunction antennas onto surface ships, MERS merges four existing topside systems into a single, mast-mounted radiating aperture. The UHF Line Of Site (LOS) Communications, Joint Tactical Information Distribution System (JTIDS), Identification Friend or Foe (IFF), and Combat Direction Finding (CDF) antenna systems comprise MERS. The broadband direct modulation photonic link has been tested against the MERS performance requirements for use in the four antenna systems. Link performance parameters including noise figure, SFDR, 1 dB compression point, close-to-carrier phase noise, and amplitude stability have been compared against system requirements with favorable narrowband results. Two fiber optic links have been packaged for MERS, one for transmit operation and one for receive

operation, and inserted into a UHF COM transmitter/receiver testbed which operates from 225 - 400 MHz. Successful transmission and reception of AM and FM modulated UHF radio signals via these photonic links has been demonstrated satisfying all system performance requirements. A final at-sea shipboard demonstration of eighteen UHF radios integrated into MERS, including transmit and receive fiber optic links, is planned. The MERS direct link RF performance for narrowband signaling is excellent out to approximately 2 GHz and can satisfy JTIDS and IFF requirements. For broadband (multi-octave) operation such as that required for the CDF antenna, the dynamic range performance is limited by second-order intermodulation distortion. To overcome this limitation, a novel push-pull fiber optic link providing extremely high dynamic range for multi-octave microwave operation has been developed [3].

A dual-channel fiber optic link for suppressing second-order intermodulation distortion is schematically shown in Fig. 3. The system uses wavelength division multiplexing (WDM) to combine and separate complementary RF modulation applied to distinct laser diodes. The parallel link configuration consists of a hybrid RF coupler for generating complementary (inverted and non-inverted) electrical outputs representative of the modulation signal. Two similar laser diode transmitters (LD1 and LD2) operating at λ_1 and λ_2 are connected to the complementary outputs of the hybrid coupler. The modulated optical energy is combined in a WDM combiner and transmitted through standard single-mode optical fiber. At the receiver end, a WDM splitter is used to separate the complementary signals whose outputs are connected to a balanced optical detector pair (PD) and electrically combined. The balanced receiver subtracts the complementary signals wherein second-order distortion is substantially suppressed provided each wavelength encounters equal transmission path lengths.
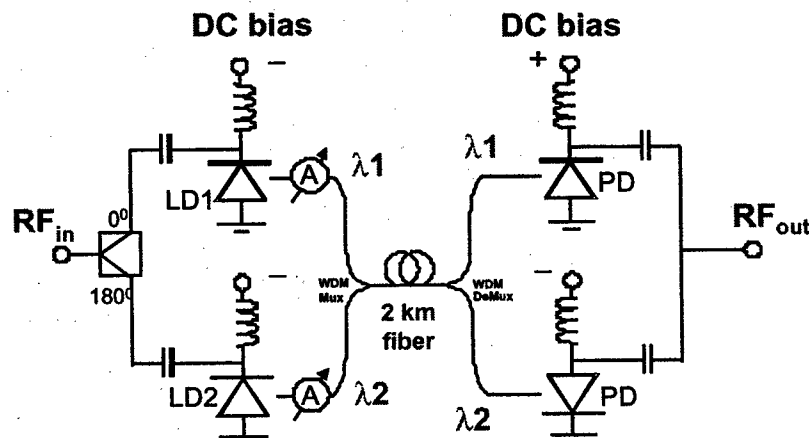
Fig 3. Schematic of a push-pull fiber optic link providing second-order distortion suppression.

To demonstrate this technique, two laser diodes, one emitting at 1309 nm and the second at 1312 nm, are operated in parallel with a balanced detector combination. A 2 km link has been used to simulate a shipboard remoting distance. Fig. 4 is a plot of the second-order and third-order limited SFDRs as a function of the two-tone modulation frequency. Third-order limited SFDR is improved slightly in comparison to that of the individual links A or B, however the second-order SFDR has been improved by >10 dB out to beyond 900 MHz. Using this push-pull fiber optic link for multi-octave applications such as the CDF antenna system, a SFDR of >80 dB in a 1 MHz bandwidth is achieved. This link linearization approach is useful for many shipboard antenna remoting applications where multi-octave RF information must be transmitted.
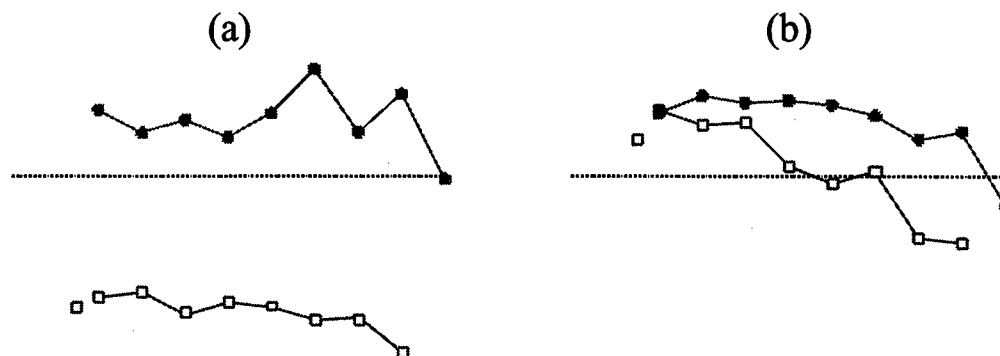
Fig. 4. (a) Second-order limited and (b) third-order limited SFDR for individual links A (crosses) and B (open squares), and for the combined (filled circles) parallel link.

In summary, broadband photonic link technology suitable for shipboard RF antenna applications has been presented. The performance attained by these broadband analog links makes them strong candidates for shipboard transmit/receive antenna remoting, with the GPS and MERS antenna systems leading the way. Additionally, a novel high dynamic range fiber optic link suitable for multi-octave operation has been demonstrated with >10 dB improvement in second-order limited SFDR. This novel push-pull fiber optic link arrangement will allow multi-octave transmission of microwave signals with the same fidelity and RF performance as narrowband transmission. This innovation should prove important as the Navy moves towards wideband multifunction antenna systems.

REFERENCES

[1]   S. A. Pappert, C. K. Sun, R. J. Orazi and T. E. Weiner, "Photonic link technology for shipboard rf signal distribution", *Proc. SPIE*, vol. 3463, p. 123-134, 1998.

[2]   J. E. Roman, L. T. Nichols, K. J. Williams, R. D. Esman, G. C. Tavik, M. Livingston and M. G. Parent, "Fiber optic remoting of an ultrahigh dynamic range radar", *IEEE Trans. Microwave Theory Tech.*, vol. 46, p. 2317-2323, 1998.

[3]   C. K. Sun & S. A. Pappert, "High Dynamic Range Fiber Optic Link," Patent Pending, U. S. Navy Case No. 79042, 1998.

PHOTONICS FOR PHASED ARRAY SYSTEMS

Paul J. Matthews

Naval Research Laboratory
Code 5651, Optical Sciences Division
Washington, DC 20375-5338

I. INTRODUCTION

The use of photonics technology in RF and microwave systems offers numerous advantages in many applications when compared to traditional microwave implementations and techniques. Photonic techniques are capable of providing microwave functionality which is light weight, compact, immune to electromagnetic interference (EMI) and potentially low cost. Additionally, by providing an enormous microwave bandwidth (hundreds of GHz) and a large time-bandwidth product, photonics is capable of providing signal processing functions that many times are difficult, if not impossible, to achieve through any other means.

Over the years, phased-array antennas have seen increased acceptance due to their many advantages over traditional fixed or mechanically steered antennas such as rapid beamsteering and reliability. However, conventional phased-array antennas have many times been hampered by issues of size, weight, cost and complexity. Due to these factors and the various potential advantages of photonic techniques, there has been an increased effort over the years to implement some of the sub-systems of a phased-array antenna optically. Additionally, photonics offers other additional benefits such as a negligible differential loss which allows for simple and flexible antenna remoting and the ability to provide wide instantaneous bandwidths through true time-delay beamforming. Because of this potential, optical control of array antennas has served as a primary motivating factor in the field of microwave photonics.

The impetus for future array antenna systems has revolved around the demands for increased capabilities including larger arrays for higher power and better angular resolution, wide bandwidths, reconfigurability, higher operating frequencies and shared apertures. In particular, photonics can serve as an enabling technology to provide many of these future capabilities. This paper will survey some of the previous photonic techniques for optical control of array antennas, highlight some of the ongoing research, address system-level issues for technology insertion and present results indicating the present and future potential of photonics for array antennas.

II. ANTENNA REMOTING AND SIGNAL PROCESSING

The use of photonics technology is clearly advantageous in the area of signal remoting. This is readily evident in the digital domain by noting the pervasiveness of optical fiber in the telecommunications industry. Analog signal remoting, especially for antenna applications often requires extreme signal purity which is many times difficult to achieve in a fiber-optic link. Some of the general concerns that are normally expressed over the insertion of photonic links into antenna systems include a limited compression dynamic range (120 to 130 dB/Hz) and spur-free dynamic range (SFDR) (100 to 110 $dB/Hz^{2/3}$), high noise figure (30 to 50 dB) and low output microwave powers (< 10 μW). This has led to much intense effort at improving the microwave performance of analog optical links. Recently, we have demonstrated a broadband, 3 GHz fiber-optic link which indicates that these concerns may be alleviated. The link demonstrated a + 5 dB microwave gain, 16 dB noise figure, 168.4 dB/Hz compression dynamic range, 119.5 $dB/Hz^{2/3}$ multi-octave SFDR and +10 dBm of output power [1].

Fiber-optic remoting links have been demonstrated in some rather stringent antenna systems with minimal or no impact on overall system performance. Several efforts have incorporated fiber-optic delay lines for calibration of wideband, high resolution radar systems [2,3]. Recently, we tested a remoting link in the Navy's high-performance AN/SPQ-9B pulsed-Doppler radar system which has very demanding SNR, SFDR and phase noise requirements with no discernable effect [4]. These results and the various techniques and demonstrations previously described indicate that there exists a great potential for the transition of photonic links into RF and microwave antenna systems.
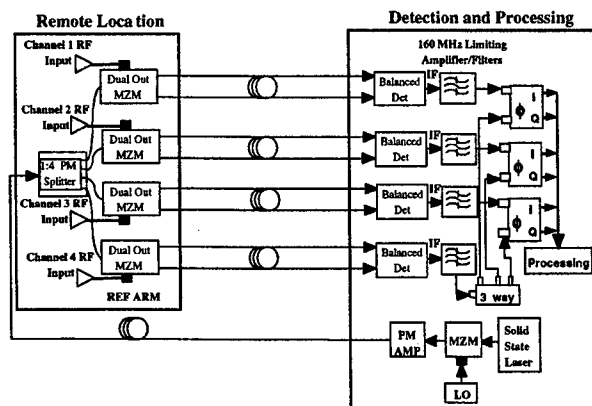
Figure 1. Schematic of a four channel angle-of-arrival optical downconverter.

The issue of antenna remoting is most apparent in receive applications which many times require signal remoting to significantly distance the unwieldy processing electronics from the aperture. In many cases, the remoted signal is subsequently down converted to an intermediate frequency (IF) before being processed. Various studies have shown that incorporating the down conversion process in the optical domain can be superior in terms of RF system parameters to fiber-optic remoting followed by microwave down conversion [5].

Recently, a photonic four-channel microwave phase detector, shown in Figure 1 was demonstrated [6]. The system exhibited RF phase accuracy of better than 2 degrees at 18 GHz with –60 dBm of input power. Anechoic chamber testing as a direction finding antenna system showed spatial resolution of better than 0.1 degrees at 10 GHz [6].

Many receive systems would also be greatly simplified by the availability of a high-speed anaolg-to-digital converter (ADC). This would allow the direct digitization of received microwave signals enabling the replacement of the multiple downconverting stages in a typical receive chain and making possible the use of digital beamforming techniques. There are currently several efforts underway to realize a photonic ADC capable of sampling rates on the order of 10 Gsps with 10-bit resolution. An architecture capable of achieving this goal has been recently demonstrated [7]. It makes use of the highly parallel signal processing capabilities of photonics by employing wavelength division multiplexing (WDM) technology. The architecture relies on optical sampling using a highly-stable, pulsed optical source. Traditional electronic ADCs are usually limited in speed and resolution by the clock timing jitter. The photonic clock used in this technique was measured to have a timing jitter of less than 70 femtoseconds at a 1 GHz clock rate. This corresponds to a 1 Gsps ADC with 12-bit resolution.

III. PHOTONIC BEAMFORMING

In general, photonic beamforming implementations may be categorized according to the intended instantaneous bandwidth of the application. A large variety of optical methods have been proposed and demonstrated for narrowband phase-steering, similar to traditional electronic techniques, as well as for wideband time-steering such as that required by many future applications such as imaging radar systems. A collection of original papers, reprinted in [8], summarizes the state of the art circa 1996.

Microwave phase shifters and electronic methods, in their various formats, have proven quite capable of generating the proper signals for driving and steering narrowband arrays. Thus, the use of photonic beamforming techniques has evolved away from its initial thrust at replacing the function of the microwave phase shifter into a search for added functionality. For this reason and because of space constraints, photonic phase-steered approaches will not be discussed here.

For much of this decade, the focus of optically controlled array antennas has centered on the use of photonic techniques for wideband true time-delay beamforming (TTD). This is due to the fact that historically, most traditional microwave implementations of TTD beamformers have suffered from severe drawbacks such as high losses, dispersion over the operating bandwidth and large size and weight. Many times these problems have rendered TTD systems impractical. Again, there have been numerous approaches to photonic TTD beamforming. These may be grouped into two main categories – switched-path delay lines (either free-space or integrated optic) and variable propagation velocity time-delays.

Switched-path optical delay lines seek to mimic the traditional microwave solution to TTD beamforming. Optical binary switched delay lines can be carried out in various fashions. Some of those proposed and demonstrated include acousto-optic, free-space, integrated optical [9] and polarization-based switching to name a few [8]. One of the most advanced demonstrations of the switched optical delay approach utilized switched optical sources and detectors. The beamformer was capable of steering a 96 element, conformal, L-band array over ±60° with a 50% bandwidth [10]. Another impressive demonstration uses wavelength division multiplexing to significantly reduce system complexity in a hybrid microwave/photonic approach [11].
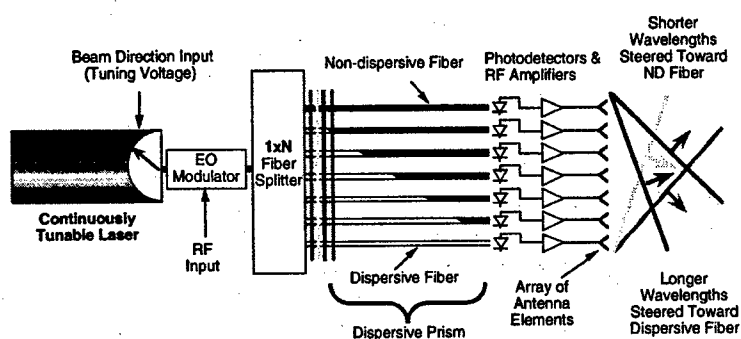
Figure 2. Schematic of a one-dimensional dispersive prism transmit beamformer.

While many of the above mentioned TTD techniques have achieved reasonably successful demonstrations, in general they have suffered from some notable drawbacks. These include system complexity, mechanical and environmental stability, the use of non-standard, custom components and inefficient use of optical power among others. These limitations have restricted the many of the demonstrations to one-dimensional, transmit systems.

The second category of photonic TTD approaches are the variable propagation velocity techniques. This method is based upon a dispersive fiber delay line proposed in [13] where a highly dispersive optical fiber is used in conjunction with a wavelength tunable laser. Changing the optical wavelength then changes the delay via the dispersion of the optical carrier signal upon which the microwave signal is modulated. Control of an array can be carried out by using a multiple wavelength source and switching in different lengths of dispersive fiber [12] or by using a wavelength tunable laser and a single length of dispersive fiber [13].

Over the past few years, we have developed a TTD beamforming system based upon dispersive fiber delay lines which alleviates many of the problems associated with photonic beamforming techniques [14]. This technique, depicted in Figure 2, uses a single tunable laser and a fiber-optic "dispersive prism" consisting multiple dispersive delay lines. The optical carrier, modulated by the desired microwave signal, is optically split to feed each element (or subarray) of an array. The fiber-optic feeds to each element have an amount of total optical dispersion corresponding to the relative position of the element in the array forming a dispersive gradient across the array. The dispersion is implemented using highly dispersive optical fiber. Upon changing the laser wavelength, the linear dispersion gradient across the array is translated to a time-delay gradient. Thus, time-delay steering of an array is carried out simply by tuning the wavelength of a single laser. This concept may be extended to two-dimensions by cascading multiple dispersive prisms.

The dispersive prism approach has been used to demonstrate both transmit and receive operation [14] which has shown squint-free, ±60° azimuthal steering over an instantaneous bandwidth of 2 to 18 GHz (see Figure 3). Two-dimensional transmit array steering squint-free steering over the full ±45° space was also demonstrated over a 6 to 18 GHz instantaneous bandwidth [15]. Multiple, independent, simultaneous beams are easily implemented by simply using additional lasers and has been demonstrated in the receive mode [16]. Due to the high time-delay resolutions attainable, the beamformer is readily adaptable to any frequency range of interest with operation in the mm-wave regime recently demonstrated [17]. Wideband nulling is also straightforward to incorporate due to the continuous, analog nature of the time-delay generation [18]. The systems have exhibited excellent amplitude and phase tracking characteristics of ~0.1 dB rms and 3.5° rms over a 2 GHz bandwidth. In general, the tracking is normally limited by the associated microwave components in the systems due to the broadband nature of the photonics.

The advantages of the dispersive prism technique lie in the simplified architecture which is optically efficient, mechanically robust, allows for easy remoting of the array and is scalable to large arrays. Additonally, rapid analog beamsteering is enabled with steering speeds on the order of 100 ns and subpicosecond time-delay resolution. Most importantly, this approach is based upon all commercially available, off-the-shelf components which have been developed by the telecommunications industry. These advantages have led to the incorporation of a two-dimensional, transmit beamformer based upon this technology into a high-level Navy demonstration array [19].
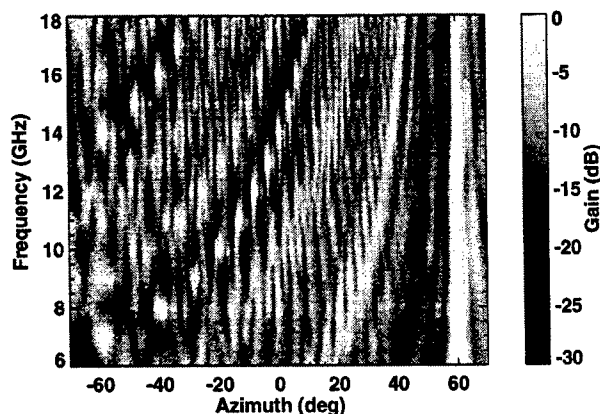
Figure 3. Measured antenna patterns of a 1-D, eight-element receive array steered to +60°.

The system was extensively field tested at an outdoor antenna range and onboard a ship.

Recent efforts at improving this beamforming approach further have centered on simplified two-dimensional architectures [20]. Research is also underway to replace the high dispersion fiber used in the system with chirped fiber Bragg gratings [21]. This leads to a significant (> 100x) increase in thermal stability of the beamformer and a corresponding decrease in the signal latency through the beamformer. An efficient receiver was recently demonstrated using this method [22].

The future challenges for the continued success of photonics techniques in array beamforming, as for any technology, involve cost issues. Practical architectures must rely on low-cost components and methods while providing a clear advanatage over competing techniques. Thus, one of the current major issues being addressed is the capability of providing a system incorporating the high-performance demonstrated in single, fiber-optic antenna remoting links into an affordable, wideband beamforming architecture.

IV. CONCLUSIONS

Photonic techniques are capable of providing improved performance and functionality for many array antenna applications. Much of this early promise has been realized and demonstrated. There are many current systems which can benefit immediately from the use of photonic technology in areas such as antenna remoting, signal processing and wideband beamforming. As the technology advances, future systems may see an even greater impact.

ACKNOWLEDGMENTS

REFERENCES

[1]. K.J. Williams, L.T. Nichols and R.D. Esman, "Photodetector nonlinearity limitations on a high-dynamic range 3 GHz fiber optic link," *Journ. Lightwave Tech.*, vol. 16, pp. 192-199, 1998.

[2]. A. Aitken, D. Shepard and D. Hall, "Calibration of wideband radar systems using fibre-optic delay lines,"*IEE Colloquium on Microwave Opto-Electronics*, London, UK, Jan. 27, 1994.

[3]. I.L. Newberg, C.M. Gee, G.D. Thurmond and H.W. Yen, "Long microwave delay fiber-optic link for radar testing," *IEEE Trans. Microwave Theory and Techn.*, vol. 38, pp. 664-666, 1990.

[4]. J.E. Roman, *et al.*, "Photonic remoting of the receiver of an ultra-high dynamic range radar," *1998 IEEE Int. Microwave Symp.*, paper TH3C-4, pp. 1521-1524, June 1998.

[5]. Lee T. Nichols, Paul D. Biernacki, and Ron D. Esman, "Dynamic range comparison of ultrawide-band photonic downconverters," *1999 Optical Fiber Comm. Conf.* , paper ThW3-1, pp. 338-340, San Diego, CA, Feb. 25, 1999.

[6]. P. D. Biernacki, *et al.*, "A four channel angle of arrival detector using optical downconversion," submitted to *IEEE Int. Microwave Symp.*, June, 1999.

[7]. T.R. Clark, M. Currie and P.J. Matthews, "Real-Time Photonic Analog-Digital Converter Based on Discrete Wavelength-Time Mapping," *1999 Int. Topical Mtg. on Microwave Photonics*, paper F-9.4, pp. 231-234, Melbourne, Australia, Nov. 17-19, 1999.

[8]. Selected papers on photonic control systems for phased array antenna, N. Riza, Ed., SPIE Milestone Series, vol. MS 136, (SPIE Optical Engineering Press, Bellingham, 1997).

[9]. K. Horikawa, *et al.*, "Silica-based integrated planar lightwave true-time-delay network for microwave antenna applications," *1996 Optical Fiber Comm. Conf.* (OFC '96), paper WB4, pp.100-101, 1996.

[10]. J.J. Lee, *et al.*, "Photonic wideband array antennas," *IEEE Trans. Antennas Prop.*, vol. 43, pp. 965-982, 1995.

[11]. A. Goutzoulis, *et al.*, "Development and field demonstration of a hardware-compressive fiber-optic true-time-delay steering system for phased-array antennas," *Appl. Opt.*, vol. 33, pp. 8173-8185, 1994.

[12]. D.T.K. Tong and M.C. Wu, "A novel multi-wavelength optically controlled phased array antenna with a programmable dispersion matrix," *IEEE Photon. Tech. Lett.*, vol. 8, pp. 812-814, 1996.

[13]. R. Soref, "Optical dispersion technique for time-delay beam steering," *Appl. Opt.*, vol. 31, pp. 7395-7397, 1992.

[14]. M.Y. Frankel and R.D. Esman, "True time-delay fiber-optic control of an ultrawideband array transmitter/receiver with multibeam capability," *IEEE Trans. Microwave Theory Techn.*, vol. 43, no. 9, pp. 2387-2394, Sept. 1995.

[15].M.Y. Frankel, P.J. Matthews and R.D. Esman, "Two-Dimensional, Fiber-Optic Control of a True Time-Steered Array Transmitter," *IEEE Trans. on Microwave Theory and Techniques*, vol. 44 (12), pp. 2696-2702, Dec. 1996.

[16]. P.J. Matthews, *et al.*, "A Wideband, Fiber-Optic, True Time-Steered Array Receiver Capable of Multiple, Independent, Simultaneous Beams," *IEEE Photon. Techn. Lett.*, vol. 10, no. 5, pp. 722-724, May, 1998.

[17].D.A. Tulchinsky, *et al.*, "Fiber-Optic Control of a Time-Steered Millimeter-Wave Transmit Array," *1999 Int. Topical Meeting on Microwave Photonics*, paper F-11.3, pp. 279-282, Melbourne, Australia, Nov. 17-19, 1999.

[18].P.J. Matthews, *et al.*, "Demonstration of a wideband, fiber-optic nulling system for array antennas," *IEEE Trans. on Microwave Theory and Techniques*, vol. 47 (7), pp. 1327-1331, July, 1999.

[19]. J. Lawrence, *et al.*, "Advanced Electronic Countermeasures Transmitter For Ship Defense," *43rd Joint Electronic Warfare Conf.*, Colorado Springs, CO, April 27-30, 1998.

[20]. M. Y. Frankel and R. D. Esman, "Reconfigurable time-steered array-antenna beam former," *Appl. Optics*, vol. 36, pp. 9261-9268, 1997.

[21].J.E. Roman, M.Y. Frankel, P.J. Matthews and R.D. Esman, "Time-Steered Array With a Chirped Grating Beamformer," *Electron. Lett.*, vol. 33 (8), pp. 652-653, April, 1997.

[22].J.B. Medberry, P.D. Biernacki, and P.J. Matthews, "Range Demonstration of an Ultra-Wideband, Continuous, Time Steered Array Using a Fiber-Optic, Cascaded Grating Prism," submitted to *2000 Int. Microwave Symp.*

Serial Feed Optical Approaches To Phased Array Antennas

H. R. Fetterman
Department Electrical Engineering, University Of California Los Angeles

H. Erlig, Y. Chang, and B. Tsap
Pacific Wave Industries

T. Itoh and Y. Qian
Department Of Electrical Engineering, University Of California Los Angeles

ABSTRACT

Photonics has been identified as an advantageous way to generate true time delays and to control phased arrays. Due to this impetus several groups have demonstrated phased arrays that were photonically controlled. Here we present the serial feed system that we have developed for optically controlling phased array antennas [1] and discuss some of the more relevant details of these systems. This serially fed architecture offers several advantages over its counterparts such as reduced cost, minimal number of photonic components, etc. However, serial systems place great constraint on the performance of the laser. This will be discussed below. Finally, an implementation with optical RF Phase Shifters is being studied which is particularly simple and versatile and promises to further reduce the complexity of the timing units in phased array systems.

The serially fed phased array was implemented in transmit [1] and receive modes [2] depicted in figures 1 (a) and (b), respectively. The systems depicted in figures 1 (a) and (b) can be broken down into 2 main sub-systems, the timing unit and the distribution unit. In the timing unit, a sequence of optical pulses of different wavelengths was generated by a rapidly tunable laser. The optical pulse sequence was reflected from a linear array of fiber Bragg gratings (FBGs) which imposed a wavelength selective time delay on the optical pulses. In this fashion the true time delays were generated. The sequence of optical pulses was subsequently distributed to the radiating elements by the distribution network. This network functioned to appropriately align the arrival time of the optical pulses on the photodetecting elements. The serial approach offered several advantages over its counterpart, the parallel architecture. As observed in figures 1 (a) and (b) this architecture minimized the number of lasers and modulators required in the system reducing cost and system complexity while maintaining full functionality.

As seen in figures 1 (a) and (b) this serial architecture is completely reliant on a rapidly tunable laser. During the past year we have examined this problem and have developed a laser system that met the requirements of the serial feed architecture. The heart of this laser system was a NEL three section laser that exhibited a 7 nm tuning band with 5 ns tuning time. By adjusting the bias currents to the DBR and Phase Control sections the laser wavelength was tunable from 1548 to 1555 nm, figure 2 (a). In figure 2 (a) the laser wavelength is shown as a function of the DBR current. During this measurement the current to the Phase Control region varied between 0 and 8 mA. Moreover, rather than using the tapped delay line indicated in figures 1 (a) and (b), which have weighted taps, we are also using a "ladder structure" shown in figure 2 (b).

We have also worked on the basic antenna array and are developing, initially, a 4x4 array using broadband quasi-Yagi antennas [3] as array elements. Four of these elements are shown in figure 3. The reflecting element in these antennas took the form of a truncated microstrip ground plane, which resulted in a compact design compatible with microstrip MMIC circuitry. The compact nature of these radiating elements resembled that of resonant antennas whereas the broad bandwidth was characteristic of travelling-wave structures. The broadband and compact nature of the quasi-Yagi antenna made it ideal as the radiating elements for the true time delay optically controlled phased array. The 4x4 array incorporating the elements described thus far is capable of performing 2D scans in addition to beam forming and related signal processing.

(a)

(b)
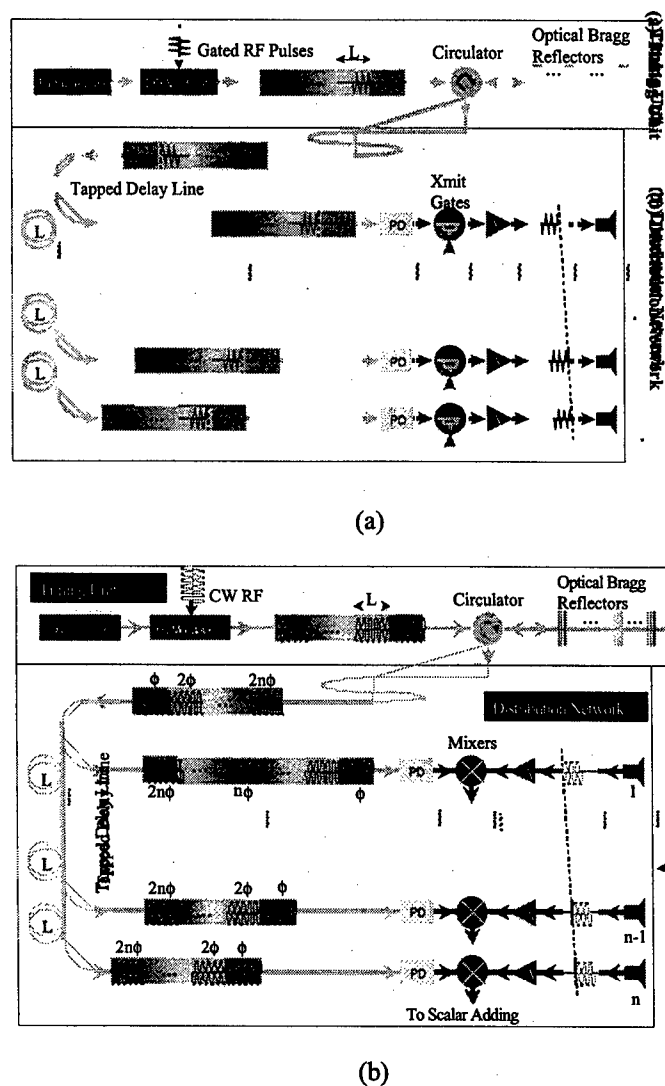
Figure 1. (a) Schematic representation of optically controlled serially fed phased array in transmit mode. (b) Schematic representation of optically controlled serially fed phased array in receive mode.

354

(a)   (b)

Figure 2. (a) Measured laser wavelength as a function of DBR current. During these measurements the current to the Phase Control region varied between 0 and 8 mA. (b) Schematic representation of "ladder" distribution network. This approach overcomes the difficulty of producing a weighted tapped line.

Figure 3. Picture showing a 1x4 array of X-band broadband quasi-Yagi antennas. These 1x4 elements form the basis for the 4x4 array.

Figure 4. Photonic RF Phase Shifter used in conjunction with the serial feed architecture. In this case the phase shifter replaces the entire timing unit with the exception of the laser.

355

Finally in a related project we have started exploring the incorporation of photonic RF Phase Shifters with the serial feed architecture. This produces a particularly simple phased array radar as shown in figure 4. As can be seen from the figure, the entire timing unit, with the exception of the laser, is replaced by the photonic RF Phase Shifter. Furthermore, in this approach a tunable laser is not required resulting in a simplification of the laser driving circuitry. The photonic RF Phase Shifters in use are shown in figure 5 (a). A microwave phase shift of 108° at 16 GHz was demonstrated from these devices as shown in figure 5 (b). In this case the phase shift was nearly linearly dependent on the phase shifter control voltage. The 108° shift was not the maximum shift obtainable from the device. The combination of phase shifter and serial feed yields a system, which is extremely inexpensive and flexible. Actual demonstrations of these approaches are now in progress.

Marker 1: 41.3¡
Marker 2: -66.8¡

(a)   (b)
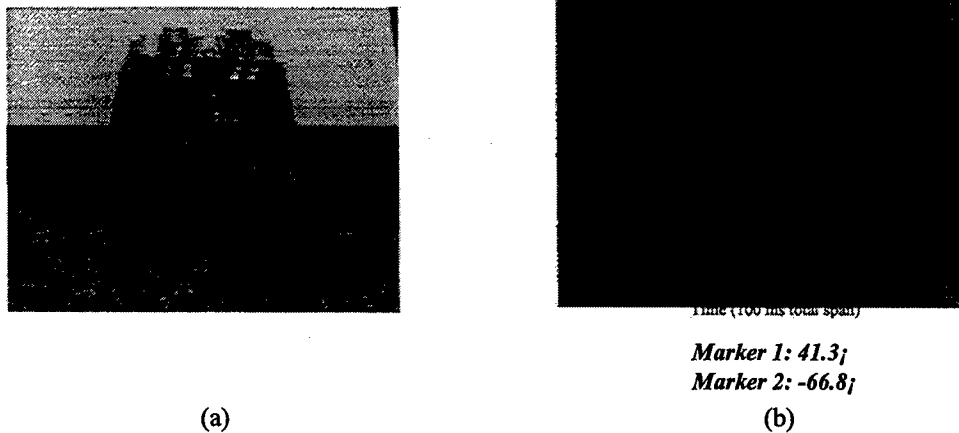
Figure 5. (a) Photograph of 4 photonic RF Phase Shifters on a chip. These devices are design from polymer modulators as the basic unit. (b) Microwave phase measured by a vector network analyzer at the output of the phase shifter. The phase shifter was driven by a 50 Hz triangular wave causing the microwave phase to vary accordingly.

ACKNOWLEDGEMENTS

REFERENCES

1. Y. Chang, B. Tsap, H. Fetterman, D. Cohen, A. Levi, I. Newberg, "Optically Controlled Serially Fed Phased-Array Transmitter," *IEEE Microwave and Guided Wave Letters*, vol. 7, no. 3, pp. 69-71, 1997.
2. B. Tsap, Y. Chang, H. Fetterman, A. Levi, D. Cohen, and I. Newberg, "Phased-Array Optically Controlled Receiver Using a Serial Feed," *IEEE Photonics Technology Letters*, vol. 10, no. 2, pp. 267-269, 1998.
3. Y. Qian, W. Deal, N. Kaneda, and T. Itoh, "Microstrip-fed quasi-Yagi antenna with broadband characteristics," *IEE Electronics Letters*, vol. 34, no. 23, pp. 2194-2196, 1998.

PROGRESS IN OPTICAL ROTMAN BEAMFORMER TECHNOLOGY

R. A. Sparks, ANRO Engineering, Inc.*
63 Great Road, Maynard, MA 01754
Tel: (978) 897-2601; Fax: (978) 897-2642; r.sparks@ieee.org

Abstract

An historical overview of optical Rotman beamformer technology is presented, beginning with the early developments and extending to the present Several practical demonstrations have confirmed their utility in selected applications where continuous electronic scanning is not required.   Integrated optic circuit implementations should permit significant size and weight reductions.

Introduction

The design of RF and microwave beamformers and feed networks for phased array antennas has been well documented in the literature [1]. Applications of photonic beamformers [2],[3], during the past two decades have been critically examined as well. Many of the demonstrated optical implementations, however, may prove to be awkward for seamless insertion in practical phased array environments. The development of the microwave Rotman lens [4] more than 35 years ago has led subsequently to several experiments that have demonstrated the optical equivalent performance of the Rotman lens principle. Recent progress in the photonic technology of Rotman beamformers is summarized in this paper.

Technical Discussion

The application of fiber optics to matched-delay filters and signal processing was first proposed at the San Diego Naval Ocean Systems Center (NOSC) laboratories in 1977, according to Pappert [5]. Novel beamforming and angle of arrival demonstrations were initiated in a series of optical experiments and theoretical analyses [6] conducted over a period of several years. The use of optical true-time-delays for RF direction finding in the 200 - 1800 MHz frequency range showed that multiple, simultaneous, and frequency independent directional responses could be obtained. Both multimode and singlemode fiber optic transmission lines were used, together with multiple GaAlAs laser sources and uniquely coupled silicon avalanche photodiodes (APD's) in 'Rotman-like' configurations. Figure 1 is a block diagram of the optical bench experimental setup for an eight-laser, multimode fiber, direction finding system constructed in the laboratory that was described as an optical two-transversal filter. A similar experiment was carried out with singlemode fiber components, and the relative performance results compared.

It appears that Cardone [7] was the first to have recognized the equivalence of these optical true-time-delay implementations and the microwave Rotman lens beamforming network developed earlier at the Rome Air Development Center, Hanscom AFB, Massachusetts. In Cardone's experiment, a three-beam optical Rotman beamforming network was fabricated in fiber, and partially tested over the 2.0 - 4.0 GHz frequency range with an eight-element linear array of horn radiators. A photograph of the bench-top laboratory experiment in Figure 2 illustrates the interconnection of multimode fiber optic components used. Computed throughput loss for the breadboard hardware was within a few dB of measured results.

Beginning in the early 1980's, interest in light weight beamformers for satellite communications motivated Paul et al [8] to investigate photonic techniques at COMSAT Laboratories. A proof-of-concept 4x4, space-fed true-time-delay optical beamforming network [9] was demonstrated with pointing directions of 0°, ±10° and + 15° from the normal to the antenna array. A photograph of the compactly constructed hardware is shown in Figure 3, and the measured far field pattern results are illustrated in Figure 4.

An elegant free-space holographic Rotman lens experiment was undertaken by Curtis a few years later [10] for ultra-wideband array antenna beamforming applications. Figure 5 illustrates the design of the optical circuit. Volume holographic beamsplitters and combiners are arranged on geometric arcs corresponding to the modified Rotman lens design equations. In the diagram, the RF modulated laser diode source is connected by means of a network of optical fibers and switches to the selected beam pointing direction. The diffractive optical elements on the feed contour split the microwave modulated optical input signal evenly in power which then radiate across the free-space lens. The output ports on the array-side focal contour consist of phase transmission holograms specifically designed for this purpose. Each hologram contains eight spatially separated gratings recorded in a common holographic substrate, each of which is pigtailed to a photodiode and 10 GHz RF amplifier for coupling to the antenna radiators. A more environmentally rugged, integrated optic Rotman lens concept, Figure 6, has been proposed for millimeter wave array antennas. A low loss material wave guiding layer such as glass replaces the free-space region of the lens with the holograms bonded to the contoured surfaces.

More recently, Sparks et al [11] carried out a detailed breadboard system demonstration using a 4-beam fiber optic Rotman lens, Figure 7, and a wideband linear array antenna. Commercially available fused biconic couplers and sixteen precise lengths of singlemode fiber were integrated with optical detectors and a telecommunications Fabry-Perot laser transmitter. The beamformer and test hardware were packaged into the antenna housing, Figure 8, and azimuthal antenna patterns for four adjacent columns of uniformly illuminated radiators were recorded on an outdoor far-field test range. Measured results when compared with computed patterns were in excellent agreement.

In the prototype experimental work that followed [12], comprehensive system performance results of a prototype fiber optic Rotman lens are described. The beamformer was designed and fabricated using silica glass planar waveguide couplers, and precision lengths of single mode optical fiber. Figure 9 is a photograph of the prototype beamformer hardware with the top covers removed to show the mounting provisions for the sixteen 1x8 and eight 1x16 couplers. The form-factored optical Rotman was integrated with a sixteen column, wideband linear antenna array to generate eight fixed beams with steering angles corresponding to ± 7.5°, ± 22.5°, ± 37.5°, and ± 52.5°. Azimuthal patterns of the integrated antenna beamformer system mounted on a test pedestal, Figure 10, were recorded for all beam pointing directions at frequency increments of 500 MHz over the 2.0 to 4.0 GHz band. The measured pattern data were compared again with calculated results giving excellent correlation.

Conclusions

Optical Rotman beamformers may be the first photonic implementation to find insertion in actual system applications. Integrated optic circuits have been designed [13] that offer practical realizations where multiple simultaneous independent beams are required. Continuous scan, optical Rotman implementations [14] have been described in the literature, also. For planar array applications slab-waveguide photonic beamforming networks have been demonstrated [15].

References

[1] R. C. Hansen, *Phased Array Antennas*, John Wiley & Sons, Inc. ;1998.
[2] D. K. Paul, "Photonic Beamforming & Steering for SATCOM Phased Arrays", WFFT Workshop Notes, 1999 IEEE MTT-S International Microwave Symposium; June 1999.
[3] P. J. Matthews, "Practical Photonic Beamforming", Tech. Digest MWP'99, pp. 271-274; 17-19 November 1999.
[4] W. Rotman and R. F. Turner, Wide-Angle Microwave Lens for Line Source Applications, pp. 623-632, Trans. IEEE AP-S, Vol. 11; November 1963.
[5] S. A. Pappert, "Ultra-Wideband Direction Finding Using Fiber Optic Transversaal Filters", NOSC Technical Report 1161; March 1987.
[6] S. A. Pappert, et al, "A Fiber Optics Matched Delay Filter for RF Direction Finding", J. Lightwave Tech., Vol. LT-3, pp. 273-275;1985.
[7] L. Cardone, "Ultra-Wideband Microwave Beamforming Technique", Microwave Journal, pp. 121-131; April 1985.

[8] [2] D. K. Paul, "Optical Technology for Communications Satellites", Encyclopedia of Telecommunications, Vol. 14, pp. 71-110, F. E. Froehlich ed., Marcel Dekker, Inc., New York; 1997.

[9] D. K. Paul, et al, "Space-Fed Optical Beam Forming Network: A Proof-of-Concept Demonstration for C-Band Phased Array Antenna", Proc. URSI Intl. Symposium on Electromagnetic Theory, pp. 531-533; August 1992.

[10] D. D. Curtis, "Holographic Rotman Lens for Phased-Array Antenna Beamforming", Proc. SPIE #2481-17; 17 April 1995.

[11] R. A. Sparks, et al ,"Experimental Demonstration of a Fiber Optic Rotman Beamformer", Tech. Digest MWP '98 pp. 127-130, October 1998.

[12] R. A. Sparks, et al, "Eight-Beam Prototype Fiber Optic Rotman Lens", Tech. Digest MWP '99, pp. 283-286; 19 November 1999.

[13] R. A. Sparks et al, "Optical Rotman Beamforming Lens for Multi-function RF/Microwave/Millimeter Wave Antenna Systems", Phase I SBIR Final Report, Contract No. N0014-97-C-0095; 15 October 1997.

[14] J. J. Lee and R. R. Stephens, "Photonic Wideband Beamformer for Multibeam Arrays", AP-S Symposium Digest, pp. 1409-1412; 1998.

[15] I. Ogawa, et al, "Two-Dimensional Multiple Beam Forming Using Slab-Waveguide-Implemented Photonic Beam Forming Network", Tech. Digest MWP'96, pp.197-200; 3-5 December 1996.
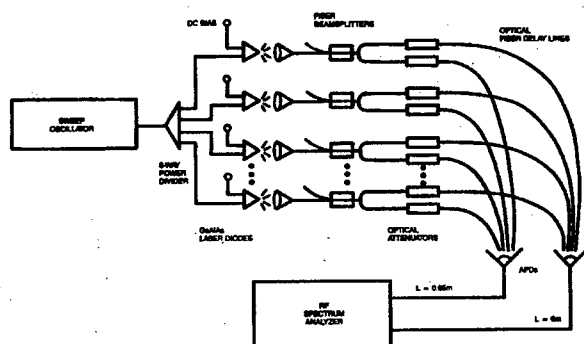
Figure 1 Optical Transversal Filter Block Diagram [5]
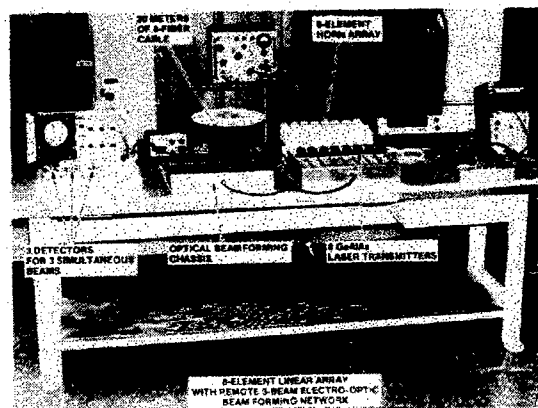
Figure 2 3-Beam Optical Rotman Beamformer [7]
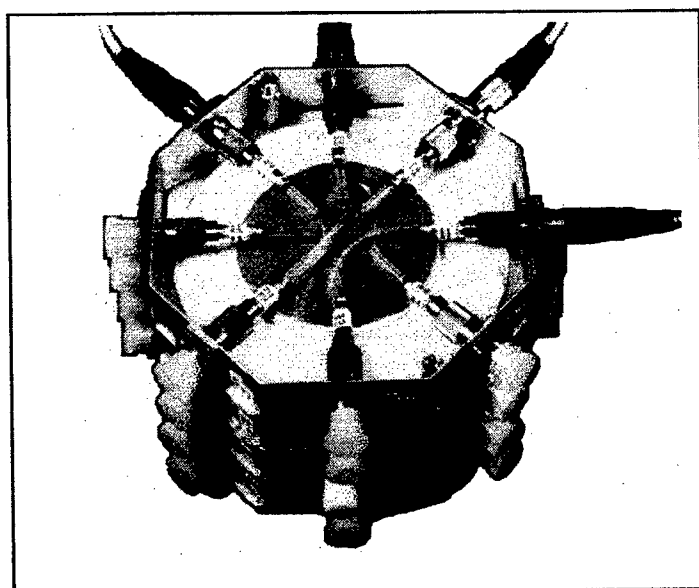
Figure 3 4x4 Space-Fed Optical BFN [9]
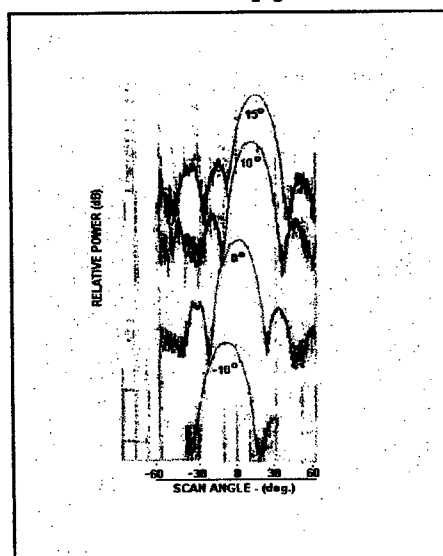
Figure 4 Far-Field Patterns [9]
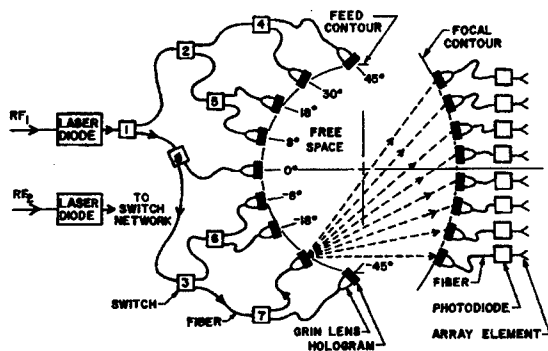
Figure 5 Holographic Rotman Lens Geometry [10]
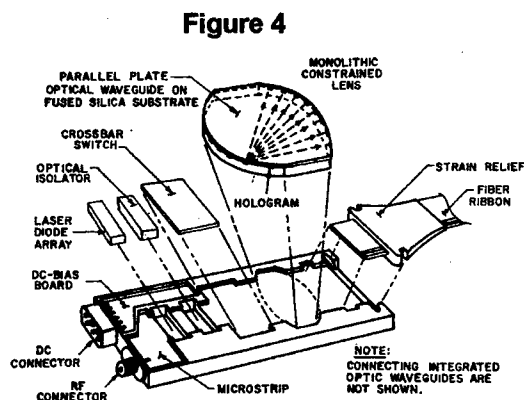
Figure 4

Figure 6 Integrated Opic Rotman Lens Concept [10]
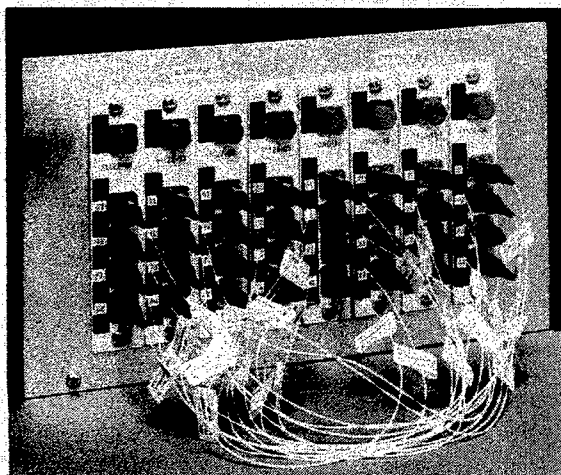
Figure 7 Breadboard 4x4 Fiber Optic Rotman Beamformer [11]
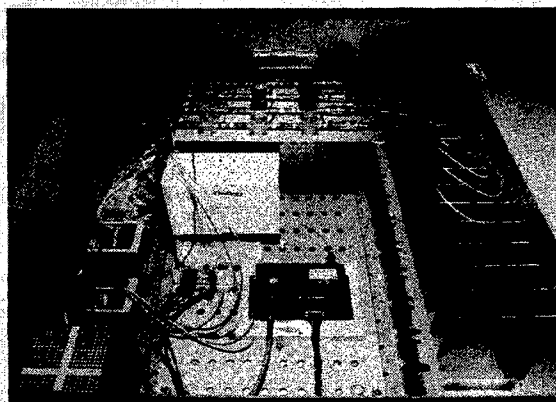
Figure 8 Breadboard Antenna Beamformer Packaged Hardware [11]
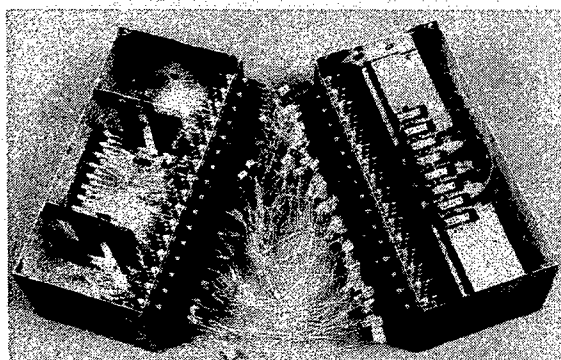
Figure 9 Prototype 8-Beam Fiber Optic Rotman Beamformer [12]

Figure 10 8-Beam Antenna Beamformer Test System [12]

Recent Advances in Opto-Electronic Signal generation

Lute Maleki , Steve Yao, Shouhua Huang, Yu Ji, Vladimir Ilchenko,
And Meirong Tu

Jet Propulsion Laboratory, California Institute of Technology
4800 Oak Grove Dr., Pasadena, CA 91109
Tel: 818-354-3688 Fax: 818-393-6773 Email: lute.maleki@jpl.nasa.gov

In the past few years the application of optoelectronic techniques to microwave signal generation has culminated in the development of the Opto-Electronic Oscillator (OEO)[1-4]. This unique device utilizes continuous light energy from a laser, in conjunction with an opto-electronic feedback loop including a long fiber delay, to produce high spectral purity signals at 10 GHz and higher frequency. This performance is useful in a variety of communications and radar applications, but is particularly useful in photonic phased arrays. This is because the output of the OEO may be selected to be an electrical reference, or a high frequency reference modulated on an optical carrier. The latter configuration can provide for significant efficiency in photonic phased arrays, since otherwise a laser transmitter system would be required for the distribution of the electric signal.

We have demonstrated the operation of OEO in several different configurations, previously. This includes the operation of a dual loop OEO, a coupled OEO (COEO) [5], and an OEO based on an integrated laser/modulator device. In this paper we will report on the demonstration of a compact 10 GHz OEO and its acceleration sensitivity performance. This latter results are of particular interest in application with moving platforms. Finally we will briefly describe our recent work towards the realization of an OEO on a chip.

COMPACT OEO

The first realization of the Opto-electronic oscillator was based on the use of a solid state (YAG) laser, and an external LiNbO$_3$ Mach-Zehnder modulator, together with a long fiber optic delay loop [1]. While the performance of this oscillator at 10 GHz was superior to all free running oscillators at 100 kHz from the carrier, the design was useful only as a laboratory demonstration. The use of the YAG laser was necessary due to the high insertion loss of the modulator, and the fiber delay loop was on its original spool of about 12 inches in diameter.. One other bulky component in the feedback loop of the first OEO was a tuned cavity bandpass filter, required to select the operation frequency. To make the OEO useful in practical applications, these three components of the oscillator had to be replaced with smaller ones.

In order to develop the compact OEO, we utilized a module from Nortel consisting of a DFB laser, and a semiconductor Mach-Zehnder modulator. Compared to the YAG laser, the realtive

intensity (RIN) noise of the laser was relatively large. We measured the RIN at the laser output to be –110dBc/Hz at 1 Hz, and –135 dBc/Hz at 10 kHz. At this level, the RIN was the limiting factor in the phase noise performance of the OEO. Results of the OEO phase noise are shown in.
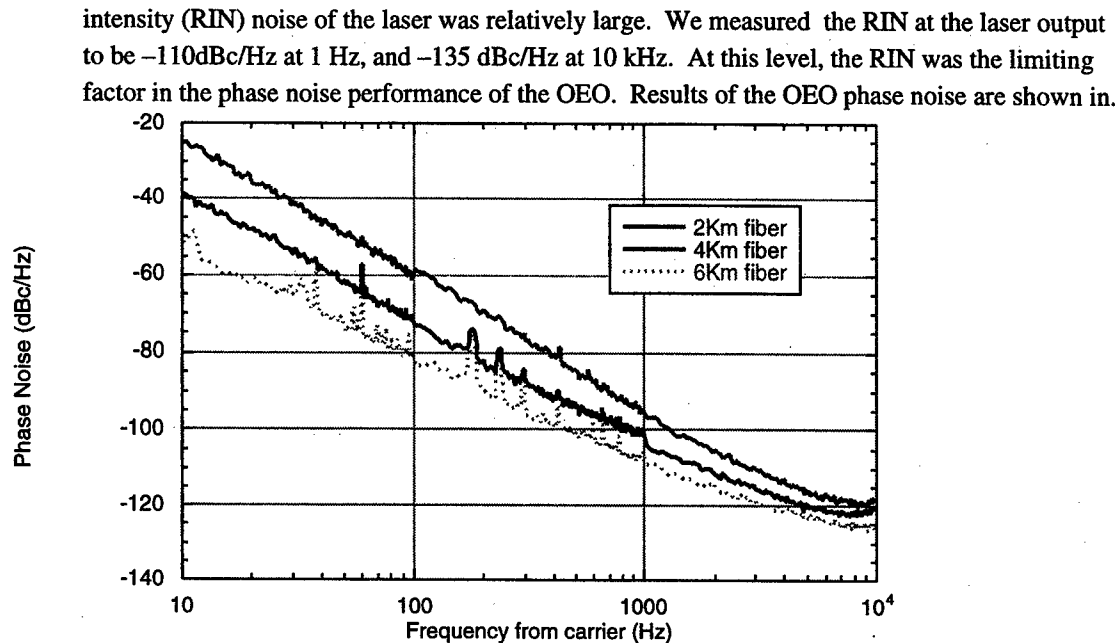
Figure 1. Noise Performance of the OEO with DFB laser.

Figure 1. The three curves correspond to optical fiber delay lines of 2, 4, and 6 Km, respectively. Notice that at about 10 KHz, the noise of all three lengths of delay are about –120 dBc. This is a deviation from the expected performance, as previously detailed in our analysis, and in experiments. The culprit here is the RIN noise of the laser which sets the floor achievable, regardless of the fiber loop length. With the floor set at about –120 dBc/Hz, longer lengths of fiber reduce the close to carrier noise more effectively, resulting in varying slopes for the three lengths of fiber. Despite this limitation, the phase noise performance of the oscillator, even with the short (2 km) length of fiber delay is comparable with some of the highest performance 10 GHz oscillators.
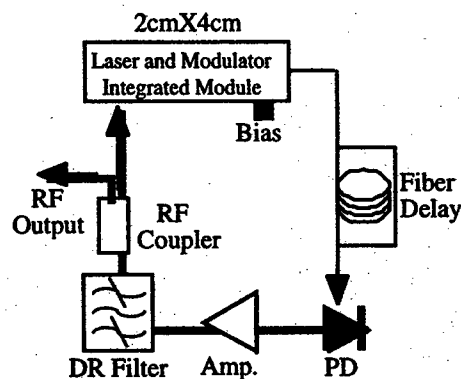
Figure 2. Schematic of the Compact OEO.

An important element in the packaging of the compact OEO is the fiber spool. It has been observed previously that winding fiber on the spool may lead to losses chiefly due to microbends. In fact our first attempt to wind the two kilometer length of fiber on a spool with diameter 9 cm resulted in a total optical loss of 30 dB. Nevertheless we developed a process for winding the fiber which at the end produced no additional loss to the 0.2 dB optical loss in this length of fiber.

The final element in the redesign of the OEO for a compact package was the 10 GHz bandpass filter. Since the OEO is essentially a multimode device, with its mode spacing inversely proportional to the length of the fiber, long lengths of fiber delay, required for lowest phase noise performance, need very high Q filters to select a single mode from all other propagating modes. For example, with a 1 km fiber length, the mode spacing is 200 kHz, requiring a filter with narrow enough bandwidth to select a mode for operation at a single frequency. Although a multi-loop scheme can be used for single mode selection [2], it increases the complexity and size of the OEO. For the realization of the compact OEO we used an ultra-narrow-bandwidth filter constructed with a dielectric resonator (DR) for single mode selection.

Dielectric resonator (DR) loaded high-Q narrow-band filters can be designed to occupy a total volume corresponding only to about 5 percent of a waveguide filter with an equivalent performance. The resonators can have a room temperature Q as high as 10^4. In addition, the temperature coefficient of a DR filter is exceptionally low, about ± 1 ppm/°C at room temperature [10].

Figure 3. Photograph of the packaged Compact OEO.

We designed and fabricated such a filter by placing a 8.7mmX4mm high dielectric constant ($\varepsilon r=35$) ceramic cylindrical disc at the center of an aluminum cavity with a size three times of the DR disc. Using a design tool based on the finite element method, we found that the TE_{04} mode has the frequency of 10GHz, and more than 90% energy can be confined in the disc. To realize optimum mode matching, a tiny wire loop probe was used for both mode excitation and coupling. By carefully adjusting the wire loop, critical coupling was achieved. At critical coupling, the insertion loss was minimized and the external Q of the filter was optimized. Fig.2 shows the filter structure, as well as the TE_{04} mode field distribution in the disc and the cavity. Measured bandwidth of this filter is 2MHz at 9.56GHz with 6dB insertion loss, with a Q about 5,000. This filter allows us to use up to 6km fiber in the OEO loop for a minimum 50 dB sidemode suppression ratio.

The packaged compact OEO which includes all components, and the fiber coil, is shown in Figure 3.

OEO-ON-CHIP DESIGN

Despite the superior performance, the size and power of the demonstrated OEO's must be reduced even further, beyond the compact OEO, for space and commercial applications. Our objective in the near future is to design and build an integrated OEO on a semiconductor chip that includes a semiconductor laser, an electro-absorption modulator, a photodetector, and a microsphere cavity. The optical microsphere is used as a high-Q resonator to replace the long optical fiber and still achievie low phase noise in a micro size. In addition, we will eliminate the power hungry RF amplifier in the opto-electronic feedback loop, by resonate-impedance matching between the electro-absorption modulator and the photodetector. The end product will be a chip sized mm-wave oscillator with low phase noise and high performance.

High-Q microspheres [6,7]with whispering-gallery modes are a novel type of solid-state optical cavity. The light in these cavities circulates inside the dielectric near the surface, undergoing continuous total internal reflection. The losses corresponding to the attenuation of light in fiber-grade silica allow for the energy storage time ranging from a few microseconds in the visible range, to potentially ~100 microseconds in the fiber-optic communication band at 1.55 micron. With the recently developed efficient waveguide coupling elements[8,9], high-Q microspheres can effectively replace fiber-optic delays in the OEO with the length up to 25km, achievable with a Q factor of 19 million at 30 GHz.

References

1. X. Steve Yao and Lute Maleki, 'High frequency optical subcarrier generator,' Electron. Lett. 30 (18), pp1525-1526 (1994).

2. X. Steve Yao and Lute Maleki , "Opto-electronic Oscillator," J. Opt. Soc. AM. B, Vol. 13, No. 8, pp. 1725-1735 (1996).

3. X. S. Yao and and L. Maleki, "Opto-electronic oscillator for photonic systems", IEEE J. Quantum Electron., Vol. 32 (7), pp. 1141-1149 (1996).

4. X. Steve Yao, L. Maleki, and J. Dick, "Opto-electronic oscillator incorporating carrier suppression noise reduction technique," 1999 IEEE Frequency control symposium, France (1999)

5. X. Steve Yao and L. Maleki, "Dual microwave and optical oscillator," Opt. Lett., Vol. 22, No. 24, pp.1867-1869 (1997).

6. V.B. Braginsky, M.L Gorodetsky, and V.S. Ilchenko, Phys lett a, 1989,v.137,p.393-397

7. M.L. Gorodetsky, A.A. Savchenkov, and V.S. Ilchenko, Opt Lett 21: (7) 453-455 (1996)

8. V.S.Ilchenko, X.S.Yao, L.Maleki, "High-Q microsphere cavity for laser stabilization and optoelectronic microwave oscillator", Proceedings SPIE, vol.3611, p.190-198 (1999)

9. V.S.Ilchenko, X.S.Yao, L.Maleki, "Pigtailing the high-Q microsphere cavity: a simple fiber coupler for optical whispering-gallery modes," Opt. Lett., Vol. 24, No. 11, pp. 723-725 (1999).

10. D. Kajfez and P. Guillon, "Dielectric Resonator," Artech House 1986

Optically Controlled Phased-Array Antenna Using Wavelength-Selective True Time Delay

B. Jalali and S. Yegnanarayanan

Optoelectronic Circuits and Systems Laboratory
Dept. of Electrical Engineering, UCLA
Los Angeles, CA 90095-1594
Phone: 310-825-9655, Fax: 310-206-2239
E-mail: jalali@ucla.edu

Abstract: A novel all-optical tunable optical delay line device is used as a true-time-delay generator for squint-free beam steering in optically-controlled microwave phased-array antennas. The mapping of optical wavelength to the microwave beam direction permits a hardware efficient architecture for the optical control unit that can easily scale to large aperture antenna arrays. The performance of a complete optically controlled phased array antenna system employing such single-chip time-delay devices is reported. Extension to two-dimensional antenna arrays with independent control of azimuth and elevation by using mid-stage optical wavelength conversion is proposed and demonstrated. An optical true-time-delay steered two-element X band antenna was assembled to verify the wide instantaneous bandwidth operation.

Key Words: Phased array antenna, True time delay, Optically controlled Beam Steering

Phased-array antenna is an enabling technology in modern radar and communication systems. Phased-array antennas offer many advantages including steering without physical movement, increased scan flexibility in two dimensions, precise elemental phase and amplitude control to obtain low spatial sidelobes, the potential for large peak and average power, and the ability to degrade gracefully due to the distributed nature of the array. The use of optical control techniques for phased-array antennas promises to alleviate many of the problems associated with traditional electronic steering systems. The unique properties of optical fiber that are suitable for this application include the ability to store large bandwidth analog signals (10s of GHz) for long times (tens of microseconds), the immunity to EMI and low mass and volume which is especially important in airborne applications. In particular, optical techniques are able to provide true time-delay beam steering that is essential for squint-free wide instantaneous bandwidth operation of high performance radar systems [1][2]. Initial efforts to realize photonic time-delay was using space-division switches along with switched laser/photodetector pairs. However, this approach suffered from excessive splitting losses and required large component count of lasers and photodetectors. In order to reduce the overall system complexity there has been a trend to utilize the wavelength domain of the optical carrier [3-5]. The first proposal to utilize the optical wavelength was by Richard Soref who suggested using chromatic dispersion in optical fibers for time-delay beam steering. Potential disadvantages include the requirements of several kilometers of fiber to realize nanosecond delays, and the concomitant bandwidth limitations of highly dispersive links. Lembo and coworkers at TRW proposed another novel approach that made use of the optical wavelength. Bragg gratings written in the fiber core were used to reflect light. Tuning the laser to the wavelength corresponding to the appropriate grating generates the desired time delay. A circulator extracts the time-delayed reflected signal and feeds it to the antenna elements. However, there exists a tradeoff between grating reflectivity and grating bandwidth. The reflectivity of a grating is proportional to the grating region length. Thus, a large grating length is required to obtain high reflectivity. At the same time, the spectral bandwidth of the grating is inversely proportional to the grating length. Thus, a high reflectivity grating has a narrower spectral bandwidth. Since the grating should be able to accommodate the RF modulation sidebands within the spectral bandwidth, this places restrictions on the maximum possible reflectivity.
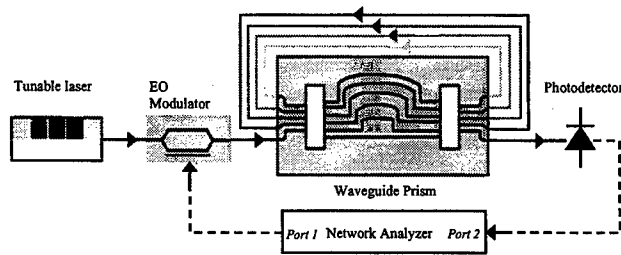
Figure 1: Experimental setup used for swept frequency measurement of the hybrid TTD device.

We proposed a key technique to enable optical control of wide-band arrays, using a novel single-chip switch-less photonic time-delay device where the microwave time-delay is selected by the optical wavelength [5]. Since all the optical energy is self-routed to the desired time-delay, this technique can easily scale to large arrays. The device we proposed eliminated the requirements for optical circulators, fiber gratings or dispersive fibers. The device can be fabricated on a single substrate using integrated waveguides, and furthermore imposes no direct trade-off between the loss and the RF bandwidth. High wavelength resolution and hence large number of delays may be realized in a single compact device. Time delays of the order of nanoseconds may be realized with sub-picosecond resolution using integrated delay lines on-chip while larger delays may be obtained off-chip.
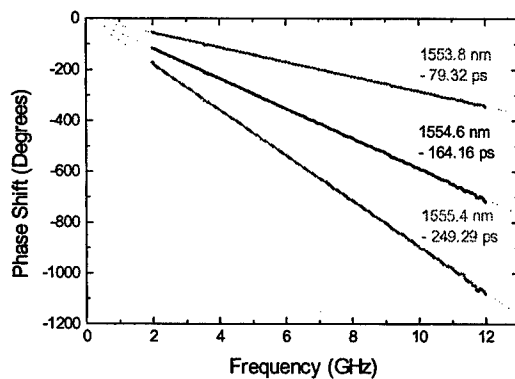
Figure 2: Swept frequency measurement of hybrid TTD device. Slope corresponds to the selected time delay.

Our first experiment to demonstrate the wavelength-selective time-delay device used an 8 channel waveguide grating with a channel spacing of 0.8 nm (100 GHz). The input and output to the device were coupled to fiber ribbon arrays and symmetric input and output fibers were connected through the external fiber delay lines to realize a hybrid delay device as shown in figure 1. The input external cavity tunable laser was modulated with the RF signal. The output from the device was fed to a photodetector and then RF phase measurements were performed using a network analyzer. The RF phase versus frequency is linear over the entire measured bandwidth of 12 GHz, demonstrating that this is a true-time-delay. The slope of the RF phase versus frequency gives the time delay. By tuning the optical signal wavelength the time delay suffered by the RF signal is varied as shown in figure 2. The stability of the RPF passband with respect to temperature variations is a critical issue and must be evaluated. Temperature induced shift in the passband frequency arises primarily due to the temperature dependence of the refractive index. This can be estimated to a reasonable degree of accuracy by the linear dependence. The temperature dependence of the passband frequency is then given by equation

$$\frac{df}{dT} = \frac{c}{n_c^2 \lambda} \frac{dn_c}{dT}$$

For the best silica-based waveguide technologies, the temperature coefficient of refractive index is $1 \times 10^{-5}/°C$, resulting in a thermal shift of approximately 1.03 GHz/°C.

We have recently proposed and demonstrated a novel technique to extend this optical wavelength-selective time-delay device to two-dimensional arrays while completely eliminating optical-electrical conversion losses [6]. This represents a departure from conventional approaches to optically controlled

Figure 3: Optically controlled two-dimensional beam steering system using a wavelength converter between azimuth and elevation beam steering units.

two-dimensional beam-steering where the optical signal at the output of the azimuth beam steering unit (BSU) is converted to an electrical signal in a photodetector, followed by an optical modulator to transfer this electrical signal to the elevation BSU. This introduces optical-electrical conversion loss and more importantly adds to the system complexity. The approach we propose for a two-dimensional optically controlled beam steering system is shown in figure 3. A tunable laser is used to select the time-delay through each stage. Each stage consists of a wavelength-selective time-delay. Typically one would need a separate photodetector after the first time-delay device, followed by an optical modulator, to transfer the analog signal to the second time-delay.

In our technique however, the broadband analog signal is transferred from one wavelength to the other using wavelength conversion. This eliminates the optical/electrical/optical conversion loss. The general method of applying a wavelength converter to transfer analog signals while remaining in the optical domain is the novel part in this work. In our particular experimental demonstration the wavelength conversion is achieved by using cross-gain modulation in a semiconductor optical amplifier (SOA) [7]. Since the gain of the SOA saturates with an increase in optical intensity, an analog signal at λ_1 modulates the gain of the SOA. A CW beam at λ_2 will sample this gain modulation, thereby copying the analog signal from λ_1 to λ_2. The maximum frequency of operation is limited only by the stimulated emission lifetime and wavelength conversion at frequencies as high as 40GHz has already been demonstrated. Thus, by cascading two individual time-delay devices, each with its own control wavelength, one can set the time delay for the azimuth and elevation to achieve independent two-dimensional optically controlled beam-steering as shown in figure3. The analog signal is inverted in the wavelength conversion process but this is of no consequence in radar applications.

In the experimental setup, the optical carrier is an external cavity tunable semiconductor laser. The RF output is applied to the Mach-Zehnder (MZ) modulator. The amplitude modulated optical signal at λ_1 is fed to a wavelength-selective time-delay chip. This true-time-delay generator chip consists of an arrayed waveguide grating (AWG) with recirculating feedback. Tuning the laser wavelength changes the time-delay experienced by the microwave signal. The optical signal at the output of the first time-delay stage serves as the pump for the SOA. The second-stage tunable laser at λ_2 serves as the CW probe signal of the SOA. Through wavelength conversion, the broadband analog signal at λ_1 is transferred to λ_2, while the internal gain in the SOA ensures loss-less operation. The optical signal at λ_2 is now applied to the second stage wavelength-selective time-delay chip. Swept frequency measurements of the RF phase versus RF frequency confirm the slope
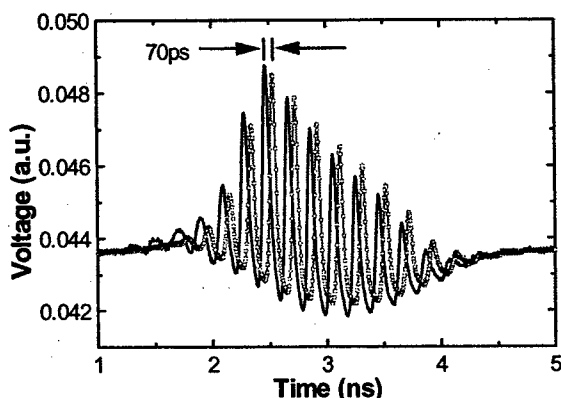
Figure 4: Time-domain response using 2ns pulsed 5GHz carrier. The response shifts by 70ps when azimuth control wavelength is changed from 1547.6nm to 1553.2nm
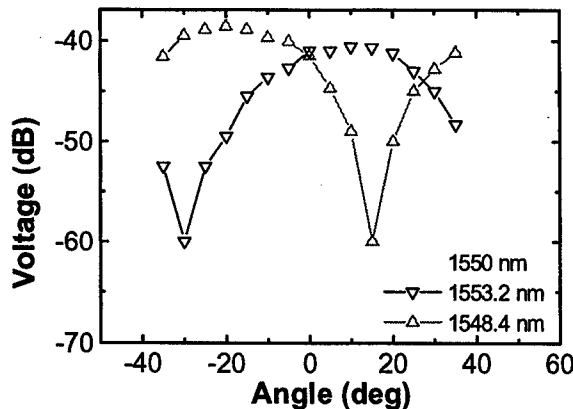
Figure 5: Angular beam pattern measurements for 2-element X-band antenna from 8-12 GHz. True time-delay beam steering by tuning optical wavelength is shown.

of each curve corresponding to the selected RF time-delay. Azimuth laser (λ_1) and elevation laser (λ_2) wavelengths are tuned to select individual time-delays. As expected, the time-delay is independent of the microwave frequency over the measured frequency range of 0-6GHz.

In order to verify the wide instantaneous bandwidth of this optical control technique, we performed time-domain measurements using an electrical pulse of 2ns on a 5GHz carrier. The time-domain data in figure 4, shows one pulse delayed by 70ps with respect to the other, while demonstrating wide instantaneous bandwidth. To further verify the wide instantaneous bandwidth, we performed a transmitter experiment. We assembled a 2-element transmitter antenna array that is driven by an optically controlled time-delay device. Angular and radial field patterns are obtained by using a horn antenna as a receiver inside a compact test range. The measured beam position is steered by tuning the optical wavelength as shown in figure 5. A 1ns pulsed 10GHz carrier signal was used. This wideband signal had frequency components extending from 8-12GHz. An important issue with this proposal is the nonlinearities that may be introduced in the wavelength converter. However, recent results have demonstrated low distortion wavelength converters for analog signals using four-wave mixing in SOA.

In conclusion, we have proposed and demonstrated a new optical technique to achieve low-loss independent control of phased-array transmitters while providing a wide instantaneous bandwidth. The mapping of optical wavelength to the microwave beam direction permits a hardware compressive architecture for the optical control unit that can easily scale to large aperture antenna arrays.

References

1. W. Ng, A. A. Walston, G. L. Tangonan, J. J. Lee, I. L. Newberg, and N. Bernstein, "The First Demonstration of an Optically Steered Microwave Phased Array Antenna using True-Time-Delay", *IEEE Journal of Lightwave Technology*, Vol. 9, pp 1124-1131, 1991.
2. H. Zmuda and E. N. Toughlian (Eds.) *Photonic Aspects of Modern Radar*, Artech House, 1994.
3. R. Soref, "Optical dispersion technique for time-delay beam steering", *Applied Optics*, 31, 7395-7397, 1992.
4. J. Lembo, T. Holcomb, M. Wickman, P. Wisseman, and J. C. Brock, "Low loss fiber optic time-delay element for phased-array antennas", *Proceedings of the SPIE*, 2155, 13-23,1994.
5. S. Yegnanarayanan, P. D. Trinh, and B. Jalali, "Recirculating Photonic Filter: A Wavelength Selective Time-Delay for Phased-Array Antennas and Wavelength Code-Division Multiple Access", *Optics Letters*, 21, 740-742, 1996.
   B. Jalali and S. Yegnanarayanan, "Method and apparatus for a wavelength selective true-time delay for an optically controlled device" United States Patent 5,793,907.
6. S. Yegnanarayanan and B. Jalali, "Optically controlled two-dimensional beam steering system for phased-array antennas", *IEEE MTT-S International Microwave Symposium Digest 1999*.
7. T. Durhuus, B. Mikkelsen, C. Joergensen, S. Danielsen, and K. E. Stubkjaer, "All-optical Wavelength Conversion by Semiconductor Optical Amplifiers", *IEEE Journal of Lightwave Technology*, 14, 942-954, 1996.

370

RF-Photonic Links for Local-Oscillator Distribution and Frequency Conversion

Daniel Yap, Willie W. Ng, Harry T.M. Wang, Keyvan R. Sayyah and David L. Persechini
HRL Laboratories, 3011 Malibu Canyon Road, Malibu, CA 90265
phone: 310-317-5360, fax: 310-317-5485, e-mail: dyap@hrl.com

Abstract

RF-photonic approaches have been evaluated for distributing electrically generated local oscillator (LO) signals as well as for performing frequency conversion with optically generated LO signals. For high-fidelity distribution of electrically generated signals, a switched RF photonic link was measured to have a residual phase noise of -145 dBc/Hz at an offset of 10 KHz from the X-band carrier. The switch isolation was better than 80 dB. For efficient frequency conversion with the RF-photonic approach, a relative conversion loss of 6.2 dB was measured for an LO modulation index of 0.97.

Introduction

A switched photonic network can be used to distribute local-oscillator signals from high-performance synthesizers to frequency converters in remotely located receiver and exciter modules. Although it would be possible to locate a set of LO synthesizers directly at each of the many frequency converters, this approach would lead to undesireable cost in terms of size, weight and power consumption. Use of centralized synthesizers whose LO signals are remoted to the antenna apertures by means of microwave cables or waveguides is limited by their bulk and dispersion. Photonics offers an attractive alternative because optical fiber cables are light weight and have minimal RF dispersion, low signal attenuation and large signal bandwidth.

Photonic remoting can be combined with optically generated LO signals and RF-photonic frequency conversion to further enhance the system functionality. Benefits of this RF-photonic approach include the large bandwidth, capable of millimeter-wave or THz LO frequencies, the ultra-high isolation between the incoming RF and LO signals, and the reduced number of mixer stages. In addition, a frequency converting link utilizing an optically generated LO is free of LO spurs or intermodulation products that would typically be observed in alternate approaches, that rely on modulating an electrically generated LO onto a lightwave carrier.

Local-Oscillator Distribution

In an RF-photonic network for distributing local-oscillator signals, a set of RF synthesizers might generate the LO signals for the various sensors. Photonic transmitters modulate the LO signals onto lightwaves carried in optical fibers. These fibers then distribute the LO signals to the destination sensors where they are detected and selected by means of optoelectronic switches. The photonic architecture has the beneficial characteristics of versatile connectivity, supporting both broadcast and point-to-point delivery of the LO signals. The capability of selecting a given LO signal from a set of candidates, which are all delivered to the frequency converter, is especially useful for multi-band or multi-function systems.

A two-channel photonic unit was demonstrated for evaluating the performance of a switched photonic link in distributing LO signals.[1] This unit, illustrated in Figure 1, consists of two separate photonic transmitter channels that are connected by optical fibers to a single 2-to-1 optoelectronic switched receiver. The self-contained, AC powered unit was constructed solely from commercially available components, to represent the capability of the current state-of-the-art in photonics. Each of the external-modulation transmitters is comprised of a distributed feedback (DFB) laser, an electro-optic modulator and a microwave amplifier, which supplies the LO drive signal for the modulator. Other components include circuits to control the laser current, the modulator bias voltage and the laser temperature. The optoelectronic switch consists of two photodetec-

tors whose microwave outputs are combined by means of a 2-to-1 Wilkinson combiner. The bias voltage of each photodetector is switched by CMOS circuits to enable the photodetector to output the LO signal ("on" state) or to suppress that signal ("off" state). A low-noise microwave amplifier is placed after the optoelectronic switch.
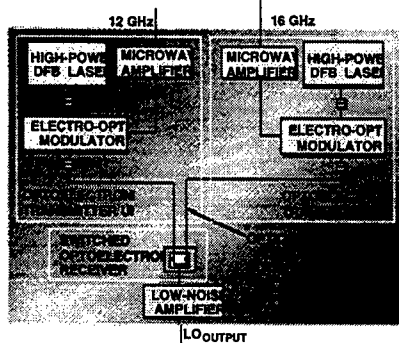
Figure 1. Block diagram of LO-distribution demonstration unit.

Each channel of the switched photonic link is set to have an overall gain of + 2 dB at 12 GHz by adjusting the output powers of the lasers and the gains of the microwave amplifiers. A link consisting of the photonic components alone would have a gain, magnitude of S_{21}, of approximately - 27 dB. Approximately 15 dB of amplification is provided by the preamplifiers before the modulators. The remaining amplification needed to achieve the desired link gain is provided by the low-noise, post-detector amplifier. The input and output ports of the photonic unit are matched quite well to a 50Ω impedance. The magnitudes of S_{11} and S_{22}, the input and output reflection coefficients, are less than -10 dB over the 8-16 GHz frequency range. To achieve low phase noise, it is important to minimize the reflections that may occur at any of the microwave or optical junctions in the unit.

The isolation of the optoelectronic switch has been measured by applying a 12 GHz LO signal to one input port of the photonic unit and a 16 GHz LO signal to the other input port. The output of the photonic unit is then observed with a microwave spectrum analyzer. The level of the 16

GHz output is somewhat lower (by 5 dB) than that of the 12 GHz output, because of the limited frequency response of the photodetector that was used, although high-power-handling photodetectors that have a flat response to beyond 20 GHz are available. The optoelectronic switch isolation was tested by alternately switching off the bias voltage to the photodetector of each channel by means of a CMOS circuit. When a channel is switched off, its associated LO signal is not observable above the noise floor of the measurement set-up, which is more than 80 dB below the signal level (as seen from Figure 2). The measured isolation of the optoelectronic switch compares well with that of a PIN-diode microwave switch, whose best performance likewise is approximately 80 dB.
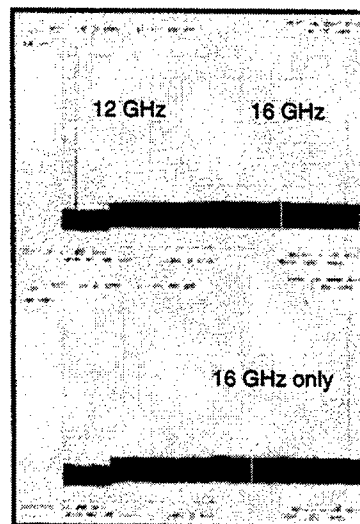
Figure 2. Measured isolation of optoelectronic receiver switch.

The photonic unit was characterized with some custom, low-noise synthesizers built by Raytheon. The absolute phase noise was measured with a Hewlett-Packard phase-noise test set. The resultant phase noise was measured for offsets as large as 40 MHz from a 12 or 16 GHz LO signal. The phase noise measured for LO signals carried through each of the two channels of the photonic unit is nearly indistinguishable from the phase

noise measured for an LO signal supplied directly from the synthesizer. A measurement of the residual or relative phase noise also was made, by splitting the LO output from a single synthesizer, passing one part through the photonic unit and using the other part as the reference for a phase-noise test set. The residual phase noise measured with an initial version of the photonic unit is shown in Figure 3. The residual phase noise is -140 dBc/Hz at frequency offsets of 10 KHz and larger from a 16 GHz carrier. This result shows that the photonic unit can be used to distribute LO signals for anticipated high-performance radar systems of the future. The residual phase noise is as low as -145 dBc/Hz at frequency offsets greater than 100 KHz. Some of the oscillations in phase noise that are observable at the large offsets could be due to the measurement set-up, since those oscillations are not seen in the prior measurements of the absolute phase noise.

the normal performance variations of amplifiers from a single manufacturing lot.

The demonstrated approach of photonic distribution and optoelectronic selection of the LO signals can be extended to systems that have many different LO frequencies and frequency converter destinations. Each additional LO frequency can be accomodated simply by adding another photonic transmitter and adding another switched photodetector to the optoelectronic switch. Addition of more frequency converter destinations requires splitting of the LO-modulated lightwave signal among more optoelectronic switches. Lasers with higher optical output power and electro-optic modulators with greater modulation efficiency could be used to ensure that the low noise levels are maintained. The photonic components are wideband. Thus, the LO frequency range covered by a photonic distribution network is limited primarily by that of the microwave amplifiers therein.

Figure 3. Measured residual phase noise of RF-photonic link.

Figure 4. Compact 9-to-1 Optoelectronic Receiver Switch.

At small offsets from the carrier, the residual phase noise of the photonic unit is due primarily to 1/f noise in the microwave amplifier that follows the optoelectronic switch. When a low-noise amplifier is used at that location, the residual phase noise measured for the photonic unit is below - 145 dBc/Hz at an offset of 10 KHz from a 9.6 GHz carrier. The residual phase noise measured for a second low-noise amplifier alone is acutally 1-2 dB worse than the noise measured for the entire photonic unit. This difference represents

To investigate the feasibility of extending this approach to large numbers of LO frequencies, a breadboad optoelectronic receiver switch was fabricated. This hybrid integrated breadboard, shown in Figure 4, combines FET switched optoelectronic photodetector chips, MMIC amplifier chips and a 9-to-1 impedance matched RF combiner. This receiver switch accomodates 9 different LO signals with frequencies between 10.5 and 16.0 GHz. The impedance-matched combiner was used to maximize the signal transfer from a single active input line to the output. In contrast, with conventional combiners, much of the signal from the selected LO input would be diverted into the other non-selected LO input ports, and thus lost.

The compact 2" x 2" size of this breadboard demonstrates that optoelectronic receiver switches could reside as part of an RF frequency converter module located at the antenna aperture.

Photonic Frequency Conversion With Optically Generated Local Oscillator

The approach for LO distribution described above can be extended to also perform frequency conversion in the photonic domain. The electrically generated LO is already modulated onto a lightwave carrier, by the electro-optic modulator. A second electro-optic modulator, to which the RF signal is applied, can be cascaded into the link to achieve the frequency conversion. Typically, a Mach-Zehnder interferometric modulator is used, as illustrated in Figure 5. The raised-cosine transfer function of the modulator effectively multiplies the LO and RF components.[2] With this approach, the modulation index, M, is generally quite small (M<<1) and results in inefficient frequency conversion. However, the electro-optic modulator used for impressing the LO onto the lightwave carrier can be overdriven to increase the effective LO power. In this case, the conversion loss can be as low as 3-6 dB.[3]

$$I_{IN} = I_o[1 + M\cos(\omega_{LO}t + \phi)] \qquad I_{OUT} = \frac{I_{IN}}{2L_{MOD}}(1 + m\sin\omega_{RF}t)$$

Photocurrent:

$$I_o = \frac{\alpha I_o L_{RF}}{2}\{1 + m\sin(\omega_{RF}t) + M\cos(\omega_{LO}t + \phi) \pm \frac{1}{2}mM\sin[(\omega_{LO}\pm\omega_{RF})t + \phi]\}$$
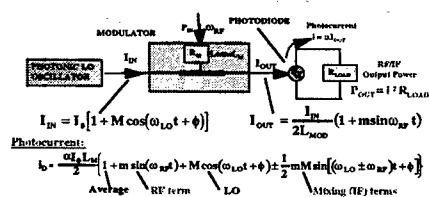
Figure 5. Illustration of photonic frequency conversion with an electro-optic modulator.

An optically generated local-oscillator signal can be achieved by heterodyning at a photodetector, which serves as a photonic mixer, two frequency-locked lasers whose optical wavelengths differ by the desired LO frequency. The heterodyning technique for LO generation enables a modulation index (M) of 1 to be achieved when the output powers of the two lasers are balanced properly. Note that when M=1, the frequency conversion loss is as low as 6 dB for a photonic link

with a net link gain of 0 dB. This RF insertion loss would be comparable to that obtained presently with electronic PIN-diode mixers. As shown in Figure 6, we have verified this result by heterodyning with two diode-pumped solid-state lasers, which have narrow emission linewidths. Useful frequency conversion, however, also requires LO signals of low phase noise. Such low-noise LO signals can be achieved by optical injection locking the two lasers to different spectral lines of a third, mode-locked laser.[4] Since the phase fluctuations of the individual lines of the mode-locked laser are highly correlated, the phase noise of the heterodyne LO signal is minimized.
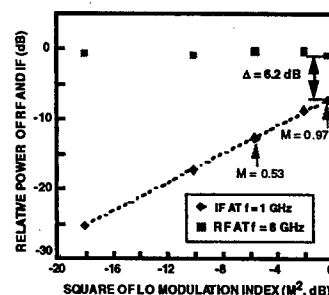
Figure 6. Measurement of photonic frequency conversion efficiency with optically generated local oscillator signals.

Conclusions

RF-photonic links for remoting, LO distribution, frequency conversion and LO generation can achieve the low phase noise, high switch isolation and high conversion efficiency needed for phase-array systems.

References
[1] D.Yap, H.W. Wang, and Y.M. So (to be published).
[2] G.K. Gopalkrishnan, et. al., IEEE Trans. Microwave Theory and Tech., v.41, p.2383 (1993).
[3] C.K. Sun, et. al., IEEE Photonics Technol. Lett., v.8, p.154 (1996).
[4] R.T. Logan, SPIE Proc., v.2844, p.312 (1996).

HIGH-PERFORMANCE LOSSLESS RF FIBER OPTIC LINK

Irwin L. Newberg
Raytheon Company
Electronic Systems
P.O. Box 902
El Segundo, CA 90245
310.334.6834

Abstract
This paper describes an RF high-performance wide-bandwidth fiber optic link that achieves significant – compared to current commercial-off-the-shelf links – improvements in key RF link parameters of bandwidth, gain, signal-to-noise ratio, noise figure, spur-free dynamic range, and noise.

Introduction
A significant breakthrough has been achieved: a wide-bandwidth RF fiber optic link without RF amplifiers that provides RF performance capability without compromising the amplifier performance when cascading the link with typical commercial off-the-shelf (COTS) RF amplifiers. This has been accomplished using several newly developed laboratory optical components and techniques to achieve a lossless wide-bandwidth, low noise and high dynamic range RF fiber optic link. The application of these links to RF signal transmission and reception, antenna remoting, multibeam/ frequency active phased-array radars, low-noise RF oscillators, RF test targets, and areas of analog signal processing can give the RF system engineer/designer a new capability for use in many RF systems. RF fiber optics have the important advantages of very wide RF bandwidths (up to 100 GHz), low susceptibility to electromagnetic interference and crosstalk, and low loss in the optical fiber (less than 0.8 dB/km).

Link Description[1]
A fiber optic link consists of a laser light source transmitter that can be RF amplitude-modulated, an optical fiber transmission medium, and a photodiode detector receiver that converts the light intensity to electrical current. The link can be treated and analyzed as an RF subsystem with the same key parameters or figures of merit used to describe an RF amplifier: bandwidth (BW), gain (G), signal-to-noise ratio (SNR), noise figure (NF), spur-free dynamic range (SFDR), and noise (N). The RF analog photonic link can be implemented by using either direct or external modulation. In the directly modulated link, the RF signal input directly amplitude-modulates an optical source (typically a diode laser transmitter). In the externally modulated link shown in Figure 1, the laser source is operated in a CW mode and the RF input amplitude-modulates the optical carrier input to the external modulator (the cascaded laser and external modulator are the transmitter). After transmission, the RF signal is recovered (demodulated, detected) via a photodiode detector (receiver) located at the link output port. While a directly modulated link is simpler to implement, the external modulation link offers more potential for achieving improved RF performance over wide bandwidths, especially for frequencies that are beyond about 5 GHz.
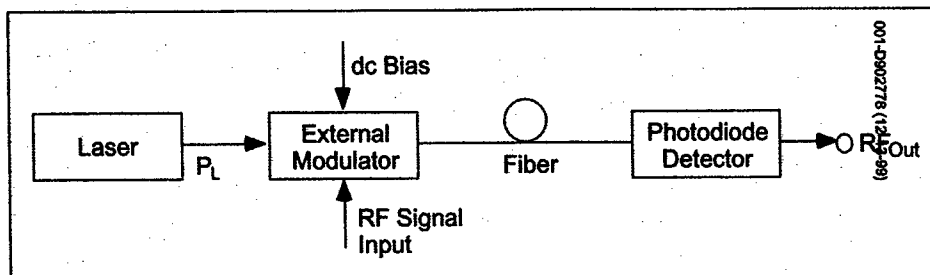
Figure 1. Generic RF analog externally modulated fiber optic link

Since only the parameters that are intrinsic to the photonic link are relevant to the link performance, the microwave amplifiers are not included in Figure 1. In practice, low-noise pre-amplifiers and post-amplifiers are typically employed before the modulator input and after the photodetector output, respectively, and those are used to establish the overall RF system parameters. The RF performance of a photonic link cascaded with microwave amplifiers can be calculated by treating the intrinsic photonic link as an RF subsystem/component with its associated RF parameters.

The laser in the externally modulated link shown in Figure 1 has an output optical power denoted by P_L. The laser can be a distributed feedback (DFB) semiconductor diode laser (operating at optical wavelenths λ of $\lambda = 1.3$ μm, micrometers, or 1.55 μm) with a fiber-coupled P_L in excess of 50 mW that can be integrated with a Mach-Zehnder (MZ) optical external modulator into a single transmitter subsystem. Using a DFB laser at $\lambda = 1.55$ μm, the optical transmitter can be put in a small package and made reliable and able to work in relatively rugged environments. In the link, an electro-optic modulator made from lithium niobate (LiNbO$_3$) is used to impress the RF signal onto the optical carrier. Although an assortment of linearized LiNbO$_3$ modulators have been reported in the literature and demonstrated, the basic MZ configuration remains the most popular design[2]. At present, MZ modulators with bandwidths in excess of 20 GHz are available as COTS items. Their optical damage threshold (at $\lambda = 1.3$ μm or 1.55 μm) is in excess of 250 mW. Other modulators (such as MZ semiconductor, MZ polymer, and electroabsortion) have not been developed and used as yet to the same extent as those using LiNbO$_3$.

Improvements in Link Parameter[1]

The external modulated link will benefit most from improved components. The link RF parameters of insertion gain, SNR, NF, and SFDR all improve with increased optical power incident on the photodetector.

With the availability of higher-power semiconductor diode lasers at optical wavelengths (λ) of $\lambda=1.3$ μm and $\lambda=1.55$ μm for use in externally modulated fiber optic links, the improvements in the link parameters are limited by the photodetector when it is excited by high amounts of incident optical power and by the increased laser relative intensity noise (RIN). With the current developments in photodetectors that can maintain a high responsiveness with low intermodulation distortion at high incident optical power levels, higher power lasers, and more efficient external modulators, large improvements in the key link parameters are possible, provided laser RIN effects can be mitigated.

Beside the four link RF figures of merit (G, SNR, NF, and SFDR), N is also key to improved link RF performance. Two types of optical noise can affect link parameters: laser RIN and detector shot noise. This N parameter affects all but the gain parameter and its effect increases with higher link optical power and the associated increased optical power on the link photodiode detector. Increased photodetector current achieves increased signal (S) and also produces increased noise.

Five techniques improve the five key link RF parameters by increasing the S and reducing the N:

- Use high levels of optical power with photodetectors that can effectively use these high optical power levels.

- Cancel laser RIN using a dual balanced photodetector receiver so the link is not RIN-limited and can thus use higher optical power levels to achieve improved link parameters.

- Reduce close-in laser noise via a feedback loop around the laser. The RIN noise from lasers decreases rapidly for frequencies greater than about a 1 MHz; thus, it is the close-in noise that needs to be significantly reduced.

- Use a photodetector without the usual 50 Ω load resistor on the output. The RF output of the link is coupled directly to an RF component that provides the link load resistance.

- Use an efficient external modulator with dual optical outputs to make available the light that is normally lost in a single output modulator.

All of these techniques have been described in the literature in general and for the link in this paper they are proposed to be used in combination in an externally modulated link that could have low, or even a small positive, RF

376

gain, with large improvements in the other link parameters. Improvements also could be achieved in directly modulated links using techniques 1, 3, and 4.

Typical commercial-off-the-shelf (COTS) components used in external modulator links have parameter ranges of BW = 18 GHz, G = –30 to –60 dB, SNR = 140 to 150 dBc, NF = 40 to 60 dB, and SFDR = 100 to 110 dB. Using the combined listed techniques to improve link performance, externally modulated links (without RF amplifiers) could achieve RF performance of BW = 2 to 18 GHz, G = 0 dB, SNR = 168 dB/Hz, NF = 19 dB and SFDR = 119 dB/Hz$^{2/3}$. These RF parameter values are calculated and based on the optical parameters of currently developed and available laboratory prototype components.

Description of Link Parameter Improvement Techniques[1]

When the RIN noise of the link establishes the noise floor, the link is said to be "RIN-limited." As long as the link is RIN limited, increasing the optical power will not improve link parameters (except gain) because both signal and RIN increase by the same amount since they are both functions of the square of the optical power and associated detector current. It is desirable for the link to be detector-shot-noise-limited because shot noise increases as a linear function of the detector current, not the square of the current like RIN noise. Thus, for a shot-noise-limited link, an increase in optical power will improve link parameters since the signal is increased by the optical power squared and the noise goes up only linearly. The use of a balanced detector to cancel RIN noise can allow the link to be shot-noise-limited. This increased link performance is then limited by the amount of RIN cancellation, optical power available, optical power levels that can damage the modulator, and photodetector power handling capability and associated linearity.

A noise-cancellation scheme that uses dual balanced detectors with a dual output external modulator minimizes RIN with increased optical power. This type of arrangement was used to demonstrate appreciable RIN suppression for a 2–18 GHz link driven by a laser diode.[3] In a balanced MZ or directional coupler modulator, two complementary output ports each have the RF modulation on the light output. These two modulator outputs allow the capturing of all the optical power from a MZ-type modulator. In an MZ single output port modulator, half the optical power is lost in the modulator substrate because the light is coherently added at the output end of the MZ modulator optical waveguide structure. This adding of the light produces the desired RF signal input AM modulation on the light carrier. Because optical power is conserved, the intensity at one output port of the dual output port modulator increases when the intensity at the other decreases, so that the RF modulated signals at each detector are 180° out of phase. The photodetectors are connected so that common-mode signals will not be passed to the amplifier, but differential signals will. The feedthrough RIN of the laser, which is in-phase at each of the output ports, will thus be rejected by this scheme and the RF signal modulation power, which is out of phase, will be added. This approach is similar to that used to cancel local oscillator noise in an RF balanced mixer.[4] The use of the dual detector will cancel the RIN that feeds through for both close-in and far-out frequencies. The RIN will be cancelled depending on how well the line lengths from the dual output modulator are matched (made equal) in length from the modulator output to where the dual detector outputs are joined. Any path length difference will decrease the RF signal-to-noise output because of the RF phase shift introduced.

The feedthrough RIN is the laser noise that is not modulated on the link RF signal inputs. Because of the noise frequency response, the close-in noise and the far-out noise need to be considered separately. The close-in noise from a laser that is modulated onto the RF signal can be significant and can be cancelled using a low-frequency (<1 MHz) feedback technique, similar to that used in diode-pumped solid state lasers.[5] This technique for laser RIN close to the carrier (<1 MHz) uses a low frequency detector to sample the laser optical signal output and feeds the detected signal back 180° out of phase to cancel (reduce) noise. This is performed on the optical output of the laser before the output goes to external modulator; thus, the low-frequency RIN is not modulated on the link input RF signal, and noise better than –135 dBc/Hz at frequencies below about 1 MHz can be obtained. The higher-frequency far-out noise is much lower than the close-in noise and will, for good DFB lasers, generally not be a problem. For a well-isolated DFB diode laser, the RIN is approximately –165 dB/Hz for frequencies above 1 MHz. At frequencies around the laser resonant frequency, the RIN is about –150 dB/Hz. This laser noise that is modulated on the RF signal input is not cancelled and is not generally considered in the description of dual balanced detector RIN reduction in the literature. Thus, using the dual detector alone without reducing low- and high-frequency noise will not produce a low-noise link. Thus the use of lasers with low far-out RIN and laser close-in RIN feedback cancellation are needed for a low-noise link.

Link SNR is improved if, instead of using a 50 Ω resistive load on the detector, the RF output of the detector is connected directly to a low-noise post amplifier located very close to the detector so the input impedance of the post amplifier becomes the load for the detector(s). The closer this RF amplifier is placed to the photodiode detectors, the farther the amplitude ripple caused by any mismatch will be moved out of the RF frequencies of interest. The amplifier output impedance can still be 50 Ω, which is needed to match RF components that follow the link. Removing the 50 Ω detector resistor increases the link output signal by 6 dB and shot noise by 3 dB, for a net signal-to-noise increase of 3 dB.

Conclusions

This paper has described a fiber optic link that can meet the demanding parameters of the latest state-of-the-art RF systems and also bring with it all the many advantages of wide bandwidth, low loss in fiber, light weight, small size, no electromagnetic interference (EMI), remoting capability, and monolithic integration using fiber optics. Previously, the link parameters restricted the use of RF fiber optic links to limited applications in RF systems. When developed, the link described herein will open the way for the use of RF fiber optic links in many RF system applications, and could provide for significant link cost reductions obtained by large-scale usage.

To quantify the link described in this paper, take a typical RF wide-bandwidth amplifier with a gain of 25 dB and measure its performance parameters of wide bandwidth, gain, signal-to-noise ratio, noise figure, spur-free dynamic range, and relative close-in and far-out noise. Now place the RF amplifier at the input to the fiber optic link described herein and measure the same parameters for the cascaded combination of amplifier and link. When the combination has substantially the same performance parameters as the amplifier measured alone, that link will have met the needed RF performance.

The challenge now is to develop this fiber optic link, which could be used in current and future radar, electronic warfare, and communications RF systems for both military and commercial use in ground, air, sea, and space applications.

Acknowledgment

References

1. Newberg, I.L., Hayes, R.R., Krikorian, K.V., Loo, R.Y., Ng, W.W., Rosen, R.A., "RF Wide Bandwidth Lossless High Performance Low Noise Transmission Link," Raytheon/HRL patent disclosure No. PD-R98047, filed June 1999.

2. Bridges, W.G. and Schaffner, J.H., "Distortion in Linearized Electro-optic Modulators," *J. Lightwave Technol.*, Vol. 43, no. 9, pp. 2184–97, Sept. 1995.

3. Wanuga, S., Ackerman, E., McDonald, J., Prince, J., and Hogue, D., "A High Performance Fiber-Optic Link using a Y Balanced EO Modulator and Various Laser Sources," *Government Microcircuits Applications Conf.* (GOMAC), Las Vegas, Nevada, Nov. 10–12, 1992, pp. 305–308.

4. Newberg, I.L., "Video-Frequency Noise Measurements in Microwave Crystal-Mixers," *Report 7848-R-4*, Electronics Systems Laboratory, Massachusetts Institute of Technology, August, 1959.

5. Kane, T.J., "Intensity Noise in Diode-pumped Single Frequency Nd:YAG Lasers and its Control by Electronic Feedback," *IEEE Photonic Technology Letters*, Vol. 2, pp. 244–46, 1990.

Photonics for airborne phased array radars

D. DOLFI*, D. MONGARDIEN*, S.TONDA*, M. SCHALLER and J. CHAZELAS
*Thomson-CSF Central Resarch Laboratory,
Domaine de Corbeville, 91401 Orsay Cedex
Thomson-CSF Detexis, Microwave Photonics Department,
2 Avenue Gay-Lussac, 78851 Elancourt France

1 Introduction

In future generation phased array radars, signal distributions will have to fulfill strict performance criteria. These include high isolation from both electromagnetic interference and crosstalk between module or subarray feeds with increased instantaneous bandwidths; dramatic reduction in size and weight regarding present fielded radars; and performance compatible with growing requirements such as low phase noise and high dynamic range.

Photonics and microwave technologies offers new opportunities for controlling many thousand array elements together with handling the wide bandwidth of shared aperture antennas. Photonics technologies will provide an interconnect solution for future airborne phased array radar antennas, which have conformality, bandwidth, EMI immunity, size,and weight requirements increasingly difficult, if not impossible, to meet using conventionnal electrical interconnect methods.

Future system requirements are reported together with results of newly developed high performance wideband analog microwave links and of demonstrated approaches for True Time Delay architectures.

2 Airborne phased array radar requirements

Airborne radars for fighter aircrafts are equipped with **active arrays** implemented, in the future, conformally to the aircraft structure.

Three main applications have been identified for conformal arrays in aircraft radars :

- **Side-looking arrays**

These arrays are disposed on the aircraft body can be desirable for backwards and / or up-downwards visibility. It appears that the curvature radiuses at these points of the body are around half a meter in the body section and can be assimilated to straight lines along the aircraft axis. Then degenerated conformal arrays are to be implemented, which can be made by stacking linear rows of T/R Modules.

- **Wing-edge arrays**

These arrays are disposed onto the leading edge of the aircraft wings or vertical fin can be desirable to increase the transverse or vertical dimension of the front array, giving access to higher separation capability between targets.

- **Nose-cone arrays**

This concept is more advanced than the previous one, it requires a 3D active array with full polarisation control on transmit/receive modes (except in circular polarisation).

Main requirements for next generation airborne radars include low phase noise (< 135 dBc/Hz) and high linearity (> 100 dBc).

Benefits and drawback associated with optical RF distributions

In this context, the main benefits of optical distributions are :
➢ a high layout flexibility, with easy 3-D, little interference with mechanical structure,
➢ high performance, independent from mechanical shape complexity, with losses only at interfaces and EMC / EMS immunity,possibility to easily mix microwave and digital signals on the same fibers and compatibility with true time delays, i.e. very wide bandwidths.

Constraints on / from Optical Distributions for conformal arrays and possible drawbacks are compared with corporate RF feeds for planar arrays as a reference.

➢ very low power levels are available at interfaces, requiring distributed gains.
➢ components require at both ends of the optical link additional power consumption / dissipation

Consequently, flexible and low cost optical interfaces for several hundreds of T/R modules must be developed according to antenna layout and constraints : environment, reliability, loss dispersion control including optical fiber connectors.
Instantaneous frequency bandwidth (up to 30 %) of future multifunction systems will require the implementation of Time Delay BeamForming Networks (TDBFN). These TDBFN require an analog optical processing of microwave signals. For a radar detection in the same direction as for emission, the optically carried transmitted and received signals, must travel through the same optical architecture in order to permit in-phase addition, over a large frequency. In this case, since these signals are spread over a dynamic range as large as 120 dB, the implementation of highly linear optoelectronic links is necessary.

3 Impedance matched microwave optical links

In order to overcome some drawbacks described above, an impedance matched complete wideband link has been built for measurements[1]. In order to improve gain and noise figure, one additional hybrid LNA stage has been designed and integrated by Miteq. Optical components from Thomson-CSF LCR are closely connected to MMICs in order to reduce parasitic bonding effects. Second generation will include Peltier cooler into transmitter housing and soon further multichip controller will be dedicated to thermal, optical power and bias control.
Active Impedance matching principle brings 15 to 20 dB inherent improvement compared to conventional technique. Additional amplification provided by Miteq LNA and intrinsic MMIC gain pushes the overall improvement up to 35 to 40 dB with respect to existing commercially available links.

Results obtained for S21 overall link using the second generation of MMICs show:
➢ A gain of 10 dB and a in the 200 MHz-12 GHz bandwidth limited today by the aviability of DFB laser.
➢ A noise figure below 20 dB in the same bandwidth and a SFDR of 70 dB measured in a 1 MHz bandwidth

A second objective for the optical links is to fabricate small size modules integrating all the requested functions like voltage and current control or thermal regulation (only for laser). To integrate, a specific housing design has been carried out with special features to integrate chip controllers, Peltier cooler, microwave and optical connectors. Different kinds of housing are in progress for assessing the component installment.

4   Optically controlled phased array antennas: Thomson–CSF approaches

4.1.1   Switched delay lines based TTD architectures

Switched architectures are obtained by combining the use of wavelength mutliplexing and fiber length switching[2]. Emerging optical switching matrix structures allow architectures to be implemented, not on base 2 but on base 4.

Expected advances with these types of components are an enhancement of losses through the use of solid-state optical amplifiers and the optimisation of the fibre/substrate interfaces. The wavelength dimension offered by optics, significantly reduces the number of switching components, taking advantage of the matrix dimensions and a proportional number of optical wavelengths.

InP based 4*4 matrices have been developped providing low power consumption, high switching speed and low insertion loss.

4.1.2   2D Optical True time optical delay architectures

The operating principle of our 2D optical architecture is detailed in ref 3
In this approach the time delays are based on polarization switched free space delay lines using 2D spatial light modulators (SLM). Experimental demonstration of an optically controlled phased array antenna, operating between 2.5 and 3.5 GHz. The 2D architecture is implemented with 6 SLMs of 4 x 4 pixels. It provides 32 delay values (5 bits), an analog control of the phase [0,2p] and permits the control of a 16 element phased array antenna. Far field patterns at different frequencies have been superposed for a given scan direction, showing no beam squint.

4.1.3   Receive mode approach

In order to overcome the limitation of linearity of commercialy avaliable optical links, we proposed an original architecture in which a channelized microwave local oscillator (LO), optically carried, is used for mixing with the received microwave signals[4].

381
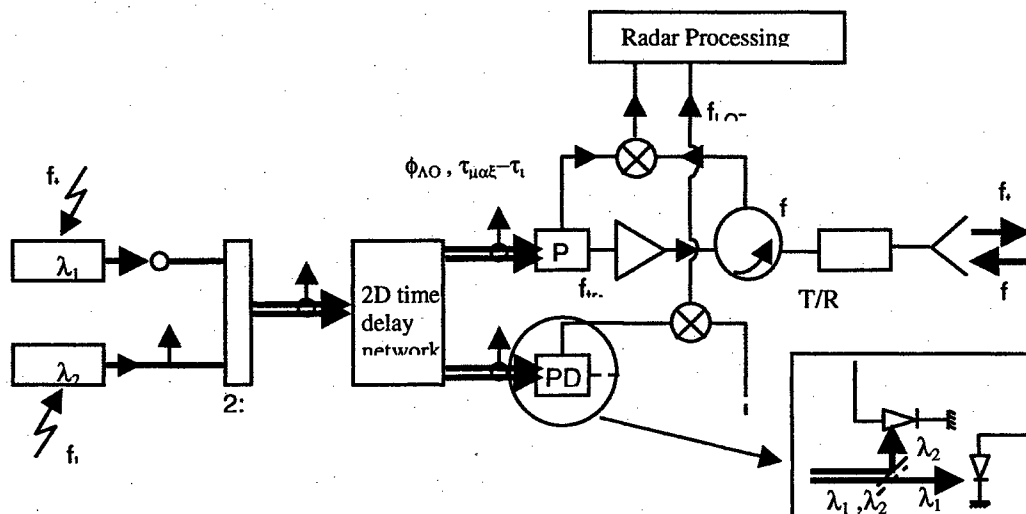
In the above figure, two cross-polarized optical beams are modulated by microwave signals at frequencies f_{tr} (signal to be transmitted) and f_{lo} (local oscillator). They travel through a 2D switching network similar to the transmit mode one. When two cross-polarized beams travel along the same channel, their polarizations remain orthogonal and they experience complementary paths. In this case, when the carrier of the frequency f_{tr} is delayed by τ_k along channel k, the cross-polarized carrier of frequency f_{lo} is delayed by τ_{max}-τ_k, where τ_{max} is the maximum available time-delay. On each channel, a dichroïc mirror switches the carriers on two different photodiodes which provides the signal to be emitted and a perfectly matched microwave LO, respectively. Because of jamming, frequency f_{lo} must stand out of the radar bandwidth Δf. The ideal homodyne processing must be replaced by an heterodyne detection, where $f_{lo} \neq f_r$ (f_r is the frequency of the received signals).

A proof of concept was recently completed, which consists of two transmit/receive modules and two delay blocks. On each channel, a laser beam is modulated at frequency f_r or f_{lo}. Phase differences equivalent to 10 ps delays at $f_i = 700$ MHz were measured that permits in-phase addition of the received signals (received signals were generated using time delays that simulate reflection from the target).

5   Conclusion

The development of the optolectronic technology offers new opportunities for introducing optical RF distribution in airborne phased array radars. It has been shown a large considerable interest for such technologies as soon as complex architectures are considered. In these cases, more technology advances are needed to give all flexibility to the system, with the help of digital beamforming. On more simple implementations, an analysis must be done in each case to balance this technology with more classic ones. In addition, one can notice that 2D optical TDBFN approaches could greatly benefit from a holographic backplane scheme, in order to solve the problems of compactness, reliability and scaling up to 10^3 transmit/receive modules.

6   Acknowledgments

7   References

[1]M. Schaller, P. Dueme, *High efficiency optical transmitter and receivermodules using integrated MMIC impedance matching and low noise 50 Ω amplifiers*, Proc GAAS IC Conference, Munich, 1999.

[2] J.J. Lee, R.Y. Loo, S. Livingston, V.I. Jones, J.B. Lewis, H.W. Yen, G. Tangonan, M. Wechsberg, *Photonic wideband array antennas*, IEEE Trans. Antenna Propag., 43, 966, 1995.

[3] D. Dolfi, P. Joffre, J. Antoine, J.P. Huignard, D. Philippet, D. Granger, *Experimental demonstration of a phased-array antenna optically controlled with phase and time delays*, Appl. Opt., 35, pp.5293-5300 1996.

[4] S.Tonda, L.Pastur, D. Dolfi, JP Huignard, T. Merlet, O. Maas and J. Chazelas, *Double heterodyne filtering of received signals in optically time-delay controlled antennas*, Proc. OMW 1998.

WA1

European Session

European Session

Some Experiences from FDTD Analysis of Broadband Phased Arrays

Henrik Holter, Hans Steyskal
Dept. of Electromagnetic Theory, Royal Institute of Technology
SE-100 44 Stockholm, Sweden

Abstract

Some experiences regarding FDTD analysis of broadband phased arrays are presented. First, a recently developed FDTD technique for unit cell analysis of periodic infinite phased arrays is recapitulated. The new technique applies to pulse excitation in oblique directions. Second, simple methods to save computer memory using a local FDTD grid in an otherwise coarse FDTD grid to model elements in finite phased arrays are examined. It is found that the local grid methods suffer from numerical instabilities. Third, the question is discussed of how large a finite broadband array needs to be in order to demonstrate low-frequency performance comparable to infinite array predictions. A considerably larger number of elements is required in the broadband case than in the normal narrowband case.

FDTD Analysis of Infinite Arrays

A novel technique for finite-difference time-domain (FDTD) analysis of linear and planar periodic infinite phased arrays has recently been developed [1, 2]. Periodic boundary conditions are implemented which reduce the computational volume to that of a single unit cell. The technique applies to pulse excitation in oblique directions in both the cardinal and inter cardinal planes. The ordinary FDTD Yee lattice is used which makes the algorithm easy to incorporate in an already existing FDTD code. The technique is exact in the sense that no additional approximations to those inherent in the ordinary FDTD technique are introduced. Alternative FDTD techniques for unit cell analysis exists, see for example [3, 4]. However, the very few coexisting techniques, which allow for pulse scan in oblique directions seem to be complicated to implement, or involve further approximations.

To shortly recapitulate the idea behind our new FDTD unit cell technique presented in [1, 2]. For simplicity, consider a unit cell in a linear infinite periodic array, as shown in Figure 1, and assume that the array is scanned to an angle θ in the positive x-direction. At boundaries A and B the tangential fields are related according to

$$f\left(x_B, y, z, t\right) = f\left(x_A, y, z, t - \tau_x\right) \tag{1}$$

$$f\left(x_A, y, z, t\right) = f\left(x_B, y, z, t + \tau_x\right) \tag{2}$$

where $\tau_x = D_x \sin\theta / c$ is the time delay between adjacent unit cells and c is the speed of light. Eq.1 implies that tangential field values at boundary B are obtained from time delayed values at boundary A, which are simply saved in a buffer for later use. On the other hand, Eq. 2, implies that time advanced field values from boundary B are used at boundary A. This poses a major problem, since the time advanced values at time $t + \tau_x$ are not known at time t. The idea is now to move the unit cell on the FDTD grid with the speed c in the positive x-direction. The fields radiating from the infinitely many array elements to the left of boundary A will never reach the

moving cell. The effect is that the boundary condition represented by Eq. 2 can be ignored. There are no reflections from boundary A and it needs not be treated in any special way. This solves the problem.
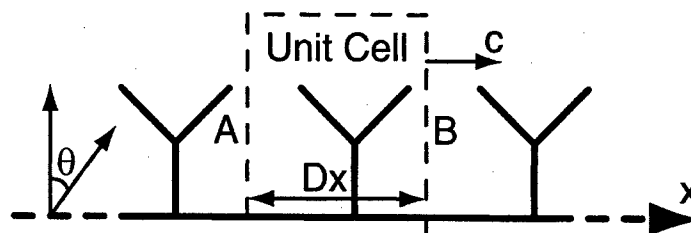
Figure 1. Side view of a linear infinite periodic array.

The new technique uses the original FDTD equations as developed by Yee 1966. The original FDTD technique has been proven to be numerical stable. Numerical stability of the new technique is therefore guaranteed. As a matter of fact, one simulation was run for 3 million time steps without becoming unstable. The technique has been used to design a broadband tapered slot phased array with bandwidth 5.9:1 over a scan volume of ±50° [5]. Mode suppressors in the form of vias between the ground planes of the stripline elements contributed to the large bandwidth [6].

Since the method is based on the original FDTD technique, it has some minor limitations. First, the same FDTD Yee cell size is used everywhere, which in principle is a waste of computer memory. Second, the geometry is modeled using a staircase approximation. Actually, these limitations are not serious, since modeling of the single unit cell does not require much computer memory. However, to address these problems, a modified version of the technique has been developed [7]. The modified technique applies to non-uniform meshes in for example FDTD and the finite-element time-domain (FETD) methods. In [7], the modified technique was applied to the FETD method.

FDTD Analysis of Finite Arrays Using a Local Fine Grid

Numerical analysis of finite phased arrays normally requires large computer resources. This problem is exacerbated in broadband phased arrays where antenna elements normally have a complex geometry, which requires high spatial resolution and consumes much computer memory. The currently existing techniques for non-uniform grids in FDTD are rather complicated to implement. An easily to implemented alternative proposed is to use a local fine FDTD grid inside a coarse FDTD grid as shown in Figure 2. We have explored this approach for phased arrays, where many local grids in the coarse grid are necessary. The problem with the local grid technique is that some or all of the fine grid field values at the fine-coarse grid boundary are unknown. We have examined two different ways to implement the local grid methods, as proposed in [8, 9]. The first method uses the wave equation together with interpolations to calculate unknown boundary field values. We found that this method becomes unstable after a fairly short period. The second method uses only interpolations to calculate unknown boundary field values. This method also eventually becomes unstable. However, the numerical simulation may well be finished before this happens. Unfortunately, the time to instability decreases with increased number of local grids. The method can therefore only be used for small arrays. As a conclusion, local FDTD grid techniques need to be further developed for the analysis of phased arrays.
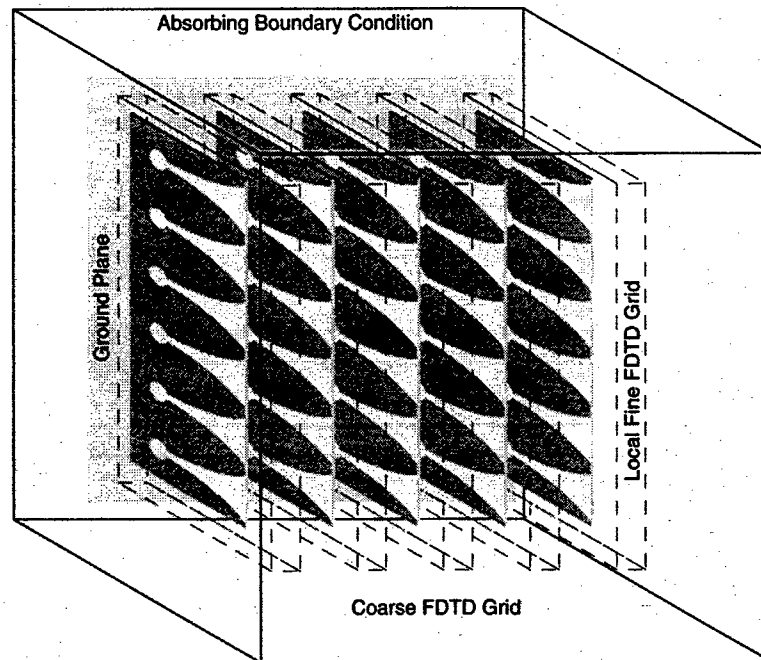
Figure 2. Finite phased array with endfire tapered slot elements. A local fine FDTD grid is used around the antenna elements to save computer memory and to decrease the simulation time.

FDTD Analysis of Finite Broadband Phased Arrays

Multi-octave arrays bring renewed interest in the old problem of array edge effects [10]. Although, at the high-frequency end, the center element of a 10×10 element array may see an essentially infinite array environment, this will not hold at the low end of a 5:1 operational band, where the array size has been reduced from 5λ×5λ to 1λ×1λ. This raises the question of how large should a finite tapered slot array model be in order to obtain low-frequency performance that can validate infinite array predictions.

We are currently investigating this question. As a preliminary result, Figure 3 shows the FDTD calculated active reflection coefficient for a series of broadband tapered slot arrays (see Figure 2), at a frequency corresponding to 0.13λ element spacing. The arrays up to 13×13 elements do not perform well. Comparing the element reflection coefficients in the 25×25 and the 49×49 arrays indicates that reasonable convergence for their behavior lies somewhere in between, say at 40×40 elements. This means that, even at this low frequency, an array of 5.2λ×5.2λ simulates both the edge and the central elements in any larger array. We have also found similar results for closely spaced dipole elements. Thus the tentative conclusion is that, for any frequency, any finite array model should be about 5λ×5λ.

Extrapolation of experimental results of a 9×8 element dual-polarized tapered slot array leads to a similar conclusion [6].
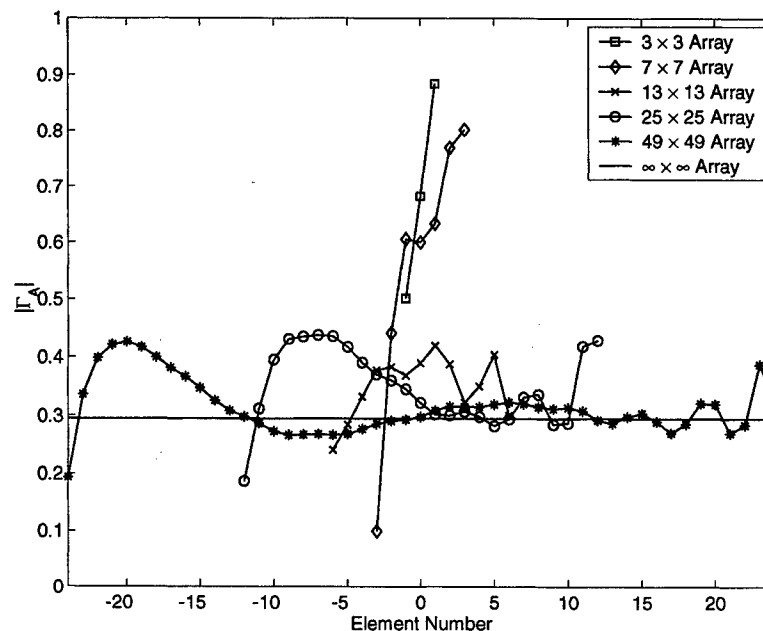
Figure 3. Active reflection coefficient for the central horizontal elements in six arrays of the type shown in Figure 2. The array is scanned to 45 degrees in the H-plane, and element spacing is 0.13λ.

References

1. H. Holter, H. Steyskal, "Broadband FDTD analysis of infinite phased arrays using periodic boundary conditions", IEE Electronics letters, Vol.35, No.10, 1999.

2. H. Holter, H. Steyskal, "Infinite phased array analysis using FDTD periodic boundary conditions-pulse scanning in oblique directions", IEEE Trans. AP., Vol. 47. No. 10, pp. 1508-1514, October 1999.

3. A. Taflove, "Advances in computational electrodynamics", Artech House, 1998, pp. 345-407.

4. G. Turner, C. Christodoulou, "FDTD analysis of phased array antennas", IEEE Trans. AP., vol.47, No. 4, April 1999, pp. 661-667.

5. T-H. Chio, D. H. Schaubert and H. Holter, "Experimental radiation and mutual coupling characteristics of dual- polarized tapered slot (TSA) arrays", Antenna and Application Symposium, Allerton Park, Illinois, September 1999.

6. H. Holter, T-H. Chio, D. H. Schaubert, "Elimination of impedance anomalies in single- and dual-polarized endfire tapered slot phased arrays", IEEE Trans. AP., Paper accepted.

7. H. Holter, "Unit cell finite-element time-domain analysis, pulse excitation in oblique directions", AP2000 Millennium Conference on Antennas & Propagation, Davos, Switzerland, April 9-14, 2000.

8. M. J. White, M. F. Iskander, Z. Huang, "Development of a multigrid FDTD code for three-dimensional applications" ", IEEE Trans. AP., Vol. 45. No. 10, pp. 1512-1517, October 1997.

9. M. W. Chevalier, R. J. Luebber, V. P. Cable, "FDTD local grid with material traverse" ", IEEE Trans. AP., Vol. 45. No. 3, pp. 411-421, March 1997.

10. R. C. Hansen, "Finite dipole arrays over a wideband", Antenna and Application Symposium, Allerton Park, Illinois, September 1999.

THE ERIEYE PHASED ARRAY ANTENNA – FROM A SYSTEMS VIEWPOINT

Martin Heed
Ericsson Microwave Systems AB, Moelndal, Sweden

Introduction

The ERIEYE airborne early warning and control (AEW&C) system is a modern, powerful system designed for medium size commuter aircraft. Thereby the operating cost, the availability as well as the life-cycle cost are outstanding.

The total system consist of the following sub-systems:
- Radar
- SSR/IFF
- ESM
- Command and control system
- Communication system
- (Navigation system)

To this date the system has been installed (in somewhat different configurations) on the Saab 340 and on the Embraer 145, but it is comparatively easy to install on other aircraft.

Below we will focus on the radar antenna, which will be described and some of the choices which were made in the design will be motivated.

Physical layout

In the antenna is included:
- the radiation elements
- the transmit/receive modules (TRMs)
- the feeding network
- the calibration network
- the cooling system

We have chosen to place these parts close together in a so-called dorsal unit as it is mounted on top of an aircraft. Thereby the active TRMs can be cooled by ram air, a simple and effective solution. In the dorsal unit is also placed SSR/IFF antennas, which we will not deal with in this paper. The layout is illustrated in the following figure.
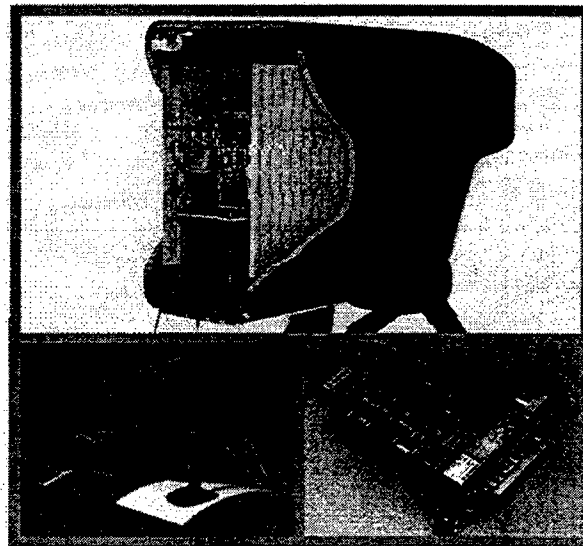
Fig. 1. The radar antenna

To be able to mount the antenna on top of a rather small commuter aircraft as the Saab 340, it is necessary to restrict both the dimensions and the weight. We have chosen to limit the active antenna area to less than 8 by 0.7 m on each side. The weight of the dorsal unit (including the IFF antennas) is below 1000 kg.

The antenna elements consist of slotted wave-guides. Each TRM is connected to one waveguide on each side of the dorsal unit. Each waveguide has vertically oriented slots, divided in an upper and a lower half with separate feedpoints. There are 192 TRMs.

The signals from all the TRMs are summed in the feeding network to a sum signal. A number a TRMs (and antenna elements) are also used as broad-beam antennas for sidelobe blanking (guard) and adaptive sidelobe cancellation.

The TRMs perform phase shifting, power amplification and switching functions on transmit. On receive they perform switching, low noise amplification, amplitude weighting and phase shifting.

Frequency choice

All long-range radars operate at S-band or below. The attenuation in clear air or rain is too large at higher frequencies.

For a radar at 6000 m altitude and a low-altitude target at 300 km range, the two-way atmospheric attenuation (in normal atmospheric conditions) is given below. In the table is also given the extra attenuation of a 100 km wide rain region with an intensity of 4 mm/h. This is a perhaps not a worst case, but the rain extent is normally more restricted for heavier rainfalls.

Frequency band:	L	S	C
Clear air att. (dB):	2.6	2.9	3.2
Extra rain att. (dB):	0.1	0.3	1.5

It is clear that lower frequencies are preferable in this respect.

Another aspect is the elevation and range coverage. It is required to detect fighter-sized targets at altitudes up to 20 km at long range. This is possible to accomplish at S-band with a single scan line. At C-band two lines are required with the extra complexity that implies.

At L-band the elevation beamwidth is too wide, the radar energy is spread out in regions where it is not required. This is illustrated in the following figure, where the single scan detection probability is plotted with a horizontal beam. The scan time is constant.
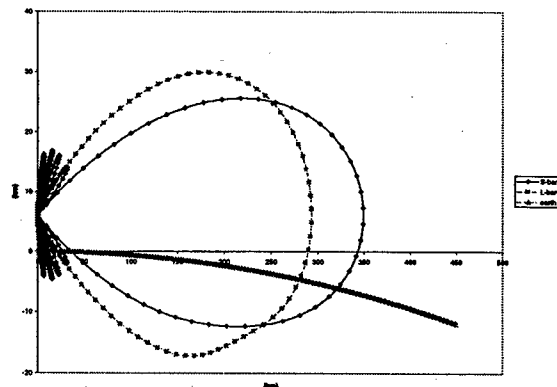
Fig. 2. Radar elevation coverage at two frequency bands

S-band is the optimum choice in this respect. This is of course under the pre-condition that the antenna aperture is limited in height as given in the former paragraph.

S-band will always have narrower beamwidths, however, which is preferable in jamming situations, as it minimises the areas with mainlobe jamming.

There are many more aspects on the choice of frequency (e.g. measurement accuracy, resolution, interference risk, available components etc.), but the three aspects given above have dominated the choice for this system.

Polarisation

Horizontal polarisation was the result of the preferred antenna design consisting of vertically oriented waveguides with broad wall slots.

Horizontal polarisation gives higher surface reflection, especially over sea. This is no disadvantage, since the net effect of the multi-path is positive. The radar range is actually improved for low-flying targets over sea.

Electronic beam steering

The main reason for choosing a phased array antenna was the requirement of low weight and drag on the aircraft, as was stated before. This

gives good operating economy and long time-on-station.

Another important feature is that the track initiation range is increased. With conventional (rotating antenna) radar, the target must be detected at a few scans before a firm track can be established. With phased-array radar, it is possible to lock on shortly after the first detection, by jumping back with the beam to the bearing of the detection. The radar then illuminates in that direction to confirm that the detection is a real target and possibly to start a new track.

In the following figure are shown: the detection probability at the search scan, the detection probability at the extra illumination and the resulting probability of track initiation.
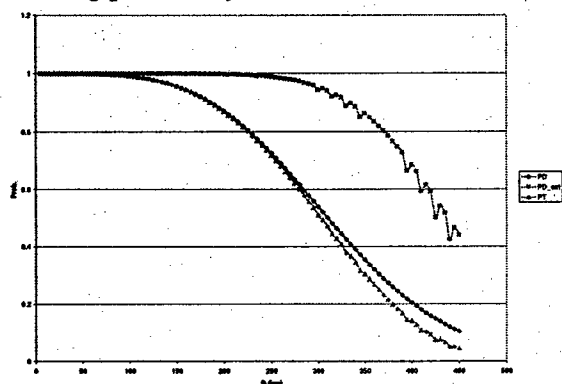
Fig. 3. Detection and track-initiation probabilities

In the next figure are shown: the cumulative probability of track initiation in a mode with extra illuminations (the so called Adaptive Radar Control, ARC, mode) and the same in a track-while-scan (TWS) mode.
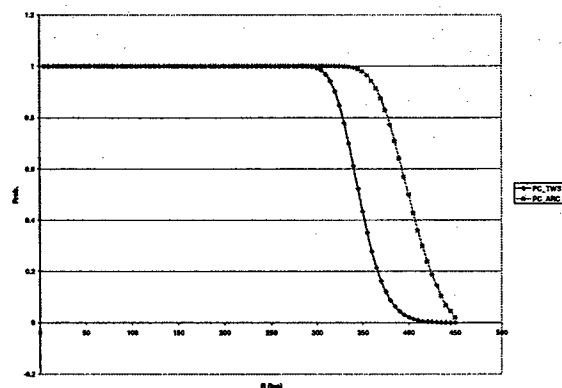
Fig. 4. Cumulative track-initiation probabilities

The cumulative track-initiation range is of greater interest than the single-scan detection range, as it is a measure of the range where tracking starts on an approaching target.

A third benefit of a phased array is that it is possible to update the tracks at a higher rate than the search scan rate. The track continuity is then improved and it is also possible to lower the scan rate to further improve the track-initiation range, as the coherent integration possible with a lower scan rate is more effective than the binary integration with a higher scan rate..

It is also possible to adjust the update rate to each target depending on the situation (adaptive tracking). If a target manoeuvre is detected the update rate for that target can be increased. The same is true in other difficult situations or if the operator chooses to give this target a higher priority.

Antenna sidelobes

It is important to get a low sidelobe level to keep both the sidelobe clutter and the sidelobe jamming low.

The distance between the radiating elements is less than half a wavelength in the horizontal plane, so that so called "grating lobes" are avoided even for very large scan angles. In the vertical plane the distance between radiating elements is a little larger, as the required scan angle is much less in that direction.

We use a certain vertical weighting function to control the elevation sidelobes. This is built into the antenna plates (the positioning of the slots) and cannot be altered afterwards.

In the horizontal dimension we use no weighting on transmit, in order to get maximum power output and to have only one type of TRM. On receive we use a Taylor weighting to get low sidelobes.

The sidelobe level is, however, not only determined by the weighting function, but also by the errors in phase and amplitude of each element. If we assume Gaussian errors with zero

mean and standard deviation of σ_a and σ_p in amplitude and phase respectively, the average sidelobe gain divided by the peak mainlobe gain (SLR) will be (in the horizontal plane):

$$SLR = SLR_0 + \frac{\sigma_a^2 + \sigma_p^2}{N_{el} \cdot \eta_a}$$

Here SLR_0 is the sidelobe level given by the weighting function, N_{el} is the number of active elements and η_a is the aperture efficiency. If we for example use a 50 dB Taylor weighting and the errors were $\sigma_a = 0.05$ (0.43 dB) and $\sigma_p = 0.05$ rad. (2.9°), the average sidelobe ratio would be 43 dB. The sidelobe level is even better in other directions.

As the system has to operate at varying surrounding air temperatures and as the active components in the TRMs tend to drift with the temperature, we have included a calibration system to keep the errors (and thus the sidelobe level) at a low level. The radar operation is interrupted for short periods now and then for calibration, so the antenna performance is always good.

With the same example of receive pattern as above and with unweighted transmit pattern, we can calculate a probable clutter spectrum:
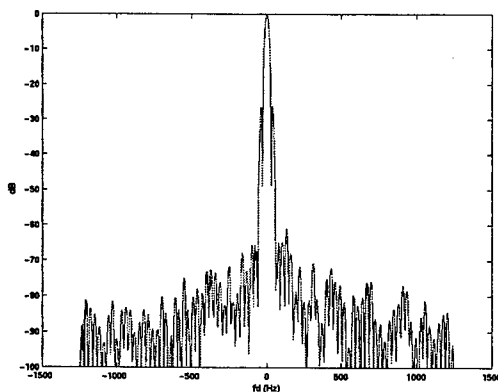
Fig. 5. Clutter spectrum

Due to the unweighted transmit pattern we get a clutter spectrum with high first sidelobes (one on each side). The first sidelobes have no influence in an AEW radar, as a small velocity region

around the main beam clutter must be discarded anyway to get rid of ground moving targets (cars, trains, etc.).

Target altitude measurement

The radar is required to be able to measure the altitude of targets.

The antenna on each side is divided into two parts: one upper and one lower part. The transmit signal from each TRM is split in two equal part, which feed each waveguide part. On receive the two signals are combined into one sum and one delta channel, which both are transferred to one TRM. By forming these two signals before any active amplification, the errors are kept at a minimum.

Reliability

One important feature of an active phased array is that the system will function (with somewhat degraded performance) even if a few TRM's would malfunction. This is commonly called "graceful degradation".

Summary

The ERIEYE antenna has been described from a systems view. The choice of frequency and polarisation were motivated and some of the advantages of using a phased array were explained. It gives longer track initiation range, better track continuity and better reliability. In this application we also have the advantage of less drag on the aircraft, thereby making it possible to use rather small aircraft.

Present EHF-Antenna activities at D.S.S.

P. Keim, K. Osterschek, M. Hofbauer, M. Reinhart, M. Weber
Dornier Satellitensysteme GmbH
P.O. Box 801169
81663 Munich, Germany

☎ +49 89 607 21724, Fax. : +49 89 607 25538, Email: Markus.weber@dss.dornier.dasa.de

Abstract

This paper gives a brief overview of the EHF antenna demonstrators designed, developed, integrated an tested at Dornier Satellitensysteme GmbH (D.S.S.)

1. Introduction

During the MILSATCOM Phase A study performed by D.S.S. for the German department of defence, the Spotbeam and Globalbeam antenna demonstrators were defined. The purpose of the two demonstrator models is to verify the electrical performance of the complete system as well as to verify the proper performance of critical technologies used within certain sub-systems of the demonstrators.

2. Spotbeam Antenna Demonstrator

The Spotbeam Antenna demonstrator forms a compact, high performance combined transmit/receive antenna. The complete demonstrator, as shown in Figure 1, consists of :

- an offset parabolic main reflector,
- a planar frequency selective surface as sub-reflector,
- the transmit feed system with zooming capabilities,
- and a fully active receive feed system.

For the transmit function, the antenna is capable of forming spot beams with variable coverage sizes in the range of 0.5° to 1.7° in diameter. The receive function allows for the formation of flexible coverages such as spot beams, contoured beams, rotational elliptical beams as well as providing sovereign nulling capabilities. A few measured examples depicting the extreme versatility of this antenna is depicted in Figure 2.

The transmit feed system, operating in the frequency range 20.2 - 21.2 GHz, consists of the :

- the horn cluster,
- Polarisation / Transition unit
- and the passive beam forming network (BFN).

The horn cluster consists of seven SCRIMP (Short Circular RIng loaded horn with Minimised cross-Polarisation) horns which are arranged in a hexagonal lattice. The polarisation and transition unit, responsible for the generation of the circular polarised transmit signal, is situated directly behind the horn cluster. A 1:6 fixed power divider and a variable power divider forms the passive BFN which is responsible for the zooming capabilities of the transmit antenna.

The receive feed system, operating in the frequency range 43.5 - 45.5 GHz, consists of the sub-systems:

- Horn cluster,
- Polarisation / Transition unit,
- waveguide bending unit ,
- and fully active beam forming network.

The horn cluster and Polarisation/transition unit operates in a similar manner as describe above for the transmit feed system. The waveguide bending unit transforms the seven hexagonal positioned receive paths from the Polarisation / transition unit into the seven planar parallel paths needed at the input of the BFN. The BFN consists of seven parallel receive paths which are added in phase via a 7:1 power combiner. Each path within the BFN consists of a waveguide to coplaner waveguide transition, LNA, VGA, a 90° Phase switch, a 90° Phase shifter and a 180° phase switch. All components are realised using MIC technology. With this receive topology, a 20 dB amplitude and 360° phase control range within each path is possible. The amplitude and phase deviation between the seven receive paths are smaller than ±1 dB, ±10 ° over the complete frequency band.

3. Globalbeam Antenna Demonstrator

A parabolic offset reflector and a 37 element, fully active receive feed system, forms the Globalbeam antenna demonstrator. A side view of the complete demonstrator is shown in Figure 3. The globalbeam antenna is capable of producing an extremely large amount of flexible coverage mode capabilities. A few coverage modes are shown in Figure 4. The receive feed system consists of the sub-systems:

- Horn cluster,
- Polarisation /Transition unit
- And the active BFN.

The horn cluster and polarisation /transition unit is based on the design given by the Spotbeam antenna demonstrator. The active BFN consists of several GaAs-MMICs realised using a 0.25µm PHEMT process. The particular chips provide the following functions: LNA, Gain Block, analogue VGA (Variable Gain Amplifier), 180° Phase Switch, 90° Phase Switch and analogue 90° Phase Shifter. The beam forming network consists of parallel branches directly attached to the polarisation/transition unit. This fully active BFN provides a continuous amplitude (15dB) and phase (360°) control range. Additional microwave components such as a novel waveguide to coplanar transition as well as power combiners completes the versatile functionality of the BFN. The amplitude and phase deviation between the 37 receive paths are smaller than ±2 dB, ±20 ° over the complete frequency band.

Acknowledgements
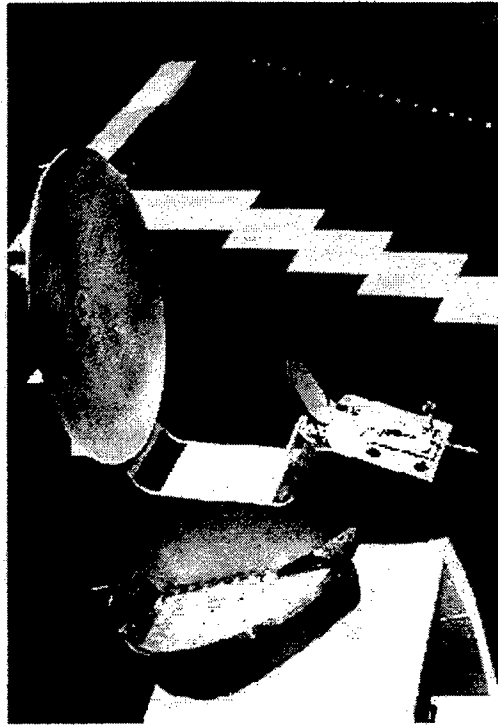
Figure 1: The Spotbeam antenna
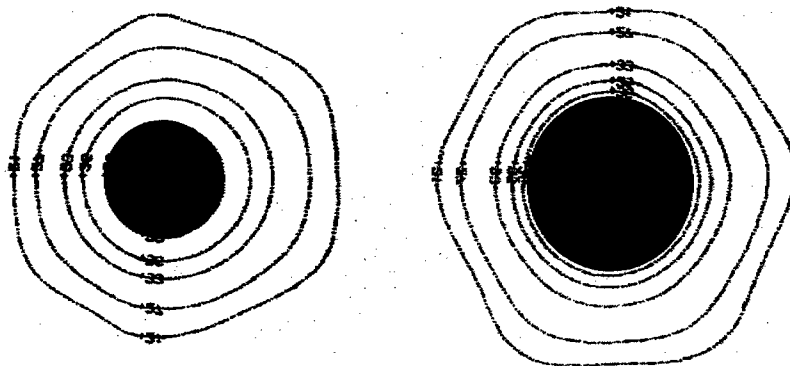
Figure 2 a: A few measured transmit coverages of the Spotbeam antenna

Figure 2b: A few measured receive coverages of the spot beam antenna
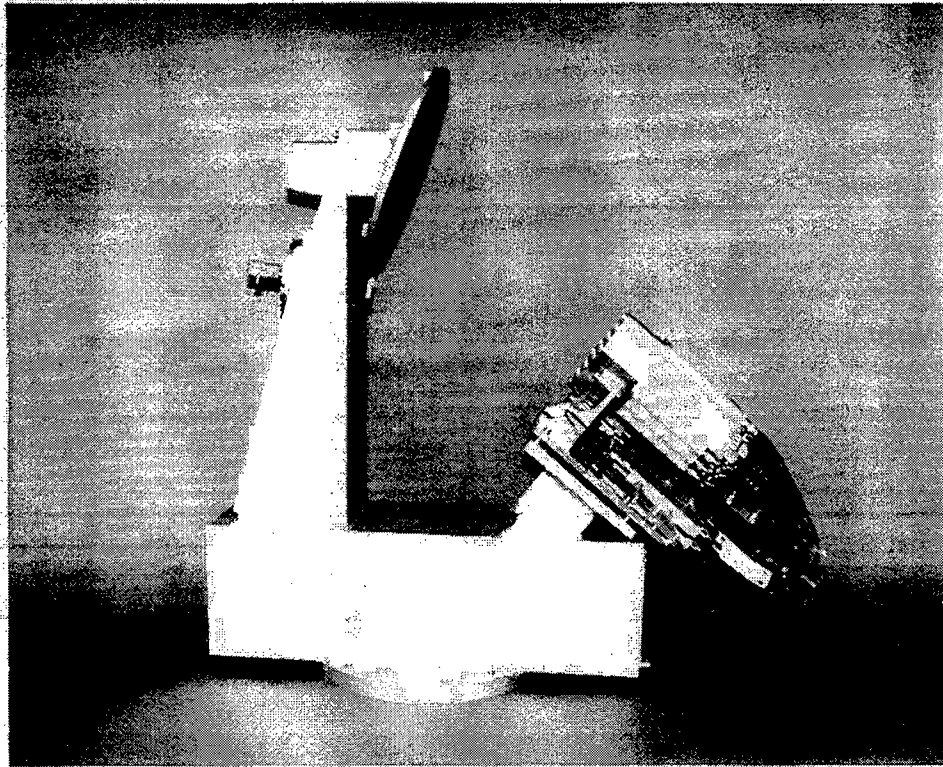
Figure 3: Side view of the Globalbeam antenna
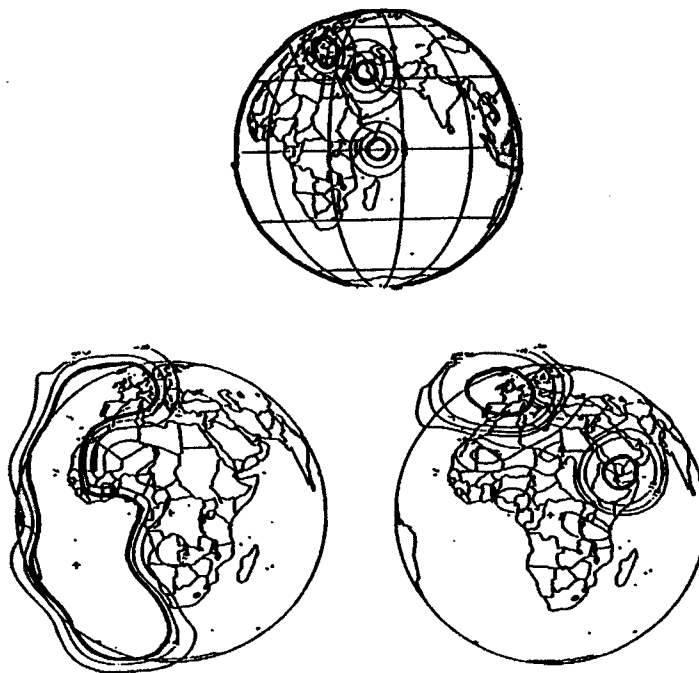
Figure 4: A few coverage mode capabilities of the Globalbeam antenna

Analysis, Design and Measurements on an active Focal Array Fed Reflector

H. LEGAY[*], F. CROQ and T. ROSTAN
* Alcatel Space Industries, 26 av. J.F. Champollion, B.P. 1187, 31037 Toulouse Cedex 1

1. Abstract

ALCATEL develops reflectors antennas with multifeed arrays for civil and military communications satellites In this paper, A X band, high gain spot beams antenna with accurate beam steering and shaping, low sidelobe levels is presented. The selected antenna is comprised of an offset parabolic reflector with overlapping feed cluster. Pattern synthesis is performed with an active beam forming network (BFN). Design rules were gained from a detailed analysis of the antenna architecture. A demonstrator was designed and measured. Low sidelobes (-25 dB), accurate steering (0.05°), good agreement between theoretical and experimental spots were demonstrated. Attention was paid to optimize the design of constitutive elements (light weight planar focal array, shaped reflector).

2. Introduction

The reflector antenna with a multifeed array is an attractive candidate for two distinct missions : multimedia satellites requiring a multibeam coverage with high directivity, and military communication satellites requiring directive beams with coverage reconfigurability and protection against electronic warfare interference.

In the first said application, the reflector focuses the RF power on a limited number of feeds. A passive Beam Forming Network combines their contributions for the synthesis of each spot.
For the military application, the BFN is active. In order to be able to scan a spot over the earth, all the feeds contribute to the synthesis of a spot. The BFN complexity is therefore higher, and is comparable to that of a Direct Radiating Array (DRA), which is another attractive candidate. However, when considering high gain spot beams in X band, the Focal Array Fed Reflector (FAFR) is preferred to the DRA mainly for its easier implementation on the platform.

ALCATEL analyzed carefully the FAFR. A parametric study was carried out and rules of the thumb were derived for assistance in the design. Theoretical models were developed and a demonstrator was defined and built. Measurements are presented. Technological developments were conducted on constitutive components.

3. General considerations on the FAFR

The FAFR consists of a parabolic reflector with a phased array located at its focus. In its passive embodiment, the scanning may be achieved by selecting one of the multiple radiating elements of the array. It is however well known that the range of scan of this method is limited by the increasing coma and astigmatism, resulting in beam broadening, loss in gain and increase of sidelobes. This phenomenon is particularly pronounced for low focal length F/D (<0.7). A second major drawback of the passive architecture is its poor efficiency. The impossibility of achieving high cross-over spots with contiguous feeds in the focal plane has been demonstrated.

This problem is alleviated with the active architecture, which uses the concept of overlapped subarrays. Several feeds contribute to the synthesis of a spot. By analogy with digital filtering, the RF energy distribution in the focal plane is spatially sampled (by small feeds), the number of which is directly connected to steering accuracy. For scanned beams, the RF energy spreads on the focal array due to the aberrations of the optical system. A higher number of feeds is required for a spot synthesis. The feeding law compensates for the phase aberrations.

The reflector size is directly derived from the directivity specification. The focal length is set according the following considerations : it must be large enough in order to minimize the phase

aberration for a beam scanned (max : ±8°) ; the optical system can be implemented of on a lateral wall of the platform ; the induced focal array grid permits the accommodation of filters and active devices.

The sidelobe control is achieved simultaneously by the optical systems for directions at least two beamwidths away from the main lobe, and for close directions by the control of the phase and magnitude combination of the feeds. Therefore, low far sidelobes can be achieved by designing properly the optical system. They are immune to the drift or failure of RF active components. On the other hand, the close sidelobes are controlled by the phase and magnitude law applied to the group of adjacent feeds. Small perturbation of this feeding law may result in sensitive degradation of the close sidelobes. The sidelobes are all the more sensitive to the instability of the law since the number of active feeds per spot is low. An on-board calibration system or an adaptative close sidelobe control process is therefore required.

4 RF Architecture

The architecture of an on-board FAFR is detailed thereafter. The received signal incident on the parabolic reflector is focused on a group of adjacent feeds. Each radiating element is connected to a RF channel, which is comprised of a filter, a calibration coupler, a Low Noise Amplifier (LNA), a phase shifter, an attenuator and switchs included in the Beam Forming Network (BFN).

The LNA must have sufficient gain, so that the losses following the amplifiers do not contribute to the noise temperature. It must also maintain the linearity in presence of high traffic and severe jamming. These considerations may require multi-gain amplifiers. The failure of a LNA has a dramatic effect on the spot characteristics. The LNA need therefore to be redounded.

The BFN includes an entrance divider, switch matrices, phase shifters and attenuators, output combiners. The entrance divider corresponds to the generation of independent spot beams fully reconfigurable. The switch matrix permits to reduce the number of phase and magnitude control per spot. Since only adjacent feeds contribute to the synthesis of a spot, remote feeds never contribute simultaneously to the synthesis of a given spot. Remote feeds located in opposite areas of the array can therefore be connected to a switch matrix which selects the feed according to the beam pointing. The order of the switch matrix depends on the coverage dedicated to the spot. The wider the coverage, the more of feeds per spot, and therefore the lower order of the matrix. The use of a switch matrix reduces the requirement on the dynamic of the feeding law which is limited by technological factors. However, the switch matrix must indicate a high isolation between its access in order to limit the far sidelobe level.

5. Demonstrator

A demonstrator has been defined according the following specifications :
- G/T=10dB/K,
- close sidelobe level < -20dB, far sidelobe level < -25 dB,
- steering capability over the earth coverage,
- shaping capability : regional and global coverage,

The objectives were :
- to validate experimentally the simulated performances,
- to underline the antenna integration,
- to identify achievable performances,
- to identify the limitations relative to the constitutive components : quantization of the law, dispersivity between the RF channels, ...,

The demonstrator is presented on Figure 1 . It is made of a 2.2 m reflector, and a focal array of 175 contiguously stacked potter horns. The BFN generates 2 spots with 16 feeds, or 1 spot with 32 feeds. The resolution was set to 0.5 dB (out of 30 dB) and 5° (out of 360°).

The RF channels were calibrated for all the phase and attenuator control states before integration with the optical system. Their dispersivity with frequency was qualified. The coupling effect between the array feeds was also qualified before integration of the antenna. The radiation pattern of the surrounded feeds appears sensitive to the environment. The pattern fluctuation was ascribed to diffraction rather than coupling between the feeds.

Low sidelobe regional and theater spots were synthesized for different pointing. They indicated good agreement between theory and measurement, as well as satisfactory performances :
- good pointing accuracy (±0.05°) ;
- low close sidelobes (<-25 dB for a scanned beam, <-30dB for Nadir spots) ;
- low far sidelobes (<-30 dB) ;
- High reconfigurability of a spot (from regional to theater).

The wide-band performances of the spots were also considered. The pattern dispersivity over the coverage and also over the null was characterized, and was correlated with the dispersivity of the optical system and the dispersivity of the active beam forming network.

6. Technological development

Attention was paid to reduce the weight of the focal array. The array grid of a focal array varies from one wavelength to one and a half wavelength, depending on the focal length. This range of diameter is particularly difficult to realize with typical planar radiating elements. Planar elements for space application are usually made of stacked resonators separated by interleaved honeycomb. The use of material substrate is forbidden, since it affects the bandwidth and the element mass. Thus, subarrays of several resonators on air substrate have a lateral spacing between 0.7 and 0.85 wavelength. Thus, planar radiating elements ranging from 0.9 to 1.4 wavelength can not be developed with the typical arrangement. A new topology was designed based on a single fed patch and seven stacked parasitic patches. It results in a 400% save of mass.

An other concern was to modify the parabolic geometry of the optical system, so that the phase aberrations observed for wide angle scanned beams was reduced and made constant regardless of the beam pointing. The goal was to have the same number of active feeds regardless of the beam pointing. A slight modification of the reflector profile improves the performances when scanning at the edge of earth. This is obtained at the expense of the nadir performances.
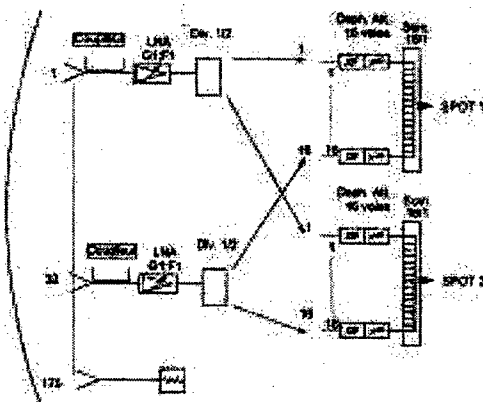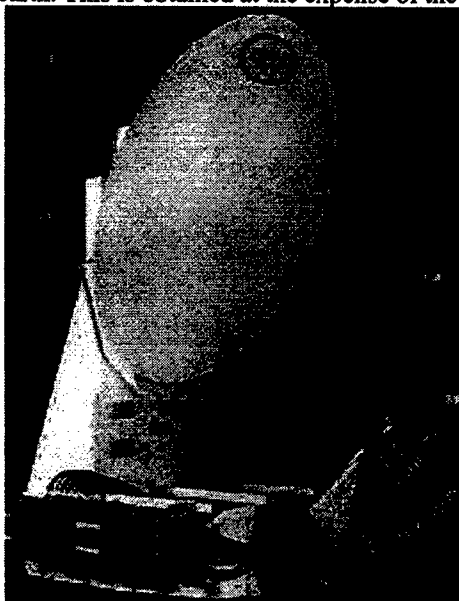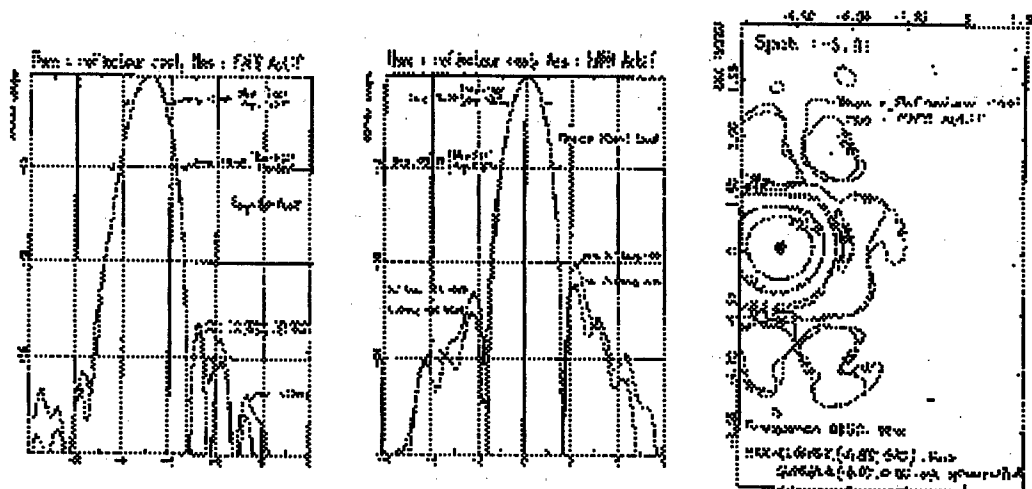

Figure 1 : FAFR Demonstrator

Figure 2 : Comparison between calculated and measured pattern (superposed on each figure)
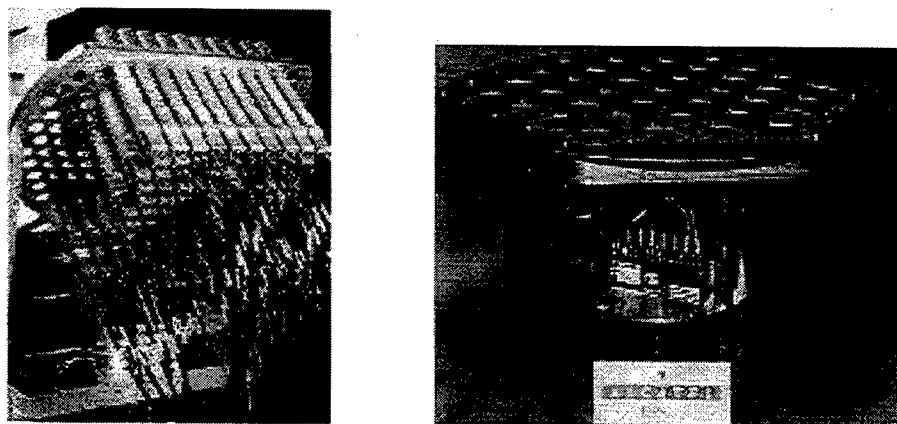

Figure 3 : Focal Array (Horn and Planar array implementation)

A Ka-band Direct Radiating Array providing multiple beams for a satellite multimedia mission

Y. CAILLOCE[*], G. CAILLE[*], I. ALBERT[**], J.M. LOPEZ[**]

* Alcatel Space Industries, 26 av. J.F. Champollion, B.P. 1187, 31037 Toulouse Cedex 1
** Centre National d'Études Spatiales, 18 av. Edouard Belin, 31401 Toulouse Cedex 4

1. Abstract

This paper deals with Direct Radiating Array pattern simulations in Ka band (transmit Tx and receive Rx). The DRA is used to generate a multiple beam coverage from a geostationary satellite to provide broadband services to fixed or mobile users in a local earth region. Particular emphasis is placed on the antenna optimization in order to reduce the number of Radiating Element (R. E.) with respect to the requirement. We have selected a typical mission corresponding to a precise ITU-filing.

2. Introduction

High data rate communication (typically from 2 to 20 Mbit/s) simultaneously to (and from) many users, leads to follow some specific constraints on the Satellite Payload: very high gain on board antennas comply with small size antennas on the users side, and decrease the power requirement of Solid State Power Amplifier transmitting around 30 GHz which are a significant part of the cost of the User Terminal. Therefore the G/T of the Satellite Rx-antennas must be very high, to achieve the link budget required for a sufficient Signal to Noise Ratio, directly related to the data rate. Maximizing G/T of Rx-satellite antennas means first minimizing noise temperature T: very low noise amplifiers, and very low ohmic losses in the whole RF path from the radiating aperture to the LNA's; it means also maximizing antenna directivity: as the Satellite Antennas radiating pattern must cover the whole useful Earth Region concerned and as the antenna directivity is inversely proportional to the area of its beam footprint, the only solution is to share it between many small circular disks called "spots". So the antenna should be a multibeam antenna.

3. Multimedia via satellite mission

Many projects are emerging, from International Public institutions (Intelsat, Eutelsat, ...) or private operators, for providing "multimedia via satellite, direct to home" services. In order to focus such Services mainly towards users located in the most populated earth regions, systems using a low number of geostationary satellites, facing these regions, appear to be the simplest ones. Traditional radio-frequency bands for communication via satellite, i.e. C and Ku ones, are nearly saturated. The only band which can offer sufficient-capacity (1 Gbit/second needs around 1 GHz available band, in each transmission sense) is the Ka-band: from 28 to 31 GHz for the up links (ground to satellite), from 18 to 21 GHz for the down links (satellite to ground). The main antenna requirements are summarized in figure 1. The coverage is composed of 44 contiguous beams disposed on a triangular lattice with 0.7 degrees beam spacing.

4. Rx and Tx Architectures

In an active DRA (Direct Radiating Array), figure 2a, amplifiers are directly connected to the R. E. So, for transmit (Tx) or receive (Rx) antennas, a large advantage is to suppress redundance switches replaced by graceful degradation (provided by a little oversizing of the array at the beginning of life). Phase-shifters allow repointing simultaneously all the beams to compensate the platform instabilities: This is done by self-pointing the antenna towards a beacon on ground, thanks to difference patterns provided by the DRA. Otherwise, platforms movements (typically ±0.1 to 0.15°) would degrade too much End Of Coverage gain and isolation between beams, whose specified contour diameter is 0.8° in the example taken here, and may be as low as 0.3° to 0.5° for other Systems.

- For Rx antenna, effective MMIC LNA's using PHEMT technology (or even more advanced ones), are very compact. Very low losses from the radiating element to the LNA provide an overall good

System Noise Temperature : this is compulsory for the very high G/T required for such mission (12 to 15 dB/K).

■ For Tx antenna, a similar architecture is also candidate, inverting the signal sense and replacing LNA's by SSPA's. This solution has the double advantage of distributing the RF power to be radiated among more than one hundred SSPA's, each of them contributing to all beams :

    – power margin to compensate rain attenuation is averaged on all beams. As the probability that rain occurs simultaneously on all the footprints is very low, power margin are much lower,

    – if the traffic demand changes, power distribution can be adjusted among various beams,

■ However, the high drawback of such architecture is the bad RF to DC efficiency of today 20GHz MMIC-SSPA's, more than twice lower than TWTA one. So an option is to use one TWTA per beam, placed in front of the passive BFN (see figure 2b). Then, the BFN must have very low losses : a double orthogonal set of waveguide Butler matrices is a good candidate.

5. BFN criticity

The present work is focused on multiple beam coverage of high gain (>42 dB) which requires a large size radiating panel, typically with a 90 λ diameter. We quantified the number of BFN's *nodes* (one *node* = one coupler, possibly unbalanced, with optimized line lengths between 2 successive nodes). The starting point is that N feeds generate M beams and we take the Rx antenna as example. In a BFN using independent layers for each beam, a splitter 1 per M is necessary after each feed and 1 per N before each beam port. As a splitter 1 towards N requires N-1 nodes, their total number is M(N-1)+N(M-1).

If using Butler matrix [1], the BFN requires (N log2 N)/2 nodes to achieve N beams (M=N) from N feeds, which is far lower (e.g. by a 73 factor if N=128 : similar gain than in FFT digital algorithms). When M≠N, this factor is a little smaller but still significant. For N=256 and M=44, 22228 nodes are necessary for the classical BFN versus 1024 for the Butler matrix. So the last one appears the only solution in term of BFN complexity ; it would be built from 2 sets of 16x8 matrices providing 64 beam ports from 256 R. E. ports (so truncated for lower numbers). Feasibility of 16x8 matrices is under assessment from numerous paper designs ; but actually built and tested ones are only 4x4 to 8x8, at least in the open literature : see [2] as example. In any case, more than 256 R. E. is not realistic.

6. Rx-DRA performances

The phase laws feeding the DRA are computed according to the specified beams lattice simulating the Butler matrix. The amplitude law is Taylor type, in order to fit the specified Side Lobe Level (SLL), while maximizing the maximal directivity. The SLL is related with the C/I : I is the sum of the power received by the useful beam, from all users in the other beams using the same frequency, referred to the useful power (C) received at the edge of coverage (EOC), i. e. worst case beam edge. Assuming EOC directivity 4.5dB below the maximum, a - 28 dB SLL is necessary to reach a 15 dB C/I requirement.

Figure 3a shows the variations of EOC directivity and isolation for the worst case beam. The directivity presents an optimum of 44.4 dBi (2.4 dB margin versus required gain) for a diameter of 900mm, with 15.7 dB compliant C/I. The figure 3b presents the number of R. E. versus array diameter: 253 R. E. corresponds to the optimal 900 mm diameter. A corresponding 4.3 dB roll-off (gain variation within the beam contour) is found (fig. 3b) : it is in accordance with theory for maximizing EOC gain if we take the assumption that the variation of the gain around its maximum is gaussian.

7. Tx-DRA performances

For distributed Tx-amplification, the main problem is the radiated power taperisation, for a maximum SSPA power, for any non-uniform excitations. For example, the linear gain factor of the Taylor circular law with SLL=-28 dB, is 0.6, losses on the antenna's EIRP are 2 dB. Hence we use an uniform feed law and the SLL optimization is performed by thinning the DRA.

The DRA dimensions are the same as the Rx ones in wavelengths, so higher by a 1.5 factor in cm. The figure 5 presents the results from the DRA thinning and the associated radiation pattern. The optimization is based on a genetic algorithm [3], well matched for this case. Thinning has enabled to save 25% of R. E. number : 189 instead of 253. The thinned DRA EOC directivity only decreases from 44.4 to 43.8 dBi for a 5.5 dB SLL improvement w.r.t the full uniform DRA (-22.5 versus -17 dB). C/I is around 17dB, so compliant with the requirement.

8. Conclusions

We have presented the predicted performances of Rx and Tx multi-beam satellite antennas in Ka band. The results of this study show that the DRA feasibility depends essentially on the BFN complexity, tightly linked with the beams number and R. E. number. A typical multimedia mission from a geostationary satellite can be achieved by Rx and Tx direct radiating arrays composed of 253 and 189 R. E. ; 8x16 Butler matrices are proposed to provide the 44 simultaneous beams. Detailed hardware design and Breadboarding will follow.

9. References

[1] R.J. Mailloux "Phased Array Antenna Handbook ", Artech House Antenna Library

[2] Piovano, B., and al., "Design and Breadboarding of wideband N x N Butler matrices for multiport amplifiers", SBMO International Microwave Conference p. 175-180, 1993.

[3] Haupt, R.L., Menozzi, J.J., McCormack, C.J., "Thinned arrays using genetic algorithms" IEEE Symposium Digest Antennas and Propagation, 1993 International, p. 712-15 vol.2
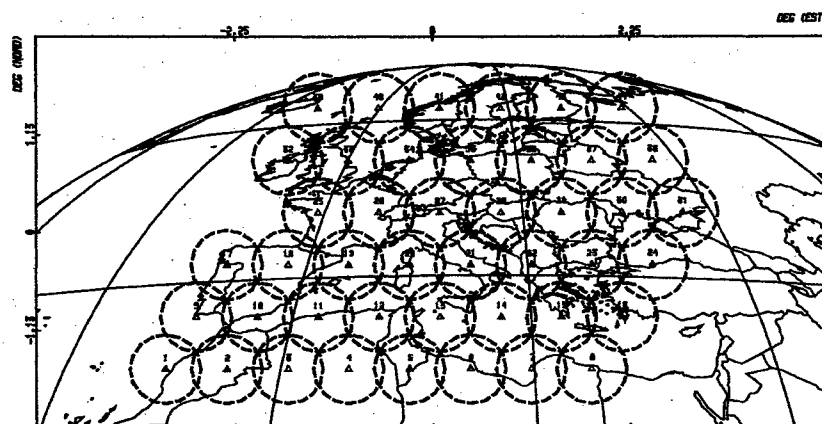
Rx/Tx band :
28350 - 30000 MHz
18550 - 20200 MHz
frequency reuse : 4

polarisation : Linear

coverage : 44 spots

spot widths : 0.8° EOC

Isolation : >15 dB (C/I)

Gain : > 42 dB EOC.

Figure 1 Example of multiple beams mission in Ka-band on Europe

a) Rx configuration with 1 LNA per R. E.   b) Tx configuration with 1 TWTA per beam
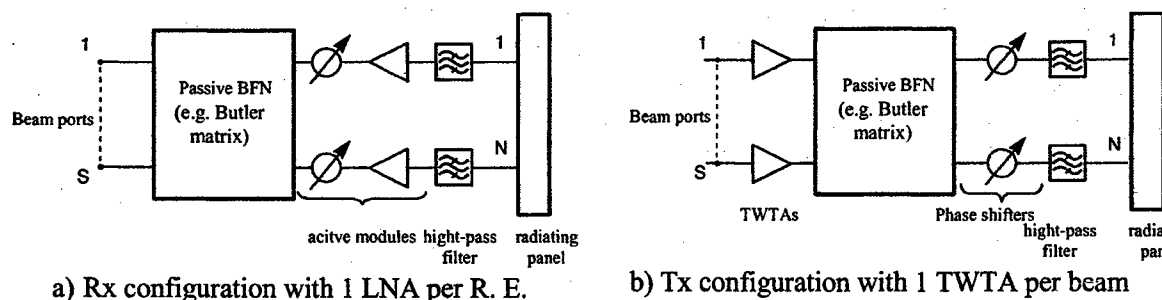
Figure 2 DRA architecture
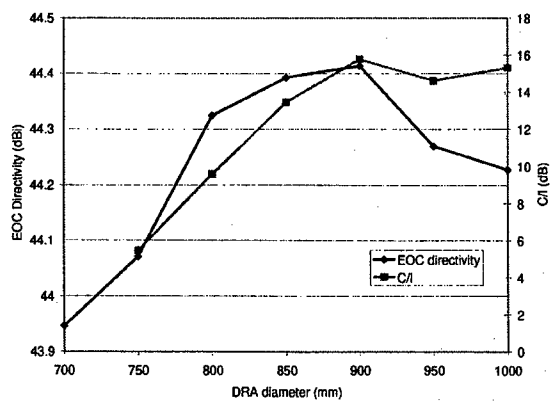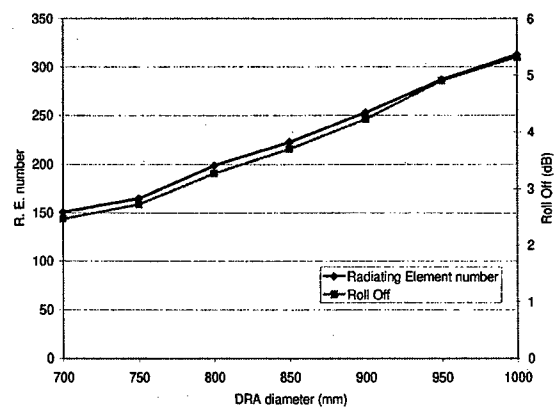
Figure 3 Rx directivity, isolation, feeds number and roll-off versus DRA diameter
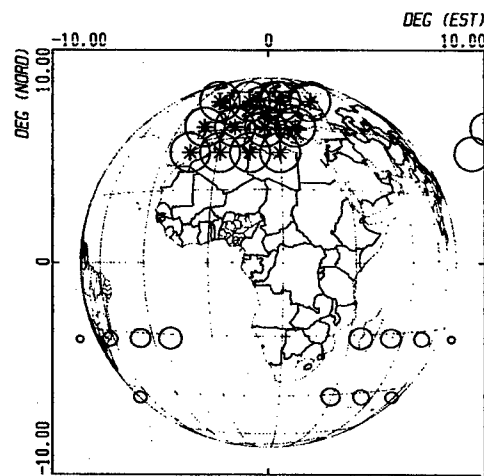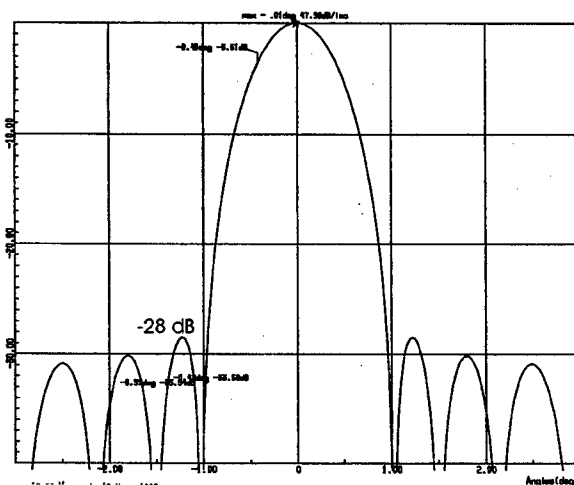
Figure 4 Rx radiation pattern and grating lobes on the oceans.
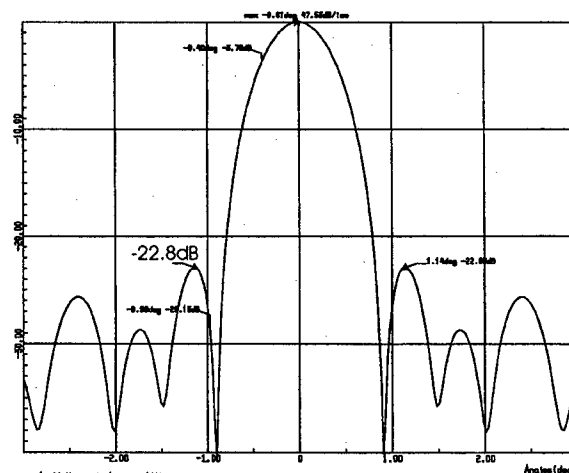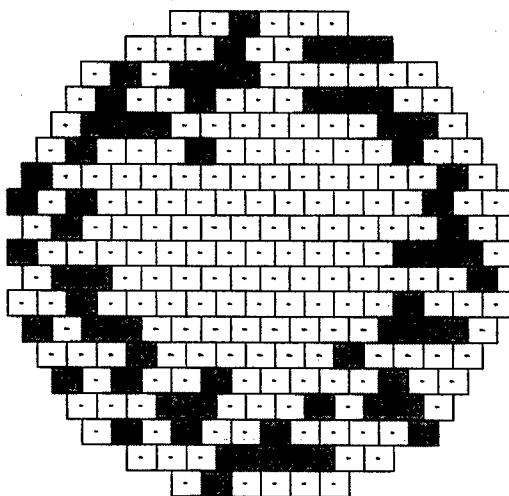
Figure 5 Tx thinned array and its radiation pattern

AN INTELLIGENT 2.45GHz BEAM-SCANNING ARRAY FOR MODERN RFID READER

Pekka Salonen, Mikko Keskilammi, Lauri Sydänheimo, Markku Kivikoski

Tampere University of Technology
Institute of electronics
P.O.Box 692
33101 Tampere, Finland

e-mail: psalonen@ele.tut.fi
tel. +358 3 365 2766
fax: +358 3 365 2620

ABSTRACT

As part of the general identification procedure, radio frequency identification (RFID) is an essential field of research in the modern industrial automation. Radio frequency identification is among the most technically advanced methods of collecting data automatically. This paper presents an intelligent 2.45GHz beam-scanning array for RFID reader. The design is based on the paper industry needs but is still applicable to other fields of industry. New current amplitude distribution is applied to feed the array elements. With this amplitude current distribution the –37.5dB side lobe level is achieved while maintaining the half power beam width at the same as Dolph-Chebyshev current amplitude distribution with the side lobe level of –30dB. Thus, the new distribution is a compromise of binomial and Dolph-Chebyshev. The system level description of the intelligent beam-scanning array is also discussed.

Key Words – Beam-scanning array, RFID, Intelligent antennas

1. INTRODUCTION

In the development of technology for paper industry the degree of automation of paper reel handling has been high for a long time, and it is still rising. Reliable paper deliveries require reliable transport systems where you can trust every link in the chain. As part of the general identification procedure, radio frequency identification (RFID) is an essential field of research in the modern industrial automation [1] – [4]. Radio frequency identification is among the most technically advanced methods of collecting data automatically. RFID technology plays an important role in controlling, detecting and tracking items and moving information efficiently with an item along its lifespan. Taking advantage of these modern RFID systems can make paper reel handling procedure faster, easier and more reliable.

The RFID system generally consists of three basic components: the transponder, the reader and the host data processing system. The part of the RFID system that most affects to the ability to read the transponder or tag is the antenna. The size of tag antenna is limited by the dimensions of tag. Thus the directivity properties can be only controlled at reader antenna. The beam-scanning array is needed because paper reels can be handled either one at the time or group.

This paper presents an intelligent five-element rectangular patch antenna array for modern beam-scanning RFID reader. In section 2, the array theory is developed which is applied to 2.45GHz antennas needed in paper industry. Section 3 presents a system level description of the beam-scanning procedure, which is controlled by a microprocessor.

2. FIVE ELEMENT NONUNIFORMLY EXCITED EQUALLY SPACED LINEAR ARRAY

The proposed beam-scanning array is composed of five elements, which are equally spaced but non-uniformly excited. This section presents the array factor (AF) derivation, which is based on the isotropic point sources. The antenna radiation pattern can be calculated by multiplying the array factor with the element factor of given antenna [5]. Thus the theory to be presented is general and can be applied to any element pattern.
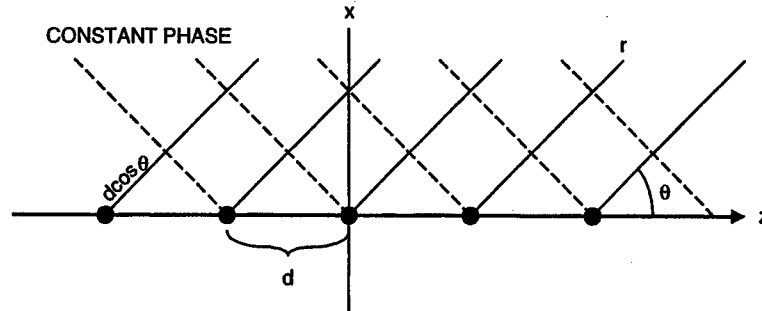
Fig. 1. Incident rays are shown in solid line and constant phase plane is shown in dashed line in zx-coordinate frame.

Let the point source separation be d as shown in fig. 1. The angle between array axis z of which unit vector is z and incident ray of which unit vector is r can be calculated by the scalar product as $z \bullet r = cos\theta$. The phase difference caused by the element spacing is thus $\beta d cos\theta$, where β is the wave number given in [6]. To obtain beam-scanning the variable phase shifter must be incorporated of which value is given by α [7]. Let A_n denote the relative amplitudes of each element where the center element relative amplitude is 1 and the phase shift $\alpha = 0°$ and the element is centered to the origin. The array factor can be evaluated

$$AF = A_1 \exp[-j2(\beta d(\cos\theta - \cos\theta_0) + \alpha)] + A_2 \exp[-j(\beta d(\cos\theta - \cos\theta_0) + \alpha)] + A_3$$
$$+ A_4 \exp[j(\beta d(\cos\theta - \cos\theta_0) + \alpha)] + A_5 \exp[j2(\beta d(\cos\theta - \cos\theta_0) + \alpha)] \tag{1}$$

where $cos\theta_0$ is the angle to the direction of which maximum is wanted. The current distribution feeding the elements of the array is symmetrical thus $A_1 = A_5$, $A_2 = A_4$. This expression can be simplified by collecting the equal amplitude exponential terms together. Thus the normalized array factor becomes

$$f(\theta, \alpha) = \frac{1}{2A_1 + 2A_2 + A_3}[2A_1 \cos(2(\beta d(\cos\theta - \cos\theta_0) + \alpha))$$
$$+ 2A_2 \cos(\beta d(\cos\theta - \cos\theta_0) + \alpha) + A_3] \tag{2}$$

The beam can be scanned by controlling the phase shift α. The RFID reader antenna should have low side lobe level. The side lobe level and the half power beam-width can be controlled by relative current amplitude. The side lobe level and the half power beam-width should be small in accurate and efficient RFID reader. The new current amplitude distribution is a compromise between binomial and Dolph-Chebyshev −30dB side lobe level distributions in which half power beam-width is identical to Dolph-Chebyshev and the side lobe level is decreased to −37.5dB. These coefficients can be calculated from normalized binomial distribution by adding 1/12 to each amplitude except the center element amplitude, thus the new coefficients are: $A_1 = A_5 = 0.25$, $A_2 = A_4 = 0.75$ and $A_3 = 1$. The resulting normalized array factor in linear scale is shown in fig. 2a, in which point source separation d is $\lambda/2$ and in fig. 2b array factor multiplied with patch element factor.

2.a)   2.b)
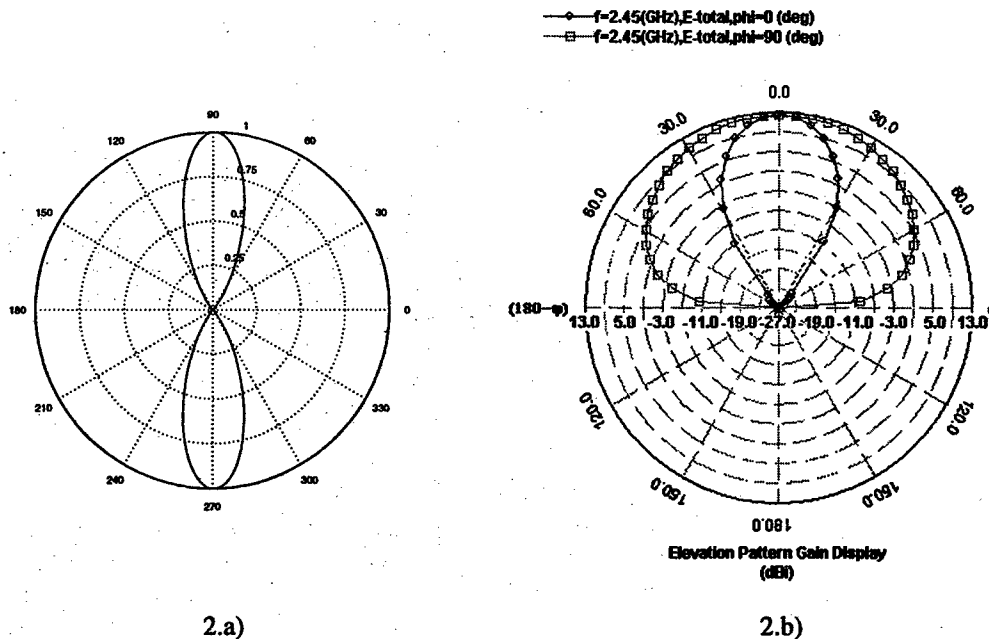
Fig. 2. a) Normalized array factor in linear scale. b) Five element patch antenna array radiation pattern in logarithmic scale.

The antenna elements used in array are rectangular patch antennas of which resonant length and width are 37.5mm. Dielectric constant is 2.54 and height from the ground plane is 3mm. The rectangular patch elements are chosen because of they do not have back radiation. Patch antennas are also light-weight, low cost and easy to manufacture. Thin structure of the patch antennas is very strong and it can withstand mechanical stress, which the antenna may confront in the transportation of heavy paper reels. The elements are feed parallel because the control of the phase scanning can be controlled easier by a microprocessor [7]. The total scan angle is 60° to avoid excessive side lobe levels i.e. 30° in both directions from the center position.

3. SYSTEM LEVEL DESCRIPTION OF THE INTELLIGENT PHASE SCANNING CONTROL

The RF front-end of the RFID reader consists of previously described parallel feed patch antenna array of which each antenna element current amplitude and phase shift can be controlled separately by a microprocessor. The transceiver is connected to the array by power combiner/divider network as shown in fig. 3. The attenuation and phase shift of each antenna element is controlled by a control bus which is eight bits wide. Four most significant bits are used to address decoding and the four least
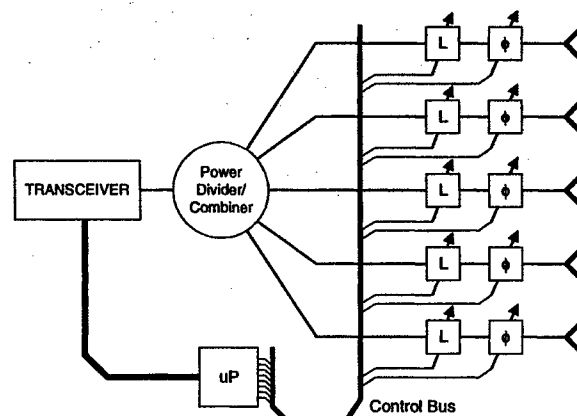
Fig. 3. Block diagram of the intelligent beam-scanning network.

409

significant bits are used to select the state of each attenuator or phase shifter. Four bits in address decoding means that it can control 16 different devices, thus the same system can control attenuators and phase shifters of eight-element array. In selecting the devise-state, the four bits means that the devise can have 16 states to choose. These values can be stored in to memory to form a look-up table. Reading the devise-states from look-up table is very fast compared to calculating the state values. However, this does not exclude the possibility to use calculation. It is just a matter of selecting of appropriate microprocessor. For this antenna array, the scan angle is $60°$. This means that the scan step is $3.75°$, which is very good resolution. However, this resolution is more than needed in this application. Also the attenuation can be controlled similarly, in which the resolution is 1/16 of the maximum amplitude.

The intelligent algorithm, which controls the array can detect the direction where the highest level signal is received and send data to that direction if requested. The RFID reader can also ask a code from a tag by sending an acknowledgement to all direction and waiting for an answer. The tag is a small passive low-cost transceiver unit attached to a paper reel containing an identification code. Thus each paper reel can be identified and its manufacturing place and date can be traced afterwards.

The microprocessor control of attenuators and phase shifters of each antenna element can be done separately, which makes this procedure adaptive. Thus the other current distributions and phase shifts are possible to form different beam shapes and properties needed in various applications i.e. the same RF front-end can be used for many other scanning or beam-forming applications.

4. CONCLUSIONS

This paper has focused on the development of intelligent planar beam-scanning array for RFID reader needed in paper industry. The operating frequency was 2.45GHz, which is part of ISM-band (Industrial, Scientific and Medical). New current amplitude distribution was applied to feed the array elements. With this amplitude current distribution the −37.5dB side lobe level is achieved while maintaining the half power beam width at the same as Dolph-Chebyshev current amplitude distribution with the side lobe level of −30dB, in which our distribution is a compromise of binomial and Dolph-Chebyshev. Patch antenna elements were chosen because of their thin structure and ease of connecting the array to a clamp truck. The control of beam-scanning was also discussed in which the intelligent algorithm controls digitally attenuators and phase shifters of the five element beam-scanning array.

REFERENCES

[1] M.Keskilammi, L.Sydänheimo, M.Kivikoski, "Modern Measurement System for Developing RF-ID Antennas", URSI'99 XXVIth General Assembly, pp. 413, Aug. 13 - 21, Toronto, Canada, 1999.

[2] M.Keskilammi, L.Sydänheimo, P. Salonen, M.Kivikoski, "Analysis of Wave Attenuation in Paper Reel", Millenium Conference on Antennas & Propagation, AP2000, Apr. 9 − 14, Davos, Switzerland, 2000, "in press".

[3] S. Beale, "The Great Paper Trace", ID Systems European Edition, pp. 22 − 26, Feb. 1997.

[4] M. Ollivier, "RFID Enhances Materials Handling", Sensor Review, vol. 15, No. 1, pp. 36 − 39, 1995.

[5] W. L. Stutzman, G. A. Thiele, "Antenna Theory and Design", 2nd Edition, New York, John Wiley & Sons, 1998.

[6] J. A. Stratton, "Electromagnetic Theory", McGraw-Hill, 1941.

[7] S. Drabovitch, A. Papiernik, H. Griffiths, J. Encinas, B. L. Smith, "Modern Antennas", IEEE Press, New York, 1998.

FOCUSER-BASED HYBRID ANTENNAS FOR ONE-DIMENSIONAL BEAM STEERING

A. S. Reutov [1] and A. V. Shishlov [2]

[1] The Moscow Institute of Physics and Technology, Dolgoprudny, Moscow Reg., Russia
[2] JSC "Radiophyzika", Moscow 123363, Geroev Panfilovtsev Str., Russia,
E-mail: apex@glasnet.ru

1. Introduction

Hybrid antenna (HA) is an effective system for limited field of view [1,2]. This system has a high gain due to a large reflector, its scan capability is achieved by use of a small feed array with controlled elements. In the existing hybrid antennas with two dimensional limited field of view [1], a realized element use factor (EUF) v is 2-3 and smaller, where $v = N / N_{min}$, N_{min} is the minimum number of controlled elements which is equal to a number of beams in the sector of beam steering [3], N is the number of controlled elements used in the antenna under consideration.

Fig. 1

In specific applications, the two-dimensional beam steering is not required, and scanning in one dimension only is sufficient. For instance, an antenna with one-dimensional field of view could be used in a ground station for communication with a satellite placed on an orbit slightly inclined to the geostatonar one. The antenna can track such a satellite because it makes oscillations along an Earth's meridian only. Another application is an airport radar with mechanical rotation in azimuth and electronic beam steering in elevation.

An example of such a HA with one-dimensional beam steering is an antenna containing a parabolic cylindrical reflector and a linear feed array of low-gain radiators located along the focal line of the reflector. Disadvantage of this system is a long feed array: its length is about the same that the reflector size. Hence, in case of a narrow beam (below 1°) and a small range of beam steering (below 10°-15°), the antenna is ineffective, i.e. $v \gg 1$.

In this paper, the HA for one-dimensional beam steering with a reflector focusing an incident plane wave to a line of a length smaller than the reflector size is considered (Fig. 1a). The reflector focusing incident radiation to a focal line (FL), is referred to as "focuser" [4,5]. Due to the doubly curved focuser shape, it is possible to reduce the feed array length in comparison with the reflector size, therefore to reduce the element number [6].

In the proposed focuser-based hybrid antenna (FHA), a linear feed array occupies a part of the focuser focal line. So, only a part of the focuser surface is excited (Fig. 1b). Controlling the phase of the array elements, we can move the excitation zone over the reflector and correspondingly to provide beam scanning (Fig. 1c,d).

The purposes of this paper are both to describe the approach to synthesis of the FHA and to analyze its beam steering capabilities and control elements efficiency.

2. Synthesis of the system

A surface of focuser is synthesized by applying geometrical optics (GO). In this approach, each point of a FL radiates a circular cone of rays [4]. The cone axis is tangential to the FL (Fig. 2).

The cone angle $\omega(\sigma)$ is determined by eikonal distribution $s(\sigma)$ over the FL as follows [4]:

$$\cos\omega(\sigma) = ds(\sigma)/d\sigma \tag{1}$$

where σ is the natural parameter of the curve.

Parametric equation of the focuser surface which transforms emergent rays of the FL to a plane wave is given by:

$$\vec{r}(\sigma,\psi) = \vec{F}(\sigma) + \vec{l}(\sigma,\psi) \cdot \left(s_0 - s(\sigma) + \left(\vec{F}(\sigma);\vec{l}_0\right)\right)\Big/\left(1 - \left(\vec{l}(\sigma,\psi);\vec{l}_0\right)\right) \tag{2}$$

Fig. 2

where $\vec{F}(\sigma)$ is the equation of the FL, $\vec{l}(\sigma,\psi)$ is the ort of a ray emitted from the point σ of the FL; ψ is the angle of ray location in the circular cone $\omega(\sigma)$; s_0 is an additive constant determining the distance from the focuser to its FL, and $\vec{l}_0$ is the ort of the plane wave.

Equation (2) determines the focuser surface as a function of two parameters: σ and ψ. In order to determine the surface, it is necessary to specify the FL shape $\vec{F}(\sigma)$, the eikonal function $s(\sigma)$ over the FL, and the direction $\vec{l}_0$. At the limit when the FL length is equal to zero, the focuser is transformed into a paraboloid. In the case of $\omega(\sigma) = const$, the focuser is transformed to a parabolic cylinder.
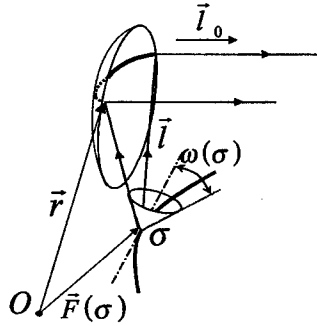
Using the GO approximation, we can evaluate the amplitude distribution $A(\vec{r})$ of the reflected field in the point $\vec{r}(\sigma,\psi)$ of the focuser surface as follows:

$$A^2\left(\vec{r}(\sigma,\psi)\right) = I(\sigma,\psi)\Big/\left|\left(\vec{l}_0;\frac{\partial}{\partial\sigma}\vec{r}(\sigma,\psi);\frac{\partial}{\partial\psi}\vec{r}(\sigma,\psi)\right)\right| \tag{3}$$

where $I(\sigma,\psi)$ is the field intensity radiated by the sources on unit length of the FL in the direction $\vec{l}(\sigma,\psi)$, $(\vec{a};\vec{b};\vec{c}) = (\vec{a};[\vec{b};\vec{c}])$ is mixed product of vectors $\vec{a}$, $\vec{b}$ and $\vec{c}$.

It is clear from equations (2) and (3), that by means of proper choice of $s(\sigma)$, it is possible to achieve the necessary amplitude distribution in the focuser aperture over a coordinate line $\vec{r}(\sigma,\psi_0)$. The amplitude in the perpendicular direction (coordinate lines $\vec{r}(\sigma_0,\psi)$) can be corrected by the pattern of the sources arranged on the FL. However, it is necessary to keep the following restrictions: a) $|s'(\sigma)| \le 1$, b) the extreme cones of the FL should touch the boundary of the reflector.

Fig 3 presents the example of FHA with two planes of symmetry. (The FL is arranged in the section presented in Fig.3). To describe the system, the following parameters are chosen: the complete size D of the reflector in the plane of scanning, the size D_0 of the excited zone of the reflector (it
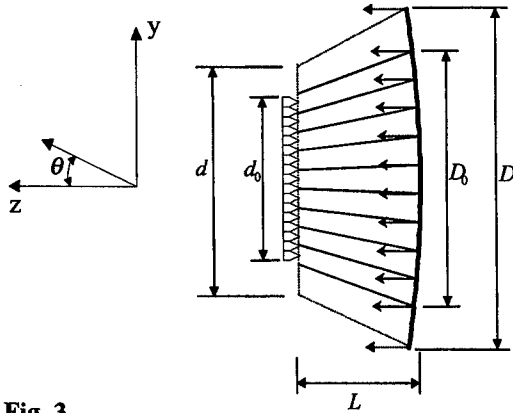
Fig. 3

defines the antenna beamwidth), the size d of the FL for the hole reflector, the size d_0 of the feed array, the depth L of the antenna, the current angle θ of observation, the angle θ_0 of beam steering.

For simplicity, in this paper, we chose a linear function $\omega(\sigma)$ and the appropriate value of $s(\sigma)$ is determined by integration of equation (1). As a model of feed, we consider a linear array of rectangular waveguides with uniform excitation ($I(\sigma) = const$).

3. Simulation of patterns and analysis of beam steering capabilities

Simulation of the FHA radiation pattern and gain has been implemented by the use of physical optics. Fig. 4 shows the dependence of antenna gain on the angle of beam steering. The feed array length d_0 is the parameter of presented curves. It defines the focuser geometry and the number of elements in the feed array. The upper curve corresponds to the system with a parabolic cylindrical reflector. The lower one corresponds to the standard system w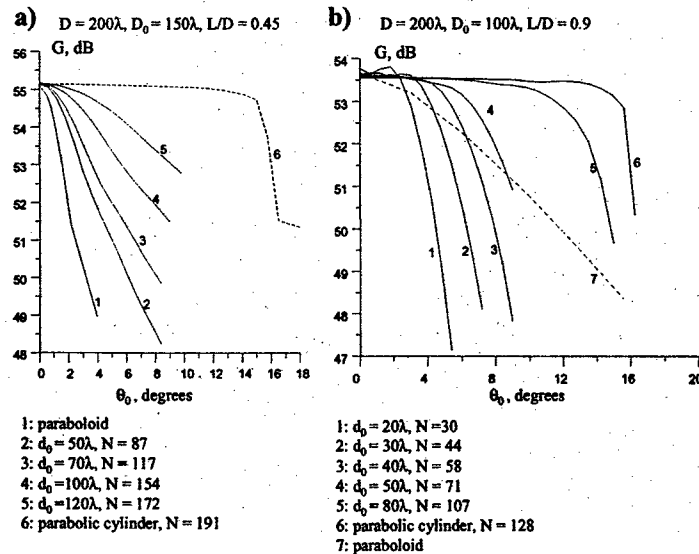ith axisymmetric parabolic reflector. In the latter case, the scanning is carried out by a transverse displacement of the feed from the paraboloid focus.

Fig 5 shows typical changes of the antenna pattern under the beam steering. These patterns correspond to curve 5 in the left part of Fig 4. Fig. 5 illustrates patterns for two cases: a) the beam is located at the center ($\theta_0 = 0$) of the scan coverage, b) it is located at the edge ($\theta_0 = 8°$) of the coverage.

a) D = 200λ, D_0 = 150λ, L/D = 0.45

b) D = 200λ, D_0 = 100λ, L/D = 0.9

1: paraboloid
2: d_0 = 50λ, N = 87
3: d_0 = 70λ, N = 117
4: d_0 = 100λ, N = 154
5: d_0 = 120λ, N = 172
6: parabolic cylinder, N = 191

1: d_0 = 20λ, N = 30
2: d_0 = 30λ, N = 44
3: d_0 = 40λ, N = 58
4: d_0 = 50λ, N = 71
5: d_0 = 80λ, N = 107
6: parabolic cylinder, N = 128
7: paraboloid

Fig. 4

As we can see, in the plane of beam steering, there are no significant changes of the pattern shape. Vice versa, in the cross plane, the side lobes level increases with increase of θ_0. The deterioration of the FHA characteristics is stipulated by two factors. The first one is the spillover. Due to this factor, the maximum angle of beam steering is determined by the margin of the reflector flare angle (Fig.1). The second factor is occurrence of the phase errors in the antenna aperture for a deflected beam. The errors appear because the reflector focuses a plane wave precisely in a line only for one chosen direction. Thus, the antenna forms exactly a plane wave only for one direction of the beam. For an inclined beam, the wave will not be plane. This effect becomes stronger by increasing the reflector depth L/D and size D/λ.
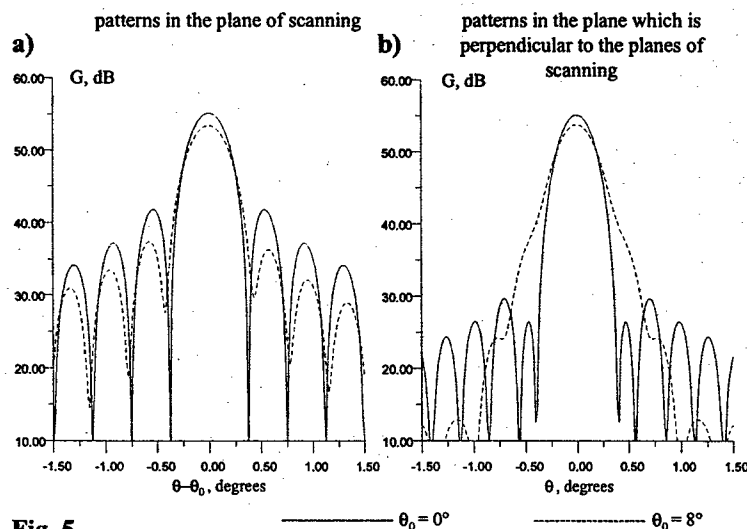
The curves in Fig. 4a correspond to focusers with $L/D = 0.45$. In this case, a main factor limiting the beam steering is occurrence of phase errors in the antenna aperture. In the second family of curves (right part in Fig. 4b), focusers have the lager L ($L/D = 0.9$) and small margins of the flare angle, thus the beam steering is essentially limited by the spillover.

With other things being equal, the smaller is the focuser curvature in the plane of scanning, the greater is the beam steering coverage. In other words, the closer is a focuser shape a

a) patterns in the plane of scanning

b) patterns in the plane which is perpendicular to the planes of scanning

Fig. 5 ———— $\theta_0 = 0°$ -------- $\theta_0 = 8°$

413

a)

beam width = 1.2°

1: Focuser $N = 36, D = 98\lambda$

2: Parabolic

cylinder $N = 58, D = 58\lambda$

θ_0, degrees

b)

beam width = 0.3°

1: Focuser $N = 78, D = 534\lambda$

2: Parabolic

cylinder $N = 212, D = 220\lambda$

Fig. 6 θ_0, degrees

parabolic cylinder, the greater is its beam steering capabilities.

In Fig.6, gain/steering angle-behavior for two systems with similar beam steering capabilities is presented. First one is the FHA with doubly curved focuser, the second one is the FHA with parabolic cylinder. We can see, the system with focuser must have larger size of reflector than appropriate system with the parabolic cylinder. However the length of the feed array and the number of elements in it is less than in the system with a parabolic cylinder. In the case of HPBW=1.2° (Fig. 6a), control efficiency is $v_F = 2.6$ for the system with parabolic cylinder and $v_C = 4.1$ for the FHA (EUF profit is 1.6). For the HPBW = 0.3° (Fig. 6b), $v_F = 3.6, v_C = 8.8$ (EUF profit is 2.7).
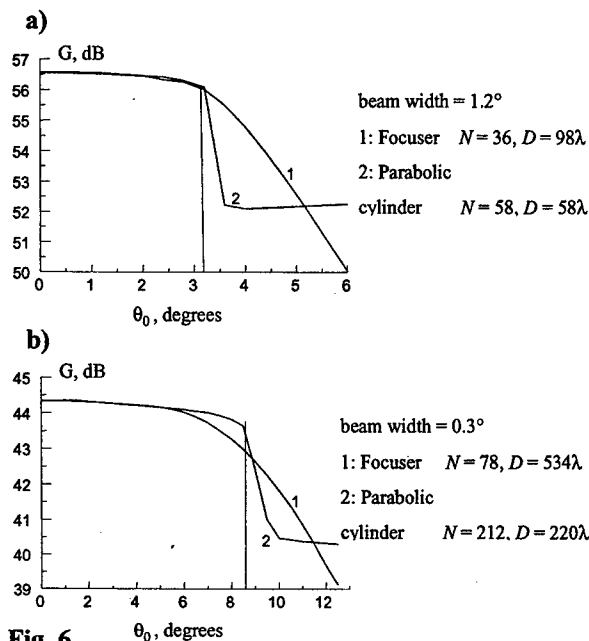
4. Conclusions

In this paper, the approach to synthesis of FHA for limited field of view in one plane is developed. From the considered examples, it can be seen that in the case of limited field of view, the FHA allows to appreciably reduce the feed array size and the controlled element number as compared with the HA with parabolic cylindrical reflector.

The considered approach to FHA synthesis can be generalized in several directions: a) offset system with no blockage, b) dual-reflector system with ordinary (commercial) main parabolic reflector and a small focuser-subreflector, c) HA with a divergent reflector for extended field of view, *etc.*

References:

[1] C. H. Tang, "Application of Limited Scan Design for the AGILTRAC-16", *20th Annual USAF Antenna Research and Development Symposium*, Univ. of Illinois, Oct. 1970.

[2] L. I. Alimova, B. Ye. Kinber, V. I. Klassen, A. V. Shishlov, "An Opportunity of Wide-Angle Beam Scanning in Hybrid Reflector Antennas", *Radiotekhnika & Elektronika*, 1981, Vol. 26,No. 12, pp.2500-2510 (in Russian).

[3] M. I. Kantorovich, V. Yu. Petrunkin, "On the Minimum Number of Elements in Antennas with Electronic Beam Steering". *Radiotekhnika & Electronica*, Vol. 6, pp. 1982-1988, Dec 1961 (in Russian).

[4] B. Ye. Kinber, S. N. Karptsov, A. V. Shishlov, "Inverse problems in optics and antenna theory". *Proceedings of the 9-th All-Union School on Diffraction and Propagation*. Kazan, 1988 (in Russian).

[5] G. Stavis, A. Dorne "Horn and Reflectors", in *Very High Frequency Techniques, vol. 1*, McGraw-Hill Book Company, New York, 1947, chap. 6.

[6] I. L. Vilenko, A. S. Reutov, A. V. Shishlov "On Synthesis of Reflector Antennas for Focusing or Scanning in One Plane", *Proceedings of the 28-th Moscow International Conference on Antenna Theory and Technology*, pp. 376-379, Moscow, 1998.

Full polarimetric pattern synthesis for an active conformal array

M.DINNICHERT

Office National d'Etudes et de Recherches Aérospatiales (ONERA)

Chemin de la Hunière, 91761 PALAISEAU, FRANCE

Email : dinni@onera.fr

Abstract

Conformal arrays offer a maximal sensor surface area for a given platform which in turn provides larger array aperture and array gain. When considering such an antenna for an airborne radar, the classical requirements for an electronically scanned antenna pattern remain, such as low sidelobe level and low cross polarization level for both sum and difference beams. This paper presents an iterative full polarimetric least-square synthesis technique for the optimization of the element excitations of an active conformal array antenna. The radiating elements are assumed to be dual polarized. Independent amplitude and phase controls are available to perform the power pattern synthesis, justifying the term of full polarimetric. For an array in its receive mode, the proposed method considers both the co and cross polarization components of the antenna pattern, making possible further array processing such as monopulse estimation. A few synthesis examples are presented for a paraboloïdal array, for the sum and difference channels.

Introduction

Conformal arrays offer a maximal sensor surface area for a given platform which in turn provides larger array aperture and array gain. When considering such an antenna for an airborne radar, the classical requirements for an electronically scanned antenna pattern remain, such as low sidelobe level for both sum and difference beams. The sidelobe level is particularly important in look down search mode and terrain mapping. Reduced electronic countermeasures (ECM) susceptibility requires also very low receive pattern sidelobes on sum and difference channels and substantial improvements in tunable bandwidth.

In the design of electronically scanned conformal array, problems arise that are different from those regarding arrays on planar surfaces. The gain of conformal arrays changes as a function of the scan angle, and also depends on the part of the radiating structure that is visible from the far field at the beam pointing position. The polarization in the far field changes as a function of the scan angle for radiating elements whose polarization is fixed with respect to the surface of the antenna. Sum and difference patterns become sensitive to the incident polarization.

The array synthesis problem for conformal arrays is of importance and a large number of papers have been devoted to it. The method presented in [1] essentially consists of a direct and inverse Fourier transform. It is therefore computationally very efficient for two dimensional planar arrays with regular lattice. But this well known Fourier transform relationship breaks down in the case of conformal arrays. Bucci extended its work to the general alternate projection approach for the synthesis of conformal arrays in the three dimensional and fully vectorial case [2,3]. This method is based on the determination of the intersection between two suitably defined sets by means of an alternate projections method. Recently, Vaskelainen presented a new array antenna synthesis method, called virtual array synthesis method [4]. This technique, which minimizes the integral of the squared difference between the array factors of the real array and a virtual array, can also be used for 3D conformal array with further developments.

The large number of available methods are essentially different in their choice of the cost function and the

algorithm used for its minimization. The basis of the method presented here is to set up the problem as a set of linear equations describing the electric field, and then solve for the excitation which produces a far field close to a desired far field. The presented method namely takes advantage of the least squares and the projection methods and proposes a conformal array synthesis in a full polarimetric case.

Problem formulation

When an electromagnetic wave with a complex polarization ratio illuminates a target, the complex polarization ratio of the scattered signal, in general, changes. This change of polarization states represents the characteristic properties of the target as expressed by the matrix S, in an orthonormal polarization basis. The scattered field from the target R is related to the incident field T transmitted via the transmit antenna by :

$$\begin{bmatrix} R_{co} \\ R_{cr} \end{bmatrix} = \begin{bmatrix} S_{co,co} & S_{co,cr} \\ S_{cr,co} & S_{cr,cr} \end{bmatrix} \begin{bmatrix} T_{co} \\ T_{cr} \end{bmatrix} \quad (1)$$

The scattered field $R = \begin{bmatrix} R_{co} & R_{cr} \end{bmatrix}^T$ is now considered as incident field on the receive antenna. We define the polarization basis in such a manner that T_{cr} is always zero, i.e. the transmitted polarization is one component of the selected basis.

Consider an array of N discrete elements arranged arbitrarily on a conformal surface. Suppose that the nth element antenna is located at x_n, y_n and z_n in a rectangular coordinate system. Each radiating element has two accesses associated to two orthogonal polarizations. These two polarizations are supposed to be axial (parallel to the antenna vertex) and circonferential and we denote the complex excitation of the axial and circonferential polarization of the nth element by w_n and o_n respectively.

The radiation pattern of a general antenna array in the direction of the unit vector $\vec{r}$ can be written in the general form :

$$F(u,v) = \frac{\sum_{i=1}^{N} w_i \cdot \left[g_i^{C,co} . R_{co} + g_i^{C,cr} . R_{cr} \right] e^{j.k_0.\vec{r}_i.\vec{r}} +}{\sum_{i=1}^{N} o_i \cdot \left[g_i^{A,co} . R_{co} + g_i^{A,cr} . R_{cr} \right] e^{j.k_0.\vec{r}_i.\vec{r}}} \quad (2)$$

where $\vec{r}_n$ is the position vector of the nth element. u and v are the classical spherical coordinates for the sampled direction, figure 2.

$$u = \sin\theta.\cos\phi \quad v = \sin\theta.\sin\phi$$

The subscript A and C represent the set of the elements axially and circonferentially polarized respectively. k_0 is the wave number and $g_n^{C,co}$ is the gain of the nth circonferentially polarized element in the direction of the unit vector for the co-polarization. Identically, $g_n^{C,cr}$ is the gain of the nth circonferentially polarized element in the direction of the unit vector for the cross-polarization.

(2) can be rearranged as follows :

$$F(u,v) = \frac{R_{co} \cdot \sum_{i=1}^{N} \left(w_i \cdot g_i^{C,co} + o_i \cdot g_i^{A,co} \right) e^{jk_0.\vec{r}_i.\vec{r}} +}{R_{cr} \cdot \sum_{i=1}^{N} \left(w_i \cdot g_i^{C,cr} + o_i \cdot g_i^{A,cr} \right) e^{jk_0.\vec{r}_i.\vec{r}}} \quad (3)$$

We note that the complex envelop of the signal at the beamformer output depends on the target properties via the R_{co} and R_{cr} values. Making this signal envelop independent of the incident polarization leads to nulling one term in (3) or at least to reduce that term to a negligible value for all the direction samples. We decide here to nulling the cross polarization component.

(3) can be easily written in matrix form.

$$F = XK \quad (4)$$

with

$$X_{ji} = \begin{bmatrix} g_i^{C,co}(u_j, v_j).e^{jk_0.\vec{r}_i.\vec{r}} & g_i^{A,co}(u_j, v_j).e^{jk_0.\vec{r}_i.\vec{r}} \\ g_i^{C,cr}(u_j, v_j).e^{jk_0.\vec{r}_i.\vec{r}} & g_i^{A,cr}(u_j, v_j).e^{jk_0.\vec{r}_i.\vec{r}} \end{bmatrix}$$

X relates all the elements gain to all the field sample points and K is the bipolarization excitation vector $\begin{bmatrix} w_1 \dots w_N, o_1 \dots o_N \end{bmatrix}^T$ of the array.

The number of rows in X is twice the number of field points (each field point has a co and cross polarization value) and the number of columns equals twice the number of elements. (4) can be solve in the least squares sense with :

$$K = \left(X^H X \right)^{-1} \left(X^H D \right) \quad (5)$$

Note that there is nothing in this formulation requiring the elements to be equally spaced or requiring identical elements. The destination vector (or required pattern) D is defined as :

$$D = \left[\vec{f}(u_j, v_j) \quad \vec{0}(u_j, v_j)\right]^T \qquad (6)$$

$\vec{f}(u,v)$ represents the pattern to be synthesized in the co-polarization and $\vec{0}$ represents the cross-polarization components to reduce to a minimum value.

The pattern requirements can be generally defined by choosing a mask, i.e. a couple of functions, say Ml and Mu, such that the pattern must lie in between. Typical masks are shown in figure 1. Note that this illustration here concerns the co-polar component only but the mask should be also defined for the cross-polar component.
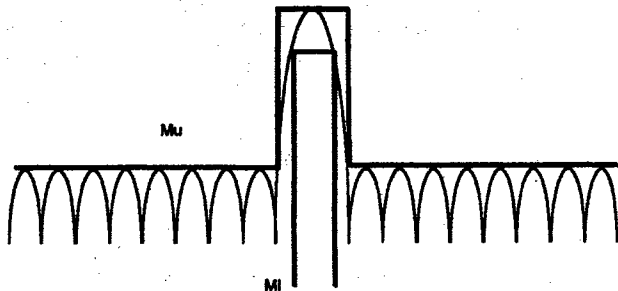

Figure 1 - Pattern requirements with masks

The shape (beamwidth and sidelobe level) of the co-polarization pattern should be very carefully selected to warrant the convergence of the process. We chose to initially define a virtual elliptical planar array in the plane perpendicular to the steered direction, figure 2. The size of the ellipse can be defined by several projection strategies. The radiation pattern of this reference array is then computed applying a elliptical taper to achieve the desired sidelobe level. From this reference pattern is built the required pattern. This procedure warrants performing a synthesis with a destination pattern in (5) that can be physically radiated by the considered conformal array.
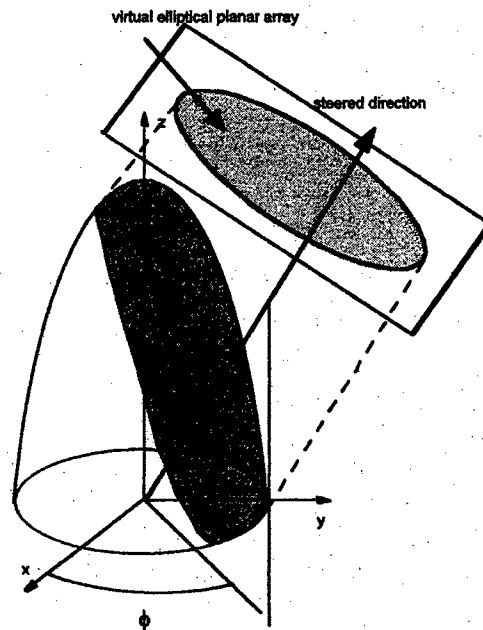

Figure 2 - Virtual array definition

For the pattern synthesis, the following iteration process can be used :

1) Calculate matrices $\left(X^H X\right)^{-1}$ and $X^H D$

2) Solve K from (5)

3) calculate F from (4)

4) Make the following projection

$$f(u,v) = \begin{cases} M_U(u,v) & \text{if} \quad |F(u,v)| > M_U(u,v) \\ F(u,v) & \text{if} \quad M_L(u,v) \leq |F(u,v)| \leq M_U(u,v) \\ M_L(u,v) & \text{if} \quad |F(u,v)| \leq M_L(u,v) \end{cases}$$

5) Calculate new $X^H D$ (D=f)

5) Calculate the new error function $e = \int_\Omega \left| f(\alpha) - D(\alpha) \right|^2 d\alpha$ where f(α) is the synthesized pattern and D(α) is the required pattern. Ω is the angular domain where f>D.

6) If the error function is not small enough return to step 2

Synthesis examples

The following synthesis examples demonstrate that the iterative least-squares method can be effectively used to synthesize doubly curved conformal arrays. The first example concerns a paraboloïd with 162 bi-polarization

patches spaced at 0,5 λ. The radius is approximately 3 λ and the antenna height is 1,5 λ. The array is steered at θ=20° and φ=30°. The sidelobe level requirements are set to -30 dB and -40 dB for the co and cross polarization components respectively, figure 3.

Figure 4 gives the excitation coefficients to be applied for the axially and circonferentially polarized elements respectively. Figure 5 illustrates the convergence rate of the algorithm (left) and the difference pattern for the same antenna but obviously with different excitation coefficients.

Conclusion

A new technique for the synthesis of conformal arrays has been presented. This approach consists of an iterative least-squares algorithm. The originality of the method is to give a solution in the case of a doubly curved conformal array for the sum and difference channels. In the examples presented in this paper, the synthesis is relatively quick, requiring few iterations. This synthesis has been presented with linearly polarized elements. But this method remains valid for any polarization basis. The problem formulation assumes that each radiating element has two ports orthogonally polarized. Some ad hoc strategies could be found to reduce the number of active ports, therefore reducing complexity, cost and power consumption of the active antenna.

Further developments at ONERA are currently considering array partitioning into subarrays and digital beamforming.

References

[1] O.M.Bucci and al « Intersection Approach to Array pattern synthesis », IEE Proceedings, Vol 137, part H, n°6

[2] O.M.Bucci, G.D'Elia « Power synthesis of conformal arrays by a generalised projection method », IEE Proc.-Microw. Antennas Propag., Vol 142, No 6

[3] O.M.Bucci, G.D'Elia « Power synthesis of reconfigurable conformal arrays with phase-only control », IEE Proc.-Microw. Antennas Propag., Vol 145, No 1

[4] L.I.Vaskelainen, « Virtual Array Synthesis Method for planar Array Antennas », IEEE Trans AP vol 46, n°3, March 1998

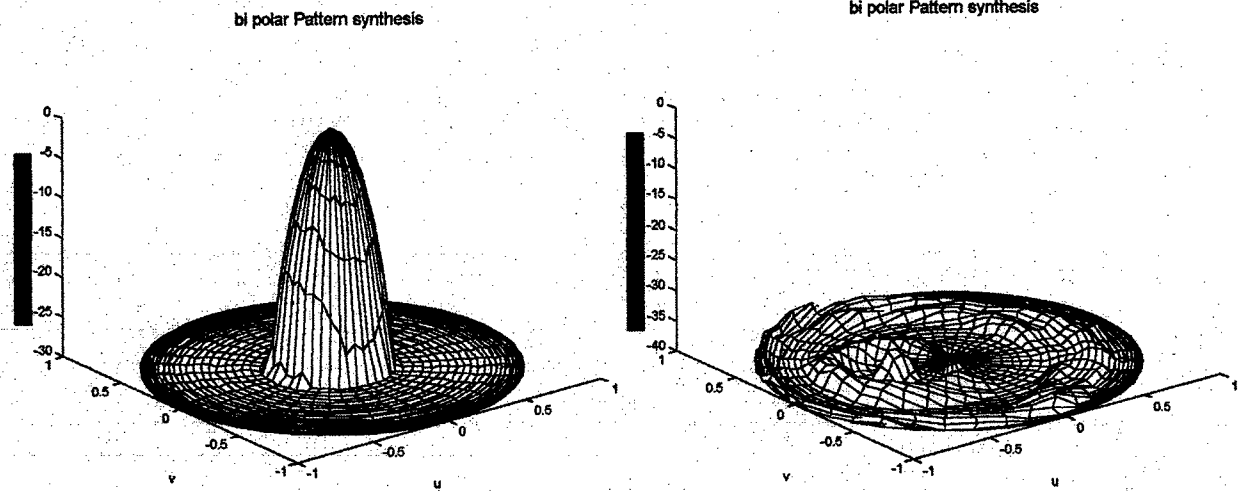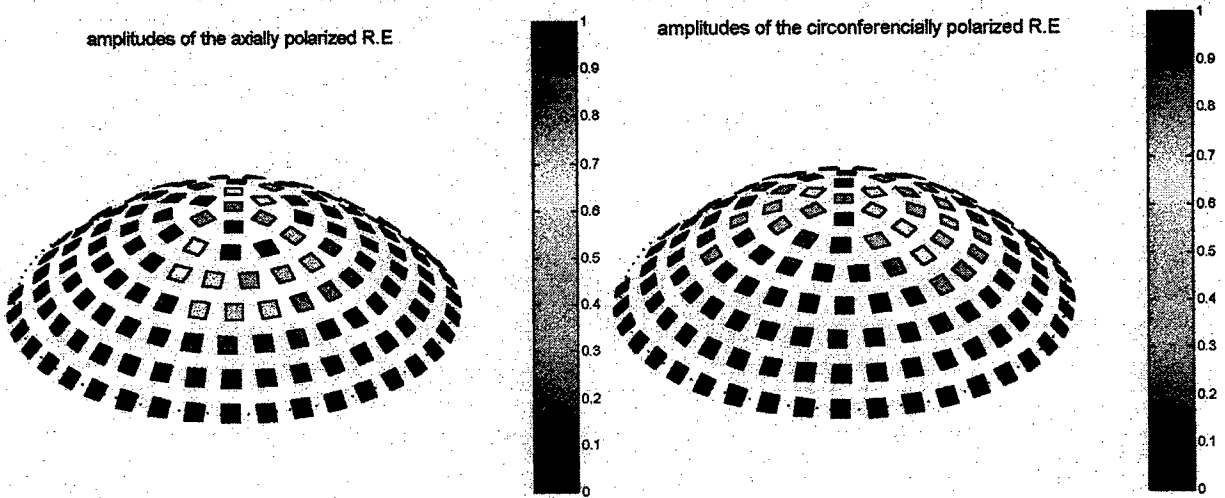Fig 3 - Co and cross polarization pattern synthesized (sum channel)

Fig 4 - Amplitudes for the axially and circonferentially polarized element (sum channel)
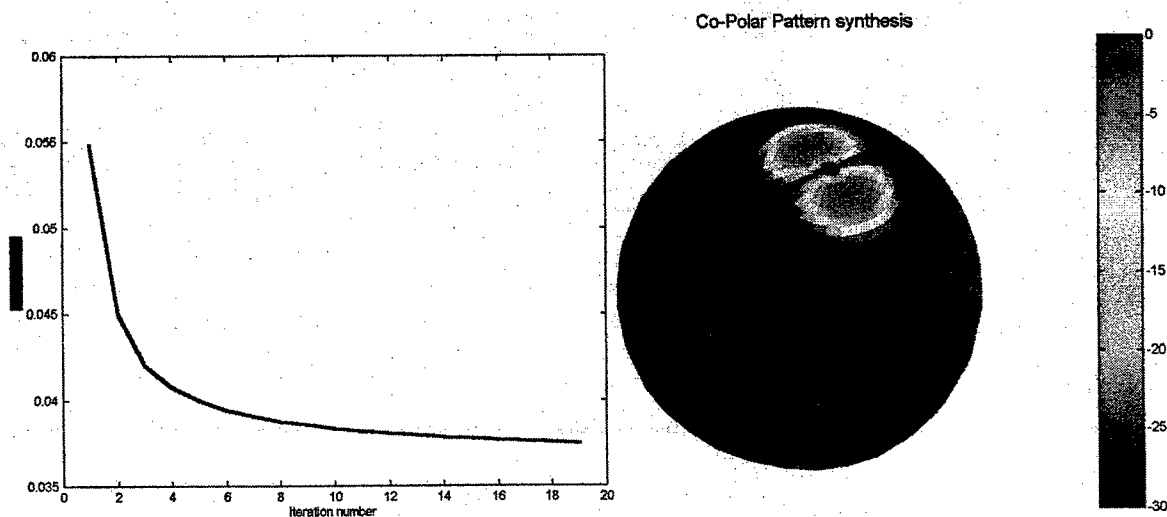

Fig 5 - Convergence rate and co-polarization pattern for the difference channel

419

PACER (Phased Array Concepts Evaluation Rig): Design, Development and Adaptive Beamforming Experiments.

P. G. Richardson, F. J. Adams, K. J. Lewis and J. C. Medley.
DERA Malvern, St. Andrews Road, Malvern, Worcs., WR14 3PS, U.K.

Introduction

PACER (Phased Array Concepts Evaluation Rig) is an experimental, receive only, phased array that has been designed and built at DERA Malvern. The array operates at X band and has been constructed as a facility to support DERA research associated with the tri-national AMSAR airborne phased array demonstrator programme, [1], and other future generation phased array radar systems. PACER is a unique facility, and the flexibility of the design offers considerable scope for practical research into adaptive array signal processing and future research associated with advanced phased array concepts (wideband operation, RCS reduction, bistatic operation, element level digitisation approaches). To date, the array has been used primarily as a source of real phased array data for validation of adaptive beamforming techniques. This paper includes some detail of the design and build of PACER in addition to the results of adaptive array signal processing experiments to demonstrate jamming rejection and estimation of the directions of closely spaced sources.

Array design

PACER is a circular planar array of approximately 600mm diameter and comprises of 1171 microstrip patch radiating elements. The fully filled array face, as shown in Figure 1, allows consideration of many beamforming configurations. However, for cost reasons, the array has initially been configured such that control of only 64 of the elements is enabled. The 64 receive elements are located in the two central horizontal staves of the array, with the remaining 1107 unused elements being terminated with 50Ω loads. The outputs of the 64 elements are combined at RF to form eight subarray channels. In the current configuration, the output of each of the subarrays is downconverted to an IF frequency of 8MHz, amplified, and then fed into a 12 bit analogue to digital converter (ADC) operating at a 40MHz clock frequency. The digitised data are transferred to a PC where they are mixed to baseband frequencies and stored for subsequent off-line adaptive processing. A schematic of the full processing architecture is given in Figure 2. The subarray configuration employed in the initial adaptive beamforming experiments is shown in Figure 3. Note that the subarrays are of unequal size in order to suppress grating lobe effects that may occur due to spatial undersampling. Further details of the array design are given in [2].

Calibration and control

To calibrate the array, a low level RF signal was injected into each of the receiving elements in turn using a probe accurately positioned on the array face. The probe was lowered into direct contact with an element by a small actuator in a manner that ensured no unwanted coupling into adjacent elements. The calibration proved to be a major undertaking, with the 6 bit amplitude and phase control implying 4096 settings for each of the elements. Three frequency settings were chosen for the calibration, giving a total of 786,432 (4096x64x3) measurements. Phase gain maps for each element channel were produced. Calibration beam patterns for the array were then obtained by selecting the amplitude and phase settings for each element that were situated closest (in the complex plane) to the required settings. Beam patterns derived from the calibration values were compared with theoretical patterns that assumed perfect amplitude and phase control, and extremely good agreement was generally achieved (see [2]).

PACER is controlled from a PC running LabView ® software. Virtual Instruments (VIs) have been written to control each of the elements. By selecting the appropriate "buttons" on the computer screen display, each attenuator and phase bit of any of the elements within a quadpack box can be switched on or off. Each quadpack of elements has been evaluated and tested by connecting to an HP 8510C network analyser via a switch matrix. The correct bias for the required gain was set, and each of the six bits of the phase shifter and attenuator chips were tested.

Digital adaptive beamforming experiments.

Prior to adaptive beamforming, experiments were performed to assess the level of the subarray channel mismatch errors, and to determine the resulting limit on the jammer cancellation. The errors were estimated using data

collected for a strong far field test source located at array broadside. The frequency of the source was varied in 1MHz steps across a 20MHz bandwidth. Amplitude and phase responses were measured at each frequency, for each subarray, using a vector voltmeter. After 'normalisation' to account for fixed amplitude and phase mismatches between channels, an 'ideal' response was defined by taking the average of the eight subarray responses at each frequency across the 20MHz bandwidth. The RMS amplitude and phase errors were then derived from the deviation of the actual subarray responses from the synthesised 'ideal' channel. This process revealed RMS amplitude and phase errors of 0.2dB and 2.5 degrees respectively. Assuming a single sidelobe jammer, and errors that are uncorrelated between channels, an estimate of the maximum achievable cancellation, C, in dB can be obtained from:

$$C \approx -10\log_{10}\left\{\frac{[\bar{a}^2 + \bar{\phi}^2]}{N}\right\} \tag{1}$$

where $\bar{a}$ is the RMS relative amplitude error, $\bar{\phi}$ is the RMS phase error and N is the number of adaptive channels. Substitution of the channel mismatch values of 0.2B amplitude and 2.5 degrees phase error into equation (1) leads to a cancellation value of 35dB. However, taking into account the sidelobe suppression already obtained with the conventionally weighted beam, jammer cancellation of around 20dB should be typically achieved with PACER. Cancellation in excess of this can be achieved applying equalisation filters at each subarray channel in order to modify the responses to more closely match that of the 'ideal' channel.

A number of adaptive beamforming experiments involving both mainlobe jamming and sidelobe jamming have been carried out with the PACER array. This paper concentrates on results of sidelobe jamming experiments involving two noise sources operating over a 2MHz bandwidth. The noise sources were located at angular separations of 21 degrees and 40 degrees from a pulsed CW signal, with a 1% duty cycle, situated at array broadside. The frequency of the transmitted signal waveform was offset to simulate a target Doppler frequency equivalent to half the pulse repetition frequency. The adaptive weights were calculated directly from the data using the SMI (Sample Matrix Inversion) algorithm. From comparison of the outputs obtained with conventional and adaptive weighting it was discovered that approximately 18dB jammer cancellation had resulted from adaptive processing. It should be noted that this level of suppression was achieved without performing channel equalisation and in the presence of severe multi-path from neighbouring buildings. The results of applying range-Doppler processing to the beam outputs are shown in Figures 4, 5 and 6. In the conventional output, in Figure 4, the signal is obscured by the jamming signal that is present throughout the entire range-Doppler detection map. In the adaptive output, Figure 5, it is clear that adaptive processing has led to significant suppression of the jamming, rendering the target detectable. For comparison purposes, the conventional output in the absence of the jamming is shown in Figure 6. The signal to noise ratio estimated from the adaptive beamformer output following range-Doppler processing was 20.9dB. For the jamming free conventional output shown in Figure 6 the estimate of the signal to noise was 29.3dB, showing that, despite leading to a significant improvement, the adaptive beamformer is still 8.4dB short of the ideal performance.

The results indicate that channel mismatch errors and multipath have limited the jammer suppression. These effects can be reduced significantly using wideband adaptive processing methods that utilise an adaptive tapped delay line architecture of the type considered in [3]. This type of processing effectively performs an adaptive equalisation of the subarray channels during the beamforming. To investigate the effectiveness of the approach, the data was processed using four taps per subarray channel. As the response of the beamformer is now frequency dependent, "all pass" constraints of the type detailed in [3] were implemented in order to maintain the gain to all signal frequencies at the look direction. The range-Doppler map that resulted is shown in Figure 7. The estimated signal to noise ratio was 25.3dB, an improvement of more than 4dB over the narrowband result.

The results of applying digital beamscanning, MUSIC, [4], and Capon, [5], direction of arrival determination algorithms to the sidelobe jamming data are shown in Figure 8. Poor performance is achieved using digital beamsteering at the subarray level due to the resultant high sidelobes. In contrast, peaks accurately located at the jammer source directions can clearly be seen in the MUSIC and Capon azimuthal power spectra. However, there are many other peaks due to weak grating lobe effects and multipath. In particular, the peaks at +13 and +30 degrees have been found to be due to grating lobes associated with the chosen subarray design. Better direction finding performance can be achieved for sources located within the mainlobe regions of the subarray beams. Figure 9 shows MUSIC spectra for two sources located close to array broadside with 1.4 degrees azimuthal separation. In this case, the two signal peaks are clear and there is far less evidence of grating effects than in the sidelobe jamming scenario.

Conclusions.

PACER is an experimental, receive only, phased array that has been constructed in-house at DERA Malvern. To date, the array has been used primarily as a facility for collecting multi-channel signal data for validation of adaptive phased array signal processing techniques. This paper has provided brief details of the array design together with the results of initial adaptive array signal processing experiments. The experiments have demonstrated successful rejection of sidelobe jamming, and it has been shown that wideband adaptive processing can help to compensate the effects of multipath and channel mismatch errors to significantly improve the jammer suppression. Results have also been presented that show accurate estimation of the directions of arrival of closely spaced signal sources via spatial super-resolution techniques. The direction finding techniques work well for sources located within the mainlobe of the individual subarray beams, but, due to grating lobe effects, the methods are not very reliable for sources lying within the subarray beam sidelobe regions. The PACER array has recently being upgraded to support 128 receive elements, and it is planned to perform further experiments with planar array configurations with an increased number of digitised channels. Although the array is currently being used to support adaptive beamforming research, the flexibility of the design ensures that there is the potential for future practical research into other advanced phased array concepts (e.g. RCS reduction, bistatic operation, wideband operation, element level digitisation).

References

[1] R. A. Blinston, "Airborne Multi-role Solid-state Active-array Radar – AMSAR", IEE and IEEE/MTT Microwaves and RF Conference Proc., Wembley, Oct. 1996, pp18-22.

[2] P. G. Richardson, F. J. Adams, G. M. Herbert, K. J. Lewis, J. C. Medley, W. Richmond, "PACER – Phased Array Concepts Evaluation Rig", Proc. of the 5th International Conference on Radar Systems, Brest, France, May 1999.

[3] O. L. Frost, "An algorithm for linearly constrained adaptive array processing", Proc. of the IEEE, Vol. 60, No. 8, Aug 1972, pp926-935.

[4] R. O. Schmidt, "Multiple emitter location and signal parameter estimation", IEEE Trans. on Antennas and Propagation, Vol. 34, No. 3, pp276-280, 1986.

[5] J. R. Capon, "High resolution frequency-wavenumber spectrum analysis, Proc. of the IEEE, Vol. 57, No. 8, pp1408-1418, Aug. 1969.
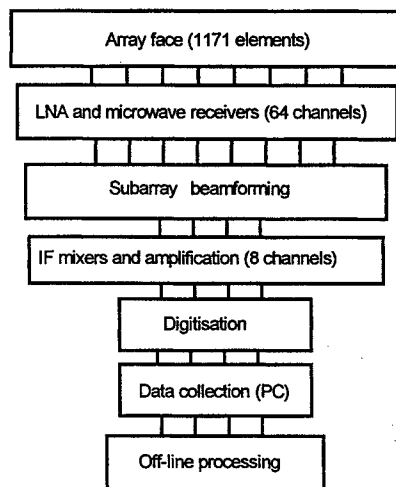
Figure 1: PACER array face showing 1171 receive elements   Figure 2: The PACER processing architecture.
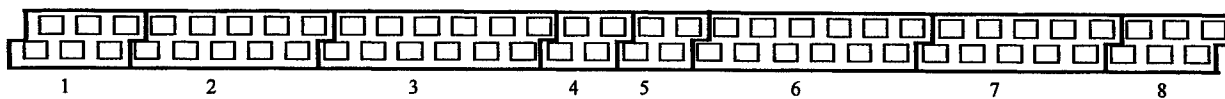
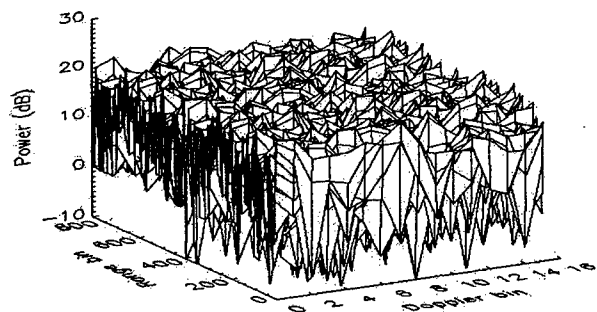Figure 3: PACER receive elements and subarray partitioning.

Figure 4: Conventional beamformer range-Doppler map, sidelobe jamming scenario
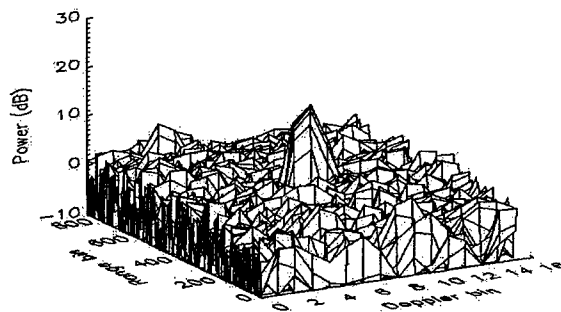

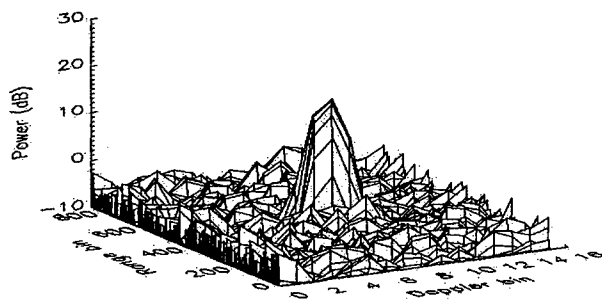Figure 5: Adaptive beamformer range-Doppler map, sidelobe jamming scenario.

Figure 6: Conventional beamformer range-Doppler map, no jamming.
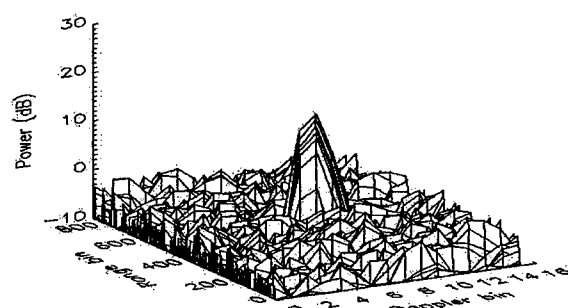

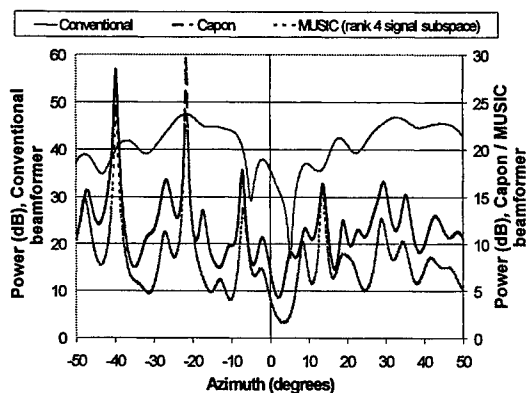Figure 7: Wideband adaptive beamformer range-Doppler map, sidelobe jamming scenario

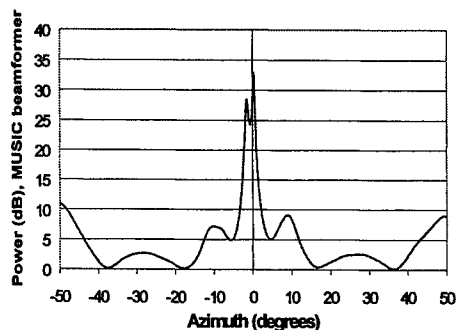Figure 8: Direction of arrival spectra, sources in subarray sidelobe region

Figure 9: MUSIC direction of arrival spectrum, sources in subarray mainlobe region

Calibration aspects of the APAR antenna unit

dr.ir. G.H.C. van Werkhoven, ir. A.K. Golshayan
Hollandse Signaalapparaten B.V.
P.O. Box 42, 7550 GD, Hengelo, the Netherlands
Fax: +31 74 248 3889
E-mail: werkhoven@signaal.nl

ABSTRACT

APAR, an acronym for Active Phased Array Radar, is a Canadian-Dutch-German program. APAR underlies the MFR scenarios within the NATO Anti-Air warfare System (NAAWS), in which all three partners have been co-operating. The system integration and testing of the engineering and development model (EDM) at factory has been concluded. The calibration of the antenna unit in the an-echoic test chamber has been a major activity, which provided new insight into the behaviour of the antenna during the calibration process.

1. INTRODUCTION

APAR is an active I/J-band multifunction radar (MFR), which will be part of the AAW-system on the German F124 and Dutch LCF frigates. Within this system APAR is responsible for weapon control support, multitarget tracking of air and surface targets, as well as for detection and tracking of sea-skimming and high diving missiles. A full description of APAR capabilities can be found in [1].

Recently the design phase of APAR has been finalized with succesfull factory acceptance tests of the Engineering Development Model (EDM). Series production models are exact copies of the EDM with an improved TR-module noise figure, such that the EDM is de facto the first of series production.

APAR consists of four independently operating non-rotating active phased array antennas. Each antenna consists of more than 3000 waveguide radiators and MMIC-based TR elements. These antennas are designed to have a wide scan range (upto 70 degrees from antenna boreside) for full 360 degrees coverage, fast electronic beam steering to support search functions and simultaneous tracking of hundreds of targets, a large frequency bandwide (upto 30%) to avoid horizontal fading due to multipath effects for low elevation targets, and ultra low sidelobes for accurate search and track as well as for a low jammer susceptibility. To maintain the low sidelobe level, an on-line calibration procedure is implemented.

The design of the antenna was started several years ago. Design features regarding the passive waveguide array, such as scan performance in relation to mutal coupling, as well as polarization and element position errors are discussed in [2]. Properties and performance of the active TR elements are presented in [3]. The emphasis in this paper is on the calibration of the combining and dividing RF networks including the active TR elements since the calibration accuracy is directly related to antenna parameters as sidelobe level and directivity.

2. ANTENNA ARCHITECTURE AND CALIBRATION PROCEDURE

The APAR waveguide array uses a dielectric sheet for wide angle impedance matching (WAIM sheet). Each waveguide radiator is connected to a TR element, which comprises of a sum channel and a combined transmit/delta elevation channel [3]. These channels are connected to separate column combiners. Electronic scanning and computation of special beamtypes is done using distributed beamsteering computers (BSC) on each column assembly, which are quickly accessible for replacement or maintenance. In receive mode the column outputs are combined once more using additional rowcombiner networks. For the sum channel a so-called combined combiner is used that leads to coupled sum and azimuth channels, thereby allowing for two i.s.o three independent channels per TR element. Together with the elevation channel, these channels form a phase-comparison monopulse antenna. In transmit mode signals from the waveform generators are distributed to the combined transmit/elevation channel using a separate row combiner and the elevation combiners.

Figure 1. Schematic view of APAR RF network layout

Alignment of all RF paths is done in two steps, an off-line calibration that has to be performed only once at Signaal's Compact Antenna Test Range (CATR), and an on-line calibration that can be performed regularly on board of the ship. During the off-line calibration transfers are measured for both plane wave incidence and for testpulse injection. The latter implies that a pilot tone is injected into each waveguide element using special testpulse waveguides that are also a part of the waveguide array. The ratio of these two transfers, referred to as the array parameter, does not include RF common paths with their active components, and is therefore considered to be stable over the life time of the system. On board of the ship the testpulse calibration is repeated and the array parameters are used as a reference to the CATR plane wave. This on-line calibration is repeated regularly to counter temperature and/or aging effects of the TR elements and RF networks.

The total error budget, after calibration, consists of a number of contributions of which TR-element errors are most dominant. The antenna design is such that sidelobe level requirements are in compliance with the total error budget, provided that all errors have a random nature. These design constraints are based upon results on several APAR prototypes, where only a limited number of elemets are used. The EDM tests have been the first occasion to measure calibration performance and pattern results using the full waveguide array. It was found that reflections at the output of the TR-elements (network side) can lead to periodic perturbations over the entire waveguide array. Such correlated effects can lead to undesired high sidelobes. This phenomenon together with solutions to reduce the sidelobe level is discussed below.

3. CALIBRATION ERRORS DUE TO TR-ELEMENT REFLECTIONS

When a radar pulse is transmitted all elements are set to receive mode. This is not the case during calibration since this is done in clusters (groups) of 16 elements simultaneously. Only these calibration elements are set to receive mode, other elements (referred to as non-calibration elements) are set to an isolate mode, which implies that there is no power to phaseshifters and variable gain attenuators, and that switches are set to 'middle' positions to minimize noise effects. The result is that these elements are poorly matched to the combining network such that large reflections occur (upto Γ_2=-2dB whereas whereas Γ_2<-10dB in receive mode. This affects the transfer function for a calibration element through the finite isolation of the column combiner, see Fig. 2, particularly if a calibration and a non-calibration element are connected through the last splitter stage of a column combiner. This effect can be diminished when elements are calibrated in pairs coinciding with the last and, to a less extend, higher splitter stages. Figure 3a shows the original cluster set. Elements in a specific cluster have the same gray tone. The elements are plotted in a 64x64 row/column notation. Note that there are currently no elements at the

outer corners of the array. A full array will be used for future tactical ballistic missile defense scenarios.
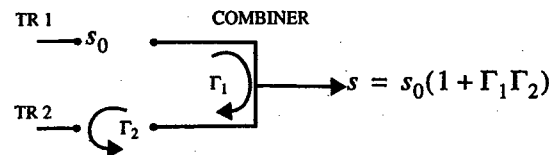

Figure 2. TR element reflections

The number of elements that lie upon a single column combiner is plotted for each cluster element, see Fig. 3b. Per column combiner there can be 1 upto 6 elements, thus this set clearly does not include the 'pairing' requirement. One can expect that the calibration results will suffer from TR-output reflections, particularly in case of an odd number of elements per column. This is tested by comparing pattern and calibration results using the orginal clusters with results obtained from a modified cluster set in which 8 adjacent top-down elements on a single column combiner are calibrated at the same time.
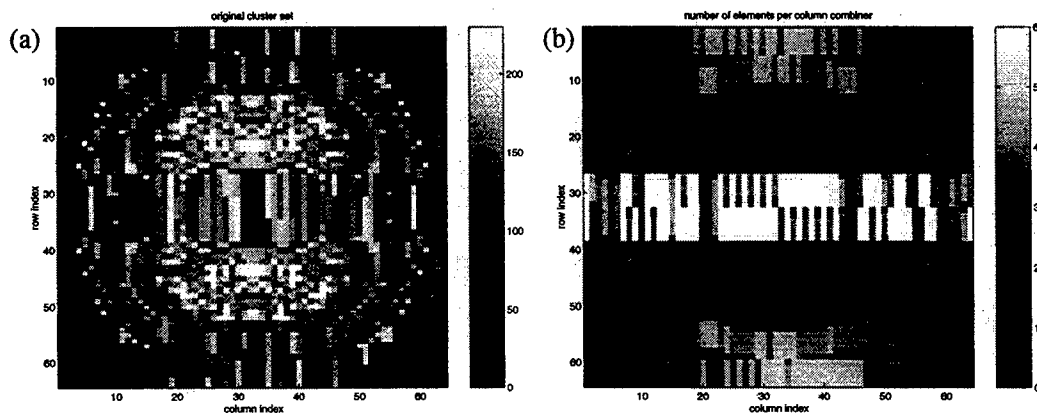
Figure 3. (a) Original cluster set, (b) number of elements per column combiner.

This assures a good output termination for the calibration elements. The relative amplitude and phase differences between the two calibration results are shown in Fig. 4. Only Sum channel is shown, similar results are obtained for the elevation channel. Clearly there is a strong correlation between the spatial distribution of errors over the waveguide array and the original cluster set depicted in Fig. 3.
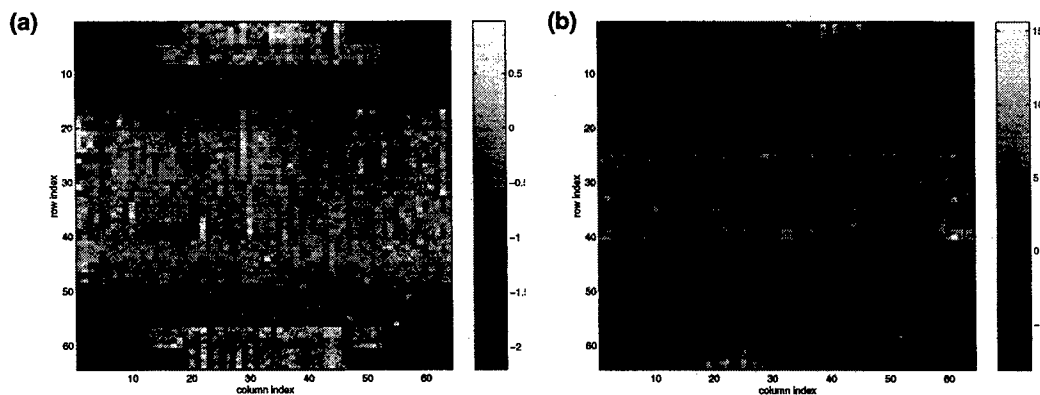
Figure 4. Relative amplitude (a) and phase differences (b) between Sum channel calibration results for original and modified cluster sets.

Oscillatory behaviour is present in both vertical and horizonal directions, however the most dominant effect is expected in the vertical (E-plane) direction.

Figure 5a. shows the measured E-plane antenna patterns for the original and modified cluster. A large broadening is present near the main lobe when the original clusters are used. This broadening is consistent with the period of the spatial oscillation. This effect is less pronounced in the H-plane pattern, as expected. In Fig. 5b the E-plane pattern is compared to a simulated pattern in which the ratio of the for mentioned calibration results is superimposed upon the desired waveguide taper. Particularly near broadside the results are in good agreement. This implies that the errors induced by TR-reflection dominate over all other error sources.

To minimize these TR-element induced waveguide ripples one must clearly improve the matching between the TR-elements and the column combiners. This is done successfully by changing the control words of the TR-elements asics, in combination with new clusters that include the fore mentioned 'pairing' constraint.
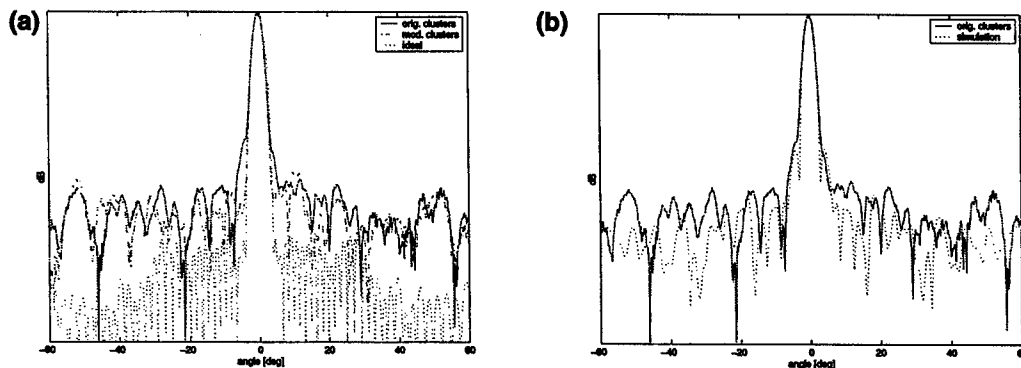
Figure 5. (a) Measured E-plane patterns using the original clusters (solid line) and modified clusters (dashed line). The dotted line corresponds to an idealized simulation. (b) Measured pattern using the original clusters compared to a simulation where the ratio of the transfers belonging to each cluster set is superimposed upon the ideal pattern.

4. CONCLUSIONS

It has been shown that the calibration performance depends strongly on a good matching between the TR-elements and the receive network. Ill-matched (non-calibration) elements can lead to undesired perturbations that extent over the waveguide face. The structure of these perturbations depends on the cluster set that is used. Improved matching was achieved by modification the software control of the TR-element components such that all non-calibration elements are set to receive mode with the lowest attenuation setting.

REFERENCES
[1] A.K. Golshayan, P. van Genderen, S. van der Schoot, 'Active Phased Array radar', Radar Brest '99.
[2] A.B. Smolders, 'Design and construction of a broadband wide-scan angle phased array antenna with 4096 radiating elements', IEEE-APS on Phased Array Systems and Technology, Boston, MA, '96.
[3] J. Bennett, K. Lewinski, P. Shearing, B. Velsher, J. van Houten, A. Tiesinga, 'Quadpack X-Band T/R Module for Active Phased Array Radar', GAAS 98 Conference Proc. p. 63, October 1998.

WA2

Wideband Phased Arrays and Time-Domain Methods

Wideband Phased Arrays and Time-Domain Methods

A proposal for a novel shared aperture radar
suitable for horizon searches

N. Fourikis

Phased Arrays Systems

3 / 48 Adelaide Tce

ASCOT PARK SA 5043 - AUSTRALIA

fourikis@camtech.net.au

Abstract: Horizon searches are particularly challenging for the defense of ships. The proposal calls for the array to be located on the deck of the ship and the generated powers are directed toward the ship's horizon with the aid of lightweight frequency selective surfaces, FSSs located on a high mast. The receive array consists of a circular array populated with wideband antenna elements capable of operation over a 3:1 frequency range while the transmit array is a linear array of elements followed by high power microwave power modules, MPMs. The proposal meets the requirements for horizon searches.

1   INTRODUCTION

While the surveillance volume of a shipboard radar system is hemispherical, horizon searches are important and particularly challenging. The threats imposed by missiles travelling at low elevation angles to ships are widely known. An Exocet missile for example can fly at an altitude of 2m above sea and the range at which the missile is in view from a ship is relatively short, typically 10-12 nmi [1].

Radars operating at S-or C-bands positioned at high masts above the ship's deck have relatively wide beamwidths which allow the systems to receive the direct as well as the indirect reflections from the target. Thus to a first approximation an interference pattern effectively prevents the radar from deriving the missile's position. Similar arguments hold for missiles travelling close to the ground and toward a high value asset.

The requirement for shipboard radars having significant power-aperture products results because the missile's radar cross section, RCS, is low and the propagation path losses are significant near the surface of the sea.
The last requirement for shipboard radar to have a large instantaneous fractional bandwidth e.g. 25% or larger is based on detailed considerations outlined in reference [1]. The important attractors of an ultrawideband radar are high range resolution and clutter rejection while its vulnerability to electronic counter measures, ECM has been acknowledged [1].

The requirements of a shipboard radar system performing horizon searches therefore are (i) Narrow beamwidth; (ii) High power-aperture product. (iii) Wide instantaneous bandwidth; and (iv) ideally continuous surveillance, ensuring no observational gaps exist.

2   THE PROBLEMS

Current multifunction radars cannot meet requirement (iv) because horizon searches are undertaken on a time sharing basis with other radar functions. As the timelines for the other radar functions increase, the time devoted to horizon searches necessarily decreases.

Let us assume that the system uses an active phased array using monolithic microwave integrated circuits, MMIC-based T / R modules. Wide-band modules operating from the upper C-band through to X- and Ku-bands can yield output powers of the order of a few Watt [2]. At higher frequency bands, the available power from MMICs operating over wide bandwidths is even lower. Tube-based amplifiers / oscillators on the other hand can deliver substantial powers at cm and mm wavelengths.

If a single aperture radar system is used in conjunction with a high power tube transmitter, the advantages offered by active phased arrays of graceful degradation and multibeaming are not attained; however such a system has been used to derive valuable experimental data [3]. The transmitter used by the reported system was a Russian-designed relativistic backward beam oscillator, BWO, capable of generating 500 MW with a pulse duration of 5 nS [3].

If requirement (ii) is to be met, heavy active phased arrays using tube-based amplifiers are required to operate at high masts, an unattractive proposition. The system's frequency of operation can be as high as possible so long as high powers over a wide bandwidth can be generated. The frequency of operation however cannot be too high above 40 GHz, if excessive propagation attenuation is not tolerated.

3   THE PROPOSAL

The microwave power module, MPM, is the ideal transmitter for active phased arrays designated for this application because it can generate significant power levels over wide bandwidths. In Table 1 we listed the pertinent electrical and physical characteristics of the Hi-band (array) and millimeter MPMs, manufactured by Northrop Grumman [4]. As can be seen the modules offer 100 W over a bandwidth extending over the 6-18 GHz and 18 to 40 GHz bands respectively. However, if the λ / 2 criterion is to be adhered to, the physical dimensions of the MPMs preclude them from use as modules in planar arrays; here λ is the shortest wavelength of operation. Similarly only the Hi-band (array) MPM can be used as a module for linear phased arrays.

Table 1   -   The essential characteristics of two Northrop Grumman MPMs [4]

Critical Parameters	Hi-band MPM (array)	Millimeter MPM
Frequency [GHz]	6-18	18-40
Nominal Output [W]	100	100
Sat. Gain [dB]	65	50
Noise Figure [dB]	13	13
Efficiency [%]	30	30
Prime Power [V]	270	270
Length, width and height [in]	6× 4 × 0.32	8× 3.5 × 0.8
Volume [in^3]	7.7	22.4
Weight [lb]	1.2	1.2

For the purposes of this paper, we shall assume that the Hi-band (array) MPM is used as a transmitter for a linear transmit array, that illuminates the ship's horizon. If however the physical dimensions of the millimeter MPM change in the future so that the $\lambda / 2$ criterion is satisfied, it can be used as module of a linear transmit array.
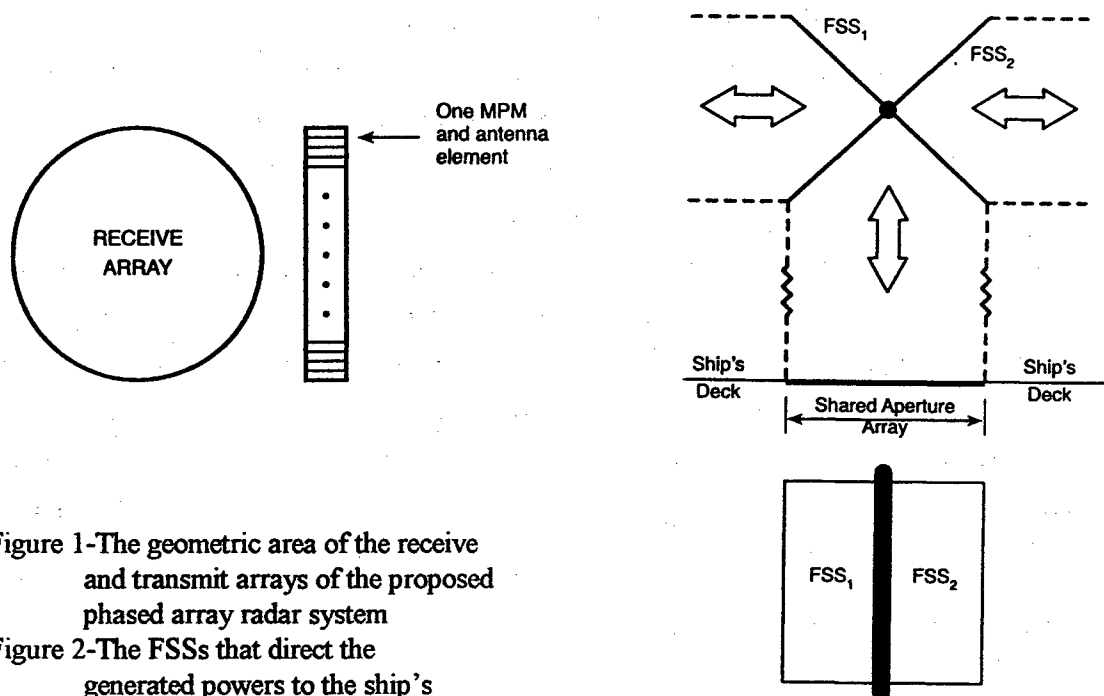

Figure 1-The geometric area of the receive
and transmit arrays of the proposed
phased array radar system
Figure 2-The FSSs that direct the
generated powers to the ship's
horizon's on either side of the ship.

In figure 1 we illustrate the receive and transmit phased arrays. The receive array is a circular planar array that generates independent and instantaneous beams that fill the transmit footprint along the ship's horizon over the 6-18 GHz frequency range. The antenna elements of both arrays can be tapered slotline antennas in the form of 'bunny ears' [5]; it has been demonstrated that these antennas can easily operate over a 3:1 frequency range. As the antennas are thin and flat, their usage in linear arrays does not represent any geometric problems.

The remaining issue of supporting a heavy phased array on the ship's high mast is resolved by the arrangement illustrated in figure 2. The phased array lies flat on the ship's deck and the lightweight frequency selective surfaces, FSS_1 and FSS_2 are located on top of a high mast. As the support axis of the FSSs is aligned with the ship's long axis of symmetry the transmitted powers are directed toward the ship's horizon. With this arrangement, the heavy phased array is located at the ship's deck and horizon searches on either side of the ship can be undertaken. We have selected the frequency bands 7.78-10 and 14-18 GHz to be transmitted on a pulse to pulse basis and the transmitted / received frequencies in GHz as a function of time for the two FSSs are shown in Table 2. The sum of t_1 and t_2 is equal to the period of the pulse of the radar, T and the instantaneous fractional bandwidths are approximately 25%. Even if we assume that the diameter of the area occupied by the receive / transmit arrays is 2m, the Rayleigh distance ($2D^2/\lambda$) is 207.8m at the lowest frequency of operation. FSSs having the same diameter at a height of say 10 to 20m will therefore be well within the Rayleigh region on the system.

Table 2. The transmitted / received frequencies in GHz as a function of time.

FSS$_1$	t$_1$	t$_2$	Next pulse t$_1$	Next pulse t$_2$
Tx	7.78-10		14-18	
Rx		7.78-10		14-18
FSS$_2$			7.78-10	
Tx	14-18			7.78-10
Rx		14-18		

The attractors of shared apertures having separate receive and transmit arrays, are outlined in reference [6]; the main attractor being the complete breakage of the nexus between the surveillance, tracking and the other important radar functions. Other transmit arrays, not shown in the figure can therefore be used for the system to perform the remaining radar functions.

4 CONCLUDING REMARKS

The structure of the proposed system is robust and can deliver high powers over wide bandwidths. Furthermore continuous monitoring of the ship's horizon is afforded by the proposed system and the long integration times improve the system's sensitivity. Lastly, the longer integration times over two different frequency bands and when the system's instantaneous fractional bandwidth is approximately 25 % enhance clutter rejection.

If increased transmit powers are required, each array antenna element can be fed by two or more MPMs connected to each antenna element via equal lengths of low-loss transmission lines. Apart from the FSSs, the MPMs are readily available and the antenna elements can be easily realized. As the arrays are on the ship's deck, relatively large arrays can be used.

5 REFERENCES

1   Skolnik M., Andrews G. and Hansen J.P. An ultrawideband microwave-radar. A conceptual design. Rec. IEEE 1995 Intern Radar Conf., p16-21

2   Vespa A., Hemmi C. and Sciarretta W. A wide-band T/R module for an airborne shared aperture array. GOMAC Digest of papers Vol XX, 7-10 Nov 1994.

3   Wardrop B. A Russian experimental high-power, short-pulse radar. GEC Journal of Technology, Vol 14, No3, 1977, p1-12.

4   Smith C. R. Power module technology for the 21st century. Proc IEEE 1995 Nat Aerospace Electronics Conf., NAECON Dayton OH USA, 22-26 May 1995, p 106-13.

5   Lee J. J.and Livingston S. Wide band bunny-ear radiating element. IEEE Antennas Propag Soc Inter Sym 1993, Vol 3, p 1604-7

6   Fourikis N. Novel shared aperture phased arrays. Microwave & Optical Tech Letters. Feb., 20, 1998, p 189-192.

A UHF Wide-Band SAR Antenna[*]

J.J. Lee*, S. Livingston, R. Sauer, G. Crandall,

Raytheon Systems Co.
R2-V518, PO Box 902, EL Segundo CA 90245
jjlee8@west.raytheon.com

1. Introduction

This UHF wide band antenna was developed for DARPA's Synthetic Aperture Radar (SAR) applications. The small array could be mounted at the belly of an aircraft (Figure 1). The operating frequency covers a 4:1 bandwidth. The antenna including the feed and a contoured ground plane was designed to fit in a shallow radome (50 cm x100 cm x100 cm). The depth of the radome is only one quarter of a wavelength at the low end of the UHF band. The small volume imposes a severe constraint in the electrical design and the packaging of the antenna, which is required to produce an EL beam pointed at 30 degree depression angle from the horizon (60 degree from the nadir).

The 3 dB beam at mid-band is about 50 degree in both elevation (EL) and azimuth (AZ) planes. Since the beam is broad enough to cover a region from 10 to 60 degree depression angle, no steering in the EL plane is required. Furthermore, the antenna must provide dual linear polarizations over a 4:1 bandwidth with VSWR less than 2:1 over 90% of the band. With the beam peak steered to 60 degree from the broadside, it is equivalent to impose a wide scan in the EL plane. To suppress grating lobes at the high end of the band, the element spacing was kept less than 25 cm. This spacing is about one-eighth of a wavelength at low end of the band, which makes it difficult to match the input impedance of the antenna because the element is electrically small.

2. Antenna Design

To meet these stringent requirements, a small array as shown in Figure 2 was developed. The antenna consists of 4x4 elements for the vertical polarization (V-pol) and 3x4 elements for the horizontal polarization (H-pol). The V-pol has four elements printed on each slab, while the H-pol has three elements on each slab. These slabs were orthogonally interleaved to form a rigid "egg-crate" structure. The radiating element is a variation of the flared notch "bunny-ear" element [1,2]. Good impedance match over a wide band was achieved by feeding each element with a tapered quasi-TEM slot line [3], which transforms a 50-ohm input impedance to a 120-ohm radiation impedance. However, the length of the feed section was restricted by the radome depth, which sets the limit of the operation at the low end.

The gain at 30 degrees depression angle was improved by tilting the elements towards the horizon. Figure 3 shows the locations and orientations of the V-pol elements in the slab before they were blended into a contiguous radiating

---

aperture (Figure 4) with a CAD program. This geometry and the active element pattern previously measured were used as inputs to compute the radiating pattern of the V-pol slab. Figure 5 is a computed array pattern in the EL plane at 540 MHz.

To ensure that the main beam points to a 30-degree depression angle over a wide band, a true time delay beam-forming network was used. Feed lengths were chosen using impulse measurements, which determined the differential time delay of the signal at each element. This was achieved by transmitting a short pulse into the antenna from the far field, with the antenna broadside turned to 60 degrees from the line of sight with respect to the transmit horn. Based on these data, a cable assembly was built to match the time delay of the incoming pulse at each element for coherent combining. The feed network was mounted on the back side of a contoured ground plane, whose profile was shaped to direct the main beam to 30-degree depression angle. The feed and radiators can transmit more than 1500 W peak power

3. Test Model

To verify the design and reduce risk, a 1/3-scale antenna was built and tested. The scale model was also used to study the mechanical issues, such as packaging, rigidity, tolerance, form and fit. The antenna was tested in an indoor range using time gating to remove ground reflections and other scattering of the chamber. Data collected include input VSWR, E- and H-plane patterns, beam widths, bandwidth, feed loss and antenna gain. Other features characterized were cross-pol isolation, back lobes, and phase linearity over the wide band. Measured data agree with design parameters very well. Fabrication of the full size antenna is underway. These results will be reported in an upcoming IEEE AP-S Symposium.

Reference

1. J. J. Lee, S. Livingston, "Wide-band bunny-ear radiating element," IEEE Antennas & Propagat. Symposium Proceedings, p. 1604, 1993.
2. J. J. Lee, R. Y. Loo, S. Livingston, et al, "Photonic Wide-band Array Antennas," IEEE Trans. Antennas and Propagation, Vol. 43, pp. 966-982, Sept., 1995.
3. J. J. Lee, " Slot-line Impedance," IEEE Trans. Microwave Theory and Tech., Vol. 39, pp.666-672, April, 1991.
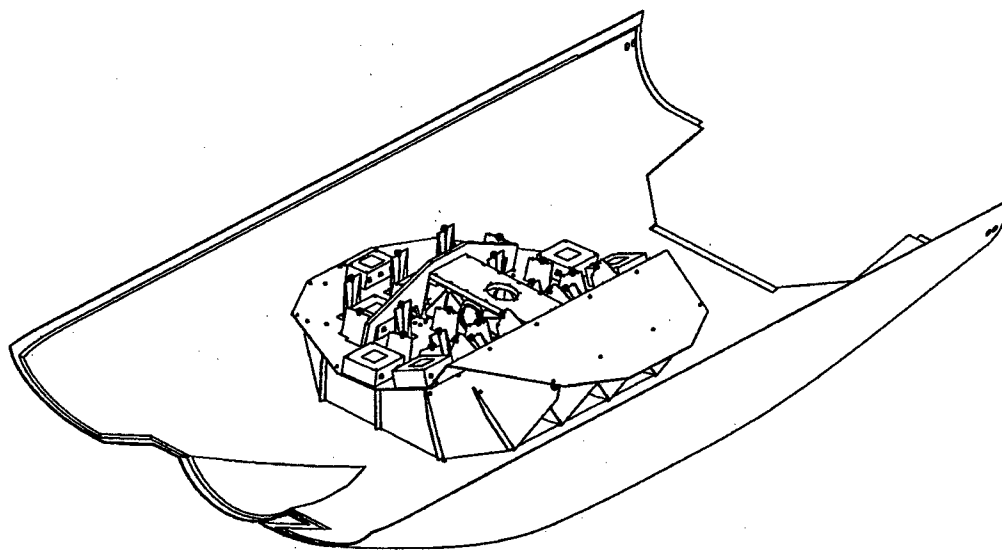
Figure 1. A wide-band UHF antenna inside a shallow radome mounted at the bottom of an aircraft.
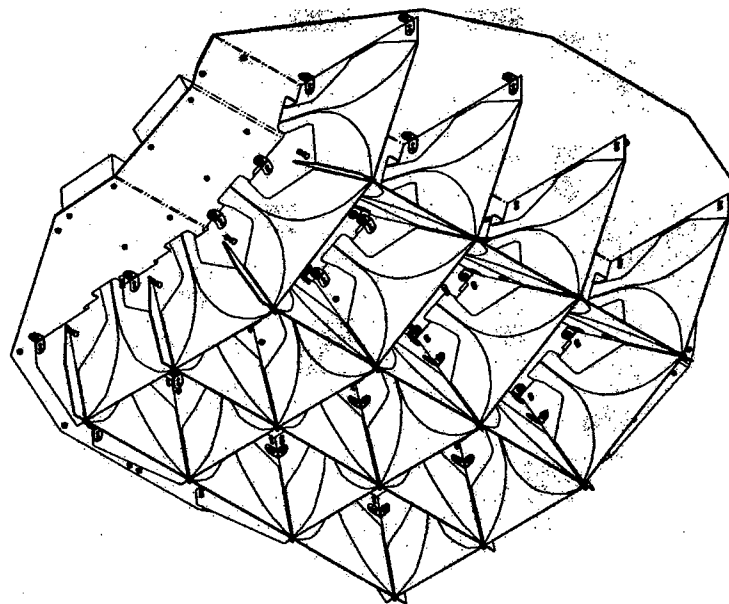

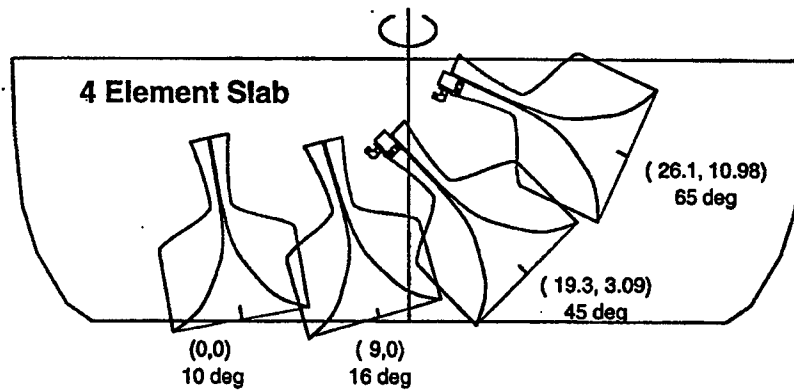Figure 2. The "egg-crate" antenna has 16 elements in V-pol and 12 elements in H-pol.

Figure 3. Geometry of tilted V-pol elements to form required EL beam (x, y dimensions in inch).
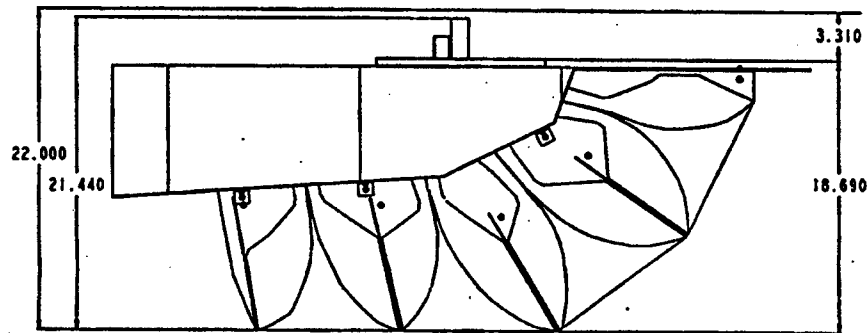

Figure 4. CAD-optimized geometry of V-pol slab and contoured ground plane profile.
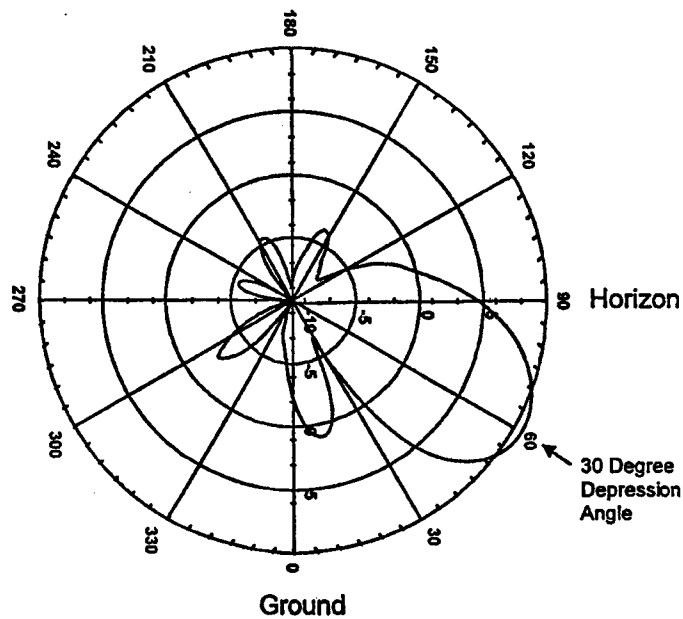

Figure 5. Computed EL beam (peaked at 30 degree depression angle).

A WIDE BAND TEM HORN ARRAY RADIATOR WITH A NOVEL MICROSTRIP FEED

Eric L. Holzman

Telaxis Communications Corporation, South Deerfield, MA 01373

ABSTRACT

We describe a TEM horn phased array radiator with a novel microstrip feed. Because the field profile in the TEM horn is uniform in amplitude and phase, multiple microstrip feeds can be inserted into a single radiator and their signals combined uniformly by the TEM horn; this particularly attractive feature makes possible low loss, wide band transmit power combining in the radiator rather than in the microwave module. Unlike Vivaldi notch and Tapered slot antennas, the TEM horn radiator field configuration resembles that of a rectangular waveguide radiator and should have high cross-polarization rejection. Using a commercially available finite element analysis tool, we have designed in detail a dual-polarized array aperture operating from 1 to 5 GHz using this radiator. The element spacing supports full quadrant scan over the entire band of operation with a predicted scan VSWR less than 3:1 up to 52 degrees in elevation. Our simulation predicts better than 25 dB cross-pol rejection in the principal planes.

INTRODUCTION

For ultra-wide band, quadrant-scan phased arrays, the selection of radiating element candidates is small. Many broadband antennas such as spirals cannot fit within the half-wavelength element spacing required for a phased array. Among the set of useable radiators, Tapered slot [1] [2] and Vivaldi Notch radiators are very popular because of their mechanical simplicity, but their cross-polarization rejection, particularly in the diagonal plane, is inferior to that of more narrow band waveguide radiators. An open-ended parallel-plate waveguide or Transverse Electromagnetic (TEM) horn antenna is inherently very broadband [3]. Its cross-pol rejection should be very high, since the TEM mode field configuration does not differ greatly from that of the TE_{10} rectangular waveguide mode.

A TEM horn antenna is formed by flaring the conducting walls of a parallel-plate waveguide in the direction of energy propagation. The throat dimensions of the horn are chosen to give a desired characteristic impedance, and the width and/or height increased to fill the phased array element lattice. Typically, exponential flaring over a half-wavelength at the lowest frequency of operation provides a good match to free-space.

Parallel-plate waveguide is not compatible with the RF output ports of most microwave modules, which may use either coaxial or planar transmission lines such as microstrip. Consequently, a feeding structure is necessary to transition the module output to the TEM horn input. We have modified the waveguide to microstrip transition of van Heuven [4] to develop a novel microstrip feed for the TEM horn [5].

CONCEPT AND THEORY

Figure 1 shows a single vertically polarized TEM horn antenna integrated with our microstrip feed. The radiator protrudes from a ground plane or metal faceplate typical of most phased array structures. The feed consists of a dielectric substrate with metal conductors on both sides. The mode of operation is quite simple. Consider a signal received by the TEM horn. Starting from the horn throat and moving left, the feed gradually rotates the vertically polarized, parallel-plate mode excited in the TEM horn
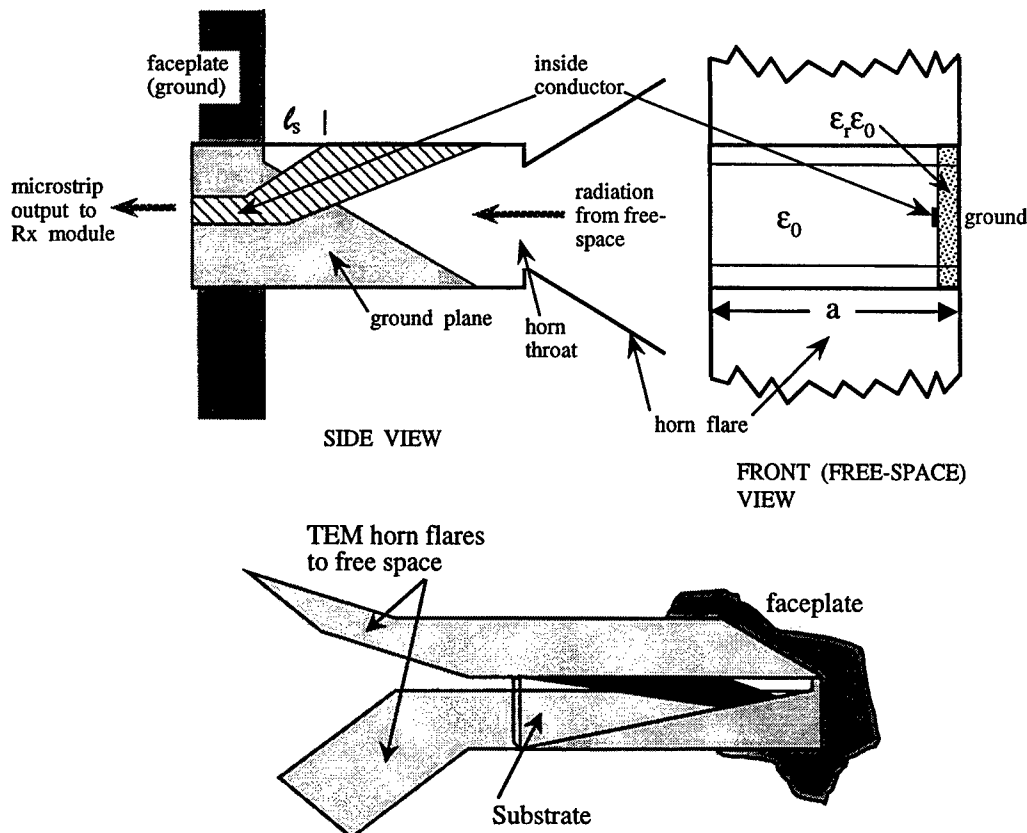
Figure 1: TEM horn with microstrip-to-parallel plate waveguide feed (not drawn to scale).

into a horizontal-polarized microstrip transmission line mode, which runs through the faceplate to the microwave modules on the other side. Since the TEM horn electric field is uniform and vertical, the substrate can be placed parallel to any vertical plane. For example, the feed can be centered in the parallel-plate waveguide or placed on an edge as shown in Figure 1. At the faceplate, there is an abrupt transition in that the parallel plate waveguide becomes rectangular waveguide. All tangential fields must go to zero along the aperture narrow walls at this point to avoid a field discontinuity and a mismatch. Use of a high dielectric constant substrate, such as Alumina (ε_r=10), insures that the electromagnetic field is concentrated in the substrate. Further, a high dielectric constant minimizes the length of the feed, which is about 40 percent of a parallel-plate mode wavelength at the lowest frequency of operation. With the substrate inserted in it, the parallel-plate waveguide is inhomogeneous, with its effective dielectric constant at the horn throat-end determined by the equation

$$\varepsilon_{e\!f\!f} = \frac{\varepsilon_r t + (a - t)}{a} \quad (1)$$

where t is the thickness of the substrate, a is the width of the parallel-plate waveguide, and we assume that the TEM horn is air-filled. The effective dielectric constant is continuously increasing as the RF energy propagates from the horn throat to the faceplate, where the mode becomes pure microstrip, and this phenomenon explains why the feed length is less than half a parallel-plate guide wavelength. As in van Heuven's transition [4], the height of the waveguide must change abruptly as we cross the horn to match the substrate-loaded feed and air-filled horn impedances. To minimize the length of the radiator is the primary design goal. However, there is a substrate length-to-height aspect ratio that gives optimum performance from the feed. So, as the feed length is increased to accommodate ever lower frequencies of operation, the height of the feed must be increased also. Another critical dimension is ℓ_s (see Figure 1), the size of the gap between the ground plane metal and flared microstrip conductor on the opposite side

of the substrate. This gap cannot be much more than one half microstrip wavelength at the highest frequency of operation; otherwise, a highly reflective resonance will move into the upper end of the band.

For transmit-only arrays, it would be advantageous to provide multiple inputs (channels) to each radiating element. We could then apply RF signals to a single radiating element that were phased differently (for multiple beams), at different frequencies (for multiple functions) or in phase at the same frequency (for power combining) without incurring the losses of a separate combining network in the microwave module. Towards this end, our radiator can contain multiple feed substrates as shown in Figure 2. We have verified the concept via simulation for the two-channel design shown in Figure 2(a); we get broad-band, uniform combining of the two input signals within the feed.
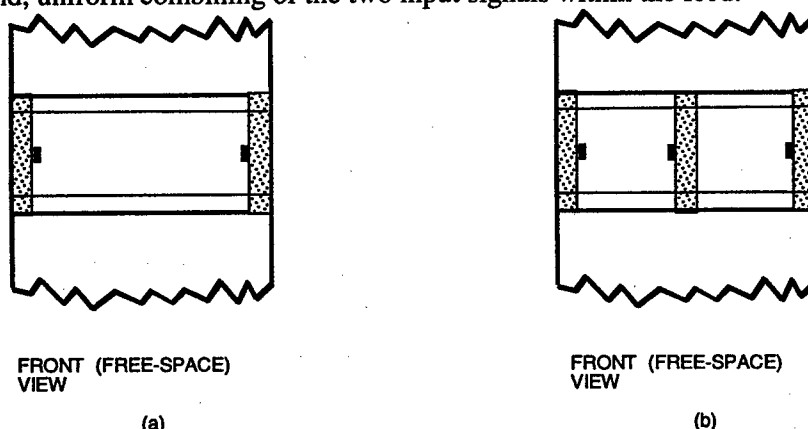

FRONT (FREE-SPACE) VIEW   FRONT (FREE-SPACE) VIEW

(a)   (b)

Figure 2. (a) Two-channel and (b) three-channel, microstrip feeds in a TEM horn

DUAL-POLARIZED ARRAY SIMULATION AND RESULTS

We have designed a dual-polarized array aperture, operating from 1 to 5 GHz, using Hewlett Packard's finite element analysis software tool, *High Frequency Structure Simulator (HFSS)*. We employ the waveguide simulator approach described by Eisenhart [6]. Figure 3 shows the aperture layout based on the geometry input to the HFSS software. To support our system concept, we use a square element lattice, rotated 45 degrees. The element spacing is selected to prevent the appearance of grating lobes in visible space at 5 GHz for a scan volume of +/-50 degrees in azimuth and -30 to +75 degrees in elevation. The TEM horn flares are 6 inches in length (half a wavelength at 1 GHz). At the horn throat, the parallel-plate waveguide is 200 mils high (abruptly changing to 170 mils on the feed side) by 400 mils wide, and the feed substrate is 25 mils thick, with a dielectric constant of 10.2. The distance ℓ_s is 550 mils. The distance from the faceplate to the TEM horn throat is 3.75 inches, about 0.4 wavelengths at 1 GHz according to equation (1). Note that equation (1) overestimates the effective dielectric constant; the waveguiding structure is not strictly parallel-plate because its cross-section includes all the space in the array lattice.

Using our HFSS model, we have generated scanned reflection coefficient data for the vertical polarization. Since the lattice is square, the performance for horizontal polarization is the same. Figures 4 and 5 show the E and H-plane performance predicted by HFSS for the infinite array environment. We can evaluate cross-polarized performance with this array model by injecting a horizontally polarized signal into the array and calculating the output at the vertically polarized ports. In the principal planes, our model predicts better than 25 dB cross-pol rejection over the 1 to 5 GHz band.

REFERENCES

[1] D. H. Schaubert, "Characteristics of Single-Polarized Phased Array of Tapered Slot Antennas," *Digest, 1996 IEEE Symposium on Phased Arrays Systems and Technology*, pp. 102-106.

[2] J. D. S. Langley, P. S. Hall and P. Newham, "Balanced Antipodal Vivaldi Antenna for Wide Bandwidth Phased Arrays," *IEE Proc.-Microw. Antennas Propag.*, Vol. 143, No. 2, April 1996, pp. 97-102.

[3] R. C. Hansen, *Phased Array Antennas*, Wiley-Interscience, 1998, pp. 146-150.

[4] J. H. C. van Heuven, "A New Integrated Waveguide-Microstrip Transition," *IEEE Trans. Microwave Theory Tech.*, Vol. 24, No. 3, March 1976, pp. 144-146.

[5] E. L. Holzman, "Broadband Antenna Element, and Array Using Such Elements," *U. S. Patent* 5,898,409, April 27, 1999.

[6] R. L. Eisenhart, "Antenna Element and Array Simulation with Commercial Software," in *Finite Element Software for Microwave Engineering*, edited by T. Itoh, G. Pelosi and P. Silvester, John Wiley & Sons, Inc., 1996.
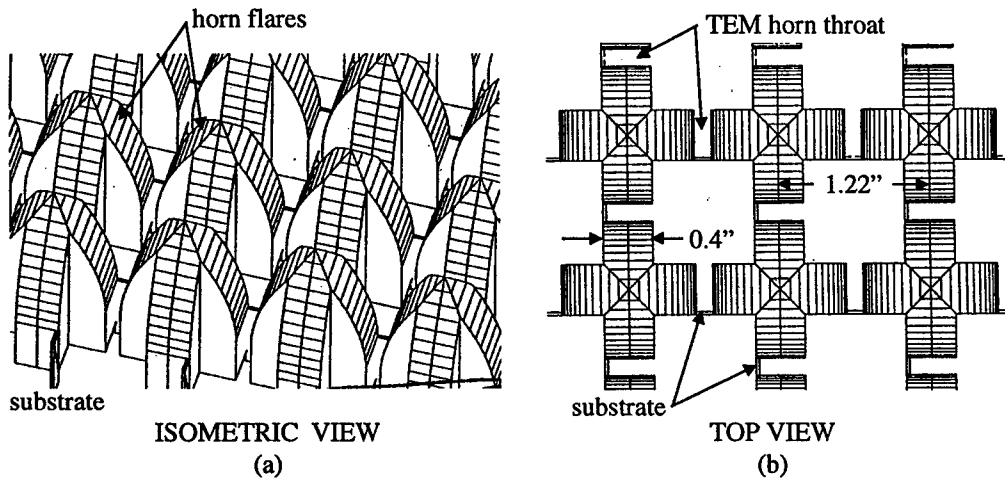
Figure 3. TEM horn in the dual-polarized array configuration with offset, orthogonal radiators.
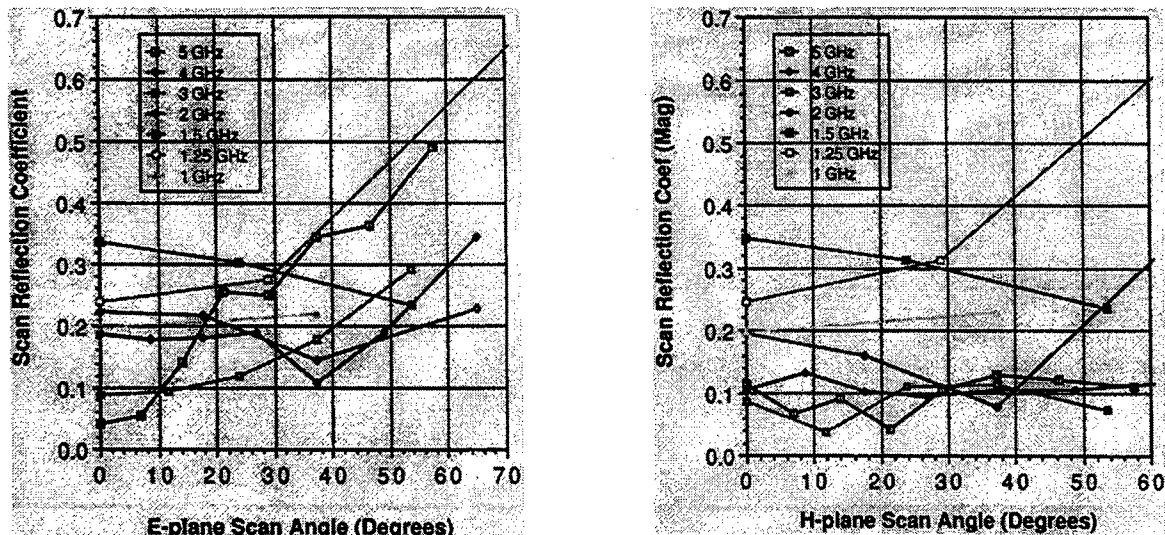

Figure 4. Predicted scan reflection coefficient in an infinite array environment.

FIELD ANALYSIS OF A RIDGED PARALLEL PLATE WAVEGUIDE ARRAY

K.K. Chan[*] and M. Rosowski[**]

[*] Chan Technologies Inc., 26 Calais Circle, Kirkland, Quebec H9H 3V3, Canada
[**] Condor Systems, 2133 Samaritan Drive, San Jose, CA 95124

Abstract

Ridged parallel plate waveguide arrays are investigated by the mode matching and generalized scattering matrix method. It is shown that the arrays have good active match and wide scan performance in the E-plane over a very broadband.

Introduction

An accurate method of analysis is presented in this paper for the ridged parallel plate waveguide (RPPW) array shown in Fig. 1. The array is assumed to scan only in the E-plane. An infinite periodic array is assumed here. The various views of a unit cell are depicted in Figs. 2 to 4. The parallel plate element has a stepped center ridge for scan impedance matching from a 50-ohm feed line. The top walls are perfect electrical conductors while the sidewalls are magnetic. Ideally, the sidewalls should be phase shift walls. For E-plane scan, the sidewalls become 0° phase shift walls. We have investigated the modal spectral of a ridged parallel plate element with 0° phase shift sidewalls and one with magnetic sidewalls using the generalized transverse resonance technique. The cutoff wave numbers of the modes are found to be identical. However, the phase shift wall element possesses some additional asymmetrical modes, which are well below cutoff and should not be excited in a symmetrical structure. Therefore the accuracy of the proposed model with magnetic sidewalls would not be compromised. The magnetic side wall model has two distinct advantages in that the determination of the modes of the ridged element are much less computationally intensive and the modes need not be regenerated for a change in the scan direction. Results will be presented that will demonstrate that the RPPW array has very broad band properties and wide scan performance.

Field Analysis

There are three steps in the characterization of the unit cell. The first step is to obtain the orthonormalized mode vectors of the ridged parallel plate element. The cross section of the element is decomposed into rectangular regions as shown in Fig. 2. A magnetic wall for symmetric modes or an electric wall for asymmetric modes is placed in the center plane. Only half the waveguide structure needs to be considered. Mode potential function for the regions is chosen so that the resultant mode vectors meet the boundary condition of the walls. The field distribution within each region is represented by a series of harmonic functions with unknown coefficients. These coefficients are determined by matching tangential electric and magnetic fields along the common interfaces between regions. The resulting boundary equations are manipulated so that a homogeneous matrix equation involving only the coefficients of a single region is obtained. The homogeneous matrix equation is real and only has a solution if its determinant vanishes. This gives rise to a characteristic equation for the TE or TM modes. Roots of the characteristic equation are the mode cutoff wave numbers. Once a root is found, the unknown coefficients can then be obtained, giving a complete description of the particular mode. To complete the procedure, the vector modal functions are normalized and their orthogonality is checked numerically. As for the TEM mode, the potential function is represented by a series of harmonic and hyperbolic terms. In this case, the boundary equations will result in an inhomogeneous matrix equation where the coefficients of a region can be found.

The next step is to characterize the various step junctions between the RPPW sections and between a RPPW section and free space. The field distribution over the cross section of a waveguide is approximated by a series of incident and reflected mode vectors with unknown coefficients. For the free space section of the unit cell, the Floquet mode vectors are used to represent the field. The mode vectors are arranged in increasing order of their cutoff wave numbers. The number of modes to be used in each section is established by the convergence condition that the highest cutoff wave number of the approximating modes should be approximately the same. A mode matching procedure is then performed by matching the tangential electric and magnetic fields across the junction interface between two waveguide sections. This will yield two coupling matrix equations between the modes of the waveguides. Manipulation of these equations produces a generalized scattering matrix description of the junction. The mode coupling integrals are all performed in close form.

The final step is to combine the generalized S-matrices of all the junctions and the in-between transmission lines in the unit cell to give an overall multi-modal S-matrix.

Results

The low frequency limit of a RPPW element is determined by its mismatch as can be clearly seen in Fig. 11. Ideally, only the fundamental TEM mode of Fig. 5 can propagate over its operating band. The high frequency limit is set by the appearance of the higher order modes. The bandwidth property of a RPPW element is investigated by using a 50-ohm line section. The cross section dimensions are defined in Fig. 4. The gap height, d, is plotted against the ridge width, s, for various element height, b, in Fig. 8 that will give a characteristic impedance of 50 ohms. All dimensions are normalized to the element width a. The first symmetric higher order mode is the TE20 mode where its E-field distribution is depicted in Fig. 6. Its cutoff wavelength, λ_{cs}, is plotted against the ridge width s in Fig. 9. The first asymmetric higher order mode is the TE10 mode. Its electric field distribution is plotted in Fig. 7. This mode is typically not excited for E-plane scan and can only be excited as a result of manufacturing tolerances that destroy the element symmetry. Its cutoff wavelength, λ_{ca}, is plotted against the ridge width s in Fig. 10. The curves of Fig. 9 and 10 show that the cutoff frequencies of the higher order modes can be raised by increasing the width of the ridge. There is an optimum value of the ridge width for a given element width and height, beyond which the cutoff frequency then starts to come back in. One can also increase the higher order mode cutoff frequency by decreasing the element width. In avoiding the TE20 mode, the optimum ridge width is only weakly dependent on the element height. The same general behavior is also observed for waveguide section with different characteristic impedance.

A stepped RPPW element, as shown in Fig. 3, was designed and optimized for a narrow ±15° E-plane scan and to operate over a 2.5:1 frequency bandwidth. No higher order mode is allowed to propagate in any of the sections within the operating band. The active match is plotted in Fig. 11 as a function of frequency for 0° scan and in Fig. 12 as a function of scan angle with frequency as a parameter. The element exhibits a worst case active return loss of −18 dB over the desired scan range and frequency band. As can be seen from the plots, this element is very broadband and can be re-optimized for a much wider scan with a small reduction in active match. The active E-plane element patterns are drawn in Fig. 13, and within the scan range, they can be represented by a $\cos^{1/2} \theta$ function.

Conclusion

A fast and accurate method has been developed to design RPPW arrays. The RPPW array element has shown to posses broad band and wide scan properties.

446

Fig. 1   Array of Ridged Parallel Plate
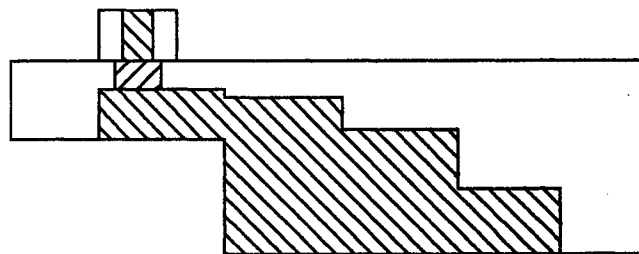Waveguide Elements – Top View

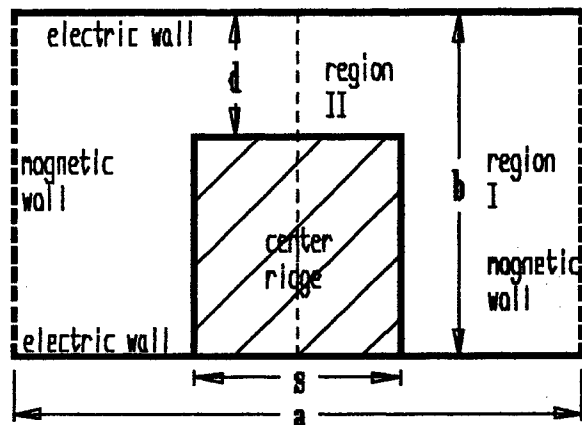Fig. 2 Ridged Parallel Plate Waveguide Element – Top View

Fig. 3 Ridged Parallel Plate Waveguide Element – Side View

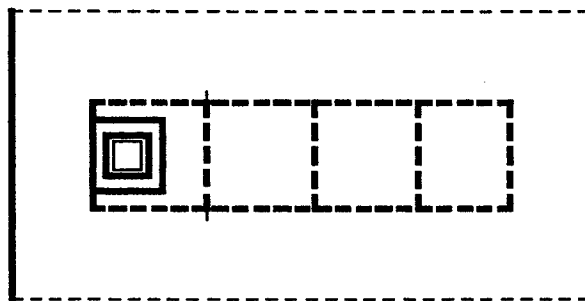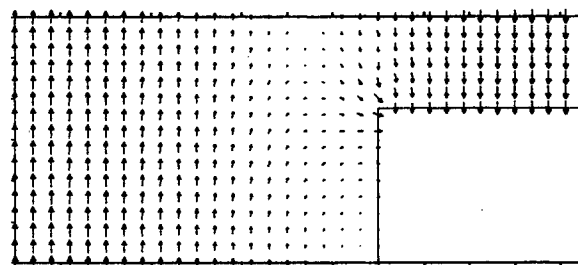Fig. 4 Ridged Parallel Plate Waveguide Section – Front View
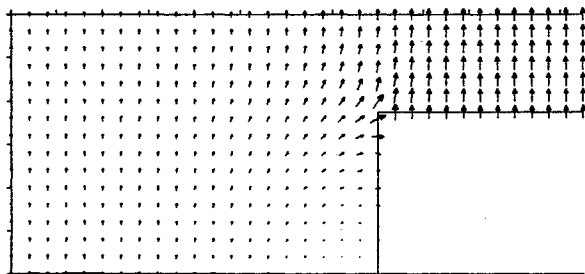

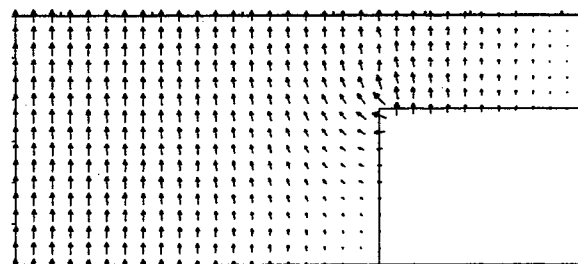Fig. 5 RPPW - TEM Mode

Fig. 6 RPPW – Symmetric TE20 Mode

Fig. 7 RPPW – Asymmetric TE10 Mode

447
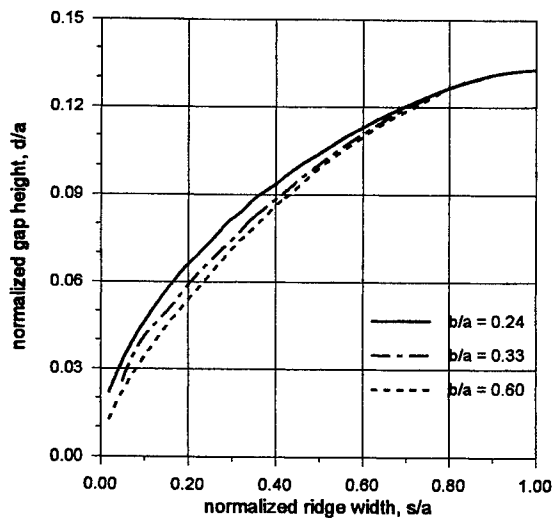
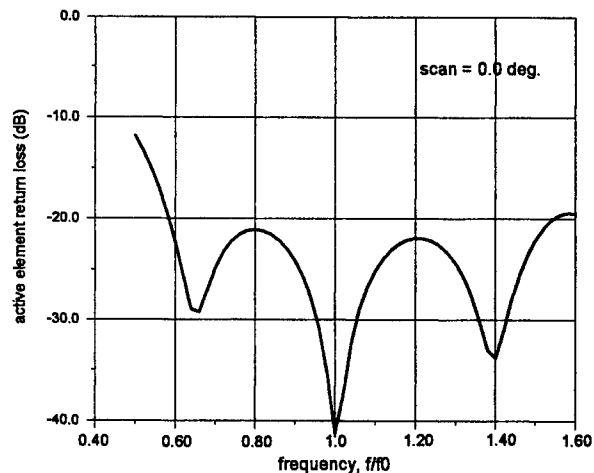Fig. 8 Dimensions of RPPW with 50-ohm impedance.

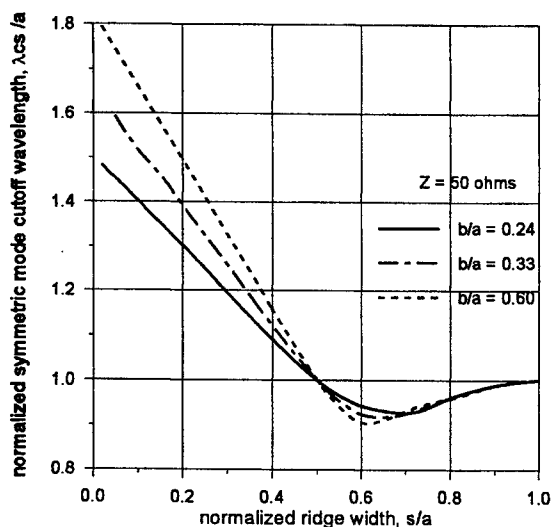Fig. 11 Active match of a RPPW array element at 0° scan.

Fig. 9 TE20mode Cutoff wavelength for 50-ohm RPPW.
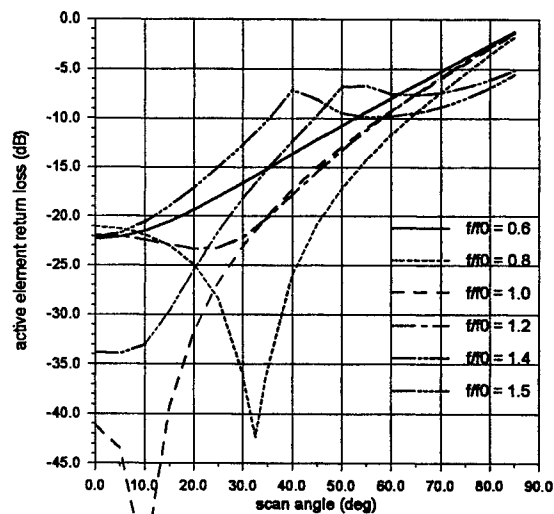

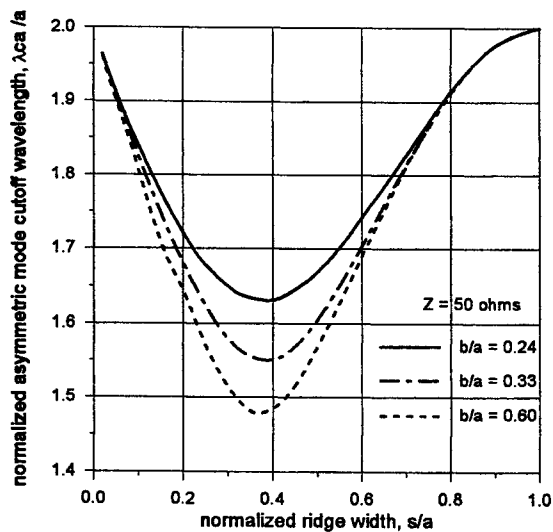Fig. 12 Active match of RPPW element under scan.

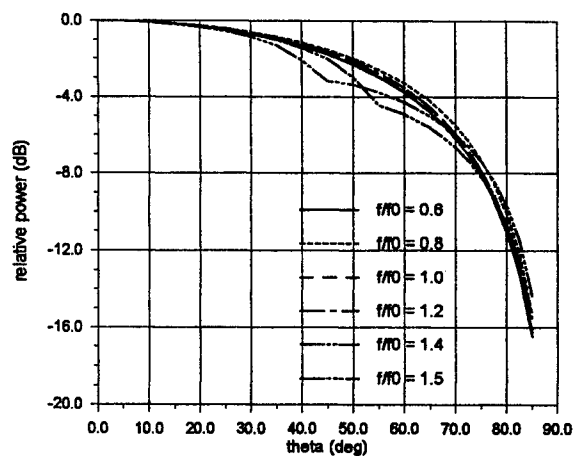
Fig. 10 TE10 mode cutoff wavelength for 50-ohm RPPW.

Fig. 13 Active E-plane element patterns.

True time delay line for short pulses based on optical path-length dispersion: experimental proof of functioning

Pál Maák, Judit Reményi, László Jakab, Péter Richter
Department of Atomic Physics, Technical University Budapest
H-1111, Budapest, Budafoki u. 8., Hungary
e-mail: maak@bigmac.eik.bme.hu, *Fax: +36 1 4634194*
István Frigyes, István Habermayer
Department of Microwave Telecommunication, Technical University Budapest
H-1111, Budapest, Goldmann Gy. Tér 3., Hungary

Abstract A true time optical delay line for short pulses by means of acousto-optic signal processing is presented. Theoretical description of the heterodyning delay line based on spatial Fourier decomposition and differential optical phase shift of the pulse frequency components is given. 2 µs time delay of 0.5 µs long pulses with maximum optical phase shift of 1.2 π was experimentally realised. Implementation of the delay line for an array with more than >10,000 antenna elements, for more than 50% fractional bandwidth is theoretically examined, and a compact optical system with involving two-dimensional acousto-optic deflector and LCD SLM is proposed.

1. Introduction

Phased array antennas have a significant role in up to date radar and communication systems. The direction of the radiated beam is varied by electronic control of the phase difference between the waves emerging from adjacent antenna array elements. Modern radar tracking and surveillance systems require bandwidth comparable with the carrier frequency. Wide frequency band phased array rise the particular problem of beam squinting, where the different frequency components are pointed to different directions, due to the constant phase shift applied [1]. In this case a short emitted pulse of large relative bandwidth will be spread out in a space region leading to serious detection limitations. This squint can be compensated by using delay lines rather than phase shifters for each radiating array element. [1,2,3].

Optical processing offers small size, low loss and wide-band systems without restriction in line length and with controllable, mostly negligible leakage [1,3]. The sizes and weights of the optical delay systems are by orders of magnitude less than of their microwave counterparts, and there is virtually no restriction in the length of the lines and bandwidth.

Several optical architectures have been investigated for both phase and time delay. Experiments involving delay path switching, using optical (also acousto-optic) [1], electronic [1,4], or polarisation switching[5,6], electronically controllable optical line stretching [1], dispersing waveguides or fibres, path-length dispersion [3, 4] have been carried out.

Our article focuses on possibilities of expanding the path-length dispersing system to time delay of short pulses by means of acousto-optic frequency modulation and deflection. The principle was introduced in [4], it was investigated in [1] and improvements proposed in [3]. As far as known by the authors, however, no experimental proof was yet given under realistic, i.e. pulsed conditions. This paper presents a pulse-delay line.

Real time delay of the pulses is achieved by introducing different phase shift along their frequency decomposition and addition of the shifted components. This optical delay line enables rising

of the bandwidth of the emitted radar signals from a few percent [2] to more than 50% of the carrier frequency. The limitation is introduced by the limited bandwidth of the acosuto-optic device and the number of the array elements to be illuminated.

We demonstrated theoretically and experimentally the possibility of time-delay of pulses introducing only 0.1-0.3 π phase shift to the different frequency components. Bandwidth considerations are being investigated and discussed.

2. The experimental setup

The architecture of the optical delay line, which demonstrates possibility of pulse delay, is presented in Figure 1. In this form this optical setup provides the necessary time delay between two adjacent pixels of the radar antenna array.
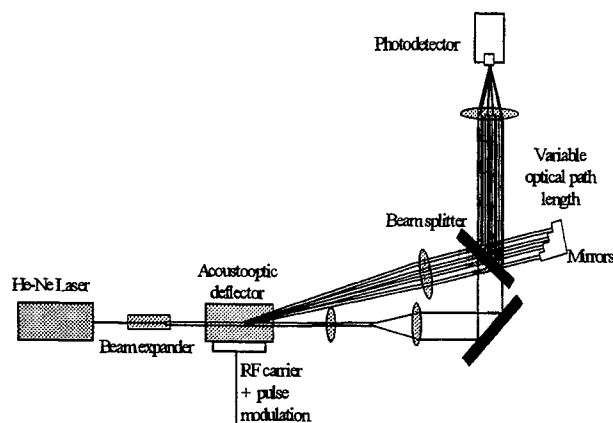
Figure 1., *Optical architecture to delay a pulse modulation of the RF signal driving two consecutive segments of the radar antenna array*

The pulse to be delayed modulates the RF carrier signal of 70 MHz driving the acousto-optic deflector. The frequency decomposition of the modulated signal is imaged in the angular distribution of the diffracted beam intensity. The diffracted beam emerging from the acosuto-optic deflector has a divergence in the interaction plane proportional to the bandwidth of the pulse modulation. The components of the diffracted beam travelling at different angles are differently phase shifted through a set of mirrors and than heterodyned on the surface of a detector. The detector signal proportional to the intensity of the interfering components, together with the added reference beam, contains a pulse modulation delayed relative to the input pulse. The principle can be easily examined mathematically by Fourier transforming the pulse modulated RF signal, introducing linearly varying phase shifts for the different frequency components and than adding the frequency components like an inverse Fourier transform.

The acousto-optic modulator included in the present experimental setup is a TeO_2 deflector operating with off-axis transversal acoustic mode in a frequency range between 53 and 96 MHz. Its maximum diffraction efficiency is > 40% in a frequency band of 40 MHz. If longer pulses and thus lower bandwidth is required, diffraction efficiency can be risen to 60% by changing the optical incidency angle. The optical aperture of the cell is of $5*5$ mm^2, corresponding to a maximal resolution of 340 points.

The task of the development is to realise the pulse delay at a carrier frequency of 1-2 GHz by involving a $LiNbO_3$ acousto-optic modulator with 1 GHz bandwidth between 1 and 2 GHz. This cell has also been developed at the Department of Atomic Physics at the TU Budapest.

The result of the mathematical modelling of the time delay mechanism is presented in Figure 2. The higher frequency components suffer the higher phase delay, leading to shorter pulse travelling time as with no phase difference introduced among the frequency components (flat mirror). In the

model continuous frequency dependent linear phase shifting is assumed, whereas experimentally the phase is delayed in 5-10 steps, depending on the tolerable distortion.
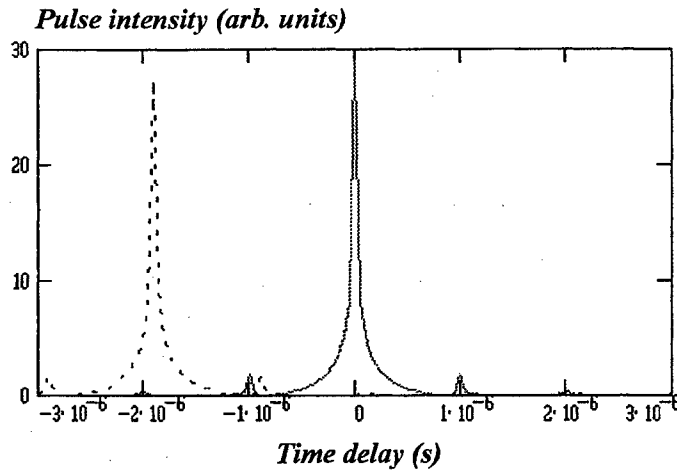
Pulse intensity (arb. units)

Time delay (s)

The delay of 1.9 μs is obtained with a phase shift of 1.2 π/MHz, corresponding to a path delay of 400 nm/MHZ.

The main advantage of this principle consists in relatively large time delays of the modulation pulse achieved with short optical path length differences of wavelength order. As a comparison, the common optical path delay technique requires path length differences of 10 m order for the same time delay value. The delay time depends on the path length difference introduced between the maximum and minimum significant frequency components in the frequency decomposition of the pulse. Introducing a path length variation of approximately 1 μm for a pulse of 0.5 μs duration a time delay of 2 μs can be achieved.
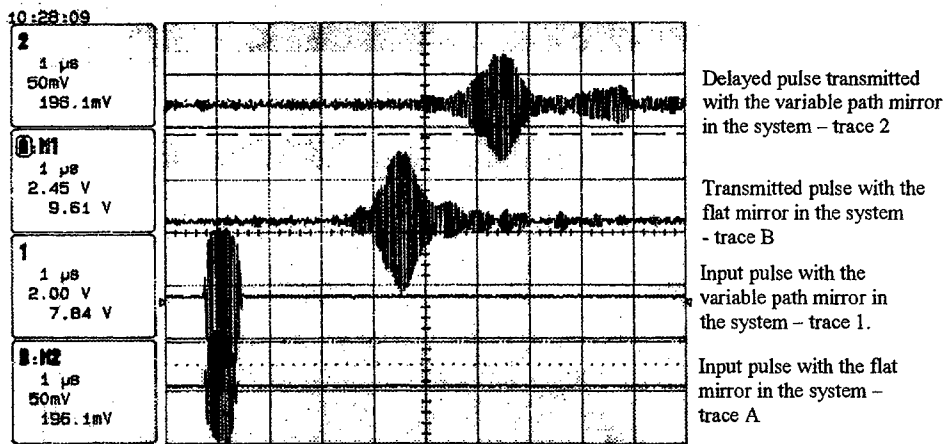
Figure 3. Measured time delay and distortion of the delayed pulse modulation

In the setup presented in Figure 1 a sputtered mirror with 5 segments is used, each providing a 400 nm path difference related to its neighbour, increasing from lower to higher frequency components. However this relatively low resolution still provides low distortion of the transmitted pulse, as shown in Figure 3.

As a demonstration of the setup possibilities a pulse transmitted with the variable path mirror is compared with a pulse transmitted with a flat mirror (Figure 3). The delay introduced by the variable path mirror is superposed to the delay of the whole optical system arising mainly from the delay introduced by the acousto-optic cell.

3. Bandwidth considerations

The bandwidth of the system is an important parameter, since it determines the minimum duration and the distortion of the transmitted pulses. The conversion elements of the actual system have relatively high bandwidth: the bandwidth of the AO driving electronics is of 90 MHz, and of the AO deflector of 45 MHz, the silicon detector head has a rise time of 1 ns (Melles Griot 13 DAH 003) and its amplifier of 1.25 ns (Melles Griot. 13 AMP 007). The main bandwidth limiting factor is the optical system, namely the heterodyning process between the diffracted and reference beams.

The acousto-optic cell performs the frequency decomposition of the input pulse, and each frequency component is added to a diffracted beam traveling through a different optical path. If not all components can be equally transmitted, mixed with the reference and added to the detector signal, the bandwidth will be reduced. In order to experimentally determine the maximum bandwidth of the system we investigated the transmission of a pulse without introducing time delaying elements (step mirrors or SLM-s) into the beam path, which can cause further bandwidth reduction.

The maximum measured bandwidth of the system has been of 1 MHz, corresponding to a pulse rise time of 0.35 μs. This was achieved by introducing a Fourier lens of 1000 mm focal length with the AO deflector in the back focal plane to determine all frequency components to propagate into the same direction and the reference beam was expanded to cover the whole diffracted pattern after mixing on the detector lens. When the diffracted beams travel parallel they will have the same incidence angle on the detector through the focusing lens, and mix in the same manner with the reference. The bandwidth was found to be reduced, if the diffracted beams carrying the frequency components were not paralleled or a lens with smaller focus (300 mm) was used. Further decrease of the bandwidth is caused by the wavefront- and phase mismatch between the particular diffracted beams and the reference. Experiments are running in order to increase the bandwidth, better wavefront matching by shaping the reference beam and beam aperture variations are proven. The results will be presented in the oral presentation

4. Conclusions

We demonstrated the possibility of true time delay of short pulses by means of path-length dispersion and acousto-optic signal processing. The main advantage of this system, compared with other optical delay techniques is the orders of magnitude shorter optical path difference required for the same delay time. Theoretical and experimental investigation of the delay principle has been carried out, and a good agreement for the delay of 0.4 −1 μs long pulses was found. Note, that the actual bandwidth is much narrower than what is needed by the practice; however the functioning of this principle is clearly demonstrated.

References

1. I. Frigyes et al.,"Optically generated true-time delay in phased array antennas", *IEEE Trans. On Microwave Theory and Techniques* , Vol. 43, No. 9., September 1995
2. H. Zmuda et al., "Photonic crossbar switch architecture for phased array beamforming applications", http://www.gerc.eng.ufl.edu/zmuda/Photonic%20Crossbar.html
3. I. Frigyes et al., "Investigations and improvements in microwave opto-electronic variable delay lines", *Intl. Microwave Symposium 1996,* San Francisco, USA, pp. 887-890
4. E. N. Toughlian, "A photonic variable RF delay line for phased array antennas", *J. of Lightwave Technology*, Vol. 8. No.12, pp. 1824-1828, December 1995
5. Nabeel A. Riza , "Transmit/receive time-delay beam-forming optical architecture for phased-array antennas", *Applied Optics*, Vol. 30. No. 32, pp. 4594-4595, 1991
6. D. Dolfi et al., "Two-dimensional optical architecture for time-delay beam forming in phased array antenna ", *Optics Letters*, Vol. 16., No. 4., pp. 235-236, February 1991

PHASED ARRAYS WITH SUB-ARRAY ARCHITECTURE

J. B. L. Rao, T. C. Cheston, J. Y. Choe, M.G. Parent and P.K. Hughes II
Naval Research Laboratory, Washington, D. C. 20375

INTRODUCTION

The instantaneous bandwidth of a phased array is severely limited if phase shifters are used at each element in the array to steer the beam. The rule of thumb is [1] that the instantaneous bandwidth (in percent), for a maximum scan angle of +/- 60 degrees, is approximately equal to the broadside beamwidth in degrees. A technique for improving the instantaneous bandwidth, by a considerable factor, is to use an array of subarrays with a phase shifter at each radiating element and time-delays (analog or digital) at the subarrays. For such an arrangement, the instantaneous bandwidth (in percent) will be approximately equal to the subarray beamwidth in degrees. However, the subarray technique can introduce severe pattern degradation in the form of grating lobes (larger sidelobes) that arise as the frequency is changed or when multiple beams are generated by combining outputs of subarrays with a digital beamformer. A scheme using overlapping subarrarys has been suggested [2, 3] to improve sidelobes performance. However, in some applications [4] that scheme cannot be practically implemented. This paper presents a simplified true time delay beam steering at the element level which is no more complex than using a phase shifter at each element of the subarray. The architecture described here makes multiple use of switched time-delays [5] and thereby significantly reduces the complexity. The method however, introduces losses and is therefore mainly applicable to active arrays, where the losses can be compensated by amplification.

All of the computations in this paper assume a linear array of 48 elements with a half wavelength spacing at the highest frequency. The array is divided into six sub-arrays with eight elements each. True time-delay digital beamforming is used at the output of the subarrays to generate one or more beams within the subarray pattern.

SUBARRAY ARCHITECTURE

Array antennas with sub-array architecture are frequently employed in phased array system. This approach is presently being used in Advanced Multifunction RF System (AMRFS) [4]. The vision of AMRFS is that a single multifunction RF System could be developed and deployed which will support the combined radar, communications and electronic warfare functional needs of the future surface Navy ships. To achieve this, parts of the multifunction array need to be dynamically allocated to separate functions. This can be implemented more easily by dividing the array antenna into subarrays and then allocating the subarrays dynamically to different functions. In order to operate over a large instantaneous bandwidth, such arrays are time-delay steered with digital time-delays at the output of the subarrays as shown in Fig. 1. In addition, digital beamforming at the subarray level will also allow the generation of cluster

multiple beams within the subarray pattern. Each element in a subarray contains a phase shifter that is controlled such that each subarray element has the correct phase at the center frequency of the instantaneous operating bandwidth (or the correct phase for the central beam, if multiple beams are to be generated). The limitations of the subarray architecture with a phase shifter at each element and true time-delays at the subarrays (hybrid scanning) are discussed next.

Performance with Wideband Signal

Subarraying with hybrid scanning can introduce severe pattern degradation in the form of grating lobes that arise as the frequency is changed. Grating lobes exist in this case, even though the subarray phase centers are correctly delayed to form a beam in a specific direction. This is because each subarray has a phase squint as the frequency is changed that causes the peak of the subarray pattern to move off the desired direction and also causes the subarray pattern nulls to move so that they do not suppress the array factor grating lobes. Fig. 2 shows the patterns of a 48 element (6 subarrays with 8 elements each) linear array with a –40 db Taylor, nbar=8 amplitude distribution. The array is scanned to 45 degrees and the patterns shown are for a frequency which is 5% above the center frequency. Clearly, the pattern exhibits no beam squint but the sidelobes become large and there is a small loss in gain. The subarray pattern is also shown in Fig. 2 for clarity.

Digital Beamforming at Subarrays

If the digital beamforming is done at the output of the subarrays, the number of multiple (cluster) beams that can be generated is limited by the beamwidth of the subarray. However, digital beamforming at the subarray level will introduce pattern degradation into the offset beams in the form of high sidelobes due to the grating lobe effect. Fig. 3 shows the off-set beam pattern for an offset angle of 3 degrees for the center frequency. Higher sidelobes are evident.

SIMPLIFIED TIME-DELAY STEERING ARCHITECTURE

The limitations of the subarray architecture with hybrid scanning discussed earlier can be eliminated if true time delay steering is introduced at the element level also. To achieve this, the electrical pathlengths from the feed to each radiating element and from there to the desired equiphase front has to be the same. This adds greatly to the complexity and cost of the antenna. The architecture presented here makes multiple use of switched time delay circuits and thereby significantly reduces the total complexity. Fig. 4 shows the architecture for a simplified true time-delay (TTD) steered series beamformer for a linear subarray. Each time-delay circuit τ shown gives a delay that can be switched from 0 to $2d/c$ where d is the inter-element spacing and c is the velocity of light. At the highest frequency the elements are spaced $\lambda/2$ to avoid grating-lobes and the maximum time-delay corresponds to 360° of phaseshift (as with a normal phase shifter). The time-delay circuits are similar to those of a diode phase shifter with switched line - lengths, and are reciprocal. When the time delays are set half way, to d/c, the various

lines feeding the elements at the aperture have fixed bias delays as shown in Fig. 4, making them all equal in length. This setting will therefore give a broadside beam which is independent of frequency. The bias delay is about a/2c at the center of the array, where 'a' is the aperture size, and reduces to zero delay at the edge. It could be implemented in stripline, taking very little space. To scan the beam, each one of the time-delay circuits in the right branch of Fig. 4 is ideally set to the same value $\tau = (d/c) + (d/c)$ Sin θ_s, where θ_s is the scan angle. Similarly, all the elements on the left branch are set to $\tau = (d/c) - (d/c)$ sin θ_s. All settings are independent of frequency.

Fig. 5 shows the patterns similar to Fig. 2, except that the simplified true time-delay steering is used at the element level. Comparing with the array pattern of Fig. 2, one notes that the sidelobes of the pattern in Fig. 5 are lower and are below −40db, as designed.

Fig. 6 shows the pattern of an offset beam, similar to that of Fig. 3, except that the true time-delays are used at the element level. As can be noted, the array pattern in Fig. 6 does not show higher sidelobes as does the array pattern in Fig. 3.

SUMMARY

The limitations of phased arrays using subarray architecture with phase shifters at the element level and true time delays at subarray level are discussed. A simplified approach for true time delay steering at the element level which eliminates these limitations, is presented. The approach uses the same number of switched delay-line phase shifters as the number of elements in the array. Hence, it is no more complex or expensive than using a typical phase shifter at each element.

REFERENCES

1. M.I. Skolnik, Radar Handbook, pp.7.49 – 7.52, McGraw Hill, Inc., 1990.

2. R.J. Mailloux, Phased Array Antenna Handbook, Artech House, Inc., Norwood, MA, 1994.

3. S.R. Rengarajan and J.B.L. Rao, "Overlapping Sub-arrays for Scanned Wideband Arrays with Improved Sidelobe Level Performances", IEEE International Conference on Phased Array Systems and Technology, May 20-26, 2000, Dana Point, CA.

4. Paul K. Hughes II and Joon Y. Choe, "Overview of Advanced Multi-function RF System (AMRFS)", IEEE International Conference on Phased Array Systems and Technology, May 20-26, 2000, Dana Point, CA.

5. T.C. Cheston and J.B.L. Rao, "Time-Delay Feed Architectures for Active Scanned Arrays", IEEE AP-S International Symposium Digest, pp. 1620-1623, 1996.
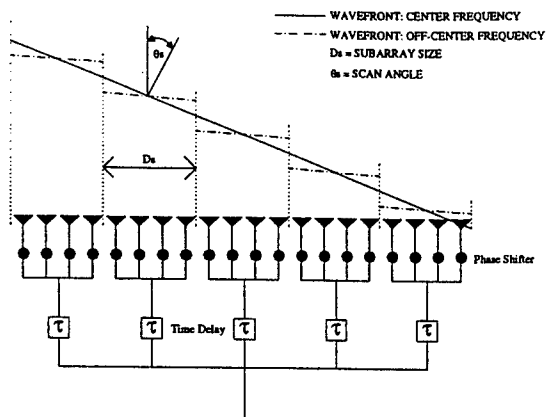
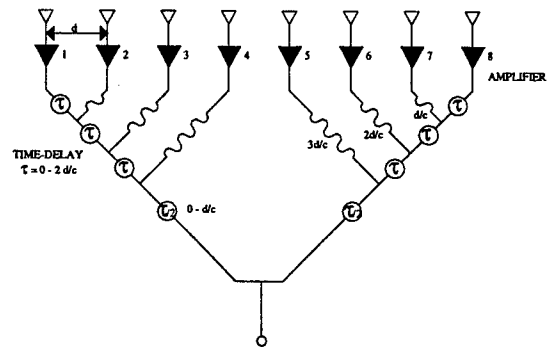Fig. 1. Array geometry showing distorted wavefront for off-center frequency

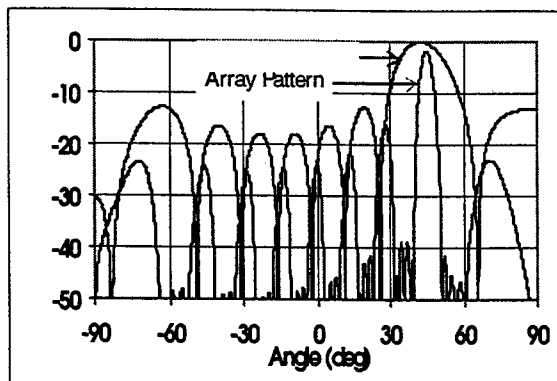Fig. 4. Simplified True Time-Delay (TTD) Steering

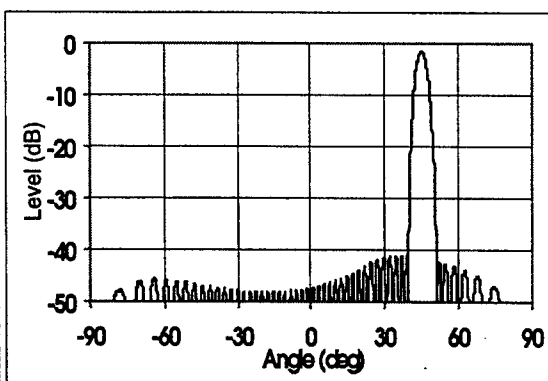Fig. 2. Patterns with Hybrid Scanning for f= 1.05 f_c and $\theta_s = 45^0$

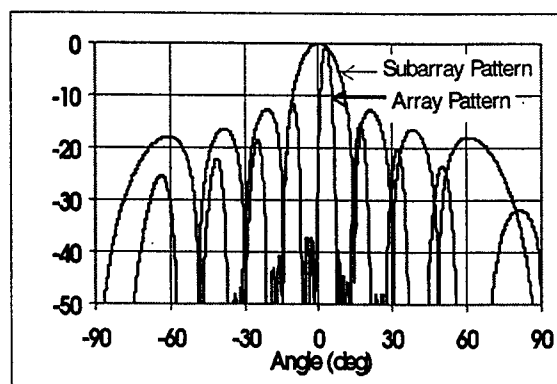Fig. 5. Pattern with TTD at each element for f= 1.05 f_c and $\theta_s = 45^0$

Fig. 3. Patterns of a cluster beam at 3^0 offset angle for Hybrid Scanning
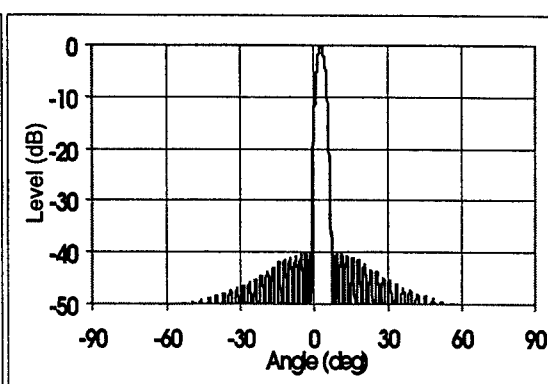

Fig. 6. Pattern of a cluster beam at 3^0 offset angle with TTD at each element

TDU Quantization Error Impact on Wideband Phased-Array Performance

Jeff Corbin and Robert L. Howard
Georgia Tech Research Institute
Atlanta, Georgia 30332

Abstract

Large, wideband phased-array antennas typically employ a time-delay subarray architecture to support wideband waveforms. Previous work [1] [2] has documented the need to appropriately size the subarrays to minimize scan angle dependent dispersion loss and preserve range resolution. However, practical issues associated with the subarray time-delay units (TDUs) also limit performance. Typically, TDUs are digitally addressed binary devices with a minimum resolution defined by the least significant bit (LSB) size (measured in time, typically nanoseconds, or path length). This paper discusses losses—in both signal-to-noise ratio (SNR) and range resolution—due to subarray to subarray time delay offsets resulting from TDU quantization errors. Simulation results are presented for wideband LFM waveforms.

Analysis

For a TDU with a least significant bit (LSB) of time delay, LSB_t, the associated quantization error is uniformly distributed between $\pm \dfrac{LSB_t}{2}$. For convenience, the LSB can also be expressed as a path length where $LSB_d = LSB_t \cdot c$, and c is the speed of light.

Subarrays are typically randomized to reduce from wideband grating lobes. Thus, the quantization error from TDU to TDU should be uniformly distributed independent of scan angle (for scan angles greater than few beamwidths). For a given TDU on the array face the commanded time delay, and thus the quantization error, is the same for both transmit and receive. Therefore one only needs to construct a one-way time delay error (ε) for each element via a uniform random distribution,

$$\varepsilon_i = U\left[-\frac{LSB_t}{2}, +\frac{LSB_t}{2}\right]$$

where $i = 1, \ldots, N$
            N = number of elements

For N subarrays, there are N^2 (from the $N \cdot N$ ways to combine the two-way signal paths) time-offset signals that coherently sum to produce the composite received signal. For an LFM waveform of pulsewidth τ, the signal—after de-ramping via stretch processing—can be expressed as,

$$\tilde{\gamma}(t) = \frac{\displaystyle\sum_{m=1}^{N}\sum_{n=1}^{N}\exp\left(-j2\pi\frac{\beta}{\tau}t\left(\varepsilon_m + \varepsilon_n\right)\right)}{N}$$

where β = Waveform bandwidth, (Hz)
            τ = Waveform pulsewidth, (sec)
            t = Independent time variable from 0 to τ, (sec)

The signal is then transformed (pulse compressed) and normalized to the peak of an ideal (no quantization error) signal. For this analysis no range sidelobe weighting was applied. Figure 1 illustrates the unweighted compressed pulses of the N^2 returns for a ten subarray antenna (prior to summation). The compressed pulses show an apparent range offset across $\pm \dfrac{LSB_d}{2}$. Figure 2 shows a histogram of the two-way time delay errors (normalized to the LSB size). The triangular distribution corresponds to the theoretical result of convolving the two uniform distributions.
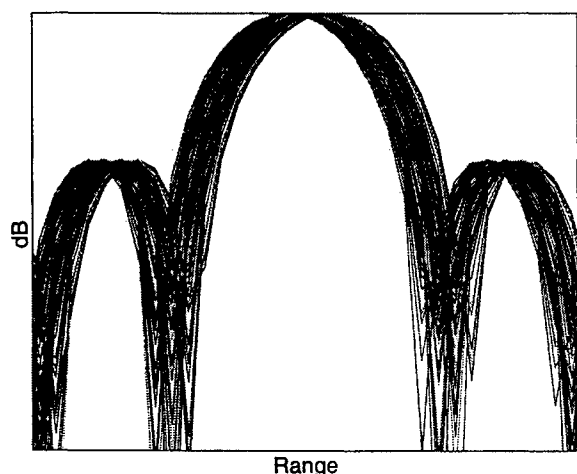

Figure 1. Compressed Pulses of Unweighted N^2 Errored Sinusoids.
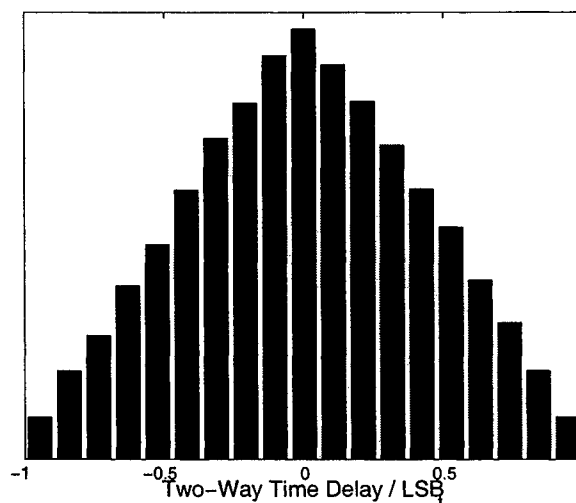
Figure 2. Distribution of Two-Way Time Delays.

The resulting compressed pulse, shown in Figure 3, will experience amplitude loss (or SNR loss) as well as pulse broadening (loss in range resolution) relative to the ideal pulse. The pulse broadening is calculated as the ratio of the errored and ideal compressed pulsewidths at the 3 dB point. Note that this 3 dB point is relative to each signal's own normalized maximum, not the normalized maximum of the ideal signal.
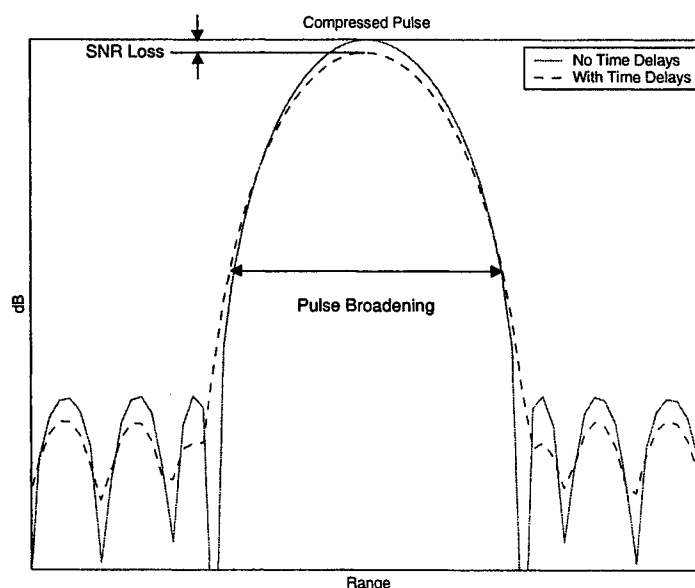
Figure 3. Signal Degradation due to Quantization.

Results

The SNR loss was calculated for arrays of 20, 40, and 80 subarrays and is plotted in Figure 4. The SNR loss is plotted in dB vs. the LSB size, $LSB_d = LSB_t \cdot c$, normalized by the waveform nominal range resolution, δ. The results for each array size were obtained via computer simulation using Monte Carlo runs. The resulting mean SNR loss and the 90% probability peak SNR loss are plotted. Each iteration of the Monte Carlo set is analogous to a single beam position for the array under simulation. Thus, when designing to account for this loss the peak SNR loss for any beam position the peak value is of interest. Depending on application, 95% or 99% values might be more appropriate. It can be seen that the smaller arrays have a higher variance relative to the mean. The lower mean for the smaller arrays was an unexpected result but probably represents that the "tails" of triangular error distribution (Figure 2) do not fill in this case. An expanded view of the SNR loss curve is shown in (b), highlighting the region of potentially acceptable losses.

Similary, the pulse broadening is shown in Figure 5. As described above, the broadening represents a degradation of range resolution and is shown for the same conditions as the SNR loss. In comparison to the SNR loss, the range resolution degradation is a minimal effect. It is anticipated that SNR loss considerations will drive most radar designs.
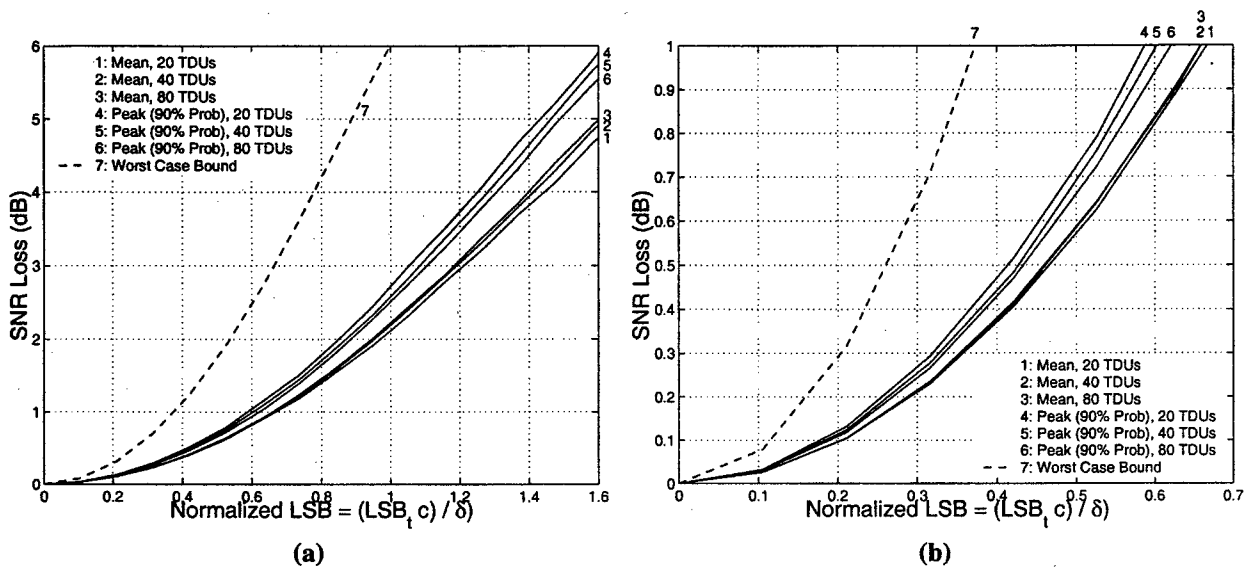

Figure 4. SNR Loss vs. Normalized TDU LSB.

Worst-Case Analysis

If the subarray locations are not randomized, for example a regularly spaced linear array, the quantization errors will not be uniformly distributed. One could consider a worst-case scenario where the time delay quantization error is set to the extreme, $\pm\dfrac{LSB_t}{2}$ (half of the elements set to $+LSB_t/2$ and the other half to $-LSB_t/2$), in order to give an indication of worst case losses. Figure 6 illustrates the unweighted compressed pulses for a ten TDU array along with the distribution of 2-way time delay errors. Obviously, these results would apply for as few as 2 TDUs. The resulting SNR loss and pulse broadening are shown on Figure 4 and Figure 5, respectively. These values represent the bound on performance.
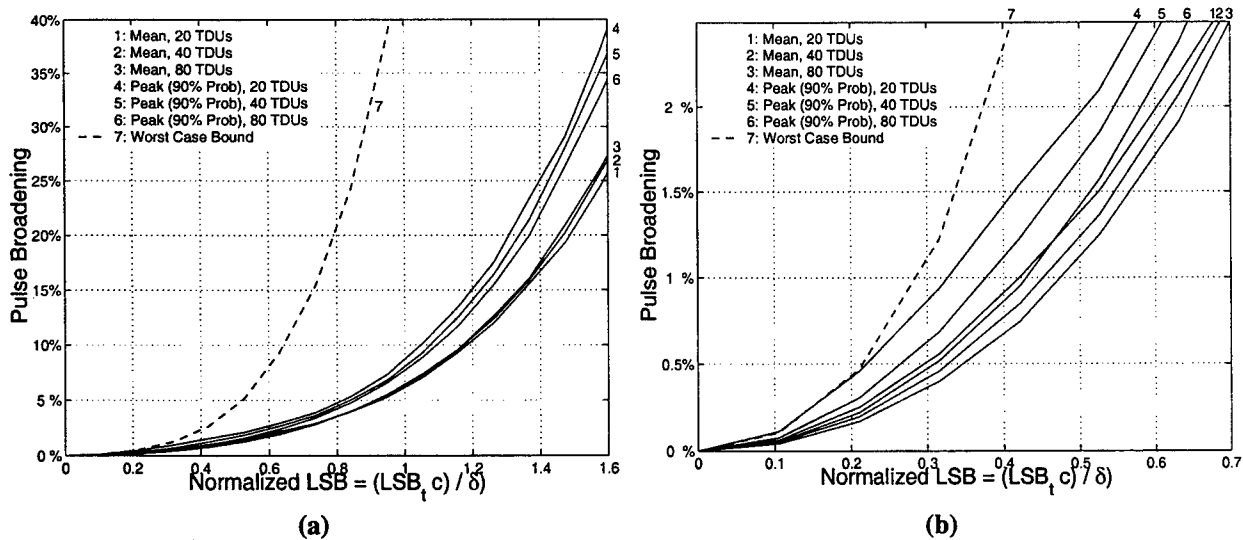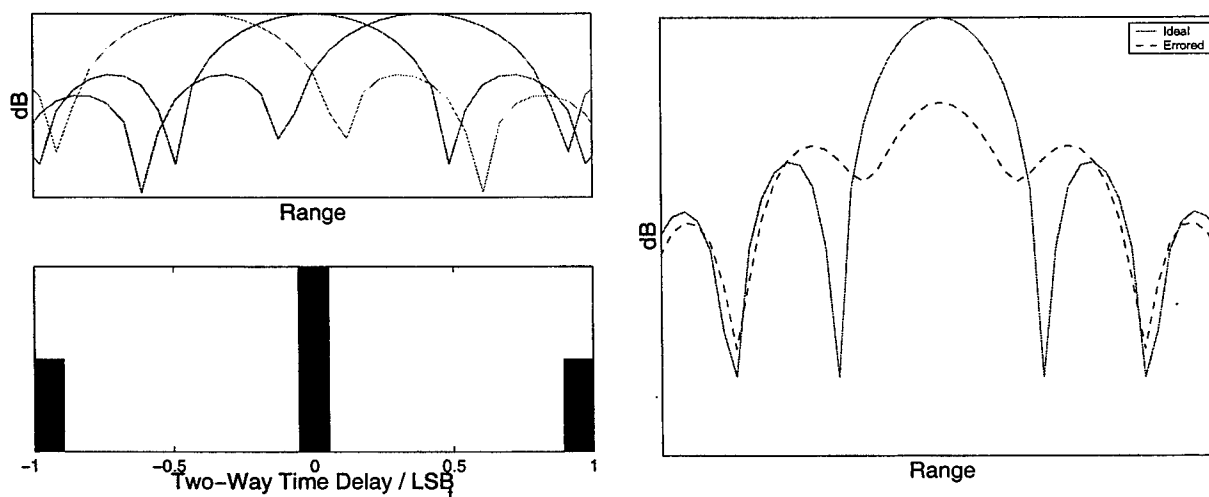
Figure 5. Pulse Broadening vs. Normalized TDU LSB.

Figure 6. Distributions of N^2 Errored Sinusoids.

Figure 7. Anomaly in Compressed Pulse.

Figure 7 shows the impact of a grossly oversized LSB. This figure illustrates that as the TDU quantization approaches the waveform range resolution, the resulting output is no longer a single degraded compressed pulse but actually resolves into separate returns. At this point, SNR loss and pulse broadening have no meaning.

References

[1] G.H.Knittel, "Relation of Radar Range Resolution and Signal-to-Noise Ratio to Phased Array Bandwidth," *IEEE Trans. Antennas Propagat.*, vol. AP-22,pp. 418-426, May 1974.

[2] Howard, R.L., L.E. Corey, and S.P. Williams, "The Relationships Between Dispersion Loss, Sidelobe Levels and Compressed Pulse Widths in Wideband Radars with Subarrayed Antennas," *1988 IEEE Antennas and Propagation Society International Symposium*, Syracuse, New York.

The phased array technology - application to time-reversal in acoustics

Didier CASSEREAU, Mathias FINK
Laboratoire Ondes et Acoustique, 10 rue Vauquelin, 75231 Paris Cedex 05, France.

Introduction

For some years, phased array systems have been developed in the domain of ultrasound ; this technology, widely used in radar and communication systems, has been proved to be particularly efficient in the frame of acoustics, for medical applications as for non destructive testing purposes.

Ultrasonic phased arrays are made of a set of piezoelectric small elements connected to electronic channels. One major advantage of ultrasonic devices is that piezoelectric transducers are reversible and can work as emitters or receivers ; they also have a linear response to an incident acoustic pressure, such that it is possible to measure both the amplitude and the phase of an acoustic field. In the transient domain, we are able to measure the temporal signal resulting from an incident pressure field.

Ultrasonic phased arrays can be used in conjunction with adaptive time delay laws, in order to achieve beam forming and focusing ; among the many applications of this feature, one can mention the medical echography systems that make an image of the human body.

In our laboratory, we have developed a new application of the phased array technology, based on the time-reversal invariance of the wave equation in a lossless propagation medium. In this paper, we briefly describe the basic principles of ultrasonic time-reversal, then we present two particular experiments using this technique that illustrate the efficiency of the acoustic phased array technology, for medical as well as non destructive testing applications.

1. Basic principles of acoustic time-reversal

The propagation of acoustic waves can be described in a similar manner than electromagnetic waves ; in the case of lossless media, the temporal dependence of the wave equation reduces to a second order derivative. Thus, the wave equation remains unchanged under the time-reversal transform $t \rightarrow -t$. Many theoretical as well as experimental works have been published in the last ten years on this subject[1-3] ; here we prefer to limit our purpose to the experimental description.

We use the phased array technology to develop 1D or 2D transducer arrays with a collection of independent piezoelectric elements. Each element is connected to its own electronic transmit/receive chain that allows to control the temporal signal emitted by each channel. This ability to emit different temporal signals on each channel is the major progress of our technology ; it is required for all time-reversal experiments.

The time-reversal experimental procedure can be described as a three-step process. We first illuminate the medium using a single element of the array, thus resulting in a widely diverging wave that propagates in the medium. The, a target (defect, tumor) generates a reflected wave that back-propagates in direction of the array that measures the resulting temporal signals on the different channels. The third and last step consists in a simultaneous reemission of the time-reversal of the previously detected signals by each channel. It has been proved that this procedure yields the generation of a wavefront that is finally focused on the target position, assuming that the propagation medium has not changed.

This three-step procedure is illustrated by figure 1.
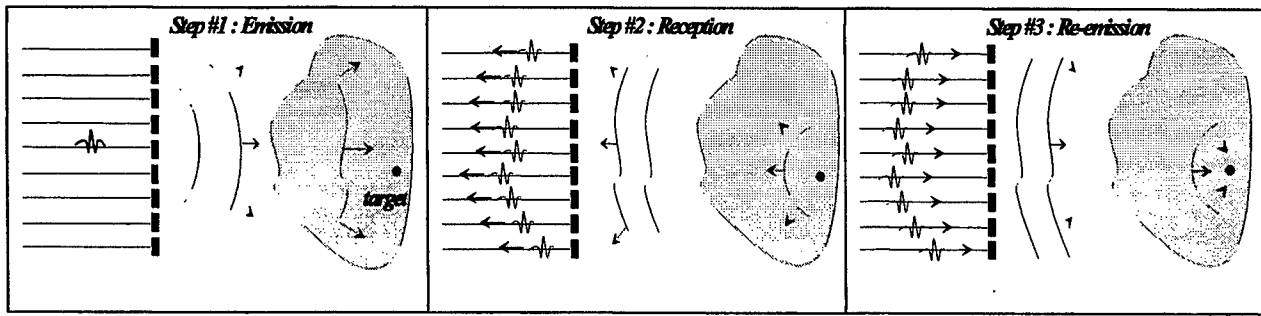
Figure 1 : *the three-step time reversal process.*

2. First application - focusing through an inhomogeneous medium

The first application illustrates the ability of the time-reversal process to compensate the strong distortions resulting from a propagation in an inhomogeneous medium, where multiple scattering occurs.[4]
In this experiment, we use a 1D periodic array of 64 elements at a central frequency of 3,3 MHz ; the sampling frequency is 20 MHz. The experiment is carried out in water, including a random set of about 2000 steel rods in front of the array. The geometry of the rods is such that high multiple scattering occurs at the considered frequency. The experiment is illustrated by figure 2.
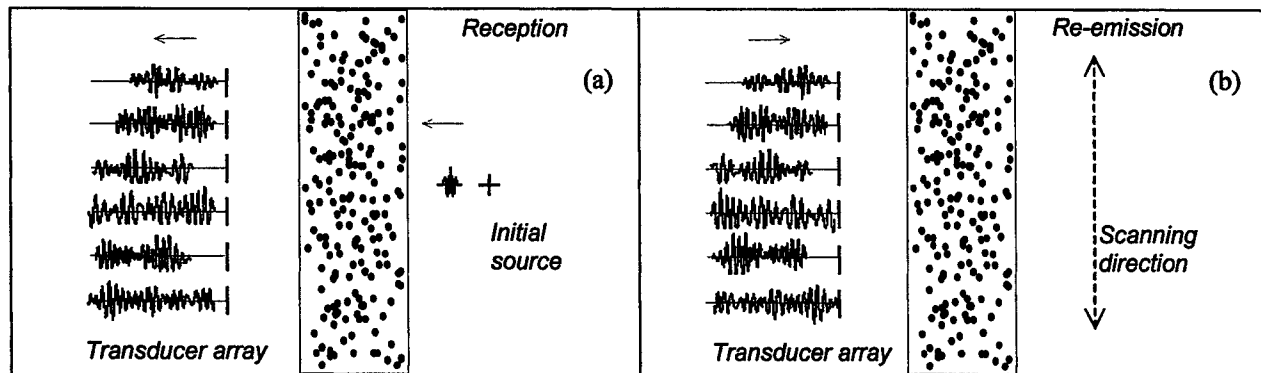

Figure 2 : *experimental setup ; (a) an active source generates a short pulse that undergoes multiple scattering before being received by the array ; (b) the time-reversed acoustic field back-propagates through the same set of rods, the resulting field is scanned around the initial source position with a hydrophone.*

The experimental results obtained in this configuration are illustrated on figure 3 :
- figure (3a) represents about 80 μs of the temporal signal detected on one particular channel of the array for an initial pulse of about 1 μs ; in fact, we could observe signals of more than 250 μs resulting from the multiple scattering that occurs in the set of rods,
- figure (3b) represents the temporal signal measured by the hydrophone at the initial source position after time-reversal and simultaneous reemission by the 64 channels of the array ; the reemitted signals are about 235 μs long, resulting in a very short pulse after back-propagation through the rods ; this figure illustrates the very efficient temporal compression that results from the self-compensations induced by the time-reversal operation,
- figure (3c) represents the directivity pattern around the initial source position (thick curve) compared to the directivity pattern without the set of rods (thin curve) ; the focal spot size is about 6 times more narrow in the presence of the rods compared to the same measurement in water.

These observations illustrate the great efficiency of the time-reversal process to focus the acoustic field through the highly heterogeneous medium. They can be interpreted in terms of an effective contribution of

widely spread multiple scattering paths in the medium, therefore resulting in a larger apparent aperture of the array.
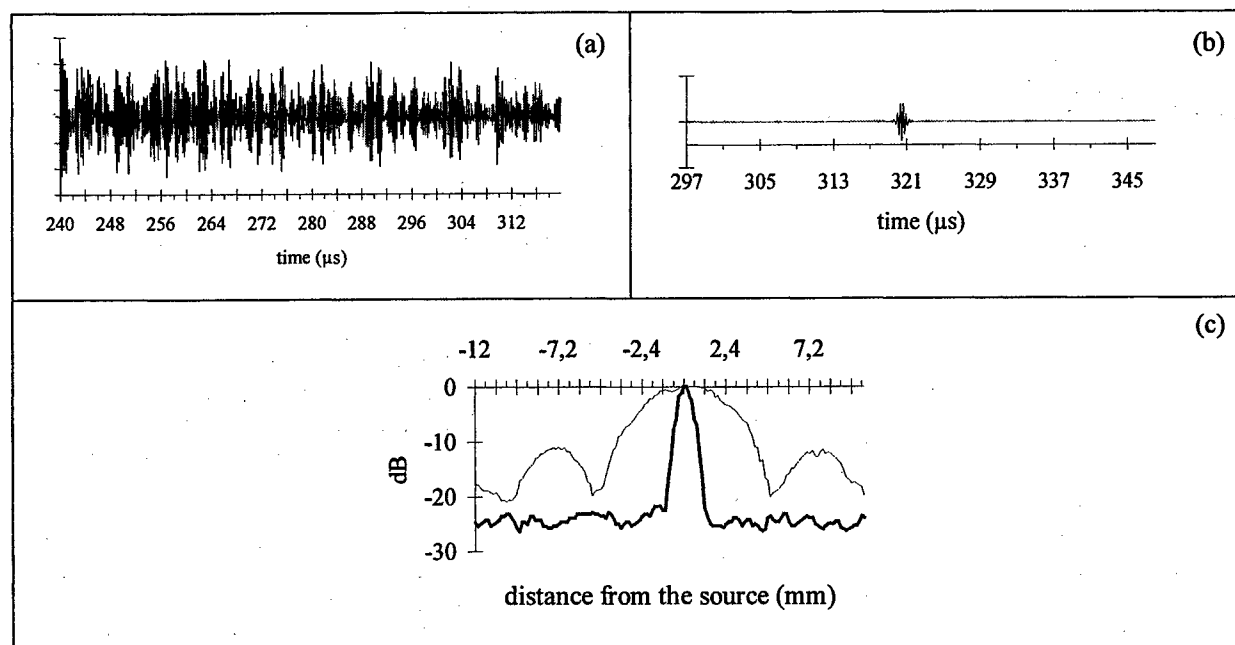
Figure 3 : *(a) temporal signal measured by one particular channel ; (b) temporal signal at the initial source position after time-reversal ; (c) focal pattern with (thick curve) and without (thin curve) rods.*

3. Second application – non destructive testing experiment

For about 10 years now, we also work on the same basic principle applied to non-destructive testing of materials, particularly for the detection of small defects (called hard-alpha) in titanium used in aeronautics (aircraft engines). Detecting small hard-alpha defects with classical methods (like pre-focused probes) is generally difficult due to the heterogeneous internal structure of titanium. Indeed, this structure generates a very noisy experimental environment while small defects have a low reflectivity.

In a time-reversal experiment, the ultrasonic phased array receives some information from both the internal heterogeneous structure (this is typically a random noise) and the defect (coherent signal). In such conditions, the time-reversal process allows to make the defect visible in spite of the noisy environment, particularly if it is iterated.[5]

In this kind of experiment, we use a 2D phased array of 121 independent transducers (an annular array where each ring is subdivided into sectors) with a central frequency of 5 MHz.

The experimental exploration of a cylindrical titanium sample is illustrated by figure 4 ; the temporal signals measured on the different channels of the array are represented in gray levels as functions of time (abscissa) and channel number (ordinates).

After the first illumination, we clearly identify the strong echoes generated by the front and back faces of the sample, but we cannot see any other structure inside the material, except the noisy structure itself. Once these temporal signals have been recorded, they are stored in memory and we select a temporal window in which the time-reversal operation is performed. Since we are working in an echographic mode, the position of the temporal window is directly related to the depth inside the material.

After two time-reversal iterations, we clearly see on figure 4b a significant signal that comes from a point inside the material ; this point corresponds to a well identified hard-alpha defect inside the sample of interest. These results illustrate how the time-reversal process allows to make the defect visible while more classical illumination techniques (as in figure 4a) cannot detect anything.
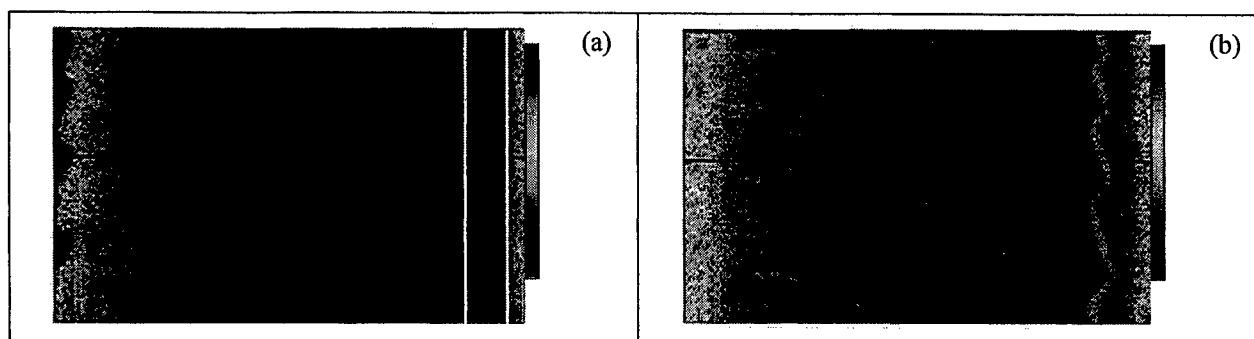
Figure 4 : *(a) temporal signal received from titanium after the first illumination, the two vertical lines identify the temporal window for the time-reversal process ; (b) after two time-reversal iterations.*

A similar experiment can be run in order to obtain an image of a titanium billet mounted on a rotating plate while the probe is moved vertically ; figure 5 shows an image of 3 different defects of dimension 0,4 0,5 and 0,6 mm.
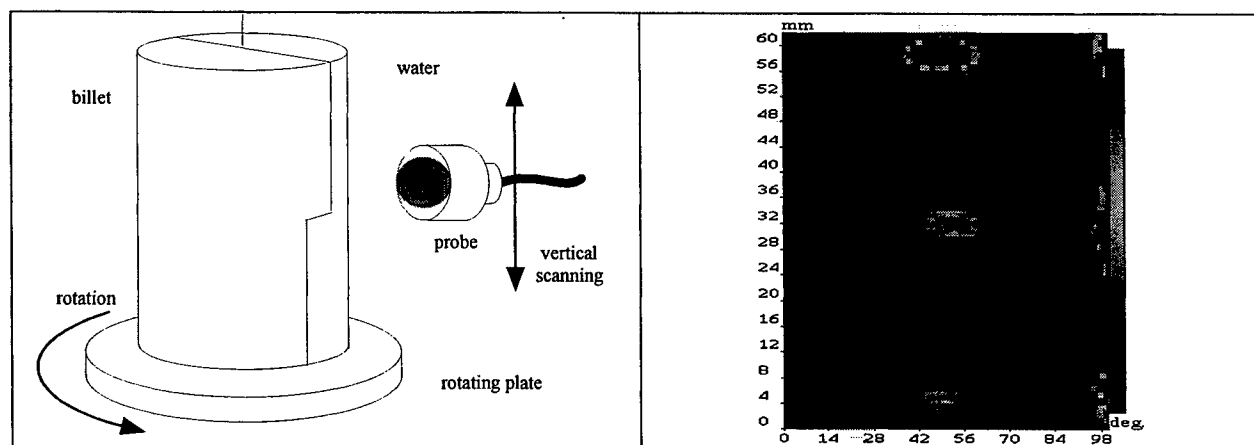
Figure 5 : *titanium billet image obtain by time-reversal.*

Conclusion

In this paper, we have briefly presented two particular experiments based on time-reversal of ultrasonic fields ; it shows how the phased array technology can be applied to ultrasonic systems. The method has been widely tested and is robust for defect detection, target location, even in the case of complex or very noisy systems.

References

1. Fink M. : Time-reversal of ultrasonic field – Part I : basic principles, *IEEE Trans. Ultrason., Ferroelec., Freq. Contr.*, vol. 39, N° 5, 1992, pp 555-566,
2. Wu F. *et al.* : Time-reversal of ultrasonic field – Part II : experimental results, *IEEE Trans. Ultrason., Ferroelec., Freq. Contr.*, vol. 39, N° 5, 1992, pp 567-578,
3. Cassereau D. *et al.* : Time-reversal of ultrasonic field – Part III : theory of the closed time-reversal cavity, *IEEE Trans. Ultrason., Ferroelec., Freq. Contr.*, vol. 39, N° 5, 1992, pp 579-592,
4. Derode A. *et al.* : Robust acoustic time reversal with high-order multiple scattering, *Phys. Rev. Lett.*, vol. 75, N° 23, 1995, pp 4206-4209,
5. Prada C. *et al.* : The iterative time-reversal process : analysis of the convergence, *J. Acoust. Soc. Am.*, vol. 97, N° 1, 1995, pp. 62-71.

Focusing with ultrasonic phased arrays – comparison between time-delay laws and time-reversal

Didier CASSEREAU

Laboratoire Ondes et Acoustique, 10 rue Vauquelin, 75005 PARIS

Introduction

For many years, ultrasonic phased arrays are widely used, for example in non destructive testing, in order to achieve beam forming and focusing. In many situations, the determination of adequate time-delay laws can be as efficient as others methods like time-reversal, with the advantage that they are much more simple and do not require complex electronic systems.[1-3]

Anyway, we could observe some limitations in the focusing ability using the time-delay laws, particularly for transducer arrays made of big elements (a few wavelengths). Developing small elements require high and expensive technology ; also, small elements have a poor dynamic in emission/reception.

In this paper, we propose a concrete situation that illustrates these difficulties, then we show how the time-reversal technique provides an efficient solution in terms of the focal pattern.

This work is based on a simulation software developed in our laboratory, PASS. This software calculates the propagation of acoustic fields generated by phased arrays, including time-delay laws and the finite aperture of the elements of the array.

1. Presentation of the problem

The problem of interest consists in focusing through a plane interface between plexiglas and steel using a 1D bar of 16 electronic channels. The geometrical configuration is illustrated by figure 1.
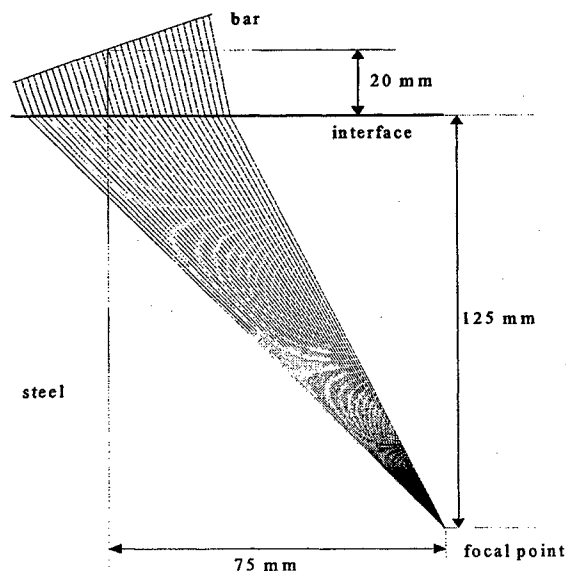
Figure 1 : *geometrical configuration of interest ; the 1D bar is rotated of 25° with respect to the plane interface, its center is located 20 mm above the interface and the desired focal point is at a depth of 125 mm with an horizontal offset of 75 mm.*

In all the following, we try to calculate the time-delay law adapted to the desired focal point for longitudinal waves in steel ; then we calculate the resulting displacement field in steel with a scanning direction that is perpendicular to the interface around the expected focal point.

The velocities and densities of the two materials are

- c_1 =2430 m/s et ρ_1 =1270 kg/m^3 (plexiglas),
- c_l =5770 m/s, c_t =3150 m/s (longitudinal and transverse velocities), ρ_2 =7700 kg/m^3 (steel).
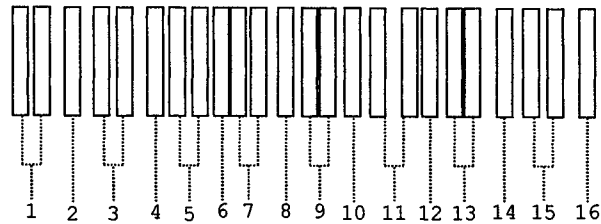
Two different bars have been designed. The first bar is made of 32 elements (periodic bar) and couples each pair of successive elements 1 and 2, 3 and 4, ... thus resulting in 16 channels. The second bar contains 24 elements only (non periodic bar) and couples elements 1 and 2, 4 and 5, 7 and 8, ... also resulting in 16 channels. The two considered bars have the same total aperture (55 mm), central frequency (4,5 MHz) and relative bandwidth (70% at –6dB).

The dimension of the elements along the axis of the bar is 1,46 mm (2,7×wavelength in plexiglas at the central frequency). The geometry of the two bars is illustrated by figure 2.
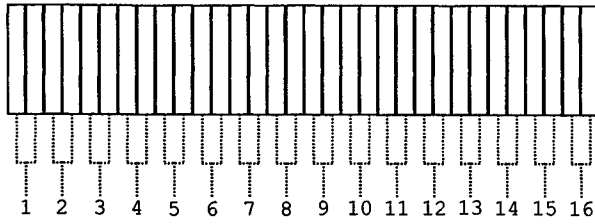

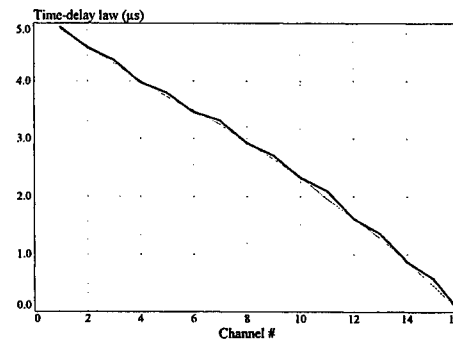**Figure 2a** : *first bar, 32 elements, 16 channels.*   **Figure 2b** : *second bar, 24 elements, 16 channels.*

Both bars have large elements, this can make the evaluation of time-delay laws more complex. The simulation software allows to choose between various algorithms for such evaluation, e.g. the average or minimum delay over the aperture of the elements. These choices yield different time-delay laws, thus also different radiated fields. We are interested in this sensibility on the computation of the time-delay law.

The time-delay laws obtained by PASS are represented on figure 3 for the first periodic (3a) and second non periodic (3b) bars. On (3a), the two curves are almost identical, while significant differences can be observed on (3b), particularly for the odd channels that couple successive elements of the array ; these differences are thus directly related to the large size of the elements.
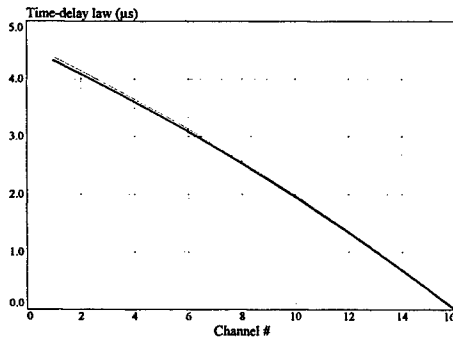

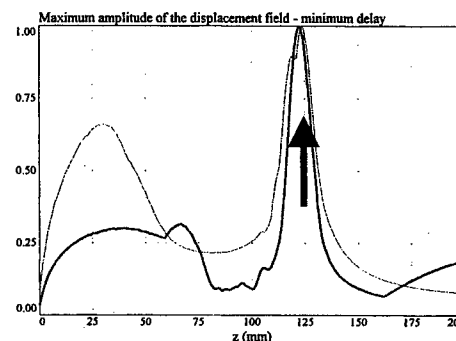**Figure 3a** : *average (thin curve) and minimum (thick curve) delays ; first periodic bar.*   **Figure 3b** : *average (thin curve) and minimum (thick curve) delays ; second non periodic bar.*

These time-delay laws are now inserted in PASS to calculate the resulting displacement field in the solid along the direction perpendicular to the interface, from z=0 (interface) to z=200 mm. The arrows indicate the position of the expected focal point.
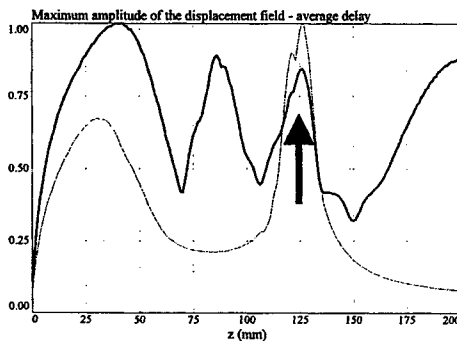
**Figure 4a** : *displacement field resulting from the average delays ; thin and thick curves correspond to the periodic and non periodic bars.*   **Figure 3b** : *displacement field resulting from the minimum delays ; thin and thick curves correspond to the periodic and non periodic bars.*

466

The different curves have been normalized to unity to allow a better comparison. We immediately observe that the periodic bar is not sensible to the computation of the time-delay law, while the non periodic bar is efficient with the minimum delays and yields a quite poor focusing with the average delays.

This example illustrates the sensitivity of the focused field with the time-delay law computation method in case of large elements.

2. The time-reversal solution

The time-reversal simulation is performed in two steps.[1-3] We first consider a point-like reflector at the desired focal point and a small emitter above the interface (the exact location of the emitter is not important). The emitter generates a short pulse that propagates to the target ; the reflected wave back-propagates in direction of the bar that works in the receiving mode, thus resulting in a set of 16 temporal signals that take into account the finite aperture of each element. Then, the bar works in the emitting mode, where each channel emits a temporal signal that results from a time-reversal operation of the signals obtained during the first step. An additional normalization can be used before re-emission in order to compensate the amplitude fluctuations that result from the various paths from the target to the elements.

In all the following, we only consider the second non periodic bar that appears more sensible to the computation of time-delay laws.
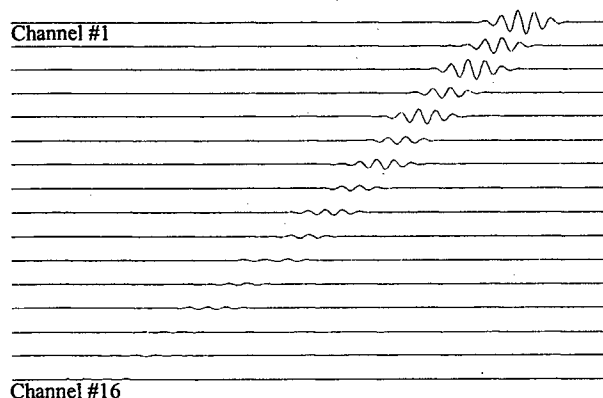
**Figure 5a** : *temporal signals emitted by the non periodic bar after time-reversal.*
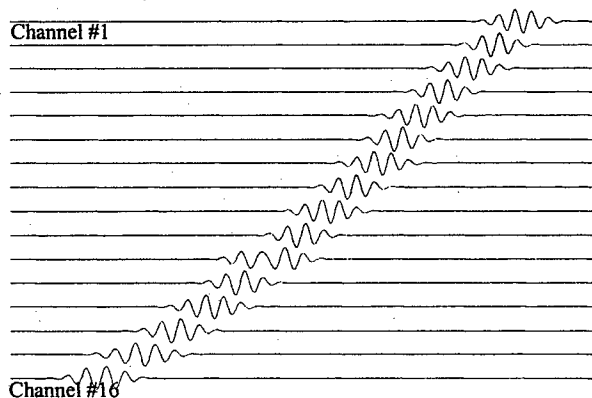
Figure 5b : *temporal signals emitted by the non periodic bar after time-reversal/normalization.*

The temporal signals to be emitted by the non periodic bar, obtained by this procedure, are represented on figure 5, without (5a) and with (5b) normalization. The temporal window shown on this figure is 5,9 µs. The temporal variations of the signals between two successive channels are visible on (5b), resulting from the variation of the aperture of the corresponding elements.

As in the previous simulations, these temporal signals are simultaneously re-emitted and PASS calculates the resulting displacement field under the interface around the expected focal point. The obtained results are shown on figure 6a, where the thin (resp. thick) curves correspond to the displacement field resulting from the temporal signals without (resp. with) normalization. Looking at this figure, we clearly see that both fields are very efficiently focused at the expected focal point.

The last step of the simulation consists in the evaluation of a time-delay law that optimally fits the temporal signals resulting from the complete time-reversal procedure. To do that, we use a classical method from general signal processing, the different delays being obtained from the computation of the cross-correlation between successive channels. Then this time-delay law is used with PASS and the resulting displacement field is shown on figure 6b. Once again the resulting displacement field appears to be effectively focused on the expected position.
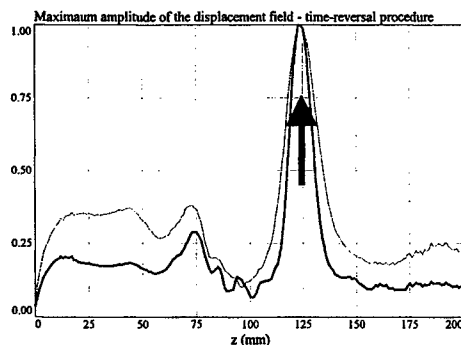
Figure 6a : *focal patterns resulting from time-reversal ; without (thin curve) and with (thick curve) normalization.*
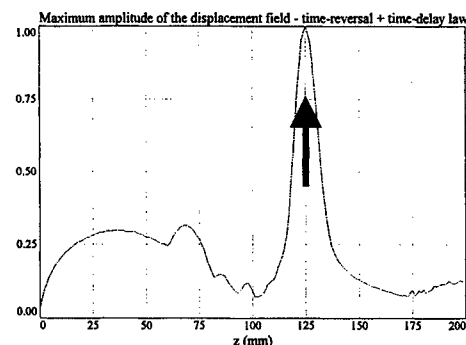
Figure 6b : *focal pattern resulting from the time-delay law obtained by cross-correlation of the temporal signal deduced from time-reversal.*

As above, the different curves are all normalized to unity.

This last simulation is interesting since it provides an objective approach to compute an adequate time-delay law, independently from the geometry of the phased array, focal point and/or interface. It is also justified by the fact that time-reversal methods require some specific and complex electronics, while phased arrays and controllable time-delay laws are much cheaper.

Conclusion

In this paper, we presented a concrete situation for which the computation of a time-delay law may yield some difficulties, particularly in the computation of the resulting focal pattern. These difficulties are directly related to the finite aperture of the elements of the array, that are generally of large size. We also proved that a time-reversal approach provides an elegant and efficient solution to these difficulties. Finally, the temporal signal obtained by time-reversal may be used to extract an adequate time-delay law ; these delays do not result from an a priori algorithm (average, minimum delays), but are the consequence of an objective approach of the problem.

We are actually working on experiments to illustrate these effects.

Acknowledgements

Bibliographie

1. Fink M. : Time-reversal of ultrasonic fields - Part I : basic principles, *IEEE Trans. Ultrason., Ferro-elec., Freq. Contr.*, vol. 39, N° 5, 1992, pp 555-566,

2. Wu F. *et al.* : Time-reversal of ultrasonic fields - Part II : experimental results, *IEEE Trans. Ultra-son., Ferroelec., Freq. Contr.*, vol. 39, N° 5, 1992, pp 567-578.

3. Cassereau D. *et al.* : Time-reversal of ultrasonic field – Part III : theory of the closed time-reversal cavity, *IEEE Trans. Ultrason., Ferroelec., Freq. Contr.*, vol. 39, N° 5, 1992, pp 579-592.

PHASED-ARRAY EFFECT IN ANTENNAS WITH TRANSIENT EXCITATION

Boryssenko A., Prokhorenko V.
Research company "Diascarb"
P.O. Box 148 Kyiv 02222 Ukraine
E-mail: diascarb@public.ua.net

Abstract

In this work the phased array effect in linear antenna with transient excitation will be under theoretical and numerical analysis. This effect is realized inherently due to specific features of transient electromagnetic radiation in long linear and other antennas. The waveform of radiated electromagnetic field of those antennas includes separated in time the pulse signal replicas that produced by specific points on antenna like its boundaries as well as any point with "strong" charge disturbance of antenna. This waveform registered by a field probe in an arbitrary observation point depends on its spatial position. The last can be principally determined by processing of the registered waveform. This signal processing involves resolution in time of indicated signal components and is in fact a beam-forming procedure of phased array antenna with transient behavior.

1. Problem Background

In contrast to antennas and arrays with both sinusoidal and narrow frequency-band excitation the electromagnetic structures with transient excitation demonstrate quite different performances [1]. Such excited by pulse (video-pulse) signals antennas are employed widely in high-resolution radars, subsurface radars, EMP simulators etc. The theoretical and experimental time-domain approaches to study transient antennas are more adequate than traditional frequency-domain technique [2]. Besides known features of transient antennas [1-4] there is an inherent effect than can be treated as some phased array behavior. For simplicity, let consider a thin monopole antenna in the Cartesian coordinates as it is shown in Fig. 1a. The two boundaries of antenna are located at $x=0$ (source termination) and $x=La$ (end point). The radius of antenna is enough small so that only the x-direction component of the vector potential function Ax should be treated that resulted in the principal component $E_x(t,x,y)$ for single-passing excitation mode [1]:

$$E_x(t,x,y) = k\left\{\int_0^{La}\frac{U'(t-(R+l)/c)}{R}dl + \int_0^{La}\frac{U(t-(R+l)/c)}{R^2}dl\right\} \quad (1)$$
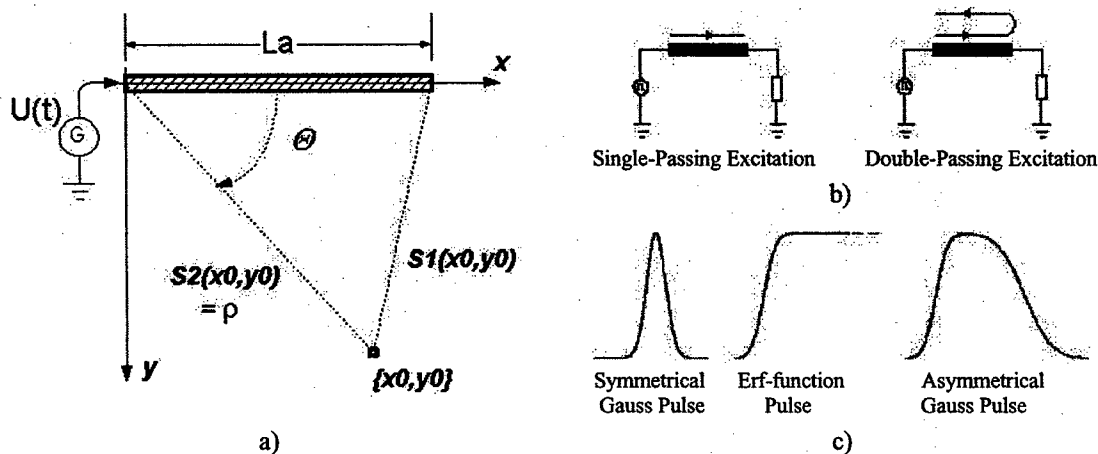

Fig. 1. Schematic presentation of linear monopole antenna in the Cartesian coordinates (a) excited in single- or double-passing mode (b) by driving signal $U(t)$ of definite waveforms (c).

Where in (1) c is the light velocity; k –coefficient; l – local auxiliary coordinate along antenna axis with the origin at $x = 0$; $R=R(x,y,l)=((x-l)^2 + y^2)^{1/2}$ is a distance on the plane xy from the point on antenna $x=l$ to observation one with coordinates $\{x,y\}$ in Fig 1a. The expression (1) has been obtained under the following assumption. The antenna is excited by pulse signal with waveform $U(t)$ like ones in Fig. 1c. Current distribution along the antenna is initially presented like traveling wave $U(t-(l+R)/c)$ until this current reaches the boundary at $x = La$. Then there are two main scenarios of antenna excitation (Fig. 1b), i.e. single-passing excitation due to matched antenna end loading or double-passing one due to boundary effect at $x=La$ with the following current disappearance on matched impedance of the driving source. Generally both modes are implemented by means of antenna distributed resistive loading.

Note that the first term in the left part (1) corresponds to the radiated far-field component while the second one is the near-field [1]. Expression for far-field radiation can be obtained analytically from (1) by noncomplex math manipulations. Thanks to axial symmetry of problem it is easy to present the electric far-field under the single-passing excitation in the polar coordinate system $\{\Theta,\rho\}$ on the plane (Fig. 1):

$$E_\Theta(t,\Theta,\rho) \cong k_1 \frac{\sin\Theta}{1-\cos\Theta} \cdot \left\{ U(t-\frac{\rho}{c}) - U(t-\frac{\rho}{c}-\frac{La}{c}(1-\cos\Theta)) \right\} \quad (2)$$

where k_1 is normalized coefficient. The expression (2) reflects that radiation of transient antenna is produced by antenna's boundary points at $x=\{0,La\}$ [3,4]. There is some physical sense in that statement because electromagnetic radiation is originated due to acceleration or deceleration the charges on antenna [5]. Evidently rapid appearance or disappearance of charges takes place on the antenna boundaries. In fact energetic and pattern features of transient radiation depends on antenna total length and its geometrical structure [1,4], which are not considered in detail here.

2. Phased Array Effect in Transient Linear Antenna

Let analyze the basic geometrical relations in antenna arrangement in Fig. 1a in accordance to introduced above a "discrete-point" model of transient radiation. Starting from evident geometrical properties in Fig. 1a one has the following expressions for time intervals that are necessary to reach the observation point from the antenna boundaries in process of pulse propagation along antenna excited in the double-passing mode (right part of Fig. 1b):

$$T1(x,y) = S1(x,y)/c \quad (3a) \quad T2(x,y) = (La + S2(x,y))/c \quad (3b) \quad T2(x,y) = (2La + S2(x,y))/c \quad (3c)$$
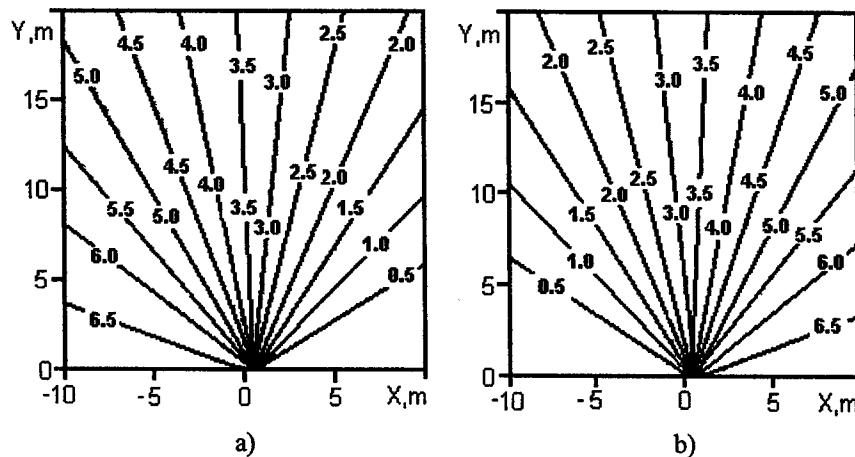

a)   b)

Fig. 2. Contour plots for $\Delta T1(x,y)$ (a) and $\Delta T2(x,y)$ (b) quantities terminated in nanosecond (ns) unit. These figures have been computed for linear antenna La = 1.0 m in the Cartesian coordinates (Fig. 1a) for square area limited by inequalities: $-10 \le x \le 10$ and $0 \le y \le 20$. Both x and y are terminated in meters (m).

Next it is reasonable to express time differences between the field events characterized by $T1,2,3(x,y)$

$$\Delta T1(x,y) = T2(x,y) - T1(x,y) \quad (4a) \qquad \Delta T2(x,y) = T3(x,y) - T2(x,y) \quad (4b)$$

Then one is able computing $\Delta T1$ and $\Delta T2$ by (4) and presenting the final results by contour plots like in Fig. 2 where is seen that there is mutual dependence between quantities $\Delta T1$ and $\Delta T2$ and spatial coordinates $\{x,y\}$ of the observation point. Such dependence establishes the one-to-one correspondence between $\{\Delta T1,\Delta T2\}$ and $\{x,y\}$ excepting only narrow domain where $x \approx La/2$.

Now let consider the problem starting rather from expressions like (1) and (2) then geometrical properties discussed above. Reaching this goal one can specify quantities $\Delta T1$ and $\Delta T2$ versus $\{x,y\}$ by computing simulated waveforms. The double passing excitation mode of antenna and set of excitation signals (Fig. 1c) are involved in simulation. The typical simulated waveform can be obtained like ones in Fig. 3 where aforementioned quantities $\Delta T1$ and $\Delta T2$ are shown. In fact exact time evolution of signal depends on correlation of antenna length La and signal electrical lengths $Ls=Ts*c$ [4] where Ts is equivalent signal duration. The array effect under investigation becomes apparent for long antenna when $La > Ls$.

In what follows one computes $\{\Delta T1,\Delta T2\}$ for chosen points $\{x,y\}$ inside the square domain $-10 \leq x \leq 10$ and $0 \leq y \leq 20$ (Fig. 2). This computation involves the specification of wanted magnitudes from simulated waveforms as shown in Fig. 3. Acting in such way one can receive total coincidence of results of presented above geometrical analysis and electromagnetic modeling as it follows from Fig. 4. In this Fig. 4 one can observe the changing of signal waveform and corresponding $\Delta T1$ and $\Delta T2$ figures versus the Cartesian coordinates of observation point inside the indicated domain. The effect of the near-field electromagnetic radiation is visible in Fig. 4 when $y \leq 5*La$ and can be employed for some goals too.

Summary

Due to the fact that transient electromagnetic events are considered in time-domain each component of electromagnetic field connected with antenna's boundaries is registered in proper time that depends on geometrical relations of task. For the sample of linear antenna with double-passing excitation considered above there are three separated replicas of radiated electromagnetic field, which are connected with pulse radiation produced by the antenna's end points. As it was shown early the features of the registered waveform depend on the coordinates of observation points $\{x,y\}$ and the general geometry of antenna. Such dependence is mostly a single-valued function excepting position $x \approx La/2$ that in turn is valuable too, for instance, to solve pointing or navigation tasks etc. Generally for implementation of radar signal processing one should solve three consequence problems, i.e. (1) target detection, (2) coordinate measurement and (3) recognition. For pulse radar operating in time-domain the problems (2) and (3) are closely matched together due to the fact that observed waveform of scattered signal is a function of both the spatial position and shape of target. The presented study gives a model of array behavior of pulse antenna that can be employed for implementing time-domain beam forming in transient antennas.
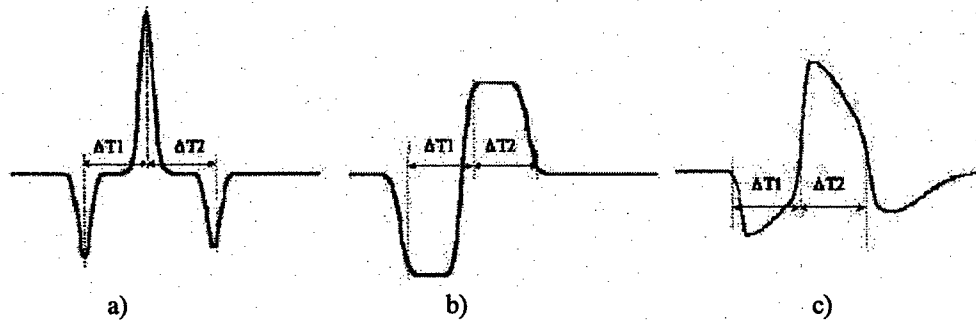
Fig. 3. Radiated waveforms due to double-passing excitation by (a) symmetrical Gauss pulse, (b) Error-function pulse and (c) asymmetrical Gauss pulse with $\Delta T1$ and $\Delta T2$ characteristic values.

471

Note that in practice for navigation and positioning tasks the measurement of spatial mutual position of receiver in observation point and transmitter with transient array can be implemented in asynchronous modes. Such working is based on estimation of the $\Delta T1$ and $\Delta T2$ characteristics without necessity for mutual synchronization of transmitter and receiver in time.

References

[1] A. Boryssenko, V. Tarasuk, "Ultra-Wide Band Impulse Antennas for Subsurface Radar Applications", *Proceedings of the 1999 Antenna Applications Symposium*, Amherst, USA, September 15-17, 1999, pp. 478-504.

[2] A. Boryssenko, V. Tarasuk, "Time-Domain Experimental Studies of Ultra-Wide Band Antennas", *Proceedings of 22nd ESTEC Antenna Workshop on Antenna Measurements*, ESTEC, Noordwijk, The Netherlands, May 1999, pp. 101-106.

[3] Zaiping N., "Radiation Characteristics of Traveling Wave Antennas Excited by Nonsinusoidal Currents", *IEEE Transactions on Electromagnetic Compatibility*, **EMC-25**, February 1983, pp.24-31.

[4] R. Gomez Martin, A. Rubio Bretones, , S. Gonzalez Garcia, "Some Thoughts About Transient Radiation by Straight Thin Wires", *IEEE Antennas and Propagation Magazine*, **AP-41**, June 1999, pp. 24-33.

[5] L. Landau , E. Lifshitz, "Field Theory", Moscow, Nauka, 1988. (In Russian).

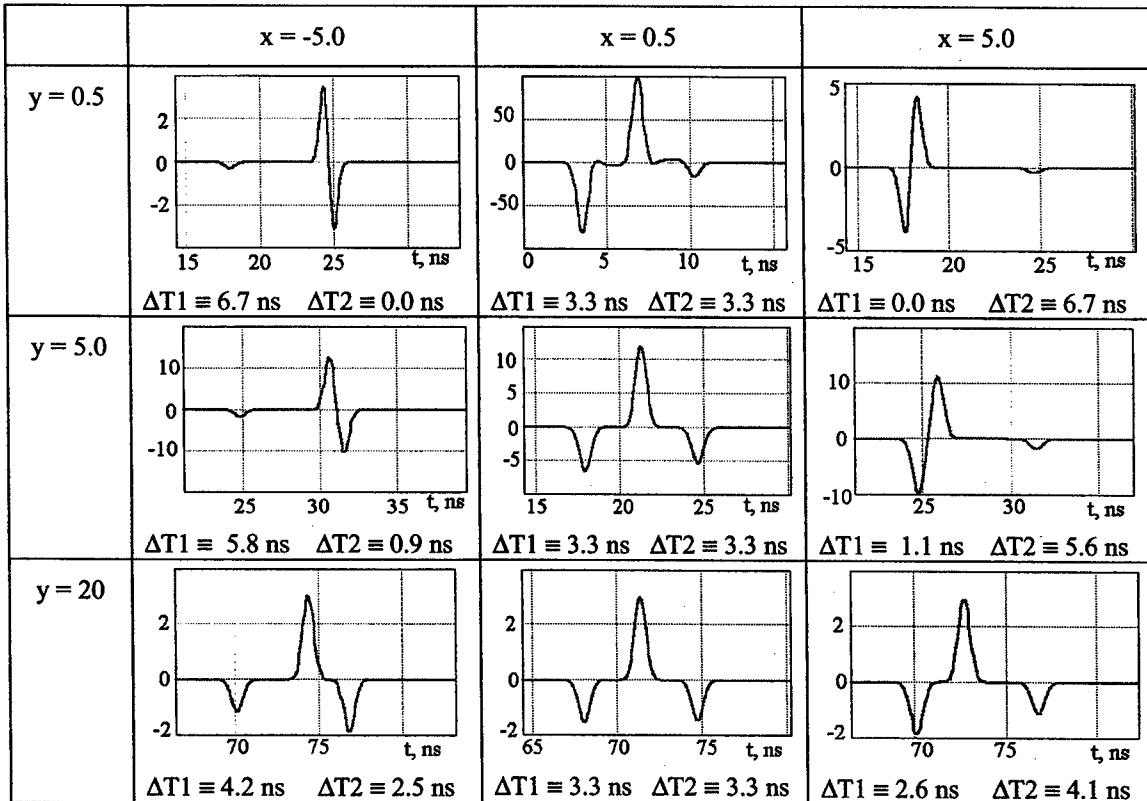|	x = -5.0	x = 0.5	x = 5.0
y = 0.5	ΔT1 $\equiv$ 6.7 ns ΔT2 $\equiv$ 0.0 ns	ΔT1 $\equiv$ 3.3 ns ΔT2 $\equiv$ 3.3 ns	ΔT1 $\equiv$ 0.0 ns ΔT2 $\equiv$ 6.7 ns
y = 5.0	ΔT1 $\equiv$ 5.8 ns ΔT2 $\equiv$ 0.9 ns	ΔT1 $\equiv$ 3.3 ns ΔT2 $\equiv$ 3.3 ns	ΔT1 $\equiv$ 1.1 ns ΔT2 $\equiv$ 5.6 ns
y = 20	ΔT1 $\equiv$ 4.2 ns ΔT2 $\equiv$ 2.5 ns	ΔT1 $\equiv$ 3.3 ns ΔT2 $\equiv$ 3.3 ns	ΔT1 $\equiv$ 2.6 ns ΔT2 $\equiv$ 4.1 ns

Fig. 4. Waveforms of principal electrical component of radiated electromagnetic field and magnitudes of ΔT1 and ΔT2 quantities computed for linear monopole antenna of the 1-m length. This antenna is located like one in Fig. 1a and excited in the double-passing mode by the current pulse source with the Gauss symmetrical waveform and pulse duration of 0.5 ns at the amplitude level 0.5 (-6dB).

WP1

System Design and Optimization

System Design and Optimization

PHASIM, an advanced phased array antenna software simulator

W.P.M.N. Keizer
TNO Physics and Electronics Laboratory
P.O. Box 96864, 2509 JG The Hague, Netherlands
keizer@fel.tno.nl

Abstract. A sophisticated phased array simulator software package for the design and analysis of planar phased array antennas is presented. This package can accurately simulate the far-field characteristics of a large variety of planar phased array configurations in both the frequency and time domain. The simulator is coded in MATLAB version 5.3. Using MATLAB, numerical engineering problems can be solved in a fraction of time of time required by programs coded in FORTRAN or C. This paper addresses an assessment of the program, discusses its use and advanced far-field analysis capabilities.

1. Introduction

Most present software packages for the calculation and analysis of the far-field behaviour of phased array antennas is written in traditional programming languages such as FORTRAN or C. However, the advent of commercially available computer algebra systems can greatly simplify the software coding of such programs due to the automatic manipulation of mathematical formulas provided by computer algebra.

In this paper the phased array software simulator PHASIM (PHased Array SIMulator) is described. It is a program for the analysis and design of planar phased array antennas of arbitrary geometry. PHASIM is coded in MATLAB Version 5.3. MATLAB (MATrix LABoratory) is a mathematical software tool that combines numeric and symbolic analysis with extended graphics and programming capabilities using a plain text proprietary language. Its matrix-oriented language is designed for efficient numerical, large scale computation and data analysis and it has hundreds of built-in numerical functions.

PHASIM offers accurate, high speed computation of the far-field patterns of planar phased antennas, advanced far-field analysis capabilities and comprehensive 2-D and 3-D visualisation of the simulated results. Execution time is minimised by coding the program as matrix operations and using 2D FFT (Fast Fourier Transform) techniques for calculating the far-field patterns. The program operates with a state-of-the-art GUI (Graphical User's Interface), provides extensive error checking of user data input, and is intuitive to use. This paper will address the main capabilities of the program, the computational approach and will present some typical results including their execution times. An earlier version of the program was described in [1]. Since then functionality of the program has been extended substantially. The latest version allows performing the far-field simulations in the frequency as well as in the time domain, and can deal with apertures split up in subarrays and with switcheable time delay units connected to a group of T/R modules. The element lattice configurations, originally restricted to rectangular and triangular types, have been extended to skew ones, which may have random row or column displacements.

2. Main capabilities

The phased array simulator PHASIM can handle planar phased array antennas with the elements spaced in rectangular, triangular and skew lattices configurations. Skew lattices having random row or column displacements of the elements can be handled as well. The elements of the array are allowed to be grouped in subarrays. Scanning of the main beam can be modelled be either phase shifters or time delay

circuits inside the T/R modules including the option to use switcheable TDUs (Time Delay Units) connected to a group of T/R modules. The radiating elements may have isotropic, cos(theta), cos(theta)^N or a dipole type radiating characteristics. For the array aperture the user can specify a circular, elliptical, rectangular or polygon shape.

In order to get low-sidelobe patterns, the program features 8 different amplitude tapers for sum patterns and 4 amplitude tapers for difference patterns. For the sum tapers the choice can be made between Uniform, Triangular, Cosine on a Pedestal, Gaussian, Blackman, Kaiser, Bessel and Taylor. For the difference patters, models are included for the tapers, odd Rectangular, odd Triangular, odd Taylor and Bayliss.

Apart from computing 2D far-field patterns, PHASIM can also generate high-resolution 1D far-field cuts. The program uses the results of the 2D far-field calculation to extract the directivity of the antenna, the main beam peak position, the 3 dB beam-width in both the u- and v-plane and the rms sidelobe level. As an option PHASIM determines also the number of sidelobes and the distribution of their peak levels. For tracking antennas with monopulse capability the program has the ability to determine the tracking slope for both the azimuth and elevation plane.

Visualisation comprises also the element layout along the aperture including the grouping in sub-arrays, the location of defective elements and the connection of the switcheable TDUs to the elements. The element excitations, phase or time delay and amplitude, can be displayed in 2-D formats and 3-D formats using pseudo contour or surface plots.

PHASIM can simulate various types of errors, such random phase and amplitude deviations in the aperture excitation, phase shifter or time delay quantisation, element failures randomly located or grouped in sectors, element location displacements and structural deformation of the aperture.

The program operates with an interactive Help Window, which gives access to an electronic on-line manual. This manual, coded as HTML (HyperText Markup Language) document, requires a Web browser to open it. PHASIM incorporates a state-of-the-art GUI and provides a high degree of user friendliness.

3. Computational approach

For arrays with periodic element lattice configurations, rectangular, triangular and skew (including the random row or column displacement) the computation of 2D far-field radiation pattern is always done by modified 2D FFT techniques performed on the element excitations. This approach reveals the AF (Array Factor), which multiplied with the element pattern gives the far-field pattern of the array under consideration. In case the elements are arbitrarily located, the 2D far-field patterns are computed by a fast brute force method based on direct summation of the radiating contributions of the array elements. All 2D far-field results are computed as a function of the direction cosine u and v.

A 2D FFT is a very efficient and high-speed computational technique for numerical evaluation of the AF. Normally, a 2D FFT can only be applied when the array elements are arranged in a rectangular lattice. However, in PHASIM this technique is extended to arrays using triangular or skew lattices. The earlier paper [1] provides information how FFT techniques can be applied to calculate the AF for triangular grids. For the present version of PHASIM a new FFT technique was developed which can also handle skew lattice configurations. This new FFT technique provides also more flexibility with respect to the spacing between the far-field directions. With conventional FFTs the spacing between the far-field directions is fully determined by the aperture element spacing, the frequency of operation and the size of the FFT. With the new FFT to calculate the AF, the spacing between the far-field directions is no longer subjected to any restriction. Another advantage of this new technique is its zoom-in capability, which allows computing the 2D far-field with a high density of the far-field directions over a limited spatial region without using a large size FFT. The program can compute high-resolution far-field pattern cuts in the u- or v-direction or in spherical co-ordinates Phi and Theta. Computation of the pattern cuts for a

fixed u- or v-direction relies on a hybrid approach consisting of the brute force method in combination with a large size (8192 points) 1D FFT. These kind of far-field cuts can be computed for any fixed value of u or v between -1 and 1. The pattern cuts for the spherical co-ordinates Phi and Theta are derived from the 2D far-field results using an interpolation scheme based on a built-in MATLAB 2D interpolation M-function.

In order to optimise execution speed, the program was mainly coded as matrix operations; in particular the far-field computations and the data visualisation parts were programmed in this way. For MATLAB this is the favourite approach since it is matrix oriented programming language. This results in a very compact code compared to the coding in FORTRAN or C which is therefore also much more easier to debug or to maintain.

4. Simulation examples

Figs 1-2 show typical simulation results obtained with PHASIM. Both figures deal with the same phased array configuration which operates with time-delay steering for scanning the beam. Two types of switcheable time delay devices are specified. At the element level a 200 ps timeshifter is applied with 6-bit resolution in combination with 103 switcheable TDUs located at the feed level. The TDUs have a 10 bit resolution and a maximum time delay range of 5000 ps. The array operates with 3407 radiating elements. Each TDU feeds 15 rows and 9 columns of elements. The plot at the top represents the far-field sum pattern on transmit of a circular phased array antenna with a triangular lattice arrangement of the elements. In this example the beam is scanned to Theta = 30 deg and Phi= 40 deg. A Blackman taper was selected for low-sidelobe performance. However, since the beam steering is done with 6-bit timeshifters, quantization lobes due to the finite time delay resolution of the timeshifters and TDUs, corrupt the low sidelobe performance. Information on the peak sidelobe performance is shown in the bottom plot.
Fig. 2 demonstrates the advantage of using time delay steering for scanning the main beam. As can be seen from the top plot, the angular position of the main beam does not vary with signal frequency. The bottom plot shows for the fixed far-field direction Theta = 30 deg and Phi = 40 deg the behaviour of the array gain and the array group delay over the frequency band 9–12 GHz.
PHASIM, running on a PC with a 500 MHz Pentium III processor, computes a 2D far-field pattern for 256*256 cosine directions in less than 0.3 sec. The far-field analysis, revealing directivity, peak direction, 3 dB beamwidth for both the u- and v plane including the rms sidelobe level takes a about the same time. The duration of the peak sidelobe analysis depends on the number of sidelobes and is usually done within 1 second including the plotting of the peak sidelobe histogram.

5. Conclusions

A sophisticated phased array simulator written in MATLAB 5.3 has been developed at TNO-FEL. The simulator can deal with various aperture shapes, a number of periodic element lattice configurations and various aperture tapers both for sum and difference patterns. High speed computation is obtained by coding the program as matrix or vector operations.

7. References

[1] Keizer, W.P.M.N., "PHASIM, a sophisticated phased array antenna software simulator implemented in MATLAB 5.2", IEEE AP-S International Symposium 1999, Orlando, pp. 2508-2511.
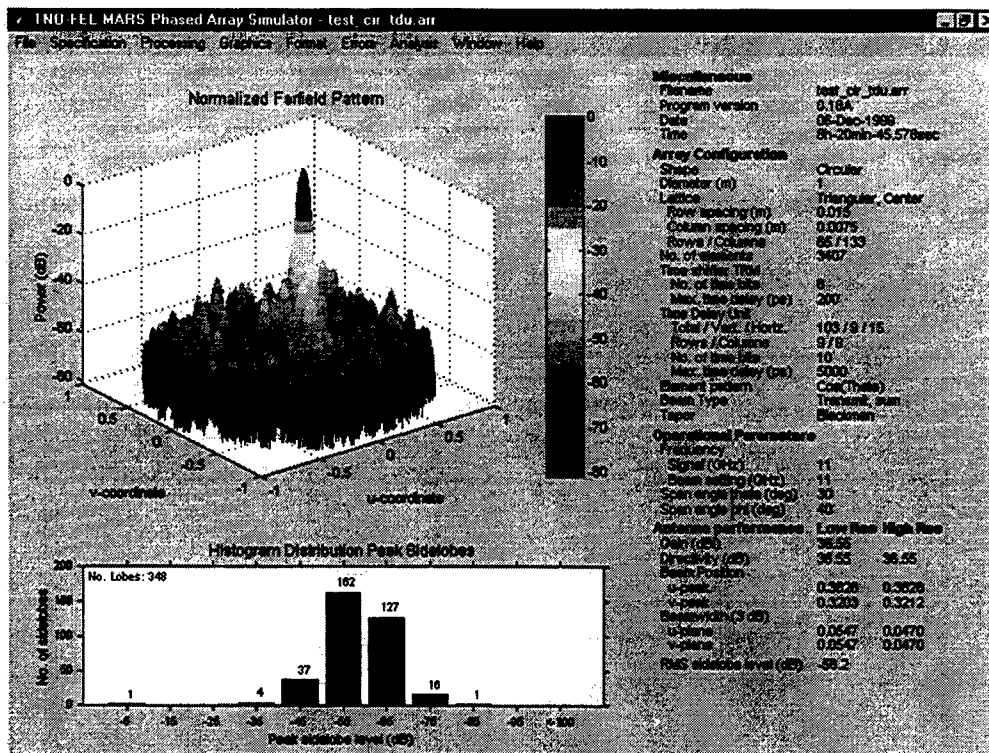
Fig. 1. Far-field results of a circular phased array at 11 GHz with the main beam scanned at Theta =30 deg and Phi = 40 deg. Beam scanning is realized by time delay steering.
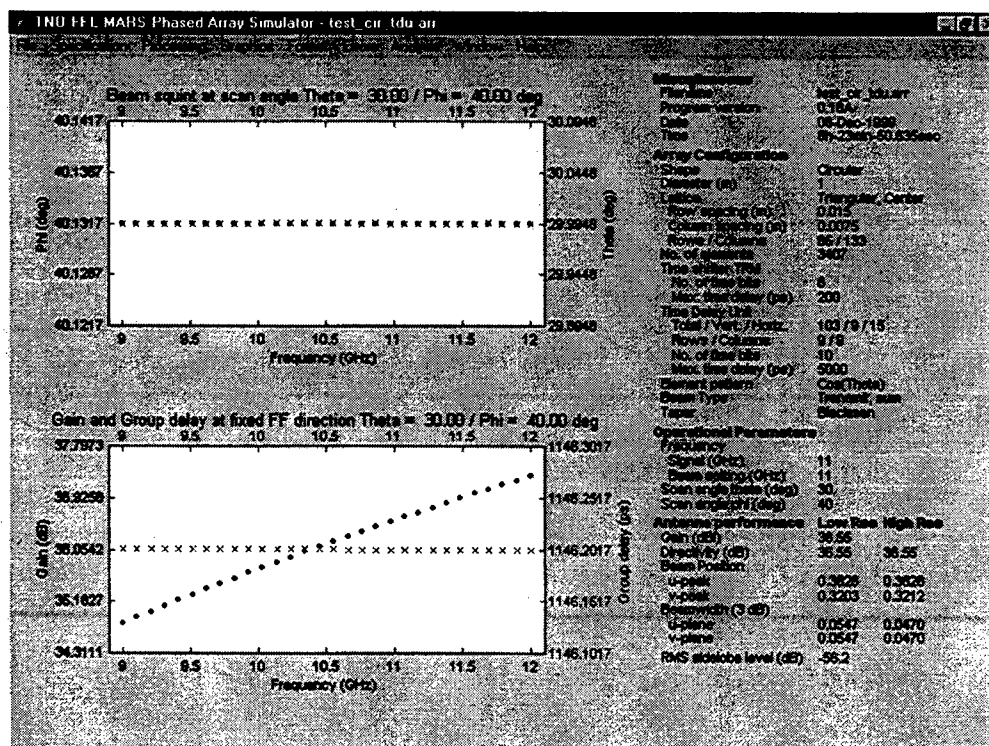

Fig.2 Beamsquint behaviour and transfer characteristic (gain and group delay) of the same phased array over the frequency band 9 –12 GHz at the scan direction Theta =30 deg and Phi = 40 deg.

480

COMPUTER AIDED DESIGN OF A PLANAR PHASED ARRAY

Nemai C. Karmakar [†] and Marek E. Bialkowski [‡]

[†]School of Electrical and Electronic Eng.
Nanyang Technological University
Nanyang Avenue, Singapore 639798
E-mail: enckarma@ntu.edu.sg

[‡] Computer Science & Electrical Eng. Dept.,
University of Queensland, St Lucia
Queensland 4072 Australia
E-mail: meb@csee.uq.edu.au

ABSTRACT

The complex design process of a planar multi-layer phased array antenna in microstrip technology can be simplified using two commercially available design tools HP-EEsof Touchstone™ and Ansoft Ensemble™. Touchstone™ is employed to analyse and optimise PIN diode switches and phase shifters while Ensemble™ is used to analyse radiating layers and associated feeding networks. The approach allows prediction of the performance of a phased array prior to its manufacturing. This is demonstrated in the design example of a 12-element circular phased array operating at L-band.

I. INTRODUCTION

Phased array antennas are increasingly being found in applications such as radar [1] and more recently in satellite and cellular communications [2], [3], [4]. The reason for this is that these antennas offer improved flexibility of beam steering using electronic means. Despite increased popularity, the design of a phased array antenna is not yet a simple task because of complex specifications this antenna has to meet. Microwave and antenna design software tools should help overcome these design complexities. Unfortunately at present, integrated software tools for the design and development of planar phased array antennas do not exist.

This paper attempts to overcome this shortcoming. It shows that the task of design and prototyping of a planar phased array in microstrip technology can be facilitated by combining two existing commercially available CAD software tools: (i) antenna design package Ensemble 6.0™ of Ansoft [5], and (ii) microwave circuit design package HP-EESof Series IV [6]. Ensemble is a tool for analysing multi-layer structures formed by planar layers of dielectrics interleaved with ground planes and arbitrarily shaped conducting sheets. As such, this software package is suitable to model radiation of multi-layer microstrip patch antennas forming the radiating layer of a planar phased array. In turn, HP-EESof Touchstone™ is a software package for the analysis, optimisation and layout production of microwave circuits that can be represented by transmission lines, lumped elements or equivalent circuit parameters. This software package can be useful in the design process of a beamforming network constituted by RF switches and phase shifters. The connection between the two software packages can be established as follows. Once the control devices of a beamforming layer are designed, they can be represented in terms of scattering matrix parameters and accommodated in Ensemble™ simulations using its *black box* utility. Using black boxes in conjunction with the power dividing network and radiating elements, Ensemble™ should be able to fully predict the radiation pattern of the array antenna prior to its manufacture. This strategy is demonstrated in the design example of a 12-element circular phased array.

II. CAD AND CAM OF A PLANAR PHASED ARRAY

Figure 1 illustrates details of the proposed integration between CAD and CAM tools in the design and development of a multi-layer phased array in microstrip technology. As seen in Figure 1, there are two streams in the proposed CAD design. In the first stream, HP-EESof Touchstone™ is used for handling

the analysis and design of switches and phase shifters in the beamforming layer. In the second stream, Ensemble™ is used to analyse a multi-layer microstrip patch antenna layer. The integration between the two CAD tools takes place via the *translation of S-parameter-to-black box* from Touchstone™ to Ensemble™.
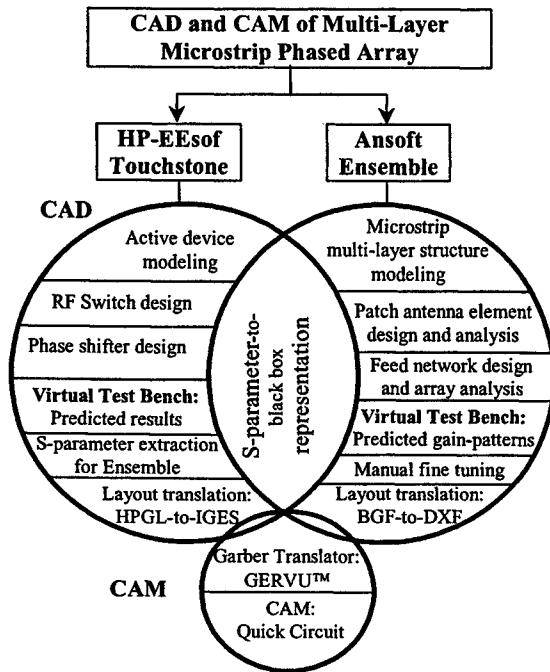

Fig. 1. Proposed integration of CAD and CAM tools in the design and development process of a planar phased array using microstrip technology.
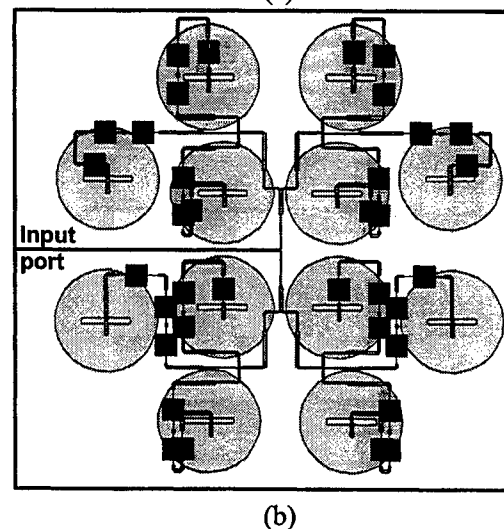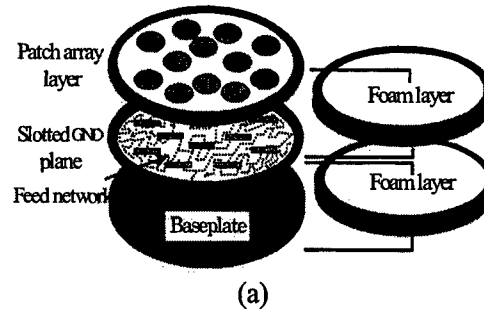

Fig. 2. Configuration of a phased array antenna: (a) schematic representation, and (b) Ensemble generated physical layout of a 2-ring 12-element circular phased array— isometric view.

The design commences with the modeling of impedance control devices, which in the present case employ a PIN diode. To this purpose, the diode is tested at two biasing conditions representing ON and OFF states. Once the scattering matrix parameters are obtained, they are fed into the simulation engine of Touchstone™, which generates numerical values of circuit parameters of the diode. Once the values of the diode circuit model are obtained, RF switches and phase shifters are designed using optimisation routines of Touchstone. The optimisation parameters involve return loss, insertion loss and a given value of phase shift over a selected frequency band. Having obtained optimal performance of switches and phase shifters, their S- parameters are translated to Ensemble™ using its *black box* facility.

In Ensemble™, a radiating layer is modelled first. In the present case a single aperture coupled patch antenna is analysed until a satisfactory performance in terms of return loss, radiation pattern, gain and ellipticity (for circularly polarised element) is obtained. When there is satisfactory performance over a given frequency band, the element is replicated in an array. The next step is to obtain a feed network in a lower layer of the array structure, which should conform to the size and location of antenna elements. Constraints introduced by the actual size of phase shifters and switches are taken into account. This process is made easier by the helpful transparent multi-layer view of the overall circuit

layout, as offered both by Ensemble™ and Touchstone™. Provided that there is physical alignment of patches, apertures and transmission lines in the beamforming layer, the analysis of the entire array in terms of return loss and radiation patterns proceeds next. At this stage, the transfer of S-parameters of control devices is already established and the complete multi-layer array performance can be simulated using the *Ensemble Simulation Engine* (ESE). Using ESE, 2-D and 3-D radiation patterns (including axial ratio) and an overall gain as a function of frequency and scan angle can be produced. Usually this analysis is time consuming if a multiple frequency scan is required and so the required calculations are performed only at selected frequency points such as the middle, lower and upper frequency points of a given band.

After achieving a satisfactory performance over the band, the multi-layer layout can be generated in a suitable format for fabrication using CAM. This task is achieved via suitable translation software. In the present version the array layout is stored using Ensemble BGF files. The usual way is to make the translation to AutoCAD DXF files or the more widely adapted Gerber format files. This is accomplished using another commercial translation software available from Ansoft or other vendors. Alternatively, the layers are re-drawn using HP-EESof Academy Layout™ leading automatically to Gerber or other popular CAM formats. Having obtained suitable layout files, the phased array layers can be etched using suitable substrates. Alternatively, *Quick Circuit™* or another equivalent milling machine can be used for the same purpose.

III. PHASED ARRRAY DESIGN AND DEVELOPMENT

The schematic diagram of a multi-layer phased array antenna in microstrip technology, which has been considered here, is shown in Figure 2(a) and its isometric view used in Ensemble is shown in Figure 2b. The array formed by two rings of 4 and 8 elements is designed for use with the Australian Mobilesat [4]. In this configuration, radiating antenna elements are in a top layer. The slotted ground plane of the beamforming network PCB is facing upward and separated by a foam layer from the radiating layer. The beamforming network, which is comprised of power splitters/combiners and phase shifters, is facing downwards. The PCB rests upon a baseplate separated with another foam layer. All layers are fastened together with screws and ring spacers. The ring spacers also help to keep uniform separation between layers. In Figure 2b, different phase shift bits are represented by *black boxes*, which carry the information about the calculated or measured S-parameters of these devices. In the present case, 3-bit phase shifters including 180°, 90° and 45° bits are used [4]. These phase shifters are designed using HP-EESof Touchstone™. First single prototypes of these devices are developed and tested and their measured results are included in the simulation of the entire beamforming network. This procedure allows for more realistic simulation of the beamforming network and is achieved using the measured S-parameters of these circuits instead of simulated ones. Calculations of the required phase shifts in order to radiate power in a given direction are obtained here using software written by the authors.

IV. RESULTS

Following the proposed design strategy, the single patch antenna element was developed and tested. Designed for 1.6GHz, the aperture coupled circular patch antenna element is 84 mm in diameter. The Ensemble simulated return loss (RL) revealed that this antenna element is well matched within the frequency band of 1.55-1.65 GHz, a result further confirmed experimentally. The gain was found to be not less than 8.5 dB over the frequency band.

Once satisfactory results from the antenna elements were achieved, the complete phased array antenna with the beamforming network including phase shifters and power dividers was simulated. The assumed inter-element spacing was 100 mm (between center-to-center of the adjacent patches). The Ensemble simulated 2D gain patterns of the 12-element circular phased antenna array [c.f. Figure 2b] are shown in Figure 3. As seen in the 2D gain patterns plot of Figure 3, the far field gain patterns are

calculated at 45° elevation at two frequency points 1.55 GHz and 1.65 GHz. The peak gain of the phased array antenna is approximately 15 dB at 45° elevation with sidelobe levels of less than 10 dB down from the main beam. This predicted gain pattern also shows reasonably low sidelobes across the entire 360° azimuth angles. Both patterns were found to agree well with the measured radiation patterns when the developed antenna was tested in an anechoic chamber [4].
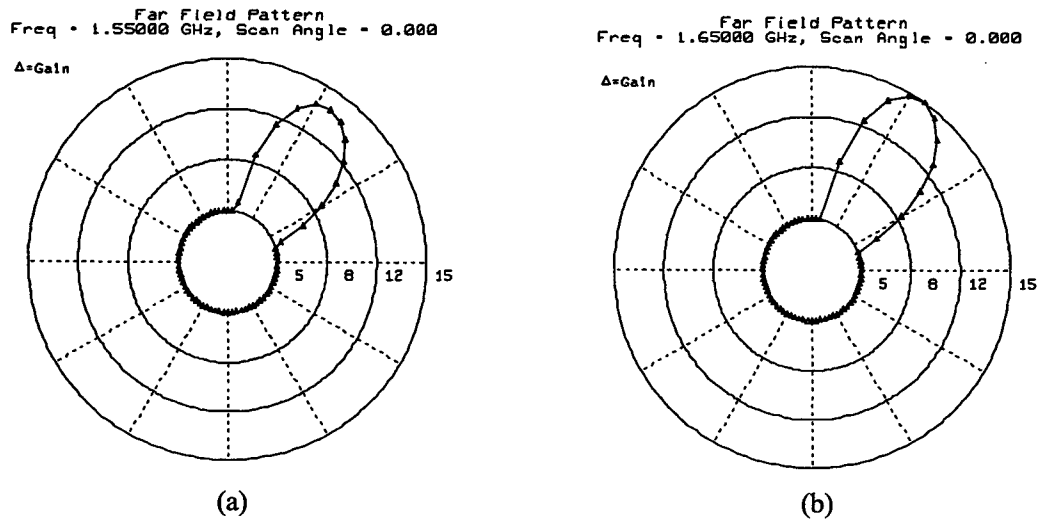

(a)   (b)

Fig 3. 2D far-field gain pattern plots of the 2-ring 12-element circular phased array at (a) 1.54 GHz and (b) 1.65 GHz.

V. CONCLUSIONS

A practical design procedure for planar phased array antennas using CAD tools has been presented. In this procedure the commercially available antenna design package Ensemble™ of Ansoft and the microwave circuit design package HP-EESof Series IV have been used. Ensemble™ has been applied to design antenna elements and to predict the performance of the entire array. HP-EESof has been used to design phase shifters in the beamforming network. The link between the two design packages has been achieved using the *black box* tool of Ensemble. Satisfactory performance of the phased array antenna has been achieved prior to its manufacturing.

REFERENCES

[1] E. Brookner, *Aspects of Modern Radar*, Norwood, MA, Artech House, 1988.
[2] L.C. Godara, "Prolog to Applications of Antenna Arrays to Mobile Communications, Part I: Performance Improvement, Feasibility, and System Consideration", *Proc. of IEEE*, Vol.85, No. 7, July 1997, pp. 1029-1060.
[3] K. Sato, K. Nishikawa and T. Hirako, "Development and Field Experiments of Phased Array Antenna for Land Vehicle Satellite Communications", *1992 IEEE MTT-S Int. Microwave Symp. Digest*, 1992, pp. 1073-1076.
[4] M.E. Bialkowski and N.C. Karmakar, "A Two-Ring Circular Phased Array for Mobile Satellite Communications", *IEEE AP-S Magazine*, Vol. 41, No. 3, June 1999, pp. 14-23.
[5] *Boulder Microwave Technologies, Inc.*, ENSEMBLE® Version 5.0, www.bmt.com.
[6] EEsof Series IV Touchstone User's Guide, Vol. 1 & 2, February 1993.

Optimal design of focusing inductive arrays for inhomogeneous medium

Elena Cherkaev[†] and Alan C. Tripp[‡]

[†] Department of Mathematics, University of Utah,
155 South 1400 East, JWB 233,
Salt Lake City, Utah 84112

[‡] Department of Geology and Geophysics,
University of Utah, 717 Browning Bldg.,
Salt Lake City, Utah 84112

Summary

The paper concerns with the optimal design of an inductive source array for inhomogeneous medium. The optimally designed array maximizes the response from an unknown inclusion in a known inhomogeneous reference medium. The problem is formulated as an optimization problem for array currents. This optimization problem is reduced to generalized eigenvalue problem and solved numerically. The source array can be hardwired or can be simulated using simpler source data. To illustrate the technique, we consider borehole source array designed for detecting a resistive bed using electromagnetic measurements in the borehole, when the invasion zone is highly conductive. The problem is known to be difficult for logging application. Comparison of the fields generated by the conventional and optimized sources show tremendous increase in depth of field penetration.

Introduction

Optimal resolution of electromagnetic images requires proper design of the applied sources. An approach to source design for direct current measurements was developed in [1, 4]. We have shown in [2, 3], that inversion algorithms with such optimized data can be computationally efficient. Dealing with an array of inductive sources, their amplitudes can be modulated using this techniques to optimize the perturbation response. This procedure is described below.

Formulation of the problem

Let a domain Ω be characterized by a dielectric permittivity ϵ, a magnetic permittivity μ, and an electric conductivity σ. We assume that $\mu = \mu_0$ everywhere, where μ_0 is the magnetic permittivity of free space, while the permittivity ϵ and the conductivity σ are spatially varying functions. Now assume that n magnetic source dipoles are confined to some subdomain Ω_0 of the domain Ω. The domains Ω and Ω_0 can be defined in various ways, depending on the particular application desired. For the numerical simulation shown below, Ω will be a three dimensional subsurface domain intersected by a fluid filled borehole which defines Ω_0. We need make no special assumptions concerning the particular geometry of Ω_0. In the regions containing the magnetic time harmonic sources J_m, the Maxwell's equations are

$$\nabla \times E + i\mu\omega H = -J_m,$$

$$\nabla \times H - (\sigma + i\epsilon\omega)E = 0. \tag{1}$$

The goal of geophysical imaging is to measure the fields H in Ω_0 which are induced by a set of sources J_m and subsequently deduce the spatially varying function σ. We will try to maximize the resolution of σ vis-a-vis a particular a-priori model by optimizing the magnitudes and phases of the impressed magnetic currents.

Suppose that the background medium is characterized by the conductivity distribution σ_0, with the fields E_0 and H_0, generated by the same magnetic currents J_m. These fields satisfy the same equations (1) with the conductivity σ_0. Let the generated response at the receivers due to J_m be H_0. The difference between the measured and calculated fields
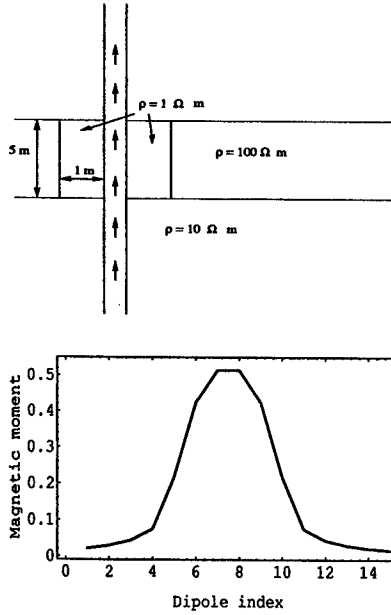
Figure 1: A cross-section of the model (top) and the optimal distribution of the moments of magnetic dipoles (bottom).

is due to the difference in conductivity distributions corresponding to the real and background medium. Hence, we formulate the problem of determining the optimal impressed magnetic currents as determining the magnetic moments of the dipoles which maximize the difference between the measured field due to the real medium and the field calculated from the a-priori model:

$$\mathcal{I} = ||H - H_0||^2_{L_2(\Omega_1)} \to \max_{J_m} . \quad (2)$$

The problem (2) is homogeneous, and the applied currents J_m should be constrained. With the chosen system of constraints the problem (2) can be reformulated as a generalized eigenvalue problem. We constrain the norm of background response due to the applied currents in ([5]) for optimization of transient currents. Here we consider l^2 constrain for the vector of the intensity of the currents which leads to an eigenvalue problem.

Optimal system of magnetic dipoles

The optimal magnetic moments of the array of dipoles which maximize the perturbation of the measured field due to the perturbation of the conductivity distribution are obtained as a solution of the optimization problem (2). Assume that the n dipoles are indexed by i and that $J = [j_1, j_2, ..., j_n]^T$ is a vector of magnetic moments. The generated field is measured using m dipoles. Let H and H_0 be the

vectors of measured fields for the media σ and σ_0. From linearity of the equations (1), it follows that an arbitrary current J and measured fields H, H_0 are related through linear operators L_σ and L_{σ_0}:

$$H = L_\sigma J, \quad \text{and} \quad H_0 = L_{\sigma_0} J . \quad (3)$$

We consider the case when the number of transmitter dipoles is equal to the number of receiver dipoles and introduce a set of basis vectors $\{J^{(k)}\}, k = 1, ..., n$, by $J^{(k)} = [j_1^{(k)}, j_2^{(k)}, ..., j_n^{(k)}]^T$, where

$$j_i^{(k)} = \begin{cases} 1, & \text{if } i = k \\ 0, & \text{otherwise} \end{cases} . \quad (4)$$

Thus the basis vector $J^{(k)}$ defines a unit magnetic current at transmitter dipole k.

With these basis vectors and the corresponding measured vectors of the magnetic fields, $H^{(k)}$, $H_0^{(k)}$, the matrices Z and Z_0 of the operators L_σ and L_{σ_0} immediately can be written as the matrices of columns:

$$Z_\sigma = \{H^{(1)}, H^{(2)}, ..., H^{(n)}\}, \quad H^{(k)} = L_\sigma J^{(k)}, \quad (5)$$

$$Z_{\sigma_0} = \{H_0^{(1)}, H_0^{(2)}, ..., H_0^{(n)}\}, \quad H_0^{(k)} = L_{\sigma_0} J^{(k)}, \quad (6)$$

where $k = 1, ..., n$. Since the basis vectors $\{J^{(k)}\}, k = 1, ..., n$, span the space of all dipole magnetic current distributions generated by this dipole system, we can consider any current J distributed among the transmitters in the array as a weighted sum

$$J = \sum_{k=1}^{n} j_k J^{(k)} \quad \text{where} \quad \sum_{k=1}^{n} j_k^2 = 1 . \quad (7)$$

The weights j_k are normalized to 1 to provide a basis for comparing different dipole arrays, since for any arbitrary array more transmitter power will of course lead to a greater field response.

For a magnetic current J the field vector given by the background σ_0 is $H_0 = Z_{\sigma_0} J$, while the vector of the field measured over σ is $H = Z_\sigma J$. Then $(Z_\sigma - Z_{\sigma_0})J$ represents the vector of the anomalous field. Suppose we wish to find a source J which maximizes the response of a perturbation $\sigma - \sigma_0$ about an a-priori conductivity model σ_0. The problem (2) can be written as

$$\lambda = \max_{J \in R^n : ||J||=1} ||(Z_\sigma - Z_{\sigma_0}) J|| . \quad (8)$$

This problem can be reduced to an eigenvalue problem for the matrix $Z_\sigma - Z_{\sigma_0}$,

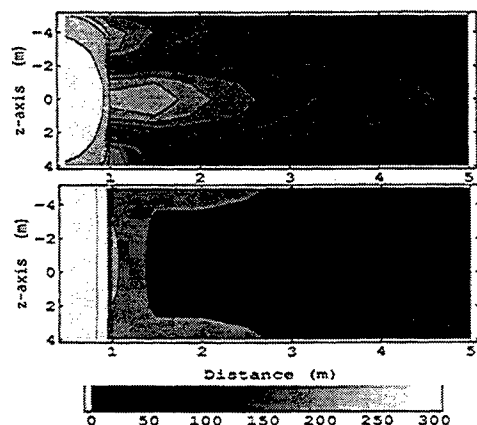$$\lambda = \max_{J \in R^n} \frac{||(Z_\sigma - Z_{\sigma_0}) J||}{||J||} . \quad (9)$$

Figure 2: Cross-plots of the amplitude of H_z for the optimal weighting (top) and uniform weighting (bottom). The frequency of excitation is 1 kHz. The contours are in units of .1 milliAmps/m.
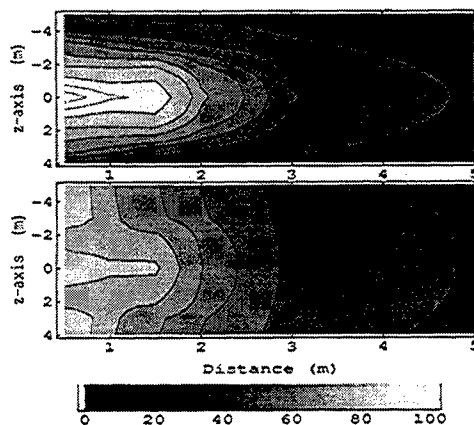

Figure 3: Cross-plots of the amplitude of E_y for the optimal weighting (top) and uniform weighting (bottom). The frequency of excitation is 1 kHz. The contours are in units of .01 mV/m.

Solution of the problem is given by a set of eigenvectors $\mathcal{J}_k$ with the eigenvalues λ_k such that

$$\tilde{\lambda} \, \mathcal{J}_k \; = \; (Z_\sigma - Z_{\sigma_0}) \, \mathcal{J}_k \; , \qquad (10)$$

where $|\tilde{\lambda}| = \lambda$. This problem can be solved numerically [6].

The equation (10) shows that the moments of the optimal dipole array $\{\mathcal{J}_k\}$, being a solution of the eigenvalue problem (8), are proportional to the values of the measured field difference. The magnetic current $\mathcal{J}_1$, which corresponds to the maximal eigenvalue λ_1, gives the most information about the difference $\sigma - \sigma_0$. The remaining eigenvalues form a monotonically decreasing sequence: $\lambda_1 \geq \lambda_2 \geq \lambda_3 \geq \; ....$ Using the magnetic currents corresponding to these subsequent eigenvalues will reveal more information about the model if the data is noise free, although the amount of information gained will diminish with each successive eigenvalue. If the data have noise, then only the eigencurrents corrsponding to the eigenvalues λ_i that are greater than the noise level contain information about the conductivity difference $\sigma - \sigma_0$. In this case, using eigencurrents for $i > N$ will not lead to useful information concerning difference $\sigma - \sigma_0$.

Numerical simulation

We demonstrate the efficacy of our technique for improving the resolution and increasing the depth of penetration for a model which is well known to have poorly resolved parameters. An array consisting of 15 vertical magnetic dipoles was placed in the borehole with a 1 m interval. The surrounding earth was modeled as a three layered structure with the resistivities 10 ohm.m, 100 ohm.m, and 10 ohm.m. The resistive 100 ohm.m bed was assumed to have a conductive 1 ohm.m invasion zone. In this situation, the currents usually concentrate in the invasion zone, and the induced current is minimal in the region of the resistive bed. That is why this resistive bed is difficult to detect with conventional sources.

We assumed that we know the geometry of the invasion zone, but not the conductivity structure beyond the invasion zone. Hence we assumed as a background a 10 ohm.m earth with a known invasion zone. We calculate numerically the responses of the background medium and of the real medium using a forward integral equations algorithm [8]. Then we calculate the distribution of the fields inside the earth outside the borehole and compare these distributions for the fields generated by the optimized source and by an array with uniformly distributed moments.

The optimal inductive source was designed specially for every model using the developed approach. It is the moment pattern that maximizes the response from the target inclusion, solving the problem (8).

Figure 1 presents the cross-section of the model used in numerical simulations, and the optimal distribution of the magnetic moments. Figures 2 and 4 (3 and 5) show the distribution of the amplitude and the phase of the vertical component of the magnetic field (and horizontal component of the electric field) inside the earth, due to the optimal source and due to the uniform array. It is clear from the figures why
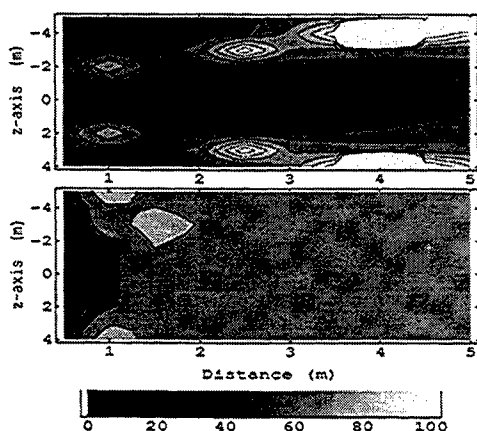
487

Figure 4: Cross-plots of the phase of H_z for the optimal weighting (top) and uniform weighting (bottom). The frequency of excitation is 1 kHz. The contours are in mrad.
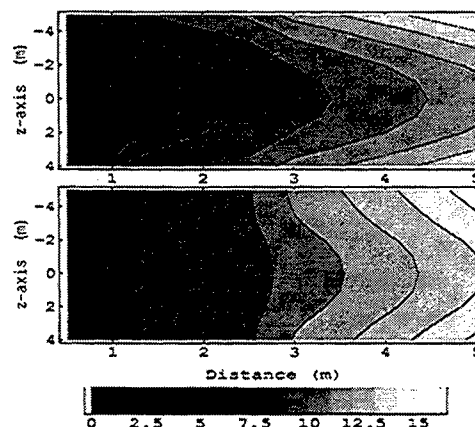
Figure 5: Cross-plots of the phase of E_y for the optimal weighting (top) and uniform weighting (bottom). The frequency of excitation is 1 kHz. The contours are in mrad.

this model is considered to have very poor resolution: currents due to the conventional array do not flow into the resistive layer, being concentrated in the very conductive invasion zone. The optimized source, on the contrary, pushes the fields away from the borehole, penetrating much deeper into the resistive bed.

Conclusions

The optimized source is constructed on the basis of a system of magnetic dipole sources which maximizes the measured response from the unknown inclusion of different conductivity. It is shown that this optimal source concentrates the energy of the scattering current in the region of the inclusion. Numerical simulations with models well known for their low resolution show that the optimized source is able to increase tremendously the depth of the field penetration.

Acknowledgement

References

[1] E. Cherkaeva and A. C. Tripp, Optimal survey design using focused resistivity arrays, IEEE, Trans. Geoscience and Remote Sensing, 34 (1996), 2, pp. 358–366.

[2] E. Cherkaeva and A. C. Tripp, Inverse conductivity problem for inexact measurements, Inverse Problems, 12 (1996), 869–883.

[3] E. Cherkaeva and A. C. Tripp, Source optimization in the inverse geoelectrical problem: in Inverse Problems in Geophysical Applications, eds. H.W. Engl, A. Louis, and W. Rundell, SIAM, 1996.

[4] E. Cherkaeva, Optimal source control and resolution in nondestructive testing, J. Structural Optimization, 1997, 13, 1, 12-16.

[5] E. Cherkaeva and A. C. Tripp, On optimal design of transient electromagnetic waveforms. Expanded Abstracts, 67th Ann. Meeting, Soc. Exploration Geophys., 1997, pp. 438–441.

[6] G.H. Golub and C.F. Van Loan, Matrix Computations, Johns Hopkins University Press, 1983.

[7] R.F. Harrington, Field computation by moment methods: New York, Macmillan, 1968.

[8] Z. Xiong, Electromagnetic modeling of three-dimensional structures by the method of system iterations using integral equations, Geophysics, 1992, 57, 1556-1561.

Formulating Wideband Array-Pattern Optimizations

Dan P. Scholnik and Jeffrey O. Coleman

scholnik@nrl.navy.mil | Naval Research Laboratory, Radar Division
jeffc@alum.mit.edu | Washington, DC 20375-5336

Abstract—Custom design of wideband digital array patterns requires a systematic approach to mapping design specifications to a program understandable by optimization engines. We show that, like in the narrowband case, wideband array patterns are closely related to multidimensional FIR filter responses, suggesting the adaptation of powerful and efficient filter design techniques to the array problem. Previously reported FIR filter design techniques are then applied to an example array-pattern design.

I. INTRODUCTION

With the continued evolution of computing power, wideband digital antenna arrays have traversed the chasm between yesterday's impracticality and today's reality. Increasingly, the traditional analog delay elements are being replaced with digital filters operating on data sampled at each element. The accompanying increase in computation complexity is offset by the precision and flexibility inherent in DSP. Fully realizing the power of a digital implementation, however, requires calculating optimal filter coefficients custom tailored to the system at hand. The powerful and efficient optimization engines [1, 2] that are required exist and often have convenient interfaces to the popular MATLAB software. What remains is to transform design specifications into a form usable by the engines.

The goal of this paper is not to argue for particular constraint choices or design strategies, as in [3], but rather to illustrate approaches to efficiently mapping common constraints to a form suitable for passing to a convex programming engine. This framework extends previous results derived for the design of single [4, 5] and multidimensional [6] FIR filters and narrow- [7] and wideband [8] arrays. In the sequel we derive the wideband array pattern and show how pattern design relates to the design of FIR filters. We then use a sample design to demonstrate the construction of an optimization program from design specifications.

II. ARRAY PATTERN DEFINITION

Consider, as a function of position x and time t, the complex field $U(x, t) = e^{j2\pi(-v \cdot x + ft)}$ of a monochromatic plane wave with spatial frequency (propagation direction) vector v and temporal frequency f. The Helmholtz equation relates spatial and temporal frequencies by $|f| = c\|v\|$, where c is the speed of propagation,

but it will be convenient to defer enforcement of this constraint until later. The output of an antenna element at position x is then the time function $y(t) = G(v, f)U(x, t)$, where $G(v, f)$ is the complex gain of the element as a function of spatial and temporal frequency. The summed output of an array of multiple elements located at positions $x \in \mathcal{X}$ is then

$$s(t) = \sum_{x \in \mathcal{X}} G_x(v, f)U(x, t)$$

We now define the array pattern as a function of v and f to be the ratio of the array output to the output $U(0, t)$ of an isotropic element located at the origin:

$$H(v, f) = \sum_{x \in \mathcal{X}} G_x(v, f)e^{-j2\pi v \cdot x}. \qquad (1)$$

This can be viewed as the Fourier transform on the four dimensional spatio-temporal variables (x, t) to transform variables (v, f) of

$$h(x, t) = \sum_{x \in \mathcal{X}} g_x(x - x, t), \qquad (2)$$

which is often a convenient way to visualize the relationship between array geometry and the array pattern.

Equation 1 is defined for all values of (v, f), which corresponds to the response to plane waves propagating at all speeds $c \in [0, \infty)$. Usually we are interested only in the array response to incident plane waves traveling at the speed of propagation c in free space, obtained by restricting the domain to the cone defined by $|f| = c\|v\|$. The more general characterization is convenient due to the Fourier transform relationship between the array pattern and the spatial and temporal definition of the array.

Although spatial frequency vector v is convenient mathematically for specifying points on the array pattern, in practice array specifications are given from the array's perspective in terms of normalized look vector $l/\|l\| = -v/\|v\|$ or in terms of angular offsets from a reference direction. Restricting our attention to two spatial dimensions provides the simplest meaningful visualization of the cone $|f| = c\|v\|$ (shown in Fig. 1(a)) that defines the domain of physical plane wave parameters. At any given frequency f, look vector l lies on a circle of radius $|f|/c = 1/\lambda$, corresponding to a 360° field of view from the array. Defining angle θ by $\sin(\theta) = l_x/\|l\|$, we see that on a semicircle (Fig. 1(b)) either θ or l_x uniquely defines l. (In three dimensions the circle becomes a spherical surface with two angles uniquely identifying l on a hemisphere.)
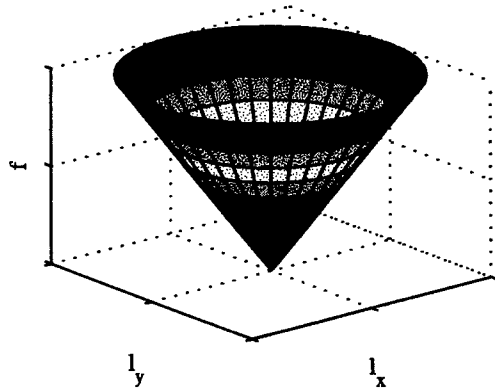
(a) The cone of physical look directions.
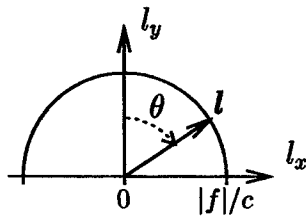
(b) A two-dimensional slice at one frequency.

Fig. 1. Restricting the array-pattern domain.

III. AN EXAMPLE DESIGN

In this section we present an example design similar to that in [3] to illustrate some of the possible types of specifications for wideband array patterns. We will restrict out attention to a linear array of isotropic antenna elements uniformly located along the x-axis of a two-dimensional space, reducing the total dimension of (x, t) to three and simplifying visualization.

The frequency response at each element is assumed to be that of an FIR filter, the set of which are to be designed. Without substantial loss of generality, let the set of element locations be $\mathcal{X} = \{kd\mathbf{e}_1 : k = -K, \ldots, K\}$ and the set of filter delays be $\mathcal{T} = \{nT : n = -N, \ldots, N\}$, with unit vector $\mathbf{e}_1 = (1, 0)^T$. The array pattern is then

$$H(v, f) = \sum_k \sum_n c_{k,n} e^{-j2\pi(kv_x d + nfT)}, \quad (3)$$

where $v = (v_x, v_y)^T$. This is the response of a two-dimensional FIR filter in three dimensions and is not a function of v_y since the array has no extent in the y dimension. The array pattern is periodic in the other two directions, with period $1/T$ in frequency f and period $1/d$ in spatial frequency v_x. Usually we want the total range of v_x to be no greater than $1/d$, so that the pattern can be uniquely specified for all look directions, thus avoiding undesired grating lobes. Since a $180°$ field of view at positive frequency f corresponds to $v_x \in [-f/c, f/c]$, this requires the familiar $d \leq c/2f = \lambda/2$ for the highest frequency of interest. Likewise, $1/T$ should be chosen larger than the desired instantaneous bandwidth of the ar-

ray. Of particular importance is that (3) is linear in the coefficients $\{c_{k,n}\}$ (and would be even with arbitrary element locations), permitting many common constraints to be expressed as upper bounds of convex functions of the coefficients. This in turn allows design of the array pattern using convex optimization tools [4, 9, 10]

Since the element locations and filter delays are symmetrically located, if the FIR filter coefficients obey the symmetry $c_{-k,-n} = c_{k,n}^*$, then the array pattern (3) is real-valued (a linear-phase response). This not only reduces by one half the number of variables to optimize but can be exploited to reduce real-time computation requirements as well. Unless a specific (nonlinear) phase response is desired, these significant benefits come with no ill effects.

The example system parameters are as follows. The RF center frequency is 1.25 GHz, the system bandwidth is $B = 400$ MHz, and the data rate is $1/T = 500$ MHz. The array is composed of 15 identical isotropic elements, each feeding an 11-tap, complex-coefficient, nonlinear-phase FIR filter with the filters obeying the symmetry discussed above. The spacing D between the elements is one half wavelength at the highest in-band frequency of 1.45 GHz in order to suppress grating lobes at all in-band frequencies. The pattern is designed to point to $45°$.

The specifications for the optimization follow, representing the pattern as an explicit function of angle θ:

min. α

s.t. $\displaystyle \int_{f \in \mathcal{F}_{\text{pb}}} \int_{\theta \in \Theta_{\text{sl}}} |H(\theta, f)|^2 \, d\theta \, df \leq \alpha \quad (4)$

$|H(\theta, f)| \leq 10^{-25/20}, \ \theta \in \Theta_{\text{sl}}, \ f \in \mathcal{F}_{\text{pb}} \quad (5)$

$\displaystyle \frac{1}{B} \int_{f \in \mathcal{F}_{\text{pb}}} |H(\theta_m, f) - \beta_m|^2 \, df \leq 10^{-50/10},$
$\qquad\qquad\qquad\qquad\qquad\qquad m = 1, \ldots, M \quad (6)$

$\displaystyle \frac{1}{M} \sum_m \beta_m = 1 \quad (7)$

$\displaystyle \sum_k \sum_n |c_{k,n}|^2 \leq \epsilon \quad (8)$

The optimization was performed in a few minutes using a convex programming engine [1] under MATLAB. The resulting response of the array pattern versus angle and frequency is shown in Fig. 2. The following sections explore the purpose and construction of the above specifications.

A. Sidelobe constraints

The sidelobe region is shown as the shaded region in Fig. 3(a). It consists of a full $180°$ field of view over the entire band minus a constant width in angle. Constraints (4) and (5) limit the L_2 and L_∞ norms over this region. The L_∞ constraint, ensuring all sidelobes lie below -25 dB, (5) is straightforward to construct. We grid along both frequency and angle, and at each grid point in the sidelobe region two linear constraints are used to bound the
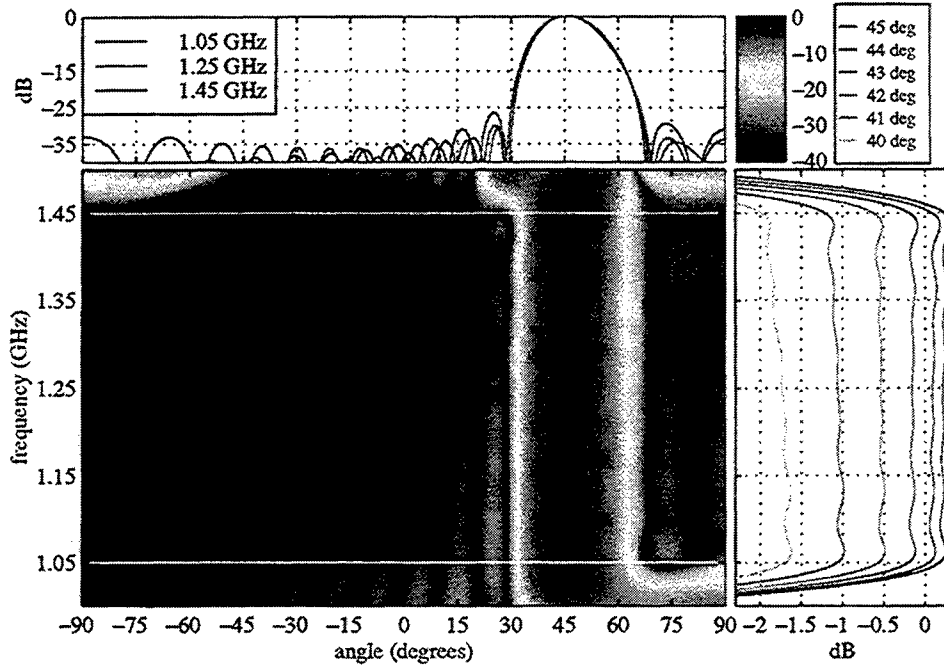
Fig. 2. Optimized wideband array pattern. The upper-left plot shows cuts across angle, and the lower-right plot show cuts across frequency.

magnitude of the (real) response. The grid spacing is chosen small enough that the array pattern cannot exceed the bound significantly between the grid points. For this example, experimentation yielded a grid spacing of $1/32T$ in f and approximately $1/128D$ in v_x.

Constraint (4) and the linear objective α together minimize the energy (squared L_2 norm) in the sidelobes, subject to the other constraints. The left side of (4) represents a quadratic form in the FIR coefficients, but it requires computation of the integral to find the quadratic kernel needed by the optimizer. This could be approximated by a double Riemann sum on a grid, with the resulting tradeoff between grid density (computation) and accuracy. Here we choose a intermediate approach. We use the test-input approach of [5] to formulate the inner integral exactly, while approximating the outer integral with a summation.

At any fixed frequency f, (3) represents the response in the variable v_x of a one-dimensional FIR filter with coefficients that are linear combinations of the array coefficients $\{c_{k,n}\}$. If we consider a zero-mean, wide-sense stationary spatial random process input with temporal frequency f and spectral density $S_{in}(v_x, f)$, the output power is

$$P_{out}(f) = \int |H(v_x, f)|^2 S_{in}(v_x, f) \, dv_x. \qquad (9)$$

The resulting quadratic kernel can be computed exactly and efficiently when the input density is specified in terms of weighted and shifted basis functions as detailed in [5]. To obtain the inner integral of (4), choose

$$S_{in}(v_x, f) = \begin{cases} \frac{c}{f \cos(\theta)}, & -\theta \in \Theta_{sl} \\ 0, & \text{otherwise.} \end{cases}$$

which effects the change of variable $v_x = -\sin(\theta)f/c \to \theta$. The double integral is now approximated by the sum

$$P_{out} = \sum_i \int |H(v_x, f_i)|^2 S_{in}(v_x, f_i) \, dv_x \, \Delta f$$

$$= \sum_i \int_{\theta \in \Theta_{sl}} |H(\theta, f_i)|^2 \, d\theta \, \Delta f$$

over the grid of frequencies $\{f_i\}$ with spacing Δf.
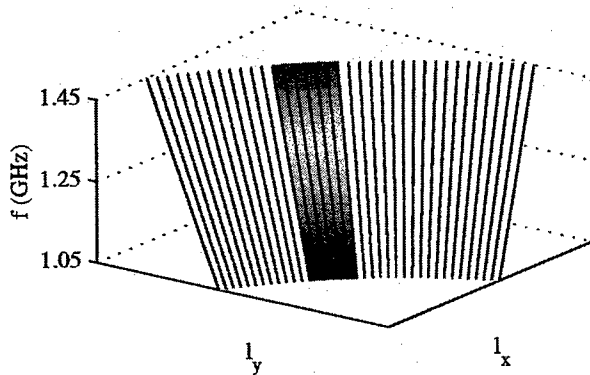
B. Mainbeam Constraints

Figure 3(b) is a blowup of the mainbeam cutout region of Fig. 3(a). The central shaded region represents angles at which we wish to control the frequency response of the array. We want the frequency response at each angle on the shaded portion of the grid (indicated by the vertical lines) to be flat while still allowing the beam to rolloff with angle. To accomplish this we allocate auxiliary variables $\{\beta_m\}$, one for each angle, to act as floating nominal-gain levels. For each angle then we approximate the left-hand side of (6) with the Riemann sum

$$\sum_i |H(\theta_m, f_i) - \beta_m|^2 \Delta f$$

over the grid of frequencies $\{f_i\}$ with spacing Δf. The resulting constraints ensure that the frequency response at each angle θ_m closely approximates β_m. The average mainlobe gain is then found by averaging the $\{\beta_m\}$, leading to a single linear equality constraint (7).

491
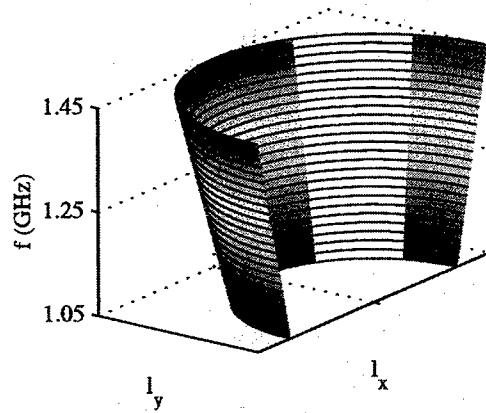
(a) The sidelobe constraint region. The horizontal lines on the shaded region represent the power distributions of narrowband spatial inputs on a grid of frequencies.

(b) A blowup of the mainbeam cutout. The mean square frequency response error along each vertical line in the shaded region and the average of the nominal gains for each are constrained.

Fig. 3. Sidelobe and mainbeam constraint regions.

C. Nonvisible Sidelobe Constraint

Constraints (4) and (5) both limit the array pattern over the sidelobe region corresponding to a 180° angular extent (the visible region) for in-band frequencies. By design, this region lies within one period of the array-pattern response. Shown in Fig. 4 is the projection of the visible region onto a $1/D$-by-$1/T$ rectangle in the (l_x, f) plane. The white region, comprised of the out-of-band and nonvisible regions, is not directly constrained, possibly resulting in extreme behavior of the array pattern. While this will not affect the response to an in-band plane wave, it will affect receiver noise. A simple solution is to limit the total power resulting from white inputs to the FIR filter of each element. A modest limit will prevent extreme responses but have minimal effect on the visible region. Constraint (8) then results from applying Parseval's relation to obtain a simpler expression for this special case.

IV. CONCLUSIONS

We have shown that under appropriate conditions the response of a wideband array can be seen as a four-
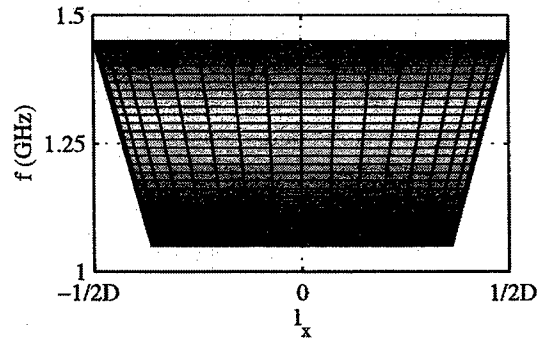

Fig. 4. Projecting the cone onto the (l_x, f) plane shows the nonvisible response region (in white).

dimensional Fourier transform, complicated by the restriction of the four-dimensional spatio-temporal frequency to a four-dimensional cone, effectively removing one dimension. The remaining three dimensions are equivalent in combination to temporal frequency and the two usual spatial pointing angles. This result suggests adapting filter design strategies to array design, particularly efficient ways to calculate the quadratic kernel on an L_2 constraint. In the example we adapted the test-input approach for L_2 constraints [5] to reduce a two-dimensional Riemann sum to a one-dimensional sum of exact integrals. This can be extended to multidimensional test inputs (as in [8]) to avoid gridding at all, with the caveat that the required autocorrelation functions can become difficult to compute exactly.

REFERENCES

[1] J. F. Sturm, "Sedumi," MATLAB toolbox, May 1998, http://www.unimaas.nl/~sturm/software/sedumi.html.

[2] R. Vanderbei, "LOQO: An interior point code for quadradic programming," Technical Report SOR 94-15, Princeton University, 1994, revised 11/30/98, to appear in Optimization Methods and Software.

[3] D. P. Scholnik and J. O. Coleman, "Optimal design of wideband array patterns," in Proc. 2000 IEEE Int'l Radar Conference, Washington, DC, May 2000, Accepted for publication.

[4] J. O. Coleman and D. P. Scholnik, "Design of nonlinear-phase FIR filters with second-order cone programming," in Proc. Midwest Symp. on Circuits and Systems (MWSCAS), Las Cruces, NM, Aug. 1999.

[5] J. O. Coleman, "Systematic mapping of quadratic constraints on embedded FIR filters to linear matrix inequalities," in Proc. 1998 Conference on Information Sciences and Systems (CISS '98), Princeton, NJ, Mar. 1998.

[6] W.-S. Lu and A. Antoniou, "Design of nonrecursive 2-D digital filters using semidefinite programming," in Proc. 1999 Int'l Symp. Circuits and Systems (ISCAS '99), Orlando, FL, May 1999.

[7] H. Lebret and S. Boyd, "Antenna array pattern synthesis via convex optimization," IEEE Trans. on Signal Processing, vol. 45, no. 3, pp. 526–32, Mar. 1997.

[8] J. O. Coleman and R. J. Vanderbei, "Random-process formulation of computationally efficient performance measures for wideband arrays in the far field," in Proc. Midwest Symp. on Circuits and Systems (MWSCAS), Las Cruces, NM, Aug. 1999.

[9] L. Vandenberghe and S. Boyd, "Semidefinite programming," SIAM Review, vol. 38, no. 1, pp. 49–95, Mar. 1996.

[10] M. S. Lobo, L. Vandenberghe, S. Boyd, and H. Lebret, "Applications of second-order cone programming," Linear Algebra and its Applications, vol. 284, pp. 193–228, Nov. 1998.

A Density Taper Technique for Low Side Lobe Applications of Hex Array Antennas

Steven S. Kuo,* Gregory P. Junker, T. K. Wu, and C. Harry Chen
TRW Antenna Products Center
One Space Park
Redondo Beach, CA 90278

Abstract: A density taper design procedure, which allocates the element positions in a hex array to reduce near-in side lobe levels, is investigated. This procedure adjusts the element positions to simulate a Taylor amplitude distribution function. This technique can be used in single power amplifier design (for every element) of transmit phased array with reduced co-channel interference. Since no attenuation of amplifier output power is required, this technique has higher power efficiency than the amplitude taper technique. The performance of this density taper technique is compared to that of a Taylor amplitude taper technique.

Introduction: Transmit phased array (TPA) technology is critical for future military and commercial satellite communication systems. These systems will be used to transmit broadband multimedia communication traffic. Such traffic demand is not uniformly distributed across the field of view. TPA technology is key to efficiently placing antenna coverage according to traffic demands. Steerable antenna beams combined with a variable dwell time pointing strategy is the optimum solution to varying non-uniform traffic demands. Placing multiple antenna beams on areas of peak demand will maximize traffic transfer around the entire communication network. Low side lobe level (SLL) is a highly desired TPA characteristic to reduce co-channel interference (CCI). CCI is the main source of system interference in a multiple-beam frequency-reuse space-based communications system (other interference sources are adjacent channel interference, adjacent system interference and cross polarization interference). CCI (and thus SLL) needs to be controlled to minimize Bit Error Rate (BER) and hence maximize the channel data rate and system capacity.

A typical planar hex array with uniform excitation amplitude and phase will produce approximate -17 dB near-in SLL as shown in Fig. 1(a). Also shown in Fig. 1(a) are the six grating lobes, which are a direct consequence of the periodicity and occur independently of any chosen amplitude distribution across the array. Side lobes can be lowered by employing tapered array illuminations, but this is accompanied with some disadvantages [1]. (1) In single power amplifier implementation of amplitude taper, the power efficiency is poor (~ 10%) thereby consuming more spacecraft power and burdening thermal management systems. Or, (2) in multiple power amplifiers implementation of amplitude taper, the cost is high because it requires design of multiple power amplifiers. Alternatively, the density-tapered array, in which the spacing between elements varies across the array following some prescribed criteria, can achieve lower side lobes while maintaining an uniform excitation amplitude for each element. Thus, the two disadvantages are removed in the density-tapered array. In this study, we explored the design procedure for density taper technique based on Taylor amplitude distribution functions for circular apertures [2,3].

Analytical Approach of Density Taper Technique: Array synthesis problems are approached by sampling the discrete array elements in such a fashion that the array aperture follows a prescribed illumination function. In the amplitude taper approach, the element spacing is uniform and the element excitation is weighted according to the illumination function as illustrated in Fig. 2(a). In the density taper approach, the element excitation is kept uniform and the element spacing is weighted according to the illumination function as illustrated in Fig. 2(b); thus the average power density will follow the

illumination function. In this study, Taylor amplitude distribution functions for circular apertures [2,3] were chosen as the illumination function. Our study cases are hex arrays of 271 elements arranged in 10 rings (with ring 1 containing 1 element), with half-power beamwidths (HPBW) of 1.53° at boresight. For the purpose of comparison, the contour plots and the pattern cuts at boresight and 9° scan for a hex array with Taylor amplitude taper are shown in Figs. 1(b) and 3(b) respectively.
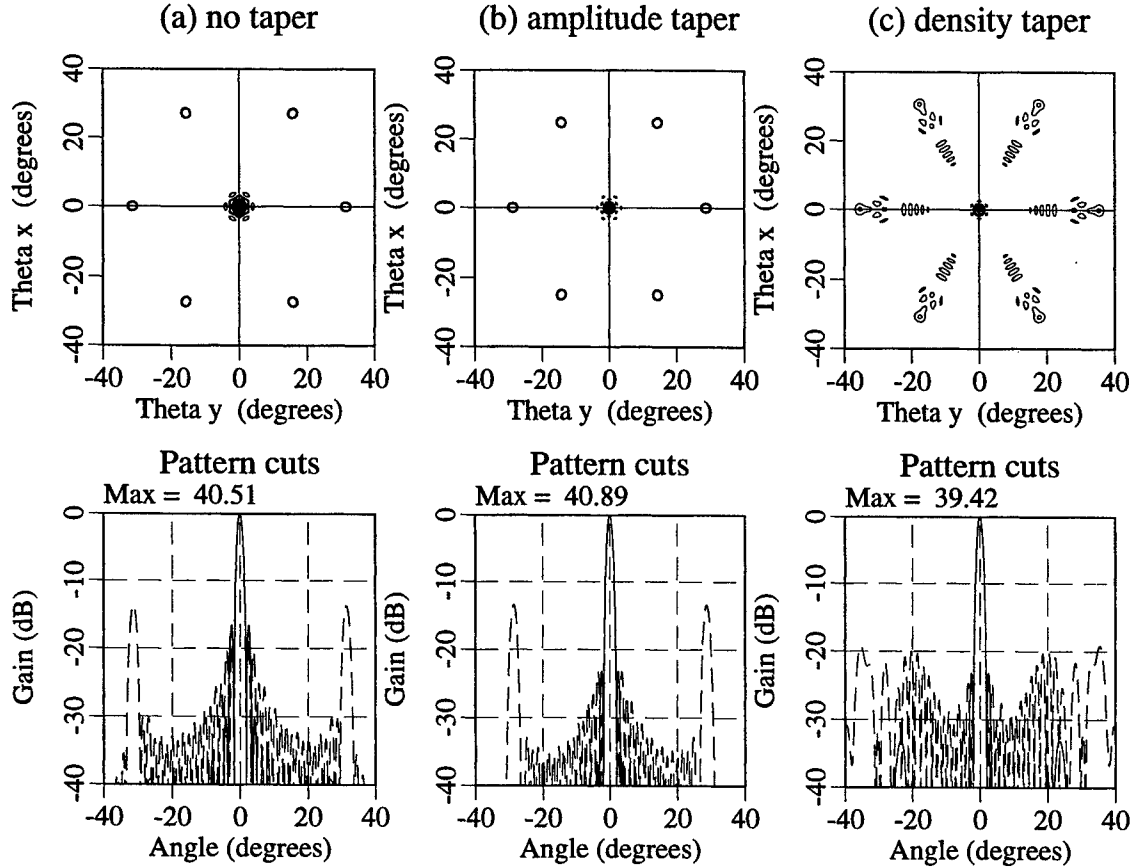

Fig. 1. Comparison of boresight antenna patterns for hex arrays with different taper techniques. In each case, the HPBW = 1.53°. The solid and dashed lines in the pattern cuts are the E- and H-plane cuts respectively.

In the density taper scheme, since each element has the same amount of input power, the basic criterion is to allocate this element with an area such that the average power density delivered by it closely resemble a Taylor amplitude distribution function. This can be regarded as a discrete simulation of a continuous illumination function. Our design procedure is:

1. choose the maximum allowed radius, r_{max}, for the array, and initial element spacing, d;
2. for ring 1, set $r_1 = 0$, number of element = 1;
3. determine the radius of each ring by

$$r_{n+1} = r_n + \frac{d}{f(r_n)}$$

where r_n is the radius of the n-th ring, and $f(r_n)$ is Taylor amplitude distribution at r_n;

4. the number of elements in the n-th ring is equal to $6 \times (n - 1)$;
5. determine the coordinate of element i in either hex or circular arrangement;
6. perform computation to determine antenna properties.
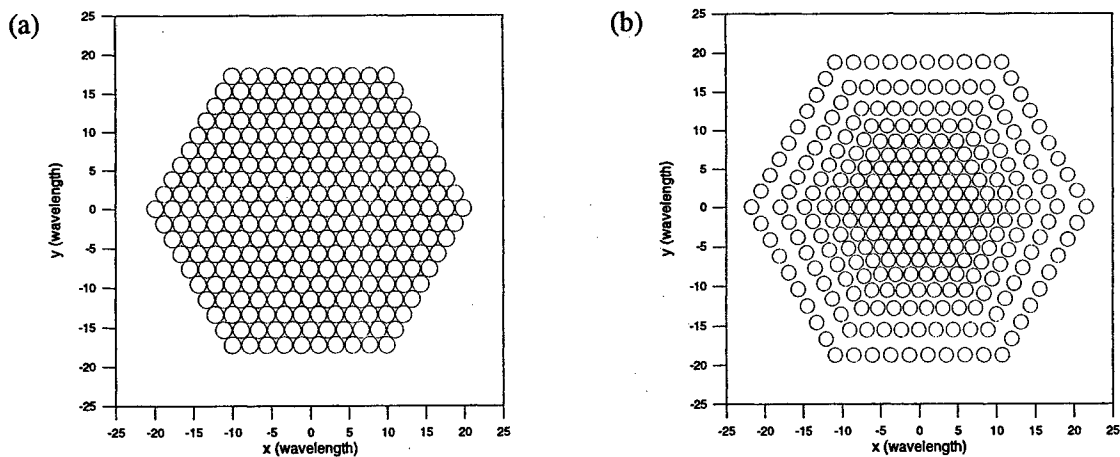
Fig. 2. (a) Illustration of a hex array layout of uniform excitation amplitude TPA and amplitude-tapered TPA. (b) Illustration of a density-tapered hex array. The element spacing gradually increases from inside out.

This procedure is similar to the graphical method suggested by Lo *et al.* [4-6], and the results from these two procedures are comparable.
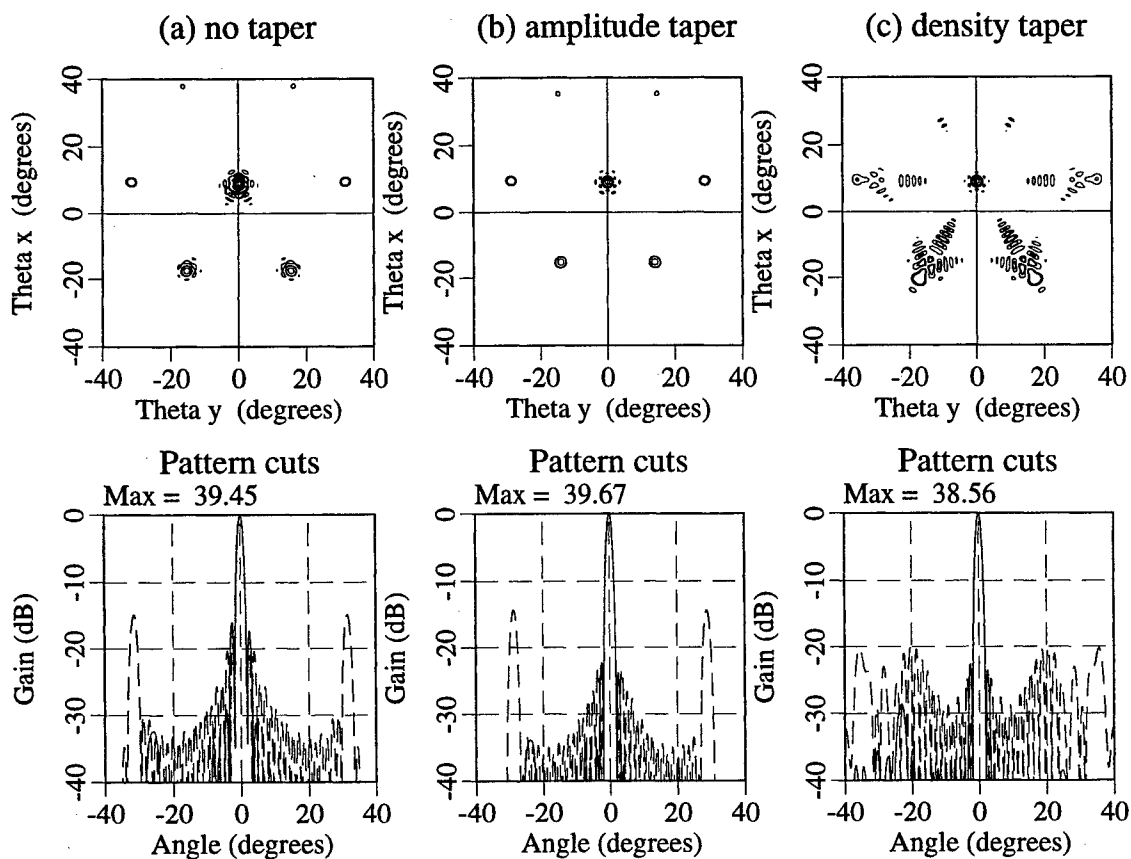

Fig. 3. Comparison of antenna patterns at 9° scan for hex arrays with different taper techniques.

Results and Discussion: The contour plots and the pattern cuts at boresight and 9° scan for a hex array with density taper using the aforementioned procedure are shown in Figs. 1(c) and 3(c) respectively, and the antenna properties are summarized in Table 1. It is shown in Table 1 that the density taper technique offers similar antenna performance as the amplitude taper technique. The decrease of directivity in the density taper case is due to the constraint of HPBW = 1.53°, which restricts the aperture size. However, the 9° scan loss for density taper case is –0.86 dB, that is more favorable compared with -1.22 dB loss in amplitude taper case. The near-in SLL is the peak SLL within 10° for the boresight, and within 19° for the 9° scan.

Table 1. Performance comparison of hex array antennas excited by different taper techniques.

	Boresight			9° Scan		
	Uniform Amplitude	Amplitude Taper	Density Taper	Uniform Amplitude	Amplitude Taper	Density Taper
Aperture Size (λ^2)	1145.21	1350.58	1329.75	1145.21	1350.58	1329.75
HPBW (°)	1.53	1.53	1.53	1.55	1.55	1.55
Directivity(dBi)	40.51	40.89	39.42	39.45	39.67	38.56
near-in SLL (dB down)	-16.73	-23.13	-23.28	-16.28	-22.57	-19.41

Conclusion: A design procedure for a density-tapered hex array proposed in this work is able to reduce the SLL to the level as in the amplitude taper case. This procedure offers comparable results as the graphical method suggested by Lo et al. [4-6]. This technique can be used in single power amplifier design (for every element) of transmit phased array with reduced co-channel interference. Since no attenuation of amplifier output power is required, the density taper technique has higher power efficiency than the amplitude taper technique.

References:
[1] Y. T. Lo, "A nonuniform linear array system for the radio telescope at the University of Illinois", 1960 Spring URSI and IRE Joint Meeting, Washington, D.C.
[2] T. T. Taylor, "Design of Circular Aperatures for Narrow Beamwidth and Low Sidelobes", *IRE Trans. Antennas Propag.*, vol. AP-8, pp. 17-22, January 1960.
[3] R. C. Hansen, "Tables of Taylor Distributions for Circular Aperture Antennas", *IRE Trans. Antennas Propag.*, vol. AP-8, pp. 23-26, January 1960.
[4] Y. T. Lo and S. W. Lee, *Antenna Handbook Volume II Antenna Theory*, New York: Van Nostrand Reinhold, 1993, and references therin.
[5] A. L. Maffett, "Array factors with nonuniform spacing parameter", *IRE Trans. Antennas Propag.*, vol. AP-10, pp. 131-136, March 1962.
[6] M. G. Andreason, "Linear arrays with variable interelement spacings", *IRE Trans. Antennas Propag.*, vol. AP-10, pp. 137-143, March 1962.

Arrays of Overlapping Sub-arrays for Improved Sidelobe Level Performance

Sembiam R. Rengarajan
California State University
Northridge, CA 91330-8346

Jaganmohan B. L. Rao
Naval Research Laboratory,
Washington, D.C. 20375

1. Introduction

Array antennas with sub-array architecture are commonly employed in phased array systems. In order to operate over wide instantaneous bandwidth, such arrays are time-delay steered with digital time delays introduced at the input of each sub-array. Phase shifters in each sub-array set the element phases such that each sub-array has the correct phase slope at the center frequency of the instantaneous operating bandwidth (for the central beam, if multiple beams are to be generated). For broadside radiation, the grating lobes of the array factor (of sub-arrays) are multiplied by the broad pattern of each sub-array. If the resulting sidelobe level is not satisfactory for the case of uniform sub-array distribution, it is possible to choose different aperture distributions for each sub-array, e.g. to make the entire array distribution correspond to that of a Taylor or Dolph Chebyshev distribution. There are two scenarios where sidelobe performance may be poor. 1) At the center frequency of a wide instantaneous bandwidth the desired antenna pattern may be synthesized. With the use of time delay steering, the array factor maintains a good pattern at band edges but for a change in beamwidth. The pattern of each sub-array squints due to the use of phase shifters. Therefore the overall pattern shows a loss in peak gain as well as degradation in sidelobes. 2) If multiple beams are to be formed in the receive mode by a digital beam former using complex weights at sub-array level, poor sidelobes result for outer beams if the phase shifts of each sub-array were set for the central beam. These two effects were discussed previously [1].

In this work, we examine the use of overlapped sub-arrays for improving the sidelobe performance. All the computations assume a linear array of 64 elements with a half wavelength spacing at the center frequency. The array is divided into 8 equally spaced sub-arrays with 8 elements for each sub-array. Time delay steering is employed at the sub-array level and elements of each sub-array have phase shifters that are set at the center frequency for the central beam. Fig. 1a and 1b show schematic representations of the array for the non-overlapping and overlapping architectures respectively. Only four elements per sub-array are shown for simplicity.

2. Analysis and discussion

2.1 Performance at edges of a wide instantaneous bandwidth

Mailloux [1] has given the patterns of the 64-element array that is time-delay steered to 45° from broadside. The time-delays are applied at the sub-array levels with element phases set to maintain the correct phase slope at the center frequency. At a frequency 10% away from the center frequency the sidelobe level relative to the main beam peak is found to be at -7.55 dB. Optimization of the sidelobe level as a function of complex weights of sub-array inputs will

produce only a small improvement since the phases have to be fixed to maintain the beam peak at the desired location.

Overlapping sub-array architecture has been employed in limited scan array applications in which scanning is achieved at the sub-arrays level [1]. In order to suppress the grating lobes of the array factor produced by the distribution of sub-arrays, the pattern of elements in each sub-array should be nearly uniform within the limited scan region and should drop to a low level outside. This is basically a pulse-type pattern that requires a sinc distribution. The pulse width has been chosen to have a value equal to one half of the spacing in u (= sin θ) space between adjacent grating lobes of the array factor. Truncating the infinite sinc distribution to a single sub-array is not adequate. Ideally we need to have a complete overlap, i.e., input to each sub-array is distributed to all elements on both sides with an amplitude distribution that samples a sinc function. However, such a system requires a rather complicated feed network. It has been implemented in linear arrays in reflectors and lenses [1]. The pattern of the central sub-array of a completely overlapping array is very close to the ideal pulse shape whereas that of the edge sub-array deviates substantially due to severe effects produced by truncation at one end. Each of the two sub-array patterns is squinted towards the broadside since the frequency is 10% above the center frequency. The patterns of the completely overlapping array produces a sidelobe level well below −25 dB. Extension of this concept to planar arrays would make the feed network extremely complex and expensive.

Instead of complete overlap, we considered overlapping of only adjacent sub-arrays. This requires that input to each sub-array be distributed to its eight elements as well as eight elements in one sub-array on each side. However, each edge sub-array overlaps to only one adjacent sub-array. The patterns of the complete array and the central and edge sub-array are shown in Fig. 2. The side lobe level is −21.2 dB. It is caused by the fact that the sub-array patterns have substantial deviation relative to the desired pulse shape because of the truncation of the sinc distribution. The results improve significantly when each sub-array overlaps to two adjacent sub-arrays, producing a sidelobe level of −24.5 dB. The sub-array pattern is closer to the pulse shape in this case.

2.2 *Sidelobe level of outer beams of multiple beams*

In digital beam forming systems, multiple simultaneous receive beams are formed by choosing appropriate complex weights for each sub-array signal for a given beam channel. An array without overlap between sub-array element distributions was considered first. The sub-arrays have been time-delay steered to point the beam at 42.5° from broadside. Element phases have been set so that each sub-array pattern points at 45° from broadside. The computations were performed at the center frequency for an outer beam at 42.5° (the central one at 45°). We first studied the array without any overlapping. The array pattern showed a sidelobe level of about −15 dB. This is due to the fact that the grating lobes of the array factor have not been sufficiently suppressed by the pattern of a single sub-array. At a frequency 10% above the center frequency the sidelobe level of the array pattern is severely degraded to −3.5 dB.

With the use of an overlapping architecture (each sub-array overlapping two adjacent ones) the sidelobe performance of the previous two cases improve significantly. These results are shown in Figs. 3 and 4 respectively. The sidelobe level in Fig. 3 is better than −26 dB whereas in Fig. 4 it is −12.6 dB. Clearly the latter value is not adequate. At 10% above the center frequency,

our computation showed that the sidelobe level of the overlapping array is below −25 dB for this outer beam (not shown). However, at this frequency an outer beam at 47.5° will have a poorer sidelobe level.

The effect of the pulse width of the synthesized pattern of each sub-array, on sidelobe performance of outer beams at ± 10% from the center frequency was studied. Previously we used a value of A, half the spacing (in u space) between adjacent grating lobes of the array factor (array of sub-arrays). A reduced value of 0.8 A was considered for the sub-array pattern width. In order to produce this pulse pattern we need a new sinc distribution to elements of overlapping sub-arrays. The array pattern and sub-array patterns of the case considered in Fig. 4 with the new pulse width (0.8 A) of the sub-array pattern has reduced the sidelobe level to −22dB.

3. Conclusion

Our studies show that partially overlapping sub-array architecture has the potential to improve the sidelobe performance compared to the non-overlapping system. Further improvements may be possible by optimizing various parameters, including the complex weights of the sub-arrays.

References

[1] R. J. Mailloux, Phased Array Antenna Handbook, Artech House, Inc., Norwood, MA, 1994.
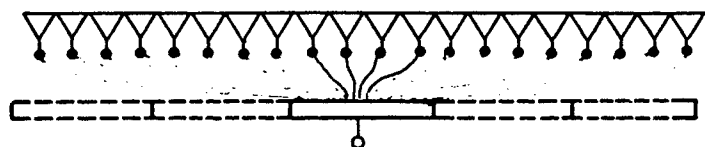
Fig. 1a A schematic view of an array of sub-arrays (no overlap)
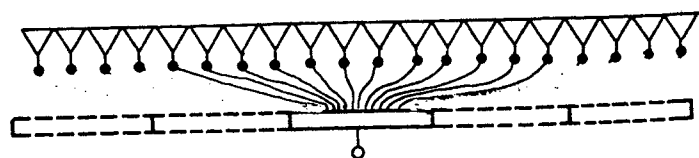
Fig. 1b A schematic view of an array of sub-arrays (one sub-array overlap)

Fig. 4. Array pattern of an outer beam (two sub-array overlap), 10% above center frequency

1 - array pattern, 2 - central sub-array pattern, 3 - edge sub-array pattern

Fig. 2 Array pattern (one sub-array overlap), 10% above center frequency
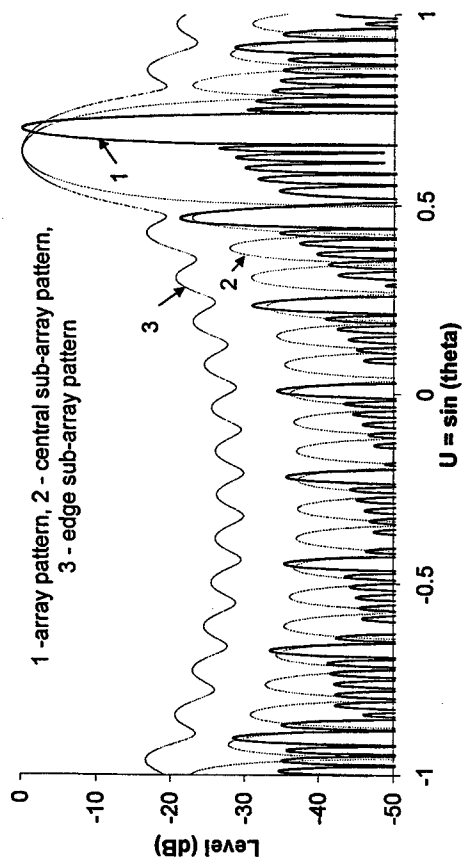
1 - array pattern, 2 - central sub-array pattern, 3 - edge sub-array pattern
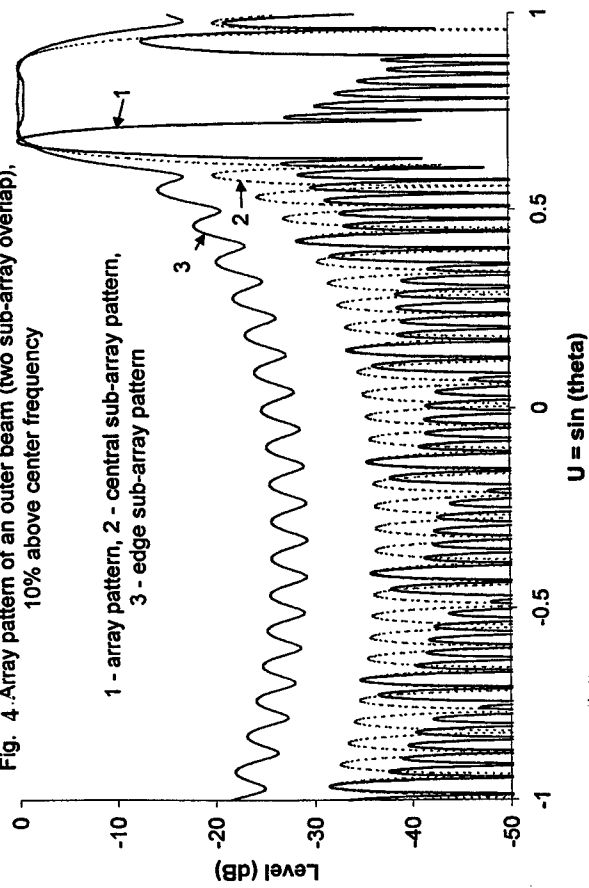
Fig. 3 Array pattern of an outer beam (two sub-array overlap), center frequency

1 - array pattern, 2 - central sub-array pattern, 3 - edge sub-array pattern
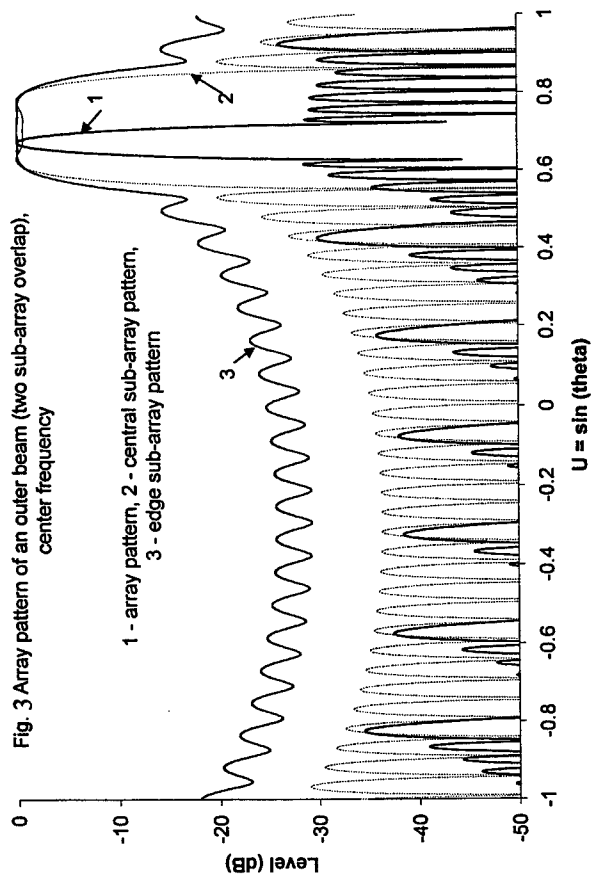
Phased Array Shaped Multi-Beam Optimization for LEO Satellite Communications Using a Genetic Algorithm

Kenneth N. Sherman
President
Satellite Software Incorporated
310 South Carson Street, Carson City, NV 89701
T: (301) 279-2015 F: (301) 424-5350
Email: ksherm@satsoft.com
www.satsoft.com

Abstract

LEO communications satellite antennas may require hundreds of high gain beams to achieve sufficient link margin, especially for mobile systems where the ground terminals have very low EIRP.

Generally, the procedure for optimizing antenna beams for shaped coverage areas starts with a set of polygons defined in antenna angle space. These polygons are filled with synthesis stations at which the desired gain is prescribed. An optimization program is then used to synthesize the excitation of the antenna in order to achieve the desired gain at each station. For multibeam coverages, if the number and size of the coverage polygons are not optimal, pattern performance will be poor. Layout is difficult at LEO because a large variation in cell size is dictated by the substantial path length variation from nadir to edge of coverage.

A genetic algorithm was developed to optimize the number and size of cells for a circularly symmetric grid. Cells were then filled with synthesis stations and a least squares optimizer used to shape the antenna pattern for each cell. A phased array antenna with circular aperture and $\cos^{1.3}\theta$ element power pattern was used. The genetic optimizer was found to quickly produce optimal cell layouts for arbitrary altitude, field of view, and directivity requirements. It was also a very good way to quickly and accurately determine the number of beams needed for a particular set of requirements.

Ground Cell Geometry

Slant range path-loss variation at GEO is only 1.3 dB from nadir to 0° elevation EOC [1] and can usually be ignored, especially if the coverage area is a small portion of the globe. This makes multibeam coverage layouts at GEO straightforward. The number of beams needed to fill a coverage area of solid angle A is simply A/Ω, where Ω is the solid angle of the beam.

Multibeam layouts at LEO are much more difficult because of the considerable slant range variation from nadir to edge of coverage. At an altitude 1200 Km, for example, the slant range varies 10.6 dB from nadir to 0° elevation EOC. Even to 15° elevation, the variation is 7.2 dB.

In order to achieve constant link margin, antenna gain must increase as a function of the angle away from nadir (fig 1) as follows:

Ideal Gain Function from 1200 Km

Fig 1
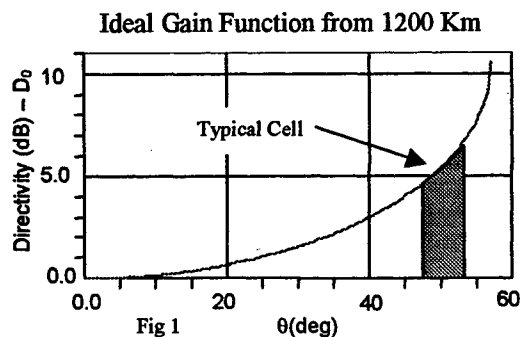
$$D = D_0 \left(\frac{R_s}{h}\right)^2 \qquad \text{(Equation 1)}$$

Where D_0 is the required directivity (ratio) at nadir, and R_s is the slant range from the earth station to the satellite at altitude h. Since required directivity increases radially from nadir outward, a circularly symmetric cell layout would appear to be the best solution, as shown in figure 5. Wedge shaped cells are arranged in rings about nadir. All cells in a particular ring have identical gain requirements except for a rotation about nadir.

Since directivity and cell area are inversely related, cells near nadir are much larger in terms of antenna angle space than at EOC.

The goal of the optimization is to choose the number of rings N, the number of cells in each ring, and the radii of each ring to maximize link margin with the fewest number of cells. It was found that a genetic optimizer worked very well for this problem.

Genetic Optimizer

A genetic algorithm [2] using steady state replacement was used. In the samples computed here, 40% of the population was replaced each generation. Tournament selection, crossover, and mutation was used to generate new individuals. Typical convergence was obtained with fewer than 10^5 evaluations of the fitness function. Note that an exhaustive evaluation of the entire solution space would require 2^{nbits} evaluations, where *nbits* is the length of the chromosome. With nbits = 35 for the smallest test case here, this is 10^{10} evaluations, an intractably large number. This is a testament to the robustness and efficiency of the genetic algorithm.
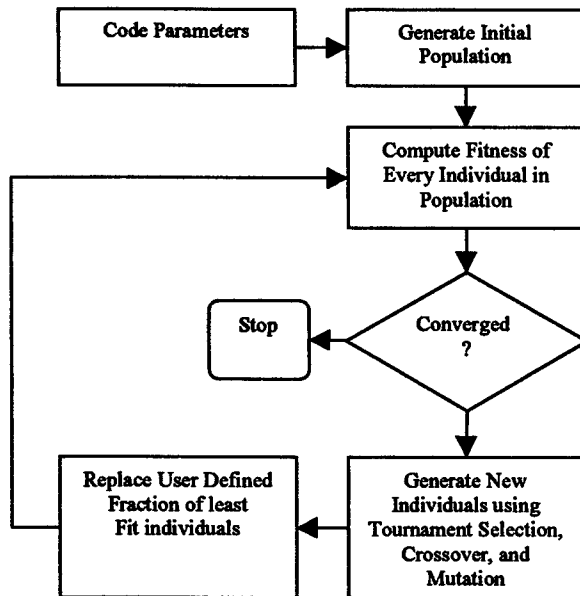
Fitness Function

The fitness function is used to determine which of two randomly selected parents is better fit to produce offspring for the next generation, and to determine which individuals are replaced each generation.

The most elegant way to compute fitness is to compute the constant C_r from the ideal gain function

$$D_r = C_r \left(\frac{R_s}{h}\right)^2$$ by integrating over a typical cell in

each ring r, then compute a least square cost function

as $f = \sum_{r=1}^{N}(C_r - D_0)^2$ However, since the ideal gain function does not appear to be integrable in closed form, this would require N numerical integrations per fitness evaluation.

Hence, a faster approach was used with the cost function written as $f = \sum_{r=1}^{N}(D_r - DD_r)^2$ where N is the number of rings, D_r is the directivity of a flat-top or uniform directivity function over a cell in ring r and DD_r is the desired directivity computed from equation 1 at the outer boundary of ring r. The error introduced by this approximation is greatest for cells in the larger, inner rings, especially for lower gain layouts with fewer rings. Note that lower values of f indicate better fitness.

By substituting the following two relationships, the ideal gain function can be written as a function of θ

$$R_s = \sqrt{-2R_e(R_e + h)\cos(\gamma) + (R_e + h)^2 + R_e^2}$$

$$\gamma = \sin^{-1}\left(\frac{(R_e + h)\ \sin(\theta)}{R_e}\right) - \theta$$

The directivity of a flat top beam in a cell at ring r is

$$D_r = \frac{4\pi}{(\cos(\theta_{r+1}) - \cos(\theta_r))\Delta\phi}$$

where θ_r and θ_{r+1} are the inner and outer radii of the ring, and $\Delta\phi$ is the phi dimension of the cell. This of course is only achievable by an infinitely large antenna. D_r was multiplied by $\cos^{1.3}(\theta)$ to match the element function used to model the phased array antenna. It was determined empirically that D_r was 2.5 dB too high for apertures of diameter 26λ, so a factor of 0.552 was also applied. For best results, it is necessary to determine this calibration factor for the particular range of antenna sizes under consideration.
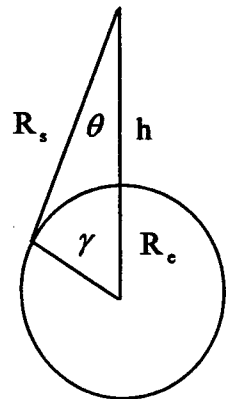
The problem would have been much more difficult to code if the optimizer were written to determine the number of rings, since a variable length chromosome

would have been required. Thus, the number of rings N is found by running the optimizer for several different values, and choosing the best results. In many cases numerically equivalent results can be obtained for different values of N, even though the cell layouts are very different.

Optimized cell layouts were obtained in minutes on a Pentium II 450 class machine. These produced very good sets of antenna patterns with D_0 very close to the value desired, once the objective function was calibrated for antenna size (a process of running several test cases for a particular aperture size).

Parameter Encoding

Chromosomes are generated by stringing together a series of genes, or coded parameters. In this problem, genes are the N-1 delta_radii (delta radii) and N ncells (number of cells per ring) parameters represented in binary coded decimal (BCD). The number of bits needed to code each parameter depends on its range and quantization level, and should be minimized to speed execution. The number of bits required is determined for each parameter as follows (see [1], equation 4)

$$N_{bits} = \log_2\left(\frac{V_{max} - V_{min}}{\Delta V} + 1\right)$$

Where $V_{max} - V_{min}$ is the range of the parameter and ΔV is the value represented by the least significant bit (LSB). Note that the number of bits is allowed to vary for each parameter. 4 to 6 bits per parameter were required for the sample results reported here. However, for problems with larger antennas and more rings (ie, higher D_0), the number of bits needed increases since quantization error must be reduced, especially for outer rings which are much smaller than inner rings.

Since inner rings are larger and need more bits to represent them, the maximum values of delta_radii for each ring r were chosen as

$$(delta\_radii_r)_{max} = \frac{\theta_{max}}{r}, \qquad \text{where}$$

$$\theta_{max} = \sin^{-1}\left(\frac{\cos(el)R_e}{R_e + h}\right) \text{ and } el \text{ is the elevation}$$

angle to the spacecraft that defines the EOC. The maximum number of cells in ring r was limited to

$$(ncells_r)_{max} = \frac{\phi_{sector}\left(r\theta_{max}/N\right)}{0.9\, bw}$$

where ϕ_{sector} is the arc length of the sector and bw is the diffraction limited 3 dB beamwidth of the antenna. For full-circle layouts $\phi_{sector} = 2\pi$.

If a chromosome containing an out-of-range parameter is produced during the optimization, for example, $ncells_r > (ncells_r)_{max}$, the fitness of that individual is set to the worst possible value. This is essential to prevent propagation of solutions containing cells narrower than the antenna beamwidth.

The number of parameters (genes) in each chromosome is 2N-1, where N is the number of rings, since ring 0 is the origin.

Random number generator

A random number generator is used to generate the initial population, select individuals for mating, and perform crossover and mutation. As the length of a chromosome increases, longer sequences of random numbers are needed to obtain a solution.

Initially, the c library function rand() from stdlib.h was used to generate the random numbers. This function repeats after a period of at most 32767, and was found to work poorly, especially for layouts of more than about 5 rings.

In order to find a global optimum in the fewest generations, a high quality random number generator such as the Mersenne Twister (MT) should be used [3]. MT produced convergence in fewer generations and with smaller populations than rand(). In fact, MT enabled excellent results to be obtained for large problems where only poor results were previously obtained with rand().

Test Cases & Conclusions

Three test cases are presented to demonstrate the effectiveness of the optimizer. All three cases are from 1200 Km altitude with EOC at 15° elevation. A 16 wavelength diameter phased array antenna with 812 elements and $\cos^{1.3}\theta$ element power pattern boresighted at nadir was used. A 90° sector was used to save time running the pattern synthesis engine, an element-level, least squares shaped beam optimizer using the steepest descent method. Computations were performed with the CPLAN Satellite Antenna Design Software package [4].

In all cases steady state replacement was used, with 40% of the population replaced each generation

(except case 1, which was 20%). Crossover probability was 0.7, and mutation probability 0.05.

Figure 5 shows the results of the three cases. The first was for N=3 rings and D_0 =15 dB. The 15 dB link margin contour is shown. It was computed by subtracting 20 Log(Rs/h) from the antenna directivity pattern in dB prior to contouring. 60 generations of a population of 400 was used. Execution time was 2 seconds on a Pentium II 450 machine.

Cases two and three are for D_0 = 20 dB and N=4 and N=5 respectively. The 20 dB link margin contour is shown. This is close to the maximum practical directivity available from the 16λ diameter antenna since the required directivity at EOC is 20+7.2 =27.2 dB. Nearly diffraction limited beams service the outer ring with peak directivities of about 30.5 dB. A diffraction limited beam centered at EOC has a peak directivity of 31.1.

Note that the 15 dB layout required 12 beams and both 20 dB layouts required 38 beams. It is no surprise that 10 Log (38/12) = 5 dB. In general, the number of beams required for a coverage can be found from $\frac{N_2}{N_1} = 10^{\left(\frac{D_{0,2}-D_{0,1}}{10}\right)}$, where $D_{0,1}$ and N_1 are found by running the optimizer for a particular test case. This is a fast and reliable way to determine the number of beams required for a constant flux LEO coverage at a particular altitude and EOC.

Many different, equally good cell layouts can be obtained by varying the number of rings, population size, and fraction of population replaced each generation. Test cases two and three illustrate this. Other criteria could be coded into the fitness function to favor a particular type of layout. The fitness function described here evaluates only directivity. However, other parameters such as adjacent beam C/I, handover, beamshape (square vs long & narrow), and constancy of cell area on the ground could be included.

Compliance Curves for the 3 Test Cases
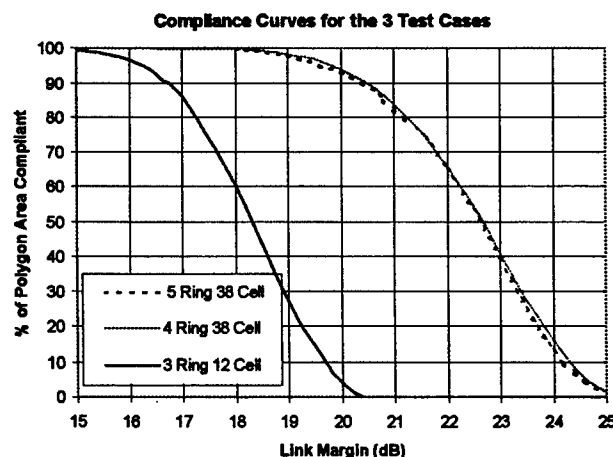
Link margin compliance is plotted above for the test cases. This is a very good metric for assessing the value of D_0 actually achieved for a coverage. The three test cased achieved 16.6, 20.5 and 20.5 dB link margin over 90% of the coverage area.

References

1. Elevation edge of coverage (EOC) is defined by the locus of points on the earth where the elevation angle to the satellite is a specified value.

2. J. Michael Johnson and Yahya Rahmat-Samii, "Genetic Algorithms in Engineering Electromagnetics," IEEE Antennas and Propagation Magazine, Vol. 39, No. 4, August 1997, pp. 7 - 21

3. M. Matsumoto and T. Nishimura, "Mersenne Twister: A 623-dimensionally equidistributed uniform pseudorandom number generator", ACM Trans. on Modeling and Computer Simulation Vol. 8, No. 1, January pp.3-30 1998. Please see http://www.math.keio.ac.jp/~matumoto/emt.html

4. CPLAN Satellite Antenna Design Software. Please see http://www.satsoft.com for more information.

Figure 5

Case 1. N=3 D_0 = 15 dB

Case 2. N=4 D_0 = 20 dB

Case 3. N=5 D_0 = 20 dB
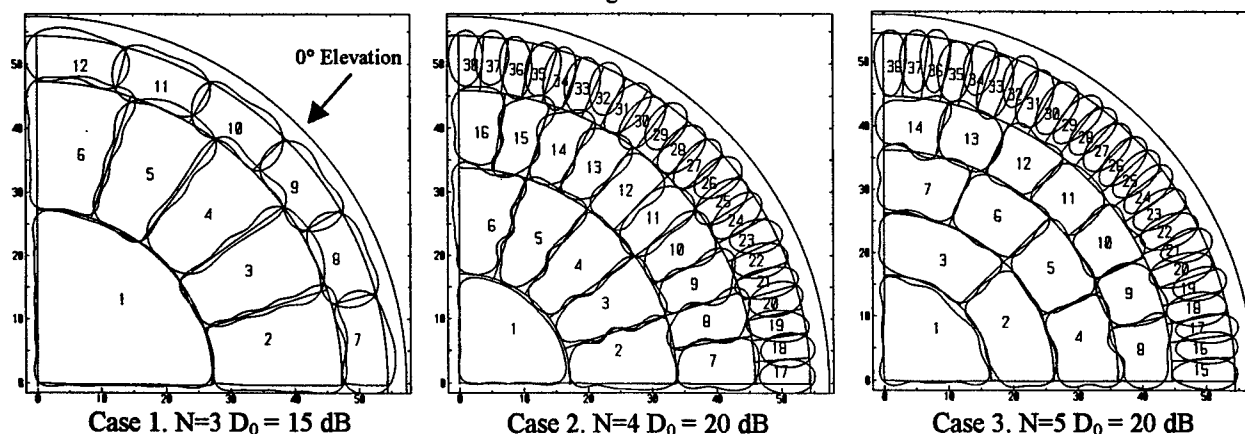
Techniques to Maximize Communication Traffic Capacity in Multi-Beam Satellite Active Phased Array Antennas for Non-Uniform Traffic Model

Erik Lier* and Daniel S. Purdy
Lockheed Martin Communications and Power Center
100 Campus Drive
Newtown, PA 18940

Abstract
In multi-beam satellite applications with frequency and polarization reuse a main challenge is to serve a high-density communication traffic region on the ground without interfering with beams at the same frequency. If the antenna is implemented as an active phased array, the challenge increases even more when the aperture has uniform amplitude excitation, which may be required for deployed arrays for thermal and efficiency reasons. Also, when all the communication channels share the same elemental amplifiers, intermodulation interference needs to be kept under control. This paper discussed these problems, and presents techniques to improve communications traffic capacity.

Problem Definition

In future high data rate global communication satellite systems in geosynchronous orbit high gain frequency reused beams will be required to cover the entire surface of the earth seen from the satellite. This can be achieved either by a multi-feed reflector antenna or active arrays.

The amount of communication traffic is assumed being highly non-uniform over the earth, with estimated high capacity requirement over Europe, Eastern and Western United States and South East Asia. The high traffic capacity regions can best be served by densely packed high gain beams with frequency and polarization reuse. The service area on the ground may be divided into hexagonal cells and served by a single beam at a fixed frequency and polarization. To cover the entire service area the high gain beams require beam hopping (TDMA). This can be achieved by active phased array antennas with a large aperture.

The analysis assumes 64 transmit beams, 4 frequency bands and 2 polarizations. This is achieved by 4 antennas, each with 16 beams and 2 frequencies. Each antenna consists of 21 tiles, each containing 8 x 8 radiating antenna elements or sub-arrays with 2.5λ spacing (see Figure 1). A Solid State Power Amplifier (SSPA) and phase shifter are behind each element. Furthermore, it is assumed that the amplitude excitation is uniform across the array. This ensures that all the SSPAs can be operated close to saturation for best antenna efficiency and optimum junction temperature.

This paper discusses techniques to increase the traffic capacity. The goal is to pack same frequency beams as close together as possible within the constraints of EIRP and C/I requirements, ensuring maximum traffic capacity over regions with high demand. The interference portion of the C/I ratio consists of co- and cross-pol interference, intermodulation interference, adjacent channel interference and inter-satellite interference. The main interference drivers are copol sidelobes and intermodulation.

Traffic Capacity Optimization Techniques

Sidelobe Interference: The use of tile architecture and uniform power illumination over the aperture result in increased sidelobe power. By selecting 21 tiles according to Figure 1 without the 4 corner tiles, the worst-case 1ˢᵗ sidelobe is being reduced from 13.2 dB for a square array to 17.2 dB, which is only 0.4 dB higher than for a circular array with uniform power distribution. Furthermore, the sidelobe interference from one beam onto the service cells of the other 7 beams at the same frequency can be suppressed by phase-only optimization. This will be further discussed below.

Intermodulation Interference: Interference from the power in the intermodulation products radiating from the antenna can be controlled by backing off the SSPAs. However, it is crucial to keep this back-off as small as possible to maximize the antenna efficiency. The goal was to run the SSPAs at 1 dB input back-off, which corresponds to -12 dB 3ʳᵈ order intermod level. Also, spatial spreading of the intermod power over the coverage area improves the C/I substantially. The results presented below are based on the Shimbo model for analyzing the non-linear amplifiers.

Synthesized Beam Templates: A beam template is defined as a cluster of 8 frequency reused beams at a given instant in time. Because of the TDMA sequence (hopping beams) the beam template could change many times per second. In regions with high traffic density the beam template would change less often. The approach is to synthesize optimum beam templates that meets the EIRP and C/I spec, and that are stored in the satellite computer for fast access.

The goal for this investigation was to pack the 8 beams as dense as possible at 1° maximum spacing. Since the 3 dB beamwidth is 0.56°, two reused beams at this spacing are within the 1ˢᵗ sidelobe of each other. A 7 cluster template as the one shown in Figure 2a will not meet the design goal within the center beam because of the high sidelobe interference from all the surrounding beams. Donut-shaped templates like the one illustrated in Figure 2b offers much better performance because each of the beams inside of the ring are in the 1ˢᵗ sidelobe of only 2 other beams. The split template shown in Figure 2c also gives good performance, offering high traffic capacity in two separate regions.

Neither of the templates in Figure 2 fully meet the C/I spec. EIRP can be traded for sidelobe interference by suppressing the sidelobe level from each beam over the 7 other reused beams. This can be achieved by phase-only optimization, at the expense of slightly reduced EIRP.

Layout of Beams with High Cross-Over Level: For multi-beam antenna applications the cross-over level between beams is typically 3 to 4 dB. The flexibility of the phased array can be utilized to trade EIRP for payload control complexity by selecting 0.7 dB cross-over level instead of 3 dB, corresponding to 0.28° cells. This improves the EIRP by approximately 3 dB when pointing error improvement is included. It also buys improved C/I performance because the cell area is ¼ of the original cell, making the sidelobe suppression easier. The disadvantage is a 4 times increased beam hop rate to cover the same service area.

Results

Table 1 shows the EIRP degradation and worst case sidelobe isolation with sidelobe suppression. The "semi uniform" sidelobe suppression suppresses the sidelobes within a 120° angle toward other service cells. A more optimum method referred to as "cell suppression" is to suppress the sidelobe over the other cells only, enlarged by the pointing error. We see that for cell templates 2b and 2c the sidelobe isolation can be suppressed to 34 dB (better than 25 dB overall sidelobe isolation) with less than 0.5 dB EIRP degradation.

Table 2 quantifies the main sources of interference from the beam template in Figure 2c, applying the total sidelobe level shown in Table 1. Without sidelobe suppression the average sidelobe level is substantial higher, forcing us to further back off the SSPAs. Miscellaneous errors are mainly amplitude and phase errors and sub-array/Supertile failures. EIRP and C/I performance with all errors included will be discussed in an accompanying paper.

Acknowledgement

References

[1] E. Lier, A. Cherrette, "A Study of Sidelobe Suppression of Active Array Satellite Antennas with Contour Beams, 1995 Int. AP-S/URSI Symposium, Newport Beach, June 1995.

Table 1: EIRP degradation and sidelobe performance for various beam templates versus sidelobe suppression.

Template	Type of Sidelobe Suppression	Worst Case Sidelobe Level (dB)	Avg. EIRP Loss (dB)
Single Beam	No suppression	-17.2	0.0
Figure 2a	Semi Uniform	-24.6 dB (inner cell) -34.1 dB (outer cells)	1.73 0.44
Figure 2b	Semi Uniform	-34.1	0.44
Figure 2c	Semi Uniform	-34.1	0.52
Figure 2c	Cell Suppression	-34.3	0.34

Table 2: Interference budget for 8 frequency reused beams and polarization reuse based on the template in Figure 2c.

Interference Sources	Interference Isolation (dB)
Average Sidelobe	25.0
Average Cross-Pol	25.0
Average Intermodulation	18.0
Allowed Miscellaneous Errors	17.5
Total C/I	14.0

Transmit Array 1 & 2

S/C Nadir Deck

Transmit Array 3 & 4

1 ft x 1 ft Tile

Dummy Tile
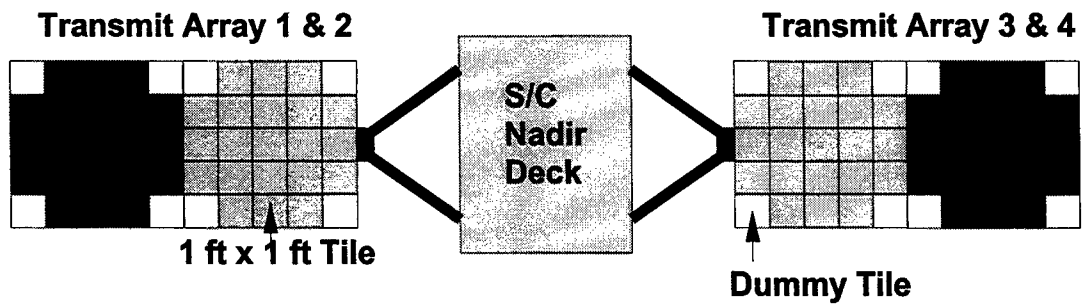
Figure 1: Example of satellite configuration using 4 deployed transmit active phased arrays with 16 beams per antenna.

a.

b.

c.

0.28°

3°

1°
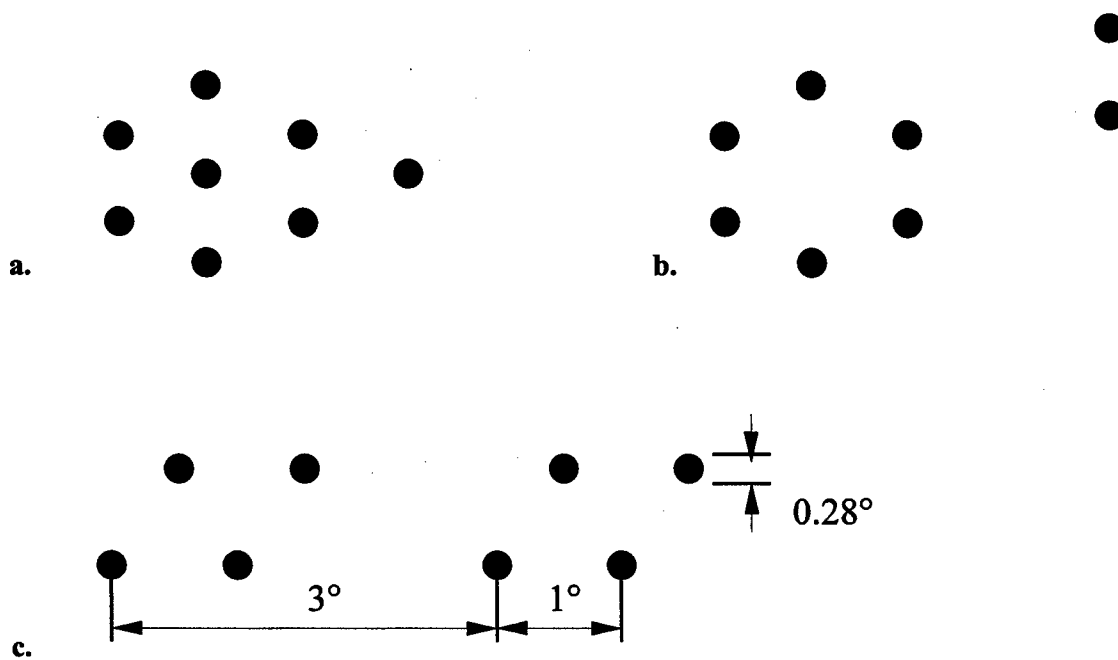
Figure 2: Beam Templates a.-c. for frequency reused beams.

An On-Board Integrated Beam Conditioning System for Active Phased Array Satellite Antennas

Erik Lier[1], Daniel Purdy[1], Jeff Ashe[2], Greg Kautz[2]
[1]Lockheed Martin Commercial Satellite Systems, Newtown, PA
[2]GE Corporate Research and Development Center, Schenectady, NY

Introduction

Future phased array satellite antennas may have multiple high directivity beams to serve a global network of small ground terminals from geostationary or low earth orbit satellites. Optimal utilization of the frequency spectrum with frequency reused beams over the earth coverage requires low sidelobe beams with high beam to beam isolation. The use of highly directive beams implies a narrow beamwidth and this in turn requires an increased beam pointing accuracy. To achieve the beam to beam isolation and associated low sidelobe performance there may be a need for accurate *calibration* and control of the amplitude and phase of each element across the array aperture to compensate for errors caused by thermal variations (diurnal and seasonal variations for space-based antennas), aging effects and elemental failures. When considering satellite applications, *attitude determination* (i.e. finding the pointing direction) of the array may also be necessary to be able to point the beams in the correct directions with minimal pointing error. The objective is to implement both the calibration and attitude determination functions while minimizing mass, power consumption and volume requirements essential to a spacecraft system.

This paper discusses an integrated on-board beam conditioning [1] or control system for a satellite-based phased array antenna as illustrated in Figure 1. The system presented takes advantage of synergy and commonality of the calibration and attitude determination subsystems. The integrated system assumes a near field calibration approach [2] based the control circuit encoding (CCE) technique [3], conventional monopulse for receive array pointing, and an orthogonally encoded monopulse technique [4] for transmit antenna pointing (attitude determination).

Description of the Technique

To calibrate the phased array one must determine the relation between the elemental control settings of the phase and amplitude controller and the actual phase and amplitude radiated at the antenna elements. The system described uses a stationary nearfield approach based on the CCE method [2-3]. The method is particularly attractive for arrays having discrete attenuation and phase control devices for beam formation. As shown in Figure 2 for a transmit array, the beamformer is encoded by applying orthogonal codes to control the phase and/or amplitude settings of each of the elements. Since each of the elements are encoded with a mutually orthogonal code, a composite signal containing each of the encoded element complex weights is received by the stationary probe. A coherent receiver and decoder (cross-correlator) are used to recover the element weights as received at the probe. The process provides the complex amplitude and phase information for the individual phase shift and attenuation devices as well as the relative complex gain amongst the elemental channels. The calibration data augmented with knowledge of the position and patterns of the element and probe allow the creation of arbitrary beam shapes. The advantage of using the orthogonal coding is that it facilitates measurements of all elements simultaneously. As compared to measuring a single element at a time the increased 'dwell' time for each element can be used to provide coherent integration gain thus improving the measurement accuracy.

For a satellite application requiring both transmit and receive operation, it is possible to take advantage of common transmit and receive array calibration functions as shown in Figure 3 [1]. Such a system is

comprised of calibration mode switch (not shown), calibration signal generators (CW tone), orthogonal code set generator, switches to select between transmit or receive array calibration, calibration RF probe / cable / boom, calibration receiver and decoder, processor and memory. The system re-utilizes existing hardware onboard the satellite including the RF signal generator, signal processor and memory for storing the orthogonal code sets used in the calibration function. The array software used by the processor to derive the amplitude and phase of each element has to account for the product of the element and probe patterns since the calibration probe is in the near field of the array antenna and in the far field of each antenna element [2].

The calibration process finds the relative amplitude and phase of each element in the array. For the transmit array the absolute amplitude or power from each element is needed in order to adjust element drive levels needed to satisfy EIRP and C/I requirements. Absolute power measurements must be achieved by monitoring power received at a ground station, by sensing bias currents with the transmitter amplifier final stage or by other means.

One of the key important factors that must be considered in the design of a calibration system is the measurement accuracy with respect to noise and interference. The figure of merit commonly used to describe accuracy is the signal-to-noise ratio (SNR). Though a detailed noise analysis is outside the scope of this paper, some qualitative remarks are provided. If the interference noise (for example, consisting of QPSK signals) behaves as additive Gaussian white noise (AGWN), then accuracy of the calibration (e.g.,SNR) is proportional to the coherent integration time in which the measurements are performed. For a multibeam satellite system that employs frequency reuse, the beam that is to be calibrated will be momentarily taken off line while the remainder of the beams will continue to transmit communications data. The communications beams will generate interference that will degrade the measurement accuracy and therefore the time required to perform the calibration will need to be sufficiently large in order to achieve the desired SNR. An analysis was conducted to assess SNR in a multibeam environment. For a limited number of beams (up to 16) it was found that the calibration SNR improves when the calibration probe is in the near field compared to in the far field. This is because the signal, which is proportional to the elemental gain, is approximately unchanged between far and near field of the array (assuming far field of the array element). However the interference noise is reduced in the near field compared to the farfield because the interfering beam patterns are defocused in the near field.

The CCE technique could be implemented as a far field / remote system by placing the calibration probe at a ground station location. The advantage would be to avoid the calibration boom and cable on the satellite. The disadvantage would be reduced SNR as discussed above, and a reference tone would be required to cancel fast varying atmospheric scintillations.

In order to provide sufficient SNR performance the calibration probe pattern must be sufficiently wide in order to cover all the array elements within the main lobe. A small element can be placed close to the array, while a larger element requires a longer boom. For a deployed array the calibration probe must be sufficiently large that the resulting beamshape can reject multipath diffraction effects from the spacecraft structure that would otherwise contribute to measurement errors. In larger arrays the probe has to be placed in front of the array to avoid an excessive boom length. A study has shown that aperture blockage from the probe and boom for a system with realistic dimensions is insignificant. For a relatively small array the probe and boom can be placed to the side of the array, so long as it is within the main beam of all elements.

The knowledge of the position of the calibration probe relative to the array antenna is needed in order to process and decode the calibration signal. Studies of probe deployment error effects are summarized in Figure 4. An axial displacement of the probe induces phase errors that result in a defocusing of the array with reduced directivity. A lateral displacement corresponds to a beam tilt. However, this beam tilt can by

510

compensated for during the beam pointing procedure following the calibration procedure. An acceptable level of calibration accuracy can be achieved if the probe positional tolerance of the calibration probe is to within 2-3λ.

Attitude determination is here defined as the process of finding the three-dimensional orientation of an array relative to the aperture plane. This is accomplished by measuring the apparent directions to terrestrial reference points. Using two or more displaced locations, the full 3D attitude may be determined. For receive antenna systems, conventional monopulse can be utilized to determine antenna pointing. The same method can be extended to transmit-only arrays [4]. The system arrangement of Figure 3 facilitates this additional function by reuse of receiver and signal generators between calibration and attitude determination. This simplifies the redundancy scheme and provides the most efficient overall beam conditioning system.

Conclusions

To provide good quality beams with high beam-to-beam isolation in multibeam satellite array application it is crucial to have a system that accurately controls the shape and pointing of the beams. The beam conditioning system presented above offers an efficient and economic method of calibrating an on-board active phased array. By taking advantage of the existing hardware on-board the satellite only a minimal amount of extra calibration hardware is required. It has several advantages over a satellite-to-ground calibration system, and is robust with respect to the positional tolerance of the on-board calibration probe. The calibration system can also be used for ground and preflight tests and calibration of the phased array antenna.

References:

[1] Erik Lier, Daniel S. Purdy, Jeff Ashe: *"An integrated beam conditioning system for a phased array antenna"*, patent pending.
[2] Erik Lier, Daniel S. Purdy Greg Kautz, Anthony Jacomb-Hood, Vladimir Volman: *"A remote nearfield phased array antenna calibration system based on orthogonal coding"*, patent pending.
[3] S.D. Silverstein, R.L.Nevin, W.E.Engelger: U.S. Patent No. 5,572,219, *"Method and Apparatus for Remotely Calibrating a Phased Array System for Satellite Communication"*, Issued Nov. 5, 1996. (Developed by General Electric / Lockheed Martin)
[4] D. Purdy, G. Kautz, E. Lier, *"Method and apparatus for monopulse operation of an array antenna"*, patent pending.
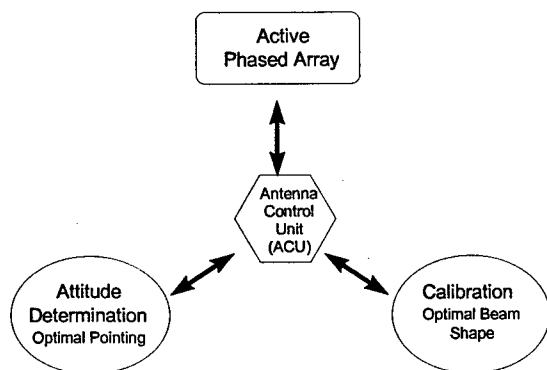
Figure 1: Beam conditioning system flow chart
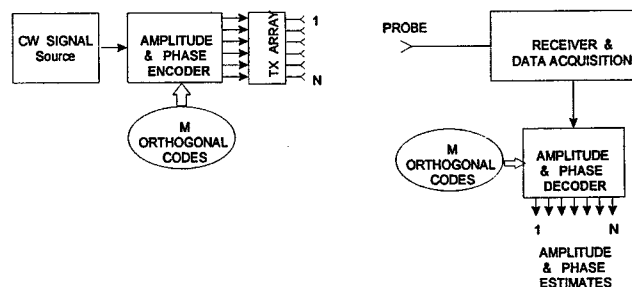
Figure 2: Illustration of CCE calibration approach
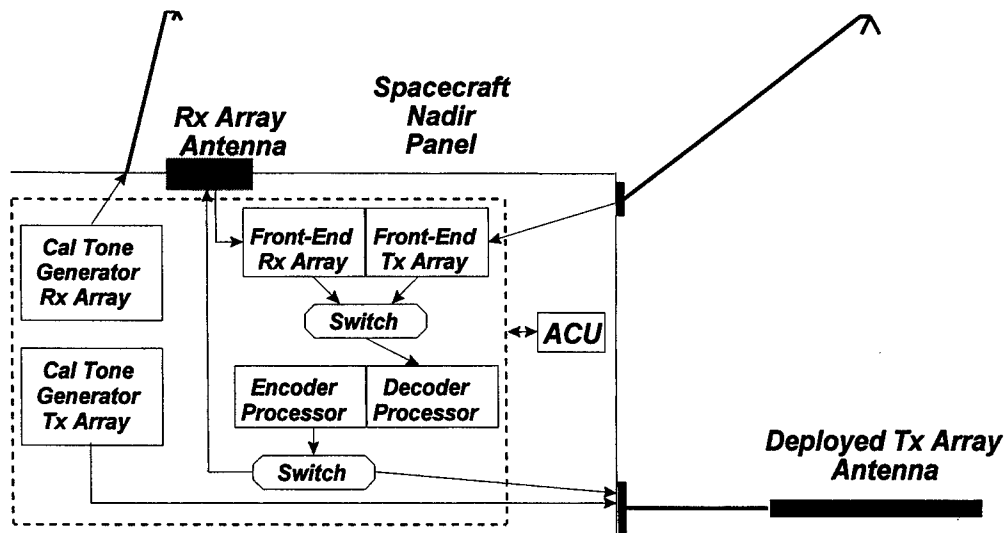
Figure 3: Block diagram of beam control system for active phased array antennas.
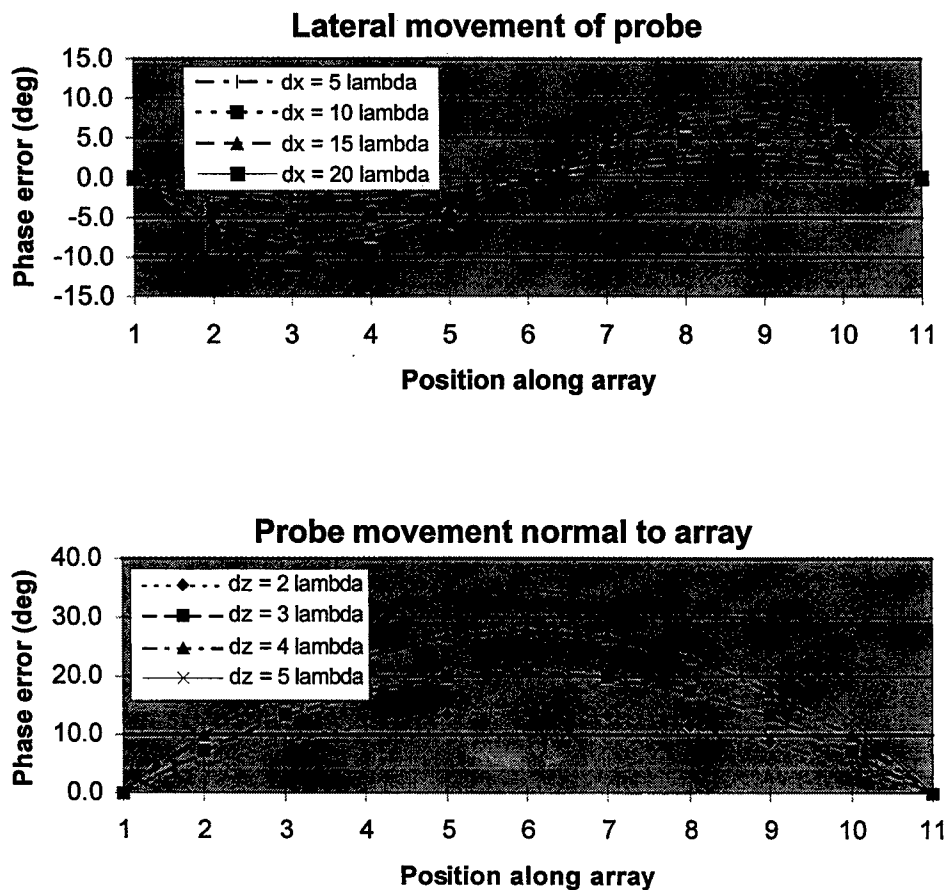
Figure 4. Calibration accuracy as a function of probe displacement from expected deployment position. (Array diameter = 120λ, Probe height above array = 300λ)

SOME ECM ASPECTS FOR PHASED ARRAY SYSTEMS

Air Marshal (Retd.) Lakhmir Singh, AVSM VSM
AIMIL Ltd.
"Naimex House"
A-8 Mohan Co-operative Indl. Estate
Mathura Road, New Delhi - 110 044
Tel : +91-11-6959818   Fax : +91-11-6959456   E-mail : aimil@vsnl.com

Introduction

This paper provides a brief overview of Electronic Counter Measure (ECM) aspects related to phased array systems and highlights techniques and concepts from available literature. It is not intended to have a comprehensive coverage of the subject. The aim is to have a discussion which may bring out certain new aspects in this important and sensitive area.

ECM Systems

The Raytheon 'design to price' shipborne ECM system employing a large number of high power TWT's was the first major phased array ECM system during 1970's and 1980's. It was developed at great expense and took several years for development. There were many modifications and upgradations. According to available reports, it served its purpose well i.e. to counter hostile radars and also make their designers to incorporate expensive ECCM.

It is also possible to exploit simple techniques for meeting certain operational requirements. For example, an improvised pair of antennae with phase discrimination circuit and display onboard an aircraft has been employed to home onto a radar or to give a warning to the pilot about a threat. The wideband IFM's (instantaneous frequency monitors) with precise phase sensing, measure frequency of unknown signals over octave or multioctave frequency bands. Sophisticated DBD's (digital bearing discriminators) find direction of arrival of unknown signals from any direction over octave frequency bands. These with other sensors provide warning systems against modern threats and missiles. Microwave frequency memory loops and digital frequency memories are effective in countering several types of threats.

Noise Jammers

Noise Jammers have been widely used, are still very effective to degrade performance of radars including phased arrays and have forced the radar designers to adopt more complex designs using improved phase shifters, components and techniques. In a phased array radar, the beam controllers (BC) are required to generate weight vectors corresponding to signal and jamming environment. The computational load on the BC is negligible if the beam is to be formed in a preset environment i.e. only with thermal noise present. It is in adapting the beam forming network to the changing noise and signal environment in real time that the problems arise. The smart jammers can adopt new waveforms and modulations to make the job of the BC more difficult.

The mathematical solution for optimum adapted weights is the product of the inverse of the element signal matrix and a given direction matrix. This is an open-loop adaptive pattern nulling process and while it is conceptually attractive it has several difficulties. Firstly with N elements in the array, the number of operations required is proportional to N^3 which in the case of an array of 2000 elements and updates of 100 times per second becomes 8×10^{11} operations per second. Secondly, the matrix may have large dynamic range and possibly ill conditioned.

This in turn means more precision arithmetic. It is not realistic to individually weigh the element signals for pattern nulling, especially in view of the fact that the number of interference sources J is far less than N(J<<N). Partially adaptive systems using a reduced number of degrees of freedom and an acceptable control of the resultant pattern will suffice.

This is a two step process. First the number of interfering jammers and their respective angular locations have to be estimated. For this purpose a search in angle with an auxiliary beam will be required. Once the jammers have been located, a retrodirective beam in that direction is created and the output of this beam is subtracted from the main beam to obtain a null in the resultant radiation pattern. So long as the number of jammers is a reasonably small figure, it is possible to use only one additional beam forming network in parallel to the main beam forming network. The retrodirective beam forming network can be time multiplexed to produce the J beams pointed at the J jammers. Thus the jammer cancellation will take place but with a degradation of the side lobes to the right and the left. Indeed even with a smart BC, the noise jammer is effective to degrade the radar performance.

Deception Decoys

Active onboard deception jammers and towed decoys are very effective to produce false targets. The cost of the decoys is an important factor. The active decoys GEN-X developed by Texas Instruments came down from US$ 16000 in lot-1 (2500 numbers) to US$ 4900 in lot-3 (3400 numbers). Due to the high cost, Raytheon has reached an agreement with Texas to drop out of the programme. Raytheon has also brought out a towed decoy ALE50 which is a straight through repeater with adequate transmit - receive antenna isolation. The ALE/50 is expected to become as common as a chaff and flare dispenser. After recent success in Kosovo, additional numbers have been ordered. Raytheon has also received an order for $ 3.2 million to develop millimetric wave free fall decoys. The millimeteric wave top attack ammunition is also used for homing onto a vehicle or tank.

Marconi's Ariel retractable towed decoy is a proven system and was effective recently in Bosnia. Marconi has teamed with Dassault Electronique to develop towed decoy for Mirage 2000. Sweden's Celsius Tech Electronics has developed BO2D decoys for Gripen and Viggen.

A recent concept 'silent hard killer' (SHARK) prescribes that before strike aircraft arrive at a target area, enemy's radars and weapon systems should be killed or at least crippled. It involves pre-emptive destruction rather than reactive suppression. The latter is time sensitive and at times too fast to be effective during the short flight time of an attack. The SHARK programme comprises of two parts : a lethal bomb or missile and a non lethal miniature decoy. The decoy is air launched before strike. It emits aircraft-like radio and radar signals and maintains a high level of flight performance for a few seconds to identify and prioritise a target that will be later destroyed by the lethal missile. The target lists and their signatures, various scenarios, concept of operations and force structure are earlier simulated to optimise deployment of SHARKS for real scoop.

Battlefield Phased Arrays

In the present day and civil security environment, there may not be many sophisticated ECM threats due to their high cost. The battlefield surveillance radars for such situations are required to be light, compact and cheap with minimum essential ECCM. Compactness means use of high frequency bands of C and X and even Ku and Ka. The cost considerations will not justify the use of the T/R module technology. Instead frequency scanning (linear or stepped) technique with a two dimensional array antenna will meet the requirement. The aim is to mount an array of resonant dipoles with phase shifters on a reflector board which is illuminated by a radiating source.

514

The array is mounted on one face of the board and the command circuits on the other face of the board. Such a system will suffer from proper look angle versus frequency relationship. However, it will be suitable for mass production. The ECCM and improvements could be added on as and when required.

Indian Phased Array Programme

A multifunction phased array radar (MFAR) operating in G band for surveillance and target tracking operations, command band transmission for guidance of missiles and a secondary surveillance radar operating in conventional D band is provided. Phased array antennae are used in all the three bands. These arrays along with their beam control processors and ventilating systems are mounted on a vehicle. Using the inherent beam agility and by employing flexible scheduling and control mechanisms, the fast agile beams are used to achieve multiple functions simultaneously under adverse operating conditions.

The main G brand array is a space fed lens array of more the 4000 elements, nearly circular in contour and about 2.4 metres in diameter. Each antenna element, called a phase control module (PCM), consists of a rear radiator, a phase shifter with associated electronics for 5 bit control of phase, and a front radiator to transmit and receive energy. Behind this array is a multi mode wave guide feed horn assembly. Focal length of the array is nearly equal to its diameter and the feed is located on the axis of the array. A radome covering the feed is attached to a box containing the microwave receiver hardware and the duplexer.

The command band array is similar to the radar band main array in concept and design, but is formed of nearly one thousand elements and has a diameter of about one meter. This array is also space fed. Its beam steering computer is identical to the quadrant processors of the main array and it is located in the same physical module.

The radar system has been designed, constructed and tested for its performance and is available for exploitation as a powerful multifunction system. It has successfully undergone extensive field evaluation against airborne targets and standalone performance established.

Future Systems

The cost and performance trade off will dictate future ECM and ECCM systems. New technologies will be mostly derived from civil market due to higher cost of technologies and lower outlays for defence barring certain key technologies and projects. More projects will be for upgradation to counter current threats in updated operational environment. Digital technology and software improvements will dominate. There will be more emphasis on surveillance, satellites and signature analysis. A great deal of effort will be spent on mathematical modelling of aircraft, vehicles and hot spots to present more difficult targets. Low (or very high) flying and shorter reaction time will continue to be required. More capabilities of millimeteric and sub millimeteric wave and optronic systems will present multisensor environment and new countermeasure requirements particularly for short range missile systems. The phased array ECM systems are characterised by more loss of RF power in the transmitter and the receiver. Therefore there is demand for higher power from TWT's and solid state devices, lower plumbing loss, better phase characteristics and spectral purity of signal sources. Improvements are required in the antenna designs, larger apertures for better angle and range resolution, digital beam forming networks and integrated systems. Improved phase shifters and time delay devices and techniques will be developed. Also adaptive RF power and time management for target and search will provide more efficient operations.

The receivers will have more dynamic range, improved processing technology and detection algorithms, both digital and analogue for better visibility under jamming interference and clutter from land, sea and atmosphere and under dense environment. Spread spectrum, exotic waveforms, frequency and pulse agility, dynamic and adaptive analysis of signal environment, prioritisation and smart libraries will be required. The list is long. In fact all technologies for the radar are also applicable to ECM.

Of course, computer hardware and software are everywhere and very important but it is the operator closely backed by the system research and development with new philosophy for concurrent design and production which will play the key role for utilisation of resources more effectively.

References

R P Shenoy, "Phased Arrays for Radar", Notes of the Advanced Course on Modern Radar Techniques & Systems, AC-MRTS 1988, 30 May - 10 June 1988, Rome, Chapter IV.

E J Carlson, "Low Probability of Intercept (LPI) Techniques and Implementations for Radar Systems", Proceedings of the 1988 IEEE National Radar Conference, USA, Pp 56-60.

E Brookner & J M Howell, "Adaptive-Adaptive Array Processing", Proceedings of the 1985 Phased Array Symposium, Rome Air Development Center, NY, USA, RADC-TR-85-171, August 1985, Pp 133-146.

Covault C, "Missile Warning Systems", AW&ST, 26 September, 1994, Pp 82-83 and 12, September, 1994, Pp 26-27.

Kirubarajan, T ; Bar-Shalom Y, Blair WD, Watson GA, "IMMPDAF for Radar Management and Tracking Benchmark with ECM", AE&ES, IEEE Trans, October, 1998, Vol 34 No.4, Pp 1115-1134.

Hans-Wener Fieweger, "New Developments in Communication, Reconnaissance and Electronic Warfare", Miltech, 2/99, Pp 96-106.

T. Kirubarajan; "IMMPDAF for Radar Management and Tracking Benchmark with ECM", IEEE Trans on AES, Vol 34, No. 4 October 1998 Pp 1115-1134.

Michael A. Dornheim, "Order for ALE-50 Doubles After Success in Kosovo", AW&ST, November 15, 1999, Pp 48-49.

Dr. George M Cleetus, L S Radhakrishnan, MC Krishnaswamy and S. Ravind, "'Rajendra' a Multifunction Radar System", Radar Symposium India-99 Proceedings, 14-17 December 1999, Pp 20-31.

WP2

Phased Array Measurement and Calibration

Invited Special Session
Chairs: Yahya Rahmat-Samii, Robert Yaccarino

Phased Array Measurement and Calibration

An Automated Process for Efficiently Measuring the Patterns of All Elements Located in a Phased-Array Antenna

Daniel S. Purdy
Lockheed Martin Corporation, Newtown, PA.
dpurdy@ieee.org

ABSTRACT: An automated technique for measuring element patterns of the elements located in a phased array antenna is described and demonstrated. The procedure utilizes Hadamard encoding applied to the beamformer in an iterative fashion as the measurement positioner moves the probe relative to the array. A coherent receiver and cross-correlator decoder are used to extract the desired element patterns. This paper experimentally shows that it is possible to measure all individual element patterns within the array simultaneously. The new technique is easily automated and eliminates the need for manually removing cables and installing terminations, as was necessary using the prior art.

Basic Problem Statement and Prior Method

It is often of great interest to the phased array designer to obtain the patterns of each of the elements located in a phased array antenna. The need for this arises from the fact that due to mutual coupling, an element immersed in an array environment will behave differently from the case where the element is removed from the array. Therefore if one is to have an accurate measure for predicting performance the element must be measured when the element is placed in the array environment. The current procedure for measuring the elements in an N element array is to apply a source to one element and place terminations on the remaining N-1 elements. A single pattern is then measured for each element and the process is repeated for all elements to be measured. Hence we refer to this as the single element approach.

One problem with the single element technique is that it can be very time consuming since elements are measured sequentially and the positioner will be required to go through the desired movement cycle for each active element. This is generally inefficient and impractical when the positioner movement and data acquisition cycle must be repeated N times. A second disadvantage, is that in some cases, it may be difficult, impractical, or impossible to shut off all but one element in the array under test. In some cases removing signals from all but one element may involve removal of a cable and replacement with a termination -- a time consuming and expensive process. If one is to rely on turning elements off using digitally controlled RF on/off switches, RF isolation may not be sufficient to allow for measurements to be performed to a suitable level of accuracy. Therefore there is a need for performing element pattern measurements in a factory or diagnostic setting that allows all elements to be characterized in an accurate, efficient and cost-effective way.

New Approach [5]

The approach described herein is believed to be novel and obtains all element patterns in an array by using orthogonal coding in conjunction with a positioning device to perform multiple simultaneous measurements for each of the elements. A block diagram showing the process flow is shown in Figure 1. The orthogonal encoding is accomplished with the use of Hadamard encoding as described in [1-4], and referred to as control circuit encoding (CCE). The CCE technique uses the beamformer control circuitry to encode the RF signal path of each element by toggling amplitude and/or phase according to a unique row (or column) of the Hadamard matrix.

A coherent RF source is connected to the input of a beamformer (encoder). The probe is located at a point, nominally in the far-field of the elements. For the m-th probe position, all elements are encoded by applying a mutually orthogonal set of codes thus allowing all elements to radiate simultaneously. A probe mounted on the positioner is connected to the coherent receiver, which receives and down-converts the composite encoded signals transmitted by the elements. A cross-correlator performs the decoding which recovers each of the element signals. A processor uses knowledge of relative probe-element position and the known probe pattern to compute the element pattern in the array environment, at each of the positions for which the fields are sampled as the probe is moved along the movement track. The process is iterated to take the pattern samples of the elements as the probe is moved relative to the array elements. So at each probe position, an orthogonal encoding and decoding measurement set is performed. The desired element patterns are reconstructed by performing M samples of the element patterns, and scaling the results by the appropriate probe-element distance and known probe pattern.

Experimental Results

The technique was demonstrated using the 16 element 2×8 C-band array of pyramidal horns discussed in [3]. Measurements were verified using two positioning arrangements; a nearfield planar scanner linear track, and a farfield compact antenna test range (CATR) with a rotational positioner.

For the linear track positioner case, a distance of 4 feet between the probe track and the array was selected. This places the probe just in the far-field of the 7 inch horn apertures however the nearfield of the array. Measurements were performed at a frequency of 4.0 GHz. The probe used was an open ended C-band (WR-229) waveguide. Figure 2-a shows a plot of all 16 element patterns which were obtained simultaneously as the probe was moved along the track. The elements as shown in [3] are arranged in a lattice 2 high and 8 wide. Therefore Figure 2-a shows pairs of element patterns grouped as the probe is moved along the width of the array. The patterns shown are the resulting product of the element and probe. Figure 2-b shows the results obtained for the case when 15 elements are terminated and the center element excited so that one single element measurement is obtained. There is excellent agreement between the single element technique and the results obtained using iterative-CCE. The element-probe pattern product is useful for the nearfield calibration system described in [4]. Knowledge of the probe pattern would allow the element pattern to be determined from the data if so desired.

Figure 3-a shows iterative-CCE element patterns obtained using the CATR in which the probe is in the farfield of the element and array. Since the array is rotated about a fixed point with the probe placed in the farfield of the array (compared to the example above) the decoding process of Figure 1 directly yields the element pattern. Shown in Figure 3-a is an overlay of all 16 element patterns in the array which were measured simultaneously. Figure 3-b shows the comparison of one element to the theoretical pattern. There is good agreement between measured and theory. The 'ripple' present in the patterns is due to the fact that the CATR has about 0.3 dB ripple present across the quiet zone. The data obtained show that the technique can rapidly measure all elements in the array and obtain element patterns using the iterative-CCE element pattern extraction technique.

References
[1] U.S. Patent No. 5,572,219 S.D. Silverstein, R.L.Nevin, W.E.Engelger, *"Method and Apparatus for Remotely Calibrating a Phased Array System for Satellite Communication,"* Issued Nov. 5, 1996. Developed by General Electric / Lockheed Martin.

[2] S. Silverstein, "Applications of orthogonal codes to the calibration of active phased array antennas for communications satellites", *IEEE Transactions on Signal Processing*, Vol. 45. No.1, January, 1997.

[3] Daniel S. Purdy, Jeffrey M. Ashe, Gregory M. Kautz, "Experimental validation of the control Circuit Encoding Technique for Calibration of Phased Arrays", *Antenna Measurement Techniques Association (AMTA)*, October, 1999, Monterey.

[4] US Patent pending: *Nearfield calibration system for phased array antennas (based on orthogonal coding)*. Erik Lier, Daniel S. Purdy, Jeffrey M. Ashe, Anthony Jacomb-Hood, Vladimir Volman, Filed June, 1999. Developed by Lockheed Martin.

[5] Daniel S. Purdy, *An Apparatus and process for efficiently determining the patterns of all elements located in a phased array antenna*. Lockheed Martin, June, 1999.
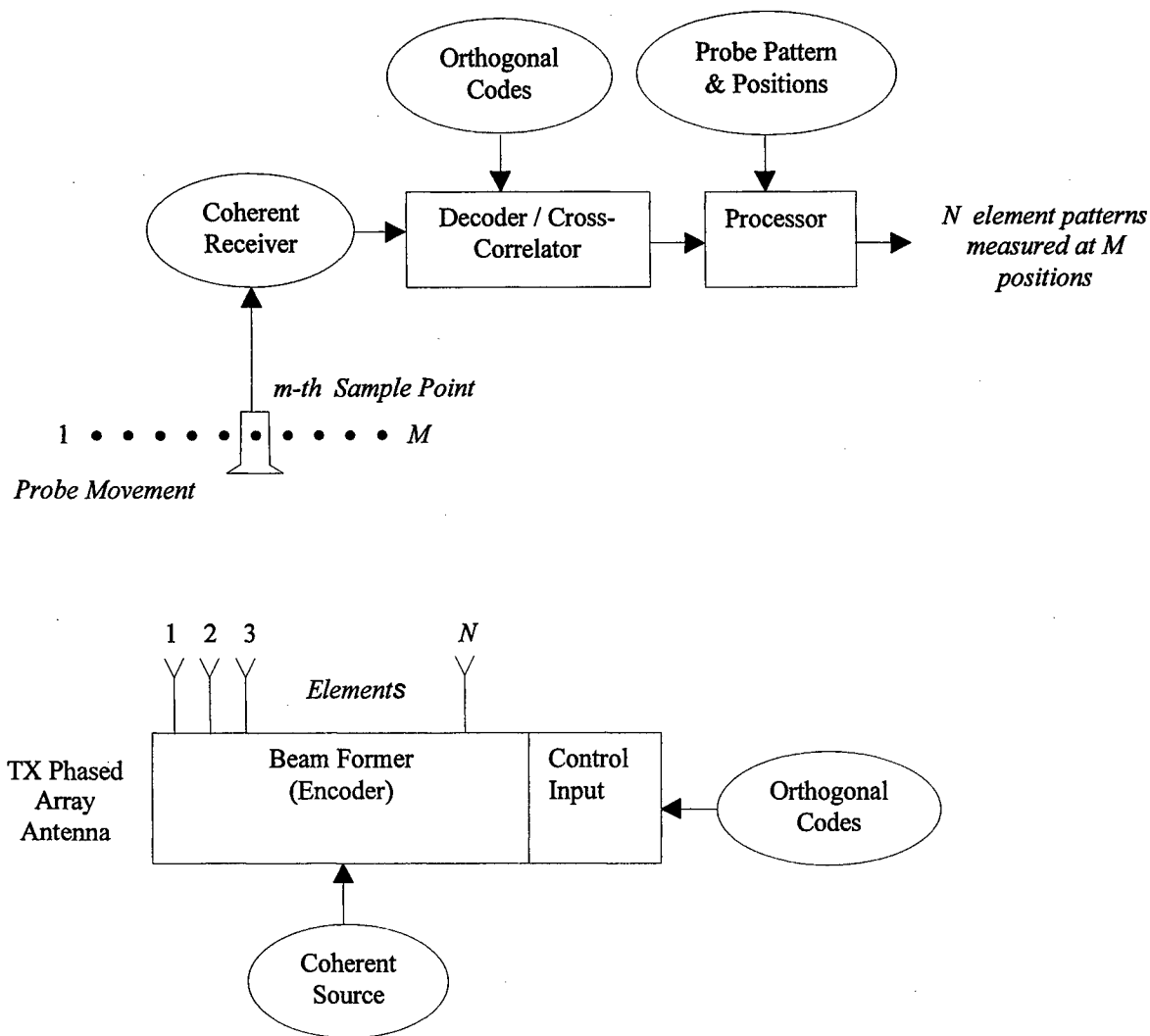
Figure 1. Iterative-CCE element pattern extraction process flow diagram.
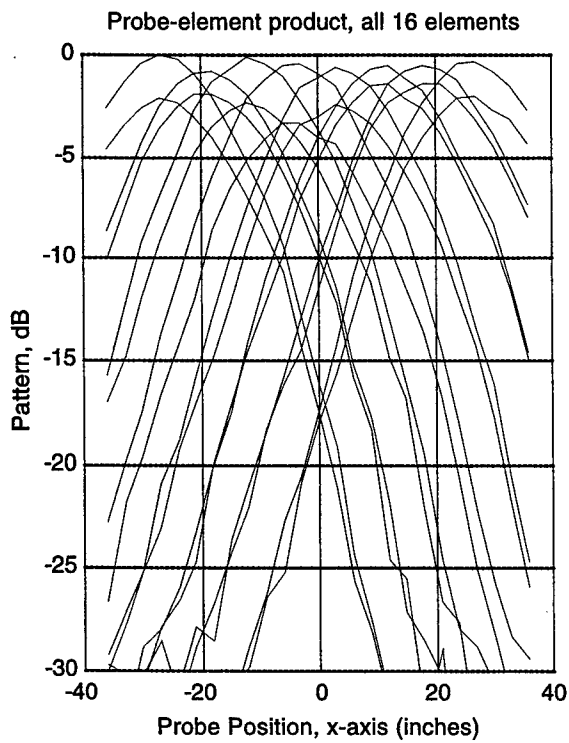
Figure 2-a. Track-probe measurements (CCE).
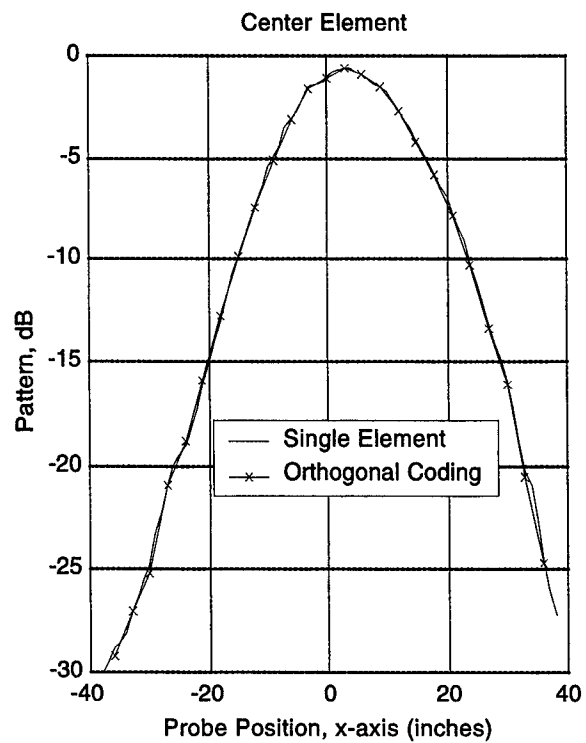
Figure 2-b. CCE vs single element.
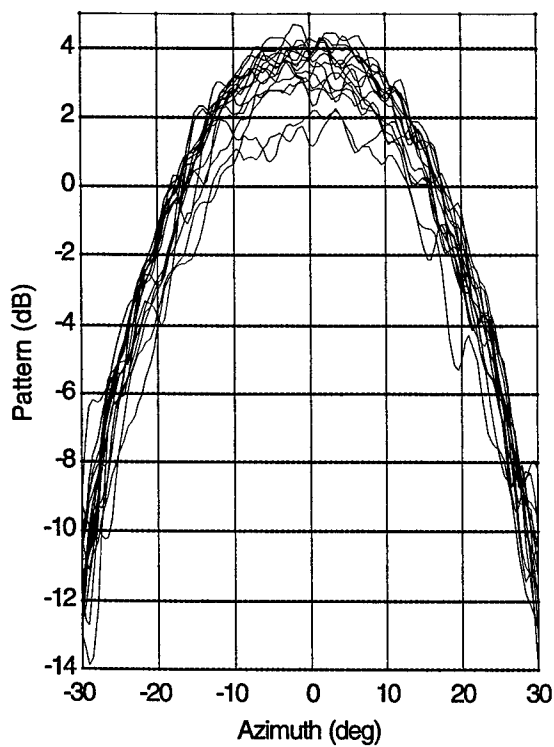
Figure 3-a. Overlay of 16 elements measurements (CCE).
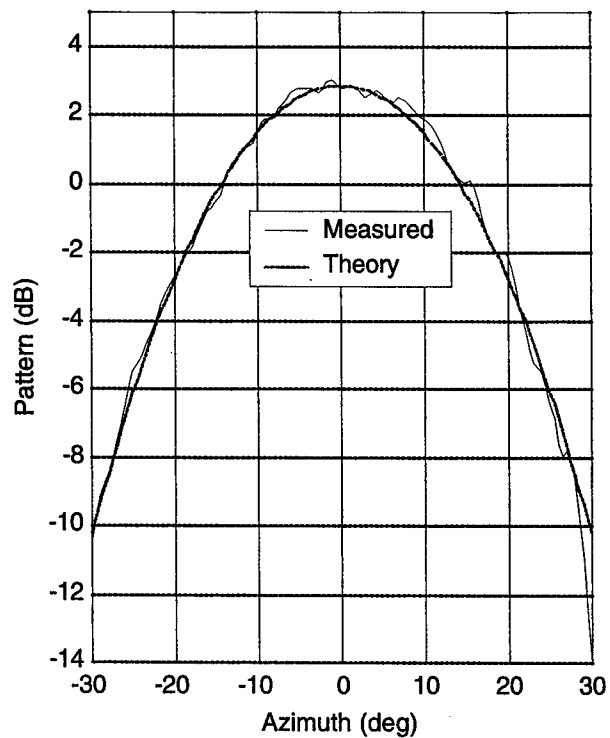
Figure 3-b. CCE vs theoretical pattern.

A COMPARISON OF CONVENTIONAL AND PHASELESS PLANAR NEAR-FIELD ANTENNA MEASUREMENTS: THE EFFECT OF PROBE POSITION ERRORS

Robert G. Yaccarino and Yahya Rahmat-Samii
University of California, Los Angeles
Department of Electrical Engineering
Los Angeles, CA 90095-1594

INTRODUCTION
In recent years, considerable progress has been made in the application of phase retrieval methods for phaseless near-field antenna measurements [1,2]. These techniques have, in fact, sufficiently matured so that accurate antenna measurements can be performed when the phase information is either unavailable or erroneous. The prohibitive cost of vector measurement equipment and high frequency measurements are two examples of applications in which phase retrieval methods may be attractive.

In this paper, a comparison of conventional (amplitude and phase) and phaseless (amplitude only) planar near-field measurements for non-ideal measuring probe locations is examined via a simulated array antenna case study. It is hypothesized that the presented phase retrieval algorithm will better reproduce the true pattern of the antenna under test (AUT) because of the diminished sensitivity of the amplitude of the near-field, as compared to the phase, with respect to the measuring probe locations.

Although methods for correcting probe position errors exist for conventional planar near-field measurements [3], they are best suited for small errors and, more importantly, require knowledge of the precise locations at which the measurements were obtained. A phase retrieval approach, on the other hand, requires no knowledge of the actual measurement locations other than the nominal location of the *two* required measurement planes, obviating the need for expensive feedback equipment, e.g. laser interferometry, and should be suitable for even rather large probe position errors, obviating the need for specialized mechanical systems at high frequencies.

PHASE RETRIEVAL ALGORITHM
The phase retrieval algorithm used in this study is based on an iterative Fourier method originally reported in [4] and adapted for use with UCLA's bi-polar planar near-field measurement system in [1]. The procedural steps required for executing this algorithm are depicted in Figure 1. The algorithm requires near-field amplitude measurements on *two* planes (steps 1 and 2) which, both in this study and the studies reported in [1], are separated by just a few wavelengths. A geometric description of the AUT's aperture plane, also commonly referred to as the object or aperture constraint, is also required. The amplitude data on each measurement plane and the AUT aperture constraint comprise the inputs to the Fourier iteration (steps 3-6) used for the phase retrieval. The product of the Fourier iteration is the complex near-field distribution on the AUT aperture plane and each of the two measurement planes. The Fourier iteration ensures, assuming successful retrieval of the phase, that the complex field distribution on these three planes are related by the Fourier transform. This relationship allows the far-field pattern of the AUT to be computed from the complex field distribution on any one of these three planes (step 7), using standard planar near-field techniques.

Fourier Iteration
An initial guess for the amplitude and phase in the aperture plane of the AUT is made and truncated to the known physical extent of the AUT (aperture constraint). This estimate is then propagated, using plane wave spectrum techniques implemented by fast Fourier transform (FFT), out to the first measurement plane. An error metric at this measurement plane is then computed by summing the squared difference of the calculated modulus and measured modulus at each point on the measurement
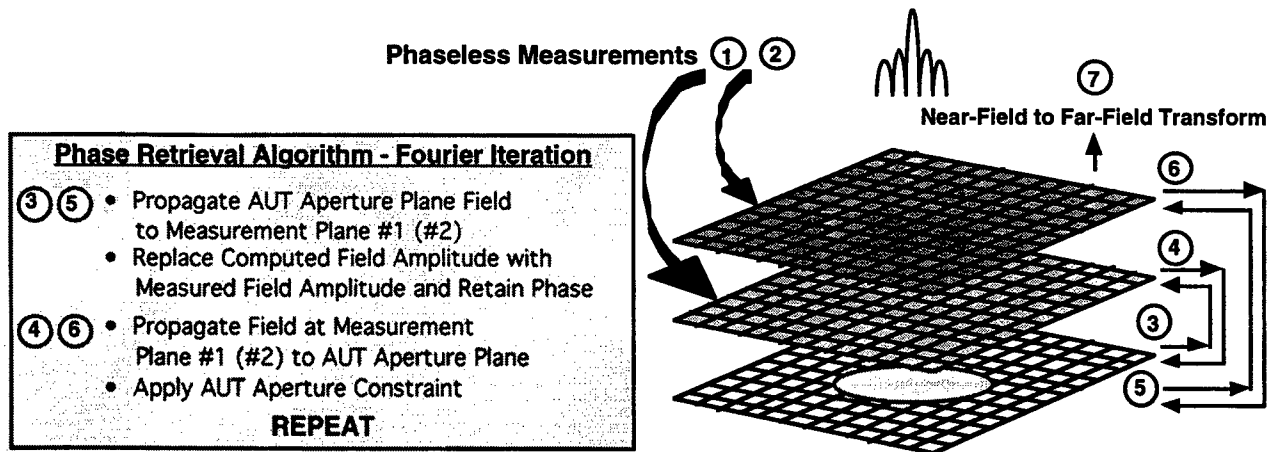
Figure 1. Phase retrieval algorithm.

plane. The computed error metric is stored, the measured modulus replaces the calculated modulus, and the result is propagated back to the AUT aperture plane.

The calculated amplitude and phase at the AUT aperture plane is again truncated to the known physical extent of the AUT and the result is propagated out to the second measurement plane. An error metric, identical to that computed at the first measurement plane, is calculated and stored, the measured modulus replaces the calculated modulus, and result is propagated back to the AUT aperture plane where the calculated amplitude and phase is again truncated to the known physical extent of the AUT.

The computed error metrics on the two measurement planes, at this point, are examined to determine whether iterations should continue. Appropriate stopping criteria include both an absolute error limit and an error convergence limit. If a stopping criterion is met then the retrieved amplitude and phase on the AUT aperture plane and the two measured planes are stored and the iterations terminate. If a stopping criterion is not met then the process is repeated until a stopping criterion is met.

SIMULATION RESULTS

A planar near-field measurement computer simulation for the waveguide-fed slot array antenna shown in Figure 2 has been performed in order to compare the effect of probe position errors on conventional and phaseless measurements. The antenna has been modeled as an array of infinitesimal magnetic dipoles whose excitations have been obtained from the aperture plane fields (holographic image) resulting from the bi-polar planar near-field measurements performed in [1].

Paralleling the measurement scenario in [1], the near-field of the antenna was computed as follows:

1. Amplitude and phase with ideal probe positions on the plane d = 6.255 λ.
2. Amplitude and phase with non-ideal probe positions on a plane nominally at d = 6.255 λ.
3. Amplitude only with non-ideal probe positions (identical to the prior simulation) on a plane nominally at d = 6.255 λ. This simulation is identical to the prior with the phase discarded.
4. Amplitude only with non-ideal probe positions (different from prior simulation) on a plane nominally at d = 8.836 λ.

The near-field was computed on a 128 x 128 square grid with a sample spacing of 0.485 λ. The non-ideal probe positions were modeled as a random set of z-directed (normal to the antenna aperture plane) displacements with a normal distribution of zero mean and 0.1 λ standard deviation.
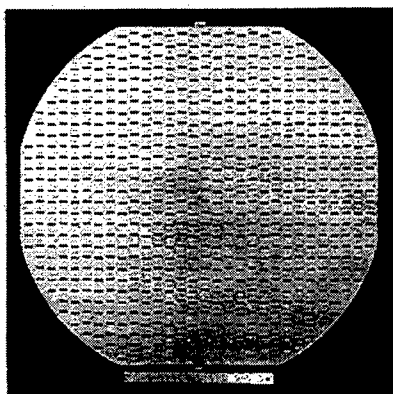
Figure 2. X-band planar waveguide-fed slot array antenna.

The phase retrieval processing of the amplitude only simulations was seeded with a pseudo-random (±3 dB amplitude, ±30° phase, uniformly distributed) estimate for the aperture plane fields. The algorithm terminated after 80 iterations at which point the error metric was reduced to -31.8 dB.

Figures 3a - 3d compare, respectively, the H-plane, E-plane, 45 degree intercardinal plane, and 135 degree intercardinal plane antenna patterns resulting from the amplitude and phase measurement with no probe position errors (reference), the amplitude and phase measurement with probe position errors, and the antenna patterns resulting from the phase retrieval processing of the amplitude only measurements with probe position errors. Figure 4 depicts the antenna patterns over the entire spectral region for the same simulation scenarios. It is obvious, particularly from the intercardinal plane results, that the antenna pattern obtained from the phase retrieval process has considerably better reproduced the true pattern of the antenna than that resulting from the amplitude and phase measurement. A quantitative comparison of some typical antenna pattern parameters justifying this conclusion appears in Table 1.

Figure 3. Comparison of a) H-plane, b) E-plane, c) 45 degree intercardinal plane, and d) 135 degree intercardinal plane far-field patterns for amplitude and phase measurement with no probe position errors (reference), amplitude and phase measurement with probe position errors, and phase retrieval with probe position errors.

527
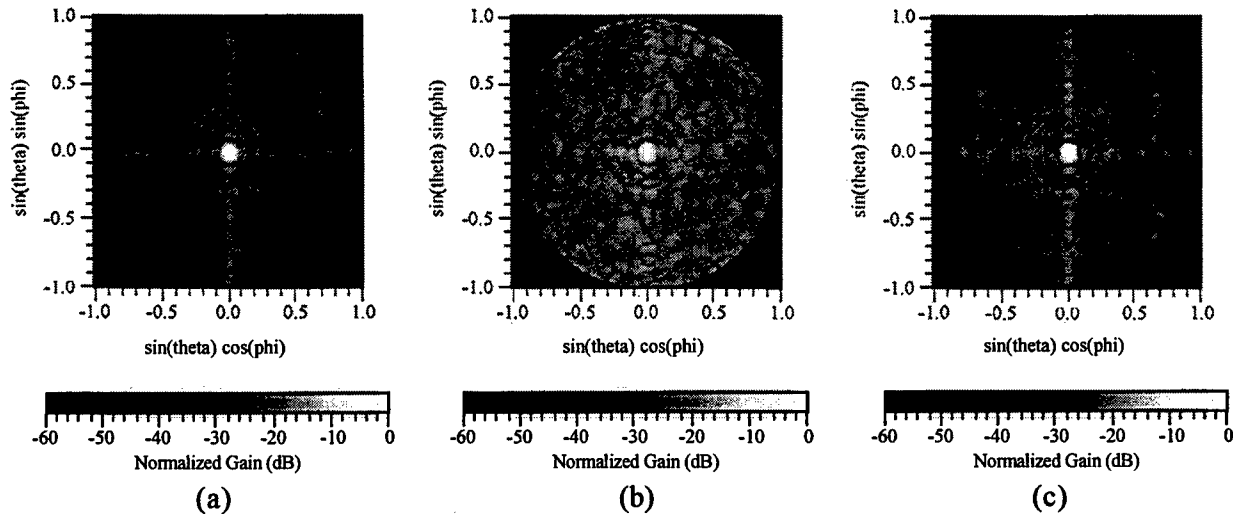
Figure 4. Far-field patterns for a) amplitude and phase measurement with no probe position errors (reference), b) amplitude and phase measurement with probe position errors, and c) phase retrieval with probe position errors.

TABLE 1. COMPARISON OF FAR-FIELD PATTERN STATISTICS.

	Reference	Amp/Phs Meas	Phase Retrieval
H-plane Beamwidth	2.92°	2.91°	2.92°
E-plane Beamwidth	3.42°	3.40°	3.39°
Directivity	35.49 dB	33.77 dB	35.55 dB
Average Sidelobe Level	-44.62 dB	-35.07 dB	-44.71 dB
Peak Sidelobe Level	-24.33 dB	-20.99 dB	-23.61 dB

CONCLUSION

The case study explored in this paper has demonstrated that the presented phase retrieval method can reproduce the true pattern of an array antenna with greater accuracy than that obtainable with a conventional amplitude and phase measurement when the measurement is contaminated with probe position errors. Distinguishing advantages of the phase retrieval processing are the absence of a requirement to know the actual measurement locations (other than the nominal location of the two required measurement planes) and the ability to obtain the true antenna pattern even when subject to relatively large probe position errors. These advantages offer the possibility, for example, of performing high frequency measurements with ordinary measurement apparatus and performing measurements "in the field" where measurement conditions are less controlled than in a laboratory environment.

Finally, although the probe position error model presented was of a random type, it is not believed that systematic errors should present any obstacles obscuring the conclusions formulated here. Future work will explore systematic error models in greater detail.

REFERENCES

[1] R.G. Yaccarino and Y. Rahmat-Samii, "Phaseless bi-polar planar near-field measurements and diagnostics of array antennas," *IEEE Trans. Antennas Propagat.*, vol. 47, pp. 574-583, March 1999.

[2] T. Isernia, G. Leone, and R. Pierri, "Radiation pattern evaluation from near-field intensities on planes," *IEEE Trans. Antennas Propagat.*, vol. 44, pp. 701-710, May 1996.

[3] L.A. Muth and R.L. Lewis, "A general technique to correct probe-position errors in planar near-field measurements to arbitrary accuracy," *IEEE Trans. Antennas Propagat.*, vol. 38, pp. 1925-1932, December 1990.

[4] A.P. Anderson and S. Sali, "New possibilities for phaseless microwave diagnostics - Part I: Error reduction techniques," *Proc. Inst. Elect. Eng.*, vol. 132, pp. 291-298, August 1985.

MUTUAL COUPLING-BASED CALIBRATION OF PHASED ARRAY ANTENNAS

Charles Shipley and Don Woods

Technology Service Corporation, 11400 West Olympic Blvd Suite 300, Los Angeles California 90064.
E-mail: cshipley@tsc.com, dwoods@tsc.com

Abstract: *Calibration of phased arrays is typically performed once during the manufacturing process, and requires large near-field or far-field antenna ranges. Technology Service Corporation (TSC) has demonstrated that by utilizing element mutual coupling characteristics, modern arrays can be accurately calibrated using only existing array elements as sources. Arrays can therefore be calibrated and re-calibrated using an automated on-board procedure, without taking the antenna out of service. This paper discusses the theory of calibration using mutual coupling, and shows successful results of tuning a modern 808-element pre-production antenna using the mutual coupling technique.*[1]

Introduction

Modern phased arrays typically have excellent performance, but still must occasionally undergo phase and amplitude calibration in order to realize their full performance potential. This must be done at least upon completion of antenna fabrication. At the factory, this initial calibration is usually done on a near-field scanning or compact range, and is typically very time consuming. Re-calibration after operational deployment is also required to maintain peak performance levels, but is typically not done, due to practical difficulties. Re-calibration is also needed if repairs or changes are made in the antenna.

TSC has developed a calibration technique that exploits the inherent mutual coupling among the radiating elements. It is readily implementable in Solid State Active Arrays (SSAA) for radar, which typically have T/R modules at every radiating element and an inherent high degree of controllability. The technique is called "Mutual Coupling Auto-Calibration", or simply "Auto-Calibration". The calibration procedure is also useful to identify failed or defective elements so that corrective algorithms can be applied.

The minimum antenna requirements are:

- Separate or isolated transmit and receive antenna ports.
- Individual control of phase, attenuation, and off-on switching of every transmit and receive module.
- A network analyzer-type device coupled to the transmit and receive ports.
- Special software loaded into the beam steering computer for the calibration mode.

Theory and Technique

There is always coupling of RF energy among the radiating elements in any array antenna. In arrays with the elements on a regular grid spacing, and made with good tolerances, this mutual coupling is the same for all like pairs of adjacent elements in the array aperture. This includes active edge elements, if there are at least two rows of dummy elements around the aperture periphery, as is common in low-sidelobe, low-RCS designs. Auto-Calibration depends on the consistency of these mutual coupling coefficients.

Auto-Calibration also depends on the ability to simultaneously transmit and receive on pairs of adjacent elements throughout the array. An SSAA design can easily accommodate this by independently switching on and off the transmit and receive channels to individual elements.

The general procedure is to compare the channels leading to all the elements in the array to determine their phase and amplitude biases. Since the mutual coupling coefficients of like element pairs are all the same, the coupling coefficients cancel from the measured transmittance between the elements. The signal differences are therefore due simply to the bias errors of the element-to-beam port channels.

The mutual coupling technique was conceived and developed at TSC without knowledge of similar previous work [Ref. 1]. That work was performed on a space-based radar array with separate transmit and receive monopole elements, and an element grid based on equilateral triangles. The TSC technique expands on that basic application by extending the technique to arrays with the more common asymmetric element spacing, to conformal arrays, and in which elements are used for both transmit and receive.

For the case of an equilateral triangle grid of monopole elements, each element pattern is circularly symmetric in the plane of the array, and the six nearest neighbor elements are at the same distance from the center element. This results in the same mutual coupling coefficient between the center element and each of the six nearest neighbors. If one transmits from the center element and receives at the other six, the received amplitude and phase will be the same, aside from the calibration biases, which are to be measured. The six received signals directly give a measure of the amplitude and phase imbalances among the six receive elements, which are the calibration coefficients.

A different situation is with isosceles triangle grids, and with equilateral triangle grids when the element patterns are not rotationally symmetric, such as with slot elements. The same coupling coefficient exists between the center element and four of the six surrounding elements. If a signal is transmitted from the center element in this arrangement, one expects the same received signal at the four symmetric elements. Those four elements can be brought into calibration by applying the proper complex multipliers to the respective received signals.

The procedure requires that the array transmit on a single element, while simultaneously receiving from an adjacent element. The transmittance measurement is stored, and a different transmit and/or receive element is selected for the next measurement. The T/R modules are switched off and on under control of the beam steering computer driven by the special Auto-Calibration software. Measurements are made of the entire array in that fashion.

Figure 1 shows how the measurements can be tied together to form calibration estimates over a slotted element array. In Step 1, four symmetric, pair-wise measurements are made, using a common transmit element. Using those results, one can form the complex calibration ratios for elements 1 through
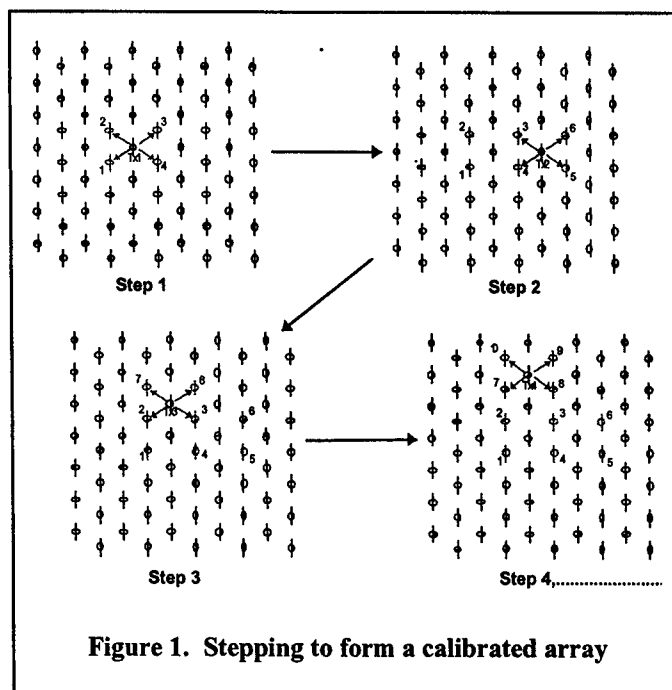
Figure 1. Stepping to form a calibrated array

530

4. In Step 2, the transmit element is changed, and four more measurements are made. With that data, elements 3 through 6 can be tied together, and those, in turn, to elements 1 and 2. Steps 3 and 4 show the transmit element being moved around, and the four measurements that are made from each position. The result after Step 4 shows that continuing in that fashion produces enough data to calibrate only the even columns, as indicated by the developing pattern of red elements.

Although we called them "steps", the measurements can be made in any order. The only requirement is to make measurements using all available element pairs. The resulting set of pair-wise measurements forms an overdetermined system of complex element weights. Although one could in theory determine a least-squares optimal set of complex calibration weights, for our tests we employed a more brute force, iterative stepping technique.

Calibration of the transmit state is performed identically to that of the receive state, but the transmit and receive elements are switched. A few minor considerations are required, e.g. to not operate receive elements in their saturated range.

The odd columns can similarly be calibrated to one another. The result is two interleaved subarrays, each of which is self-calibrated; but they cannot be referenced to each other by using adjacent element measurements. We call this condition is the "two-array ambiguity".

Figure 2 shows non-adjacent elements that can be used to find the amplitude and phase that will tie together the two separately calibrated arrays indicated by the red elements, "A", and the green elements, "B". Since the array is precisely fabricated, geometrically identical pairs of elements have the same mutual coupling coefficients. These are indicated by m_1 and m_2. We make the four separate pair-wise measurements by transmitting on T_a and T_b, and receiving on R_a and R_b. The four measurements can be combined as a ratio to obtain $(R_b/R_a)^2$. This complex ratio ties together the two interlaced subarrays to complete the full calibration.
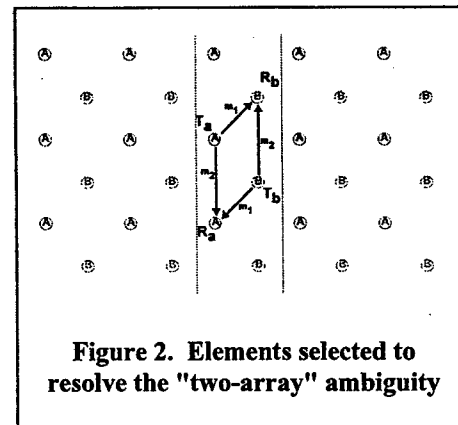
Figure 2. Elements selected to resolve the "two-array" ambiguity

One minor point is that we require the square root of the complex ratio $(R_b/R_a)^2$, which has a sign ambiguity. The far-field pattern will have a null on boresight if the wrong sign is selected. There are simple techniques to determine the proper sign. One can use a compact range or far field measurements once during fabrication to determine the values of m_1 and m_2, which will resolve the sign.

Results
The Auto-Calibration technique was thoroughly tested by the Northrop-Grumman Corporation (NG), under subcontract to TSC. The test array is a sophisticated, high performance SSAA, circular, with 808 elements on an isosceles triangle grid. The tests were extremely successful. The phase and amplitude alignment of the element channels using the TSC technique exceeded the performance of the compact range alignment routinely done by NG. In fact, Auto-Calibration uncovered a previously unknown leakage problem within the pre-production array on which the technique was first tested.
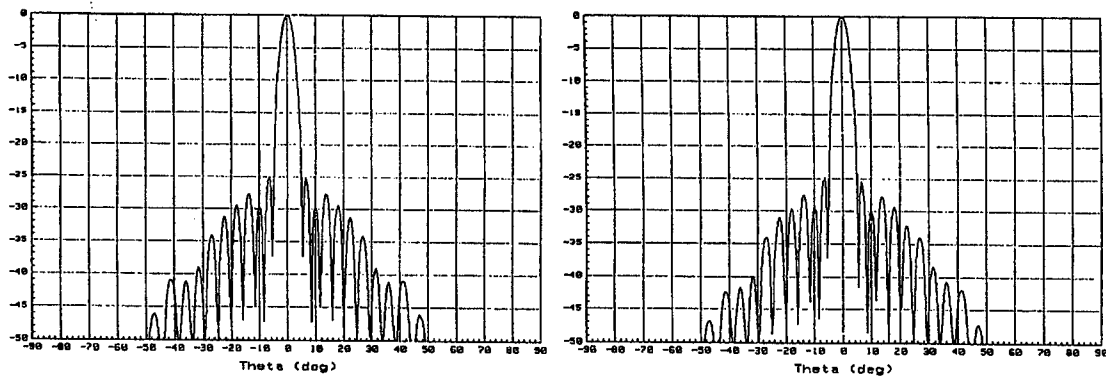
Figure 3. Theoretical and calibrated elevation patterns

The array was set to use 25 dB Taylor weighting. Figure 3 shows the theoretical elevation pattern on the left, and the pattern achieved by Auto-Calibration on the right. The calibration was started with random settings on the phase shifters and amplitude attenuators. The measure of merit is how well the calibrated pattern approaches the theoretical pattern. The results are excellent; the patterns are virtually identical.
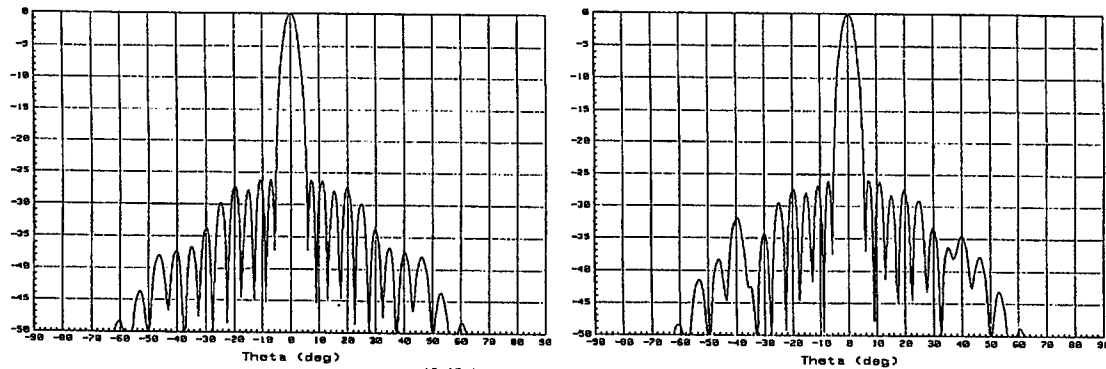
Figure 4. Theoretical and calibrated azimuth patterns

Figure 4 shows the results for the azimuth patterns. These are not quite as good as for elevation, but are still very good. The higher sidelobes beyond 40 degrees in azimuth result from residual RF leakage between element column pairs behind the aperture. An analysis of the residual amplitude and phase errors shows that Auto-Calibration will support sidelobe levels of -53 dB in the 800-element array.

Reference

[1] H.M. Aumann, A.J. Fenn, F.G. Willwerth, "Phased Array Antenna Calibration and Pattern Prediction Using Mutual Coupling Measurements", *IEEE Trans. Antennas Propagation*, Vol 37, No 7, pp 844-850, July 1989.

Phased Array Calibration

Ron Sorace, *Hughes Space & Communications Co., El Segundo, CA*

Since accurate pointing of a beam of a phased array antenna demands precise control of phase and amplitude, periodic calibration of the gain and phase of the electronics is essential. Calibration may be performed by pointing a beam of an array at a fixed location and transmitting or receiving signals that permit calibration of individual elements. To calibrate the entire array, the procedure must be repeated for each element. Note that pointing a beam at a fixed station assumes that dependence of calibration on direction is negligible. If parameters are sensitive to pointing direction, then an alternative such as multiple stations must be implemented.

To calibrate a beam for a single element of an array, the phases of all elements for that beam are set to the current corrected phase state for pointing the beam at a fixed station, and the phase settings for the beam position are regarded as the 0° state. Typically, the phase corresponding to the beam for the element being calibrated is cycled through all possible phase settings [1], and the received or transmitted power is measured at each setting. The potential impact on the service of the array depends on the number of repetitions, the number of phase settings, and the time for measurement at each setting. The proposed method of calibration reduces the overhead by performing measurements at four orthogonal phase settings [2]. This yields sufficient information to obtain a maximum likelihood estimate of the calibration offset.

Figure 1. Array Calibration Signal Structure
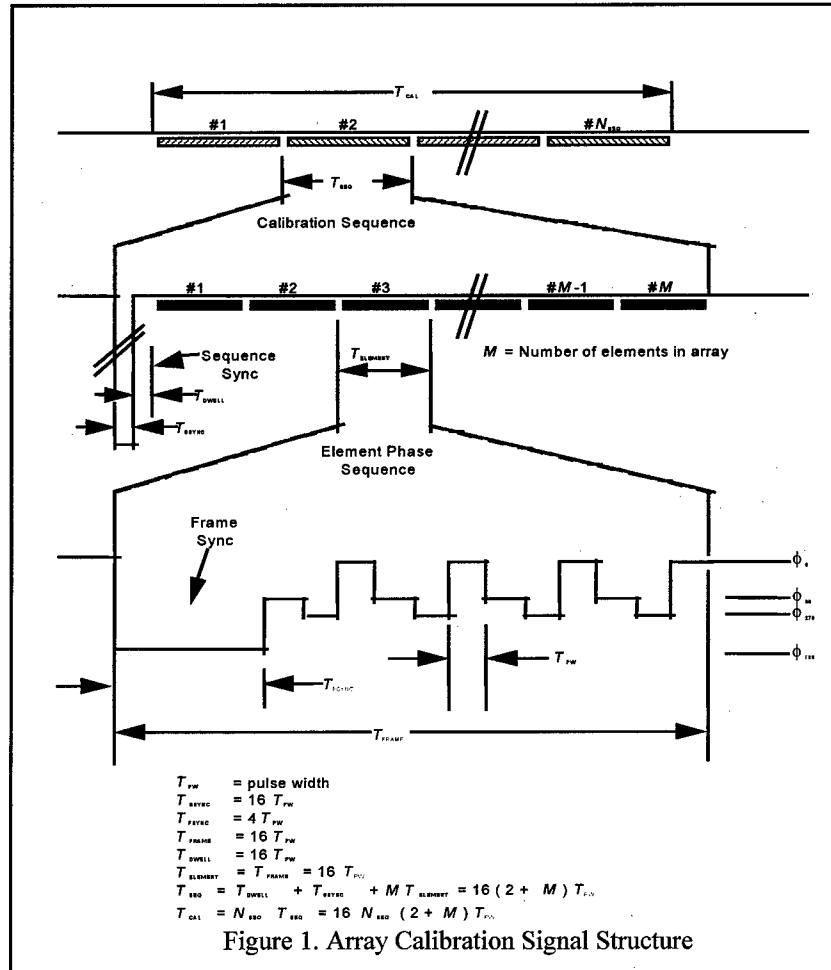
Figure 1 illustrates the calibration sequence generated by the array. The sequence, which is repeated N_{SEQ} times, starts with a synchronization time T_{SSYNC} during which the phase of every odd-numbered element is switched by 180° to produce a signal null. This null is followed by a dwell time T_{DWELL} during which all array elements remain at their 0° state and one repetition of the element phase sequence for each element in the array. The individual element phase sequence starts with a phase transition from the 0° state ϕ_0 to the 180° state ϕ_{180} for a time T_{FSYNC} to provide unambiguous synchronization and a power measurement P_{180} at the receiver. Subsequently, the phase is toggled by 90° , 270°, and 0° between states ϕ_{90}, ϕ_{270}, and ϕ_0 with corresponding power measurements P_{90}, P_{270}, and P_0

Ron Sorace (ronald.sorace@hsc.com)
HSC, P.O. Box 92919, SC/S13/G343
Los Angeles, CA 90009

being performed. The times given in Figure 1 are representative of the timing parameters for the calibration sequence. The sample interval of T_s must be chosen according to the Nyquist criterion, and the filter bandwidth must be chosen to limit the input noise while passing the desired signal.

Special cases occur within the frame pattern when the element phase error δ_k is close to one of four values. When δ_k is approximately either 90° or 270°, P_0 and P_{180} are approximately equal, and the transition from ϕ_0 to ϕ_{180} may not be detected. However, the transition from ϕ_{180} to ϕ_{90} at the end of the frame will be detected as will the transitions from ϕ_{270} to ϕ_{180} and from ϕ_{180} to ϕ_{90} at the start of the second repetition of the phase pattern. Similarly, when δ_k is approximately either 45° or 235°, P_{180} and P_{90} are approximately equal, so the transition from ϕ_{180} to ϕ_{90} may not be detected. In this case the transition from ϕ_0 to ϕ_{180} at the beginning of the long pulse will be detected as will the same transition at the start of the second repetition of the phase pattern. Thus, the phase pattern can be correctly synchronized in all cases.

The measurement system is depicted in Figure 2 and consists of a narrowband filter followed by a quadratic detector whose output voltage is proportional to the power of the RF signal. Quadratic detection is preferable to a correlation receiver which requires carrier recovery that is susceptible to timing variation.

The received voltage at the input to the power detector when all elements are set to their nominal phases can be written $r(t) = \sum_{m=1}^{M} a_m \cos(\omega t + \delta_m) + n(t)$ where ω is the transmitted frequency, δ_m is the phase offset of the mth element relative to its nominal value, a_m is the RF voltage from the mth element, and $n(t)$ is narrowband noise which is uncorrelated between samples. The narrowband noise is given by $n(t) = n_c(t)\cos\omega t - n_s(t)\sin\omega t$ where $n_c(t)$ and $n_s(t)$ are the inphase and quadrature components, respectively. These components are independent and

Figure 2. Measurement System

identically distributed Gaussian processes having zero mean and variance $\sigma^2 = N_0 B$ with $N_0/2$ the noise power density and $2B$ the bandwidth of the filter. Introducing a phase of θ on the kth element yields

$$r(t) = \left[\sum_{\substack{m=1 \\ m \neq k}}^{M} a_m \cos\delta_m + a_k \cos(\theta + \delta_k) + n_c(t) \right] \cos\omega t - \left[\sum_{\substack{m=1 \\ m \neq k}}^{M} a_m \sin\delta_m + a_k \sin(\theta + \delta_k) + n_s(t) \right] \sin\omega t$$

at the input to the power detector. The output from the power detector is the square of the envelope of its input $q = \left(A_c + v_c + n_c \right)^2 + \left(A_s + v_s + n_s \right)^2$ where $A_c = \sum_{\substack{m=1 \\ m \neq k}}^{M} a_m \cos\delta_m$, $A_s = \sum_{\substack{m=1 \\ m \neq k}}^{M} a_m \sin\delta_m$,

$v_c = a_k \cos(\theta + \delta_k)$, and $v_s = a_k \sin(\theta + \delta_k)$. The output of the power detector is sampled at a time interval $T_s \gg 1/B$ so that the samples are uncorrelated. The sampled output of the power detector is $q_\lambda = \left(A_c + v_c + n_{c\lambda} \right)^2 + \left(A_s + v_s + n_{s\lambda} \right)^2$ where the variables $n_{c\lambda}$ and $n_{s\lambda}$ are Gaussian variables as described previously. For each element the statistic q_λ is a noncentral chi-squared random variable with two degrees of freedom, density $p(q_\lambda) = \left(2\sigma^2 \right)^{-1} \exp\left[-\left(q_\lambda + \lambda \right) / 2\sigma^2 \right] I_0 \left(\dfrac{\sqrt{q_\lambda \lambda}}{\sigma^2} \right)$, and

noncentral parameter $\lambda = \left(A_c + v_c \right)^2 + \left(A_s + v_s \right)^2$. The mean and variance of the statistic q_λ are

$\mu = E\{q_\lambda\} = \lambda + 2\sigma^2$ and $\sigma_q^2 = Var\{q_\lambda\} = 4\sigma^2\lambda + 4\sigma^4$, respectively, and $I_0(\cdot)$ denotes the modified Bessel function of the first kind of order zero.

If L independent samples of the output of the power detector are averaged to form the statistic $\overline{q}$, then the statistic $\overline{q}$ is a noncentral chi-squared random variable having $2L$ degrees of freedom with noncentral parameter $\overline{\lambda} = \frac{1}{L}\sum_{\lambda=1}^{L}\left[\left(A_c + v_c\right)^2 + \left(A_s + v_s\right)^2\right] = \lambda$. The density of $\overline{q}$ is

$$p(\overline{q}) = \left(\frac{2\sigma^2}{L}\right)^{-1}\left(\frac{\overline{q}}{\lambda}\right)^{\frac{L-1}{2}}\exp\left[-\frac{\overline{q}+\lambda}{2\sigma^2/L}\right]I_{L-1}\left(\frac{\sqrt{\overline{q}\lambda}}{\sigma^2/L}\right)$$

with mean $\overline{\mu} = E\{\overline{q}\} = \mu = E\{q\} = \lambda + 2\sigma^2$ and variance $\overline{\sigma}^2 = Var\{\overline{q}\} = \left(4\sigma^2\lambda + 4\sigma^4\right)/L$. The statistic $\overline{q}$ is an unbiased estimate of μ since $E\{\overline{q}\} = \frac{1}{L}\sum_{\lambda=1}^{L}E\{q_\lambda\} = E\{q\} = \lambda + 2\sigma^2$, and this estimate is asymtotically efficient.

Although the gradient of the likelihood function gives maximum likelihood estimates for the phase variation δ_k and the amplitude variation a_k, the estimate of μ is a biased estimate of λ that may be solved for δ_k and a_k. The bias in the sample mean may be removed by considering of the differences $\overline{q}_{270} - \overline{q}_{90} = 4a_k\left(A_c\sin\delta_k - A_s\cos\delta_k\right)$ and $\overline{q}_0 - \overline{q}_{180} = 4a_k\left(A_c\cos\delta_k + A_s\sin\delta_k\right)$ which are unbiased estimates. Note that the element index k is understood for the statistics $\overline{q}$, and the power is measured for each phase setting of each element. Since only the phase of the kth element is varying, the sum of the other element voltages forms the reference, i.e., $A_s \cong 0$, which gives $\overline{q}_{270} - \overline{q}_{90} \cong 4a_kA_c\sin\delta_k$ and $\overline{q}_0 - \overline{q}_{180} \cong 4a_kA_c\cos\delta_k$. Hence, the estimates of the phase and amplitude variations become

$$\hat{\delta}_k = \tan^{-1}\left(\frac{\overline{q}_{270} - \overline{q}_{90}}{\overline{q}_0 - \overline{q}_{180}}\right) \qquad \text{and} \qquad \hat{a}_k = \frac{\sqrt{\left(\overline{q}_{270} - \overline{q}_{90}\right)^2 + \left(\overline{q}_0 - \overline{q}_{180}\right)^2}}{4A_c}.$$

The deviations of these estimates are readily derived from first order differentials

$$\hat{\sigma}_\delta^2 \cong \sum_\theta\left(\frac{\partial\hat{\delta}_k}{\partial\overline{q}_\theta}\right)^2\sigma_\theta^2 = \frac{\sigma^2/L}{2a_k^2A_c^2}\left(\sigma^2 + A_c^2 + A_s^2 + a_k^2\right) \text{ and } \hat{\sigma}_a^2 \cong \sum_\theta\left(\frac{\partial\hat{a}_k}{\partial\overline{q}_\theta}\right)^2\sigma_\theta^2 = \frac{\sigma^2/L}{2A_c^2}\left(\sigma^2 + A_c^2 + A_s^2 + a_k^2\right).$$

Since the elements are driven approximately equally, $a_m \cong a_k$ for all m and $A_c \cong (M-1)a_k$. Using the approximation $A_s \cong 0$ gives errors $\hat{\sigma}_\delta^2 \cong \frac{N_0B}{4LP_k}\left[1 + \frac{N_0B}{2P_k\left(M-1\right)^2}\right]$ and $\hat{\sigma}_a^2 \cong \frac{N_0B}{2L}\left[1 + \frac{N_0B}{2P_k\left(M-1\right)^2}\right]$

where $P_k = a_k^2/2$ denotes the power of the kth element. A plot of the deviation of the phase error estimate $\hat{\sigma}_\delta$ indicates that an accuracy of $2°$ requires approximately twelve iterations at a signal-to-noise power ratio of approximately 13 dB per element. Since the residual phases of all elements other than the kth element were disregarded, the estimates of δ_k and a_k are relative to the aggregate of the other elements. Note that this reference varies depending on which element is being tested. Hence, caution must be exercised to update the element corrections only after calibration of the entire array.

The transition in the phase sequence at the initiation of calibration must be immediately detectable to achieve synchronization. A transition in phase from θ to ϕ is detected by comparing the difference $q_\theta - q_\phi$ to a threshold τ which is set nominally at the mid-point of the range $\tau = \left(q_\theta - q_\phi\right)/2 \cong 4(M-1)P_k$. The probability of this transition being detected is $P_{\theta\phi} = \Pr\{q_\theta - q_\phi > \tau\}_\phi = \int_0^\infty p(q_\phi)\int_{q_\phi+\tau}^\infty p(q_\theta)\,dq_\theta dq_\phi$. In particular, the false alarm rate is

535

$P_{fa} = \Pr\{q_\theta - q_\phi > \tau \mid \theta = \phi\} = \int_0^\infty p(q_\theta) \int_{q_\theta + \tau}^\infty p(q_\theta') \, dq_\theta' \, dq_\theta$, and the probability of detection is

$P_D = \Pr\{q_\theta - q_\phi > \tau \mid \theta - \phi = \pi\} = \int_0^\infty p(q_\phi) \int_{q_\phi + \tau}^\infty p(q_\theta) \, dq_\theta \, dq_\phi$ where $p(\cdot)$ is the noncentral chi-squared density.

These integrals are difficult to evaluate, but the variable $q = q_\theta - q_\phi$ may be approximated by a Gaussian distribution with mean $E\{q\} = \lambda_\theta - \lambda_\phi$ and variance $\sigma_q^2 = 4\sigma^2(\lambda_\theta + \lambda_\phi + 2\sigma^2)$ to obtain

$$P_{fa} = \frac{1}{\sqrt{2\pi}\sigma_{fa}} \int_\tau^\infty e^{-q^2/2\sigma_{fa}^2} dq = 1 - Q(\tau/\sigma_{fa}) = 1 - Q\left(\frac{M-1}{M} \sqrt{\frac{P_k}{N_0 B}} \middle/ \sqrt{1 + \frac{N_0 B}{2 P_k M^2}} \right)$$

and

$$P_D = Q\left(\frac{(M-1)}{\sqrt{(M-1)^2+1}} \sqrt{\frac{P_k}{N_0 B}} \middle/ \sqrt{1 + \frac{N_0 B}{2 P_k \left[(M-1)^2 + 1 \right]}} \right)$$

where $\sigma_{fa}^2 \cong 8\sigma^2(2P_k M^2 + \sigma^2)$, $\mu_D \cong 8(M-1)P_k$, $\sigma_D^2 \cong 8\sigma^2(2P_k \left[(M-1)^2 + 1 \right] + \sigma^2)$, and the standard Gaussian distribution function is $Q(z) = (1/\sqrt{2\pi}) \int_{-\infty}^z e^{-x^2/2} dx$. Observe that a false alarm rate of 10^{-6} requires a signal-to-noise power of approximately 13 dB and indicates a probability of detection in excess of 99% for a thirty-six element array.

The quantization step size of the A/D converter must be sufficiently small to measure the smallest voltage change that will occur at the output of the detector. To cover the range of the possible inputs, the ratio of the A/D converter full scale reading to that of its least significant bit must be greater than or equal to the ratio of the full scale voltage to the minimum detectable voltage step. The smallest voltage change that is measured is $\Delta q_{RF} = \bar{q}_{90} - \bar{q}_{270} = 4(M-1)a_k^2 \sin\delta$, and the full scale voltage is proportional to the peak RF power $P_{PEAK} \approx M^2 a_k^2$, so the minimum number of bits to detect a change of δ in the phase of a single element in the absense of noise is $B_{min} = \log_2\left(\frac{P_{PEAK}}{\Delta P_{RF}} \right) = \log_2\left[\frac{M^2}{4(M-1)\sin\delta} \right]$. The required minimum number of bits for a measurement resolution of $\delta = 2°$ for a thirty-six element array is 8.05. However, the signal-to-quantization-noise ratio must be at least 10 dB greater than the signal-to-noise-power ratio to preclude degradation from quantization. For a peak loaded A/D converter this ratio is approximately $SQN = 6.02B + 1.77$ dB, so that eight bits is almost 40 dB above the signal-to-noise-power ratio.

In summary, calibration of a phased array may be accomplished remotely by cycling the phases of elements through only four orthogonal phases and using a maximum likelihood algorithm for optimal accuracy. For a given calibration measurement the corrected estimates $\tilde{\delta}_k$ and $\tilde{\alpha}_k$ of the phase and amplitude errors may be computed recursively from the previous corrections. Adjustment of the calibration and amplitude corrections must be performed iteratively until acceptable accurracy is achieved.

References

[1] Katagi, T., Konishi, Y., Tamai, Y., and Iida, Y. "A Large Deployable Active Phased Array Antenna for Satellite Use," *Proceedings of the American Institute of Aeronautics and Astronautics*, AIAA-94-1070-CP, pp. 1075-1084, 1994.

[2] Sorace, R., Reinhardt, V., and Chan, C. " Phased Array Calibration by Orthogonal Phase Sequence," Hughes Patent Disclosure PD-970039, December 15, 1997.

[3] Collin, R.E. and Zucker, F.J. *Antenna Theory, Part 1*, Ch. 5, Mc-Graw-Hill, New York, 1969.

[4] Skolnik, M.I. *Radar Handbook*, Ch. 9, Mc-Graw-Hill, New York, 1970.

WP3

Adaptive Array Antennas

Adaptive Array Antennas

Adaptive Clutter Cancellation for Element-Digitised Airborne Radar

J. L. Mather[†], H. D. Rees[†], M. Cook[‡], J. Wood[‡]

† Signal Processing Group, DERA, St. Andrew's Road, Malvern, Worcs., WR14 3PS, U.K.
Email: mather@signal.dera.gov.uk Internet: http://spg.dera.gov.uk/
‡ Marconi Electronic Systems Ltd, Marconi Research Centre, Chelmsford, UK.

Abstract

We describe a multi-layer adaptive beamforming method, for a large element-digitised array radar (EDAR). Range-dependent gain adaption (RDGA) at each array element offers effective cancellation of clutter. Simulations of airborne intercept (AI) radar demonstrate the power of this approach and illustrate its robustness to random phase and amplitude errors in the array.

1. Introduction

The performance and availability of digital technology - from analogue-to-digital converters (ADCs) to digital signal processing - continue to increase, whilst costs plummet. There has been similar progress in the technology for producing microwave integrated circuits.

As a result, it is now realistic to consider element-level digitisation for large phased array radars, as opposed to the current state-of-the-art, which is based on sub-array digitisation. Benefits include

- improved ability to compensate for mismatches in analogue components (or the ability to use cheaper, less well-matched analogue components);

- the ability to form multiple simultaneous low-sidelobe receive-beams, accelerating surveillance; and

- new opportunities for the design of the adaptive beamforming system, offering improved cancellation of unwanted signals.

The challenge is to exploit the additional degrees of freedom without demanding unrealistic numbers of data samples, and without requiring unrealistically high levels of computation for calculation of the beamforming weights.

In this paper, we concentrate on the problems and potential for adaptive beamforming in a fully-digitised forward-looking airborne phased array, such as might be fitted in a fighter aircraft. Section 2 reviews the basic processing scheme [1]. Section 3 provides simulation results, and shows the effect of random phase and amplitude errors on the clutter cancellation performance.

2. Element digitised array radar

2.1 Cancellation of clutter from airborne radar

In simple terms, detection of targets by an airborne radar may be limited by (a) thermal noise; (b) jamming or other interference; (c) clutter. For a particular power-aperture product, thermal noise sets the ultimate limit. In phased arrays, fixed taper weighting can keep sidelobe gains low, reducing sensitivity to sidelobe jamming and clutter. However, at low altitude, clutter breaks through and masks targets. Phased arrays can be designed to adapt their gain to the environment. To date, in large arrays, individual elements have been grouped into (typically 16) sub-arrays, the outputs of which are weighted adaptively and then summed. Due to the small number of degrees of freedom, it is possible to suppress only a limited number of point-source jammers. Spatial adaption has been largely ignored for cancellation of distributed clutter.

Two approaches can be taken to increase the number of degrees of freedom. Firstly, a tapped delay line can be used on each sub-array output to create a Doppler-frequency dependent weight vector. This leads to space-time adaptive processing (STAP) [2], which is very well suited to removing the clutter seen from a sideways-looking airborne radar. A second method is to increase the number of sub-arrays. This can be increased until the array is completely digitised. However, if the usual sample-matrix inversion adaptive algorithm is similarly extended, element digitised adaptive beamforming becomes impractical for large arrays because too many data samples are required to estimate the covariance matrix, and the number of digital operations to invert the covariance matrix becomes too large. Below, we describe a new processing architecture, which allows us to calculate element-level weights without these problems.

2.2 Range Dependent Gain Adaption (RDGA)

Within a single range gate, clutter observed by the radar subtends a limited solid angle. Range dependent gain adaption (RDGA) involves calculating an adapted beamforming weight vector for each range gate. Thus, it is not necessary to maintain ultra-low sidelobes for all

angles of arrival - only for angles corresponding to the clutter within the range gate of interest. An $n \times m$ matrix of data is used to calculate the weight vector, where n is the number of antenna elements and m is the number of pulses. At high PRF, range ambiguous clutter returns are received. This is indicated in Fig. 1, where the radar is at an altitude h above a flat earth. A target is at a distance of $R_t = n_t R_a + d_t$, where n_t is an integer, R_a is the range ambiguity given by $R_a = cT/2$, T is the pulse repetition interval (PRI) and $c = 3 \times 10^8$ m/s. After an initial period of n_t pulses has elapsed, the target return lies in all m samples. Each sample contains clutter from rings on the ground located between distances of $R_a + d_t - a$ to $R_a + d_t + a$, $2R_a + d_t - a$ to $2R_a + d_t + a$, ..., $pR_a + d_t - a$ to $pR_a + d_t + a$, where $a = c\tau/2$ and τ is the pulse length.

To cancel the clutter spatially, broad gain minima must be formed over the clutter bands. Sidelobes may increase in other directions. This reduces array efficiency, but does not increase sensitivity to other interference since signals corresponding to intermediate ranges have been gated out. Although we have described a high pulse-repetition-frequency (HPRF) mode of operation, the method can be extended easily for low and medium PRF.

2.3 Domain Factorisation

In this paper, we consider a planar array of $n = 1387$ elements, whose locations are shown in the bottom right of Fig. 2. We assume that all elements have been matched, using digital correction. Element-level weights are calculated by breaking down the processing into smaller stages, or *domains*, as illustrated in Fig. 2. The first domain, shown in the top left of Fig. 2, consists of $n_1 = 19$ elements taken around the array centre. The second domain, of $n_2 = 49$ points, is shown in the top right of Fig. 2. The third domain, of $n_3 = 55$ points (in randomised positions, to minimise grating effects [1]) is shown at the bottom left. In domain q, a weight vector
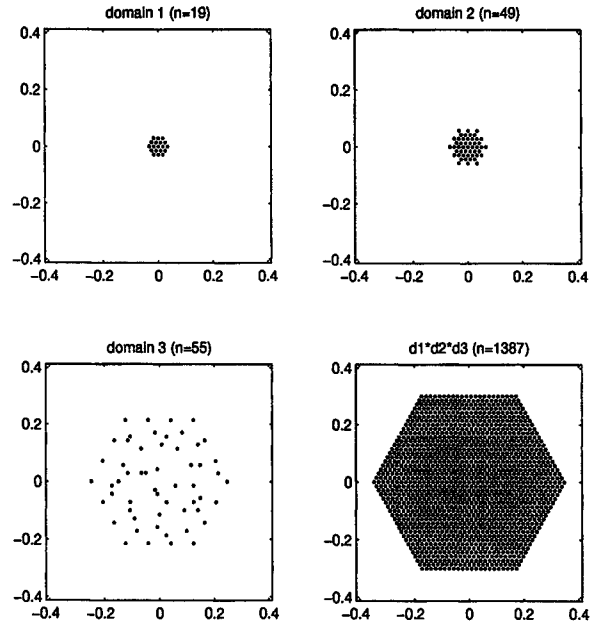
Figure 2. Three-layer domain factorisation of a 1387 element X-band array. Axes show dimensions in metres.

$w^{(q)}$ of dimension $n_q \times 1$ is calculated adaptively from an $n_q \times m$ matrix of signals $X^{(q)}$, where m is the number of time samples.

Define the data at a single domain element to be the $1 \times m$ vector $x(r)$ where r is the position vector of the element. The $n_1 \times m$ matrix $X^{(1)}$ which is used to calculate the weights in domain 1 is given by

$$X^{(1)} = \left[x_1^{(1)} \ x_2^{(1)} \ ... \ x_{n_1}^{(1)} \right]^T, \tag{1}$$

where T denotes the matrix transpose. $x_i^{(1)}$ is the data time-series from the ith element in domain 1, given by
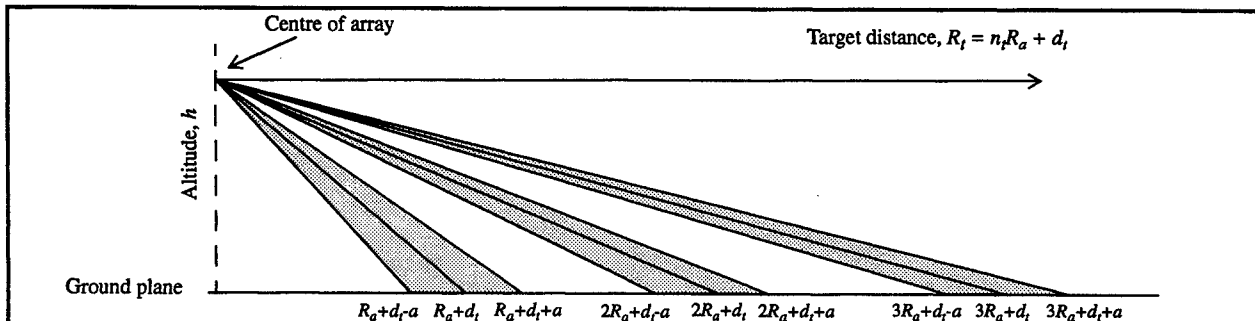
Figure 1. Using a HPRF waveform, clutter is received from multiple ambiguous ranges. Adaption to the clutter is achieved by calculating a unique weight vector for this range gate.

$x_i^{(1)} = x(r_i^{(1)})$, where $r_i^{(1)}$ is the position vector of the ith element.

Having obtained the domain 1 weight vector $w^{(1)} = \left[w_1^{(1)} \; w_2^{(1)} \; ... \; w_{n_1}^{(1)} \right]^T$, shifted versions of domain 1 then form n_2 overlapping sub-arrays, centred about the domain 2 points. The inputs to domain 2 are then

$$x_j^{(2)} = \sum_{i=1}^{n_1} w_i^{(1)} x(r_i^{(1)} + r_j^{(2)}), \qquad (2)$$

where $r_j^{(2)}$ is the position vector of the jth point in domain 2 and $j=1,2 ... n_2$. The $n_2 \times m$ matrix of domain 2 data is

$$X^{(2)} = \left[x_1^{(2)} \; x_2^{(2)} \; ... \; x_{n_2}^{(2)} \right]^T. \qquad (3)$$

The weight vector $w^{(2)} = \left[w_1^{(2)} \; w_2^{(2)} \; ... \; w_{n_2}^{(2)} \right]^T$ is then calculated by adapting to the data in $X^{(2)}$. The input signals to domain 3 are

$$x_k^{(3)} = \sum_{i=1}^{n_1} \sum_{j=1}^{n_2} w_i^{(1)} w_j^{(2)} x(r_i^{(1)} + r_j^{(2)} + r_k^{(3)}), \qquad (4)$$

where $r_k^{(3)}$ is the position vector of the kth point in domain 3, and $k=1,2 ... n_3$. The $n_3 \times m$ data matrix for domain 3 is

$$X^{(3)} = \left[x_1^{(3)} \; x_2^{(3)} \; ... \; x_{n_3}^{(3)} \right]^T. \qquad (5)$$

From $X^{(3)}$, a weight vector $w^{(3)} = \left[w_1^{(3)} \; w_2^{(3)} \; ... \; w_{n_3}^{(3)} \right]^T$ is calculated, and the $1 \times m$ output from the array is

$$y = \sum_{i=1}^{n_1} \sum_{j=1}^{n_2} \sum_{k=1}^{n_3} w_i^{(1)} w_j^{(2)} w_k^{(3)} x(r_i^{(1)} + r_j^{(2)} + r_k^{(3)}). \qquad (6)$$

The weighting in equation (6) is a convolution of the weights for each domain, and the array beam pattern is the product of the patterns of each domain.

2.4 Weight Computation

Beamforming weights can be calculated using diagonally-loaded Sample Matrix Inversion. The loaded covariance matrix in domain q is

$$R_l^{(q)} = \frac{1}{m} X^{(q)} X^{(q)H} + \gamma^{(q)} I \qquad (7)$$

where H denotes the complex conjugate transpose, $\gamma^{(q)}$ is a loading factor, and I is the identity matrix. The $n_q \times 1$ weight vector is then calculated using [3]

$$w^{(q)} = \frac{R_l^{(q)-1} c^{(q)}}{c^{(q)H} R_l^{(q)-1} c^{(q)}} \qquad (8)$$

$c^{(q)}$ is the look-direction vector of the form

$$c^{(q)} = \left[e^{i k_0 \cdot r_1^{(q)}} \; e^{i k_0 \cdot r_2^{(q)}} \; ... \; e^{i k_0 \cdot r_{n_q}^{(q)}} \right]^T \qquad (9)$$

where $k_0 = k n_0$ and n_0 is a unit vector in the look direction, and $k = 2\pi/\lambda$, where λ is the wavelength. Diagonal loading reduces weight jitter in each domain, desensitises the weights to insignificant signals and reduces the influence of signals incident near to the look-direction.

In the results presented here, $\gamma^{(q)}$ is chosen to satisfy a norm constraint on the adaptive weights at the qth stage of domain factorisation. This has been found to improve performance in the presence of main-beam jamming.

Main beam clutter can cause severe distortion of the adapted beams, if it is allowed to influence the weight calculation. However, it is easily dealt with by temporal pre-filtering of the data at each domain level.

3. Simulation results

We have simulated an AI radar in level flight at $300 \mathrm{ms}^{-1}$ at an altitude of 2000 feet. A medium PRF waveform is used (14.285kHz, with a bandwidth of 4MHz). There are 128 pulses, and (for efficiency in computing the RDGA weights) groups of 35 adjacent range-gates have been averaged into the covariance matrix, providing the equivalent of 4480 data samples - far more than is actually needed. We have simulated a peak transmitter power of 10W per element, with 12.5% duty ratio. There is no aperture shading on transmit, but a randomly chosen 1% of elements do not transmit. (This raises the transmit sidelobes to a realistic level.)

In our simulation the clutter is modelled using

$$\sigma^0 = \gamma \sin\theta + \gamma_{cv} \exp(-(90-\theta)^2/\psi_0^2) \qquad (10)$$

where σ^0 is the clutter cross-section, θ is the grazing angle, $\gamma = 0.2$, $\gamma_{cv} = 10$, and $\psi_0 = 10^0$. The first term in equation (10) is a constant gamma model for the

clutter, and the second term simulates the altitude line return.

Fig. 3 shows range-Doppler maps for (a) a fixed beamformer, pointed perpendicular to the array face, (b) EDAR/RDGA processing of data from perfectly matched receivers, and (c) EDAR/RDGA processing with random amplitude and phase errors (0.2dB and 2.5 degrees RMS, respectively). There are 25 targets at different ranges and Dopplers (visible on a regular grid in Fig. 3(b)) and sidelobe clutter. Target strengths are equivalent to a $1m^2$ object at a range of 50km. In the absence of errors, EDAR domain-factored RDGA processing removes almost all of the sidelobe clutter. In the presence of errors, there is increased breakthrough of the strongest clutter returns (although, in practice, the closest range returns would be eclipsed). Performance may be improved by (i) reducing the number of range-gates over which the covariance matrix is averaged; (ii) increasing the number of elements in domain 3; (iii) potentially more accurate calibration of an element-digitised array. Nevertheless, our results show resilience to this type of error. The plots are scaled to give constant thermal noise level in each range-Doppler cell, equal to kTB, where k is Boltzmann's constant, $T = 290K$ and B is the bandwidth.

4. Conclusions

Using domain factorisation, adaptive processing of a large element-digitised phased array can be achieved with realistic sample support. Range-dependent gain adaption enables effective spatial adaption for cancellation of distributed clutter. However, random calibration errors can cause some breakthrough of altitude line clutter. Future work should examine the potential for reducing errors by element-level calibration.

5. References

[1] *Element accessed array radar processing.* G.D. Wills, H.D. Rees, I.D. Skidmore, pp 196 - 207, Proc. SPIE Advanced Signal Processing, Algorithms, Architectures and Implementations VIII, 22 - 24 July, 1998, San Diego, CA.

[2] *Space Time Adaptive Processing.* R. Klemm, IEE Publications, 1999.

[3] *Adaptive filter theory, 2nd Ed.* S. Haykin, Prentice Hall Inc, 1991.

This work was carried out as part of Technology Group TG9 of the MoD Corporate Research Programme.

© British Crown Copyright 1999. Published with the permission of the Defence Evaluation and Research Agency on behalf of the Controller HMSO.
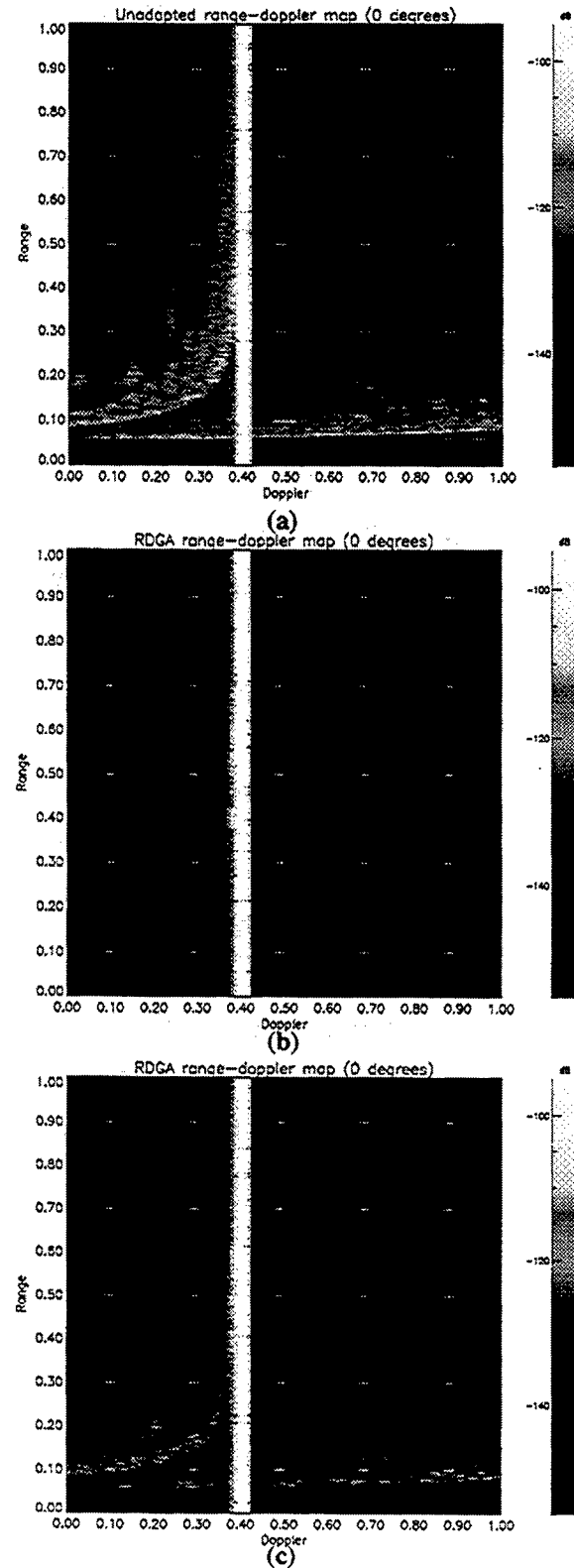
Figure 3. Normalised range-Doppler maps for scenario with sidelobe clutter and 25 targets. (a) Fixed beam (b) EDAR/RDGA (no errors) (c) EDAR/RDGA with errors.

EFFECTS OF MUTUAL COUPLING AND CHANNEL MISMATCH ON SPACE-TIME ADAPTIVE PROCESSING ALGORITHMS[1]

Tapan K. Sarkar[1], Raviraj S. Adve[2] and Michael C. Wicks[2]

[1] *Division of Electrical Engineering and Computer Science*
Syracuse University
121 Link Hall
Syracuse, NY 13244

[2] *Research Associates for Defense Conversion, Inc.*
10002 Hillside Terrace, Marcy, NY 13403
E-mail: adver@rl.af.mil

[3] *Air Force Research Laboratory*
Sensors Directorate
26 Electronic Parkway
Rome, NY 13441-4514

Abstract

The paper discusses the impact of mutual coupling on Space-Time Adaptive Processing (STAP) algorithms. To do so, simulations are used to illustrate the impact on the structure of the covariance matrix. Examples using measured data illustrate the effects of mutual coupling and channel mismatch.

INTRODUCTION

Space-Time Adaptive Processing (STAP) algorithms were originally developed mainly for proof-of-concept, assuming an idealized scenario. The main assumption is a linear array of equi-spaced, isotropic, point, sensors. Under this assumption, the array elements sample but do not re-radiate the incident fields. In addition, each element of the array is assumed to be exactly like every other element, i.e. the channels are perfectly matched. In the real world, each array element must have some physical size leading to mutual coupling between the elements. In addition, the channels are mis-matched due to manufacturing errors.

The effort of moving STAP from theory to practice has been significantly advanced by the availability of the Multi-Channel Airborne Radar Measurements (MCARM) database. The MCARM elements are reduced depth notch radiators. In applying STAP algorithms to measured data, researchers ignored the real world effects of mutual coupling and channel mismatch. However, electromagnetic analysis of antenna arrays shows that these effects severely degrade the performance of statistical [1] and direct data domain algorithms [2]. Reference [1] uses a simplistic analysis to illustrate the effects of mutual coupling. However the impact on the structure of the covariance matrix has not been studied. In the ideal case of a linear array of point sensors, the interference covariance matrix is Toeplitz (Toeplitz-block-Toeplitz in the space-time case). Furthermore, in the space-time case, the number of significant eigenvalues may be estimated *a-priori*. Both assumptions fail in the case of mutual coupling.

In applying STAP algorithms to measured data, another phenomenon, channel mismatch, must be taken into consideration. For example, under the ideal case the spatial steering vector forms a column of an appropriate DFT matrix. Certain algorithms therefore use a DFT to transform spatial data to the angle domain. In the real world, channel mismatch and mutual coupling affect the spatial steering vectors and a DFT is not optimal.

This paper uses both measured data and simulations to illustrate the effects of channel mismatch and mutual coupling on adaptive beamforming. For the simulations, the difference between the covariance matrices with and without mutual coupling is investigated. The simulations use a Method of Moments (MOM) analysis to evaluate the mutual coupling between the elements of a linear array of half-wavelength dipoles. For measured data, the algorithm investigated is the Joint Domain Localized (JDL) adaptive algorithm. Improved detection performance by accounting for channel mismatch and mutual coupling is illustrated.

METHOD OF MOMENTS ANALYSIS OF MUTUAL COUPLING

In this work we use the MOM [3] to analyze the antenna and hence the mutual coupling. The MOM reduces to a matrix equation, the integral equation relating the incident field to the currents on the antenna. As we will show, the elements of the matrix quantize the mutual coupling between the antenna elements.

There are assumed to be N_e $z-$directed wires in the array, lying in the $x - y$ plane. The array elements are of length L and radius a, with $a \ll L$. A linear polarized, narrowband, electric field, $\mathbf{E}^{inc}$, is incident on the array. Under the thin wire assumption, the current approximately flows only in the direction of the wire axes (here the z-direction), the surface current and charge densities on the wire can be approximated by line currents (I) and charge on the wire axes (they lie in the $y = 0$ plane) and the boundary condition can be applied to the axial component of $\mathbf{E}$ on the wire axes i.e. the boundary condition is applied to E_z on the wire axes. Using these assumptions, and the boundary condition that the total electric field on the axis of the wires must be identically zero, the integral equation that characterizes the behavior of the antenna array is

$$E_z^{inc}(z) = j\omega\mu_0 \int_{axes} I(z')\frac{e^{-jkR}}{4\pi R}dz' - \frac{1}{j\omega\epsilon_0}\frac{\partial}{\partial z}\int_{axes} \frac{\partial I(z')}{\partial z'}\frac{e^{-jkR}}{4\pi R}dz' \quad z \in axes. \tag{1}$$

We solve this equation for the currents using the MOM. The basis functions used are the piecewise sinusoids as described by Strait et.al. [4]. The weighting functions are the same piecewise sinusoids i.e. a Galerkin formulation is used. This formulation is chosen because it yields analytic expressions for the elements of the matrix, hence eliminating the need for numerical integration. The resulting matrix equation can be written as

$$\mathbf{V} = \mathbf{ZI} \Rightarrow \mathbf{I} = \mathbf{YZ}, \tag{2}$$

where $\mathbf{I}$ is the MOM current vector with the coefficients of the expansion of the current in the above basis. $\mathbf{Z}$ is the MOM impedance matrix. $\mathbf{Y}$ is the MOM admittance matrix, the inverse of the impedance matrix. The matrices are of order $N \times N$, where N is the number of unknowns used in the MOM formulation. The entries of $\mathbf{V}$ and $\mathbf{Z}$ are given by

$$\mathbf{V}_i = \frac{E_0 e^{jkx_m \cos\phi \sin\theta}}{k\sin(k\Delta z)\sin^2\theta}2e^{jkz_{q,m}\cos\theta}\left[\cos(k\Delta z\cos\theta) - \cos(k\Delta z)\right], \tag{3}$$

where θ and ϕ are the elevation and azimuth direction of arrival of the incident field.

$$\mathbf{Z}_{i,l} = \int_{z_{q-1,m}}^{z_{q+1,m}} f_{q,m}(z)\left\{\left[j\omega\mu_0\int_{z_{p-1,n}}^{z_{p+1,n}} f_{p,n}(z')\frac{e^{-jkR}}{4\pi R}dz' - \frac{1}{j\omega\epsilon_0}\frac{\partial}{\partial z}\int_{z_{p-1,n}}^{z_{p+1,n}} \frac{df_{p,n}(z')}{dz'}\frac{e^{-jkR}}{4\pi R}dz'\right]\right\}dz, \tag{4}$$

where $i = [(m-1)P + q]$. $l = [(n-1)P + p]$ and $f_{q,m}$ is the q-th basis function on the m-th element.

Note that the entries of the voltage vector are directly related to the incident field and are hence free of the effects of mutual coupling. The entries of the impedance matrix are the interaction between the field due to the current source $f_{p,n}$ at the location corresponding to the basis function $f_{q,m}$. Therefore, by their very nature, the entries of the impedance matrix are a measure of the mutual coupling between the sections of the array.

Using the MOM admittance matrix and the voltage vector, we can show that the voltages measured at the ports of the array are given by

$$\mathbf{V}^{meas} = \mathbf{Z}_L\mathbf{Y}_{port}\mathbf{V} \tag{5}$$

where, $\mathbf{Y}_{port}$ is the $N_e \times N$ matrix of the rows of $\mathbf{Y}$ that correspond to the ports of the N_e elements. $\mathbf{Z}_L$ is the $N_e \times N_e$ diagonal matrix with the port loads as its entries.

EFFECTS OF MUTUAL COUPLING AND CHANNEL MISMATCH

STAP algorithms were traditionally developed assuming a linear array of isotropic point sensors. This section illustrates effects of mutual coupling and channel mismatch using simulations and measured data.

Simulated Data

In the case of an ideal array, the spatial interference covariance matrix is Toeplitz. In the space-time case, the space-time data vector can be arranged such that the covariance matrix is Toeplitz-Block-Toeplitz. However, this is true only under the ideal case. Under the ideal case each element of the array is independent of the others and the correlation between elements is only a function of the distance between them. However, in the true case,

Table 1: Covariance matrices: without and with mutual coupling

Without Mutual Coupling							With Mutual Coupling						
0.92	0.59	0.59	0.41	0.37	0.22	0.23	0.80	0.76	0.57	0.44	0.28	0.23	0.01
0.59	0.85	0.58	0.66	0.43	0.42	0.23	0.76	0.96	0.75	0.54	0.35	0.29	0.10
0.59	0.58	0.86	0.60	0.59	0.41	0.38	0.57	0.75	0.82	0.66	0.45	0.40	0.20
0.41	0.66	0.60	1.00	0.63	0.64	0.34	0.44	0.54	0.66	0.86	0.68	0.59	0.39
0.37	0.43	0.59	0.63	0.88	0.62	0.56	0.28	0.35	0.45	0.68	0.83	0.77	0.50
0.22	0.42	0.41	0.64	0.62	0.90	0.60	0.23	0.29	0.40	0.59	0.77	1.00	0.71
0.23	0.23	0.38	0.34	0.56	0.60	0.88	0.01	0.10	0.20	0.39	0.50	0.71	0.73
Measure of "Non-Toeplitzity"=0.1926							Measure of "Non-Toeplitzity"=0.4827						
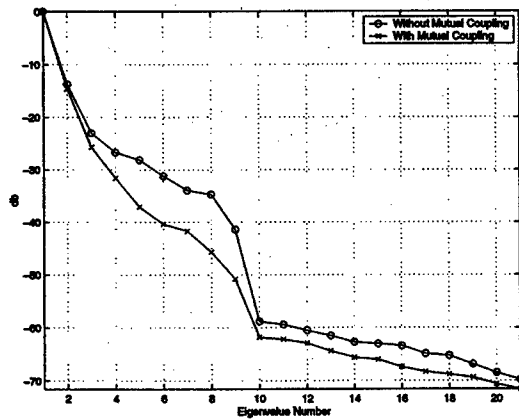
Figure 1: Eigenvalue spread without and with mutual coupling.
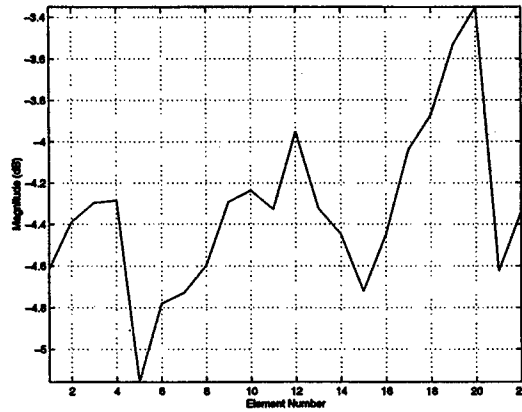
Figure 2: Magnitude of measured steering vector.

each element in the array sees a different environment. The correlation between two elements is a function of the distance between them and also the location of the elements in the array. Solving for the adaptive weights using a Toeplitz solver will lead to incorrect solutions.

To illustrate this point, Table 1 presents the magnitude of the covariance matrix for the case with and without mutual coupling. The array is made up of 7 elements spaced $\lambda/2$ apart. Each element is of length $\lambda/2$ and radius $\lambda/200$. The clutter is 25dB above the noise floor. 28 secondary data vectors are used to estimate the covariance matrix. The covariance matrices are normalized to the maximum absolute value. The "Non-Toeplitzity" of the matrix is defined as mean squared summed error between the matrix and its Hermitian.

For an ideal array, the number of significant clutter eigenvalues is set by the number of pulses in a coherent pulse interval (CPI), number of elements and speed of the platform. In general [5],

$$N_{eig} \simeq N + \beta(M-1), \tag{6}$$

where β is the number of half inter-element spacings covered in a single pulse period. In this example, the seven element array of Table 1 is used in conjunction with three pulses forming the CPI. The speed of the aircraft is set such that $\beta = 1$. The number of eigenvalues is therefore approximately 9. We use 84 secondary data vectors to estimate the 21×21 covariance matrix. The eigenvalue spread for the case without and with mutual coupling is given in Fig.1. As can be seen, the eigenvalue plot for the case without mutual coupling shows a sharp cut off at the 9th eigenvalue. For the case with mutual coupling, the cut off is significantly less.

Measured Data

In using STAP algorithms to detect weak signals in interference, the effects of mutual coupling and channel mismatch are usually ignored. However, as we shall see, both have significant effects on the performance of STAP algorithms. Here the effect is illustrated on the JDL algorithm which adaptively processes data within a Localized Processing Region (LPR) in angle-Doppler space.

The MCARM database is a collection of measured data taken over several flights with several acquisitions

547
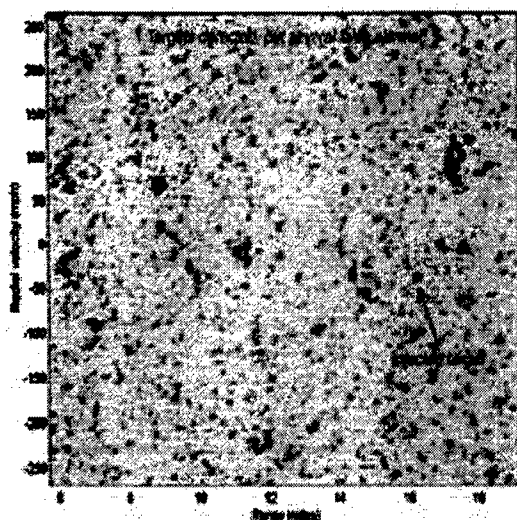
Figure 3: STAP performance assuming ideal array.
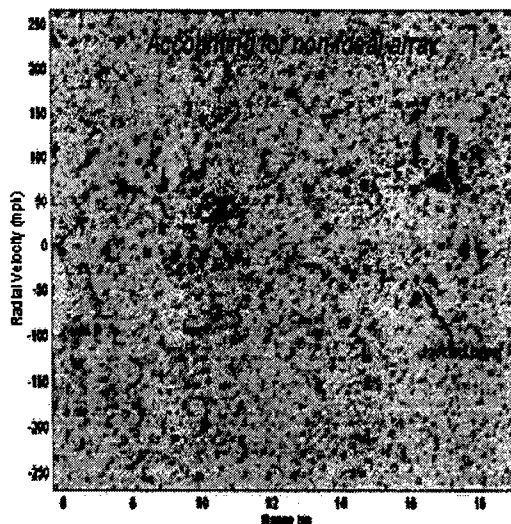
Figure 4: STAP performance accounting for mutual coupling and channel mismatch.

per flight. Also provided with the database is a set of measured steering vectors. These steering vectors account for the mutual coupling and channel mismatch and must be used to transform the space-time data to the angle-Doppler domain. In the ideal case, the magnitude of the steering vector at each element is constant. In the measured case, as shown in Fig. 2, the magnitude may fluctuate significantly.

In past applications of JDL to the MCARM database, the data is transformed to the angle-Doppler domain using the measured steering vectors, but the space-time steering vector is not. It is assumed that the steering vector follows the ideal case. Figure 3 illustrates the performance of the STAP algorithm for the case that the array is assumed to be ideal. The data is from acquisition 575 on flight 5. A weak target is injected in range bin 290. There are many false alarms and the target cannot be easily detected. Figure 4 illustrates the performance after accounting for the non-ideal array. As is seen, the false alarms are significantly reduced and the weak target can be detected.

CONCLUSIONS

This paper provides a brief review of the effects of mutual coupling and channel mismatch on the performance of STAP algorithms. Accounting for the non-ideal array can significantly improve STAP performance.

References

[1] I.J. Gupta and A.A. Ksienski. Effect of mutual coupling on the performance of adaptive arrays. *IEEE Transactions on Antennas and Propagation*, 31(5):785–791, September 1983.

[2] Raviraj S. Adve and Tapan K. Sarkar. Accounting for the effects of mutual coupling in adaptive antennas. In *Proceedings of the 1997 IEEE National Radar Conference*, May 1997. Syracuse, NY.

[3] R.F. Harrington. *Field Computation by Moment Methods*. Robert E. Kreiger Publishing Co., 1982.

[4] B.J. Strait, T.K. Sarkar, and D.C. Kuo. Special programs for analysis of radiation by wire antennas. Technical Report AFCRL-TR-73-0399, Syracuse University, June 1973.

[5] J. Ward. Space-time adaptive processing for airborne radar. Technical Report F19628-95-C-0002, MIT Linclon Laboratory, December 1994.

Experimental Analysis of DOA Estimation and BER Performance using Adaptive Array Antenna System

Ami Kanazawa[†], Takashi Fukagawa[‡], Youichi Nakagawa[‡], Hiroyuki Tsuji[†] and Hiroyo Ogawa[†]

[†] Communications Research Laboratory, MPT of Japan

[‡] Matsushita Research Institute Tokyo Inc.

Abstract

This paper reports the experimental results of the DOA estimation and BER improvement using adaptive array antenna system we have proposed. We evaluate the accuracy of the DOA estimation in outdoor using the MUSIC, ESPRIT, and fast DOA algorithm. Moreover, we show the improvement of the BER performance through the beamforming control of the adaptive array antenna with the DCMP algorithm.

1. Introduction

Adaptive array techniques in mobile communication system can improve channel capacity by reducing co-channel interference and multipath fading. Estimating the direction of arrival (DOA) of the signals and determining the antenna weights are the important technologies, on which many studies have been made [1][2]. As for DOA algorithm, the multiple signal classification (MUSIC) and estimation signal parameters via rotational in variance techniques (ESPRIT) algorithms are well-known. They are based on the eignen structure of the signal. On the other hand, another fast DOA algorithm without the eigen structure has been proposed [3]. In this paper we evaluate the performance of the above algorithms using an adaptive array antenna system through the experimental results. The array antenna system which we developed consists of DOA estimation, weight adaptation, and beamforming blocks. Moreover, we clarify that the bit error rate (BER) can be improved by beamforming technique. In Section 2, we describe the system concept using the array antenna system. In Section 3, we explain our experimental system, then in Section 4, we report the results of our experiments in both an unechoic chamber and outdoor, line-of-sight (LOS) environment. Finally, we summarize our major findings.

2. The system using adaptive array antenna

2.1. System concept

Figure 1 shows the system concept using adaptive array system. The base station (BS) has the array antenna, searches the directions of the mobile stations (MSs) and forms the beam for the target MSs. These controls improve not only carrier to interference ratio (CIR) and BER but also the utilization of frequency resources through adaptive beam control.

2.2. Experimental system

Figure 2 shows our experimental adaptive array system we have developed. Figure 3 depicts the block diagrams of the system. The array antenna system consists of array antenna block, frequency conversion block, and digital processing block. The array antenna has equi-spaced eight elements with micro-strip patch antennas. The distance between adjacent antennas is half a wavelength. Two dummy elements are

(a)   (b)

Fig, 2 The exterior of the adaptive array antenna system
(a) The control part of the adaptive array system
(b) 8 element linear array antenna

Fig. 1 The system concept using the adaptive array system

Table 1 Experimental system parameter

Array antenna	microstrip patch antenna vertical polarization
RF frequency	2.335 GHz
IF frequency	450 kHz
Modulation	π/4-DQPSK, 42 kbps

placed at both ends of the elements to equalize their characteristics. The frequency 2.335 GHz of the RF signals received at the array elements is converted to 450 kHz by the down converters and analog filters in the frequency conversion block. Then, the IF signals are sent to the digital processing block, which consists of A/D converter, a DOA estimation block, a weight adaptation block, and a beamforming block. The IF signals are digitized by the A/D converter, which operates at 1.8 MHz sampling clock rate and 12 bit resolution. The digitized IF signals are then converted to the I and Q base-band signals. The data bus transfers the I/Q channel data to the DOA estimation, weight adaptation, and beamforming blocks. The DOA estimation block applies three types of DOA estimation algorithms, such as the MUSIC or ESPRIT (eigen space based algorithm) or a fast DOA algorithm [3] to the received data. The weight adaptation block calculates the optimum weight vector based on the estimated DOA, the beamforming block synthesizes the data by using the calculated weight vector.

We can also operate each block independently. Therefore, we can examine both the reliability of the DOA algorithms and the effect of beamforming, using each block independently.

In our experiments, the DOA estimation block use 1024 samples from each element for the calculation of the MUSIC and ESPRIT. For the fast DOA algorithm, it used one sample from each element for the calculation because it is a recursive type algorithm. The CPU performance is 200MIPS. When one signal impinges on the array, it takes about 70 ms for the calculation with the MUSIC or ESPRIT algorithm and about 0.7 ms for the calculation with the fast DOA algorithm.

3. Experimental results
3.1 Accuracy of DOA estimation

We first examined the performance of the MUSIC and ESPRIT algorithms which estimate the DOA of the signals in an unechoic chamber. We set the array antenna (Rx) on a turntable and performed experiments under two different conditions. In condition I, a single transmitter was set in front of the array antenna. In condition II, two transmitters were

used. The configurations of these experiments are illustrated in Figs. 3 and 4. In the experiments, we set the power of the transmitter 1 (Tx1) and the transmitter 2 (Tx2) so as to receive the signals at the level of −91.4dBm at Rx. The distance between Tx1 and Rx was 10 m.

The accuracy of the DOA estimation in condition I is shown in Fig 6. The merge of the estimation errors was within 3 degrees in both algorithms through the angle of incident from −80 to 80 degrees. We also examined the DOA estimation when the height of Tx1 is lower than that of Rx. We set the angle of elevation between Tx1 and Rx at about 7 degrees. We found that the accuracy of the DOA estimate degraded slightly when $|\theta|$ becomes large. From the result, our system can guarantee the accuracy of the DOA estimation within $|\theta| \leq 60$ degrees in this case.

In condition II, the two transmitters in front of the array
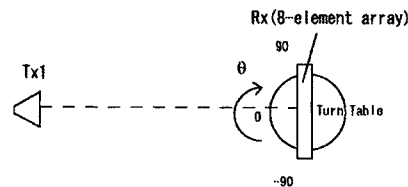
Fig. 4 Experimental configuration in situation I.
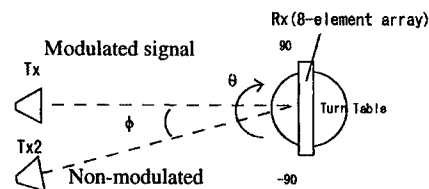
Fig. 5 Experimental configuration in situation II.
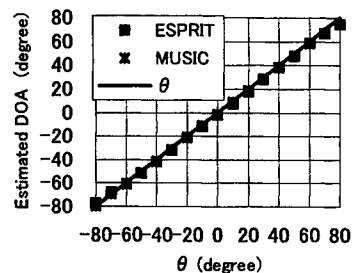
(a) In the case that Tx1 and Rx was same height
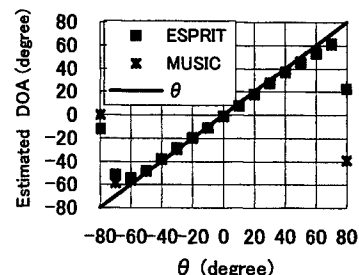
(b) In the case that the elevation angle was 7 degrees.
Fig. 6. Result of DOA estimation (situation I)

Fig.3 Experimental system configuration

antenna were located at an interval of ϕ degrees. Figure 7 shows the results obtained by the ESPRIT when $\phi = 5$ and 20. The accuracy of the DOA estimate was poor compared to that in condition I. As ϕ became smaller, the estimation error increased.

3.2 Tracking and beamforming experiment (LOS)

We examined the performance of DOA estimation and the effect of the beamforming control using our system. For investigation of the beamforming control, the algorithm which calculates the optimum weight vector is need to receive the desired signal avoiding the interference.

We use the directionally constrained minimization power (DCMP) algorithm [4] that is shown as follows,

$$w(m+1) = P \cdot [w(m) - \mu x(m)y^*(m)] + F \qquad (1)$$

$$y(m) = w^H(m)x(m) \qquad (2)$$

$$w(0) = F \qquad (3)$$

$$P = I - C(C^H C)^{-1} C^H \qquad (4)$$

$$F = C(C^H C)^{-1} H^* \qquad (5)$$

where $x(m)$ is the array input signal, $y(m)$ is the output signal at a discrete time m, I is M-by-M identity matrix, u is the step size parameter that satisfies

$$0 < \mu < \frac{2}{3\text{trace}(E[x(m)x^H(m)])}, \qquad (6)$$

C is a matrix of array responses for the constraint direction
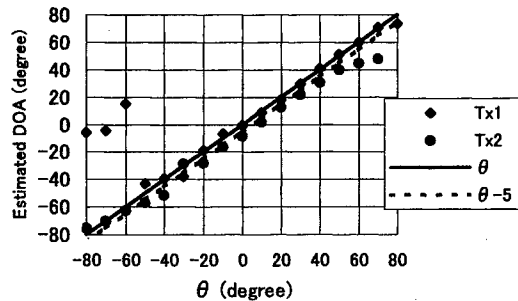
(a)$\phi = 5$
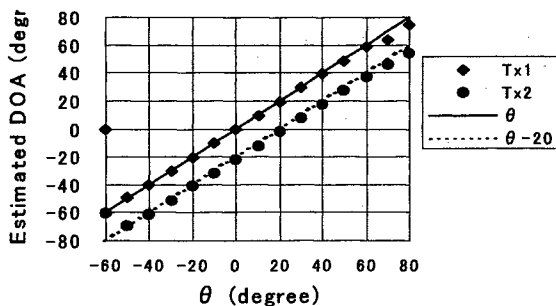
(b)$\phi = 20$

Fig.7 Result of DOA estimation (situation II)

and H is the vector of the complex-valued gain for the constraint direction. C and H satisfy the following equation:

$$C^T w = H. \qquad (7)$$

We calculated the weight vector in (1) using 1024 samples.

Figure 8 shows the configuration of the outdoor experiments. A slightly higher place, we positioned Rx parallel to the street. The maximum angle of elevation from the street to the Rx was about 12 and the minimum was about 3 degrees. On the basis of the results in an unechoic chamber, we examined the accuracy of DOA estimation at the range between –60 and 60 degrees.

We performed the experiments in the same conditions as in the unechoic chamber. We used a single transmitter (Tx1) in condition I and two transmitters in condition II.

In condition I, we positioned the Tx1 at several points to change the DOA of its signal. At each point, the transmission power level of Tx1 was set so as to receive the signals at the level of –85 dBm at BS. Figure 9 shows the results of the DOA estimation in condition I. In condition II, we located the Tx1 and Tx2 as shown in Fig. 8. The results of the DOA estimates are shown in Fig. 10. From figs. 9 and 10, we found that the BS could estimate the DOA almost perfectly.

Then we measured the BER to investigate the effect of beamforming in condition II. Tx1 transmitted a modulated signal as a desired signal and Tx2 transmitted a non-modulated (carrier only) signal as a interference signal. We measured the BER in three different cases:

In case 1: the BS receives the signal with a single element.

In case 2: the BS receives the signal with the array antenna in which all eight elements have the same antenna weights.

In case 3: the BS receives the signal with the array antenna where the weight vector is calculated by DCMP algorithm.

Throughout the experiment we changed the transmission level of Tx2 , while we fixed the transmission level of Tx1. In order to set the constant transmission level of Tx1, we first measured the BER at the transmission level used in Tx1 in situation I for both case 1 and case 2. Then, we established the transmission level x at which the BS could receive a signal with BER of 1e-4. For case 1, the received level at BS was -80 and for case 2, the received level was –85 dBm when Tx1 was set at 0 degrees. Using these results, we set the level of Tx1 to $(x+3)$ dBm and observed results at the 1e-4 BER level. For
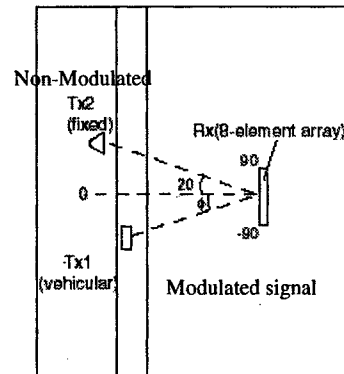
Fig.8 Experimental configuration in outdoor

551

case 3, the transmission level of Tx1 was fixed at the same level at in case 2.

Figure 11 shows the BER. In case 2, the CIR improved about 10 from case 1 dB to achieve BER = 10^{-3}. In case 3, it improved more than 5 dB.

Finally, we examined the reliability of a fast DOA algorithm calculation [3]. This algorithm was developed to track users moving at high velocity because the DOA estimation algorithm applied in eigen space requires much time. This algorithm is applied as follows,

1) The BS estimates the transmitter position using MUSIC or ESPRIT algorithm as initial value.
2) The fast DOA algorithm is used to calculate the DOA and velocity at sampling time m.
3) m is set to $m+1$. When 1000 times repetitions are finished, return to step 1), if not, return to step 2).

In our experiment, Tx1 (a vehicle) moved down the street at 60 km/h. To find the actual position of Tx1, BS started estimating the DOA when Tx1 passed a certain mark. Figure 12 shows the accuracy of the DOA estimation. In this scenario, the square shows the results calculated by ESPRIT, and the solid line shows the results calculated by the fast DOA algorithm. The crosses show the actual positions calculated by the time and velocity. This figure indicates that using the fast DOA algorithm resulted in extremely accurate estimates.

4. Conclusions

In this paper, we report the results of the DOA estimation and BER improvement using our experiments in LOS enviroment of an unechoic chember and outdoor. From the results, we showed the accuracy of DOA estimation using the MUSIC and ESPRIT in outdoor and the feasibility of the fast DOA algorithm.

Moreover, we showed the improvement of the BER through the beamforming with the DCMP algorithm. In the near future, we will examine the effect of the DOA estimation and BER improvement in urban area.

Acknowlegement

References

[1] L. C. Godara, "Application of antenna arrays to mobile communications, part II: beam-forming and direction-of-arrival considerations", Proc. of IEEE, vol. 85, no. 8, pp. 1195-1245, Aug. 1997.

[2] S. Haykin, "Adaptive filter theory," Prentice-Hall, Inc., 1996.

[3] T. Kishigami, Y. Nakagawa, T. Fukagawa, M. Hasegawa, T. Fukuchi, and H. Tsuji, "A study on adaptive array antenna with a novel fast DOA algorithm for mobile communications", Asia-Pacific Microwave conference, pp. 523-526, Dec. 1998.

[4] K. Takao, M. Fujita, and T. Nishi, " An adaptive antenna array under directional constraint," IEEE Trans. Antennas & Propag., vol. AP-24, no. 5, pp. 662-669, Sept. 1976
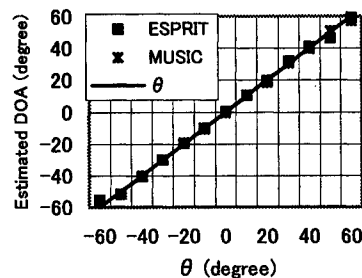
Fig 9. DOA estimation (one transmitter)
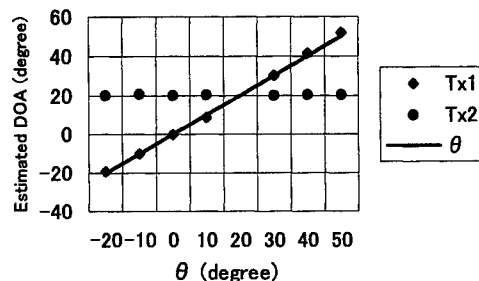
Fig. 10. DOA estimation using ESPRIT (two transmitters)
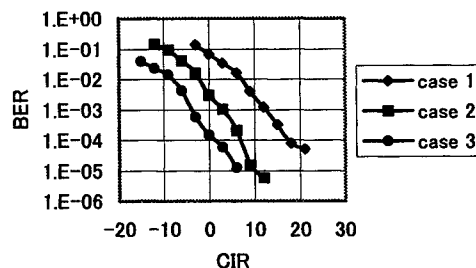
Fig. 11 BER performance
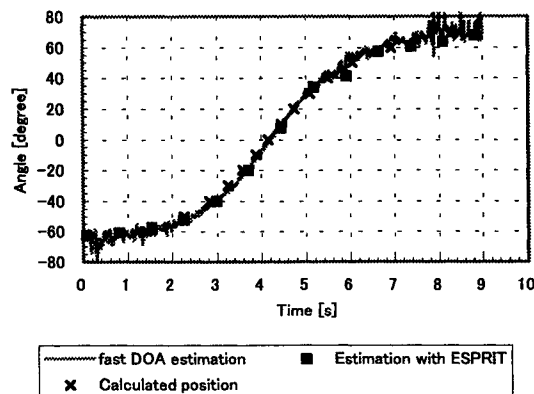
Fig. 12 DOA estimation with a first DOA algorithm

A Generalized Eigenspace-Based Beamformer with Robust Capabilities

Ann-Chen Chang[1], Ching-Tai Chiang[2] and Yuan-Hwang Chen[1]

[1]Dept. of Electrical Engineering, National Sun Yat-Sen University, Kaohsiung, Taiwan 804, ROC

[2]Dept. of Electronic Engineering, Southern Taiwan University of Technology, Tainan, Taiwan, ROC

Abstract — This paper presents a robust beamforming based on the generalized eigenspace-based (GEIB) technique. It has been shown that the GEIB beamformer demonstrates the advantage of less sensitivity to small pointing errors over the eignespace-based (ESB) technique. However, the GEIB still couldn't deal with the large pointing error near the edge of mainlobe. Shaping the noise subspace with the estimated steering vector, we propose an effective technique to achieve more robust capabilities than the GEIB and ESB.

I. INTRODUCTION

When the interferers are uncorrelated with the desired signal, the conventional beamformers have been shown to achieve good output SINR by suppressing the interferers while enhancing the reception of the desired signal. In practical circumstances, there exist the steering vector errors due to the pointing errors or inaccurate calibration of sensors. The desired signal may be viewed as an interferer and tends to be suppressed [1]. For solving this problem, several robust methods were proposed in the literature [2] to reduce the array sensitivity. The GEIB [3] has robust capabilities to the small pointing errors and achieves higher output SINR than the linear constrained minimum variance beamformer (LCMVB) [2], especially when the constraints are not preserved. However,

we note that the output SINR of the GEIB is degraded when the desired signal impinges upon the array from the direction near the mainlobe edge. To cure this problem, the ESB beamformer in [4] uses the subarray partition scheme to estimate the actual steering vector of the desired signal and construct the signal subspace (SS). Due to the mismatch between the estimated ideal steering vector of the desired signal and the actual one, the desired signal may be suppressed in the ESB method. In the situation of the large pointing error and high input SNR, the desired signal may be viewed as an interferer and tends to be suppressed.

In this paper, we present an effective technique for the GEIB against the pointing error. Firstly, we propose an appropriate scheme to estimate the actual steering vector by using the full array data. Then, using the orthogonality property between the steering vector and the noise subspace, we shape the estimated steering vector to approximate the correct steering vector. Secondly, with the actual estimated steering vector, the actual bearing angle of the desired signal can be obtained by using the concept of constructing steering vector. Finally, the actual bearing angle of the desired signal to improve the performance of the GEIB at a large pointing error nears the mainlobe beamwidth.

II. GEIB AND PROBLEM DESCRIPTION

A. The GEIB Beamformer

Consider P narrowband uncorrelated sources impinging on an M elements uniform linear array. The direction vector of the ith source is given by

$$\mathbf{a}_i = \begin{bmatrix} 1 & \cdots & \exp(j2\pi(M-1)\frac{d}{\lambda}\sin\theta_i) \end{bmatrix}^T \quad (1)$$

where d is the spacing between two adjacent elements, λ is the wavelength of the carrier, θ_i is the impinging angle with respect to the broadside of the array, and the superscript T is the transpose operator. Thus, the received array data can be represented as an $M \times 1$ vector form

$$\mathbf{x}(t) = \sum_{i=1}^{P} s_i \mathbf{a}_i + \mathbf{n} \quad (2)$$

where the ith source s_i is assumed to be the complex Gaussian process with power equal to σ_i^2, and the noise $\mathbf{n}$ is spatially and temporally white Gaussian noise with power σ_n^2.

Next, we describe the GEIB [3], which combines the features of the ESB beamformer and the LCMVB. Minimizing the array output power subject to the linear constraints $\mathbf{C}^H\mathbf{W}_c = \mathbf{f}$, the LCMVB [2] generates a weight vector

$$\mathbf{W}_c = \mathbf{R}^{-1}\mathbf{C}(\mathbf{C}^H\mathbf{R}^{-1}\mathbf{C})^{-1}\mathbf{f} \quad (3)$$

where the superscript H denotes the complex conjugate transpose. $\mathbf{C}$ and $\mathbf{f}$ are the constraint matrix and response vector, respectively. The correlation matrix of the array input vector $\mathbf{R} = E[\mathbf{x}\mathbf{x}^H]$. The weight vector $\mathbf{W}_c$ in (3) can be expressed as the summation of two orthogonal components [3]

$$\mathbf{W}_c = \mathbf{E}_s\mathbf{E}_s^H\mathbf{W}_c + \mathbf{E}_n\mathbf{E}_n^H\mathbf{W}_c = \mathbf{W}_s + \mathbf{W}_n \quad (4)$$

where $\mathbf{E}_s$ spans the SS, while $\mathbf{E}_n$ spans the noise subspace (NS). Thus, $\mathbf{W}_s = \mathbf{E}_s\mathbf{E}_s^H\mathbf{W}_c$ is the weight projected in the SS, and $\mathbf{W}_n = \mathbf{E}_n\mathbf{E}_n^H\mathbf{W}_c$ is the weight projected in the NS. Due to the GEIB without preserving the constraints, this approach can reduce the output noise power to the noise power level of unit gain constraint beamformer. Therefore, we only use the weight of GEIB with second-order derivative constraints unpreserved to analyze performance. Then, the weight vector is

$$\mathbf{W}_G = \frac{1}{\mathbf{a}_d^H\mathbf{E}_s\mathbf{E}_s^H\mathbf{W}_c}\mathbf{E}_s\mathbf{E}_s^H\mathbf{W}_c \quad (5)$$

B. Problem Description

Let the desired signal be the source incident from directional angle θ_1. For the case of correct steering, $\mathbf{a}_d$ is equal to $\mathbf{a}_1$. Otherwise, the steering vectors mismatch $\mathbf{a}_d \neq \mathbf{a}_1$. According to the result presented in [4], the output SINR approaches to zero when the desired signal is impinging on the array near the mainlobe edge. If the beamformer could deal with this problem, one can call this beamformer has robust capability. Fig. 1 depicts the sensitivity of the ESB technique of [4] and [5] in terms of the output SINR versus θ_1. The simulation conditions are the same as the Fig. 4(a) of [4] with the steering angle $\theta_d = 0°$ and SNR = 20dB. However, both of them can not deal with the pointing error near the mainlobe edge.

III. THE PROPOSED ROBUST TECHNIQUE

Here, we directly use the full array output data and the ESB beamforming [5] to estimate the steering vector of the desired signal. The optimal weight vector is $\mathbf{W}_E = \mathbf{E}_s\Lambda_s^{-1}\mathbf{E}_s^H\mathbf{a}_d$ where $\Lambda_s = \mathbf{E}_s^H\mathbf{R}\mathbf{E}_s$. Then the output of array is

$$y(t) = \mathbf{W}_E^H\mathbf{x}(t) = \sum_{i=1}^{P} s_i g_i + \mathbf{W}_E^H\mathbf{n} \quad (6)$$

where $g_i = \mathbf{W}_E^H\mathbf{a}_i$ denotes the array gain for the ith

signal. Based on the assumptions that M > P and a_d is suitably close to a_1, we can say that the interferers could be nulled under array optimal condition and (6) can be approximated as

$$y(t) \approx s_1 g_1 + W_E^H n \qquad (7)$$

Equation (7) reveals that the output of the array can be used as a reference to find the actual steering vector a_1. Consider the cross-correlation matrix R_{xy} between $x(t)$ and $y(t)$,

$$R_{xy} = RW_E \approx \sigma_1^2 g_1^* a_1 + \sigma_n^2 W_E \qquad (8)$$

From (8), let $M \times 1$ vector

$$V = RW_E - \sigma_n^2 W_E = \sigma_1^2 g_1^* a_1 \qquad (9)$$

Then, the steering vector a_1 is approximately proportional to V with a proportion constant equal to $\sigma_1^2 g_1^*$. The above technique of estimated steering vector is similar to the method of [4]. Due to the effects of pointing errors, the computed weight vector does not remain in the SS, and consequently, W_n is not equal to zero. From the observation on the cause the desired signal cancellation, we can mitigate the problem by finding a vector Ψ orthogonal to NS. Specifically, it leads us to formulate the problem:

$$\underset{\Psi}{\text{minimize}} \parallel \Psi - V \parallel^2 \text{ subject to } \Psi^H E_n = 0^T \quad (10)$$

Thus, the solution of the problem is given by

$$\Psi_0 = (I - E_n E_n^H) V \qquad (11)$$

where I is the $M \times M$ identity matrix. To make the first entry equal to one for the actual steering vector, we define a vector shown as $F = (\phi_1)^{-1} \Psi_0$, where ϕ_1 denotes the first entry of Ψ_0. Since the amplitude of each entry of the actual steering vector is equal to one, an appropriate estimate of the actual steering vector can be obtained from F by finding the optimal solution for the following optimization problem

Minimize $\parallel \hat{a} - F \parallel^2$

Subject to $\hat{a}_{d1} = 1$ and $\left| \hat{a}_{dm} \right| = 1, \ m > 1$ (12)

where $\hat{a}_{dm}$ denotes the mth entry of $\hat{a}$. The optimization problem formulated in (12) has a closed-form solution given by $\hat{a}_d$ with its mth entry $\hat{a}_{dm} = f_m / |f_m|$, for m = 1, 2, ..., M, where f_m denotes the mth entry of F [4].

In order to compensate the difference between the estimated and the actual steering vectors, we use the high order derivative constrains. Based on the concept of constructing steering vector, we present a method for finding the incident directional angle of desired signal, which was shown as follows:

$$\hat{\theta}_d = \frac{1}{M-1} \sum_{i=2}^{M} \sin^{-1} \left(\frac{\tan^{-1} \frac{\text{Im}\{ \hat{a}_{di} \}}{\text{Re}\{ \hat{a}_{di} \}}}{(i-1)2\pi \frac{\lambda}{d}} \right) \qquad (13)$$

where Re$\{x\}$ and Im$\{x\}$ denotes the real and complex parts of x. Substituting $\hat{\theta}_d$ of (13) into the constraint matrix of (5). We can obtain the optimal weight vector W_G for the GEIB.

IV. COMPUTER SIMULATION

An 18-element linear uniform array with half wavelength is used for simulation. All elements are assumed identical and omnidirectional with a unit gain. The classical beamwidth of the array is approximately $6.34°$. 2 uncorrelated interferers with equal power, which interfer-noise ratio INR = 10dB, are impinging on the array from $-40°$ and $50°$, respectively. Let the ideal steering angle $\theta_d = 0°$ and the sample correlation matrix is 200 data snapshots. $\sigma_n^2 = 1$ is the average power of the background noise. Fig. 2 plots the beampatterns of

555

the proposed technique and the GEIB under pointing error 6°. Fig. 3 shows the output SINR versus the input SNR under pointing error = 4°. From these aforementioned results, we see that the proposed technique is much more robust to the pointing error than the method [4] and the GEIB [3], especially as the input SNR.

V. CONCLUSION

This paper has presented a technique for GEIB beamformer with robust capabilities. For uniform linear array, we propose a method to estimate the incident angle of the desired signal by the received full array data vector. Based on the actual results, the proposed robust technique achieves the same convergence speed and mitigates pointing error. Even though the pointing error nears the mainlobe edge, the output SINR of the proposed method is still proportional to the input SNR.

REFERENCE

[1] N.K. Jablon, "Adaptive beamforming with the generalized sidelobe canceller in the presence of array imperfections," IEEE Trans., vol. AP-34, pp. 996-1012, Aug. 1986.

[2] O.L. Forst III, "An algorithm for linearly constrained adaptive array processing," Proc. IEEE, vol. 60, pp.926-935, Aug. 1972.

[3] J.L. Yu and C.C. Yeh, "Generalized eigenspace-based beamformers," IEEE Trans., vol. SP-43, pp. 2453-2461, Nov. 1995.

[4] C.C. Lee and J.H. Lee, "Eigenspace-based adaptive array beamforming with robust capabilities," IEEE Trans., vol. AP-45, pp. 1711-1716, Dec. 1997.

[5] L. Chang and C.C. Yeh, "Effect of pointing errors on the performance of the projection beamformer," IEEE Trans., vol. SP-41, pp. 1045-1056, Aug. 1993.
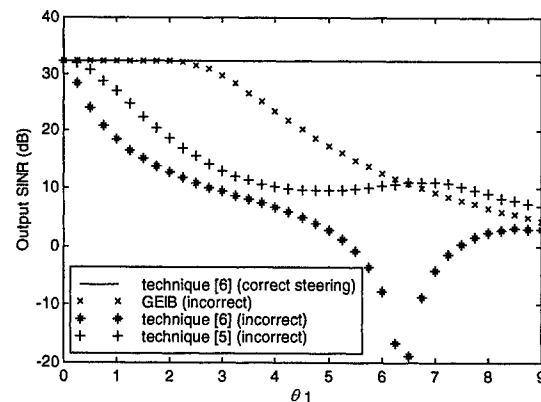
Fig. 1 Output SINR versus θ_1. SNR = 20dB.
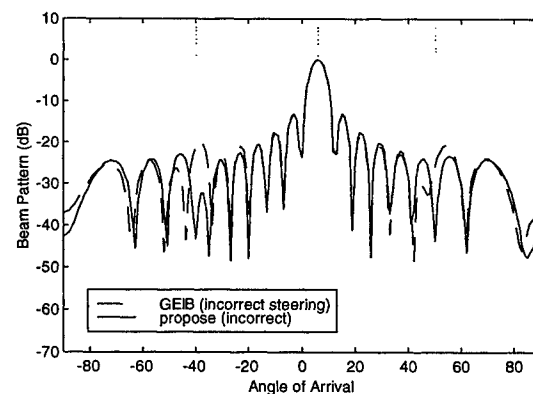
Fig. 2 Output beampatterns. SNR = 10dB.
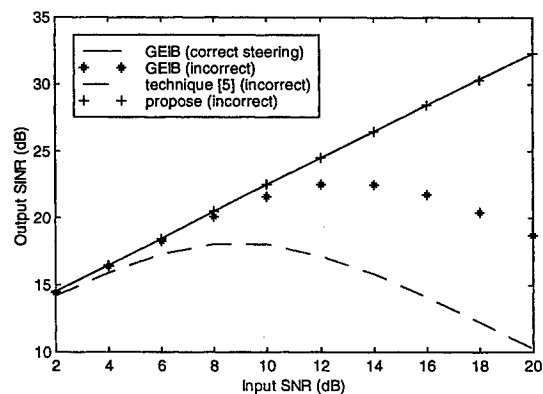
Fig. 3 Output SINR versus the input SNR.

Adaptive Wide Null Steering for Digital Beamforming Array with the Complex Coded Genetic Algorithm

Yilong Lu and Beng-Kiong Yeo
School of Electrical and Electronic Engineering
Nanyang Technological University
Singapore 639798
eMail: eylu@ntu.edu.sg

Abstract— This paper presents adaptive wide null steering for digital beamforming (DBF) array with the versatile and powerful genetic algorithm. In this approach, the complex weights of a DBF array are directly coded as the chromosomes for GA. The GA is able to precisely suppress the sidelobe level, using multiple deep nulls – collectively termed as a wide null – to cover a stretch of azimuth directions. Depending on the prescribed depth of the desired suppression, its proximity to the main beam and the width of the wide null, the original sidelobe level (*SLL*) of the beam pattern can be maintained. More importantly, this GA approach is applicable for arrays of any configuration, as shown by the numerical results.

I. Introduction

Antenna pattern null forming and steering are very important in some critical wireless communication and radar applications, especially when used in modern digital beamforming adaptive array systems [1]-[4]. Traditionally, adaptive nulling is within a fairly narrow angle to reject a strong interfering source, at a specific azimuth direction. But in most applications, the interfering signals could be incident from many different directions. Due to increasing electromagnetic pollution of the environment, beamforming techniques that allow the placement of more than one null in the antenna pattern at specific jamming directions are becoming more important, [5]. Since a wideband jammer will appear to cover an angular sector of the pattern due to the frequency dependence of the antenna. Hence, the term *wide null* has been used, [6] and [7], to describe this suppression in the *SLL* of an angular sector.

Usually, the wide nulls produced should be deep and wide enough to accommodate frequency fluctuations and interference from mobile jammers. This is overcome in conventional techniques by placing two adjacent nulls in the radiation pattern [8].

In this study, a GA based on [9] is applied to adaptive wide null steering. The GA operates directly on the complex weight of each element in the array without the need for additional elements or a change in the position of original ones. The approach is elaborated in the following text, with the assumption that the reader has sufficient background knowledge on the relevant antenna theories.

II. Problem Formulation

For an arbitrary array, the array factor can be expressed by the general function, AF:

$$AF(\theta, \phi) = \mathbf{w}^T \mathbf{S}(\theta, \phi) \qquad (1)$$

$$
\begin{aligned}
\mathbf{w} &= \{w_n\}^T, w_n \in C^n, \\
\mathbf{S} &= \{e^{jk\mathbf{r}_n \cdot \hat{a}_r}\}^T, \\
\mathbf{r}_n &= \hat{a}_x x_n + \hat{a}_y y_n + \hat{a}_z z_n, \\
\hat{a}_r &= \hat{a}_x \sin\theta \cos\phi + \hat{a}_y \sin\theta \sin\phi + \hat{a}_z \cos\theta
\end{aligned}
$$

where $\mathbf{w}$ is a column vector with the complex weighting coefficients, $\mathbf{w}$ is the generic steering column vector, C^n is the set or subset of all complex numbers, $\mathbf{r_n}$ is the element location vectors, $\hat{a}_n$ is unit vector of distance ray of spheric coordinate, and θ and ϕ are the elevation and azimuth angles, respectively.

The key part of adaptive digital beamforming is to find proper weighting coefficient vector $\mathbf{w}$ to achieve desired pattern shape, including sidelobe suppression and null formation, steering.

III. The Genetic Algorithm

Genetic Algorithm is a stochastic optimization technique based on the concepts of biologic genetics and natural selection. GAs feature a group of candidate solutions (population) on the response surface. The variables are represented as genes on a chromosome. The algorithm mimics Mother Nature's process to create children from the generation of parents. Through natural selection and the genetic operators, mutation and recombination, chromosomes with better fitness are found. The potential survival of the next generation depends on the "fitness" values associated with individuals. Thus, parents with good attributes should be preserved and survived to successive generations while poor fitness parents are destroyed.

The mathematics of this theorem were originally developed using the binary representation [10], although recent work [11] has now extended it to include integer and real number representations. Numerous comtemporary GA applications can be found in [12].

A. Encoding The Variables

Since, the steering vector $\mathbf{S}$, varies for different array configurations, this approach applies floating-point ge-

netic operations on complex array weighting vectors. Similar to [9], each chromosome is a vector of complex numbers and the length of the vector is equivalent to the number of array elements.

B. Initial Population of Random Individuals

An initial population of at least 100 random samples is generated. No inserton of any near solutions is performed, except the replacement of the weakest individual with a classic Chebyshev design of specified SLL for a linear array. For a circular array, a near-solution obtained through minimisation of mean square error [13] is inserted instead.

C. Mating Scheme

After fitness evaluation, the kth generation, of a G_k population of P number of individuals is sorted in a descending order of fitness. Arithmetical crossover is performed [13], where two parents produce two children. Using a modified *Emperor-Selective (EMS)* selection scheme from [9], the best individual in G_k gets to mate with every other even sample in the population.

D. Steady-State Replacement

The *cPop* children population so produced is ranked according to their fitness, and allowed to compete with G_k to form *tPop*1 of P individuals.

Meanwhile, a non-uniform multi-modal mutation operator is applied to two subpopulations. Firstly, a mutant population *mPop*1 is created from $X(X \le P)$ mutants of the fittest individual. Then, every individual of the original population G_k, is mutated based a user-defined mutation probability P_m, to give *mPop*2, the second subpopulation.

Since, most of the fitter individuals from *mPop*1 and *mPop*2 may be the mutated versions of the current best sample. In a fixed size population, too many of the above will increase the selective pressure in favour of the best individual or local maxima, resulting in a loss of diversity. Thus, unlike [9], only the best $Y(Y \le P)$ individuals from *mPop*1 and *mPop*2 are selected to produce *tPop*2, the population of best individuals produced through unary transformation.

Finally, the new population of P individuals that form the next generation G_{k+1} are those from the best of *tPop*1 and *tPop*2.

E. Quarantined Subpopulation

To ensure implicit parallelism, $R\%$ of the population determined by a user-defined Rejuvenation Ratio, is earmarked for replacement by randomly generated samples. This is carried out whenever the the fitness difference, D, between the fittest and weakest individuals of the sub-population, is below a user-specified Trigger Level, T, the user-specified minimum fitness difference.

The randomly generated **junior** population of $R * P$ individuals is seeded with the same near-solutions as the original population. In addition, it is allowed to grow or "be groomed" on its own for the next predefined Z number of generations before it can interact with the **senior** population. This "Auto-Grooming" technique has so far yielded better results than pure restarts of the GA.

F. Ideal Beam Pattern

A template, formed by the shape of the main lobe, the specified SLL and prescribed nulls, is casted over the array pattern produced by each candidate, to compute their cumulative difference, shown in Fig. 1, as a form of fitness measure in dB. The ideal array pattern is one that conforms to the all the above specifications.

G. Termination Criteria

The maximum number of generations must be defined together with the desired fitness level. By satisfying either one of the above criteria, the GA will terminate. A log file of the GA progress in terms of the increasing fitness per generation, and the matrix containing the chromosomes of the current population are saved onto the hard disk. By reviewing the above data, it is possible to improve the performance of the GA through fine-tuning the Gaussian distribution of mutational changes or by introducing new heuristic marriage routines. The decreasing cumulative error of each generation in dB can be extracted from the fitness log.

H. Convergence Observation

The best sample of each generation may be produced through linear crossover after EMS selection or from a mutated individual. Usually, the offsprings of fit individuals from the previous generation show greater fitness, in the beginning of a GA run. However, when approaching convergence, the mutation operation may tend to produce better individuals.

IV. Simulation Results

In this section, two examples are presented to show the effectiveness of the approach.

A. Linear Array Pattern Wide Nulling

A classic Chebyshev linear array design of a specific SLL is used as a reference. In simulation, the array consists of 32 identical dipoles, each spaced at half a wavelength apart.

For this linear array of N identical elements, the steering vector is

$$\mathbf{S}(\phi) = \{e^{jkd*(n-\frac{(N+1)}{2})*(\cos\phi - \cos\phi_m)}\}, \qquad (2)$$

where ϕ_m is the main beam pointing direction, and ϕ is the azimuth angle, provided the elevation is fixed at $90°$. Thus, the same set of optimum weights for the

main beam at broadside can be used for other directions, if the above S vector is recalculated for the new beam pointing direction.

In the following, the number of generations for GA to arrive at a particular beam pattern are averaged from a total of 20 runs. The dot-dash lines in each subsequent figure depict the template casted for that particular case.

Fig. 2(a) depicts an example with a *SLL* of −30 dB and a wide null of −50 dB stretching from 20 to 40 degrees azimuth. In this instance, the main beam retains the same shape, half-power beamwidth and *SLL* are from Chebyshev design. The beam is later steered to extend from 30 to 50 degrees and 50 to 70 degrees, respectively, while maintaining the prescribed specifications as mentioned above.

B. Circular Array Pattern Wide Nulling

A near-solution obtained through minimization of mean square error technique [?] is inserted into the initial population. Similarly, in simulation the circular array consists of 32 identical dipoles, each spaced at half a wavelength apart along the circumference.

For this circular array of N identical elements, the steering vector is

$$\mathbf{S}(\phi) = \{e^{jka*(\cos(\phi-\phi_n)-\cos(\phi_m-\phi_n))}\}, \qquad (3)$$

where $ka = N/2$ and $\phi_n = \frac{(2\pi n)}{N}$. The ϕ_m is the main beam pointing direction, and ϕ is the azimuth angle, provided the elevation is fixed at 90°. Once again, the same set of optimum weights for the main beam at a particular direction can be used for other directions, if the above S vector is recalculated for the new beam pointing direction.

Fig. 3(a)-(c) show the adaptive null beamforming with variable null width and depth of the circular array with a *SLL* of −25 dB. It shows the the flexibility of this simple approach by merely casting a different template for candidate evaluation. Thus, the example has proven that this GA approach can be applied to any arbitrary array configuration.

V. Conclusions

A genetic algorithm is proposed for the independent wide nulling of linear and circular arrays, while maintaining as much of the original sidelobe level as possible. The null steering is kept independent of the main beam steering and it has shown that the GA can be applied to any arbitrary array.

By imposing an ideal template over the candidate patterns, multiple wide nulls of varying widths and depths are realized through altering the complex weights of the array elements. However, wider widths, deeper sidelobe suppression or more wide nulls, would come at a price of higher *SLL*.

Though, direct real-time processing is not possible, the weighting vectors for different interference scenarios can be precomputed and stored in a look-up table in the beamforming computer. So that once the sidelobe to be canceled has been determined, the appropriate weighting vector can be issued immediately in real-time without delays due to matrix operations or iterations.

References

[1] Special Issue on adaptive antennas, *IEEE Trans. Antennas Propagat.*, vol. AP-24, 1976.

[2] H. Steyskal, "Simple method for pattern nulling by phase perturbation," *IEEE Trans. Antennas Propagat.*, vol. AP-31, pp. 163-166, Jan. 1983.

[3] T.B. Vu, "Method of null steering without using phase-shifters," *Inst. Elec. Eng. Proc.*, vol. 131, pt. H, no. 4. Aug. 1984.

[4] J. E. Hudson, *Adaptive Array Principles*, Chippenham, Wiltshire: Antony Rowe Ltd, 1989.

[5] K. A. Al-Mashouq, I. El-Azhary, M. S. Afifi, A. S. Al-Ruwais, and P. S. Excell, "Multiple nulls formation and low interference of future arrays for small earth stations," *Proc. ARABSAT Symp.*, King Saud Univ., Riyadh, Saudi Arabia, pp. 434-443, 1987.

[6] El-Azhary, M. S. Afifi and P. S. Excell, "Fast cancellation of sidelobes in the pattern of a uniformly excited array using external elements," *IEEE Trans. Antennas Propagat.*, vol. 38, no. 12, Dec. 1990.

[7] Tie Gao, Yanchang Guo and Jianxin Li. "Wide null and low sidelobe pattern synthesis for phased array antennas," *Proceedings of Asia-Pacific Microwave Conference*, vol.1, pp.42-45, 1993.

[8] P. Owen and J.C. Mason, "The use of linear programming in the design of antenna patterns with prescribed nulls and other constraints," *Int. J. Comput. Math. Elec. Electron. Eng.*, vol. 3, no. 4, pp. 201-215, 1984.

[9] B. K. Yeo and Y. Lu, "Array failure correction with a genetic algorithm", *IEEE Trans. Antennas Propagat.*, vol. 47, pp. 823-828, May. 1999.

[10] J. H. Holland, *Adaptation in Natural and Artificial Systems*, Ann Arbor: The University of Michigan Press, 1975.

[11] D. Whitley, *Foundations of Genetic Algorithms II*, San Mateo, CA: Morgan Kaufmann Publishers, 1993.

[12] Lance Chambers, *Practical Handbook of Genetic Algorithms : Applications*, CRC Press, vol.1, pp45-46, 1995.

[13] K. K. Yan and Y. Lu, "Sidelobe reduction in array pattern synthesis using genetic algorithm," *IEEE Trans. Antennas Propag.*, vol. 45, pp.1117-1121, Jul 1997.
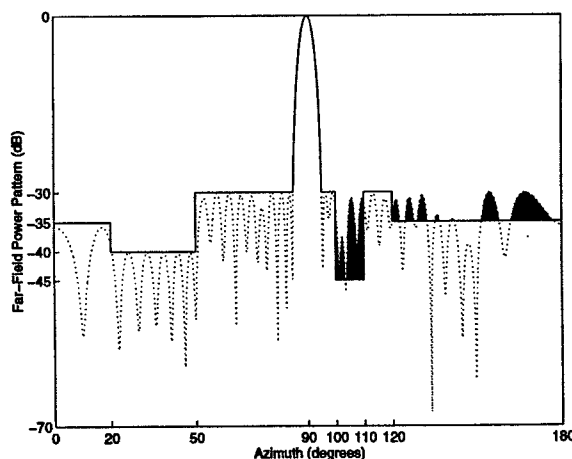
Fig. 1. The ideal template casted over an individual for a multiple null steering operation.
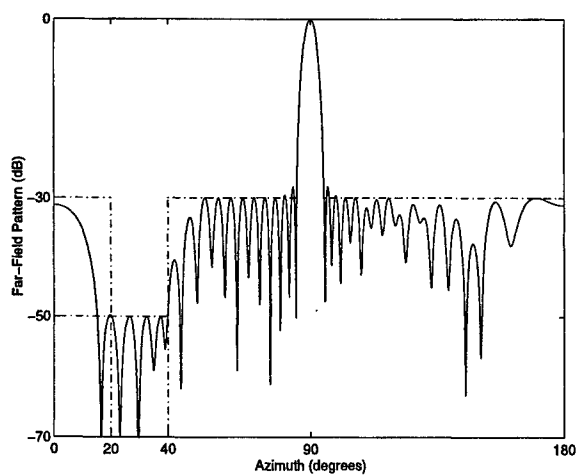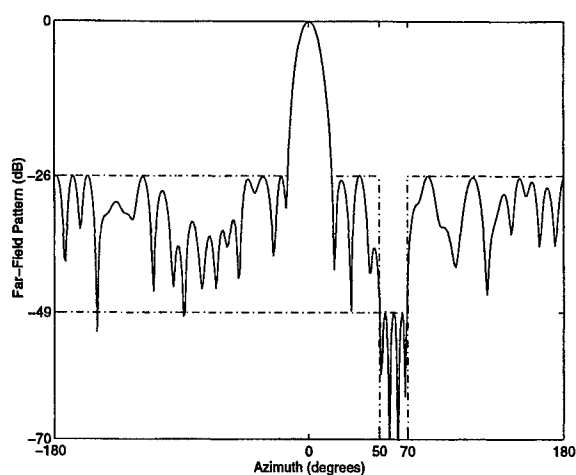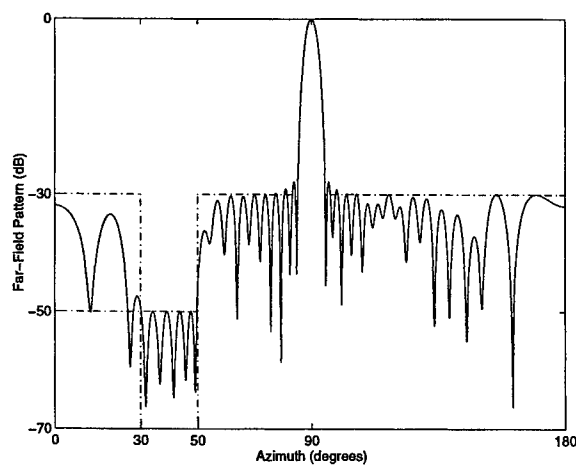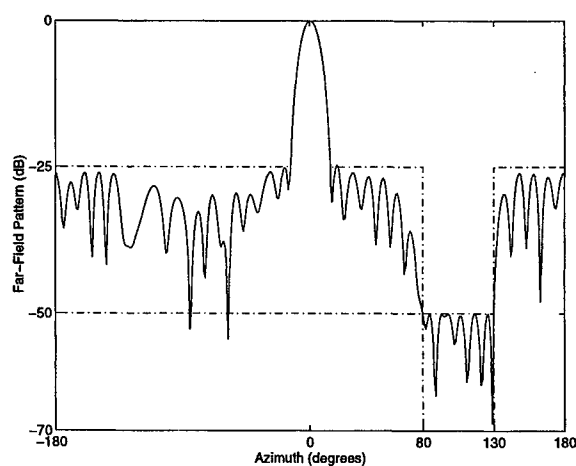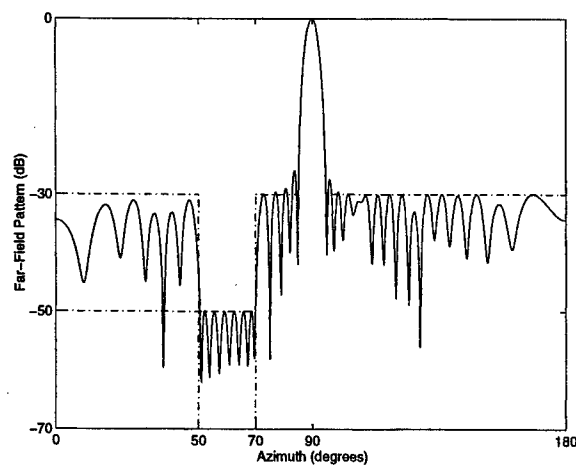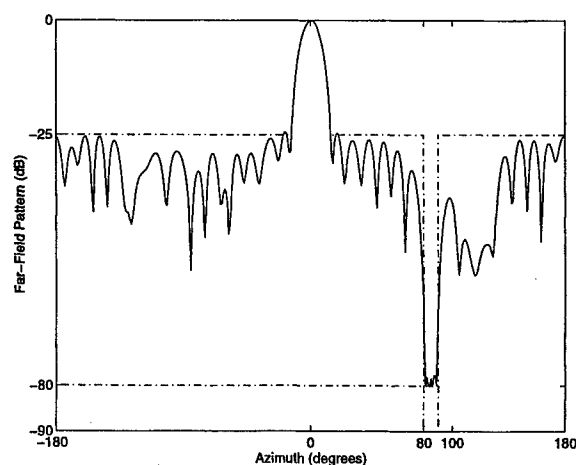
Fig. 2. Wide null of 20 degree width and 20 dB depth with respect to *SLL* being adaptively steered from azimuth, (a) 20 to 40 degrees, (b) 30 to 50 degrees and (c) 50 to 70 degrees.

Fig. 3. Beamforming and steering of null with variable width and depth for a circular array of 32 dipole elements, (a) −49 dB from 50 to 70 degrees to (b) −50 dB from 80 to 130 degrees (c) −77.75 dB from 80 to 90 degrees

SPATIAL BEAMFORMER WEIGHTING SETS FOR CIRCULAR ARRAY STAP

Kathleen L. Virga* and Hongbin Zhang
Department of Electrical and Computer Engineering
University of Arizona, Tucson AZ 85721-0104

I. Introduction. An experimental, circular, electronically scanned array is being fabricated by Raytheon as part of the Office of Naval Research sponsored UHF Electronically Scanned Array (UESA) program. Space-Time Adaptive Processing (STAP) techniques applied to circular arrays are of particular interest on this project. STAP refers to adaptive nulling techniques in the angle-Doppler domain to place nulls in the direction of clutter or jammers [1]. All forms of adaptive processing follow the flow of Fig. 1, and perform best when the interference is statistically stationary [2]. Traditionally STAP techniques have been applied to linear arrays and, until recently much less attention has been directed at employing STAP techniques for circular arrays. In this paper we explore the spatial beamformer weights (or antenna distribution) that form an interference-free pattern in the presence of multiple jammers for circular arrays of directional elements. The goal is to create patterns that have high directivity, low sidelobes, yet multiple nulls in specified angular directions. This information may be used in pre- or post- processing algorithms by providing information of the spatial beamformer weights between an optimum linear STAP processor and a circular array.

II. Array Geometry and Synthesis Procedure. The UESA array uses 60 directional elements arranged in a circular configuration. Each element is directed so that its maximum radiation is in the outward radial direction. In these simulations, a sector of the 60 elements are used to transmit and receive at any one time. An array radius of 5.48λ is assumed. The array function for this array is

$$\vec{E}(\theta,\phi) = \sum_{n=1}^{N} I_n \vec{f}_n(\theta,\phi) e^{j2\pi \cdot 5.48\cos(\phi - n\Delta\phi)} \tag{1}$$

where N is the number of "on" elements, $\vec{f}_n(\theta,\phi)$ is the element pattern of the nth element at the observation angle ϕ. I_n is the complex excitation of the nth array element and in this case $\Delta\phi = 6°$. The element patterns used in these simulations are shown in Fig. 2. Simulations using a cosine element factor or a Vivalidi element factor were conducted. A uniform phase pattern is assumed. Arrays with 16, 20, and 26 elements, which correspond to sector sizes of 96°, 120° and 156°, respectively, were considered.

To obtain the set of I_n's that make up the optimal beamformer weighting vector, **g**, for the interference-free signal a design program based upon Genetic Algorithm (GA) optimization was developed [3]. The GA cost function maximizes the patttern directivity and allows for the user to specify a peak sidelobe level. This design algorithm allows computed or measured element pattern data as part of the pattern function. This is an important feature for the synthesis of circular arc arrays of directional elements, since the element factor of each element must be included under the summation given in (1). The apparent element factor changes per element and observation angle, since each element is pointed so that the maximum of its element factor is pointed radially outward. Also, a particular element's pattern may not contribute to the overall array pattern for large observation angles, since the element may be blocked by the array curvature and electronics. Figs. 3 and 4 compare the results of two different simulations that

optimize the pattern for maximum directivity for a UESA array with 16 elements. Fig. 3a uses a cosine element pattern and Fig. 3b uses the Vivalidi element pattern. Fig. 3 shows that the patterns using the cosine element factor are smoother than the patterns using the Vivalidi element. Fig. 4a shows that the optimum amplitude distribution depends upon the particular element factor used. The GA optimization using the cosine element factor converges to a uniform amplitude distribution, while the optimization with the Vivaldi element factor does not. Fig. 4b shows that both simulations converge to a co-phasal phase distribution. This is not surprising as the phase of the element patterns in both cases were assumed to be uniform.

The flow diagram of the process that implements spatial nulling is given in Fig. 1. In this process, the optimal beamformer weighting vector, **g**, of the interference free signal is determined by the GA synthesis. The spatial covariance matrix of the observed signal vector is given by **R**, where **R** is computed by taking the expected value of the complex conjugate of the observed signal, x(t) multiplied by the transpose of x(t). The observed signal includes information about the desired signal, the interference due to jammers, and the circular array geometry. From signal detection theory, the optimum weighting vector (or optimum filter) for an interference free signal is computed by $\mathbf{w}=\mathbf{R}^{-1}\mathbf{g}$ [1]. The resulting vector, **w**, contains the new beamformer weights that when applied to the circular array gives a pattern with high directivity, low sidelobes, and nulls that are located at the angles corresponding to the jammer locations.

III. Results. This process has been applied to several different types of circular arrays and has shown good performance. Cases with 3, 7, 9, and 11 jammers were considered. In some cases, the jammers were located very close to one another, in order to test the feasibility of the algorithm to null out all the jammers. Fig. 5 shows the GA optimized pattern of the UESA array with 20 Vivaldi elements. In this case, the cost function was specified to maximize boresight directivity with a 25dB peak sidelobe level. Fig. 6 shows the GA optimized amplitude distribution for this pattern case as well as the cases for a cost function specified to only maximize directivity and a cost function to maximize directivity with a 20dB peak sidelobe level. The GA optimized phase distribution for each case is co-phasal. Fig. 7 shows the resulting patterns after applying the optimal filtering process. Fig. 7a shows a case with 7 jammers and Fig. 7b shows a case with 9 jammers. The circles on the horizontal axis indicate the angular location of the jammers. Fig. 8 shows the resulting beamformer weighting function, **w**, for these cases as well as the non-jammer (GA) and other jammer cases. These results show that the process works well to produce highly directive, low sidelobe patterns with multiple spatial nulls. This process is more desirable than a process that only uses the GA algorithm to directly compute the patterns with multiple spatial nulls. A direct GA process would be overall more time consuming at computing the beamformer weights for several pattern cases when only the position and number of jammers is changed.

[1] J. Ward., "Space-time adaptive processing for airborne radar," MIT Lincoln Laboratory technical report 1015, Dec. 1994.

[2] M. Zatman, "Circular array STAP," 1999 IEEE Radar Conference, Boston, MA

[3] C. W. Brann and K. L. Virga, "Generation of Optimal Distribution Sets for Single-Ring Cylindrical Arc Arrays", *1998 IEEE Antennas & Propag,Symposium Digest*, pp. 732-735.
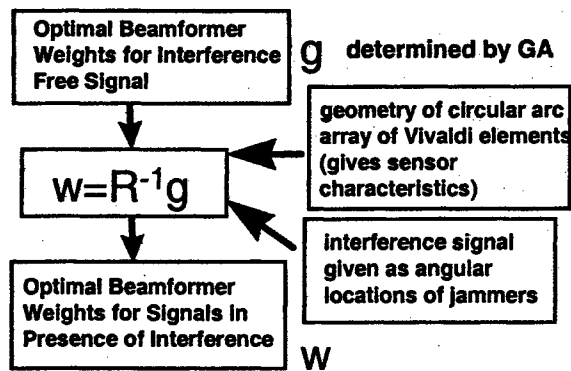
Fig. 1 Adaptive processing flow diagram
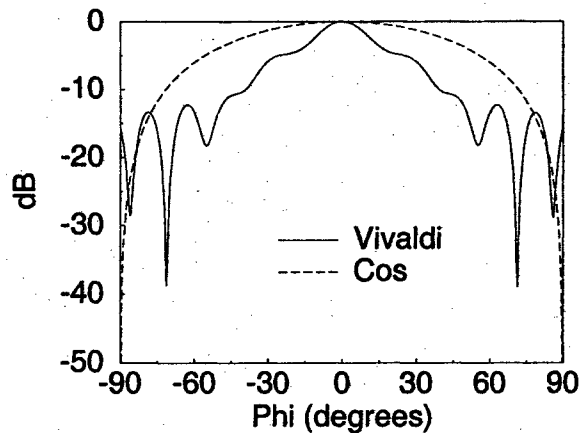
Fig. 2 Element factor patterns. Element pattern maximum at 0 degrees.
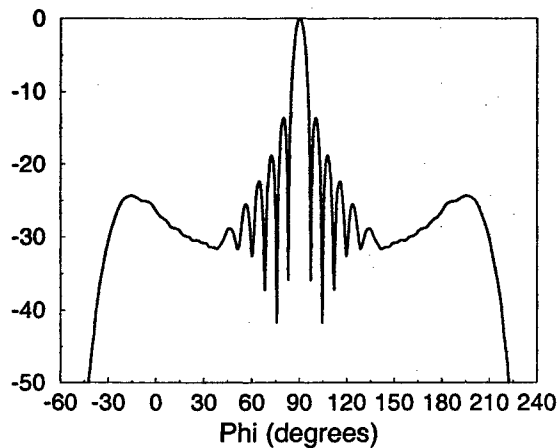
a) Cosine element factor
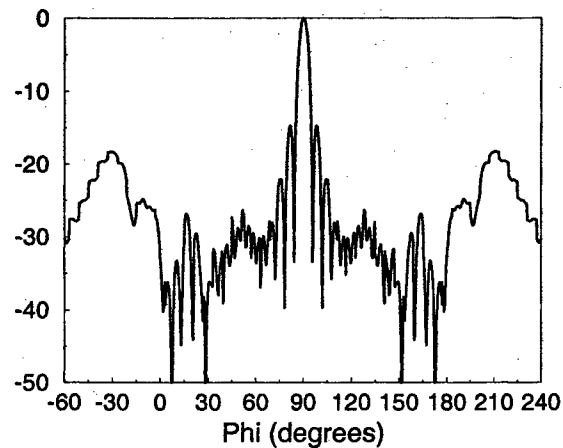
b) Vivaldi element factor

Fig. 3 Optimized patterns for 16 element UESA array (optimized for maximum directivity). Array boresight at 90 degrees.
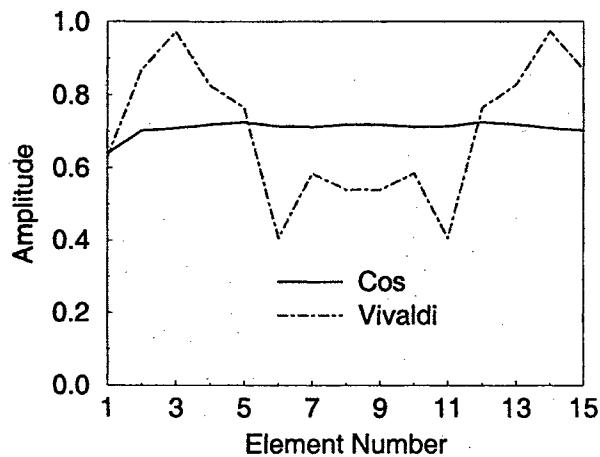
a) Amplitude distribution
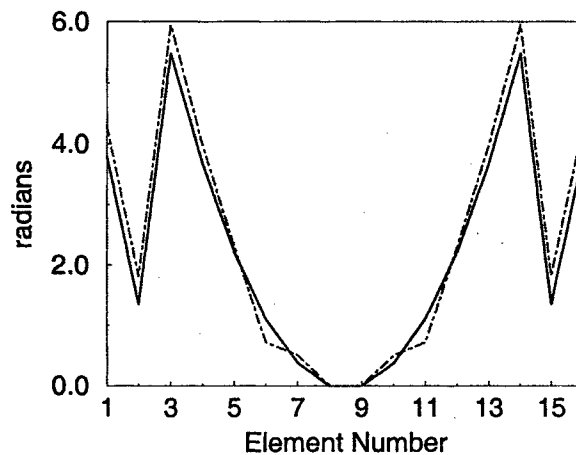
b) Phase distribution

Fig. 4 Distributions for array patterns shown in Fig. 3
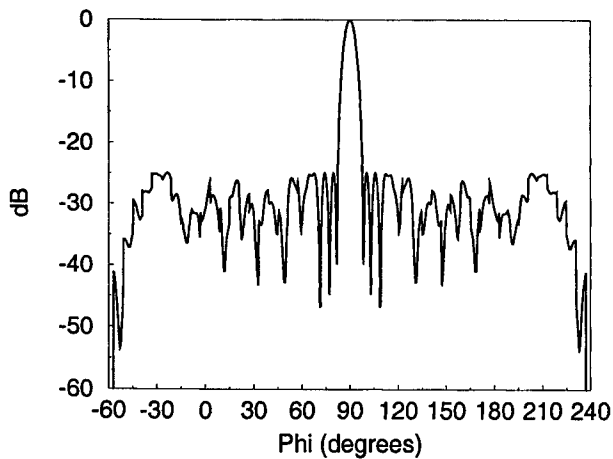
Fig. 5 Pattern for 20 element UESA array
(optimized for max. directivity & 25dB sidelobes)
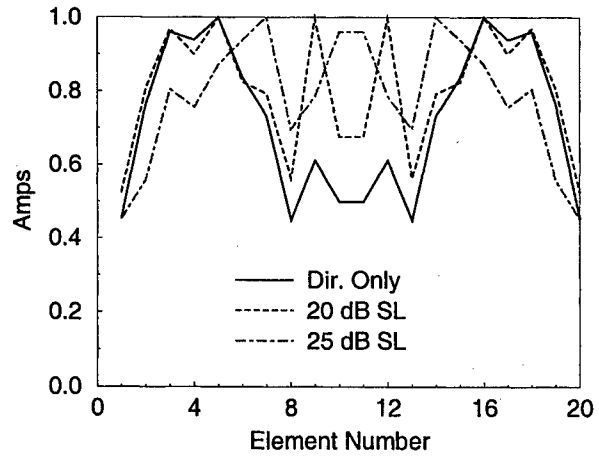
Fig. 6 Amplitude distributions for
20 element UESA array
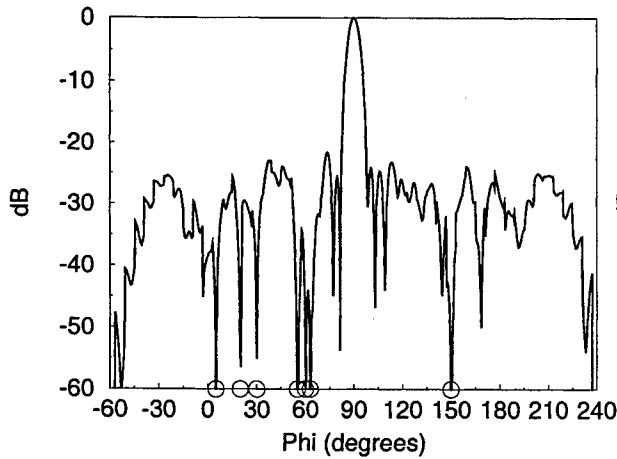
a) 7 jammers
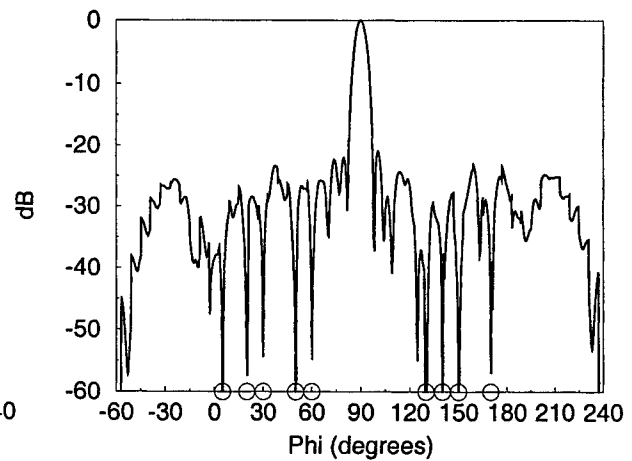
b) 9 jammers

Fig. 7 Patterns of 20 element UESA array in presence of jammers after applying optimum filtering process in Fig. 1. Original interference-free signal optimized for max. directivity & 25dB sidelobes.
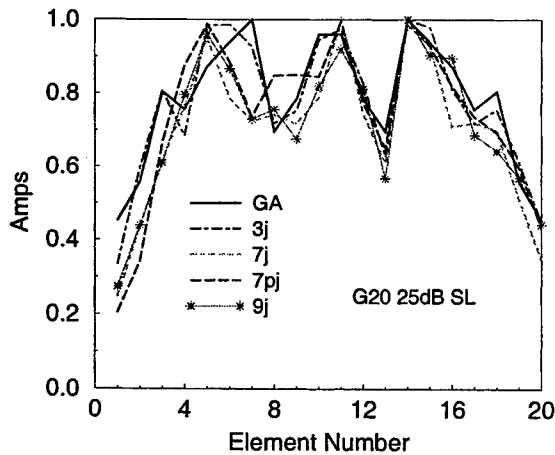
a) Amplitude
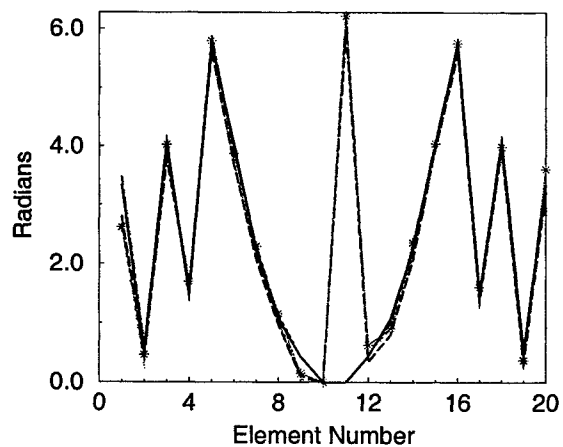
b) Phase

Fig. 8 Optimal beamformer weights for 20 element UESA array in presence of jammers after applying optimum filtering process in Fig. 1. Original interference-free signal optimized for max. directivity and 25 dB sidelobes.

Short Course Summaries

Phased Array Antenna Measurements

Dr. Donald G. Bodnar — MI Technologies

Course Description

This short course is designed for engineers, scientists, managers, and technicians who need to understand the principles of the various state-of-the-art antenna measurement techniques in use today for phased array antennas. The course covers far-field range, anechoic chamber, compact range, and near-field range measurement techniques. Measured results are used to demonstrate each technique. The course emphasizes concepts, procedures, and applications while detailed mathematical treatments are minimized. Data collection time, calibration and high power testing are covered.

Instructor Biography

Donald Bodnar is the Director of Business Development for Microwave Instrumentation Technologies, LLC. He joined MI Technologies from the United States Air Force Research Laboratory (AFRL), Dayton, OH, where he served as Chief Scientist, Sensors Directorate. Prior to his service at Dayton, he was Chief Scientist of the United States Air Force Rome Laboratory Rome, NY. He joined the Air Force from the Georgia Institute of Technology, Atlanta, GA, where he held positions including Chief Scientist of the Microwave & Antenna Technology Laboratory and Interim Director of the Advanced Technology Laboratory. His technical specialty is antennas, especially scanning reflector antennas and the polarization characterization of antennas using both theoretical and experimental methods. He has performed near-field and far-field antenna and RCS measurements using compact, near-zone and far-zone measurement techniques. Dr. Bodnar has taught graduate and undergraduate courses at the Georgia Institute of Technology in antennas, electromagnetic theory, materials, and computer programming, and he teaches in several antenna short courses. He is a Fellow of the IEEE, a past President and a past Vice President of the IEEE Antennas and Propagation Society, past Chairman of the IEEE Antenna Standards Committee, and is the author or co-author of over 100 publications. Dr. Bodnar holds a doctorate degree and a bachelor's degree in electrical engineering from the Georgia Institute of Technology and a master's degree in electrical engineering from the Massachusetts Institute of Technology.

Antenna Arrays for Wireless Communications

Prof. R. Janaswamy — Naval Posgraduate School

Course Description

In this half-day short course we will discuss the principles and applications of antenna arrays used in the wireless communications area. Topics will include small scale fading of signals, coherence time, coherence bandwidth, transmit/receive spatial diversity, max-ratio/equal-gain/selection combining techniques, adaptive antennas, angular spread of arrival, spatial correlation, array spacing, effect of element mutual coupling, capacity improvement, implementation issues, etc.

Instructor Biography

Ramakrishna Janaswamy earned his Ph.D. degree in electrical engineering in 1986 from the University of Massachusetts, Amherst. From August 1986 to May 1987, he was an Assistant Professor of electrical engineering at Wilkes University, Wilkes Barre, PA. In September 1987 he joined the Department of Electrical and Computer Engineering, Naval Postgraduate School, Monterey, CA, where is currently an Associate Professor. His research interests are in the general area of antennas and radiowave propagation prediction techniques.

Dr. Janaswamy was the recipient of the IEEE R. W. P. King Prize Paper Award of the Transactions on Antennas and Propagation in 1995. He also received a Certificate of Recognition for Research Contributions in 1995 from ONR/ASEE and a Certificate of Recognition for Outstanding Research in 1991 from the Naval Postgraduate School, Monterey, CA. He he is a Senior Member of IEEE and member of USNC/URSI, Commissions B and F.

All You Ever Wanted to Know About Practical Phased-Array Systems—But Were Afraid to Ask

Dr. Eli Brookner — Raytheon

Course Description

This tutorial is based on the book entitled *Practical Phased Array Antenna Systems*, edited by Dr. Brookner. The tutorial and book will provide an ideal introduction to principles of phased array antenna design. With an explicitly tutorial approach, the book offers a concise, introductory-level survey of the fundamentals without dwelling on extensive mathematical derivations or abstruse theory. Its presentation focuses on step-by-step design procedures and provides practical results using extensive curves, tables and illustrative examples. The course notes will update the book relative to recent development and future trends in phased-array systems.

Instructor Biography

Dr. Brookner is a Consulting Scientist at Raytheon Company where he has worked on the COBRA DANE, PAVEPAWS, BMEWS, COBRA JUDY, GBR, ASTOR, Space-Based Radar and next generation IRIDIUM phased array programs, among others. He has published four books, the most recent being *Tracking and Kalman Filtering Made Easy*, (John Wiley & Sons, Inc., 1998). He has taught his radar course to over 8,000 around the world. He is a fellow of the IEEE and AIAA

Design and Applications of Printed Array Antennas

Dr. John Huang — JPL

Course Description

This course offers special insight into practical design techniques for printed array antennas. Design procedures and guidelines will be presented. Topics such as single-element design, radiation mechanism, array configurations, microstrip power divider design, parallel/series feeds, bandwidth enhancement, multilayer design with aperture coupling, fabrication procedures, etc. will be discussed. The emerging technologies of microstrip reflectarray and inflatable/thin-membrane array and their design techniques will also be one of the topics. Sample cases of actual microstrip arrays at microwave and millimeter-wave frequencies with detailed dimensions will be given. This course is ideal for antenna designers, microwave engineers, system engineers, and non-specialists who wish to learn the basics of printed antennas.

Instructor Biography

Dr. John Huang received his Master degree in electrical engineering from the University of California, Berkeley and his Ph.D degree in electrical engineering from the Ohio State University. He had worked at the Naval Weapons Center, China Lake, California for six years, and is currently with the Jet Propulsion Laboratory since 1980. He has developed numerous mobile and satellite antennas which include phased arrays. He also has pioneered several innovative microstrip array configurations, received four U.S. patents, and received more than fifteen NASA certificates of recognition. He is currently developing inflatable phased arrays for space application. He is an IEEE Fellow and has published over 60 technical journal articles, conference papers, and book chapters. He has been invited as session chairperson and speaker in numerous international conferences. He has been invited several times to teach a short course on microstrip array design over the recent years.

A Holistic View of Arrays and the Emerging Opportunities for Signal Processing at Radio Frequencies

Dr. Nicholas Fourikis — Phased Array Systems

Course Description

Arrays performing the radar/EW, or communications functions as well as arrays dedicated to the derivation of radiometric images of celestial sources or of the Earth's surface have been treated in separate textbooks/treatises in the past. As all phased arrays share the same theory, we have adopted a holistic view of all phased arrays. Furthermore, we shall demonstrate that there is a continuum between radar arrays having short integration times and radiometric/radioastronomy arrays having longer integration times.

The approach taken enriches and deepens one's understanding of array systems and allows a designer imbued in one discipline to use the techniques/approaches developed by another discipline. Lastly, the integration of several diverse functions into one phased array is often required for the defense of a high value platform e.g. ship/aircraft or the efficient management/control of air traffic.

During the short course we shall consider current systems and their precursors as well as systems that are in the proposal/planning/developmental stages. While the first two sets of systems help the reader reconstruct the vector of evolution, the consideration of future systems provides the reader with a philosophy of minimum surprises.

Instructor Biography

Nicholas Fourikis, MSc, PhD, formerly with the Australian DoD and the Commonwealth Scientific and Industrial Organization, has published extensively in the fields of radar/radiometric array systems and radioastronomy. As Australian National Leader, he participated in several international defense committees coordinating R&D in radar phased arrays. Dr Fourikis is the sole author of two books: *Phased Array-Based Systems and Applications,* a John Wiley & Sons Publication, Feb. 1997; and *Advanced Arrays Systems and RF Technologies,* an Academic Press publication, due to appear in 2000. He is a senior member of the IEEE, has pioneered R&D work toward wideband multifunction arrays, and is the co-discoverer of five interstellar molecules.

AUTHOR INDEX

574

NOTES

NOTES